

nature

THE INTERNATIONAL WEEKLY JOURNAL OF SCIENCE



PLURIPOTENCY UNDER THE MICROSCOPE

A decade of iPS cells — what we've learned **PAGE 310**

MEDICINE

DRUG REDISCOVERY

*Mining the pharmaceutical
back catalogue*

PAGE 314

PUBLIC HEALTH

SUSTAINABLE SEAFOOD

*Fewer fish could spell
more nutrient deficiency*

PAGE 317

SCIENCE AT THE MOVIES

FOLLOWING NEMO

*Pixar's fabulous fish guy
on the cast of Finding Dory*

PAGE 325

NATURE.COM/NATURE

16 June 2016 £10

Vol. 534, No. 7607

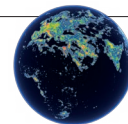


THIS WEEK

EDITORIALS

COMMUNICATION *Nature*
experiments with new
article summaries **p.296**

WORLD VIEW Map out a
future to tackle the
worst wildfires **p.297**



MILKY WAY Majesty of dark
heavens invisible to
many places **p.300**

Turning point

The result of next week's crucial UK referendum on whether or not to remain in the European Union will have worldwide repercussions.

The people of the United Kingdom will next week vote to either leave or remain in the European Union. At stake is not only the future of the United Kingdom and its place in the world, but also the future of Europe itself.

For science and research, the benefits that flow from being part of the EU are obvious. Free movement of people makes it easier for researchers in one EU state to live and work in others, which in turn promotes access to a plethora of multi-country collaborations. Belonging to the EU gives member states ready access to a huge pool of diverse scientific expertise and shared research facilities (see page 307).

The EU itself will spend more than €120 billion (US\$135 billion) between 2014 and 2020 on research, collaboration and innovation, including around €40 billion in beefing up scientific infrastructure in its poorer regions. Some €13 billion will go to one of the EU's greatest research successes, the highly competitive European Research Council, created in 2007 to award research grants to scientists of any nationality. Not surprisingly perhaps, a *Nature* survey in March showed that an overwhelming majority of UK researchers are in favour of remaining. Leading scientists from many disciplines have taken to the pages of newspapers and to the airwaves to plead the case for staying in the EU, making science a theme of the political campaign.

COOPERATION

The benefits of EU regulations to research and innovation in the life sciences were highlighted in a report published on 11 June by the UK House of Commons Science and Technology Committee. But it also noted shortcomings, for example in the translating of EU legislation into national laws. Some countries — Britain included — often implement national laws that go over and above that required by the EU (a practice known as gold-plating), resulting in variation between countries. The report also argued that the EU's application of the 'precautionary principle' in regulations needs to be more closely based on robust scientific evidence.

Scientists in Britain and elsewhere will have their own complaints about the way the EU works. But the UK referendum should not be a vote on whether or not the EU is perfect — how could it be? The question must be whether the unique system of cooperation that it represents does what it sets out to do.

It is *Nature's* view that when it comes to science and science-based regulation, the EU is much greater than the sum of its parts. Over time, it has replaced a maze of regulations and technical standards in its 28 member states — on everything from the life sciences to car parts — with common EU-wide regulations. Its environmental-protection laws are also widely recognized as world-leading.

Such cooperation has helped Europe to become the research and economic powerhouse that it is today. And the strength of UK science

has allowed Britain to have an outsized say in shaping EU research and regulations. Outside the EU, its influence would be greatly diminished.

Many of those who have been pushing for Britain to leave complain of diminished sovereignty. But in the modern globalized world, a willingness to pool aspects of sovereignty is the only way for a country such as the United Kingdom to have any strong say in shaping international rules, from financial regulation to air pollution. Climate change, the environment, use of natural resources, energy security and sustainable agriculture: all are examples of science-based issues on which Europe can be much more effective as a bloc than any mem-

***"It is time to
build a better,
stronger EU, not
tear it down."***

ber state alone — not to mention countering terrorism, or managing the potential threat of Russia on Europe's eastern flank. At a time when so many of Europe's most important challenges are increasingly regional and global, it is time to build a better, stronger EU,

not tear it down. The 'Brexit' camp insists that a split from the EU will allow Britain to make more of its own decisions. It might, but many of those decisions would carry much less weight.

It is difficult to get multiple nation states to agree to sacrifice some autonomy for what is in their collective interest. It requires hard work and, of course, often plodding negotiation and compromise. Britain undervalues that effort at its peril.

Built from the ruins of a Europe devastated by the Second World War, the EU has, despite its defects, woven together often-fractious, if not belligerent, nations into a bloc that has secured peace and democracy and has helped to build a Europe that has common values and rights. It has also managed to peacefully assimilate many former Soviet states under the democratic and societal obligations of the EU umbrella.

Continued engagement of the United Kingdom in the EU is vital, and its citizens bear a heavy responsibility on 23 June. So do the representatives on both sides of the debate, who have tended to stray into hyperbole and exaggeration. For example, a central claim of the 'Leave' campaign has been that a Brexit would free up £350 million (US\$500 million) a week that could be spent on the National Health Service and other public services. This is simply false. That figure is Britain's gross contribution to the EU; when the money Britain receives back is taken into account, it is less than £250 million a week. The reality is that the United Kingdom is in full control of the vast majority of its public spending; its net contribution to the EU budget was around £8.8 billion, or slightly more than 1% of its total public spending of £735 billion, in 2014–15. As the Confederation of British Industry concludes: "The UK's net budgetary contribution is a small net cost relative to the benefits."

We urge UK readers to critically examine the issues and to get out and vote — because every vote in this crucial election will matter. ■

Under the sea

If life in the oceans is to be preserved, people must get to know the wonders of the deep.

It was World Oceans Day last week, and the annual event highlighted once again just how poorly studied two-thirds of our planet's surface is. But this year's tag line, "Healthy Oceans, Healthy Planet", should remind us that we do know some things about the sea — notably, how much people depend on it.

Millions of people rely directly on food taken from ocean waters, and millions more depend on money from fishing, tourism and other marine activities. But across the world, these relationships are often undermined.

Nowhere is this more apparent right now than at the world's coral reefs. Bathed in warming waters, reefs everywhere are bleaching as the corals on them sicken and turn white. Many will die, and so will animals that live on them.

The outlook for corals is bleak, but it is not yet hopeless. Online this week, we publish one approach that could point to ways to rescue them from the brink (J. E. Cinner *et al. Nature* <http://dx.doi.org/10.1038/nature18607>; 2016). A huge analysis of data on fish found at more than 2,500 reefs identifies 15 'bright spots' — reefs in a better state than models suggest they should be — and then digs into the factors that might be responsible. Bright spots include unpopulated, unfished regions such as the Chagos islands, and areas that are close to towns and are fished, such as Kiribati and the Solomon Islands. The study also pinpoints 35 'dark spots' where conditions were surprisingly poor, such as Montego Bay in Jamaica and Lord Howe Island in the Tasman Sea between Australia and New Zealand.

The researchers used information on a reef's habitat, depth, nearby human population and amount of fishing to model how many fish could live at each site.

Such insights can help to steer conservation efforts. And conservation of coral reefs is a popular cause. More difficult is the protection and preservation of what lies deeper.

Although there is a huge public appetite for documentaries that detail the wonders found under the surface of our seas, to many people the oceans are a mysterious, even threatening, place. This feeling is reflected in — and doubtless enhanced by — the approach of storytellers. From storms and sharks to mystery and other-worldliness, the oceans are made to seem an unknown and unknowable place: it is never safe to go back in the water.

What we do know about life beneath the waves does sometimes make its way into the public consciousness. The 2003 animated film *Finding Nemo*, for example, delighted not just the public but also marine biologists, many of whom were impressed that the ocean they knew had been represented with such fidelity in how the animals moved and interacted (talking fish notwithstanding).

"To many people the oceans are a mysterious, even threatening place."

On page 325, we interview one of the people responsible for that accuracy: Adam Summers of the University of Washington in Friday Harbor. (He also worked on the sequel, *Finding Dory*, which lands this week.) Summers rightly points out that although filmmakers often need to bend or even break the truth to tell stories, facts can add something, too.

As a biomechanist, his contribution was both to supply general fish facts, such as insights about the whale-shark character, and to give precise feedback on how the animals could move realistically even when they were doing things that no marine animal could actually do. If you watch and are amazed by the octopus sequences in the film, you will see the result of imbuing teams of highly talented animators with the knowledge of professional scientists.

There are many marine researchers who reach out to the public and inspire a love of the sea by discussing their work. This should be applauded. But there are also many who only really talk to other ocean scientists about their work (a problem far from unique to the field).

If more landlubbers are to engage with the oceans, and understand and appreciate them as researchers do, then all involved must do more to emphasize more widely the wonders of the depths and the threats that face them.

Finding Nemo and *Finding Dory* may please scientists with their accuracy, but it would be a tragedy and a disaster if future generations had to watch them to find out what a coral reef looked like. ■

Nature distilled

We need your views on an experiment to convey the latest research in digestible form.

Since 1869, *Nature* has set itself two goals, which can be boiled down to presenting science and its implications to the public, and presenting them to professional researchers. Public outreach is important for science — it is the public that pays for most of it — and with much of our magazine content and the brief summaries of research papers made accessible to journalists in advance, much good science is available to them. But what of the professional researchers — how can *Nature* best present science to you?

Any journal that tries to publish the most important results that it is sent, in all fields of science, will run into the same problem. Every bit of our output, we hope, is useful and interesting to somebody somewhere. But even the most optimistic of our editors would concede that the pool of readership for each of these specific advances is only a small subsection of our audience, professional researchers included. To the outside world, science is science. To those who read *Nature*, science is a multiplicity of

specialisms — and specialists.

We know that most of you are specialists, and that you don't read most of what we present to you. You're busy people. It is hard enough to follow the literature that you need to read. Even the titles of research papers in an unfamiliar field can look incomprehensible. But if you're anything like us, one reason you got into science in the first place was curiosity about the world — and not just the tiny piece of it that you now focus on. Wouldn't it be useful and interesting to keep better track of the rest? Or at least, the rest that is published in *Nature*, and therefore already judged to be important?

We think so, and this week we begin an experiment to see how many of you agree. We have revisited 15 recently published *Nature* papers and asked the authors to produce two-page summaries of each. The summaries remain technical — these are not articles suitable for the popular press — but they try to communicate both the research advance and why it matters. The authors of these papers have been enthusiastic — they want the broadest possible readership — and we thank them for their cooperation. Now we want to know what you think. The first three summaries are published online this week (see go.nature.com/1uhcy3x). The rest will be released in the coming weeks. Please take a look. Be brave — pick a topic that you expect to struggle with — and then fill in the online survey to let us know what you think. ■



Science can map a solution to a fast-burning problem

Wildfires such as those that hit Canada last month are a growing worry, writes Marc-André Parisien, but risk-assessment models can limit future damage.

Rain has fallen on the explosive wildfire that ripped through the Fort McMurray region of Canada last month, but the inferno is likely to burn until the snow falls later in the year. The raging fire was a true force of nature. It sent out embers that skipped natural barriers such as the Athabasca River, hundreds of metres wide, and created its own weather system: pyrocumulus clouds that generated lightning, which ignited another fire some 30 kilometres away. The fire was unstoppable.

Unfortunately, the largest residential community in the Canadian boreal forest was in its way, and the resulting scenes of devastation drew attention from around the world. The fire is projected to be the costliest natural disaster in the nation's modern history. A repeat of last month's scenes is unacceptable, so what can be done? One thing is certain: there is now a tacit understanding among all Canadians that something must change.

Science has the tools to drive that change. Canada and other fire-prone regions should develop new maps of fire risk and use them to guide development and mitigation efforts. Similar maps are already produced around the world for areas prone to flooding and earthquakes, and it is unfortunate that so little has been done so far to measure wildfire risk. This is especially true across Canada, where hundreds of communities embed themselves in one of the most flammable places on Earth.

Wildfire spreads through a boreal forest with a speed and intensity not seen in other landscapes. But a fire's impact depends on factors that we can measure. With data on fire ignitions, weather, vegetation and topography, we can build models to demonstrate how we expect a region to burn should it catch fire. These can show two things that are important to guide policy: the probability of burning, and the likely fire intensity. The first shows the chances of a fire taking hold, and the second indicates how severe the consequences will be.

These maps show which areas, if they ignite, will burn at such a high temperature that attempts to fight the fire will never succeed. The only option is to evacuate, or not to live there in the first place. The maps can also identify parts of the forest where, because of the nature of the landscape and flora, fire would be easier to prevent and tackle. This knowledge can be used to allocate money and effort to places where mitigation is more likely to work.

A range of possible policies can minimize fire risk. Wood shingles used to build houses can be replaced by metal and asphalt; vents and gaps that can admit embers can be blocked; and flammable landscape can be reduced. Some houses burned down in Fort McMurray because homeowners had planted conifer trees and shrubs — a poor

choice, given that conifers burn much more readily than do deciduous trees in this part of the world. The surrounding forests can be managed too. Prescribed burning of vegetation and other measures can set up effective firebreaks.

This is not always easy or popular. I lived in one of these communities as a child. Many people make a conscious decision to live in the forest and don't want to see it altered. To fell trees and mandate the type of shrubbery they are allowed to plant can feel like a violation. But using fire-risk maps can sometimes show that the most effective intervention might be a few kilometres upstream of the prevailing wind. Fire management does not always require changes on people's doorsteps. Indeed, the recent blaze started as four separate fires — and it was the one that started the farthest from the town that caused the greatest damage.

After the Fort McMurray fire, our team at the Canadian Forest Service went back and produced fire-risk maps for the region. They, correctly, showed that a fire in the area was likely to take hold, and that when it did it would be unstoppable.

We need to set up a systematic framework to construct more of these maps. In Canada, this would demand a partnership between the federal government and provinces and municipalities that directly manage boreal wildlands. In other countries, similar partnerships could be formed to great benefit. We would also need to consult and engage with the people who live and work in the forest. It would not be cheap, but a Canada-wide framework to assess wildfire risk would still

be a fraction of the cost of a major fire incident. The good news is that we already have much of the data, as well as the tools and the expertise.

Continued human expansion into the Canadian boreal forest for natural-resource extraction and housing is inevitable. It is too late for Fort McMurray, but risk-assessment maps can guide this new development and direct it to low-risk areas. Some of these places are obvious: new settlements could take advantage of natural firebreaks such as large lakes to help shield them. Other preferable areas could be more surprising and would be identified only with the help of these maps; for example, landscape and vegetation in such areas might combine in unusual ways to reduce risk.

In a warmer and drier future climate, more fires are expected. We need to use our knowledge of boreal fire dynamics to find better ways to live and work safely in this hazardous environment. ■

Marc-André Parisien is a fire researcher with the Canadian Forest Service in Edmonton, Canada.
e-mail: marc-andre.parisien@canada.ca

SETTING UP A
NATIONWIDE
FRAMEWORK
WOULD BE A
FRACTION
OF THE COST OF
A MAJOR
INCIDENT.

RESEARCH HIGHLIGHTS

Selections from the
scientific literature

GENE EDITING

CRISPR blocks cancer growth

Knocking out genes in cancer genomes with the CRISPR–Cas9 technique decreases the ability of cancer cells to multiply.

William Hahn at the Dana Farber Cancer Institute in Boston, Aviad Tsherniak at the Broad Institute of Harvard and MIT in Cambridge — both in Massachusetts — and their colleagues silenced certain genes in 33 cancer-cell lines using CRISPR–Cas9, which can be programmed to snip DNA at specific locations. They found that in parts of the genome with multiple copies of a gene, the number of DNA breaks made by the CRISPR system was linked to a drop in cell proliferation, an outcome not seen with another gene-silencing tool called RNA interference. This effect could be the result of how CRISPR-made DNA cuts are repaired.

The results suggest that cancer cells are sensitive to site-specific DNA damage, and have implications for how experiments using CRISPR should be interpreted. Targeting genomic regions that have many repeated sequences could be a new therapeutic strategy, the authors suggest. *Cancer Discov.* <http://doi.org/bjzn> (2016)

ENERGY

Excess nitrogen spoils biofuels

Nitrogen fertilizer can boost the growth of crops for biofuel production, but applying too much can cut the climate benefits in half.

Ethanol fuel made from

plant cellulose is a promising form of renewable energy. Philip Robertson at Michigan State University in Hickory Corners and his colleagues applied various amounts of nitrogen fertilizer to experimental plots of switchgrass (*Panicum virgatum*) for three years. They measured emissions of the greenhouse gas nitrous oxide (N₂O) and the leaching of nitrate, a water pollutant. The authors found that fertilizer boosted yields in the first year, but that the increase declined with subsequent applications.

Levels of both emissions and leaching grew exponentially with increases in fertilizer.

The team suggests that minimizing fertilizer use will be crucial for maintaining the environmental benefits of cellulosic biofuel.

Environ. Res. Lett. 11, 064007 (2016)

NANOSCIENCE

Tiny carbon rods blow off steam

Nanometre-sized rods of carbon can expel water in puffs of vapour when the

of the creature that is not transparent — has fibre-like cells in a range of shapes that channel bioluminescence while leaking light at different rates.

The authors modelled how the light travels through the various cell shapes. They suggest that the squid could activate different populations of cells to vary the intensity and distribution of the light passing through them, allowing the animal to camouflage itself at any depth.

J. R. Soc. Interface 13, 20160230 (2016)



BIOPHYSICS

How squid hide their eyes

A transparent squid may camouflage itself by activating specialized cells in its eyes.

Many marine creatures emit light to hide shadows that might be seen by predators below. To find out how animals control this bioluminescence, Amanda Holt and Alison Sweeney at the University of Pennsylvania in Philadelphia used transmission electron microscopy to study the eyes of the squid *Galiteuthis* (pictured). They found that the underside of the eye — one of the few parts

air is already humid.

Materials such as carbon and silica gels typically pick up moisture as humidity increases. But Satish Nune and his colleagues at the Pacific Northwest National Laboratory in Richland, Washington, found that their carbon-based nanorods take up water at low humidity and then give off about half of it when the relative humidity exceeds 50–80%. The team thinks that water condenses between adjacent rods and then capillary forces draw the rods together until the water bursts from the ends of the

MBARI

rods and evaporates.
Nature Nanotechnol. <http://dx.doi.org/10.1038/nnano.2016.91> (2016)

EVOLUTION

Fish keep coming out of water

Fish have evolved to live on land multiple times, suggesting that the crucial transition from water to land during the evolution of terrestrial life may not have been unusual.

Terry Ord and Georgina Cooke at the University of New South Wales in Kensington, Australia, looked at data on the behaviour and ecology of living fish and identified 33 different families that include amphibious species, some of which seldom leave the land. In one family, the blenny fish (Blenniidae), amphibious lifestyles evolved 3–7 times. The duo observed one primarily aquatic species of blenny (*Praealticus labrovittas*) emerging onto land on warm days on the western Pacific island of Guam.

The ability to survive on land could help fish to cope with the low oxygen levels of warm seawater, and prevent them getting stuck in tidal pools, the authors propose.
Evolution <http://doi.org/bjzq> (2016)

MICROBIOLOGY

A wealth of anti-CRISPR proteins

Proteins that inhibit the activity of the CRISPR–Cas bacterial defence system could be widespread.

Viruses and other microbes often successfully transfer genes to bacteria, despite the presence of the bacterial CRISPR–Cas system, which recognizes and attacks foreign DNA or RNA. Karen Maxwell and Alan Davidson at the University of Toronto in Canada and their colleagues had previously described nine families of

anti-CRISPR protein that help certain viruses to infect *Pseudomonas* bacteria. Now, using bioinformatics, the team has identified five more anti-CRISPR protein families in a range of microorganisms that inhibit CRISPR–Cas systems in *Pseudomonas aeruginosa* and *Pectobacterium atrosepticum*.

Anti-CRISPR proteins could have an important role in gene transfer between bacteria, including the spread of genes involved in antibiotic resistance, the authors say.

Nature Microbiol. <http://dx.doi.org/10.1038/nmicrobiol.2016.85> (2016)

BIOMATERIALS

Liquid-like solid lets cells grow

A scaffold made of tightly packed hydrogel particles allows cultured cells to grow in custom 3D configurations.

Developed by Thomas Angelini and his colleagues at the University of Florida in Gainesville, the scaffold is made of a liquid-like solid material that temporarily becomes fluid when force is applied, and rapidly solidifies after the force is removed. Angelini's team 3D-printed clusters of various types of cell inside the liquid-like solid, creating multicellular structures in the shape of a sphere, a loop and a simple flower (pictured).

In contrast to other, stiffer scaffolds used for 3D cell



culture, this one is not easily damaged when cells are injected into it, and does not need to be broken down by enzymes to allow cells to grow and migrate.

ACS Biomater. Sci. Eng. <http://doi.org/bjzp> (2016)

NEUROSCIENCE

Myelin clogs up immune cells

The insulating layer around nerve fibres breaks down as mice age, and this could lead to immune dysfunction.

The myelin layer coats nerves to speed up signal transmission. Mikael Simons at the Max Planck Institute for Experimental Medicine in Göttingen, Germany, and his colleagues used electron microscopy to study the brains of mice. They found that the amount of myelin fragments increased with age and that the pieces were taken up by immune cells in the brain called microglia, which engulf debris and foreign materials. During this process, insoluble fatty aggregates accumulated in the microglia and the ability of the cells to take up material declined.

The authors suggest that microglia become overwhelmed with the growing amount of myelin debris, making them less able to function in the ageing brain.

Nature Neurosci. <http://dx.doi.org/10.1038/nn.4325> (2016)

DEVELOPMENTAL BIOLOGY

Dragon lizard gets sex change

A shift in egg-incubation temperature can result in a genetically male lizard having a mix of male and female traits.

The sex of some reptile species is determined by genetics, but in others it depends on egg-incubation temperature. Richard Shine at the University of Sydney in Australia and his colleagues studied hatchlings and juveniles of the central bearded dragon (*Pogona vitticeps*; male pictured). In this species, sex is normally controlled genetically, but incubation temperatures of 32°C and above can produce sex-reversed females from male embryos. The team incubated eggs at constant temperatures between 26°C and 34°C, and found that although sex-reversed females are capable of laying eggs — and even produce more eggs than genetic females — they are similar to males in their morphology and behaviour.

This mix of traits could enhance fitness under certain conditions, which could cause a rapid elimination of sex-determination genes, the authors say.

Proc. R. Soc. B 283, 20160217 (2016)

➔ **NATURE.COM**

For the latest research published by Nature visit:

www.nature.com/latestresearch

SEVEN DAYS

The news in brief

EVENTS

Nobel support

As the British people prepare for a 23 June vote on whether to leave or remain in the European Union, 13 Nobel laureates have lent their support to staying in. In a letter published on 10 June in the newspaper *The Daily Telegraph*, the laureates, including physicist Peter Higgs and geneticist Paul Nurse, warned that UK science would suffer in the event of a 'Brexit'. "Science thrives on permeability of ideas and people, and flourishes in environments that pool intelligence, minimise barriers, and are open to free exchange and collaboration," they argue, stressing that the EU provides just that environment. See page 307 for more.

Cyberattack

The University of Calgary in Canada said on 7 June that it had paid a ransom worth Can\$20,000 (US\$15,600) in untraceable Bitcoins to hackers who had encrypted much of the university's past 50 years of research data. A spokeswoman

STANDING UP FOR SCIENCE

Nominations are invited for the John Maddox Prize, which rewards an individual in any country who has promoted sound science and evidence on a matter of public interest. The £2,000 (US\$3,000) prize puts emphasis on those who have faced difficulty or hostility for their efforts. The prize is awarded by *Nature* and the London-based Sense About Science, and is supported by the Kohn Foundation. The deadline for nominations is 1 August 2016. See go.nature.com/9rvd1t.



Brighter nights for Earth

The glow of artificial light denies one-third of humanity the sight of the Milky Way. The 'new world atlas of artificial night sky brightness', produced with recently available imaging data from NASA's high-resolution Suomi National Polar-orbiting Partnership satellite, maps global night pollution in improved detail. Released on 10 June, it shows that nocturnal light pollution (pictured) is worst in Italy and South Korea, with Canada and Australia the least affected of industrialized countries (F. Falchi *et al. Sci. Adv.* **2**, e1600377; 2016). The authors calculate that the ongoing conversion from high-pressure sodium lamps to white LED lighting could lead to a doubling of the undesired brightness of the night sky.

for the university said that no personal or university data had been released to the public. Most of the researchers affected regained access to their data within three days, she said. The university was confident that it could restore most missing data from back-ups, and that it had purchased the decryption keys from the hackers only as a last resort.

Elemental choice

Three newcomers to the periodic table are to be called nihonium, moscovium and tennessine in reference to Japan, Moscow and

Tennessee, where scientists first created them. A fourth entry, oganesson, is to be named in honour of 83-year-old Russian scientist Yuri Oganessian, who helped to discover it — only the second time that a chemical element has been named after a living scientist. The International Union of Pure and Applied Chemistry proposed the names and symbols of the four elements with atomic numbers 113, 115, 117 and 118 — short-lived artificial elements that do not occur in nature — on 8 June. See go.nature.com/1vowh1u for more.

PEOPLE

Scottish adviser

Sheila Rowan became chief scientific adviser to the Scottish government on 13 June. The University of Glasgow physicist is part of the US-based Advanced Laser Interferometer Gravitational-Wave Observatory (LIGO) collaboration, which in 2015 made the first direct observation of gravitational waves. In an appointment lasting three years, Rowan is tasked with providing the Scottish government with expert advice on science-related issues, and with championing the use of science in policy development.

Jerome Bruner dies

Psychologist Jerome Seymour Bruner died at the age of 100 on 5 June. Working at Harvard University in Cambridge, Massachusetts, then at the University of Oxford, UK, and New York University, Bruner was a pioneer of cognitive psychology before turning his attention to developmental and educational psychology. He coined the term 'scaffolding' to describe how children build on the knowledge they have, and proposed a teaching approach based on it. He was on the science advisory committees during the presidencies of John F. Kennedy and Lyndon B. Johnson.

RESEARCH

LIGO strikes again

Nine months after the first discovery of gravitational waves made science history, news broke on 14 June that a similar event has been observed. On 26 December, the twin detectors of the Advanced Laser Interferometer Gravitational-Wave Observatory (LIGO) in Louisiana and Washington

FURIONI ET AL./PREPARED BY FABIO FALCHI

state detected the tell-tale sign of two black holes spiralling into each other and merging about 429 million parsecs away. Researchers reported the finding this week, at a meeting of the American Astronomical Society in San Diego, California.

FUNDING

NIH windfall

The US National Institutes of Health (NIH) is poised to receive its second major budget increase in two years. On 7 June, the US Senate voted to add US\$2 billion to the agency's annual budget, bringing it to \$34 billion. The boost will have to be reconciled with the US House of Representatives' spending bill, which has yet to be released. The windfall is to be focused on specific programmes, including a precision-medicine initiative and research on Alzheimer's disease, but does not include any money for the Cancer Moonshot initiative promoted by US vice-president Joe Biden.

ENVIRONMENT

Deer prion in moose

The discovery in Norway of two moose infected with chronic wasting disease suggests that the neurodegenerative disorder might be gaining traction in Europe. The fatal, infectious



prion disease is related to bovine spongiform encephalopathy ('mad cow disease'), and was thought to be limited to deer, elk and moose in North America and South Korea. In April, researchers at the Norwegian Veterinary Institute in Oslo detected it for the first time in Europe in a wild reindeer (*Rangifer tarandus tarandus*; see *Nature* <http://doi.org/bjz5>; 2016). Since May, at least three Norwegian moose (*Alces alces*, pictured) have tested positive for the disease, which is caused by abnormal proteins. Researchers don't yet know how the disease spread to Europe, or in which species it originated in Norway.

POLICY

Chemical bill

The US Senate on 7 June approved a bill to overhaul and strengthen the 1976 Toxic

Substances Control Act, which has been widely criticized as ineffective. Companies have registered some 85,000 chemicals with little or no safety review by government regulators. Roughly 700 new chemicals enter the marketplace each year. The updated legislation would grant the US Environmental Protection Agency authority to investigate hazardous chemicals, both new and old, that are used in consumer products or commercial and industrial processes. US President Barack Obama, who strongly supports the reform, is expected to sign the legislation into law.

Climate pledges

US President Barack Obama and Indian Prime Minister Narendra Modi agreed to a suite of climate goals during a meeting at the White House

COMING UP

18 JUNE

Crew members Tim Peake, Yuri Malenchenko and Tim Kopra return to Earth from the International Space Station.
go.nature.com/1unqtlj

20–24 JUNE

The 11th International Conference on Permafrost takes place in Potsdam, Germany.
icop2016.org

on 7 June. The two leaders pledged to push for a 2016 amendment to the Montreal Protocol on Substances that Deplete the Ozone Layer to reduce the use of heat-trapping hydrofluorocarbons, which are commonly used in air-conditioning units. They also announced a string of clean-energy partnerships, and Obama promised to ratify the 2015 Paris climate agreement as early as this year.

Visa overhaul

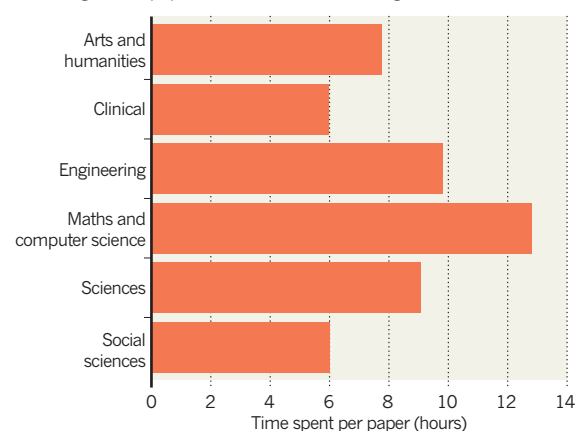
The European Commission has proposed changes to the visa scheme for highly educated prospective migrants, to facilitate the legal immigration of skilled workers. The existing Blue Card system, adopted in 2009, has failed to attract much foreign talent to the European Union because of restrictive admission conditions and conflicting national visa rules, EU migration commissioner Dimitris Avramopoulos said on 7 June. A relaxed EU-wide scheme would enable immediate work permits and quicker access to long-term residence. The United Kingdom, Ireland and Denmark are exempted from the proposed visa scheme.

TREND WATCH

Scientists spend an average of 8.4 hours per article reviewing papers submitted for publication. But reviewing times differ with subject area and reviewer age, according to a survey of opinions and attitudes towards peer review by the London-based Publishing Research Consortium. On average, reviewers spend twice as long on papers in mathematics and computer sciences as on papers in clinical and social sciences. Academics who are older than 65 take half the time of those under 36.

PEER REVIEW BY THE HOUR

Reviewing maths papers is most time-consuming.



NEWS IN FOCUS

SPACE Thousands of volunteers will comb the ground for meteorites **p.304**

THERAPIES Biotechnology successes create cost conundrum **p.305**

SPECIAL REPORT Five core ways that the EU has changed science **p.307**



MEDICINE When old drugs find new uses, prices could be slashed **p.314**

MAURO FERMARELLO/SPL



Many pets are treated like family members — and that is often reflected in the veterinary care that they receive.

BUSINESS

Demand for pet medicines sparks a biotech boom

Longer-lived animals inspire a new breed of care — from antibodies to cell therapies.

BY HEIDI LEDFORD

Little Jonah once radiated pain. The 12-year-old Maltese dog's body was curled and stiff from the effort of walking with damaged knees. But after Kristi Lively, Jonah's veterinary surgeon, enrolled him in a clinical trial of a therapeutic antibody to treat pain, his owner returned to the Village Veterinary Medical Center in Farragut, Tennessee, with tears in her eyes. Her tiny companion trotted easily alongside her. "I got my dog back," she said.

Such cutting-edge treatments were once reserved for humans. But in recent years, the changing nature of pet ownership has sparked a boom in sophisticated therapies for animals — and many are now approaching the market. On 9 June, the company that sponsored the antibody trial, Nexvet of Dublin, presented its results at the American College of Veterinary Internal Medicine Forum in Denver, Colorado. Other companies are working on bone-marrow transplants, sophisticated cell therapies and cancer vaccines.

"When I was a child and just wanted to be

a veterinarian, certainly I didn't imagine I'd be doing what I'm doing now," says Heather Wilson-Robles, a veterinary oncologist at Texas A&M University in College Station, who is engineering canine immune cells to fight cancer.

Cancer, arthritis and other diseases associated with old age are becoming more common as pets live longer, thanks in part to better treatment by their owners. "A generation ago, as beloved as Snoopy was, he lived in the backyard in the doghouse," says Steven St. Peter, president of Aratana Therapeutics, ►

► a pet-therapy company in Leawood, Kansas. Now, pets are considered family members, often sharing beds with owners who are willing to pay hefty veterinary bills.

Many standard pet treatments are human drugs given at lower doses to account for animals' smaller size. But antibodies and cell therapies generally cannot be used across species without provoking an unwanted immune response. And some human treatments simply will not work in pets: many common pain medications are toxic to cats.

Nexvet, which has raised more than US\$80 million from investors since it was founded in 2011, takes antibodies that have been approved as human medicines and alters their structures to make them effective in cats or dogs. Moving from a drug lead to safety testing takes about 18 months, says chief executive Mark Heffernan, who estimates that Nexvet's antibody therapies for pain will cost around \$1,500 a year. The company is now looking into developing antibodies that block a protein called PD-1, thereby unleashing the immune system to fight cancer. This approach has shown tremendous promise for treating cancer in people.

Aratana is also developing antibody therapies for pets, and has applied for regulatory approval of a cancer vaccine that uses a bacterium to target malignant cells. The company

hopes to move into cell therapies, and to develop a way to manufacture stem cells from fat for use against joint pain. St. Peter wants his company to be the first to win approval from the US Food and Drug Administration for a stem-cell therapy — ahead of firms developing such treatments for people.

Other forms of cell therapy could also result in new veterinary remedies. Last July, veterinary oncologist Colleen O'Connor founded a cancer-treatment company in Houston, Texas, called CAVU Biotherapies. To treat lymphoma, CAVU aims to isolate a sick dog's immune cells, rejuvenate them in culture, and then infuse them back into the dog's blood to stimulate an immune response. O'Connor used a similar approach in 2011 to treat Dakota, a bichon frise that belonged to then-US Senator Kent Conrad (Democrat, North Dakota). The dog, a Capitol Hill fixture known as the '101st senator', entered remission but later died of cancer.

For many pet owners, cost is no object. Steven Suter, a veterinary oncologist at North Carolina State University in Raleigh, runs a bone-marrow transplant clinic for dogs that

claims to cure 33% of lymphomas. Suter's clinic was booked solid after it opened in 2008, despite offering treatment that can cost a dog owner up to \$24,000. Still, Suter has worked to drive down the cost of care: to filter stem cells from blood, his clinic uses second-hand machines that were donated by a physician with a soft spot for schnauzers. Earlier this year, several major pet-insurance companies added bone-marrow transplants to the lists of procedures that they will pay for.

But when it comes to the latest pet treatments, some animals might be more equal than others. Cats are "physiologically finicky", Suter says, noting that they may be too small to allow bone-marrow transplants using his usual machines. And O'Connor notes that cats' immune systems also differ wildly from those of both humans and dogs — meaning that more basic research must be done before sophisticated immunotherapies can be deployed against feline ailments.

At Lively's clinic, many dog and cat owners were grateful that their animals could participate in Nexvet's clinical trial. But about a month after the trial ended, the effects of the antibody therapy began to fade. Jonah's owner was among the clients who called Lively, desperate for a way to access the treatment again. "It's tough," Lively says. "They'll have to wait until this product comes to market." ■

"A generation ago, as beloved as Snoopy was, he lived in the backyard in the doghouse."

ASTRONOMY

France launches massive meteor-spotting network

Tracking space rocks that reach Earth will give insight into the early Solar System.

BY TRACI WATSON

Scientists in France have launched an unprecedented campaign to catch shooting stars, an effort that will rely on thousands of volunteers to comb the ground for bits of space rock.

The Fireball Recovery and InterPlanetary

Observation Network (FRIPON), inaugurated on 28 May, already includes 68 cameras that scan the skies for meteors, which are seen when bits of asteroid, comet or other planetary material streak through Earth's atmosphere. By the end of this year, some 100 cameras will blanket France, organizers say. That would make it one of the biggest

and densest meteor-spotting networks in the world.

"If tomorrow a meteorite falls in France, we will be able to know where it comes from and roughly where it has landed," says Jérémie Vaubaillon, an astronomer at the Paris Observatory and one of organizers of the system.

Meteorites — chunks of stone that have



TOP NEWS



First rodent found with human-like menstrual cycle
go.nature.com/21jq422

MORE NEWS

- Muddled language hampers efforts to fix reproducibility go.nature.com/10ncgxz
- South Korean scientists fight plan to scrap military exemptions go.nature.com/1se3bqi
- Brazil's scientists protest against ministry merger go.nature.com/1pqstbv

NATURE PODCAST



Pimping proteins; modifying metalloenzymes; and conserving coral reefs
nature.com/nature/podcast

FOTANDY/GETTY

fallen from space and reached Earth's surface — provide valuable insights into everything from the history of the Solar System to the identity of asteroids that could potentially collide with Earth. Snagging such objects is “the one chance you get to see Solar System material in your hands,” says David Clark, who studies meteors at the University of Western Ontario in London, Canada. “We simply don't have enough of this stuff.”

FIRE IN THE SKY

Especially prized are meteorites that were tracked on their inward journey. Scientists can use data about the journey to reconstruct the object's trajectory and reveal where in the Solar System it came from. People manage to retrieve just one to three meteorites with known trajectories each year, says Peter Jenniskens, an astronomer at the SETI Institute in Mountain View, California.

FRIPON's organizers dream of collecting one tracked meteorite per year from the French landscape. By comparison, researchers with the large and dense Spanish Meteor Network have scored 2 in the past 12 years.

The French network's cameras are very densely and evenly spaced, sitting roughly 70–80 kilometres apart at laboratories, science museums and other buildings — close enough together to yield good information about where meteorites land. “That increases your chance of finding something,” says Jenniskens.

FRIPON is also the first fully connected and automated network, says principal investigator François Colas, of the Paris Observatory.



Fisheye cameras will cover France as part of the meteor-spotting network.

When a camera detects a meteor, it sends a message to a central computer in Paris. If two or more cameras spot the fireball, FRIPON scientists receive an e-mail describing where it was seen. Eventually, the e-mail will include automatically generated information about the object's probable landing zone, pinpointing it to an area roughly 1 kilometre by 10 kilometres.

The researchers will then face the arduous job of searching this area to find the object. At first, scientists will conduct the ground searches. But in the next few years, FRIPON organizers plan to train an army of citizen

scientists to walk the French landscape looking for bits of meteorite — and to hand over any finds.

Perhaps one in 1,000 volunteers will actually turn up for a search, estimates Brigitte Zanda, a meteorite specialist at the National Museum of Natural History in Paris, who heads the volunteer effort. Organizers hope to field a search team of 30 people in every part of France, so they will have to recruit hundreds of thousands of people, she says. “It's ambitious.” But hundreds of people have already signed up, even though the official recruitment drive is just getting under way. ■

DRUG PRICING

Gene therapies pose million-dollar conundrum

Economists, investors and medical insurers can't work out how to pay for cutting-edge drugs.

BY ERIKA CHECK HAYDEN

Drugs that act by modifying a patient's genes are close to approval in the United States, and one is already available in Europe. The developments mark a triumph for the field of gene therapy, once considered controversial.

But with estimated price tags of at least US\$1 million per patient, how will anyone pay for these treatments? The question is just one in a broader debate about how to finance a range of super-expensive drugs that are now

available, thanks to an explosion in genetic and molecular-biology research over the past 20 years.

“Advances in science are presenting a social affordability question like never before,” says economist Mark Trusheim at the Massachusetts Institute of Technology in Cambridge. “Do we want to convert the science into therapies that we actually would have to pay for?”

Trusheim spoke at the Biotechnology Innovation Organization (BIO) meeting in San Francisco, California, on 6–9 June, which featured much discussion about how society

will pay for the rising costs of new drugs. At the American Society of Clinical Oncology meeting in Chicago, Illinois, on 3–7 June, dozens of talks and abstracts focused specifically on the growing cost of cancer care. Cancer drugs that unleash the power of the immune system cost up to \$40,000 per year.

Gene therapies that are close to US approval include treatments for haemophilia B, sickle-cell anaemia and the neurodegenerative disease cerebral adrenoleukodystrophy. A therapy under development at Spark Therapeutics in Philadelphia, Pennsylvania, for a type of ►

► blindness is considered the most advanced.

Many of the treatments deliver corrective genes using a modified virus that is considered safer than vectors used in earlier attempts. But many of the target disorders are rare, limiting the population that can be treated. And there are often no previously approved drugs that work similarly, removing the pressure on companies to lower their prices.

Such therapies could cost \$1 million per patient, estimate haematologist Stuart Orkin of Harvard Medical School in Boston, Massachusetts, and Philip Reilly, an investor with Third Rock Ventures in Boston (S. H. Orkin and P. Reilly *Science* **352**, 1059–1061; 2016). Reilly co-founded Cambridge-based Bluebird Bio, which is working on several of the gene therapies that are close to market.

That's the same price as Glybera, the gene therapy given the green light by European regulators in 2012, which has been taken by only one person so far. Experts attribute this low uptake to the high price and to doubts about its efficacy. If newer gene therapies are to do better, they will have to produce convincing data that they are worth the money, Trusheim says.

For medicines that are already approved, one increasingly popular solution is a deal between insurers and drug companies that ties payments to how well medicines perform. Last November, for example, Boston-based

Harvard Pilgrim Health Care, a major New England insurer, announced that it will cover treatment for its clients with Repatha (evolocumab), one of a new class of cholesterol-lowering medication that is made by Amgen and costs \$14,000. But if patients don't reach pre-agreed cholesterol levels, or if Harvard Pilgrim ends up paying more than it has budgeted for, Amgen will refund the insurer.

“Advances in science are presenting a social affordability question like never before.”

on the rise around the world: one study found ‘pay-for-performance’ deals across 14 countries in 2013, predominantly in Europe and the United States, but also in middle-income countries such as China and Brazil.

These deals may work for some conditions, such as haemophilia B, for which several drugs might be approved. But for others, such as adrenoleukodystrophy, only one company is developing a product, so there won't be the incentive for companies to negotiate, Trusheim says.

At the BIO meeting, investors and economists

Networks set up by insurance companies to gather and share data from health centres make such deals possible, says Michael Sherman, chief medical officer at Harvard Pilgrim. And they are

discussed a range of alternative solutions, including the medical equivalent of a mortgage or annuity, in which insurance companies or governments might spread the cost of a one-time treatment over many years, as long as a patient continues to benefit from it. One complication of such arrangements in the United States is that patients often move between insurers, so it is unclear who would continue to make these payments on a patient's behalf.

The difficulties of paying for the fruits of the biotechnology revolution are something that governments are already struggling with. The state of Arkansas last year settled a lawsuit filed by three people who said they had been denied access to the \$300,000 cystic fibrosis drug Kalydeco (ivacaftor) because of the cost. And in April, the Japanese government imposed a 50% price cut on a new hepatitis C treatment, Sovaldi (sofosbuvir). A US federal judge in Seattle, Washington, ruled on 27 May that states cannot delay treatment with Sovaldi, which costs up to \$84,000, because of price concerns.

But those working on gene therapy are confident that a solution is out there. “Let's say that a gene therapy that really made a world of difference in the life of a small child should cost a million dollars for one event,” Reilly says. “I can think of many things in medicine that cost that much or more, and we don't think twice about that.” ■



The EU affects science from the collaborative opportunities that the bloc creates to the billions of euros that it distributes for research and innovation.

EUROPEAN UNION

Boon or burden: what has the EU ever done for science?

More than 500 million people and 28 nations make up the European Union. It will lose one of its richest, most populous members, if the United Kingdom votes to leave on 23 June. Ahead of a possible 'Brexit', Nature examines five core ways that the EU shapes the course of research.

SCIENTIST SUPERHIGHWAY

Science doesn't respect national boundaries, so it helps if scientists don't have to either — and EU rules and programmes encourage researchers to hit the road.

EU citizens have the right to live and work in any country in the bloc, and the European Commission's Marie Skłodowska-Curie actions pay for 9,000 scientists each year to move to or within the EU. The actions fill a gap left by national funders, which are often reluctant to fund researchers outside their country, says Caroline Whelan, a senior scientific officer at Science Europe, the Brussels-based organization of national research councils. The EU Erasmus exchange programme has transplanted more than 3.3 million students, and 470,000 teaching and administrative staff, since 1987.

Although there is little information on how such programmes affect scientists' overall mobility, they boost opportunities for

collaboration. And because Marie Skłodowska-Curie fellows often return to their home country, they redistribute skills and knowledge. "This is fantastic for Eastern Europe and other less-well developed countries to build research capacity," says Lidia Borrell-Damian, director for research and innovation at the European University Association in Brussels.

A 2011–13 study found that 31% of EU academics had worked outside their country of residence in the previous decade. And leading scientists say that hiring from abroad helps them to respond to local skills shortages. The survey also found that 80% of those who had worked internationally saw a positive effect on their research skills, and 60% thought that mobility had strongly increased their research output (see go.nature.com/28wvqta).

But the experiences were not all positive: more academics said that their job options had decreased as a result of moving than said that opportunities had increased, for example.

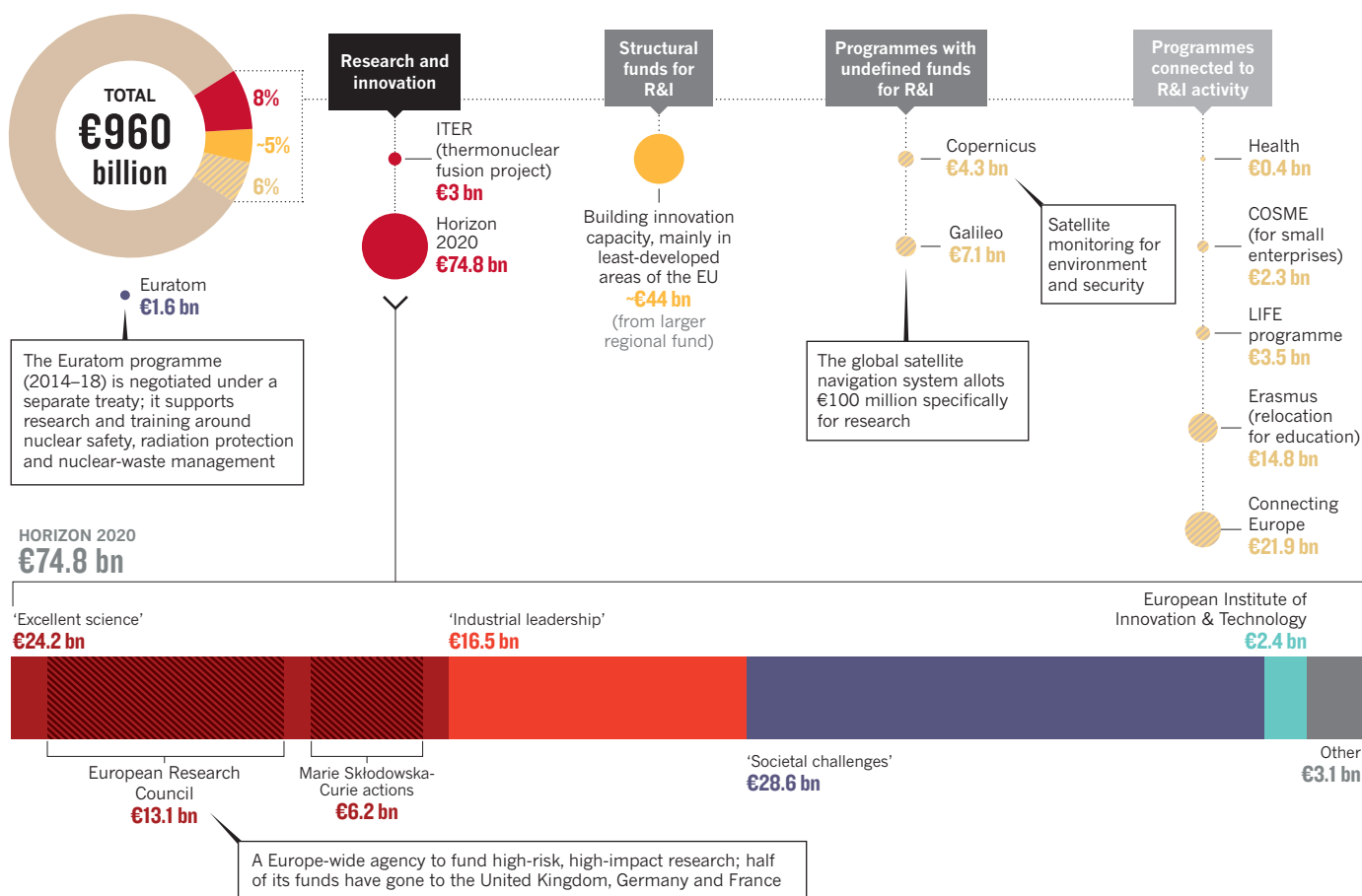
Another downside of mobility is that much of the flow goes just one way, says Maria Helena Nazaré, a physicist and former rector of the University of Aveiro in Portugal. "I think that's already creating problems." Countries such as the United Kingdom, the Netherlands and Sweden tend to be net attractors for the Marie Skłodowska-Curie actions, whereas Spain, Greece and Italy lose talent. Nazaré also notes that transferring pension and benefits between countries can be tough.

Still, the commission is committed to further greasing the wheels. Funding aimed at encouraging mobility has soared in the past two decades to €6.2 billion (US\$6.9 billion) in 2014–20 — and the commission is tackling the pensions issue. It is also growing its EURAXESS portal, an EU-wide website that lists jobs and support for moving researchers, and has revamped its 'scientific visa' package for non-EU researchers. Notably, the United Kingdom has opted out of the visa, together with Denmark. ▶

VIKTOR DRACHEV/AFP/GETTY

EU SPENDING

The European Union has dedicated more than €120 billion (almost 13%) of its 2014–20 budget to research and innovation (R&I). A host of other EU-funded programmes also support or are connected to R&I activities, but don't define the amount of their investment.



SOURCES: EU REG 2015/1017; EPRS

UNIQUE SCIENCE

Scientists like to complain loudly about some aspects of the commission's 'Framework' funding programmes, which are dedicated to research and innovation (see 'EU spending').

To access a vast pot of cash geared to meeting 'Societal Challenges' — which amounts to an estimated €28.6 billion of the €74.8 billion available under Horizon 2020, the Framework programme for 2014–20 — they must meld themselves into large multinational collaborations, and adjust their research to fit EU strategic goals. But these constraints have fostered many valuable projects.

"I am a big fan of these programmes," says Nadia Rosenthal, scientific director of the Jackson Laboratory in Bar Harbor, Maine, who has collaborated with several EU consortia on mouse-genetics projects, which she says generated world-class science. "The coordination of talents they can achieve would be very hard to pull off in the United States — or in the UK alone, if it were not connected to Europe."

Take research into the health effects of low-dose radiation, which people may encounter during a CT scan or if they live within a few tens of kilometres of the site of the Fukushima disaster in Japan. So small are the risks — if they exist at all — that such research is low on most

funding agencies' list of priorities.

But the issue is of perennial concern to the public. And studying it requires collaboration between radiation-protection agencies and academics, as well as the use of large data sets, which can be gathered only by multiple collaborating nations.

These factors make low-dose-radiation studies perfect fodder for EU funding, says Thomas Jung, head of radiation protection and health at the German Federal Office of Radiation Protection in Munich, which has participated in the series of low-dose-radiation projects that the commission has supported since 2010.

Societal Challenges funding has also supported projects that others shy away from, such as transplanting cells derived from the brains of fetuses into the brains of people with Parkinson's disease. In 2003, researchers around the world abandoned this controversial line of research — which tries to replace the neurons whose loss causes the illness's symptoms — after many trial participants failed to benefit and no one could work out why. Then, in 2014, the commission-funded TRANSEURO trial began.

TRANSEURO aims to transplant neurons into 150 people with Parkinson's in the United Kingdom, Sweden, France and Germany using harmonized clinical protocols to help establish

which conditions work best. The large collaboration, which joins 14 biomedical laboratories, clinics and companies, is essential, says TRANSEURO's coordinator, neurologist Roger Barker at the University of Cambridge, UK. "Without the EU, I doubt this would have happened."

Trust between companies is crucial to the Advanced Immunization Technologies (ADITEC) project, which aims to create a generic toolbox to speed up vaccine development. Under the confidentiality agreements of the consortium, which the commission has funded since 2011, companies are comfortable sharing the components of their proprietary vaccines. The project has already produced the first direct comparison of different companies' 'adjuvants', substances that strengthen immune responses (N. P. H. Knudsen *et al. Sci. Rep.* **6**, 19570; 2016). "We had always thought it would be impossible to compare them," says ADITEC coordinator Rino Rappuoli, chief scientist of GSK Vaccines in Siena, Italy.

LIFTED THE EAST

In late 2000, when NATO sponsored a meeting on science in Central and Eastern Europe, much of the region was a world apart from the EU. Years of communist thinking had nourished

the illusion that the mere existence of institutes and research facilities was more important than their actual performance.

Attitudes have changed, partly thanks to the EU, which absorbed the Czech Republic, Estonia, Hungary, Latvia, Lithuania, Poland, Slovakia and Slovenia in 2004, then Bulgaria and Romania in 2007 and Croatia in 2013.

These countries have had a low rate of success in winning grants from the Framework programmes. But all of the former communist states are recipients of the commission's 'structural funds' — subsidies designed to reduce social and economic disparities, a goal of the EU. How the funds are used is decided locally, but of the €170 billion available for 'cohesion and regional development' in 2007–13, the commission pushed for €20 billion to be spent on research. In 2014–20, almost €44 billion is meant to be used for science and innovation in poorer regions.

The cash has been most effective when used to refurbish universities and provide labs with the equipment needed to train students and entice researchers to stay, says Peter Tindemans, secretary-general of science-advocacy group EuroScience in Strasbourg, France.

The funds have also financed the €850-million Extreme Light Infrastructure, a pan-European laser facility under construction at sites in the Czech Republic, Hungary and Romania. The facility is expected to attract leading talent from around the world to the region, but Tindemans cautions that improvements to the research environment must come first. "You can't jump-start scientific development solely with large infrastructures," he says.

FOSTERING EXCELLENCE

To win cash from EU funding programmes, researchers must often fit their work into broader societal or economic goals. But one corner of the European funding apparatus is all about science for science's sake.

Set up in 2007 to raise the quality of research across Europe, the European Research Council (ERC) awards generous grants that are open to any discipline, come with minimum bureaucracy and are judged solely on the quality of the application.

The ERC budget has grown from €7.5 billion in 2007–13 to €13.1 billion for 2014–20. At up to €2.5 million over 5 years per researcher, its grants are longer and larger than those of most national funders. The approach seems to work: 7% of ERC-generated papers come in the top 1% of the most highly cited articles by discipline, publication type and year.

Not everyone is happy with the 'excellence at all costs' approach. Since the ERC's inception, half of the grants it awarded under its three core schemes have gone to just three countries: the United Kingdom, Germany and France.

But the ERC system lifts the quality of research beyond the projects that it funds.

EUROPEAN, BUT NOT EU

Although separate, CERN and ESA receive EU funds.

Before the EU began to have a major role in coordinating Europe-wide research in the 1990s, the task fell mainly to pan-European research organizations such as the CERN particle-physics laboratory.

Established by treaty in 1952 by 11 countries, CERN, near Geneva, Switzerland, was born in the same post-war spirit of peace as led to the formation of the EU. But the lab pre-dates the EU's main forerunner, the European Economic Community, which had no remit for

research, by about five years. CERN now has 21 member states and is a major recipient of EU funds, including for a 2020 upgrade of its Large Hadron Collider, which scientists used to discover the Higgs boson.

Another organization that grew up alongside the EU is the European Space Agency (ESA). It arose from a 1975 merger between the European Space Research Organisation and the European Launch Development Organisation. Both were created in the 1960s to guarantee Europe independent access to space.

ESA has racked up a string of successes, including the Rosetta mission that put a lander on a comet in 2014. The EU is now the biggest single contributor to the 22-nation-strong agency, accounting for some 20% of its budget. ESA and the EU are partners in the multibillion-dollar Copernicus Earth observation system and in the Galileo global satellite navigation system.

Rosetta's Philae lander touches down on a comet.



Either in an attempt to win more of its grants or simply inspired by the ERC, member states are redesigning national policies to make their science more competitive, says Jose Labastida, head of the ERC's scientific department. He cites Poland's National Science Centre, set up in 2011, as an example.

And 17 countries have run schemes that fund ERC runners-up — applicants who met the quality threshold but were unsuccessful — essentially reusing the agency's high-quality peer-review process. "The ERC has raised the scientific level all over Europe," says Catherine Cesarsky, an astronomer at the French Atomic Energy Commission near Paris.

RESEARCH MELTING POT

Science thrives on collaboration — and the EU has partnered with other agencies (see 'European, but not EU') and creates myriad opportunities for researchers to pool ideas and cooperate.

Most of the funding for the EU's Framework programmes is reserved for projects in which partnerships are formed by at least three organizations from different countries. The last programme, FP7, which ran from 2007 to 2013, spent €41.7 billion of its €50.5-billion budget on some 26,000 joint projects, generating more than 500,000 pairs of collaborative links between research organizations, according to the commission. The Framework programmes also fund mobility grants that foster collaboration.

In less-well-off countries, meanwhile, structural funds equip researchers to work with their counterparts in more scientifically

developed nations, says Rémi Barré, an emeritus researcher at the National Conservatory of Arts and Crafts in Paris.

The gradual political, economic and research integration of the EU's member states has created an environment that is conducive to collaboration, according to geneticist Paul Nurse, head of the Crick Institute in London. Research is now embedded across the EU's activities, from the bloc's negotiation of the COP21 climate accord in December 2015 to its environmental-protection policies and regulatory bodies such as the London-based European Medicines Agency.

Contact between science ministers from different member states and researchers has become the norm, says Frank Gannon, former head of the intergovernmental European Molecular Biology Organization. By contrast, he recalls how fragmented European research was a few decades ago when he was a researcher in Ireland. "The sense of isolation of a researcher was massive." ■

Reporting by Alison Abbott, Declan Butler, Elizabeth Gibney, Quirin Schiermeier and Richard Van Noorden

CLARIFICATION

The News Feature 'The material code' (*Nature* **533**, 22–25; 2016) did not make it clear that the director of the Materials Genome Project is Kristin Persson, and that she has an affiliation with the University of California, Berkeley.

A DECADE OF iPS CELLS

Induced pluripotent stem cells were supposed to herald a medical revolution. But ten years after their discovery, they are transforming biological research instead.

BY MEGAN SCUDELLARI

“We have colonies.” Shinya Yamanaka looked up in surprise at the postdoc who had spoken. “We have colonies,” Kazutoshi Takahashi said again. Yamanaka jumped from his desk and followed Takahashi to their tissue-culture room, at Kyoto University in Japan. Under a microscope, they saw tiny clusters of cells — the culmination of five years of work and an achievement that Yamanaka hadn’t even been sure was possible.

Two weeks earlier, Takahashi had taken skin cells from adult mice and infected them with a virus designed to introduce 24 carefully chosen genes. Now, the cells had been transformed. They looked and behaved like embryonic stem (ES) cells — ‘pluripotent’ cells, with the ability to develop into skin, nerve, muscle or practically any other cell type. Yamanaka gazed at the cellular alchemy before him. “At that moment, I thought, ‘This must be some kind of mistake,’” he recalls. He asked Takahashi to perform the experiment again — and again. Each time, it worked.

Over the next two months, Takahashi narrowed down the genes to just four that were needed to wind back the developmental clock. In June 2006, Yamanaka presented the results to a stunned room of scientists at the annual meeting of the International Society for Stem Cell Research in Toronto, Canada. He called the cells ‘ES-like cells,’ but would later refer to them as induced pluripotent stem cells, or iPS cells. “Many people just didn’t believe it,” says Rudolf Jaenisch, a biologist at the Massachusetts Institute of Technology in Cambridge, who was in the room. But Jaenisch knew and trusted Yamanaka’s work, and thought it was “ingenious.”

The cells promised to be a boon for regenerative medicine: researchers might take a person’s skin, blood or other cells, reprogram them into iPS cells, and then use those to grow liver cells, neurons or whatever was needed to treat a disease. This personalized therapy would get around the risk of immune rejection, and sidestep the ethical concerns of using cells derived from embryos.

Ten years on, the goals have shifted — in part because those therapies have proved challenging to develop. The only clinical trial using iPS cells was halted in 2015 after just one person had received a treatment.

But iPS cells have made their mark in a different way. They have become an important tool for modelling and investigating human diseases, as well as for screening drugs. Improved ways of making the cells, along with gene-editing technologies, have turned iPS cells into a lab workhorse — providing an unlimited supply of once-inaccessible human tissues for research. This has been especially valuable in the fields of human development and neurological diseases, says Guo-li Ming, a

neuroscientist at Johns Hopkins University in Baltimore, Maryland, who has been using iPS cells since 2006.

The field is still experiencing growing pains. As more and more labs adopt iPS cells, researchers struggle with consistency. “The greatest challenge is to get everyone on the same page with quality control,” says Jeanne Loring, a stem-cell biologist at the Scripps Research Institute in La Jolla, California. “There are still papers coming out where people have done something remarkable with one cell line, and it turns out nobody else can do it,” she says. “We’ve got all the technology. We just need to have people use it right.”

FROM SKIN TO EYES

Six weeks after presenting their results, Yamanaka and Takahashi published¹ the identities of the genes responsible for reprogramming adult cells: *Oct3/4*, *Sox2*, *Klf4* and *c-Myc*. Over the next year, three laboratories, including Yamanaka’s, confirmed the results and improved the reprogramming method^{2–4}. Within another six months, Yamanaka and James Thomson at the University of Wisconsin–Madison managed to reprogram adult cells from humans^{5,6}. Labs around the world rushed to use the technique: by late 2009, some 300 papers on iPS cells had been published.

Many labs focused on working out what types of adult cell could be reprogrammed, and what the resulting iPS cells could be transformed into. Others sought to further improve the reprogramming recipe, initially by eliminating⁷ the need to use *c-Myc*, a gene with the potential to turn some cells cancerous, and later by delivering the genes without them integrating into the genome, a looming safety concern for iPS-cell-based therapies.

Another big question was how similar iPS cells really were to ES cells. Differences started to emerge. Scientists discovered⁸ that iPS cells retain an ‘epigenetic memory’ — a pattern of chemical marks on their DNA that reflects their original cell type. But experts argue that such changes should not affect the cells’ use in therapies. “There might be some differences from ES cells, but I believe they are really not relevant,” says Jaenisch.

By 2012, when Yamanaka won half of the Nobel Prize in Physiology or Medicine for the work, the first human trial of an iPS-cell-based therapy was being planned. Masayo Takahashi, an ophthalmologist at the RIKEN Center for Developmental Biology (CDB) in Kobe, Japan, had been developing ES-cell-based treatments for retinal diseases when Yamanaka first published his reprogramming method. She quickly switched to iPS cells, and eventually began to collaborate with Yamanaka.

In 2013, her team made iPS cells from the skin cells of two people



Shinya Yamanaka won a Nobel prize for his work on reprogramming adult cells to an embryonic-like state.

with age-related macular degeneration, an eye condition that can lead to blindness, and used them to create sheets of retinal pigment epithelium (RPE) cells for a clinical trial. Not long after, CDB researchers working on another cell-reprogramming technique — stimulus-triggered acquisition of pluripotency, or STAP — came under investigation for misconduct (see go.nature.com/1xbnlzn). Although unconnected to the iPS-cell trial, the furore made it difficult for Takahashi to advance her study: it created a “headwind in the calm sea” in which she had been working, she says. Yet her team pushed ahead, and on 12 September 2014, doctors implanted the first RPE sheets into the right eye of a woman in her seventies. Takahashi says that the therapy halted the woman’s macular degeneration and brightened her vision.

But as the lab prepared to treat the second trial participant, Yamanaka’s team identified two small genetic changes in both the patient’s iPS cells and the RPE cells derived from them. There was no evidence that either mutation was associated with tumour formation, yet “to be on the safe side” Yamanaka advised Takahashi to put the trial on hold. She did.

The suspension gave pause to other researchers interested in the field, says Paul Knoepfler, a stem-cell biologist at the University of California, Davis: “The world is watching to see how it progresses.” But the difficulties iPS cells have faced getting to the clinic aren’t that unusual, says David Brindley, who studies stem-cell regulation and manufacturing at the University of Oxford, UK. It generally takes about 20 years to move a scientific discovery to clinical and commercial adoption, so iPS cells “are following roughly the same trajectory”, he says.

In the United States, the Astellas Institute for Regenerative Medicine in Marlborough, Massachusetts (formerly Advanced Cell Technology), has several iPS-cell-based therapies in its pipeline, including ones for macular degeneration and glaucoma, says chief scientific officer Robert Lanza. For any such therapy, it takes years to work out a suitable method for making the right cell types in large enough quantities, and with enough purity. “iPS cells are the most complex and dynamic therapies that have ever been proposed for the clinic,” says Lanza. “I’m the first one who wants to see these cells in the clinic, but an abundance of caution is needed.”

The other great challenge is working out what will be required to get

such treatments approved. Loring hopes to start an iPS-cell-therapy trial for Parkinson’s disease in the next two years. But it won’t be easy: the treatment uses cells derived from individual patients, and Loring plans to do a complex series of checks and validations for each cell line to demonstrate its safety to the US Food and Drug Administration.

Developing and testing a therapy in even one person has been educational, says Yamanaka: it took one year and US\$1 million. He expects future therapies to use donor-derived iPS cells from a cell bank, rather than making them for each patient.

Takahashi plans to compare banked iPS cells side-by-side with those derived from patients, to observe any differences in immune reaction. She intends to apply to the Japanese government to resume her macular-degeneration trial “very soon”, but when asked, would not specify a timeline.

“THE WORLD IS WATCHING TO SEE HOW IT PROGRESSES.”

CELLULAR IMPROVEMENTS

Although cell therapy has suffered setbacks, other areas of research have blossomed.

Methods for making iPS cells “are more refined and elegant than they were even five years ago”, says Knoepfler.

But most reprogramming techniques are inefficient: only a small fraction of cells end up fully reprogrammed. And, like all cell lines, iPS cells vary from one strain to another. That has made it hard to establish controls in experiments.

Marc Tessier-Lavigne, a neuroscientist at the Rockefeller University in New York City, confronted this challenge with colleagues at the New York Stem Cell Foundation when they began to work with iPS cells made from people with early-onset Alzheimer’s disease and frontotemporal dementia. They quickly realized that comparing a patient’s iPS cells with those from a healthy control didn’t work — the cells behaved too differently in culture, probably the result of disparities in genetic background or gene expression. “So we turned to gene editing,” says Tessier-Lavigne.

The CRISPR–Cas9 gene-editing tool, which has gained huge popularity in recent years, has enabled researchers to introduce disease-associated mutations into a sample of iPS cells and then compare them with the original, unedited cell lines. Jaenisch’s lab uses CRISPR–Cas9 with iPS cells daily. “We can do any manipulations we want to do,” he says.

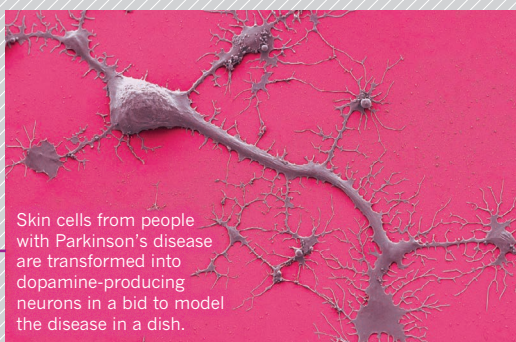
New, refined gene-editing methods are proving even more useful. In April, for example, Dominik Paquet and Dylan Kwart in Tessier-Lavigne’s

INDUCING A REVOLUTION

Shinya Yamanaka's discovery spurred thousands of publications on the identity, characteristics and many uses of iPS cells in research.

- 2006** Yamanaka, of Kyoto University in Japan, reveals that just four genes can reprogram adult mouse cells into embryonic-like, 'pluripotent' iPS cells.
- 2007** Yamanaka and James Thomson at the University of Wisconsin-Madison both report creation of human iPS cells.

2008



Skin cells from people with Parkinson's disease are transformed into dopamine-producing neurons in a bid to model the disease in a dish.

2009

Several teams start to demonstrate that iPS cells can be created without inserting genes into the genome.

2010

2011



Yamanaka (pictured with King Carl XVI Gustaf of Sweden) and John Gurdon at the University of Cambridge, UK, receive the Nobel Prize in Physiology or Medicine for revealing that adult cells can be reprogrammed.

2013

2014

Researchers in Japan begin the first, and so far only, test of iPS-derived cells in people, attempting to treat a degenerative eye condition.

2015

The Japanese trial is halted.

lab demonstrated⁹ a technique for introducing specific point mutations into iPS cells using CRISPR, and editing just one copy of a gene, rather than both. This allowed them to generate cells with precise combinations of Alzheimer's-associated mutations, and to study the effects.

But because iPS cells resemble embryonic cells, they are not always ideal for studying late-onset diseases such as dementia. So researchers are exploring ways to stress cells or introduce proteins that age them prematurely. "It's a valid concern that hasn't been resolved, but there are a number of approaches to really try to tackle it," says Tessier-Lavigne.

The fact that iPS cells mimic early human development has proved useful in another field — the sprint to discover whether and how infection with the Zika virus in pregnant women might lead to microcephaly, a condition in which a baby's head is smaller than expected. Ming and her colleagues have used iPS cells to create brain organoids — 3D bits of tissue that resemble developing organs. When they exposed these to Zika, they found¹⁰ that the pathogen preferentially infects neural stem cells over newly formed neurons, leading to increased death of the neural stem cells and a decrease in the volume of a layer of neurons in the cortex, resembling microcephaly.

Other groups have used iPS cells to create organoids such as mini-guts and mini-livers, and the list of disease-related discoveries using iPS cells is growing. It includes showing how a gene duplication in glaucoma causes the death of nerve-cell clusters¹¹, and recapitulating genetic and cellular alterations associated with Huntington's disease¹².

iPS cells have also been used with some success in drug discovery: they provide a plentiful source of patient-derived cells to screen or test experimental drugs. In 2012, for example, neural stem cells made from people with a nerve-cell-development disease were used to screen nearly 7,000 small molecules and identify a potential drug for the condition¹³. And this year, a team reported¹⁴ generating sensory neurons from iPS cells made from people with an inherited pain disorder. The researchers showed that a sodium-blocking compound reduced the excitability of neurons and decreased pain in the patients. It would be great to use iPS cells to predict whether people will respond to a particular drug, says Edward Stevens, a research fellow at the Pfizer Neuroscience and Pain Research Unit in Cambridge, UK, who led the work, but there will need to be much more evidence that such a strategy works.

Even after a decade of reprogramming cells (see 'Inducing a revolution'), researchers don't know in detail how the process actually occurs. For now, the field is focused on systematically verifying cell lines' identity and safety, by checking their genomes, gene-expression patterns and more. One such effort, the European Bank for Induced Pluripotent Stem Cells, centred in Cambridge, UK, publicly launched its catalogue of standardized iPS cells for use in disease modelling this March. Yamanaka is also involved in banking iPS cells for future therapies, collecting varieties that would be immunologically compatible across a broad population.

The greatest future challenges, he says, are not scientific. Researchers are going to need strong support from the pharmaceutical industry and governments to move forward with cell therapies; for drug discovery and disease modelling, researchers must be persistent and patient. iPS cells can only shorten the discovery process, not skip it, he says. "There's no magic. With iPS cells or any new technology, it still takes a long time." ■

Megan Scudellari is a science journalist in Boston, Massachusetts.

1. Takahashi, K. & Yamanaka, S. *Cell* **126**, 663–676 (2006).
2. Okita, K., Ichisaka, T. & Yamanaka, S. *Nature* **448**, 313–317 (2007).
3. Wernig, M. *et al.* *Nature* **448**, 318–324 (2007).
4. Maherali, N. *et al.* *Cell Stem Cell* **1**, 55–70 (2007).
5. Takahashi, K. *et al.* *Cell* **131**, 861–872 (2007).
6. Yu, J. *et al.* *Science* **318**, 1917–1920 (2007).
7. Nakagawa, M. *et al.* *Nature Biotechnol.* **26**, 101–106 (2007).
8. Kim, K. *et al.* *Nature* **467**, 285–290 (2010).
9. Paquet, D. *et al.* *Nature* **533**, 125–129 (2016).
10. Qian, X. *et al.* *Cell* **165**, 1238–1254 (2016).
11. Tucker, B. A. *et al.* *J. Stem Cell Res. Ther.* **3**, 161 (2014).
12. HD iPSC Consortium *Cell Stem Cell* **11**, 264–278 (2012).
13. Lee, G. *et al.* *Nature Biotechnol.* **30**, 1244–1248 (2012).
14. Cao, L. *et al.* *Sci. Transl. Med.* **8**, 335ra56 (2016).

THOMAS DEERING/NCMIR/SPL

POOL/YOMIURI SHIMBUN/AP



New tricks for old drugs

Faced with skyrocketing costs for developing new drugs, researchers are looking at ways to repurpose older ones — and even some that failed in initial trials.

BY NICOLA NOSENGO

When a young physician opted to do a short stint in Grant Churchill's pharmacology lab as part of his medical training, he asked for a task that would quickly teach him the tools of the trade. "So I thought, 'I have a good project for you,'" says Churchill.

That was in 2010, and Churchill's group at the University of Oxford, UK, was looking for ways to treat bipolar disorder without using lithium — a drug that often works well, but is plagued with side effects. So Churchill asked the physician, Justyn Thomas, to screen all of the 450 compounds in the US National Institutes of

Health (NIH) Clinical Collection, a library of drugs that had passed safety tests in humans but, for various reasons, had never reached the market. "That stuff is just sitting there, and it doesn't take much effort," says Churchill, "so you think you just have to try."

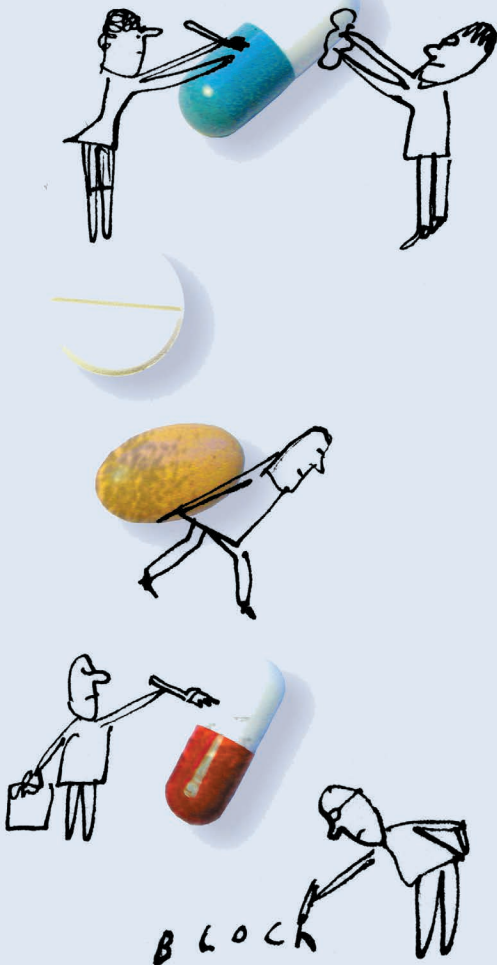
Thomas pipetted a few drops of each compound into Petri dishes filled with bacteria that had been genetically engineered to manufacture the human enzyme suppressed by lithium — and eventually got a hit. A compound originally intended for people who had experienced a stroke also damped production of the

enzyme, suggesting that it might give patients the same benefits as lithium¹. After experiments in mice showed that the drug, ebselen, could get through the chemical barrier that protects the brain — something only a few compounds can do — Churchill's group did a small-scale trial and found that ebselen could be used safely in healthy volunteers².

The University of Oxford has now teamed up with a pharmaceutical company to run clinical trials of ebselen for bipolar disorder. The researchers are able to skip the phase I safety trials because the drug had already passed them, and are going straight to phase II: testing the drug's efficacy against bipolar disorder. Churchill is well aware that ebselen could fail this trial, or the larger, more stringent ones needed to test whether the drug works better than lithium. But he is already proud of what his team has achieved. "As an academic group with no company money," he says, "we were able to go from identification of the molecule to a human trial with a very limited budget."

Such stories are becoming more and more common: taking drugs that have been developed for one disorder and 'repositioning' them to tackle another is an increasingly important strategy for researchers in industry and academia alike. These efforts take inspiration from some classic success stories. One is sildenafil, an angina medication developed in 1989 that

SERGE BLOCH



is now marketed as Viagra and used to treat erectile dysfunction. Another is azidothymidine, which failed as a chemotherapy drug but emerged in the 1980s as a therapy for HIV.

Increasingly, the serendipity responsible for those earlier discoveries is giving way to systematic searches for candidates. Partly, this is the result of advances in technology. These include big-data analytics that can now uncover molecular similarities between diseases; computational models that can predict which compounds might take advantage of those similarities; and high-throughput screening systems that can quickly test many drugs against different cell lines.

But for the pharmaceutical industry, the real impetus is economics. Getting a drug to market currently takes 13–15 years and between US\$2 billion and \$3 billion on average, and the costs are going up — even though the number of drugs approved every year per dollar spent on development has remained flat or decreased for most of the past decade³ (see ‘Eroom’s law’). The 3,000 or so drugs that have been approved by at least one country therefore represent a vast untapped resource if they can be used against another condition — as do the thousands more that stalled in clinical trials. Many of them, like ebselen, can probably skip the phase I trials and pose a substantially lower risk of producing dramatic side effects in later phases — thereby

slashing those development costs compared with completely new compounds. Some estimates suggest that repositioning a drug costs on average \$300 million and takes around 6.5 years. “My feeling is that the proportion of drugs that in theory could be repositioned is probably around 75%,” says Bernard Munos, a senior fellow at FasterCures, a drug-development advocacy organization in Washington DC, and a member of the advisory council of the National Center for Advancing Translational Sciences (NCATS) at the NIH.

But the fraction is probably quite a bit smaller in practice, he concedes. Repositioned drugs still have to make it through phase II and III clinical trials for their new purpose — trials that respectively eliminate 68% and 40% of every compound that gets that far. And many drugs also face economic barriers, such as being off-patent, that could dissuade pharmaceutical companies from getting involved. “Can some repositioning projects work? Sure. Can it work systematically as a profitable business model? That, I don’t believe,” says John LaMattina, a former president of research and development at Pfizer, and now a senior partner at the health-care technology research firm PureTech in Boston, Massachusetts.

Nonetheless, some 30 articles on cases of drug repositioning are now being published in scientific journals every month — a sixfold increase since 2011. A dedicated journal, *Drug Repurposing, Rescue and Repositioning*, was launched last year. Three or four drug-repositioning companies are created every year. And some estimates⁴ suggest that the number of repositioned drugs entering the regulatory-approval pipeline is rising, and could account for about 30% of all drugs approved every year.

“We’ve gone past the stage where we had to explain to everyone what we were talking about,” says Andreas Persidis, chief executive of Biovista in Charlottesville, Virginia, one of about 40 companies that now specialize in drug repositioning. “Now it’s a recognized field, and we’re in the typical second stage of scientific trends, when lots of people jump on the bandwagon.”

STARTING POINT

The easiest target for repositioning is generic drugs. They have been on the market for years, their safety profiles are well known and they are easy and cheap to obtain for clinical trials because their original patents have expired. And, if they involve new formulations or applications to new disorders, they can still be covered by patents or be granted three

years of market exclusivity by the US Food and Drug Administration (FDA). So they remain attractive targets for companies.

Biovista, for example, starts by automatically scanning through all the publicly available information on generic compounds, from scientific papers and patents to the database of adverse events compiled by the FDA. Then

it creates a kind of cellular social network, mapping all the connections that it has found between drugs, molecular pathways, genes and other biologically relevant entities. The thinking is that the more connections that a drug has in common with a disease, the more likely it is to be a good candidate for repositioning.

This is how Biovista discovered that pirlindole — a generic antidepressant that was developed and is used in Russia — might be a potential treatment for

multiple sclerosis. In mouse models⁵, the drug slows down the progression of the disease, and is now about to progress to a proof-of-concept study in humans. The company has secured a new patent on pirlindole, as well as on another candidate treatment for multiple sclerosis, still another for epilepsy and three for cancer.

Another source of knowledge is what doctors see in the clinic. “Every drug that’s been around for some years has about 20 off-label uses, two-thirds of which are started by practising physicians,” says Moshe Rogosnitzky, who heads one of the first academic centres for drug repositioning, established last year at Ariel University in Israel. “But the other doctors don’t know about them, because clinicians have a hard time publishing their results.”

So Rogosnitzky and his group systematically canvas these practitioners in Israel and 12 other countries, try to work out a mechanism of action for each reported effect and help the physicians to get patent protection and attract money for further trials. They also help more people to get the drug on an off-label basis. Next July, the group will start a phase II trial to reposition a generic angina drug, called dipyridamole, to treat dry eye disease, a frequent complication for people who have undergone bone-marrow transplants and risk losing their sight because their eyes stop producing tears.

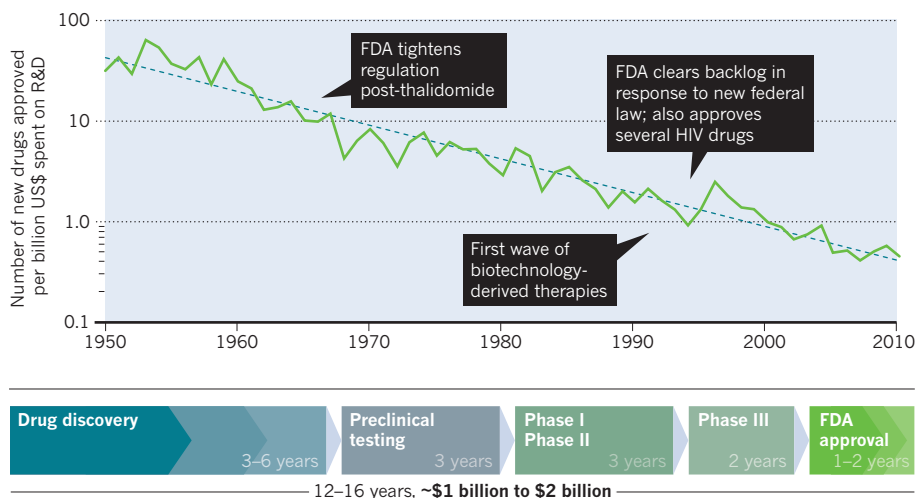
FAILED BUT NOT FORGOTTEN

Another favourite target is the long list of failed drugs. Most of them pass phase I trials, but do not get past phase II because they don’t have the same effect in humans that they had in animals. “Still, there are not many compounds that have some biological activity and are safe in humans, so for heaven’s sake let’s try to do something else with them,” says Gregory Petsko, a

“My feeling is that the proportion of drugs that in theory could be repositioned is probably around 75%.”

EROOM'S LAW

The efficiency of research and development of new drugs in the United States halves every nine years or so. Drug developers sometimes call this Eroom's law — Moore's law for microprocessors in reverse. Repositioning drugs could help to counter this decline.



A SHORTER TIMESCALE

Because most repositioned drugs have already passed the early phases of development and clinical testing, they can potentially win approval in less than half the time and at one-quarter of the cost.

Drug repositioning

~6 years, ~\$300 million

neuroscientist at Weill Cornell Medical College in New York City. The problem is that, apart from really old ones like ebselen, they tend to be locked in the industry's drawers.

"Sometimes, companies make official announcements when they abandon a molecule, but in most cases they don't," says Hermann Mucke, a biochemist who in 2000 founded the Vienna-based firm HM Pharma Consultancy, which now makes a business from hunting through discontinued compounds. "So we monitor a number of sources and look for drugs that have quietly disappeared from pipelines, or for clinical trials that were announced and never led to a publication." When they feel there may be room for repositioning, Mucke and his staff approach the owner of the drug and try to strike a deal that will allow them to do further tests and development — and share in any profits that result. They are also creating a database of drugs that have been approved but are no longer manufactured, and of drugs that have been abandoned during development. "We are developing it for our own use," he says. "But if we can find investors, we would like to turn it into a public resource."

In the absence of such a public resource, both the UK Medical Research Council (MRC) and NCATS have struck deals with major pharmaceutical companies, convincing them to pick some abandoned compounds from their pipelines and release enough information for academic groups to work out whether repositioning might be feasible. "There's a lot of research that could be done but is not happening, simply because academic people are not aware of what pharmaceutical companies are doing," says Christine Colvis, who heads

the NCATS drug-repurposing effort.

Although the MRC programme officially aims to help researchers to understand the biology of diseases, many of the groups that it funds end up doing interesting repositioning work, too. At the University of Manchester, UK, for example, physician-scientist Jacky Smith is testing a compound that was originally developed to treat heartburn to see whether it can help people with chronic cough.

The NCATS programme has drawn criticism, however. "It's good that some groups have had access to some drugs, but that leaves out the vast majority of us," says Petsko. "And there's no guarantee that the compounds in those lists were really the most interesting ones." NCATS spent \$12.7 million on 9 projects in 2013, and 8 of those have progressed to phase II trials. They include a former psoriasis drug that is being tested as a smoking-cessation therapy, a failed diabetes pill that is getting a second chance as a treatment for alcoholism, and a failed cancer drug that is now a potential therapy for Alzheimer's disease. A year from now, says Colvis, the first results of those studies will be published, and if all goes well, at least some of them will progress further. In the meantime, NCATS invested \$2 million last year in another round of projects.

TURNING THE TABLES

In the long run, says Munos, drug repositioning could disrupt big pharma's business model in much the same way that digital music upended big record companies in the 1990s. "When current efforts start resulting in a flow of market approval," he says, "and we see many small companies developing drugs for a few millions of dollars, there will be a lot of interesting

competition with traditional companies."

That optimism is not universal, however. "Not all repositioning projects that work on paper are really feasible," says Tudor Oprea, a bioinformatics researcher at the University of New Mexico in Albuquerque who monitors the field in addition to doing his own repositioning work. For instance, he says, side effects that would be acceptable for a life-threatening disease might not be acceptable for a chronic one. And the standard business case for repositioning — that costs are slashed because safety tests are already in the bag — works only if the dose and mode of administration remain similar. If the new disease requires a significantly higher dose, the drug will have to go through phase I trials again. In the end, says Oprea, development costs can be similar to those for a new molecule.

LaMattina wonders whether the opportunities are really as plentiful as proponents suggest. When companies test a new molecule, he says, they do a wide array of tests on various targets and cell types because they want to anticipate the effects. So if a drug really has interesting effects beyond the expected one, industry scientists will find out for themselves. "It's a bit naive to think that companies overlook all these opportunities to do business," he says. "It's typically people in academia, who don't know what happens in the industry, who think they can do it."

But Persidis argues that many companies are too specialized to benefit from all the repositioning opportunities they have in-house. They may have expertise and market penetration in neurology, but not in oncology, and moving a drug from one field to the other could be out of their strategy. "People like us keep getting business," he says, "and that's because larger companies do appreciate having an external partner looking at their drugs from a different angle."

In the end, says Atul Butte, a bioinformatician at the University of California, San Francisco, drug repositioning is a complement to the discovery of new molecules, rather than an alternative. "We just need more of both," he says. "In modern medicine, we're becoming better at figuring out that each disease is actually five or ten different ones. There are simply not enough companies out there to develop new drugs to treat them all." ■

Nicola Nosengo is a freelance writer in Rome.

1. Singh, N. *et al.* *Nature Commun.* <http://dx.doi.org/10.1038/ncomms2320> (2013).
2. Singh, N. *et al.* *Neuropsychopharmacology* **41**, 1768–1778 (2016).
3. Scannell, J. W., Blanckley, A., Boldon, H. & Warrington, B. *Nature Rev. Drug Discov.* **11**, 191–200 (2012).
4. American Chemical Society. *International Year of Chemistry 2011: Activities Report of the American Chemical Society* (ACS, 2011); available at go.nature.com/1tbzmxn.
5. Lekka, E., Deftereos, S. N., Persidis, A., Persidis, A. & Andronis, C. *Drug Discov. Today Ther. Strateg.* **8**, 103–108 (2011).

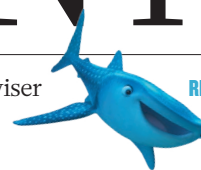
SOURCES: J. W. SCANNELL *ET AL.* *NATURE REV. DRUG DISCOV.* **11**, 191–200 (2012); CYTHERA PHARMACEUTICALS

COMMENT

POLICY Rubric for prioritizing action on the Sustainability Development Goals **p.320**

PHYSICS A fond history of the Cavendish, a lab with few rivals **p.323**

FILM Biomechanics adviser to *Finding Dory* in conversation **p.325**



REPRODUCIBILITY A call to shun predatory journals **p.326**

MICHAEL D. KOCK



Women from a traditional sea-harvesting community fishing in Mozambique.

Fall in fish catch threatens human health

Christopher Golden and colleagues calculate that declining numbers of marine fish will spell more malnutrition in many developing nations.

How will the 10 billion people expected to be living on Earth by 2050 obtain sufficient and nutritious food? This is one of the greatest challenges humanity faces. Global food systems must supply enough calories and protein for a growing human population and provide important micronutrients such as iron, zinc, omega-3 fatty acids and vitamins.

Deficiencies of micronutrients — so called because the body needs them only in tiny amounts — can increase the risks of perinatal and maternal mortality, growth retardation, child mortality, cognitive deficits and reduced immune function¹. The associated burdens of disease are large. Forty-five per cent of mortality in children

under five is attributable to undernutrition; nutritional deficiencies are responsible for 50% of years lived with disability in children aged four and under¹.

Fish are crucial sources of micronutrients, often in highly bioavailable forms. And fish populations are declining. Most previous analyses have considered only how people will be affected by the loss of protein derived from fish. We calculate that this is the tip of the iceberg. Combining data on dietary nutrition, and fish catch, we predict that more than 10% of the global population could face micronutrient and fatty-acid deficiencies driven by fish declines over the coming decades, especially in the developing nations at the Equator (see ‘Troubled

Waters.’ This new view underlines the need for nutrition-sensitive fisheries policies.

NUTRITIONAL RISK

Presently, 17% of the global population is zinc deficient, with some subpopulations being particularly at risk¹. Nearly one-fifth of pregnant women worldwide have iron-deficiency anaemia and one-third are vitamin-A deficient¹. We estimate that 845 million people (11% of the current global population) are poised to become deficient in one of these three micronutrients if current trajectories in fish-catch declines continue.

Considering nutrients found only in foods derived from animals, such as vitamin B₁₂, and DHA omega-3 fatty acids ►

► (almost exclusively derived from meat consumption, see Supplementary Information; go.nature.com/25oll0p), we calculate that 1.39 billion people worldwide (19% of the global population) are vulnerable to deficiencies because fish make up more than 20% of their intake of these foods by weight.

IMPACT ASSESSMENT

To make this sobering new assessment, we coupled two databases from 2010, the most recent year for which both had data. The new Global Expanded Nutrient Supply (GENuS) database combines food balance sheets (total quantity of food production and imports minus livestock feed, post-harvest losses, and exports) and production or trade data from the Food and Agriculture Organization of the United Nations (FAO) with estimates of food group intake by age and sex². It estimates per capita edible supplies for 225 foods, paired with regional food composition tables to infer nutrient supplies by country. GENuS is supported by the Bill and Melinda Gates Foundation and the Winslow Foundation.

We categorized populations as nutritionally vulnerable if their nutrient supply was less than double the estimated average requirement (EAR), and if they derived from fish more than 10% of their vitamin A or zinc, or more than 5% of their iron. We chose to double the EAR for two reasons. First, even in countries where the national average intake is greater than the EAR, large variability of intake may still mean that a significant part of the population is eating less well. If we had used the EAR as our threshold, more than 50% of a nation's population would need to be deemed at risk of nutritional deficiency, which we feel is an irresponsibly high proportion required for raising an alarm. Second, our GENuS-derived estimates measure food supply rather than food intake, and are generally regarded as overestimates of true intake³.

The Sea Around Us database, released in 2016, provides a portrait of marine fisheries catch between 1950 and 2010 for every coastal nation³. Over 15 years, a team of researchers in every coastal country collated information from government documents, academic research and maritime records to reconstruct the numbers of fish caught. This database measures the contribution of subsistence, artisanal and industrial marine fisheries to food supply at the country level more accurately than previous estimates³. This database was funded by the Pew Charitable Trust and the Paul G. Allen Family Foundation and is maintained by staff at the University of British Columbia in Vancouver, Canada.

These global marine catch data are alarming. Conservative estimates by the FAO characterize global fisheries as stable, but acknowledge that global catch has declined by 0.38 million tonnes per year since 1996 (ref. 4). The Sea Around Us estimates summarized

earlier this year³ paint a much bleaker picture, in which fish catch peaked in 1996 and has been falling by 1.22 million tonnes (roughly 1%) per year since — three times faster than the decline reported by FAO. The degradation of marine habitat by destructive fishing practices, industrial pollution, climate change and coastal development for urbanization and aquaculture is likely to further degrade ocean ecosystems and reduce fisheries yields. Such patterns call into question the ability of wild fisheries to support future demand for fish.

PERFECT STORM

The health impacts of fishery declines will hit some places harder than others. A perfect storm is brewing in the low-latitude developing nations. This is where human nutrition is most dependent on wild fish, and where fisheries are most at risk from illegal fishing, weak governance, poor knowledge of stock status, population pressures and climate change.

Sharp declines in the health of fisheries were first described in the twentieth century in high-latitude regions where industrial fishing began, such as the northwest Atlantic Ocean. Developed countries have compensated with intensive agricultural production, by importing goods (including fish), vitamins, supplements and fortified foods. Since the 1990s, the major declines in fish stocks have been in lower latitudes and developing nations. This rapid degradation probably results from the increasing industrialization of fisheries, poor governance and the accelerated expansion of foreign fishing in these regions.

These sensitivities in the tropics will be only exacerbated by climate change. Ocean warming and shifts in net primary production are likely to drive remaining fish and shellfish species from low to high latitudes, potentially reducing catch globally by more than 6% and by as much as 30% in some regions (such as the tropics) by 2050 relative to recent decades⁵. Fish will also probably get smaller in the tropics: ocean warming and associated declines in oxygen content are projected to reduce the average biomass of fish communities by around 20% during this period⁶. Coral reefs, essential ecosystems for many tropical coastal subsistence and artisanal fisheries, will be heavily degraded by warming and ocean acidification. Mangroves — nurseries for many fish that are crucial in developing nations — continue to decline. Also under threat are global inland freshwater fisheries, another crucial source of nutrition and livelihood for hundreds of millions of people around the world⁷.

In these same regions, fish play an important part in the avoidance of diseases associated with malnutrition. Nearly all countries that depend heavily on fish for nutrition are situated in the developing world (46 of 49); we

defined these as nations in which more than 20% of the population's animal-based food by weight is seafood. Furthermore, countries with the highest levels of undernourishment and the weakest governance are often net exporters of seafood to well-nourished countries with strong governance⁸.

Poor people have fewer alternatives to make up for these impending shortfalls in access to micronutrients. Meat, eggs, vitamin supplements and imported fish can be prohibitively expensive. Communities are often forced to rely on what they can harvest locally or on less-healthy processed foods.

FARMED FISH

Could global increases in fish farming meet the nutritional shortfalls we predict for poor equatorial populations? With today's production and distribution patterns, we think not. Aquaculture has expanded globally by more than an order of magnitude over the past three decades⁹. Farmed fish exceeded wild catch destined for human consumption for the first time in 2014 (ref. 10). However, aquaculture has not yet developed significantly in many low-income countries where food and technology is in short supply (particularly sub-Saharan Africa and the Pacific Islands¹¹). Such regions still largely depend on domestic, subsistence and artisanal fishing. These small-scale fisheries include the pirogue fleets of West Africa, the spearfishers of the world's coral reefs, and shore-based gathering of shellfish in mangrove creeks.

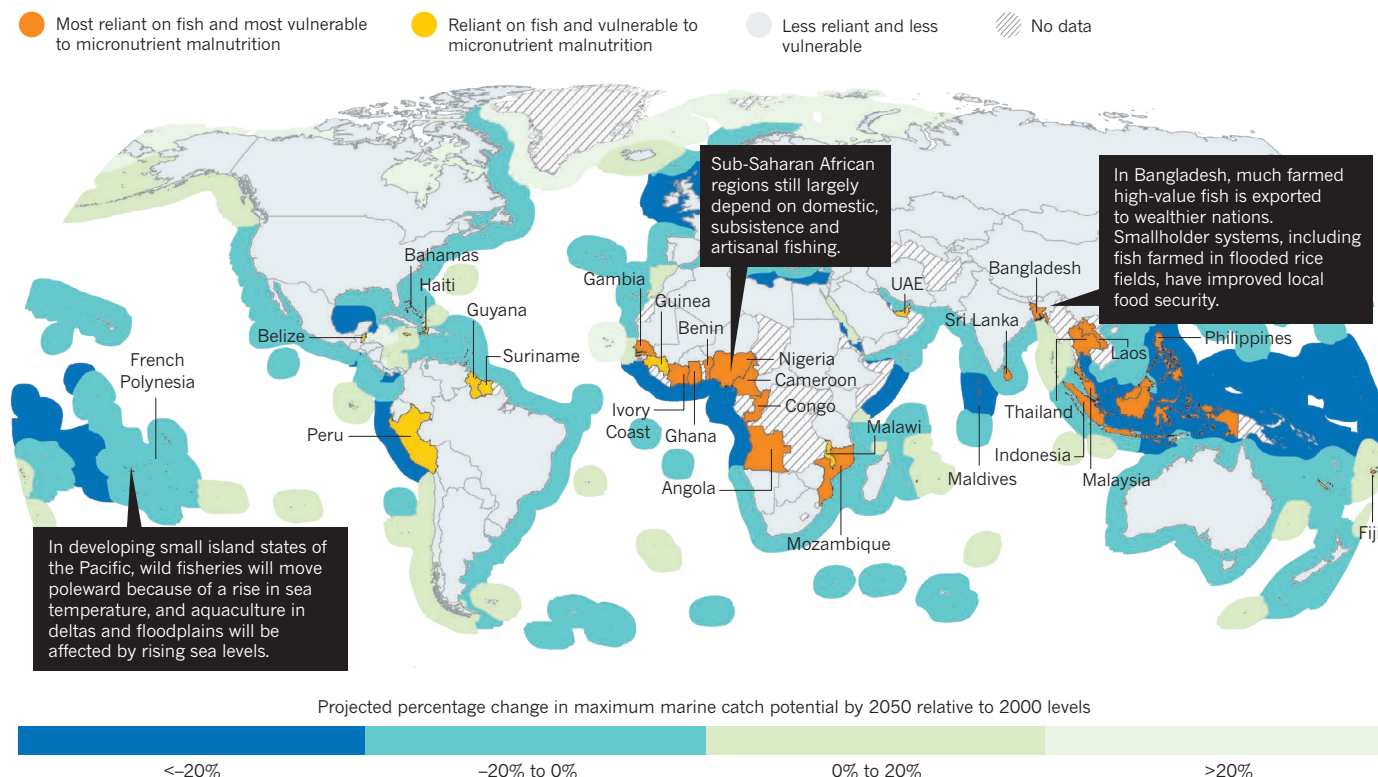
Where aquaculture is growing, much of it has been aimed at wealthier consumers in domestic cities or in international markets, rather than local rural areas¹². Globally, developing countries export higher value fish (caught and farmed) and import lower-value food from industrial fisheries in developed countries¹³. For example, shrimp, tilapia and Mekong catfish grown in developing and transitional countries such as Bangladesh, China, Indonesia, Ecuador, Thailand and Vietnam are mostly exported to the wealthy countries of Europe and North America, or consumed by the growing middle-classes in the megacities of these economies. The benefits of these export-oriented industries to livelihoods and nutrition of the coastal poor are unclear and cannot be inferred from national seafood balance data or national economic growth statistics¹³. Moreover, commercial aquaculture can displace coastal and inland fisheries, and small-scale aquaculture producers may not always profit from engagement in global value chains.

Farmed fish may also be of lower nutritional value¹². Aquaculture species that are most affordable, such as carp, are often not as rich in omega-3 fatty acids as are the wild species currently accessible to impoverished communities, such as sardines and mackerels. Oil-rich wild fish are also the basis for

“Poor people have fewer alternatives.”

TROUBLED WATERS

In the low-latitude developing nations, human nutrition is most dependent on wild fish, and fisheries are most at risk from illegal fishing, weak governance, poor knowledge of stock status, population pressures and climate change. These countries urgently need effective strategies for marine conservation and fisheries management to rebuild stocks for nutritional security.



aquaculture feeds. Because supplies of these wild-fish have little potential for expansion under current management policies, plant-based feeds are increasingly used, further altering the nutritional composition of farmed fish. And aquaculture generally focuses on fewer species than those caught from the wild. A global fish supply dominated by aquaculture, as it is currently practiced, would lead to a drop in the diversity, and thus nutritional quality, of many diets¹².

Yet, when explicitly planned to improve local well-being, aquaculture can be a crucial contribution to local diets and economies. For example, in Bangladesh, smallholder integrated systems in which fish are raised in rice paddies have improved local food security¹⁴. Small indigenous fish, rich in nutrients, can be grown for household consumption in ponds together with carp, tilapia or catfish as cash crops. Less-intensive and more-diverse forms of aquaculture may have the most potential to meet the nutrition and food-security needs of the poor.

This promise may, however, be constrained by lack of suitable sites. Both inland and coastal production are under increasing pressure from urbanization and industrialization. In the same small island states likely to be hit hardest by shifts in the distribution of marine species⁵, prospects for increasing aquaculture are at best mixed. Much aquaculture production is concentrated in river deltas and

floodplains, brackish-water lagoons and other low-lying tropical coastal areas. These areas will be heavily affected by sea-level rise, ocean acidification and increased storm intensity. Non-intensive aquaculture technologies face many challenges and are currently minor contributors to global production.

NEXT STEPS

Next-generation models that integrate data on human health and fisheries, such as those explored here, with climate and population models need to play an important part in estimating the human health burdens of environmental change and the enormous public health dividends of natural-resource management. These models can also be used to identify hotspot countries that urgently need more effective strategies for marine conservation and fisheries management to rebuild stocks for nutritional security³.

Aquaculture also needs reform so that undernourished people can access nutritious products. The following can help: boosting investment in less intensive and domestically oriented aquaculture of cheap and nutritious species; farming species lower in the food chain to reduce dependence on wild-caught fish meal; and allocating coastal land and water resource rights to small-scale aquaculture (as has already been done for fisheries).

The analytical methods currently in use to inform fisheries and aquaculture policies

require refinement. Data on food-price fluctuations are needed for local economic models of fish supply and dietary substitution, and empirical research is required to understand and model how populations around the world will adapt to changes in fish supply and market prices. We need better data on freshwater fisheries and aquaculture, as well as on the nutrient composition of foods and nutritional status of more human populations around the world. Improvements should include separating data on farmed and wild fish to better characterize vulnerability to micronutrient deficiencies.

Addressing these emerging problems will require new interdisciplinary partnerships among fisheries scientists, aquaculture technologists, ecosystem managers, nutrition and public-health specialists, development economists, granting agencies and policymakers. As a first step, new funding streams are required to support the emerging discipline of planetary health, dedicated to characterizing and quantifying the human health impacts of accelerating global environmental change. For example, our work has been supported by the Wellcome Trust, the US National Socio-Environmental Synthesis Center and the Rockefeller Foundation. A second step would be more interaction between health agencies (such as the World Health Organization, the United Nations children's fund UNICEF, and health

ministries) and ocean-management agencies (such as the FAO, the UN Environmental Programme, regional fisheries management organizations, and ministries of fisheries and the environment).

Mitigating losses of biodiversity and income have been at the heart of fisheries-management policies. In our view, there should be a much stronger emphasis on human health. This would mirror recent shifts in agricultural policy that respond to rising burdens of diet-related diseases.

These policy changes are possible. We believe that improvements in fisheries management and marine conservation can serve as nutritional delivery mechanisms. A meta-analysis of nearly 5,000 fisheries worldwide found that applying sound management reforms to global fisheries could increase catch by more than 10%¹⁵. Without these changes, the health of the poor is at risk. ■

Christopher D. Golden is a research scientist at the Harvard T.H. Chan School of Public Health, and associate director of the Planetary Health Alliance at the Harvard University Center for the Environment, Harvard University, Cambridge, Massachusetts, USA.

Edward H. Allison, William W. L. Cheung, Madan M. Dey, Benjamin S. Halpern, Douglas J. McCauley, Matthew Smith, Bapu Vaitla, Dirk Zeller and Samuel S. Myers.
e-mail: golden@hsph.harvard.edu

1. Black, R. E. *et al.* *Lancet* **382**, 427–451 (2013).
2. Smith, M. R., Micha, R., Golden, C. D., Mozaffarian, D. & Myers, S. S. *PLoS ONE* **11**, e0146976 (2016).
3. Pauly, D. & Zeller, D. *Nature Comm.* **7**, 10244 (2016).
4. Food and Agriculture Organization of the United Nations. *The State of World Fisheries and Aquaculture (SOFA) 2010* (FAO, 2011).
5. Cheung, W. W. L. *et al.* *Ecol. Model.* **325**, 57–66 (2016).
6. Cheung, W. W. L. *et al.* *Nature Clim. Change* **3**, 254–258 (2013).
7. Youn, S. J. *et al.* *Glob. Food Sec.* **3**, 142–148 (2014).
8. Smith, M. D. *et al.* *Science* **327**, 784–786 (2010).
9. World Bank. *Fish to 2030: Prospects for Fisheries and Aquaculture* (World Bank, 2014).
10. OECD/Food and Agriculture Organization of the United Nations. *OECD–FAO Agricultural Outlook 2015–2024* (2015); available at http://dx.doi.org/10.1787/agr_outlook-2015-en
11. Hall, S. J. *et al.* *Proc. Nat. Acad. Sci.* **110**, 8393–8398 (2013).
12. Thilsted, S. *et al.* *Food Policy* **61**, 126–131 (2016).
13. Asche, F., Bellemare, M. F., Roheim, C., Smith, M. D. & Tveteras, S. *World Dev.* **67**, 151–160 (2015).
14. Dey, M. M. *et al.* *Food Policy* **43**, 108–117 (2013).
15. Costello, C. *et al.* *Proc. Nat. Acad. Sci. USA* **113**, 5125–5129 (2016).

Full author details and Supplementary Information accompany this article online at go.nature.com/25oll0p.



Solar lights are used by vendors in rural western India, where lack of electricity has stymied development.

Map the interactions between Sustainable Development Goals

Måns Nilsson, Dave Griggs and Martin Visbeck present a simple way of rating relationships between the targets to highlight priorities for integrated policy.

Next month in New York, the United Nations' 2030 Agenda on Sustainable Development will have its first global progress review. Adopted by the UN General Assembly in 2015, the agenda represents a new coherent way of thinking about how issues as diverse as poverty, education and climate change fit together; it entwines economic, social and environmental targets in 17 Sustainable Development Goals (SDGs) as an 'indivisible whole'.

Implicit in the SDG logic is that the goals depend on each other — but no one has specified exactly how. International negotiations gloss over tricky trade-offs. Still, balancing interests and priorities is what policymakers do — and the need will surface when the goals are being implemented. If countries ignore the overlaps and simply start trying to tick off targets one by one, they risk perverse outcomes. For example, using coal to improve energy access (goal 7) in Asian

nations, say, would accelerate climate change and acidify the oceans (undermining goals 13 and 14), as well as exacerbating other problems such as damage to health from air pollution (disrupting goal 3).

If mutually reinforcing actions are taken and trade-offs minimized, the agenda will be able to deliver on its potential. For example, educational efforts for girls (goal 4) in southern Africa would enhance maternal health outcomes (part of goal 3), and contribute to poverty eradication (goal 1), gender equality (goal 5) and economic growth (goal 8) locally.

The importance of such interactions is built into the SDGs: 'policy coherence' is one of the targets. The problem is that policymakers and planners operate in silos. Different ministries handle energy, agriculture and health. Policymakers also lack tools to identify which interactions are the most important to tackle, and evidence to show how particular interventions and policies help or hinder progress towards the goals. Many preconceptions that influence decisions are outdated or wrong, such as the belief that rising inequalities are necessary for economic growth, or that mitigating climate change is bad for productivity growth in the long term¹.

To make coherent policies and strategies, policymakers need a rubric for thinking systematically about the many interactions — beyond simply synergies and trade-offs — in order to quickly identify which groups could become their allies and which ones they will be negotiating with. And they need up-to-date empirical knowledge on how the goals and interventions of one sector affect another positively or negatively.

As a first step, we propose a seven-point scale of SDG interactions (see 'Goals scoring') to organize evidence and support decision-making about national priorities. This should help policymakers and researchers to identify and test development pathways that minimize negative interactions and enhance positive ones. And it is globally applicable so that countries can compare and contrast, and learn from each other and over time.

SEVEN INTERACTION TYPES

We rate seven possible types of interactions, from the most positive (scoring +3) to the most negative (−3). These can be applied at any level — among goals and targets, to individual policies or to actions (see 'The wins and losses en route to zero hunger').

For practical policymaking, the process should start from a specific SDG — in line with a minister's mandate — and map out, score and qualify interactions in relation to the other 16 goals and their targets.

Positive interactions lend themselves to building strategies across sectors. The three negative types will be subject to trade-offs, and the target of extra regulations and policies, such as bans. But negative-scoring

GOALS SCORING

The influence of one Sustainable Development Goal or target on another can be summarized with this simple scale.

Interaction	Name	Explanation	Example
+3	Indivisible	Inextricably linked to the achievement of another goal.	Ending all forms of discrimination against women and girls is indivisible from ensuring women's full and effective participation and equal opportunities for leadership.
+2	Reinforcing	Aids the achievement of another goal.	Providing access to electricity reinforces water-pumping and irrigation systems. Strengthening the capacity to adapt to climate-related hazards reduces losses caused by disasters.
+1	Enabling	Creates conditions that further another goal.	Providing electricity access in rural homes enables education, because it makes it possible to do homework at night with electric lighting.
0	Consistent	No significant positive or negative interactions.	Ensuring education for all does not interact significantly with infrastructure development or conservation of ocean ecosystems.
−1	Constraining	Limits options on another goal.	Improved water efficiency can constrain agricultural irrigation. Reducing climate change can constrain the options for energy access.
−2	Counteracting	Clashes with another goal.	Boosting consumption for growth can counteract waste reduction and climate mitigation.
−3	Cancelling	Makes it impossible to reach another goal.	Fully ensuring public transparency and democratic accountability cannot be combined with national-security goals. Full protection of natural reserves excludes public access for recreation.

interactions might also attract public investment in technologies and solutions that over time might push the needle up the scale.

There are four main considerations when applying the scale. First, is the interaction reversible or not? For example, failing on education (goal 4) could irreversibly damage social inclusion (goal 8). Loss of species owing to lack of action on climate change (goal 13) is another irreversible interaction. Conversely, converting land use from agriculture to bioenergy production (goal 7) might counteract food security (goal 2) and poverty reduction (goal 1) but could be reversed.

Second, does the interaction go in both directions? For instance, providing energy to people's homes benefits education, but improving education does not directly provide energy.

A third consideration is the strength of the interaction: does an action on one goal have a large or small impact on another? Negative interactions can be tolerable if they are weak, such as the constraints that land resources might put on the development of transport infrastructure.

Fourth, how certain or uncertain is the

interaction: is there evidence that it will definitely happen or is it only possible?

CONTEXT MATTERS

Countries must interpret the SDGs according to their national circumstances and levels of development, so interaction scores will vary. Differences in geography, governance and technology make it dangerous to rely on generalized knowledge.

The regional resource base makes a big difference. For instance, bioenergy production is widely assumed to counteract food security through land competition. But in the Nordic region, bioenergy markets have reinforced the agricultural and forest production systems — offering new and more diversified market opportunities and increasing farmers' and forest owners' resilience². Introducing technologies can render interactions more positive. For example, a transition to electric cars, fuelled by low-carbon power, could make personal-car-based mobility more consistent with climate-change goals.

Negative interactions may be the result of weakness in institutions, legal rights or governance procedures, which marginalize vulnerable groups. For example, poorly governed industrialization and infrastructure development (goal 9) in emerging economies or agricultural productivity

"There is no formal platform for sharing knowledge related to the goals."

efforts (goal 2) can counteract local livelihoods and increase inequalities (working against goal 10).

Timescale matters: intensifying food production to end hunger in places where resources are scarce may be feasible in the short term, but over time can deplete fisheries and forests. And spatial scale matters, too: for instance, industrial development may cause pollution and adversely affect the local environment and people's health, but may also generate wealth that can support national health infrastructure. Politicians might mandate that health plans directly benefit the local community.

This conceptual framework is a starting point for building an evidence base to

characterize the goal interactions in specific local, national or regional contexts. There is no formal platform for sharing such knowledge yet, but the International Council for Science (ICSU) is beginning to use the framework and populate it with empirical evidence³. The ICSU is bringing together research teams of leading experts from universities and institutes around the world to develop thematic case studies, starting with the SDGs for health, energy and food. Each team will define the expertise needed to characterize and quantify the domain's interactions with all other SDGs, organize existing knowledge about these interactions, and identify key gaps and priorities.

Many knowledge gaps will surface. For

example, the relationship between urban developments and human health and well-being is only beginning to be studied. Filling the gaps will be costly and will require contributions from research councils and funders such as the European Union's Horizon 2020 framework, as well as governments and universities. The UN should consider how best to track interactions in its SDG monitoring systems, which is now being designed. Tracking interactions will be more complicated than monitoring single sectors, but it could be done in detail in a few key places, such as for the nine SDG pilot countries, which include Uganda and Vietnam.

This interactions framework is intuitive, relatively easy to use and broadly replicable. It will facilitate the accumulation of knowledge and policy learning across countries. To further ensure that the research meets governments' needs, the ICSU and other knowledge brokers such as the Organisation for Economic Co-operation and Development and the UN should convene a series of dialogues and workshops around interactions and how to apply them to policy-making. A first opportunity to put SDG interactions on the agenda is at next month's high-level political forum, where 22 countries, including Germany and Colombia, will report back on their early action plans. ■

Måns Nilsson is research director at the Stockholm Environment Institute, Stockholm, Sweden, and professor of the practice of policy analysis at the KTH Royal Institute of Technology, Stockholm, Sweden. **Dave Griggs** is professor in sustainable development at the Monash Sustainability Institute, Monash University, Melbourne, Australia, and Warwick University, Coventry, UK. **Martin Visbeck** is professor in physical oceanography at GEOMAR Helmholtz Centre for Ocean Research Kiel and Kiel University, Kiel, Germany. e-mail: mans.nilsson@sei-international.org

1. Organisation for Economic Co-operation and Development. *OECD Economic Outlook Volume 2015 Issue 2* (OECD, 2015).
2. Hakkila, P. *Biomass Bioenergy*, **30**, 281–288 (2006).
3. International Council for Science. *A Draft Framework for Understanding SDG Interactions* (ICSU, 2016); available at <http://bit.ly/sdg-interactions>
4. Foley, J. A. *et al. Nature* **478**, 337–342 (2011).
5. Food and Agriculture Organization of the United Nations. *Agriculture, Forestry and Other Land Use Emissions by Sources and Removals by Sinks* (FAO, 2015).

CORRECTION

Reference 1 in the Comment 'Create a global microbiome effort' (N. Dubilier *et al. Nature* **526**, 631–634; 2015) gave incorrect page numbers. It should have read: Alivisatos, A. P. *et al. Science* **350**, 507–508 (2015).



A hydropowered irrigation pump in use at the Kabwadu Women's Banana Farm in Zambia.

WORKED EXAMPLE

The wins and losses en route to zero hunger

In sub-Saharan Africa, ending hunger (goal 2) interacts positively with several other goals — including poverty eradication (goal 1), health promotion (goal 3) and achieving quality education for all (goal 4). Addressing chronic malnourishment is 'indivisible' from addressing poverty — which gains the interaction a score of +3. Tackling malnourishment reinforces (+2) educational efforts because children can concentrate and perform better in school. Not addressing food security would counteract (–2) education, when the poorest children have to help provide food for the day.

Food production interacts with climate-change mitigation (goal 13) in several ways, because agriculture represents 20–35% of total anthropogenic greenhouse-gas

emissions⁴. Climate mitigation constrains (–1) some types of food production, in particular those related to meat (methane release from livestock constitutes nearly 40% of the global agricultural sector's total emissions)⁵. Yet food production is reinforced (+2) by a stable climate. Securing food from fisheries is also reinforced by protecting the climate, because that limits ocean warming and acidification.

Finally, in some parts of sub-Saharan Africa, promoting food production can also constrain (–1) renewable-energy production (goal 7) and terrestrial ecosystem protection (goal 15) by competing for water and land. Conversely, limited land availability constrains (–1) agricultural production.



CAVENDISH LAB./UNIV. CAMBRIDGE

Ernest Rutherford (right) and Jack Ratcliffe in the Cavendish Laboratory in 1932.

PHYSICS

Crucible of science

Graham Farmelo ponders Malcolm Longair's study of the Cavendish, a physics laboratory with few rivals.

Physics laboratories are a relatively recent innovation. They started to spring up 150 years ago, centuries after investigators began trying to understand the inanimate world using observation and rational thought. Chemists were ahead of the game — their first laboratories appeared a quarter of a millennium earlier (D. Lowe *Nature* **521**, 422; 2015).

In 1927, Ernest Rutherford spoke at the opening of the H. H. Wills Physics Laboratory at the University of Bristol, UK. He said: "Our pure science laboratories should in the main be set aside for fundamental

research." Those that did research relating to industry should be funded by the government or manufacturers, in places "where the research workers can come into close contact with manufacturing conditions". Rutherford was at the time director of the Cavendish Laboratory at the University of Cambridge, UK — a world-leading institution for experimental physics. Today, his purism looks

**Maxwell's
Enduring Legacy:
A Scientific History
of the Cavendish
Laboratory**
MALCOLM LONGAIR
Cambridge University
Press: 2016.

almost quaint, with most academic physics laboratories relying heavily on support from industry and other sources.

In what is patently a labour of love, the astronomer Malcolm Longair now gives us a comprehensive scientific history of the Cavendish in *Maxwell's Enduring Legacy*. Longair, who was the lab's head from 1997 to 2005, describes its inception well. Its early development in the 1870s, on a small site near the centre of town, was bankrolled by the university's chancellor, William Cavendish. He was among those who wanted to ensure that Cambridge could continue to supply top-notch graduates to help to administer the increasingly technological British Empire. Several sceptics, particularly among the champions of the prestigious natural-sciences course, the Tripos, argued that experimental training was unnecessary. The mathematician Isaac Todhunter wrote: "Experimentation is unnecessary for the student." He believed that "the student should be prepared to accept whatever the master told him".

The venture made an excellent start, Longair shows, when James Clerk Maxwell was appointed its first director. A strong mathematician with almost superhuman physical intuition, he was determined to nurture experimentation, and had extraordinarily wide interests. He was as eager to explore the new technology of wireless telegraphy as he was to master modern topological mathematics. After his death in 1879 at just 48, the university appointed as his successor John William Strutt, Lord Rayleigh, a versatile physicist who went on to discover argon and win a Nobel prize. Strutt's five years in the post consolidated the reputation of the lab. He was succeeded by theorist J. J. Thomson, who, although not a dexterous experimenter, discovered the electron at his bench there in 1897. With Thomson at the helm, the Cavendish rivalled the mighty Imperial Physical Technical Institute in Berlin as the world's pre-eminent centre for experimental physics.

The next director, Rutherford, died unexpectedly in 1937 after a botched operation. In the quest to find his successor, Longair says, the crystallographer Lawrence Bragg was the "obvious choice". This surprised me. In 1992, theoretical physicist Rudolf Peierls, who knew the lab well, told me that Rutherford's deputy James Chadwick (discoverer of the neutron) was the widely tipped successor, and that the failure to appoint him led to "a minor scandal". Either way, Bragg proved a far-sighted leader, and his promotion of crystallography yielded impressive results. Notably, Francis Crick and James Watson gave the Cavendish one of its greatest triumphs by identifying the structure of DNA in 1953.

The quantum theorist Nevill Mott, appointed director in 1954, continued the policy of diversification and expansion. Teaching and research activity doubled, ▶

► and the lab's Radio Astronomy Group, led by Martin Ryle, had a series of successes, most famously the discovery of pulsars by Jocelyn Bell Burnell in 1967, working with her supervisor Antony Hewish (A. Hewish *et al.* *Nature* **217**, 709–713; 1968). By this time, the Cavendish was so large that its director was not so much a powerful commander-in-chief as chair of a company, as Longair aptly describes it.

The lab's research had outgrown its space: the number working there had risen from around a dozen in the 1870s to some 40 times that number. In 1973, the next director, Brian Pippard, moved the Cavendish to much larger premises in West Cambridge, the workplace of about 1,000 people. Longair chronicles this move and presents the achievements of Pippard and his successors as Cavendish Professor of Physics, Sam Edwards and Richard Friend, with detail that will satisfy the most assiduous reader of annual reports. The breadth and depth of the areas of physics now being explored by the laboratory are remarkable: all its previous specialities, as well as everything from optoelectronics to medical physics, thin-film magnetism and the physics that underlies studies of the sustainability of the global economy.

Longair's history is in the form of a well-organized modern physics book, most of its 22 sections replete with charts, tables and lucid technical explanations presented neatly in boxes. Abundant diagrams, photographs, line drawings, floor-plans and facsimiles of historical documents give fascinating insights into the lab's development. Very much the account of an insider, the book would have benefited from a wider international perspective.

It would also have been interesting to hear more about the challenges that the lab faces to preserve its eminence. Rutherford kept an eye on almost every research project — no longer feasible for even the most energetic director — and took personal responsibility for keeping his fiefdom fleet of foot so that it could respond quickly to developments. The main challenge of directing the laboratory today, I imagine, is to ensure that the elephant can keep dancing. ■

Graham Farmelo is a by-fellow at Churchill College of the University of Cambridge, UK, and author of *Churchill's Bomb*.
e-mail: graham@grahamfarmelo.com

MEDICAL RESEARCH

Citizen medicine

Sally Frampton and Sally Shuttleworth explore a show on public involvement in the evolution of vaccination.

The introduction of vaccination in the late eighteenth century is often viewed as a defining moment, when modern medicine began to stem the ravages of disease. But it has not just been down to pioneering doctors: members of the public have been significant in shaping the development of vaccination, both as practitioners and as critics. *Vaccination: Medicine and the Masses*, an exhibition at the Royal College of Surgeons' Hunterian Museum in London, seeks to unravel those threads with photographs, letters, pamphlets, specimens and medical devices.

The exhibition is part of Constructing Scientific Communities (<http://conscicom.org>), a project on citizen science past and present for which we are researcher (S.F.) and principal investigator (S.S.). In 1798, physician Edward Jenner published *An Inquiry into the Causes and Effects of the Variolæ Vaccinæ* (a draft manuscript features in the exhibition). It showed that protection from the deadly, disfiguring disease smallpox could be conferred by exposure to the much milder cowpox. Jenner's experiments convinced fellow medics, but were themselves inspired by the observations of farming communities in south-west England that milkmaids (prone to cowpox infection, acquired by handling the udders of infected animals) hardly ever caught smallpox.

Local knowledge and volunteers remain key to successful vaccination programmes. The Global Polio Eradication Initiative, for example, has involved more than 20 million volunteers since it began in 1988, many working in dangerous conditions (H. J. Larson and I. Ghinai *Nature* **473**, 446–447; 2011). One story highlighted in the exhibition focuses on Ali Maow Maalin, the Somali cook who was the last person to be infected with naturally occurring smallpox. After he recovered, Maalin campaigned for polio eradication. He died of malaria in 2013, while carrying out polio vaccinations.

But public resistance has also dogged vaccination, as the exhibition makes clear. In the nineteenth and twentieth

Vaccination: Medicine and the Masses
Hunterian Museum,
London.
Until 17 September
2016.

centuries, pamphlets from Britain's National Anti-Vaccination League and others played on fears that the procedure poisoned children's blood and

laid them open to a host of diseases. Resistance grew to the British government's compulsory smallpox-vaccination programme, established in 1853. By 1907, the programme was effectively abolished.

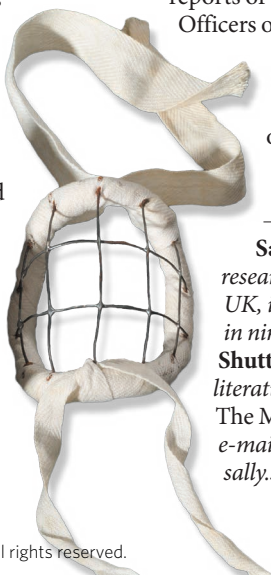
The diseases have changed, but scepticism remains dangerous — not least because of the lingering impact of Andrew Wakefield's discredited work hinting at a link between the measles, mumps and rubella (MMR) jab and autism, published almost 20 years ago. US and UK outbreaks of measles in recent years have had a strong correlation with vaccine refusal.

As highlighted by Constructing Scientific Communities, citizen science now benefits from digital platforms such as Zooniverse, which enable projects that range from identifying galaxies to analysing cancer cells. That potential makes it timely now to look back to when barriers between professional and amateur science had not yet been erected. Researchers are looking, for instance, at mass involvement in Victorian public-health movements such as the drive to stop air and water pollution, and at the local natural-history groups whose records still serve as benchmarks. With Zooniverse, we are creating projects drawing on historical records of the era: *Diagnosis London*, for instance, will enable people to analyse reports of the nineteenth-century Medical Officers of Health for London.

Like *Vaccination*, these projects offer fascinating insights into the lives of people faced with an array of public-health challenges, and into the medical science that is running to keep up with them. ■

Sally Frampton is a postdoctoral researcher at the University of Oxford, UK, investigating public involvement in nineteenth-century medicine. **Sally Shuttleworth** is professor of English literature at Oxford. Her latest book is *The Mind of the Child*.
e-mails: sally.frampton@ell.ox.ac.uk;
sally.shuttleworth@st-annes.ox.ac.uk

A nineteenth-century 'shield', used to protect vaccination sites.



Correspondence

Ban predators from the scientific record

Predatory journals are threatening the credibility of science. By faking or neglecting peer review, they pollute the scholarly record with fringe or junk science and activist research. I suggest that every publishing stakeholder could contribute to reining in these journals.

Universities and colleges should stop using the quantity of published articles as a measure of academic performance. Researchers and respectable journals should not cite articles from predatory journals, and academic library databases should exclude metadata for such publications.

Companies that supply services to publishers, including those that license journal-management software or provide standard identifiers, should decline to work with predatory publishers.

Scholarly databases such as Scopus and Thomson Reuters Web of Science need to raise the bar for acceptance, eliminating journals and publishers that use flawed peer-review practices. The US National Center for Biotechnology Information should do the same for PubMed and PubMed Central.

Finally, advocates of open-access publication must stop pretending that the author-pays model is free of serious, long-term structural problems (see J. Beall *Nature* **489**, 179; 2012). Just because it works well in a few cases doesn't mean it always works.

Jeffrey Beall *Auraria Library, University of Colorado Denver, USA.*
jeffrey.beall@ucdenver.edu

Hail local fieldwork, not just global models

We contend that science's 'publish-or-perish' culture, which selects for rapid publication in high-ranking journals, has contributed to the

demise of field-based studies (see K.-D. Dijkstra *Nature* **533**, 172–174; 2016).

Top-tier journals tend to favour large-scale analyses that answer big, general questions (see J. M. Fitzsimmons and J. H. Skevington *Nature* **466**, 179; 2010), presumably because they help to boost journal impact factors. Unlike basic ecological and observational studies, such analyses seldom involve the collection of new, local field data. Instead, they depend mainly on modelling of published information, often over scales that would be logistically and economically challenging for conventional field investigations.

Because publication in leading journals is science's currency to capture funding, funders also tend to select against field-based research studies — including those with undeniable reach and importance, such as long-term biodiversity monitoring (see T. Birkhead *Nature* **514**, 405; 2014).

Given the current biodiversity crisis, journals and funding agencies — as well as the scientific community — must act to reverse this trend.

Catarina Ferreira *Trent University, Peterborough, Canada.*
C. Antonio Ríos-Saldaña *BioCórima, Arteaga, Mexico.*
Miguel Delibes-Mateos *Institute for Advanced Social Studies (IESA-CSIC), Córdoba, Spain.*
catferreira@gmail.com

A code of conduct for data on epidemics

As a long-term champion of open-access research data on pandemic viruses and a member of the Italian Parliament, I urge Brazil to hasten the reform of its current biosecurity legislation. This would enable sharing of vital Zika virus samples and information, as recently called for by the World Health Organization (see M.-P. Kieny *et al. Nature* **533**, 469; 2016, and go.nature.com/1o4x3dp).

Data sharing for viruses has been disappointingly patchy since I first ignited the debate by depositing my unpublished sequence data for H5N1 avian influenza virus in a public database, rather than in the established password-protected system (see *Nature* **440**, 255–256; 2006). When the 2009 H1N1 swine flu virus emerged, the importance of data sharing was evident in the rapid response to the pandemic. However, the first isolate of the Middle East respiratory syndrome (MERS) coronavirus from Saudi Arabia was controversially submitted for patenting in 2013 (see go.nature.com/1uu7ldd). And in last year's Ebola virus epidemic, there were significant gaps in the availability and posting of online sequence data (N. L. Yozwiak *et al. Nature* **518**, 477–479; 2015).

To overcome such hurdles, I suggest that the United Nations and relevant stakeholders should develop guidelines for scientists, institutions and governments. These should harmonize codes of conduct on sharing information about emerging biological threats — including pathogens that are resistant to antimicrobials.

Ilaria Capua *Italian Chamber of Deputies, Italy.*
ilariacapua1@gmail.com

Archive computer code with raw data

As the leader of a young research group, I recognize the need to archive more than just the raw data that underpin scientific papers. Archiving computer code is also important for safeguarding scientific integrity and for facilitating ongoing projects.

Most scientific journals demand that researchers make their primary data publicly available in the interest of reproducibility. Access to the associated computer code enables statistical analyses and calculations to be validated (see *Nature* **514**, 536; 2014).

The more explicit the links between the data, the code and the resulting outputs (including tables and figures), the easier it is to reproduce the findings.

Software tools such as knitr and R Markdown allow the description and code of a statistical analysis to be combined into a single document, providing a pipeline from the raw data to the final results and figures. Outputs are updated by re-running the scripts using version-control tools such as Git and GitHub.

My group has elected to use these tools and to include R Markdown files as supplementary information to our publications (see, for example, M. A. Stoffel *et al. Proc. Natl Acad. Sci. USA* **112**, E5005–E5012; 2015). I suggest that journals encourage this practice to help to fight the reproducibility crisis.

Joseph I. Hoffman *University of Bielefeld, Germany.*
joseph.hoffman@uni-bielefeld.de

Tea but not dinner with Karl von Frisch

In the 1960s, I had reason to discuss with my friend the late Annemarie Weber, a muscle physiologist, the morality of ethologist Karl von Frisch's decision to continue his studies on honeybee communication during the Second World War (see M. L. Winston *Nature* **533**, 32–33; 2016).

Annemarie's father, Hans Weber, had been removed from his post as professor at the University of Tübingen because he was an opponent of the Nazis. Too famous to be harmed, he was instead transferred to a minor university in East Prussia. Her precise but nuanced response to me was: "After the war, my father would have tea with von Frisch — but dinner, never."

Michael Katz *March of Dimes Foundation, White Plains, New York, USA.*
mkatz@marchofdimes.org

GENOMICS

The language of flowers

The complete DNA sequences of the two wild parents of the garden petunia provide valuable genetic insights into this model plant, and will improve the optimization of other crop plants for agriculture.

SANDRA KNAPP & DANI ZAMIR

The domestication of plants is often thought to apply mainly to food crops, but cultivation has also been widely used to enhance the beauty of ornamental plants. Writing in *Nature Plants*, Bombarely *et al.*¹ report the genome sequences of two progenitor species of *Petunia hybrida*, a plant domesticated for its flowers. These genomes are a notable addition to the known sequences of members of the nightshade family (Solanaceae)². They will enable researchers to unravel fundamental mechanisms in evolution, ecology and gene function, and will help to bring an understanding of the relationships between plant genomes closer.

Petunia is used as a model organism, but one might nonetheless wonder why the genome of a popular flower is of interest. With global consumption of floriculture products estimated to be worth around US\$30 billion per year, however, much research is aimed at optimizing productivity, flower shape, colour, vase-life and fragrance. Previous studies³ have identified many of the genes that influence *Petunia* flower characteristics, highlighting both the evolutionary conservation and diversification of function between different ornamental varieties. Bombarely *et al.* now provide a powerful

platform for the ornamental-flower industry to translate this information to other species, increasing the development of new commercial varieties and species in this economically important research field.

The flowers of wild petunias come in diverse shapes and colours⁴. Cultivated petunias are a hybrid between two wild species — the pink-flowered *Petunia inflata* and the white-flowered *Petunia axillaris*. Bombarely *et al.* sequenced both of these genomes, and generated transcriptomic data (which detail all the messenger RNA molecules in a cell) from three unrelated cultivated *P. hybrida* lines. These data provide a superb resource for analysing not only the genes that confer particular *Petunia* characteristics, but also the genomics of hybridity.

The authors found that most of the genes expressed in the cultivated species are from *P. axillaris* — 15,000, compared with only 600 from *P. inflata*. This is partly attributable to the use of the white background colour derived from *P. axillaris* as a playground for colour manipulation in the cultivated species. An alternative explanation is gene conversion, in which one parental set of genes comes to predominate. Gene conversion has long been thought to be confined to species called polyploids, in which chromosome doubling has

occurred during evolution. Bombarely and colleagues suggest that gene conversion similar to that commonly seen in polyploid Solanaceae crops such as tobacco might also occur in hybrids such as *Petunia* that are not polyploid.

Colour and scent are crucial for attracting pollinators^{3,5}. *P. axillaris* is moth-pollinated and produces volatile compounds that give its night-blooming flowers their strong scent, whereas *P. inflata* is bee-pollinated and has little scent. Bombarely *et al.* find that gene sequence alone cannot explain these differences. But the ‘ecosystem’ of the genome is complex, consisting of many layers of regulation that do not alter DNA sequence. The authors show that the circadian clock that regulates scent production is highly diversified in Solanaceae species, perhaps pointing to a key role for the biochemical pathways that regulate circadian rhythms in driving adaptation to different environmental niches, and thus diversification.

In terms of colour, the *Petunia* genomes provide a powerful resource for understanding the genomic basis of the biosynthetic pathway for pigments called anthocyanins, and for analysing how gene position and duplication can contribute to diversification of traits, influencing speciation⁶. Both parental species share the same core anthocyanin pathway, and, as expected, the white-flowered *P. axillaris* has lost some peripheral components over the course of evolution. But some of the genes encoding transcription factors that regulate the expression of anthocyanin-pathway components reside in exceptionally dynamic regions of the genome. The authors provide evidence that large and extremely rapid rearrangements in these regions were involved in diversification of the Solanaceae.



Figure 1 | A diverse family of crops. Crops of the Solanaceae family have been bred to produce diverse agricultural and ornamental products, including fruits (tomatoes), flowers (petunias) and tubers (potatoes). Bombarely *et al.*¹ report the genome sequences of two progenitor species of the domesticated *Petunia*, which will help researchers to dissect the genetic basis of crop productivity.

FROM LEFT: FOTODISK/GETTY; ONEPONY/GETTY; THE GARDEN SMALL HOLDER/GETTY

Human domestication of many Solanaceae-related ancestors has resulted in related modern crops that have similar sets of genes but highly variable characteristics. For example, petunia, aubergine, tomato, pepper, potato and tobacco are all derived from members of the Solanaceae family, and sweet potato and coffee are members of the same clade, a larger grouping called the euasterids. Each species has been bred to enhance the productivity of different organs (Fig. 1). Thanks to Bombarely and colleagues' work, the genomes of this unique cluster of closely related crops are all now available², which allows us to investigate a major biological question — what are the genetic factors that dictate a plant's balance between vegetative, photosynthetic carbon-dioxide-fixing organs (known as the source), and the reproductive organs consumed by humans (the sink) that store chemical energy in the form of carbohydrates⁷?

Answers to this question will be useful for optimizing crop productivity across many plant species, because the balance between vegetative and reproductive development determines how much chemical energy will be converted to agricultural yield. The fact that different organs constitute sinks in solanaceous crops and their relatives could enable us to identify genes that regulate the source–sink balance beyond those that control specific

sink–organ traits. Such knowledge will allow identification of evolutionary or breeder-selected sink–source innovations in one species that could then be deployed in other crops by using the plant breeder's rapidly expanding molecular toolbox⁸.

The rich diversity of petunias, combined with our new understanding of the genes that regulate this ornamental beauty, will facilitate a deeper understanding of the genetic language that regulates the glory of flowers. A bigger challenge, however, is to understand naturally occurring variability and diversification, and to use this knowledge to better conserve the biodiversity on which our future depends.

If we are to use genomics to unpick evolutionary relationships between solanaceous and other species, each genome must be considered in the context of the organism's characteristics and the selection pressures that it faces in the wild. A major barrier to linking genomes and traits is a lack of consensus on how to annotate qualitative and quantitative traits in a computable manner⁹. A step towards this goal is the database developed by the Solanaceae Genome Network (<https://solgenomics.net>), which presents an ontology to describe traits from different plant species in a common framework¹⁰.

The next step is to link genomes and traits in a bioinformatics framework that can associate

specific DNA sequences with traits that arise at different stages of organismal development and in different environments. Finally, perhaps the greatest challenge in linking the genome to the traits that it encodes is social — persuading the scientific community to deposit its data in open-source platforms so that others can use them. ■

Sandra Knapp is in the Department of Life Sciences, Natural History Museum, London SW7 5BD, UK. **Dani Zamir** is in the Faculty of Agriculture, Hebrew University of Jerusalem, Rehovot, Israel.
e-mails: s.knapp@nhm.ac.uk;
dani.zamir@mail.huji.ac.il

1. Bombarely, A. *et al.* *Nature Plants* <http://dx.doi.org/10.1038/nplants.2016.74> (2016).
2. Lyons, E., Freeling, M., Kustu, S. & Inwood, W. *PLoS ONE* **6**, e16717 (2011).
3. Gerats, T. & Vandenbussche, M. *Trends Plant Sci.* **10**, 251–256 (2005).
4. Stehmann, J. R. *et al.* in *Petunia* (eds Gerats T. & Strommer T.) 1–26 (Springer, 2009).
5. Sheehan, H. *et al.* *Nature Genet.* **48**, 159–166 (2016).
6. Venail, J., Dell'olivo, A. & Kuhlemeier, C. *Phil. Trans. R. Soc. Lond. B* **365**, 461–468 (2010).
7. White, A. C., Rogers, A., Rees, M. & Osborne, C. P. *J. Exp. Bot.* **67**, 31–45 (2016).
8. Puchta, H. *Genome Biol.* **17**, 51 (2016).
9. Deans, A. R. *et al.* *PLoS Biol.* **13**, e1002033 (2015).
10. Fernandez-Pozo, N. *et al.* *Nucleic Acids Res.* **43**, D1036–D1041 (2014).

IMMUNOTHERAPY

Cancer vaccine triggers antiviral-type defences

An immunotherapy approach targets nanoparticles to dendritic cells of the immune system, leading to an antitumour immune response with antiviral-like features. Initial clinical tests of this approach show promise.

JOLANDA DE VRIES & CARL FIGDOR

Preventive vaccines are perhaps the most effective form of immunotherapy. But in a paper online in *Nature*, Kranz *et al.*¹ describe a vaccination strategy against cancer that targets existing tumours by recruiting immune mechanisms normally used against viral infection. The authors used nanoparticles carrying tumour RNA to simulate the intrusion of a viral pathogen into the bloodstream. When the nanoparticles reach lymphoid tissues, including the spleen and lymph nodes, they activate antiviral defence mechanisms in immune cells such as dendritic cells. The dendritic cells translate RNA obtained from the nanoparticles to express and present tumour antigens (molecules used by the immune response as attack targets) to the T cells of the immune system, priming these cells to launch an antitumour immune response.

Why is it so difficult to effectively vaccinate against cancer? One reason is that cancer cells are similar in many ways to normal cells and the immune system avoids attacking the self.

Only relatively modest immune responses occur with vaccines containing antigens that are also expressed on healthy tissue. Strong immune responses can be expected only when cancer cells express antigens that are not usually expressed in normal adult cells.

Another reason is that the growth of a cancer is not accompanied by strong inflammatory signals such as those that occur during microbial infection and which initiate a strong immune response. This leads to tumour microenvironments in which immune cells tolerate, or even promote, cancer growth². Antitumour vaccines must therefore work when the disease has already taken hold, and often when it has spread throughout the body. Last, and in a key contrast to preventive vaccinations against viruses, most cancers coexist and coevolve with our immune systems over years, resulting in an immunosuppressive tumour microenvironment that adds an extra obstacle for immunotherapy.

In vaccine approaches for a range of diseases, specialized antigen-presenting cells have a pivotal role. Dendritic cells in particular are

extremely well suited to handling and presenting antigens to activate T cells. Cultured dendritic cells that have been loaded with antigens *in vitro* can boost immunity when given to patients with cancer, but up to now the clinical efficacy of this strategy has been limited³. Most of these vaccines use dendritic cells that have been derived *in vitro* from white blood cells called monocytes. *Ex vivo* activation of different dendritic-cell subsets that naturally circulate in the blood has also been investigated, using several types of dendritic cell including plasmacytoid dendritic cells, which produce high levels of the immune-response protein interferon- α (IFN α) upon viral infection⁴.

Immunologists have also explored vaccines aimed at directly activating the patient's own dendritic cells *in vivo*, which avoids laborious and expensive *in vitro* culture⁵. Such a vaccine requires at least three components: an 'address label' (a dendritic-cell-specific antibody or ligand molecule such as a carbohydrate)^{6–8} that targets the dendritic cell; a tumour antigen; and a compound that readies the dendritic cells to fully activate T cells (usually a ligand for a Toll-like receptor (TLR)). Nanoparticles containing antigen and TLR ligands, along with targeting antibodies or other ligands, have proved effective in animal models⁹, and initial clinical trials using conjugates of dendritic-cell-targeting antibodies bound to a tumour antigen are under way (see ref. 10 for examples).

Kranz *et al.* have developed a different type of nanoparticle vaccine that does not require antibodies or ligands to target the dendritic cells. Instead, they made nanoparticles consisting of RNA–lipid complexes¹¹. They first demonstrated that, by making the nanoparticles

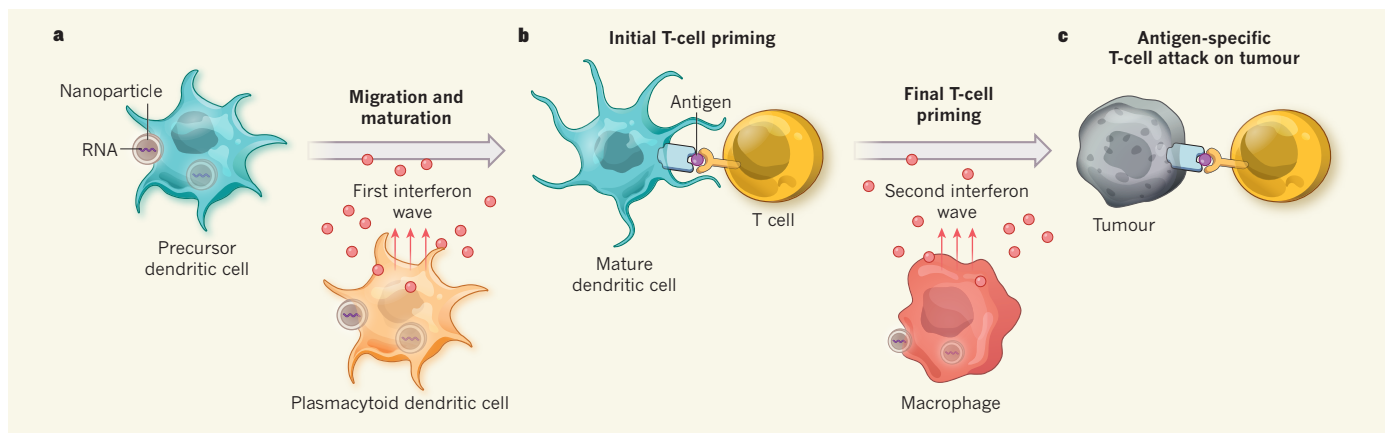


Figure 1 | An antitumour nanoparticle vaccine. **a**, Kranz *et al.*¹ prepared nanoparticles (lipid complexes containing RNA that encodes tumour antigens), and report that they target dendritic cells and macrophages in mice. Nanoparticle uptake by precursor dendritic cells causes them to develop into mature antigen-presenting dendritic cells that migrate to the T cells. Uptake of nanoparticles by plasmacytoid dendritic cells promotes secretion

of an initial wave of interferon protein that helps to prime the first steps of T-cell activation. **b**, Translating the RNA within the nanoparticles, the mature dendritic cells express tumour antigens and present them to the T cells. Nanoparticle uptake by macrophages leads to a second wave of interferon release, which fully primes the T cells against specific antigens. **c**, The primed T cells then attack tumour cells.

slightly negatively charged by manipulating the RNA-to-lipid ratio, the particles can be directed to dendritic-cell-containing compartments in the spleen and other lymphoid tissues when intravenously injected into mice. By using nanoparticles that carried RNA encoding a fluorescent protein, the authors observed that the distribution within the body was more dependent on the overall charge of the nanoparticle than on the type of lipid used. Fluorescence was observed in antigen-presenting dendritic cells and in macrophages, another type of antigen-presenting cell (both of which express the molecular marker CD11c) in the marginal zone of the spleen and in other lymphoid organs. Fluorescence was not observed in mice depleted of CD11c-expressing cells. Plasmacytoid dendritic cells did not fluoresce but showed other signalling responses that suggest that they have taken up nanoparticles.

The researchers found that uptake of the nanoparticle RNA occurred by a cell-membrane-based process called micropinocytosis. Uptake was highest in macrophages. However, the highest expression of RNA-encoded fluorescent marker was observed in dendritic cells, indicating that they are more effective than macrophages at enabling the ingested RNA to reach the cytoplasm and be translated into protein.

Intriguingly, the authors observed two transient waves of IFN α after nanoparticle injection (Fig. 1): the first was produced by plasmacytoid dendritic cells and peaked at 2–3 hours after injection; it was followed by a macrophage-produced wave around 6–8 hours later. By testing an array of genetically modified mice, the authors show that IFN α secretion is mediated by the receptor TLR and that the first wave is necessary for precursor dendritic cells to mature and migrate to encounter T cells in

the spleen and lymph nodes. This leads to a full-blown T-cell response (helped by the second wave of IFN α secretion) against a range of antigens in tumour models in mice, generating robust and long-lasting antitumour responses.

Kranz *et al.* extended their research to an initial clinical study in patients with melanoma, using nanoparticles carrying RNA encoding tumour antigens, and present results from the first three patients treated. Impressively, immune responses were observed — although it is still early days, and a larger, randomized trial will be needed to validate these findings. All three patients produced IFN α and developed strong T-cell responses against the immunizing antigens, even though a smaller dose of nanoparticles was used than in the mouse studies. The T-cell responses involved both CD4-type and CD8-type T cells; the activation of cytotoxic CD8 T cells is typical of an antiviral response, and having both types of T-cell response usually improves anticancer action.

The authors used intravenous injection to deliver the nanoparticles, but it would be interesting to explore other administration routes, which might alter their distribution. It would be worth examining the tissue distribution of radiolabelled nanoparticles in humans, as in the mouse experiments, to see if they also mainly target CD11c-expressing cells. Other immune-system cells that are marked by CD11c, such as neutrophils and monocytes, also have a high phagocytic capacity, and might therefore be able to take up nanoparticle materials and become activated. If so, it is not clear what contribution these other cell types might make to producing immune-system signals such as cytokines.

Kranz and colleagues' study highlights the role of IFN α in obtaining robust T-cell responses against tumours. Notably, CD8 (as

well as CD4) T-cell responses were observed in both the mouse and human studies. Although CD8 T cells have long been known as the major class of immune cells acting in tumour eradication, different subtypes of dendritic cells stimulate different types of CD8 T cells³, and the contribution of CD4 T cells may have been underestimated. The responses in the three cancer patients are interesting given the different types of tumour antigen that were explored (including antigens that are not usually expressed in adult tissue and new antigens that arose owing to mutation within the tumour cells). This nanomedicine platform may give a strong boost to the vaccine field, and the results of forthcoming clinical studies will be of great interest. ■

Jolanda de Vries and Carl Figdor are in the Department of Tumor Immunology, Radboud Institute for Molecular Life Sciences, Radboud University Medical Center, 6525 GA Nijmegen, the Netherlands.
e-mails: jolanda.devries@radboudumc.nl; carl.figdor@radboudumc.nl

1. Kranz, L. M. *et al.* *Nature* <http://dx.doi.org/10.1038/nature18300> (2016).
2. Joyce, J. A. & Fearon, D. T. *Science* **348**, 74–80 (2015).
3. Palucka, K. & Banchereau, J. *Nature Rev. Cancer* **12**, 265–277 (2012).
4. Tel, J. *et al.* *Cancer Res.* **73**, 1063–1075 (2013).
5. Tacke, P. J., de Vries, I. J., Torensma, R. & Figdor, C. G. *Nature Rev. Immunol.* **7**, 790–802 (2007).
6. Bonifaz, L. C. *et al.* *J. Exp. Med.* **196**, 1627–1638 (2002).
7. Bonifaz, L. C. *et al.* *J. Exp. Med.* **199**, 815–824 (2004).
8. Tacke, P. J. *et al.* *Blood* **106**, 1278–1285 (2005).
9. Cruz, L. J. *et al.* *J. Control. Release* **144**, 118–126 (2010).
10. <https://clinicaltrials.gov/ct2/results?term=dec-205&Search=Search>
11. Kuhn, A. N. *et al.* *Gene Ther.* **17**, 961–971 (2010).

Radboud Institute for Molecular Life Sciences,
Radboud University Medical Center, 6525 GA
Nijmegen, the Netherlands.
e-mails: jolanda.devries@radboudumc.nl;
carl.figdor@radboudumc.nl

1. Kranz, L. M. *et al. Nature* **534**, 396–401 (2016).

2. Joyce, J. A. & Fearon, D. T. *Science* **348**, 74–80 (2015).
3. Palucka, K. & Banchereau, J. *Nature Rev. Cancer* **12**, 265–277 (2012).
4. Tel, J. *et al. Cancer Res.* **73**, 1063–1075 (2013).
5. Tacke, P. J., de Vries, I. J., Torensma, R. & Figdor, C. G. *Nature Rev. Immunol.* **7**, 790–802 (2007).
6. Bonifaz, L. C. *et al. J. Exp. Med.* **196**, 1627–1638 (2002).

7. Bonifaz, L. C. *et al. J. Exp. Med.* **199**, 815–824 (2004).
8. Tacke, P. J. *et al. Blood* **106**, 1278–1285 (2005).
9. Cruz, L. J. *et al. J. Control. Release* **144**, 118–126 (2010).
10. <https://clinicaltrials.gov/ct2/results?term=dec-205&Search=Search>
11. Kuhn, A. N. *et al. Gene Ther.* **17**, 961–971 (2010).

This article was published online on 1 June 2016.

COMPUTATIONAL MATERIALS SCIENCE

Predictions of pinning

A multiscale model has been implemented that provides accurate predictions of the behaviour of ferroelectric materials in electric fields, and might aid efforts to design devices such as sensors and digital memory. SEE LETTER P.360

PATRYCJA PARUCH & PHILIPPE GHOSEZ

Hotter temperatures are probably the last thing that you would want when climbing out of a deep valley on a summer hike in the mountains. However, when physical interfaces — such as propagating cracks, or the edges of moving domains in certain materials — become pinned by a potential-energy minimum, higher temperatures that amplify thermal fluctuations might be exactly what is needed to activate slow, highly nonlinear motion over the restrictive energy barriers¹. These barriers can be randomly distributed when associated with defects and disorder in a system, or periodic when arising from potential-energy variations that occur across the atomic planes of crystals, past which certain types of interface move

sequentially². On page 360, Liu *et al.*³ explore this second scenario for the movement of electrically polarized domains in ferroelectric materials, which are used in many optical devices, sensors and digital memory. The study provides an insightful description of domain motion in relation to the microscopic physics that underlies the properties of ferroelectric systems, and is generalizable to many different domain-wall geometries.

Ferroelectric materials are characterized by spontaneous electric polarization that can be reversed by an external electric field. Polarization can develop along two or more directions depending on the crystal symmetry of the material. Regions that have different directions of polarization are called ferroelectric domains, and typically coexist in any ferroelectric sample, separated by thin interfaces

known as domain walls (Fig. 1a).

The domain structure and its evolution in an external electric field are intimately linked to the dynamics of polarization reversal. When an electric field is applied to a sample, polarization aligned with the field direction becomes energetically most favourable. Domains with this orientation therefore grow at the expense of their neighbours, either through the formation and growth of new domains, or by the motion of existing domain walls (Fig. 1b).

Domain-wall motion is a particularly interesting model system for the theoretical study of pinned elastic interfaces, which exhibit complex dynamic behaviours⁴ due to the interplay between elastic behaviour (which tends to maintain a flat configuration) and the effects of local potential-energy variations. For ferroelectric domains at zero kelvin, no motion would occur until the electric field reached a critical value. At finite temperatures, however, thermal activation allows a highly nonlinear dynamic response that depends on the dimensionality of the system and the type of pinning, even for fields well below the critical value^{5,6}. Understanding the dynamics of this domain-wall motion is not only of academic interest, but is also crucial for technological applications of ferroelectric materials.

However, obtaining a general, widely

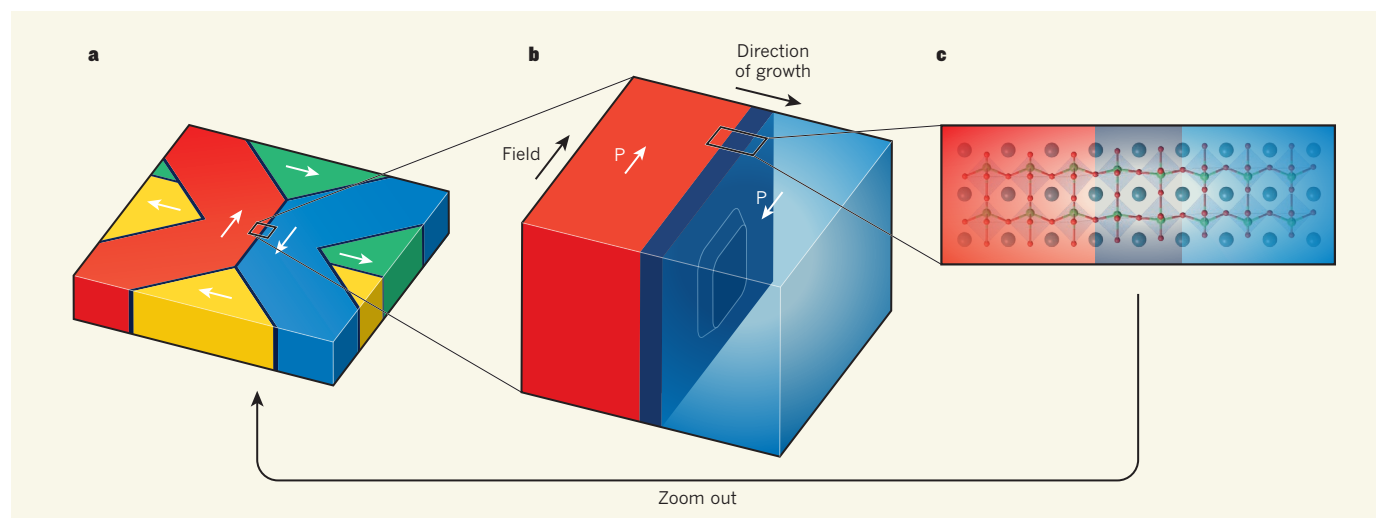


Figure 1 | Modelling domain motion in ferroelectric materials.

a, Ferroelectric materials consist of domains that are electrically polarized in different directions (arrows) and separated by domain walls. **b**, When an electric field is applied to a ferroelectric material, domains polarized in the direction of the field grow at the expense of others (P, polarization). The square ‘nucleus’ represents the initial growth of the red domain into the blue domain. **c**, Liu *et al.*³ report a theoretical description of domain-wall

motion that depends on the potential-energy variation associated with the crystal lattices of ferroelectric materials. The method starts by calculating the structure and energetics of a few hundred atoms at the atomic scale and quantum level, then progressively ‘zooms out’ to a larger scale (up to 850,000 atoms; not shown), before finally deriving an analytical description of the bulk material that internalizes key parameters derived in the first two steps, but does not explicitly consider the microscopic details.

applicable description is complicated by the wide diversity of ferroelectric materials, from almost-perfect single crystals, through mono- and polycrystalline thin films that generally have higher densities of defects than single crystals, to ceramics, which can be porous and have multiple grain boundaries (interfaces between the microscopic crystals that make up the bulk material). If defects dominate domain-wall pinning, then highly variable, sample-specific motion is expected.

Nonetheless, all of these materials have something in common: the intrinsic microscopic variation of potential energy across the atomic planes of their crystal lattices acts as a periodic pinning potential that restricts domain-wall motion. Liu and colleagues focus on this simple universal feature, and show that, in many cases, a theoretical description of its effects provides surprisingly accurate predictions of the macroscopic, technologically relevant behaviour of real samples.

To achieve this, the authors implemented a multiscale theoretical approach that progressively internalizes the microscopic electronic and ionic degrees of freedom of ferroelectric systems. They started from first-principles calculations based on quantum mechanics, which provided key information about the structure and energetics of model ferroelectric materials, but which were limited by computational resources to encompass a few hundred atoms at zero kelvin (Fig. 1c). Using the first-principles results, they built model interatomic potentials that allowed them to study much larger systems — of up to 845,000 atoms — and to explore the motion of a field-driven domain wall at finite temperatures using classical molecular-dynamics simulations.

The data acquired from these two scales served as ingredients for an analytical, phenomenological model of domain-wall motion in the bulk material, considered as a continuous medium that does not explicitly take into account the atomic structure. The authors also explain how their approach can be ingeniously generalized to domain walls in crystals of different symmetries in both purely ferroelectric and ferroelectric–ferroelastic systems (which exhibit spontaneous deformation as well as electrical polarization).

Liu and colleagues' *ab initio*, multiscale approach does not rely on empirical parameters, and thus allows several assumptions in existing theories of domain-wall motion to be re-examined — for instance, by allowing a more realistic understanding of the shape of critical nuclei (the initial regions of polarization that form and grow into new ferroelectric domains; Fig. 1b) — and corrected as necessary. Their work demonstrates that zero-temperature microscopic quantities calculated from first principles are relevant to descriptions of complex macroscopic phenomena at finite temperatures, and it provides a

concrete process for the rapid calculation of the latter from the former. This process could be integrated into high-throughput *ab initio* platforms for material design and is a new tool for optimizing ferroelectrics⁷.

Although the model does not consider disorder or defects in materials, in many cases its predictions of coercive fields (the electric fields needed to reverse the polarization) are in excellent agreement with experimental measurements⁸, emphasizing the key role of periodic crystal pinning in ferroelectric systems. Moreover, even for studies of ferroelectric domain walls in which periodic pinning is clearly insufficient to describe domain-wall behaviour⁹, Liu and co-workers' results will be useful for comparing the relative energies needed for motion of different types of domain wall, and determining whether switching is purely ferroelectric, or proceeds by linked, ferroelastic steps.

Finally, it should be possible to use other microscopic periodic pinning potentials — such as those artificially induced during the growth of ferroelectric materials on specially prepared substrates — in the molecular-dynamics simulations used to generate the analytical models, and in the analytical

models themselves. This could be used to engineer domain-wall pinning sites for future nanoelectronics applications¹⁰. ■

Patrycja Paruch is in the Department of Quantum Matter Physics, University of Geneva, 1211 Geneva 4, Switzerland.

Philippe Ghosez is in the group of Theoretical Materials Physics of the CESAM Research Unit, University of Liège, 4000 Liège, Belgium. e-mails: philippe.ghosez@ulg.ac.be; patrycja.paruch@unige.ch

1. Barabási, A.-L. & Stanley, H. E. *Fractal Concepts in Surface Growth* (Cambridge Univ. Press, 1995).
2. Blatter, G., Feigelman, M. V., Geshkenbein, V. B., Larkin, A. I. & Vinokur, V. M. *Rev. Mod. Phys.* **66**, 1125 (1994).
3. Liu, S., Grinberg, I. & Rappe, A. M. *Nature* **534**, 360–363 (2016).
4. Giamarchi, T., Kolton, A. B. & Rosso, A. in *Jamming, Yielding, and Irreversible Deformation in Condensed Matter* (eds Miguel, M. C. & Rubi, M.) 91–108 (Springer, 2006).
5. Nattermann, T., Shapir, Y. & Vilfan, I. *Phys. Rev. B* **42**, 8577 (1990).
6. Nattermann, T. *J. Phys. C* **16**, 4125 (1983).
7. Marzari, N. *Nature Mater.* **15**, 381–382 (2016).
8. Jo, J. Y. *et al.* *Phys. Rev. Lett.* **99**, 267602 (2007).
9. Paruch, P. & Guyonnet, J. *C.R. Phys.* **14**, 667–684 (2013).
10. Catalan, G., Seidel, J., Ramesh, R. & Scott, J. F. *Rev. Mod. Phys.* **84**, 119 (2012).

CELL REPROGRAMMING

Brain versus brawn

The mechanisms that underlie enforced transitions between mature cell lineages are poorly understood. Profiling single skin cells that are induced to become neurons reveals that, unexpectedly, they often become muscle. SEE LETTER P.391

BRUNO DI STEFANO & KONRAD HOCHEDLINGER

Differentiated cells maintain their identity after development, ensuring specialized tissue function throughout adult life. However, they can be experimentally forced to change their identity — for instance, skin cells called fibroblasts can be reprogrammed to become more-primitive, embryonic-like stem cells¹, or transdifferentiated into other specialized cell types such as muscle², blood³ or neural cells⁴. These techniques are invaluable for studying cell plasticity and hold promise as possible tools for treating degenerative diseases, but the process is typically slow and inefficient. On page 391, Treutlein *et al.*⁵ address these shortcomings by presenting a molecular road map of fibroblasts as they convert to neurons, and provide intriguing evidence that such neuronal transdifferentiation often entails an unanticipated tug-of-war between alternative outcomes.

Reprogramming and transdifferentiation experiments typically involve overexpression

of regulatory transcription factors that bind to DNA and induce gene-expression patterns characteristic of a specific cell type⁶. One of the groups that carried out the current study previously identified⁴ three brain-specific transcription factors — Brn2, Ascl1 and Myt1l, collectively known as BAM factors — whose overexpression *in vitro* converts fibroblasts into cells that resemble brain-derived neurons. This group also demonstrated⁷ that overexpression of Ascl1 alone can induce transdifferentiation into neuron-like cells, albeit with lower efficiency than the BAM cocktail. With either approach, most cells resist transdifferentiation, but the reasons for this remain unclear.

Single-cell RNA sequencing is a useful tool for assessing global gene-expression patterns in rare cell types within mixed cell populations⁸. Treutlein *et al.* apply this technology to neuronal transdifferentiation mediated by either BAM or Ascl1 alone. They measure total RNA levels in 405 single cells after 0, 2, 5 and 22 days of culture. They then use sophisticated computational tools to visualize data obtained from the cultures as a two-dimensional

CELL REPROGRAMMING

Brain versus brawn

The mechanisms that underlie enforced transitions between mature cell lineages are poorly understood. Profiling single skin cells that are induced to become neurons reveals that, unexpectedly, they often become muscle.

BRUNO DI STEFANO &
KONRAD HOCHEDLINGER

Differentiated cells maintain their identity after development, ensuring specialized tissue function throughout adult life. However, they can be experimentally forced to change their identity — for instance, skin cells called fibroblasts can be reprogrammed to become more-primitive, embryonic-like stem cells¹, or transdifferentiated into other specialized cell types such as muscle², blood³ or neural cells⁴. These techniques are invaluable for studying cell plasticity and hold promise as possible tools for treating degenerative diseases, but the process is typically slow and inefficient. In a paper online in *Nature*, Treutlein *et al.*⁵ address these shortcomings by presenting a molecular road map of fibroblasts as they convert to neurons, and provide intriguing evidence that such neuronal transdifferentiation often entails an unanticipated tug-of-war between alternative outcomes.

Reprogramming and transdifferentiation

experiments typically involve overexpression of regulatory transcription factors that bind to DNA and induce gene-expression patterns characteristic of a specific cell type⁶. One of the groups that carried out the current study previously identified⁴ three brain-specific transcription factors — Brn2, Ascl1 and Myt1l, collectively known as BAM factors — whose overexpression *in vitro* converts fibroblasts into cells that resemble brain-derived neurons. This group also demonstrated⁷ that overexpression of Ascl1 alone can induce transdifferentiation into neuron-like cells, albeit with lower efficiency than the BAM cocktail. With either approach, most cells resist transdifferentiation, but the reasons for this remain unclear.

Single-cell RNA sequencing is a useful tool for assessing global gene-expression patterns in rare cell types within mixed cell populations⁸. Treutlein *et al.* apply this technology to neuronal transdifferentiation mediated by either BAM or Ascl1 alone. They measure total RNA levels in 405 single cells after 0, 2, 5 and 22 days of culture. They then use sophisticated

computational tools to visualize data obtained from the cultures as a two-dimensional representation and thus reconstruct the progression of the fibroblasts into neurons over time.

These experiments reveal that transdifferentiating fibroblasts transit through two discernible stages, which the authors dub initiation and maturation (Fig. 1). During initiation, the cells cease to express genes that are characteristic of fibroblasts, stop proliferating and transiently activate genes whose expression marks neuronal progenitor cells. These changes take place in most cells and are orchestrated by Ascl1. By contrast, only a subset of cells progresses to maturation. This phase is characterized by the activation of genes that establish, and subsequently maintain, a mature neuronal lineage, and involves all three BAM factors. Thus, the transition from initiation to maturation represents a bottleneck during fibroblast-to-neuron conversion, correlating with the low efficiency of transdifferentiation.

One plausible explanation for this bottleneck is that rare cell types in the mixed cultures are uniquely susceptible to transdifferentiation. This would predict the existence of a transcriptionally distinct subset of fibroblasts. However, when examining gene expression in 73 individual fibroblasts, Treutlein *et al.* find no evidence for distinct subsets, and cultures seem remarkably homogeneous, making this possibility unlikely.

Another possibility is that the viral vector used by the authors to deliver the transcription factors into cells is silenced. To address this point, Treutlein *et al.* compare the expression of the introduced *Ascl1* transgene in dozens of single cells. Although *Ascl1* is initially expressed in most fibroblasts, the transgene is frequently silenced as cells transition to the maturation phase. These data suggest that viral silencing accounts, at least in part, for the low efficiency of neuronal transdifferentiation.

Perhaps the most surprising result emerges from a comparison of gene-expression data in single cells that activate the neuronal marker gene *Tau* after receiving either Ascl1 alone or the BAM factors. This analysis reveals that cells that receive only Ascl1 adopt a muscle-like (myogenic) gene-expression program despite activating *Tau*, whereas *Tau*-expressing cells that received BAM assume the expected neuronal fate. Unfortunately, the frequency with which Ascl1 expression alone gives rise to bona fide neurons and the functionality of the myogenic cells remain unclear. Nonetheless, these data suggest that Myt1l and Brn2 not only promote neuronal identity, but also prevent acquisition of a competing myogenic fate (Fig. 1).

Treutlein and colleagues' study underscores the power of single-cell technology to deconstruct complex cell-fate transitions across

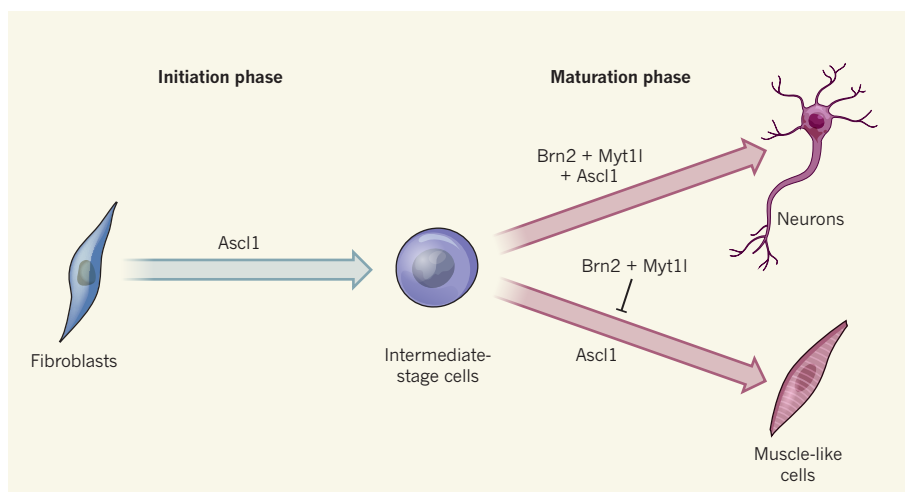


Figure 1 | A tug-of-war between cell types. Expression of the brain-specific transcription factors Brn2, Ascl1 and Myt1l in skin cells called fibroblasts triggers the cells' direct conversion into neurons. Treutlein *et al.*⁵ discover that this neuronal transdifferentiation involves two waves of transcriptional change, initiation and maturation. Most cells progress through initiation and take on an intermediate identity in a process orchestrated by Ascl1. During maturation, only a few cells turn on genes associated with mature neurons. The authors find that the three factors promote the acquisition of a proper neural fate in such cells. Brn2 and Myt1l seem to actively prevent transdifferentiation towards muscle — a fate that is promoted by Ascl1.

different lineages and time. Key questions that remain are why and how the *Ascl1* transgene is silenced in fibroblasts, and whether an understanding of this inhibition would help to reveal the mechanisms that normally safeguard cell identity. Of note, recent data^{9,10} suggest that the mechanisms that facilitate viral-transgene silencing also act as barriers to reprogramming and transdifferentiation, suggesting a functional connection between these processes.

Another unresolved question is how *Ascl1* supports transdifferentiation into myogenic cells, given that it is not normally expressed in muscle. *Ascl1* belongs to a class of 'pioneer' factors¹¹ that can associate with and regulate dormant regions of the genome that are inaccessible to other transcription factors. As such, its forced expression in fibroblasts might trigger nonspecific binding to hundreds of DNA sequences, including inactive muscle genes. Alternatively, *Ascl1* might partner with another transcription factor that redirects it to muscle genes. A potential candidate partner is the protein MEF2, which is highly expressed both in fibroblasts and during muscle development, and has been shown¹² to interact with *Ascl1*.

Regardless of the mechanisms that give rise to myogenic cells, Treutlein and colleagues' results have several practical implications. For example, the data suggest that identifying transdifferentiated neurons using a single marker such as *Tau* is insufficient, because the gene is also activated in cells that acquire a myogenic fate. The authors' findings further imply that the general trend of reducing the set of transdifferentiation-inducing transcriptional regulators to a minimum, as was the case here and in previous studies, may have unintended consequences.

This is particularly relevant in a therapeutic setting, in which it is crucial to transplant well-defined, homogeneous cell populations. A case in point is the finding¹³ that liver-like cells transdifferentiated from fibroblasts seem to be more similar to progenitors of the intestinal lining than to liver cells, and accordingly give rise to functional intestinal cells in mice. It is tempting to speculate that removing, adding or exchanging transcription factors from other transdifferentiation cocktails, combined with a more in-depth molecular analysis of the generated cell types, might uncover other similar shifts in cell fate or maturity. ■

Bruno Di Stefano and Konrad Hochedlinger are in the Department of Molecular Biology, Massachusetts General Hospital, Boston, Massachusetts 02114, USA, and in the Department of Stem Cell and Regenerative Biology, Harvard University and Harvard Medical School, and the Harvard Stem Cell Institute, Cambridge, Massachusetts.

e-mail: khochedlinger@mgh.harvard.edu

1. Takahashi, K. & Yamanaka, S. *Cell* **126**, 663–676 (2006).
2. Davis, R. L., Weintraub, H. & Lassar, A. B. *Cell* **51**, 987–1000 (1987).
3. Feng, R. *et al.* *Proc. Natl Acad. Sci. USA* **105**, 6057–6062 (2008).
4. Vierbuchen, T. *et al.* *Nature* **463**, 1035–1041 (2010).
5. Treutlein, B. *et al.* *Nature* <http://dx.doi.org/10.1038/nature18323> (2016).
6. Graf, T. *Cell Stem Cell* **9**, 504–516 (2011).
7. Chanda, S. *et al.* *Stem Cell Rep.* **3**, 282–296 (2014).
8. Shapiro, E., Biezuner, T. & Linnarsson, S. *Nature Rev. Genet.* **14**, 618–630 (2013).
9. Cheloufi, S. *et al.* *Nature* **528**, 218–224 (2015).
10. Yang, B. X. *et al.* *Cell* **163**, 230–245 (2015).
11. Iwafuchi-Doi, M. & Zaret, K. S. *Genes Dev.* **28**, 2679–2692 (2014).
12. Black, B. L. & Olson, E. N. *Annu. Rev. Cell Dev. Biol.* **14**, 167–196 (1998).
13. Morris, S. A. *et al.* *Cell* **158**, 889–902 (2014).

Stem cell function and stress response are controlled by protein synthesis

Sandra Blanco¹, Roberto Bandiera¹, Martyna Popis¹, Shobbir Hussain², Patrick Lombard¹, Jelena Aleksic¹, Abdulrahim Sajini¹, Hinal Tanna³, Rosana Cortés-Garrido¹, Nikoletta Gkatza¹, Sabine Dietmann¹ & Michaela Frye¹

Whether protein synthesis and cellular stress response pathways interact to control stem cell function is currently unknown. Here we show that mouse skin stem cells synthesize less protein than their immediate progenitors *in vivo*, even when forced to proliferate. Our analyses reveal that activation of stress response pathways drives both a global reduction of protein synthesis and altered translational programmes that together promote stem cell functions and tumorigenesis. Mechanistically, we show that inhibition of post-transcriptional cytosine-5 methylation locks tumour-initiating cells in this distinct translational inhibition programme. Paradoxically, this inhibition renders stem cells hypersensitive to cytotoxic stress, as tumour regeneration after treatment with 5-fluorouracil is blocked. Thus, stem cells must revoke translation inhibition pathways to regenerate a tissue or tumour.

Protein synthesis is a fundamental process for all cells, but its precise regulatory roles in development, stem cells and cancer are not well understood. We recently identified post-transcriptional methylation of transfer RNA (tRNA) at cytosine-5 (m^5C) by NSUN2 as a novel mechanism to repress global protein synthesis^{1,2}. Loss of *Nsun2* causes hypomethylation of tRNAs, allowing endonucleolytic cleavage by angiogenin and accumulation of 5' tRNA fragments^{1,3}. These fragments repress cap-dependent protein translation^{4–7}.

Correct RNA methylation is essential for development and tissue homeostasis. Loss-of-function mutations in human *NSUN2* cause growth retardation and neurodevelopmental defects including microcephaly^{1,8–10}. In mouse, *Nsun2*-associated microcephaly can be rescued by inhibiting angiogenin-mediated tRNA cleavage¹. In adult tissues (testis and skin), NSUN2 is only expressed in a subpopulation of committed progenitors, in which its activity balances self-renewal and differentiation^{11,12}.

Here, we reveal that the interplay between RNA methylation and translation shapes stem cell fate. Using skin as a model, we demonstrate that stem cells have lower protein synthesis than committed cells in both homeostasis and tumorigenesis. Low translation functionally contributes to maintaining stem cells, and is not merely a consequence of quiescence or cell cycle state. By genetically deleting *Nsun2* in a tumour mouse model, we find that protein synthesis is globally repressed; however, distinct transcripts escape this repression and establish a translational programme crucial to stimulate stem cell functions. Unexpectedly, the selective alteration of translation is remarkably effective in rendering stem cells sensitive to cytotoxic stress.

Protein synthesis is low in stem cells

In skin, the best-characterized stem cell populations reside in the hair follicle¹³. Hair follicle stem cells (HFSCs) are periodically activated at the onset of hair growth (anagen), which is followed by phases of regression (catagen) and rest (telogen) (Extended Data Fig. 1a)^{14,15}. HFSCs located in the bulge express the stem cell markers CD34, K19 (also known as KRT19) and LGR5 (Fig. 1a)^{16,17}.

To visualize HFSCs and their progeny, we genetically labelled K19- and LGR5-expressing bulge stem cells with a tdTomato (tdTom) reporter (Fig. 1a, b and Extended Data Fig. 1a)^{16,18}. To measure global

protein synthesis we quantified incorporation of O-propargyl-puromycin (OP-puro) into nascent proteins (Fig. 1b)¹⁹. Protein synthesis was uniformly low in the interfollicular epidermis, but highly dynamic in hair follicles throughout the hair cycle (Extended Data Fig. 1b). In telogen, highly translating cells at the follicle base were not stem cells, as they were negative for tdTom (Fig. 1c, d and Extended Data Fig. 1c). In late anagen, OP-puro co-localized with tdTom in committed progenitors located in the hair bulb (Fig. 1e, f and Extended Data Fig. 1d, arrows). The highest translation was displayed above the hair matrix, which contains committed progenitors that divide a finite number of times before differentiating (Fig. 1e, f and Extended Data Fig. 1d, arrowheads)²⁰.

Co-labelling of OP-puro with markers for all hair lineages identified the Henle's and Huxley's layers of the inner root sheath (IRS) as the lineages with highest translation (Fig. 1g–k and Extended Data Fig. 1e, f)^{21,22}. Both IRS layers exclusively contain committed and differentiated cells²².

To quantify protein synthesis fully in distinct epidermal populations, we flow-sorted bulge stem cells (CD34⁺/ITGA6⁺), non-bulge cells (CD34[−]/ITGA6⁺), and differentiated cells (CD34[−]/ITGA6[−]) (Fig. 2a–c)¹⁷. To capture epidermal cells giving rise to the highly translating IRS, we enriched for OP-puro^{high} cells (top 2.5% in rate of translation) (Fig. 2b). The selection for high translation did not perturb the proportion of cell populations found in the epidermis (Extended Data Fig. 2a–d). Quantification of OP-puro incorporation confirmed that protein synthesis was highest in differentiated populations in late anagen (Fig. 2d). Translation in bulge stem cells significantly increased from telogen to anagen (Fig. 2d), suggesting a correlation between translation rate and stem cell activation.

Next, we focused on HFSCs and their progeny and quantified protein translation in tdTom⁺ cells that were sorted into bulge stem cells, non-bulge cells, and differentiating cells (Fig. 2e, f). Translation rates significantly increased in bulge HFSCs from telogen to anagen (Fig. 2e, f). In addition, the average translation rate increased in differentiating cells in late anagen, and was around twofold higher compared to the background cells (tdTom[−]) (Fig. 2d–f and Extended Data Fig. 2e, f). These results were robust to the specific threshold used to identify cells as highly translating (top 2.5–50%) (Extended Data Fig. 3a–c).

¹Wellcome Trust—Medical Research Council Cambridge Stem Cell Institute, Department of Genetics, University of Cambridge, Tennis Court Road, Cambridge CB2 1QR, UK. ²Department of Biology & Biochemistry, University of Bath, Claverton Down, Bath BA2 7AY, UK. ³University of Cambridge, CR-UK, Cambridge Institute, Li Ka Shing Centre, Robinson Way, Cambridge CB2 0RE, UK.

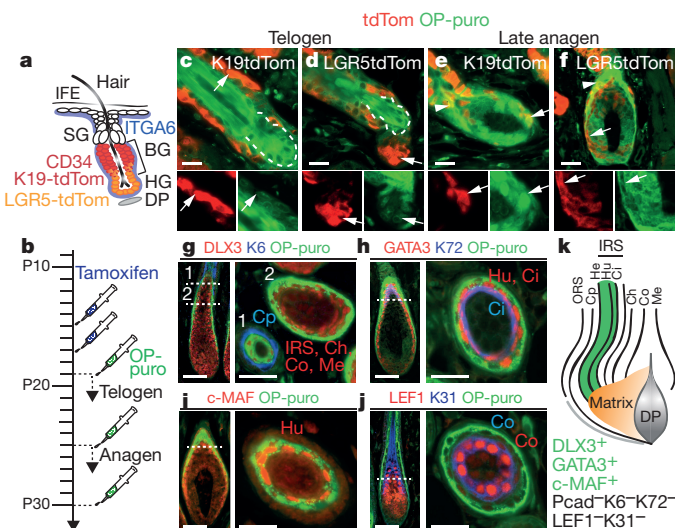


Figure 1 | HFSCs synthesize less protein than their progeny.

a, Epidermal populations analysed. BG, bulge; DP, dermal papilla; HG, hair germ; IFE, interfollicular epidermis; SG, sebaceous gland. **b**, Treatment regimes. P, postnatal day. **c–f**, Detection of tdTom and OP-puro in back skin of K19/LGR5Cre tdTom mice in telogen (**c**, **d**) and late anagen (**e**, **f**). Arrows indicate tdTom⁺ cells (magnification, bottom panels). Arrowheads indicate tdTom⁺/OP-puro^{high} cells. Dotted line indicates lower bulge. **g–j**, OP-puro and hair follicle lineage marker detection (late anagen). Dotted lines indicate cross-section (1, 2). **k**, Schematic summary of **g–j**. Ch, cuticle; Ci, cuticle of inner root sheet; Co, cortex; Cp, companion layer; He, Henle's layer; Hu, Huxley's layer; Me, medulla; ORS, outer root sheet. OP-puro⁺ layers (green). Scale bars, 50 μ m.

Thus, as stem cells proceed into a fully committed progenitor state, protein translation steadily increases.

Proliferation does not dictate translation

Protein synthesis was highest in growing hair follicles. However, cellular division alone did not explain translation rates as the greatest protein synthesis was found in differentiating but non-dividing (Ki67[−]) cells (Fig. 2g). Although the percentage of cycling (S/G2/M) cells correlated with increasing translation rates (Extended Data Fig. 3d, e), differentiating (CD34[−]/ITGA6[−]) and non-dividing (G1/G0) cells represented the population with the highest translation (Extended Data Fig. 3f, g).

To test directly whether protein synthesis was determined by lineage commitment instead, we measured the translation rate in bulge HFSC and their offspring (tdTom⁺) along the cell cycle. In late anagen, non-cycling (G1/G0) tdTom⁺ cells synthesized significantly more protein than their cycling (S/G2/M) counterparts (Fig. 2h and Extended Data Fig. 3h). Thus, increasing translation rates correlated with stem cell commitment and differentiation rather than proliferation (Extended Data Fig. 4p).

Low translation in tumour-initiating cells

To test whether low protein synthesis simply reflected a quiescent state, we investigated translation rates in cancer-initiating cells, which exhibit both high self-renewal and proliferation capacity. We used *K5-Sos* mice, which constitutively activate RAS in basal epidermal cells and develop well-differentiated tumours resembling human squamous tumours^{23,24}.

Undifferentiated progenitors expressed markers for tumorigenesis and tumour-initiating cells (ITGB1, ITGA6, CD44, CD34, PDPN)^{25–29} and exhibited lower protein synthesis than committed progenitors (Fig. 3a, d and Extended Data Fig. 4a–c, f–j). Translation was highest in suprabasal and differentiating committed progenitors (K10⁺), but absent in terminally differentiated, non-tumorigenic cells (Fig. 3a, b). In cancer, elevated translation has been associated with increased proliferation³⁰. However, in our data, high translation was uncoupled

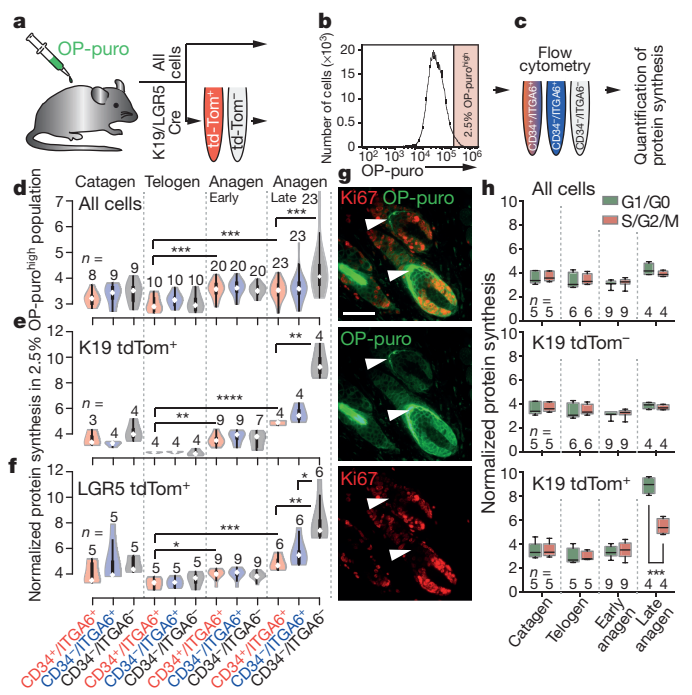


Figure 2 | Protein synthesis correlates with differentiation.

a–c, Experimental set up. **d–f**, Violin plots of normalized protein synthesis in OP-puro^{high} cells sorted for the indicated epidermal populations (**c**). **g**, Ki67 and OP-puro detection (late anagen). Arrowheads indicate Ki67[−]/OP-puro⁺ cells. Scale bar, 50 μ m. **h**, Box plots of protein synthesis in cycling (S/G2/M) and non-dividing (G1/G0) OP-puro^{high} cells. n = mice. * P < 0.05, ** P < 0.01, *** P < 0.001, **** P < 0.0001 (two-tailed Student's t -test). Source Data for this figure is available in the online version of the paper.

from proliferation because both OP-puro^{high} and OP-puro^{low} cells expressed Ki67 (Fig. 3c), and protein synthesis did not correlate with cycling cells (Fig. 3e).

Thus, similar to normal skin, stem and progenitor cells in tumours produced less protein than their committed progeny.

Low translation maintains tumour stem cells

To test whether low translation is a cause or a consequence of a stem cell state requires the ability to modulate protein synthesis. An excellent system is the genetic deletion of the RNA-methyltransferase NSUN2. NSUN2 modulates global translation by protecting tRNAs from cleavage¹. In normal skin, NSUN2 is restricted to distinct hair follicle populations¹¹ that overlap with OP-puro^{high} cells in early and late anagen (Extended Data Fig. 4k, l). *Nsun2* deletion delayed HFSC differentiation in adult¹¹ and developing skin (Extended Data Fig. 4m–o). NSUN2 is upregulated in epithelial tumours and homogeneously expressed in mouse and human squamous cell carcinomas (Extended Data Fig. 5a)^{31,32}, and its expression is restricted to highly translating cells in *K5-Sos* tumours (Fig. 3f).

We deleted *Nsun2* in *K5-Sos* mice, and measured OP-puro incorporation into the tumours of the offspring. As expected, *Nsun2* ablation reduced protein synthesis in tumours (Fig. 3g–i and Extended Data Fig. 4d, e). *K5-Sos/Nsun2*^{−/−} mice developed more tumours that appeared earlier, grew larger, and reduced their life span (Fig. 4a and Extended Data Fig. 5b–d).

Nsun2^{−/−} tumours appeared more proliferative; however, 5-ethynyldeoxyuridine (EdU)/5-bromodeoxyuridine (BrdU) pulse-chase experiments revealed that high EdU incorporation reflected an increased undifferentiated population, but not a faster division rate (Fig. 4b, c and Extended Data Fig. 5e, f). *Nsun2*^{−/−} tumours were poorly differentiated and in a later stage of tumorigenesis, as shown by increased expression of stem cell and tumour progression markers (Fig. 4d–i and Extended Data Fig. 5f–j).

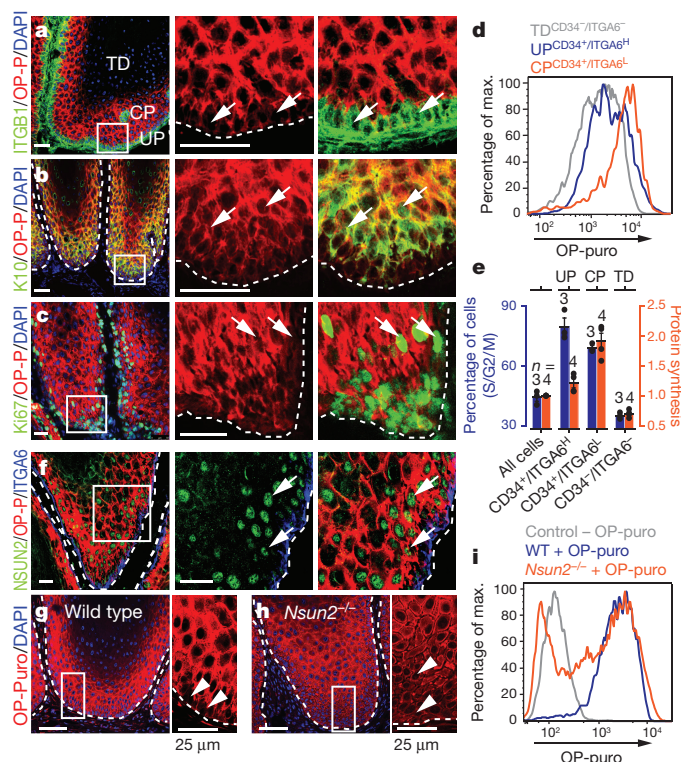


Figure 3 | Tumour-initiating cells synthesize less protein than their progeny. **a–c**, Co-labelling OP-puro (OP-P) with the indicated markers. Arrows indicate marker-positive cells. Boxed areas in the left-hand panels are shown magnified in the panel to the right. **d**, Flow cytometry for OP-puro incorporation. **e**, Percentage of dividing cells (S/G2/M) and normalized protein synthesis (mean \pm standard deviation (s.d.); n = mice). **f**, Co-staining OP-puro, NSUN2, ITGA6. Arrows indicate OP-puro⁺/NSUN2⁺ cells. Boxed areas in the left hand-panel are shown magnified in the panel to the right. **g–i**, OP-puro detection in sections (**g**, **h**) or by flow cytometry (**i**). Boxed areas in the left-hand panels are shown magnified in the panel to the right. Arrowheads indicate OP-puro^{low} cells. Nuclei are stained with 4',6-diamidino-2-phenylindole (DAPI). Scale bars, 50 μ m (**a**, **b**, **c**, **f**, **g**, left, **h**, left); 25 μ m (**g**, right, **h**, right). Dotted line indicates basal membrane. All analyses are in *K5-Sos* tumours. WT, wild type. Source Data for this figure is available in the online version of the paper.

To test for the cell-intrinsic potential to initiate tumours, we injected *Nsun2*^{−/−} tumour cells subcutaneously into nude mice (Extended Data Fig. 6a). Only *Nsun2*^{−/−} cancer cells reconstituted the original squamous tumour with high proliferative potential and elevated levels of ITGB1 and PDPN (Extended Data Fig. 6b–f). Thus, *Nsun2* deletion enhances the self-renewal potential of tumour-initiating cells in a cell-autonomous manner.

Furthermore, in human skin cancers, NSUN2 expression was inversely correlated with malignancy when we compared protein expression levels in normal skin and cutaneous cancers of increasing tumour/node/metastasis (TNM) stages (Fig. 4j) and Extended Data Fig. 6g–m).

These results indicate that the reduction of translation rates caused by *Nsun2* deletion increased the tumour-initiating population.

tRNA fragments modulate translation

A likely mechanism for the translational repression in *Nsun2*-deficient tumours was that 5' tRNA fragments inhibit protein synthesis⁴. Using RNA-bisulfite sequencing^{1,33}, we confirmed that in tumours, NSUN2-dependent methylation occurred at most tRNAs (65%), but only at a small proportion of messenger RNA exons (2%) and introns (Fig. 5a, b, Extended Data Fig. 7a–e and Supplementary Tables 1, 2)^{1,2,34–39}. In the few methylated mRNAs, NSUN2-target sites were enriched close to transcriptional start sites, but were uncorrelated with RNA abundances (Extended Data Fig. 7f, g and Supplementary Tables 1, 3). In contrast,

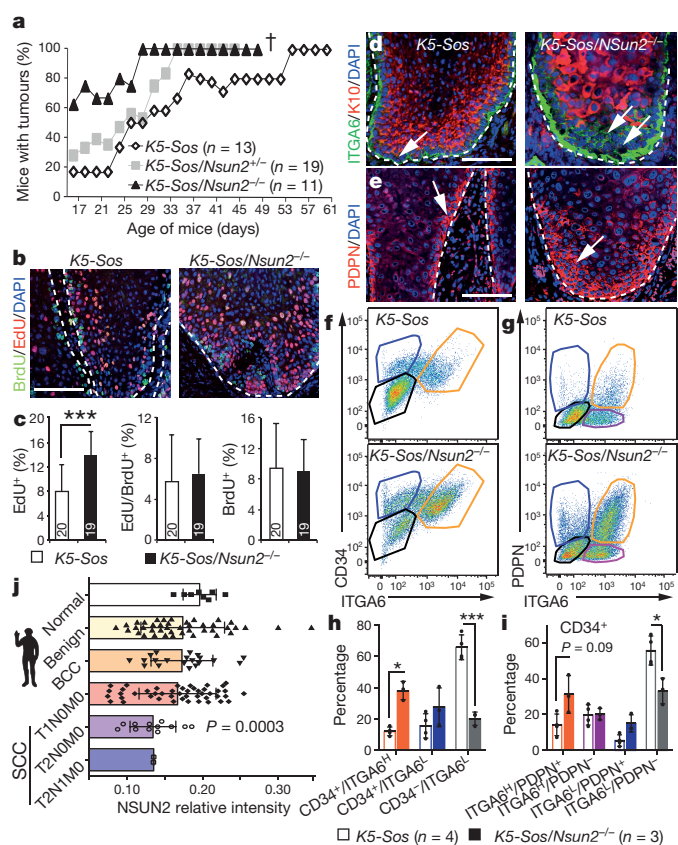


Figure 4 | *Nsun2* deletion promotes stem cell identity and tumorigenesis. **a**, Tumour incidence. Daggers indicate that the mice died. **b**, **c**, Detection (**b**) and quantification (**c**) of pulsed-chased BrdU⁺ and EdU⁺ cells in tumours (see Methods). n = 5 slides \times 3 mice. **d**, **e**, Immunostaining for ITGA6, K10 (**d**) and PDPN (**e**). Arrows indicate marker-positive cells. Nuclei are stained with DAPI; dotted line indicates basal membrane. Scale bars, 100 μ m. **f–i**, Flow cytometry (**f**, **g**) and quantification (**h**, **i**) of marker-positive tumour cells. n = mice (mean \pm s.d.). **j**, NSUN2 protein expression in human normal skin or tumours (mean \pm s.d.). * P < 0.05, *** P < 0.001 (two-tailed Student's *t*-test). Source Data for this figure is available in the online version of the paper.

hypomethylation of tRNAs directly caused by loss of *Nsun2* led to the accumulation of 5' tRNA fragments (Fig. 5c, d, Extended Data Fig. 7i–l and Supplementary Tables 2, 4).

We performed ribosome profiling to evaluate how 5' tRNA fragments influenced translation in mouse tumours and patient-derived NSUN2-deficient fibroblasts (Extended Data Fig. 8a, b and Supplementary Tables 5, 6a–c). We verified the high quality of our data by testing for triplet periodicity of ribosomal footprints⁴⁰, increased ribosomal density near translational start sites⁴¹, and correlation between RNA expression levels and translation (Extended Data Fig. 8c–j)⁴².

The distinct translational programme in *Nsun2*^{−/−} mouse tumours was not driven by transcriptional alteration, as the changes in protein synthesis caused by *Nsun2* removal were decoupled from the corresponding changes in RNA expression levels (Fig. 5e and Extended Data Fig. 8e). The differences in translation were more likely to be caused by accumulated 5' tRNA fragments than by changes in mRNA methylation, because translation of NSUN2-methylated mRNAs remained unaltered (Extended Data Fig. 7h).

In summary, the undifferentiated cellular phenotype of *Nsun2*^{−/−} tumours was primarily driven by translational, and not transcriptional changes.

Translational signatures in NSUN2^{−/−} cells

Accumulation of 5' tRNA fragments can activate a cap-independent stress-response programme⁴; and stress stimuli can increase ribosomal

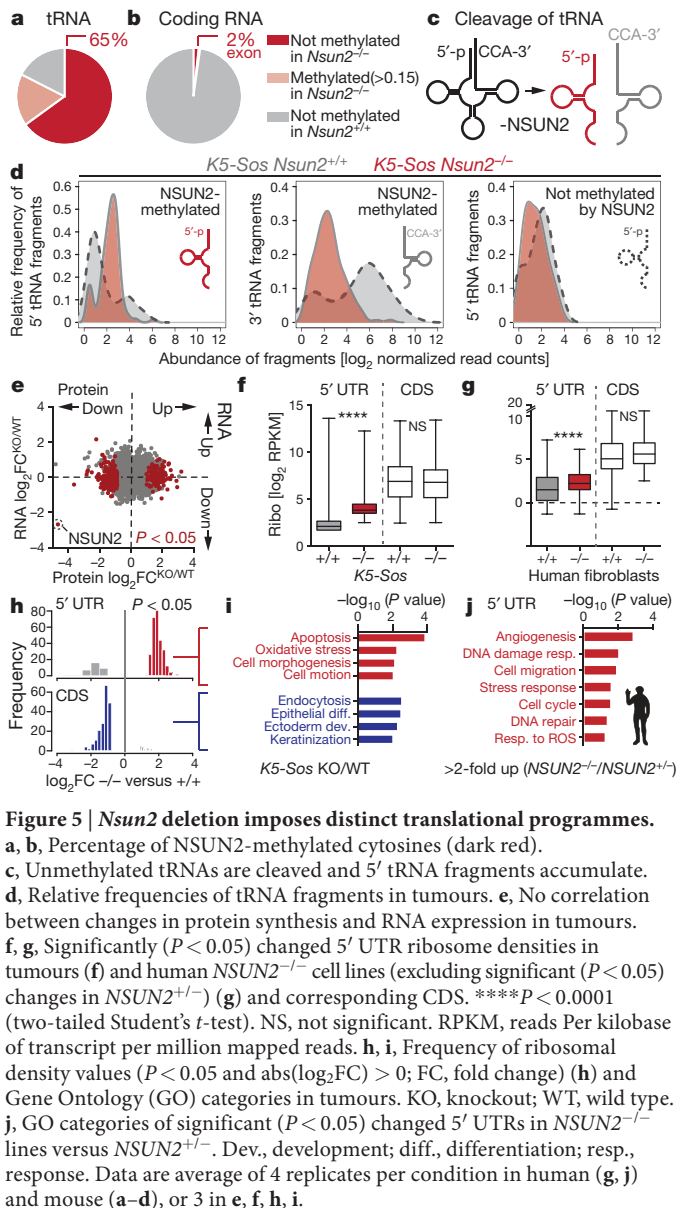


Figure 5 | *Nsun2* deletion imposes distinct translational programmes. **a, b**, Percentage of NSUN2-methylated cytosines (dark red). **c**, Unmethylated tRNAs are cleaved and 5' tRNA fragments accumulate. **d**, Relative frequencies of tRNA fragments in tumours. **e**, No correlation between changes in protein synthesis and RNA expression in tumours. **f, g**, Significantly ($P < 0.05$) changed 5' UTR ribosome densities in tumours (**f**) and human *NSUN2*^{-/-} cell lines (excluding significant ($P < 0.05$) changes in *NSUN2*^{+/+}) (**g**) and corresponding CDS. **** $P < 0.0001$ (two-tailed Student's *t*-test). NS, not significant. RPKM, reads per kilobase of transcript per million mapped reads. **h, i**, Frequency of ribosomal density values ($P < 0.05$ and $abs(\log_2 FC) > 0$; FC, fold change) (**h**) and Gene Ontology (GO) categories in tumours. KO, knockout; WT, wild type. **j**, GO categories of significant ($P < 0.05$) changed 5' UTRs in *NSUN2*^{-/-} lines versus *NSUN2*^{+/+}. Dev., development; diff., differentiation; resp., response. Data are average of 4 replicates per condition in human (**g, j**) and mouse (**a–d**), or 3 in **e, h, i**.

density in 5' untranslated regions (UTRs)^{43,44}. Consistent with such a stress response, 5' UTRs in NSUN2-deficient cells showed increased ribosome densities (Fig. 5f, g, Extended Data Fig. 8k, l

and Supplementary Tables 7–9). The increased ribosome density in 5' UTRs is probably due to the occurrence of upstream open reading frames (uORFs)^{41,45}. Functionally, uORFs repress translation by sequestering initiation events or facilitating downstream re-initiation and translation^{45–48}, which may explain why protein synthesis of the corresponding coding sequences (CDS) remained unaltered (Fig. 5f, g).

Although the underlying mechanisms are unclear, differential ribosome density in 5' UTRs should alter the protein production of distinct genes. Indeed, transcripts with increased ribosome density in 5' UTRs were linked to apoptosis, stress response, cell shape and migration (Fig. 5h–j). In tumours, transcripts with reduced ribosome density in the CDS were related to differentiation (Fig. 5h, i). Thus, the ribosome profiling data correlated well with the phenotypic reduction of epidermal differentiation of *Nsun2*-deficient tumours; and the cell-intrinsic NSUN2-controlled translational programme(s) related to stress responses and cell motility was conserved between species.

To identify the translational programme that directly depended on RNA methylation, we performed ribosomal profiling after rescuing *NSUN2*^{-/-} human fibroblasts with the wild-type or enzymatically dead constructs of NSUN2 (Extended Data Fig. 9a–d). Modulators of cell adhesion and motility represented a quarter of translational repressed transcripts that depended on the enzymatic activity of NSUN2 (Extended Data Fig. 9e–g and Supplementary Tables 10a–c). Consequently, motility and adhesion were reduced and differentiation increased in primary human keratinocytes when NSUN2 was repressed or enzymatic-dead versions overexpressed (Extended Data Fig. 9h–m).

Thus, the undifferentiated stem cell state in *Nsun2*-deficient tumours was primarily driven by differential translation of proteins regulating cell migration, adhesion and stress responses (Extended Data Fig. 10a, b and Supplementary Fig. 1).

Low translation impairs stress responses

To test whether the stress-related programme in *Nsun2*^{-/-} tumours altered their sensitivity to external stress *in vivo*, we applied the cytotoxic agent 5-fluorouracil (5FU). 5FU is commonly used to treat squamous cell carcinomas⁴⁹. While wild-type tumours only showed a mild reduction in growth, 5FU-treatment blocked progression of *Nsun2*^{-/-} tumours (Fig. 6a and Extended Data Fig. 10c, d). *Nsun2*^{-/-} tumour cells were unable to re-enter the cell cycle after drug treatment, despite induction of p53 being detectable in all samples (Fig. 6b, c and Extended Data Fig. 10e, f). We obtained similar results using cisplatin (Extended Data Fig. 10g–i). 5FU-treated *Nsun2*^{-/-} tumour cell layers were reduced, and the remaining ITGA6⁺ basal cells unusually co-expressed the differentiation marker K10 (Fig. 6d, arrows). Thus, *Nsun2*-deficient tumours fail to activate survival pathways in response to stress.

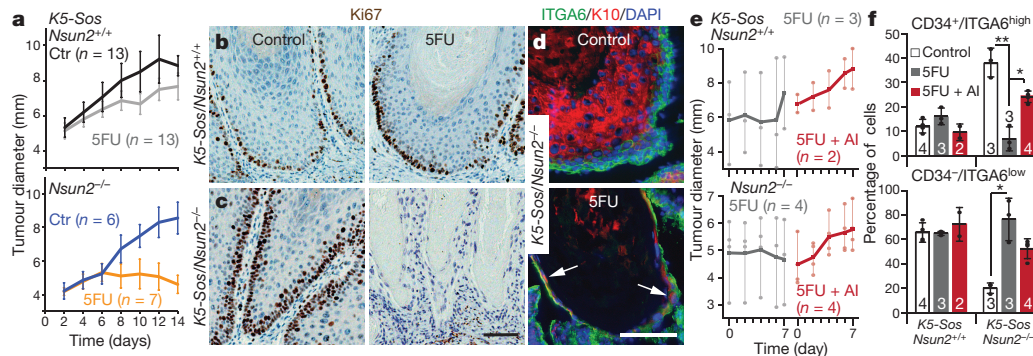


Figure 6 | *Nsun2* deletion sensitizes tumour-initiating cells to cytotoxic stress. **a–c**, Tumour size (mean \pm standard error of the mean (s.e.m.)) (**a**) and Ki67 detection (**b, c**) in control (Ctr) or 5FU-treated mice. **d**, K10 and ITGA6 detection in treated *Nsun2*^{-/-} tumours. Arrows indicate K10⁺/ITGA6⁺-positive cells. **e**, Tumour size in mice treated with 5FU and/or

angiogenesis inhibitor (AI) (horizontal line, mean). **f**, Quantification of tumour-initiating cells in tumours shown in **e** (mean \pm s.d.). * $P < 0.05$, ** $P < 0.01$ (two-tailed Student's *t*-test). *n* = mice. Scale bars, 100 μ m. Source Data for this figure is available in the online version of the paper.

Finally, we asked whether the increased sensitivity to 5FU depended on angiogenin-mediated cleavage of non-methylated tRNAs. We rescued tRNA cleavage by administering the angiogenin inhibitor N65828 (refs 1, 50). The high toxicity of this drug combination only allowed treatment for up to 7 days. Nevertheless, *Nsun2*^{-/-} tumours failed to regress, and the survival of undifferentiated tumour-initiating cells (CD34⁺/ITGA6^{high}) significantly increased when they were exposed to both drugs (Fig. 6e, f), indicating that tRNA fragments reduce the survival of *Nsun2*^{-/-} tumour-initiating cells.

In conclusion, combining cytosine-5 RNA methylation inhibitors with conventional chemotherapeutic agents may provide an effective anti-cancer strategy for solid tumours (Extended Data Fig. 10j).

Discussion

Similar to the haematopoietic system¹⁹, epidermal stem cells produce less protein than their immediate progenitors, and forced entry into the cell cycle is not sufficient to reverse this translation repression. Instead, global protein synthesis in normal and tumour cells is determined by lineage commitment, but not by proliferation.

We identify RNA methylation as an important pathway to modulate global protein synthesis and cell fate. Both protein synthesis and NSUN2 expression are low in epidermal stem cells, but increase upon commitment to differentiate. NSUN2-mediated methylation protects tRNA from cleavage into non-coding 5' tRNA fragments, thereby promoting protein translation and differentiation¹. External stress stimuli inhibit NSUN2 activity¹, permitting cleavage into 5' tRNA fragments, which then decrease protein synthesis in human cells⁴. Inhibition of post-transcriptional methylation in squamous tumours promotes stem cell function and tumorigenesis. However, re-activation of cytosine-5 RNA methylation pathways is required to exit the specific translation inhibition programme after cytotoxic stress. Thus, activation of RNA methylation or inhibition of tRNA cleavage is essential for cell survival of tumour-initiating cells in response to cytotoxic stress (see Supplementary Discussion).

Online Content Methods, along with any additional Extended Data display items and Source Data, are available in the online version of the paper; references unique to these sections appear only in the online paper.

Received 2 October 2014; accepted 21 April 2016.

- Blanco, S. *et al.* Aberrant methylation of tRNAs links cellular stress to neuro-developmental disorders. *EMBO J.* **33**, 2020–2039 (2014).
- Tuorto, F. *et al.* RNA cytosine methylation by Dnmt2 and NSun2 promotes tRNA stability and protein synthesis. *Nature Struct. Mol. Biol.* **19**, 900–905 (2012).
- Schaefer, M. *et al.* RNA methylation by Dnmt2 protects transfer RNAs against stress-induced cleavage. *Genes Dev.* **24**, 1590–1595 (2010).
- Ivanov, P., Emara, M. M., Villen, J., Gygi, S. P. & Anderson, P. Angiogenin-induced tRNA fragments inhibit translation initiation. *Mol. Cell* **43**, 613–623 (2011).
- Spriggs, K. A., Bushell, M. & Willis, A. E. Translational regulation of gene expression during conditions of cell stress. *Mol. Cell* **40**, 228–237 (2010).
- Sobala, A. & Hutvagner, G. Small RNAs derived from the 5' end of tRNA can inhibit protein translation in human cells. *RNA Biol.* **10**, 553–563 (2013).
- Gebetsberger, J., Zywicki, M., Künzi, A. & Polacek, N. tRNA-derived fragments target the ribosome and function as regulatory non-coding RNA in *Haloflex volcanii*. *Archaea* **2012**, 260909 (2012).
- Khan, M. A. *et al.* Mutation in NSUN2, which encodes an RNA methyltransferase, causes autosomal-recessive intellectual disability. *Am. J. Hum. Genet.* **90**, 856–863 (2012).
- Martinez, F. J. *et al.* Whole exome sequencing identifies a splicing mutation in NSUN2 as a cause of a Dubowitz-like syndrome. *J. Med. Genet.* **49**, 380–385 (2012).
- Abbasi-Moheb, L. *et al.* Mutations in NSUN2 cause autosomal-recessive intellectual disability. *Am. J. Hum. Genet.* **90**, 847–855 (2012).
- Blanco, S. *et al.* The RNA-methyltransferase Misu (NSun2) poises epidermal stem cells to differentiate. *PLoS Genet.* **7**, e1002403 (2011).
- Hussain, S. *et al.* The mouse cytosine-5 RNA methyltransferase NSun2 is a component of the chromatoid body and required for testis differentiation. *Mol. Cell Biol.* **33**, 1561–1570 (2013).
- Fuchs, E. Cell biology: more than skin deep. *J. Cell Biol.* **209**, 629–632 (2015).
- Plikus, M. V. & Chuong, C. M. Macroenvironmental regulation of hair cycling and collective regenerative behavior. *Cold Spring Harb. Perspect. Med.* **4**, a015198 (2014).
- Müller-Röver, S. *et al.* A comprehensive guide for the accurate classification of murine hair follicles in distinct hair cycle stages. *J. Invest. Dermatol.* **117**, 3–15 (2001).
- Jaks, V. *et al.* Lgr5 marks cycling, yet long-lived, hair follicle stem cells. *Nature Genet.* **40**, 1291–1299 (2008).
- Trempe, C. S. *et al.* Enrichment for living murine keratinocytes from the hair follicle bulge with the cell surface marker CD34. *J. Invest. Dermatol.* **120**, 501–511 (2003).
- Youssef, K. K. *et al.* Identification of the cell lineage at the origin of basal cell carcinoma. *Nature Cell Biol.* **12**, 299–305 (2010).
- Signer, R. A., Magee, J. A., Salic, A. & Morrison, S. J. Haematopoietic stem cells require a highly regulated protein synthesis rate. *Nature* **509**, 49–54 (2014).
- Fuchs, E. Scratching the surface of skin development. *Nature* **445**, 834–842 (2007).
- Hirai, Y., Nose, A., Kobayashi, S. & Takeichi, M. Expression and role of E- and P-cadherin adhesion molecules in embryonic histogenesis. II. Skin morphogenesis. *Development* **105**, 271–277 (1989).
- Joshi, R. S. The inner root sheath and the men associated with it eponymically. *Int. J. Trichology* **3**, 57–62 (2011).
- Sibilia, M. *et al.* The EGF receptor provides an essential survival signal for SOS-dependent skin tumor development. *Cell* **102**, 211–220 (2000).
- Egeblad, M., Nakasone, E. S. & Werb, Z. Tumors as organs: complex tissues that interface with the entire organism. *Dev. Cell* **18**, 884–901 (2010).
- Malanchi, I. *et al.* Cutaneous cancer stem cell maintenance is dependent on β -catenin signalling. *Nature* **452**, 650–653 (2008).
- Atsumi, N. *et al.* Podoplanin, a novel marker of tumour-initiating cells in human squamous cell carcinoma A431. *Biochem. Biophys. Res. Commun.* **373**, 36–41 (2008).
- Schober, M. & Fuchs, E. Tumour-initiating stem cells of squamous cell carcinomas and their control by TGF- β and integrin/focal adhesion kinase (FAK) signaling. *Proc. Natl Acad. Sci. USA* **108**, 10544–10549 (2011).
- Owens, D. M., Romero, M. R., Gardner, C. & Watt, F. M. Suprabasal $\alpha 6 \beta 4$ integrin expression in epidermis results in enhanced tumorigenesis and disruption of TGF β signalling. *J. Cell Sci.* **116**, 3783–3791 (2003).
- Lin, H. C. *et al.* High-level $\beta 1$ -integrin expression in a subpopulation of highly tumorigenic oral cancer cells. *Clin. Oral Investig.* **18**, 1277–1284 (2014).
- Ruggero, D. Translational control in cancer etiology. *Cold Spring Harb. Perspect. Biol.* **5**, a012336 (2013).
- Frye, M. & Watt, F. M. The RNA methyltransferase Misu (NSun2) mediates Myc-induced proliferation and is upregulated in tumors. *Curr. Biol.* **16**, 971–981 (2006).
- Frye, M. *et al.* Genomic gain of 5p15 leads to over-expression of Misu (NSun2) in breast cancer. *Cancer Lett.* **289**, 71–80 (2010).
- Schaefer, M., Pollex, T., Hanna, K. & Lyko, F. RNA cytosine methylation analysis by bisulfite sequencing. *Nucleic Acids Res.* **37**, e12 (2009).
- Hussain, S. *et al.* NSun2-mediated cytosine-5 methylation of vault noncoding RNA determines its processing into regulatory small RNAs. *Cell Reports* **4**, 255–261 (2013).
- Hussain, S., Aleksic, J., Blanco, S., Dietmann, S. & Frye, M. Characterizing 5-methylcytosine in the mammalian epitranscriptome. *Genome Biol.* **14**, 215 (2013).
- Khoddami, V. & Cairns, B. R. Identification of direct targets and modified bases of RNA cytosine methyltransferases. *Nature Biotechnol.* **31**, 458–464 (2013).
- Zhang, X. *et al.* The tRNA methyltransferase NSun2 stabilizes p16^{INK4} mRNA by methylating the 3'-untranslated region of p16. *Nature Commun.* **3**, 712 (2012).
- Tang, H. *et al.* NSun2 delays replicative senescence by repressing p27 (KIP1) translation and elevating CDK1 translation. *Aging* **7**, 1143–1158 (2015).
- Xing, J. *et al.* NSun2 promotes cell growth via elevating cyclin-dependent kinase 1 translation. *Mol. Cell Biol.* **35**, 4043–4052 (2015).
- Baranov, P. V. & Michel, A. M. Illuminating translation with ribosome profiling spectra. *Nature Methods* **13**, 123–124 (2016).
- Ingolia, N. T., Lareau, L. F. & Weissman, J. S. Ribosome profiling of mouse embryonic stem cells reveals the complexity and dynamics of mammalian proteomes. *Cell* **147**, 789–802 (2011).
- Schwanhäusser, B. *et al.* Global quantification of mammalian gene expression control. *Nature* **473**, 337–342 (2011).
- Gerashchenko, M. V., Lobanov, A. V. & Gladyshev, V. N. Genome-wide ribosome profiling reveals complex translational regulation in response to oxidative stress. *Proc. Natl Acad. Sci. USA* **109**, 17394–17399 (2012).
- Ingolia, N. T., Ghaemmaghami, S., Newman, J. R. & Weissman, J. S. Genome-wide analysis in vivo of translation with nucleotide resolution using ribosome profiling. *Science* **324**, 218–223 (2009).
- Calvo, S. E., Pagliarini, D. J. & Mootha, V. K. Upstream open reading frames cause widespread reduction of protein expression and are polymorphic among humans. *Proc. Natl Acad. Sci. USA* **106**, 7507–7512 (2009).
- Schleich, S. *et al.* DENR-MCT-1 promotes translation re-initiation downstream of uORFs to control tissue growth. *Nature* **512**, 208–212 (2014).

47. Lu, P. D., Harding, H. P. & Ron, D. Translation reinitiation at alternative open reading frames regulates gene expression in an integrated stress response. *J. Cell Biol.* **167**, 27–33 (2004).
48. Morris, D. R. & Geballe, A. P. Upstream open reading frames as regulators of mRNA translation. *Mol. Cell. Biol.* **20**, 8635–8642 (2000).
49. Longley, D. B., Harkin, D. P. & Johnston, P. G. 5-Fluorouracil: mechanisms of action and clinical strategies. *Nature Rev. Cancer* **3**, 330–338 (2003).
50. Kao, R. Y. *et al.* A small-molecule inhibitor of the ribonucleolytic activity of human angiogenin that possesses antitumor activity. *Proc. Natl Acad. Sci. USA* **99**, 10066–10071 (2002).

Supplementary Information is available in the online version of the paper.

Acknowledgements We thank J. Marioni and D. Odom for their advice on analysing the sequencing data. This work was funded by Cancer Research UK, Worldwide Cancer Research, the Medical Research Council (MRC), the European Research Council, and EMBO. Research in M.F.'s

laboratory is supported by a core support grant from the Wellcome Trust and MRC to the Wellcome Trust-Medical Research Cambridge Stem Cell Institute.

Author Contributions M.F., S.B. and R.B. designed experiments and performed data analysis. S.B., R.B., M.P., S.H., A.S., H.T., R.C.-G. and N.G. performed experiments. P.L., J.A. and S.D. performed bioinformatics analysis. M.F., S.B. and R.B. wrote the manuscript.

Author Information Mouse next-generation sequencing data have been deposited in the Gene Expression Omnibus under accession number GSE72067. Human data have been deposited in dbGAP under accession number phs000645.v2.p1. Reprints and permissions information is available at www.nature.com/reprints. The authors declare no competing financial interests. Readers are welcome to comment on the online version of the paper. Correspondence and requests for materials should be addressed to M.F. (mf364@cam.ac.uk).

METHODS

Transgenic mice. *Rosa-CAG-LSL-tdTomato* (ref. 51), *K19-CreER* (ref. 52) and *Lgr5-CreERT2* (ref. 53), *Nsun2*^{-/-} (or homozygous *Nsun2*^{Gt(D014D11)Wist})¹¹, and *K5-Sos-F* (in a *wa2/wa2* background)²³ mutant mice have been described previously. Balb/C athymic nude mice purchased from Charles River were used in transplantation experiments. All mice were housed in the Wellcome Trust—Medical Research Council Cambridge Stem Cell Institute Animal Unit. All mouse husbandry and experiments were carried out according to the local ethics committee under the terms of a UK Home Office license PPL80/2231 and PPL80/2619.

To conditionally induce *tdTomato*-reporter lines for expression of Cre-recombinase, *Rosa-CAG-LSL-tdTomato* mice were crossed with *K19-CreER* or *Lgr5-CreERT2* mice. To activate CreER, only male mice were treated with two intraperitoneal (i.p.) injections of 50 µl of a tamoxifen (Sigma-Aldrich) solution (40 mg ml⁻¹) in corn oil at postnatal day 15 and 17.

To measure protein synthesis *in vivo*, mice were i.p. injected with O-propargyl-puromycin (OP-puro) (Medchem Source LLP) at a concentration of 50 mg per kg of body weight dissolved in PBS at pH 6.4–6.6 1 h before being killed. Skin samples were collected at Catagen (postnatal day (P)17), telogen (P19), early anagen (P25) and late anagen (P30).

To induce squamous tumours in an *Nsun2*^{-/-} background, we used *K5-Sos* transgenic mice. These mice express a dominant-negative form of son of sevenless (SOS) under control of the keratin 5 (K5) promoter and develop spontaneous cutaneous tumours with 100% penetrance²³. *K5-Sos*^{Fxwa2/wa2} mice were crossed with *Nsun2*^{+/-} mice carrying a gene trap in the *Nsun2* allele (*Nsun2*^{Gt(D014D11)Wist}). Spontaneous skin papillomas developed mainly in the tail of *K5-Sos*^{Fxwa2/+} mice 2 weeks after birth but they did not develop into malignant squamous cell carcinomas²³.

Histology, tissue and cell stainings, antibodies and imaging. Tissues or tumours were either embedded in OCT and frozen or fixed overnight with 4% paraformaldehyde, transferred to 70% EtOH and embedded in paraffin. Samples were then cut at 4 µm (paraffin) or 10 µm (frozen). Immunofluorescence staining, LacZ and haematoxylin and eosin staining of frozen or paraffin-embedded tissues or cells were performed as described previously¹¹. For immunohistochemistry, ImmPRESS reagents (Vector Labs) or IHC Detection Kit (Ventana Medical Systems) and DISCOVERY automated IHC staining system (Ventana Medical Systems) were used.

Primary antibodies were used at the following dilutions: rabbit polyclonal to RFP (for *tdTomato*) (1:1,000; Rockland, 600-401-379), mouse monoclonal to DLX3 (1:200, Abnova, H00001747-A01), rabbit polyclonal to K6 (1:200, Abcam, ab24646), mouse monoclonal to GATA3 (1:50, Santa Cruz Biotech, sc-268), guinea pig polyclonal to K31 and K72 (1:200, Progen, GP-hHa1 and GP-K6ir52), rabbit polyclonal anti c-MAF (1:100, Bethyl, A300-613A), mouse monoclonal to LEF1 (1:50, Santa Cruz Biotech, sc-81470), goat polyclonal to P-cadherin (1:100, R&D systems, FAB761A), rabbit monoclonal antibody to Ki67 (1:200; SP6, Vector Labs, VP-RM04), mouse monoclonal anti-mouse K15 (1:1,000; ref. 54), β-catenin (1:200, Santa Cruz Biotech, sc-7199), rat monoclonal anti-ITGB1 (1:200, clone HMβ1-1, BioLegend, 102203), rabbit polyclonal anti-mouse K10 (1:500; Covance, PRB-159P), rabbit polyclonal anti-NSUN2 (1:500; Aviva Systems Biology, ARP48811_P050), rabbit polyclonal anti-human NSUN2 (MetA, 1:500; ref. 31), rat monoclonal anti-ITGA6 (1:500; GoH3, eBioscience, 14-0495), rat monoclonal anti-CD44 (1:200, IM7, BioLegend, 103004), anti-mouse podoplanin (1:500, clone 8.1.1, eBioscience, 14-5381), rat monoclonal anti-BrdU (1:100; Abcam, ab6326), rabbit polyclonal anti-laminin-α5 (1:100, Abcam, ab75344), mouse monoclonal anti-cytokeratin 8 (1:100, TROMA-I, DSHB, US), rabbit polyclonal to Slug (1:200, Cell Signaling, 9585P), chicken polyclonal anti-GFP (1:200, Abcam, ab13970), rabbit polyclonal anti-p53 (1:100, CM5, Novocastra, NCL-p53-CM5p), and rabbit anti human involucrin (SY5 clone, 1:200, Abcam, ab80530). Alexa Fluor 555-, Alexa Fluor 647- and Alexa Fluor 488-conjugated secondary antibodies (Thermo Fisher Scientific) were added at a dilution of 1:1,000 for 1 h at room temperature. Apoptotic cells were visualized staining sections with DeadEnd Fluorometric TUNEL System (Promega) or immunostained for rabbit polyclonal anti-cleaved Caspase3 (1:200, Cell Signaling, 9664). Nuclei were labelled with DAPI or haematoxylin. Slides were mounted in glycerol supplemented with Mowiol 4-88 mounting medium (Sigma-Aldrich).

White field images were acquired using an Olympus IX80 microscope and a DP50 camera. Fluorescence images were acquired either on a Zeiss Axioplan microscope or using a confocal microscope (Leica TCS SP5) at 1,024 × 1,024 dpi resolution. All the images were further processed with Photoshop CS5 (Adobe) software.

Isolation of mouse keratinocytes from normal skin and skin tumours. To isolate keratinocytes from mouse back skin, shaved skin was floated on 0.25% trypsin without EDTA (Thermo Fisher Scientific) for 2 h at 37°C. Then the epidermis

was scraped off the dermis, and cells were disaggregated by gentle mincing with a scalpel and pipetting. For back skin in late anagen the dermis was further minced and digested for 30 min at 37°C in low-calcium medium containing 1.25 mg ml⁻¹ of collagenase type I, 0.5 mg ml⁻¹ of collagenase type II, 0.5 mg ml⁻¹ of collagenase type IV (all from Worthington) and 0.1 mg ml⁻¹ of hyaluronidase (Sigma-Aldrich).

To disaggregate cells from squamous tumours, the tumours were minced with a scalpel and incubated for 1–2 h at 37°C in low-calcium medium containing 1.25 mg ml⁻¹ of collagenase type I, 0.5 mg ml⁻¹ of collagenase type II, 0.5 mg ml⁻¹ of collagenase type IV (all from Worthington) and 0.1 mg ml⁻¹ of hyaluronidase (Sigma-Aldrich). Then pieces were further incubated for another hour with trypsin without EDTA (Thermo Fisher Scientific) and cells disaggregated by scraping with a scalpel blade. Trypsin was inactivated by washing the cell suspension with low-calcium media containing 10% of FBS (Thermo Fisher Scientific).

In vivo measurement of protein synthesis by flow cytometry and microscopy. Quantification of protein synthesis from back skin was performed using only male mice. Back skin or cutaneous tumours were collected and further processed for flow cytometry or histology analysis (described earlier). For flow cytometry analysis cells were dissociated as described earlier. For staining of dissociated cells or frozen sections, samples were first fixed with 1% paraformaldehyde in PBS for 15 min on ice. Next samples were washed in PBS, and then permeabilized in PBS supplemented with 3% fetal bovine serum (Sigma-Aldrich) and 0.1% saponin (Sigma-Aldrich) for 5 min at room temperature. To conjugate OP-puro to a fluoro-chrome, an azide-alkyne cycloaddition was performed using the Click-iT Cell Reaction Buffer Kit (Thermo Fisher Scientific) and 5 µM of Alexa Fluor 488 or Alexa Fluor 647 conjugated to azide (Thermo Fisher Scientific). After the 30-min reaction, the cells were washed twice in PBS with 3% fetal bovine serum and 0.1% saponin and then resuspended in PBS. When indicated cells were further stained for cell surface markers and DAPI as described later.

To visualize protein synthesis together with antibody staining in skin or tumour paraffin embedded or frozen sections; frozen sections were first fixed with 1% paraformaldehyde in PBS for 15 and paraffin sections were first de-waxed and progressive rehydration sections were then blocked and stained with primary antibodies overnight at 4°C. Next, the sections were washed and stained with secondary antibodies for 1 h at room temperature. After washes sections were stained using the Click-iT Cell Reaction Buffer Kit with Alexa Fluor-647 or -488 azide (Thermo Fisher Scientific) as described earlier.

Quantification of protein synthesis rates. Protein synthesis rates in specific cell populations were calculated by normalizing the mean of OP-puro signal of each population of interest to the signal of the whole epidermal or tumour cell preparation, using the following formula: mean OP-puro_{population of interest}/mean OP-puro_{all epidermal or tumour cells (CD117-negative; CD31-negative; CD45-negative)}. The mean of OP-puro incorporation was averaged from several mice collected in multiple independent experiments. OP-puro fluorescence signal between experiments was calibrated by including in each run BD rainbow calibration particles 8 peaks (BD Bioscience). Samples from PBS-injected mice were also stained for OP-puro and the fluorescence signal was used to determine the background signal.

Flow cytometry and cell cycle analysis. Flow cytometry was performed for cells dissociated from normal skin, skin tumours or cells growing in culture. Cell dissociation from skin or tumours was performed as described earlier. Cells in culture were trypsinized for 5 min before performing the staining. Analysis of specific epidermal or tumour populations, live cells, or fixed cells previously stained for OP-puro as indicated earlier were incubated in 2% of BSA with combinations of antibodies to the following cell-surface markers: PE-Cy7-conjugated CD117 (1:100, clone 2B8, BD Bioscience, 558163), PE-Cy7-conjugated CD31 (1:50, PE-CAM1, eBioscience, 563651), PE-Cy7-conjugated CD45 (1:100, BD Pharmingen, 552848), PE- or eFluor-450-conjugated ITGA6 (1:500, clone GoH3, eBioscience, 12-0495 and 48-0495), eFluor-660- or FITC-conjugated CD34 (1:50, RAM34, eBioscience, 50-0341 and 11-0341), biotinylated CD44 (clone IM7, BioLegend, 103004) and PE-conjugated PDPN (eBioscience, 12-5381-82). After incubation for 30 min at 4°C, cells were washed twice in PBS. Biotinylated antibodies were visualized by incubation with Alexa Fluor-488-conjugated streptavidin (Thermo Fisher Scientific) for 10 min. For cell cycle analysis cells were further stained with DAPI. *tdTomato*⁺ cells were detected using PE-Texas Red channel.

Cells were gated using forward versus side scatter to eliminate debris and aggregates. Surface markers CD117, CD31 and CD45 were used to gate out endothelial cells, melanocytes and blood cells when analysing cell preparations from skin or tumours. Data acquisition was performed on a BD LSRFortessa analyser (BD Biosciences). Data were analysed by FlowJo software.

Measurement of tumour growth and tumour treatments. Both male and female mice were used in these experiments. To evaluate the effect of *Nsun2* deletion on the formation of skin tumours we measured the presence (number of tumours), the growth of the tumours, the percentage of mice with tumours as well the survival

of the mice throughout the length of the experiment (approximately 6–8 weeks). To monitor tumour occurrence and growth mice were weighed, the number of all tumours formed all over the body were counted and the growth of each tumour monitored every other day from P16 (the earliest time at which *K5-Sos-F* mice start developing papillomas). Papillomas in the tail tended to fuse into one covering the whole tail, and therefore were counted as one tumour from the beginning of the experiments. Other tumours also developed in ears, mouth, back skin or feed. The growth of each tumour was monitored by measuring the diameter of the widest area of the tumour using a precision calliper allowing discriminating size modifications >0.1 mm. When animals have to be treated with drugs, experiments started also at the third week of age. The end point of the experiments was determined by health deterioration and casualties or by the length of the treatments when mice were under a treatment regime. *K5-Sos^{Fxwa2/+}Nsun2^{+/-}* (referred as *K5-Sos/Nsun2^{+/-}*) survived longer than *K5-Sos^{Fxwa2/+} × Nsun2^{-/-}* (*K5-Sos/Nsun2^{-/-}*) and *K5-Sos^{Fxwa2/+} × Nsun2^{+/-}* (*K5-Sos/Nsun2^{+/-}*). All mouse tumour experiments were carried out according to the local ethics committee under the terms of a UK Home Office license PPL80/2231 and PPL80/2619. Following these regulations the mean diameter of a tumour should not normally exceed 1.4 cm (PPL80/2619, 19b 7). While *K5-Sos/Nsun2^{-/-}* and *K5-Sos/Nsun2^{+/-}* had to be killed before mice reached 2 months of age due to the size and aspect of the tumours and weight loss or general health deterioration due to excessive tumour burden, *K5-Sos/Nsun2^{+/-}* only reached the deterioration state later than 2 months of age. For the analysis in Fig. 4a we measured the percentage of mice with tumours for each indicated day. The average number of tumours in each mouse genotype is shown in Extended Data Fig. 5c. Note that data points are shorter for *K5-Sos/Nsun2^{-/-}* and *K5-Sos/Nsun2^{+/-}* as mice survival was shorter. The diameter of the tumours was normalized to the size of each mouse (body weight) in Extended Data Fig. 5b to eliminate genotype variance because *K5-Sos/Nsun2^{-/-}* mice are significantly smaller than *K5-Sos/Nsun2^{+/-}*.

Cutaneous tumours in transgenic *K5-Sos/Nsun2^{+/-}* and *K5-Sos/Nsun2^{-/-}* mice were topically treated with 5-Fluorouracil (5FU) (Efudix 5% Fluorouracil Cream, Meda Pharmaceuticals) every second day for 2 weeks. 5FU inhibits thymidylate synthases leading to the upregulation of p53 and cell death⁴⁹. Tumours were also treated with 5FU in combination with an angiogenesis inhibitor (AI; N65828, NCI, US)^{1,50} administered by i.p. injections at 2 mg kg⁻¹ in PBS pH 7.4 every alternative day to 5FU treatment. Owing to the high toxicity of the drug combination, we were only able to simultaneously treat with 5FU and AI for a short period of time (up to 7 days). Cisplatin (CDDP) (Sigma) was dissolved in PBS and injected intraperitoneally at 14 mg kg⁻¹ every other day. All treatments started when the first cutaneous lesions appeared and the end point was indicated by the length of the treatment, after which all mice were killed. Control mice were administered PBS. **BrdU and EdU labelling.** To measure proliferation, *K5-Sos* mice were injected i.p. with 50 mg of BrdU per kg of body weight, 23 h later with 20 mg kg⁻¹ of EdU. One hour later mice were killed and tumour samples were processed for histology as described previously. BrdU was visualized as described previously¹¹. EdU was stained with Click-iT EdU Alexa Fluor 488 Imaging Kit (Thermo Fisher Scientific). Images of random areas of the slide were collected using a confocal microscope (Leica SP5). Numbers of BrdU- and EdU-positive cells were quantified using Volocity software (PerkinElmer).

Tumour graft assay. Epidermal keratinocytes from *K5-Sos/Nsun2^{+/-}* and *K5-Sos/Nsun2^{-/-}* cutaneous tumours were isolated as described earlier. GFP-expressing dermal fibroblasts were isolated from healthy skin of newborn *APC-eGFP* mice. For this, skin was first incubated in a 1:1 solution of 5% dispase (BD Biosciences) at 37 °C for 1 h. The epidermis was then peeled from the dermis. The dermis was incubated with 0.2% collagenase in low-calcium medium for 30 min at 37 °C to yield a single-cell suspension. The dermis suspension was filtered through a 70-µm cell strainer. 1×10^6 of viable epidermal keratinocytes from *K5-Sos/Nsun2^{+/-}* or *K5-Sos/Nsun2^{-/-}* tumours were injected subcutaneously in athymic nude mice. To allow successful engrafting, the tumour cells were injected with 1×10^6 of viable GFP dermal fibroblasts. The GFP-expressing dermal fibroblasts integrated into the dermis but failed to contribute to tumour formation (Extended Data Fig. 6c). Experiments were done in triplicates. Nude mice were killed 1 month after transplantation and tumour size was measured with a calliper.

RNA extraction and quantitative RT-PCR. Total RNA from mouse skin tumours was prepared using Trizol reagent (Thermo Fisher Scientific) and double-stranded cDNA was generated with Superscript III First-Strand Synthesis kit (Thermo Fisher Scientific). Real-time PCR amplification and analysis was conducted in StepOne™ Real-Time PCR Systems (Applied Biosystems) using pre-designed probe sets and TaqMan Fast Universal PCR Master Mix (2×) (Applied Biosystems). The following probes were used to amplify selected genes *Nsun2* (Mm00520224_m1), $\alpha 6$ integrin (Mm01333831_m1), *Cd34* (Mm00519283_m1),

Krt10 (Mm03009921_m1) and involucrin (Mm00515219_s1). *Gapdh* expression (4352932E) was used to normalize samples using the ΔC_t method.

Mouse SCC and TMA staining and quantification. Mouse squamous cell carcinomas (SCCs) were obtained from a TPA/DMBA chemical induction treatment for 20 weeks and frozen tissues were provided by C. Blanpain. Frozen sections were stained as described earlier.

Tissue microarrays (TMAs) for human skin tumours of increased malignancy according to the TNM classification were purchased from Abcam (ab178287 and ab178288). Immunohistochemistry was performed using IHC Detection Kit (Ventana Medical Systems) and DISCOVERY automated IHC staining system (Ventana Medical Systems) with a polyclonal antibody for human NSUN2 (Meta, 1:1,000; ref. 31). Images of each tumour section were acquired with a Zeiss AxioPlan microscope and NSUN2 expression levels were quantified for each individual cell in each tissue (quantified as average between all cells in all sections) using CellProfiler image software.

Cell culture, viral infections and siRNA knockdown. Four lines of human dermal fibroblasts were used. Two independent cell lines of *NSUN2^{-/-}* human dermal fibroblasts were derived from two patients and referred as *NSUN2^{-/-}* line 1 and line 2 in this study, and one line of *NSUN2^{+/-}* fibroblasts was derived from the mother of the patients described previously⁹; these three lines were provided by J. Gleeson. *NSUN2^{+/-}* human dermal fibroblasts were purchased from Thermo Fisher Scientific (C-013-5C) and were derived from an age- and gender-matched individual compared to *NSUN2^{+/-}* fibroblasts. Human fibroblasts were grown in MEM (Thermo Fisher Scientific) supplemented with 20% fetal bovine serum (FBS) as described previously⁹. ZHC human epidermal keratinocytes (Cellworks distributed, ZHC-1116) were grown in KBM-Gold medium (Lonza). All cells were kept in a humidified atmosphere at 37 °C and 5% CO₂.

To rescue expression of NSUN2 or express NSUN2 catalytically dead mutants in *NSUN2^{-/-}* fibroblasts or ZHC keratinocytes, full-length human NSUN2 (pB-NSUN2), inactive mutants C271A (pB-NSUN2-C271A), K190M (pB-NSUN2-K190M) or C321A (pB-NSUN2-C321A) or the empty vector (pB-empty) were infected via retrovirus as described previously⁵⁵. To knock down NSUN2 expression in human keratinocytes, cells were transfected with control siRNA (AllStars negative control siRNA (Qiagen, 1027292) or human NSUN2 short interfering (siRNA) (Flexitube siRNA Qiagen, SI02655548) using Lipofectamine RNAiMax transfection reagent (Thermo Fisher Scientific) according to the manufacturer's instructions.

Migration assays. For migration analysis in Boyden chambers, human primary keratinocytes were transfected with siRNAs as described earlier. Transfections were carried twice every 48 h and migration assay was performed 24 h after the second transfection. Cells were treated with mitomycin C for 2 h to arrest cell cycle progression. After mitomycin C treatment cells were trypsinized and counted and seeded on Boyden chambers (transwell inserts of 8 µm, 24-well plates, BD Biosciences). 8×10^4 cells were seeded with KBM growing medium (Lonza) without human recombinant (hr)EGF. Media containing 10 ng ml⁻¹ of hrEGF (Lonza) was placed under the transwell inserts as a chemoattractant to attract cells. Media without chemoattractant was placed under the transwell inserts in control experiments. Cells were allowed to migrate for 6 or 12 h, after which the inserts were washed once with PBS, fixed with 4% PFA for 10 min, and cells were stained with DAPI. Cells from the upper side of the membrane were scratched off with a cotton bud and washed off with PBS several times. Cells on the bottom side of the membrane were imaged with a colony scan microscope. Cells were then quantified with the software CellProfiler.

For motility analysis of human keratinocytes, 10^4 cells were seeded in 24-well ImageLock plates (Essen Instruments) in growing medium and kept for 26 h at 37 °C in 5% CO₂. Cell mobility was recorded with an automated IncuCyte microscope (Essen Instruments). Images were collected at 15-min intervals. Two-dimensional cell migration was analysed by using the MTracking function of ImageJ software. Two-dimensional migration tracks were generated by manually tracing the nucleus of each cell. Migrated distance was obtained by measuring the linear distance travelled between the first and last position (after 26 h) of each tracked cell.

tRNA sequencing library preparation. Small RNA libraries were generated from snap-frozen skin papillomas from 4-week-old mice. Four independent biological replicates were used. For tRNA library generation we followed the protocols described previously¹. Briefly total RNA was extracted using Trizol reagents (Thermo Fisher Scientific) and treated with DNase (Turbo DNase, Thermo Fisher Scientific). Ribosomal RNA was removed with Ribo-zero (Epicentre, Illumina). The remaining RNA fraction was size-selected using MirVana Isolation Kit (Thermo Fisher Scientific). Using MirVana RNA purification columns with two sequential filtration steps with different ethanol concentrations, an RNA fraction highly enriched in RNA species ≤ 200 nucleotides was obtained. The

small RNA fraction (approximately 200 ng) was first treated with 0.1 M Tris-HCl pH 9.0 and 1 mM EDTA for 30 min at 37 °C to de-aminoacylate mature tRNAs and later T4-PNK (NEB) treated to ensure phosphorylated 5' ends and 3' OH ends to proceed with RNA adaptor ligation and library preparation. tRNA libraries were generated using TruSeq Small RNA Preparation Kit (Illumina). Briefly, 3' adenylated and 5' phosphorylated adapters suitable for Illumina RNA sequencing were ligated to the small RNA fraction. RNA was reverse-transcribed at 50 °C for 1 h (SuperScript III cDNA synthesis kit, Thermo Fisher Scientific), followed by PCR amplification with Phusion DNA polymerase (Thermo Fisher Scientific). All samples were multiplexed and sequenced in HiSeq platform (Illumina).

Bisulfite sequencing library preparation. To generate bisulfite sequencing libraries, RNA was prepared and bisulfite treated as described previously³³. Briefly RNA was extracted with Trizol reagents (Thermo Fisher Scientific) from snap-frozen skin tumours from 4-week-old mice. Four independent biological replicates were used. Total RNA was extracted and DNase treated (Turbo DNase, Thermo Fisher Scientific). Samples were Ribo-zero treated (Epicentre, Illumina) to deplete them from rRNA. At least 1.5 µg of the remaining RNA fraction was bisulfite converted as follows: RNA was mixed in 70 µl of 40% sodium bisulfite pH 5.0 and DNA protection buffer (EpiTect Bisulphite Kit, Qiagen). The reaction mixture was incubated for three to four cycles of 5 min at 70 °C followed by 1 h at 60 °C and then desalted with Micro Bio-spin 6 chromatography columns (Bio-Rad). RNA was desulfonated by adding an equal volume of 1 M Tris (pH 9.0) to the reaction mixture and incubated for 1 h at 37 °C, followed by ethanol precipitation. 2',3'-Cyclic phosphate and 5'-hydroxyl termini produced during the bisulfite/desulfonation reaction were end-repaired with T4 PNK (New England Biolabs). About 120 ng of bisulfite-converted RNA was used to generate bisulfite-seq (BS-Seq) libraries. Because bisulfite treatment and desulfonation cleaves long RNAs into fragments of about 100 nucleotides, we then used TruSeq Small RNA preparation kit (Illumina) to generate libraries suitable for Illumina sequencing as described previously¹. Briefly, RNA adapters suitable for Illumina sequencing were ligated to bisulfite-converted RNAs, reverse transcribed at 50 °C for 1 h with SuperScript III and 2 mM of each dNTP (SuperScript III cDNA synthesis kit, Thermo Fisher Scientific) followed by PCR amplification. All samples were multiplexed and sequenced on a HiSeq platform (Illumina).

Preparation of Ribo-seq libraries. Two types of experiments were performed on mouse skin tumours (from *K5-Sos* mice) and human dermal fibroblasts samples from each set of conditions: ribosomal profiling (Ribo-seq) and mRNA-seq. All samples were sequenced using the HiSeq platform (Illumina). A minimum of three replicates was performed for each sample. Dermal fibroblasts were grown and infected when indicated as described earlier and with the constructs indicated in each experiment. For cells or tissue collection, none were pre-treated with cycloheximide, however, cycloheximide was present in the following steps. Cells were washed with PBS (without cycloheximide) twice and lysis buffer (20 mM Tris-Cl (pH 7.4), 150 mM NaCl, 5 mM MgCl₂, 1 mM dithiothreitol (DTT) (Sigma), 1% Triton X-100 (Sigma), 25 U ml⁻¹ of Turbo DNase I (Thermo Fisher Scientific) containing 100 µg ml⁻¹ of cycloheximide (Sigma) was added straight to the cells. Papillomas were dissected from the mice, snap frozen in liquid nitrogen and later homogenized in lysis buffer containing 100 µg ml⁻¹ of cycloheximide. Cycloheximide was added to the lysis buffer to arrest translation elongation while the polysome fraction was being purified and mRNA fragments were recovered. We then proceeded with ribosome footprint purification without snap freezing the lysates as indicated previously⁵⁶. All the steps for cell or tissue lysis, nuclease footprinting, polysome fractionation, mRNA footprint purification and gel size-selection were performed as indicated previously⁵⁶. Briefly, lysates were further triturated by passing them ten times through a 26-G needle. Nuclei and debris were removed by centrifugation at 13,000 r.p.m. for 10 min. Supernatant was digested with RNaseI (100 U µl⁻¹, Thermo Fisher Scientific) for 45 min at room temperature. Digestion was blocked with SupersaseIN (Thermo Fisher Scientific) and lysate was layered on a 1 M sucrose cushion and separated by ultracentrifugation at 45,000 r.p.m. in a 70Ti rotor for 9 h at 4 °C. Pellets were resuspended in Qiazol and RNA fragments lower than 200 nucleotides were extracted using miR-Neasy kit (Qiagen) followed by ethanol precipitation. Size selection of footprints with a length of 26–34 nucleotides was performed on 15% TBE-urea gel (Thermo Fisher Scientific). Footprints were 3'-dephosphorylated with T4 polynucleotide kinase (10 U, NEB). From this step and to prepare libraries suitable for Illumina sequencing we slightly modified the original protocol⁵⁶. mRNA footprints were then treated with Ribo-zero (Epicentre Illumina) to deplete rRNA. By using this extra step of rRNA depletion (together with the use of DNA oligonucleotides to deplete rDNA by subtractive hybridization in a later step) we were able to reduce rRNA contamination to only ~60% of all reads. mRNA footprints recovered from Ribo-zero were then prepared for Ribo-seq using TruSeq Small RNA Preparation Kit (Illumina). Briefly, 3'-adenylated and 5'-phosphorylated adapters suitable

for Illumina RNA sequencing were ligated to the recovered mRNA fragments. RNA was reverse transcribed at 50 °C for 1 h (SuperScript III cDNA synthesis kit, Thermo Fisher Scientific), followed by rDNA depletion by subtractive hybridization (as indicated in the original protocol) using oligonucleotides listed previously⁵⁶ and following the protocol recommendations. Recovered complementary DNAs were PCR amplified with no more than 12 PCR cycles. All samples were multiplexed and sequenced in HiSeq platform (Illumina).

Preparation of mRNA-seq libraries. mRNA-seq libraries were generated from mouse skin tumours from 4-week-old *K5-Sos/Nsun2*^{+/+} and *K5-Sos/Nsun2*^{-/-} mice, from mouse healthy back skin from 3.5–4-week-old *Nsun2*^{+/+} or *Nsun2*^{-/-} mice (without tumours) and from human dermal fibroblasts (*NSUN2*^{+/+}, *NSUN2*^{+/-} and *NSUN2*^{-/-}) growing in culture and infected when indicated. At least four replicates were performed for each sample. All samples were multiplexed and sequenced using the HiSeq platform (Illumina). Total RNA was extracted using Trizol (Thermo Fisher Scientific) from cells in culture or snap-frozen tissues. Total RNA was DNase (Turbo DNase, Thermo Fisher Scientific) and Ribo-zero (Epicentre, Illumina) treated. rRNA-depleted RNA was used to generate mRNA-seq libraries using NEXTFlex Directional RNA-seq Kit V2 (Illumina). All samples were multiplexed and sequenced in HiSeq platform (Illumina).

Next-generation sequence data analyses. For all data analyses, FastQC was used for the initial assessment of the quality and basic processing of the reads (<http://www.bioinformatics.babraham.ac.uk/projects/fastqc>). Sequencing adapters were trimmed from the 5' and the 3' ends of the reads using cutadapt (v.1.4.2; <https://pypi.python.org/pypi/cutadapt/1.4.2>).

RNA BS-seq analysis. To determine RNA methylation levels in mouse *K5-Sos* tumours, two complementary protocols for the analysis of BS-seq data were used. **Alignment to the genome.** BS-seq reads were aligned to mouse reference genome (GRCm38/mm10) with Bismark (<http://www.bioinformatics.babraham.ac.uk/projects/bismark>; v.0.13.1; options: '-directional -n 0 -l 40'). Methylation levels for all cytosines with at least coverage of ≥5 reads (5× coverage) in both *K5-Sos/Nsun2*^{+/+} and *K5-Sos/Nsun2*^{-/-} tumour samples were inferred with Bismark 'methylation_extractor'. Cytosine positions displaying a difference in RNA methylation of at least 10% between *K5-Sos/Nsun2*^{+/+} and *K5-Sos/Nsun2*^{-/-} tumour samples were extracted based on the ENSEMBL (GRCm38, Release 74; <http://www.ensembl.org/info/data/ftp>) transcript annotations and tRNA gene predictions in the mouse (GRCm38/mm10) reference genome obtained from GtRNAdb (<http://lowelab.ucsc.edu/GtRNAdb>).

Alignment to representative transcripts. Sequences for ENSEMBL transcripts and tRNAs were extracted in FASTA format. All transcript isoforms were considered, and in addition the longest gene at full length including introns was retained as a representative sequence to identify RNA methylation sites in introns. Cs were converted to Ts in the reference transcript sequences, and in the processed BS-seq reads. Alignment of converted BS-seq reads against converted transcript sequences were performed using bowtie (v.1.1.1; <http://bowtie-bio.sourceforge.net>; options '-m 500 -v 2 -a -best -strata'). Following alignments, the reads that aligned in the sense direction were obtained, and the original transcript sequences and reads were used to compile RNA methylation (C/(C+T) levels considering only cytosines with at least 5× coverage. Heatmaps displaying either C or T in the aligned reads at each cytosine position were generated using custom PERL scripts and matrix2png (<http://www.chibi.ubc.ca/matrix2png/>) for visualization. Cytosine positions on the heatmaps were reported relative to the annotated transcriptional start sites of the transcripts.

tRNA-seq data analysis. The abundance of tRNA fragments was determined according to a previously published protocol¹. Adaptor-trimmed tRNA-seq reads (>20 nucleotides and <200 nucleotides in length) were mapped to the mouse reference genome (GRCm38/mm10) using bowtie (v.1.1.1; <http://bowtie-bio.sourceforge.net>; options '-m1 -v2 -a -best -strata') considering only reads that map uniquely to the genome. To account for the polymerization of CCA 3' ends onto mature tRNAs, the remaining unmapped reads were trimmed of CCA[CCA] ends and realigned using the same options. Annotations were conducted based on tRNA genes predicted for the mouse reference genome (GRCm38/mm10) and downloaded from GtRNAdb (<http://lowelab.ucsc.edu/GtRNAdb>). Reads that exceeded the annotated tRNA gene start or end by more than 10% were discarded. All distinct reads, which were shorter than 90% of the annotated tRNA gene length, were considered as tRNA fragments. Counts per fragments were normalized, and the differential abundances of fragments processed from the 5' or 3' halves of the tRNAs were statistically evaluated using the R/Bioconductor DESeq package (<http://bioconductor.org/packages/release/bioc/html/DESeq.html>). tRNA fragment abundances are given by log₂(DESeq-normalized counts).

mRNA-seq and Ribo-seq data analyses. Ribosome profiling data was processed following established protocols⁵⁷. The first 5' base of the adaptor-trimmed Ribo-seq reads was removed, as this is usually an artefact of reverse transcription⁵⁶.

For removing abundant contamination from digested rRNA present in the libraries, the reads were aligned to a collection of rRNA sequences obtained from GenBank and UCSC using bowtie (options: '-n 2--seedlen = 23'). Reads aligning to rRNA were discarded, with the average rRNA contamination per sample being around 60%. Only reads with at least 24 nucleotides and less than 30 nucleotides length were retained in accordance with the observed length distribution of ribosome footprints⁴⁴.

Both the Ribo-seq and mRNA-seq reads were aligned to the human (GRCh37/hg19) and to the mouse (GRCm38/mm10) reference genomes using Tophat2 (v.2.1; options: '-read-mismatch 1(2)--max-multihits 1 -GTF') guided by ENSEMBL gene models (release 76), allowing for two mismatches per read for human and one mismatch per read for mouse, and unique alignments only.

To determine mRNA abundance, mRNA-seq read counts for the full transcript were calculated using htseq-count (<http://www-huber.embl.de/HTSeq/doc/overview.html>), data sets were normalized, and the statistical significance of differential expression was evaluated by using the R/Bioconductor DESeq2 package (<https://bioconductor.org/packages/release/bioc/html/DESeq2.html>).

To evaluate differences in translation, the following additional Ribo-seq data analyses and normalizations were performed.

Alignment to representative regions. Coding sequences (CDS) and 5' UTRs were downloaded from ENSEMBL including 'protein_coding' and 'nonsense-mediated decay' types of transcripts. Intron sequences were excluded. Ribo-seq reads, which uniquely aligned to the genome in the initial alignment step using Tophat2, were aligned to 5' UTR or CDS sequences using bowtie (options: '-m 1000 -v1'), allowing for multiple mappings to overlapping regions of the same gene.

Statistical analysis of differential ribosome footprint densities and normalization. In concordance with other studies performed in yeast or mammalian cells^{41,58}, we observed a characteristic 5' 'ramp' of ribosome footprints at the translation start site of the CDS for our samples. It has been suggested that these excess footprints are a result of cycloheximide-inflicted accumulation of ribosomes⁵⁶. To prevent any artefactual bias in our analysis, we followed the instructions for normalization described previously⁵⁹. Read counts were extracted that aligned to either (1) all full-length CDS (see Supplementary Tables 6–10) or (2) all CDS sequences without the initial 150 nucleotides (50 codons) corresponding to the ribosomal ramp (see Supplementary Table 5 and Fig. 5e). For both data sets, statistical tests were performed with the R/Bioconductor DESeq package. The two sets of DESeq scaling factors were subsequently used for normalization of data sets. The DESeq-normalized counts for all regions were divided by their length in kb to define ribosome footprint densities.

Analysis of ribosome footprint densities at 5' UTRs. Reads that mapped uniquely to the genome by using Tophat2 were mapped to the 5' UTR sequences with bowtie (options: '-m 1000 -v1'). Differences in ribosome footprint densities on the full 5' UTRs were evaluated by using the DESeq scaling factors obtained from the analysis of CDS (Supplementary Tables 7–9) for normalization, and DESeq to perform statistical tests for differences. DESeq-normalized counts for 5' UTRs were divided by their length in kb to define ribosome footprint densities.

Analysis of triplet periodicity. Footprints of length 28 nucleotides were extracted, since they report with high precision on the position of the ribosome⁴⁴. The frequencies of the 5' starts of the footprints, which were aligned close to the annotated translation initiation sites, were aggregated for all genes.

Heatmap analysis. For the heatmap analysis in Extended Data Fig. 8d, we specifically selected the 43,625 representative and well-annotated protein-coding transcripts from GENCODE that overlap ENSEMBL transcript structures ('ensembl_havana'). The positions of the start codons were obtained from the ENSEMBL 'Gene sets' gtf file (<http://www.ensembl.org/info/data/ftp/index.html>). Heatmaps of ribosome footprint densities (RPKM) were generated for regions $\pm 1,500$ nucleotides around the start codon by using ngsplot (<https://github.com/shenlab-sinai/ngsplot>).

If not indicated otherwise, Gene Ontology categories represent GOTERM_BP_FAT in DAVID (<http://david.ncifcrf.gov>).

Protein extraction and western blot analysis. To extract proteins from squamous tumours, samples were snap frozen in liquid nitrogen, transferred to lysis buffer (1% NP-40, 200 mM NaCl, 25 mM Tris-HCl, pH 8, 1 mM DTT) including protease inhibitor cocktail (Roche) and homogenized and cleared by centrifugation at 13,000 r.p.m. To extract proteins from cells in culture, the same lysis

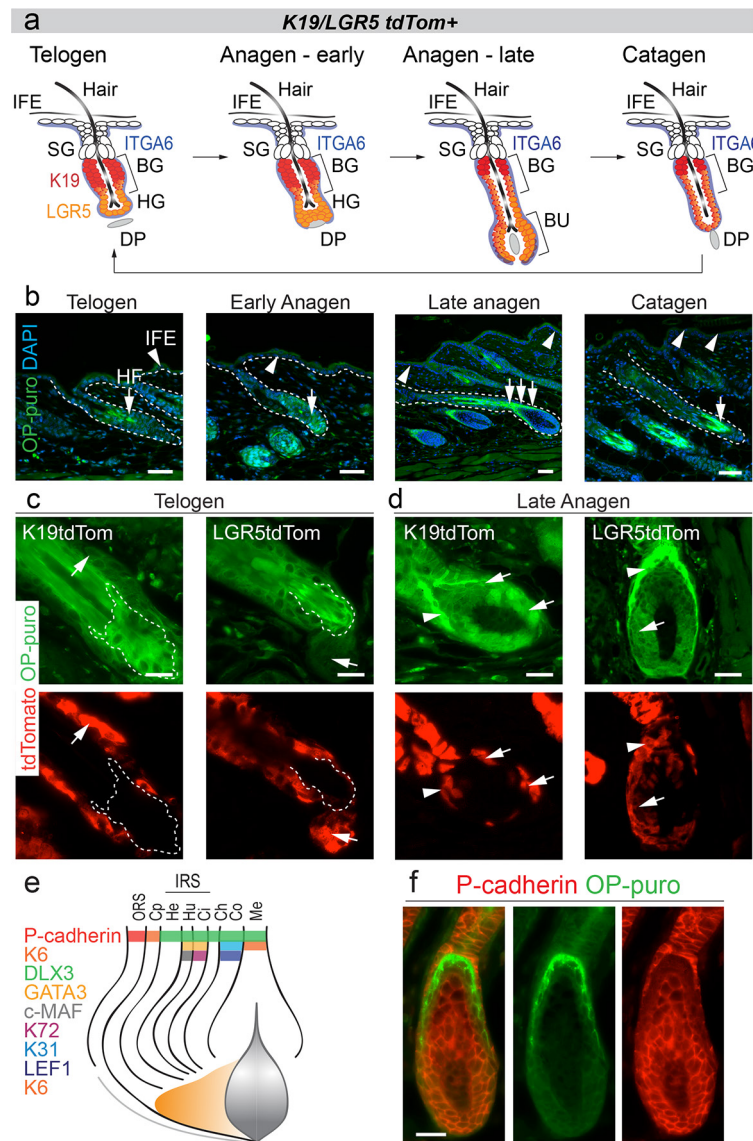
buffer was added to the plate and scratched the cells from the plate surface, left lysing for 20 min in ice and cleared by centrifugation. Total protein quantification was performed using BCA Protein Assay (Thermo fisher). Equal amounts of protein were run in polyacrylamide gels. Western blotting was performed as described previously¹¹. The following primary antibodies were used for western blot analyses: anti-PSAT (Protein Tech Group, 10501-1-AP), anti-THBS1 (Santa Cruz, sc-65612), anti-SEN2 (Protein Tech Group, 10795-1-AP), anti-calreticulin (Abcam, ab2907), anti-INHBA (Sigma-Aldrich, SAB1408593), anti-NSUN2 (Aviva Systems Biology, ARP48811_P050), anti-K19 (Abcam, ab52625), anti-CD44 (IM7, Biolegend, 103004), anti-BCL10 (H197, Santa Cruz, sc-5611), anti-semaphorin 3A (SEMA3A) (Abcam, ab23393), anti-PSMD11 (Abcam, ab66346), anti-SPHK1 (Cell Signaling, 3297), anti-APT1 (Abcam, ab31841), anti-Slug (Cell Signaling, 9585P), anti-Snail (Abcam, ab180714), anti-SOD2 (Abcam, ab13534), anti-CLSPN (Bethyl Laboratories, A300-266A), anti-ZAK (Sigma, HPA017205), anti-CHAF1B or CAF1 p60 (Abcam, ab180371). Polyclonal α -tubulin (Abcam, ab15246) was used as a loading control. Band intensity was quantified with Image J software.

Statistical methods. Group data are always represented by mean and s.d., unless otherwise indicated in figure legends. To test statistical significance between samples, unpaired two-tailed Student's *t*-tests were used. To test for significance of populations (that is, stem cells versus differentiated cell populations) within one sample (mouse) we used the paired Student's *t*-test. To analyse the differences among group means we used analysis of variance (ANOVA). Violin plots were created using the vioplot package (<https://cran.r-project.org/package=vioplot>) in R. The outline of the violin plots represents the kernel probability density of the data at different values. Violin plots include a marker for the median of the data and a box indicating the interquartile range⁶⁰. Boxplots were created with Prism 6 software. The box extends from the 25th to 75th percentiles and the line in the middle of the box is plotted at the median. The whiskers show minimum to maximum. Scatter plots, linear regression lines and coefficient of correlation (r^2) were calculated using Prism 6 software by computing non-parametric Spearman correlation and two-tailed *P* values.

Sample sizing and collection. No statistical methods were used to predetermine sample size, but at least three samples were used per experimental group and condition. The number of samples used in each experiment is indicated in Figs 1–6, in the legends of Extended Data Figs 1–10 and in Source Data files.

Samples and experimental animals were randomly assigned to experimental groups. Sample collection was also assigned randomly. Experimental procedures *in vitro*, sample collection and data analysis were performed blindly whenever possible. Whenever possible automated quantifications were performed using the appropriate software. Most animal procedures (that is, mouse treatments) were performed blindly by individuals unaware of the experimental design.

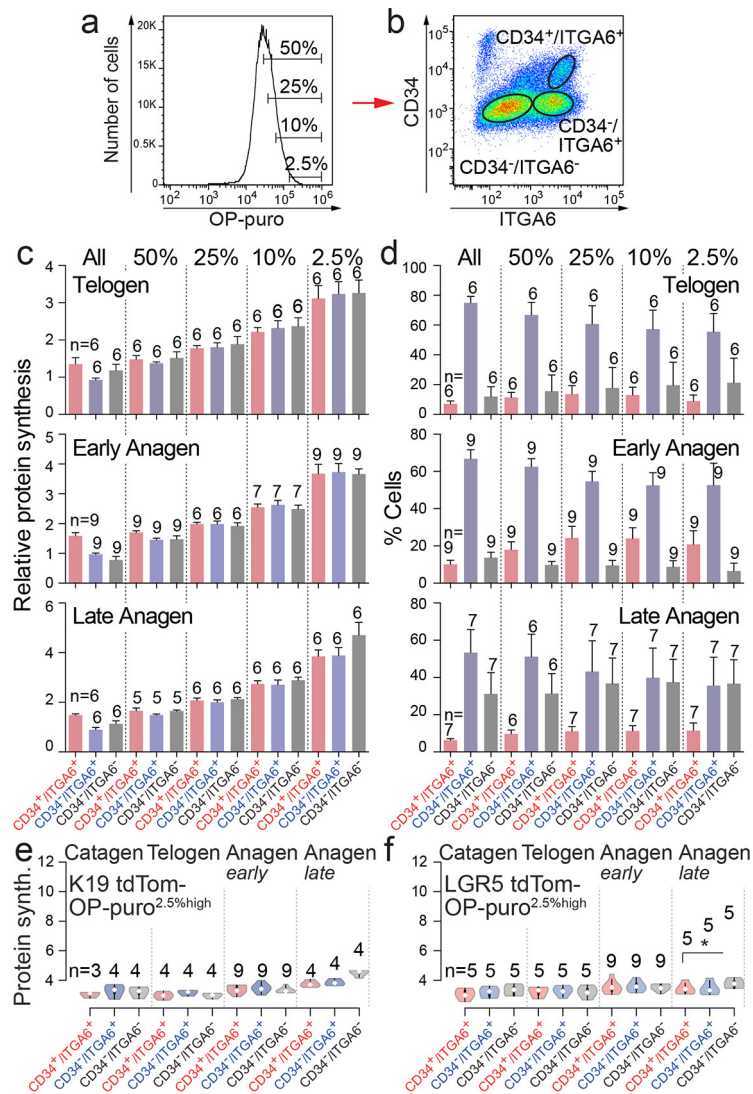
- Madisen, L. *et al.* A robust and high-throughput Cre reporting and characterization system for the whole mouse brain. *Nature Neurosci.* **13**, 133–140 (2010).
- Means, A. L., Xu, Y., Zhao, A., Ray, K. C. & Gu, G. A CK19^{CreERT} knockin mouse line allows for conditional DNA recombination in epithelial cells in multiple endodermal organs. *Genesis* **46**, 318–323 (2008).
- Barker, N. *et al.* Identification of stem cells in small intestine and colon by marker gene Lgr5. *Nature* **449**, 1003–1007 (2007).
- Braun, K. M. *et al.* Manipulation of stem cell proliferation and lineage commitment: visualisation of label-retaining cells in whole mounts of mouse epidermis. *Development* **130**, 5241–5255 (2003).
- Hussain, S. *et al.* The nucleolar RNA methyltransferase Misu (NSun2) is required for mitotic spindle stability. *J. Cell Biol.* **186**, 27–40 (2009).
- Ingolia, N. T., Brar, G. A., Rouskin, S., McGeachy, A. M. & Weissman, J. S. The ribosome profiling strategy for monitoring translation *in vivo* by deep sequencing of ribosome-protected mRNA fragments. *Nature Protocols* **7**, 1534–1550 (2012).
- Ingolia, N. T. Genome-wide translational profiling by ribosome footprinting. *Methods Enzymol.* **470**, 119–142 (2010).
- Schneider-Poetsch, T. *et al.* Inhibition of eukaryotic translation elongation by cycloheximide and lactimidomycin. *Nature Chem. Biol.* **6**, 209–217 (2010).
- Weinberg, D. E. *et al.* Improved ribosome-footprint and mRNA measurements provide insights into dynamics and regulation of yeast translation. *Cell Reports* **14**, 1787–1799 (2015).
- Hintze, J. L. & Nelson, R. D. Violin plots: a box plot-density trace synergism. *Am. Stat.* **52**, 4 (1998).



Extended Data Figure 1 | Protein synthesis in epidermal populations.

a, Hair cycle stages and genetic lineage marking using K19- and LGR5 tdTom mice. Cell surface markers to isolated bulge stem cells are CD34 and ITGA6. Telogen: stem cells ($CD34^+/ITGA6^+$) are quiescent and resting in the bulge (BG). Early anagen: stem cells divide and give rise to committed progenitors in the hair germ (HG), which then grow downwards into the bulb (BU) surrounding the dermal papilla (DP). Late anagen: cells differentiate upwards to form the hair. Catagen: intermediate phase, when the hair bulb degenerates into a new resting bulge. IFE, interfollicular epidermis; SG, sebaceous glands. Mouse transgenes label K19- (red) and LGR5- (orange) positive stem cells and their progeny. **b**, OP-puro detection in mouse epidermis at all hair cycle stages. Dotted

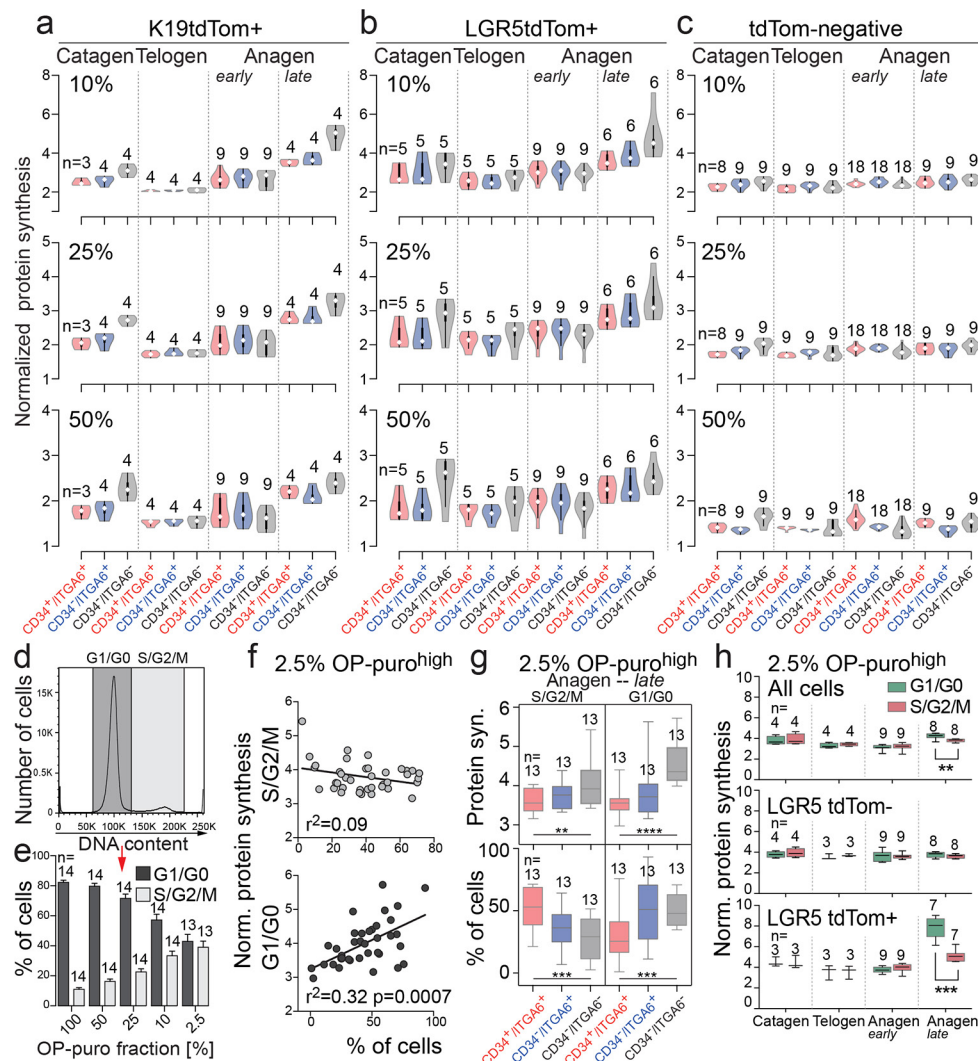
lines indicate hair follicle and epidermal basal layer. Arrows indicate OP-puro^{high} cells in the hair follicle. Arrowheads indicate OP-puro^{low} cells in the interfollicular epidermis. Nuclei are stained with DAPI. **c**, **d**, tdTom and OP-puro detection in back skin of *K19tdTom* and *Lgr5tdTom* mice in telogen and late anagen. Arrows indicate tdTom⁺ cells. Arrowheads indicate Tomato⁺/OP-puro^{high} cells. Dotted line indicates lower bulge. Merged panels from **c**, **d** are shown in Fig. 1c–f. **e**, Hair follicle lineages and differentiation markers used in Fig. 1g–j. Ci, cuticle of inner root sheet; Ch, cuticle; Co, cortex; Cp, companion layer; He, Henle's layer; Hu, Huxley layer; IRS, inner root sheet; Me, medulla; ORS, outer root sheet. **f**, P-cadherin and OP-puro detection in a late anagen. Scale bars, 50 μ m.



Extended Data Figure 2 | Quantification of protein synthesis in epidermal populations. **a, b**, Top 2.5%, 10%, 25% and 50% translating epidermal cells (OP-puro^{high}) (**a**) were sorted for CD34 and ITGA6 (**b**). **c**, Protein synthesis in CD34⁺/ITGA6⁺, CD34⁻/ITGA6⁺ and CD34⁻/ITGA6⁻ epidermal populations in the top 2.5%, 10%, 25%, 50% or 100% (all) translating cells at indicated hair follicle stages. **d**, Percentage of CD34⁺/ITGA6⁺, CD34⁻/ITGA6⁺ and CD34⁻/ITGA6⁻ cells in the

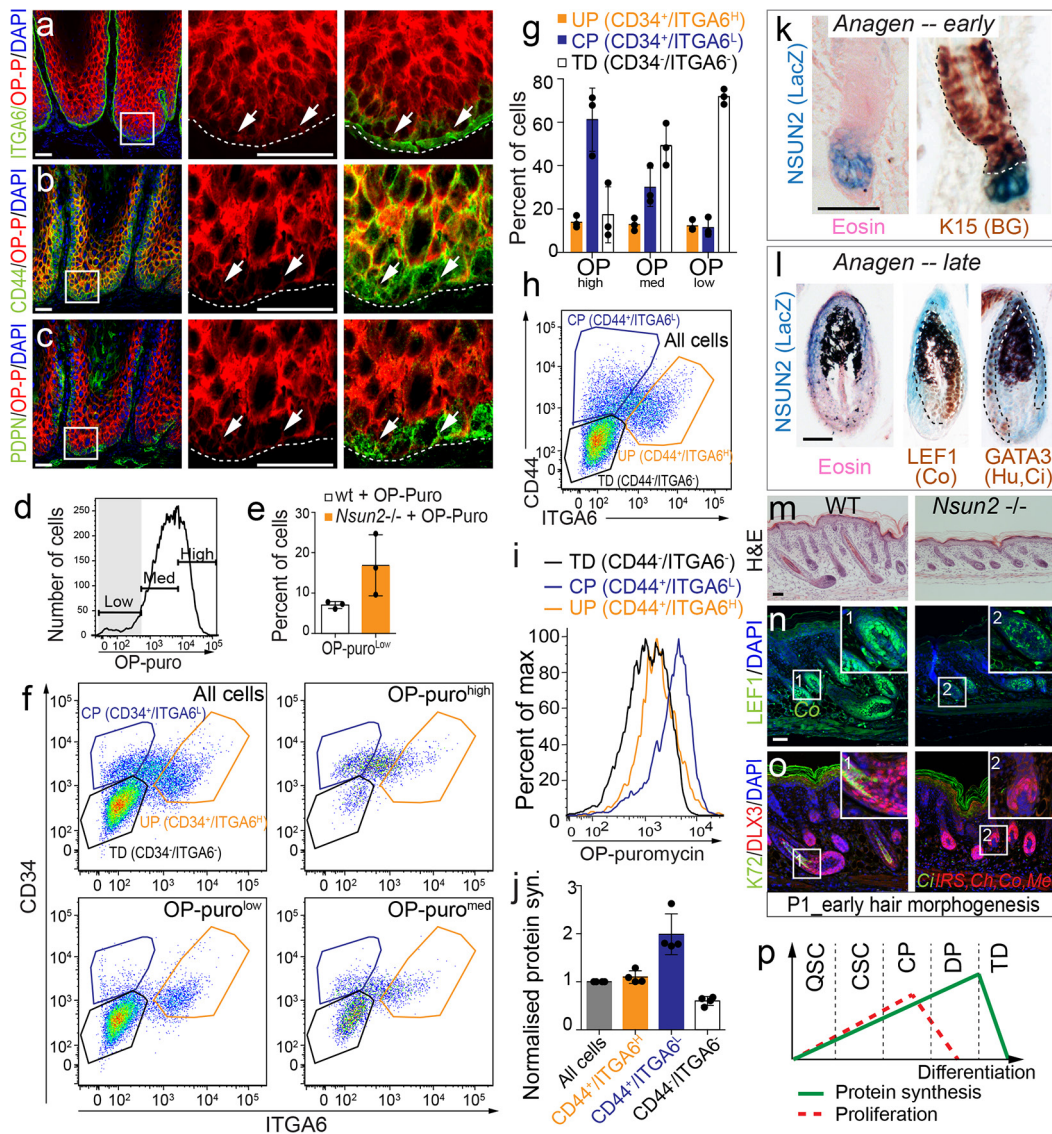
top 2.5%, 10%, 25%, 50% or 100% (all) of translating epidermal cells at indicated stages of the hair cycle. Error bars show mean \pm s.d.

e, f, Violin plots of protein synthesis in top 2.5% OP-puro^{high} cells in tdTom⁻ epidermal cells sorted for CD34 and ITGA6 from K19-tdTom (**e**) or Lgr5-tdTom mice (**f**) at all stages of the hair cycle. (n = mice). Source Data for this figure is available in the online version of the paper.



Extended Data Figure 3 | Protein synthesis and cell cycle analyses in epidermal cells. **a–c**, Violin plots of protein synthesis in indicated epidermal populations sorted for K19-tdTom-positive (**a**) and LGR5-tdTom-positive (**b**) and -negative (**c**) populations. Protein synthesis is shown for top 10%, 25% or 50% OP-puro^{high} cells. **d**, **e**, Cell cycle analysis (**d**) and percentage of cells in G1/G0 or S/G2/M in the top 2.5%, 10%, 25% or 50% OP-puro^{high} cells in late anagen (**e**). Data represent mean \pm s.d. **f**, Scatter plots correlating protein synthesis in the 2.5% OP-puro^{high} population with percentage of cells in S/G2/M (top) and G1/G0 (bottom) using all samples independent of hair cycle stage. Linear

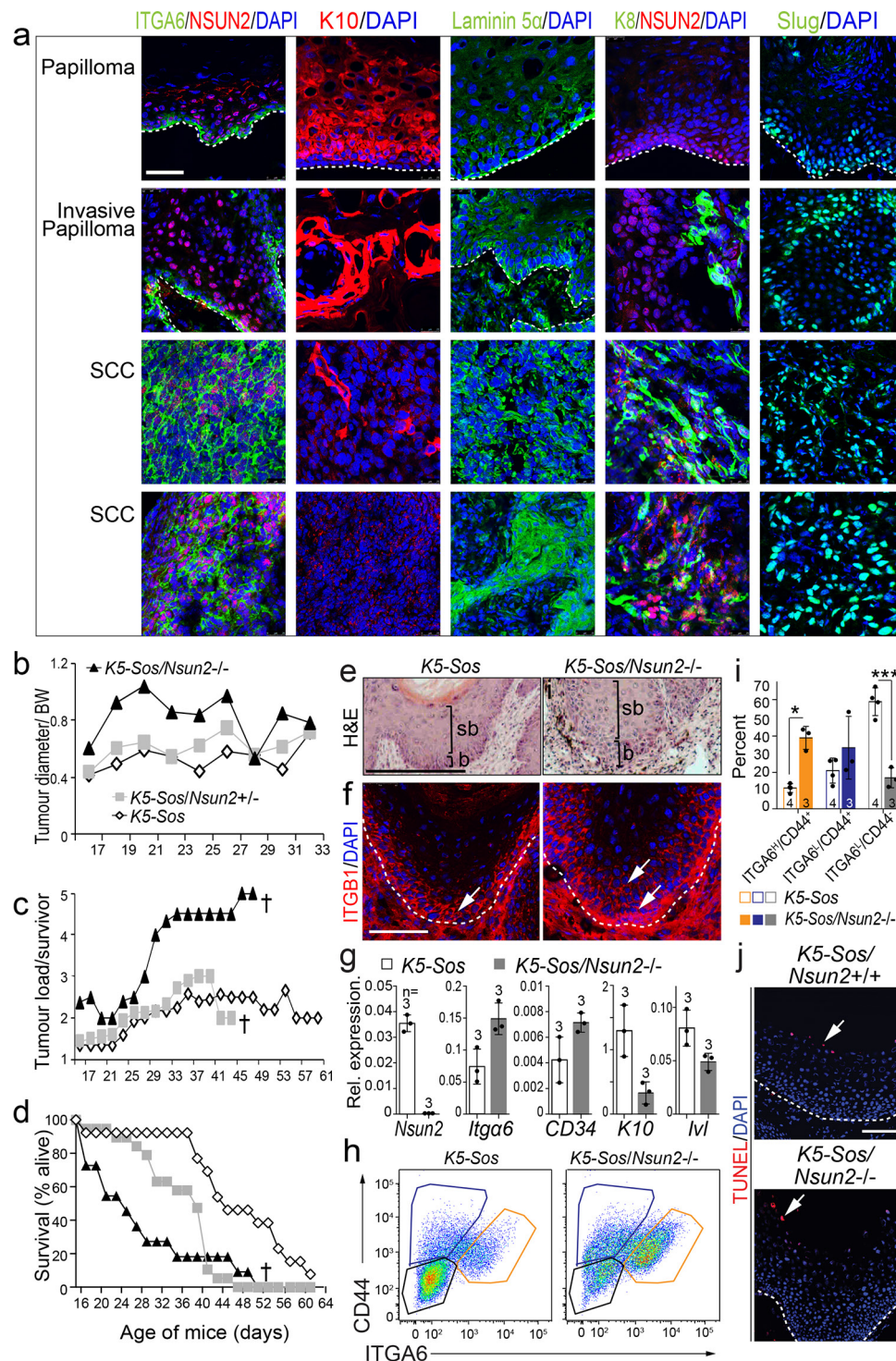
regression, correlation coefficient (r^2) and P value are shown. **g**, Box plots of protein synthesis (top) and number of cycling cells (bottom) in the top 2.5% translating cell populations (OP-puro^{high}). **h**, Box plots of protein synthesis in cycling (S/G2/M) and non-dividing (G1/G0) cells in the 2.5% OP-puro^{high} population isolated from *Lgr5-tdTom* mice. Shown are all cells (top), tdTom⁻ (Tom⁻) (middle) and tdTom⁺ (Tom⁺) (bottom) cells at the indicated hair cycle stages. ** $P < 0.01$, *** $P < 0.001$, **** $P < 0.0001$, two-tailed Student's t -test. n = mice. Source Data for this figure is available in the online version of the paper.



Extended Data Figure 4 | Protein synthesis in squamous tumours.

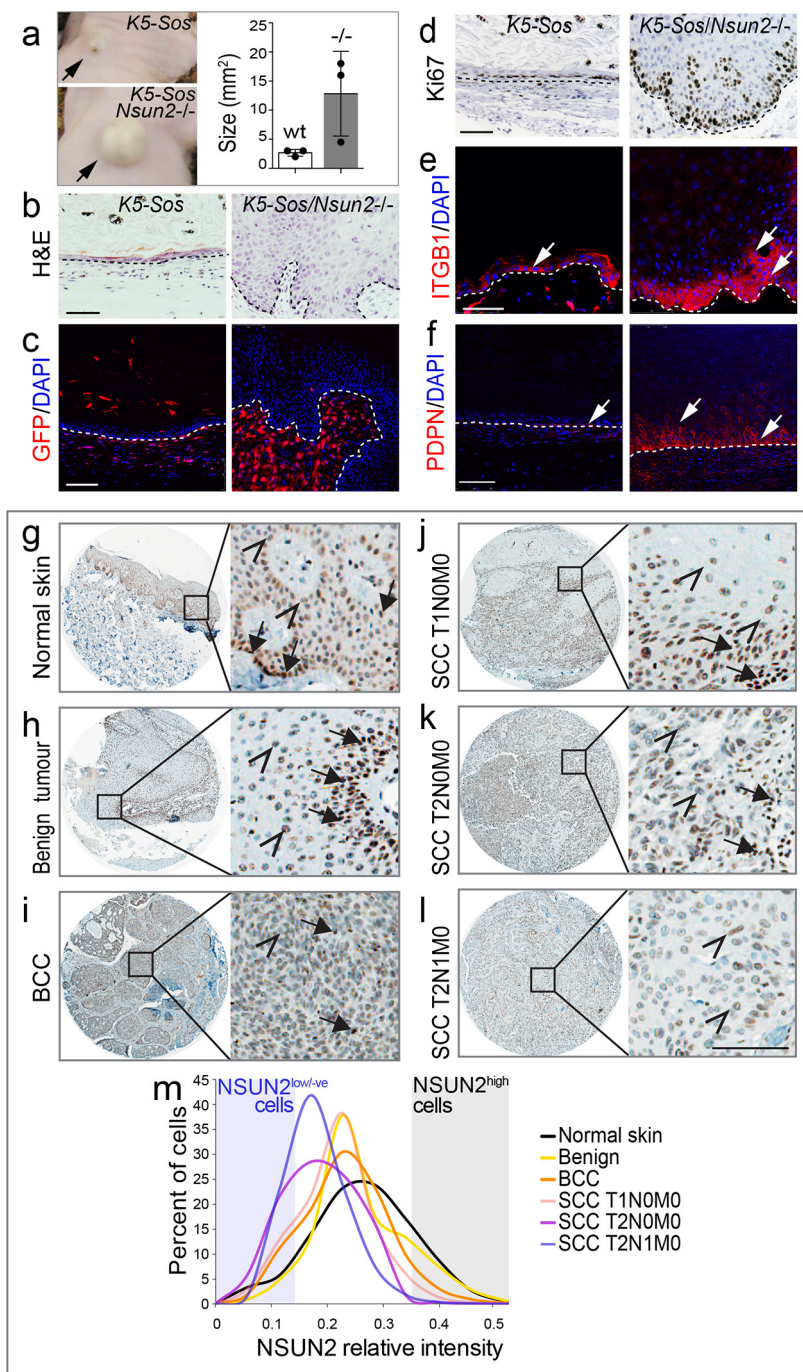
a–c, Co-labelling of OP-puro with markers for undifferentiated basal cells: ITGA6 (**a**), CD44 (**b**) and PDPN (**c**) in mouse tumours. Nuclei are stained with DAPI. Arrows indicate low translating and marker-positive cells. Dotted line indicates invasive front of the tumour. Boxed areas are magnified on the right. **d**, Gating of low, medium and high OP-puro cells in *Nsun2*^{+/+} (wild type) and *Nsun2*^{-/-}; *K5-Sos* skin tumours analysed in **e–g**. **e**, Percentage of OP-puro^{low} cells in tumours from *Nsun2*^{+/+} (wild type) and *Nsun2*^{-/-}; *K5-Sos* mice. **f, g**, Flow cytometry for ITGA6 and CD34 in unfractionated epithelial cells from mouse tumours (all cells) or epithelial cells with high, medium and low OP-puro incorporation (**f**) and quantification (**g**) (mean \pm s.d.; $n = 3$ mice). **h**, Flow cytometry for ITGA6 and CD44 in unfractionated epithelial cells from mouse tumours.

i, j, Histogram (**i**) and quantification (**j**) showing OP-puro incorporation of cells as gated and quantified in **h** (mean \pm s.d.; $n = 4$ mice). **k, l**, Detection of endogenous expression of NSUN2 (LacZ) in early (P23) (**k**) and late (P30) anagen (**l**) hair follicles. Sections were co-stained with eosin or markers for bulge stem cells K15 and the hair lineages Huxley's (Hu), cuticle (Ci) (GATA3), and cortex (Co) (LEF1). **m–o**, Haematoxylin and eosin staining (**m**) and immunostaining for LEF1 (**n**), K72 and DLX3 (**o**) in wild-type (WT) and *Nsun2*^{-/-} skin at P1. Nuclei are stained with DAPI. Insets: magnified boxed area (1, 2). Scale bars, 50 μ m. **p**, Correlation between proliferation and protein synthesis with differentiation of quiescent (QSC) or committed stem cells (CSC), committed progenitors (CP), differentiating progenitors (DP), and terminally differentiated (TD) cells. Source Data for this figure is available in the online version of the paper.



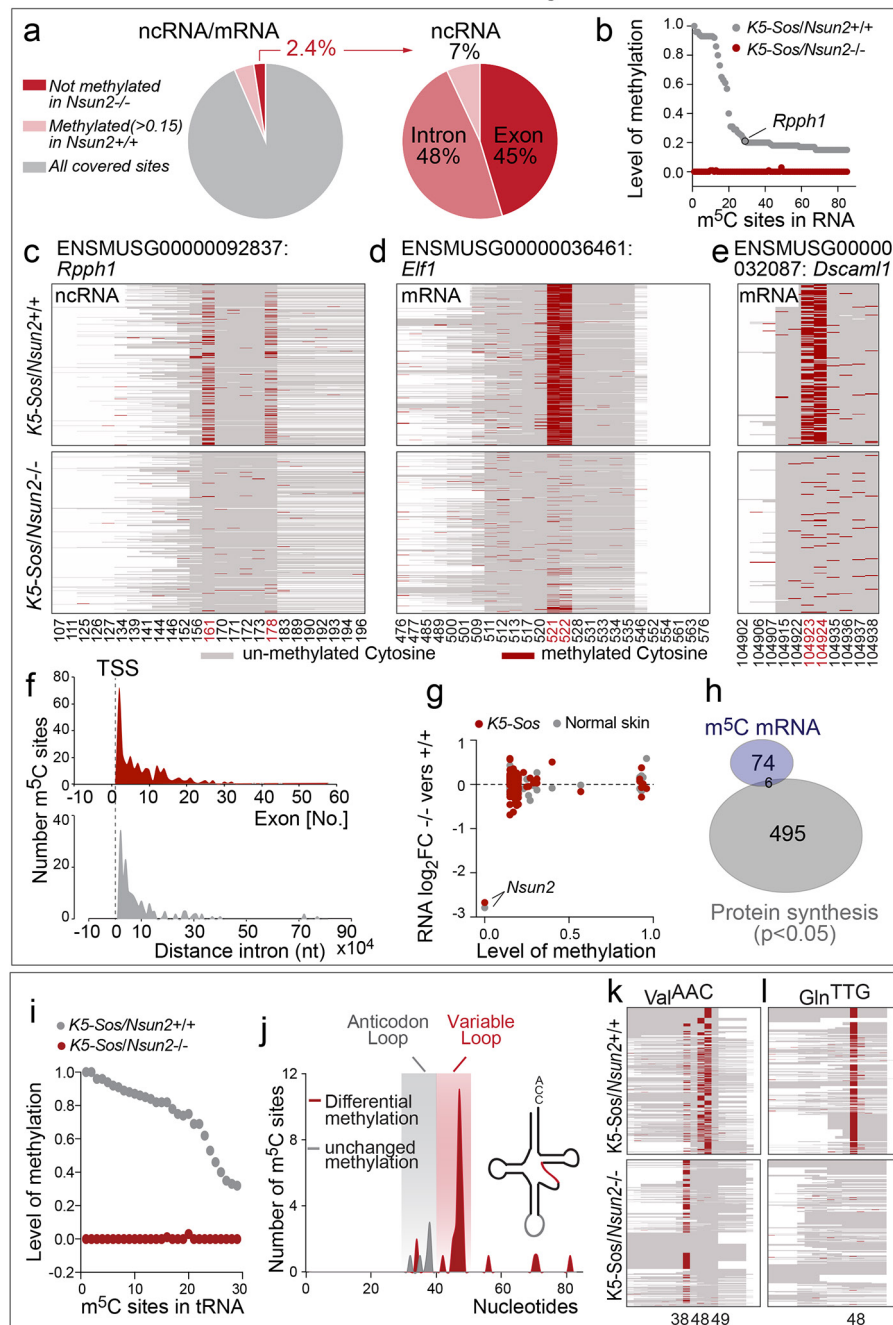
Extended Data Figure 5 | NSUN2 in mouse skin squamous cell carcinomas. **a**, Immunostaining for NSUN2, ITGA6, K10 (differentiation marker), laminin 5α and K8 (tumour progression markers), and Slug (epithelial to mesenchymal transition-related gene) at different stages of DMBA-TPA-induced malignant progression to squamous cell carcinoma (SCC). **b–d**, Quantification of tumour diameter normalized to body weight (BW) (**b**), tumours per mouse (**c**), and mouse life span (**d**) in K5-Sos/Nsun2^{+/-} (K5-Sos), K5-Sos/Nsun2^{+/-} and K5-Sos/Nsun2^{-/-} littermates. Measurements start at P16. Data collection discontinued when mice died (indicated by a dagger). Data represent mean, *n* ≥ 5 mice of each genotype. **e**, **f**, Haematoxylin and eosin staining (**e**) and immunostaining for ITGB1 (**f**) in sections from K5-Sos (K5-Sos/Nsun2^{+/-}) and K5-Sos/Nsun2^{-/-} skin tumours. **b**, basal undifferentiated cells;

sb, suprabasal layers. Arrows indicate ITGB1⁺ cells. **g**, Relative mRNA expression levels of the indicated transcripts in skin tumours (mean ± s.d.; *n* = mice). **h**, Flow cytometry using ITGA6 and CD44 in K5-Sos/Nsun2^{-/-} and control K5-Sos (K5-Sos/Nsun2^{+/-}) tumours. **i**, Percentage of cells in cell populations as gated in **h** (mean ± s.d.; *n* = mice). **P* < 0.05; ****P* < 0.001 (two-tailed Student's *t*-test) (**i**). **j**, TdT-mediated dUTP nick end labelling (assay) (TUNEL) assay on sections of K5-Sos tumours expressing (K5-Sos/Nsun2^{+/-}) or lacking Nsun2 (K5-Sos/Nsun2^{-/-}). Arrows indicate TUNEL⁺ (apoptotic) cells. Nuclei are stained with DAPI. Dotted line indicates boundary of epithelia and stroma (**f**, **j**). Scale bars: 25 μm (**a**), 100 μm (**e**, **f**, **j**). Source Data for this figure is available in the online version of the paper.



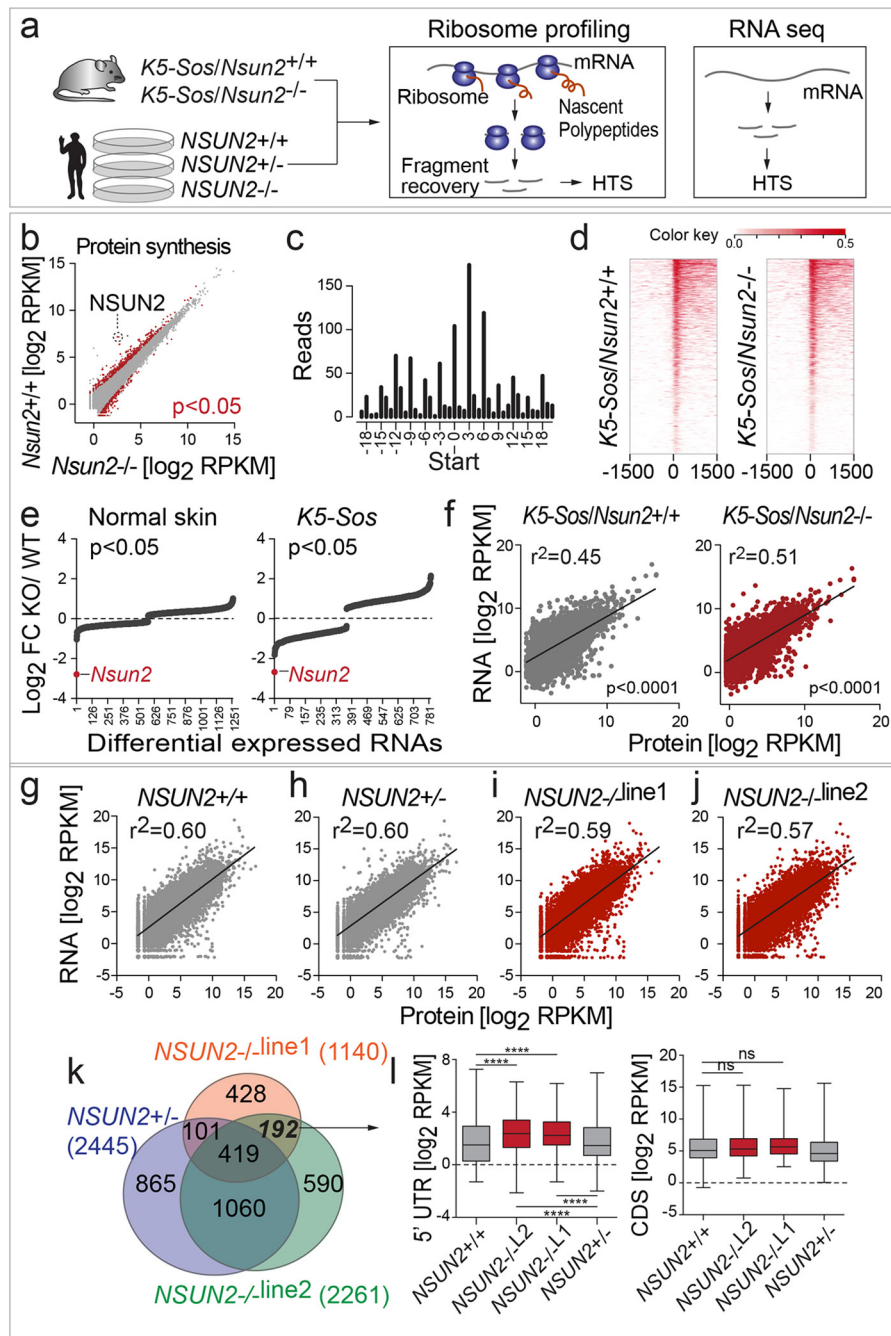
Extended Data Figure 6 | Deletion of *Nsun2* enhances self-renewal of tumour-initiating cells in a cell-autonomous manner and NSUN2 expression in human skin tumours. **a**, Tumour size after grafting of *K5-Sos*/*Nsun2^{+/+}* (*K5-Sos*) and *K5-Sos/Nsun2^{-/-}* tumour cells subcutaneously into nude mice (mean \pm s.d.; $n = 3$ mice). **b–f**, Histology (haematoxylin and eosin staining) (**b**), staining for GFP (**c**), Ki67 (**d**), ITGB1 (**e**) and PDPN (**f**) in grafted tumour sections. Dotted line indicates boundary between epithelia and stroma. Arrows indicate basal and suprabasal

expression. Nuclei are stained with DAPI. **g–l**, Immunohistochemistry for NSUN2 in human normal skin, benign tumours, malignant basal cell carcinomas (BCC) and squamous cell carcinomas (SCC) with increased malignancy (stages classified using the TNM system). Arrows indicate NSUN2^{high} cells. Arrowheads indicate NSUN2^{low} cells. **m**, Distribution of cells shown in **g–l** according to NSUN2 protein levels. ($n \geq 3$ samples). Scale bars, 100 μ m. Source Data for this figure is available in the online version of the paper.



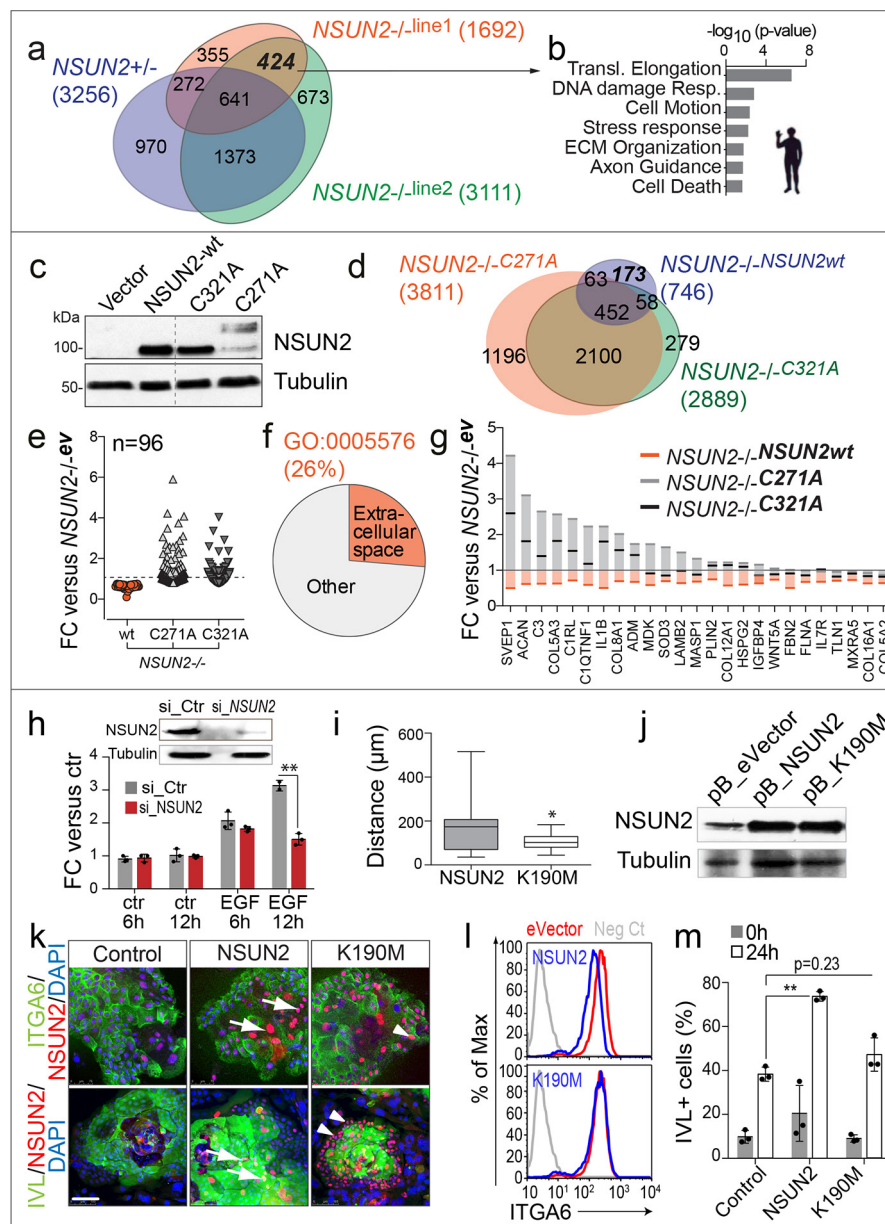
Extended Data Figure 7 | NSUN2-dependent RNA methylation of coding and non-coding RNA in mouse tumours. **a**, Percentage of NSUN2-methylated sites (>0.15 m⁵C in *Nsun2*^{+/+}; <0.05 m⁵C in *Nsun2*^{-/-}) out of all covered sites (left) and in non-coding RNA (ncRNA) or introns and exons (right). **b**, Methylation level in coding and non-coding RNAs (>0.15 m⁵C in *Nsun2*^{+/+}; <0.05 m⁵C in *Nsun2*^{-/-}; coverage >10 reads). **c–e**, Examples of NSUN2-targeted non-coding RNA (*Rpph1*) and mRNA (*Elf1* and *Dscaml1*) in *Nsun2*^{+/+} (top) and *Nsun2*^{-/-} (bottom) tumours. **f**, Number of NSUN2-methylated sites in exons 1 to 60 (top) or distance from the transcriptional start site (TSS) in introns (bottom). Plotted sites: >0.1 m⁵C in *Nsun2*^{+/+}; <0.05 m⁵C in *Nsun2*^{-/-}; coverage >10 reads. **g**, No correlation between NSUN2 methylation shown in **b** and RNA abundance in normal skin or *K5-Sos* skin tumours. *Nsun2* is

highlighted as a control. **h**, Venn diagram with no significant overlap between NSUN2-methylation targets shown in **b** and differentially translated mRNAs ($P < 0.05$; measured as ribosome density of *Nsun2*^{+/+} versus *Nsun2*^{-/-} tumours). **i–l**, NSUN2 methylation in tRNAs (>0.15 m⁵C in *Nsun2*^{+/+}; <0.05 m⁵C in *Nsun2*^{-/-}; coverage >10 reads) (**i**). Number and location of lost (red) or unchanged (grey) m⁵C sites in *K5-Sos/Nsun2*^{-/-} tumours. Nucleotide position in tRNA is shown on the x-axis (**j**). Examples of NSUN2-targeted tRNAs in *Nsun2*^{+/+} (top) and *Nsun2*^{-/-} (bottom) *K5-Sos* tumours (**k**, **l**). Heatmaps show methylated (red) and unmethylated (grey) cytosines. Cytosines are shown on the x-axis, and sequence reads on the y-axis. Numbers indicate the m⁵C position in the RNA (**c–e**; **k**, **l**). Bisulfite-seq and RNA-seq data represent average of 4 replicates per condition.



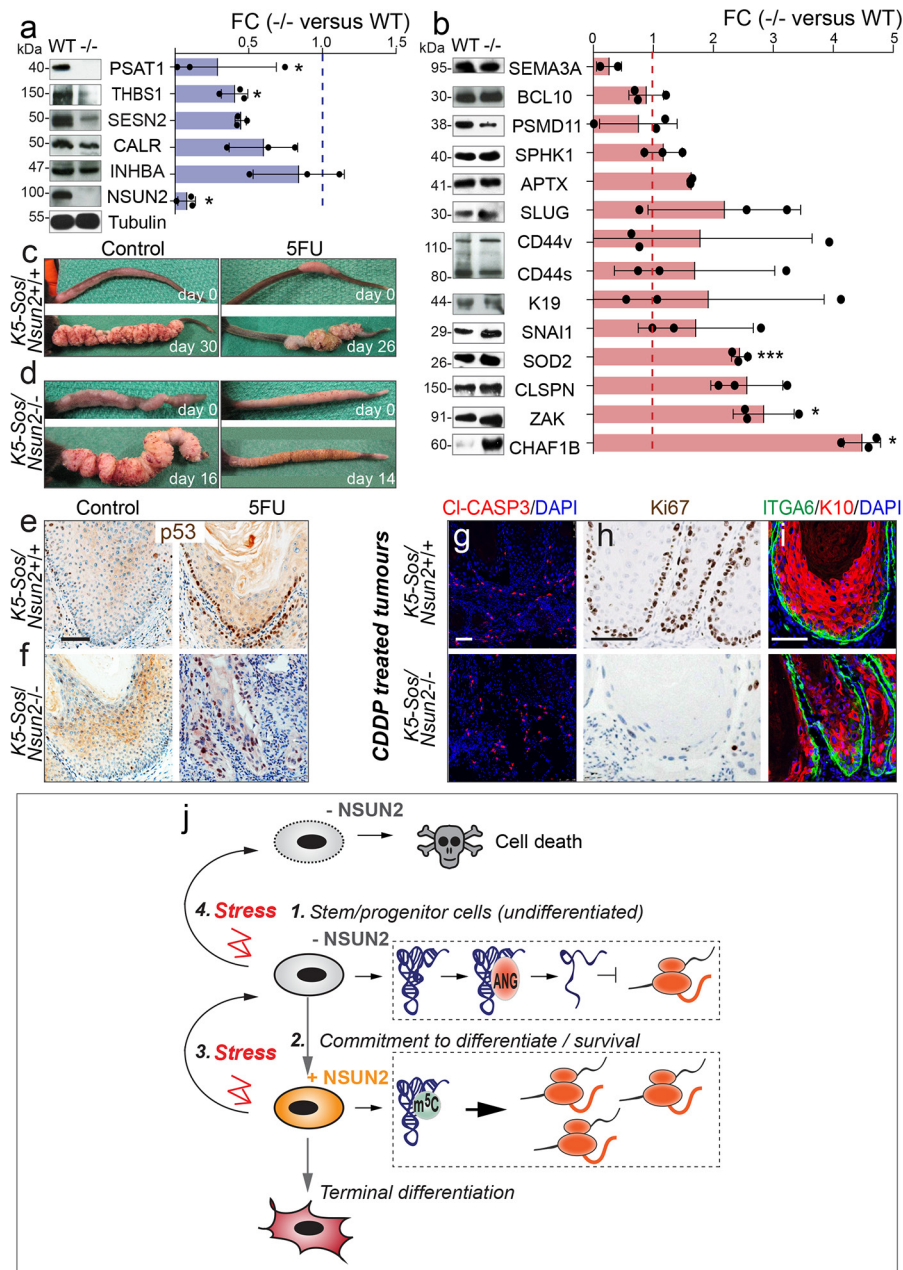
Extended Data Figure 8 | *Nsun2* deletion drives translational changes independent of mRNA expression. **a**, Ribosome profiling and RNA-sequencing experiments (see Fig. 5) using *Nsun2*-expressing (*Nsun2^{+/+}*) and *Nsun2*-deficient (*Nsun2^{-/-}*) *K5-Sos* skin tumours, or cultured human skin fibroblasts (*NSUN2^{-/-}*.line1 and *NSUN2^{-/-}*.line2 and healthy donors: *NSUN2^{+/+}*, *NSUN2^{+/-}*). HTS, high-throughput sequencing. **b**, Correlation between protein synthesis (ribosome footprint density) in *Nsun2^{+/+}* and *Nsun2^{-/-}* tumours. **c**, Example of triplet periodicity in ribosome footprints (*K5-Sos/Nsun2^{+/+}*, replicate 1) shown as number of reads against nucleotide position relative to the translational start site for all ORFs. **d**, Heatmaps showing ribosome footprint reads around the translational start site (0) in *Nsun2^{+/+}* and *Nsun2^{-/-}* tumours (3 replicates per condition; ribosome density >0; colour indicates RPKM values of

footprints). **e**, Log₂ fold change (FC) per transcript in normal skin (left) and tumour samples (right) of significant ($P < 0.05$) expression differences. *Nsun2* RNA levels (red). **f-j**, Scatter plots, linear regression lines and coefficient of correlation (r^2) of mRNA expression and protein synthesis (density of ribosome footprints per kb) in *Nsun2^{+/+}* (grey) and *Nsun2^{-/-}* (red) mouse tumours (**f**) and human fibroblasts relative to *NSUN2^{+/+}* cells. **k**, Venn diagram of transcripts with significant ($P < 0.05$) different ribosome footprint density in the 5' UTR in *NSUN2^{+/+}*, *NSUN2^{-/-}*.line1 and *NSUN2^{-/-}*.line2 human fibroblasts relative to *NSUN2^{+/+}* cells. **l**, Box plots of ribosome footprint read counts in the 5' UTR (left) and corresponding CDS (right) of the 192 transcripts in **k**. **** $P < 0.0001$ (two-tailed Student's *t*-test).



Extended Data Figure 9 | RNA methylation-dependent changes of protein synthesis. **a**, Venn diagram of transcripts with differential protein synthesis in *NSUN2*^{+/-} and *NSUN2*^{-/-} human fibroblasts relative to *NSUN2*^{+/+} cells. **b**, GO terms enriched in 424 commonly differentially translated transcripts in *NSUN2*^{-/-} lines (**a**). **c**, Western blot for NSUN2 and tubulin in *NSUN2*^{-/-} human fibroblasts rescued with viral constructs expressing wild-type NSUN2 (NSUN2-wt), two catalytically dead mutants (C271A and C321A) or the empty vector. **d**, Venn diagram of differentially translated transcripts in the indicated rescued cells relative to empty vector-infected control cells. Translation of 173 out of 746 of transcripts (23%) depended on the enzymatic activity of NSUN2. **e–g**, Differential translation of transcripts relative to *NSUN2*^{-/-} cells (infected with empty vector) showing reduced translation in the presence of wild-type NSUN2 but not the enzymatic-dead versions of NSUN2 (C271A, C321A), corresponding GO categories (**f**) and examples (**g**). **h**, Boyden chamber migration assay towards epidermal growth factor (EGF) or control medium (ctr) using primary human keratinocytes transduced with a siRNA for *NSUN2* (si_ *NSUN2*) or a scrambled construct (si_ *ctr*).

Data represent mean \pm s.d. ($n = 3$ assays). Western blot confirms downregulation of NSUN2 in the presence of the siRNA construct. **i, j** Reduced motility in keratinocytes expressing the enzymatic-dead NSUN2 construct (K190M) (K190M: $n = 13$; NSUN2: $n = 19$ cells) (**i**). Western blot confirms equal protein expression levels of K190M and NSUN2 (**j**). **k**, Reduced differentiation in primary human keratinocytes expressing the enzymatic-dead NSUN2 (K190M). Staining for NSUN2, ITGA6 or involucrin (IVL) and nuclei (DAPI). Control: empty vector (left); NSUN2: wild-type NSUN2 (middle); K190: enzymatic-dead NSUN2 (right). Arrows indicate NSUN2-expressing ITGA6⁺/IVL⁺ cells. Arrowheads indicate K190M-expressing ITGA6⁺/IVL⁻ cells. **l**, Flow cytometry for ITGA6 of keratinocytes transduced with NSUN2 (blue line, top panel), K190M (blue line, bottom panel) or the empty vector (eVector) (red line). Negative control (grey line) represents unstained cells. **m**, Quantification of IVL⁺ infected keratinocytes grown in suspension for 24 h to stimulate differentiation. * $P < 0.05$, ** $P < 0.01$ (two-tailed Student's t -test) (**h–m**). Scale bar, 100 μ m. Source Data for this figure is available in the online version of the paper.



Extended Data Figure 10 | Protein expression differences, drug treatment of *Nsun2*^{-/-} tumours and graphical summary.

a, b, Western blot analysis of translationally repressed (**a**) or induced (**b**) mRNAs in *Nsun2*^{-/-} compared to *Nsun2*^{+/+} (WT) skin tumours with quantification of band densitometry on the right (mean \pm s.d.; $n = 3$ mice). * $P < 0.05$, *** $P < 0.001$ (two-tailed Student's t -test). **c, d**, Control and 5FU-treated tumours, before and after treatment. **e, f**, Immunohistochemistry for p53 in tumours shown in **c, d**. **g–i**, Immunostaining for cleaved caspase 3 (CI-CASP3) (**g**), Ki67 (**h**), ITGA6 and K10 (**i**) in *K5-Sos* tumours expressing (+/+) or lacking (-/-) *Nsun2* and treated with CDDP (see Methods). Scale bars, 100 μ m. **j**, Graphical

summary: (1) quiescent undifferentiated stem and progenitor cells are characterized by the absence of NSUN2 and low global protein synthesis; (2) upregulation of NSUN2 counteracts angiogenin-mediated cleavage of tRNAs through site-specific methylation of tRNAs, allowing increased translation of lineage-specific transcripts driving terminal differentiation; (3) cytotoxic stress inhibits NSUN2 and global protein synthesis in particular of lineage-specific transcripts and promotes an undifferentiated quiescent cell state. Yet cell survival after the insult requires re-methylation of tRNAs by NSUN2 (see (2)); (4) the inability to upregulate NSUN2 in response to the cytotoxic insult leads to cell death. Source Data for this figure is available in the online version of the paper.

Dual targeting of p53 and c-MYC selectively eliminates leukaemic stem cells

Sheela A. Abraham^{1*}, Lisa E. M. Hopcroft^{1*}, Emma Carrick^{2,3}, Mark E. Drotar¹, Karen Dunn¹, Andrew J. K. Williamson^{2,3}, Koorosh Korfi^{1,4}, Pablo Baquero⁴, Laura E. Park¹, Mary T. Scott¹, Francesca Pellicano¹, Andrew Pierce^{2,3}, Mhairi Copland¹, Craig Nourse⁴, Sean M. Grimmond⁵, David Vetrie⁴, Anthony D. Whetton^{2,3,6*} & Tessa L. Holyoake^{1*}

Chronic myeloid leukaemia (CML) arises after transformation of a haemopoietic stem cell (HSC) by the protein-tyrosine kinase BCR-ABL. Direct inhibition of BCR-ABL kinase has revolutionized disease management, but fails to eradicate leukaemic stem cells (LSCs), which maintain CML. LSCs are independent of BCR-ABL for survival, providing a rationale for identifying and targeting kinase-independent pathways. Here we show—using proteomics, transcriptomics and network analyses—that in human LSCs, aberrantly expressed proteins, in both imatinib-responder and non-responder patients, are modulated in concert with p53 (also known as TP53) and c-MYC regulation. Perturbation of both p53 and c-MYC, and not BCR-ABL itself, leads to synergistic cell kill, differentiation, and near elimination of transplantable human LSCs in mice, while sparing normal HSCs. This unbiased systems approach targeting connected nodes exemplifies a novel precision medicine strategy providing evidence that LSCs can be eradicated.

BCR-ABL1 is a chimaeric oncogene arising from the t(9;22)(q34;q11) chromosomal translocation. The resultant protein tyrosine kinase (PTK) drives signalling events¹ and transforms HSCs. BCR-ABL activity in HSCs causes CML, which if untreated, is fatal.

Tyrosine kinase inhibitors (TKIs), such as imatinib mesylate, are standard CML treatment and have improved survival, justifying the use of single-target therapies². However, these drugs do not kill the LSCs that maintain the disease³, resulting in ever-increasing costs to sustain remissions. TKI discontinuation in the best 10–20% of TKI responders led to relapse rates of 50–60%, reinforcing the need to understand and target CML LSCs⁴ with curative therapies. Recent studies suggest that LSC survival is BCR-ABL-kinase independent⁵ and BCR-ABL has functionality beyond PTK activity, explaining the shortcomings of TKIs⁶.

We have applied systems biology approaches to patient material to identify key protein networks that perpetuate the CML phenotype, aiming to elucidate potentially curative therapeutic options. Using unbiased transcriptomic and proteomic analyses, the transcription factors p53 and c-MYC are identified as having defining roles in CML LSC survival. We demonstrate an integral relationship between p53 and c-MYC in the maintenance of CML, and importantly, a potential therapeutic advantage they have as drug targets over BCR-ABL for eradication of CML LSCs.

p53 and c-MYC mediate the CML network

To interrogate perturbations in BCR-ABL signalling of potential therapeutic value, isobaric-tag mass spectrometry (MS) was used to compare treatment-naïve CML and normal CD34⁺ cells. Fifty-eight proteins were consistently deregulated in three CML samples (Methods and Supplementary Table 1). Dijkstra's algorithm⁷ and the MetaCore knowledge base (<https://portal.genego.com/>) were used to identify p53 and c-MYC as central hubs (Supplementary Table 2) in a CML network of 30 proteins (Fig. 1a) predominantly downstream of the transcription

factors, with significant enrichment for p53/c-MYC targets (Fisher's exact test, $P = 0.001$). While the majority of proteins downstream of p53 were downregulated, those downstream of c-MYC included proteins up- or downregulated in CML, in keeping with c-MYC acting as an activator and repressor of gene transcription⁸. The deregulated network suggests an altered dependency on p53 and c-MYC in CML CD34⁺ cells.

This data set represents the first—to our knowledge—relative quantitative comparison of CML to normal CD34⁺ cells using MS. Importantly, CML-initiating cells reside within the CD34⁺CD38[−]Lin[−] subpopulation and may differ to bulk CD34⁺ cells. To substantiate the CML proteome observations and investigate regulation in LSCs, we examined relevant, primary CML transcriptomic data. Network protein levels correlated well with respective gene levels, in both LSCs (four independent data sets; Fig. 1b and Extended Data Fig. 1a–c) and CD34⁺ progenitors (Extended Data Fig. 1d, e). Correlations were stronger for the 30 network candidates compared to all 58 deregulated proteins; seven data sets showed significant gain in r^2 for network candidates (Extended Data Fig. 1a, d). The mutual information (MI) of proteomic/transcriptomic data for network proteins was significantly greater than random (Fig. 1c and Extended Data Fig. 1b, e). This consistent messenger RNA/protein correspondence, in both progenitors and LSCs, confirmed that the network was transcriptionally regulated, compatible with c-MYC and p53 function.

p53 and c-MYC have key roles in oncogenesis and appear in many cancer networks. To distinguish true regulatory effectors, we assessed the bias towards outgoing versus incoming signalling ($\text{degree}_{\text{out}}/\text{degree}_{\text{in}}$ ($d_{\text{out}}/d_{\text{in}}$)) for p53 and c-MYC. We generated networks from deregulated proteins in (1) primary MS data sets^{9–11}, (2) cell lines transduced with oncogenic PTKs driving haematological malignancies¹², and from (3) 50 randomly generated protein sets. Our network falls outside the expected random distribution and no other data set exhibits

¹Paul O'Gorman Leukaemia Research Centre, Institute of Cancer Sciences, University of Glasgow, Gartnavel General Hospital, 1053 Great Western Road, Glasgow G12 0YN, UK. ²Stem Cell and Leukaemia Proteomics laboratory, University of Manchester, Manchester M20 3LJ, UK. ³Manchester Precision Medicine Institute, University of Manchester, Manchester M20 3LJ, UK. ⁴Institute of Cancer Sciences, University of Glasgow, Gartcube Estate, Glasgow G61 1QH, UK. ⁵University of Melbourne Centre for Cancer Research, University of Melbourne, Victoria 3010, Australia. ⁶Stoller Biomarker Discovery Centre, University of Manchester, Manchester M20 3LJ, UK.

*These authors contributed equally to this work.

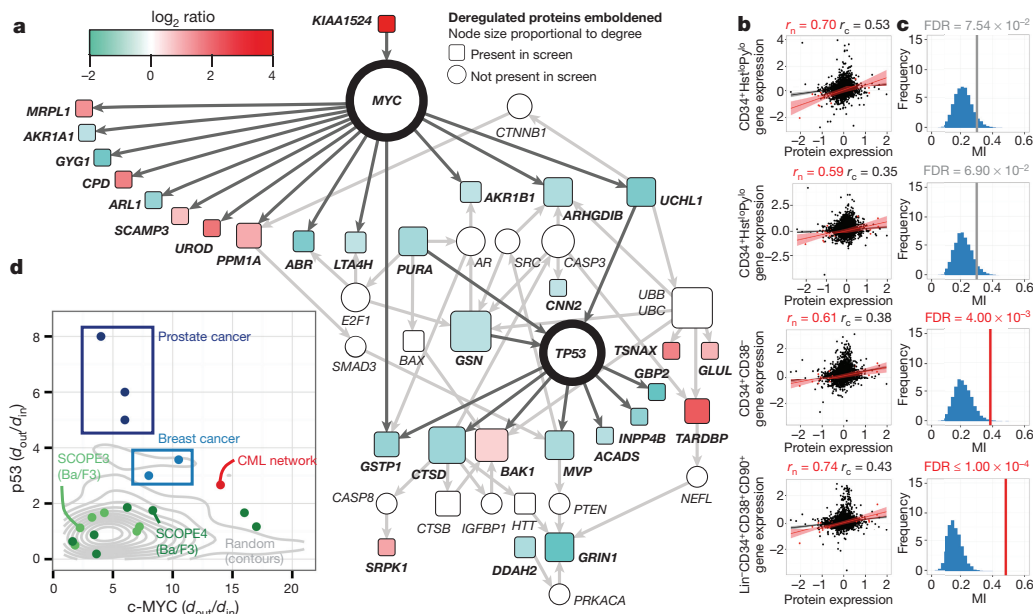


Figure 1 | p53 and c-MYC network in CML regulation. **a**, Network analysis reveals that c-MYC and p53 are central in a putative CML network ($n=3$ patient samples, $n=2$ normal samples). **b**, Correlation between proteomic/transcriptomic deregulation in primitive CD34⁺Hst^{lo}Py^{lo} (G0) (top two panels); CD34⁺CD38⁻ (second panel from the bottom) and Lin⁻CD34⁺CD38⁻CD90⁺ CML cells (bottom panel). Filled black circles indicate all protein/genes; filled red circles indicate network proteins/

genes. r_c , full candidate list correlation; r_n , network correlation. **c**, Gene/protein MI for the CML network (red, false discovery rate (FDR) < 0.05; grey, FDR < 0.10); FDR calculated using 10,000 re-samplings (blue histogram). **d**, The d_{out}/d_{in} ratio for p53 and c-MYC in haematological PTK-regulated cell lines ($n=3$ BaF/3 technical replicates per transfected oncogene), other primary cancers and random protein networks.

greater downstream bias for p53 and c-MYC (Fig. 1d). These data support a novel network in, and unique to, CML, centred on p53 and c-MYC.

Validation of network candidates

The CML network revealed well-characterized p53/c-MYC targets and proteins not previously associated with CML pathogenesis (Supplementary Table 3). To validate proteomic predictions (Fig. 1a), gelsolin, CIP2A (also known as KIAA1524), UCHL1, aldose reductase, p53 and c-MYC were assessed using western blotting and immunofluorescence (Fig. 2a, b). Protein expression of gelsolin, CIP2A, UCHL1 and aldose reductase were consistent with CML network predictions (Fig. 2a). Immunofluorescence was confirmatory, highlighting the dramatic difference in CIP2A expression between normal and CML cells, and the intracellular localization of gelsolin and aldose reductase (Fig. 2b). CML cells also expressed increased c-MYC and decreased p53 levels (Fig. 2a, b), correlating well with appropriate modulation of downstream targets. We therefore hypothesized that simultaneous p53 activation and c-MYC inhibition would kill LSCs. To assess dual hub requirement for CML survival, lentiviral short hairpin RNA (shRNA) constructs (Extended Data Fig. 2a) were employed. Knockdown of HDM2 (also known as MDM2; E3 ligase/negative regulator for p53), c-MYC, or both, in CML CD34⁺ cells reduced viability and enhanced apoptosis; the combined effects were synergistic. In colony-forming cell (CFC) assays, effects were more dramatic with single or combined knockdown, strengthening the hypothesis that p53 and c-MYC are critical for the survival of CML cells (Fig. 2c–e and Extended Data Fig. 2b, c). We then investigated synergistic interactions between p53 and c-MYC, testing clinically tractable inhibitors.

RITA and CPI-203 synergize to drive CML CD34⁺ cell kill

To target identified hubs, we selected RITA (also known as NSC652287), which binds p53 and blocks its degradation, and CPI-203, a bromodomain and extra terminal protein (BET) inhibitor hindering transcription by disrupting chromatin-dependent

signal transduction^{13,14}. As anticipated¹⁵, c-MYC was downregulated 8 h after CPI-203 treatment (Extended Data Fig. 3a). CPI-203 also reduced p53 at 8 h. RITA subtly increased p53 by 8 h, further enhanced by 24–48 h. Dasatinib (Das) at 150 nM (a concentration achievable in patients to fully inhibit BCR-ABL¹⁶) gradually reduced p53 levels and inhibited phosphorylation of STAT5 as previously observed^{17,18}. RITA with CPI-203 for 8 h reduced both p53 and c-MYC, suggesting a dominant effect of CPI-203 at this early time point, but by 48 h markedly increased p53 (Extended Data Fig. 3a–c).

RITA or CPI-203 treatment of CML CD34⁺ cells for 72 h reduced viability in a concentration-dependent manner and induced significant apoptosis; combining drugs resulted in further significant changes in these parameters (Fig. 3a, b and Extended Data Fig. 3d). Labelling with the cell division tracker carboxyfluorescein succinimidyl ester (CFSE) and CD34 antibody showed that as CML cells divided in the presence of CPI-203, there was clear and rapid loss of CD34 expression not seen with RITA (Fig. 3c), suggesting that c-MYC (a predominant target of CPI-203; ref. 15) inhibition induces differentiation of CML CD34⁺ cells. Differentiation was further suggested by skewing of the morphology, size and number of CFCs (Fig. 3d). RITA decreased CFCs but did not affect colony types (Fig. 3d, e). By inducing apoptosis and differentiation, the drugs may synergize and enhance elimination of CML. By measuring drug–dose response¹⁹, combination therapy was potentially synergistic with combination indices (CIs) ranging from 0.07 to 0.34 (Fig. 3a). Nutlin-3a (Nut), another HDM2 inhibitor, produced similar results. The effects of RITA and Nut were p53 dependent, as K562 cells lacking p53 were non-responsive (Extended Data Fig. 3e and 4a, b). Since CPI-203 ± RITA reduced p53 at the early time point, sequential inhibition of HDM2 and c-MYC was tested using chemical and genetic approaches. Neither inhibition of HDM2 before c-MYC nor vice versa improved cell kill compared with simultaneous knockdown or drug inhibition, or compared with nilotinib (Nil) (Extended Data Fig. 4c, d).

CML patients receive a TKI, irrespective of response. We therefore assessed RITA and CPI-203 effects in imatinib-mesylate-pre-treated

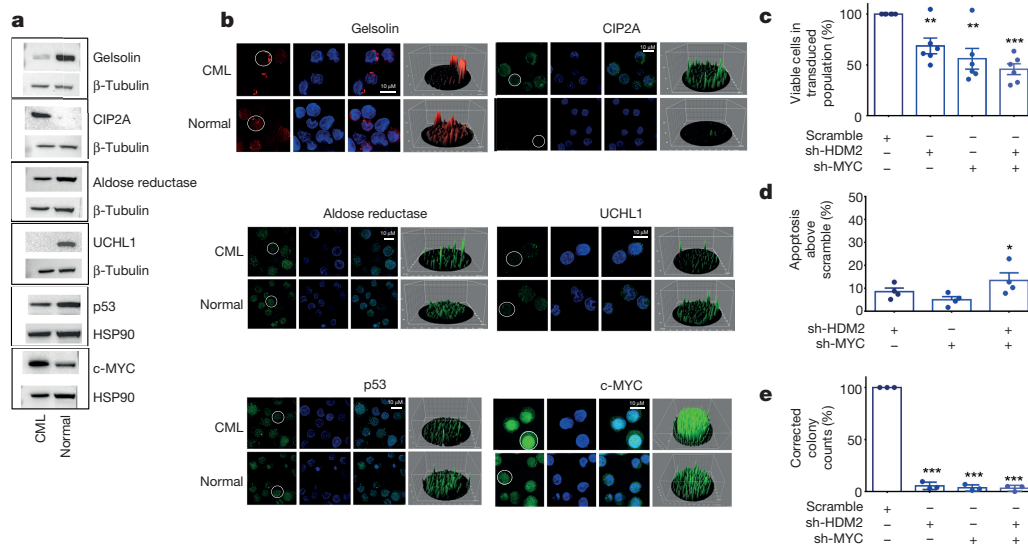


Figure 2 | Validation of proteomic network. **a**, Network proteins, p53 and c-MYC western blots using CML and normal CD34⁺ cells. For gel source data, see Supplementary Fig. 1. **b**, Network proteins validated by immunofluorescence in CML and normal CD34⁺ cells labelled green or red (far left), with the nucleus stained blue using 4',6-diamidino-2-phenylindole (DAPI; second left), overlays of images (second right), and

three-dimensional fluorescent signal (far right). **c**, CML CD34⁺ cells after HDM2, c-MYC, or scramble knockdown ($n = 6$ patient samples). **d**, Apoptosis after knockdown ($n = 4$ patient samples). **e**, CFCs from knockdown ($n = 3$ patient samples). Values normalized to scrambled control, mean \pm standard error of the mean (s.e.m.) (P values: two-tailed Student's t -test; * $P < 0.05$, ** $P < 0.01$, *** $P < 0.001$).

CML CD34⁺ cells. Imatinib mesylate neither ameliorated nor enhanced the efficacy of RITA and/or CPI-203 (Extended Data Fig. 4e).

RITA and CPI-203 eliminate LSCs

The CML network suggested an altered dependency on p53/c-MYC signalling. We therefore hypothesized that normal cells may be less susceptible to the drug combination. Treatment of normal CD34⁺ cells with single agents or combinations had no significant effects on cell counts. However, increased apoptosis was observed at higher CPI-203 concentrations (2 or 5 μ M) and with the highest combination (RITA 25 nM, CPI-203 5 μ M; Extended Data Fig. 5a, b). In CML cells, significant apoptosis was observed with all four CPI-203 and combination concentrations (Fig. 3b), confirming a therapeutic window.

To confirm the *in silico* results that led to the prediction (Fig. 1b, c and Extended Data Fig. 1c) that an altered dependency on p53 and c-MYC extended to primitive LSCs, we exposed CML LSCs to the drug

combination. LSCs were defined as either CFSE^{max} or CD34⁺CD38⁻. As shown previously¹⁶, in comparison to untreated control, over 5 days the CFSE^{max} population persisted in response to Das and Nil, but was significantly reduced by CPI-203 alone and by combination treatment (Figs 3c and 4a, b). Over 72 h, RITA with CPI-203 was also effective in synergistically eliminating residual CD34⁺CD38⁻ cells (CI = 0.3–0.8; Extended Data Fig. 5c).

HSCs and LSCs are most stringently defined by their engraftment capacity at 16 weeks. We exposed CML CD34⁺ cells to RITA, CPI-203, the combination, or Das for 48 h before transplantation into sublethally irradiated NSG mice (Extended Data Fig. 5d). Human CD45⁺ cells were detectable in peripheral blood at 8, 12 and 16 weeks and in bone marrow at 16 weeks post-transplantation. Das had no significant effect on NSG-repopulating CML LSCs, representing the most primitive long-term engrafting cells. In contrast RITA, CPI-203, and the combination reduced engraftment as indicated by decreased CD45⁺,

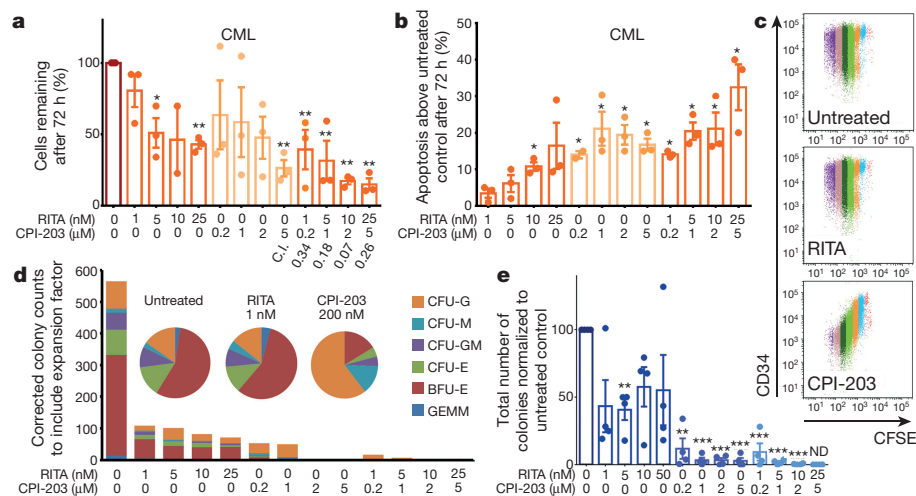


Figure 3 | Modulation of p53 and c-MYC demonstrates CML sensitivity. **a**, **b**, Drug titrations: cell viability with CIs ($n = 3$ patient samples) (**a**) and apoptosis ($n = 3$ patient samples) (**b**). **c**, CFSE/CD34-labelled cells. Cell divisions are multicoloured. Representative of $n = 3$ patient samples. **d**, CFCs from treated cells. BFU, burst-forming unit; CFU, colony-forming

unit; E, erythrocyte; G, granulocyte; GEMM, granulocyte, erythrocyte, monocyte, megakaryocyte. Representative of $n = 3$ patient samples. **e**, Averaged CFCs ($n = 3$ patient samples). ND, not detected. One experiment is represented in **d**, mean \pm s.e.m. (P values: two-tailed Student's t -test; * $P < 0.05$, ** $P < 0.01$, *** $P < 0.001$).

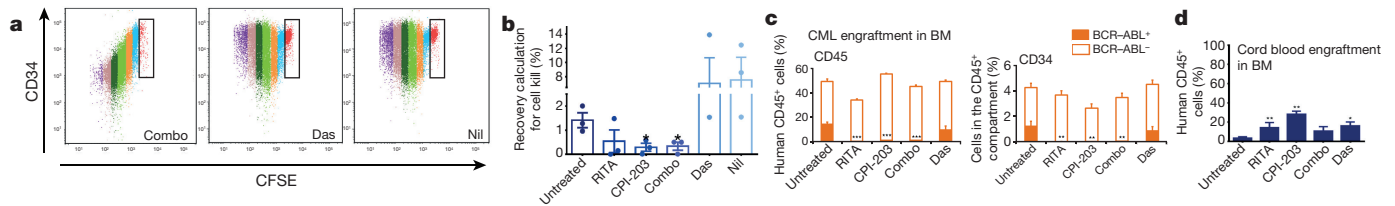


Figure 4 | p53 and c-MYC abrogation in normal and primitive CML cells. **a**, CFSE/CD34-labelled CML cells. Combo, combination. **b**, Recovery of CFSE^{max} CML cells after 5 days treatment ($n = 3$ patient samples). **c**, Bone marrow (BM) analyses of human CML, replicated twice

CD34⁺, CD33⁺, CD11b⁺, CD19⁺ and CD14⁺ cells (Extended Data Fig. 5e, f). Using a CML sample known to engraft both BCR-ABL⁺ and BCR-ABL⁻ cells by double-fusion fluorescence *in situ* hybridization (D-FISH), there was a marked decrease in the long-term-engrafting potential of RITA-, CPI-203- or combination-treated leukaemic cells, with no significant effect on non-leukaemic populations (Fig. 4c, d and Extended Data Fig. 5g, h). Experiments using cord blood CD34⁺ cells confirmed the selectivity of RITA and CPI-203 for BCR-ABL⁺ versus BCR-ABL⁻ stem cells (Fig. 4d).

Mechanism of LSC kill and clinical scope

To understand the mechanism(s) underlying reduction of CML stem and progenitor cells in response to RITA and CPI-203, RNA sequencing (RNA-seq) was performed. Of the 12,248 genes sequenced, 2,134 were identified as synergistically modulated by combination treatment; 166 demonstrated extreme synergy (Fig. 5a). Moreover, 81% of the genes differentially expressed in response to the combination were deregulated in the same direction with RITA or CPI-203 ($\chi^2(1) = 891.93$, $P < 0.01$). While transcriptional responses to RITA or CPI-203 were enriched for p53/apoptosis or c-MYC/differentiation (not found with Nil), respectively, the combination induced enhanced or additional enrichment of these molecular signatures and pathways (Fig. 5b, Extended Data Fig. 6a–c and Supplementary Tables 5–7). Furthermore, stem/progenitor markers CD34 and CD133 were dramatically down-regulated by CPI-203 and the combination, but not by RITA or Nil (Extended Data Fig. 7b). The enrichment in the p53/apoptosis and c-MYC/differentiation pathways paralleled the *in vitro* phenotypic effects observed. Limited overlap in gene membership of the signatures identified *in silico* demonstrates that distinct molecular components contribute to single and combined drug responses (Fig. 5c).

CML stem cell persistence is an issue for all CML patients, however, many also exhibit or acquire TKI resistance or demonstrate a more aggressive clinical phenotype²⁰. These represent patients in whom novel agents targeting p53 and c-MYC would first be tested. To investigate whether the deregulated p53/c-MYC network is present in both TKI-responder (TKI-R) and TKI-non-responder (TKI-NR) patients²¹, and in more advanced forms of CML²⁰, we considered data from CD34⁺ CML cells derived from suitable patient cohorts. Transcriptional expression of the network components was highly correlated across all CML versus normal comparisons, irrespective of TKI response or clinical phenotype (Fig. 5d). In keeping with these *in silico* data, CD34⁺ cells from a TKI-NR patient showed high levels of apoptosis after treatment with RITA and/or CPI-203 (Extended Data Fig. 7c), suggesting that these drugs should be of therapeutic value for such patients.

RG7112/7388 and CPI-203/0610 therapy

To progress the drug combination towards the clinic, we used complementary preclinical mouse models and introduced RG7112 and RG7388, both HDM2 inhibitors²², and CPI-0610, a BET inhibitor²³, drugs already advanced in clinical trials in humans. In the SCL-tTA-BCR-ABL1 double transgenic (DTG) leukaemia mouse model BCR-ABL1, driven from the stem cell promoter (SCL), is inducible in HSCs

(2 patient samples), with a minimum of $n = 6$ mice per arm. **d**, Bone marrow analyses of human cord blood replicated once, $n = 5$ mice per arm; mean \pm s.e.m. (P values: two-tailed Student's t -test; * $P < 0.05$, ** $P < 0.01$, *** $P < 0.001$).

by tetracycline withdrawal (tTA), resulting in a transplantable CML-like disease with increased myeloid counts and splenomegaly^{16,17,24}.

After irradiation, C57BL/6 CD45.1⁺ mice were used as recipients and CD45.2⁺ mice as DTG bone marrow donors (Extended Data Fig. 8a). After transplantation (to synchronize leukaemia development and assess transplantable LSCs), CML was induced. In mice and/or rats, RG7112 at 50–200 mg kg⁻¹ and CPI-0610 at 15–60 mg kg⁻¹ have demonstrated on-target effects in tumours^{22,23}. Excellent tolerability was achieved with modest doses of RG7112 (50 mg kg⁻¹ once daily) and CPI-0610 (15 mg kg⁻¹ twice daily, both for 4 weeks), selected to demonstrate synergy. White blood cell and neutrophil counts returned to non-leukaemic control levels with the drug combination, but not with single treatments (Fig. 6a and Extended Data Fig. 8b). While CPI-0610, Nil, and the combination significantly reduced spleen size (Fig. 6b), only the combination significantly reduced donor leukaemic CD45.2⁺ cells in the bone marrow (protected by the niche), while simultaneously allowing recovery of host normal CD45.1⁺ cells; CD45.1:CD45.2 ratio changed from 20:80 (untreated) to 40:60 (combination) (Extended Fig. Data 8c). At the stem cell level, donor leukaemic Lin⁻Sca-1⁺c-Kit⁺ (CD45.2⁺ LSK) cells were reduced by >60% by the combination, while host LSKs were unaffected. None of the single arms reduced LSKs (Fig. 6b–d), supporting the synergistic effects demonstrated *in vitro*.

To confirm that these therapeutic *in vivo* effects extended to human CML, two cohorts of sublethally irradiated NSG mice were transplanted

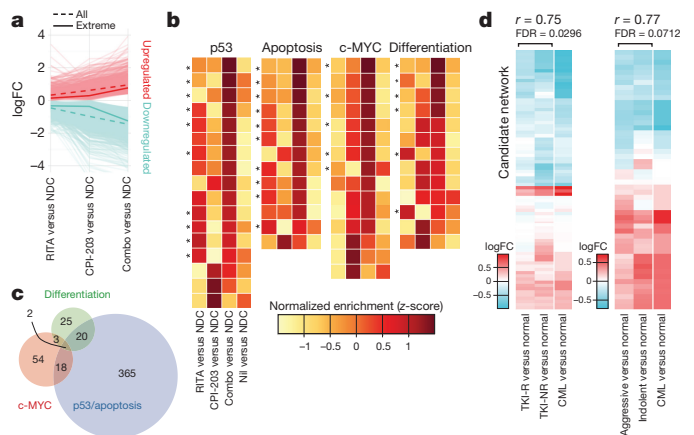


Figure 5 | Mechanism and clinical relevance of treatment. **a**, Molecular synergy for 100 nM RITA, 1 μ M CPI-203 and RITA plus CPI-203 (Combo) 24 h treatment (NDC, no drug control; $n = 3$ patient samples per arm); mean expression of 'all' and 'extreme' synergistic genes summarized as indicated. FC, fold change. **b**, Enrichment of p53 (far left), apoptosis (second left), c-MYC (second right) and differentiation (far right) Molecular Signatures Database (MSigDB) signatures. Asterisks indicate significant enrichment specific to combination treatment. **c**, Gene membership of three functional signatures. **d**, Comparison of transcriptional profiles of TKI-R, TKI-NR and baseline CML versus normal (left), and aggressive, indolent and baseline CML versus normal (right) for our candidate network (Fig. 1a). FDRs calculated by 10,000 permutations.

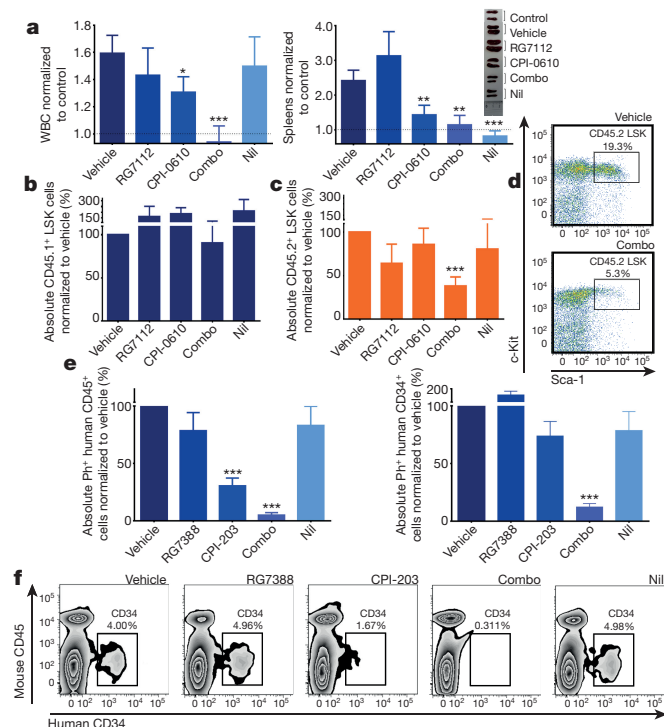


Figure 6 | Targeting p53 and c-MYC in CML elicits synergistic kill in BCR-ABL⁺ LSCs. **a**, White blood cell (WBC) counts and spleen weights normalized to control (dotted line) (experiments replicated twice, minimum $n = 7$ mice per arm; vehicle, no drug control). Combo, combination treatment. **b–d**, Bone marrow stained for CD45.1/2 and further gated on Lin[−]Sca-1⁺c-Kit⁺ (LSK). Drug treatments (experiments replicated twice, minimum $n = 5$ mice per arm). **e, f**, NSG mice *in vivo* treatment: bone marrow stained for human Philadelphia chromosome (Ph)⁺CD45⁺ (left) and further gated on CD34⁺ cells (right). **g**, Representative CD34⁺ dotplots (experiments replicated twice (2 patient samples), minimum $n = 9$ mice per arm); mean \pm s.e.m. (P values: two-tailed Student's *t*-test; * $P < 0.05$, ** $P < 0.01$, *** $P < 0.001$).

with independent CML CD34⁺ samples and treated with RG7388 and CPI-203 (75–100 mg kg^{−1} and 6–7.5 mg kg^{−1}, respectively) for 3–4 weeks. Of the single agents, only CPI-203 showed a consistent effect. The drug combination, however, eliminated 95% of Ph⁺CD45⁺ and 88% of CD45⁺CD34⁺ subsets (Fig. 6e, f). These results were significant as compared to vehicle ($P < 0.001$) or Nil ($P = 0.0016$ (CD45⁺); $P = 0.0047$ (CD45⁺CD34⁺)) and as compared to RG7388 ($P = 0.0017$ (CD45⁺); $P = 0.0004$ (CD45⁺CD34⁺)) or CPI-203 ($P = 0.0046$ (CD45⁺); $P = 0.0008$ (CD45⁺CD34⁺)), respectively (Fig. 6e, f), again suggesting a high degree of synergy.

Discussion

This work demonstrates the potential of unbiased, systems approaches to uncover new therapeutic options by analysing primitive stem cell subsets from primary material. We found that p53 and c-MYC work together with BCR-ABL to shape LSC phenotype and show that modulation of both p53 and c-MYC is critical to drive synergistic enhancement of apoptosis and differentiation seen *in vitro*, *in vivo*, at the stem cell level and the molecular level by RNA-seq.

p53 and c-MYC have individually been identified as proteins in CML pathobiology^{17,25–30} and cancer^{31–33}, but have not previously been considered for dual targeting. In recent CML studies, enhanced LSC kill converged on p53 as the mediator of apoptosis^{17,25,34}. CML LSCs are also susceptible to enhancement or depletion of c-MYC. After deletion of the E3 ligase FBXW7, c-MYC increases with p53, resulting in cell cycle entry and p53-dependent apoptosis^{29,30}. However, FBXW7 may not represent a viable drug target based on its role in haematopoiesis,

tissue stem cells and, importantly, as a tumour suppressor. Currently, there is interest in drugging the spliceosome machinery, particularly for MYC-driven cancers, however, a therapeutic window remains to be established and exploited with well-tolerated agents^{35,36}. BET inhibition is a rapidly expanding market with multiple agents in phase 1–2 development. These agents are well tolerated and demonstrate efficacy in haematological malignancies. Resistance to BET inhibitors evolves through epigenetic mechanisms³⁷, however, our combination approach will be less susceptible to resistance.

Over the last decade CML has been transformed from a fatal cancer to a manageable disease with lifelong therapy. Despite recognition that LSCs prevent cure, the paradigm established by TKIs means that novel drugs must be safe, supported by a clear therapeutic window and easy to administer. As a result, few preclinical studies have reached the clinic and trials fail owing to toxicity and poor recruitment^{24,38}. CML is often regarded as a simple cancer, driven solely by BCR-ABL, yet we do not understand why targeting BCR-ABL does not eradicate LSCs, nor cure CML. Our work shows that BCR-ABL reprograms potent oncoproteins and tumour suppressors, to establish a signalling network that underlies the propagation of CML. Critically, we found that simultaneous perturbation of p53 and c-MYC, mechanistically driving modulation of p53, apoptosis, c-MYC and differentiation pathways, improved selective kill of LSCs as compared to TKIs. Nil was ineffective against these pathways, potentially explaining why TKIs are not sufficient to cure CML. The fact that the aberrant network was similarly regulated in TKI-Rs, TKI-NRs, and patients with aggressive and indolent CML, coupled with the availability of well-tolerated oral agents in an advanced stage of development, now offers an entirely novel approach for the treatment of CML, with the therapeutic potential to address CML LSC persistence and improve outcome for CML patients.

Online Content Methods, along with any additional Extended Data display items and Source Data, are available in the online version of the paper; references unique to these sections appear only in the online paper.

Received 8 March; accepted 26 April 2016.

Published online 8 June 2016.

- O'Hare, T., Zabriskie, M. S., Eiring, A. M. & Deininger, M. W. Pushing the limits of targeted therapy in chronic myeloid leukaemia. *Nature Rev. Cancer* **12**, 513–526 (2012).
- Druker, B. J. *et al.* Activity of a specific inhibitor of the BCR-ABL tyrosine kinase in the blast crisis of chronic myeloid leukemia and acute lymphoblastic leukemia with the Philadelphia chromosome. *N. Engl. J. Med.* **344**, 1038–1042 (2001).
- Graham, S. M. *et al.* Primitive, quiescent, Philadelphia-positive stem cells from patients with chronic myeloid leukemia are insensitive to STI571 *in vitro*. *Blood* **99**, 319–325 (2002).
- Mahon, F. X. *et al.* Discontinuation of imatinib in patients with chronic myeloid leukaemia who have maintained complete molecular remission for at least 2 years: the prospective, multicentre Stop Imatinib (STIM) trial. *Lancet Oncol.* **11**, 1029–1035 (2010).
- Corbin, A. S. *et al.* Human chronic myeloid leukemia stem cells are insensitive to imatinib despite inhibition of BCR-ABL activity. *J. Clin. Invest.* **121**, 396–409 (2011).
- Neviani, P. *et al.* PP2A-activating drugs selectively eradicate TKI-resistant chronic myeloid leukemic stem cells. *J. Clin. Invest.* **123**, 4144–4157 (2013).
- Dijkstra, E. W. A note on two problems in connexion with graphs. *Numer. Math.* **1**, 269–271 (1959).
- Van Dang, C. & McMahon, S. B. Emerging concepts in the analysis of transcriptional targets of the MYC oncoprotein: are the targets targetable? *Genes Cancer* **1**, 560–567 (2010).
- Boichenko, A. P. *et al.* A panel of regulated proteins in serum from patients with cervical intraepithelial neoplasia and cervical cancer. *J. Proteome Res.* **13**, 4995–5007 (2014).
- Liu, Y. *et al.* Glycoproteomic analysis of prostate cancer tissues by SWATH mass spectrometry discovers N-acylthanolamine acid amidase and protein tyrosine kinase 7 as signatures for tumor aggressiveness. *Mol. Cell. Proteomics* **13**, 1753–1768 (2014).
- Sutton, C. W. *et al.* Quantitative proteomic profiling of matched normal and tumor breast tissues. *J. Proteome Res.* **9**, 3891–3902 (2010).
- Pierce, A. *et al.* Eight-channel iTRAQ enables comparison of the activity of six leukemogenic tyrosine kinases. *Mol. Cell. Proteomics* **7**, 853–863 (2008).

13. Issaeva, N. *et al.* Small molecule RITA binds to p53, blocks p53–HDM-2 interaction and activates p53 function in tumors. *Nature Med.* **10**, 1321–1328 (2004).
14. Wong, C. *et al.* The bromodomain and extra-terminal inhibitor CPI203 enhances the antiproliferative effects of rapamycin on human neuroendocrine tumors. *Cell Death Dis.* **5**, e1450 (2014).
15. Mertz, J. A. *et al.* Targeting MYC dependence in cancer by inhibiting BET bromodomains. *Proc. Natl Acad. Sci. USA* **108**, 16669–16674 (2011).
16. Hamilton, A. *et al.* Chronic myeloid leukemia stem cells are not dependent on Bcr-Abl kinase activity for their survival. *Blood* **119**, 1501–1510 (2012).
17. Li, L. *et al.* Activation of p53 by SIRT1 inhibition enhances elimination of CML leukemia stem cells in combination with imatinib. *Cancer Cell* **21**, 266–281 (2012).
18. Shah, N. P. *et al.* Transient potent BCR-ABL inhibition is sufficient to commit chronic myeloid leukemia cells irreversibly to apoptosis. *Cancer Cell* **14**, 485–493 (2008).
19. Chou, T. C. Drug combination studies and their synergy quantification using the Chou-Talalay method. *Cancer Res.* **70**, 440–446 (2010).
20. Yong, A. S., Szydlo, R. M., Goldman, J. M., Apperley, J. F. & Melo, J. V. Molecular profiling of CD34⁺ cells identifies low expression of CD7, along with high expression of proteinase 3 or elastase, as predictors of longer survival in patients with CML. *Blood* **107**, 205–212 (2006).
21. McWeeney, S. K. *et al.* A gene expression signature of CD34⁺ cells to predict major cytogenetic response in chronic-phase chronic myeloid leukemia patients treated with imatinib. *Blood* **115**, 315–325 (2010).
22. Tovar, C. *et al.* MDM2 small-molecule antagonist RG7112 activates p53 signaling and regresses human tumors in preclinical cancer models. *Cancer Res.* **73**, 2587–2597 (2013).
23. Albrecht, B. K. *et al.* Identification of a benzoisoxazoloazepine inhibitor (CPI-0610) of the bromodomain and extra-terminal (BET) family as a candidate for human clinical trials. *J. Med. Chem.* **59**, 1330–1339 (2016).
24. Zhang, B. *et al.* Effective targeting of quiescent chronic myelogenous leukemia stem cells by histone deacetylase inhibitors in combination with imatinib mesylate. *Cancer Cell* **17**, 427–442 (2010).
25. Hurtz, C. *et al.* BCL6-mediated repression of p53 is critical for leukemia stem cell survival in chronic myeloid leukemia. *J. Exp. Med.* **208**, 2163–2174 (2011).
26. Lanza, F. & Bi, S. Role of p53 in leukemogenesis of chronic myeloid leukemia. *Stem Cells* **13**, 445–452 (1995).
27. Gómez-Casares, M. T. *et al.* MYC antagonizes the differentiation induced by imatinib in chronic myeloid leukemia cells through downregulation of p27(KIP1). *Oncogene* **32**, 2239–2246 (2013).
28. Winter, G. E. *et al.* Systems-pharmacology dissection of a drug synergy in imatinib-resistant CML. *Nature Chem. Biol.* **8**, 905–912 (2012).
29. Takeishi, S. *et al.* Ablation of Fbxw7 eliminates leukemia-initiating cells by preventing quiescence. *Cancer Cell* **23**, 347–361 (2013).
30. Reavie, L. *et al.* Regulation of c-Myc ubiquitination controls chronic myelogenous leukemia initiation and progression. *Cancer Cell* **23**, 362–375 (2013).
31. Dang, C. V. MYC, metabolism, cell growth, and tumorigenesis. *Cold Spring Harb. Perspect. Med.* **3**, a014217 (2013).
32. Vousden, K. H. & Prives, C. Blinded by the light: the growing complexity of p53. *Cell* **137**, 413–431 (2009).
33. Wade, M., Li, Y. C. & Wahl, G. M. MDM2, MDMX and p53 in oncogenesis and cancer therapy. *Nature Rev. Cancer* **13**, 83–96 (2013).
34. Zhang, H., Li, H., Ho, N., Li, D. & Li, S. Scd1 plays a tumor-suppressive role in survival of leukemia stem cells and the development of chronic myeloid leukemia. *Mol. Cell. Biol.* **32**, 1776–1787 (2012).
35. Hsu, T. Y. *et al.* The spliceosome is a therapeutic vulnerability in MYC-driven cancer. *Nature* **525**, 384–388 (2015).
36. Koh, C. M. *et al.* MYC regulates the core pre-mRNA splicing machinery as an essential step in lymphomagenesis. *Nature* **523**, 96–100 (2015).
37. Fong, C. Y. *et al.* BET inhibitor resistance emerges from leukaemia stem cells. *Nature* **525**, 538–542 (2015).
38. Prost, S. *et al.* Erosion of the chronic myeloid leukaemia stem cell pool by PPAR γ agonists. *Nature* **525**, 380–383 (2015).

Supplementary Information is available in the online version of the paper.

Acknowledgements We thank all CML patients and UK haematology departments who contributed samples; A. Hair for sample processing; J. Cassels for cell sorting; A. Michie and V. Helgason for assisting with the *in vivo* research and providing cord blood samples; C. Wells, P. Bailey and J. Cole for discussions regarding the RNA-seq analysis. We acknowledge the Cancer Research UK (CR-UK) Glasgow Centre (C596/A18076) and the CR-UK Beatson Institute (C596/A17196) for providing animal care and housing facilities. We acknowledge Constellation Pharmaceuticals for providing CPI-203, CPI-0610 and part funding M.E.D., Roche for providing RG7112, RG7388 and part funding M.E.D. and the SPIRIT Trials Management Group for access to CML samples. This study was supported by the Glasgow and Manchester Experimental Cancer Medicine Centres (ECMC), which are funded by CR-UK and the Chief Scientist's Office (Scotland). We acknowledge the funders who have contributed to this work: MRC stratified medicine infrastructure award (A.D.W.), CR-UK C11074/A11008 (F.P., L.E.M.H., T.L.H., A.D.W.); LLR08071 (S.A.A., E.C.); LLR11017 (M.C.); SCD/04 (M.C.); LLR13035 (S.A.A., K.D., A.D.W. and A.P.); LLR14005 (M.T.S., D.V.); KKL690 (L.E.P.); KKL698 (P.B.); LLR08004 (A.D.W., A.P. and A.J.W.); MRC CiC (M.E.D.); The Howat Foundation (fluorescence-activated cell sorting (FACS) support); Friends of Paul O'Gorman (K.D. and FACS support); ELF 67954 (S.A.A.); British Society for Haematology start-up fund (S.A.A.); MR/K014854/1 (K.D.).

Author Contributions A.D.W. and T.L.H. supervised the entire study and research. S.A.A., L.E.M.H., A.D.W. and T.L.H. designed the research, analysed and interpreted data, and wrote the manuscript. S.A.A. conceived the hypothesis, supervised *in vivo* research, prepared samples for proteomic and RNA-seq, performed all *in vitro* work including western blotting, immunofluorescence, cloning and knockdown studies, clonogenic studies, flow cytometry and all mouse *in vivo* studies including tissue processing-FISH preparation and slide interpretation, engraftment determination and analysis of primitive stem cell subsets. L.E.M.H. designed and performed all *in silico* work including global omics handling, integration and analysis (MS, RNA-seq and microarray data); network analyses; correlation/MI calculations; functional enrichment analyses and permutation experiments for calculation of *P* values. E.C. performed proteomic work. A.J.K.W. performed proteomic work and generated relative proteomic quantification. M.E.D. performed virus preparation, prepared drugs for *in vivo* work and assisted with *in vivo* studies. K.D. provided maintenance and care for all mouse colonies and assisted with *in vivo* work. P.B. and L.E.P. provided assistance with *in vivo* studies and D-FISH preparation. F.P. and M.T.S. provided assistance with *in vivo* studies. D.V. provided analysed datasets and analysed/interpreted RNA-seq data. S.M.G. supervised and interpreted RNA-seq. C.N. performed RNA-seq experiments. K.K. and M.C. provided analysed datasets. A.P. supervised proteomic studies. All authors reviewed/edited the manuscript.

Author Information The CML and normal CD34⁺ mass spectrometry proteomics data have been deposited to the ProteomeXchange Consortium via the PRIDE partner repository with the dataset identifiers PXD001502, PXD001503, PXD001504; SCOPE3/SCOPE4 data are also available using PXD001505 and PXD002782 respectively. Transcriptomic data are publicly available via the accession codes E-MTAB-2581, E-MTAB-2508, E-MIMR-17 at ArrayExpress (<https://www.ebi.ac.uk/arrayexpress/>) and GSE47927, GSE5550, GSE24739, GSE14671 at GEO (<http://www.ncbi.nlm.nih.gov/geo/>). RNA-seq data (fastq) have been deposited in the European Nucleotide Archive under accession number PRJEB9942. Reprints and permissions information is available at www.nature.com/reprints. The authors declare competing financial interests: details are available in the online version of the paper. Readers are welcome to comment on the online version of the paper. Correspondence and requests for materials should be addressed to T.L.H. (Tessa.Holyoake@glasgow.ac.uk).

METHODS

Patient samples. Patient samples (PS) were leukapheresis products taken at time of diagnosis with chronic-phase CML, with written informed consent in accordance with the Declaration of Helsinki and approval of the Greater Glasgow and Clyde National Health Service Trust Institutional Review Board. CD34⁺ cells were enriched using CliniMACS (Miltenyi Biotec), with stem cell subsets purified by FACS. CML CD34⁺ samples were cultured in serum-free medium (SFM) supplemented with growth factors as described previously¹⁶. Normal CD34⁺ cells were CD34-enriched leukapheresis products or cord blood maintained as described for CML CD34⁺ samples. All PS and relevant clinical data are summarized in Supplementary Table 4. All *in vitro* work was performed with a minimum of 3 PS (3 biological replicates) unless otherwise indicated. Unless otherwise indicated each PS was analysed as an individual sample replicated once in an experiment.

Cell lines. The HeLa cell line was obtained from the German Collection of Microorganisms and Cell Cultures (DSMZ; originally deposited by ATCC). HeLa cells were subcultured in RPMI 1640 (10% FCS plus 2 mM L-glutamine, 100 units ml⁻¹ penicillin and 100 µg ml⁻¹ streptomycin (Gibco - Life Technologies)) (passage 3). The K562 cell line (DSMZ) was subcultured in IMDM (10% FCS plus 2 mM L-glutamine, 100 units ml⁻¹ penicillin and 100 µg ml⁻¹ streptomycin (passage <6)); the cell lines were not authenticated between passage 2–6. Cell lines were mycoplasma negative in DAPI, microbiological culture, RNA hybridization and PCR assays.

CML cytoplasmic preparations for MS. CML and normal CD34⁺ cells were thawed and cultured overnight as described²⁴. Cytoplasmic preparations were prepared using the Active Motif Nuclear Extraction Kit (Active Motif).

Materials. RITA (CAS 213261-59-7; catalogue no. 10006426), Nutlin-3a (CAS 675576-98-4; catalogue no. 18585) (Cayman Chemical) and Nil (CAS 641571-10-0) (Selleck Chemicals) were stored as per manufacturer's instructions. CPI-203 and CPI-0610 were obtained from Constellation Pharmaceuticals and kept as a solid powder at room temperature. Das (Selleck Chemicals) was kept as a stock solution (10 mg ml⁻¹) in dimethylsulfoxide (DMSO; Sigma-Aldrich) and prepared and stored in aliquots at -20 °C. Imatinib mesylate (LC Laboratories) was stored at 100 mM in distilled water at 4 °C. RG7112 and RG7388 were supplied by Roche. A list of all antibodies used is provided in Supplementary Table 8.

Proteomics. Methods used have been described¹². Twenty micrograms of protein was isobarically tagged (iTRAQ reagent, ABSciex). Peptides were identified by Reverse phase liquid chromatography tandem mass spectrometry (RP-LC-MS/MS) on three different instruments: ABSciex Q-STAR Elite, Thermo LTQ Orbitrap Velos, ABSciex TripleTOF 5600. For the 5600 and Elite, dried peptide fractions were resuspended in 15 µl 3% (v/v) acetonitrile, 0.1% (v/v) formic acid and 20 mM citric acid. For each analysis, a 5 µl peptide sample was loaded onto a nano ACQUITY UPLC Symmetry C18 Trap (5 µm, 180 µm × 20 mm) and separation of the peptides was performed using nanoACQUITY UPLC BEH C18 Column (1.7 µm, 75 µm × 250 mm). For the Orbitrap, 10% of the peptide sample was loaded onto Acclaim PepMap µ-PreColumns, analytical separation of the peptides was performed using Acclaim PepMap RSLC C18 Columns. Data were acquired using the information-dependent acquisition (IDA) protocol.

Elite and 5600 data were processed by a 'thorough' search against the UniProtKB/SwissProt human database containing 532,146 sequence entries using ProteinPilot Software 4.1, revision number 460, Paragon Algorithm 4.0.0.0. Orbitrap data were analysed using Proteome Discoverer 1.3. The data were searched using the MASCOT node of Proteome Discoverer with the UniProtKB database (release 2011_11). The proteins observed in the three data sets demonstrated that using multiple instruments enhanced coverage (Extended Data Fig. 1).

Analysis and integration of MS proteomic data. MS data sets were filtered for peptides observed in all channels (one normal sample was removed from all experiments due to poor labelling). Deregulated proteins were identified using a threshold of mean ± 2 s.d. on CML versus normal log₂ ratios. This candidate list was refined to include only those proteins corroborated by (1) log ratio changes of ±0.5 in murine Ba/F3 ± BCR-ABL MS data¹², (2) a complementary CD34⁺ cell proteomics data set³⁹, and/or (3) all instruments within the current experimental data set. A parallel, manual inspection retained candidates if (1) log ratios were ≈ ±1.3, or (2) log ratios were lower and neither alternative instrument reported differential expression in the opposite direction; this manual selection step was blinded. Together, these filtering steps reduced the candidate list to 58 proteins (see Supplementary Table 1).

Formation of candidate network. The MetaCore implementation (13 June 2012) of Dijkstra's shortest path algorithm⁷, a general purpose algorithm that identifies the shortest paths between 'seed' nodes of interest in a graph, was used to build a network around the 58 deregulated proteins (the graph used was the fully manually annotated MetaCore KB). Paths between seeds were limited to length = 2 and all shortest paths of the minimum length were retained in the resulting network. Topology statistics (Supplementary Table 2) were calculated using the igraph package in R.

Transcriptomic data analysis. Three bulk CD34⁺ (1–3) and four primitive LSC (4–7) CML chronic phase versus normal data sets are discussed: (1) E-MTAB-2581: Affymetrix Human Gene 1.0 ST Array transcriptional data from newly diagnosed CML chronic phase and normal progenitor cells (CD34⁺CD38⁺) from G-CSF-mobilized peripheral blood. mRNA was extracted using the RNeasy Mini Kit (Qiagen) and DNase I treated on columns using the RNase (RNase)-Free DNase Set (Qiagen). Affymetrix GeneChip analysis was performed using 50 ng of RNA to the manufacturer's instructions; (2) Gene Expression Omnibus (GEO) accession GSE47927 (ref. 40); (3) GEO accession GSE5550 (ref. 41); (4) ArrayExpress accession E-MTAB-2581 (as described in (1) but for CD34⁺CD38⁻ cells); (5) GEO accession GSE47927 (ref. 40); (6) GEO accession GSE24739 (ref. 42); and (7) ArrayExpress accession E-MTAB-2508 (ref. 43).

CEL files were obtained directly from collaborators or public repositories. All transcriptional data were RMA normalized with the exception of GSE5550 for which only the VSN⁴⁴ normalized data were available. log₂ scale expression values were analysed using limma⁴⁵ (*P* value correction by Benjamini–Hochberg⁴⁶). In calculating the correlations and MI statistics (Fig. 1b, c and Extended Data Fig. 1), multiple probesets corresponding to single genes were median averaged.

Calculating correlations across multiple data sets. Ensembl's web services were used to map between (1) human and murine data sets via orthologues and (2) human transcriptomic and proteomic data sets via HUGO Gene Nomenclature Committee (HGNC) symbols. The Bioconductor package biomaRt (v.2.18.0) was used in R (v.3.0.1). Pearson's product moment correlation coefficients (*r*) were calculated across data sets for the 58 candidates and the 30 networked candidates (*r_c* and *r_n* respectively in Extended Data Fig. 1a, d). Resulting *r*² values quantify the proportion of variability captured by the linear relationship and *r*²_Δ is defined as *r*²_n/*r*²_c, that is, the ratio of *r*² for the 30 networked candidates to the *r*² for the 58 candidates. FDRs for the *r*²_Δ observed were generated by considering 10,000 random samplings of each data set and counting the number of random samples meeting or exceeding the *r*²_Δ and *r*²_n statistics.

Calculation of MI. We calculated the MI values for 10,000 random subsets (of size 30) to generate a distribution of MI values that we would expect by chance (expression values binned between -3 and 3, bin width = 0.1; entropy package in R); these are the values summarized by the distributions plots in Fig. 1c and Extended Data Fig. 1b, e. The FDR values represent the proportion of random subsets that generate an MI greater than or equal to the MI for the network.

Calculation of proteomic/primitive transcriptional consistency FDR. Of the 30 proteins in Extended Data Fig. 1c, 21 showed consistency of deregulation in at least three of the primitive transcriptional data sets and the bulk proteomic data set. To assess how likely it would be to observe such consistency by chance, the data were randomly permuted 10,000 times and permutations exhibiting similar deregulation consistency (that is, deregulation correspondence across four data sets) were recorded.

Topological analysis of p53/c-MYC in other MS data sets. Comparison of leukaemogenic PTK proteomic effects and three primary proteomics data sets, describing two types of breast cancer¹¹ (3 ductal carcinoma *in situ* and 4 invasive carcinoma breast cancer patient samples with matched normal samples), three types of prostate cancer¹⁰ (24 non-aggressive, 16 aggressive, 25 metastatic prostate cancer patient samples and 10 normal samples) and cervical⁹ cancer, were obtained directly from the authors. In each data set, deregulated proteins were identified using *z*-scores ± 2 when considering cancer versus normal log₂ ratios and subjected to the same MetaCore network building process as described earlier. In the case of the cervical cancer data set no network could be found and the data were removed from the analysis. In addition, 50 sets of 58 random proteins were generated from the list of all proteins observed across the three MS data sets and subjected to the same network building process. The ratio *d*_{out}/*d*_{in} was calculated to quantify the bias of outgoing to incoming connections to/from p53 and c-MYC (Fig. 1d).

TKI-R/TKI-NR and aggressive/indolent CML transcription. The PB 'validation' set TKI-R/TKI-NR samples in GEO data set GSE14671 were integrated with a material-matched CML versus normal data set (CD34⁺CD38⁺ cell data from ArrayExpress E-MTAB-2581) using COMBAT⁴⁷ (Bioconductor package inSilicoDb v.1.10.1). All probeset-to-probeset mappings between the Affymetrix HG U133+2 and Affymetrix HuGe 1.0 ST chips (obtained via Bioconductor's biomaRt package) were retained and used by COMBAT. The TKI-R and TKI-NR samples were compared to the integrated normal data (using limma) to generate logFC values representing differential expression (see left two lanes in each panel of Fig. 5e). The pattern of differential expression in the TKI-R/TKI-NR versus normal comparisons was then compared to that of CML versus normal, as calculated separately by limma in the material-matched data sets (E-MTAB-2581) (see right lane in each panel of Fig. 5e) to provide a baseline CML versus normal comparison. Transcriptional profiles for probe pairs corresponding to the 30 members of the candidate network were identified using HGNC symbols (data corresponding to TARDBP were removed due to the large number (66) of corresponding probe pairs).

An FDR was calculated using 10,000 re-samplings of the merged data set to describe the likelihood of observing a correlation as high or greater by chance. The transcriptional data for the aggressive and indolent samples in ArrayExpress data set E-MIMR-17 were processed as described above, but integrated with the CML and normal CD34⁺ data set GSE5550 using all probeset-to-probeset mappings between the Affymetrix U133a and Affymetrix HG Focus chips (again obtained using biomaRt).

Enrichment of MSigDB signatures. For the candidate network analysis (the results of which are shown in Supplementary Table 3), MSigDB signatures (C2: curated genesets) were accessed via the c2BroadSets object in GSVAdata v.1.0.0 using R. Enrichment scores were calculated using the hypergeometric distribution as implemented by dhyper(). Signatures corresponding to CML, c-MYC and p53 related biology were extracted using appropriate regular expressions on the signature name. In the RNA-seq analysis (Fig. 5b), the MSigDB signatures (C2: curated genesets) were identified as significantly differentially expressed in the TMM/VOOM-normalized RNA-seq data using GSVA⁴⁸ and limma⁴⁹. Significant pathways were identified using an FDR = 0.05 threshold on corrected *P* values⁴⁶. The p53, apoptosis, c-MYC and differentiation signatures were extracted using appropriate regular expressions on the signature name.

Enrichment of PANTHER pathways. The top 1,500 differentially expressed genes (as ranked by increasing *P* value, calculated by limma⁴⁹) were identified comparing treated/untreated samples. These genes and their logFCs for each arm were uploaded to PANTHER (<http://www.pantherdb.org/>) and subjected to a Mann-Whitney *U*-test⁵⁰ to identify enrichment of PANTHER pathways. Extended Data Figure 6b shows enrichment results (without Bonferroni correction) including the hypothesized direction of pathway deregulation.

Cell counting and apoptosis assays. CML CD34⁺ cells were seeded at $1-2 \times 10^6$ cells ml⁻¹ before drug treatment and counted by trypan blue (Sigma-Aldrich) exclusion. Apoptosis was quantified by staining with annexin-V-APC and DAPI. In specified experiments, CML and human cord CD34⁺ cells were labelled with CD34-APC and CD38-FITC or PerCP-Cy5.5 and sorted using the FACSARIA (BD). The selected CD34⁺CD38⁻ cells were analysed 72 h after drug treatments. To measure the dose-effect relationship of each drug and its combination and to determine synergy, CIs were calculated using the Calcsyn software package (BioSoft). Except where documented, all results are expressed as a mean \pm s.e.m.

CFC assay. CD34⁺ cells were treated for 72 h at the indicated concentrations of RITA, CPI-203 and Das. Drug-treated cells (2,000 cells per plate) were washed and seeded in Methocult H4435 (STEMCELL Technologies). CML cells were transduced with lentivector constructs and sorted then washed and seeded into methylcellulose. Colonies were assessed 10–14 days after plating.

Western blotting. CD34⁺ cells were lysed in RIPA buffer with inhibitors and western blots were performed as per standard protocols.

Immunofluorescence microscopy. CML CD34⁺ cells were left untreated or treated with the indicated drugs for 24 h. Cells were harvested and spotted onto slides coated with poly-L-lysine and fixed with 3.7% (w/v) formaldehyde and permeabilized using a 0.25% (w/v) Triton-PBS solution for 15 min. Cells were blocked with 5% (w/v) BSA-PBS and stained with primary and secondary antibodies. Cells were concurrently stained with DAPI. Cells were imaged using a Zeiss Imager M1 AX10 fluorescence microscope (Carl Zeiss) and subjected to deconvolution (AxioVision software; Carl Zeiss) for image manipulation. Fluorescent signal was measured in three dimensions by Image Processing and Analysis in Java (Image J) program.

Tracking cell divisions. CFSE (Molecular Probes) and CD34 staining were performed and cell divisions were identified as described previously³.

Lentivirus transduction. The pCMV-VSV-G and pCMV-HIV1 were provided by J. Rossi. The pLKO-GFP came from K. Kranc. The following optimized pLKO vectors were purchased from Open Biosystems and subcloned into the pLKO-GFP vector: (1) TRCN000003380: MDM2 shRNA bacterial stock NM_002392. x-1495s1c1 (ref. 51); (2) TRCN0000355728: MDM2 shRNA bacterial stock NM_002392.3-1496s21c1; (3) TRCN0000174055: c-MYC shRNA bacterial stock NM_002467.2-1377s1c2 (ref. 52); (4) TRCN0000039642: c-MYC shRNA bacterial stock NM_002467.2-1377s1c1 (ref. 53).

Transduction of HeLa cell lines was performed at a MOI 1–10 with 70–95% of the cells expressing GFP after 48 h. For transduction, CD34⁺ cells were cultured in medium supplemented with growth factors (IL-3 25 ng ml⁻¹, IL-6 10 ng ml⁻¹, Flt-3L 100 ng ml⁻¹, SCF 50 ng ml⁻¹, TPO 100 ng ml⁻¹) for 48 h, followed by two exposures to concentrated virus-containing supernatants (multiplication of infection = 5) via spinoculation. Cells were harvested 48 h after second transduction and analysed or sorted for GFP positivity.

Transduced viable cells (assessed as annexin-V⁻/DAPI⁻ percentages multiplied by the absolute cell count) are presented as a percentage of CML CD34⁺ cells transduced with scramble control.

Immunodeficient mouse engraftment. For the *ex vivo* drug studies CML (2×10^6 cells per mouse) or cord blood (2×10^5) CD34⁺ cells were cultured with the indicated drugs (RITA 70 nM, CPI-203 1 μ M and Das 150 nM). After 48 h cells were transplanted via tail vein into female 8–10-week-old sublethally irradiated (2.5 Gy) NOD.Cg-Prkdcscid1l2rgtm1Wjl/SzJ NSG mice (The Jackson Laboratory). Human cells were assessed by anti-human CD45 antibody analysed by flow cytometry. Specific cell subsets were detected using antibodies to human CD34, CD33, CD11b, CD14 and CD19 (mouse antibody table in Supplementary Table 8).

For the *in vivo* drug treated NSG experiments, CML (2×10^6 cells per mouse) CD34⁺ cells were transplanted via tail vein into female 8–10-week-old sublethally irradiated (2.5 Gy) NSG mice (The Jackson Laboratory). After 4 weeks, mice were treated with RG7388 (75–100 mg kg⁻¹, oral gavage once daily), CPI-203 (6–7.5 mg kg⁻¹, intraperitoneally twice daily) or Nil (50 mg kg⁻¹, oral gavage once daily) for 3–4 weeks. Two CML samples were assessed separately, each performed with 4–5 mice per drug arm per experiment. Results presented represent data from both experiments (each experiment normalized to vehicle). To quantify the frequency of BCR-ABL⁺ cells within the engrafted human CD45⁺ cells, dual-fusion D-FISH was performed as previously described³.

Transgenic mouse model. Inducible (tetracycline (TET)-based) DTG (SCLTAXBCR-ABL1) donor mice in a C57BL/6 (CD45.2) background were a gift from D. G. Tenen. B6.SJL-Ptprca^a Pep^b/BoyJ (CD45.1) recipients (a mixture of female and males between 8–10 weeks old) were purchased from Charles River Laboratories.

Bone marrow transplantation and analysis of disease. Bone marrow cells of DTG mice (1×10^6) were injected into the tail veins of 10-week-old irradiated (2 doses of 4.25 Gy, 3 h apart) recipients. TET was continued for 2 weeks after radiation. Tail veins bleeds were performed weekly after TET removal and Gr1/Mac1 percentages (flow cytometry), white blood cells, neutrophils and haemoglobin (Hemovet) were monitored.

DTG *in vivo* drug treatment. Drugs were administered to DTG mice 5 weeks after transplantation, over a 4-week period. Nil 75 mg kg⁻¹ once daily, CPI-0610 15 mg kg⁻¹ twice daily and RG7112 50 mg kg⁻¹ once daily, all by oral gavage. For no drug control mice were administered the vehicles at the same concentrations and volumes as used for the combination arm.

Flow analysis. Peripheral blood, bone marrow and spleen cells were stained using appropriate antibodies and analysed using a FACSCanto or FACSARIA machine (BD Biosciences).

Husbandry. All experiments were performed in accordance with the local ethical review panel, the UK Home Office Animals Scientific Procedures Act, 1986, and UK Co-ordinating Committee on Cancer Research (UKCCCR) and National Cancer Research Institute (NCRI) guidelines.

Animals were kept in regulated facilities, monitored daily, and all experiments were carried out in compliance with UK Home Office guidelines. Mice were genotyped by Transnetyx.

RNA-sequencing.

Sample preparation. CML CD34⁺ cells were seeded in 48-well plates at $1-2 \times 10^6$ cells ml⁻¹, before drug treatment (RITA 50 nM, CPI-203 1 μ M, Nil 5 μ M) for 24 h. After treatment, RNA was extracted using RNeasy Plus Mini Kit (Qiagen). **Library generation.** RNA-seq libraries were generated using TruSeq Stranded Total RNA (part no. 15031048 Rev. E October 2013) kits. Ribosomal depletion was performed on 1 μ g of RNA using Ribo-Zero Gold before a heat fragmentation step aimed at producing libraries with an insert size between 120–200 bp. Complementary DNA was synthesized from the enriched and fragmented RNA using SuperScript II Reverse Transcriptase (Invitrogen) and random primers. The cDNA was converted into double-stranded DNA in the presence of dUTP to prevent subsequent amplification of the second strand. After 3' adenylation and adaptor ligation, libraries were subjected to 15 cycles of PCR to produce RNA-seq libraries. Before sequencing, RNA-seq libraries were qualified and quantified via Caliper's LabChip GX (part no. 122000) instrument using the DNA High Sensitivity Reagent kit (product no. CLS760672). Quantification of libraries for clustering was performed using the KAPA Library Quantification Kits for Illumina sequencing platforms (kit code KK4824) in combination with Life Technologies QuantStudio 7 real-time PCR instrument. Libraries were finally pooled in equimolar ratios and sequenced on Illumina's NextSeq500 platform using 75 bp paired-end high-output runs.

Alignment and analysis. Sequencing reads were aligned to the genome (GRCh38/release 80 primary assembly as obtained via <ftp.ensembl.org>) using Subread (v.1.4.6-p3)⁵⁴. RNA-SeQC was used to confirm adequate mapping quality and gene-level counts were calculated using Subread's featureCounts algorithm⁵⁵. Count data for each arm were normalized independently by TMM⁵⁶ (as implemented in the Bioconductor package edgeR) and Voom⁵⁷ (as implemented in the Bioconductor package limma). Genes with <3 cpm in three samples were removed from further analysis. Differential expression was identified using limma⁴⁹ (using Benjamini-Hochberg⁴⁶ correction).

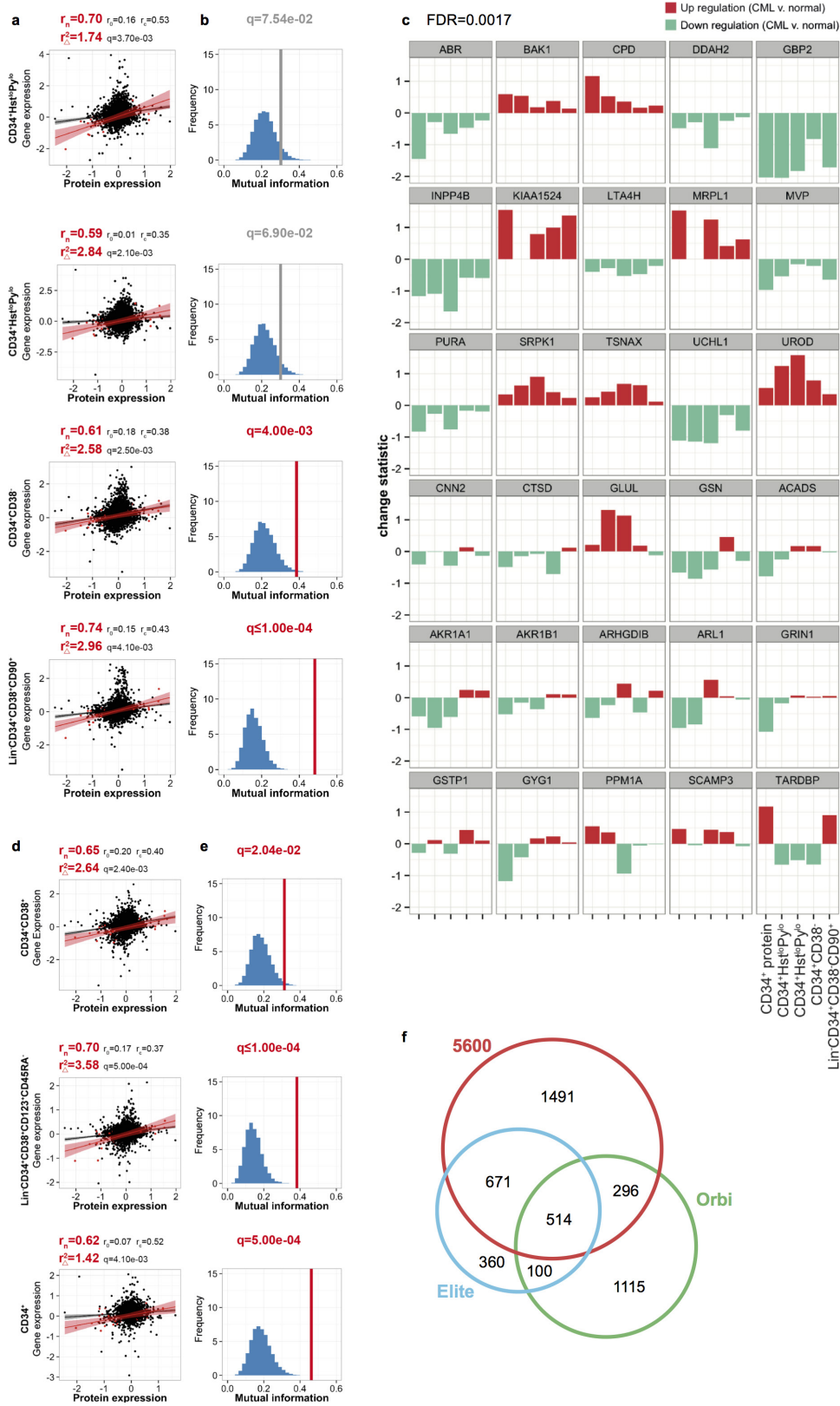
Definition of synergy. Genes were described as loosely synergistic if (1) RITA, CPI-203 and combined treatment all induced deregulation in the same direction, (2) the deregulation in response to the combined treatment was significant ($q < 0.05$), and (3) the deregulation induced by the combined treatment was greater than both RITA and CPI-203 in isolation. A more extreme definition had an additional criteria of the log ratio of the observed and additive effect being >0.6 (corresponding to a 150% increase).

Statistical analysis. No statistical methods were used to predetermine sample size. For *in vitro* experiments a minimum of 3 patient samples were chosen as a sample size to ensure adequate power. For all animal studies, each experiment was replicated twice in the laboratory with a minimum number of 5 mice per arm, unless indicated. NSG mice were excluded from analyses if they died of radiation poisoning (within 10 days of being irradiated, out of a 16-week procedure). For DTG mice, mice were excluded from analysis if leukaemic cells (CD45.2) failed to engraft host mice (CD45.1⁺) and therefore would not develop leukaemia. This was determined 1 week before drug treatment. Patient samples were only excluded if clinical data identified patient sample as entering blast crisis. Pre-established criteria also included that if a sample data point deviated 2 standard deviations from the mean, it was to be excluded, but this was not applied to the data in main or extended data. Group allocation to mice was done as mice were either purchased and subsequently numbered or weaned, to remove any investigator bias. For both NSG and DTG mice studies, all mice were randomly assigned treatment groups, ensuring all animals were of equal health and leukaemic status, within normal variability. Mice were assessed at predetermined time points: NSG mice were assessed at 8 and 16 weeks and DTG mice were assessed 4 weeks after drug treatment, so there was minimized bias as to assessing outcome. All mice were cared for equally in an unbiased fashion by animal technicians and investigator. No blinding was done.

Unless indicated, data are presented as the mean \pm s.e.m. and *P* values were calculated by two-tailed Student's *t*-test using GraphPad Prism software. Significant statistical differences ($*P < 0.05$, $**P < 0.01$, $***P < 0.001$) are indicated.

Code availability. All computer code was implemented in R and is available from the authors upon request.

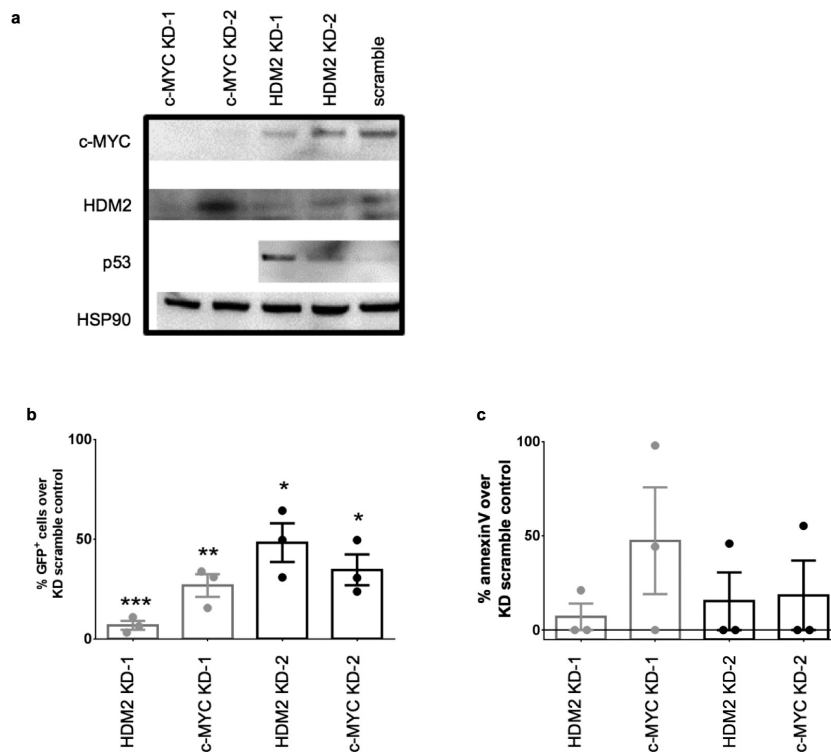
39. Pizzatti, L., Sá, L. A., de Souza, J. M., Bisch, P. M. & Abdelhay, E. Altered protein profile in chronic myeloid leukemia chronic phase identified by a comparative proteomic study. *Biochim. Biophys. Acta* **1764**, 929–942 (2006).
40. Cramer-Morales, K. *et al.* Personalized synthetic lethality induced by targeting RAD52 in leukemias identified by gene mutation and expression profile. *Blood* **122**, 1293–1304 (2013).
41. Diaz-Blanco, E. *et al.* Molecular signature of CD34⁺ hematopoietic stem and progenitor cells of patients with CML in chronic phase. *Leukemia* **21**, 494–504 (2007).
42. Affer, M. *et al.* Gene expression differences between enriched normal and chronic myelogenous leukemia quiescent stem/progenitor cells and correlations with biological abnormalities. *J. Oncol.* **2011**, 798592 (2011).
43. Graham, S. M., Vass, J. K., Holyoake, T. L. & Graham, G. J. Transcriptional analysis of quiescent and proliferating CD34⁺ human hemopoietic cells from normal and chronic myeloid leukemia sources. *Stem Cells* **25**, 3111–3120 (2007).
44. Huber, W., von Heydebreck, A., Sülthmann, H., Poustka, A. & Vingron, M. Variance stabilization applied to microarray data calibration and to the quantification of differential expression. *Bioinformatics* **18** (suppl. 1), S96–S104 (2002).
45. Smyth, G. K. in *Bioinformatics and Computational Biology Solutions using R and Bioconductor* (eds Gentleman, R., Dudoit, S., Irizarry, R. & Huber, W.) 397–420 (Springer, 2005).
46. Benjamini, Y. & Hochberg, Y. Controlling the false discovery rate: a practical and powerful approach to multiple testing. *J. R. Stat. Soc. B* **57**, 289–300 (1995).
47. Johnson, W. E., Li, C. & Rabinovic, A. Adjusting batch effects in microarray expression data using empirical Bayes methods. *Biostatistics* **8**, 118–127 (2007).
48. Hänzelmann, S., Castelo, R. & Guinney, J. GSVA: gene set variation analysis for microarray and RNA-seq data. *BMC Bioinformatics* **14**, 7 (2013).
49. Smyth, G. K. Linear models and empirical Bayes methods for assessing differential expression in microarray experiments. *Stat. Appl. Genet. Mol. Biol.* **3**, e3 (2004).
50. Clark, A. G. *et al.* Inferring nonneutral evolution from human-chimp-mouse orthologous gene trios. *Science* **302**, 1960–1963 (2003).
51. Xu, X. L. *et al.* Retinoblastoma has properties of a cone precursor tumor and depends upon cone-specific MDM2 signaling. *Cell* **137**, 1018–1031 (2009).
52. Wolfer, A. *et al.* MYC regulation of a “poor-prognosis” metastatic cancer cell state. *Proc. Natl Acad. Sci. USA* **107**, 3698–3703 (2010).
53. Sheth, A. *et al.* Inhibition of human mitochondrial peptide deformylase causes apoptosis in c-myc-overexpressing hematopoietic cancers. *Cell Death Dis.* **5**, e1152 (2014).
54. Liao, Y., Smyth, G. K. & Shi, W. The Subread aligner: fast, accurate and scalable read mapping by seed-and-vote. *Nucleic Acids Res.* **41**, e108 (2013).
55. Liao, Y., Smyth, G. K. & Shi, W. featureCounts: an efficient general purpose program for assigning sequence reads to genomic features. *Bioinformatics* **30**, 923–930 (2014).
56. Robinson, M. D. & Oshlack, A. A scaling normalization method for differential expression analysis of RNA-seq data. *Genome Biol.* **11**, R25 (2010).
57. Law, C. W., Chen, Y., Shi, W. & Smyth, G. K. voom: Precision weights unlock linear model analysis tools for RNA-seq read counts. *Genome Biol.* **15**, R29 (2014).



Extended Data Figure 1 | See next page for caption.

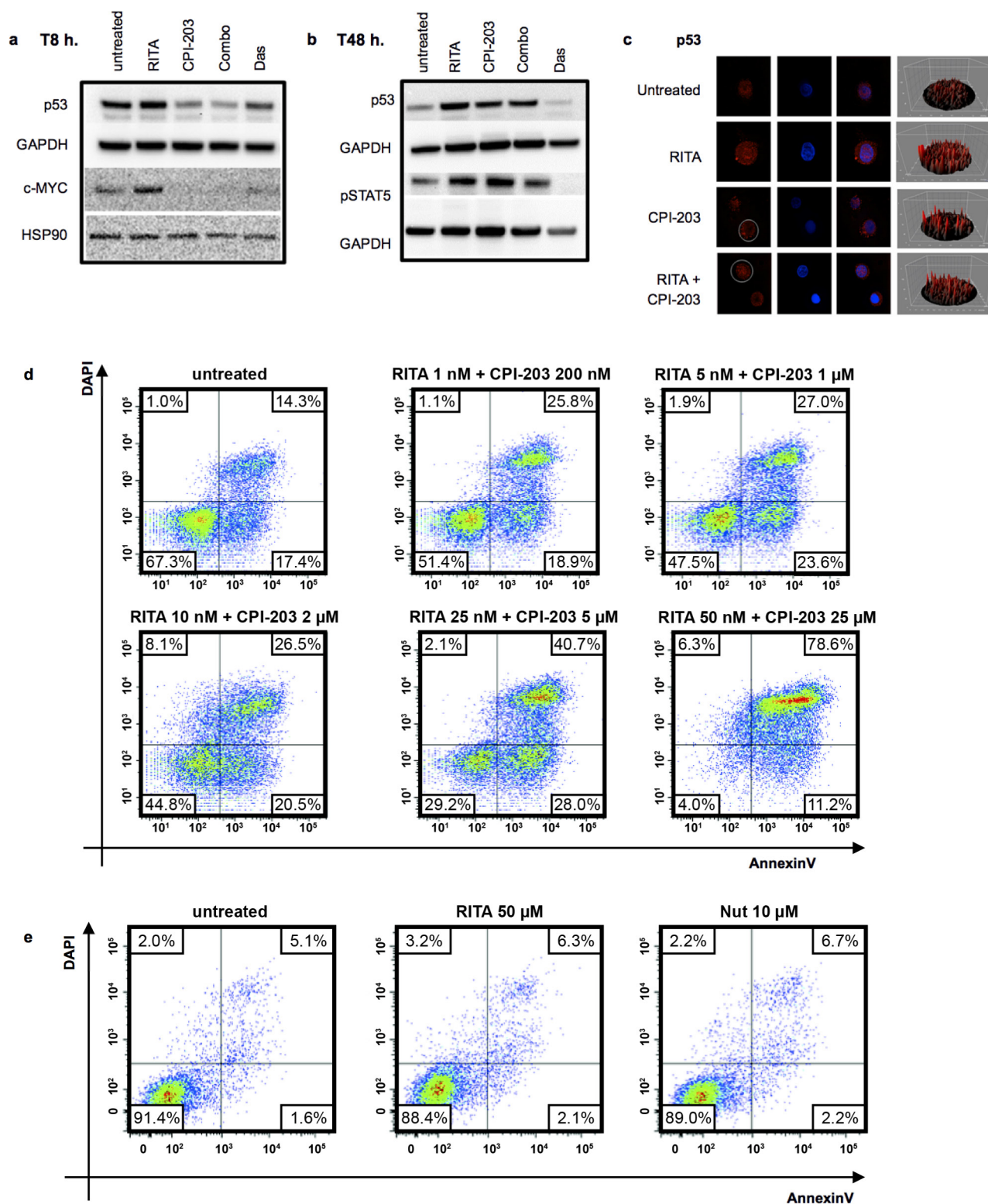
Extended Data Figure 1 | BCR-ABL drives a proteomic signature mediated by p53 and c-MYC. a, b, Equivalent to Fig. 1b, c with additional information regarding the correlations calculated from the complete list of 58 candidate proteins (r_c) in addition to the correlations for the candidate network (r_n) and the background (r_0). Also shown is the gain in r^2 obtained for the candidate network as compared to the r^2 obtained for the candidate list as a whole (r^2_{Δ}). FDR calculated from 10,000 re-samplings. **c,** Expression changes of the network components (shown as bar plots) in the context of quiescent and primitive CML cells; data shown in each panel (left to right) are (1) CD34⁺ protein log₂ ratios ($n = 3$ patient samples, $n = 2$ normal samples); (2) CD34⁺Hst^{lo}Py^{lo} transcript logFC (ArrayExpress accession E-MTAB-2508); (3) CD34⁺Hst^{lo}Py^{lo} transcript logFC (GEO accession GSE24739); (4) CD34⁺CD38⁻ logFC (ArrayExpress accession E-MTAB-2581); and (5) Lin⁻CD34⁺CD38⁻CD90⁺ logFC (GEO accession GSE47927).

Down-/upregulation is indicated by turquoise/red, respectively. Where multiple probesets were found for individual genes, the probeset corresponding to the maximal log ratio was selected. **d, e,** Correlation of the candidate network in progenitor (CD34⁺) CML cells: CD34⁺CD38⁺ progenitor (top); common myeloid progenitor Lin⁻CD34⁺CD38⁺CD123⁺CD45RA⁻ (middle); and CD34⁺ cells (bottom). As in **a, b**, correlations for the background (r_0), candidate list (58 proteins, r_c) and candidate network (Fig. 1a, r_n) are shown. Also shown is the gain in r^2 obtained for the candidate network as compared to the r^2 obtained for the candidate list as a whole (r^2_{Δ}). FDR calculated from 10,000 re-samplings; MI statistics corresponding to FDRs < 0.05 are coloured red, FDRs < 0.10 are coloured grey. **f,** A Venn diagram showing the overlap in protein identification of the three MS instruments: ABSciex Q-STAR Elite (Elite), Thermo LTQ Orbitrap Velos (Orbi) and ABSciex TripleTOF 5600 (5600).



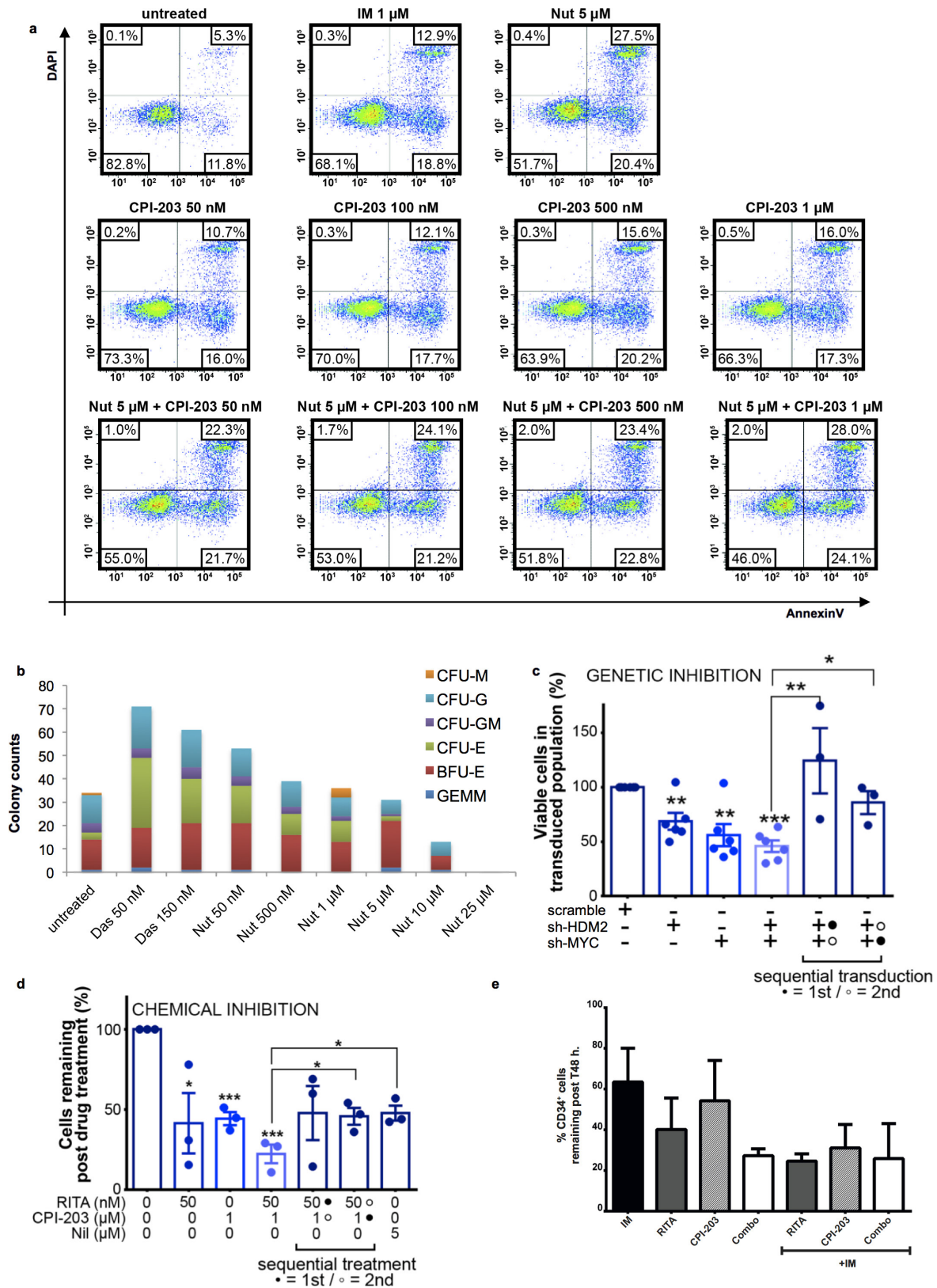
Extended Data Figure 2 | Validation of network candidates. **a**, HDM2 and c-MYC knockdown using shRNA constructs. Western blots of c-MYC, HDM2, p53 and HSP90 in HeLa cells transduced with lentiviral constructs specific for either c-MYC (2 constructs), HDM2 (2 constructs) or scrambled control (1 construct). KD, knockdown. **b**, **c**, CML CD34⁺ cells were transduced with either lentiviral (GFP) shRNA constructs to HDM2 (constructs 1, 2), c-MYC (constructs 1, 2) or scramble control

(1 construct). **b**, Transduced viable GFP⁺ cells (assessed as annexin-V⁻/DAPI⁻/GFP⁺ percentages multiplied by the absolute cell count) are presented as a percentage of CML CD34⁺ cells transduced with scramble control ($n=3$ patient samples). **c**, Early apoptosis levels (assessed as annexin-V⁺/DAPI⁻/GFP⁺) after transduction of CML CD34⁺ cells ($n=3$ patient samples) as described in **b**. Statistical significance was calculated by a two-tailed Student's *t*-test and error bars represent the s.e.m.



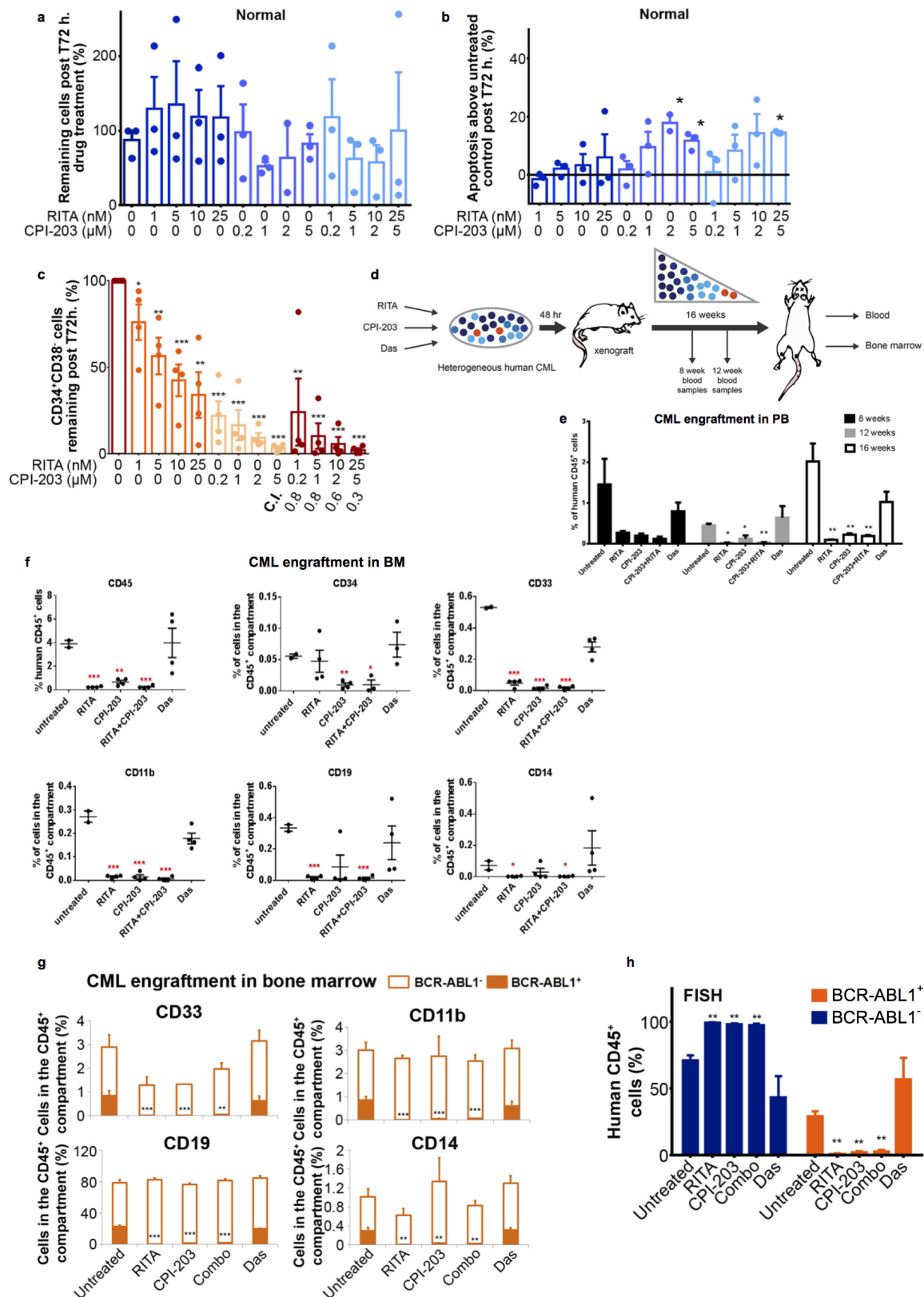
Extended Data Figure 3 | RITA and CPI-203 synergize to eliminate CML CD34⁺ cells. **a, b,** Western blots of CML CD34⁺ cells untreated or treated with 50 nM RITA; 1 μ M CPI-203; or the combination of 50 nM RITA and 1 μ M CPI-203 or 150 nM Das for 8 h (**a**) and 48 h (**b**). **c,** p53 (red, nucleus in blue) 24 h after treatment in CML CD34⁺ cells. **d,** RITA, CPI-203 and combination drug treatment eliminates CD34⁺ CML cells

through mechanisms probably dependent on apoptosis; after 72 h of drug treatment apoptosis levels were assessed (annexin V/DAPI) using flow cytometry techniques. **e,** RITA or Nut cannot induce death of K562 cells that lack p53. K562 cells were treated with either 50 μ M RITA or 10 μ M Nut and after 72 h of drug treatment, apoptosis levels were assessed (annexin V/DAPI) using flow cytometry techniques.



Extended Data Figure 4 | RITA and CPI-203 synergize to eliminate CML cells. **a**, CD34⁺ CML cells were treated with Nut and CPI-203 for 72 h with apoptosis levels assessed (annexin V/DAPI) using flow cytometry techniques. **b**, Treatment of CD34⁺ CML cells with Nut results in the elimination of early and late progenitor cells as assessed by the functional colony-forming capacity of drug-treated CML cells. **c**, Sequential drug treatments ($n = 3$ patient samples; drug one for 24 h,

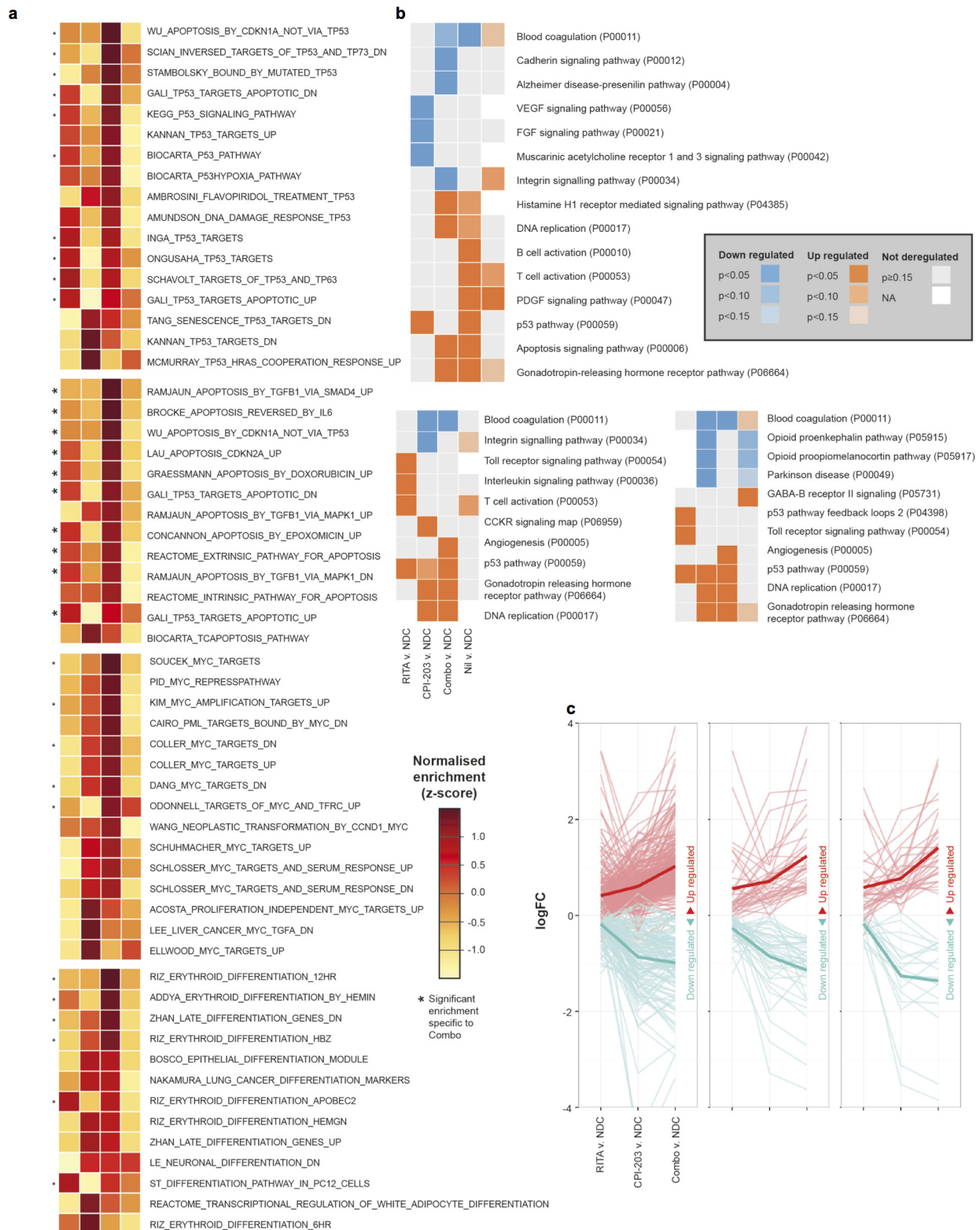
then both for 48 h). **d**, Sequential knockdown treatments ($n = 3$ patient samples; knockdown one for 24 h, then both for 48 h), mean \pm s.e.m. (P values: two-tailed Student's t -test; * $P < 0.05$, ** $P < 0.01$, *** $P < 0.001$). **e**, CML CD34⁺ primary samples were pre-treated or not with imatinib mesylate (1 μ M) for 8 h followed by RITA (50 nM), CPI-203 (1 μ M) or the combined treatment (RITA plus CPI-203) for 72 h (right three columns). Cell counts were obtained using trypan blue exclusion.



Extended Data Figure 5 | RITA and CPI-203 selectively eliminate LSCs.

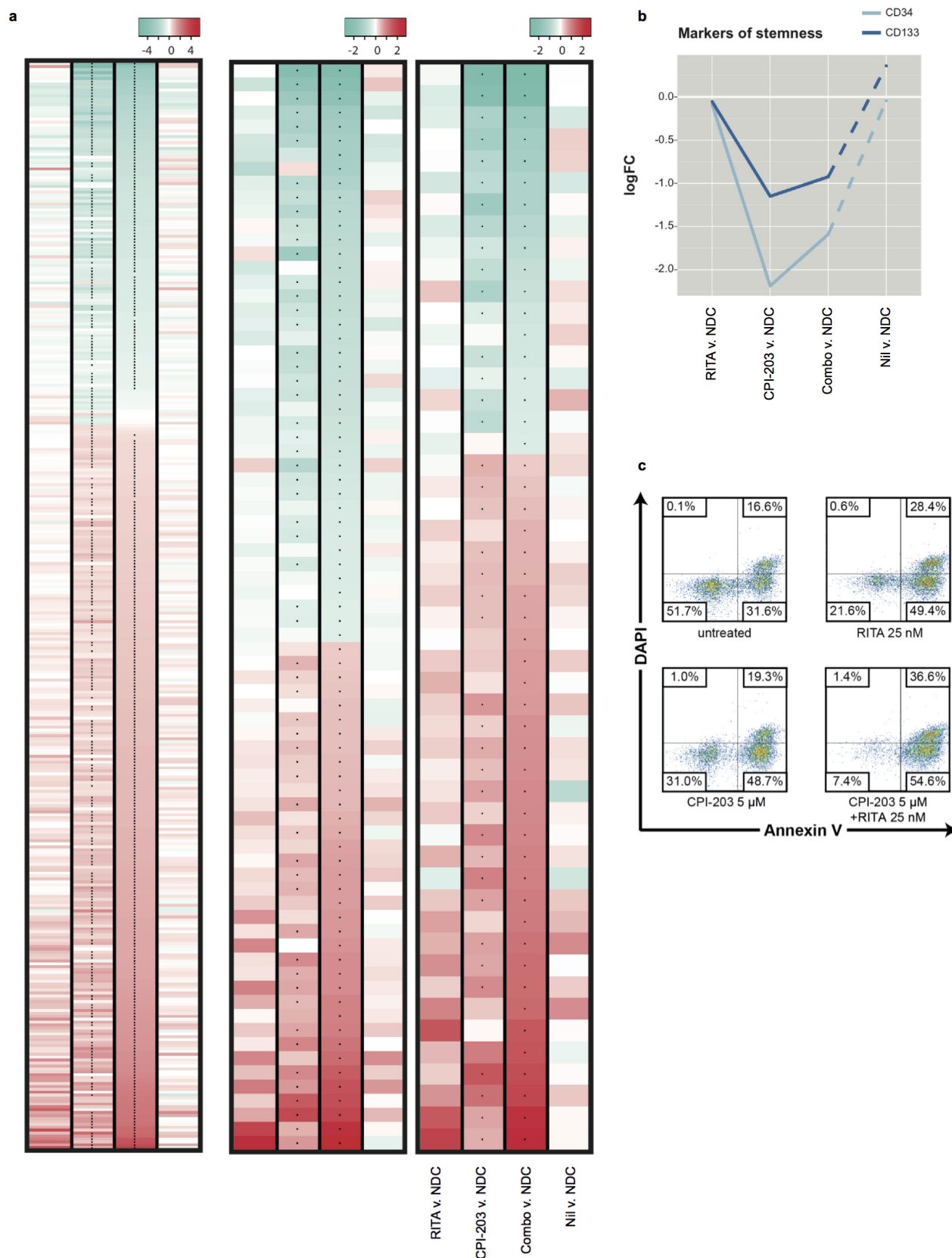
a, b, Viable cell counts ($n = 3$ patient samples) (**a**); apoptosis in normal CD34⁺ cells ($n = 3$ patient samples) in response to RITA and/or CPI-203 (**b**). **c**, Gated CML CD34⁺CD38⁻ cells 72 h after treatment ($n = 4$ patient samples). **d**, *Ex vivo* protocol for CML/cord blood CD34⁺ cells in NSG mice ($n = 5$ mice per arm). **e, f**, Targeting p53 and c-MYC in CML eliminates NSG repopulating leukaemic stem cells. CML CD34⁺ cells were treated with RITA (70 nM) and/or CPI-203 (1 μM) or Das (150 nM) for 48 h and recovered cells were injected intravenously into 8–12-week-old,

sublethally irradiated (2.5 Gy) NSG mice (2–4 mice per arm). **e**, Percentage of human CD45⁺ cell levels in peripheral blood (PB) at 8, 12 and 16 weeks. **f**, Percentages of human CD45⁺, CD34⁺, CD33⁺, CD11b⁺, CD19⁺ and CD14⁺ cells in the bone marrow at 16 weeks. **g**, CML bone marrow analyses of CD33, CD11b, CD19 and CD14 from a CML sample determined to engraft both BCR-ABL-positive and -negative cells. **h**, D-FISH analyses of bone marrow human engraftment studies shown in **g** performed twice (2 patient samples) with a minimum of $n = 6$ mice per arm; mean \pm s.e.m. (P values: two-tailed Student's t -test; * $P < 0.05$, ** $P < 0.01$, *** $P < 0.001$).



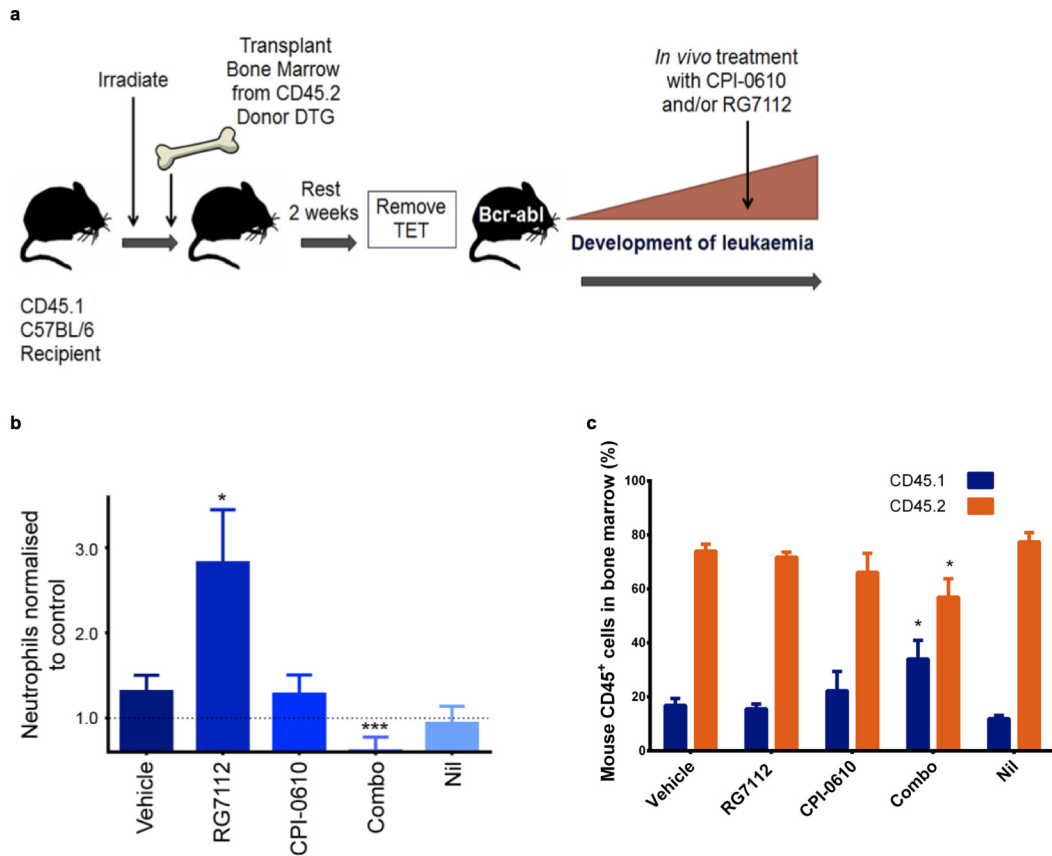
Extended Data Figure 6 | Mechanism of LSC elimination and clinical scope. **a**, Enrichment of p53 (top); apoptosis (second from top); c-MYC (second from bottom); and differentiation MSigDB signatures (bottom) in the four treatment arms ($n = 3$ CML patient samples per arm) (columns named as per **b**). Equivalent to Fig. 5b, but with named MSigDB signatures. **b**, Enrichment of PANTHER pathways in the four treatment arms. Pathway enrichment calculated from the top 1,500 genes, as ranked

by increasing P value (top); only those genes exhibiting an absolute FC of >0.5 in each arm (bottom left); only those genes exhibiting a $P < 0.05$ each arm (bottom right). **c**, Assessing molecular synergy of the combined RITA plus CPI-203 treatment, as compared to the individual RITA and CPI-203 arms of the RNA-seq experiments in the three *in silico* functional signatures: p53/apoptosis (left); c-MYC (middle); and differentiation (right). Mean expression is shown as a solid line.



Extended Data Figure 7 | Mechanism of LSC elimination and clinical scope continued. **a**, Gene expression patterns (logFC, $n = 3$ patient samples per arm) shown for the members of the three broad signatures identified *in silico*: p53/apoptosis (left); c-MYC (middle); and differentiation (right) ($*q < 0.05$); data are ordered by increasing logFC in response to combination treatment, from downregulation at the top to

upregulation at the bottom. Corresponding expression data are provided in Supplementary Tables 5–7. **b**, Differential expression of CD34 and CD133 (markers of stemness) in the four arms of the RNA-seq experiment. **c**, Apoptosis levels assessed (annexin V⁺/DAPI) using flow cytometry on a TKI-NR CD34⁺ sample after 72h treatment with RITA and CPI-203 as indicated.



Extended Data Figure 8 | RG7112 and CPI-0610 as a combination decrease BCR-ABL⁺ cells. **a, b,** DTG mice *in vivo* treatment (**a**): neutrophils normalized to control (dotted line) (**b**). **c,** Bone marrow cells stained for CD45.1/2. Drug treatment arms (minimum of $n = 7$ mice) mean \pm s.e.m. (P values: two-tailed Student's t -test; * $P < 0.05$, ** $P < 0.01$, *** $P < 0.001$).

TRPV1 structures in nanodiscs reveal mechanisms of ligand and lipid action

Yuan Gao^{1,2}, Erhu Cao^{1†}, David Julius¹ & Yifan Cheng^{2,3}

When integral membrane proteins are visualized in detergents or other artificial systems, an important layer of information is lost regarding lipid interactions and their effects on protein structure. This is especially relevant to proteins for which lipids have both structural and regulatory roles. Here we demonstrate the power of combining electron cryo-microscopy with lipid nanodisc technology to ascertain the structure of the rat TRPV1 ion channel in a native bilayer environment. Using this approach, we determined the locations of annular and regulatory lipids and showed that specific phospholipid interactions enhance binding of a spider toxin to TRPV1 through formation of a tripartite complex. Furthermore, phosphatidylinositol lipids occupy the binding site for capsaicin and other vanilloid ligands, suggesting a mechanism whereby chemical or thermal stimuli elicit channel activation by promoting the release of bioactive lipids from a critical allosteric regulatory site.

Transporters and ion channels reside in biological membranes, where lipids have important structural and regulatory roles^{1–3}. However, structural characterization of protein–lipid interactions is challenging in detergent-based systems, making implementation of more native, lipid-based environments an important goal. For crystallographic approaches, this has been achieved through the use of lipidic-cubic phase systems^{4,5} or formation of two-dimensional crystals in lipid bilayers⁶. For single-particle electron microscopy, one approach is to reconstitute proteins into spherical liposomes for random spherically constrained single-particle reconstruction⁷. Another is to use lipid nanodiscs, hockey-puck-like structures in which a lipid bilayer patch is encircled by an amphipathic scaffolding protein⁸. Both approaches mimic the native lipid environment and can enhance functionality and thermal stability^{9,10}. Moreover, nanodisc-embedded proteins are often monodisperse and especially suitable for single-particle electron cryo-microscopy (cryo-EM)^{11,12}. Nevertheless, membrane protein structures determined with these systems have achieved limited resolution to date, failing to reveal detailed protein–lipid interactions.

Cryo-EM can now be used to obtain structures of many biological macromolecules at near-atomic resolution^{13–15}. An important next goal is to enable cryo-EM to define interactions between small molecules and their protein targets at the atomic level. The heat- and capsaicin-activated ion channel, TRPV1, is an excellent model with which to address these challenges. This sensory receptor is modulated by membrane lipids and their metabolites, and activated or inhibited by various ligands, including vanilloid compounds and peptide toxins^{16,17}. Moreover, TRPV1 structures in multiple conformational states have recently been determined by cryo-EM under conditions in which purified channel protein was stabilized with an amphipathic polymer^{18,19}. These structures provide a standard against which other preparations can be assessed. Here we show that high-resolution structures can be obtained when TRPV1 is embedded in a nanodisc, and use this system to characterize channel–lipid interactions, revealing novel structural mechanisms underlying ligand binding and channel gating.

Structure of TRPV1 in lipid nanodiscs

We reconstituted purified TRPV1 protein into lipid nanodiscs generated with different membrane scaffold proteins (MSPs) (Extended Data Fig. 1). For structural analysis, we favoured preparations using MSP2N2, which forms nanodiscs of ~150 Å diameter and is sufficient to accommodate TRPV1 without imposing spatial constraint (Extended Data Fig. 1d). Indeed, cryo-EM images of frozen hydrated samples revealed monodispersed TRPV1–nanodisc particles. Two-dimensional class averages showed TRPV1 tetramers with distinct channel features floating within the nanodisc (top view) (Fig. 1a). Transmembrane helices and cytoplasmic domains were clearly visible within a disc-like density contributed by the lipid bilayer (side views). Importantly, the presence of the bilayer and MSP did not preclude accurate image alignment.

We determined three structures of TRPV1 in nanodiscs, including unliganded, agonist-bound, and antagonist-bound states at resolutions of 3.2, 2.9 and 3.4 Å, respectively (Fig. 1b and Extended Data Figs 2–4). These structures can be compared directly to those previously obtained in amphipol^{18,19}. Generally speaking, density maps determined with nanodiscs were of superior quality. This is especially evident when

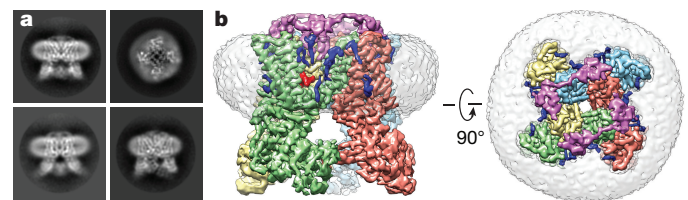


Figure 1 | TRPV1 structures determined in lipid nanodisc. a, Side and top views of reference-free two-dimensional class averages of TRPV1 in nanodiscs, showing transmembrane helices and lipid bilayer. The size of the class average windows is 233 Å. **b**, Side and top views of three-dimensional reconstruction of TRPV1–ligand–nanodisc complex. Individual channel subunits are colour-coded with two molecules of DkTx (purple) atop the channel and a molecule of RTX (red) in the vanilloid-binding pocket. Densities of the nanodisc (grey) and well-resolved lipids (blue) are also shown.

¹Department of Physiology, University of California, San Francisco, California 94143, USA. ²Keck Advanced Microscopy Laboratory and Department of Biochemistry and Biophysics, University of California, San Francisco, California 94143, USA. ³Howard Hughes Medical Institute, University of California, San Francisco, California 94143, USA. †Present address: Department of Biochemistry, University of Utah School of Medicine, Salt Lake City, Utah 84112-5650, USA.

examining side-chain densities within transmembrane regions or connecting loops that face lipids, such as S1 and S2 helices and the S2–S3 linker (Extended Data Fig. 5a–f). Interestingly, improvements were not limited to transmembrane regions, but also extended to cytoplasmic domains, enabling us to build a model including previously unresolved regions (Extended Data Fig. 6a, b). These improved density features may reflect enhanced stability of the channel in the nanodisc, but other technical advances also contribute (Extended Data Table 1a). The nanodisc- and amphipol-stabilized structures of a given conformational state are essentially identical, albeit with some specific differences that may relate to lipid and/or ligand binding (see later).

Two layers of continuous density corresponding to lipid head groups mark the bilayer boundaries and surround the channel (Fig. 1a, b and Extended Data Fig. 7a). Furthermore, well-resolved lipid-like densities associate with various regions of the channel, indicative of well-ordered lipids that form specific protein interactions (Fig. 1b and Extended Data Fig. 7b, c). These include annular lipids that fill crevices between subunits and reside within the outer leaflet surrounding pore-forming domains of the channel, reminiscent of voltage-gated potassium channels²⁰. We also observed lipids in hydrophobic clefts, as exemplified by a density within the lower segment of the S1–S4 domain, whose shape and local environment suggest that it represents a molecule of phosphatidylcholine (Extended Data Fig. 7c). Indeed, we observed a similar density in this location for TRPV1 in amphipol¹⁹, suggesting that an endogenous, tightly bound lipid helps stabilize a hydrophobic crevice within the S1–S4 domain, which remains stationary during channel gating¹⁸.

Lipid–channel–toxin tripartite complex

TRPV1 can be stably trapped in its fully open state when exposed to resiniferatoxin (RTX)—an ultra-potent vanilloid agonist^{18,21}—plus double-knot toxin (DkTx), a bivalent tarantula peptide that consists of two nearly identical inhibitor cysteine knot (ICK) motifs joined by a short (7-amino-acid) linker²². Two DkTx molecules bind to one TRPV1 tetramer such that each knot assumes a specific orientation with respect to the channel, suggesting that two DkTx molecules adopt an antiparallel configuration¹⁸. In our nanodisc structure, we initially applied C4 symmetry to achieve optimal resolution, yielding a 2.9 Å map of the nanodisc-stabilized, RTX/DkTx-activated channel, compared to 3.8 Å for the amphipol-stabilized complex (Fig. 2a and Extended Data Fig. 8). To gain further information about non-equivalent regions of the toxin, we applied C2 symmetry independently, which was insufficient to reveal specific features associated with each knot and their relationship to one another, indicating that some particle images were misaligned by 90° around the symmetry axis. Focused classification on the toxin and adjacent regions enabled us to partially separate the two possible orientations to obtain an improved C2 averaged map, as evidenced by more pronounced features within the antiparallel linker connecting the ICK knots (Fig. 2b and Extended Data Fig. 8).

With improved maps, we rebuilt and refined the atomic model of the fully open channel with associated ligands. For DkTx, three canonical disulfide bonds are clearly resolved, as are most side chains in regions that interact with TRPV1 (Fig. 2a and Extended Data Fig. 8b). Here we find that residues involved in the channel interaction are highly conserved between ICK knots, consistent with the fact that the side-chain densities of these residues were well resolved even when C4 symmetry was applied. Interestingly, the density of the linker domain is also well resolved (Fig. 2c), revealing a taut and constrained conformation that probably contributes to the high-avidity interaction with the channel²².

The nanodisc system enabled us to determine where interactions occur with respect to the lipid bilayer. Two hydrophobic fingers from each ICK knot insert into the bilayer (Fig. 2a) and several phospholipid densities at these sites are well resolved, probably reflecting their stabilization through specific toxin interactions (Fig. 2c, d and Extended Data Fig. 7b). For example, a tryptophan side chain in finger 1 (Trp11 of knot 1 and Trp53 of knot 2) interacts with the aliphatic tail of a phospholipid whose head group forms a polar interaction with Arg534 in TRPV1,

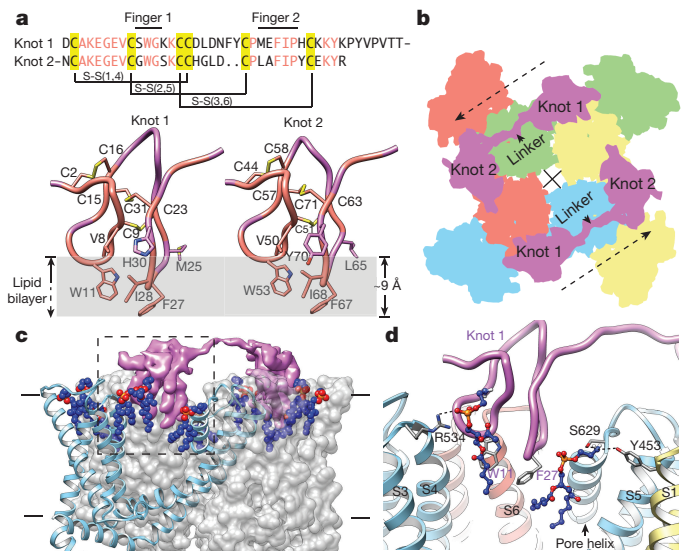


Figure 2 | Structural details of tripartite toxin–channel–lipid complex. **a**, Sequence of DkTx (top) showing location of intramolecular disulfide bonds and finger-like loops formed primarily by residues conserved between toxin knots (orange). Hydrophobic residues enable fingers to penetrate the lipid bilayer by ~9 Å (bottom). **b**, Schematic top-down view showing antiparallel arrangement of two DkTx molecules (purple) binding at subunit interfaces of a TRPV1 homo-tetramer (subunits are colour-coded). **c**, Cutaway view depicting one DkTx molecule interacting with two adjacent TRPV1 subunits (grey) and associated lipids (blue spheres; red and orange spheres depict phosphate head groups). Superimposed ribbon diagram (light blue) denotes location of transmembrane α -helices for one channel subunit. **d**, Detailed view of boxed region in **c** showing interactions between lipids and amino acid side chains from channel and toxin (dotted line, hydrogen bond). Helices from three neighbouring channel subunits are colour-coded as in **b**.

located in the extracellular loop connecting the S3 and S4 helices. This sort of tripartite complex between toxin, lipid, and channel is also seen proximal to finger 2, where a phenylalanine side chain (Phe27 of knot 1 and Phe67 of knot 2) is stabilized through hydrophobic interaction with an aliphatic lipid tail. Furthermore, the lipid head group is coordinated by the side chain of Ser629 at the top of the channel's pore helix domain, as well as by interaction with Tyr453 from S1 of the adjacent channel subunit (Fig. 2d). Thus, together with the newly refined apo model, we see that gating-associated side-chain movements within outer pore loops and pore helices are more clearly visualized compared with our previous structures in amphipols (Extended Data Fig. 5b). These new observations demonstrate how potential side-chain clashes between DkTx and the apo channel are relieved through lateral shifts in the outer pore loops and pore helices, primarily through reorientation of aromatic side chains (Fig. 3a). Moreover, they suggest a structural mechanism for how toxin binding stabilizes the open state.

The nanodisc preparation also reveals local distortions in the lipid environment associated with toxin binding. For example, insertion of DkTx into the bilayer results in lateral and upward displacement of a phospholipid adjacent to finger 1, as well as lateral and downward displacement of another phospholipid proximal to finger 2 (Fig. 3b). The resulting energetic penalty may be compensated by toxin–channel interactions, as well as by new interactions formed between the channel and displaced lipids (Figs 2d and 3b). Such a tripartite arrangement probably determines the overall affinity and kinetics of toxin binding.

A resident lipid in the vanilloid pocket

A particularly striking density within the vanilloid-binding pocket of the apo channel can be confidently interpreted as a phosphatidylinositol lipid whose branched acyl chains extend upwards between S4 of one subunit and S5 and S6 of an adjacent subunit, within a hydrophobic

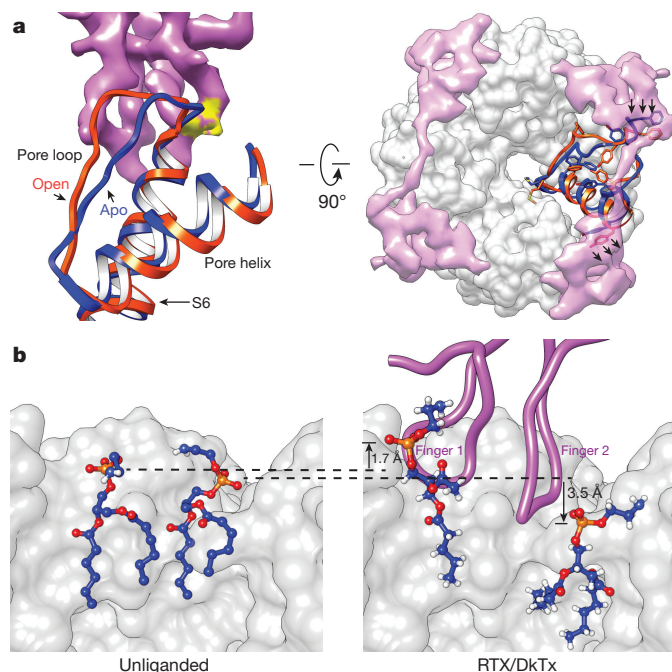


Figure 3 | Movement of protein and lipids associated with toxin binding. **a**, Movement of pore loop, pore helix, and part of S6 domain from closed (blue) to open (orange) states upon DkTx (purple) binding. Without such movement, one finger of DkTx would clash (yellow region) with the unliganded channel at the top of S6. Top-down view (right) shows two DkTx molecules atop TRPV1 (grey density). Toxin binding is associated with lateral shifts of the pore helix and loop (arrows), as well as large rearrangements of aromatic side chains within these regions. **b**, Two annular lipids (shown in blue, with phosphate in orange and oxygen in red) at the channel–toxin interface undergo both lateral and vertical movements upon DkTx binding. Dashed lines mark original position of phosphate groups in the absence of toxin (left); arrows indicate displacement of lipids in the presence of toxin (right).

cleft facing the lipid bilayer. The inositol ring is bounded on each side by S3 and the elbow of the S4–S5 linker, with the TRP domain below (Fig. 4a). Polar interactions, such as that between Arg557 at the bottom of S4 and the hydroxyl group of the phosphate on position 1, or between Glu570 in the S4–S5 linker and a hydroxyl group on position 6 of the inositol ring, further enhance stability (Fig. 4a and Extended Data Fig. 9a). Detailed analysis of the local protein environment suggests that additional phosphate groups at positions 3, 4 and/or 5 of the inositol ring could form electrostatic interactions with Arg409 in a cytoplasmic N-terminal segment preceding S1 or Lys571 and Arg575 within the S4–S5 linker (Fig. 4a and Extended Data Fig. 9a, b). If so, then this pocket could favour a range of phosphatidylinositide species.

A similar, albeit less well-resolved density was observed at this locale in our amphipol-stabilized structure¹⁹, suggesting that a tightly associated lipid is retained during channel purification. This, or other associated lipids, may derive from the soybean lipid extract that was added to improve protein stability, but it is also possible that they are of cellular origin.

Mechanism of vanilloid action

We next examined the structure of the vanilloid pocket when occupied by various ligands (Extended Data Fig. 9c, d). With nanodiscs, we could discern ligand structures in much greater detail compared to amphipol-stabilized structures. For example, RTX could be precisely fit by its atomic structure (Fig. 4b), and in a manner consistent with mutagenesis and modelling studies^{23–28}. For the capsaicin-like homovanillyl ester moiety, key interactions include a hydrogen bond between Thr550 and the carbonyl oxygen proximal to the vanilloid moiety, as well as between Ser512 and Arg557 and the vanilloid moiety at the hydroxyl

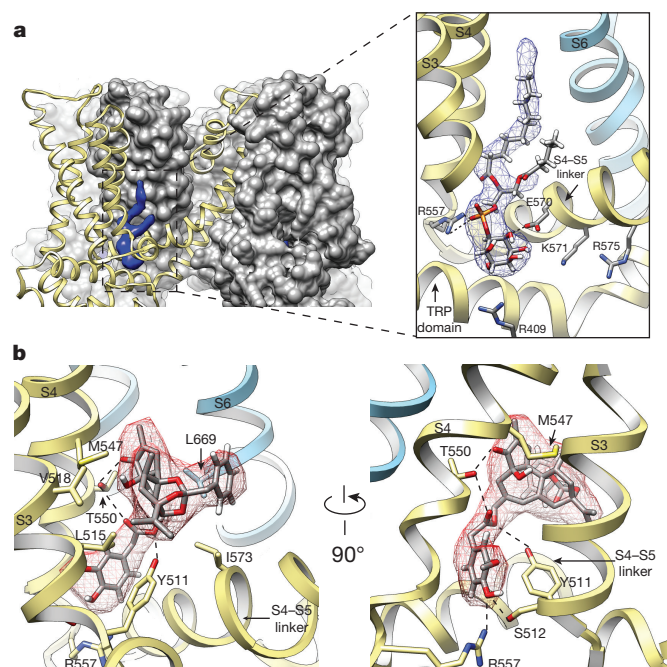


Figure 4 | Shared binding pocket for phosphatidylinositol lipids and vanilloid ligands. **a**, Surface representation of TRPV1 (grey) in cutaway view revealing location of bound co-factor (blue). Superimposed ribbon diagram (yellow) denotes location of transmembrane α -helices for one channel subunit. Detailed view of boxed region shows how co-factor density (blue mesh) accommodates a molecule of phosphatidylinositol. Positive and negative side chains from S4 and the S4–S5 linker, respectively, can form ionic interactions with negatively charged phosphate or hydroxyl moieties on the inositol ring. Helices from a neighbouring subunit (light blue) are also shown. **b**, Density for RTX (red mesh) is well fit by its atomic structure. Residues essential for RTX sensitivity (Y511, M547, T550) lie in close proximity to the ligand and can engage in electrostatic or hydrophobic interactions. Densities for phosphatidylinositol and RTX define overlapping, but non-identical sites (see also Extended Data Fig. 9).

group. Tyr511, which assumes distinct rotomers in apo versus liganded TRPV1 structures¹⁸, engages in hydrogen bonding with the ester oxygen of RTX. The five-membered diterpene ring component of RTX is stabilized by hydrophobic interactions with several amino acids, including Leu515, Val518, Met547 and Ile573, as well as Leu669 from a neighbouring subunit. These residues form a hydrophobic pocket that accommodates the heterocyclic region of the drug, probably accounting for high-affinity binding of this potent agonist.

Comparison of apo versus RTX-bound states suggests that vanilloid agonists function by displacing the resident phosphatidylinositol lipid. Indeed, RTX docks within the same pocket otherwise occupied by one acyl chain of the lipid. Absence of the other acyl chain allows for reorientation of Tyr511 to further stabilize RTX binding (Extended Data Fig. 9c, d). At the same time, RTX binding coordinates interaction between Arg557 and Glu570 to re-occupy the space vacated by the inositol head group, consequently pulling the S4–S5 linker away from the central axis to facilitate opening of the lower gate (Fig. 5 and Extended Data Fig. 9e). This mechanism is further supported by analysis of a capsazepine-bound structure (determined in either amphipol or nanodisc), in which this competitive vanilloid antagonist²⁹ occupies the same hydrophobic pocket as RTX, but apparently without facilitating the key interaction between Arg557 and Glu570 (Fig. 5 and Extended Data Fig. 9f). Indeed, mutations at these sites abrogate capsaicin-evoked responses, whereas charge-swapping mutations (R557E and E570R) partially restore channel function^{28,30}, consistent with our model. Parenthetically, we did not observe appreciable movement within the

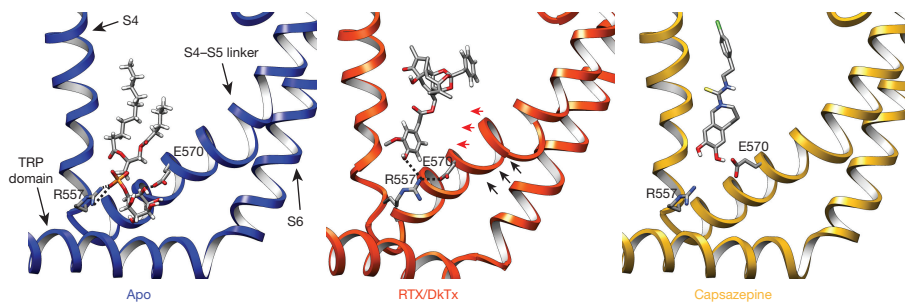


Figure 5 | Structural rearrangements associated with vanilloid binding. **a**, Ribbon diagrams depicting relative locations of S4, S4–S5 linker, S6 and TRP domain helices in the presence of phosphatidylinositol (blue, left), RTX (orange, middle), or capsaizepine (gold, right). The vanillyl ring of

S1–S4 region (Extended Data Fig. 9e), indicating that the static nature of this voltage-sensor-like domain, as previously described¹⁸, is not merely an artefact of amphipol packing.

Concluding remarks

Membrane proteins have been reconstituted into lipid nanodiscs and studied by single-particle cryo-EM^{11,12}, but our results now show that this system can be taken to atomic resolution, enabling detailed structural analysis of lipid–protein interactions in a more native or stable environment. A main concern about using nanodiscs for cryo-EM was that the bilayer mass would weaken the power of image alignment and limit the achievable resolution of imbedded proteins. Our results now show that this is not a problem. Indeed, as in the case of amphipol-stabilized TRPV1, the transmembrane core reached the highest resolution, indicating that image alignment was not adversely affected by the nanodisc. In addition to enabling visualization of specific, tightly bound lipids, the nanodisc provides a defined contour for the bilayer in relation to protein structure while revealing local deformations such as those associated with toxin binding.

Biophysical and biochemical studies suggest that amphipathic ICK toxins, such as hanatoxin and SGTx1, first partition into the lipid bilayer, then engage their channel target through moderate-affinity protein–protein interactions³¹. Furthermore, binding affinity may be enhanced by formation of a toxin–lipid–channel trimolecular complex^{32,33}. Our DkTx-bound TRPV1 structure supports this concept by showing that hydrophobic fingers of the toxin insert almost half-way (~9 Å) through the outer leaflet of the bilayer, interaction surfaces between DkTx and TRPV1 are not extensive, and membrane lipids form bridging interactions between toxin and channel (Fig. 6a). Indeed, we achieved considerably better resolution for the RTX/DkTx-bound channel, probably reflecting enhanced stability of such a tripartite complex. Overall, our findings are consistent with recent modelling studies based on an NMR structure of DkTx³⁴. Finally, DkTx is uniquely bivalent, and our structure suggests that the taut linker region connecting the two ICK knots has evolved to perfectly match the distance between subunit-binding sites, which, together with the specific antiparallel orientation of toxin binding, probably contributes to the remarkable avidity and specificity of the DkTx–TRPV1 interaction.

Many TRP channels function as ‘receptor-operated’ channels that are modulated by phospholipase-C-mediated phosphatidylinositol-4,5-bisphosphate (PtdIns(4,5)P₂) hydrolysis^{35,36}. However, structural mechanisms governing phosphatidylinositol-mediated regulation remain poorly understood. For TRPV1, it is not clear whether PtdIns(4,5)P₂ or other phosphatidylinositides bind directly to the channel, or function as obligatory co-factors, allosteric inhibitors, or both^{2,37}. Moreover, channel domains that specify phosphatidylinositide sensitivity have not been unambiguously identified. We now show that phosphatidylinositides function as endogenous, tightly bound co-factors that stabilize TRPV1 in its resting state by serving as competitive vanilloid antagonists and negative allosteric modulators. At the same time, phosphatidylinositides may function as positive, obligatory co-factors whose binding to

RTX uniquely stabilizes the interaction between Arg557 and Glu570 to facilitate movement of the S4–S5 linker away from the central axis of the channel (indicated by red arrows), thereby facilitating opening of the lower gate through coupled movements (indicated by black arrows).

TRPV1 in the closed state primes the channel for subsequent activation by vanilloids or other stimuli (Fig. 6b). Thus, our structures suggest a dual role for phosphatidylinositides through interactions at this single site. Moreover, structure–function studies suggest that regions within the TRPV1 C terminus interact with PtdIns(4,5)P₂ (refs 38–41) and thus additional mechanisms may contribute to phosphatidylinositide regulation of TRPV1 or other TRP subtypes. Our findings, together with those describing PtdIns(4,5)P₂ interactions with inwardly rectifying potassium channels⁴², demonstrate that phosphatidylinositides can interact with membrane proteins in diverse ways. It is tempting to speculate that temperature-dependent displacement of endogenous phosphatidylinositides contributes to heat-evoked activation of TRPV1 (Fig. 6c).

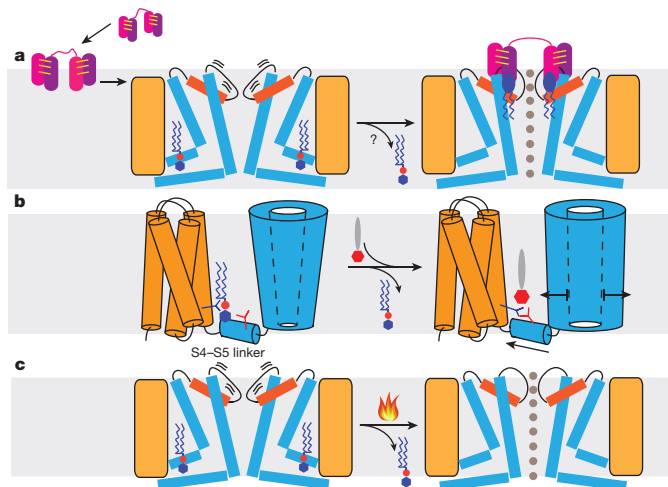


Figure 6 | Mechanistic models for TRPV1 activation. **a**, Proposed mechanism for DkTx action. Two hydrophobic fingers (purple and pink) of each ICK knot (joined by three intramolecular disulfide bonds, yellow lines) enable the toxin to partition into the lipid bilayer (grey shade) and subsequently target TRPV1. In the closed state, the upper pore region of the channel (orange, pore helix; thick line, pore loop) undergoes brief spontaneous excursions to an open state, enabling DkTx to dock. Several annular lipids (blue ellipse with zigzag tails) bind at the channel–toxin interface to further stabilize the open state through formation of a tripartite complex. Resident phosphatidylinositides (blue hexagon attached to red sphere with zigzag tails) in the vanilloid pocket may leave upon toxin binding to facilitate allosteric opening of the lower gate. **b**, Proposed mechanism for vanilloid agonist action. Phosphatidylinositide co-factor binds in vanilloid pocket to stabilize the channel in its closed state. Vanilloid agonist (red hexagon attached to grey ellipse) displaces phosphatidylinositide to facilitate formation of a salt bridge between Arg557 (dark blue branch) and Glu570 (red branch), consequently pulling the S4–S5 linker away from the channel's central axis to open the lower gate. **c**, Heat may open the channel through a similar mechanism involving thermal displacement of resident phosphatidylinositides.

Online Content Methods, along with any additional Extended Data display items and Source Data, are available in the online version of the paper; references unique to these sections appear only in the online paper.

Received 9 December 2015; accepted 31 March 2016.

Published online 18 May 2016.

- Hilgemann, D. W. Getting ready for the decade of the lipids. *Annu. Rev. Physiol.* **65**, 697–700 (2003).
- Hille, B., Dickson, E. J., Kruse, M., Vivas, O. & Suh, B. C. Phosphoinositides regulate ion channels. *Biochim. Biophys. Acta* **1851**, 844–856 (2015).
- Lee, A. G. Biological membranes: the importance of molecular detail. *Trends Biochem. Sci.* **36**, 493–500 (2011).
- Caffrey, M. A lipid's eye view of membrane protein crystallization in mesophases. *Curr. Opin. Struct. Biol.* **10**, 486–497 (2000).
- Landau, E. M. & Rosenbusch, J. P. Lipidic cubic phases: a novel concept for the crystallization of membrane proteins. *Proc. Natl Acad. Sci. USA* **93**, 14532–14535 (1996).
- Gonen, T. et al. Lipid-protein interactions in double-layered two-dimensional AQP0 crystals. *Nature* **438**, 633–638 (2005).
- Wang, L. & Sigworth, F. J. Structure of the BK potassium channel in a lipid membrane from electron cryomicroscopy. *Nature* **461**, 292–295 (2009).
- Bayburt, T. H., Grinkova, Y. V. & Sligar, S. G. Self-assembly of discoidal phospholipid bilayer nanoparticles with membrane scaffold proteins. *Nano Lett.* **2**, 853–856 (2002).
- Banerjee, S., Huber, T. & Sakmar, T. P. Rapid incorporation of functional rhodopsin into nanoscale apolipoprotein bound bilayer (NABB) particles. *J. Mol. Biol.* **377**, 1067–1081 (2008).
- Ritchie, T. K. et al. Reconstitution of membrane proteins in phospholipid bilayer nanodiscs. *Methods Enzymol.* **464**, 211–231 (2009).
- Eftremov, R. G., Leitner, A., Aebersold, R. & Raunser, S. Architecture and conformational switch mechanism of the ryanodine receptor. *Nature* **517**, 39–43 (2015).
- Frauenfeld, J. et al. Cryo-EM structure of the ribosome–SecYE complex in the membrane environment. *Nature Struct. Mol. Biol.* **18**, 614–621 (2011).
- Bai, X. C., McMullan, G. & Scheres, S. H. How cryo-EM is revolutionizing structural biology. *Trends Biochem. Sci.* **40**, 49–57 (2015).
- Cheng, Y. Single-particle cryo-EM at crystallographic resolution. *Cell* **161**, 450–457 (2015).
- Kühlbrandt, W. Cryo-EM enters a new era. *eLife* **3**, e03678 (2014).
- Bevan, S., Quallo, T. & Andersson, D. A. Trpv1. *Handb. Exp. Pharmacol.* **222**, 207–245 (2014).
- Julius, D. TRP channels and pain. *Annu. Rev. Cell Dev. Biol.* **29**, 355–384 (2013).
- Cao, E., Liao, M., Cheng, Y. & Julius, D. TRPV1 structures in distinct conformations reveal activation mechanisms. *Nature* **504**, 113–118 (2013).
- Liao, M., Cao, E., Julius, D. & Cheng, Y. Structure of the TRPV1 ion channel determined by electron cryo-microscopy. *Nature* **504**, 107–112 (2013).
- Long, S. B., Tao, X., Campbell, E. B. & MacKinnon, R. Atomic structure of a voltage-dependent K⁺ channel in a lipid membrane-like environment. *Nature* **450**, 376–382 (2007).
- Szallasi, A. & Blumberg, P. M. Resiniferatoxin, a phorbol-related diterpene, acts as an ultrapotent analog of capsaicin, the irritant constituent in red pepper. *Neuroscience* **30**, 515–520 (1989).
- Bohlen, C. J. et al. A bivalent tarantula toxin activates the capsaicin receptor, TRPV1, by targeting the outer pore domain. *Cell* **141**, 834–845 (2010).
- Chou, M. Z., Mtui, T., Gao, Y. D., Kohler, M. & Middleton, R. E. Resiniferatoxin binds to the capsaicin receptor (TRPV1) near the extracellular side of the S4 transmembrane domain. *Biochemistry* **43**, 2501–2511 (2004).
- Gavva, N. R. et al. Molecular determinants of vanilloid sensitivity in TRPV1. *J. Biol. Chem.* **279**, 20283–20295 (2004).
- Hanson, S. M., Newstead, S., Swartz, K. J. & Sansom, M. S. P. Capsaicin interaction with TRPV1 channels in a lipid bilayer: molecular dynamics simulation. *Biophys. J.* **108**, 1425–1434 (2015).
- Jordt, S. E. & Julius, D. Molecular basis for species-specific sensitivity to “hot” chili peppers. *Cell* **108**, 421–430 (2002).
- Phillips, E., Reeve, A., Bevan, S. & McIntyre, P. Identification of species-specific determinants of the action of the antagonist capsazepine and the agonist PPAHV on TRPV1. *J. Biol. Chem.* **279**, 17165–17172 (2004).
- Yang, F. et al. Structural mechanism underlying capsaicin binding and activation of the TRPV1 ion channel. *Nat. Chem. Biol.* **11**, 518–524 (2015).
- Bevan, S. et al. Capsazepine: a competitive antagonist of the sensory neurone excitant capsaicin. *Br. J. Pharmacol.* **107**, 544–552 (1992).
- Boukalova, S., Marsakova, L., Teisinger, J. & Vlachova, V. Conserved residues within the putative S4-S5 region serve distinct functions among thermosensitive vanilloid transient receptor potential (TRPV) channels. *J. Biol. Chem.* **285**, 41455–41462 (2010).
- Lee, S. Y. & MacKinnon, R. A membrane-access mechanism of ion channel inhibition by voltage sensor toxins from spider venom. *Nature* **430**, 232–235 (2004).
- Milescu, M. et al. Interactions between lipids and voltage sensor paddles detected with tarantula toxins. *Nature Struct. Mol. Biol.* **16**, 1080–1085 (2009).
- Milescu, M. et al. Tarantula toxins interact with voltage sensors within lipid membranes. *J. Gen. Physiol.* **130**, 497–511 (2007).
- Bae, C. et al. Structural insights into the mechanism of activation of the TRPV1 channel by a membrane-bound tarantula toxin. *eLife* **5**, e11273 (2016).
- Hardie, R. C. TRP channels and lipids: from *Drosophila* to mammalian physiology. *J. Physiol.* **578**, 9–24 (2007).
- Qin, F. Regulation of TRP ion channels by phosphatidylinositol-4,5-bisphosphate. *Handb. Exp. Pharmacol.* **179**, 509–525 (2007).
- Rohacs, T. Phosphoinositide regulation of TRPV1 revisited. *Pflügers Arch.* **467**, 1851–1869 (2015).
- Cao, E., Cordero-Morales, J. F., Liu, B., Qin, F. & Julius, D. TRPV1 channels are intrinsically heat sensitive and negatively regulated by phosphoinositide lipids. *Neuron* **77**, 667–679 (2013).
- Prescott, E. D. & Julius, D. A modular PIP2 binding site as a determinant of capsaicin receptor sensitivity. *Science* **300**, 1284–1288 (2003).
- Ufret-Vincenty, C. A. et al. Mechanism for phosphoinositide selectivity and activation of TRPV1 ion channels. *J. Gen. Physiol.* **145**, 431–442 (2015).
- Ufret-Vincenty, C. A., Klein, R. M., Hua, L., Angueyra, J. & Gordon, S. E. Localization of the PIP2 sensor of TRPV1 ion channels. *J. Biol. Chem.* **286**, 9688–9698 (2011).
- Hansen, S. B., Tao, X. & MacKinnon, R. Structural basis of PIP2 activation of the classical inward rectifier K⁺ channel Kir2.2. *Nature* **477**, 495–498 (2011).

Acknowledgements We thank our laboratory colleagues, past and present, for many helpful discussions and manuscript critiques, C. Paulsen and E. Green for helping with initial screening for nanodisc reconstitution, and E. Palovcak for providing scripts for focused classification. This work was supported by grants from the National Institutes of Health (R01NS047723, R37NS065071 and R01NS055299 to D.J., S10OD020054, R01GM098672, P01GM111126 and P50GM082250 to Y.C.). Y.C. is an Investigator with the Howard Hughes Medical Institute.

Author Contributions Y.G. carried out protein purification, nanodisc reconstitution, and detailed cryo-EM experiments, including data acquisition, image processing, atomic model building and refinement of TRPV1–nanodisc complexes. E.C. carried out cryo-EM experiments of the TRPV1–capsazepine complex solubilized in amphipol. All authors contributed to experimental design, data analysis, and manuscript preparation.

Author Information The three-dimensional cryo-EM density maps of the TRPV1–nanodisc complexes without low-pass filter and amplitude modification have been deposited in the Electron Microscopy Data Bank under accession numbers EMD-8118 (TRPV1–nanodisc), EMD-8117 (TRPV1–RTX/DkTx–nanodisc), EMD-8119 (TRPV1–capsazepine–nanodisc) and EMD-8120 (TRPV1–capsazepine in amphipol). Particle image stacks after motion correction related to TRPV1–nanodisc and TRPV1–RTX/DkTx–nanodisc have been deposited in the Electron Microscopy Pilot Image Archive (<http://www.ebi.ac.uk/pdbe/emdb/empir/>) under accession number EMPIAR-10059. Atomic coordinates for the atomic model of TRPV1 in nanodisc, TRPV1–RTX/DkTx in nanodisc and TRPV1–capsazepine in nanodisc have been deposited in the Protein Data Bank under accession numbers 5IRZ, 5IRX and 5ISO. Reprints and permissions information is available at www.nature.com/reprints. The authors declare no competing financial interests. Readers are welcome to comment on the online version of the paper. Correspondence and requests for materials should be addressed to D.J. (david.julius@ucsf.edu) or Y.C. (ycheng@ucsf.edu).

METHODS

Protein expression, purification and nanodisc reconstitution. A minimal functional rat TRPV1 construct was expressed and purified as previously described¹⁹. Membrane scaffold proteins MSP2N2 and MSP1E3 were expressed and purified from *Escherichia coli*, and detergent-solubilized TRPV1 protein was incorporated into lipid nanodisc as previously described¹⁰, with modifications. Briefly, 2.5 mg soybean polar lipid extract (Avanti) dissolved in chloroform was dried using argon stream and residual chloroform was further removed by vacuum desiccation (~3 h). Lipids were then rehydrated in buffer (20 mM HEPES, 150 mM NaCl, 2 mM TCEP, 14 mM DDM, pH 7.4) and sonicated, resulting in a clear lipid stock at 10 mM concentration. Purified MBP-TRPV1 protein (0.7–1.5 mg ml⁻¹) solubilized in 0.5 mM DDM was mixed with the soybean lipid stock and MSP2N2 (~3 mg ml⁻¹) at various molar ratios and incubated on ice for 30 min. Specifically, we achieved the best result using the ratio TRPV1 monomer:MSP:soybean lipid = 1:1.150–1:1.5:225 for MSP2N2 and 1:1:100 for MSP1E3. Bio-beads SM2 (20 mg per 1 ml mixture, Bio-Rad) were added to initiate the reconstitution by removing detergents from the system and the mixture was incubated at 4 °C for 1 h with constant rotation. A second batch of Bio-beads (equal amount) together with TEV protease (40 µg per 1 mg TRPV1) was then added and the sample was incubated at 4 °C overnight. Bio-beads were then removed and the reconstitution mixture cleared by centrifugation before subsequent separation on a Superose 6 column (GE) in buffer (20 mM HEPES, 150 mM NaCl, 2 mM TCEP, pH 7.4). Reconstitution was assessed by size-exclusion chromatography, SDS-PAGE, and negative-stain EM (Extended Data Fig. 1). The peak corresponding to tetrameric TRPV1 reconstituted in lipid nanodisc was collected for analysis by both negative-stain and cryo-EM. TRPV1–nanodisc particles were mono-dispersed as assessed by negative-stain EM (Extended Data Fig. 1c). No statistical methods were used to predetermine sample size. The experiments were not randomized. The investigators were not blinded to allocation during experiments and outcome assessment.

EM data acquisition and analysis. Grids of TRPV1–nanodisc complexes for negative-stain EM were prepared following an established protocol⁴³. Specifically, 2.5 µl of purified TRPV1–nanodisc complex (0.05–0.1 mg ml⁻¹) was applied to glow-discharged EM grids covered by a thin layer of continuous carbon film and stained with 0.75% (w/v) uranyl formate. Negatively stained EM grids were imaged on a Tecnai T12 microscope (FEI Company) operated at 120 kV. Images were recorded at a nominal magnification of $\times 52,000$ and a defocus set to $-1.5 \mu\text{m}$ using a 4k \times 4k scintillator-based charge-coupled device camera (UltraScan 4000, Gatan), corresponding to a pixel size of 2.02 Å on the specimen.

For cryo-EM, 2.5 µl of purified TRPV1–nanodisc complex (~0.5 mg ml⁻¹ concentration and supplied with 2.5% (v/v) glycerol) was applied to a glow-discharged Quantifoil grid (holey carbon film with 1.2-µm hole size and 1.3-µm hole spacing on 400-mesh Cu grid), blotted with a Vitrobot Mark III (FEI Company) using 8-s blotting time with 100% humidity at 5 °C, and plunge frozen in liquid ethane cooled by liquid nitrogen. For preparation of TRPV1–nanodisc in complex with agonists or antagonist, reconstituted channel complex was mixed with RTX (final concentration 50 µM; molecular weight 628 Da) and DkTx (final concentration 20 µM; molecular weight 8.5 kDa), or capsazepine (20 µM; molecular weight 377 Da), 20 min before vitrification, as described earlier.

Cryo-EM images of frozen hydrated TRPV1–nanodisc particles were collected on a TF30 Polara electron microscope (FEI Company) equipped with a field emission electron source and operated at 300 kV. Images were recorded at a nominal magnification of $\times 31,000$ using a K2 Summit direct electron detector camera (Gatan) operated in super-resolution counting mode following an established protocol⁴⁴. Images have a calibrated physical pixel size of 1.22 Å per pixel on the specimen. The dose rate on the camera was set to be 8.2 counts (corresponding to 9.9 electrons) per physical pixel per second. The total exposure time was 6 s, leading to a total accumulated dose of 41 electrons per Å² on the specimen. Each image was fractionated into 30 subframes, each with an accumulation exposure time of 0.2 s. All dose-fractionated cryo-EM images were recorded using a semi-automated acquisition program UCSFImage4 (ref. 45). Images were recorded with a defocus in a range from -0.7 to $-2.2 \mu\text{m}$.

Image processing. Defocus of all images was determined using CTFFIND4 (ref. 46). Negative-stain EM images were 2 \times 2 binned for particle picking and subsequent image processing. SamViewer, an interactive image analysis program written in Python, was used for all two-dimensional image display and manual particle picking. Individual particles were manually picked, boxed out from the micrograph and normalized to have a mean of 0 and a standard deviation of 1. Usually a total of 1,000–2,000 particles were picked manually. For two-dimensional classification, particles were first corrected for contrast transfer function (CTF) by flipping the phase using 'ctffaply' (written by X. Li), and then subjected to ten cycles of correspondence analysis, *k*-means classification and multi-reference alignment, using SPIDER operations 'CA S', 'CL KM' and 'AP SH' (ref. 47). Two-dimensional class

averages generated from manually picked particles then served as references for a subsequent automatic particle picking procedure implemented in a Python script 'samautopick.py', as previously described¹⁹. All picked particles were then screened visually and particles without clear, defined structural features were removed interactively. The selected particles were again subjected to the same two-dimensional analysis and two-dimensional class averages were assessed (Extended Data Fig. 1).

For cryo-EM images, dose-fractionated super-resolution image stacks of frozen hydrated TRPV1–nanodisc images were first binned 2 \times 2 by Fourier cropping, resulting in a pixel size of 1.22 Å, for motion correction and further image processing. Each image stack was subjected to whole-frame motion correction⁴⁴, followed by correction at individual pixel level using the program UcsfDfCorr (written by S. Zheng). A sum of all corrected subframes, calculated following a dose weighting scheme⁴⁸, was used for further processing. Particle picking was performed similarly to as described earlier. Selected particles after visual screening were boxed out, and subjected directly to maximal-likelihood-based three-dimensional classification procedures implemented in RELION⁴⁹. A previous density map of TRPV1 solubilized in amphipol (Electron Microscopy Data Bank accession 5778) was low-pass filtered to a resolution of 60 Å and used as an initial reference for three-dimensional classification. Stable classes from three-dimensional classification were then iteratively refined and reclassified to obtain the most homogeneous subset for the final three-dimensional reconstruction. All refinements followed the gold-standard refinement procedure, in which the data set was divided into two half sets, and refined independently. Once refinement was converged, the final data set was subjected to the 'post-processing' procedure of RELION, in which a soft mask was calculated and applied to the two half-maps before the corrected Fourier shell coefficient (FSC) was calculated. Temperature-factor estimation and map sharpening were also performed in this step using an automated procedure. C4 symmetry was applied in all three-dimensional classification and refinement steps unless specifically noted. The final resolution was estimated using the FSC = 0.143 criterion⁵⁰ on corrected FSC curves in which the influences of the mask were removed. Local resolution was estimated from unbinned and unsharpened raw density maps using ResMap⁵¹. The number of particles in each data set and other details related to data processing are summarized in Extended Data Table 1b. Conformations of TRPV1 alone or with ligands are very similar whether determined in amphipol or nanodisc.

For the TRPV1–RTX/DkTx nanodisc data set, two three-dimensional reconstructions were first determined independently to resolutions of 2.95 Å with C4 symmetry and 3.24 Å with C2 symmetry. These two reconstructions are very similar. We then performed a three-dimensional classification focusing on DkTx and its peripheral region in TRPV1, following a procedure outlined in Extended Data Fig. 8a. Specifically, a volume that includes DkTx and peripheral densities in TRPV1 was masked out from the C2-symmetrized three-dimensional reconstruction. The density after masking was back-projected and convoluted with the CTF to yield a two-dimensional image for all individual particles using its assigned Euler angles and defocus parameters from the reconstruction. These images were first scaled and normalized to the corresponding experimental particle images and then subtracted from the experimental particle images, resulting in a particle stack in which every particle image contains only signals for the focused region. These procedures were implemented into a Python script 'projection_subtraction.py' (written by E. Palovcak) using the `filt_ctf` and `math.sub.optimal` functions from the SPARX and EMAN2 libraries, respectively^{52,53}. The modified particle images were then subjected to three-dimensional classification in RELION with a soft mask around DkTx, and without further alignment. Two major classes representing two possible orientations of DkTx (as judged by the linker region) were identified, and unsorted particles belonging to each class were separated and used for two independent reconstructions with pre-determined Euler angles. These two reconstructions were aligned to each other using 'fit in map' in UCSF Chimera⁵⁴ and summed, yielding a density map with enhanced two-fold symmetry feature. This density map was used as the reference model for a second round of focused three-dimensional classification to further optimize the classification result.

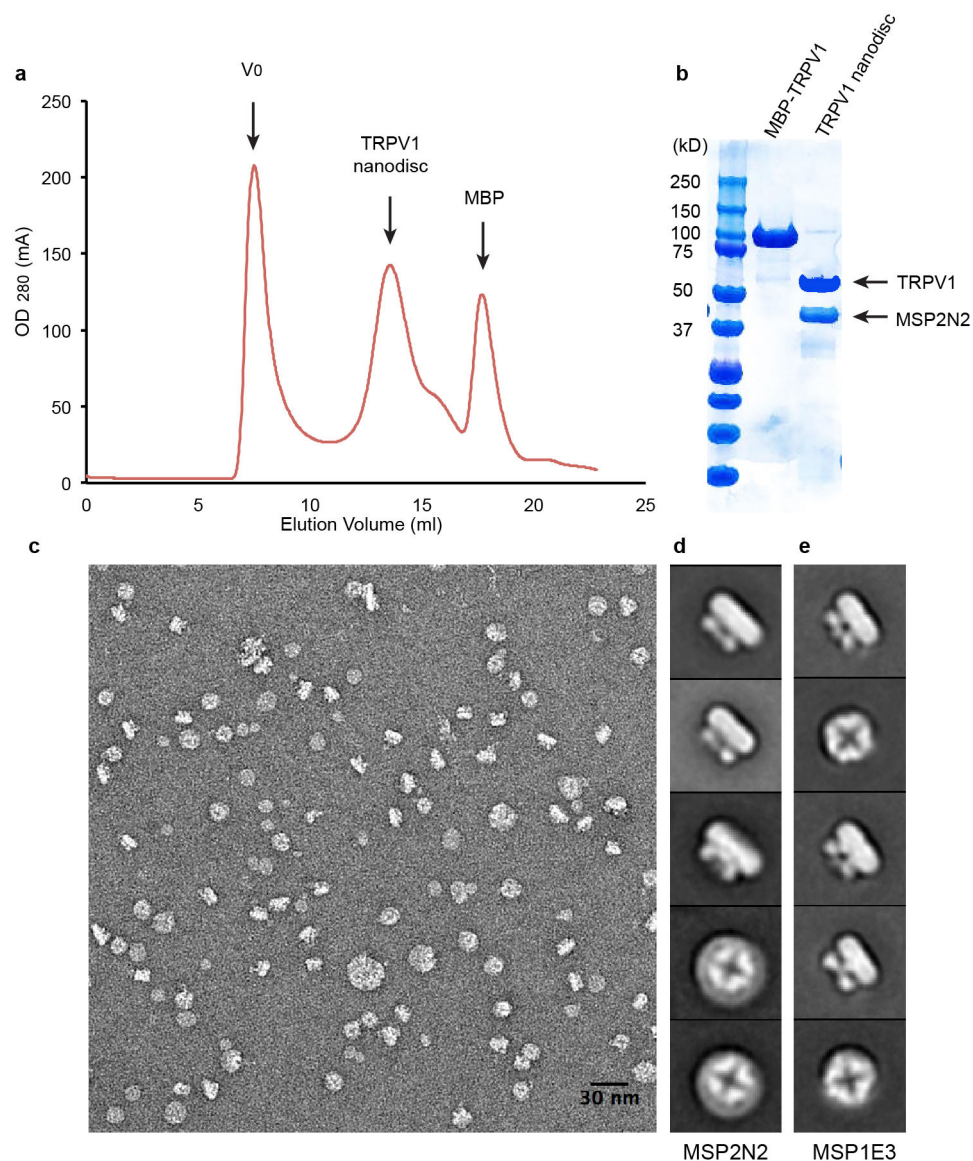
We also determined the structure of capsazepine-bound TRPV1 in amphipol A8-35 (Anatrache). In brief, TRPV1 (~0.5 mg ml⁻¹) in amphipol was mixed with capsazepine (final concentration 50 µM) at 4 °C for ~30 min before application to grids. Procedures for grid preparation, data acquisition and image processing were the same as described¹⁹. The final resolution of the reconstruction (3.8 Å) was calculated using the 'post-processing' procedure of RELION, in which a soft mask was calculated and applied to the two half-maps using default parameters.

Model building. Atomic models of TRPV1 in apo (Protein Data Bank (PDB) accession 3J5P) or fully open states (PDB accession 3J5Q), previously determined when the channel was solubilized in amphipol, were initially docked into maps of unliganded or agonist-bound TRPV1–nanodisc complex using UCSF Chimera. With improved resolution and stability afforded by the nanodisc system, we were

able to remodel side chains and local geometry to higher accuracy. TRPV1 models were first adjusted and real-space refined using COOT⁵⁵. Unliganded TRPV1 model was then used for modelling capsaizipine-bound structure with minor adjustment due to high similarity between the two structures. DkTx was remodelled according to the improved map from focused analysis (see earlier). All models for ligands or associated lipids, except for RTX, were generated using elBOW⁵⁶ module in PHENIX⁵⁷ together with their geometric constraints. RTX model and constraints were generated using a web server 'PRODRG'⁵⁸. For simplicity, all annular lipids in the structure were modelled as phosphatidylethanolamine (PE), and the acyl chains of all lipids were modelled as 1–8 carbon length according to specific densities. Models for all ligands were docked into densities and refined using COOT. Full models of TRPV1 (residue 335–751, corresponding to well-resolved regions in maps) in complex with ligands and lipids were then subjected to global refinement and minimization in real space using the module 'phenix.real_space_refine'⁵⁹ in PHENIX. For cross-validation⁶⁰, the refined structures were first randomly displaced by 0.1 Å and then refined against one of the half maps generated in RELION following the same procedures described earlier. FSC curves were calculated between the refined model and half map 1 ('work', used in test refinement), the refined model and half map 2 ('free', not used in test refinement), and the refined model and summed map. The small gap between the work and the free FSC curves indicated little effect of over-fitting of atomic models. The geometries of all models were assessed using the 'comprehensive model validation' section in PHENIX and MolProbity⁶¹, and detailed information was listed in Extended Data Table 1b.

Figures were prepared using UCSF Chimera and two-dimensional electron microscopy images were extracted using SamViewer.

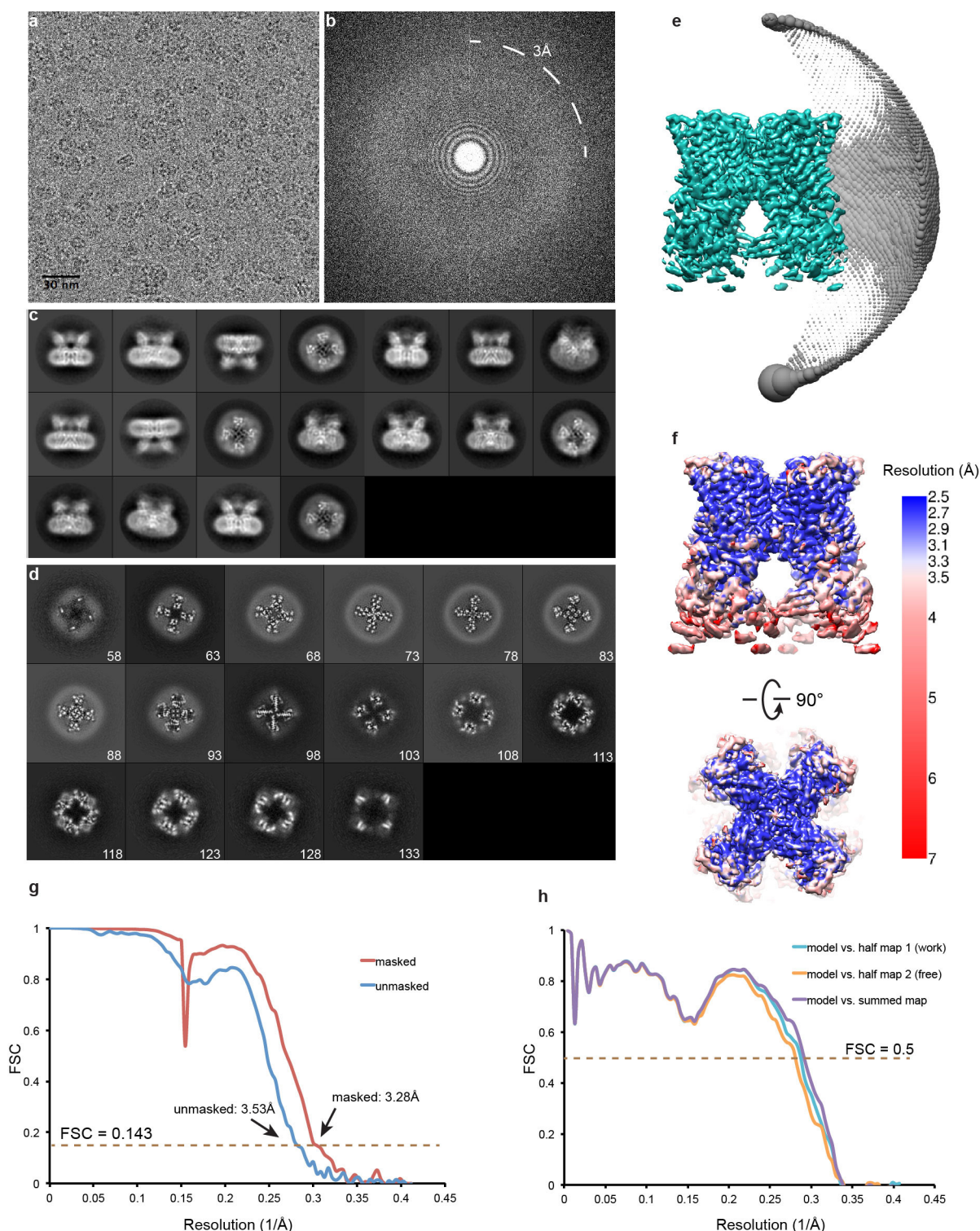
43. Booth, D. S., Avila-Sakar, A. & Cheng, Y. Visualizing proteins and macromolecular complexes by negative stain EM: from grid preparation to image acquisition. *J. Vis. Exp.* **58**, 3227 (2011).
44. Li, X. *et al.* Electron counting and beam-induced motion correction enable near-atomic-resolution single-particle cryo-EM. *Nature Methods* **10**, 584–590 (2013).
45. Li, X., Zheng, S., Agard, D. A. & Cheng, Y. Asynchronous data acquisition and on-the-fly analysis of dose fractionated cryoEM images by UCSFImage. *J. Struct. Biol.* **192**, 174–178 (2015).
46. Rohou, A. & Grigorieff, N. CTFFIND4: fast and accurate defocus estimation from electron micrographs. *J. Struct. Biol.* **192**, 216–221 (2015).
47. Frank, J. *et al.* SPIDER and WEB: processing and visualization of images in 3D electron microscopy and related fields. *J. Struct. Biol.* **116**, 190–199 (1996).
48. Grant, T. & Grigorieff, N. Measuring the optimal exposure for single particle cryo-EM using a 2.6 Å reconstruction of rotavirus VP6. *eLife* **4**, e06980 (2015).
49. Scheres, S. H. W. RELION: implementation of a Bayesian approach to cryo-EM structure determination. *J. Struct. Biol.* **180**, 519–530 (2012).
50. Scheres, S. H. W. & Chen, S. Prevention of overfitting in cryo-EM structure determination. *Nature Methods* **9**, 853–854 (2012).
51. Kucukelbir, A., Sigworth, F. J. & Tagare, H. D. Quantifying the local resolution of cryo-EM density maps. *Nature Methods* **11**, 63–65 (2014).
52. Hohn, M. *et al.* SPARX, a new environment for cryo-EM image processing. *J. Struct. Biol.* **157**, 47–55 (2007).
53. Tang, G. *et al.* EMAN2: an extensible image processing suite for electron microscopy. *J. Struct. Biol.* **157**, 38–46 (2007).
54. Pettersen, E. F. *et al.* UCSF Chimera—a visualization system for exploratory research and analysis. *J. Comput. Chem.* **25**, 1605–1612 (2004).
55. Emsley, P., Lohkamp, B., Scott, W. G. & Cowtan, K. Features and development of Coot. *Acta Crystallogr. D* **66**, 486–501 (2010).
56. Moriarty, N. W., Grosse-Kunstleve, R. W. & Adams, P. D. electronic Ligand Builder and Optimization Workbench (elBOW): a tool for ligand coordinate and restraint generation. *Acta Crystallogr. D* **65**, 1074–1080 (2009).
57. Adams, P. D. *et al.* PHENIX: a comprehensive Python-based system for macromolecular structure solution. *Acta Crystallogr. D* **66**, 213–221 (2010).
58. van Aalten, D. M. F. *et al.* PRODRG, a program for generating molecular topologies and unique molecular descriptors from coordinates of small molecules. *J. Comput. Aided Mol. Des.* **10**, 255–262 (1996).
59. Afonine, P. V., Headd, J. J., Terwilliger, T. C. & Adams, P. D. New tool: phenix.real_space_refine. *Computational Crystallography Newsletter* **4**, 43–44 (2013).
60. Amunts, A. *et al.* Structure of the yeast mitochondrial large ribosomal subunit. *Science* **343**, 1485–1489 (2014).
61. Chen, V. B. *et al.* MolProbity: all-atom structure validation for macromolecular crystallography. *Acta Crystallogr. D* **66**, 12–21 (2010).



Extended Data Figure 1 | Reconstitution of TRPV1 into lipid nanodisc.

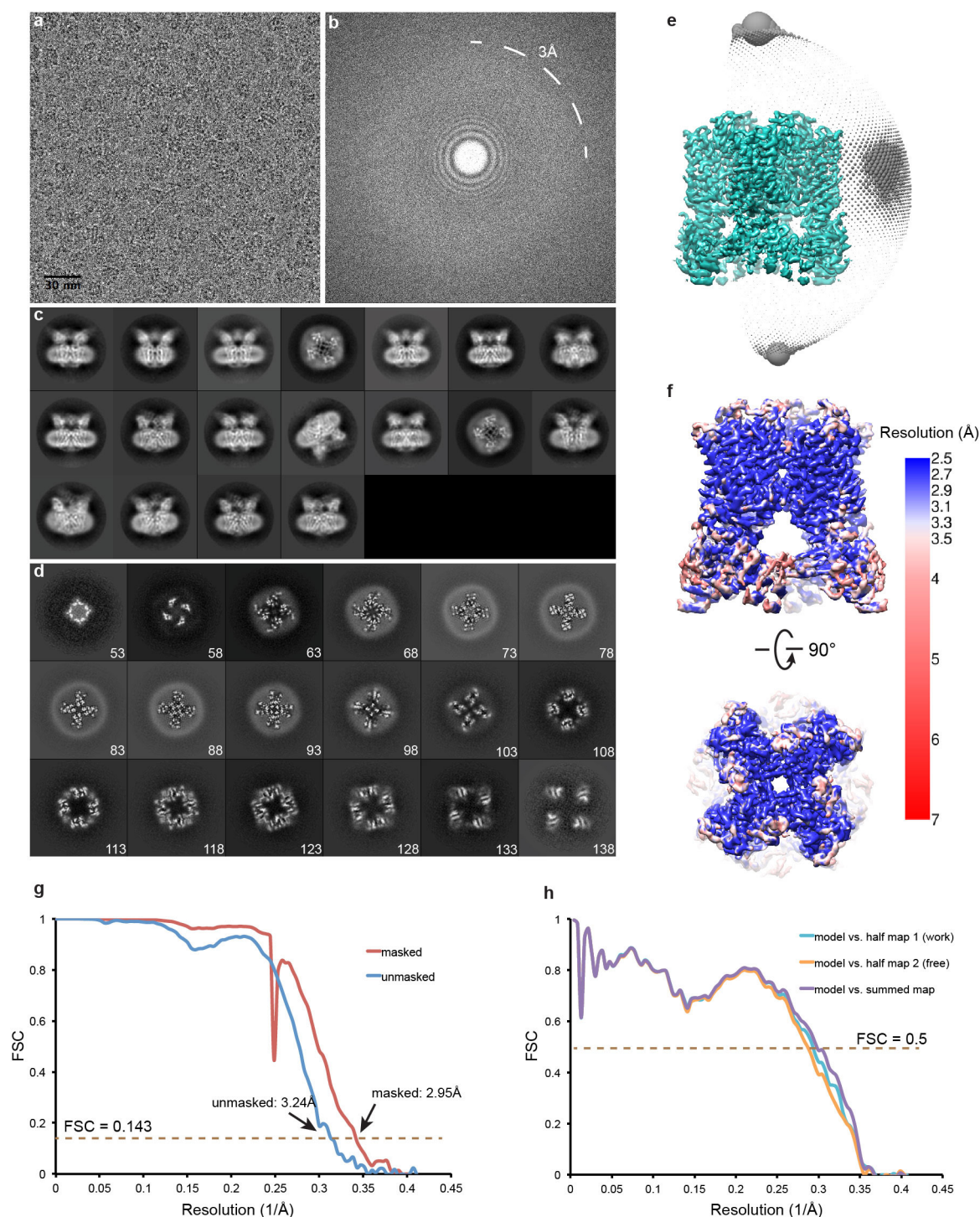
a, Size-exclusion chromatography of TRPV1 channel reconstituted into lipid nanodisc using MSP2N2. Void volume and peaks corresponding to TRPV1 and cleaved MBP are indicated. **b**, SDS-polyacrylamide gel electrophoresis (SDS-PAGE) of detergent-solubilized MBP-TRPV1 fusion protein and material from nanodisc reconstituted with TRPV1 following MBP cleavage (middle peak in **a**). Note the presence of both bands for TRPV1 and MSP2N2. **c**, Representative micrograph of negative-stained

TRPV1-nanodisc sample showing mono-dispersed and homogeneous particles. **d**, Reference-free two-dimensional class averages of particles in **c**, revealing band-like density contributed by the lipid disc (side view) and tetrameric arrangement of channel subunits (top view). **e**, Two-dimensional class averages of the same protein reconstituted into MSP1E3 nanodisc, which is smaller in diameter. Note the extra space within the disc offered by MSP2N2 scaffold protein in **d**. The size of the class average window is 258 Å.



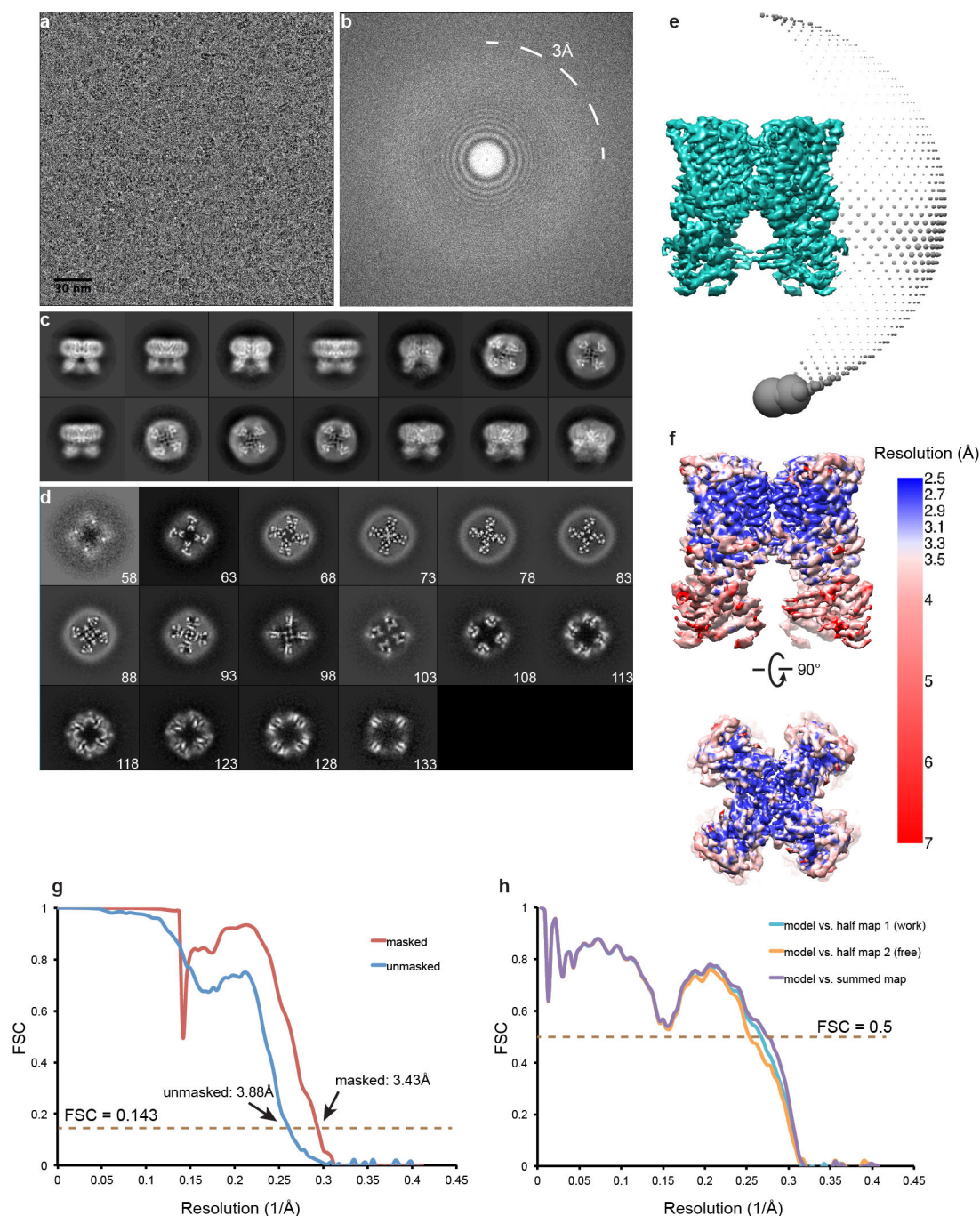
Extended Data Figure 2 | Single-particle cryo-EM of unliganded TRPV1 in lipid nanodisc. **a**, Representative raw micrograph of apo TRPV1 in nanodisc. **b**, Fourier transform of image in **a**. Note that Thon rings are visible at up to 3 Å. **c**, Gallery of two-dimensional class averages, with size of window as 233 Å. **d**, Slices through the unsharpened density map at different levels along the channel symmetry axis (numbers start from extracellular side). **e**, Euler angle distribution of all particles included in the calculation of the final three-dimensional reconstruction. Position of each sphere (grey) relative to the density map (green) represents its

angle assignment and the radius of the sphere is proportional to the amount of particles in this specific orientation. **f**, Final three-dimensional density map coloured with local resolution in side and top views. **g**, Fourier shell coefficient (FSC) curves between two independently refined half maps before (blue) and after (red) the post-processing in RELION. **h**, FSC curves for cross-validation: model versus summed map (purple), model versus half map 1 (used in test refinement, cyan), model versus half map 2 (not used in test refinement, orange). Small differences between the 'work' and 'free' curves indicate little effect of over-fitting.



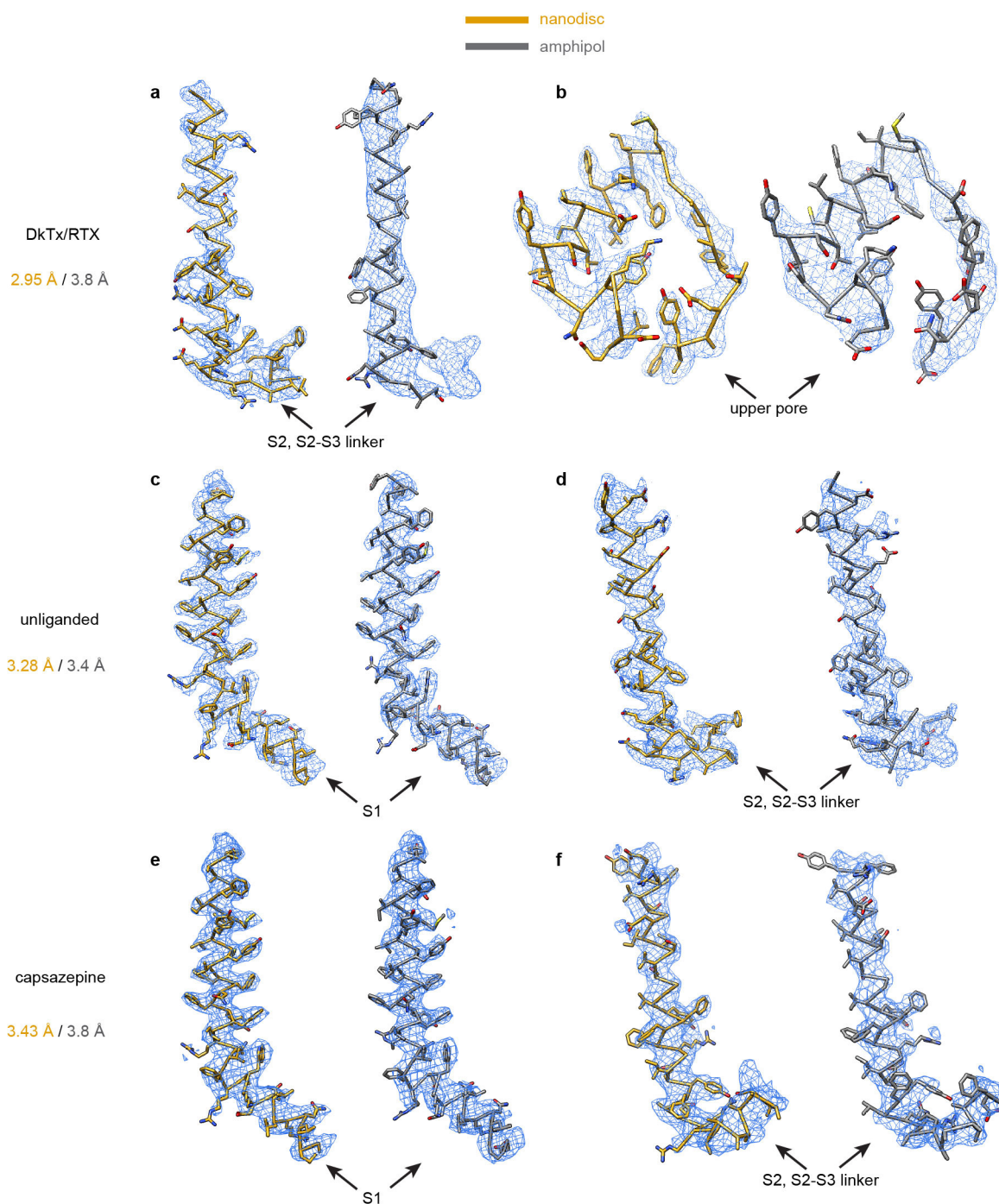
Extended Data Figure 3 | Single-particle cryo-EM studies of agonist-bound TRPV1 in lipid nanodisc. **a**, Representative raw micrograph of TRPV1-RTX/DkTx in nanodisc. **b**, Fourier transform of image in **a**. **c**, Gallery of two-dimensional class averages, with size of window as 233 Å. **d**, Slices through the unsharpened density map at different levels along the channel symmetry axis (numbers start from extracellular side). **e**, Euler angle distribution of all particles included in the calculation of the final three-dimensional reconstruction. Position of each sphere (grey) relative to the density map (green) represents its angle assignment and the radius

of the sphere is proportional to the amount of particles in this specific orientation. **f**, Final three-dimensional density map coloured with local resolution in side and top views. **g**, FSC curves between two independently refined half maps before (blue) and after (red) the post-processing in RELION. **h**, FSC curves for cross-validation: model versus summed map (purple), model versus half map 1 (used in test refinement, cyan), model versus half map 2 (not used in test refinement, orange). Small differences between the 'work' and 'free' curves indicate little effect of over-fitting.



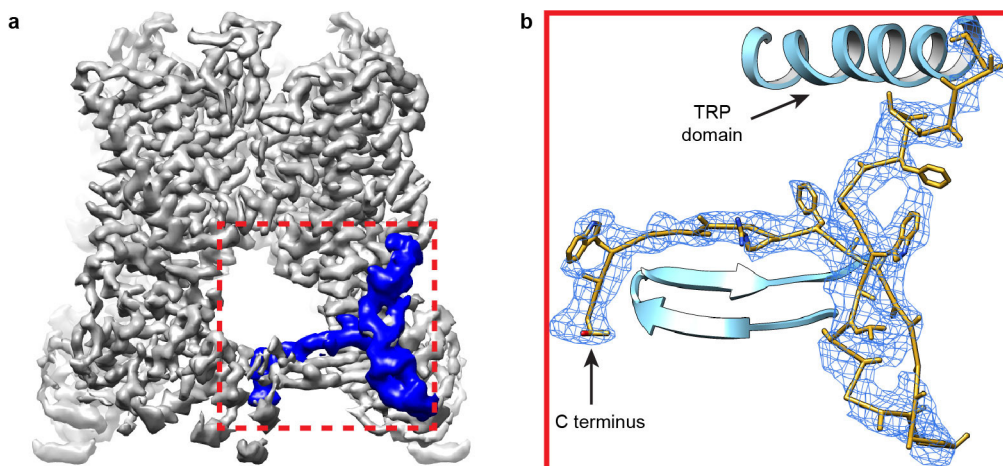
Extended Data Figure 4 | Single-particle cryo-EM studies of antagonist-bound TRPV1 in lipid nanodisc. **a**, Representative raw micrograph of TRPV1–capsazepine complex in nanodisc. **b**, Fourier transform of image in **a**. **c**, Gallery of two-dimensional class averages, with size of window as 233 Å. **d**, Slices through the unsharpened density map at different levels along the channel symmetry axis (numbers start from extracellular side). **e**, Euler angle distribution of all particles included in the calculation of the final three-dimensional reconstruction. Position of each sphere (grey) relative to the density map (green) represents its angle assignment and

the radius of the sphere is proportional to the amount of particles in this specific orientation. **f**, Final three-dimensional density map coloured with local resolution in side and top views. **g**, FSC curves between two independently refined half maps before (blue) and after (red) the post-processing in RELION. **h**, FSC curves for cross-validation: model versus summed map (purple), model versus half map 1 (used in test refinement, cyan), model versus half map 2 (not used in test refinement, orange). Small differences between the ‘work’ and ‘free’ curves indicate little effect of over-fitting.



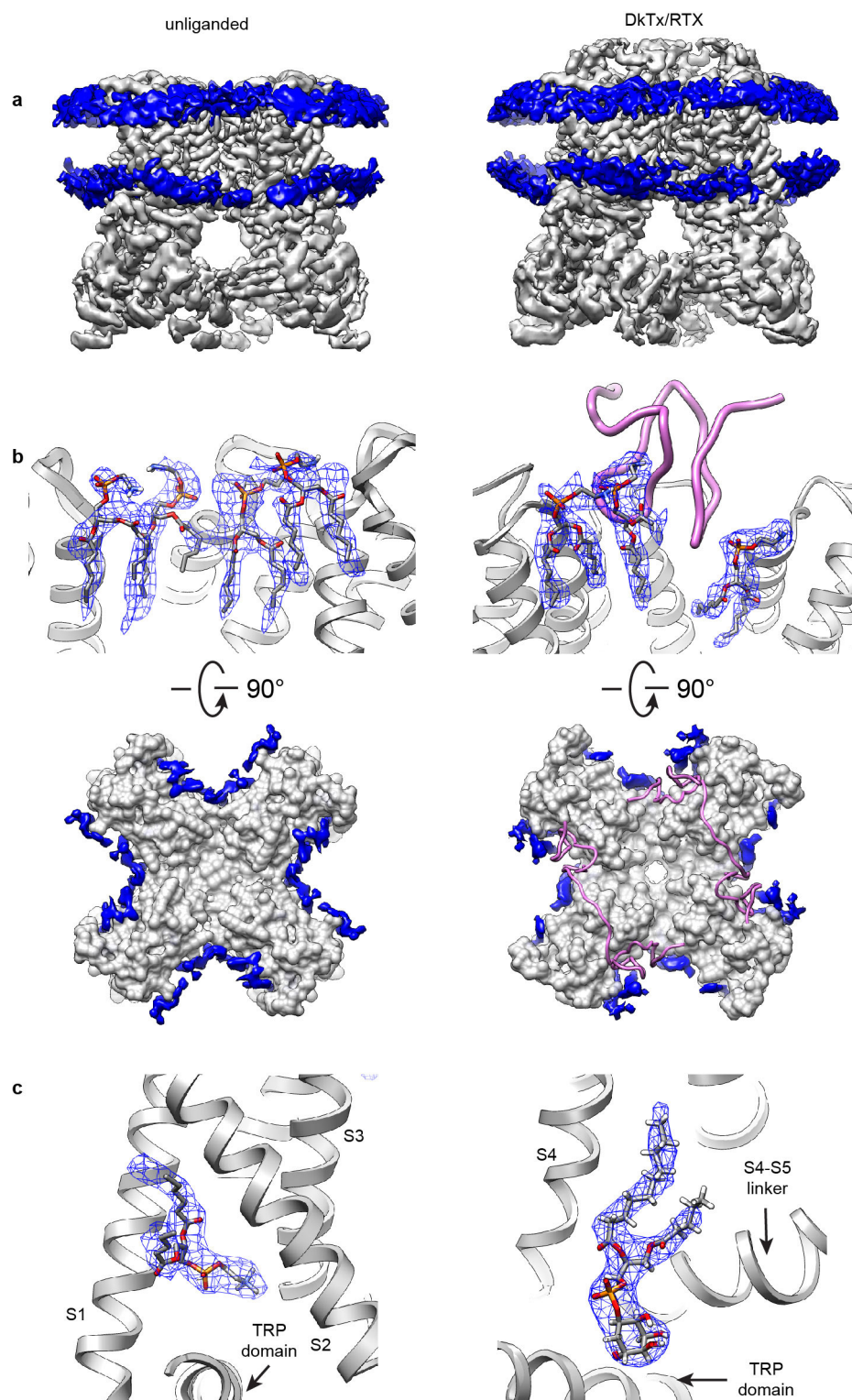
Extended Data Figure 5 | Improved resolution for structures determined in nanodisc. Comparison of density maps (blue mesh) determined from nanodisc- and amphipol-stabilized TRPV1 at various regions of the channel facing the lipid bilayer or at the bilayer surface. Refined atomic models (gold, nanodisc; grey, amphipol) are fit to

corresponding densities. Side-chain densities were considerably improved in nanodisc-stabilized TRPV1–DkTx/RTX structure (a, b), and notable improvement was also seen for unliganded (c, d) and capsazepine-bound (e, f) channels in nanodisc.



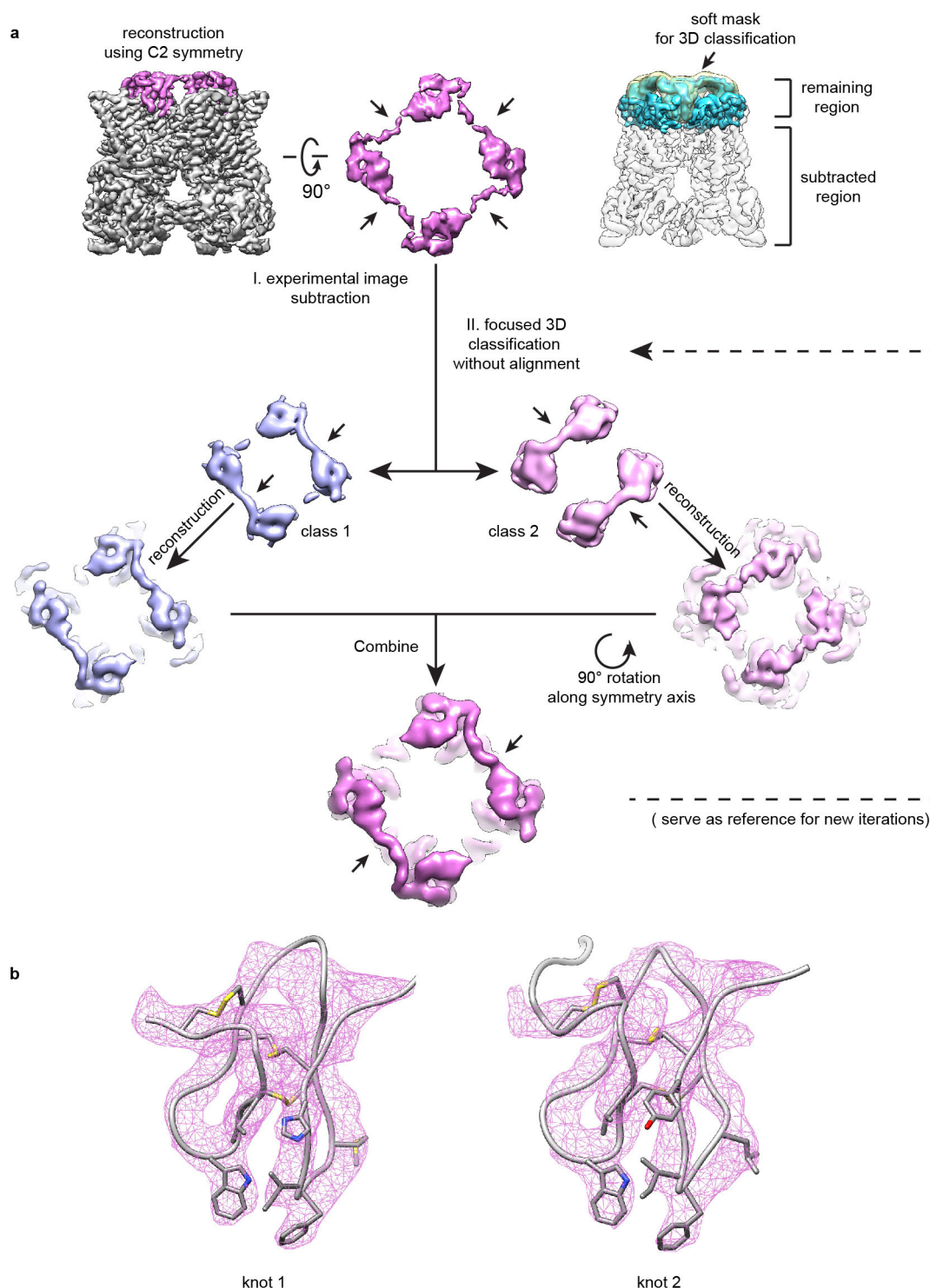
Extended Data Figure 6 | Newly resolved TRPV1 cytoplasmic region in nanodisc-stabilized structure. **a**, A region in the TRPV1 C terminus, previously unresolved in amphipol-stabilized structures (blue) is clearly resolved in the nanodisc-stabilized structure. **b**, Enlarged view of boxed

region in **a** showing density map (blue mesh) and superimposed model (gold). Previously resolved TRP domain and N-terminal β -strands are depicted in ribbon diagram format (cyan).

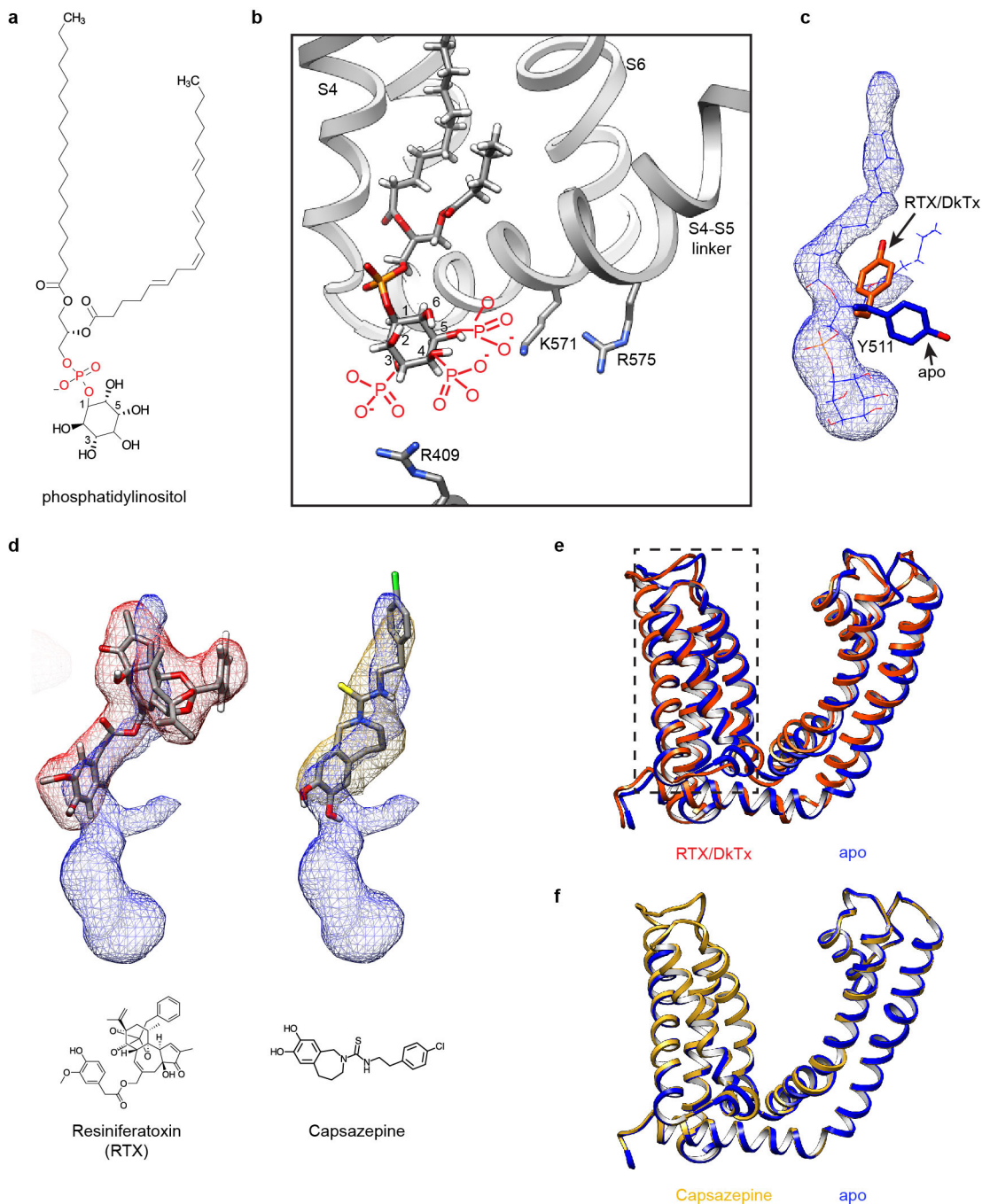


Extended Data Figure 7 | Categories of lipid densities observed in TRPV1 structures. **a**, Two continuous layers of density (blue) contributed by lipid head groups of bilayer within nanodisc are shown for apo channel (left) and channel in complex with RTX–DkTx (right). **b**, Atomic model of annular lipids could be built into well-resolved densities (blue mesh) surrounding the channel protein. DkTx is shown as ribbon diagram

(pink). Top-down views show distribution of resolved annular lipids (blue) in inter-subunit crevices at the outer leaflet of the membrane. **c**, Well-resolved densities (blue mesh) in the structures representing a phosphatidylcholine molecule (left) and a phosphatidylinositol molecule (right). Transmembrane helices of TRPV1 close to the binding site are also shown as ribbon diagrams (grey).



Extended Data Figure 8 | Focused analysis of DkTx density map. a, Flow-chart showing procedures of focused three-dimensional classification of DkTx and proximal regions (see Methods for details). **b**, Atomic models for both knots of DkTx are superimposed on density maps (pink mesh).



Extended Data Figure 9 | Lipid co-factor and vanilloids at the vanilloid binding site of TRPV1. a, Chemical structure of phosphatidylinositol.

b, Local environment of the phosphatidylinositol-binding site may accommodate multiple phosphatidylinositide species with phosphate substituents at the 3, 4 and/or 5 positions of the inositol ring (drawn in red). Adjacent regions of the channel are shown as ribbon diagram (grey). **c**, Tyr511 assumes two possible orientations that differ in apo versus agonist-bound states of the TRPV1 channel. In the apo state, one acyl chain of the resident phosphatidylinositol lipid (blue mesh superimposed with atomic model) prevents the Tyr511 side chain from assuming the

upward rotamer position. **d**, Density maps of vanilloids (resiniferatoxin, red mesh; capsaizipine, gold mesh) superimposed with density of the bound phosphatidylinositol lipid (blue mesh), suggesting that they occupy overlapping, but not identical sites. Atomic models for both drugs and their chemical structures are also shown. **e**, Overlap of transmembrane region of one TRPV1 subunit corresponding to apo (blue) and RTX/DkTx-bound (orange) states. Note the relatively small conformational change of the voltage sensor-like domain (S1–S4, boxed region). **f**, Overlap of transmembrane region of one TRPV1 subunit corresponding to apo (blue) and capsaizipine-bound (gold) states.

Extended Data Table 1 | Summary of data sets and statistics

a

	Unliganded		DkTx/RTX		Capsazepine	
	nanodisc	amphipol	nanodisc	amphipol	nanodisc	amphipol
Defocus range (μm)	-0.7 – -2.2	-1.5 – -3.0	-0.7 – -2.2	-1.5 – -3.0	-0.7 – -2.2	-0.8 – -2.2
Number of images	1000	946	1200	~1000	1219	1002
Motion correction	UcsfDfCorr	MotionCorr	UcsfDfCorr	MotionCorr	UcsfDfCorr	MotionCorr
Initial particle #	159193	97166	218787	148670	198831	81709
Final particle #	30689	35645	73929	36158	80725	47477
Resolution (\AA)	3.28	3.28	2.95	3.8	3.43	3.8

b

	unliganded	DkTx/RTX	capsazepine
Data collection/processing			
Voltage (kV)	300	300	300
Magnification	31000	31000	31000
Defocus range (μm)	-0.7 – -2.2	-0.7 – -2.2	-0.7 – -2.2
Pixel size (\AA)	1.2156	1.2156	1.2156
Total electron dose ($\text{e}^-/\text{\AA}^2$)	41	41	41
Exposure time (s)	6	6	6
Number of images	1000	1200	1219
Number of frames per image	30	30	30
Initial particle number	159193	218787	198831
Final particle number	30689	73929	80725
Resolution (unmasked, \AA)	3.53	3.24	3.88
Resolution (masked, \AA)	3.28	2.95	3.43
Refinement			
Number of atoms	12504	13162	11808
Protein	11804	12558	11708
Ligand	700	604	100
R.m.s deviations			
Bond lengths (\AA)	0.0082	0.0127	0.0141
Bond angles ($^\circ$)	1.25	1.42	1.37
Ramachandran			
Favored (%)	92.8	88.86	89.62
Allowed (%)	7.2	11.02	10.12
Outlier (%)	0	0.12	0.26
Molprobit score	1.83	1.91	1.83

a, Comparison of imaging/data-processing variables between nanodisc and amphipol datasets. b, Statistics of three-dimensional reconstruction and model refinement.

Fission and reconfiguration of bilobate comets as revealed by 67P/Churyumov–Gerasimenko

Masatoshi Hirabayashi^{1†}, Daniel J. Scheeres¹, Steven R. Chesley², Simone Marchi³, Jay W. McMahon¹, Jordan Steckloff⁴, Stefano Mottola⁵, Shantanu P. Naidu² & Timothy Bowling⁶

The solid, central part of a comet—its nucleus—is subject to destructive processes^{1,2}, which cause nuclei to split at a rate of about 0.01 per year per comet³. These destructive events are due to a range of possible thermophysical effects⁴; however, the geophysical expressions of these effects are unknown. Separately, over two-thirds of comet nuclei that have been imaged at high resolution show bilobate shapes⁵, including the nucleus of comet 67P/Churyumov–Gerasimenko (67P), visited by the Rosetta spacecraft. Analysis of the Rosetta observations suggests that 67P's components were brought together at low speed after their separate formation⁶. Here, we study the structure and dynamics of 67P's nucleus. We find that sublimation torques have caused the nucleus to spin up in the past to form the large cracks observed on its neck. However, the chaotic evolution of its spin state has so far forestalled its splitting, although it should eventually reach a rapid enough spin rate to do so. Once this occurs, the separated components will be unable to escape each other; they will orbit each other for a time, ultimately undergoing a low-speed merger that will result in a new bilobate configuration. The components of four other imaged bilobate nuclei have volume ratios that are consistent with a similar reconfiguration cycle, pointing to such cycles as a fundamental process in the evolution of short-period comet nuclei. It has been shown^{7,8} that comets were not strong contributors to the so-called late heavy bombardment about 4 billion years ago. The reconfiguration process suggested here would preferentially decimate comet nuclei during migration to the inner solar system, perhaps explaining this lack of a substantial cometary flux.

Along the neck of 67P's nucleus (the Hapi region) are two straight cracks, each a few hundred metres long and separated from each other by 750 metres (Fig. 1a, b)^{9,10}. The morphology of these cracks is distinguishable from that of other cracks observed on the surface of the nucleus (Extended Data Fig. 1). Previous studies suggested that the straight cracks have been created by tidal forces¹⁰, but this would have required a close Jupiter flyby within a narrow range of distances. Episodes of past rapid rotation might also have caused stress fractures within the nucleus, and are feasible as the nucleus' spin rate can undergo substantial changes per orbit, with its spin period decreasing by 0.36 hours to 12.4 hours during its 2009 perihelion passage^{9,11}. To analyse this possibility, we used elastic and plastic finite-element models (FEMs) to study the strength and failure of 67P at different spin periods (see Methods). We used a reduced-resolution version of the SHAP 2 shape model (see Methods)¹², fixed the total mass at 1.0×10^{13} kg (ref. 9), and assumed the material properties to be uniformly distributed, resulting in a nuclear bulk density of 535 kg m^{-3} (ref. 13).

The elastic FEM analysis shows that, with faster spin rates, tensile stresses peak at the observed crack locations. Figure 1c, d shows the maximum principal stress distributions on the surface at spin periods

of 12.4 hours and 9 hours. For periods shorter than 9 hours, the peak stresses always appear at the crack locations, with the direction of the maximum principal stress moving away from and perpendicular to the crack planes (Fig. 1d)—implying that the cracks are of an open type (mode I)¹⁴, consistent with their appearance¹⁰.

The plastic FEM analyses identified three failure regimes for the nucleus (see Fig. 2 and Methods). Type I is compressive failure, which occurs at spin periods longer than about 9 hours. Compression would cause crushing failure around the neck's surface, with the interior not at its yield stress. Type II is a crack-forming failure, which occurs at spin periods of around 7–9 hours, with tensional failure occurring on side A of the neck and portions of the interior near side B remaining in compression below yield stress. In type III failure, which occurs

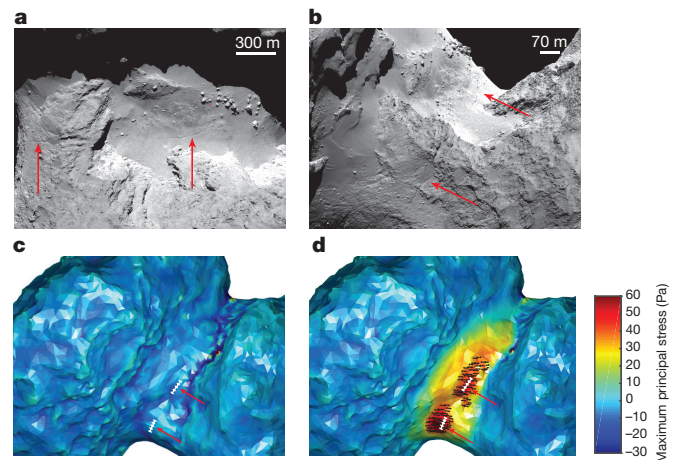


Figure 1 | Locations of the straight cracks and stress peaks on the surface of the Hapi region of 67P. **a, b**, Two straight cracks, viewed from different angles, in the Hapi region⁹. Data are available at the European Space Agency (ESA) image browser (<http://imagearchives.esac.esa.int>), with identification numbers N20140808T062034578ID30F22 (**a**) and N20140826T074254573ID30F22 (**b**). Image credit: ESA/Rosetta/MPS for OSIRIS Team MPS/UPD/LAM/IAA/SSO/INTA/UPM/DASP/IDA; original images processed by ESA/Rosetta/SGS/PSA&ESDC to create image for Archive Imager Browser. **c**, Contour plot of the maximum component of the principal stress at a spin period of 12.4 h. **d**, Contour plot of the maximum component of the principal stress at a spin period of 9 h. The black arrows in **d** show the vector field of the stress component that is larger than 40 Pa. The white lines in **c, d** indicate the locations of the observed cracks. The spin axis is in the out-of-plane direction. ANSYS Academic APDL version 15.03 was used for an elastic FEM analysis to compute the maximum principal stress distributions, under the assumption that the nucleus initially had no cracks on the neck.

¹Department of Aerospace Engineering Sciences, University of Colorado Boulder, 429 UCB, Boulder, Colorado 80309, USA. ²Jet Propulsion Laboratory, California Institute of Technology, 4800 Oak Grove Drive, Pasadena, California 91109, USA. ³Southwest Research Institute, 1050 Walnut St, Suite 300, Boulder, Colorado 80302, USA. ⁴Department of Earth, Atmospheric and Planetary Sciences, Purdue University, 550 Stadium Mall Drive, West Lafayette, Indiana 47907, USA. ⁵German Aerospace Center (DLR), Institute of Planetary Research, Rutherfordstr. 2, 12489 Berlin, Germany. ⁶Department of the Geophysical Sciences, University of Chicago, 5734 S. Ellis Avenue, Chicago, Illinois 60637, USA. [†]Present address: Department of Earth, Atmospheric and Planetary Sciences, Purdue University, 550 Stadium Mall Drive, West Lafayette, Indiana 47907, USA.

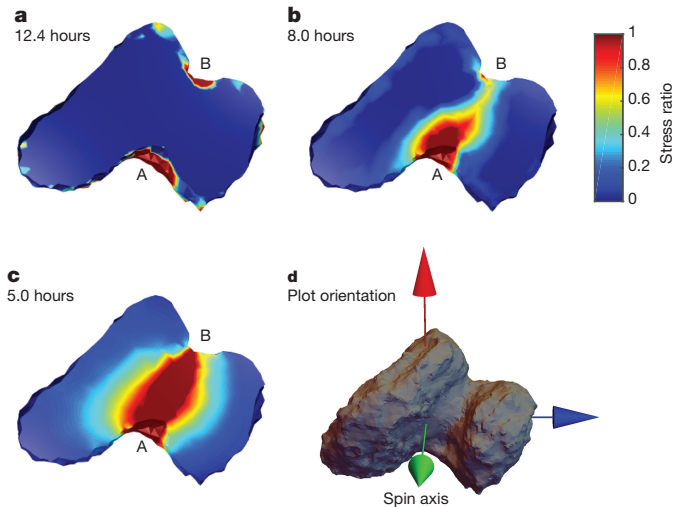


Figure 2 | Terminal failure states for the 67P nucleus. We used a plastic FEM analysis to compute terminal failure states. The colours show the ratio of the present stress state to the yield stress on the cross-section. Regions with a unity stress ratio are at yield and indicate failure²⁹. **a**, Type I failure is compressive surface failure, so there are no failed regions in the interior. The plot shows the case for a spin period of 12.4 h and a cohesive strength of 1 Pa. **b**, Type II failure involves a tensile failure on side A, but structurally stable regions on side B. The figure shows an example at a spin period of 8 h and a bulk cohesive strength of 30 Pa. **c**, Type III failure involves tensile failure across the neck region. The centrifugal force exceeds the gravitational force in this condition. This describes the case for a spin period of 5 h and a bulk cohesive strength of 250 Pa. **d**, The orientation of the body. The maximum, intermediate and minimum moments of the inertia axes are shown with green, red and blue arrows, respectively.

when spin periods are shorter than about 7 hours, centrifugal forces exceed gravitational forces, and the tensile failure region spreads across the neck.

In type I failure, compressed materials should experience shear cracks, with additional splits occurring at the crack tips¹⁴—features that are not observed at these cracks¹¹. Moreover, compressive failure does not occur unless the cohesive strength is less than about 10 Pa (Fig. 3); this is much smaller than the reported compressive strength for 67P, of the order of kilopascals^{15,16}. Type III failure also seems unlikely for this nucleus: given the existing cracks on the Hapi region, under a type III regime the concentration of stress in the interior should cause failure to propagate across the entire neck and separate the lobes (see Extended Data Fig. 2 and Methods).

We therefore conclude that a type II failure resulted in the formation of the observed cracks on the Hapi region. Formation conditions for the cracks predict a bulk cohesive strength of about 10–200 Pa (Fig. 3), compatible with the reported cohesive strength of this nucleus¹⁶ and with that of other comet nuclei¹⁷. Our results also predict that the present nucleus configuration will immediately undergo a type III failure and fission into two lobes if the spin period reaches about 7 hours.

By computing the total energy of the fissioned system, we find that, at the 7-hour split limit, the system would have a negative total energy and be Hill stable, which means the distance between the two lobes would be bounded, preventing them from escaping one another¹⁸ (see Methods). Instead, they would enter a brief period of orbiting each other, eventually re-impacting at speeds less than escape speed ($\sim 1 \text{ m s}^{-1}$), which should, given our strength constraints, preserve the bilobate structure of the nucleus¹⁹. We confirmed that these results were insensitive to possible heterogeneity or variation in the bulk density (Extended Data Figs 3–6 and Methods).

The results of our structural analysis raise the question of how the spin period could exceed 9 hours without transitioning beyond the

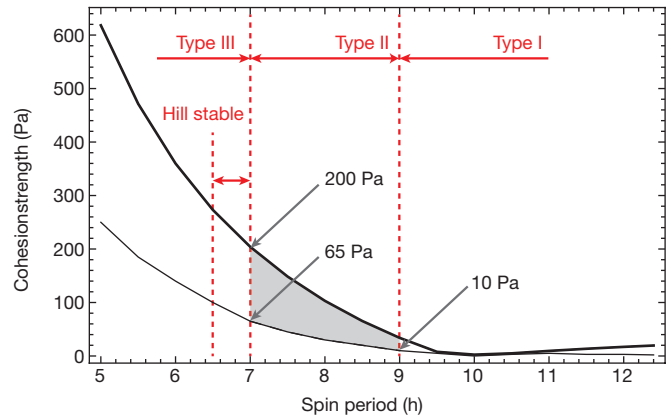


Figure 3 | Failure types and conditions at different spin periods.

The thick and narrow black lines show results obtained from the elastic and plastic FEM analyses, respectively. If the cohesive strength is below the thick line, cracks should appear at the stress peaks. If cohesive strength is below the narrow line, the nucleus splits into two. Given that the cracks on 67P have already formed, the lines delineate upper and lower bounds to the bulk cohesive strength at a given spin period. The boundary between type I failure and type II failure is determined by when stress peaks first appear in the neck. The boundary between types II and III is determined by when the gravitational and centrifugal forces are balanced across the neck. The type I compressive failure condition is less than ~ 10 Pa, and much lower than the reported compressive strength, $\sim 1 \text{ kPa}$. In a type III failure, the existing cracks would experience tension in excess of its strength and fail catastrophically. Therefore, the shaded region indicates the bulk cohesive strength of the nucleus. Taking the lowest and highest values of this region, we derive strength limits of between ~ 10 Pa and ~ 200 Pa. We note that the findings shown here are relatively insensitive to variations in density and mass distribution (see Methods). The Hill stability condition is determined by finding when the total energy at fission is zero (see Methods).

7-hour split limit for its components to separate during its present shape configuration. To analyse this, we applied results from an earlier study²⁰ that correlated nucleus spin variation with uniform gas emission normal to the surface, appropriately scaled by the incident sunlight. This is analytically similar to the YORP effect, enabling these techniques to be applied to computing the spin acceleration for the given nucleus shape²¹. Since sublimation pressure varies strongly with heliocentric distance, the spin acceleration of 67P will primarily occur near perihelion and will be a function of ϕ_p , the subsolar latitude at perihelion in the nucleus frame (see Methods). Figure 4a and b give the scaled spin acceleration at perihelion as a function of ϕ_p , and as a function of heliocentric distance. To assess the past evolution of the spin period, we integrated 1,000 clones backwards in time for 5,000 years, choosing initial conditions with uncertainties proportional to the present orbital uncertainty (see Methods). The timescale used is compatible with the activity lifetime of typical Jupiter family comets (JFCs)—thousands of years (ka)—and is much shorter than their dynamical lifetime of around $4 \times 10^2 \text{ ka}$ (ref. 22).

Even relatively distant flybys of Jupiter will modify a comet's orbit, which in turn can yield large changes in the subsolar latitude at perihelion. Over multiple encounters, this yields a chaotically changing outgassing torque and causes the subsolar latitude (Fig. 4c) and the perihelion distance (Fig. 4d) to become uniformly distributed between $\pm 40^\circ$ in just over 1 ka, and between 2 AU and 5 AU within 0.5 ka, respectively. Variation in ϕ_p shows that the spin rate becomes completely random within the activity lifetime and makes it plausible for the nucleus to pass into and out of a spin period of 7–9 hours, forestalling spin-induced fission. Over a longer time span, this randomization also allows the nucleus to eventually exceed a 7-hour spin period and undergo fission and reconfiguration, also implying that the nucleus could have undergone repeated reconfigurations since its formation. Given that the orbit of 67P is typical among

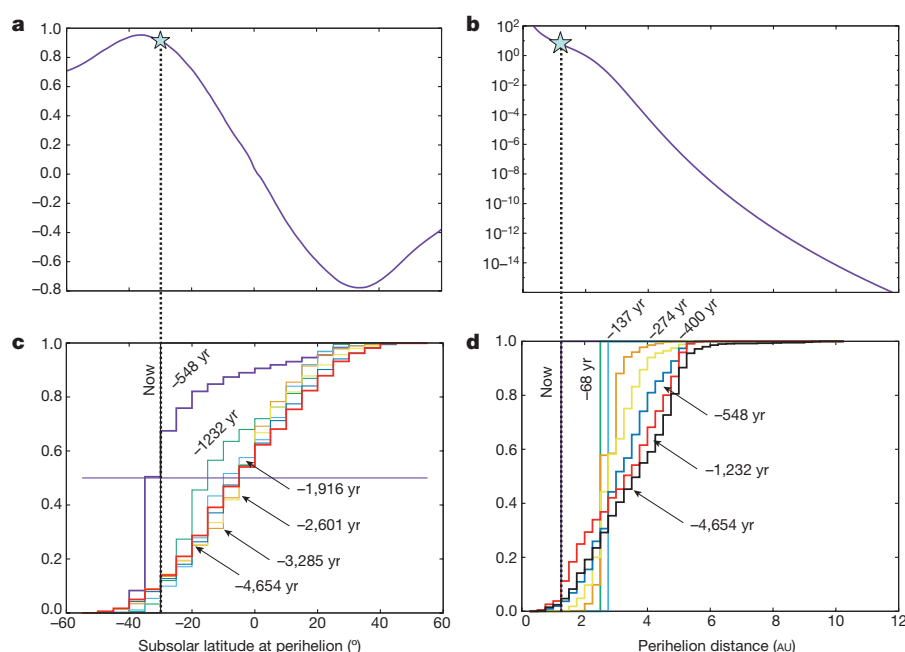


Figure 4 | Dynamical variation of factors controlling spin acceleration. **a**, Profile of the relative spin acceleration as a function of the subsolar latitude at perihelion, ϕ_p . **b**, Intensity of sublimation (proportional to rotational acceleration) as a function of perihelion distance³⁰. **c**, **d**, Cumulative distribution of ϕ_p and perihelion distance, respectively, obtained from 1,000 Monte Carlo simulations, starting with the present-day

state and uncertainties and propagating backwards in time for 5 ka (see Methods). The y-axes show: **a**, rotational acceleration relative to an ideal value (present rotational acceleration is indicated by the star); **b**, sublimation intensity relative to an ideal value (again, the star indicates present scaling); **c**, **d**, cumulative distribution function of the latitude (**c**) or radius (**d**).

JFCs, this proposed mechanism is common to the population as a whole.

Tidal forces experienced during close Jupiter flybys could also be responsible for the formation of the observed cracks; however, with an elastic FEM analysis we find that 67P must pass within three radii of Jupiter to experience strong enough tidal forces. Our orbital simulations show that such close flybys are very unlikely to have occurred over the past 5 ka, with none occurring within our sample. Other processes such as thermal fatigue and sublimation are unlikely to have formed the observed cracks on the Hapi region, as the straight cracks are not polygonal—a typical morphology resulting from thermal fatigue (Extended Data Fig. 1a)—and are not eroded by sublimation⁹. Our plastic FEM analysis shows that the parallel set of cracks on the Hathor region²³ (Extended Data Fig. 1b) cannot be due to rotational failure, because the reported compressive strength^{15,16} is much higher than the modelling-derived value that causes compressive failure (Fig. 3). This reinforces the idea that these fractures pre-date the merger of the lobes or are due to earlier reconfiguration cycles.

Finally, bilobate nuclei observed by spacecraft encounters or ground-based radar have component volume ratios consistent with their nuclei being trapped in a similar cycle to that of 67P's nucleus. For bilobate nuclei with a volume ratio between their lobes larger than about 0.2, the total energy of these systems will be negative after fission. This means that they are bounded in a similar way to some rubble pile asteroids^{24,25}; however additional sublimation effects could further erode or spin up the individual lobes before re-impact²⁶. Taking material density to be constant, we computed the volume ratios of the imaged bilobate nuclei of comets 1P/Halley, 8P/Tuttle, 19P/Borrelly, 67P and 100P/Hartley 2; we found that all of these nuclei had a volume ratio higher than 0.2 (see Extended Data Fig. 7 and Methods). Observed nuclei with a single component might either be primordial, or have been part of a multi-component object, from which smaller parts are more easily shed^{18,27}.

The reconfiguration cycles of short-period cometary nuclei constitute a new evolutionary process that could affect their ability to survive during migration into the inner solar system. The evolution sequences proposed here might enhance erosion and reduce the lifetime of

cometary nuclei, potentially explaining the negligible cometary flux found during the late heavy bombardment^{7,8,28}.

Online Content Methods, along with any additional Extended Data display items and Source Data, are available in the online version of the paper; references unique to these sections appear only in the online paper.

Received 14 January; accepted 14 March 2016.

Published online 1 June 2016.

1. Rickman, H. *et al.* Comet 67P/Churyumov-Gerasimenko: constraints on its origin from OSIRIS observations. *Astron. Astrophys.* **583**, A44 (2015).
2. Guilbert-Lepoutre, A. *et al.* On the evolution of comets. *Space Sci. Rev.* **197**, 271–296 (2015).
3. Chen, J. & Jewitt, D. On the rate at which comets split. *Icarus* **108**, 265–271 (1994).
4. Boehnhardt, H. in *Comets II* (eds Festou, M., Keller, H. U. & Weaver, H. A.) 301–316 (Univ. Arizona Press, 2004).
5. Keller, H. U. *et al.* Isolation, erosion, and morphology of comet 67P/Churyumov-Gerasimenko. *Astron. Astrophys.* **583**, A34 (2015).
6. Massironi, M. *et al.* Two independent and primitive envelopes of the bilobate nucleus of comet 67P. *Nature* **526**, 402–405 (2015).
7. Kring, D. A. & Cohen, B. A. Cataclysmic bombardment throughout the inner solar system 3.9–4.0 Ga. *J. Geophys. Res.* **107**, 4 (2002).
8. Strom, R. G., Malhotra, R., Ito, T., Yoshida, F. & Kring, D. A. The origin of planetary impactors in the inner solar system. *Science* **309**, 1847–1850 (2005).
9. Sierks, H. *et al.* On the nucleus structure and activity of comet 67P/Churyumov-Gerasimenko. *Science* **347**, <http://dx.doi.org/10.1126/science.aaa1044> (2015).
10. El-Maarry, M. R. *et al.* Fractures on comet 67P/Churyumov-Gerasimenko observed by Rosetta/OSIRIS. *Geophys. Res. Lett.* **42**, 5170–5178 (2015).
11. Mottola, S. *et al.* The rotation state of 67P/Churyumov-Gerasimenko from approach observations with the OSIRIS cameras on Rosetta. *Astron. Astrophys.* **569**, L2 (2014).
12. Barnes, T. & Farnham, T. Shape models of 67P/Churyumov-Gerasimenko v1.0, RO-C-multi-5-67P-shape-v1.0. NASA Planetary Data System and ESA Planetary Science Archive <http://pdssbn.astro.umd.edu/holdings/ro-c-multi-5-67p-shape-v1.0/dataset.html> 2015.
13. Preusker, F. *et al.* Shape model, reference system definition, and cartographic mapping standards for comet 67P/Churyumov-Gerasimenko—stereo-photogrammetric analysis of Rosetta/OSIRIS image data. *Astron. Astrophys.* **583**, A33 (2015).
14. Pollard, D. D. & Fletcher, R. C. *Fundamentals of Structural Geology* 1st edn (Cambridge Univ. Press, 2005).

15. Biele, J. *et al.* The landing(s) of Philae and inferences about comet surface mechanical properties. *Science* **349**, aaa9816–aaa9816-6 (2015).
16. Groussin, O. *et al.* Gravitational slopes, geomorphology, and material strengths of the nucleus of comet 67P/Churyumov-Gerasimenko from OSIRIS observations. *Astron. Astrophys.* **583**, A32 (2015).
17. Steckloff, J. K. *et al.* Dynamic sublimation pressure and the catastrophic breakup of comet ISON. *Icarus* **258**, 430–437 (2015).
18. Scheeres, D. J. Rotational fission of contact binary asteroids. *Icarus* **189**, 370–385 (2007).
19. Jutzi, M. & Asphaug, E. The shape and structure of cometary nuclei as a result of low-velocity accretion. *Science* **348**, 1355–1358 (2015).
20. Keller, H. U., Mottola, S., Skorov, Y. & Jorda, L. The changing rotation period of comet 67P/Churyumov-Gerasimenko controlled by its activity. *Astron. Astrophys.* **579**, L5 (2015).
21. Scheeres, D. J. The dynamical evolution of uniformly rotating asteroids subject to YORP. *Icarus* **188**, 430–450 (2007).
22. Levison, H. F. & Duncan, M. J. The long-term dynamical behavior of short-period comets. *Icarus* **108**, 18–36 (1994).
23. Thomas, N. *et al.* Morphological diversity of comet 67P/Churyumov-Gerasimenko. *Science* **347**, aaa0440-1–aaa0440-6 (2015).
24. Pravec, P. *et al.* Formation of asteroid pairs by rotational fission. *Nature* **466**, 1085–1088 (2010).
25. Jacobson, S. A. & Scheeres, D. J. Dynamics of rotationally fissioned asteroids: source of observed small asteroid systems. *Icarus* **214**, 161–178 (2011).
26. Steckloff, J. K. & Jacobson, S. A. The formation of striae with cometary dust tails by a sublimation-driven YORP-like effect. *Icarus* **264**, 160–171 (2016).
27. Hirabayashi, M., Sánchez, D. P. & Scheeres, D. J. Internal structure of asteroids having surface shedding due to rotational instability. *Astrophys. J.* **808**, 63 (2015).
28. Marchi, S. *et al.* The onset of the lunar cataclysm as recorded in its ancient crater populations. *Earth Planet. Sci. Lett.* **325–326**, 27–38 (2012).
29. Kohnke, P. 2009, *Theory Reference for the Mechanical APDL and Mechanical Applications*, 12th edn (ANSYS, Inc.).
30. Marsden, B. G., Sekanina, Z. & Yeomans, D. K. Comets and nongravitational forces. *Astron. J.* **78**, 211–225 (1973).

Acknowledgements M.H. acknowledges the use of ANSYS Academic APDL, version 15.03. D.J.S. and M.H. were supported by NASA grants NNX14AL16G, NNX14AB08G and NNA14AB03A. S.R.C. carried out his work at the Jet Propulsion Laboratory, California Institute of Technology under a contract with NASA. S.M. acknowledges support by the Jet Propulsion Laboratory.

Author Contributions M.H. conducted structure analysis. D.J.S., S.R.C., J.W.M. and M.H. analysed orbital and spin evolution. S.P.N. produced reduced data sets for the analysis. M.H., D.J.S., S. Ma., J.S., S. Mo. and T.B. discussed the meaning of the discovered relationships. M.H. wrote the paper with guidance from D.J.S. T.B. generated high-resolution figures. All authors commented on the manuscript.

Author Information Reprints and permissions information is available at www.nature.com/reprints. The authors declare no competing financial interests. Readers are welcome to comment on the online version of the paper. Correspondence and requests for materials should be addressed to M.H. (thirabayashi@purdue.edu) or D.J.S. (scheeres@colorado.edu).

METHODS

Finite-element models. The meshes used here consist of ten-node tetrahedral elements, generated by using the shape model made on the basis of OSIRIS imagery. The shape model used is a reduced-resolution version of the SHAP 2 model¹², which consists of 7,597 vertices and 15,190 faces. Using this polygonal model, we developed FEM mesh models by a Delaunay triangulation algorithm³¹ and then improved their quality by modifying the shape of each element. The mesh models finally obtained consist of a 105,006-node mesh and a 21,289-node mesh for plastic FEM and elastic FEM, respectively.

We assumed the nucleus to be rotating uniformly in space and to be affected only by gravitational and centrifugal forces. We followed the technique of ref. 32, defining the boundary condition such that six degrees of freedom in node displacement were constrained to cancel out translational and rotational motion. To consider the tidal effect of Jupiter on the 67P nucleus, we also computed the tidal force components that can distort the structure of the nucleus, and applied the elastic FEM technique of ref. 33. Furthermore, we assumed isotropic deformation.

We used an elastic FEM to determine where failure appears initially in the nucleus, as in ref. 33. We calculated elastic solutions for spin periods from 5 h to 12.4 h, with a 0.5-h interval between simulations. When tensile peaks first appear on the surface at a given spin period, we stored the locations and the maximum components of the principal stress.

We carried out a plastic FEM to determine the final failure types of the nucleus. We simulated the same spin period cases as in the elastic computation³². We modelled the yield condition of cometary materials by the Drucker–Prager criterion³⁴:

$$f(\sigma_{ij}) = \alpha I_1 + \sqrt{J_2} - k = 0$$

where i and j are indices ranging from 1 to 3, I_1 and J_2 are the stress invariants, and α and k are the parameters defined using a friction angle, θ , and cohesive strength, c , as follows:

$$\alpha = \frac{2 \sin \theta}{\sqrt{3} (3 - \sin \theta)}$$

$$k = \frac{6c \cos \theta}{\sqrt{3} (3 - \sin \theta)}$$

Because the details of a flow law for cometary materials are unknown, we simplified our model by using an associated flow law^{32,34}:

$$\dot{\epsilon}_{ij}^p = \dot{\lambda} \frac{\partial f(\sigma_{ij})}{\partial \sigma_{ij}}$$

where $\dot{\epsilon}_{ij}^p$ is the plastic ('p') strain rate, σ_{ij} is the stress component, and $\dot{\lambda}$ is a constant rate (the scale factor of the strain rate).

We assumed an elastic/perfectly plastic flow law in the analysis. This choice guarantees that failure regions in the actual case are wider than those in our results. The plastic strain rate of brittle materials is faster than that of elastic/perfectly plastic materials^{35,36}. Early Rosetta results and observations suggest that materials in the 67P nucleus are highly brittle^{10,23,37}.

We fixed Young's modulus, Poisson's ratio and the angle of internal friction at 1.0×10^7 Pa, 0.25 and 35° , respectively^{38,39}. These are typical values for geological materials, although the results obtained are not a strong function of them^{33,40}. Also, in our FEM analyses we assumed that the distribution and properties of the material are uniform in a given region and that the nucleus has no cracks initially.

Identifying failure types.

Boundary between types I and II. We determined the boundary between failure types I and II by searching for the spin periods at which tensile stress peaks appear on the surface of the neck. Because the elastic FEM simulations indicate that such peaks always show up first at the regions comparable to the locations of the observed cracks, we computed elastic solutions for the different spin period cases, and found the spin period condition at which the stress becomes tensile in the neck. Using the plastic FEM analysis, we identified that a type I failure is characterized by compression, while a type II failure includes tensional failure on side A.

Boundary between types II and III, and crack propagation. A shorter spin period causes plastic deformations to progress across the nucleus neck. The presence of the straight cracks in the present configuration indicates that this failure mode has begun, but has not progressed across the entire region.

Because the existing cracks cause stress to be concentrated at their tips, we also investigated the possibility of crack propagation resulting from tension. For mode I cracks, a crack-tip stress is expressed as a function of $K_I/\sqrt{2\pi r}$, where K_I is a mode I stress-intensity factor, and r is radial distance from the crack-tip⁴¹. This form indicates that a tensile loading always gives a non-zero growth rate^{42–45}. Therefore, we

conclude that when centrifugal forces exceed gravitational forces in the neck, existing cracks will propagate across the neck, and the body will split into two components. We defined this force balance point as the boundary between failure types II and III.

To demonstrate that this force balance condition leads to crack propagation across the neck, we use the 535 kg m^{-3} uniform density case as an example. The force balance condition was obtained at a 7-h rotation period. From the elastic solution for the neck cross-section, we confirmed that 90% of the region reaches tension (Extended Data Fig. 2). Although 10% of the cross-section is still compressive as a result of a bending moment, as the cracks propagate, the compressive region eventually disappears.

Hill stability calculation. We analysed the initial conditions for a fissioned system to determine the Hill stability condition. If a system is Hill stable, then the orbital motions of the separated components are mutually bounded and cannot escape⁴⁶. For a system initiated from a cohesive fission, as with 67P, the generic fate is for the components to eventually collide with one another, albeit at low speeds that will be less than escape speed. We derive a sufficient condition for Hill stability, which is that the total energy (including translational and rotational kinetic energy plus mutual potential energy) is negative. If the spin period at the boundary between a type II and a type III failure satisfies the sufficient condition, then the system is Hill stable.

To obtain the shortest spin period for the sufficient condition, we first sliced the nucleus through its neck to consider the head and the body to be separated components. Then, we numerically calculated the total energy of the system, which is given as:

$$E = \frac{1}{2} \frac{M_1 M_2}{M_1 + M_2} \mathbf{v} \cdot \mathbf{v} + \frac{1}{2} \boldsymbol{\omega} \cdot (I_1 + I_2) \cdot \boldsymbol{\omega} - U$$

where E is the total energy, U is the mutual potential, \mathbf{v} is the relative velocity vector and equals the mutual spin rate times the distance between the mass centres, M is the mass of component 1 or 2, I is the inertia tensor for component 1 or 2, and $\boldsymbol{\omega}$ is the angular velocity vector, assumed to be oriented along the maximum moment of inertia of the 67P nucleus. Thus the spin period at which the total energy becomes zero can be solved for.

Variation in the bulk density. The Rosetta-derived bulk density of 67P's nucleus is reported to be $535 \pm 35 \text{ kg m}^{-3}$ (ref. 13). We investigated how the uncertainty range in this measurement changes the results of our structural analysis. Assuming a constant material density, we computed the failure type and conditions for the cases of bulk densities of 500 kg m^{-3} and 570 kg m^{-3} (Extended Data Fig. 3). To obtain proper sizes of the nucleus for these cases, we fixed the total mass at $1.0 \times 10^{13} \text{ kg}$. Because of this choice, the size for the 500 kg m^{-3} bulk density case is 7% larger than the original size, while that for the 570 kg m^{-3} bulk density case is 6% smaller than the original size. The results showed that all the cases experience the same failure types—that is, types I, II and III—and that the spin period range of type II changes by only 0.5 h.

The hypothesis of a gentle contact also implies that the bulk density at the contact zone where the two lobes touch may differ from the bulk density of the individual lobes^{1,6,19}. Fixing the size and mass as before, we tested two extreme cases that account for high and low bulk density of the neck. The first case considers that the nucleus has a 300-m-width neck with a zero bulk density. The second case includes the 300-m-width neck with a bulk density of $1,000 \text{ kg m}^{-3}$. The elastic analysis identified two stress peaks on the spots comparable to those for the uniform density case (Extended Data Fig. 4).

Considering the same spin period cases as Fig. 2—that is, 5 h, 8 h and 12.4 h—we confirmed that these heterogeneous density cases also undergo the same failure types as in the homogeneous conditions (Extended Data Figs 5 and 6). To obtain plastic solutions for these cases, we determined critical cohesive strengths for different spin periods (Extended Data Fig. 3). Because we fix the mass and volume, if the neck region has a low (high) density, the bulk density of the lobes becomes high (low). Such density conditions produce strong (weak) centrifugal forces and weak (strong) gravitational forces acting on the neck, because of the relation of the distance between mass elements³³. These different configurations cause the low-density neck and the high-density neck to have higher cohesive strength or lower cohesive strength, respectively, in order to keep the original shape. On the basis of this consideration, we chose the critical cohesive strengths for the 5-h and 8-h cases. However, for the 12.4-h case the cohesive strength for failure is too small to follow such trends.

Spin acceleration as a function of subsolar latitude. In the text, the spin acceleration is given as a function of the subsolar latitude (ϕ_p) of the nucleus at perihelion. For each latitude, this profile is made by computing the insolation of each surface facet with respect to the Sun model (accounting for shadowing), summing the net torque from the normal forces on all lit facets of the SHAP 2 shape, and then

averaging it over one rotation^{21,47}. The resulting curve (Fig. 4a) shows how the sign and strength of the rotational acceleration over one orbit change with the latitudinal location of the Sun. Combining this curve with the results of the Monte Carlo analysis of orbital evolution (see below) establishes that, over time, the spin acceleration varies both positively and negatively in almost the same proportions. To avoid additional uncertainties in our analysis, we fixed the spin axis at right ascension (RA) = 69.3° and declination (Dec.) = 64.1° (ref. 9). Even if the spin axis is constant in the inertial frame, ϕ_p varies substantially owing to the orbital evolution.

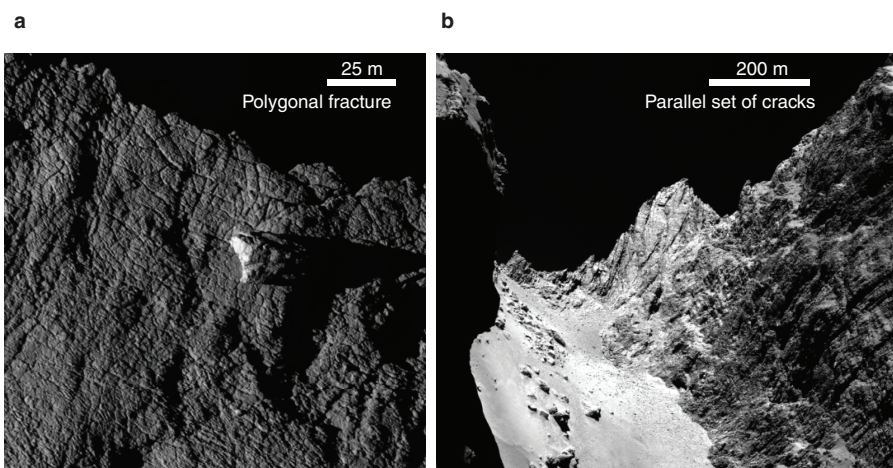
Monte Carlo analysis of orbital evolution. We propagated 1,000 orbital clones of 67P to reveal the range of orbital evolution during the past 5 ka. The orbital solution (designated JPL K084/23) included six orbital elements and three non-gravitational acceleration parameters, namely A1, A2, and A3 (in the formulation of ref. 30). The data set for the orbital solution extends from 6 July 1988 to 17 July 2015, and includes 4,072 observations of the comet's right ascension and declination. To account for the potentially substantial long-term evolution in non-gravitational accelerations, we randomly drew clones from a Gaussian distribution ten times broader than that derived from the *a posteriori* nine-by-nine covariance matrix associated with the orbit estimate. Each clone was propagated 5 ka backwards in time using a dynamical model that incorporates the point mass gravitational effects of the Sun, eight planets, the Moon, and four massive minor planets (1 Ceres, 2 Pallas, 4 Vesta and 134340 Pluto). General-relativity perturbations from the Sun's monopole were included, as were the non-gravitational accelerations on the comet according to the randomly drawn parameters (A1, A2, A3). For each clone, we recorded the osculating orbital elements at 100-day intervals and the close approach circumstances for all Jupiter encounters within 0.5 au. Note that earlier studies¹ did not include the detailed perturbation effects implemented in our model.

Computation of the volume ratio. There are seven reported cometary nuclei whose shapes have been detected, and five out of them are considered to have bilobate shapes⁵. Assuming a constant material density, we computed the volume ratio of the smaller component to the larger one²⁴ for each bilobate object (Extended Data Fig. 7) as a proxy for a volume ratio.

For comets 67P and 103P/Hartley 2, we used the degraded SHAP 2 model¹² and the EPOXI-derived shape model⁴⁸, respectively. For each body, we searched for the smallest cross-section and split the body through it. Then, we calculated the volume of each component. For 1P/Halley⁴⁹ and 19P/Borrelly⁵⁰, only a few images were available. After finding their neck regions, we cut the bodies through them. Then, assuming that the lengths in the minimum and intermediate principal axes are equal, we computed their volume ratios. 8P/Tuttle was observed by ground-based radar, and its shape was well determined⁵¹; therefore, we referred directly to the reported values.

Code availability. The input file to ANSYS for elastic computation for the 9-h case is available upon request from M.H. (thirabayashi@purdue.edu). The code used to compute the dependence of generated torque on the subsolar latitude is available upon request from J.W.M. (jay.mcmahon@colorado.edu). We have opted not to make the orbital evolution code available because it is proprietary and its release requires a licensing agreement.

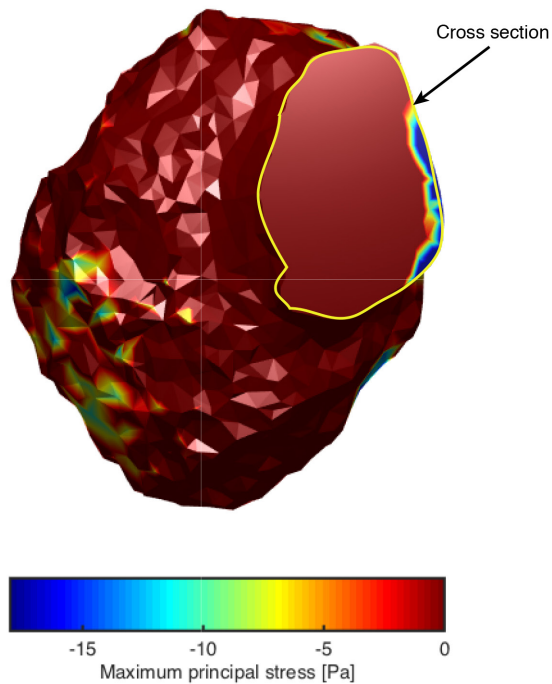
31. Si, H. TetGen, a Delaunay-based quality tetrahedral mesh generator. *ACM Trans. Math. Software* **41**, 11 (2015).
32. Hirabayashi, M. & Scheeres, D.J. Stress and failure analysis of rapidly rotating asteroid (29075) 1950 DA. *Astrophys. J. Lett.* **798**, L8 (2015).
33. Hirabayashi, M. & Scheeres, D. J. Analysis of asteroid (216) Kleopatra using dynamical and structural constraints. *Astrophys. J.* **780**, 160 (2014).
34. Chen, W. F. & Han, D. J. *Plasticity for Structural Engineers* Ch. 2 (Springer, 1988).
35. Byerlee, J. Friction of rocks. *Pure Appl. Geophys.* **116**, 615–626 (1978).
36. Willam, K. J. & Warnke, E. P. Constitutive model for the triaxial behaviour of concrete. In *IABSE Reports of the Working Commissions* **19**, III-1–III-30 (1974).
37. El-Maarry, M. R. *et al.* Regional surface morphology of comet 67P/Churyumov-Gerasimenko from Rosetta/OSIRIS images. *Astron. Astrophys.* **583**, A26 (2015).
38. Lambe, T. W. & Whitman, R. V. *Soil Mechanics* Ch. 11, 12 (John Wiley, 1969).
39. Jaeger, J. C., Cook, N. G. W. & Zimmerman, R. *Fundamentals of Rock Mechanics* Ch. 6 (John Wiley, 2009).
40. Hirabayashi, M. Failure modes and conditions of a cohesive, spherical body due to YORP spin-up. *Mon. Not. R. Astron. Soc.* **454**, 2249–2257 (2015).
41. Unger, D. J. *Analytical Fracture Mechanics* 25–28 (Dover, 1995).
42. Gross, D. & Seelig, T. *Fracture Mechanics* Ch. 2, 4 (Springer, 2011).
43. Wiederhorn, S. M. & Bolz, L. H. Stress corrosion and static fatigue of glass. *J. Am. Ceram. Soc.* **53**, 543–548 (1970).
44. Goodman, D. J. Critical stress intensity factor (K_{IC}) measurements at high loading rates for polycrystalline ice in *Physics and Mechanics of Ice* 129–146 (Springer, 1980).
45. Atkinson, B. K. Subcritical crack growth in geological materials. *J. Geophys. Res.* **89**, 4077–4114 (1984).
46. Scheeres, D. J. Stability in the full two body problem. *Celestial Mech. Dyn. Astron.* **83**, 155–169 (2002).
47. McMahon, J. W. & Scheeres, D. J. Improving space object catalog maintenance through advances in solar radiation pressure modeling. *J. Guid. Control Dyn.* **38**, 1366–1381 (2015).
48. Farnham, T. L. & Thomas, P. C. Plate shape model of comet 103P/Hartley 2 V1.0, DIF-C-HRIV/MRI-5-HARTLEY2-SHAPE-V1.0. *NASA Planetary Data System* <https://pds.nasa.gov> (2013).
49. Sagdeev, R. Z. *et al.* Television observations of comet Halley from Vega spacecraft. *Nature* **321**, 262–266 (1986).
50. Keller, H. U., Britt, D., Buratti, B. J. & Thomas, N. In situ observations of cometary nuclei in *Comet II* (eds Festou, M. C., Keller, H. U. & Weaver, H. A.) 211–222 (Univ. Arizona Press, 2004).
51. Harmon, J. K., Nolan, M. C., Giorgini, J. D. & Howell, E. S. Radar observations of 8P/Tuttle: a contact-binary comet. *Icarus* **207**, 499–502 (2010).



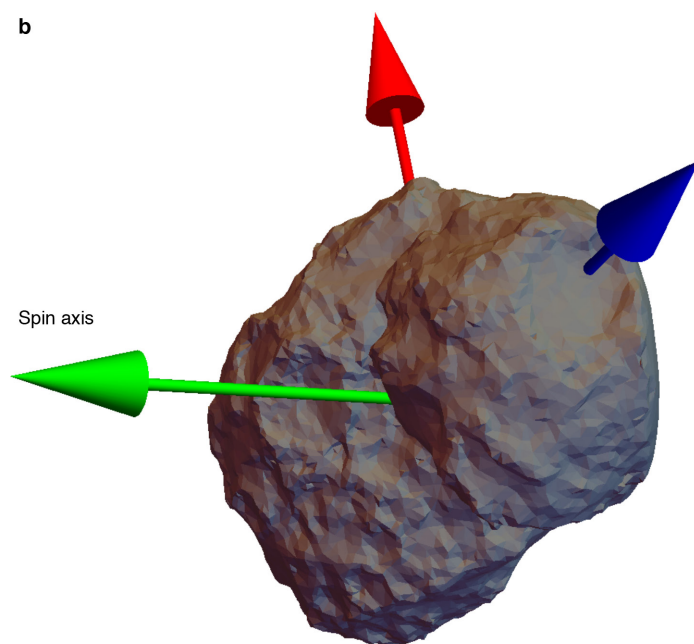
Extended Data Figure 1 | Different types of crack observed on the 67P nucleus. **a**, Polygonal cracks on the Apis region at the edge of the large lobe; these cracks are presumably generated by thermal contraction¹⁰. **b**, Parallel sets of cracks on the Hathor region²³. Images available at

<http://blogs.esa.int/rosetta/2015/08/18/do-comet-fractures-drive-surface-evolution/> (**a**) and at <http://sci.esa.int/rosetta/55310-hapi-and-hathor/> (**b**). Image credits: ESA/Rosetta/MPS for OSIRIS Team MPS/UPD/LAM/IAA/SSO/INTA/UPM/DASP/IDA.

a

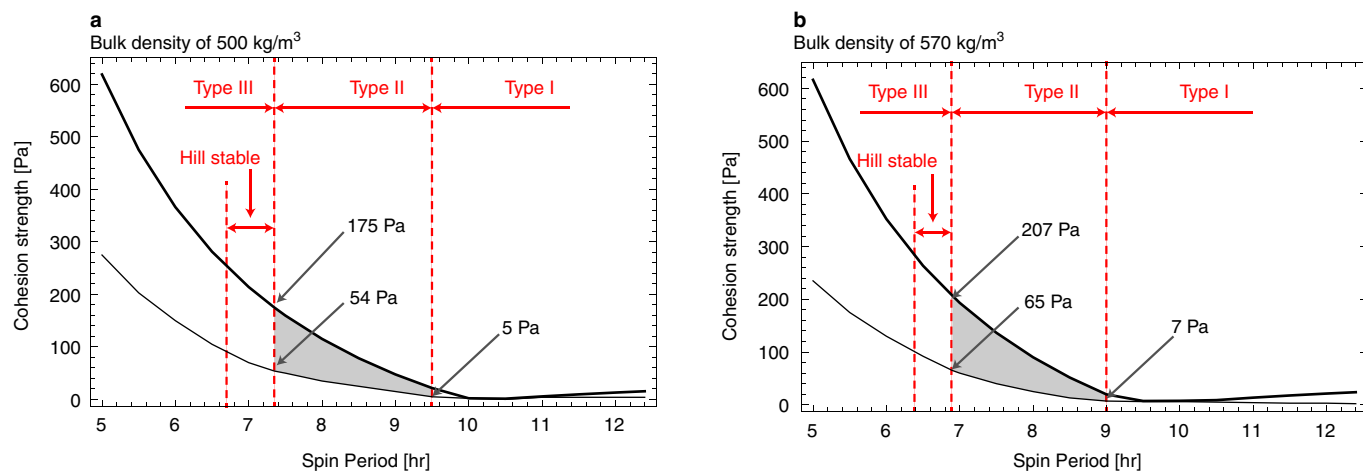


b

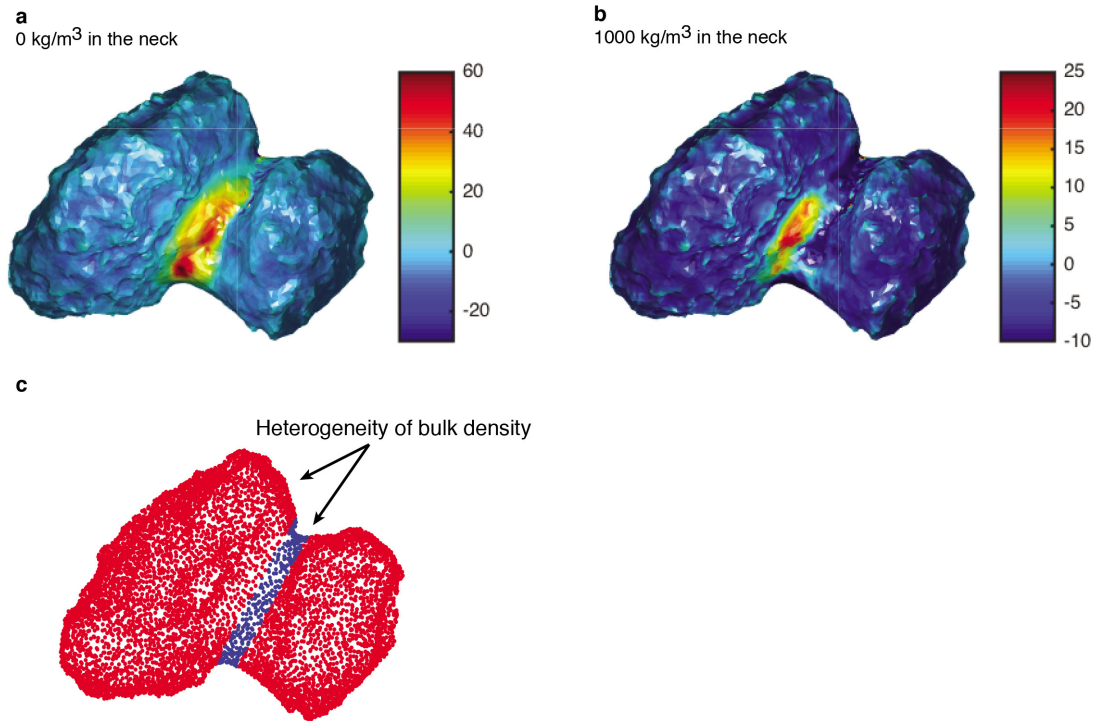


Extended Data Figure 2 | Tensile regions on the neck cross-section at the force balance point. The bulk density is assumed to be 535 kg m^{-3} . **a**, The maximum component of the principal stress at the force balance point, which is 7 h. The region enclosed by the yellow line indicates the

neck cross-section. The red region indicates tensile regions. **b**, Body orientation. Green arrow, maximum moment of inertia axis; red arrow, intermediate moment of inertia axis; blue arrow, minimum moment of inertia axis.

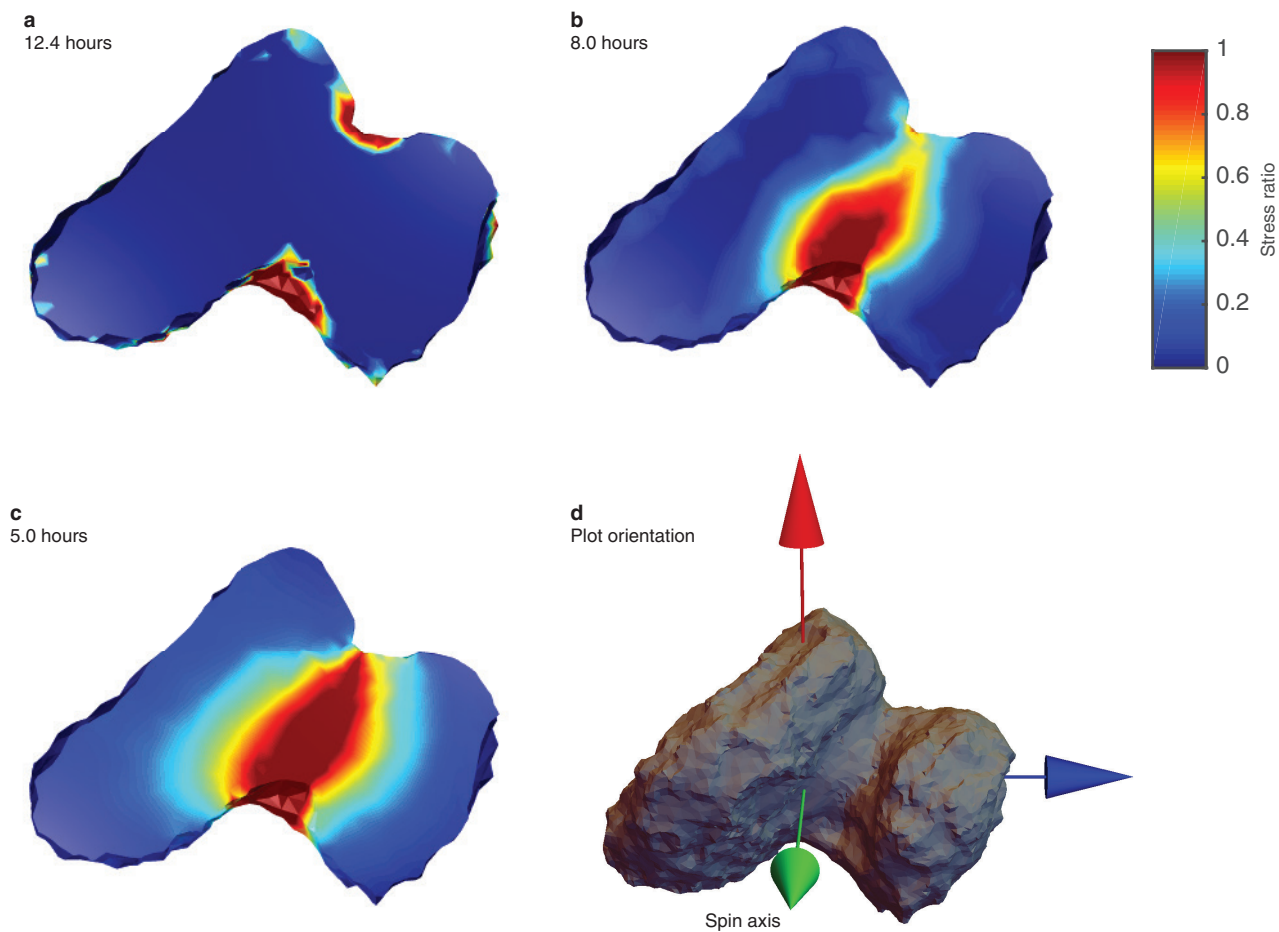


Extended Data Figure 3 | Failure types and conditions for different bulk density cases. **a**, The bulk density is 500 kg m^{-3} . **b**, The bulk density is 570 kg m^{-3} .



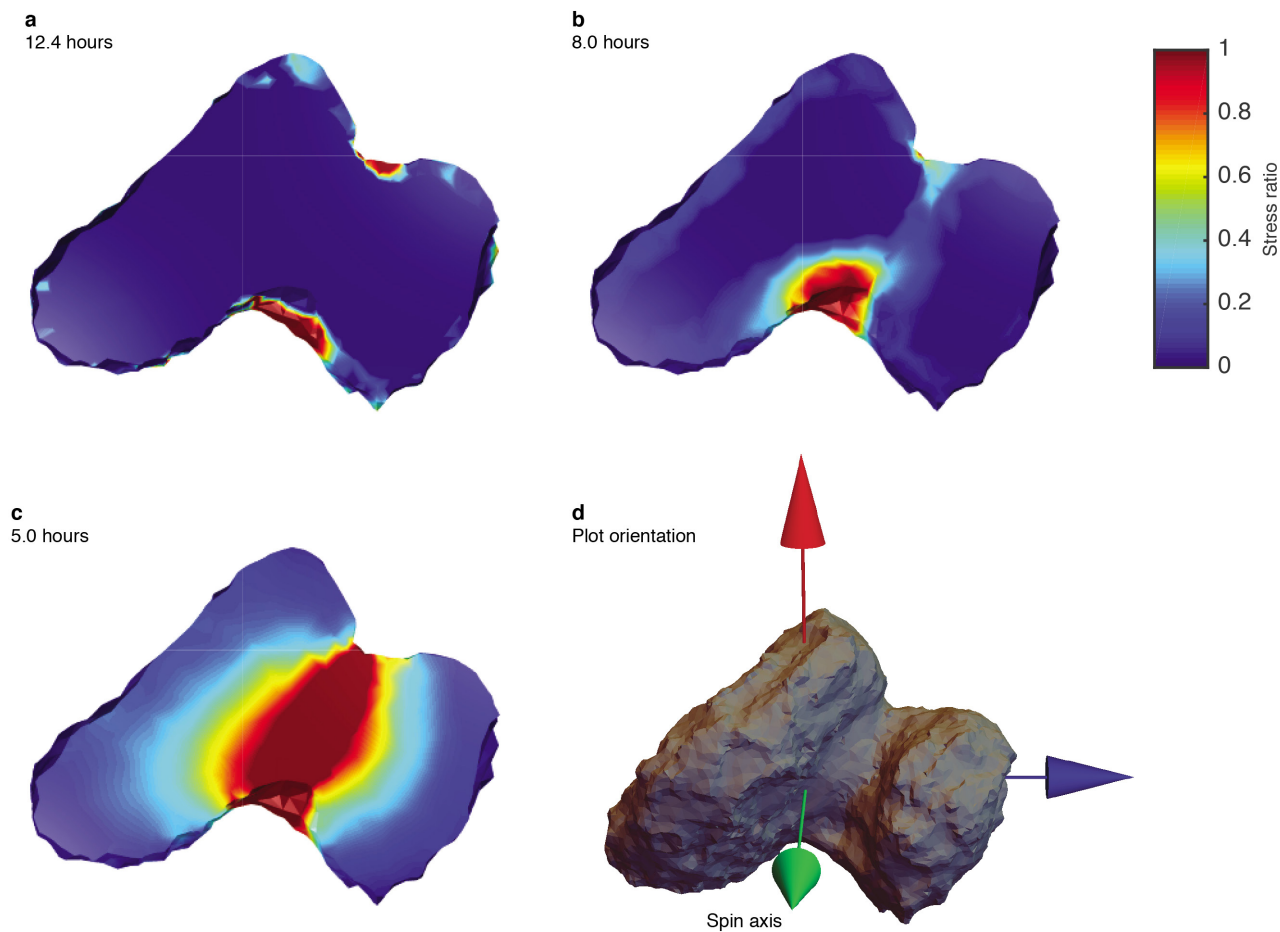
Extended Data Figure 4 | Elastic analysis for heterogeneous density cases. The spin period was fixed at 9 h. The contour plots show the maximum component of the principal stress, with units of pascals. **a**, The bulk density of the neck is zero. The other regions have a bulk

density of 578 kg m⁻³. **b**, The bulk density of the neck is 1,000 kg m⁻³, leading to a bulk density of 498 kg m⁻³ in the other regions. **c**, Schematic plot of the bulk density distribution.



Extended Data Figure 5 | Plastic analysis for a neck density of 0 kg m^{-3} . The cross-sections displayed are the same as in Fig. 2. The averaged density is fixed at 535 kg m^{-3} . The colours describe the stress ratio.

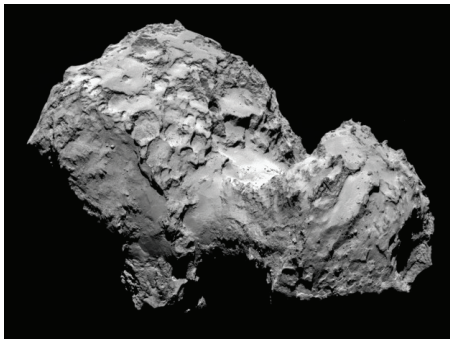
a, Type I failure at 12.4 h. The cohesive strength used was 4 Pa. **b**, Type II failure at 8 h. The cohesive strength was 45 Pa. **c**, Type III failure at 5 h. The cohesive strength was 300 Pa. **d**, Body orientation.



Extended Data Figure 6 | Plastic analysis for a bulk density of $1,000 \text{ kg m}^{-3}$. The cross-sections displayed are the same as in Fig. 2. The averaged density is fixed at 535 kg m^{-3} . The colours describe the stress

ratio. **a**, Type I failure at 12.4 h. The cohesive strength used was 5 Pa. **b**, Type II failure at 8 h. The cohesive strength was 25 Pa. **c**, Type III failure at 5 h. The cohesive strength was 200 Pa. **d**, Body orientation.

a
67P/Churyumov-Gerasimenko
Volume ratio: 0.58



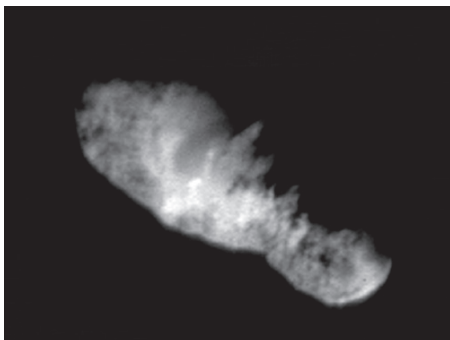
b
103P/Hartley 2
Volume ratio: 0.32



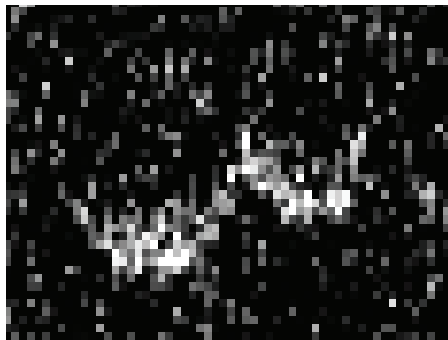
c
1P/Halley
Volume ratio: 0.30



d
19P/Borrelly
Volume ratio: 0.22



e
8P/Tuttle
Volume ratio: 0.47



Extended Data Figure 7 | Volume ratios of cometary nuclei imaged from spacecraft encounters or ground-based radar. **a**, 67P/Churyumov-Gerasimenko. Image credits: ESA/Rosetta/MPS for OSIRIS Team MPS/UPD/LAM/IAA/SSO/INTA/UPM/DASP/IDA. **b**, 103P/Hartley 2. Image credit: EPOXI mission MRI-VIS frame 5004057 from NASA's Planetary

Data System. **c**, 1P/Halley. Image credit: ESA/MPS. **d**, 19P/Borrelly. Image credit: PIA03500, Courtesy by NASA/JPL-Caltech. **e**, 8P/Tuttle. Image credit: Arecibo Observatory scans 800300017-19; resolution $1\ \mu\text{s} \times 0.5\ \text{Hz}$ (see ref. 51 for more information).

Mean first-passage times of non-Markovian random walkers in confinement

T. Guérin¹, N. Levernier², O. Bénichou² & R. Voituriez^{2,3}

The first-passage time, defined as the time a random walker takes to reach a target point in a confining domain, is a key quantity in the theory of stochastic processes¹. Its importance comes from its crucial role in quantifying the efficiency of processes as varied as diffusion-limited reactions^{2,3}, target search processes⁴ or the spread of diseases⁵. Most methods of determining the properties of first-passage time in confined domains have been limited to Markovian (memoryless) processes^{3,6,7}. However, as soon as the random walker interacts with its environment, memory effects cannot be neglected: that is, the future motion of the random walker does not depend only on its current position, but also on its past trajectory. Examples of non-Markovian dynamics include single-file diffusion in narrow channels⁸, or the motion of a tracer particle either attached to a polymeric chain⁹ or diffusing in simple¹⁰ or complex fluids such as nematics¹¹, dense soft colloids¹² or viscoelastic solutions^{13,14}. Here we introduce an analytical approach to calculate, in the limit of a large confining volume, the mean first-passage time of a Gaussian non-Markovian random walker to a target. The non-Markovian features of the dynamics are encompassed by determining the statistical properties of the fictitious trajectory that the random walker would follow after the first-passage event takes place, which are shown to govern the first-passage time kinetics. This analysis is applicable to a broad range of stochastic processes, which may be correlated at long times. Our theoretical predictions are confirmed by numerical simulations for several examples of non-Markovian processes, including the case of fractional Brownian motion in one and higher dimensions. These results reveal, on the basis of Gaussian processes, the importance of memory effects in first-passage statistics of non-Markovian random walkers in confinement.

It has long been recognized that the kinetics of reactions is influenced by the properties of the transport process that brings reactants into contact^{1,2}. Transport can even be the rate-limiting step, and in this diffusion-controlled regime, the reaction kinetics is quantified by the properties of the first encounter between molecules². First-passage time (FPT) properties have been studied intensively in the past few decades^{1,3,15} and are now well understood when the stochastic motion of the reactants satisfies the Markov property, that is, is memoryless (uninfluenced by previous states, only by the current state). Under this assumption, exact asymptotic formulas characterizing the FPT of a tracer to a target located inside^{6,7,16} or at the boundary¹⁵ of a large confining volume have been obtained. These studies reveal that the geometrical parameters, as well as the complex properties of the stochastic transport process (such as subdiffusion), can have a strong impact on the reaction kinetics^{3,6,7}.

However, as a general rule, the dynamics of a given reactant results from its interactions with its environment and cannot be described as a Markov process. Indeed, although the evolution of the set of all microscopic degrees of freedom of the system is Markovian, the dynamics restricted to the reactant only is not. This is typically the case

for a tagged monomer, whose non-Markovian motion results from the structural dynamics of the whole chain to which it is attached^{9,17,18}, as observed for example, in proteins¹⁹. Other experimentally observed examples of non-Markovian dynamics include the diffusion of tracers in crowded narrow channels⁸ or in complex fluids such as nematics¹¹ or viscoelastic solutions^{13,14}. Even in simple fluids, hydrodynamic memory effects and thus non-Markovian dynamics have been recently observed¹⁰. So far, most theoretical results on the first-passage properties of non-Markovian processes have been limited to specific examples^{17,18,20–22} or to unconfined systems, where non-trivial persistence exponents characterizing its long time decay have been calculated^{23–25}. However, in many situations, geometric confinement has a key role in first-passage kinetics^{3,6,7}. Here, we develop a theoretical framework with which to determine the mean FPT of non-Markovian random walkers in confinement.

More precisely, we consider a non-Markovian Gaussian stochastic process $x(t)$, defined in unconfined space, which represents the position of a random walker at time t , starting from x_0 at $t = 0$. As the process is non-Markovian, the FPT statistics in fact depend also on $x(t)$ for $t < 0$. For the sake of simplicity, we assume that at $t = 0$ the process of constant average x_0 is in the stationary state (see Supplementary Information for more general initial conditions), with increments $x(t + \tau) - x(t)$ independent of t . The process $x(t)$ is then entirely characterized by its mean square displacement (MSD): $\psi(\tau) = \langle [x(t + \tau) - x(t)]^2 \rangle$. Such a quantity is routinely measured in single particle tracking experiments and in fact includes all the memory effects in the case of Gaussian processes. At long times, the MSD is assumed to diverge and thus, typically, the particle does not remain close to its initial position. Last, the process is continuous and non-smooth²⁵ ($\langle \dot{x}(t)^2 \rangle = +\infty$), meaning that the trajectory is irregular and of fractal type, similar to standard Brownian motion. Note that the class of random walks that we consider here covers a broad spectrum of non-Markovian processes used in physics, and in particular the examples mentioned above.

The random walker is now confined in a domain of volume V with reflecting walls, and we focus on its mean FPT to reach a target of position $x = 0$ (see Fig. 1). Note that this setting also gives access to the reaction kinetics of a reactant in the presence of a concentration $c = 1/V$ of targets in infinite space. Although the theory can be developed in any space dimension (see Supplementary Information for an explicit treatment of the two-dimensional and three-dimensional cases), it is presented here for clarity in one dimension (see Fig. 1b). Our starting point is the following generalization of the renewal equation¹

$$p(0, t) = \int_0^t d\tau F(\tau) p(0, t | \text{FPT} = \tau) \quad (1)$$

which results from a partition over the first-passage event. In this equation, $p(0, t)$ stands for the probability density of being at position $x = 0$ at time t , F is the FPT density and $p(0, t | \text{FPT} = \tau)$ is the probability that

¹Laboratoire Ondes et Matière d'Aquitaine, University of Bordeaux, Unité Mixte de Recherche 5798, CNRS, F-33400 Talence, France. ²Laboratoire de Physique Théorique de la Matière Condensée, CNRS/Université Pierre et Marie Curie, 4 Place Jussieu, 75005 Paris, France. ³Laboratoire Jean Perrin, CNRS/Université Pierre et Marie Curie, 4 Place Jussieu, 75005 Paris, France.

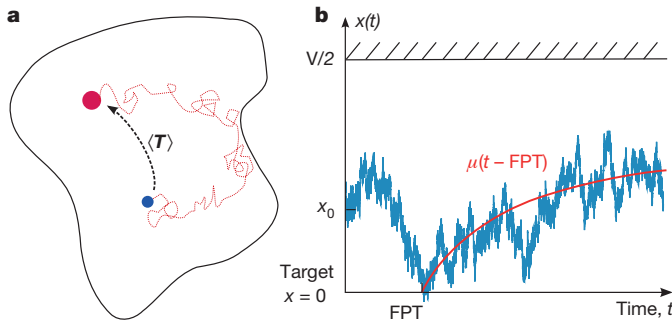


Figure 1 | Mean FPT of a random walker in confinement. **a**, What is the mean time $\langle T \rangle$ needed for a random walker starting at x_0 (blue dot) to reach a target (red dot) in a confining volume V ? Here we answer this question for random walkers with memory. **b**, In one dimension, the problem is to quantify the FPT of a random trajectory (in blue) in the presence of a reflecting boundary. We show here that $\langle T \rangle$ is controlled by the average trajectory $\mu(\tau)$ (in red) followed by the walker in the future of its first passage to the target.

$x=0$ at time t given that the first-passage event occurred at time τ . Owing to the confinement, for large times $p(0, t)$ reaches the stationary value $1/V$. Next, subtracting $1/V$ on both sides of equation (1) and integrating over t from 0 to infinity yields an exact expression for the mean FPT:

$$\frac{\langle T \rangle}{V} = \int_0^\infty dt [q_\pi(t) - p(0, t)] \quad (2)$$

where $q_\pi(t)dx$ is the probability of observing the random walker in the interval $[0, dx]$ at time t after the first passage to the target. The exact formula (2) is a generalization of the expression obtained for Markovian processes^{6,26} and holds for any non-smooth non-Markovian process

with stationary increments (even non-Gaussian). Even if $q_\pi(t)$ is a priori a non-trivial quantity because it is conditioned by first-passage events, this equation is of great practical use in determining the mean FPT, as shown below.

To proceed further, we first consider the large volume limit $V \rightarrow \infty$ (where it is assumed that all boundary points are sent to infinity) and, second, we assume that the stochastic process in the future of the FPT, defined by $y(t) \equiv x(t + \text{FPT})$, is Gaussian with mean $\mu(t)$ and the same covariance as the initial process $x(t)$ (see Fig. 1b). Simulations and the perturbation theory below show the broad validity of this approach. Equation (2) then leads to:

$$\langle T \rangle = V \int_0^\infty dt \frac{e^{-\mu(t)^2/2\psi(t)} - e^{-x_0^2/2\psi(t)}}{[2\pi\psi(t)]^{1/2}} \quad (3)$$

Relying on a generalization of equation (1) to link the n times probability distribution functions of $x(t_1)$, $x(t_2)$, ... and the FPT density, we obtain an equation for the probability of the future trajectories $y(t)$ leading to (see Supplementary Information for details):

$$\int_0^\infty \frac{dt}{\sqrt{\psi(t)}} \{ [\mu(t+\tau) - \mu(t)K(t, \tau)] e^{-\mu(t)^2/2\psi(t)} - x_0[1 - K(t, \tau)] e^{-x_0^2/2\psi(t)} \} = 0 \quad (4)$$

where $\mu(0) = 0$ and $K(t, \tau) = [\psi(t+\tau) + \psi(t) - \psi(\tau)]/[2\psi(t)]$. Equation (4), which allows for a self-consistent determination of the mean future trajectory $\mu(t)$, together with equation (3), provide the mean FPT and constitute our main result.

At this stage, several remarks can be made. (1) The mean FPT depends linearly on the confining volume V , which extends the result obtained for Markovian processes⁶. (2) Our approach reveals the key role of the mean trajectory $\mu(t)$ followed by the walker in the future of the first-passage event. In other words, even if the real motion is

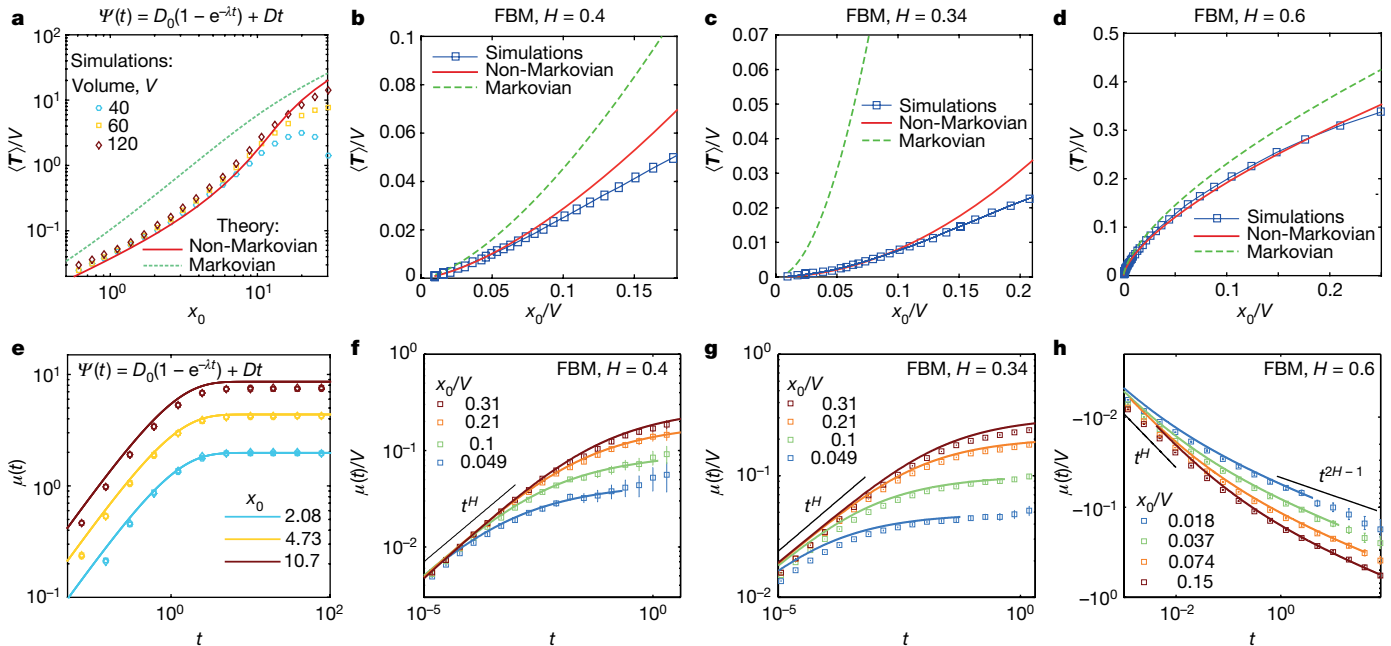


Figure 2 | Mean FPT of one-dimensional non-Markovian random walks. Mean FPT as a function of the initial position x_0 (**a–d**) and average reactive trajectory $\mu(t)$ in the future of the FPT as a function of time t (**e–h**) for various one-dimensional Gaussian stochastic processes. Solid lines are predictions of the non-Markovian theory from equations (3) and (4); dashed lines are the Markovian approximation (in which $\mu(t) = 0$); and symbols represent numerical simulations using the circulant matrix algorithm (see Supplementary Information). In **a** and **e**, the correlator $\Psi(t)$ is indicated with $D = 1$, $D_0 = 30$, $\lambda = 1$ (arbitrary units). Time is in units of $1/\lambda$ and lengths are in units of $(D/\lambda)^{1/2}$. In **e** symbols represent different

volumes (hexagons, $V = 40$; squares, $V = 60$; and diamonds, $V = 120$); the superposition confirms that $\mu(t)$ does not depend on V . In **b–d** and **f–h**, fractional Brownian motion (FBM) is shown for $K = 1$ (arbitrary units). Time is in units of $V^{1/H}/K^{1/2H}$. Note that the theory is derived for the limit of large volume, or equivalently $x_0 \ll V$. When significant, error bars give the s.e.m. of the numerical simulations. Number n of simulated trajectories: in **a** and **e** $n = 173,285$ (for $V = 40$), $n = 180,641$ (for $V = 60$), and $n = 96,623$ (for $V = 120$); in **b** and **f** $n = 19,224$; in **c** and **g** $n = 22,422$; and in **d** and **h** $n = 40,685$.

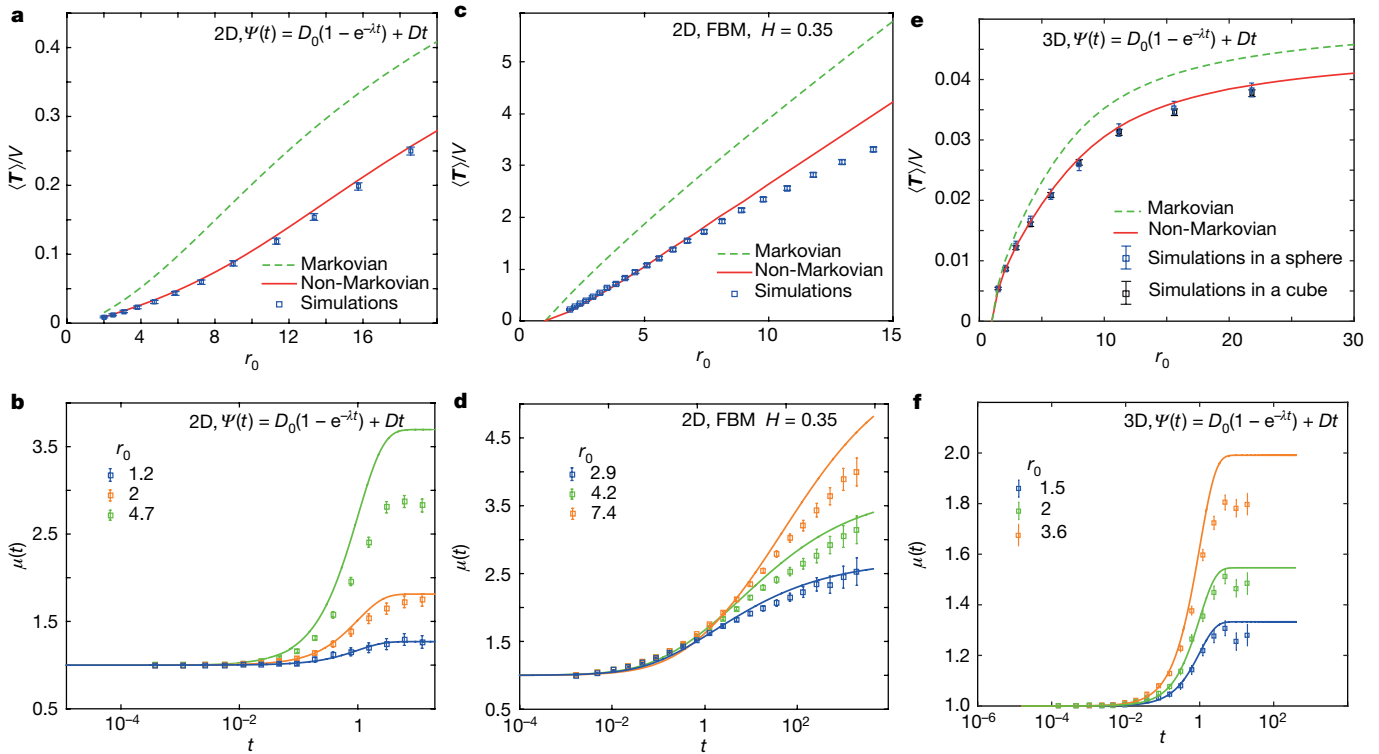


Figure 3 | Mean FPT of two- and three-dimensional non-Markovian random walks. Mean FPT to a target of radius $a = 1$ (arbitrary units) as a function of the initial position r_0 (a, c, e) and average reactive trajectory $\mu(t)$ in the future of the FPT as a function of time t (b, d, f) for different two-dimensional (2D) (a–d) and three-dimensional (3D) (e, f) Gaussian stochastic processes. Solid lines are predictions of the non-Markovian theory from equations (3) and (4); dashed lines are the Markovian approximation, in which $\mu(t)$ remains equal to the radius $a = 1$ of the target; and symbols represent numerical simulations using the circulant matrix algorithm. In a and b, the correlator $\Psi(t)$ of each coordinate in two

stopped at the first encounter with the target, the mean FPT is controlled by the statistical properties of the fictitious path that the walker would follow if allowed to continue after the first encounter event. (3) Assuming that $\psi(t) \propto t^{2H}$ at large times, with $0 < H < 1$, it can be shown from the asymptotic analysis of equation (4) that:

$$\mu(t) \simeq x_0 - A t^{2H-1} (t \rightarrow \infty) \quad (5)$$

where A is a coefficient depending on the entire MSD function $\psi(t)$ (at all timescales) and on x_0 (it generally has the same sign as x_0). Thus, for processes that are subdiffusive at long times (so that the MSD grows slower than linearly with time, $H < 1/2$), $\mu(t)$ comes back to the initial position x_0 of the walker, which is consequently not forgotten. On the contrary, asymptotically superdiffusive walkers ($H > 1/2$) keep going away from the target in the future of the FPT with a non-trivial exponent. These behaviours reflect the anticorrelation and correlation of successive steps of subdiffusive and superdiffusive walks, respectively. Note that even for asymptotically diffusive processes ($H = 1/2$), $\mu(t)$ tends to a non-vanishing constant, in contrast to a pure (Markovian) Brownian motion. (4) The importance of non-Markovian effects can be appreciated by comparing the mean FPT to the result obtained by setting $\mu(t) = 0$, which amounts to neglecting the memory of the trajectory before the first passage. As shown by equation (5), $\mu(t)$ is actually not small, so that memory effects are important. They are especially marked for $H < 1/3$, where setting $\mu(t) = 0$ in equation (3) leads to an infinite mean FPT, as opposed to our finite non-Markovian prediction.

We now confirm the validity of these analytical results by comparing them to numerical simulations of representative examples of non-Markovian processes defined by the MSD $\psi(t)$. First, the choice

dimensions is indicated for $D = 1$, $D_0 = 30$, $V = 100$, $\lambda = 1$ (arbitrary units). Time is in units of $1/\lambda$ and lengths are in units of a . In c and d, fractional Brownian motion in two dimensions is shown, with $K = 1$, $V = 60^2$ (arbitrary units). Time is in units of $a^{1/H}/K^{1/2H}$ and lengths in units of a . In e and f, the correlator $\Psi(t)$ of each coordinate in three dimensions is indicated for $D = 1$, $D_0 = 10$, $\lambda = 1$ (arbitrary units). Time is in units of $1/\lambda$ and lengths in units of a . The confining volume is a sphere of radius $R = 70$ or a cube of volume $V = 116^3$. When significant, error bars give the s.e.m. of the numerical simulations. Number n of simulated trajectories: in a and b $n = 35,334$, in c and d $n = 37,314$; and in e and f $n = 16,900$.

$\psi(t) = D_0(1 - e^{-\lambda t}) + Dt = \psi_D(t)$ corresponds to the generic case where the position $x(t)$ is coupled to other degrees of freedom at the single timescale $1/\lambda$ (Fig. 2a, e). It is typically relevant to tracers moving in nematics¹¹ or solutions of non-adsorbing polymers²⁷.

Second, the choice $\psi(t) = Kt^{2H}$ where $0 < H < 1$ and K is a positive transport coefficient (Fig. 2b–d, f–h), corresponds to the fractional Brownian motion used in fields as varied as hydrology²⁸, finance²⁹ and biophysics^{13,30}; it is a particularly good description of anomalous diffusion in various physical situations such as telomere motion³⁰ or tracer diffusion in viscoelastic fluids¹³. This process is strongly non-Markovian, as shown by its long-range correlation functions. For fractional Brownian motion, the solution of equation (4) is of the form:

$$\mu(t) = x_0 \tilde{\mu}_H(t K^{1/2H}/x_0^{1/H})$$

so that the mean FPT reads:

$$\langle T \rangle = V \beta_H x_0^{1/H-1} K^{-1/2H} \quad (6)$$

with β_H a numerical coefficient given in Supplementary Information. This equation gives the explicit dependence of the mean FPT on x_0 and generalizes the results obtained for Markovian processes⁶.

Third, the theory can be extended to higher dimensions with the supplementary assumption that the random walk is isotropic. Two-dimensional and three-dimensional versions of both of the choices of $\psi(t)$ considered above have been analysed explicitly (Fig. 3).

In fact, as shown in the Supplementary Information, the theory is exact at order ε^2 when one considers a MSD function of the type $\psi(t) = Dt + \varepsilon\psi_1 + \varepsilon^2\psi_2 + \dots$ where the small parameter ε measures the

deviation from a Markovian process (see Supplementary Information). Figures 2 and 3 reveal very good quantitative agreement between the analytical predictions and the numerical simulations far beyond this perturbative regime. Both the volume and the source–target distance dependence of the mean FPT are unambiguously captured by the theoretical analysis, at all the length scales involved in the problem. Note that, even if the theoretical prediction relies on large-volume asymptotics, numerical simulations show that it is accurate even for small confining systems (with various shapes of confining volumes, such as spherical or cubic). The very different nature of these examples (one, two or three dimensions, diffusive, superdiffusive or subdiffusive at long times...) demonstrates the wide range of applicability of our approach. Remarkably, the amplitude of memory effects is important in the examples shown in Figs 2 and 3, where the multiplicative factor between Markovian and non-Markovian estimates of the mean FPT can be up to 15 (Fig. 2c). As discussed above, this factor is even infinite for the fractional Brownian motion as soon as $H < 1/3$. Interestingly, even for the process defined by $\psi(t) = \psi_D(t)$ above, which is diffusive both at short and long times, for which one could thus expect memory effects to be negligible, this factor is not small (typically 5; see Fig. 2a). The accuracy of our analytical predictions for the mean FPT traces back to the quantitative prediction for the trajectories in the future of the FPT $\mu(t)$, as shown in Figs 2 and 3. The strong dependence of $\mu(t)$ on the starting point x_0 , predicted by our approach and confirmed numerically, is a direct manifestation of the non-Markovian feature of the random walks. Together, our results demonstrate and quantify the importance of memory effects in the first-passage properties of non-Markovian random walks in confined geometry.

Received 19 November 2015; accepted 6 April 2016.

- Redner, S. *A Guide to First-Passage Processes* (Cambridge Univ. Press, 2001).
- ben Avraham, D. & Havlin, S. *Diffusion and Reactions in Fractals and Disordered Systems* (Cambridge Univ. Press, 2000).
- Bénichou, O. & Voituriez, R. From first-passage times of random walks in confinement to geometry-controlled kinetics. *Phys. Rep.* **539**, 225–284 (2014).
- Shlesinger, M. F. Mathematical physics: search research. *Nature* **443**, 281–282 (2006).
- Lloyd, A. L. & May, R. M. Epidemiology—how viruses spread among computers and people. *Science* **292**, 1316–1317 (2001).
- Condamine, S., Bénichou, O., Tejedor, V., Voituriez, R. & Klafter, J. First-passage times in complex scale-invariant media. *Nature* **450**, 77–80 (2007).
- Bénichou, O., Chevalier, C., Klafter, J., Meyer, B. & Voituriez, R. Geometry-controlled kinetics. *Nat. Chem.* **2**, 472–477 (2010).
- Wei, Q.-H., Bechinger, C. & Leiderer, P. Single-file diffusion of colloids in one-dimensional channels. *Science* **287**, 625–627 (2000).
- Panja, D. Anomalous polymer dynamics is non-Markovian: memory effects and the generalized Langevin equation formulation. *J. Stat. Mech.* **2010**, P06011 (2010).
- Fransosch, T. *et al.* Resonances arising from hydrodynamic memory in Brownian motion. *Nature* **478**, 85–88 (2011).
- Turiv, T. *et al.* Effect of collective molecular reorientations on Brownian motion of colloids in nematic liquid crystal. *Science* **342**, 1351–1354 (2013).
- Démery, V., Bénichou, O. & Jacquin, H. Generalized Langevin equations for a driven tracer in dense soft colloids: construction and applications. *New J. Phys.* **16**, 053032 (2014).
- Ernst, D., Hellmann, M., Köhler, J. & Weiss, M. Fractional Brownian motion in crowded fluids. *Soft Matter* **8**, 4886–4889 (2012).
- Mason, T. G. & Weitz, D. Optical measurements of frequency-dependent linear viscoelastic moduli of complex fluids. *Phys. Rev. Lett.* **74**, 1250 (1995).
- Holcman, D. & Schuss, Z. The narrow escape problem. *SIAM Rev.* **56**, 213–257 (2014).
- Bénichou, O., Meyer, B., Tejedor, V. & Voituriez, R. Zero constant formula for first-passage observables in bounded domains. *Phys. Rev. Lett.* **101**, 130601–130604 (2008).
- Guérin, T., Bénichou, O. & Voituriez, R. Non-markovian polymer reaction kinetics. *Nat. Chem.* **4**, 568–573 (2012).
- Bénichou, O., Guérin, T. & Voituriez, R. Mean first-passage times in confined media: from Markovian to non-Markovian processes. *J. Phys. A* **48**, 163001 (2015).
- Kou, S. & Xie, X. S. Generalized Langevin equation with fractional Gaussian noise: subdiffusion within a single protein molecule. *Phys. Rev. Lett.* **93**, 180603 (2004).
- Wilemski, G. & Fixman, M. Diffusion-controlled intrachain reactions of polymers. 1. Theory. *J. Chem. Phys.* **60**, 866–877 (1974).
- Hanggi, P. & Talkner, P. First-passage time problems for non-Markovian processes. *Phys. Rev. A* **32**, 1934–1937 (1985).
- Masoliver, J., Lindenberg, K. & West, B. J. First-passage times for non-Markovian processes: correlated impacts on bound processes. *Phys. Rev. A* **34**, 2351–2363 (1986).
- Krug, J. *et al.* Persistence exponents for fluctuating interfaces. *Phys. Rev. E* **56**, 2702 (1997).
- Molchan, G. Maximum of a fractional Brownian motion: probabilities of small values. *Commun. Math. Phys.* **205**, 97–111 (1999).
- Bray, A. J., Majumdar, S. N. & Schehr, G. Persistence and first-passage properties in nonequilibrium systems. *Adv. Phys.* **62**, 225–361 (2013).
- Noh, J. D. & Rieger, H. Random walks on complex networks. *Phys. Rev. Lett.* **92**, 118701 (2004).
- Ochab-Marcinek, A. & Holyst, R. Scale-dependent diffusion of spheres in solutions of flexible and rigid polymers: mean square displacement and autocorrelation function for FCS and DLS measurements. *Soft Matter* **7**, 7366–7374 (2011).
- Mandelbrot, B. B. & Wallis, J. R. Noah, Joseph, and operational hydrology. *Wat. Resour. Res.* **4**, 909–918 (1968).
- Cutland, N. J., Kopp, P. E. & Willinger, W. Stock price returns and the Joseph effect: a fractional version of the Black–Scholes model. In *Seminar on Stochastic Analysis, Random Fields and Applications* 327–351 (Springer, 1995).
- Burnecki, K. *et al.* Universal algorithm for identification of fractional Brownian motion. A case of telomere subdiffusion. *Biophys. J.* **103**, 1839–1847 (2012).

Supplementary Information is available in the online version of the paper.

Acknowledgements This work was supported by ERC grant FPTOpt-277998.

Author Contributions All authors contributed equally to this work.

Reviewer Information Nature thanks K. Lindenberg and the other anonymous reviewer(s) for their contribution to the peer review of this work.

Author Information Reprints and permissions information is available at www.nature.com/reprints. The authors declare no competing financial interests. Readers are welcome to comment on the online version of the paper. Correspondence and requests for materials should be addressed to O.B. (benichou@lptmc.jussieu.fr) or R.V. (voiturie@lptmc.jussieu.fr).

Intrinsic ferroelectric switching from first principles

Shi Liu¹, Ilya Grinberg^{2,3} & Andrew M. Rappe²

The existence of domain walls, which separate regions of different polarization, can influence the dielectric¹, piezoelectric², pyroelectric³ and electronic properties^{4,5} of ferroelectric materials. In particular, domain-wall motion is crucial for polarization switching, which is characterized by the hysteresis loop that is a signature feature of ferroelectric materials⁶. Experimentally, the observed dynamics of polarization switching and domain-wall motion are usually explained as the behaviour of an elastic interface pinned by a random potential that is generated by defects^{7,8}, which appear to be strongly sample-dependent and affected by various elastic, microstructural and other extrinsic effects^{9–12}. Theoretically, connecting the zero-kelvin, first-principles-based, microscopic quantities of a sample with finite-temperature, macroscopic properties such as the coercive field is critical for material design and device performance; and the lack of such a connection has prevented the use of techniques based on *ab initio* calculations for high-throughput computational materials discovery. Here we use molecular dynamics simulations¹³ of 90° domain walls (separating domains with orthogonal polarization directions) in the ferroelectric material PbTiO₃ to provide microscopic insights that enable the construction of a simple, universal, nucleation-and-growth-based analytical model that quantifies the dynamics of many types of domain walls in various ferroelectrics. We then predict the temperature and frequency dependence of hysteresis loops and coercive fields at finite temperatures from first principles. We find that, even in the absence of defects, the intrinsic temperature and field dependence of the domain-wall velocity can be described with a nonlinear creep-like region and a depinning-like region. Our model enables quantitative estimation of coercive fields, which agree well with experimental results for ceramics and thin films. This agreement between model and experiment suggests that, despite the complexity of ferroelectric materials, typical ferroelectric switching is largely governed by a simple, universal mechanism of intrinsic domain-wall motion, providing an efficient framework for predicting and optimizing the properties of ferroelectric materials.

In ferroelectric materials, domain walls separate regions with different polarization orientations. In response to an external perturbation that favours one polarization state over another, the domain wall will move to increase the size of the domain favoured by the perturbation, potentially leading to polarization switching of the whole material. The translational motion of the 180° domain wall has been studied experimentally^{9,10,12,14} and theoretically^{15–18}. The dynamical behaviour of a domain wall is usually understood as an elastic interface moving in a fluctuating pinning potential that is created by defects^{7,8}. Under relatively weak electric fields (E), the propagation of domain walls at finite temperature (T) can be described with a creep process^{9,10}:

$$v \propto \exp\left[-\frac{U}{k_B T} \left(\frac{E_{C0}}{E}\right)^\mu\right] \quad (1)$$

where v is the domain-wall velocity, U is a characteristic energy barrier, k_B is Boltzmann's constant, E_{C0} is a critical field at which depinning occurs at 0 K and μ is the dynamical exponent determined by the nature

of the defects. The dynamical exponent $\mu = 1$ is usually ascribed to the random field defects, which break the symmetry of the ferroelectric double-well potential^{9,10}, whereas $\mu = 0.5$ is an indication of random bond disorder, which locally modifies the symmetric ferroelectric double-well potential depth^{11,12}. Another widely used equation that characterizes the switching and domain-wall motion is Merz's law, which takes the form $v = v_0 \exp(-E_a/E)$, where v_0 is the domain-wall velocity under an infinite field and E_a is the temperature-dependent activation field^{14,15}. Merz's law can be viewed as a reformulation of equation (1) with $\mu = 1$ and $E_a = UE_{C0}/(k_B T)$. When the electric field becomes larger than the crossing field E_{C0} , the wall experiences a pinning–depinning transition¹⁰, with the velocity becoming temperature-independent and given by:

$$v \propto (E - E_{C0})^\theta \quad (2)$$

where θ is a velocity exponent that reflects the dimensionality (D) of the wall. A classical theory based on a nucleation-and-growth mechanism was developed by Miller and Weinreich¹⁵ to explain the intrinsic origin of Merz's law and creep behaviour. However, the Miller–Weinreich model assumes the dominant role of depolarization energy during nucleation, which incorrectly leads to an atomically sharp triangular critical nucleus and implausibly high activation fields for nucleation^{9,11}. Multiscale simulations for 180° domain walls in defect-free PbTiO₃ revealed a square critical nucleus with diffusive and bevelled interfaces that substantially reduces the nucleation barrier and hence leads to much lower activation fields for domain-wall motion, suggesting an intrinsic origin for $\mu = 1$ (ref. 17).

Unlike the motion of 180° domain walls, switching processes in ceramics, thin films and single-crystal ferroelectrics are not well understood. The presence of a variety of extrinsic features, the possible role of ferroelastic effects in non-180° switching and the long (microsecond–millisecond) timescales typically studied for switching make it challenging to relate the observed hysteresis loops to the microscopic properties of ferroelectric materials. Because of the strong clamping effect of the substrate^{19,20}, the intrinsic dynamics of non-180° domain walls cannot be studied in high-quality ferroelectric thin films; instead, most recent experimental and theoretical studies of non-180° domain walls have focused on static properties¹⁹. Here, we use a multiscale approach to computationally model the switching process. We first obtain the missing quantitative understanding of the intrinsic dynamics of non-180° domain walls and encapsulate it in a simple and general model for domain-wall speed. The model is then used in coarse-grained simulations on long timescales that enable accurate calculation of ferroelectric-switching hysteresis loops and coercive fields.

We quantitatively estimate the velocity of a 90° domain wall in defect-free PbTiO₃ over a wide range of temperatures and electric fields using large-scale molecular dynamics simulations (see Methods). Figure 1 presents the velocity as a function of applied electric field for various temperatures, revealing an intrinsic ‘creep–depinning’ transition. In the low-field region ($E < 0.5 \text{ MV cm}^{-1}$), the velocity strongly depends on temperature and has a strong nonlinear dependence on the electric field. In the high-field region ($E > 0.5 \text{ MV cm}^{-1}$), the temperature

¹Geophysical Laboratory, Carnegie Institution for Science, Washington DC 20015, USA. ²The Makineni Theoretical Laboratories, Department of Chemistry, University of Pennsylvania, Philadelphia, Pennsylvania 19104, USA. ³Department of Chemistry, Bar-Ilan University, Ramat Gan 5290002 Israel.

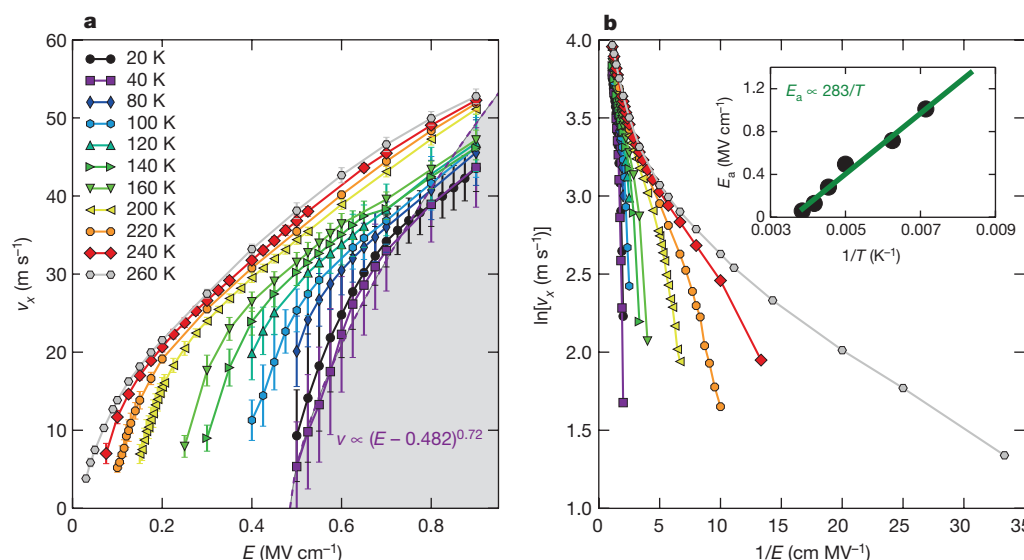


Figure 1 | Domain-wall velocity from molecular dynamics simulations. **a**, Temperature (T)- and field (E)-dependent domain-wall velocity (v_x) data reveal an intrinsic creep–depinning transition. The domain-wall velocity data at 40 K are in the flow region (shaded area) and are fitted to equation (2). We find $\theta = 0.72$, $E_{C0} = 0.482 \text{ MV cm}^{-1}$ (dashed purple line, boundary of the shaded area). The solid lines are guides for the eye. The error bars are standard deviations of v_x . **b**, Plot of $\ln(v_x)$ versus $1/E$ curves for different temperatures (see legend in **a**). The inset shows the temperature dependence of the activation field $E_a = UE_{C0}/(k_B T)$ in the creep-like region at low fields.

dependence of the domain-wall velocity becomes weaker, as seen by the overlap of the velocity data obtained at different temperatures. Plotting $\ln(v)$ versus $1/E$ (Fig. 1b), we find that $\ln(v)$ has a linear relationship with $1/E$ in the low-field region. This confirms that for relatively low electric fields and high temperatures the velocity of the 90° domain wall follows Merz's law ($\mu = 1.0$), showing a creep-like response even in the absence of defects. The inset in Fig. 1b shows the temperature dependence of the activation field $E_a = UE_{C0}/(k_B T)$ above 140 K. The nearly linear relationship between E_a and $1/T$ shows that UE_{C0}/k_B is temperature-independent in the creep-like region with a value of 283 K MV cm^{-1} . By fitting the velocity data at 40 K with equation (2), we find that $\theta = 0.72$ and $E_{C0} = 0.48 \text{ MV cm}^{-1}$. The crossing field for the 90° domain wall is lower than that for the 180° domain wall (1 MV cm^{-1}) in $\text{Pb}(\text{Zr}, \text{Ti})\text{O}_3$ (PZT) thin films¹⁰; this is expected, because *ab initio* calculations have shown that the 90° domain wall in PbTiO_3 is lower in energy than the 180° domain wall in PZT¹⁶. The values of the dynamical exponent are the same ($\mu = 1$) for 90° and 180° domain walls¹⁷. This indicates a universal intrinsic response for ferroelectric domain walls under low driving force. The observed intrinsic creep–depinning transition can be explained with a nucleation-and-growth mechanism. At low fields, the large size of the critical nucleus and the high nucleation barrier relative to thermal fluctuations make nucleation the rate-limiting step and lead to an Arrhenius dependence of the velocity in the creep region. At high fields, the nucleus size and nucleation barrier approach zero and the domain-wall velocity is growth dominated, resulting in near-linear dependence on electric fields and a weak temperature dependence.

We now develop an analytical model for nucleation at a non- 180° domain wall based on our molecular dynamics simulations for 90° domain walls. As shown in Fig. 2a, a 90° domain wall in x - y coordinates can be viewed as a special 180° domain wall in X - Y coordinates: the polarization component parallel to the domain wall (P_Y) is reversed by 180° across the boundary, while the polarization component perpendicular to the domain wall (P_X) remains almost unchanged (bottom of Fig. 2a). This transformation allows us to treat all types of non- 180° domain walls as a 180° domain wall and allows a convenient estimate of the relative energies of different types of domain walls based on the Landau–Ginzburg–Devonshire (LGD) expression for the energy per unit area (σ) of the 180° domain wall ($\sigma_{180\text{DW}}$). Detailed examinations of nucleation events at the domain wall ($X = 0$) at low temperature ($T = 20 \text{ K}$) reveal a diamond-like nucleus in the Y - Z plane (Fig. 2b), with substantial diffuseness at the boundary characterized by a gradual polarization change. With this microscopic picture of nucleation, we use LGD theory to relate the nucleation energy to the fundamental characteristics of the material (see Methods). The nucleation energy

U_{nuc} includes two important energy terms: polarization–electric-field coupling (PE) and interfacial energy. Contrary to the assumption of the classical Miller–Weinreich model, the depolarization energy is quite small and does not make a substantial contribution to the nucleation energy (see Methods for a detailed analysis of elastic and depolarization energy).

At the lowest approximation, P_X and P_Z remain unchanged across the domain wall and, therefore, the nucleation energy depends only on P_Y . The profile of P_Y for a domain wall containing a nucleus of size $l_1 \times l_2 \times l_3$ can be described as:

$$P_Y = \frac{2P_s}{\sqrt{2}} f(X, l_1, \delta_1) f(Y + Z, \sqrt{2}l_2, \delta_2) f(Y - Z, \sqrt{2}l_3, \delta_3) + \frac{P_s}{\sqrt{2}} g(X, l_1, \delta_1) \quad (3)$$

$$\text{where } f(x, l, \delta) = \frac{1}{2} \left[\tanh\left(\frac{x + l/2}{\delta/2}\right) - \tanh\left(\frac{x - l/2}{\delta/2}\right) \right], \quad g(x, l, \delta) = \tanh\left(\frac{x - l/2}{\delta/2}\right),$$

P_s is the bulk polarization and δ_i characterizes the diffuseness of the nucleus along direction i . Figure 2c shows the polarization profile in the Y - Z and X - Y planes generated by equation (3). Evaluating this P_Y profile in the LGD energy expression for different parameter values (l_1 and l_2) allow us to identify the critical nucleus size and to estimate the nucleation activation energy (ΔU_{nuc}). According to Avrami theory of transformation kinetics, ΔU_{nuc} can be related to the activation field in Merz's law as $E_a \approx \frac{1}{D+1} \frac{\Delta U_{\text{nuc}}}{k_B T} E$, where D is the dimensionality¹⁷. By applying this relation with $D = 2$ and using parameters (see Methods) obtained from our classical bond-valence potential, we obtain E_a values for a range of temperatures. As shown in Fig. 2d, the activation fields predicted from the analytical model agree well with molecular dynamics results. To apply the model to other types of non- 180° domain walls, only a simple modification of the input parameters is required, with the necessary values obtained from first-principles density functional theory (DFT) calculations of the particular domain wall (see Methods).

The availability of an analytical model that uses DFT inputs enables rapid estimation of hysteresis loops and coercive fields (E_c ; see Methods). Because the structure and polarization of Ti-rich PZT are similar to those of PbTiO_3 , we compare the simulated values of the PbTiO_3 E_c to various experimental values for PZT materials. We find that our theoretical coercive fields (Fig. 3a) using parameters of 90° -domain-wall motion agree well over a large frequency range with the experimental E_c values (5 – 20 kV cm^{-1})^{21–24}. The E_c values based on 180° -domain-wall motion are quite large and exhibit the correct frequency dependence (Fig. 3c), in agreement with experimental results obtained in thin films (with thickness larger than the critical size of the nucleus)²⁵. This suggests that the 180° switching in ceramics proceeds via sequential 90° -domain-wall motion²³, owing to the much smaller

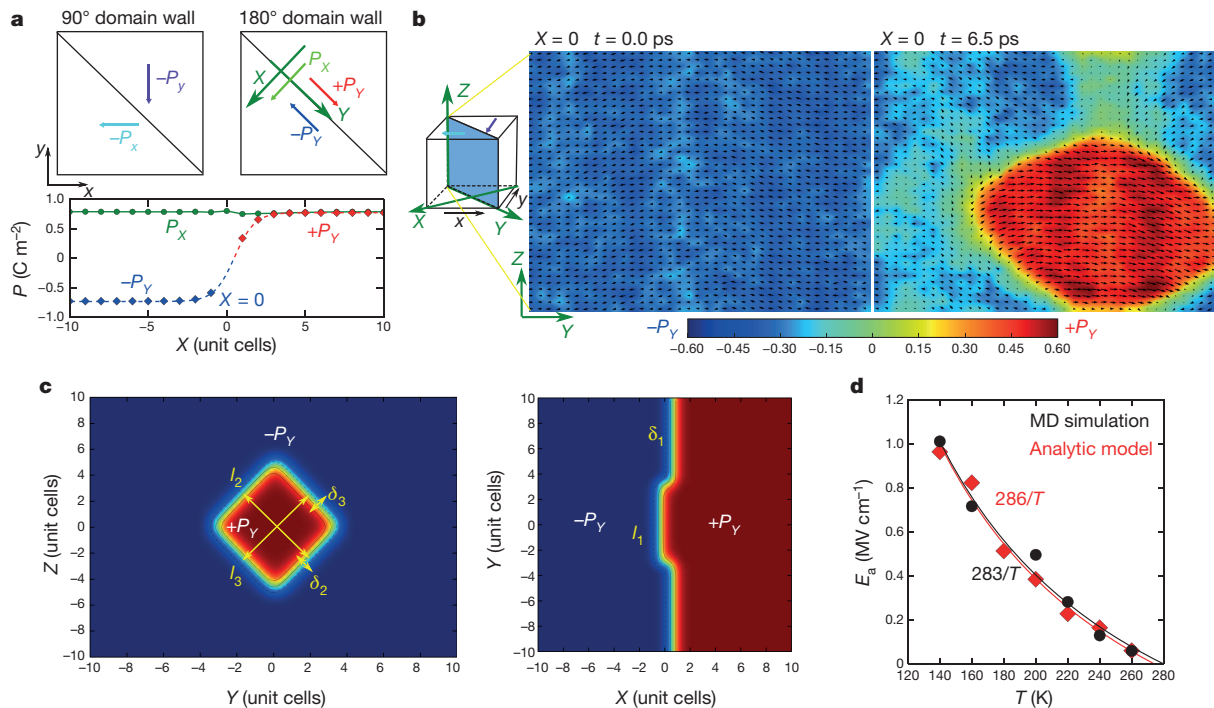


Figure 2 | LGD model of nucleation at domain walls. **a**, Schematic of mapping a 90° domain wall in x - y coordinates to a 180° domain wall in X - Y coordinates. The bottom panel shows the polarization P profile of a 90° domain wall in X - Y coordinates. The change in P_X across the domain wall ($X=0$) is small. **b**, Simulated nucleation process at the domain wall in the Y - Z plane (blue-shaded plane in the schematic). The black arrows scale with the local dipole magnitudes of each unit cell in the Y - Z plane. The background of each arrow is coloured on the basis of the magnitude of the Y component of the local dipole. At $t=0$ ps, the Y - Z interface at

$X=0$ has dipoles aligned along $-Y$. In the presence of electric field, a diamond-like nucleus forms at $t=6.5$ ps. **c**, Polarization profile of a nucleus generated by equation (3). The size of the nucleus is defined as $l_1 \times l_2 \times l_3$; $\delta_{1,2,3}$ characterize the diffusiveness of the polarization. **d**, Comparison of the activation fields E_a obtained from molecular dynamics (MD) simulations with the results of the LGD model. The analytical model reproduces molecular dynamics activation fields using bond-valence-potential-based parameters together with the molecular dynamics temperature dependence of local polarization.

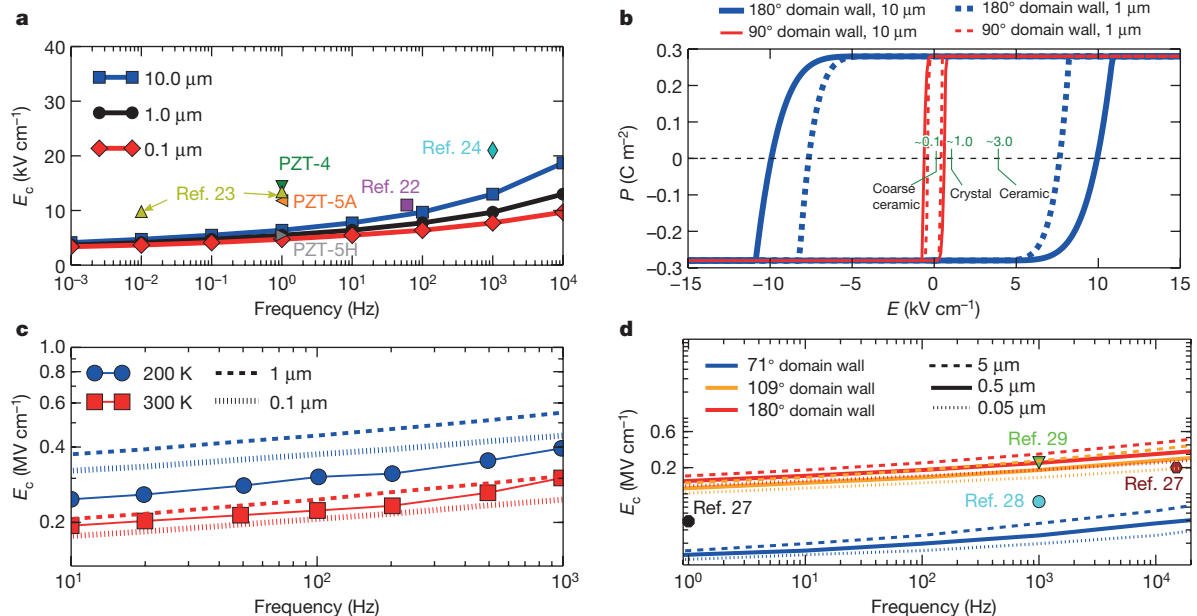


Figure 3 | Hysteresis loops and coercive fields for several materials simulated using first-principles data. **a**, Simulated frequency dependence of coercive fields E_c for PZT ceramics for various domain sizes (see legend) at 300 K. Theoretical values are comparable to various experimental values^{22–24} in ceramics. PZT-4, -5A and -5H refer to different PZT ceramics in ref. 21. **b**, Hysteresis loops of BaTiO₃ with a domain size of 1 μ m (dashed lines) and 10 μ m (coarse grain). The green labels refer to experimental values of coercive fields. **c**, Frequency- and

temperature-dependent coercive fields for PZT thin films. Experimental data (solid lines with filled circles and squares) are taken from ref. 25. A domain size of 0.1 μ m (vertically dashed lines) and 1 μ m (dashed lines) is used to obtain the theoretical values. **d**, Theoretical coercive fields for different domain walls in BiFeO₃ with a domain size of 0.5 μ m (solid lines), 0.05 μ m (vertically dashed lines) and 5 μ m (dashed lines), compared to experimental values^{27–29}.

intrinsic nucleation barrier at the 90° domain wall. Thus, the switching and coercive fields in PZT are largely determined by the intrinsic properties of the appropriate domain-wall-motion mechanism. Similarly to the PZT results, we find that switching in BaTiO₃ ceramics is governed by the motion of 90° domain walls (Fig. 3b), with the predicted coercive field of around 0.1 kV cm⁻¹ at 300 K close to the experimental value for coarse-grain BaTiO₃ ceramics²⁶.

Polarization reversal in BiFeO₃ is another test of our model, owing to the importance of octahedral rotations and the presence of three types of domain walls in rhombohedrally polarized BiFeO₃. DFT calculations revealed that the 71° domain wall has the highest energy, followed by the 180° domain wall, with the lowest energy for the 109° domain wall. The higher energy of the 71° domain wall is attributed to the mismatch of oxygen octahedral rotations across the domain boundary. We introduce a second order parameter (oxygen octahedral rotation, Θ) into our LGD-based nucleation-and-growth model (see Methods). Using DFT domain-wall energies, our analytical model predicts that E_c is lowest for the 71° domain wall, followed by the 109° and 180° domain walls. The predicted coercive fields for 180° domain walls are comparable with experimental values in thin films^{27–29}. The ability of our simple analytical model to estimate E_c accurately indicates that the value of the coercive field is largely determined by the intrinsic properties of the material, with the nucleation barrier on the domain wall controlling the dynamics of polarization reversal.

The dominant role of intrinsic domain-wall motion explains the consistent differences in E_c of the tetragonal and rhombohedral ferroelectrics. For example, an increase in E_c of approximately 80% is observed across the rhombohedral–tetragonal compositional phase transition at the morphotropic phase boundaries in lead-free (Ba, Ca) TiO₃–Ba(Zr, Ti)O₃ and Bi-rich BiScO₃–Bi(Zr, Ti)O₃–PbTiO₃ ceramic systems³⁰. Analysis of our LGD nucleation model incorporating the changes in octahedral rotations across the 71° domain wall shows that the ratio of the coercive fields for 90° and 71° domain walls is approximately two (see Methods). This suggests that the switching in rhombohedral and tetragonal ferroelectrics proceeds via a multistep switching mechanism that involves a series of 71° and 90° steps, respectively, and that the higher E_c of the tetragonal ferroelectrics is a direct consequence of the larger nucleation energy for 90°-domain-wall motion. The unified framework presented here relates microscopic zero-kelvin quantities to macroscopic material parameters at finite temperature and thus suggests an avenue for rational material design.

Online Content Methods, along with any additional Extended Data display items and Source Data, are available in the online version of the paper; references unique to these sections appear only in the online paper.

Received 28 January; accepted 13 April 2016.

- Xu, R., Karthik, J., Damodaran, A. R. & Martin, L. W. Stationary domain wall contribution to enhanced ferroelectric susceptibility. *Nat. Commun.* **5**, 3120 (2014).
- Chaplya, P. M. & Carman, G. P. Dielectric and piezoelectric response of lead zirconate–lead titanate at high electric and mechanical loads in terms of non-180° domain wall motion. *J. Appl. Phys.* **90**, 5278–5286 (2001).
- Karthik, J. & Martin, L. Pyroelectric properties of polydomain epitaxial Pb(Zr_{1-x}Ti_x)O₃ thin films. *Phys. Rev. B* **84**, 024102 (2011).
- Seidel, J. *et al.* Conduction at domain walls in oxide multiferroics. *Nat. Mater.* **8**, 229–234 (2009).
- Liu, S. *et al.* Ferroelectric domain wall induced band gap reduction and charge separation in organometal halide perovskites. *J. Phys. Chem. Lett.* **6**, 693–699 (2015).
- Jin, L., Li, F. & Zhang, S. Decoding the fingerprint of ferroelectric loops: comprehension of the material properties and structures. *J. Am. Ceram. Soc.* **97**, 1–27 (2014).

- Ioffe, L. B. & Vinokur, V. M. Dynamics of interfaces and dislocations in disordered media. *J. Phys. C* **20**, 6149–6158 (1987).
- Chauve, P., Giamarchi, T. & Le Doussal, P. Creep and depinning in disordered media. *Phys. Rev. B* **62**, 6241–6267 (2000).
- Tybell, T., Paruch, P., Giamarchi, T. & Triscone, J.-M. Domain wall creep in epitaxial ferroelectric Pb(Zr_{0.2}Ti_{0.8})O₃ thin films. *Phys. Rev. Lett.* **89**, 097601 (2002).
- Jo, J. *et al.* Nonlinear dynamics of domain-wall propagation in epitaxial ferroelectric thin film. *Phys. Rev. Lett.* **102**, 045701 (2009).
- Paruch, P., Giamarchi, T., Tybell, T. & Triscone, J.-M. Nanoscale studies of domain wall motion in epitaxial ferroelectric thin films. *J. Appl. Phys.* **100**, 051608 (2006).
- Pertsev, N. A. *et al.* Dynamics of ferroelectric nanodomains in BaTiO₃ epitaxial thin films via piezoresponse force microscopy. *Nanotechnology* **19**, 375703 (2008).
- Liu, S., Grinberg, I., Takenaka, H. & Rappe, A. M. Reinterpretation of the bond-valence model with bond-order formalism: an improved bond-valence-based interatomic potential for PbTiO₃. *Phys. Rev. B* **88**, 104102 (2013).
- Merz, W. J. Domain formation and domain wall motions in ferroelectric BaTiO₃ single crystals. *Phys. Rev.* **95**, 690–698 (1954).
- Miller, R. C. & Weinreich, G. Mechanism for the sideways motion of 180° domain walls in barium titanate. *Phys. Rev.* **117**, 1460–1466 (1960).
- Meyer, B. & Vanderbilt, D. *Ab initio* study of ferroelectric domain walls in PbTiO₃. *Phys. Rev. B* **65**, 104111 (2002).
- Shin, Y.-H., Grinberg, I., Chen, I.-W. & Rappe, A. M. Nucleation and growth mechanism of ferroelectric domain-wall motion. *Nature* **449**, 881–884 (2007).
- Liu, S., Grinberg, I. & Rappe, A. M. Exploration of the intrinsic inertial response of ferroelectric domain walls via molecular dynamics simulations. *Appl. Phys. Lett.* **103**, 232907 (2013).
- Pramanick, A., Prewitt, A. D., Forrester, J. S. & Jones, J. L. Domains, domain walls and defects in perovskite ferroelectric oxides: a review of present understanding and recent contributions. *Crit. Rev. Solid State Mater. Sci.* **37**, 243–275 (2012).
- Gao, P. *et al.* Atomic-scale mechanisms of ferroelastic domain-wall-mediated ferroelectric switching. *Nat. Commun.* **4**, 2791 (2013).
- Hooker, M. W. *Properties of PZT-based Piezoelectric Ceramics Between –150 and 250°C*. Report No. NASA/CR-1998-208708, <http://ntrs.nasa.gov/search.jsp?R=19980236888> (NASA, 1998).
- Lente, M. & Eiras, J. 90° domain reorientation and domain wall rearrangement in lead zirconate titanate ceramics characterized by transient current and hysteresis loop measurements. *J. Appl. Phys.* **89**, 5093–5099 (2001).
- Lente, M., Picinin, A., Rino, J. & Eiras, J. 90° domain wall relaxation and frequency dependence of the coercive field in the ferroelectric switching process. *J. Appl. Phys.* **95**, 2646–2653 (2004).
- Kong, L. & Ma, J. PZT ceramics formed directly from oxides via reactive sintering. *Mater. Lett.* **51**, 95–100 (2001).
- Yang, S. M. *et al.* ac dynamics of ferroelectric domains from an investigation of the frequency dependence of hysteresis loops. *Phys. Rev. B* **82**, 174125 (2010).
- Wu, K. & Schulze, W. A. Effect of the ac field level on the aging of the dielectric response in polycrystalline BaTiO₃. *J. Am. Ceram. Soc.* **75**, 3385–3389 (1992).
- Wang, J. *et al.* Epitaxial BiFeO₃ multiferroic thin film heterostructures. *Science* **299**, 1719–1722 (2003).
- Shelke, V. *et al.* Reduced coercive field in BiFeO₃ thin films through domain engineering. *Adv. Mater.* **23**, 669–672 (2011).
- Guo, E.-J., Dörr, K. & Herklotz, A. Strain controlled ferroelectric switching time of BiFeO₃ capacitors. *Appl. Phys. Lett.* **101**, 242908 (2012).
- Suchomel, M. R. *Greater Functionality of Bismuth and Lead Based Perovskites*. PhD thesis, Univ. Pennsylvania, <http://repository.upenn.edu/dissertations/AAI3179819> (2005).

Acknowledgements S.L. was supported by the NSF through Grant DMR-1124696, Grant CBET-1159736, and the Carnegie Institution for Science. I.G. was supported by the US ONR under Grant N00014-12-1-1033. A.M.R. was supported by the US DOE under Grant DE-FG02-07ER46431. Computational support was provided by the US DOD through a Challenge Grant from the HPCMO, and by the US DOE through computer time at NERSC.

Author Contributions S.L., I.G. and A.M.R. designed and analysed the simulation approaches. S.L. performed the molecular dynamics simulations. All authors discussed the results and implications of the work and commented on the manuscript at all stages.

Additional Information Reprints and permissions information is available at www.nature.com/reprints. The authors declare no competing financial interests: details are available in the online version of the paper. Correspondence and requests for materials should be addressed to S.L. (slu@carnegiescience.edu) and A.M.R. (rappe@sas.upenn.edu).

METHODS

Molecular dynamics simulations of 90° domain walls. To understand the intrinsic dynamics of non-180° domain walls, we study the motion of the 90° domain wall in defect-free PbTiO₃ as an example and then generalize the obtained results to other types of non-180° domain walls. We perform constant-temperature constant-pressure (NPT; N is the (constant) number of particles) molecular dynamics simulations over a wide range of temperatures and electric fields using a bond-valence-based classical potential and extract velocity data for the 90° domain wall^{13,18,31,32}. We use a $40 \times 40 \times 40$ supercell with the polarization direction changing from $[0\bar{1}0]$ to $[100]$ across the boundary (Extended Data Fig. 1a). Owing to the use of an orthorhombic supercell, the domains are homogeneously strained, making the relative angle between the orientations of the polarization axes of neighbouring domains exactly 90°, rather than $2\arctan(a/c)$ as is geometrically required for a tetragonal ferroelectric with short-axis lattice constant a and long-axis lattice constant c . The electric field is applied along the $[100]$ direction; this will cause the domain wall to move along the $[110]$ direction (with velocity v_{DW}) as a result of the 90° switching of $[100]$ dipoles to $[0\bar{1}0]$ dipoles at the domain boundary (Extended Data Fig. 1b). When dipoles in one layer of unit cells are switched by 90°, the wall moves by $\sqrt{a^2 + c^2}/2$, and the cells initially with their long axis (c) along $[100]$ will now have their short axis (a) along $[100]$, causing $L_{[100]}$ (the cell dimension along $[100]$) to be reduced by $(c - a)$ (Extended Data Fig. 2a). Therefore, the domain-wall velocity v_{DW} can be estimated from the change in the cell dimension $dL_{[100]}$ using:

$$v_{DW} = \frac{dL_{[100]}}{2dt} \frac{\sqrt{a^2 + c^2}}{2(c - a)} = v_x \frac{\sqrt{a^2 + c^2}}{2(c - a)}$$

with $v_x = dL_{[100]}/2dt$ (the factor of 1/2 is due to the presence of two walls in the simulated supercell). Owing to the stochastic behaviour of nucleation, 20 simulations with slightly different initial structures are carried out for a given temperature and electric field to obtain the velocity average and standard deviation.

It is known that for PbTiO₃ the values of the lattice constants depend on temperature. The lattice constants of PbTiO₃ are calculated under different temperatures with molecular dynamics simulations; we find that $\sqrt{a^2 + c^2}/[2(c - a)]$ depends on the temperature weakly and is in the 5–6 range (Extended Data Fig. 2b). This temperature dependence has a different origin from the temperature dependence of the domain-wall velocity. For the polarization switching process, the relevant kinetic quantity is v_{DW}/a , which is the effective (switching-related) domain-wall velocity (v_{eff}) in terms of the unit-cell lattice constant a . Therefore, to connect the domain-wall velocity at a given temperature with the experimentally observed switching rate estimated from the switching current, the obtained velocity v_{DW} must be divided by the lattice constant at that particular temperature. We find that v_{eff} exhibits the temperature dependence predicted by equation (1). Owing to the temperature dependence of the lattice constants, the domain-wall velocity measured by v_{DW} deviates somewhat from equation (1). We consider v_{eff} as the intrinsic velocity of the domain wall. Nevertheless, when studying the effect of the electric field on switching at a given temperature, v_x can also be used because it differs from the intrinsic, switching-related domain-wall velocity v_{eff} by a constant multiplicative factor for each temperature. The temperature and field dependence of v_x are presented in Fig. 1 because v_x is the quantity that is most easily and directly obtained from our molecular dynamics simulations. A v_x of $10\text{--}50\text{ m s}^{-1}$ corresponds to a domain-wall velocity of $50\text{--}250\text{ m s}^{-1}$ or a change in supercell dimension of $1\text{--}5\text{ Å}$ per 10 ps —about $4\text{--}20$ unit cells per 10 ps . All simulations are carried out for $10\text{--}50\text{ ps}$ and therefore allow domain-wall movement that can be detected by examination of the changes in the supercell dimensions and total polarization. Our approach for extracting the domain-wall velocity from the change in supercell dimension resembles the experimental switching-current measurement. Experimentally, the domain-wall velocity is extracted by measuring the switching current, which is equivalent to dP/dt . We find from molecular dynamics simulations that v_x scales linearly with dP/dt for various temperatures (Extended Data Fig. 2c), showing that v_x is a good indicator of domain-wall velocity for theory–experiment comparison.

The thermal broadening of domain walls is taken into account in finite-temperature molecular dynamics simulations. Increased thermal broadening of the wall diminishes the polarization at the interface of the two domains, leading to a lower nucleation energy, faster domain-wall motion and a lower coercive field. As the temperature approaches the critical temperature, the coercive field is expected to become low, and the domain-wall motion will take place in the flow regime even at low fields. Additionally, the smearing out of the domain wall may lead to a transition from layer-by-layer switching to multilayer switching whereby several unit cells in adjacent layers switch simultaneously.

LGD nucleation model. The nucleation energy U_{nuc} that captures the most important energy terms can be expressed as $U_{\text{nuc}} = \Delta U_E + \Delta U_i$ where the polarization-field coupling term ΔU_E is:

$$\Delta U_E = -E \int_{-\infty}^{\infty} dX \int_{-\infty}^{\infty} dY \int_{-\infty}^{\infty} dZ [P_{\text{nuc}}(X, Y, Z) - P_{\text{DW}}(X, Y, Z)] \quad (4)$$

and the interfacial energy ΔU_i is:

$$\Delta U_i = \int_{-\infty}^{\infty} dX \int_{-\infty}^{\infty} dY \int_{-\infty}^{\infty} dZ \{ [U_g(P_{\text{nuc}}) + U_{\text{loc}}(P_{\text{nuc}})] - [U_g(P_{\text{DW}}) + U_{\text{loc}}(P_{\text{DW}})] \}$$

Here $P_{\text{nuc}}(X, Y, Z)$ and $P_{\text{DW}}(X, Y, Z)$ are the polarization profiles of a domain wall with and without the nucleus, respectively. U_{loc} is the local energy penalty due to the deviation of the local polarization from the ground-state bulk value (P_s): $U_{\text{loc}}(P) = A_{\text{loc}}[1 - (P/P_s)^2]^2$, where A_{loc} is the energy difference between the ferroelectric phase and the paraelectric phase. U_g is the gradient energy due to the polarization changes ($\partial_j P_i$) at the domain wall: $U_g(P_i) = \sum_j g_{ij} (\partial_j P_i)^2$, where g_{ij} is the coefficient for the gradient of the i th component of P along direction j . The value of g_{ij} can be derived from the energy and diffusiveness of the domain wall. The contributions from elastic strain energy (ε^2) and strain–polarization coupling (εP^2) terms could be implemented into equation (3). However, we find that the elastic energy change is not significant (see below) and is therefore omitted in the following analysis.

Elastic energy contribution to nucleation energy. We calculate the effective lattice constants (defined in Extended Data Fig. 1a) in X – Y coordinates and find that they remain almost unchanged across the domain wall (Extended Data Fig. 3a). This finding suggests that the elastic energy cost at domain boundaries is not significant in an ideal crystal. Extended Data Fig. 3b, c shows the distributions of strain gradient in the presence of a diamond-like nucleus (illustrated in Fig. 2b). It can be seen that the unit cells of the nucleus have essentially the same lattice constants as the rest of the PbTiO₃ unit cells at the domain wall. Therefore, the elastic energy contribution to the nucleation energy (change in elastic energy during nucleation) is negligible and does not have to be treated explicitly. We have therefore omitted explicit strain and strain–polarization coupling terms from our LGD nucleation model at the lowest approximation. Additionally, although the LGD theory presented in the main text does not explicitly refer to elastic interactions, these are included implicitly. It can be shown that inclusion of strain and strain–polarization coupling terms merely renormalizes the fourth-order LGD parameter. Because the parameters for the LGD model are obtained from DFT calculations in which strain polarization coupling is included, these elastic energetics are included in the A_{loc} parameter that specifies the dependence of local energy on local polarization. (Similarly, because the supercell size is allowed to vary in the NPT simulations, elastic energy is taken into account in molecular dynamics simulations as well.) Therefore, a deviation from the preferred value of polarization automatically implies a change in the unit-cell parameters, and the energy of this change is included in our model as the local energy penalty (U_{loc}).

Analysis of the Miller–Weinreich nucleation model. The original work of Miller and Weinreich¹⁵ (illustrated in Extended Data Fig. 4) is based on the following assumptions: (1) the nucleus boundary is oriented at a 90° angle relative to the original domain wall; (2) the nucleus is located at the surface of the material and has a net non-zero boundary charge ($\rho_1 + \rho_2 > 0$); (3) the boundary of the nucleus has the same interface energy as that of the planar domain wall (σ_w) on which the nucleus is located; and (4) the σ_p parameter that characterizes the strength of the depolarization interactions is large relative to the magnitude of the local interface energy characterized by σ_w . The assumption that $\sigma_p \gg \sigma_w$ leads to the triangular (red in Extended Data Fig. 4) nucleus shape.

Owing to the lack of reliable experimental or first-principles data for the domain-wall energy, the model was assumed to be correct in ref. 15 and so was used to parameterize the domain-wall energy with the available domain-wall velocity data. This allowed the fitting of the electric-field/domain-wall-velocity relationships in many experiments. Despite this success, two major studies have cast serious doubt on the model. First, first-principles calculations of domain-wall energy per unit area (σ_w) were found to be markedly higher than the fit values and, conversely, inserting the accurate, calculated values into the Miller–Weinreich model gave velocities that were markedly lower than those observed experimentally⁹. Second, multiscale modelling of the nucleation process on the domain wall for 180° domain walls shows that the critical nucleus is not a tall, narrow, sharp triangle, as suggested in ref. 15. Instead, the observed nucleus is a diffuse, bevelled square¹⁷. We show that rather than the $\sigma_p \gg \sigma_w$ limit assumed in ref. 15, the actual nucleation takes place in the $\sigma_w \gg \sigma_p$ limit, with the local interface energy playing the dominant role and governing the energetics of nucleation and growth.

Reduced depolarization energy. For simplicity, we discuss the relative energies of the depolarization and local interface terms adopting the triangular shape and form of the nucleus energy expression of ref. 15 (presented in Extended Data Fig. 4), so that these terms are discussed in the framework traditionally used to model nucleation on the domain wall. Four factors contribute to the reduced role of depolarization energy in nucleation.

First, the bevelled shape of the nucleus effectively reduces σ_w . Because the depolarization energy of the Miller–Weinreich model arises from the electrostatic interactions between the charges along the boundary of the nucleus, the magnitude of σ_p exhibits a logarithmic dependence on the width of the nucleus (a). Although the boundary of the nucleus was assumed to be sharp in ref. 15 and at a 90° angle to the domain wall, the actual nucleus boundary has a bevelled shape, as shown in previous molecular dynamics studies¹⁷. This decreases the effective domain-wall area or, alternatively, the effective local-domain-wall energy ($\sigma_{\text{eff},w}$) for a given nucleus of width a . According to equation (9) in ref. 15 (also presented in Extended Data Fig. 4), the magnitude of the width of the critical nucleus a^* is determined by the ratio between σ_w and the PE terms in the limit $\sigma_p \gg \sigma_w$ and in the limit $\sigma_w \gg \sigma_p$. Thus, for all cases, a decrease in σ_w leads to a smaller critical width a^* and therefore a smaller critical depolarization energy σ_p^* . The logarithmic dependence of σ_p is not weak for the small nuclei observed in our molecular dynamics simulations. Therefore, a decrease in the local interface energy due to the bevelled shape of the nucleus, which favours smaller critical nucleus size, also substantially decreases the magnitude of σ_p^* .

Second, the dielectric constant is enhanced at the domain wall and therefore the screening at the domain wall is stronger than in the bulk of the material. Recent experimental¹ and theoretical work³³ has shown that the dielectric constant at the domain wall is larger than that in the bulk. This is confirmed by our molecular dynamics simulations that show that the local dipole fluctuations and therefore the dielectric constant at the 90° domain wall are enhanced by a factor of two relative to the bulk value. Owing to the presence of the dielectric constant in the denominator of the formula for σ_p , the actual σ_p value is then reduced by another factor of two relative to the original Miller–Weinreich estimate.

Third, the diamond shape of the nucleus shows an interaction cancellation effect. An additional effect is present for the elongated-diamond-like nuclei found in this work. Unlike the Miller–Weinreich model, which is not charge neutral, the elongated diamond shape observed in our molecular dynamics simulations exhibits both positive (ρ_1 and ρ_2) and negative ($-\rho_3$ and $-\rho_4$) boundary charges (Extended Data Fig. 5) so that the total charge at the nucleus boundary (Q_{tot}) is zero. Therefore, the repulsive energy penalty due to the interaction between ρ_1 and ρ_2 , and between $-\rho_3$ and $-\rho_4$, is cancelled by the attractive energy gain of the interaction between ρ_1 and $-\rho_3$, and between ρ_2 and $-\rho_4$. This changes the dependence of σ_p on a from $\ln[2a/(eb)]$ to $\ln[(a/eb)]$ (the $4P_s^2b/[\ln(2)]$ contribution (in which ϵ is the dielectric constant) to σ_p (see Extended Data Fig. 4 for definitions of e and b) arises from the interaction between the charges on the two opposite sides of the triangle; see the text following equation (4) in ref. 15). Although this change would have a minor effect on the large nucleus assumed in ref. 15, it is highly important for the small nucleus observed in our molecular dynamics simulations.

Finally, the boundary of the nucleus has a much smaller depolarization charge. We find that the average boundary charge between the nucleus and the original domain as integrated from the polarization changes on the 90° domain wall observed in our molecular dynamics calculations (Extended Data Fig. 5) is about two times smaller ($\Delta P = 0.7 \text{ C m}^{-2}$) than that predicted by the sharp polarization change ($\Delta P = 2P_s = 1.41 \text{ C m}^{-2}$) that would be used in a Miller–Weinreich-like model. Such a small polarization change is due to the greatly decreased value of P_Y at the domain wall relative to the bulk value. First-principles calculations¹⁶ show that the diffuseness of the 90° domain wall means that P_Y at the domain wall layer is only about 50% of the bulk value. This large decrease in P_Y is also found in our calculations (Fig. 2a). It is this domain wall layer that undergoes the nucleation and growth process governing the domain-wall motion, and therefore the appropriate value of P to be used for estimating the depolarization charge is much smaller than the Miller–Weinreich estimate based on the bulk value P_s . The much smaller charge generated at the boundary of the nucleus decreases the strength of electrostatic interactions and σ_p by a further factor of approximately four.

Despite the small σ_p , our nucleus still exhibits an elongated shape; this is due to the greater magnitude of the local energy σ_w for the domain wall at which P changes along the P direction than that for the domain wall at which P changes along a direction transverse to the P direction, as found in ref. 17 for 180°-domain-wall motion. This is also unlike the assumption in ref. 15 that σ_w is the same as the energy of the flat domain wall for all nucleus boundaries.

In summary, rather than the $\sigma_p \gg \sigma_w$ limit assumed in ref. 15, the actual nucleation takes place in the $\sigma_w \gg \sigma_p$ limit, with the local interface energy playing the dominant role and governing the energetics of nucleation and growth. This not

only justifies our analytical model that neglects the small depolarization energy term, but also represents a new understanding of the physics that is important for ferroelectric switching.

Quantitative analysis of σ_p reduction. We quantitatively evaluate the impact of the effects described above (bevelled shape, high dielectric constant, cancellation effect and small depolarization charge) on the depolarization energy term (σ_p). To take the modification of the boundary structure into account, we write down a modified version of the Miller–Weinreich formula:

$$\begin{aligned} U_{\text{nuc}} &= -2P_s E a l c + 2s\sigma_w c \sqrt{a^2 + l^2} + U_d \\ U_d &= \frac{8f_c^2 P_s^2 c^2 a^2}{f_\epsilon \epsilon} \ln \left(\frac{f_Q a}{eb} \right) = 2\sigma_p b a^2 / l \\ \sigma_p &= \frac{4f_c^2 P_s^2 c^2}{f_\epsilon \epsilon} \ln \left(\frac{f_Q a}{eb} \right) \end{aligned} \quad (5)$$

where σ_w is the energy of the planar 90° domain wall, $s = 0.41$ is a factor that accounts for the reduction in the interface area of the nucleus due to its bevelled shape, as described previously¹⁷ ($\sigma_{\text{eff},w} = s\sigma_w$), f_c is the scaling factor between the actual charge at the nucleus and the boundary charge assumed in the Miller–Weinreich model, f_ϵ is the scaling factor between the values of the dielectric constant (ϵ) at the domain wall and in the bulk, and f_Q is a factor reflecting the effect of the interactions between the charged domain boundaries at the net-neutral ($Q_{\text{tot}} = 0$) and net-charged ($Q_{\text{tot}} \neq 0$) boundaries of the nucleus, with $f_Q = 2$ for the original, charged, triangular, Miller–Weinreich nucleus and $f_Q = 1$ for a net-neutral, diamond-like nucleus.

To determine the dimensions and the energy of the critical nucleus, we evaluate U_{nuc} for a wide range of a and l values and identify those that give the lowest energy for each nucleus area $A = al$. Here, we use the DFT σ_w value of 35 mJ m^{-2} for the 90° domain wall and standard parameters for PbTiO_3 (dielectric constant $\epsilon = 60$, bulk polarization component in the plane of the 90° domain wall $P_s = 0.53 \text{ C m}^{-2}$, $b = 3.9 \text{ \AA}$, $c = 4 \text{ \AA}$ and $e = 2.718$). The plots of the nucleus energy versus area (A) for different values of s , f_c , f_ϵ and f_Q under an applied field of 0.1 MV cm^{-1} , which is typical of the low range of field magnitudes used in molecular dynamics simulations, are shown in Extended Data Fig. 6. We also show the dependence of the nucleus aspect ratio (l^*/a^* , where l^* is the length of critical nucleus; see Extended Data Fig. 5) on the ratio of σ_p and σ_w , and the σ_p values obtained for different values of s , f_c , f_ϵ and f_Q .

Examination of Extended Data Fig. 6 shows several important differences between the results of the classical Miller–Weinreich approach and the results obtained for a Miller–Weinreich-like nucleus with realistic boundaries. First, even for $s = f_c = f_\epsilon = 1$, the obtained $a^* = 12.5b$ and $l^* = 47b$ values are relatively small. For such a small a^* , the dependence of σ_p on $\ln[(a/(eb))]$ is not weak and, therefore, reduction of a^* due to the effects described above (smaller effective domain-wall area due to bevelled shape) has a strong effect on σ_p . Taken together, the various effects lead to a reduction in σ_p by a factor of about 30 relative to the Miller–Weinreich estimate for nucleation at the 90° domain wall under an applied field of 0.1 MV cm^{-1} . This results in $\sigma_p \approx 5.7 \text{ mJ cm}^{-2}$, much smaller than the local interface energy characterized by the effective domain-wall energy $\sigma_{\text{eff},w} = 15.4 \text{ mJ cm}^{-2}$. The small value of σ_p justifies our neglect of electrostatic interactions in the analytical model of the nucleus, and the much smaller σ_p/σ_w ratio corresponds to an aspect ratio of the critical nucleus (l^*/a^*) that is close to one.

As illustrated in Extended Data Fig. 7, similar effects can be obtained for nucleation on the 180° domain wall under an applied field of 0.3 MV cm^{-1} using the DFT 180°-domain-wall σ_w value of 132 mJ m^{-2} and standard parameters for PbTiO_3 (dielectric constant $\epsilon = 60$, bulk polarization $P_s = 0.75 \text{ C m}^{-2}$, $b = 3.9 \text{ \AA}$, $c = 4 \text{ \AA}$ and $e = 2.718$).

Model parameters for non-180° domain walls. The nucleation model discussed here is similar to the model in ref. 17. The mapping scheme discussed therein allows the treatment of a non-180° domain wall as a generalized 180° domain wall lying in the Y – Z plane with polarization changing from $+P_Y$ to $-P_Y$ along X . The following five parameters are required to estimate the nucleation energy at the domain wall under a given temperature T : $P_s(T)$, $A_{\text{loc}}(T)$, g_{YY} , g_{YX} and g_{YZ} , where:

$$\begin{aligned} P_Y(T) &= \gamma P_s(T) \\ A_{\text{loc}}(T) &= A_{\text{loc}}(0) \frac{P_s^4(T)}{P_s^4(0)} \\ A_{\text{loc}}^Y(0) &= \gamma^4 A_{\text{loc}}(0) \end{aligned}$$

$$g_{YX} \approx g_{YZ} = \left[\frac{3\sigma_{DW}^{YX}}{8P_Y(0)} \right]^2 \frac{1}{A_{loc}^Y(0)} = A_{loc}^Y(0) \left[\frac{\delta_X}{2P_Y(0)} \right]^2$$

$$g_{YY} = \left[\frac{3\sigma_{DW}^{YY}}{8P_Y(0)} \right]^2 \frac{1}{A_{loc}^Y(0)} = A_{loc}^Y(0) \left[\frac{\delta_Y}{2P_Y(0)} \right]^2$$

Here P_s is the total local polarization, γ is the fraction of the polarization variation across the domain boundary (for example, $\gamma = \sqrt{2}/2$ for a 90° domain wall), A_{loc} is the energy difference between the ferroelectric phase and the high-symmetry paraelectric phase, σ_{DW}^{YX} is the energy of a domain wall with normal along X and neighbouring dipoles along Y , and δ_X is the polarization diffuseness parameter over which the polarization changes across the domain boundary. By analogy, σ_{DW}^{YY} is the energy of a domain wall with normal along Y and neighbouring dipoles along Y (head-to-head or tail-to-tail domain wall), and δ_Y is the associated diffuseness parameter. $P_s(0)$ and $A_{loc}(0)$ are extracted from zero-kelvin DFT calculations. The temperature dependence of $P_s(T)$ is taken from experiments when available. The values of g_{YY} and g_{YZ} can be determined on the basis of the domain-wall energy (σ_{DW} , calculated from DFT) or diffuseness parameters (δ , calculated from molecular dynamics). In practice, g_{YY} , g_{YX} and g_{YZ} are of the same order and therefore $g_{YX} \approx g_{YY}$ is a useful approximation.

For BaTiO₃, DFT calculations using the PBEsol density functional³⁴ with $a = 3.986$ Å and $c/a = 1.01$ give $A_{loc}(0) = 3.48 \times 10^7$ J m⁻³, $\sigma_{180DW} = 11$ mJ m⁻², $\sigma_{90DW} = 3.89$ mJ m⁻², $P_s(0) = 0.283$ C m⁻² and $g_{YX} = 0.61 \times 10^{-11}$ m³ F⁻¹. These parameters are used for simulating the hysteresis loop in Fig. 3b. For PbTiO₃, we use experimental lattice constants ($a = 3.9$ Å and $c = 4.15$ Å) for DFT calculations with PBEsol and obtain $A_{loc}(0) = 5.05 \times 10^8$ J m⁻³, $\sigma_{180DW} = 175$ mJ m⁻², $\sigma_{90DW} = 67$ mJ m⁻², $g_{YX} = 1.21 \times 10^{-11}$ m³ F⁻¹. The temperature dependence of polarization is taken from ref. 35, with $P_s(0) = 0.872$ C m⁻². These parameters are used for predicting the coercive fields of PbTiO₃-based ceramics and thin films in Fig. 3a, c.

LGD model for BiFeO₃ and other rhombohedral ferroelectrics with O₆ rotations. 71° , 109° and 180° domain walls are all observed in BiFeO₃. The energetics of these three types of domain walls have been investigated with DFT in several studies^{36–38}. In ref. 36, $\sigma_{71DW} = 152$ mJ m⁻², $\sigma_{109DW} = 62$ mJ m⁻² and $\sigma_{180DW} = 73$ mJ m⁻² was reported using LDA+U. In ref. 38, $\sigma_{71DW} = 128$ mJ m⁻², $\sigma_{109DW} = 33$ mJ m⁻² and $\sigma_{180DW} = 98$ mJ m⁻² was reported with GGA+U. From equation (5), we deduce that $\sigma_{DW}^{YX} \propto P_Y \sqrt{A_{loc}^Y g_{YX}}$. Assuming the polarization gradient coefficient is isotropic, the energy of a non- 180° domain wall (σ_{DW}^2) can be related to that of a 180° domain wall: $\sigma_{DW}^2 = \gamma^3 \sigma_{180DW}$. Therefore, for a given ferroelectric, $\sigma_{71DW}:\sigma_{90DW}:\sigma_{109DW}:\sigma_{180DW} = 0.192:0.354:0.544:1$. This relationship works well for 90° and 180° domain walls in BaTiO₃ and PbTiO₃ (ref. 16), and reasonably well for 109° and 180° domain walls in BiFeO₃ (refs 36, 38). However, the 71° domain wall is found to have the highest energy in BiFeO₃, which is attributed to the mismatch of oxygen octahedral rotation across the domain boundary^{36,38}. To capture this feature, we introduce a second order parameter, oxygen octahedra rotation (Θ), into the LGD model of BiFeO₃. Therefore, the 71° domain wall in BiFeO₃ has the following extra energy term:

$$U_\Theta = \frac{1}{2} K \int_{-\infty}^{\infty} dX \int_{-\infty}^{\infty} dY \int_{-\infty}^{\infty} dZ [\Theta_{DW}(X, Y, Z) - \Theta_{bulk}(X, Y, Z)]$$

where K is the harmonic angle constant and $\Theta_{bulk}(X, Y, Z) \approx 8^\circ$ (ref. 38). The value of K (6.106×10^9 J m⁻³ rad⁻²) is optimized such that the LGD model reproduces the DFT value of σ_{71DW} with the gradient coefficient ($g_{YX} = 0.32 \times 10^{-11}$ m³ F⁻¹) estimated from σ_{109DW} . The following term is then added to equation (3) when estimating the nucleation energy:

$$\Delta U_\Theta = \frac{1}{2} K \int_{-\infty}^{\infty} dX \int_{-\infty}^{\infty} dY \int_{-\infty}^{\infty} dZ [\Theta_{nuc}(X, Y, Z) - \Theta_{DW}(X, Y, Z)]$$

where an analytical equation similar to equation (4) is used to describe the angle profile $\Theta_{nuc}(X, Y, Z)$. Other parameters are $A_{loc}(0) = 5.81 \times 10^8$ J m⁻³, $P_s(0) = 0.987$ C m⁻² and $T_0 = 1,120$ K.

Coarse-grained simulation of P - E hysteresis loop. The coercive field reflects the ease of domain reversal and is one of the most important characteristic parameters of ferroelectrics for practical applications. For the domain-reversal process achieved via domain-wall motion, the change in the polarization under an applied electric field directly correlates with the distance moved by the domain wall, the velocity of which can be estimated using Merz's law. We extract the pre-exponential

factor v_0 in Merz's law from molecular dynamics simulations in the creep-like region and obtain E_a for PbTiO₃ from the LGD model with parameters calculated with DFT PBEsol³⁹. With these values of v_0 and E_a , we then simulate the hysteresis loops at 300 K and obtain the frequency dependence of E_c for varying domain sizes (Fig. 3a). Following the experimental set-up used in most hysteresis-loop measurements, a triangular electric field $E(t)$, with frequency f , maximum magnitude E_0 and time t , is used in the simulation:

$$E(t) = \begin{cases} 4fE_0t & 0 < t < \frac{1}{4f} \\ -4fE_0t + 2E_0 & \frac{1}{4f} < t < \frac{3}{4f} \\ 4fE_0t - 4E_0 & \frac{3}{4f} < t < \frac{1}{f} \end{cases}$$

At $t = 0$, the domain of size d is fully poled with saturation polarization $-P_s$. Assuming the domain reversal is achieved via domain-wall motion, the polarization at time t can be calculated using:

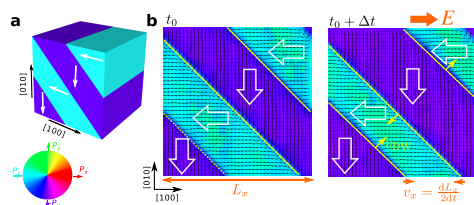
$$P(t) = -P_s + \frac{\int_0^{1/f} v(t) dt}{d} P_s \quad (6)$$

where $v(t)$ is the domain-wall velocity at time t and is calculated using Merz's law: $v(t) = v_0 \exp[-E_a/E(t)]$. When the value of $P(t)$ obtained from equation (6) is larger than P_s (such that the domain is already fully reversed), $P(t)$ is set to P_s . Plotting $P(t)$ with respect to $E(t)$ gives the hysteresis loop. The coercive field E_c is the magnitude of the electric field when $P(t) = 0$. On the basis of the molecular dynamics simulation results, we used $v_0 = 300$ m s⁻¹ for predicting room-temperature coercive fields. We find that the coercive field is not sensitive to the value of v_0 , as demonstrated by the moderate change in coercive fields in response to orders of magnitude change in d (which is equivalent to changing v_0 for fixed d) shown in Fig. 3. This indicates that the magnitude of the coercive field is largely determined by the activation field.

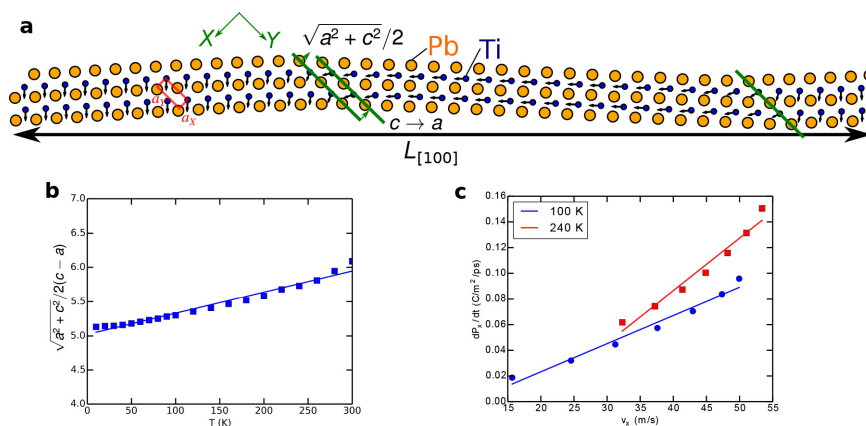
Comparison of coercive fields for tetragonal and rhombohedral ferroelectrics. The values of P_s , $A_{loc}(0)$, σ_{90DW} , g_{YX} and g_{YX} are derived from PbTiO₃. These parameters are used for simulating the hysteresis loop and coercive field of tetragonal (T) ferroelectrics. The value of σ_{71DW} is estimated as $0.542\sigma_{90DW}$ (as explained above). To account for the possible octahedral rotations across the 71° domain wall, we use the angle constant derived from BiFeO₃ when simulating the coercive field for rhombohedral (R) ferroelectrics; we find that $E_c^T/E_c^R \approx 1.8$.

Effect of supercell size. We carried out a benchmark study on the effect of supercell size (Extended Data Fig. 8). We calculated the domain-wall velocity with $40 \times 40 \times 40$, $50 \times 50 \times 40$, $60 \times 60 \times 40$ and $65 \times 65 \times 40$ supercells at 200 K and 240 K. The key finding is that the values obtained with the $40 \times 40 \times 40$ supercell do not substantially deviate from values found using the larger supercells (within 10 m s⁻¹). Most importantly, the v_x - E slope is similar for supercells of different sizes, showing that the domain-wall dynamics obtained with a $40 \times 40 \times 40$ supercell are robust against supercell size.

- Shin, Y.-H., Cooper, V. R., Grinberg, I. & Rappe, A. M. Development of a bond-valence molecular-dynamics model for complex oxides. *Phys. Rev. B* **71**, 054104 (2005).
- Jablonski, M. L. *et al.* Asymmetric response of ferroelastic domain-wall motion under applied bias. *ACS Appl. Mater. Interfaces* **8**, 2935–2941 (2016).
- Wojdeł, J. C. & Íñiguez, J. Ferroelectric transitions at ferroelectric domain walls found from first principles. *Phys. Rev. Lett.* **112**, 247603 (2014).
- Perdew, J. P. *et al.* Restoring the density-gradient expansion for exchange in solids and surfaces. *Phys. Rev. Lett.* **100**, 136406 (2008).
- Rossetti, G. A. Jr, Cline, J. P. & Navrotsky, A. Phase transition energetics and thermodynamic properties of ferroelectric PbTiO₃. *J. Mater. Res.* **13**, 3197–3206 (1998).
- Diéguez, O., Aguado-Puente, P., Junquera, J. & Íñiguez, J. Domain walls in a perovskite oxide with two primary structural order parameters: first-principles study of BiFeO₃. *Phys. Rev. B* **87**, 024102 (2013).
- Ren, W. *et al.* Ferroelectric domains in multiferroic BiFeO₃ films under epitaxial strains. *Phys. Rev. Lett.* **110**, 187601 (2013).
- Wang, Y. *et al.* BiFeO₃ domain wall energies and structures: a combined experimental and density functional theory + U study. *Phys. Rev. Lett.* **110**, 267601 (2013).
- Zhao, Y. & Truhlar, D. G. Construction of a generalized gradient approximation by restoring the density-gradient expansion and enforcing a tight Lieb–Oxford bound. *J. Chem. Phys.* **128**, 184109 (2008).

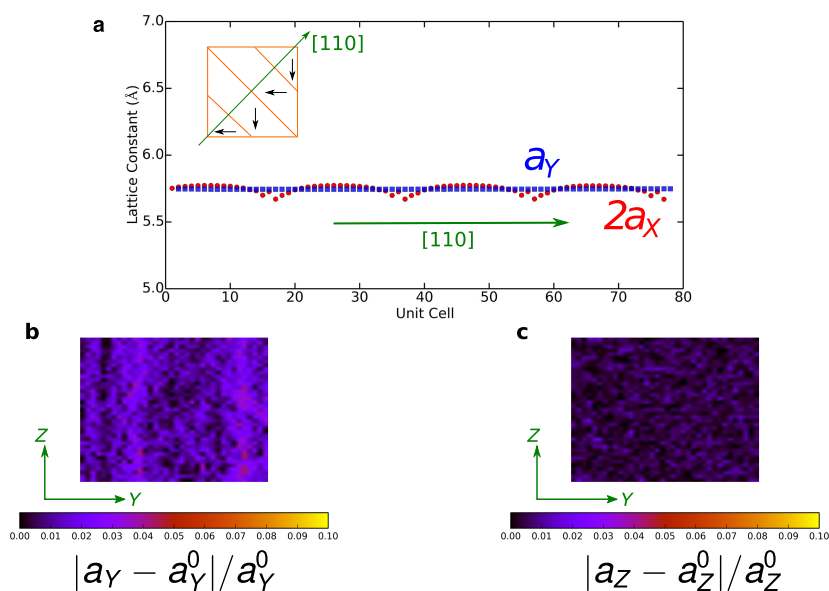


Extended Data Figure 1 | Large-scale molecular dynamics simulations of 90°-domain-wall motions. **a**, Schematic of a $40 \times 40 \times 40$ supercell with 90° domain walls used in molecular dynamics simulations. The colours of the domains correspond to the polarization (P) wheel shown at the bottom. White arrows represent the polarization directions of domains. **b**, Simulated domain evolution under a $[100]$ -oriented electric field (E). The dashed yellow lines show the positions of 90° domain walls. The electric field is turned on at time t_0 . The domain-wall velocity v_{DW} along $[110]$ (yellow arrows) is estimated on the basis of the change in the supercell dimension (L_x) along $[100]$ from t_0 to $t_0 + \Delta t$. The black arrows scale with the local dipole of each unit cell. The domain wall motion is achieved via the 90° switching of $[\bar{1}00]$ dipoles to $[0\bar{1}0]$ dipoles.



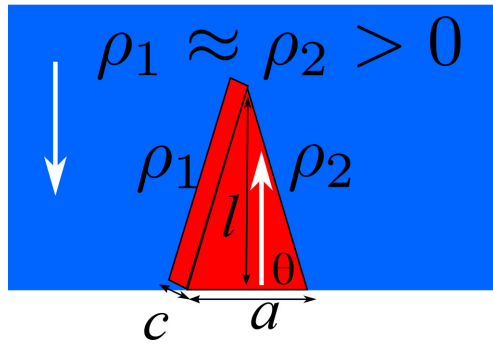
Extended Data Figure 2 | Lattice constants of supercells used in molecular dynamics simulations. **a**, Pb (orange) and Ti (blue) sublattices in a PbTiO_3 supercell with 90° domain walls. The boundaries are marked by green lines. a_X and a_Y are effective lattice constants of the domain-wall unit cell defined in the transformed X - Y coordinates and shown by the red rectangle. When dipoles in one layer of unit cells switch by 90° ($c \rightarrow a$),

the wall moves by $(a^2 + c^2)^{1/2}/2$ along the $[110]$ direction. **b**, Temperature (T) dependence of $\sqrt{a^2 + c^2}/[2(c - a)]$ obtained from molecular dynamics simulations (squares). It depends on temperature weakly (blue line). **c**, Plot of polarization change (dP_x/dt) versus cell-dimension change (v_x). The solid curves show linear fits at 100 K (blue) and 240 K (red).



Extended Data Figure 3 | Elastic energy contribution to nucleation energy. **a**, Effective lattice constants across 90° domain walls. The inset is the top view of the $40 \times 40 \times 40$ supercell used in molecular dynamics simulations; black arrows indicate the polarization direction. The effective lattice constants (a_X and a_Y) are defined in X - Y coordinates, as explained in Extended Data Fig. 1. The averaged lattice constants for

each layer of cells across the domain wall along the $[110]$ direction are plotted. **b**, **c**, Distributions of strain gradient at the domain wall in the presence of a nucleus. a_Y^0 and a_Z^0 are the effective lattice constants along Y and Z in the absence of nucleus ($t = 0$ ps in molecular dynamics simulations), respectively.



Extended Data Figure 4 | Schematic of a triangular-shaped nucleus, as in the Miller–Weinreich model. The triangular-shaped nucleus (red) has a polarization direction (white arrows) that is antiparallel to its neighbouring domains (blue). The depolarization charges $\rho_{1,2}$ at two boundaries are of the same sign, giving rise to repulsive energy penalty. The expressions for nucleation energy (U_{nuc}), depolarization energy (U_d),

Nucleation Energy

$$U_{\text{nuc}} = -2P_s E a l c + 2\sigma_w c(a^2 + l^2)^{\frac{1}{2}} + U_d$$

Depolarization Energy

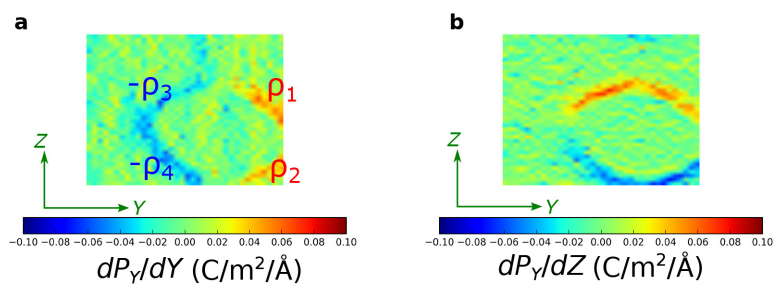
$$U_d = 8P_s^2 \frac{c^2}{\epsilon} \frac{a^2}{l} \ln \frac{2a}{eb} = 2\sigma_p b a^2 / l$$

$$\sigma_p = 4P_s^2 \frac{b}{\epsilon} \ln \frac{2a}{eb}$$

Dimensions of critical nucleus

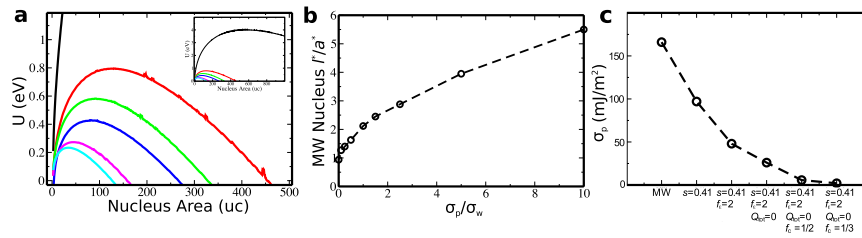
$$a^* = \frac{\sigma_w}{P_s E} \frac{\sigma_w + 2\sigma_p}{\sigma_w + 3\sigma_p} \quad l^* = \frac{\sigma_w^{\frac{1}{2}}}{(P_s E (\sigma_w + 3\sigma_p)^{\frac{1}{2}})}$$

depolarization-contributed domain-wall energy (σ_p) and the dimensions for the critical nucleus a^* and l^* are taken from the original work of Miller and Weinreich, ref. 15; c and b are lattice constants ($c \approx b$ in PbTiO_3 and BaTiO_3), e is the base of natural logarithm, and ϵ is the dielectric constant. The σ_p/σ_w ratio determines the aspect ratio of the critical nucleus (l^*/a^*).



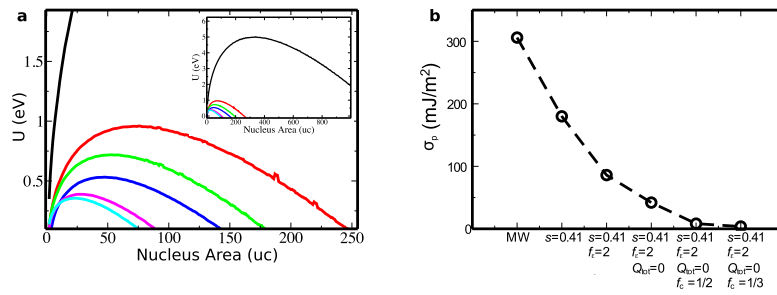
Extended Data Figure 5 | Distributions of polarization gradient at the domain wall in the presence of a nucleus. a, b, The polarization gradients (dP_Y/dY , **a**; dP_Z/dZ , **b**) are highest at the boundary of the nucleus. The maximum polarization gradient is around $0.08 \text{ C m}^{-2} \text{ \AA}^{-1}$,

much smaller than the value estimated by the classical theories in ref. 15 ($0.25 \text{ C m}^{-2} \text{ \AA}^{-1}$). This difference is due to the diffuse nature of the boundary. The total boundary charge ($\rho_1 + \rho_2 + \rho_3 + \rho_4$) is zero.



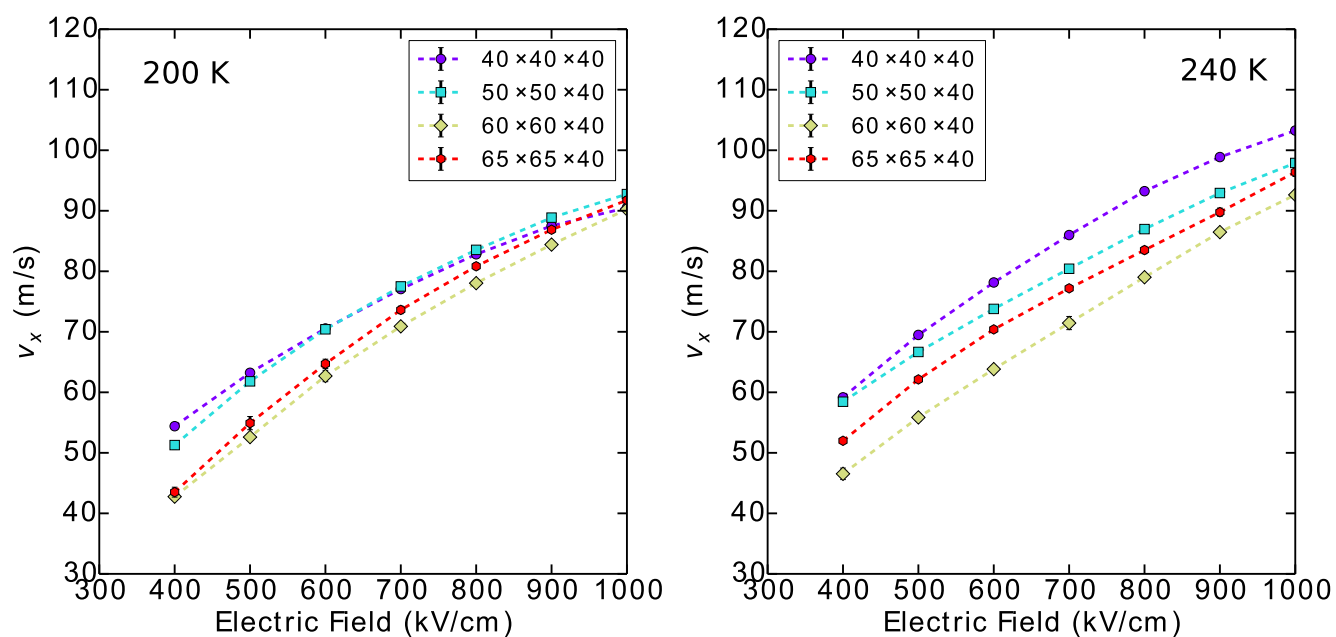
Extended Data Figure 6 | Results for the Miller–Weinreich model of nucleation on the PbTiO₃ 90° domain wall using various conditions for the interface boundary. **a**, Nucleus energy U as a function of Miller–Weinreich nucleus area (al , given in terms of the number of unit cells (uc)) for the original Miller–Weinreich model (black) and Miller–Weinreich models with $s = 0.41, f_c = 1, Q_{\text{tot}} \neq 0$ and $f_c = 1$ (red), $s = 0.41, f_c = 2, Q_{\text{tot}} \neq 0$ and $f_c = 1$ (green), $s = 0.41, f_c = 2, Q_{\text{tot}} = 0$ and $f_c = 1$ (blue), $s = 0.41, f_c = 2$,

$Q_{\text{tot}} = 0$ and $f_c = 1/2$ (magenta), and $s = 0.41, f_c = 2, Q_{\text{tot}} = 0$ and $f_c = 1/3$ (cyan). Inset, zoomed-out view showing all the curves. **b**, Aspect ratio of the Miller–Weinreich nucleus (l^*/a^*) as a function of the ratio between σ_p and σ_w . The Miller–Weinreich assumption that $l^* \gg a^*$ is not valid for realistic values of σ_p and σ_w . **c**, σ_p for different interface conditions. The actual σ_p is much smaller than the estimate used by Miller and Weinreich (MW; ref. 15).

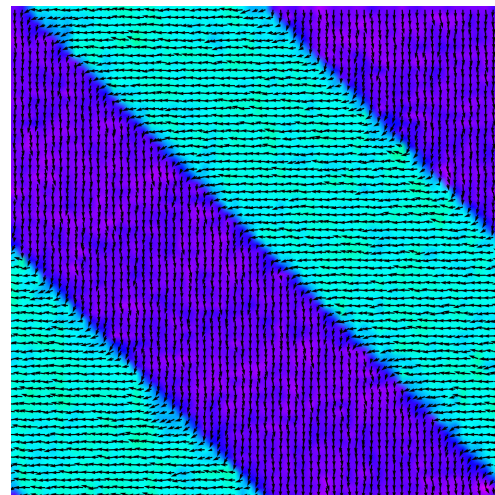
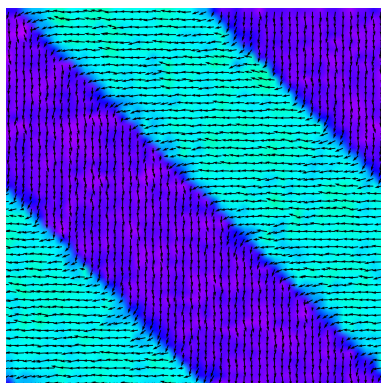
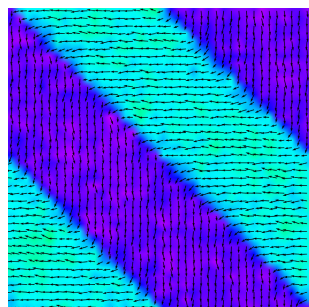


Extended Data Figure 7 | Results for the Miller–Weinreich model of nucleation on the PbTiO_3 180° domain wall using various conditions for the interface boundary. **a**, Nucleus energy U as a function of Miller–Weinreich nucleus area (al , given in terms of the number of unit cells (uc)) for the original Miller–Weinreich model (black) and Miller–Weinreich models with $s = 0.41$, $f_c = 1$, $Q_{\text{tot}} \neq 0$ and $f_c = 1$ (red), $s = 0.41$, $f_c = 2$,

$Q_{\text{tot}} \neq 0$ and $f_c = 1$ (green), $s = 0.41$, $f_c = 2$, $Q_{\text{tot}} = 0$ and $f_c = 1$ (blue), $s = 0.41$, $f_c = 2$, $Q_{\text{tot}} = 0$ and $f_c = 1/2$ (magenta), and $s = 0.41$, $f_c = 2$, $Q_{\text{tot}} = 0$ and $f_c = 1/3$ (cyan). Inset, zoomed-out view showing all the curves. **b**, σ_p for different interface conditions. The actual σ_p is much smaller than the estimate used by Miller–Weinreich (MW; ref. 15).



40x40x40, 320,000 atoms **50x50x40, 500,000 atoms** **65x65x40, 845,000 atoms**



Extended Data Figure 8 | Test of domain-wall velocity (v_x) convergence with supercell size. The colours of the domains in the bottom panels correspond to those in Extended Data Fig. 1. The error bars are standard deviations.

Self-assembly of microcapsules via colloidal bond hybridization and anisotropy

Chris H. J. Evers¹, Jurriaan A. Luiken², Peter G. Bolhuis² & Willem K. Kegel¹

Particles with directional interactions are promising building blocks for new functional materials and may serve as models for biological structures^{1–3}. Mutually attractive nanoparticles that are deformable owing to flexible surface groups, for example, may spontaneously order themselves into strings, sheets and large vesicles^{4–6}. Furthermore, anisotropic colloids with attractive patches can self-assemble into open lattices and the colloidal equivalents of molecules and micelles^{7–9}. However, model systems that combine mutual attraction, anisotropy and deformability have not yet been realized. Here we synthesize colloidal particles that combine these three characteristics and obtain self-assembled microcapsules. We propose that mutual attraction and deformability induce directional interactions via colloidal bond hybridization. Our particles contain both mutually attractive and repulsive surface groups that are flexible. Analogously to the simplest chemical bond—in which two isotropic orbitals hybridize into the molecular orbital of H₂—these flexible groups redistribute on binding. Via colloidal bond hybridization, isotropic spheres self-assemble into planar monolayers, whereas anisotropic snowman-shaped particles self-assemble into hollow monolayer microcapsules. A modest change in the building blocks thus results in much greater complexity of the self-assembled structures. In other words, these relatively simple building blocks self-assemble into markedly more complex structures than do similar particles that are isotropic or non-deformable.

Deformability and mutual attraction have recently been combined for the self-assembly of nanoparticles by grafting flexible polymers onto the surface of mutually attractive particles. This results in isotropic clusters¹⁰ and self-assembled strings, sheets and large vesicles^{4,5}. For micrometre-sized colloids, on the other hand, coupling mutual attraction and anisotropy leads to patchy particles. Attractive domains, or patches, have induced self-assembly into open lattices and the colloidal equivalents of molecules and micelles^{7–9}. Here, we combine these three properties—mutual attraction, anisotropy and deformability—by synthesizing snowman-shaped particles that consist of a deformable core and a non-deformable lobe or protrusion. In the first part of this Letter, mutual attraction is combined with deformability, resulting in anisotropic or directional interactions as the flexible surface groups redistribute on binding (Fig. 1e). This process is analogous to bond hybridization in quantum chemistry. When two hydrogen atoms bind and form H₂, for example, the electrons around each atom redistribute, that is, two isotropic orbitals hybridize into the molecular orbitals of H₂. Similarly, when mutually attractive, deformable particles bind, the flexible surface groups redistribute resulting in directional interactions. We refer to this effect as colloidal bond hybridization. We observe fundamentally new behaviour on combining colloidal bond hybridization with anisotropy, that is, for particles that are mutually attractive and deformable as well as anisotropic. These snowman-shaped particles self-assemble into microcapsules and form spherical cavities at high particle concentrations. We hypothesize that mutual attraction,

anisotropy and deformability are sufficient to stabilize curved structures and we support this hypothesis with computer simulations.

We create isotropic as well as anisotropic building blocks that are mutually attractive and deformable. Before discussing the more complex anisotropic particles, we consider the basic principles of colloidal bond hybridization using mutually attractive, isotropic, deformable particles. These poly(styrene-*co*-acrylic acid) spheres are synthesized by copolymerization in water (Fig. 1a, b), and acrylic acid and styrene are incorporated at different stages of the polymerization process^{11,12}. Hence the particles consist of a hydrophobic polystyrene-rich core and a hydrophilic poly(acrylic acid)-rich brush. The particles are mutually attractive as hydrophobic polystyrene groups are present both in the interior of the particles and the brush. Furthermore, dynamic light scattering shows that the poly(acrylic acid)-rich brush can rearrange on the order of 0.1 μm, rendering the particles deformable (Extended Data Fig. 1).

Mutually attractive, isotropic, deformable particles self-assemble into planar monolayers in water (Fig. 1c, d). The monolayer sheets are hexagonally ordered and move freely in the solution (Supplementary Video 1). We hypothesize that a colloidal equivalent of bond hybridization drives the formation of the monolayers. The polymer brush contains hydrophobic styrene groups as well as hydrophilic acrylic acid groups (Fig. 1e, shown in yellow and blue). The attraction between the hydrophobic groups promotes compact structures, whereas excluded volume effects of the hydrophilic parts favour unbound particles. To accommodate both effects, the polymer brush rearranges on binding: hydrophobic parts interact in-plane, whereas hydrophilic parts expand out-of-plane. Consequently, directional interactions are induced and planar monolayers are formed (Fig. 1e).

This segregation process is similar to phase segregation in the self-assembly of block copolymers¹³. In our system, however, copolymers are anchored to the surface of micrometre-sized particles. Consequently, the molecular segregation of the polymers induces directional interactions on the colloidal length scale. Our observations are also in line with results for polymer-grafted nanoparticles that are mutually attractive, isotropic and deformable^{4–6,14} but here directional interactions are induced for particles that are two orders of magnitude larger than in previous work. Finally, DNA-coated colloids can also form crystalline monolayers¹⁵, but for these particles a functionalized surface induces directional interactions.

Below, we combine colloidal bond hybridization with anisotropy, which results in fundamentally new behaviour. Anisotropic building blocks are synthesized by growing a rigid protrusion onto the deformable spheres of Fig. 1 (Extended Data Fig. 2). The second lobe is grown by swelling with additional styrene^{16–18}. Furthermore, we increase the attraction between the deformable lobes by functionalizing the poly(acrylic acid)-rich brush with hydrophobic groups¹⁹ (Extended Data Fig. 10). Next, the particles are washed by centrifugation. Finally, we obtain snowman-shaped particles that consist of a deformable lobe and a non-deformable lobe (Fig. 2a).

¹Van 't Hoff Laboratory for Physical and Colloid Chemistry, Debye Institute for Nanomaterials Science, Utrecht University, Padualaan 8, 3584 CH Utrecht, The Netherlands. ²Van 't Hoff Institute for Molecular Sciences, University of Amsterdam, PO Box 94157, 1090 GD Amsterdam, The Netherlands.

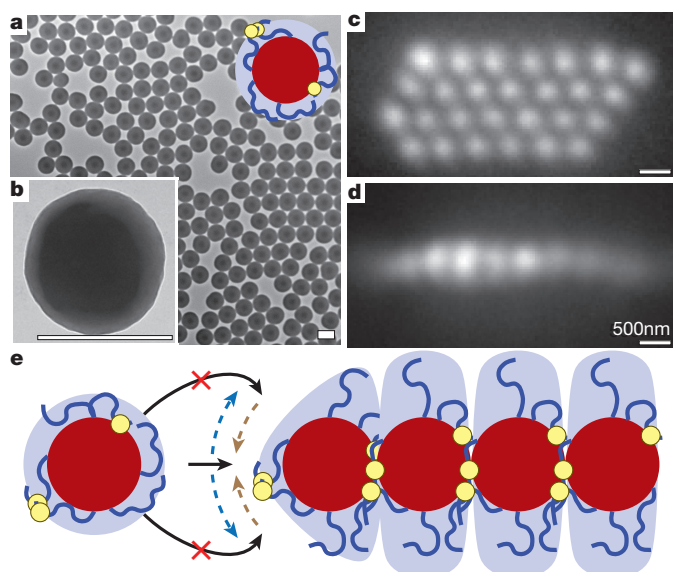


Figure 1 | Self-assembled planar monolayers. **a, b,** Mutually attractive, isotropic, deformable particles (**a, b**, TEM images) consist of a polystyrene-rich core (red), a deformable poly(acrylic-acid)-rich brush (blue) and mutually attractive moieties (yellow). **c, d,** In water, the particles self-assemble into planar hexagonal monolayers seen from the top (**c**) and side (**d**) by reflected light microscopy. **e,** In colloidal bond hybridization, surface groups of deformable particles redistribute on binding; mutually attractive moieties move towards the contact area (brown arrows), whereas hydrophilic chains move into the solution (blue arrows). Hence, new bonds are formed in-plane (black arrow) and not out-of-plane (crossed black arrows). Scale bars, 500 nm.

These mutually attractive, anisotropic, deformable particles self-assemble into monolayer microcapsules (Fig. 2). The microcapsules can be observed with scanning electron microscopy (SEM) after sintering or freeze drying (Fig. 2a, Extended Data Fig. 3). Owing to the relatively large size of the particles, however, we can study these structures in solution using optical microscopy (Fig. 2g–j). The microcapsules consist of a particle monolayer whereas the interior is water-filled (Fig. 2c, Supplementary Video 3). Furthermore, most particles align tangentially to the surface of the microcapsules, with the protrusions pointing either slightly inwards or slightly outwards (Fig. 2a, b, Extended Data Fig. 3).

For particles with a large lobe of $0.540\ \mu\text{m}$ in diameter, the mean diameter of the microcapsules is $3.7 \pm 0.8\ \mu\text{m}$, corresponding to about 10^2 particles per microcapsule. Most particles have six nearest neighbours, but pentagons occur frequently as expected from the Euler characteristic of a sphere (Fig. 2a, Supplementary Video 2). The structure of the microcapsules, however, has no overall icosahedral symmetry. Furthermore, excess styrene is removed before the microcapsules are formed, so unlike colloidosomes—which are formed on emulsion droplets²⁰—no template is involved.

By systematically varying the complexity of the particles, we identified that in our system mutual attraction, anisotropy and deformability are required for self-assembly into microcapsules (Extended Data Fig. 4a–d). First, before functionalization with mutually attractive groups, no microcapsules are found for any of the anisotropic, deformable particles in Fig. 2d–f, demonstrating the importance of mutual attraction. Second, for hydrophobically functionalized, deformable, but isotropic spheres, no microcapsules are observed. Finally, for functionalized, anisotropic, but non-deformable snowman-shaped particles, no microcapsules are observed. These three characteristics seem sufficient to induce self-assembly into microcapsules, and are relatively easy to implement experimentally. In contrast, particles with four orthogonally attractive patches, which have previously been predicted to induce self-assembly into microcapsules, have not been

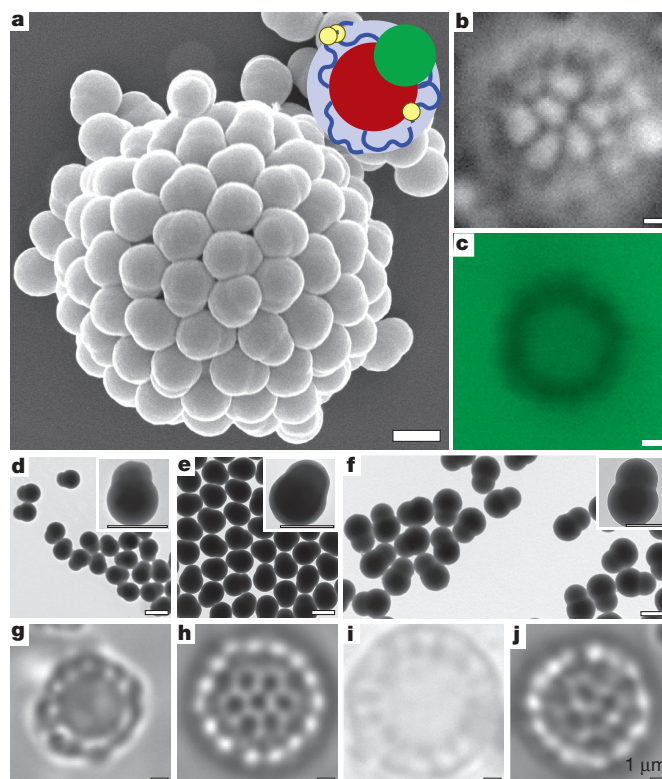


Figure 2 | Self-assembled monolayer microcapsules. **a,** Deformable, anisotropic, mutually attractive particles (inset) consist of a core (red) with hydrophilic (blue) and hydrophobic (yellow) moieties and a rigid protrusion (green), and self-assemble into microcapsules (SEM image after sintering). **b, c,** In solution the particles align tangentially (**b**; reflected light microscopy) and the microcapsules are water-filled (**c**; confocal fluorescence microscopy with dyed water phase). **d–f,** The synthesized particles have large lobes with diameters of 445 nm (**d**), 540 nm (**e**) and 626 nm (**f**, TEM images). **g–i,** For each size (bright field microscopy) self-assembled microcapsules are found on functionalization with fluoresceinamine. **j,** On functionalization with *tert*-butylamine (bright field microscopy), self-assembled microcapsules are also found. Scale bars, $1\ \mu\text{m}$.

experimentally realized yet²¹. Moreover, the self-assembling tendency is robust, as both monolayer microcapsules and planar monolayers are found for snowman-shaped particles with large lobes of diameters ranging from 445 nm to 626 nm, and for hydrophobic functionalization with either *tert*-butylamine or fluoresceinamine (Fig. 2d–j, Extended Data Fig. 5).

At high particle concentrations, mutually attractive, anisotropic, deformable particles form curved hollow structures or cavities, and these are probably intermediates in the formation of the microcapsules. The tendency to form cavities is robust, as similar structures are observed for five different experimental conditions. The first condition is at the edge of an evaporating droplet on a glass slide (Fig. 3a–e). The evaporation of a droplet of particles in water causes a particle flow towards the glass–water–air contact line that is known as the coffee-stain effect²². For our particles, hemispherical cavities are spontaneously formed in the resulting dense layer near the contact line (Fig. 3b–e, Extended Data Fig. 6a–d). The second condition is for a droplet that is confined between two parallel glass slides (Fig. 3f–j, Supplementary Video 4). Again, a dense layer is formed at the contact line, but this layer is two-dimensional with circular cavities. The third condition is at particle volume fractions of ~ 0.2 , where a highly fluctuating ‘cavity phase’ is formed (Fig. 3k–n, Supplementary Video 5). In this phase, we observe coexisting regions on the order of $1\text{--}10\ \mu\text{m}$ with either high particle concentrations or virtually no particles, that is, dense curved structures around cavities. For the fourth condition,

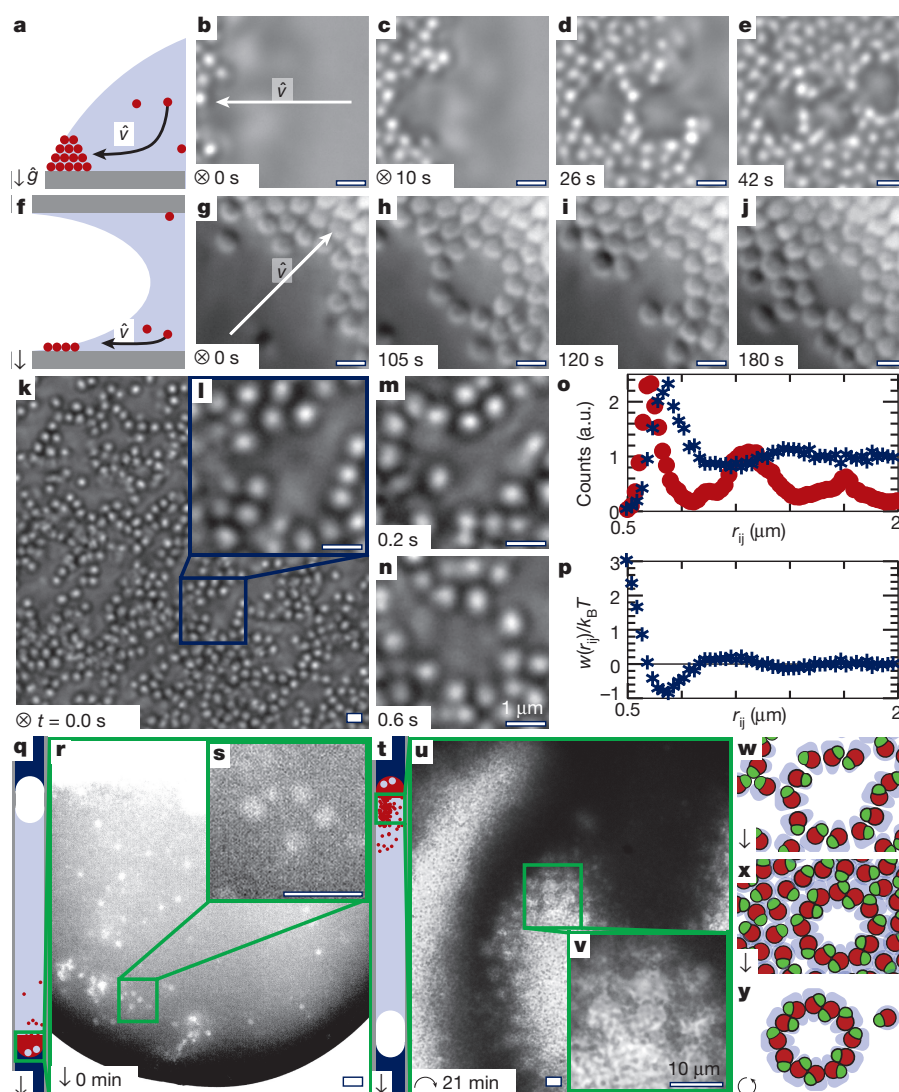


Figure 3 | Cavity formation on densification. **a–n**, Cavities are observed at the edge of an evaporating droplet (**a–e**, multilayer; **f–j**, monolayer) and in a cavity phase (**k–n**). Scale bars, 1 μm . **o, p**, The histograms of the interparticle distance r_{ij} (**o**) peak at 0.72 μm (cavity phase, blue asterisks) and at 0.62 μm (microcapsules, red circles), and the effective pair potential $w(r_{ij})$ (**p**) has a minimum of $-0.8k_B T$. a.u., arbitrary units. **q–v**, Cavities are also observed after centrifugation in a thin cell (**q–s**, bright regions), and upon turning the

cell upside down (**t–v**). Scale bars, 10 μm . **w, x**, Particles form a cavity phase on densification (**w**), and are pushed into close contact on centrifugation (**x**). **y**, We propose that after redispersion, the particles that surrounded cavities are found as microcapsules. Large arrows indicate the flow, \vec{v} ; small arrows indicate the gravitational field, \vec{g} ; t denotes time. In **a, f, q** and **t**, particles are coloured red, the solvent is light blue, glue is dark blue and glass is grey. In **w–y**, cores are red, protrusions are green and deformable brushes are light blue.

on centrifuging particles in a capillary, cavities are observed in the sediment (Fig. 3q–s and Extended Data Fig. 7a). Finally, on diluting the sediment, the formation of circular cavities is again observed (Fig. 3t–v, Supplementary Video 6).

For all five conditions, the diameters of the cavities are comparable to the diameters of the microcapsules. Furthermore, by systematically varying the complexity of the building blocks, we conclude that—as for the formation of the microcapsules—mutual attraction, anisotropy and deformability all greatly influence the formation of the cavities (Extended Data Fig. 4). For isotropic particles, we proposed that mutual attraction and deformability induce the observed self-assembly into planar monolayers by colloidal bond hybridization. On the basis of the above observations, we hypothesize that adding anisotropy to mutually attractive and deformable colloids induces a shift from planar to curved structures, resulting in microcapsules and cavities.

The formation of microcapsules is a rare event as only 1 in every 10^4 particles ends up in a microcapsule. This can be ascribed to the specific orientation of many particles that is required for the formation of microcapsules, and the initially weak attractive interactions. The

latter becomes apparent as the minimum in the effective pair potential is comparable to the thermal energy, $k_B T$ (where k_B is Boltzmann's constant and T is temperature; Fig. 3p), and particles do not form lasting clusters on collision (Supplementary Video 5). Furthermore, for particles in such non-lasting clusters, the centre-to-centre distance distribution peaks at a distance that is 0.1 μm larger than for particles in microcapsules (Fig. 3o). The difference in the centre-to-centre distance can be attributed to the hydrophilic chains with an estimated length of about 0.1 μm . These chains need to move out of the binding site on bond formation (Fig. 1e).

We propose that both the specific orientation and the formation of lasting bonds are induced by centrifugation with cavities as intermediates. The synthesis consists of several centrifugation steps and centrifugation induces the formation of spherical cavities with a similar size and shape as the microcapsules (Fig. 3q–s). Centrifugation thus aligns the particles in a specific microcapsule-like orientation. Furthermore, on centrifugation, particles are pushed close together. This could push the hydrophilic chains out of the binding side, and induce the formation of irreversible bonds that arise from van der

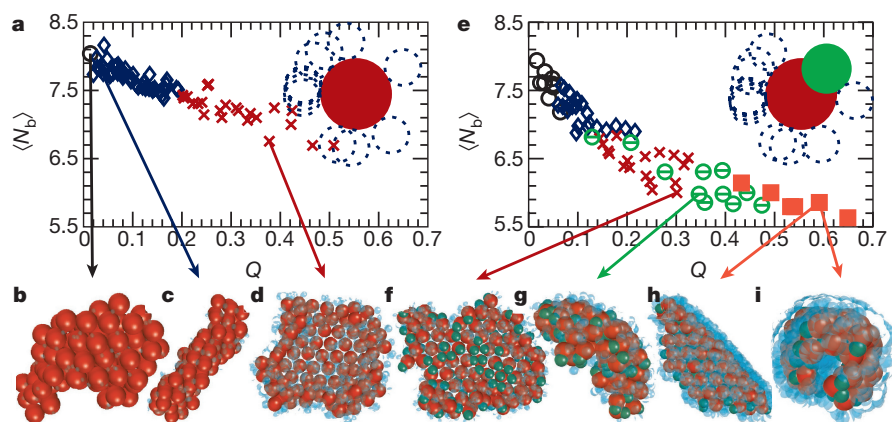


Figure 4 | Monte Carlo simulations. **a**, The average number of bonds, $\langle N_b \rangle$, decreases with the covered surface fraction, Q . Inset, deformable spheres are modelled as attractive spheres (red in all panels) with f mobile penetrable hard spheres (blue in all panels). **b–d**, This results in compact clusters (**b**, black circles in **a**, **e**), bilayers (**c**, blue diamonds in **a**, **e**) and monolayers (**d**, red crosses in **a**, **e**). **e**, The average number of bonds for

snowman-shaped particles. Inset, snowman-shaped particles are modelled as deformable spheres with a rigid protrusion (green in **e–i**). **f–i**, From flat monolayers (**f**, red crosses in **e**), the structure changes to curved monolayers with in-plane protrusions (**g**, green bisected circles in **e**) and out-of-plane protrusions (light red squares in **e**) seen from the side (**h**) and the front (**i**) at high Q values.

Waals forces between the colloids at close proximity. Although we have no direct, real-space proof of the formation mechanism, microcapsules could be formed as follows: first, particles form a dense sediment with cavities (Fig. 3w); next, centrifugation pushes the particles closer together and irreversible bonds are formed (Fig. 3x); finally, after shaking, the particles that surrounded cavities are found as microcapsules (Fig. 3y).

We test the key hypothesis that combining colloidal bond hybridization with anisotropy can stabilize curved monolayers using Monte Carlo simulations. First, we develop a simple model for mutually attractive, isotropic, deformable particles. Next, we extend this model with anisotropy.

Mutually attractive, isotropic, deformable particles are modelled as central spheres with f satellite spheres each (Fig. 4a). The size ratio between the central and the satellite spheres is q and the latter are penetrable hard spheres that model the flexible surface groups. Penetrable hard spheres can interpenetrate other satellite spheres, but have excluded volume interactions with the central spheres. Mutual attraction is captured by a square-well interaction between the central spheres, and deformability is incorporated as the satellite spheres can freely move over the surface of the central sphere.

To verify if colloidal bond hybridization can induce directional interactions—that is, if rearrangement of surface groups can stabilize monolayers—we start Monte Carlo simulations in a hexagonal planar configuration. Different morphologies are observed when the size and the number of satellite spheres are varied (Extended Data Fig. 8b, i–k). These two variables can be combined in the covered surface fraction, $Q = \frac{fq^2}{4(1+q)^2}$. On plotting the average number of bonds, $\langle N_b \rangle$, as a function of Q , all of the data collapse onto a single curve (Fig. 4a). Furthermore, the transitions between the different morphologies occur at well-defined Q values, showing that the Q dictates the morphology (Fig. 4a, Extended Data Fig. 8b). If Q is small, the particles reorganize into compact aggregates with many bonds to maximize the attractive interaction between the central spheres (Fig. 4b). When the size or number of satellite spheres is increased, however, they redistribute out-of-plane and mechanically stable bilayers and monolayers are observed (Fig. 4c, d). Colloidal bond hybridization can thus induce directional interactions and stabilize monolayers for isotropic particles, which agrees well with the results in Fig. 1.

Starting with unbound particles (Extended Data Fig. 8a, c–h), we qualitatively reproduce simulation results that have been obtained using a more detailed model with tethered chains⁴. Hence we conclude that, although simple, our model captures the main ingredients that

induce directional interactions: mutual attraction and deformability. As our model does not contain any molecular details, we expect this behaviour to be generic. This expectation is in line with experimental systems of polymer-grafted nanoparticles where both mutual attraction and deformability can be identified and directional interactions are induced^{4,5}.

We model mutually attractive, anisotropic, deformable particles by adding a rigid sphere to the deformable sphere (Fig. 4e, Extended Data Fig. 9). The rigid sphere models the polystyrene protrusion in the most primitive way, and its hydrophobicity is captured by a short-range attraction with other rigid and central spheres. As for isotropic particles, the values for the average number of bonds collapse on a single curve as a function of Q (Fig. 4e, equation (11)), and planar monolayers are stable at moderate Q values (Fig. 4f). On increasing the size and the number of satellite spheres further, however, curved monolayers with protrusions pointing just out-of-plane (Fig. 4g) are observed, whereas for large and many satellite spheres, all protrusions point inwards (Fig. 4h, i).

We conclude that, as hypothesized, colloidal bond hybridization can stabilize monolayers and anisotropy induces a shift from planar to curved structures. Furthermore, hemispherical monolayers with in-plane protrusions (Fig. 4i, Supplementary Video 7) resemble segments of the experimentally observed microcapsules.

Here we combined mutual attraction, anisotropy and deformability in colloidal model particles. Mutual attraction and deformability are thought to cause surface groups to rearrange on binding, which is a colloidal equivalent of bond hybridization, whereas anisotropy induces curvature. These three characteristics are probably sufficient to induce self-assembly into microcapsules, a process that—to the best of our knowledge—had not been realized before in a colloidal model system. We note that although the details are different, the same three properties can also be identified in the building blocks of viruses^{23–25}, suggesting that these characteristics could also be important in the assembly of virus microcapsules. The mechanism we find is fundamentally different from previous work, where directional interactions are induced by rigid patches^{7–9}, structural rearrangements on changing the solvent²⁶ or electric fields²⁷. Quantification of the attraction strength, anisotropy, number of particle lobes and deformability lead to a large parameter space that remains to be systematically explored. Theoretical work that extends previous studies¹⁴ is needed to predict self-assembled structures from these properties. Independently controlling these properties seems impossible for proteins; colloidal particles, on the other hand, are promising building blocks to address this challenge.

Online Content Methods, along with any additional Extended Data display items and Source Data, are available in the online version of the paper; references unique to these sections appear only in the online paper.

Received 27 February 2015; accepted 22 March 2016.

Published online 8 June 2016.

- Zhang, Z. & Glotzer, S. C. Self-assembly of patchy particles. *Nano Lett.* **4**, 1407–1413 (2004).
- Glotzer, S. C. & Solomon, M. J. Anisotropy of building blocks and their assembly into complex structures. *Nature Mater.* **6**, 557–562 (2007).
- Yi, G.-R., Pine, D. J. & Sacanna, S. Recent progress on patchy colloids and their self-assembly. *J. Phys. Condens. Matter* **25**, 193101 (2013).
- Akcora, P. *et al.* Anisotropic self-assembly of spherical polymer-grafted nanoparticles. *Nature Mater.* **8**, 354–359 (2009).
- Nikolic, M. S. *et al.* Micelle and vesicle formation of amphiphilic nanoparticles. *Angew. Chem. Int. Ed.* **48**, 2752–2754 (2009).
- Luiken, J. A. & Bolhuis, P. G. Anisotropic aggregation in a simple model of isotropically polymer-coated nanoparticles. *Phys. Rev. E* **88**, 012303 (2013).
- Chen, Q., Bae, S. C. & Granick, S. Directed self-assembly of a colloidal kagome lattice. *Nature* **469**, 381–384 (2011).
- Wang, Y. *et al.* Colloids with valence and specific directional bonding. *Nature* **491**, 51–55 (2012).
- Kraft, D. J. *et al.* Surface roughness directed self-assembly of patchy particles into colloidal micelles. *Proc. Natl Acad. Sci. USA* **109**, 10787–10792 (2012).
- Larson-Smith, K. & Pozzo, D. C. Scalable synthesis of self-assembling nanoparticle clusters based on controlled steric interactions. *Soft Matter* **7**, 5339–5347 (2011).
- Wang, P. H. & Pan, C.-Y. Preparation of styrene/acrylic acid copolymer microspheres: polymerization mechanism and carboxyl group distribution. *Colloid Polym. Sci.* **280**, 152–159 (2002).
- Hu, X., Liu, H., Ge, X., Yang, S. & Ge, X. Preparation of submicron-sized snowman-like polystyrene particles via radiation-induced seeded emulsion polymerization. *Chem. Lett.* **38**, 854–855 (2009).
- Bates, F. S. Polymer-polymer phase behavior. *Science* **251**, 898–905 (1991).
- Asai, M., Cacciuto, A. & Kumar, S. K. Quantitative analogy between polymer-grafted nanoparticles and patchy particles. *Soft Matter* **11**, 793–797 (2015).
- Geerts, N. & Eiser, E. Flying colloidal carpets. *Soft Matter* **6**, 664–669 (2010).
- Sheu, H. R., El-Aasser, M. S. & Vanderhoff, J. W. Uniform nonspherical latex particles as model interpenetrating polymer networks. *J. Polym. Sci. A* **28**, 653–667 (1990).
- Mock, E. B., De Bruyn, H., Hawkett, B. S., Gilbert, R. G. & Zukoski, C. F. Synthesis of anisotropic nanoparticles by seeded emulsion polymerization. *Langmuir* **22**, 4037–4043 (2006).
- Kraft, D. J., Groenewold, J. & Kegel, W. K. Colloidal molecules with well-controlled bond angles. *Soft Matter* **5**, 3823 (2009).
- Marchand-Brynaert, J., Deldime, M., Dupont, I., Dewez, J.-L. & Schneider, Y.-J. Surface functionalization of poly(ethylene terephthalate) film and membrane by controlled wet chemistry: chemical characterization of carboxylated surfaces. *J. Colloid Interf. Sci.* **173**, 236–244 (1995).
- Dinsmore, A. D. *et al.* Colloidosomes: selectively permeable capsules composed of colloidal particles. *Science* **298**, 1006–1009 (2002).
- Chen, T., Zhang, Z. & Glotzer, S. C. Simulation studies of the self-assembly of cone-shaped particles. *Langmuir* **23**, 6598–6605 (2007).
- Deegan, R. D. *et al.* Capillary flow as the cause of ring stains from dried liquid drops. *Nature* **389**, 827–829 (1997).
- Berg, J. M., Tymoczko, J. L. & Stryer, L. *Biochemistry* (ed. Stryer, L.) (W. H. Freeman and Company, 2002).
- Tompa, P. & Fuxreiter, M. Fuzzy complexes: polymorphism and structural disorder in protein–protein interactions. *Trends Biochem. Sci.* **33**, 2–8 (2008).
- Freund, S. M. V., Johnson, C. M., Jaulent, A. M. & Ferguson, N. Moving towards high-resolution descriptions of the molecular interactions and structural rearrangements of the human hepatitis B core protein. *J. Mol. Biol.* **384**, 1301–1313 (2008).
- Groschel, A. H. *et al.* Guided hierarchical co-assembly of soft patchy nanoparticles. *Nature* **503**, 247–251 (2013).
- Crassous, J. J. *et al.* Field-induced assembly of colloidal ellipsoids into well-defined microtubules. *Nature Commun.* **5**, 5516 (2014).

Supplementary Information is available in the online version of the paper.

Acknowledgements We thank B. G. P. van Ravenstein for providing non-deformable, fluorescein functionalized snowman-shaped particles, S. I. R. Castillo for taking the SEM images, and J. D. Meeldijk and C. T. W. M. Schneijdenberg for help with freeze drying and TEM. This work is part of the research programmes VICI 700.58.442 and TOP-GO 700.10.355, which are financed by the Netherlands Organization for Scientific Research. We thank A. van Blaaderen and M. Dijkstra for discussions, and M. de Jong for reading the manuscript.

Author Contributions All authors designed the research; C.H.J.E. synthesized the particles and analysed the self-assembled structures; J.A.L. performed and analysed the Monte Carlo simulations. W.K.K. and P.G.B. supervised the project. All authors discussed the results and implications and wrote the paper.

Author Information Reprints and permissions information is available at www.nature.com/reprints. The authors declare no competing financial interests. Readers are welcome to comment on the online version of the paper. Correspondence and requests for materials should be addressed to C.H.J.E. (c.h.j.evers@uu.nl) or W.K.K. (w.k.kegel@uu.nl).

METHODS

Chemicals. Unless stated otherwise, the following chemicals were used as received: acrylic acid (AA, 99%), aluminium oxide (Al_2O_3 , puriss, $\geq 98\%$), *tert*-butylamine ($\geq 99.5\%$), divinylbenzene (DVB, 55%, mixture of isomers), fluorescein sodium salt (F6377), fluoresceinamine (mixture of isomers, $\geq 75\%$), *N*-(3-Dimethylaminopropyl)-*N'*-ethylcarbodiimide hydrochloride (EDC, purum, $\geq 98.0\%$), 2-(*N*-Morpholino)ethanesulfonic acid (MES, $\geq 99\%$), sodium phosphate dibasic (Na_2HPO_4 , BioXtra, $\geq 99\%$), sodium phosphate monobasic dihydrate ($\text{NaH}_2\text{PO}_4 \cdot 2\text{H}_2\text{O}$, BioUltra, $\geq 99\%$) and styrene (ReagentPlus, $\geq 99\%$), were obtained from Sigma-Aldrich or its subsidiaries; 2,2'-azobis(2-methylpropionitrile) (AIBN, 98%), potassium chloride (KCl, *pro analysi*) and potassium persulfate (reagent ACS, 99+%) were obtained from Acros Organics; hydroquinone (puriss, $\geq 99.5\%$) was obtained from Riedel-de Haën; glycerol (Ph Eur) was obtained from Bufa; ethanol (100%) was obtained from Interchemia; potassium hydroxide (KOH) was obtained from Emsure; hydrochloric acid (HCl, 37%) was obtained from Merck; and Millipore water (MQ) was obtained with a Synergy water purification system.

Synthesis. The synthesis is outlined in Extended Data Fig. 2a and involved the emulsifier-free polymerization of cross-linked poly(styrene-*co*-acrylic acid) (CPSAA) spheres, the formation of protrusions by swelling with styrene, heating and polymerizing and the covalent linking of hydrophobic moieties to the carboxylic groups.

Cross-linked poly(styrene-*co*-acrylic acid) spheres of $0.530 \pm 0.014 \mu\text{m}$ in diameter are prepared by emulsifier-free polymerization of styrene, acrylic acid and divinylbenzene following refs 11 and 12. 90 ml MQ and 11 ml styrene were passed over an Al_2O_3 column; 761 μl freshly opened AA and 55 μl DVB were added to a 250 ml three-neck round-bottom flask. The flask was constantly and vigorously stirred with a glass stirrer under a nitrogen flow. Quantitatively, 0.05 g potassium persulfate was dissolved as an initiator and added to the flask with 10 ml MQ. After 15 min, the nitrogen inlet was raised above the liquid level, and after a further 15 min, the flask was immersed in an oil bath at 70°C to start the polymerization. After 20 h, a milky-white dispersion was obtained. Excess reactants were removed by centrifugation (Beckman Coulter Allegra X-12R). On centrifugation, the particles settle at the bottom of the sample, whereas unreacted chemicals were in the so-called supernatant. The dispersion was washed by centrifugation at 2.1×10^3 g three times and the supernatant was replaced by MQ.

Cross-linked polystyrene (CPS) spheres are prepared in a similar method. For these particles 225 ml MQ, 23.5 ml styrene and 0.7 ml DVB were added to a 500-ml one-neck round-bottom flask. The flask was constantly and vigorously stirred with a polytetrafluoroethylene-coated stir bar and immersed in an 80°C oil bath. 0.78 g potassium persulfate in 37.5 ml MQ was then added. After 24 h a milky-white dispersion was obtained, which was washed three times by centrifugation and redispersed in MQ.

To form a protrusion, the CPSAA spheres were swollen with styrene, heated and polymerized, in line with refs 16–18. In a typical experiment, the solid mass fraction—as determined by drying—was brought to 3%–6% with MQ. About 5 ml of the dispersion was magnetically stirred with a polytetrafluoroethylene-coated stir bar in a glass tube. Styrene was added with a swelling ratio $S = m_{\text{st}}/m_{\text{s}}$ = 3–7 with m_{st} and m_{s} being the mass of added styrene and the solid mass in the dispersion, respectively. After one to two days of stirring, the tube was immersed in an 80°C oil bath for two hours under continuous stirring to form a styrene protrusion. Next, 500 μl of an aqueous hydroquinone solution (45 mg in 50 ml) and 5 mg AIBN in 250 μl styrene were added, and the tube was again immersed in the oil bath at 80°C for 24 h to polymerize the protrusion. Finally, a milky-white dispersion was obtained. A millimetre-sized solid white aggregate was often found that could easily be removed.

Hydrophobic moieties are covalently linked to carbodiimide-activated carboxylic groups on the CPSAA particles by a method adapted from ref. 19. In a typical synthesis, a 0.1 M MES buffer (1.95 g in 100 ml MQ), and a 0.2 M phosphate buffer (6.72 g Na_2HPO_4 and 0.41 g $\text{NaH}_2\text{PO}_4 \cdot 2\text{H}_2\text{O}$ in 250 ml MQ) were prepared. 2.5 ml of the dispersion was centrifuged and the supernatant was replaced by an EDC/MES solution (45 mg EDC quantitatively added with 40 ml of the MES buffer) to activate the AA groups. The dispersion was tumbled at 60 rpm for one hour, and washed by centrifugation at 2.1×10^3 g with an MES buffer and twice with MQ. The dispersion was again centrifuged and after removal of the supernatant, 0.028 mmol fluoresceinamine or *tert*-butylamine was quantitatively added with 30 ml phosphate buffer to covalently bind fluoresceinamine or *tert*-butylamine to the activated AA groups. The tube was wrapped in aluminium foil, and after tumbling at 60 rpm overnight, the dispersion was washed three times with a phosphate buffer, once with an MES solution and five times with MQ. Finally, a milky-white dispersion was obtained. The covalent linkage of fluoresceinamine was verified by varying the fluoresceinamine coupling method and studying the resulting washed

particles using fluorescence microscopy (Extended Data Fig. 10). The preparation of non-deformable, fluoresceinamine-functionalized snowman-shaped particles was previously described in ref. 28.

TEM. Transmission electron microscopy (TEM) images were taken with a Philips TECNAI 10 at 100 kV and 16 bit. Samples were prepared by drying a diluted dispersion droplet on a polymer coated copper grid under illumination with a heat lamp. The image levels were linearly rescaled using ImageMagick so that 99.9% of all of the values were between the lower and upper level thresholds.

Figure 1a was obtained at 9.7 nm per pixel and Fig. 1b at 0.95 nm per pixel. Figure 2d, e was obtained at 3.5 nm per pixel, Fig. 2f at 6.8 nm per pixel and the insets in Fig. 2d–f at 0.95 nm per pixel. Extended Data Fig. 2b, d was obtained at 4.9 nm per pixel, and Extended Data Fig. 2c, e at 0.95 nm per pixel. Extended Data Fig. 5a–d was obtained at 0.95 nm per pixel.

Particle sizes were measured using Gaussian ring transformations in Wolfram Mathematica 10 (<https://www.wolfram.com/mathematica/>). For spherical particles, a gradient transform was computed using discrete derivatives of a Gaussian. Circles were detected by iteratively convolving with Gaussian rings and finding the maxima. **SEM.** By freeze drying or sintering, self-assembled structures could be preserved and studied using SEM. For freeze-drying, 1 μl of the dispersion was deposited on a polymer-coated copper grid. The grid was vitrified in liquid nitrogen and mounted on a cryotransfer unit that was then brought under a vacuum. The temperature was increased to -90°C at 5°C min^{-1} and kept constant for about six hours to allow the water to sublimate.

For sintering, the sample was heated above the glass transition temperature of polystyrene at about 100°C . First, the dispersion was centrifuged and after redispersion in 1:1 glycerol:water, it was immersed in an 105°C oil bath for 30 min. The dispersion was washed three times by centrifugation with MQ and 1 μl was placed on a polymer-coated copper grid. After drying, the sample was coated with a ~ 6 -nm-thick layer of platinum.

Both samples were studied with a FEI XL30 FEG operated at 5–10 kV, and images were obtained at 8 bit. The image levels were linearly rescaled using ImageMagick, from the value of the pixel with the lowest intensity to the brightest pixel. Figure 2a was obtained at 6.5 nm per pixel. Extended Data Fig. 3c–e, h–j was obtained at 3.5 nm per pixel, 1.9 nm per pixel, 3.5 nm per pixel, 11 nm per pixel, 6.9 nm per pixel and 11 nm per pixel, respectively.

Optical microscopy. Bright-field, fluorescence and reflected light microscopy images were captured with a Nikon Ti-E inverted microscope unless stated otherwise. The Nikon Ti-E was operated with a Nikon TIRF 100 \times numerical aperture 1.49 objective, intermediate magnification of 1.5 \times , and a Hamamatsu ORCA Flash camera at 16 bit. For reflected light microscopy, a Nikon Intensilight C-HGFI light source was used with a Nikon D-FLE filter block. For fluorescence microscopy, the same light source was used with a Semrock FITC-3540C filter block. The reflected light microscopy images in Fig. 3k–n were obtained with a Nikon Ti-U inverted microscope with a Nikon Plan Apo VC 100 \times numerical aperture 1.40 objective, intermediate magnification of 1.5 \times , and a Lumenera Infinity X camera at 8 bit. The bright field microscopy images in Fig. 3r–s, u–v, Extended Data Fig. 4i–v and Extended Data Fig. 7 were obtained with a Nikon Eclipse LV100POL microscope with its focal plane parallel to the gravitational field, a Nikon Plan Fluor ELWD 40 \times numerical aperture 0.6 objective and a QImaging MicroPublisher 5.0 camera at 8 bit. Finally, confocal microscopy images were captured with a Nikon TE2000-U, with a Nikon Plan Apo 100 \times numerical aperture 1.40 objective, a 488-nm laser and a 590-nm detector at 12 bit. For images obtained with the Ti-E and the TE2000-U, bitmaps were extracted from the microscopy files using bconvert 5.1.7 (Open Microscopy Environment). The image levels were linearly rescaled using ImageMagick.

Figure 1c and d was obtained with the Ti-E in reflected light mode at 40 nm per pixel and image levels were linearly rescaled from the value of the darkest to the brightest pixel. Figure 2b was obtained with the Ti-E in reflected light mode at 43 nm per pixel, and levels were linearly rescaled from the value of the darkest pixel to the brightest pixel. Figure 2c was obtained with the TE2000-U in confocal fluorescence mode at 35.72 nm per pixel, and levels were linearly rescaled from zero to the value of the brightest pixel. Fluorescein sodium salt was added to the water phase, and the image was false coloured green. Figure 2g–j was obtained with the Ti-E in bright-field mode at 43 nm per pixel, and levels were linearly rescaled from zero to the value of the brightest pixel. Figure 3b–e was obtained with the Ti-E in bright field mode at 40 nm per pixel, and levels were linearly rescaled from zero to the value of the brightest pixel. Figure 3g–j was obtained with the Ti-E in reflected light mode at 43 nm per pixel and levels were linearly rescaled from the value of the darkest pixel to the brightest pixel. Figure 3k–n was obtained with the Ti-U in reflect light mode at 29 nm per pixel, and levels were linearly rescaled from the value of the darkest pixel to the brightest pixel. Figure 3r, s, u, v was obtained with the LV100POL at 86 nm per pixel. For Fig. 3s, v levels were linearly rescaled

from the value of the darkest pixel to the brightest pixel, and these thresholds were also used for Fig. 3r, u. Extended Data Fig. 2f, g was obtained with the Ti-E in fluorescence mode at 43 nm per pixel, and levels were linearly rescaled from zero to the value of the brightest pixel. Extended Data Fig. 4a was obtained with the Ti-E in bright field mode at 43 nm per pixel, and levels were linearly rescaled from zero to the value of the brightest pixel. Extended Data Fig. 4e–h was obtained with the Ti-E in bright field mode at 40 nm per pixel, and levels were linearly rescaled from zero to the value of the brightest pixel. Extended Data Fig. 4i–v was obtained with the LV100POL at 86 nm per pixel. For Extended Data Fig. 4m–o, t–v, levels were linearly rescaled from the value of the darkest pixel to the brightest pixel, and these thresholds were also used for Extended Data Fig. 4i–k, q–s. For Extended Data Fig. 4l, p, levels were linearly rescaled from zero to the value of the brightest pixel. Extended Data Fig. 5e–h was obtained with the Ti-E in bright field mode at 43 nm per pixel, and levels were linearly rescaled from zero to the value of the brightest pixel. The images in Extended Data Fig. 6 were obtained with the Ti-E in bright field mode at 40 nm per pixel, and levels were linearly rescaled from zero to the value of the brightest pixel. The images in Extended Data Fig. 7 were obtained with the LV100POL at 86 nm per pixel. Image levels were linearly rescaled using the thresholds from Fig. 3s and Extended Data Fig. 4m–o. Extended Data Fig. 10a–d was obtained with the Ti-E in fluorescence mode at 43 nm per pixel, levels were linearly rescaled from zero to the value of the brightest pixel, and the images were false coloured in green.

Typically, a sample was prepared by placing 0.5–2 μl of the dispersion between a microscope slide (Menzel-Gläser) and a #1.5 cover slip (Menzel-Gläser) with two #0 cover glasses (VWR) as spacers. Before use, the slides were cleaned with MQ, ethanol and Kimtech precision wipes. The cells were then sealed with glue (Norland NOA81, after ultraviolet curing) or scotch tape. The evaporating droplets between two glass slides (Fig. 3f–j) were studied in cells as described above, but without sealing the sides of the cell. Evaporating droplets on a glass slide (Fig. 3a–e, Extended Data Fig. 4e–h and Extended Data Fig. 6), on the other hand, were studied by placing 0.5 μl of the dispersion onto a cleaned #1.5 cover slip (Menzel-Gläser). Droplets evaporated spontaneously and for each dispersion four (two for non-deformable particles) time series were obtained of a $89\mu\text{m} \times 89\mu\text{m}$ region near the contact line (Extended Data Fig. 6). High-concentration samples (Fig. 3k–n, Supplementary Video 5) were studied after sedimentation in the gravitational field in a similar cell to that described above. Thin cells in Fig. 3q–v, Extended Data Fig. 4i–v and Extended Data Fig. 7 were prepared in a capillary and sealed with glue, while preventing contact between uncured glue and the dispersion. A $0.020 \times 0.200 \times 50\text{ mm}^3$ capillary (VitroCom 5002-050, Kimtech cleaned) was half-filled with the dispersion. Next, the capillary was pressed onto a microscopy slide (Menzel-Gläser) with tweezers and a foam cushion and nitrogen gas was blown from the filling side to push the dispersion to the middle of the tube. While blowing, the other side was sealed with a glue droplet (Norland NOA81) to prevent the dispersion from flowing back. Finally, the other side was sealed with glue, the glue was cured with ultraviolet light, and the cells were centrifuged in centrifuge tubes (VWR SuperClear).

Interparticle distance distributions were obtained by analysing reflected light microscopy time series with Mathematica. For each frame, the gradient transform was computed using discrete derivatives of a Gaussian, and the gradients were circle transformed by convolving with a circle. The original image was multiplied pixel per pixel with the circle transform, and the local maximums were identified as particles. The histogram for particles in the cavity phase (Fig. 3o, blue) was normalized with a fitted function through the distribution of 10^7 distances between random points on a plane with the same size as the microscopy images, and the resulting histogram was scaled to 1 at large interparticle distances. The effective pair potential (Fig. 3p) was calculated using $w(r_{ij})/k_B T = -\ln(g(r_{ij}))$, where $g(r_{ij})$ is the measured interparticle distance distribution. The histogram for particles in a microcapsule (Fig. 3p, red) was scaled so that the maximum has the same height as the maximum of the cavity phase histogram.

The number of particles per microcapsule was estimated from the first peak in the interparticle distance distribution of a microcapsule, $r_{ij}^* = 0.62\mu\text{m}$, by assuming a hexagonal orientation and a spherical microcapsule surface,

$$N_{\text{part}} = \frac{A_{\text{tot}}}{A_{\text{part}}} = \frac{4\pi R_m^2}{\frac{\sqrt{3}}{2} r_{ij}^*{}^2} \quad (1)$$

with A_{tot} the surface area of a microcapsule, A_{part} the surface area per particle and R_m the radius of the microcapsules. For particles with a large lobe with a diameter of $0.540\mu\text{m}$, the radii of 30 microcapsules, $R_m = 1.9 \pm 0.4\mu\text{m}$, was determined as for transmission electron microscopy (TEM). Finally, the estimated number of particles per microcapsule was $N_{\text{part}} = 10^2$.

Dynamic light scattering. Cross-linked poly(styrene-co-acrylic acid) spheres were added to 1 mM KOH, and using a Malvern Zetasizer Nano ZS, equipped

with an MPT-2 autotitrator, pH was stepwise decreased from 9.8 to 3.4 by adding 1 mM HCl. Cumulant analysis gave the apparent size and polydispersity index. The influence of electrostatic interactions was studied by replacing the solvents with 1 mM KOH/9 mM KCl and 1 mM HCl/9 mM KCl. The influence of the carboxylic acid groups was studied by using cross-linked polystyrene spheres instead of CPSAA spheres.

Simulation model. We model the colloids as hard spheres of diameter σ . The attractive forces between the particles, due to van der Waals interactions and the hydrophobic (polystyrene) component of the brush for example, are captured using a square-well potential:

$$U_{c-c}(R) = \begin{cases} \infty & R \leq \sigma \\ -\varepsilon_c & \sigma < R \leq \sigma + \Delta \\ 0 & R > \sigma + \Delta \end{cases} \quad (2)$$

where Δ is the width of the well, ε_c is the attraction strength and R is the centre-to-centre distance between the colloids. We then model the grafted acrylic acid polymers as penetrable hard spheres or satellite spheres with diameter relative to the hard spheres q (ref. 29) that can move freely across the surface at a fixed distance $(\sigma + q\sigma)/2$, thereby allowing the brush to adapt its configuration to the environment. The penetrable hard spheres are free to overlap each other, that is, $U_{\text{PHS-PHS}} = 0$, but have a hard-sphere interaction with the colloids:

$$U_{\text{PHS-c}}(r) = \begin{cases} \infty & r \leq (\sigma + q\sigma)/2 \\ 0 & r > (\sigma + q\sigma)/2 \end{cases} \quad (3)$$

where r is the centre-to-centre distance between the colloid and polymer.

To obtain snowman-shaped particles, we attach a protrusion to each colloid, modelled here as a hard sphere with radius r_p , with its centre located at the colloid surface. The protrusion hydrophobicity is captured by a weak square-well attraction between protrusions with strength $U_{p-p} = -\varepsilon_p$ over the range $2r_p < R \leq 2r_p + \Delta$. The colloids and protrusions interact through a square-well potential with depth $U_{c-p} = -\sqrt{\varepsilon_c \varepsilon_p}$, that is, the geometric mean of the interaction strengths, over the range $\sigma/2 + r_p < R \leq \sigma/2 + r_p + \Delta$. Lastly, the protrusions have a hard-sphere interaction with the polymers:

$$U_{\text{PHS-p}}(r) = \begin{cases} \infty & r \leq r_p + q\sigma/2 \\ 0 & r > r_p + q\sigma/2 \end{cases} \quad (4)$$

Given a system containing N particles at positions \mathbf{R}^N , each grafted with f polymers at positions \mathbf{r}^f , the total energy for the system is then given by

$$U(\mathbf{R}^N, \mathbf{r}^{fN}) = \sum_{i,j}^N \{U_{c-c}(\mathbf{R}_{ij}) + U_{c-p}([\mathbf{R}_i + \mathbf{u}_i] - \mathbf{R}_j) + U_{c-p}(\mathbf{R}_i - [\mathbf{R}_j + \mathbf{u}_j]) + U_{p-p}([\mathbf{R}_i + \mathbf{u}_i] - [\mathbf{R}_j + \mathbf{u}_j])\} + \sum_{i,j}^N \sum_k^f \{U_{\text{PHS-c}}(\mathbf{r}_{i,k} - \mathbf{R}_j) + U_{\text{PHS-p}}(\mathbf{r}_{i,k} - [\mathbf{R}_j + \mathbf{u}_j])\} \quad (5)$$

where $\mathbf{r}_{i,k}$ denotes the position of the k th polymer of the i th particle and $\mathbf{u}_i = M(\Omega_i)\Delta\mathbf{u}$ is the vector pointing from the centre of the colloid of the i th particle to the protrusion. $M(\Omega_i)$ is the rotation matrix for the orientation Ω_i of the i th particle and $\Delta\mathbf{u}$ is the vector in the reference frame from the centre of the colloid to the protrusion⁶.

Simulation details. We employ Monte Carlo simulations in the canonical ensemble to study the aggregation behaviour of mutually attractive, anisotropic, deformable colloids. We perform two types of simulations: initiating from the soluble phase and increasing the interaction strength from $\varepsilon_c = (3-9)k_B T$ in steps of $1k_B T$ in system (i) and initiating from a square planar monolayer in a hexagonal packing arrangement with fixed interaction strength $\varepsilon_c = 9k_B T$ in system (ii). We set $N = 98$ and the box length L is set such that the colloid packing fraction equals $\phi_c = 0.001$; periodic boundary conditions apply in all directions. The protrusions have a radius $r_p = 0.35\sigma$, they are weakly attractive relative to the colloids ($\varepsilon_p = \varepsilon_c/5$) and are randomly oriented below and above the monolayer in system (ii). Lastly, the square-well width is set to $\Delta = 0.1\sigma$.

We perform 4×10^4 equilibration Monte Carlo cycles and another 150×10^4 production cycles for each step in system (i). For each Monte Carlo cycle we attempt 50 colloid displacement moves over a fixed maximum distance (0.25L), 50 colloid moves with variable maximum displacement such that $25\% < P_{\text{acc}} < 40\%$, 50 quaternion rotations of the protrusion and another 50 of the entire nanoparticle, 50 cluster moves³⁰ over a fixed distance (0.15L) and 50/2 quaternion rotations of polymers. We disable the expensive cluster moves for system (ii), allowing us to

greatly increase the number of equilibration cycles to 2×10^6 and the number of production cycles to 10×10^6 .

For both systems we perform simulations for every combination of functionality $f \in \{2, 4, 6, 8, 10, 12\}$ and polymer size $q \in \{0.20, 0.25, \dots, 0.70\}$, and we repeat all simulations in the absence of protrusions. We repeat the simulations initiated from the hexagonal monolayer an additional four times and all of the resulting data plots and morphologies are averages over these runs.

Simulation data analysis. We evaluate the average number of bonds per particle using the expression

$$\langle N_b \rangle = \frac{1}{N} \sum_{i \neq j}^N \theta(\sigma + \Delta - r_{ij}) \quad (6)$$

where θ is the Heaviside step function. Here, particles are in contact when the centre-to-centre distance $r_{ij} = |\mathbf{r}_i - \mathbf{r}_j|$ between their bodies is less than $\sigma + \Delta$.

We define Q as the surface which is covered by surface groups divided by the total available surface,

$$Q \equiv \frac{fA_q}{A_{\text{tot}} - A_{\text{ex}}} \quad (7)$$

where A_q is the surface area covered by a satellite sphere, $A_{\text{tot}} = 4\pi((\sigma + \sigma q)/2)^2$ is the total area of the sphere over which the satellite spheres move and A_{ex} is the surface area excluded by the presence of the protrusion.

A_q and A_{ex} are the curved surface areas of spherical caps. These areas are given by $A_{\text{cap}} = 2\pi R_{\text{cap}} h_{\text{cap}}$, where R_{cap} is the radius of the sphere and $h_{\text{cap}} = R_{\text{cap}} - R_{\text{cap}} \cos \theta_{\text{cap}}$ is the height of the cap. θ_{cap} is the angle between the edge of the cap, the centre of the sphere and the centre of the cap. Inserting this into the equation for A_{cap} gives

$$A_{\text{cap}} = 2\pi R_{\text{cap}}^2 (1 - \cos \theta_{\text{cap}}) \quad (8)$$

For the satellite spheres, $R_{\text{cap}} = (\sigma + \sigma q)/2$ and the law of cosines gives

$$\cos \theta_{\text{cap}} = \frac{\left(\frac{\sigma + q\sigma}{2}\right)^2 + \left(\frac{\sigma + q\sigma}{2}\right)^2 - \left(\frac{q\sigma}{2}\right)^2}{2\left(\frac{\sigma + q\sigma}{2}\right)\left(\frac{\sigma + q\sigma}{2}\right)} = 1 - \frac{q^2}{2(1+q)^2} \quad (9)$$

and for the excluded surface area, $R_{\text{cap}} = (\sigma + \sigma q)/2$ and

$$\cos \theta_{\text{cap}} = \frac{\left(\frac{\sigma}{2}\right)^2 + \left(\frac{\sigma + q\sigma}{2}\right)^2 - \left(\frac{p\sigma + q\sigma}{2}\right)^2}{2\left(\frac{\sigma}{2}\right)\left(\frac{\sigma + q\sigma}{2}\right)} = 1 - \frac{2pq + p^2}{2 + 2q} \quad (10)$$

with $p = 2r_p/\sigma$ the dimensionless protrusion diameter.

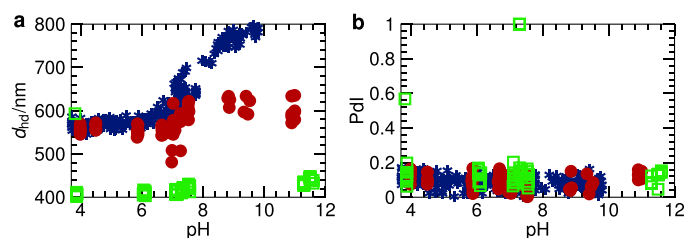
Inserting equations (8)–(10) into equation (7) gives

$$Q = \frac{fq^2}{(1+q)(4+4q-2pq-p^2)} \quad (11)$$

For particles without protrusions, $p = 0$, this reduces to

$$Q = \frac{fq^2}{4(1+q)^2} \quad (12)$$

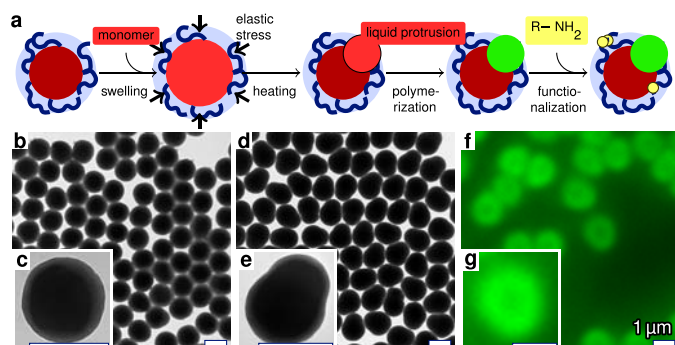
28. van Ravensteijn, B. G. P., Kamp, M., van Blaaderen, A. & Kegel, W. K. General route toward chemically anisotropic colloids. *Chem. Mater.* **25**, 4348–4353 (2013).
29. Asakura, S. & Oosawa, F. On interaction between two bodies immersed in a solution of macromolecules. *J. Chem. Phys.* **22**, 1255 (1954).
30. Bhattacharyay, A. & Troisi, A. Self-assembly of sparsely distributed molecules: an efficient cluster algorithm. *Chem. Phys. Lett.* **458**, 210–213 (2008).



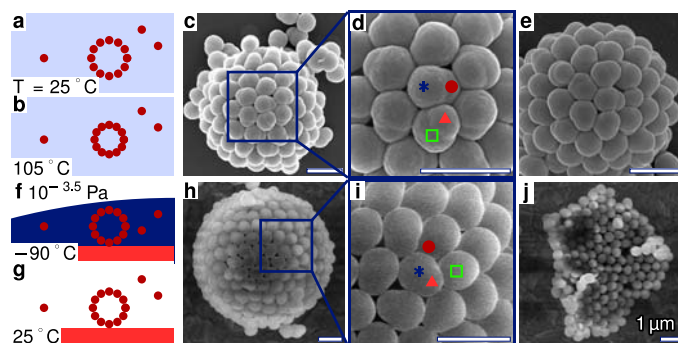
Extended Data Figure 1 | pH-induced structural rearrangements.

a, For poly(styrene-*co*-acrylic acid) spheres with a TEM diameter $d = 0.530 \pm 0.014 \mu\text{m}$, the apparent hydrodynamic diameter, d_{hd} , is measured using dynamic light scattering. At ionic strength $I \approx 1$ mM, d_{hd} equals $0.79 \mu\text{m}$ at pH 10, but decreases to $0.57 \mu\text{m}$ at pH 3 (blue). On screening electrostatic interactions at $I \approx 10$ mM (red), or for polystyrene spheres without acrylic acid (green), however, the measured diameter remains almost constant with pH. We conclude that at high pH, the electrostatic repulsion between acrylic acid groups triggers the poly(acrylic acid)-rich brush to expand by about $0.1 \mu\text{m}$ into the solution.

b, The measured polydispersity index, Pdl, stays constant, indicating that changing the pH does not induce aggregation.

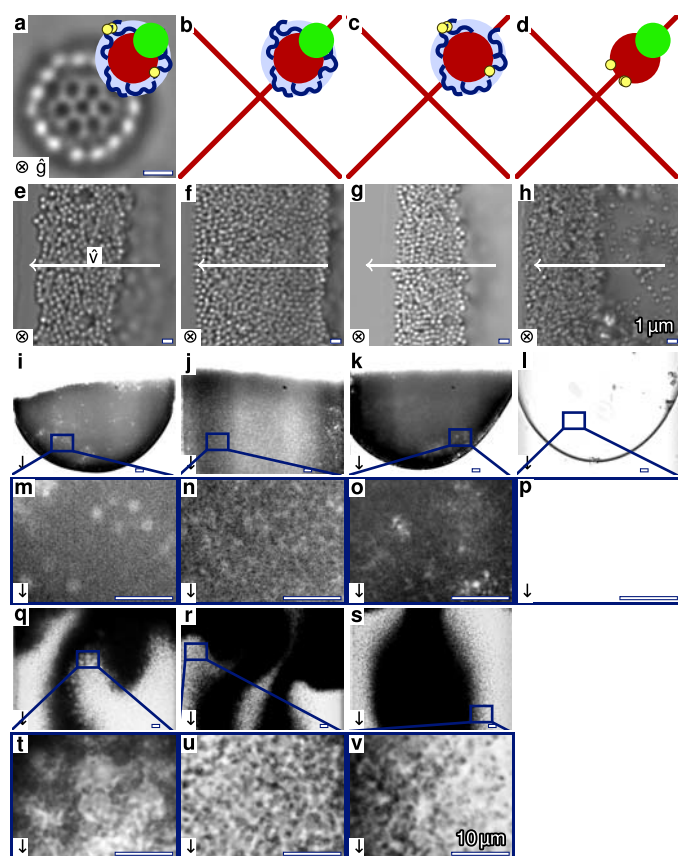


Extended Data Figure 2 | Synthesis. **a–g**, Schematic outline (**a**) and microscopy images (**b–g**) of the synthesis of mutually attractive, anisotropic, deformable particles. Poly(styrene-*co*-acrylic acid) spheres (**b**, **c**, TEM) with a hydrophobic core (red in **a**) and a deformable brush (blue in **a**) are swollen with monomer, heated, and polymerized, resulting in snowman-like particles (**d**, **e**, TEM) with a deformable lobe and a rigid protrusion (green in **a**). Hydrophobic molecules (yellow in **a**) are covalently linked to the acrylic acid groups, resulting in fluorescent particles when fluoresceinamine is used (**f**, **g**, fluorescence microscopy).

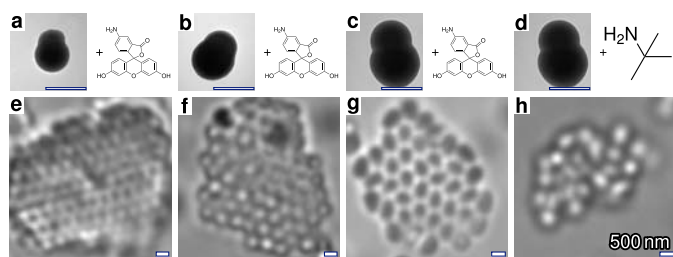


Extended Data Figure 3 | SEM images of self-assembled microcapsules.

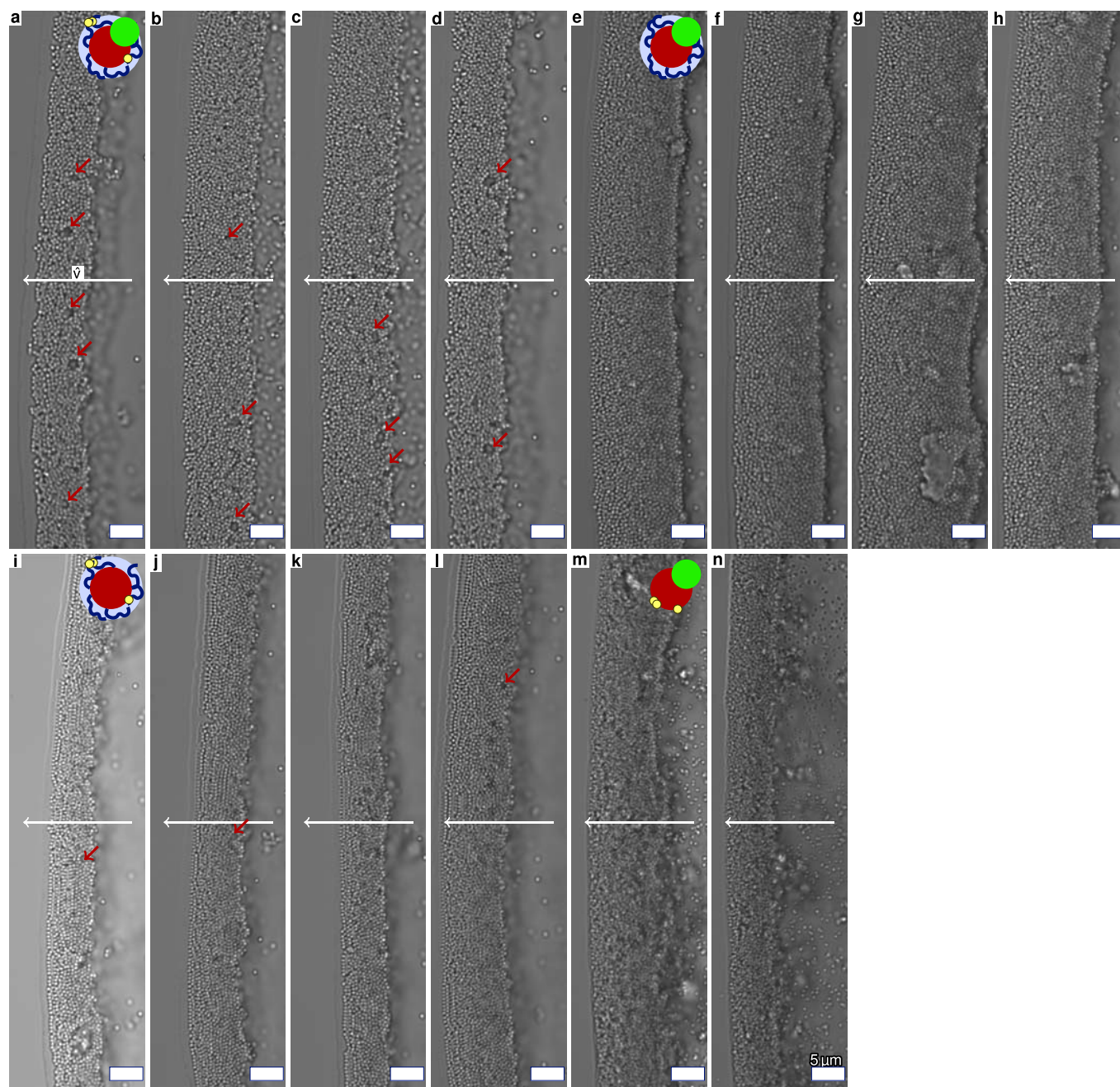
To prevent disintegration upon drying, microcapsules are studied after sintering (a–e) or freeze-drying (f–j). During sintering, the solvent (light blue) is heated in order to partly merge the particles (red) (a, b). During freeze-drying, vitrified water (dark blue) is sublimated under vacuum (f, g). Particles in the microcapsules have six (blue asterisks) or five (green squares) neighbours, and both protrusions that point slightly inwards (red circles) and outwards (light red triangles) are found (d, i). Besides microcapsules, also planar monolayers (j) are observed.



Extended Data Figure 4 | Formation of microcapsules and cavities on varying the complexity of the particles. **a–d**, The complexity of particles (a) that are deformable (blue), anisotropic (green) and functionalized with mutually attractive groups (yellow) is varied, resulting in non-functionalized particles (b), isotropic particles (c) and non-deformable particles (d). Microcapsules are only found in the first case. **e–h**, All particles are studied using bright field microscopy at the edge of an evaporating droplet (e–h), in a sediment after centrifugation (i–p), and upon diluting the sediment (q–v). The entire images of e–h can be found in Extended Data Fig. 6 and magnifications of i–k can be found in Extended Data Fig. 7b–d. The arrows indicate the directions of the particle flow, \hat{v} , or the gravitational field, \hat{g} .

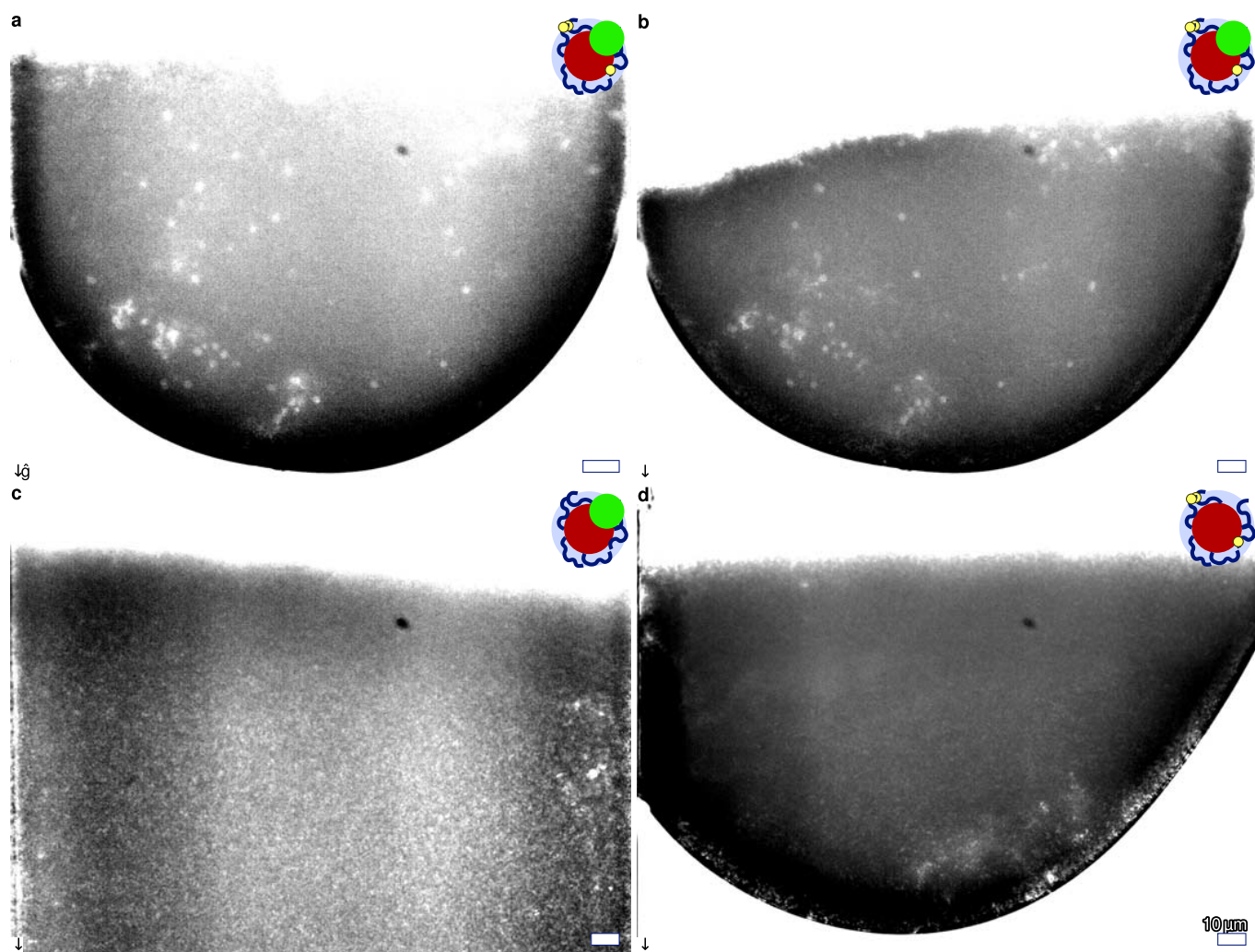


Extended Data Figure 5 | Monolayer sheets. For mutually attractive, anisotropic, deformable particles with varying sizes (**a–c**), not only hollow microcapsules (Fig. 2), but also two-dimensional hexagonal planar monolayers (**e–g**) are observed using bright field microscopy. Both fluoresceinamine (**a–c**, **e–g**) and *tert*-butylamine (**d**, **h**) are used as hydrophobic moieties and for both moieties monolayers are observed.

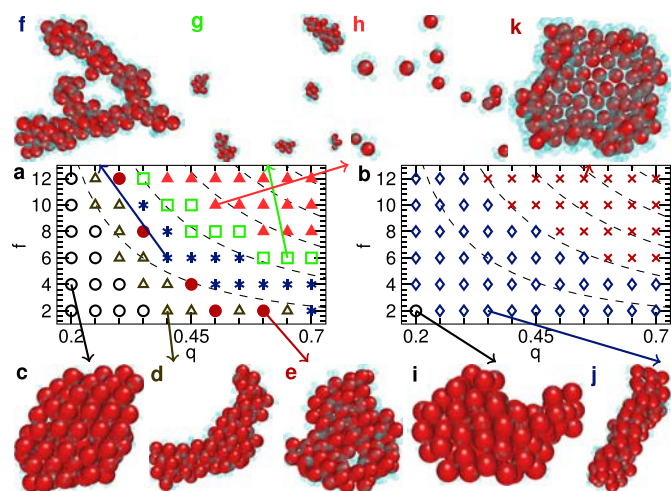


Extended Data Figure 6 | Formation of cavities at the contact line. The complexity of mutually attractive, anisotropic, deformable particles (**a–d**) is varied resulting in non-functionalized particles (**e–h**), isotropic particles (**i–l**) and non-deformable particles (**m, n**). For each particle type, part of the contact line of an evaporating droplet is studied four times (twice for

non-deformable particles). Many cavities are found for mutually attractive, anisotropic, deformable particles (red arrows), whereas for isotropic particles many fewer cavities are found and the other particles did not show any cavities. Crops of these images can be found in Extended Data Fig. 4. The white arrows indicate the direction \hat{v} .

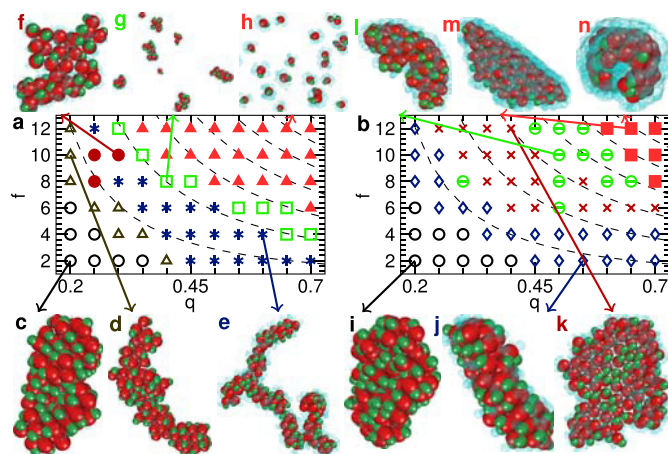


Extended Data Figure 7 | Centrifuged sediments. Magnifications of the bright field microscopy images in Fig. 3r (a) and Extended Data Fig. 4i–k (b–d). a–d, For mutually attractive, anisotropic, deformable particles, spherical cavities are observed in the sediment (a, b), whereas the sediments of similar non-functionalized and isotropic particles show no (c) and fewer (d) cavities.



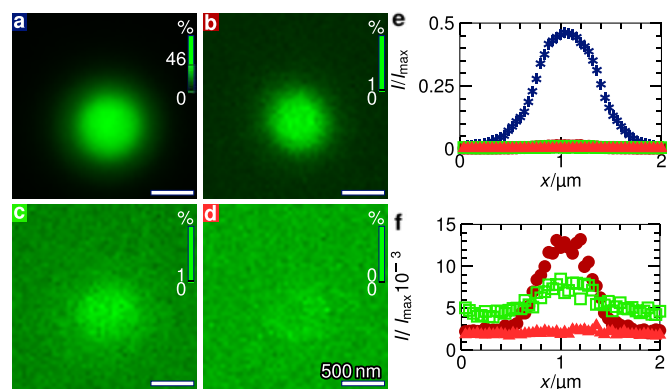
Extended Data Figure 8 | Clusters of isotropic particles.

a, b, Morphology diagrams of mutually attractive, isotropic, deformable particles as a function of the dimensionless diameter of the satellite spheres, q , and the number of satellite spheres, f . **c–k**, Representative snapshots with cores (red) and satellite spheres (blue). **a**, When unbound particles are used as the initial configuration and q and f are increased, compact (**c**, open circles), cylindrical (**d**, open triangles), flattened (**e**, filled circles), rod-like (**f**, asterisks) and finite-size (**g**, open squares) clusters as well as unbound particles (**h**, filled triangles) are found. **b**, When the initial configuration is a hexagonal monolayer, compact clusters (**i**, open circles), bilayers (**j**, open diamonds) and monolayers (**k**, crosses) are observed. The transitions between different morphologies are parallel to isolines for the covered surface fraction, $Q = 0.1$ to 0.5 (dashed lines in **a** and **b**).



Extended Data Figure 9 | Clusters of anisotropic particles.

a, b, Morphology diagrams of clusters of mutually attractive, anisotropic, deformable particles as a function of the dimensionless diameter of the satellite spheres, q , and the number of satellite spheres, f . **c–n**, Representative snapshots with cores (red), protrusions (green) and satellite spheres (blue). **a**, When unbound particles are used as the initial configuration, increasing f and q results in compact (**c**, open circles), cylindrical (**d**, open triangles), rod-like (**e**, asterisks), flattened (**f**, filled circles) and finite-size (**g**, open squares) clusters as well as unbound particles (**h**, filled triangles). **b**, When the initial configuration is a hexagonal monolayer, compact clusters (**i**, open circles), bilayers (**j**, open diamonds), planar monolayers (**k**, crosses), curved monolayers with in-plane protrusions (**l**, bisected circles) and curved monolayers with out-of-plane protrusions (**m–n**, filled squares) are found. The transitions between different morphologies are parallel to isolines for the covered surface fraction, $Q = 0.1$ to 0.7 (dashed lines in **a** and **b**).



Extended Data Figure 10 | Functionalized CPSAA spheres.

a–d, Fluorescence microscopy images for variations on the fluoresceinamine coupling method. **e, f**, Normalized fluorescence intensity, I/I_{\max} , as a function of the distance, x , on the horizontal line through the fluorescence maximum. Poly(styrene-*co*-acrylic acid) spheres were activated and functionalized as described in Methods (**a, e, f**, blue asterisks). Polystyrene spheres were similarly activated and functionalized (**b, e, f**, red circles). CPSAA was similarly treated without adding *N*-(3-dimethylaminopropyl)-*N'*-ethylcarbodiimide hydrochloride (**c, e, f**, green squares). CPSAA was similarly treated without adding fluoresceinamine (**d–f**, light red triangles). The vertical bars indicate the image level thresholds.

Concerted nucleophilic aromatic substitution with $^{19}\text{F}^-$ and $^{18}\text{F}^-$

Constanze N. Neumann¹, Jacob M. Hooker^{2,3} & Tobias Ritter^{1,2,4}

Nucleophilic aromatic substitution ($\text{S}_{\text{N}}\text{Ar}$) is widely used by organic chemists to functionalize aromatic molecules, and it is the most commonly used method to generate arenes that contain ^{18}F for use in positron-emission tomography (PET) imaging¹. A wide range of nucleophiles exhibit $\text{S}_{\text{N}}\text{Ar}$ reactivity, and the operational simplicity of the reaction means that the transformation can be conducted reliably and on large scales². During $\text{S}_{\text{N}}\text{Ar}$, attack of a nucleophile at a carbon atom bearing a ‘leaving group’ leads to a negatively charged intermediate called a Meisenheimer complex. Only arenes with electron-withdrawing substituents can sufficiently stabilize the resulting build-up of negative charge during Meisenheimer complex formation, limiting the scope of $\text{S}_{\text{N}}\text{Ar}$ reactions: the most common $\text{S}_{\text{N}}\text{Ar}$ substrates contain strong π -acceptors in the *ortho* and/or *para* position(s)³. Here we present an unusual concerted nucleophilic aromatic substitution reaction ($\text{CS}_{\text{N}}\text{Ar}$) that is not limited to electron-poor arenes, because it does not proceed via a Meisenheimer intermediate. We show a phenol deoxyfluorination reaction for which $\text{CS}_{\text{N}}\text{Ar}$ is favoured over a stepwise displacement. Mechanistic insights enabled us to develop a functional-group-tolerant ^{18}F -deoxyfluorination reaction of phenols, which can be used to synthesize ^{18}F -PET probes. Selective ^{18}F introduction, without the need for the common, but cumbersome, azeotropic drying of ^{18}F , can now be accomplished from phenols as starting materials, and provides access to ^{18}F -labelled compounds not accessible through conventional chemistry.

$\text{S}_{\text{N}}\text{Ar}$ reactions generally take place via either an addition–elimination or elimination–addition mechanism. Both two-step mechanisms display

a high-energy intermediate, either an aryne species (elimination–addition) or a Meisenheimer complex (addition–elimination)^{2,4}. A concerted displacement of the leaving group by an incoming nucleophile could avoid the formation of high-energy intermediates and thus broaden the scope of suitable electrophiles. Displacements at primary aliphatic centres, where charge build-up in a hypothetical $\text{S}_{\text{N}}1$ mechanism is unfavourable, commonly take place via a concerted mechanism involving the σ^* ($\text{C}_{\text{alkyl}}\text{–leaving group (LG)}$) orbital ($\text{S}_{\text{N}}2$ mechanism). For aromatic substrates, a direct substitution pathway involving the σ^* orbital of the arene–LG bond (σ^* ($\text{C}_{\text{aryl}}\text{–LG}$)) is deemed to be impossible: the σ^* orbital is shielded because its large lobe points inwards into the arene ring (Fig. 1a)⁵. Concerted $\text{S}_{\text{N}}\text{Ar}$ substitutions via the π -orbital framework are considered “possible but restricted to aromatic structures devoid of the ring activation to generate an intermediate sigma complex of some stability”². The intramolecular Newman–Kwart rearrangement has been reported to occur through concerted displacement for a wide range of arene substrates, albeit mostly with high activation barriers (35–43 kcal mol^{−1}) that reduce synthetic utility⁶. Here we show that the deoxyfluorination reaction of phenols with the reagent PhenoFluor (Fig. 2b) reported by our group^{7,8} proceeds via a concerted pathway with electron-rich as well as electron-poor substrates, and how a detailed mechanistic analysis enabled us to design a deoxyfluorination reaction of phenols with ^{18}F . A concerted reaction with activation energies between 20 and 25 kcal mol^{−1} is observed because the concerted pathway is favoured, rather than because the classic two-step mechanism is disfavoured, which sets our reaction apart from previous transformations that proceed with substantially higher activation

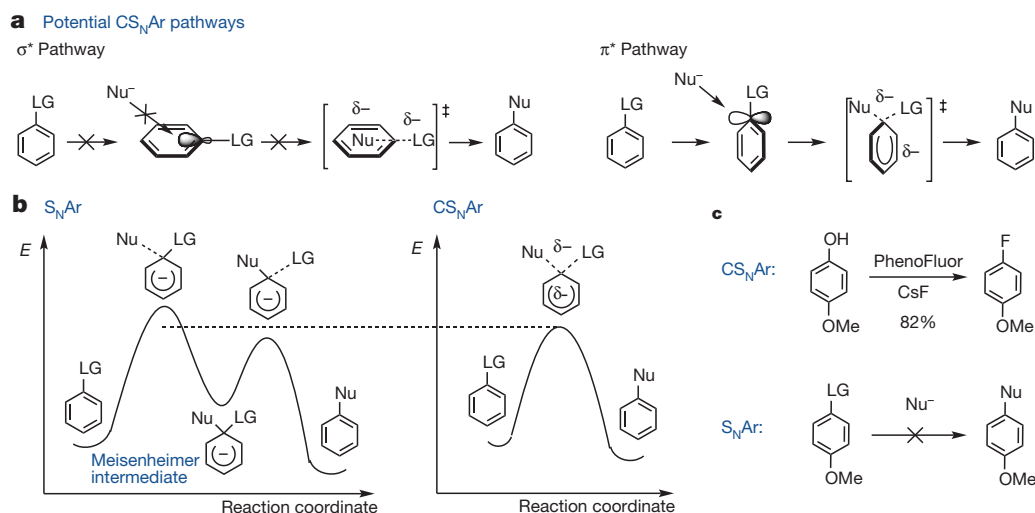


Figure 1 | Comparison of orbital interactions and energy profiles in $\text{S}_{\text{N}}\text{Ar}$ and $\text{CS}_{\text{N}}\text{Ar}$. **a**, The aromatic ring blocks the approach of the nucleophile to the $\sigma^*_{\text{C-LG}}$ orbital; attack on the π -framework is feasible. **b**, The energy profiles of $\text{S}_{\text{N}}\text{Ar}$ and $\text{CS}_{\text{N}}\text{Ar}$ differ in the number of

transition states and in the magnitude of the activation energies. **c**, Minimization of charge build-up in the transition state renders nucleophilic displacement feasible even on electron-rich arenes in $\text{CS}_{\text{N}}\text{Ar}$ reactions.

¹Department of Chemistry and Chemical Biology, Harvard University, Cambridge, Massachusetts 02138, USA. ²Division of Nuclear Medicine and Molecular Imaging, Department of Radiology, Massachusetts General Hospital, Boston, Massachusetts 02114, USA. ³Athinoula A. Martinos Center for Biomedical Imaging, Massachusetts General Hospital and Harvard Medical School, Charlestown, Massachusetts 02129, USA. ⁴Max-Planck-Institut für Kohlenforschung, Kaiser-Wilhelm-Platz 1, D-45470 Mülheim an der Ruhr, Germany.

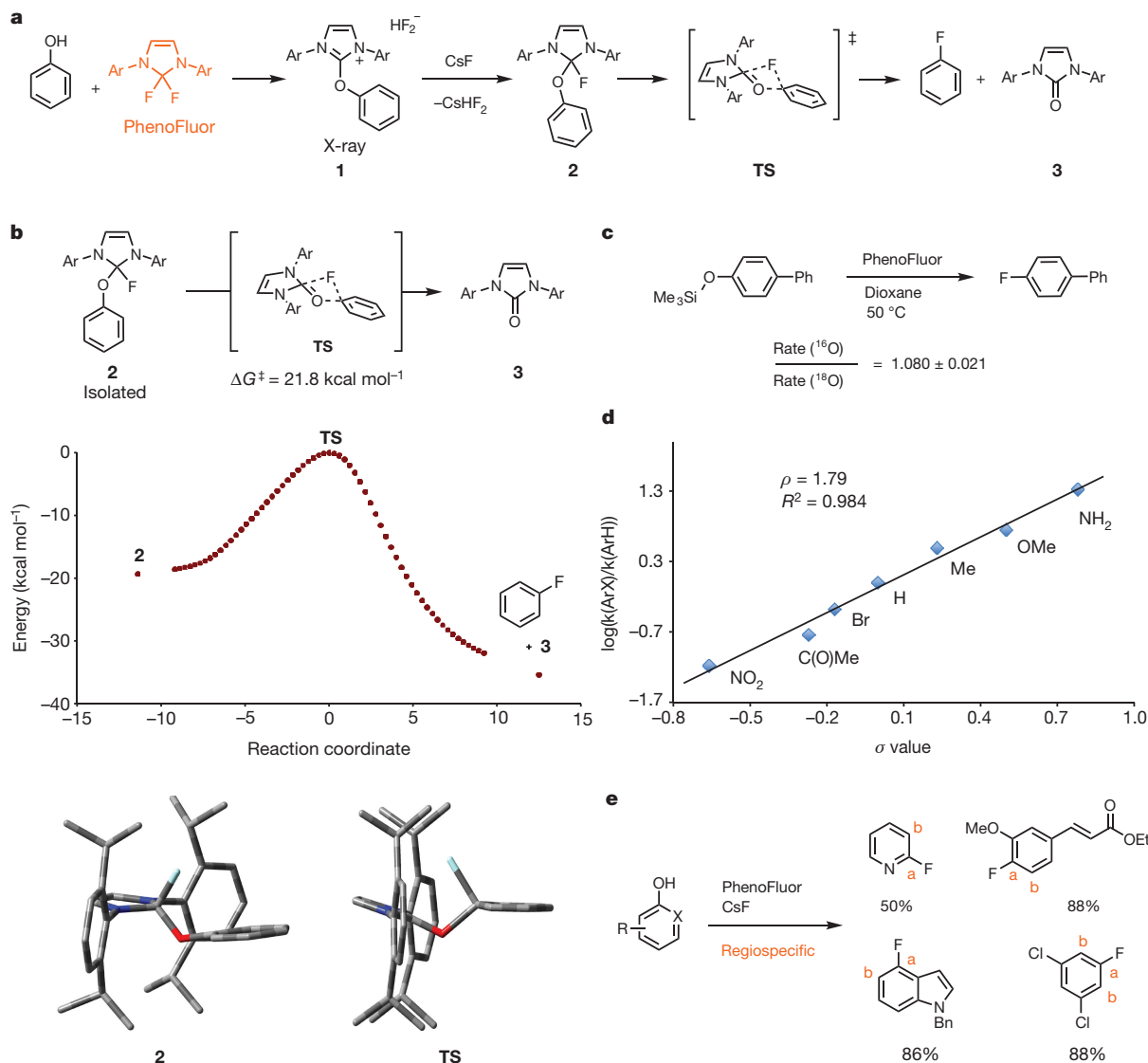


Figure 2 | Proposed mechanism of PhenoFluor-mediated deoxyfluorination. **a**, After formation of uronium intermediate **1**, external CsF abstracts hydrogen fluoride (HF) to form tetrahedral adduct **2**, which undergoes concerted nucleophilic substitution via fluoride shift (Ar = 2,6-diisopropylphenyl). **b**, The intrinsic reaction coordinate obtained from DFT calculations (B3LYP/6-31G(d), toluene solvent model) shows a single barrier between tetrahedral adduct **2** and reaction products (Ar = 2,6-diisopropylphenyl). Structures obtained from DFT calculations are shown for **2** and TS. $\Delta G^\ddagger = 21.8 \pm 0.2 \text{ kcal mol}^{-1}$

barriers^{1,3,6,9}. Gas-phase nucleophilic aromatic substitutions can take place by concerted nucleophile attack and loss of the leaving group, but only isolated cases of intermolecular $\text{CS}_\text{N}\text{Ar}$ reactions in solution or ionic melt have been reported^{10–16}.

The orbital interactions involved in a concerted mechanism are similar to those of classical addition–elimination pathways, but the extent of bond formation and cleavage in the transition state is crucially different: in the transition state of $\text{CS}_\text{N}\text{Ar}$, both the nucleophile and leaving group are attached to the arene by partial rather than full bonds. Loss of the leaving group in the rate-determining step allows the negative charge associated with nucleophilic attack to be located on the incoming nucleophile and the departing leaving group, as opposed to the arene in conventional $\text{S}_\text{N}\text{Ar}$. We propose that selection of leaving groups and reaction conditions tailored to a concerted displacement make it possible to utilize the minimization of charge build-up on the arene to lower the activation barrier (Fig. 1b), which expands the scope of

was measured for the transformation of **2** to aryl fluoride and urea **3**. **c**, The primary $^{16}\text{O}/^{18}\text{O}$ kinetic isotope effect is consistent with cleavage of the C–O bond during the rate-limiting step (Supplementary Fig. 15). Silylated phenols react with PhenoFluor to form tetrahedral intermediate without CsF. **d**, Hammett plot for the deoxyfluorination of *para*-substituted phenols at 110 °C. **e**, Regioselective product formation occurs for substrates prone to nucleophilic attack at position **b** if arynes were formed^{14,30}.

electrophiles to include deactivated substrates that feature strong π -donors in the *para*-position (Fig. 1c). The PhenoFluor-mediated deoxyfluorination reaction allows the interconversion of 4-hydroxyanisole to 4-fluoroanisole at only 110 °C (refs 7, 8)—far below the temperature commonly observed for aromatic substitutions on unactivated arenes^{3,6,9}.

We propose a reaction sequence for the deoxyfluorination reaction in which fluoride attacks the imidazolium core of the reagent to yield tetrahedral intermediate **2** before participating in concerted displacement on the arene (Fig. 2a); independently synthesized and characterized tetrahedral intermediate **2** is converted to aryl fluoride and urea **3** under the reaction condition (Fig. 2b). A single transition state (TS) was localized in a density functional theory (DFT) study (B3LYP/6-311++G(d,p)), toluene solvent model) with partial bonds between the nucleophile and arene as well as the leaving group and the arene, the characteristic feature of a concerted transformation¹⁷. An internal

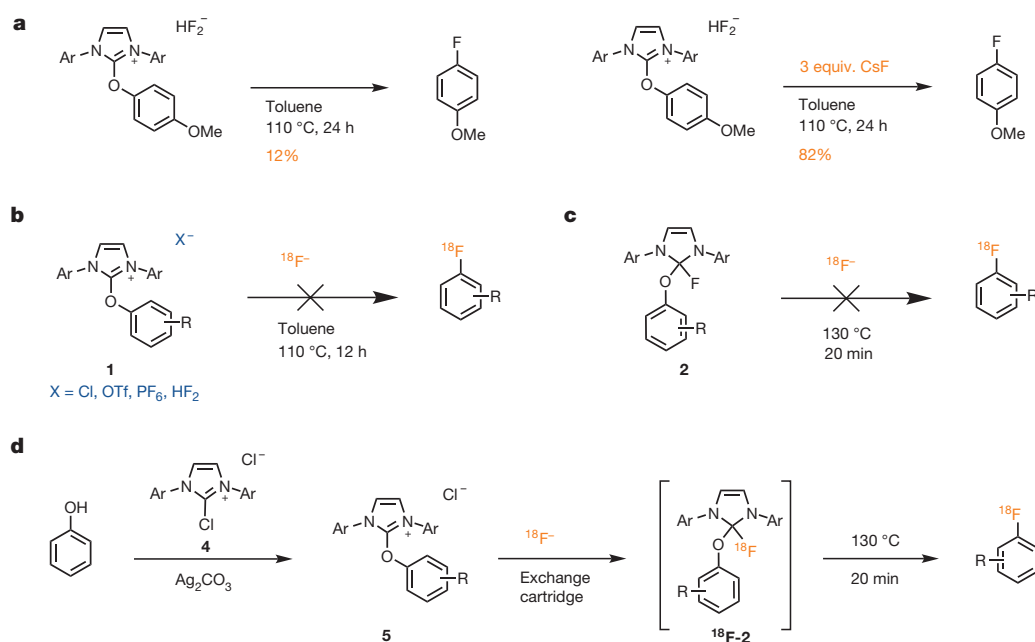


Figure 3 | ^{18}F isotopologue 2. **a**, CsF abstracts HF from the HF_2^- counteranion: without CsF, deoxyfluorination occurs via a different mechanism in which HF_2^- attacks the arene. DFT studies reveal that the barrier for C–F bond formation is 6.0 kcal mol^{-1} lower with a fluoride instead of a bifluoride nucleophile (see Supplementary Fig. 29).

b, Treatment of uronium 1 with ^{18}F does not give aryl fluoride owing to the lack of anion exchange between X and ^{18}F -fluoride in solution. **c**, No ^{18}F incorporation is observed. **d**, Anion exchange with extraneous fluoride takes place on an anion exchange cartridge (Ar = 2,6-diisopropylphenyl).

reaction coordinate analysis revealed that the transition state connects tetrahedral intermediate 2 to urea 3 and aryl fluoride, which excludes the existence of additional maxima along the reaction path.

Crucial to the proposal of a concerted substitution mechanism is that loss of the leaving group occurs concurrently with attack of the incoming nucleophile. The rate observed for the fluorination of ^{16}O -4-phenyl-phenol is 1.08 ± 0.02 times as fast as the rate of fluorination of ^{18}O -4-phenyl-phenol, corresponding to a large primary kinetic isotope effect (Fig. 2c)¹⁸. A primary $^{16}\text{O}/^{18}\text{O}$ kinetic isotope effect shows that cleavage of the C–O bond (and therefore loss of the LG) occurs during the rate-determining step^{17,19,20}. The rate of deoxyfluorination with PhenoFluor is greater for electron-deficient than for electron-rich substrates, and the continuity in the Hammett plot reveals that no change in mechanism or rate-determining step occurs when the electron density on the phenol is varied (Fig. 2d). A single electron transfer (SET) mechanism, in which an electron is transferred from the phenol arene to the positively charged imidazolium core, is inconsistent with the observed Hammett plot: for rate-determining electron transfer, reaction rates should be fastest for electron-rich substrates, which is not the case. SET occurring under pre-equilibrium conditions followed by rate-determining fluoride attack, in which case a positive ρ value would be expected, is unlikely due to the primary $^{16}\text{O}/^{18}\text{O}$ isotope effect. Fast and reversible fluoride attack followed by rate-limiting expulsion of the leaving group would give rise to a negative ρ value in the Hammett plot. The regioselectivity of the deoxyfluorination reaction discounts an aryne mechanism (Fig. 2e).

Eyring plots were constructed for a selection of substrates, which revealed $\Delta G^\ddagger = 20.3 \pm 0.1\text{ kcal mol}^{-1}$ for 4-nitrophenol, $\Delta G^\ddagger = 21.0 \pm 0.2\text{ kcal mol}^{-1}$ for 4-cyanophenol, $\Delta G^\ddagger = 21.2 \pm 0.5\text{ kcal mol}^{-1}$ for 4-trifluoromethylphenol and $\Delta G^\ddagger = 23.4 \pm 0.2\text{ kcal mol}^{-1}$ for phenol, respectively. Computational activation barriers $\Delta G^\ddagger = 20.8\text{ kcal mol}^{-1}$ for 4-nitrophenol and $\Delta G^\ddagger = 25.0\text{ kcal mol}^{-1}$ for phenol are in good agreement with the experimental values. Compared to classical $\text{S}_\text{N}\text{Ar}$ reactions, the increase in activation energies as the aromatic system becomes more electron-rich is far less pronounced for concerted $\text{S}_\text{N}\text{Ar}$ reactions, which is also apparent from the smaller Hammett ρ values; conventional $\text{S}_\text{N}\text{Ar}$ reactions have ρ values ranging

from 3 to 8, compared with 1.8 for the $\text{CS}_\text{N}\text{Ar}$ reaction reported here (Fig. 3c)¹⁰. Limited delocalization of negative charge onto the aromatic substrate in the transition state can thus extend the scope of nucleophilic aromatic substitution to electron-rich substrates.

The barrier for $\text{CS}_\text{N}\text{Ar}$ in the presented deoxyfluorination is low relative to hypothetical $\text{S}_\text{N}\text{Ar}$ reactions on electron-rich arenes. First, facile loss of the leaving group is crucial for a concerted nucleophilic aromatic substitution reaction²¹. Unlike in a two-step sequence, where a second smaller activation barrier is associated with loss of the leaving group, a concerted transformation has a single barrier to which both nucleophilic attack, disruption of aromaticity, and loss of the leaving group contribute. A neutral leaving group (urea 3) will aid in stabilizing the partial negative charge that resides on both the nucleophile and the leaving group in the transition state²¹. An earlier transition state with a lower reaction barrier will occur for $\text{CS}_\text{N}\text{Ar}$ reactions if loss of the leaving group is energetically favourable¹. Formation of urea 3 is highly exergonic, and because partial C–O cleavage occurs in the transition state, the exergonicity of the overall transformation is expected to lower the activation barrier for deoxyfluorination, an effect also apparent in the ^{18}F displacement of arenes from triarylsulfonium salts²². Compared with the Newman–Kwart rearrangement, which can take place on substrates deactivated by electron-donating substituents, the PhenoFluor-mediated deoxyfluorination proceeds with considerably lower reaction barriers, probably due to the higher enthalpic gain associated with leaving group loss. Second, rearrangement of solvent molecules is commonly a large contributor to the activation barriers of nucleophilic aromatic substitutions, particularly when anionic nucleophiles are employed²³. Association of the (bi)fluoride nucleophile with the cationic uronium 1 solubilizes the nucleophile in the non-polar solvent toluene, and can subsequently form neutral tetrahedral adduct 2. We propose that the contribution of solvation to the activation barrier is small because neither the associated reaction partners nor the transition state carry an overall charge and little nuclear motion is required to proceed from 2 to TS. Computational data indicate that the use of a non-polar solvent favours the occurrence of a concerted deoxyfluorination reaction (Supplementary Fig. 46).

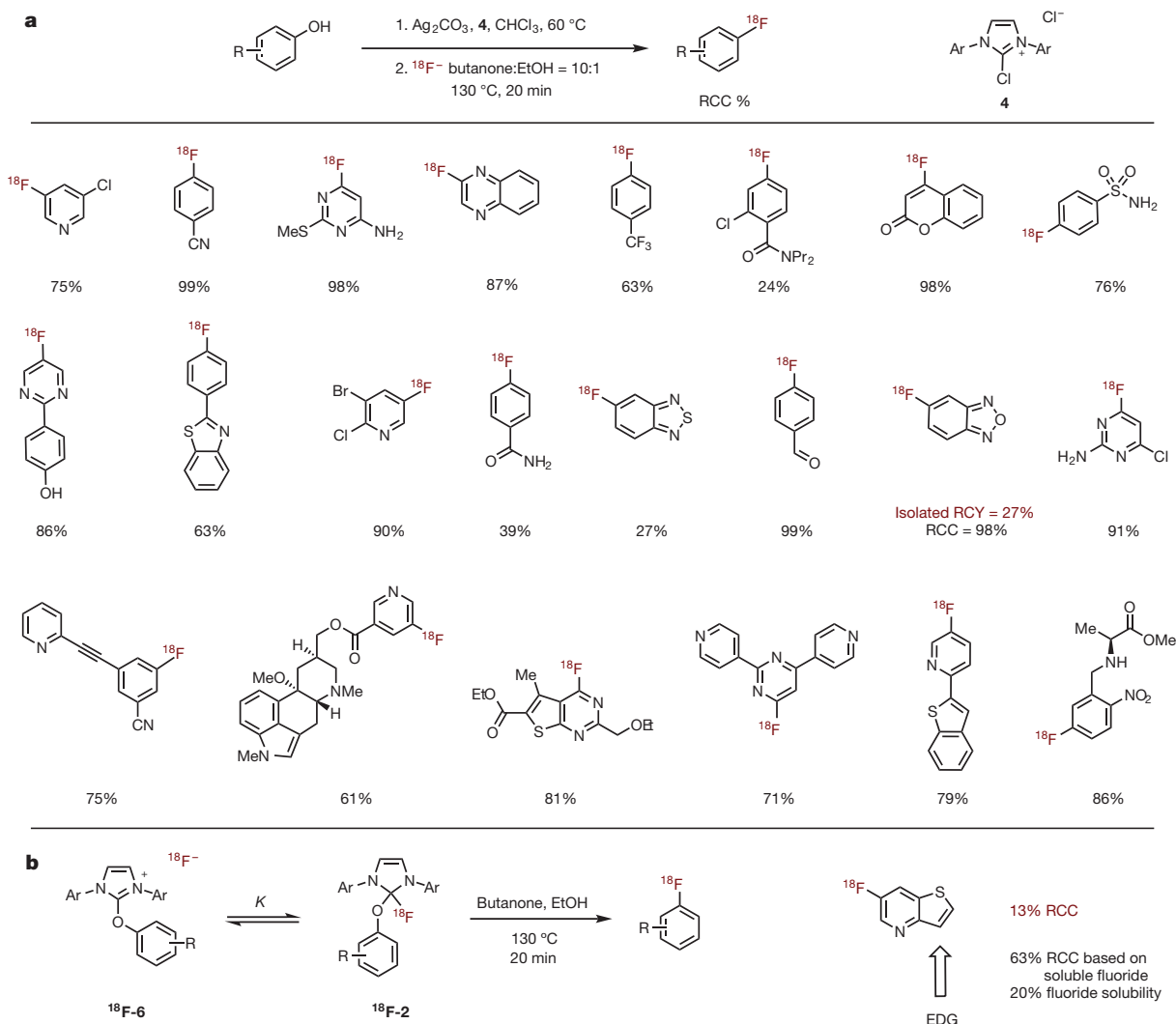


Figure 4 | Deoxyfluorination of phenols and heterophenols with ^{18}F .
a, Decay-corrected radiochemical conversions were determined by comparing the amount of ^{18}F incorporated into the product to the amount of ^{18}F not incorporated. **b**, Electron-rich phenols will result in a smaller

equilibrium constant K , resulting in fluoride expulsion and decomposition before productive deoxyfluorination from tetrahedral intermediate ^{18}F -2 can occur. Ar = 2,6-diisopropylphenyl.

^{18}F -fluoride is a desirable nucleophile for the development of $\text{CS}_\text{N}\text{Ar}$ reactions, particularly concerted deoxyfluorination: phenols are easily accessible and their high polarity facilitates purification of aryl fluoride product from phenol starting material²⁴. However, in addition to the two equivalents of fluoride inherent to PhenoFluor itself, additional fluoride must be added for efficient deoxyfluorination (Fig. 3a), which, a priori, renders PhenoFluor-mediated deoxyfluorination effectively useless for ^{18}F chemistry. Even attempts towards a low specific-activity radiodeoxyfluorination initially proved fruitless: both isolated reaction intermediate **1** (and derivatives featuring different counteranions) and tetrahedral intermediate **2** did not react with external ^{18}F -fluoride to yield ^{18}F -aryl fluoride products (Fig. 3b, c). Mechanistic work (Supplementary Information) revealed that fluoride was not incorporated into tetrahedral intermediate **2** via attack by external fluoride on uronium **1** or anion metathesis; instead the fluoride on the aryl fluoride originated from PhenoFluor. We thus devised a strategy to alter the mechanism of fluoride incorporation into **2** to access ^{18}F -**2** in high specific activity: while anion exchange of **1** with ^{18}F does not occur in solution, productive anion exchange occurs on an anion exchange cartridge (Fig. 3d).

^{18}F -fluoride is typically prepared by proton bombardment of ^{18}O - H_2O , and ^{18}F -fluoride is subsequently trapped on an ion-exchange cartridge. Elution of the radioisotope is commonly achieved with an aqueous solution of a base¹⁹. Here we can use uronium **5** directly for elution of

^{18}F -fluoride from the anion exchange cartridge. Uronium **5** can readily be prepared from chloroimidazolium chloride **4** and a suitable phenol and used after simple filtration. The elution procedure obviates the need for azeotropic drying of ^{18}F -fluoride, and subsequent heating of the resulting solution of ^{18}F -**2** directly provides aryl fluoride.

No special care is required to exclude air or moisture from the ^{18}F -deoxyfluorination reaction, and the radiolabelled product can be conveniently separated from the reaction precursor. A wide variety of functional groups including amines and phenols as well as thioethers and amides are tolerated, and arenes as well as heteroarenes undergo radio-deoxyfluorination with high radiochemical conversion (Fig. 4a). Substrates containing carboxylic acids did not undergo ^{18}F -deoxyfluorination because carboxylic acids inhibit the formation of uronium **5**. Competing nucleophilic aromatic substitution of activated chloride does not occur under the reaction conditions. Classical $\text{S}_\text{N}\text{Ar}$ chemistry is the most widely applied method for the synthesis of PET probes but suffers from a very limited reaction scope, and protic functional groups are commonly not tolerated. Modern methods^{25–29}, while capable of introducing ^{18}F -fluoride into a more diverse range of structures, often suffer from the need for complex starting materials, operating or purification procedures. Heterocycles are present in many bioactive compounds but are often problematic substrates for metal-mediated fluorination protocols with ^{18}F ;

several heterocycles undergo PhenoFluor deoxyfluorination with high radiochemical conversion. To highlight the operational simplicity of ^{18}F -deoxyfluorination, ^{18}F -5-fluorobenzofurazan was synthesized from 34 mCi aqueous ^{18}F -fluoride and subjected to high-performance liquid chromatography purification. Within 34 min from the end of bombardment, 9.3 mCi of isolated and purified ^{18}F -5-fluorobenzofurazan could be obtained in 27% non-decay-corrected radiochemical yield (RCY) with a specific activity of $3.03\text{ Ci }\mu\text{mol}^{-1}$.

We have established that tetrahedral intermediate **2** is in equilibrium with uronium fluoride **6** (Fig. 4b and Supplementary Fig. 36). Clean first-order decay of **2** was observed in the presence of added fluoride, but a marked deviation from first-order kinetics was observed for the deoxyfluorination of silylated phenols in the absence of added fluoride. Hence, the fluoride anion in **6** probably engages in unproductive processes, such as precipitation or other fluoride sequestrations. In ^{19}F deoxyfluorination, excess CsF negates such potential side reactions, but for radiofluorination, fluoride is present in small quantities (nmol). For most compounds shown in Fig. 4, potential decomposition of **2** does not disrupt productive fluorination, but when more electron-rich phenols are employed, the equilibrium constant K between **6** and tetrahedral intermediate **2** decreases. We have already shown that more electron-rich substrates can afford acceptable radiochemical conversions, when the conversion is based on soluble fluoride (Fig. 4b). While fluoride sequestration from **6** currently precludes the isolation of electron-rich ^{18}F aryl fluorides in high radiochemical yields, efficient C– ^{18}F bond formation bodes well for mechanism-based strategies to increase K , which would render electron-rich arenes accessible.

Received 21 November 2015; accepted 10 March 2016.

Published online 18 May 2016.

- Fernández, I., Frenking, G. & Uggerud, E. Rate-determining factors in nucleophilic aromatic substitution reactions. *J. Org. Chem.* **75**, 2971–2980 (2010).
- Terrier, F. *Modern Nucleophilic Aromatic Substitution* 1–94 (Wiley, 2013).
- Chéron, N., El Kaïm, L., Grimaud, L. & Fleurat-Lessard, P. Evidences for the key role of hydrogen bonds in nucleophilic aromatic substitution reactions. *Chemistry* **17**, 14929–14934 (2011).
- Picazo, E., Houk, K. N. & Garg, N. K. Computational predictions of substituted benzyne and indolyne regioselectivities. *Tetrahedr. Lett.* **56**, 3511–3514 (2015).
- Crampton, M. R. in *Organic Reaction Mechanisms—2010: An Annual Survey Covering the Literature Dated January to December 2010* (ed. Knappe, A. C.) 175–190 (Wiley, 2012).
- Lloyd-Jones, G. C., Moseley, J. D. & Renny, J. S. Mechanism and application of the Newman-Kwart O→S rearrangement of *O*-aryl thiocarbamates. *Synthesis* **2008**, 661–689 (2008).
- Tang, P., Wang, W. & Ritter, T. Deoxyfluorination of phenols. *J. Am. Chem. Soc.* **133**, 11482–11484 (2011).
- Fujimoto, T., Becker, F. & Ritter, T. PhenoFluor: practical synthesis, new formulation, and deoxyfluorination of heteroaromatics. *Org. Process Res. Dev.* **18**, 1041–1044 (2014).
- Glukhovtsev, M. N., Bach, R. D. & Laiter, S. Single-step and multistep mechanisms of aromatic nucleophilic substitution of halobenzenes and halonitrobenzenes with halide anions: *ab initio* computational study. *J. Org. Chem.* **62**, 4036–4046 (1997).
- Fry, S. E. & Pienta, N. J. Effects of molten salts on reactions. Nucleophilic aromatic substitution by halide ions in molten dodecyltributylphosphonium salts. *J. Am. Chem. Soc.* **107**, 6399–6400 (1985).
- Hunter, A. *et al.* Stepwise versus concerted mechanisms at trigonal carbon: transfer of the 1,3,5-triazinyl group between aryl oxide ions in aqueous solution. *J. Am. Chem. Soc.* **117**, 5484–5491 (1995).
- Renfrew, A. H. M., Taylor, J. A., Whitmore, J. M. J. & Williams, A. A single transition state in nucleophilic aromatic substitution: reaction of phenolate ions with 2-(4-nitrophenoxy)-4,6-dimethoxy-1,3,5-triazine in aqueous solution. *J. Chem. Soc. Perkin Trans. 2* **1993**, 1703–1704 (1993).
- Dub, P. A. *et al.* C–F bond breaking through aromatic nucleophilic substitution with a hydroxo ligand mediated via water bifunctional activation. *Bull. Chem. Soc. Jpn* **86**, 557–568 (2013).
- Goryunov, L. I. *et al.* Di- and trifluorobenzenes in reactions with Me_2EM ($\text{E} = \text{P}, \text{N}$; $\text{M} = \text{SiMe}_3, \text{SnMe}_3, \text{Li}$) reagents: evidence for a concerted mechanism of aromatic nucleophilic substitution. *Eur. J. Org. Chem.* **2010**, 1111–1123 (2010).
- Nawaz, F. *et al.* Temporary intramolecular generation of pyridine carbenes in metal-free three-component C–H bond functionalisation/aryl-transfer reactions. *Chemistry* **19**, 17578–17583 (2013).
- Renfrew, A. H. M., Taylor, J. A., Whitmore, J. M. J. & Williams, A. Timing of bonding changes in fundamental reactions in solutions: pyridinolysis of a triazinylpyridinium salt. *J. Chem. Soc. Perkin Trans. 2* **1994**, 2383–2384 (1994).
- Williams, A. The diagnosis of concerted organic mechanisms. *Chem. Soc. Rev.* **23**, 93–100 (1994).
- Sawyer, C. B. & Kirsch, J. F. Kinetic isotope effects for reactions of methyl formate-methoxy- ^{18}O . *J. Am. Chem. Soc.* **95**, 7375–7381 (1973).
- Lasne, M.-C. *et al.* in *Contrast Agents II* Vol. 222 (ed. Krause, W.) Ch. 7, 201–258 (Springer, 2002).
- Matsson, O. & MacMillar, S. Isotope effects for fluorine-18 and carbon-11 in the study of reaction mechanisms. *J. Labelled Comp. Radiopharm.* **50**, 982–988 (2007).
- Yamabe, S., Minato, T. & Kawabata, Y. The importance of the $\sigma^*-\pi^*$ orbital mixing for the nucleophilic displacement on the unsaturated carbon. *Can. J. Chem.* **62**, 235–240 (1984).
- Mu, L. *et al.* ^{18}F -radiolabeling of aromatic compounds using triarylsulfonium salts. *Eur. J. Org. Chem.* **2012**, 889–892 (2012).
- Sun, H. & DiMaggio, S. G. Room-temperature nucleophilic aromatic fluorination: experimental and theoretical studies. *Angew. Chem. Int. Ed.* **45**, 2720–2725 (2006).
- Neumann, C. N. & Ritter, T. Late-stage fluorination: fancy novelty or useful tool? *Angew. Chem. Int. Ed.* **54**, 3216–3221 (2015).
- Tredwell, M. *et al.* A general copper-mediated nucleophilic ^{18}F fluorination of arenes. *Angew. Chem. Int. Ed.* **53**, 7751–7755 (2014).
- Gao, L. *et al.* Metal-free oxidative fluorination of phenols with ^{18}F fluoride. *Angew. Chem. Int. Ed.* **51**, 6733–6737 (2012).
- Ichihashi, N. *et al.* Copper-catalyzed ^{18}F fluorination of (mesityl)(aryl)iodonium salts. *Org. Lett.* **16**, 3224–3227 (2014).
- Lee, E., Hooker, J. M. & Ritter, T. Nickel-mediated oxidative fluorination for PET with aqueous ^{18}F fluoride. *J. Am. Chem. Soc.* **134**, 17456–17458 (2012).
- Lee, E. *et al.* A fluoride-derived electrophilic late-stage fluorination reagent for PET imaging. *Science* **334**, 639–642 (2011).
- Bronner, S. M., Goetz, A. E. & Garg, N. K. Overturning indolyne regioselectivities and synthesis of indolactam V. *J. Am. Chem. Soc.* **133**, 3832–3835 (2011).

Supplementary Information is available in the online version of the paper.

Acknowledgements We thank the Patty and Michael Phelps Foundation and the National Institutes of Health (NIH) National Institute of General Medical Sciences (GM088237) for funding. Radioisotope production and use were enabled by a shared instrument grant from the NIH (1S1ORR017208). We thank S. Arlow and C. Kleinlein for preliminary mechanistic work and H. Lee for assistance with X-ray crystallography. We thank N. A. Stephenson for a synthetic precursor for **S6** as well as the ^{19}F -standard for this substrate.

Author Contributions C.N.N. designed and performed the experiments, with input from T.R. and J.M.H. C.N.C. analysed the data. T.R. directed the project. C.N.N. and T.R. prepared the manuscript with input from J.M.H.

Author Information Atomic coordinates and structure factors for the reported crystal structures have been deposited in the Cambridge Crystallographic Data Centre under accession number CCDC-1419728. Reprints and permissions information is available at www.nature.com/reprints. The authors declare no competing financial interests. Readers are welcome to comment on the online version of the paper. Correspondence and requests for materials should be addressed to T.R. (ritter@mpi-muelheim.mpg.de).

Seafloor geodetic constraints on interplate coupling of the Nankai Trough megathrust zone

Yusuke Yokota¹, Tadashi Ishikawa¹, Shun-ichi Watanabe¹, Toshiharu Tashiro¹ & Akira Asada²

Interplate megathrust earthquakes have inflicted catastrophic damage on human society. Such an earthquake is predicted to occur in the near future along the Nankai Trough off southwestern Japan—an economically active and densely populated area in which megathrust earthquakes have already occurred^{1–5}. Megathrust earthquakes are the result of a plate-subduction mechanism and occur at slip-deficit regions (also known as ‘coupling’ regions)^{6,7}, where friction prevents plates from slipping against each other and the accumulated energy is eventually released forcefully. Many studies have attempted to capture distributions of slip-deficit rates (SDRs) in order to predict earthquakes^{8–10}. However, these studies could not obtain a complete view of the earthquake source region, because they had no seafloor geodetic data. The Hydrographic and Oceanographic Department of the Japan Coast Guard (JHOD) has been developing a precise and sustainable seafloor geodetic observation network¹¹ in this subduction zone to obtain information related to offshore SDRs. Here, we present seafloor geodetic observation data and an offshore interplate SDR-distribution model. Our data suggest that most offshore regions in this subduction zone have positive SDRs. Specifically, our observations indicate previously unknown regions of high SDR that will be important for tsunami disaster mitigation, and regions of low SDR that are consistent with distributions of shallow slow earthquakes and subducting seamounts. This is the first direct evidence that coupling conditions might be related to these seismological and geological phenomena. Our findings provide information for inferring megathrust earthquake scenarios and interpreting research on the Nankai Trough subduction zone.

Recurring interplate megathrust earthquakes have occurred along the Nankai Trough subduction zone between the Philippine Sea plate and the Amur plate, and the next earthquake in this region is predicted to occur in the near future^{1–5}. This subduction zone is frequently discussed in terms of segmented source regions known as the Nankaido, Tonankai and Tokai regions, and the past 300 years of historical records² describe the occurrence of earthquakes of magnitude 8 in these segments (notably the 1707 Hōei, 1854 Ansei-I and Ansei-II, 1944 Tonankai and 1946 Nankaido earthquakes). Moreover, earthquakes with magnitudes up to 9 are thought to have occurred along each segment⁵.

Because megathrust earthquakes are driven by accumulated interplate slip deficit, these historical earthquakes are thought to have occurred on an interplate boundary with a high SDR^{6,7}. Therefore, to assess the scale of future earthquakes and associated tsunamis, it is necessary to understand the whole interplate distribution of SDRs. Although many geodetic studies have attempted to obtain this information for the Nankai Trough, they have not been successful. This is because the previous geodetic observation network was biased to land areas and so could not capture total geodetic information on the seafloor above the interplate boundary^{8–10}. Although small-scale seafloor geodetic observations have been carried out¹², they were limited to the Kumano-nada region.

Accordingly, over the past decade we have taken a new approach to obtaining total seafloor geodetic information, by means of a broad-scale seafloor observation network using a combined global positioning system and acoustic ranging (GPS-A) technique^{11,13,14}. We have improved the precision and frequency of our GPS-A observations since 2000 and they are amongst the highest global standards (see Methods and Extended Data Fig. 1).

We observe 15 seafloor sites in a wide seafloor region along the Nankai Trough (Fig. 1). Six sites were established before the 2011 Tohoku-oki earthquake. Nine further sites were deployed subsequently because data from the original six sites were insufficient to expose a complete picture of interplate SDRs¹⁵.

Extended Data Figs 2–4 show time series of the estimated horizontal coordinates of seafloor sites for each epoch, relative to their locations in the first observations at these sites. The reference frame is International Terrestrial Reference Frame (ITRF) 2005 (ref. 16). The positions are presented with respect to the stable part of the Amur plate (with stability determined by the MORVEL velocity model¹⁷). The position data for each epoch are summarized in Supplementary Table 1. Raw data from the six original sites involved coseismic deformation steps owing to the occurrence of the Tohoku-oki earthquake. We removed these steps from the raw data according to a coseismic source model, established using onshore and seafloor geodetic data¹⁸. In addition, the raw data from all sites involved postseismic deformations resulting from afterslip and viscoelastic relaxation following the Tohoku-oki earthquake. We removed this nonlinear deformation by using a postseismic model, calculated by means of a three-dimensional finite-element method¹⁹.

The corrected data gave us seafloor velocity fields that reflect strain accumulation processes that occurred when all sites moved at stable displacement rates owing to subduction of the Philippine Sea plate under the upper Amur plate. Extended Data Figs 2–4 present linear trends fitted to the time series using a robust regression method (the *M* estimation method); Table 1 lists each velocity. The lines fitted to the east–west and north–south time series in Extended Data Figs 2–4 represent the estimated linear site velocities and are shown with their 95% confidence intervals, which are used for the confidence ellipses in Fig. 1. Vertical velocities were not detected, because they were less than the detection limit (3–4 cm year^{−1}).

Long periods of observation at the six original sites made the confidence ellipses small. These velocity fields are also compared with onshore global navigation satellite system (GNSS) data (Fig. 1), calculated for the stable period from March 2006 to December 2009, and with the rates of convergence of the Philippine Sea plate to the Amur plate (calculated using the MORVEL model; see Fig. 1). Our seafloor data are roughly consistent with the orientation of plate convergence and with onshore velocities. Therefore, all offshore regions on the interplate boundary have positive SDRs.

These new data have great potential for advancing the estimation of SDR distributions²⁰. Onshore data cannot resolve offshore interplate

¹Hydrographic and Oceanographic Department, Japan Coast Guard, 3-1-1, Kasumigaseki, Chiyoda-ku, Tokyo 100-8932, Japan. ²Institute of Industrial Science, University of Tokyo, 4-6-1 Komaba, Meguro-ku, Tokyo 153-8505, Japan.

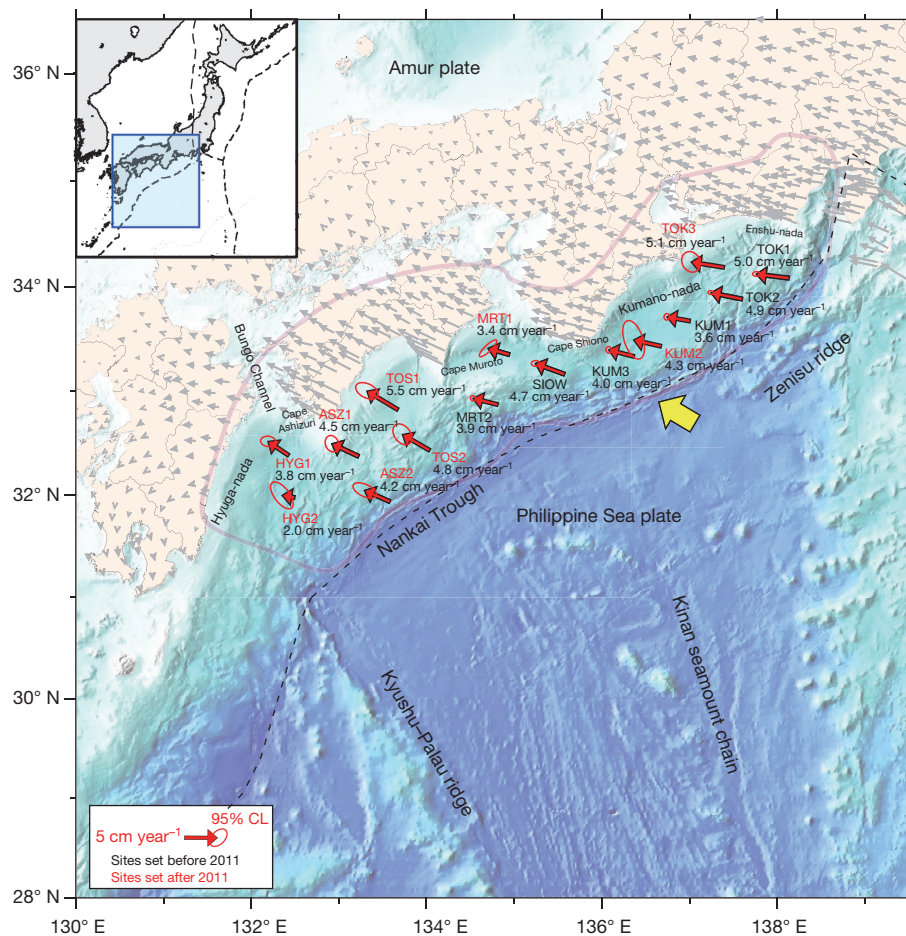


Figure 1 | Seafloor velocity field, based on seafloor geodetic observations at 15 seafloor sites along the Nankai Trough. Seafloor velocity vectors are shown with red arrows; each ellipse indicates the 95% confidence level. Onshore velocity vectors were calculated for the period from March 2006 to December 2009 using GEONET stations, and are shown with light grey arrows. Seafloor sites are named with four characters (including a letter and a number). The yellow arrow indicates the

convergence of the Philippine Sea plate under the Amur plate, calculated (using the MORVEL model¹⁷) to be occurring at a rate of 6.5 cm year^{-1} . The purple region is the region of maximum earthquake sources, provided as the worst-case scenario by the Central Disaster Management Council of the Japanese Government⁵. Seafloor topography is based on the J-EGG500 data set from the Japan Oceanographic Data Center (JODC) of the JHOD.

boundaries (see Methods). In contrast, our seafloor data can show the offshore heterogeneity (although regions adjacent to the trench axis—other than those near the TOK1 and ASZ2 sites—cannot be resolved). Figure 2a shows the SDR distribution model established using seafloor geodetic data (see Methods and Supplementary Tables 2 and 3 for more details).

Along the Nankai Trough, subducting seamounts are located in three regions^{21–23} at which very-low-frequency earthquakes (VLFs) have been activated²⁴. Below, we discuss mainly the relation of the shallow SDR distribution with these seismological and geological features and with the latest and predicted megathrust earthquake source regions, from west to east. The distribution of deep SDRs in our model is robustly similar to that obtained in past studies using only onshore data^{8–10}.

For region A, one edge could not be resolved enough in the model. Only at the shallowest site in region A, namely HYG2, could we directly catch a glimpse of the undersea SDR. The displacement rate at HYG2 was lower than the rates at adjacent sites (namely HYG1, ASZ1 and ASZ2; confidence levels 95%, 95% and 90%) according to our tests of parallelism between each east–west component. These data and our model suggest that the region of VLFE occurrence that extends to the east of the Kyushu–Palau ridge has a lower SDR than do adjacent undersea regions. This spatial relationship suggests that the subducting ridge not only activates shallow VLFs, but also forms the low-SDR region (this is a ‘low-coupling’ condition).

In region B, the deep region of high SDRs corresponds with the source region of the Nankaido earthquake of 1946. This region extends to the shallow side near the trench axis, which showed no slip in the

Table 1 | Velocity of each site with respect to the Amur plate

Site name	Position		Velocity (cm year^{-1})			Standard deviation and correlation (cm year^{-1})		
	Latitude	Longitude	Absolute	East (E)	North (N)	σ (E)	σ (N)	Corr (E, N)
TOK1	34.08	138.14	5.0	−4.9	0.9	0.2	0.1	0.0
TOK2	33.88	137.61	4.9	−4.8	1.0	0.2	0.1	−0.1
TOK3	34.18	137.39	5.1	−5.1	0.8	0.4	0.5	−0.1
KUM1	33.67	137.00	3.6	−3.6	0.7	0.1	0.2	0.1
KUM2	33.43	136.67	4.3	−4.2	1.0	0.5	0.9	−0.5
KUM3	33.33	136.36	4.0	−3.9	1.0	0.2	0.2	−0.1
SIOW	33.16	135.57	4.7	−4.4	1.6	0.2	0.2	0.0
MRT1	33.35	134.94	3.4	−3.3	1.0	0.4	0.4	0.9
MRT2	32.87	134.81	3.9	−3.8	1.0	0.2	0.2	−0.1
TOS1	32.82	133.67	5.5	−4.7	2.8	0.6	0.4	−0.4
TOS2	32.43	134.03	4.8	−4.2	2.4	0.5	0.5	−0.4
ASZ1	32.37	133.22	4.5	−4.1	1.9	0.3	0.4	−0.2
ASZ2	31.93	133.58	4.2	−3.9	1.7	0.6	0.4	−0.5
HYG1	32.38	132.42	3.8	−3.1	2.1	0.4	0.3	−0.1
HYG2	31.97	132.49	2.0	−2.0	0.3	0.6	0.7	−0.6

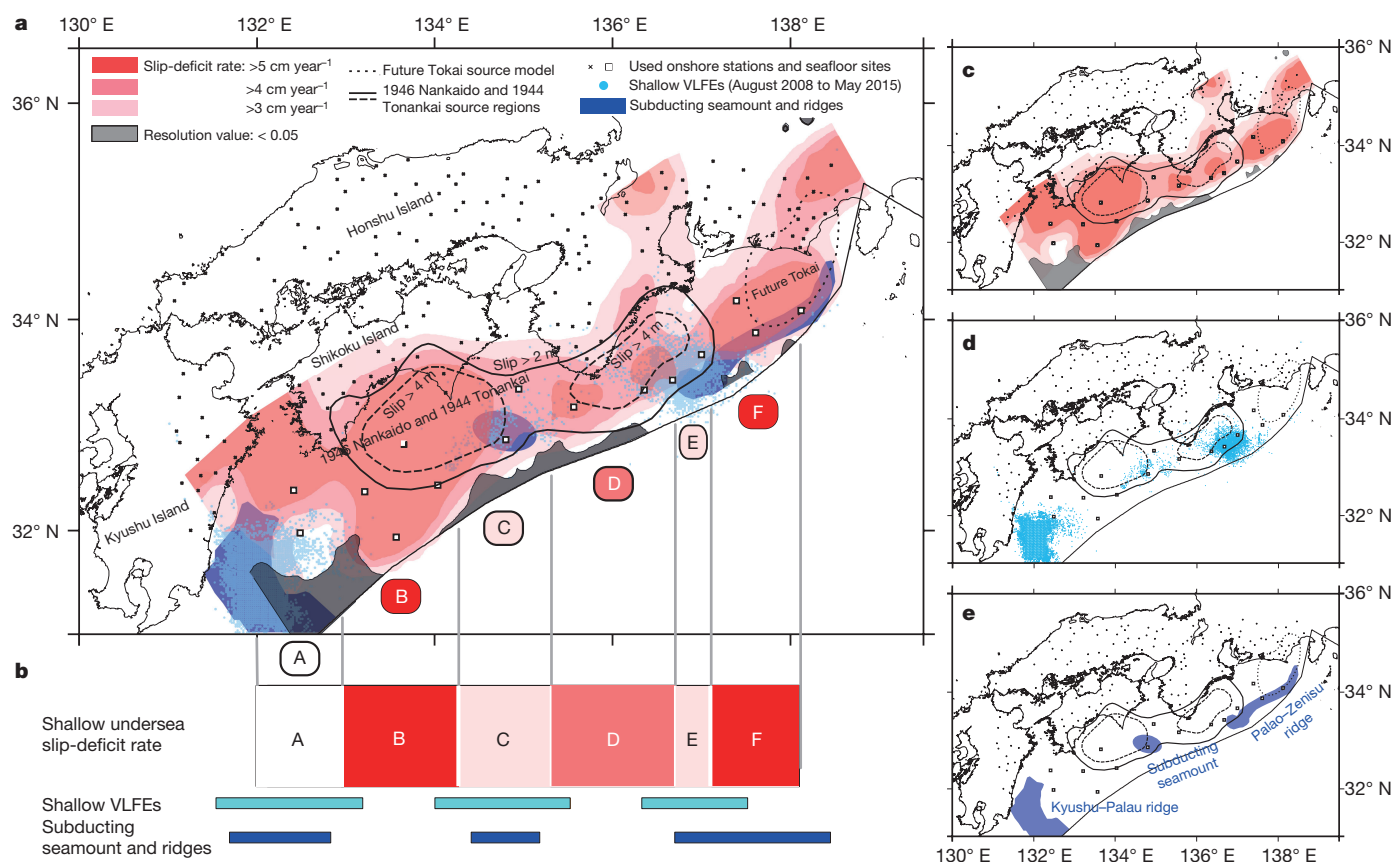


Figure 2 | Interplate SDR distribution as indicated by onshore and seafloor geodetic data. a, Contour map showing the SDR distribution (for SDRs of more than 3 cm year⁻¹) obtained using onshore and seafloor geodetic data. Light blue dots indicate shallow VLFs²⁴; darker blue regions denote subducting seamount and ridges^{21–23}. Dotted lines delimit regions indicated to be sources of future earthquakes by the Tokai model⁵;

solid lines denote the regions of assumed large slip (more than 2 metres) resulting from the 1946 Nankaido and 1944 Tonankai earthquakes². **b**, A schematic illustration of the segmented source regions along the shallow side of the Nankai Trough. Darker pink shading shows regions with high SDRs. **c–e**, Separate figures showing SDR distribution, shallow VLFs and subducting seamounts.

latest event. We detected no conspicuous activity of the VLFs or subducting seamount in this near-trench region. In this high-SDR region, there are patches of ‘overshot’ SDR (where movement has been roughly 6.5 cm year⁻¹, more than the convergence rate), as in past studies^{8,9}. These patches probably result from interseismic viscoelastic effects⁷, or from underestimation of the convergence rate.

The broad area of high SDRs is segmented in the eastern region, C, which is estimated to have a lower SDR than the neighbouring regions, B and D. Additionally, the zones of VLFE activity and subducting seamount in region C are located together, as in region A. This spatial correspondence is additional evidence that the three phenomena (VLFE activity, subducting seamount and SDR) have a physical correlation.

In region D, where the Kii Peninsula protrudes to the south, the obtained SDR distribution corresponds with the source regions for the 1946 Nankaido and 1944 Tonankai earthquakes. The high-SDR region F also corresponds with the Tokai region, in which major earthquakes have occurred and future earthquakes are predicted⁵. However, region F reaches into the southwest, which had no slip in the 1944 Tonankai earthquake and was not indicated as the future Tokai earthquake model⁵. Regions D and F are partitioned by the low-SDR region E.

Below the shallow seafloor, from regions D to F, the Paleo–Zenisu ridge is subducting in the area nearest to the trench axis. However, intensive VLFE activity is located in the middle region, E. Therefore, the VLFE activity correlates with the low SDR of region E rather than with the subduction (although note that the resolving power is insufficient in the shallower south region compared with in our deep, seafloor sites).

Observation studies^{25,26} in subduction zones worldwide suggest a relationship between the low-SDR condition and the subducting areas in front of topographic features, including seamounts. VLFE activity has also been predicted to be related to the low-SDR condition²⁷. For the Nankai Trough, indirect seismological evidence from seafloor studies inferred the physical relationship of the low-SDR condition with ridges and VLFs^{23,28}—a relationship that is probably the result of elevated pore-fluid pressure and a complicated fracture network. Our discovery of the three low-SDR regions A, C and E is direct evidence that subducting seamounts generate VLFE activity, which in turn causes a low SDR. Our findings also suggest that VLFs might be activated in the low-SDR region in front of subducting seamounts worldwide.

Figure 2b illustrates the segmented source regions discovered through our observations. This ‘shallow’ segmentation is inconsistent with the well known ‘deep’ segmentation² of the Nankai Trough source region. Because the shallow, high-SDR patches control the scale of tsunamis that result from megathrust ruptures, they are important for assessment and early warning. For example, the Tohoku-oki earthquake had a large amount of very shallow slip²⁹, which led to a devastating tsunami. The high-SDR regions B and F are located on the outer shallow zones of the most recent and predicted earthquake sources; there have been no historical records of earthquakes in regions B and F since 1854 (ref. 2). Thus these shallow regions have accumulated slip deficit since at least this time and could drive shallow ruptures and tsunamis.

Low SDRs are suggested for regions A, C and E, which segment and separate the high-SDR (megathrust earthquake source) regions, thereby possibly regulating earthquake dynamics. For example, the 1944

Tonankai earthquake began in region D and was halted in region E, in front of region F^{1,3,4}. However, when a rupture breaks through a segment boundary, a larger event is possible. The 1946 Nankaido earthquake progressed from region D through region C, finally reaching the deep side of region B^{1,3,4}.

Our observations and our model for SDR distribution reflect crustal deformation in the past few years only. We plan to perform continuous observations over decades to investigate the stability of interplate SDR distributions. We can also determine whether decadal-scale changes in crustal deformation—like those observed in eastern Japan²⁹—occur in this subduction zone.

Online Content Methods, along with any additional Extended Data display items and Source Data, are available in the online version of the paper; references unique to these sections appear only in the online paper.

Received 4 November 2015; accepted 25 February 2016.

Published online 23 May 2016.

- Kanamori, H. Tectonic implications of the 1944 Tonankai and the 1946 Nankaido earthquakes, Japan. *Phys. Earth Planet. Inter.* **5**, 129–139 (1972).
- Ando, M. Source mechanism and tectonic significance of historical earthquakes along the Nankai Trough, Japan. *Tectonophysics* **27**, 119–140 (1975).
- Sagiya, T. & Thatcher, W. Coseismic slip resolution along a plate boundary megathrust: the Nankai Trough, southwest Japan. *J. Geophys. Res.* **104** (B1), 1111–1129 (1999).
- Baba, T. & Cummins, P. R. Contiguous rupture areas of two Nankai Trough earthquakes revealed by high-resolution tsunami waveform inversion. *Geophys. Res. Lett.* **32**, L08305 (2005).
- Central Disaster Management Council of the Japanese Government. <http://www.bousai.go.jp/jishin/nankai/index.html> (in Japanese; accessed 27 April 2015).
- Moreno, M., Rosenau, M. & Oncken, O. 2010 Maule earthquake slip correlates with pre-seismic locking of Andean subduction zone. *Nature* **467**, 198–202 (2010).
- Wang, K., Hu, Y. & He, J. Deformation cycles of subduction earthquakes in a viscoelastic Earth. *Nature* **484**, 327–332 (2012).
- Ito, T. & Hashimoto, M. Spatiotemporal distribution of interplate coupling in southwest Japan from inversion of geodetic data. *J. Geophys. Res.* **109**, B02315 (2004).
- Hok, S., Fukuyama, E. & Hashimoto, C. Dynamic rupture scenarios of anticipated Nankai-Tonankai earthquakes, southwest Japan. *J. Geophys. Res.* **116**, B12319 (2011).
- Yoshioka, S. & Matsuoka, Y. Interplate coupling along the Nankai Trough, southwest Japan, inferred from inversion analyses of GPS data: effects of subducting plate geometry and spacing of hypothetical ocean-bottom GPS stations. *Tectonophysics* **600**, 165–174 (2013).
- Asada, A. & Yabuki, T. Centimeter-level positioning on the seafloor. *Proc. Jpn Acad. B* **77**, 7–12 (2001).
- Tadokoro, K. *et al.* Interseismic seafloor crustal deformation immediately above the source region of anticipated megathrust earthquake along the Nankai Trough, Japan. *Geophys. Res. Lett.* **39**, L10306 (2012).
- Spiess, F. N. *et al.* Precise GPS/acoustic positioning of seafloor reference points for tectonic studies. *Phys. Earth Planet. Inter.* **108**, 101–112 (1998).
- Gagnon, K., Chadwell, C. D. & Norabuena, E. Measuring the onset of locking in the Peru-Chile trench with GPS and acoustic measurements. *Nature* **434**, 205–208 (2005).
- Yokota, Y. *et al.* Heterogeneous interplate coupling along the Nankai Trough, Japan, detected by GPS-acoustic seafloor geodetic observation. *Prog. Earth Planet. Sci.* **2**, 10 (2015).
- Altamimi, Z., Collilieux, X., Legrand, J., Garayt, B. & Boucher, C. ITRF2005: a new release of the International Terrestrial Reference Frame based on time series of station positions and Earth Orientation Parameters. *Geophys. J. Int.* **112**, B09401 (2007).
- DeMets, C., Gordon, R. G. & Argus, D. F. Geologically current plate motions. *Geophys. J. Int.* **181**, 1–80 (2010).
- Iinuma, T. *et al.* Coseismic slip distribution of the 2011 off the Pacific Coast of Tohoku Earthquake (M9.0) refined by means of seafloor geodetic data. *J. Geophys. Res.* **117**, B07409 (2012).
- Sun, T. & Wang, K. Viscoelastic relaxation following subduction earthquakes and its effects on afterslip determination. *J. Geophys. Res.* **120**, 1329–1344 (2015).
- Yabuki, T. & Matsu'ura, M. Geodetic data inversion using a Bayesian information criterion for spatial distribution of fault slip. *Geophys. J. Int.* **109**, 363–375 (1992).
- Kodaira, S., Takahashi, N., Nakanishi, A., Miura, S. & Kaneda, Y. Subducted seamount imaged in the rupture zone of the 1946 Nankaido earthquake. *Science* **289**, 104–106 (2000).
- Park, J.-O., Moore, G. F., Tsuru, T., Kodaira, S. & Kaneda, Y. A subducted oceanic ridge influencing the Nankai megathrust earthquake rupture. *Earth Planet. Sci. Lett.* **217**, 77–84 (2004).
- Yamamoto, Y. *et al.* Imaging of the subducted Kyushu-Palau Ridge in the Hyuga-nada region, western Nankai Trough subduction zone. *Tectonophysics* **589**, 90–102 (2013).
- National Research Institute for Earth Science and Disaster Prevention. Activity of very-low-frequency earthquakes in and around Japan (November, 2014–May, 2015). *Report of the Coordinating Committee for Earthquake Prediction, Japan* (in Japanese) **94**, 5–7 (2015).
- Chlieh, M., Avouac, J. P., Sieh, K., Natawidjaja, D. H. & Galetzka, J. Heterogeneous coupling of the Sumatran megathrust constrained by geodetic and paleogeodetic measurements. *J. Geophys. Res.* **113**, B05305 (2008).
- Perfettini, H. *et al.* Seismic and aseismic slip on the Central Peru megathrust. *Nature* **465**, 78–81 (2010).
- Hirose, H. *et al.* Slow earthquakes linked along dip in the Nankai subduction zone. *Science* **330**, 1502 (2010).
- Yamashita, Y. *et al.* Migrating tremor off southern Kyushu as evidence for slow slip of a shallow subduction interface. *Science* **348**, 676–679 (2015).
- Ozawa, S. *et al.* Preceding, coseismic, and postseismic slips of the 2011 Tohoku earthquake, Japan. *J. Geophys. Res.* **117**, B07404 (2012).
- Colombo, O. L. in *GPS for Geodesy*, 2nd edn (eds Kleusberg, A. & Teunissen, P.) 537–567 (Springer, 1998).

Supplementary Information is available in the online version of the paper.

Acknowledgements We thank R. Burgmann and J.-P. Avouac for reviews of, and comments on, the manuscript. We thank O.L. Colombo of the NASA Goddard Space Flight Center for the kinematic GPS software IT (Interferometric Translocation)³⁰, and the Geospatial Information Authority of Japan (GSI) for high-rate GPS data for kinematic GPS analysis, and for daily coordinates of the sites on the GSI website. T. Iinuma and T. Sun calculated the coseismic and postseismic deformations, respectively, of the 2011 Tohoku-oki earthquake. Comments from K. Wang and A. Kato improved our manuscript. We thank T. Yabuki of the JHOD for the Bayesian inversion software. Additionally, many among the staff of the JHOD—including the crew of the vessels *Shoyo*, *Takuyo*, *Meiyo* and *Kaiyo*—have supported our observations and data processing. Some figures were produced using GMT software, developed by P. Wessel and W. H. F. Smith.

Author Contributions Y.Y. carried out the inversion analysis. T.I. designed the study and performed the statistical processing. Y.Y. and S.W. performed the resolution tests. Y.Y., T.I., S.W. and T.T. processed the GPS-A seafloor geodetic data. A.A. constructed the GPS-A system.

Author Information Reprints and permissions information is available at www.nature.com/reprints. The authors declare no competing financial interests. Readers are welcome to comment on the online version of the paper. Correspondence and requests for materials should be addressed to Y.Y. (eisel@jodc.go.jp).

METHODS

Seafloor geodetic observations. Because radio waves scatter in seawater, we instead measure seafloor movements using GPS observations above the sea and acoustic ranging under the sea. This is the GPS-A method, which is a unique approach to monitoring an absolute horizontal movement directly above an off-shore interplate boundary. The technique was proposed in the 1980s (ref. 31) and established in the 1990s and later^{11,13,14}. However, the precision of observation in these previous studies was lower than in our method, so they achieved a low-precision observation result and needed an uneconomically long observation period. Since 2000, the JHOD has been developing highly precise and sustainable observation techniques and has provided valuable data for geodesy and seismology—such as data on the preseismic, coseismic and postseismic seafloor deformations of the 2011 Tohoku-oki earthquake^{32–34}.

Extended Data Fig. 1 shows our seafloor geodetic observation system^{11,35–37}. It consists of a seafloor unit with four acoustic mirror-type transponders, and an on-board unit with an undersea on-board acoustic transducer, a GPS antenna/receiver and a dynamic motion sensor. Before 2007, the on-board acoustic transducers were mounted at the stern of survey vessels for a drifting survey. After 2008, we provided a hull-mounted system to perform a line-controlled sailing survey³⁷ for stability and efficiency.

This system acquires three kinds of data. Kinematic GPS data are gathered to determine the absolute position of the survey vessel. Attitude data on the survey vessel are also obtained on board by a dynamic motion sensor, to determine the coordinates of the on-board transducer relative to those of the GPS antenna. Distance data from the on-board transducer to the seafloor acoustic transponders are measured by the acoustic ranging technique. The obtained round-trip acoustic travel times are transformed to the ranges using profiles of sound speed in seawater. These profiles are obtained using temperature and salinity profilers—namely a conductivity temperature depth profiler (CTD), an expendable conductivity temperature depth profiler (XCTD) and expendable bathythermographs (XBTs)—every few hours.

The consecutive absolute positions of the on-board transducer were determined by kinematic GPS analysis using IT software³⁰ and attitude data on the survey vessel. The position references are the onshore GEONET stations conducted by the Geospatial Information Authority of Japan (GSI)³⁸. The resulting position of the seafloor transducer was determined using a linearized inversion method based on a least-squares formulation, combining the absolute on-board transducer positions and the ranges to the seafloor acoustic transponders. This final analysis was constrained by the positional relationship of the grouped transponders for all epochs³⁶. This analysis cannot provide substantive information on the positioning error of each epoch, because we combine the independent observations to estimate all the positions.

To stabilize the estimates, we acquire acoustic ranging data of 3,000–5,000 shots for one observation at each site, each observation taking about 24 hours. The observation uncertainty of this technique is up to just 2–3 cm in the horizontal component in each epoch. However, the vertical component has much uncertainty, because we observe the seafloor only from the upper region (much as the GNSS does). The detection limit of the vertical velocity is 3–4 cm year^{−1}.

Data processing. Raw seafloor geodetic observation data—relating to the Amur Plate in the MORVEL data set¹⁷—are shown as red circles before the Tohoku-oki earthquake and blue circles after this earthquake in Extended Data Figs 2–4. We deducted coseismic and nonlinear postseismic effects resulting from the Tohoku-oki earthquake from these raw data. We calculated the coseismic effects on the basis of the coseismic source model¹⁸, which was established using many onshore stations of the GNSS network (namely GEONET, Tohoku University, and others), seafloor geodetic data^{33,39}, and data obtained from ocean-bottom pressure gauges installed by the Earthquake Research Institute, University of Tokyo. We calculated the postseismic effects on the basis of the deformation model¹⁹, established using this coseismic slip model and coordinated to match the GSI's onshore data and seafloor data (observed by Tohoku University and us³⁴) following the Tohoku-oki earthquake by means of the three-dimensional spherical-Earth finite-element model. The prototype of this viscoelastic model was established⁴⁰ by including not only the mantle wedge and the oceanic mantle but also the lithosphere–asthenosphere boundary, and is based on the afterslip model developed in ref. 29. The model¹⁹ used for the calculation of postseismic effects has been revised with regard to shallow afterslip. These coseismic and postseismic effects are shown in Extended Data Figs 2–4. These effects are large in eastern sites, near the source region of the Tohoku-oki earthquake, and very small in western sites. The deducted data are shown as red circles in Extended Data Figs 2–4; these final data and the raw data are in Supplementary Table 1.

For estimations of site velocities, we used a robust regression method (*M* estimation method) with Turkey's biweight function. This method mitigates the negative

influences of outliers, which are mainly due to disturbances of an undersea sound speed structure.

Interplate SDR inversion method. We constructed the SDR distribution model by means of a geodetic inversion using the method of ref. 20. This method includes two prior-constraint constants (α and σ). We determined the best estimates of these 'hyperparameters' by minimizing the Akaike Bayesian information criterion (ABIC)⁴¹ and obtained an optimal model. The SDR distribution model was coordinated to match our seafloor geodetic data and onshore GNSS data.

We set a fault model with approximately 800 km in the strike direction of 237°, and approximately 300 km in the dip direction on the plate boundary. Our fault model was deployed simply on the interplate boundary model known as the CAMP standard model⁴². We used a B-spline function as a basis function and calculated the SDR values by distributing subfaults on the plate boundary. We calculated Green's functions using the formulation of ref. 20, considering a homogeneous elastic half-space. We deployed this broader model around our seafloor sites. Thus, we also used the onshore GNSS data of GEONET around our fault model. These onshore data were calculated for the stable period from March 2006 to December 2009. In order to avoid biases in the inversion and keep the resolution of the SDR model smooth, we subsampled the GEONET stations. Weight functions were set equally in all onshore and offshore stations. Model boundary conditions are detailed below in the section 'Model boundary condition effect'.

The northern edge of our model would be affected by block motions, because the block boundaries around western Japan are located near the northern boundary of our model region. However, a detailed investigation of block motions⁴³ showed that the maximum deformation rate of the block boundary (the median tectonic line) does not greatly affect the undersea SDR distribution (the distribution is shifted by less than 8 mm year^{−1} in the northernmost region of Shikoku Island and by 3 mm year^{−1} in the eastern region). Intraplate deformation has a negligible effect in this SDR model calculation. Although splay faults^{22,44,45} also have implications for the generation of megathrust earthquakes and tsunamis, these smaller-scale fault geometries cannot be monitored and discussed by our present seafloor geodetic observation network.

Our SDR distribution model is shown in Fig. 2 and Extended Data Fig. 5b. Hyperparameter values for the prior constants (α and σ) were 1.6×10^{-1} and 1.3×10^{-1} . Our data improve the previous model, which used only onshore data (Extended Data Fig. 5a). The calculated SDR values for subfaults, and a comparison between observed and calculated data, are described in Supplementary Tables 2 and 3, respectively.

Resolution of the SDR inversion. We carried out checkerboard resolution tests in order to examine the SDR model. We generated synthetic data for the checkerboard-like SDR distributions (Extended Data Fig. 6a) with 2σ errors of 0.3 cm year^{−1} and 1.5 cm year^{−1} for onshore and seafloor data, respectively. The synthetic data were inverted using the same parameters and settings as for the SDR inversion. Extended Data Fig. 6 shows the resulting distributions, using only onshore data (Extended Data Fig. 6b) or both onshore and seafloor data (Extended Data Fig. 6c). An unsolved offshore region in Extended Data Fig. 6b was solved clearly in Extended Data Fig. 6c.

Extended Data Fig. 6 also shows resolution values as diagonal elements of the resolution matrix, calculated for onshore data only (Extended Data Fig. 6d) or for both onshore and seafloor data (Extended Data Fig. 6e). The resolution matrix is represented as $R = (H^T H + \alpha^2 G^T G)^{-1} H^T H$ where H is the static-response-function matrix; α is the hyperparameter of smoothness²⁰; G is the spatial smoothness matrix²⁰; and the superscript T denotes the transposed matrix.

Undersea areas with low values, shown in Extended Data Fig. 6d, were improved by the seafloor data (Extended Data Fig. 6e), although the region adjacent to the trench axis cannot be resolved even with our seafloor network because there is no site (other than those near the TOK1 and ASZ2 sites).

We also set Green's functions to zero for outer subfaults of the interplate boundary (on the south of the trench). These subfaults affect neighbour low-resolution subfaults through spatial smoothing. Thus, the resolving power for the shallowest subfaults to the south of our seafloor sites was not sufficient (Extended Data Fig. 6c).

Model boundary condition effect. We examined the boundary condition of this inversion model. Each test was calculated using the best hyperparameters, determined by minimizing the ABIC.

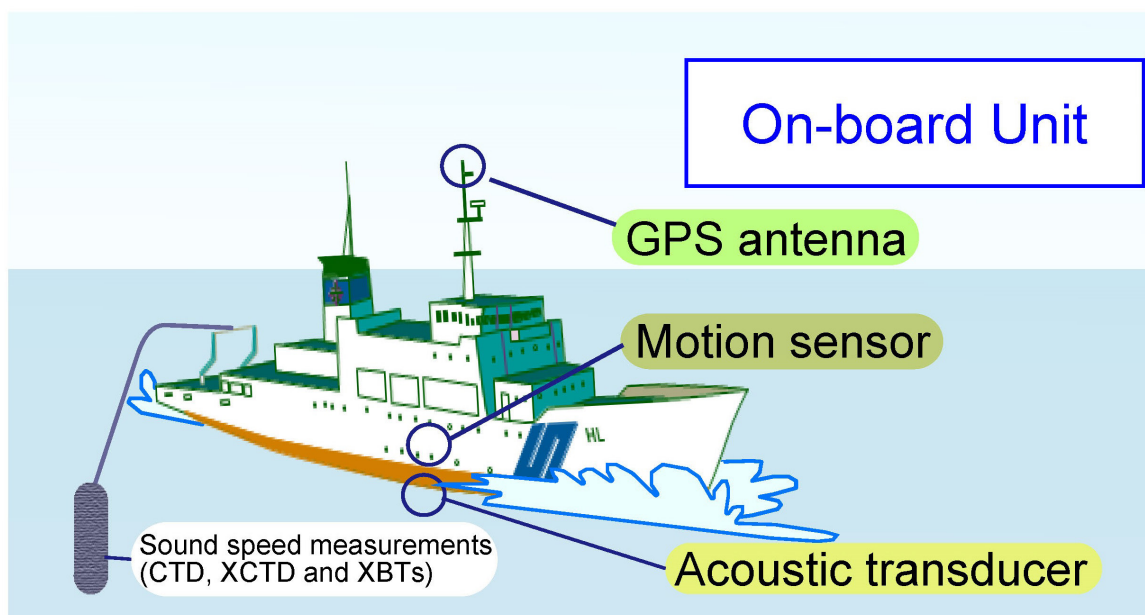
In the resulting SDR model, we used a 'zero backslip (full creeping)' condition at the trench side boundary, and a free condition at the other boundaries. We also used the free condition at all the boundaries; zero backslip at all the boundaries; or a 6.5 cm year^{−1} constraint at the south edge (the other boundaries being in the free condition), in order to examine the model boundary condition effect (Extended Data Figs 7a–c). The results suggest that the boundary condition did not control the main part of the undersea SDR calculation, except in low-resolution shallow

areas. There were small differences in the r.m.s. of misfits between observations and calculations in these cases.

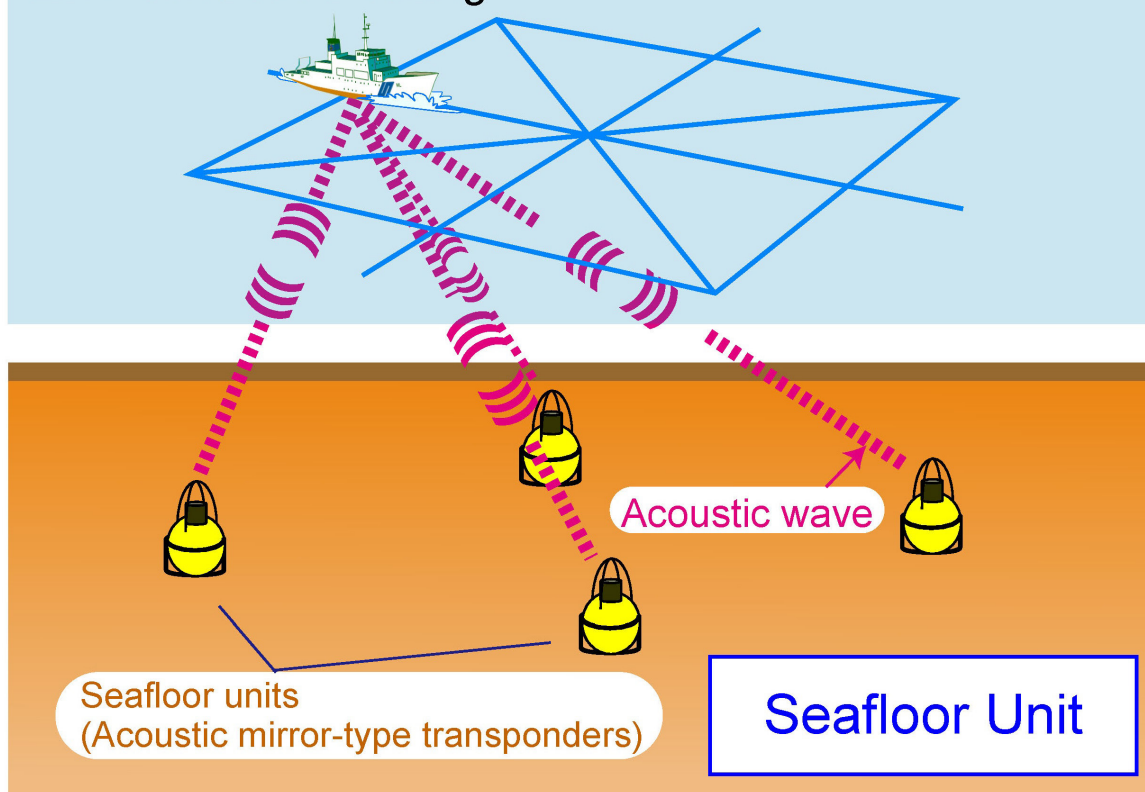
VLFE distribution. The VLFE distribution in Fig. 2a, d was determined by automatic analysis²⁴ using the method of ref. 46. This approach separates VLFs and ordinary earthquakes automatically by comparing them with the Hi-net catalogue produced by the National Research Institute for Earth Science and Disaster Resilience. (Aftershocks following the magnitude-7 event could not be fully differentiated.) We plotted the unordinary events (mainly VLFs) from the period 1 August 2008 to 10 May 2015 without including the aftershocks resulting from the Kii Peninsula earthquake of 2004. We also plotted all the events detected in the period 1 June 2003 to 10 May 2015 (Extended Data Fig. 8).

Subducting seamounts. The previous reflection and refraction surveys^{21–23} were carried out broadly along the Nankai Trough, guided by past geomagnetic studies and by known seismic and bathymetric information. These surveys detected three subducting seamounts (Fig. 2a, e) in front of the visible bathymetric features (the Kyushu–Palau ridge, the Kinan seamount chain and the Zenisu ridge) shown in Fig. 1. The VLFs were activated around these regions.

31. Spiess, F. N. Suboceanic geodetic measurements. *IEEE Trans. Geosci. Remote Sensing* **GE-23**, 502–510 (1985).
32. Sato, M. *et al.* Interplate coupling off northeastern Japan before the 2011 Tohoku-oki earthquake, inferred from seafloor geodetic data. *J. Geophys. Res.* **118**, 1–10 (2013).
33. Sato, M. *et al.* Displacement above the hypocenter of the 2011 Tohoku-oki earthquake. *Science* **332**, 1395 (2011).
34. Watanabe, S. *et al.* Evidence of viscoelastic deformation following the 2011 Tohoku-oki earthquake revealed from seafloor geodetic observation. *Geophys. Res. Lett.* **41**, 5789–5796 (2014).
35. Fujita, M. *et al.* GPS/acoustic seafloor geodetic observation: method of data analysis and its application. *Earth Planets Space* **58**, 265–275 (2006).
36. Matsumoto, Y., Fujita, M. & Ishikawa, T. Development of multi-epoch method for determining seafloor station position. *Rep. Hydrograph. Oceanograph. Res.* **26**, 16–22 (2008; in Japanese).
37. Sato, M. *et al.* Improvement of GPS/acoustic seafloor positioning precision through controlling the ship's track line. *J. Geodesy* **87**, 825–842 (2013).
38. Sagiya, T., Miyazaki, S. & Tada, T. Continuous GPS array and present-day crustal deformation of Japan. *Pure Appl. Geophys.* **157**, 2303–2322 (2000).
39. Kido, M., Osada, Y., Fujimoto, H., Hino, R. & Ito, Y. Trench-normal variation in observed seafloor displacements associated with the 2011 Tohoku-Oki earthquake. *Geophys. Res. Lett.* **38**, L24303 (2011).
40. Sun, T. *et al.* Prevalence of viscoelastic relaxation after the 2011 Tohoku-oki earthquake. *Nature* **514**, 84–87 (2014).
41. Akaike, H. in *Bayesian Statistics* (eds Bernardo, J. M., DeGroot, M. H., Lindley, D. V. & Smith, A. F. M.) 143–166 (Valencia Univ. Press, 1980).
42. Hashimoto, C., Fukui, K. & Matsu'ura, M. 3-D modelling of plate interfaces and numerical simulation of long-term crustal deformation in and around Japan. *Pure Appl. Geophys.* **161**, 2053–2068 (2004).
43. Loveless, J. P. & Meade, B. J. Geodetic imaging of plate motions, slip rates, and partitioning of deformation in Japan. *J. Geophys. Res.* **115**, B02410 (2010).
44. Park, J.-O., Tsuru, T., Kodaira, S., Cummins, P. R. & Kaneda, Y. Splay fault branching along the Nankai subduction zone. *Science* **297**, 1157–1160 (2002).
45. Moore, G. *et al.* Three-dimensional splay fault geometry and implications for Tsunami generation. *Science* **318**, 1128–1131 (2007).
46. Asano, Y., Obara, K. & Ito, Y. Spatiotemporal distribution of very-low frequency earthquakes in Tokachi-oki near the junction of the Kuril and Japan trenches revealed by using array signal processing. *Earth Planets Space* **60**, 871–875 (2008).



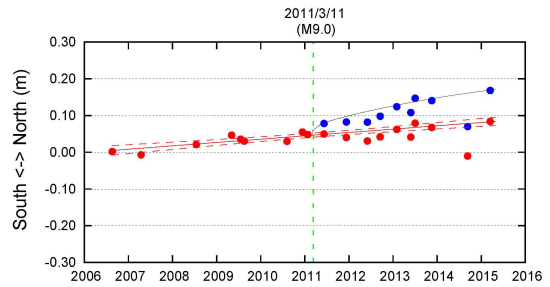
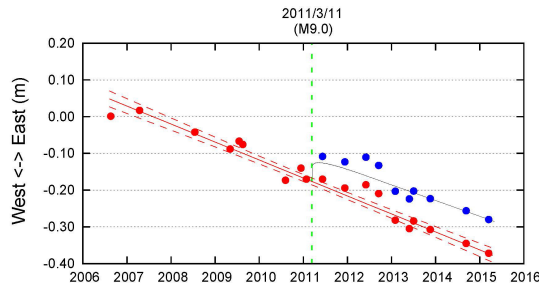
Line-controlled sailing



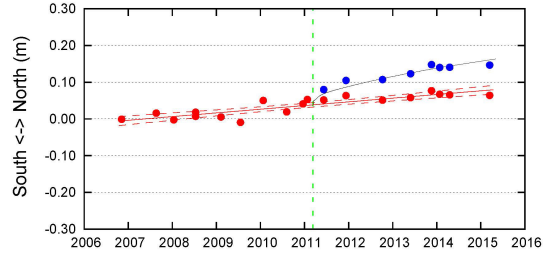
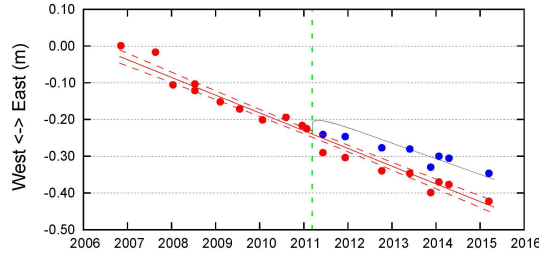
Extended Data Figure 1 | Our GPS-A seafloor geodetic observation system. The system, comprising on-board and seafloor sensors, was developed as described in ref. 11 and improved as described in ref. 35.

This diagram was modified from refs 15, 34, 37. CTD, conductivity temperature depth profiler; XCTD, expendable conductivity temperature depth profiler; XBT, expendable bathythermographs.

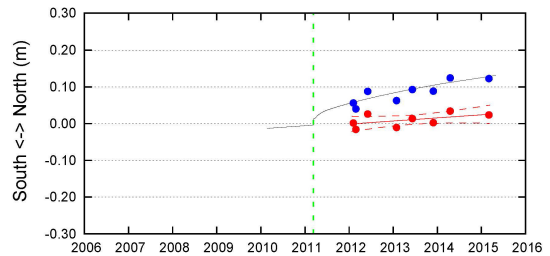
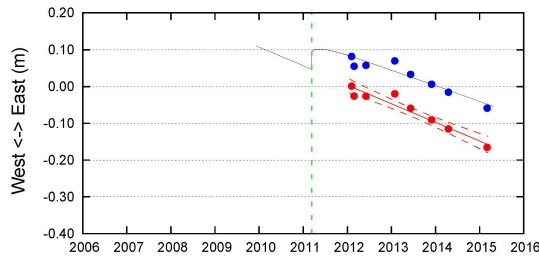
(1) TOK1



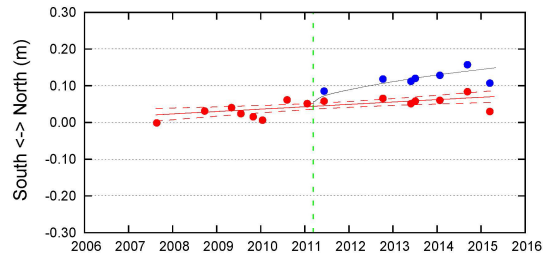
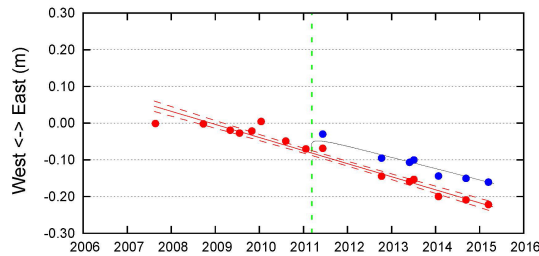
(2) TOK2



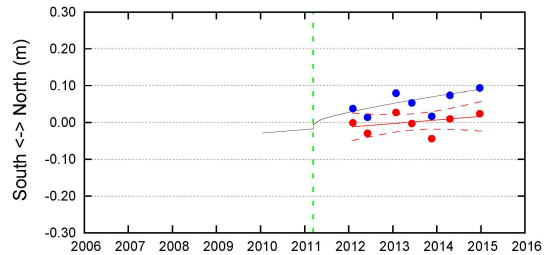
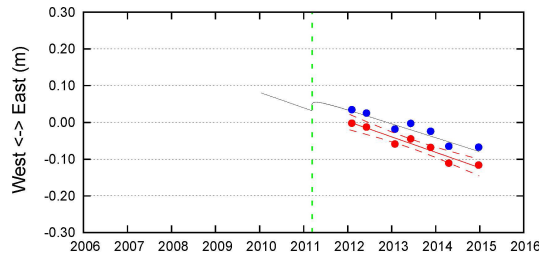
(3) TOK3



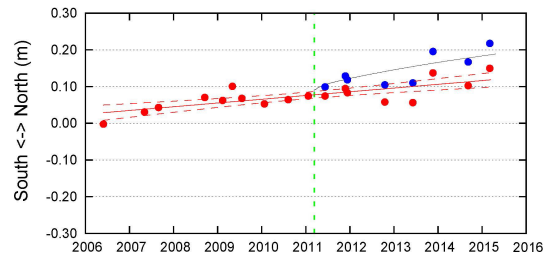
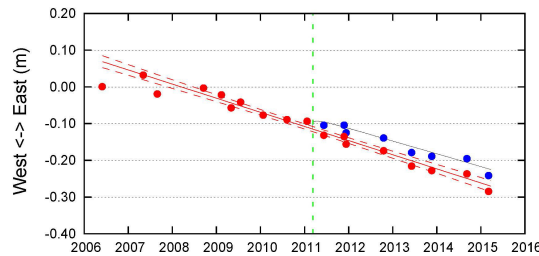
(4) KUM1



(5) KUM2



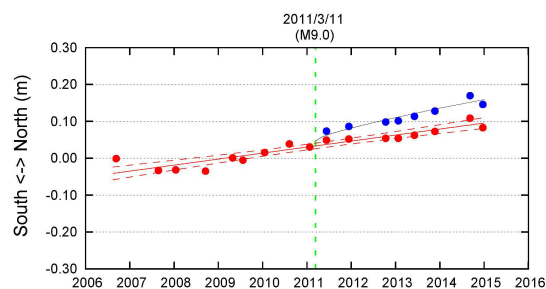
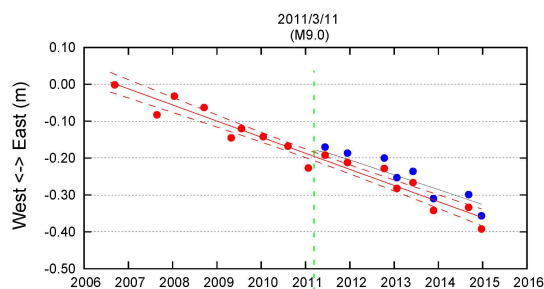
(6) KUM3



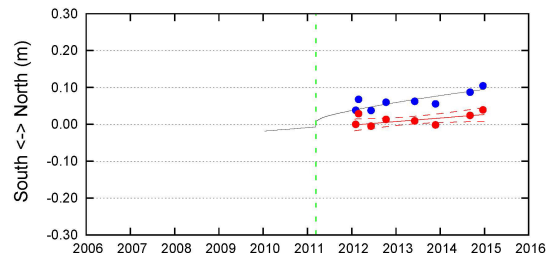
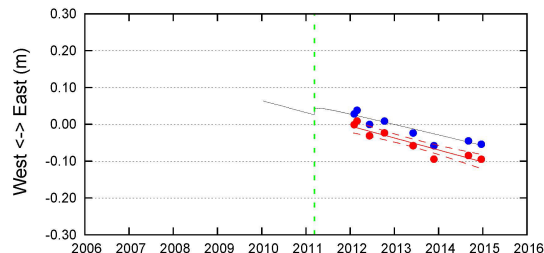
Extended Data Figure 2 | Horizontal movements of seafloor sites over time. Time series for east–west (left column) and north–south (right column) displacements of seafloor sites TOK1, TOK2, TOK3, KUM1, KUM2 and KUM3 from 2006 onwards. The position reference is the Amur plate. Blue circles indicate raw observations before deductions of the coseismic and postseismic effects that resulted from

the magnitude-9.0 Tohoku-oki earthquake of 11 March 2011. Red circles indicate the corrected final results. The linear trends and the 95% two-sided confidence intervals are shown with red solid and dashed lines, respectively. Grey lines show the calculated coseismic and postseismic deformations following the Tohoku-oki earthquake^{18,19}.

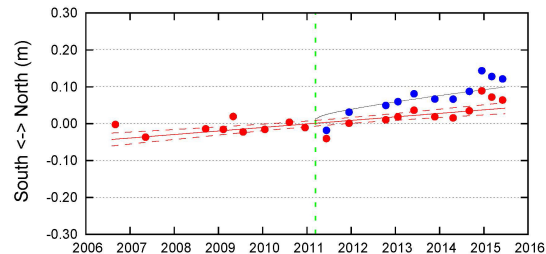
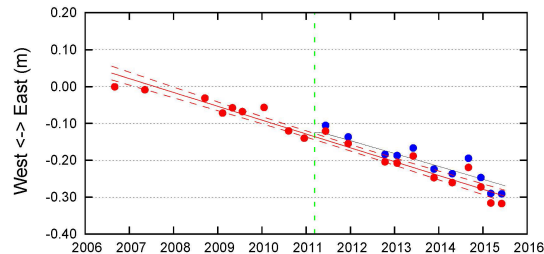
(7) SLOW



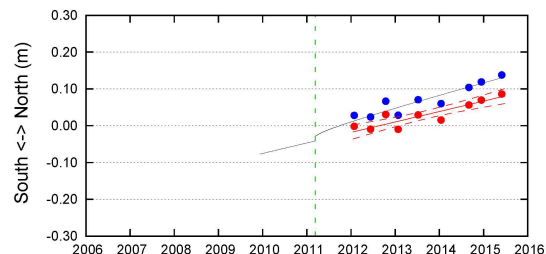
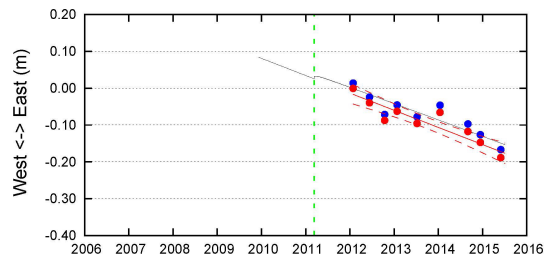
(8) MRT1



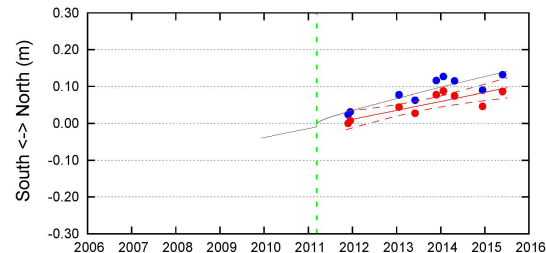
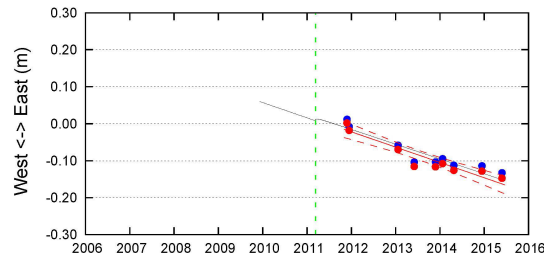
(9) MRT2



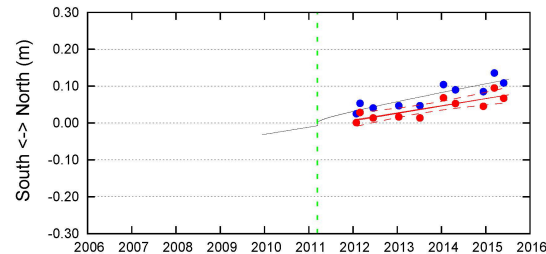
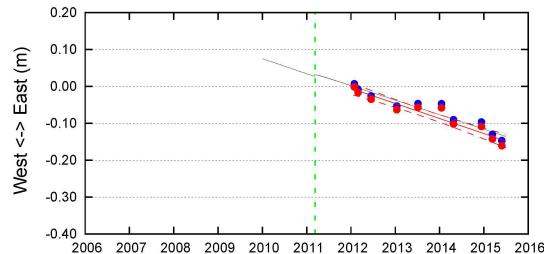
(10) TOS1



(11) TOS2

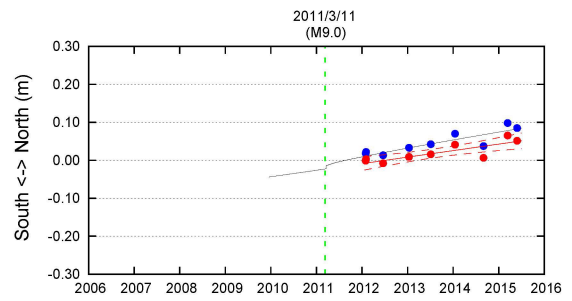
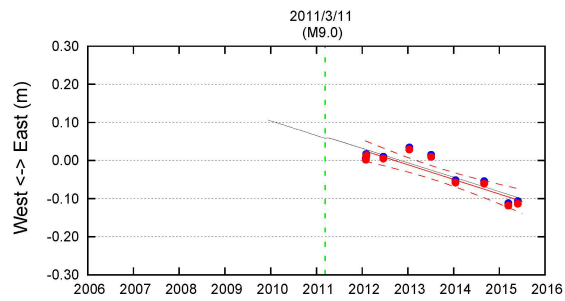


(12) ASZ1

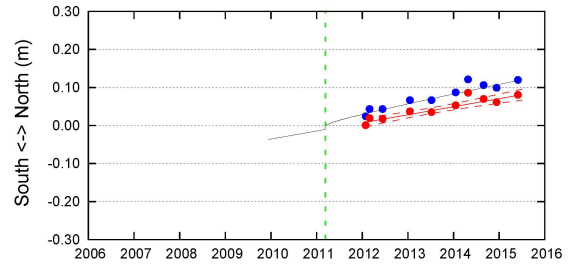
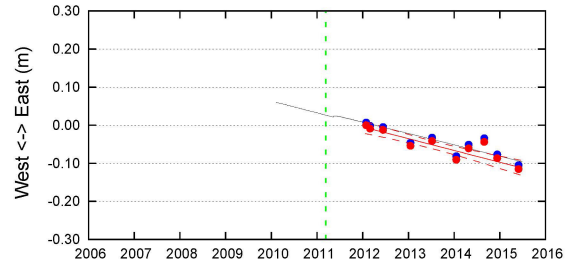


Extended Data Figure 3 | Horizontal movements of seafloor sites over time. Time series showing east–west (left column) and north–south (right column) displacements of seafloor sites SLOW, MRT1, MRT2, TOS1, TOS2 and ASZ1. Colours are as in Extended Data Fig. 2.

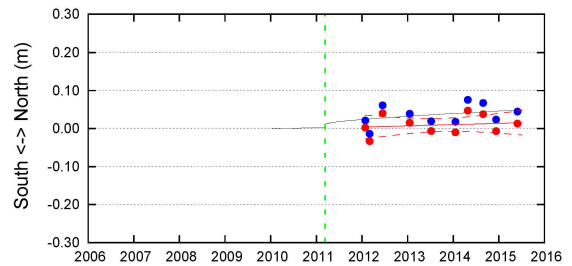
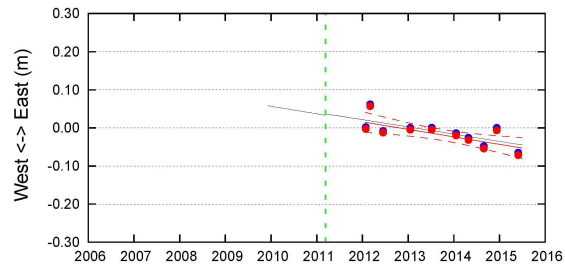
(13) ASZ2



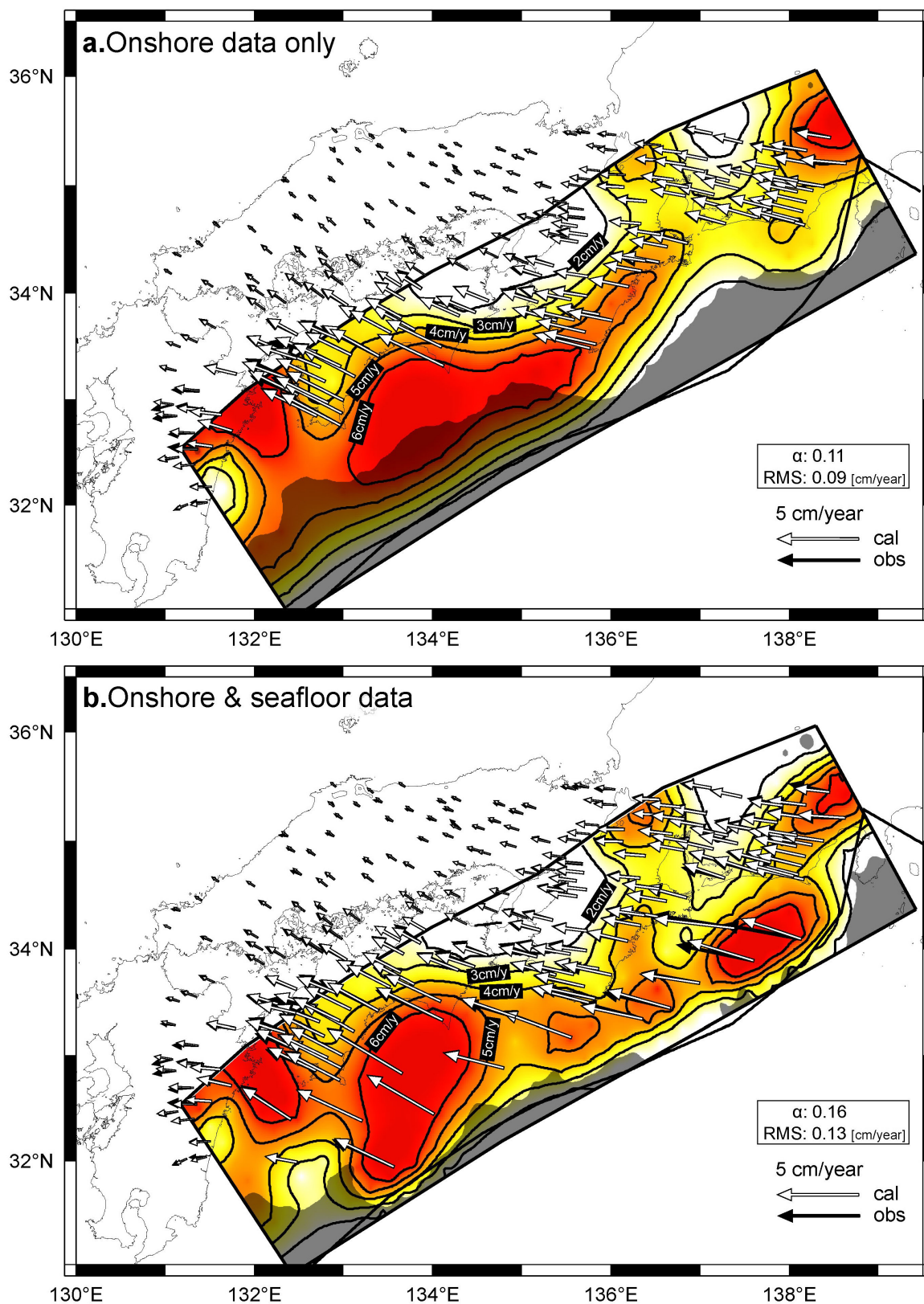
(14) HYG1



(15) HYG2



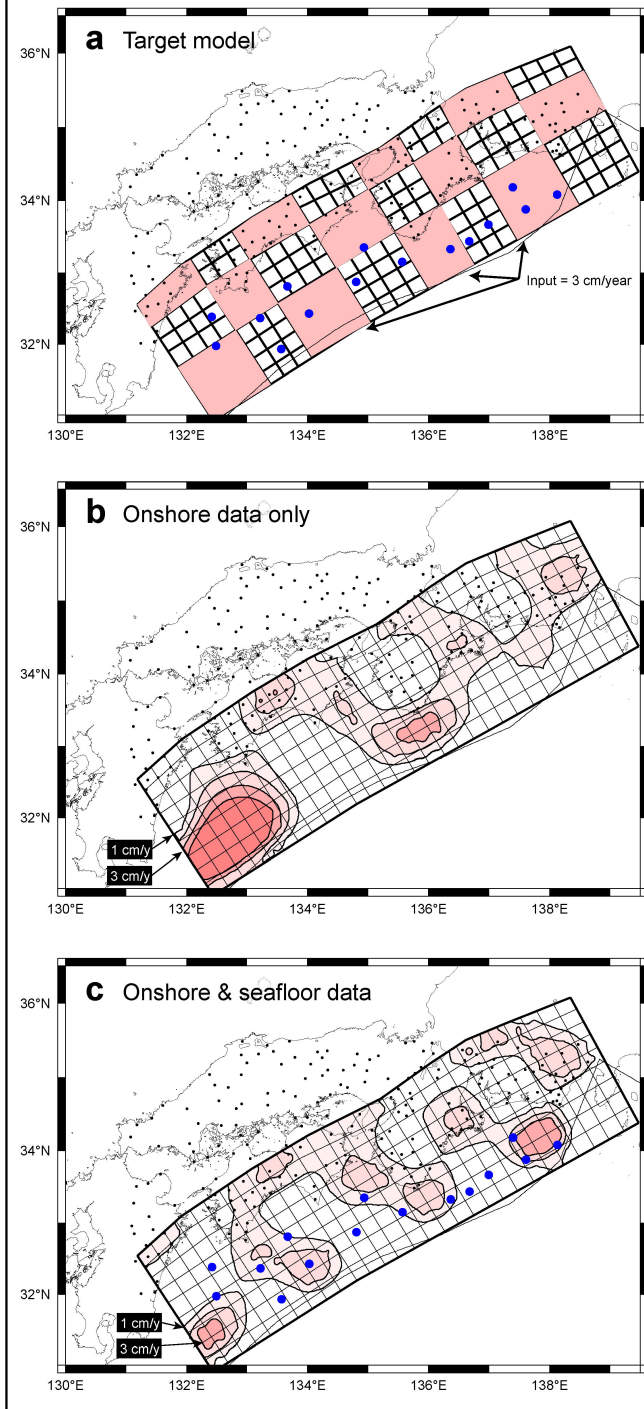
Extended Data Figure 4 | Horizontal movements of seafloor sites over time. Time series showing east–west (left column) and north–south (right column) displacements of seafloor sites ASZ2, HYG1 and HYG2. Colours are as in Extended Data Fig. 2.



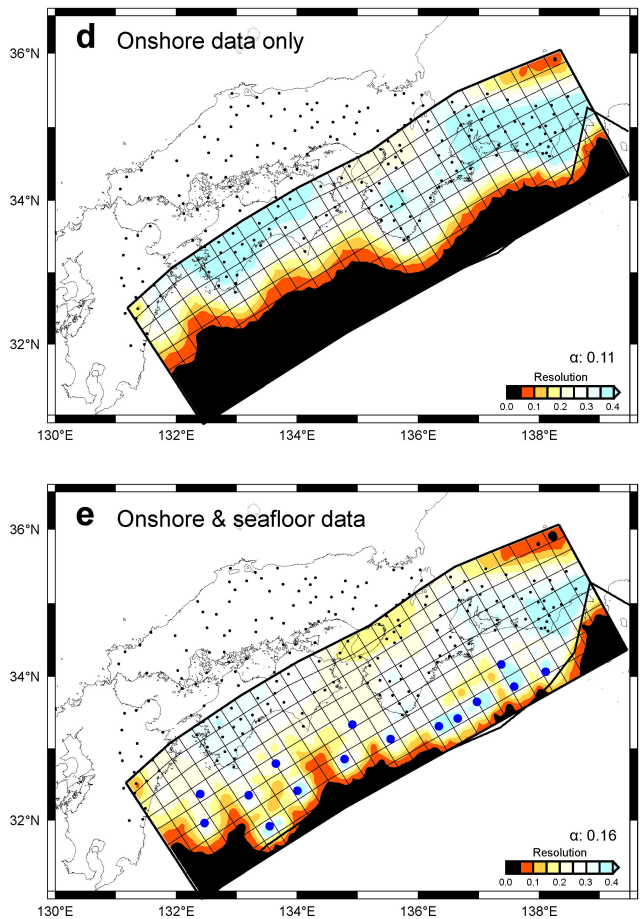
Extended Data Figure 5 | Comparison of calculated SDR distributions obtained using onshore data only versus onshore plus seafloor data.
a, b, SDR distributions (for SDRs of more than 2 cm year⁻¹) calculated using only onshore data (a) or using onshore and seafloor data (b).

Black and white vectors indicate the observed data and the calculated velocities, respectively. Grey shading indicates areas with resolution values lower than 0.05 (calculated in Extended Data Fig. 6d, e). α is the hyperparameter of smoothness.

Checkerboard resolution test

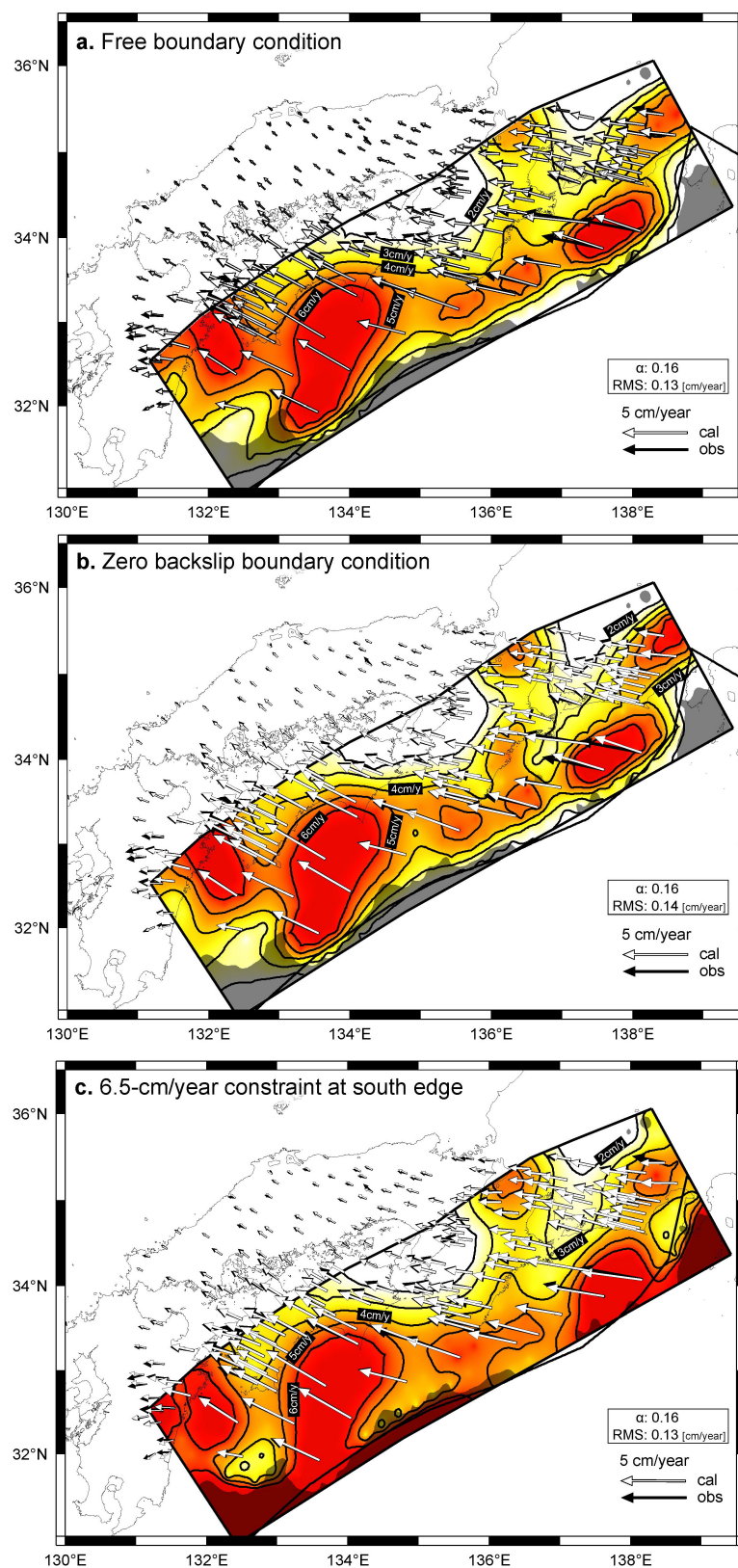


Resolution value



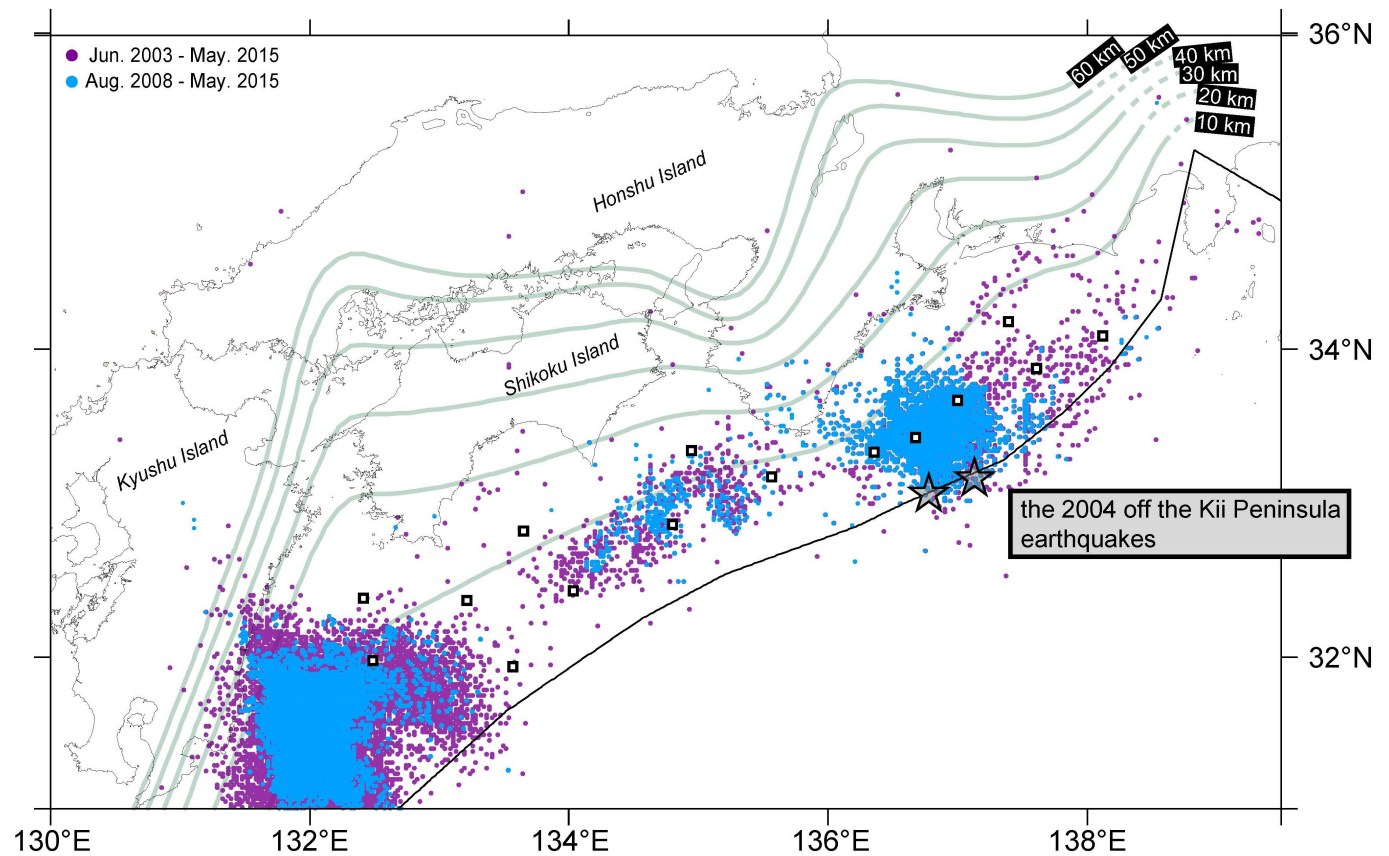
Extended Data Figure 6 | Checkerboard resolution tests and distributions of resolution values. a–c, Results of checkerboard resolution tests for the SDR inversions. a, Input checkerboard-like SDR distribution. b, c, The checkerboard distributions calculated from using onshore data only (b) or using both onshore and seafloor data (c).

d, e, Resolution values as diagonal elements of the resolution matrix, calculated using onshore data only (d) or using onshore and seafloor data (e). Black and blue dots denote the onshore and seafloor sites, respectively, used in each calculation. α is the hyperparameter of smoothness.



Extended Data Figure 7 | Examination of boundary condition effects. **a–c**, Estimated SDR distributions (for SDRs of more than 2 cm year^{-1}) calculated with **a**, the free condition; **b**, zero backslip at all boundaries; and **c**, a 6.5 cm year^{-1} constraint at the south edge (the other boundaries

being in the free condition). Grey shading indicates areas with resolution values lower than 0.05, calculated in Extended Data Fig. 6e. α is the hyperparameter of smoothness.



Extended Data Figure 8 | Events determined using analysis of automatic VLFE detection²⁴. Purple and blue dots denote events in the periods 1 June 2003 to 10 May 2015, and 1 August 2008 to 10 May 2015,

respectively. Grey stars indicate epicentres of the 2004 earthquakes off the Kii Peninsula. Pale green lines indicate the depths of the plate boundary determined using the CAMP model⁴².

Neural correlates of single-vessel haemodynamic responses *in vivo*

Philip O'Herron¹, Pratik Y. Chhatbar¹, Manuel Levy¹, Zhiming Shen¹, Adrien E. Schramm¹, Zhongyang Lu¹ & Prakash Kara¹

Neural activation increases blood flow locally. This vascular signal is used by functional imaging techniques to infer the location and strength of neural activity^{1,2}. However, the precise spatial scale over which neural and vascular signals are correlated is unknown. Furthermore, the relative role of synaptic and spiking activity in driving haemodynamic signals is controversial^{3–9}. Previous studies recorded local field potentials as a measure of synaptic activity together with spiking activity and low-resolution haemodynamic imaging. Here we used two-photon microscopy to measure sensory-evoked responses of individual blood vessels (dilation, blood velocity) while imaging synaptic and spiking activity in the surrounding tissue using fluorescent glutamate and calcium sensors. In cat primary visual cortex, where neurons are clustered by their preference for stimulus orientation, we discovered new maps for excitatory synaptic activity, which were organized similarly to those for spiking activity but were less selective for stimulus orientation and direction. We generated tuning curves for individual vessel responses for the first time and found that parenchymal vessels in cortical layer 2/3 were orientation selective. Neighbouring penetrating arterioles had different orientation preferences. Pial surface arteries in cats, as well as surface arteries and penetrating arterioles in rat visual cortex (where orientation maps do not exist¹⁰), responded to visual stimuli but had no orientation selectivity. We integrated synaptic or spiking responses around individual parenchymal vessels in cats and established that the vascular and neural responses had the same orientation preference. However, synaptic and spiking responses were more selective than vascular responses—vessels frequently responded robustly to stimuli that evoked little to no neural activity in the surrounding tissue. Thus, local neural and haemodynamic signals were partly decoupled. Together, these results indicate that intrinsic cortical properties, such as propagation of vascular dilation between neighbouring columns, need to be accounted for when decoding haemodynamic signals.

To determine how neural activity leads to changes in cerebral blood flow, the haemodynamic responses of individual vessels need to be compared to neural activity in the surrounding tissue¹¹. While sensory-evoked responses of individual vessels have been measured in the somatosensory cortex and olfactory bulb of rodents, these studies have not measured vessel responses to the full range of stimuli for which the neighbouring neural tissue is responsive. Thus, the degree to which vascular signals match local neural activity has been difficult to assess. Here we compare neural and vascular responses to a full range of stimulus orientations in cat primary visual cortex to determine if vascular responses can be predicted from local neural activity. Additionally, the primary visual cortex of the cat, similar to that of primates including humans, is organized into precise maps such that different columns of neural tissue are optimally activated by different stimulus orientations (Fig. 1a). Therefore the orientation selectivity of vessel responses can be linked to the spatial scale of neurovascular coupling. For example, if blood

flow in a single cortical vessel is sensitive to neural activity over a large spatial scale covering many orientation columns, then the vessel should dilate to a broad range of stimulus orientations. By contrast, if the vascular response is controlled very locally, that is, within the scale of an orientation column, then individual vessels may be highly orientation selective.

We first labelled blood vessels in the cat primary visual cortex with the fluorescent indicators Texas Red Dextran or Alexa 633 (see Methods)¹², and measured the dilation responses to drifting grating stimuli of different orientations. Veins and capillaries, which were distinguished from arteries by a number of means¹² (see Methods), were not included in this initial analysis because they rarely exhibit rapid sensory-evoked dilation^{12–14}. Our data set included all other blood vessels, provided that they were sufficiently labelled and imaged in tissue with minimal movements from respiration. All blood vessels in this data set dilated in response to drifting grating visual stimuli ($P < 0.05$ analysis of variance (ANOVA)). Specifically, we found that parenchymal arterioles in layer 2/3 typically dilated more strongly in response to one or two of the stimulus orientations presented (Fig. 1b), whereas pial surface arteries dilated to all orientations nearly equally (Fig. 1c). For each vessel, we computed the orientation selectivity index (OSI; see Methods), such that when a vessel dilates equally to all stimulus orientations the OSI = 0 and when a vessel responds only to a single orientation the OSI = 1. The OSI was much greater for parenchymal arterioles than for pial surface arteries (OSI parenchymal arteriole mean \pm standard error of the mean (s.e.m.) = 0.21 ± 0.01 ; $n = 79$ vessels and OSI surface artery mean \pm s.e.m. = 0.06 ± 0.01 ; $n = 24$ vessels; $P < 10^{-10}$; Mann–Whitney test; Fig. 1d).

To illustrate further the role of an organized map of neocortical neurons in generating tuned parenchymal vessel responses, we also measured dilation changes in rat primary visual cortex. Because cortical neurons in rats are not organized in an orientation map¹⁰, each parenchymal vessel is surrounded by neurons displaying a variety of orientation preferences (Fig. 1e). In rats, we found no orientation selectivity in cortical layer 2/3 parenchymal arterioles (Fig. 1f; OSI mean \pm s.e.m. = 0.06 ± 0.01 ; $n = 16$ vessels) or pial surface arteries (Fig. 1g; OSI mean \pm s.e.m. = 0.05 ± 0.01 ; $n = 21$ vessels) (Fig. 1h).

To compare the orientation selectivity of cat parenchymal vessels to spiking activity in the surrounding tissue, we performed calcium imaging using Oregon Green BAPTA-1 AM (OGB-1 AM) or GCaMP6s, along with vascular imaging from the same sites (see Methods). Figure 2a shows a penetrating arteriole that dilates most strongly to the same stimulus orientation as preferred by the immediately adjacent cortical neurons. However, the vessel also dilated when other stimulus orientations were presented, despite minimal or non-existent responses in the nearby neurons. As a result, the vessel had a substantially broader OSI (0.20) than the neuronal spiking activity (OSI = 0.82, average across six adjacent neurons labelled in Fig. 2a). As a penetrating arteriole is likely to be sensitive to neural activity from more than just the immediately adjacent cells, we examined whether spiking activity over

¹Department of Neuroscience, Medical University of South Carolina, Charleston, South Carolina 29425, USA.

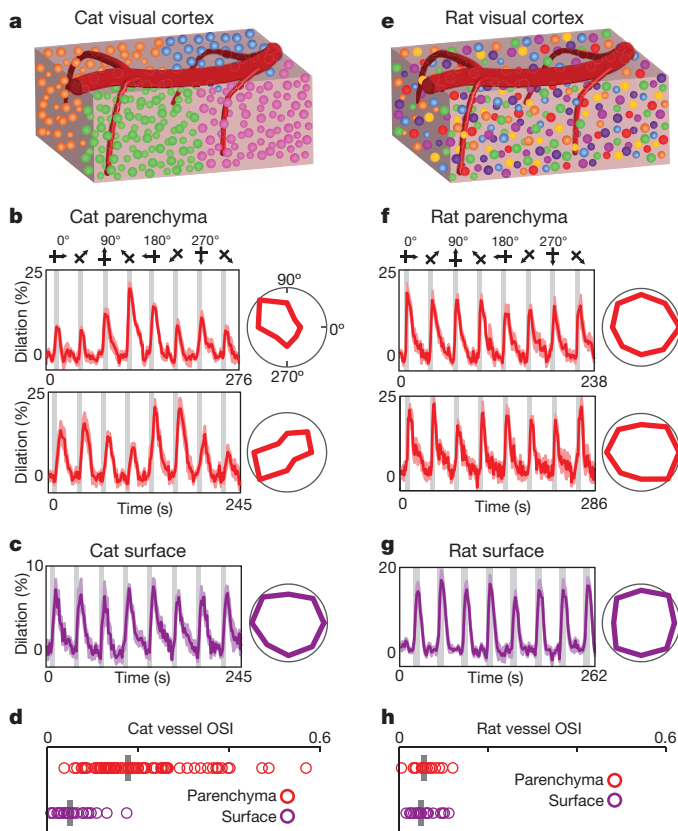


Figure 1 | Selectivity of blood vessel dilation to sensory stimuli in species with and without cortical orientation maps. **a**, Schematic of cat visual cortex showing the columnar organization of neurons by orientation preference and a pial surface artery with multiple branches penetrating the parenchyma. Different colours of neuronal cell bodies represent their different preferred stimulus orientations. **b**, Time courses and polar plots (averages of six (top) and eight (bottom) trials) of the changes in dilation of two layer 2/3 arterioles in cat visual cortex to visual stimulation. Error bands represent s.e.m. and grey bars represent the periods of visual stimulation. In this and subsequent figures, stimuli were gratings that drifted in eight different directions of motion and polar plots are normalized to the maximum response. **c**, Time course and polar plot of responses from a surface artery in cat (average of four trials). **d**, Population distribution and median OSI for parenchymal ($n = 79$ vessels in 18 cats) and surface ($n = 24$ vessels in 9 cats) vessels. **e**, Schematic of rat visual cortex where neurons with different orientation preferences are intermingled. **f**, **g**, Time courses and polar plots of responses from two parenchymal arterioles (averages of seven (top) and eight (bottom) trials) and a surface artery (average of five trials) in rat visual cortex. **h**, Population distribution and median OSI for parenchymal ($n = 16$ vessels in 6 rats) and surface ($n = 21$ vessels in 7 rats) vessels.

a larger region might explain the broad orientation selectivity of the parenchymal vessels. Previous work has shown that occlusion of a single penetrating arteriole in the neocortex leads to tissue death in regions with approximately 400 μm diameter¹⁵, suggesting that this is the region of tissue that an individual penetrating arteriole supplies (see also Supplementary Information). Therefore we compared vascular responses to calcium signals integrated over 400- μm -diameter windows around each parenchymal artery (Fig. 2b, c). The orientation preference of these regions of spiking activity matched those of the arteries at their centres (Fig. 2d; $R = 0.94$, $n = 19$ pairs, $P < 10^{-8}$). However, the orientation selectivity of the spiking activity was higher than the corresponding artery in all regions examined (Fig. 2e; $P < 10^{-9}$, paired t -test). Because the spacing of penetrating arterioles is heterogeneous (see Supplementary Information), we also examined the selectivity of neural responses in a wide range of window sizes around each vessel (100–600 μm diameter). We found that for all window sizes the spiking

activity OSI was still at least 60% higher than the vessel dilation OSI (Fig. 2f; $P < 10^{-5}$ at each window size).

Our calcium imaging results suggest that additional sources of neural activity (besides spiking in the local tissue around the vessel) may be contributing to sensory-evoked vasodilation. Experimental and theoretical work has implicated synaptic glutamate release as a driver of haemodynamic responses¹⁶. In particular, calculation of the energy budget of the neocortex estimated that, of all the cellular processes performed, excitatory synaptic activity has the largest metabolic demand¹⁷. Therefore, to measure directly excitatory synaptic activity over different spatial scales and compare it to single-vessel responses, we labelled neurons in the cat visual cortex with a glutamate sensor (iGluSnFR; see Methods). We found that glutamate activity (like neuronal spiking) is organized in direction and orientation maps (Fig. 3 and Extended Data Fig. 1). However, glutamate signals were generally less orientation selective than spiking activity. Integrating over 400- μm -diameter windows, the OSI for calcium (mean \pm s.e.m. = 0.59 ± 0.02 ; $n = 19$ regions) was sharper than that for glutamate (mean \pm s.e.m. = 0.44 ± 0.02 ; $n = 37$ regions; $P < 0.001$, Mann–Whitney test). To determine if excitatory synaptic activity alone could account for single-vessel haemodynamic responses, we integrated the glutamate signals over 400- μm -diameter regions around individual arteries (Fig. 3a, b) and compared these to vessel responses from the same sites (Fig. 3b–e). We found that the visual stimulus that produced the largest glutamate signal in a 400 μm window matched the visual stimulus that resulted in the largest vessel dilation (Fig. 3c; $R = 0.90$, $n = 37$ pairs, $P < 10^{-13}$). However, a 400- μm region of synaptic activity was always more selective than its corresponding penetrating arteriole (Fig. 3d; $P < 10^{-11}$, paired t -test). The mismatch between orientation selectivity in individual blood vessels and synaptic activity was confirmed for a range of glutamate response window sizes (100–600 μm diameter; Fig. 3e; $P < 10^{-5}$ at each window size).

The broader tuning of the vascular response relative to synaptic and spiking activity (Figs 2 and 3) suggests that vessels can respond to sensory stimuli that evoke little to no concomitant neural activity in the surrounding tissue. This phenomenon can be directly observed by comparing the response amplitudes of vessel dilation and neural activity to individual stimulus conditions. Extended Data Figure 2a, b shows an example in which two visual stimuli (135° and 180°) evoked robust dilations in a penetrating arteriole but essentially no glutamate release in the region around the blood vessel. Across the data sets of synaptic and spiking activity, we compared the amplitude of each vessel's response to each sensory stimulus against the neural response around the vessel to the same stimulus (Extended Data Fig. 2c). Our analysis confirmed that there are many instances where there is a non-existent (or very small) synaptic or spiking response to a visual stimulus despite a robust dilation response. In general, there are very few instances where a stimulus failed to evoke a dilation response of some magnitude.

Like orientation tuning, direction selectivity is a hallmark feature of the primary visual cortex and represents the capacity of a neuron to respond preferentially to one direction of stimulus motion at the optimal stimulus orientation. We found direction maps for excitatory synaptic activity (Fig. 3) that were qualitatively similar to direction maps of spiking activity (Fig. 2). However, the directionality index¹⁰ (DI) over 400- μm -diameter windows was greater for spiking activity than for synaptic responses (DI spiking mean \pm s.e.m. = 0.59 ± 0.07 ; $n = 19$ regions; DI synaptic mean \pm s.e.m. = 0.33 ± 0.03 ; $n = 37$ regions; $P < 0.01$; Extended Data Fig. 3a). Blood vessel responses appeared to have little direction selectivity, even when surrounded by iso-direction territories of spiking activity, for example, Fig. 2b vessels 2 and 4. Indeed, across the population, the direction selectivity of vessels was smaller than that of regions of spiking activity (DI vessel mean \pm s.e.m. = 0.30 ± 0.02 ; $n = 79$ vessels; $P < 0.0005$). The population mean DI of vessels and synaptic activity were similar (Extended Data Fig. 3a; $P = 0.70$) although

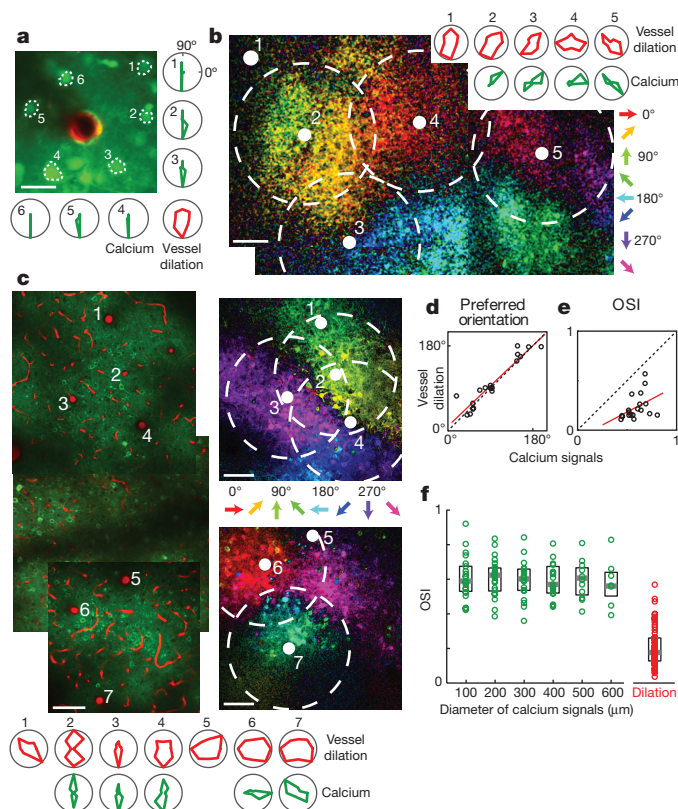


Figure 2 | Stimulus selectivity of single vessels and of spiking activity in the surrounding tissue. **a**, *In vivo* anatomical image of a small region of layer 2/3 cat visual cortex labelled with OGB-1 AM (green) and an arteriole labelled with Alexa 633 (red). Polar plots show the sensory evoked calcium responses from six neurons and the dilation of the arteriole. **b**, Pixel-based direction map and polar plots of responses from another cat labelled with OGB-1 AM and Alexa 633. The pixels are colour-coded by their preferred stimulus, with the brightness indicating the response strength. Red polar plots show the dilation responses of the five vessels indicated by solid white circles on the direction map. Green polar plots show the calcium responses pooled in 400- μ m-diameter windows around four of these vessels (dashed circles). No calcium responses are shown for the region around vessel number 1 because this vessel was near the edge of the imaging field. **c**, Direction map and polar plots of responses from cat visual cortex labelled with GCaMP6s and blood vessels labelled with Texas Red Dextran. Left, tiled *in vivo* anatomical images of a large region of layer 2/3 where the positions of seven penetrating arterioles are numbered. Right, pixel-based direction maps of neural responses. The polar plots at the bottom show the vessel dilation responses (red) and the calcium responses (pooled over 400- μ m-diameter regions) around five of these vessels (green). **d**, Correlation between the preferred orientation of the vessel dilation and the preferred orientation of calcium responses in 400- μ m-diameter windows around each vessel ($R = 0.94$; $P < 10^{-8}$; $n = 19$ windows in 8 cats; regression line shown in red). **e**, No significant correlation between calcium and vessel OSI ($R = 0.41$; $P = 0.08$). **f**, Distribution of OSI for calcium responses across tissue regions of different window sizes ($n = 11$ cats) and for the population of dilation responses ($n = 18$ cats). Solid bars are medians and boxes indicate the interquartile range. For all window sizes, calcium responses were more selective than the vessel dilation ($P < 0.0001$, Mann–Whitney test). Pixel maps shown are averages of five to six trials. Scale bars, 25 μ m (**a**) and 100 μ m (**b**, **c**).

there was no correlation between the direction selectivity of a particular vessel and the glutamate signals in the surrounding tissue (Extended Data Fig. 3b; $R = 0.20$; $n = 37$ pairs; $P = 0.23$).

While vessel dilation responses over the population of parenchymal arterioles did not match neural orientation selectivity, we tested the possibility that the smallest vessels would show similar selectivity to neural responses. Larger penetrating arterioles (with baseline diameter $> 15 \mu$ m) may perfuse larger regions of tissue than small penetrating

arterioles and their finer branches. Therefore, these smaller vessels (typically 8–15- μ m baseline diameter) may be sensitive to vasodilators from smaller regions of neural tissue and thus have sharper orientation tuning. Indeed we found that OSI was inversely correlated with baseline vessel diameter in cat layer 2/3 (Extended Data Fig. 4a; $R = 0.37$, $P < 0.001$). We compared the dilation responses of these small vessels (baseline diameter $\leq 15 \mu$ m, mean = 11.8 μ m) to those with baseline diameter $> 15 \mu$ m (based on consistency of Alexa 633 labelling¹²; see Methods). We found that the small vessels were slightly more tuned (OSI mean \pm s.e.m. = 0.24 ± 0.02 ; $n = 35$) than the larger ones (OSI mean \pm s.e.m. = 0.18 ± 0.01 ; $n = 44$; $P < 0.05$; Extended Data Fig. 4a, b). Importantly, however, the OSI of these small vessels was still lower than synaptic and spiking activity over the full range of window sizes ($P < 0.005$; see Extended Data Fig. 4b, c).

Capillaries are the smallest vessels in the neocortex and therefore may be even more tuned for stimulus orientation than small arterioles. However, whether capillaries have the capacity to dilate *in vivo* to sensory stimuli is controversial^{13,14,18,19}. This is probably due to inconsistent criteria for defining capillaries and distinguishing them from pre-capillary arterioles as well as to the difficulty of detecting dilation in very small vessels even with two-photon microscopy resolution^{13,14,18,19}. However, a small dilation in a capillary that is undetectable with two-photon microscopy would still lead to easily detectable changes in red blood cell (RBC) velocity. Because RBC size is slightly larger than the capillary lumen diameter, a very small dilation in a capillary could produce a dramatic reduction in the resistance to flow (see figure 2e in ref. 20). Therefore, we measured the stimulus-evoked changes in RBC velocity in a set of micro-vessels that would probably be classified as capillaries based on their high tortuosity and small diameter (4–7 μ m; see Methods)^{21,22}. We found that the orientation selectivity on the basis of blood velocity in these capillaries (OSI mean \pm s.e.m. = 0.30 ± 0.04 ; $n = 15$ vessels) was no different from what was found for dilation of the ≤ 15 - μ m-diameter vessels ($P = 0.16$; Extended Data Fig. 4a, b). To determine if the tuning of capillaries was due to these vessels being in unusually broadly tuned windows of neural activity, we compared the OSI of neural activity around capillaries with what was found around parenchymal arterioles. The OSIs of 400- μ m-diameter windows of spiking activity around capillaries (mean \pm s.e.m. = 0.60 ± 0.03 ; $n = 13$) and around arterioles (mean \pm s.e.m. = 0.59 ± 0.02 ; $n = 19$) were indistinguishable ($P = 0.94$, Mann–Whitney test). Thus, stimulus-evoked changes even in capillaries were still not as selective as the responses in adjacent neural tissue.

Our results suggest that blood flow increases in parenchymal vessels are partially driven by local neural activity (which would generate the match in orientation preference) and also by an additional global component arising from adjacent functional columns (which would induce the dilation to non-preferred orientations). One possibility is that this global component is due to the propagation of dilatory signals along vessel walls. Specifically, the lack of orientation tuning in surface arteries could result from the dilation of penetrating arterioles from many different orientation domains propagating back to a surface artery. Then the propagation of dilation along the surface artery and down into multiple penetrating arterioles could broaden the locally driven dilation signal, leading to dilation in adjacent regions of tissue that have no concomitant neural activity. Previous studies in rodents have demonstrated the propagation of dilation from the parenchyma up to the cortical surface²³ and along the surface over distances of at least 1 mm (refs 24–26) at rapid speeds²⁵, but these have not been linked to the stimulus selectivity of vessel or neural responses. Consistent with this propagation of dilation hypothesis, we found that in cat visual cortex parenchymal vessels dilate before the surface vessels and that the dilation to the preferred orientation came before the dilation to the stimulus that was oriented orthogonal to the preferred orientation, that is, at the null orientation (see Supplementary Information and Extended Data Fig. 5). Alternative

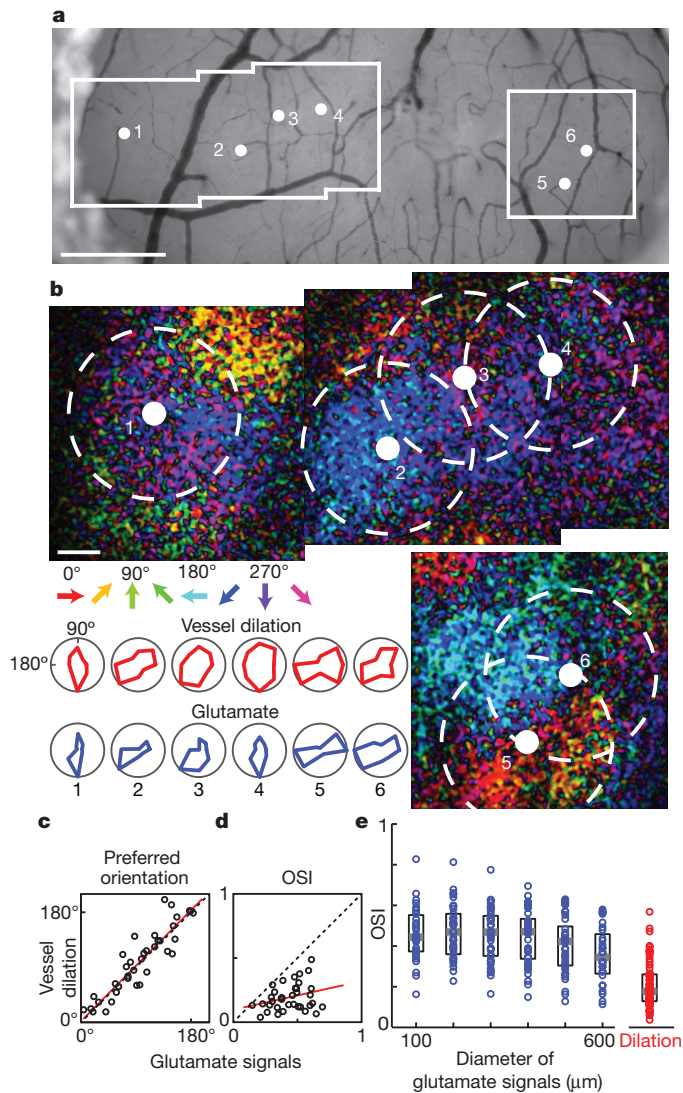


Figure 3 | Stimulus selectivity of single vessels and of excitatory synaptic activity in the surrounding tissue. **a**, Bright-field image of the surface of cat visual cortex showing the location of six penetrating arterioles and the regions targeted for two-photon imaging. **b**, Direction maps and polar plots of glutamate responses from cortical neurons labelled with iGluSnFR and dilation from blood vessels labelled with Texas Red Dextran. The positions of the arterioles and the 400-μm-diameter windows of pooled glutamate responses in cortical layer 2/3 are indicated by solid white and dashed circles, respectively. Red polar plots show the dilation responses and blue plots show the pooled glutamate activity in the windows around each arteriole. **c**, Correlation between the preferred orientation of the dilation responses and the preferred orientation of glutamate activity in 400-μm-diameter windows around each vessel for all cat data ($R = 0.90$, $P < 10^{-13}$; $n = 37$ windows in 5 cats). **d**, No significant correlation between glutamate and vessel OSI ($R = 0.28$, $P = 0.08$; linear regression line shown in red). **e**, Distribution of OSI for glutamate activity across windows of different sizes ($n = 5$ cats) and for the population of dilation responses ($n = 18$ cats). Solid bars are medians and boxes indicate the interquartile range. For all window sizes, the glutamate responses were more selective than vessel dilation ($P < 10^{-5}$, Mann–Whitney test). Pixel maps shown are averages of 8–10 trials. Scale bars, 500 μm (**a**) and 100 μm (**b**).

hypotheses on the origin of the selectivity of vessel dilation are discussed in Supplementary Information.

In conclusion, our results have a number of implications for the interpretation of haemodynamic signals in relation to neural activity. We provide direct single-vessel evidence for the untuned global signal in the pial vasculature that has been found in low-resolution

haemodynamic imaging studies^{27,28}. After subtracting the global signal, these earlier studies often suggested that the residual tuned vascular responses were of capillary origin^{27,28}. We show that individual penetrating arteries also display stimulus-specific responses. Furthermore, the orientation selectivity of these parenchymal vessels is an order of magnitude higher than what is obtained with intrinsic signal optical imaging²⁹. We also demonstrate that an organized functional map of neural responses is required for attaining tuned haemodynamic signals (see also ref. 30). Furthermore, by sampling responses over the full range of a stimulus parameter and by directly measuring synaptic and spiking activity along with single-vessel responses in precisely defined spatial regions of tissue, we overcome many of the technical limitations of earlier studies that examined neurovascular coupling. The difficulties inherent in correlating low-resolution vascular signals with electrophysiological metrics of neural activity and in interpreting glutamate pharmacology has led to controversy regarding the spatial scale over which synaptic versus spiking activity matches vascular signals (see Supplementary Information). Here we establish that the sensory stimulus that elicits the largest synaptic or spiking response also produces the largest haemodynamic signal. However, the complete selectivity profile of neither synaptic nor spiking activity in the local tissue around a vessel can be inferred from the tuning curves of haemodynamic signals. Thus, vascular signals are partially decoupled with local neural signals, over distances of at least 300 μm.

Online Content Methods, along with any additional Extended Data display items and Source Data, are available in the online version of the paper; references unique to these sections appear only in the online paper.

Received 14 July 2015; accepted 1 April 2016.

Published online 25 May 2016.

1. Raichle, M. E. & Mintun, M. A. Brain work and brain imaging. *Annu. Rev. Neurosci.* **29**, 449–476 (2006).
2. Grinvald, A., Lieke, E., Frostig, R. D., Gilbert, C. D. & Wiesel, T. N. Functional architecture of cortex revealed by optical imaging of intrinsic signals. *Nature* **324**, 361–364 (1986).
3. Heeger, D. J., Huk, A. C., Geisler, W. S. & Albrecht, D. G. Spikes versus BOLD: what does neuroimaging tell us about neuronal activity? *Nature Neurosci.* **3**, 631–633 (2000).
4. Logothetis, N. K., Pauls, J., Augath, M., Trinath, T. & Oeltermann, A. Neurophysiological investigation of the basis of the fMRI signal. *Nature* **412**, 150–157 (2001).
5. Sirotnin, Y. B. & Das, A. Anticipatory haemodynamic signals in sensory cortex not predicted by local neuronal activity. *Nature* **457**, 475–479 (2009).
6. Maier, A. *et al.* Divergence of fMRI and neural signals in V1 during perceptual suppression in the awake monkey. *Nature Neurosci.* **11**, 1193–1200 (2008).
7. Wang, Z. & Roe, A. W. Columnar specificity of microvascular oxygenation and blood flow response in primary visual cortex: evaluation by local field potential and spiking activity. *J. Cereb. Blood Flow Metab.* **32**, 6–16 (2012).
8. Logothetis, N. K. What we can do and what we cannot do with fMRI. *Nature* **453**, 869–878 (2008).
9. Ekstrom, A. How and when the fMRI BOLD signal relates to underlying neural activity: the danger in dissociation. *Brain Res. Rev.* **62**, 233–244 (2010).
10. Ohki, K., Chung, S., Ch'ng, Y. H., Kara, P. & Reid, R. C. Functional imaging with cellular resolution reveals precise micro-architecture in visual cortex. *Nature* **433**, 597–603 (2005).
11. Kleinfeld, D. *et al.* A guide to delineate the logic of neurovascular signaling in the brain. *Front. Neuroenergetics* **3**, 1 (2011).
12. Shen, Z., Lu, Z., Chhatbar, P. Y., O'Herron, P. & Kara, P. An artery-specific fluorescent dye for studying neurovascular coupling. *Nature Methods* **9**, 273–276 (2012).
13. Drew, P. J., Shih, A. Y. & Kleinfeld, D. Fluctuating and sensory-induced vasodynamics in rodent cortex extend arteriole capacity. *Proc. Natl Acad. Sci. USA* **108**, 8473–8478 (2011).
14. Hillman, E. M. C. *et al.* Depth-resolved optical imaging and microscopy of vascular compartment dynamics during somatosensory stimulation. *Neuroimage* **35**, 89–104 (2007).
15. Shih, A. Y. *et al.* The smallest stroke: occlusion of one penetrating vessel leads to infarction and a cognitive deficit. *Nature Neurosci.* **16**, 55–63 (2013).
16. Attwell, D. *et al.* Glial and neuronal control of brain blood flow. *Nature* **468**, 232–243 (2010).
17. Howarth, C., Gleeson, P. & Attwell, D. Updated energy budgets for neural computation in the neocortex and cerebellum. *J. Cereb. Blood Flow Metab.* **32**, 1222–1232 (2012).
18. Hall, C. N. *et al.* Capillary pericytes regulate cerebral blood flow in health and disease. *Nature* **508**, 55–60 (2014).

19. Hill, R. A. *et al.* Regional blood flow in the normal and ischemic brain is controlled by arteriolar smooth muscle cell contractility and not by capillary pericytes. *Neuron* **87**, 95–110 (2015).
20. Blinder, P. *et al.* The cortical angiome: an interconnected vascular network with noncolumnar patterns of blood flow. *Nature Neurosci.* **16**, 889–897 (2013).
21. Kleinfeld, D., Mitra, P. P., Helmchen, F. & Denk, W. Fluctuations and stimulus-induced changes in blood flow observed in individual capillaries in layers 2 through 4 of rat neocortex. *Proc. Natl Acad. Sci. USA* **95**, 15741–15746 (1998).
22. Chhatbar, P. Y. & Kara, P. Improved blood velocity measurements with a hybrid image filtering and iterative Radon transform algorithm. *Front. Neurosci.* **7**, 106 (2013).
23. Tian, P. *et al.* Cortical depth-specific microvascular dilation underlies laminar differences in blood oxygenation level-dependent functional MRI signal. *Proc. Natl Acad. Sci. USA* **107**, 15246–15251 (2010).
24. Berwick, J. *et al.* Fine detail of neurovascular coupling revealed by spatiotemporal analysis of the hemodynamic response to single whisker stimulation in rat barrel cortex. *J. Neurophysiol.* **99**, 787–798 (2008).
25. Chen, B. R., Bouchard, M. B., McCaslin, A. F. H., Burgess, S. A. & Hillman, E. M. C. High-speed vascular dynamics of the hemodynamic response. *Neuroimage* **54**, 1021–1030 (2011).
26. Chen, B. R., Kozberg, M. G., Bouchard, M. B., Shaik, M. A. & Hillman, E. M. A critical role for the vascular endothelium in functional neurovascular coupling in the brain. *J. Am. Heart Assoc.* **3**, e000787 (2014).
27. Vanzetta, I., Sloviter, H., Omer, D. B. & Grinvald, A. Columnar resolution of blood volume and oximetry functional maps in the behaving monkey; implications for fMRI. *Neuron* **42**, 843–854 (2004).
28. Fukuda, M. *et al.* Localization of activity-dependent changes in blood volume to submillimeter-scale functional domains in cat visual cortex. *Cereb. Cortex* **15**, 823–833 (2005).
29. Rao, S. C., Toth, L. J. & Sur, M. Optically imaged maps of orientation preference in primary visual cortex of cats and ferrets. *J. Comp. Neurol.* **387**, 358–370 (1997).
30. Li, Y., Van Hooser, S. D., Mazurek, M., White, L. E. & Fitzpatrick, D. Experience with moving visual stimuli drives the early development of cortical direction selectivity. *Nature* **456**, 952–956 (2008).

Supplementary Information is available in the online version of the paper.

Acknowledgements We thank A. Shih for comments on the manuscript. This work was supported by grants from the National Institutes of Health (NS088827), National Science Foundation (1539034), and Whitehall and Dana Foundations to P.K.

Author Contributions P.K. conceived and supervised the project. All authors collected data. P.O'H. and P.Y.C. analysed data. P.O'H., M.L. and P.K. wrote the paper. All authors commented on and approved the final manuscript.

Author Information Reprints and permissions information is available at www.nature.com/reprints. The authors declare no competing financial interests. Readers are welcome to comment on the online version of the paper. Correspondence and requests for materials should be addressed to P.K. (kara@muscc.edu).

METHODS

Animals and surgery. All surgical and experimental procedures were approved by the Institutional Animal Care and Use Committee at Medical University of South Carolina. Cats ($n = 25$ of either sex; postnatal day 28 to >2.5 kg adult) were anaesthetized with isoflurane (1–2% during surgery, 0.5–1.0% during imaging) and paralyzed with a continuous infusion of vecuronium bromide ($0.2 \text{ mg kg}^{-1} \text{ h}^{-1}$, intravenously). Cats were artificially ventilated through a tracheal cannula, and the end tidal CO_2 was regulated at 3.5–4.5%. Heart rate, respiration rate, temperature and electroencephalogram were also monitored. Long Evans rats ($n = 10$ males, postnatal days 31–45) and C57BL/6J mice ($n = 1$ male, postnatal day 63) were initially anaesthetized with a bolus infusion of fentanyl citrate (0.04 – 0.06 mg kg^{-1}), midazolam (3.75 – 6.25 mg kg^{-1}), and dexmedetomidine (0.19 – 0.31 mg kg^{-1}). The one mouse was used for a control experiment to confirm that the iGluSnFR sensor was not being saturated during sensory stimulation (see later). During two-photon imaging, continuous intraperitoneal infusion with a lower concentration mixture (fentanyl citrate: 0.02 – $0.03 \text{ mg kg}^{-1} \text{ h}^{-1}$; midazolam: 1.50 – $2.50 \text{ mg kg}^{-1} \text{ h}^{-1}$; and dexmedetomidine: 0.10 – $0.25 \text{ mg kg}^{-1} \text{ h}^{-1}$) was administered using a catheter connected to a syringe pump.

For all animals, craniotomies (2–3 mm square) were opened over the primary visual cortex (area 18), the dura was reflected, and the craniotomies were sealed with agarose (1.5–3% dissolved in artificial cerebrospinal fluid (ACSF)) and a glass coverslip. When the calcium indicator OGB-1 AM was used, before the placement of the coverglass, a pipette was inserted into the craniotomy and the dye was injected with air pressure puffs. The dye loading procedure has been described in detail³¹.

In cats, we also used the genetically encoded indicators GCaMP6s³² and iGluSnFR³³ to measure calcium and glutamate activity respectively. Two-to-four weeks before the imaging session, viral injections of AAV2/9.hSyn.GCaMP6s.WPRE.SV40 or AAV2/1.hSyn.iGluSnFR.WPRE.SV40 were performed under sterile surgery conditions. Cats were anaesthetized with 1–2% isoflurane and vital signs were monitored. One to three craniotomies were performed over the primary visual cortex (area 18) and small holes were made in the dura. Aliquots of virus (5 μl) were diluted in PBS and mannitol (5:9:6 ratio of virus:PBS:mannitol) to titres of $\sim 10^{12}$ genomes ml^{-1} with 50–200 nl of Fast Green dye (Sigma) added to visualize the injection. Glass pipettes containing the virus solution were lowered 500–800 μm into the cortex and pressure puffs were administered over 15–20 min until approximately 1 μl had been injected. After 10 min, the pipettes were slowly retracted, the craniotomies were sealed with agarose (3% dissolved in ACSF), the scalp was sutured closed and the animals were recovered and returned to their housing. All animals were treated similarly and so randomization and blinding were not required. No statistical methods were used to predetermine sample size.

Two-photon imaging. For vascular imaging, three fluorescent dyes were used as we described previously¹². Alexa 633 fluor hydrazide selectively labels artery walls, while Texas Red dextran (70 kDa) and fluorescein dextran (2,000 kDa) indiscriminately label the entire vascular lumen. Fluorescein dextran has similar excitation and emission properties as our neuronal labels OGB-1 AM, GCaMP6s, and iGluSnFR. Therefore, fluorescein dextran was not used for vessel dilation measurements in animals where neuronal imaging was performed because sufficient contrast between a vessel wall and background is more difficult to obtain when two green labels are used simultaneously. Fluorescein dextran was typically used for the measurement of RBC velocity and was only injected after the neural imaging was completed.

Fluorescence was monitored with a custom-built microscope (Prairie Technologies) coupled with a Mai Tai (Newport Spectra-Physics) mode-locked Ti:sapphire laser (810 nm or 920 nm) with DeepSee dispersion compensation. Excitation light was focused by a $\times 40$ (NA 0.8, Olympus), $\times 20$ (NA 1.0, Olympus) or $\times 16$ (NA 0.8, Nikon) water immersion objective and beam expansion optics. Full frame imaging of neural activity and vessel dilation were typically obtained at approximately 0.8 Hz. All the blood velocity data and the dilation of a small number of vessels were measured with line scans rather than full frame imaging by using line acquisition rates between 0.4 and 4.2 kHz.

Visual stimulation and size of imaged region. Drifting square-wave grating stimuli were presented on a 17-inch LCD monitor. The gratings were presented at 100% contrast, 30 cd m^{-2} mean luminance, 1.5–2.0 Hz temporal frequency. As depicted in the various time courses (for example, Fig. 1) these stimuli were presented at eight directions of motion in 45° steps and each of these eight stimuli was interspersed with blank periods (equiluminant grey screen). Because vascular responses decay slowly, we used long blank periods (at least four times the stimulus duration) when measuring blood vessel responses. We also presented the eight visual stimuli in pseudo-random order. These steps ensured that a particular response would not be influenced by a residual response to the previous stimulus. The duration of the stimulation period, for example, 6 s, and the duration of the blank period, for example, 24 s, was always identical across all epochs in a stimulus sequence. Each of the eight stimuli was repeated at least

three times and in the vast majority of the data, 5–10 trials were used. Unlike arteriole dilation, neural transients return to baseline nearly immediately upon extinguishing the visual stimulus^{12,34} (see also Extended Data Figs 1 and 2). Therefore, for epochs of data collection involving only calcium or glutamate imaging, either sequential or pseudo-random sequences were used. While some neural and vascular data were collected simultaneously, our analyses benefited from collecting them sequentially for the following reasons. Neural data was typically collected in $600 \times 600 \mu\text{m}$ square regions to allow the pooling of large regions of activity (see Figs 2b, c and 3b) and multiple $600 \times 600 \mu\text{m}$ square regions were often imaged in a single craniotomy to obtain maps where many orientation and direction domains were represented (see Figs 2b, c, 3b and Extended Data Fig. 1). Higher pixel resolution was needed for resolving blood vessel dilation so we usually obtained the vessel responses immediately after the neural responses using higher optical zooms that were centred on the blood vessels of interest. Because of the optical zoom customization per imaged site and the differences in recovery of neural versus vascular responses to baseline, the selected duration of visual stimulation for a particular experiment ranged from 2 to 8 s and the duration of blank periods ranged from 6 to 35 s.

Data-analysis overview. Images were analysed in Matlab (Mathworks) and ImageJ (National Institutes of Health). Data with movements of several μm in XY or Z were excluded. Data with small drift movements were realigned by maximizing the correlation between frames.

Quantifying vessel dilation. We analysed dilation responses only in surface arteries and penetrating arterioles because veins and capillaries do not typically dilate to sensory stimuli less than 10 s in duration^{12–14}. When veins dilate in response to very long duration sensory stimuli, these responses are relatively weak and extremely slow, unlike the rapid and large responses of arteries and arterioles¹³. Surface arteries and penetrating arterioles are distinguished from veins using Alexa 633 as an artery-specific dye, by their orange versus purplish hue under bright-field illumination, and by the tone of the vessel walls and the speed and direction of blood flow during two-photon imaging¹². Distinguishing capillaries from pre-capillary arterioles has been inconsistent in the literature^{13,14,18,19}. Here we categorize capillaries as vessels with 4–7 μm baseline diameter²¹, high tortuosity and complete lack of Alexa-633 labelling¹². Vessel diameter was determined in full-frame images by one of two methods. When the vessel had a circular profile (as was the case for most of the parenchymal arterioles), a region of interest was manually drawn around each vessel and a circle was fit to the pixels in the region that passed a luminance threshold (Extended Data Fig. 6). For vessels with an elongated profile (typical for pial surface vessels), a cross-section was taken through the vessel walls and the peaks in luminance (for the wall-labelling Alexa 633) or peaks in the pixel-by-pixel luminance difference along the line (for lumen labels) were used to compute the diameter¹² (see Extended Data Fig. 7). For the few instances where diameter was measured using line-scans, we averaged the data along the time axis over all the lines in an image (usually 1,000 lines) or obtained two data points per image by sequentially averaging half the lines in each image. Since each line was only 0.25–2.5 ms in duration, averaging across these lines still provided sufficient temporal resolution for capturing the onset, peak and recovery of sensory-evoked dilation. The diameter was computed from these line scans in the same way as for the cross-section (Extended Data Fig. 8). For all methods of dilation measurement, images were usually oversampled by interpolating between pixels from 2 to 20 times to allow the algorithm to compute diameter values with a spatial resolution that was finer than the pixel size in the raw data images. To compute the vascular response to each condition, a stimulus response window was defined. Because of the slow onset and offset of the vascular response, we could not simply assign the response period to correspond to the period when the stimulus was displayed on the monitor. Instead, for each vessel we selected the response period by examining the average response across all stimulus conditions and then selected the imaging frames that best approximated this response interval. Shifting this time window by adding or removing data points did not appreciably change the responses. The mean response across this time window was divided by the baseline level for each condition to get the percentage change in diameter. Responsive vessels were defined by ANOVA across baseline and eight directions over multiple trials ($P < 0.05$). The orientation selectivity index (OSI) was defined as:

$$\text{OSI} = \text{abs} \left(\frac{\sum_k r_k e^{i2\theta_k}}{\sum_k r_k} \right)$$

where θ_k is the orientation of each stimulus and r_k is the mean response across trials to that stimulus³⁵. Note that $\text{OSI} = 1$ – circular variance. The preferred orientation was defined as: $\arctan(\sum_k r_k \cos(2\theta_k) / \sum_k r_k \sin(2\theta_k))$. The directionality index (DI) was computed as $1 - r_{\text{null}}/r_{\text{pref}}$, where r_{pref} is the response amplitude to the preferred stimulus and r_{null} is the response to the stimulus with the same orientation

drifting in the opposite direction. Computing the OSI based on flow rather than diameter by scaling the diameter values to the 4th power (Poiseuille's law) did not affect our results.

Measuring onset latency to dilation. To compare the latencies of pial arteries and parenchymal arterioles, we fit a linear regression line to the rising phase of the dilation (20–80% of the peak response) of each vessel. For parenchymal vessels, we used only the response to the preferred orientation because of potential latency differences between dilation to the preferred and other stimulus orientations (see later). For the pial vessels, we pooled the response to all stimulus conditions because these vessels are untuned to stimulus orientation. We used the time at which the regression line crossed the pre-stimulus baseline level as the onset latency¹². This regression line metric on the average response is applicable when responses are large and relatively stable from trial to trial—as is the case for pial vessels to any stimulus orientation and for parenchymal vessels to the preferred stimulus orientation.

Since parenchymal vessels are orientation selective (Fig. 1b, d), responses to the null orientation are the weakest and, by definition, smallest in amplitude and more noisy from trial to trial. Thus, to compare the latency between the response to the preferred and null orientations in parenchymal vessels, we used a statistical test, the standardized mean difference (SMD, specifically Hedge's *g*; refs 36, 37), in which vessels are weighted by the trial-by-trial variance in latency values (see Extended Data Fig. 5a). We first smoothed each trial's time course with a three-frame running average. We then performed linear regression on the same interval as earlier (20–80% of the peak). We took the difference in the average onset latency across trials between the responses to preferred and null stimuli and standardized this difference by the pooled variability across the two conditions. The population summary SMD was obtained by using a random-effect model. This model weighs each vessel by the inverse variance of its SMD and factors in the heterogeneity present across the individual vessel data³⁷. As a control for spurious effects, the preferred and null responses were assigned randomly for each trial and the analysis was repeated (Extended Data Fig. 5b).

Quantifying blood velocity. Velocity data was analysed as described previously²². Briefly, line scans were first pooled into blocks of 250, 500, or 1,000 lines. The angle of the RBC streaks in each image was used to determine the velocity of that block and a time course of velocity measurements was extracted. Baseline and stimulus windows were defined similarly to the dilation data and equivalent OSI and statistical analyses were performed.

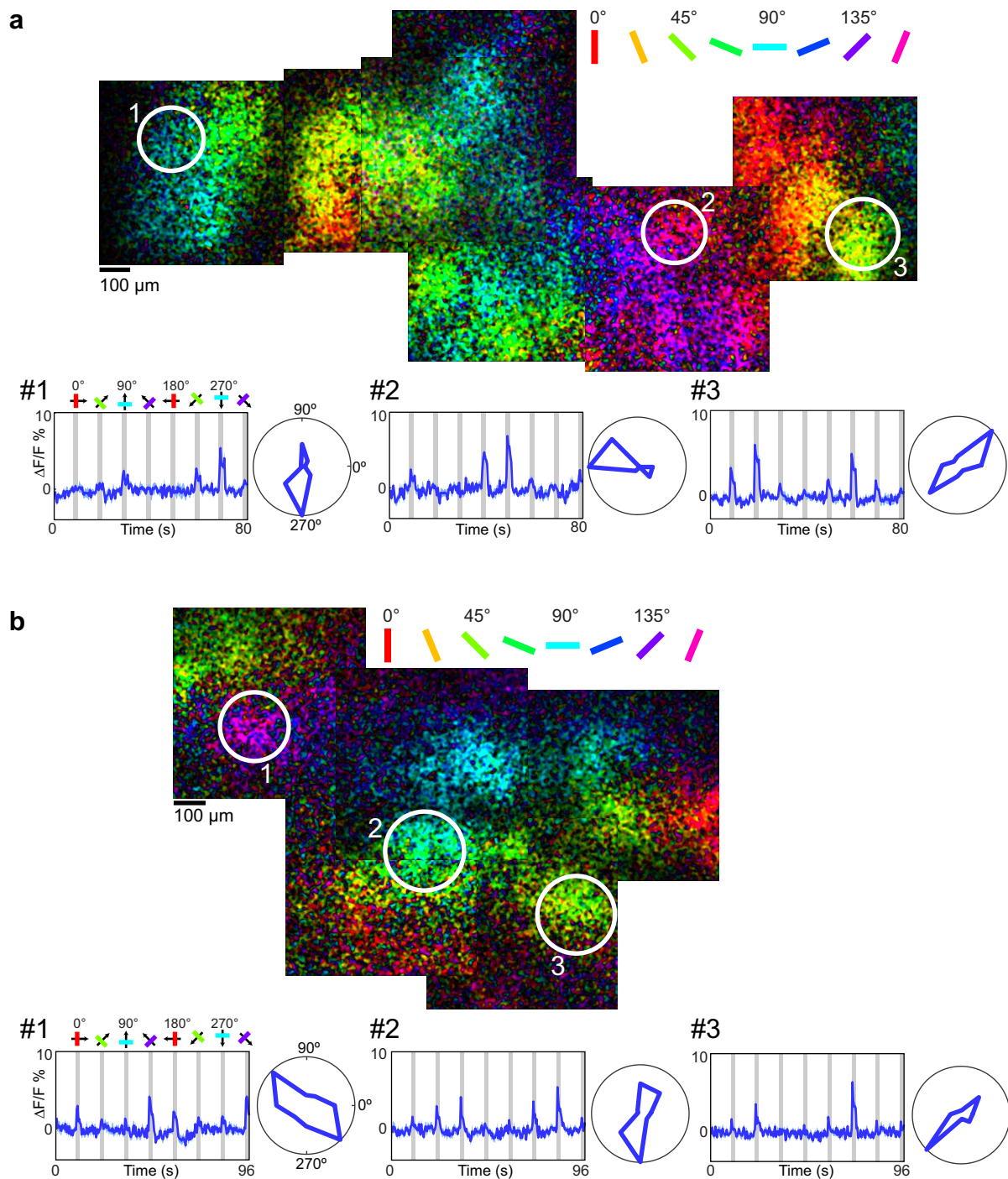
Analysis of calcium and glutamate responses. Calcium and glutamate signals were analysed the same way. Raw images were first smoothed with a 4 μ m Gaussian filter. The mean fluorescence of each pixel within a given 100–600- μ m-diameter window around a vessel was computed for each blank and stimulus epoch. A *t*-test was performed on the difference in stimulus and baseline fluorescence for each condition in each trial and if the distribution was significantly higher than zero ($P < 0.05$), the pixel was included in the integration window. We also performed this analysis without excluding the unresponsive pixels and the responses were indistinguishable. In some data sets, part of the 100–600- μ m-diameter analysis window fell outside of the image boundary and so there would be fewer pixels from those domains contributing to the overall response. Therefore, to avoid biasing the overall response of the integrated region, we divided the 100–600- μ m-diameter analysis window into wedges before averaging the data over the full window. Each wedge was 1/16 of the circle and was further divided into sections of 50 μ m radial length. Thus, a 100- μ m-diameter window had 16 sections whereas a 400- μ m-diameter window had 64. The pixels with significant responses within each section were averaged together to create a time course. The time course was then normalized by a sliding baseline of the mean fluorescence of each blank interval ($\Delta F/F$). Each time course was then weighted by the total number of pixels represented by its section, because sections farther from the vessel contain more pixels. Finally, the time courses of all the sections were averaged together to obtain the time course of the entire region. For inclusion in the population data set, responses from the 100–600- μ m-diameter analysis windows had to pass the following criteria. First, each wedge had to have at least 30% of the imaged pixels passing the initial *t*-test to ensure that windows with wedges having no response and/or weak labelling would be removed. Second, at least 80% of the circular area

of the window had to be within the image to ensure that a sizeable region of tissue whose orientation preference could dramatically affect the overall response was not being missed. In addition, at least 10% of each wedge had to be within the image to ensure that each wedge had some representation. For data that passed all these criteria, the responses to each condition were computed by averaging the imaging frames during stimulus presentation and across trials. Before the OSI was computed, if any conditions showed a negative response (below the baseline level), then the absolute value of the minimum response was added to all responses (to make the minimum equal zero). We have recently published a mechanistic rationale for applying such a correction in fluorescence imaging of neural responses—stimulus-evoked dilation of surface arteries can block fluorescence from the underlying tissue and make a very small response actually appear negative¹². We also analysed the data without this correction and, in addition, when only including the first 1 s of the response (to avoid the slower surface artery interference¹²). Although there were small changes in the OSI values of individual windows, the overall results did not change in either case. The neural response amplitudes, OSI and DI were all computed using the same formulae as for the vessel data. Population distribution statistics on OSI and DI measurements used the Mann–Whitney test.

Additional control for calcium imaging. Spiking activity in the neuropil should also contribute to metabolic needs and hence neurovascular coupling. Therefore, when integrating the calcium signals in the tissue surrounding each artery, we included all pixels that passed a signal-to-noise criterion (see earlier) and not only those corresponding to cell bodies. However, the neuropil may include a mixture of calcium signals from synaptic events in dendritic spines and spiking in axons arriving from regions outside of the integration window we selected. Therefore, as a control, we compared the orientation selectivity in 400- μ m-diameter windows with and without including the neuropil. Masks excluding the neuropil were generated in the same way as described earlier except that the pixels within each wedge were constrained to the cell bodies. Cell body masks were first created using an automated algorithm that applied a series of morphological filters to identify the contours of cell bodies based on intensity, size and shape¹⁰. Cell outlines were visually inspected and errors were corrected manually. Then a *t*-test was performed on each pixel of these masks and the wedges were created in the same manner as before. Because of the sparse distribution of cell bodies, we did not enforce the 30% significantly responding imaged pixels criterion but all other criteria applied. The orientation selectivity with the two mask types was indistinguishable (Extended Data Fig. 9).

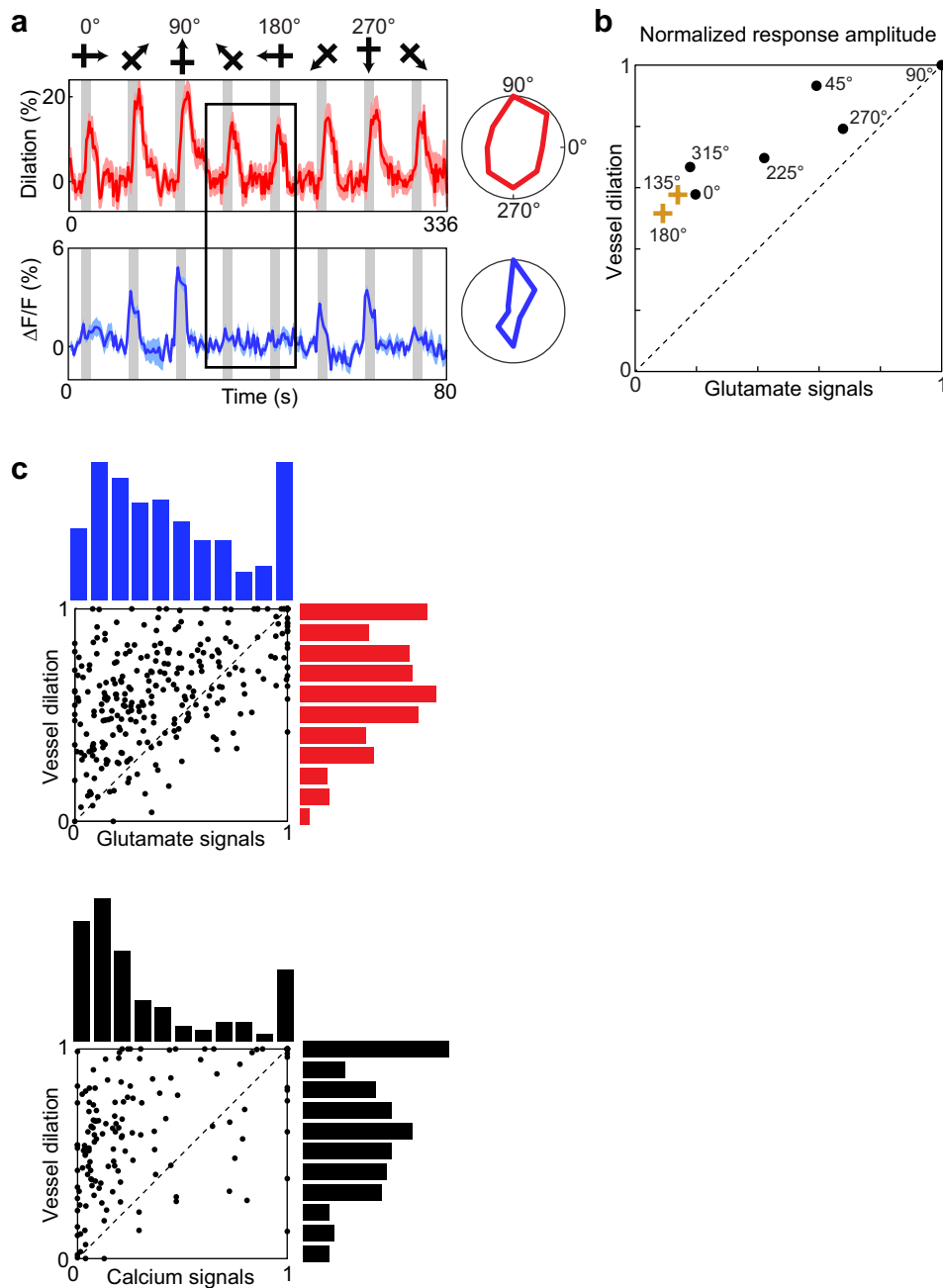
Control to show that visual stimulation was not saturating the iGluSnFR sensor. With visual stimulation, the glutamate signals peaked at $<10\%$ $\Delta F/F$. To determine if the iGluSnFR sensor responded linearly and responded over a greater range than that obtained with visual stimulation, we used iontophoresis to apply large doses of exogenous glutamate. We lowered a pipette containing 0.5 M glutamate into layer 2/3 of the visual cortex of a mouse that was labelled with iGluSnFR. We applied a range of currents (10, 20, 40, 60, 80 nA) and found that the fluorescence signals increased linearly ($R > 0.99$; $P < 0.0001$) and peaked at $\sim 60\%$ $\Delta F/F$ (data not shown). Thus, our *in vivo* imaging with iGluSnFR (for example, Extended Data Fig. 10) is probably revealing the true spatial profile of glutamate direction maps (Fig. 3) and orientation maps (Extended Data Fig. 1).

31. O'Herron, P. *et al.* Targeted labeling of neurons in a specific functional micro-domain of the neocortex by combining intrinsic signal and two-photon imaging. *J. Vis. Exp.* **70**, e50025 (2012).
32. Chen, T.-W. *et al.* Ultrasensitive fluorescent proteins for imaging neuronal activity. *Nature* **499**, 295–300 (2013).
33. Marvin, J. S. *et al.* An optimized fluorescent probe for visualizing glutamate neurotransmission. *Nature Methods* **10**, 162–170 (2013).
34. Kara, P. & Boyd, J. D. A micro-architecture for binocular disparity and ocular dominance in visual cortex. *Nature* **458**, 627–631 (2009).
35. Ringach, D. L., Shapley, R. M. & Hawken, M. J. Orientation selectivity in macaque V1: diversity and laminar dependence. *J. Neurosci.* **22**, 5639–5651 (2002).
36. Hedges, L. V. & Olkin, I. *Statistical Method for Meta-analysis* (Academic, 2014).
37. Chhatbar, P. Y. *et al.* Transcranial direct current stimulation post-stroke upper extremity motor recovery studies exhibit a dose-response relationship. *Brain Stimul.* **9**, 16–26 (2016).



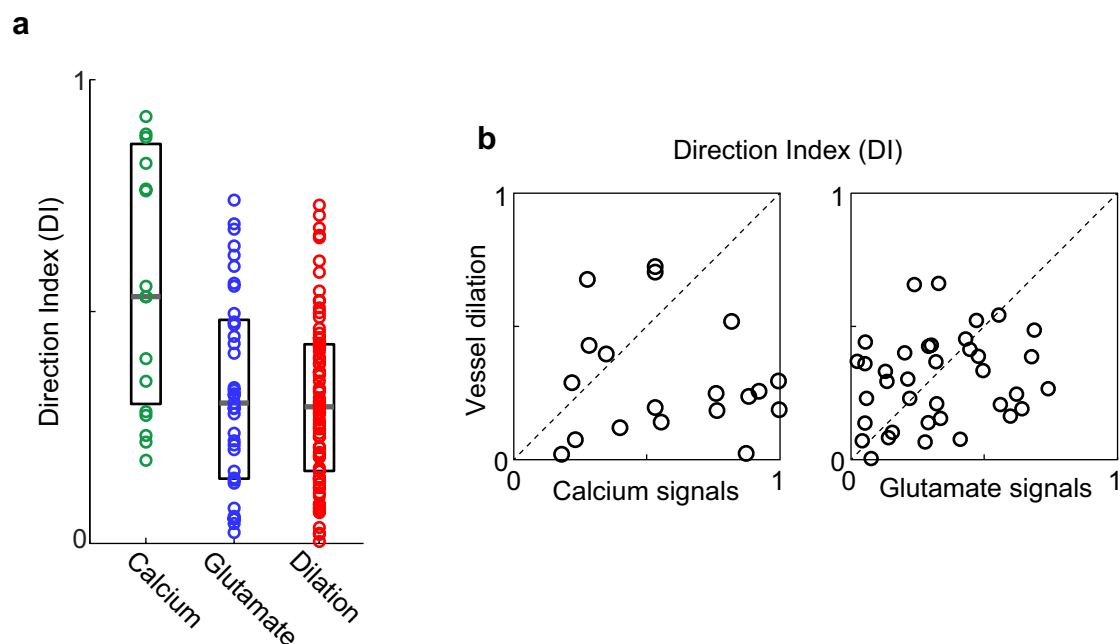
Extended Data Figure 1 | Glutamate release is organized into orientation maps. a, Region of cat visual cortex labelled with iGluSnFR. Pixels are colour-coded by preferred orientation with the brightness indicating the response strength. Time courses and polar plots (averages of

four trials) are shown for three regions of tissue with different orientation preferences. **b,** Orientation maps of iGluSnFR responses from a different cat. Time courses and polar plots are averages of ten trials.



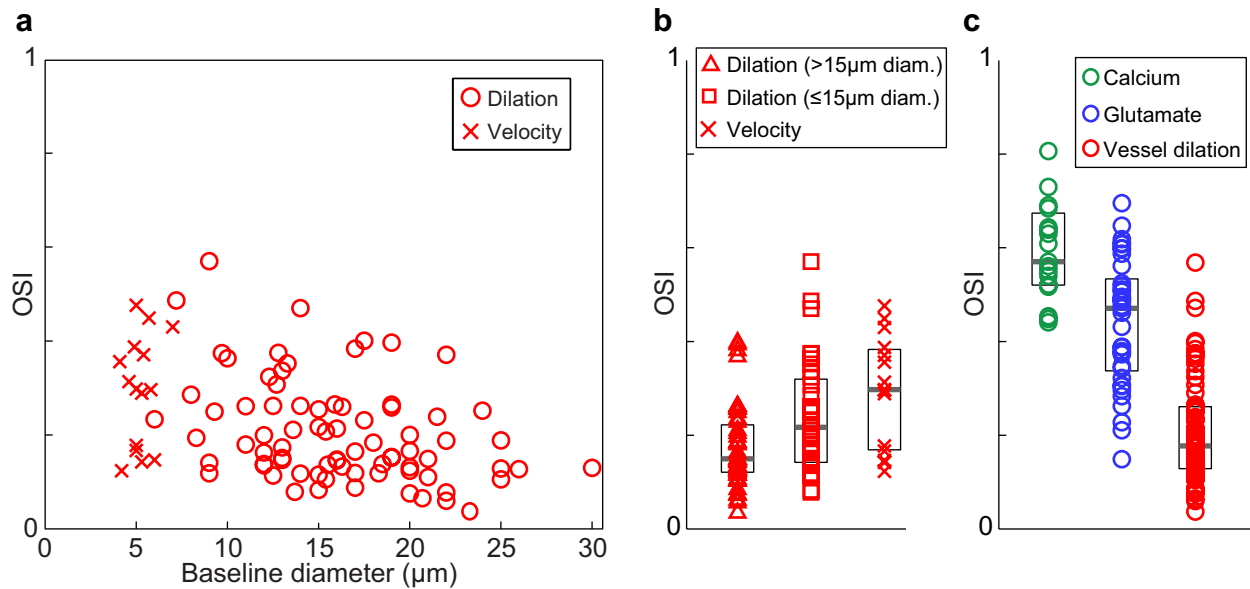
Extended Data Figure 2 | Arteriole dilation in the absence of glutamate signalling or local spiking. **a**, Time courses and polar plots of arteriole dilation (red) and the release of glutamate in a 400- μm -diameter window surrounding an arteriole (blue). Averages of eight trials are shown for vessel dilation and ten trials for glutamate responses. In time courses, error bands represent s.e.m. and grey bars represent the periods of visual stimulation. The responses to the 135° and 180° stimuli (outlined by the black box over the time courses) are large for the vessel dilation but virtually non-existent for the glutamate activity. **b**, Quantifying the relative amplitude of the vessel and neural responses to each of the eight stimulus directions for the single cat experiment shown in **a**. Each data point in the scatterplot represents the average response of the vessel and of the neural

tissue surrounding it to a single direction of visual stimulation, normalized by the response to the best direction. **c**, Quantifying the relative amplitude of vessel and neural responses across all cat experiments. Top panel shows glutamate versus dilation data ($n = 37$ windows and vessels in 5 cats) and the bottom panel shows calcium versus dilation responses ($n = 19$ windows and vessels in 8 cats). Each data point in the scatterplot is as described in **b**. The histograms at the top and right show the distributions of neural and dilation responses, respectively. In both population scatterplots, there are many data points in the top left quadrant, indicating stimuli that drove robust dilation responses but minimal glutamate or calcium responses. All data are from cat visual cortex layer 2/3.



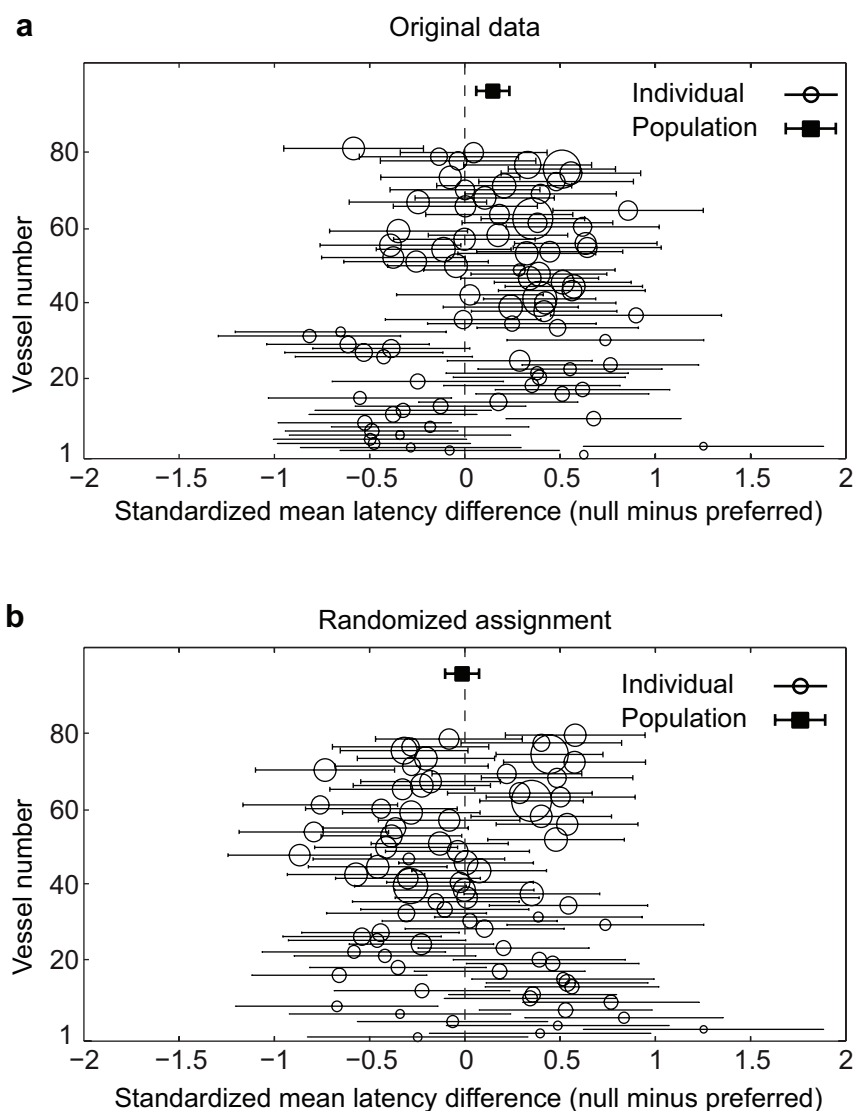
Extended Data Figure 3 | Direction selectivity of parenchymal vessels and of local spiking and synaptic activity. **a**, Population distributions of the direction index of calcium (green, $n = 19$ windows in 8 cats), glutamate (blue, $n = 37$ windows in 5 cats) and vessel dilation (red, $n = 79$ vessels in 18 cats) responses. All data were obtained from cat visual cortex and neural responses were pooled over 400- μm -diameter windows. The DI of spiking activity was greater than the DI of synaptic responses ($P < 0.01$, Mann–Whitney test) and the DI of vessel dilation ($P < 0.0005$,

Mann–Whitney test). The DI of synaptic activity was not different from the DI of vessel dilation ($P = 0.70$, Mann–Whitney test). Solid bars are medians and boxes show the interquartile range. **b**, For each vessel that had a corresponding 400- μm -diameter window of calcium or glutamate activity, the vessel direction index is plotted against the corresponding neural direction index. There was no significant correlation for calcium ($R = 0.2$, $P = 0.43$, $n = 19$ pairs) or glutamate ($R = 0.2$, $P = 0.23$, $n = 37$ pairs).



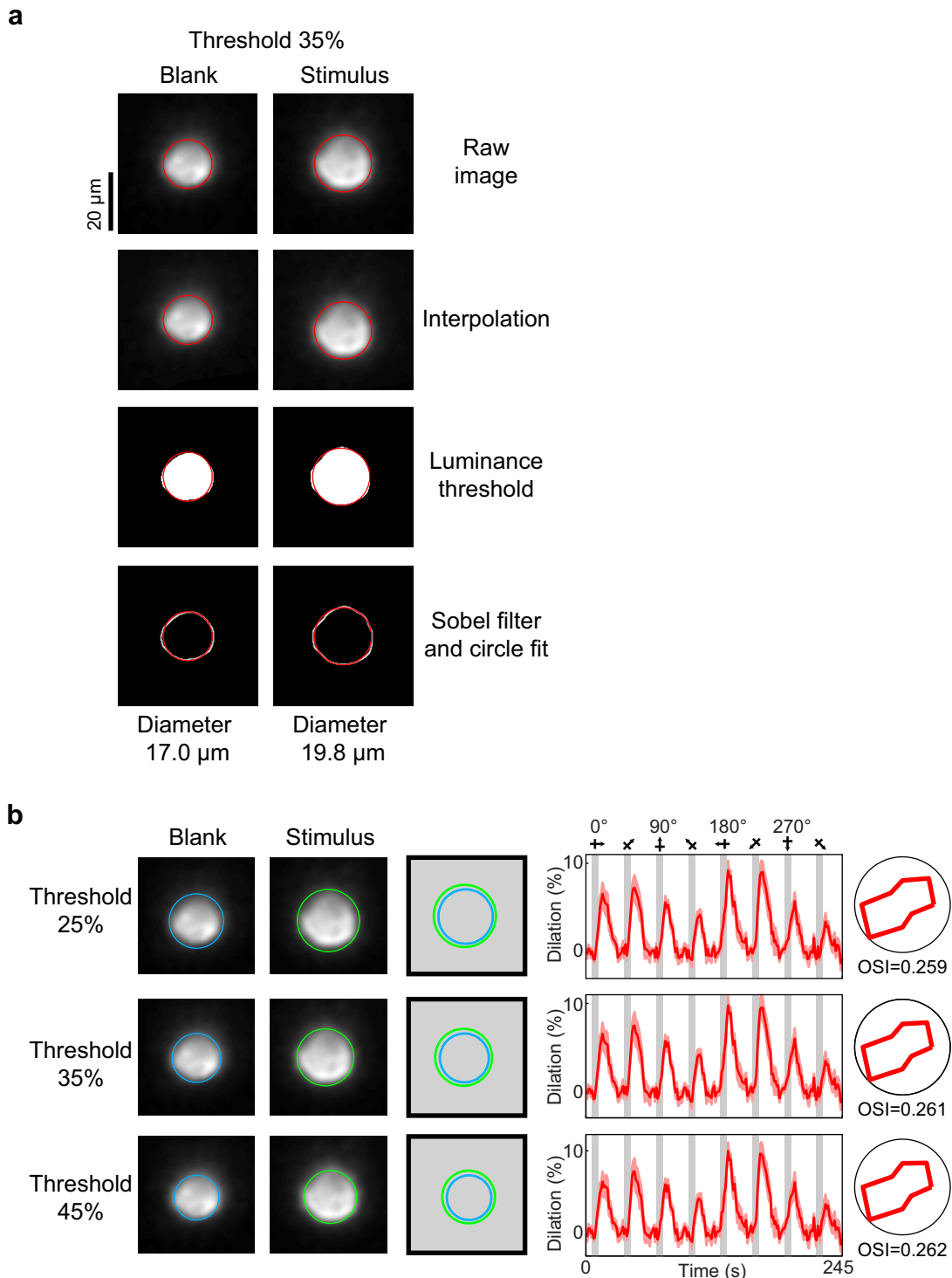
Extended Data Figure 4 | Dilation and velocity responses in parenchymal blood vessels with different baseline diameters. **a**, The diameter of all vessels and their OSI values from cat visual cortex layer 2/3. For arterioles, OSI was determined based on dilation ($n = 79$ vessels in 18 cats) whereas for capillaries, OSI was calculated from blood velocity measurements ($n = 15$ vessels in 7 cats). **b**, The distribution of OSI for the three subgroups of layer 2/3 vessels analysed in our study ($>15 \mu\text{m}$,

$n = 44$ vessels in 15 cats; $\leq 15 \mu\text{m}$, $n = 35$ vessels in 14 cats; capillaries, $n = 15$ vessels in 7 cats). The OSI of the $\leq 15 \mu\text{m}$ vessels was greater than the OSI of the $>15 \mu\text{m}$ vessels ($P < 0.05$, Mann-Whitney test). The OSI of the $\leq 15 \mu\text{m}$ vessels was not different from the OSI of the capillaries ($P = 0.16$, Mann-Whitney test). Solid bars are medians and boxes indicate the interquartile range. **c**, The OSI distribution of dilating vessels and 400 μm-diameter windows of calcium and glutamate responses.



Extended Data Figure 5 | Onset latency of dilation in parenchymal vessels. **a**, Vessel-by-vessel comparison of the onset latency difference between the response to preferred and orthogonal (null) stimulus orientations. Each whisker diagram represents a single vessel with the circle position indicating the standardized mean difference (SMD; calculated as Hedge's g) in latency. The whisker length represents the 95% confidence interval (CI) of the SMD. The size of the circle represents the weight given to the vessel when calculating the population summary SMD.

The population summary SMD is shown by the solid square with the error bands giving the 95% CI. The population average shows that parenchymal vessels responded significantly faster for the preferred than the null stimulus orientation. **b**, As a control, the analysis shown in **a** was repeated after randomizing the assignment of preferred and null on individual trials for each vessel. All data are from cat visual cortex layer 2/3 ($n = 79$ vessels in 18 cats).

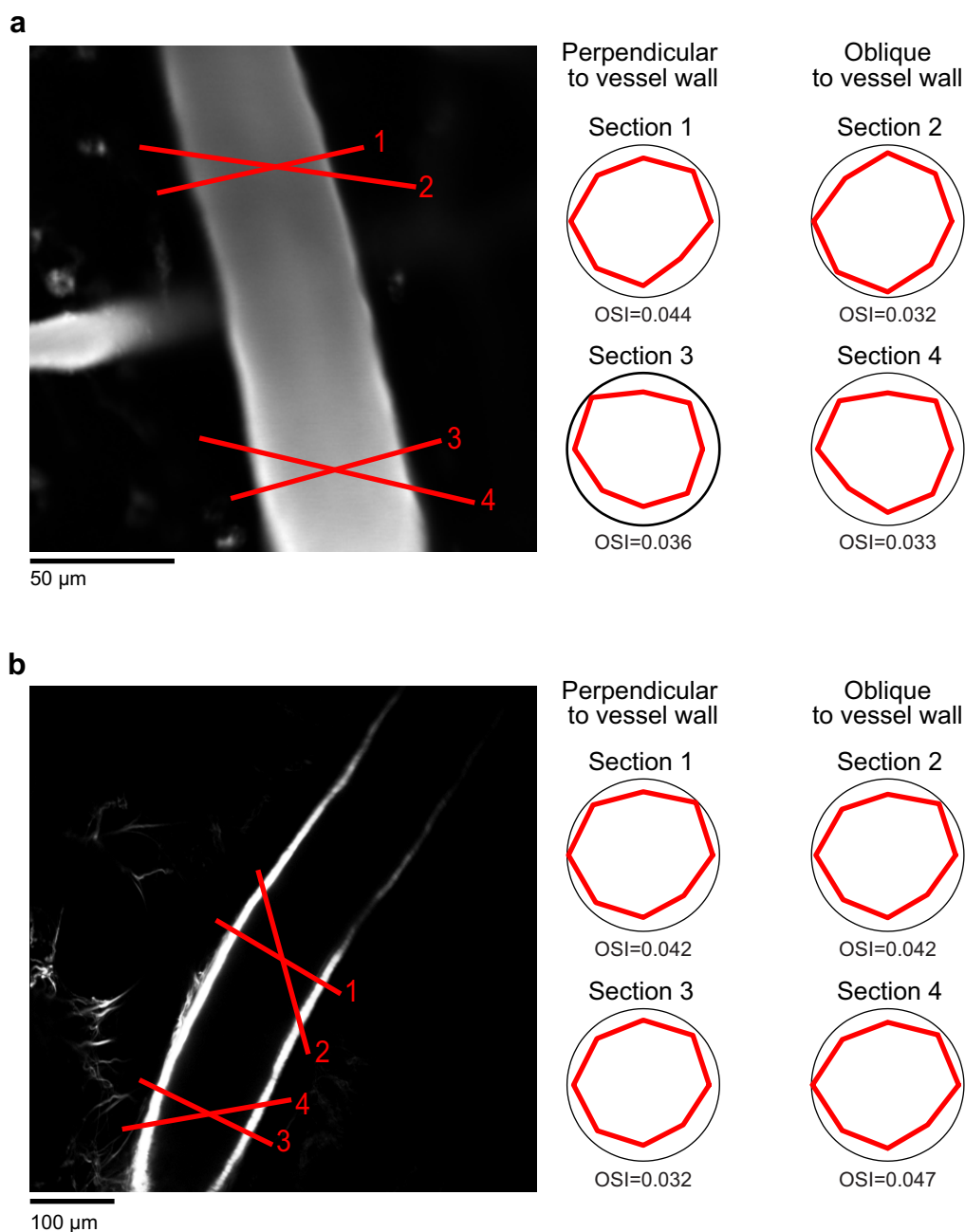


Extended Data Figure 6 | Dilation measurements with circle fitting.

a, The steps of the circle fitting algorithm are illustrated for a blank and a stimulus frame corresponding to the penetrating arteriole shown in the bottom panel of Fig. 1b. The raw image data (first panel) is oversampled by linear interpolation between pixels (second panel). Then a luminance threshold (a fraction of the gradient between the brightest and darkest pixel of the image) is applied (third panel). Finally, a two-dimensional sobel filter is applied to the thresholded pixels to detect the edge of the vessel (fourth panel). The circle fit is only applied to the pixels in the

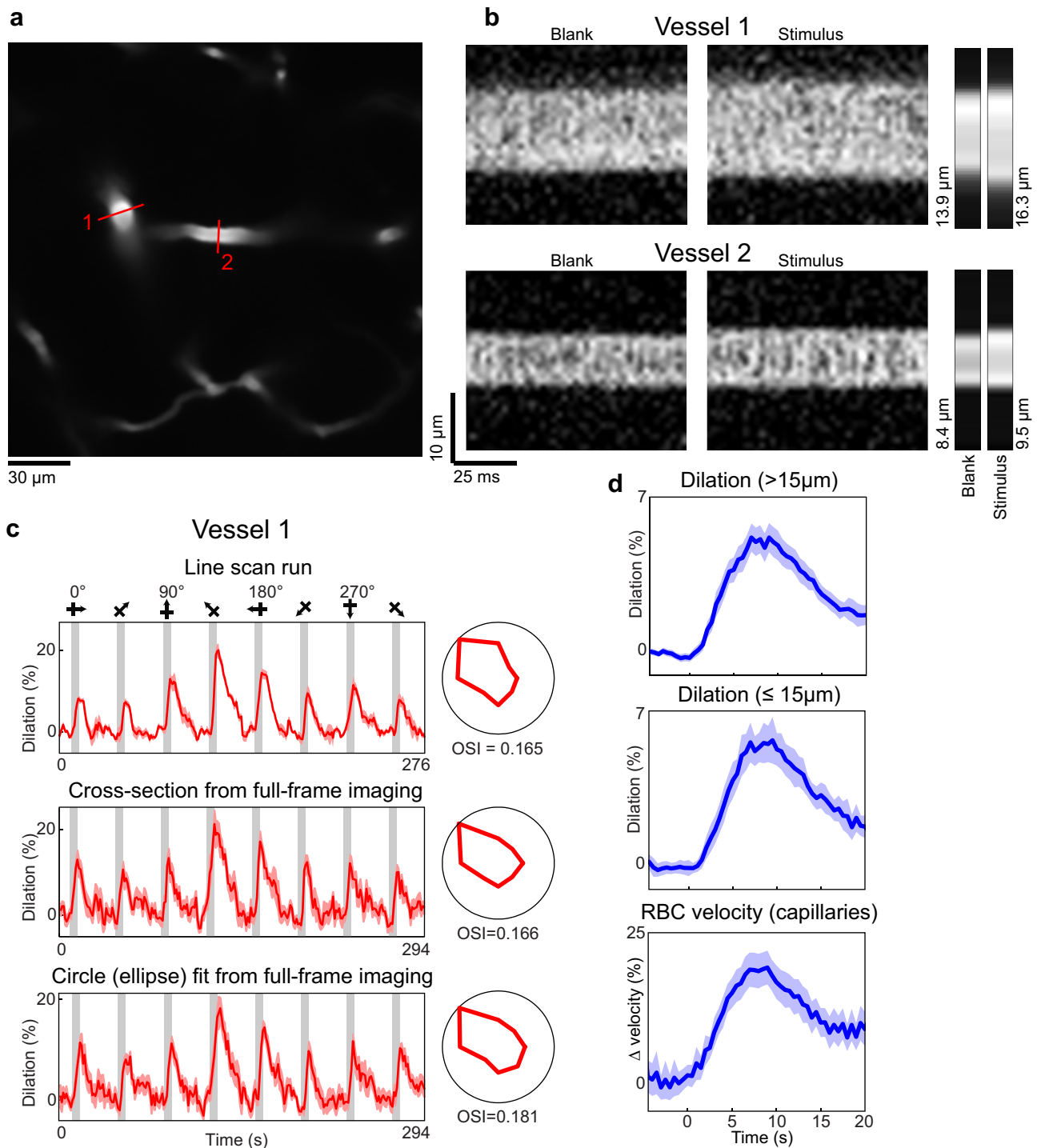
fourth panel but it is overlaid on all the panels for illustration purposes.

b, As the threshold is increased, fewer pixels pass the threshold and therefore the baseline diameter changes. However, the percentage change in diameter across baseline and stimulus presentations (the response amplitude) and the response selectivity remain the same. Note that for vessel geometries needing an elliptical fit rather than a circular fit (see Extended Data Fig. 8c and Methods), the shorter axis of the fitted ellipse was used to estimate the vessel diameter.



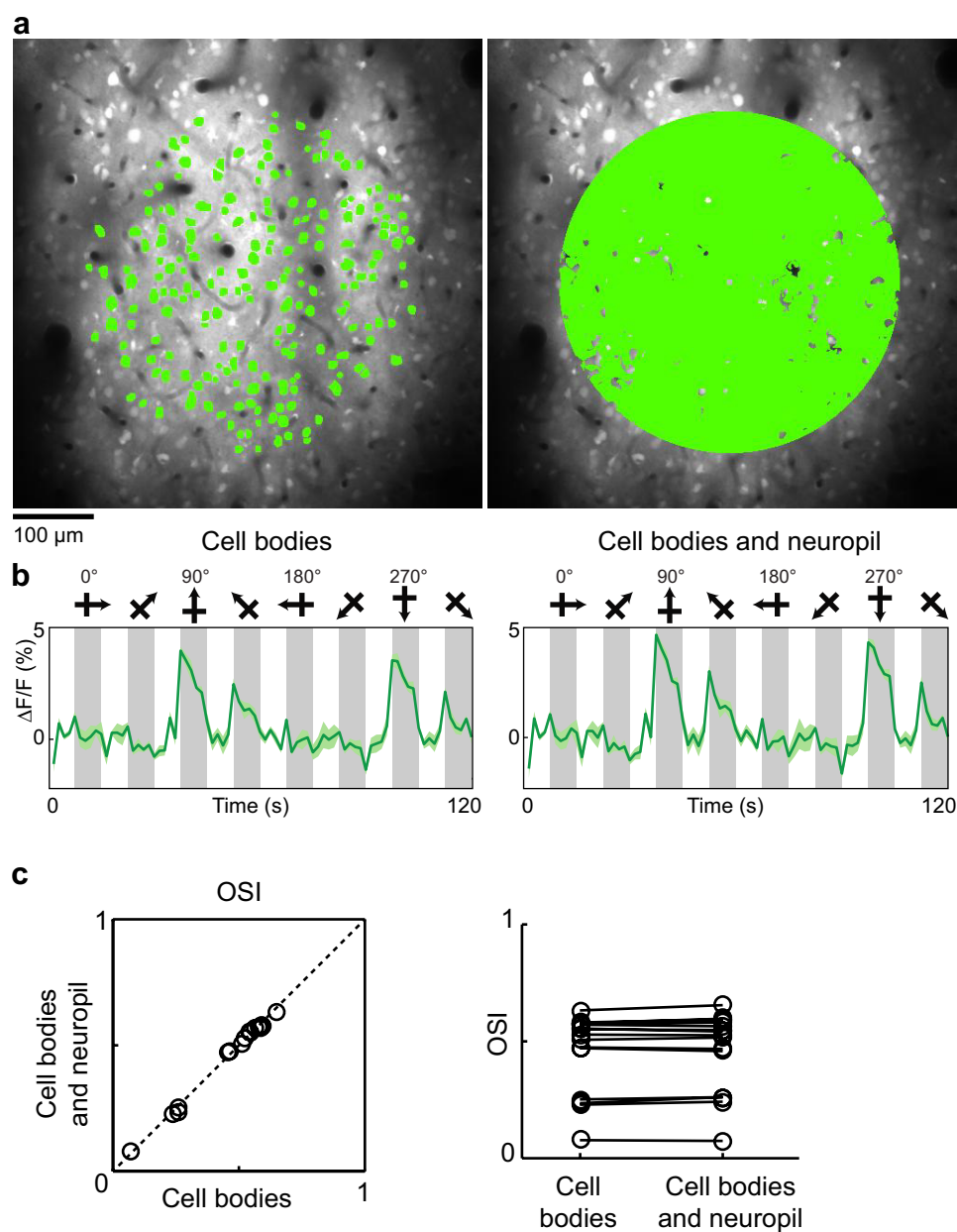
Extended Data Figure 7 | Dilation measurements using the cross-section algorithm do not depend on the precise location and angle of the selected cross-section. a, Example cat pial artery (from Fig. 1c) labelled with Texas Red Dextran. **b,** Another pial artery from a different

cat labelled with the artery-specific dye Alexa 633. Both arteries show similar tuning for cross-sections drawn $>100\mu\text{m}$ apart and also drawn perpendicular and obliquely relative to the vessel walls.



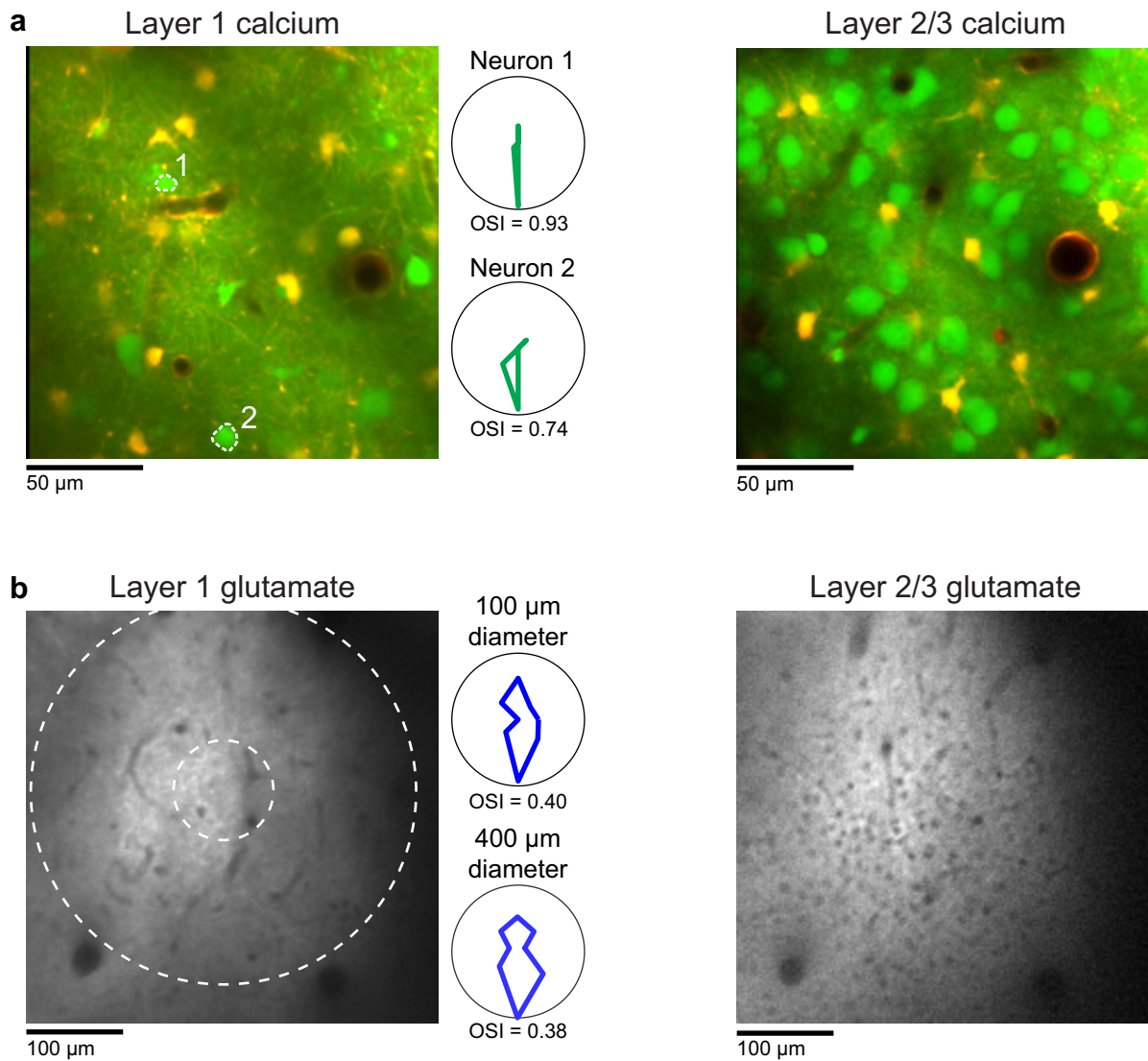
Extended Data Figure 8 | Dilation measurements in small arterioles and comparison of dilation measurement techniques. **a**, A penetrating artery (#1, the responses of which are shown in the top panel of Fig. 1b) and its daughter branch (#2) in cat layer 2/3 labelled with Texas Red Dextran. Red lines indicate the position of the laser scan path across the vessels for line-scan diameter measurements. **b**, Individual line-scans are stacked next to each other to create X-time (XT) images. The four large rectangular panels are XT images of a blank and stimulus frame for each of two vessels shown in **a**. The small panels to the right are the average across the image (~ 0.96 s) for each of the four frames. The computed diameter values are also shown. These images were oversampled by interpolating between pixels (by 5 times for vessel 1 and by 20 times for vessel 2) before the diameter was calculated. **c**, The time courses and polar plots of the

responses for three different diameter measurements are shown for vessel 1—as a line-scan, a cross-section from a full-frame imaging run (seven trials), and the circle fit from the full-frame imaging run. In this particular example we used an ellipse rather than a circle because of the elongation of the vessel due to its diving obliquely to the imaging plane. **d**, Time courses of the vessel responses to preferred stimulus orientations for the three groups of vessels shown in Extended Data Fig. 4b. The responses for each vessel were aligned by stimulus onset and binned in 400-ms bins. The population average was then smoothed with a three-frame running average. Mean responses in dark colours and light bands indicate s.e.m. Note that the similar error bands and temporal profiles indicate that the smallest vessels had a similar quality of responses to the larger ones.



Extended Data Figure 9 | Comparison of orientation selectivity in regions of calcium responses with and without neuropil. **a**, *In vivo* anatomical image of cells labelled with OGB-1 AM in cat visual cortex and selection of two different masks for quantitative analysis of orientation selectivity. Left, a 400 μm -diameter mask comprising soma pixels only. Right, a 400 μm -diameter mask comprising all significantly responding pixels (see Methods). **b**, The time courses of calcium responses computed

from the two masks. Time courses are averages of five trials, error bands represent s.e.m. and grey bars represent the periods of visual stimulation. **c**, For a population of 16 imaged regions (from 7 cats), the OSI was computed with the two masks and found to be indistinguishable (cell bodies only OSI mean \pm s.e.m. = 0.46 ± 0.04 ; cell bodies and neuropil OSI mean \pm s.e.m. = 0.47 ± 0.04 ; $P = 0.12$, paired t -test).



Extended Data Figure 10 | Orientation-selective responses in layer 1 neurons and synapses. **a**, Region of cat visual cortex labelled with OGB-1 AM (to measure spiking activity) and SR101 (to distinguish astrocytes). Note the much sparser density of neuronal cell bodies in layer 1 (left) compared with the higher density of cells deeper in layer 2/3 (right). The polar plots are the responses of the two layer 1 neurons labelled in the image.

b, Region of cat visual cortex labelled with iGluSnFR (to measure synaptic activity). Again the density of cell bodies (the small black holes) in layer 1 (left) is much lower than in layer 2/3 (right). The polar plots are the responses of a 400-µm- and 100-µm-diameter window of layer 1 glutamate activity.

Towards clinical application of pronuclear transfer to prevent mitochondrial DNA disease

Louise A. Hyslop^{1,2}, Paul Blakeley³, Lyndsey Craven⁴, Jessica Richardson¹, Norah M. E. Fogarty³, Elpida Fragouli⁵, Mahdi Lamb¹, Sissy E. Wamaitha³, Nilendran Prathalingam^{1,2}, Qi Zhang^{1†}, Hannah O'Keefe¹, Yuko Takeda¹, Lucia Arizzi^{1,2}, Samer Alfarawati⁵, Helen A. Tuppen⁴, Laura Irving^{1†}, Dimitrios Kalleas^{1†}, Meenakshi Choudhary², Dagan Wells⁶, Alison P. Murdoch², Douglass M. Turnbull⁴, Kathy K. Niakan³ & Mary Herbert^{1,2}

Mitochondrial DNA (mtDNA) mutations are maternally inherited and are associated with a broad range of debilitating and fatal diseases¹. Reproductive technologies designed to uncouple the inheritance of mtDNA from nuclear DNA may enable affected women to have a genetically related child with a greatly reduced risk of mtDNA disease. Here we report the first preclinical studies on pronuclear transplantation (PNT). Surprisingly, techniques used in proof-of-concept studies involving abnormally fertilized human zygotes² were not well tolerated by normally fertilized zygotes. We have therefore developed an alternative approach based on transplanting pronuclei shortly after completion of meiosis rather than shortly before the first mitotic division. This promotes efficient development to the blastocyst stage with no detectable effect on aneuploidy or gene expression. After optimization, mtDNA carryover was reduced to <2% in the majority (79%) of PNT blastocysts. The importance of reducing carryover to the lowest possible levels is highlighted by a progressive increase in heteroplasmy in a stem cell line derived from a PNT blastocyst with 4% mtDNA carryover. We conclude that PNT has the potential to reduce the risk of mtDNA disease, but it may not guarantee prevention.

Predicting the risk of serious disease in children of women who carry mtDNA mutations is complicated by a number of factors. Mutations in mtDNA can be either homoplasmic (all copies of mtDNA are mutated) or heteroplasmic (mixture of mutated and wild-type mtDNA). In the case of heteroplasmy, women produce oocytes with widely varying mutation loads³. While pathogenicity is generally proportional to the ratio of mutated to wild-type mtDNA, the severity of disease for a given mutation load can vary, even among homoplasmic individuals⁴. The resulting unpredictability in the risk of transmitting disease raises profoundly difficult reproductive decisions for women from affected families. While preimplantation genetic diagnosis (PGD) can be used to reduce the risk of mtDNA disease by identifying embryos with low mutation loads⁵, it is not useful for women who are homoplasmic for pathogenic mtDNA mutations⁶. In such cases, it may be possible to reduce the risk of transmission by transplanting the oocyte nuclear DNA to an enucleated donor oocyte free of pathogenic mtDNA mutations.

Progression through female meiosis offers a number of opportunities for transplanting nuclear DNA. Proof-of-concept studies^{7,8} indicate that transplantation of the nuclear genome between human oocytes arrested at metaphase of meiosis II (MII) is associated with a high incidence of abnormal fertilization⁷. An alternative approach

is to transplant the nuclear genome after fertilization, when the haploid maternal and paternal genomes are separately packaged in large, clearly visible pronuclei. First performed in mouse zygotes more than three decades ago⁹, PNT is typically performed during the G2 phase of the 1st mitotic cell cycle. Using this approach, we have previously demonstrated that PNT between abnormally fertilized human zygotes is technically feasible². However, their limited capacity for onward development has been a major barrier to further investigation of the therapeutic potential of PNT.

Here we investigate the effect of PNT on normally fertilized human zygotes. We found that the procedures (Extended Data Fig. 1a, b) previously used for abnormally fertilized zygotes² resulted in reduced survival. Because developmental competence is correlated with accelerated division to the two-cell stage¹⁰, we asked whether the timing of PNT might be too close to the onset of 1st mitosis in normally fertilized zygotes (Fig. 1a). To address this, we undertook a series of experiments in which the pronuclei were transplanted shortly after they first appear (~8 h after insemination; Fig. 1b and Supplementary Videos 1, 2). Initially, we added sucrose to the enucleation medium to facilitate enucleation and fusion by inducing shrinkage of the cytoplasm (Fig. 1b). However, this was later abandoned to reduce the karyoplast mtDNA content and had minimal effect on survival (see later). Our data indicate that early PNT (ePNT) promotes survival (92% versus 59% for late PNT (ltPNT); $P < 0.01$; Fig. 1c). Moreover, ePNT zygotes showed normal pronuclei abutment and division to the two-cell stage (Extended Data Fig. 1c, d), indicating that sperm centriole function was not disrupted¹¹.

Blastocyst formation, which is essential for implantation, occurs at 5–6 days after fertilization *in vitro*, and is marked by allocation of cells to the inner cell mass (ICM), or to an outer layer of trophectoderm cells¹². The morphology of the ICM and trophectoderm correlates well with implantation and is used to assess blastocyst quality in clinical *in vitro* fertilization (IVF) programmes (Extended Data Fig. 2a–d). While the increased survival of ePNT zygotes (series I) resulted in improved blastocyst formation compared with ltPNT, both approaches produced few good quality blastocysts (Extended Data Fig. 2e, f). Control experiments in which pronuclei were replaced in the same zygote (autologous ePNT) indicated that blastocyst quality was compromised by the manipulations (Fig. 2a and Extended Data Fig. 2f). To address this, we modified the manipulation medium, removing Ca^{2+} and Mg^{2+} and reducing by tenfold the concentration of the fusogen, haemagglutinating virus of Japan envelope (HVJ-E)⁸. In addition, we switched from a two-step to a single-step culture medium,

¹Wellcome Trust Centre for Mitochondrial Research, Institute of Genetic Medicine, Biomedicine West Wing, Centre for Life, Times Square, Newcastle upon Tyne NE1 3BZ, UK. ²Newcastle Fertility Centre, Biomedicine West Wing, Centre for Life, Times Square, Newcastle upon Tyne NE1 4EP, UK. ³The Francis Crick Institute, Human Embryo and Stem Cell Laboratory, Mill Hill Laboratory, Mill Hill, London NW7 1AA, UK. ⁴Wellcome Trust Centre for Mitochondrial Research, Institute of Neuroscience, Newcastle University, The Medical School, Framlington Place, Newcastle upon Tyne NE2 4HH, UK. ⁵Reprogenetics UK, Institute of Reproductive Sciences, Oxford Business Park North, Oxford OX4 2HW, UK. ⁶University of Oxford, Nuffield Department of Obstetrics and Gynaecology, John Radcliffe Hospital, Oxford OX3 9DU, UK. [†]Present addresses: Department of Cell Biology, Academy of Military Medical Sciences, No. 27th Taiping Road, HaiDian, Beijing 100850, China (Q.Z.); Gateshead Fertility Unit, Gateshead Health NHS Trust, Queen Elizabeth Hospital, Sheriff Hill, Gateshead NE9 6SX, UK (L.I.); St Mary's Hospital, Department of Reproductive Medicine, Old Saint Mary's Hospital, Oxford Road, Manchester M13 9WL, UK (D.K.).

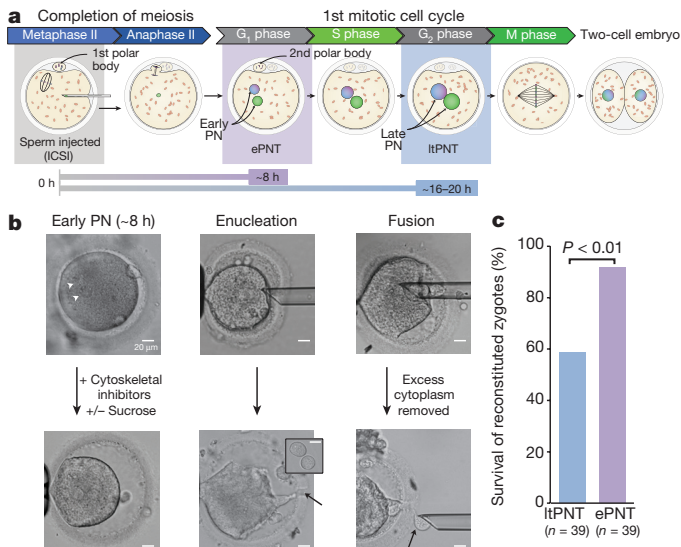


Figure 1 | Early PNT promotes survival of normally fertilized zygotes after PNT. **a**, Progression from MII arrest to completion of the 1st mitosis showing timings of ePNT and ItPNT. ICSI, intracytoplasmic sperm injection. **b**, Images show the steps involved in ePNT. Left, arrowheads indicate the pronuclei (PN). Middle, enucleation pipette inserted through a laser-induced opening in the zona pellucida (arrow, bottom). Bottom, enucleated zygote (cytoplasm). Inset shows two karyoplasts, each consisting of a single pronucleus surrounded by a small amount of cytoplasm. Right, karyoplasts treated with HVJ-E and inserted under the zona pellucida. Bottom, arrow indicates removal of excess cytoplasm (see Supplementary Video 2). **c**, Survival of reconstituted ePNT and ItPNT zygotes ($P < 0.01$). Comparisons by χ^2 test.

in which embryos remained for the duration of culture. Under these conditions (ePNT series II), blastocyst formation and quality did not differ between unmanipulated controls and technical controls (Fig. 2a, b). Similarly, heterologous ePNT, which involved reciprocal transfers between zygotes from fresh and vitrified oocytes, had no detectable effect on blastocyst quality (Fig. 2b, c). Consistent with

the improved quality, nuclear counts indicated that ePNT blastocyst cell numbers were equivalent to controls (Extended Data Fig. 2g, h). However, heterologous ePNT resulted in reduced blastocyst formation (Fig. 2b), possibly due to an effect of vitrification at the MII stage¹³, which was not ameliorated by delaying vitrification until after exit from MII (Extended Data Fig. 3a–f).

Analysis of aneuploidy by array-based comparative genomic hybridization (array-CGH) indicated that while the majority of poor quality ePNT blastocysts were aneuploid for multiple chromosomes (Fig. 2d and Extended Data Fig. 4), the overall incidence of aneuploidy was comparable between ePNT and control blastocysts, and was similar to a reference data set of IVF blastocysts, in which female age was matched to the karyoplast donors (Fig. 2e). These data indicate that the ePNT procedure does not result in an increased incidence of aneuploid blastocysts.

We next determined whether ePNT alters the pattern of gene expression in human blastocysts by performing RNA sequencing (RNA-seq) on single cells microdissected from ePNT and control blastocysts (Extended Data Fig. 5a, b). For reference, we also included a previously published series of unmanipulated blastocysts¹⁴. The ePNT blastocysts included in these experiments were generated by fusion of cytoplasts and karyoplasts with the same (autologous and homologous ePNT), or different (heterologous ePNT), mitochondrial genotypes (Extended Data Fig. 5b).

To test for differences in global gene expression, we performed principal component analysis (PCA) on normalized RNA-seq data (Extended Data Fig. 5c). We first determined whether PCA is sufficiently sensitive to detect differences in global gene expression between good and poor quality blastocysts. Plotting PC1 against PC2, which together account for the largest contributions to variation in global gene expression, revealed a high proportion of outliers among samples from poor quality blastocysts (Fig. 3a, b). By contrast, samples from good quality ePNT blastocysts clustered closely with controls (Fig. 3c). To determine whether additional principal components, however minor, might distinguish differences between good quality ePNT and control blastocysts, we plotted all combinations of the first ten principal components. In each combination we found that ePNT samples cluster with controls (Extended Data Fig. 6a). Furthermore,

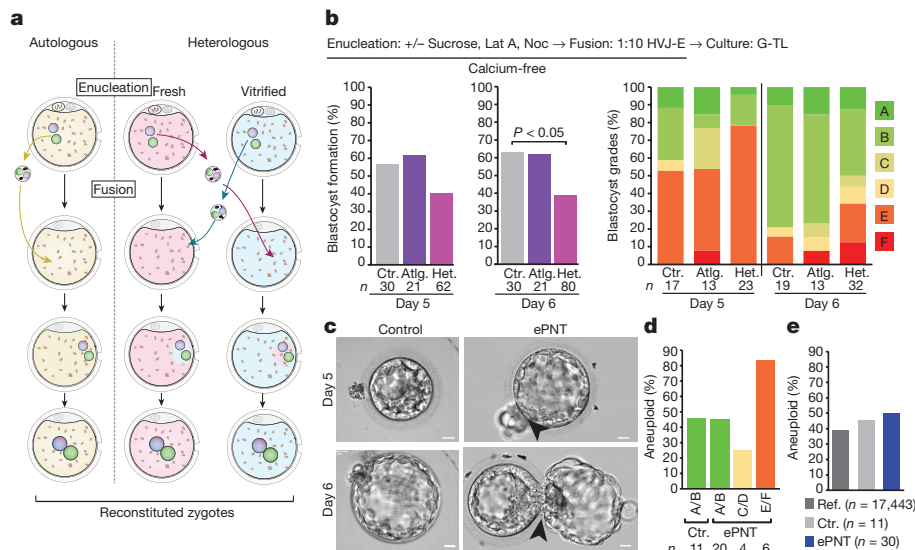


Figure 2 | Blastocyst development after ePNT. **a**, Autologous ePNT (left) and heterologous ePNT (right). **b**, Blastocyst formation and quality (series II). Zygotes ($n = 131$ from 30 donors) were either unmanipulated (control (Ctr.), $n = 30$), or used for autologous (Atlg.; $n = 21$) or heterologous (Het.; $n = 80$) ePNT. Heterologous ePNT blastocyst formation was reduced compared with control ($P < 0.05$; χ^2 test). Blastocyst quality is similar between the three groups (not significant; Fisher's exact test). Lat A, latrunculin A; Noc, nocodazole. **c**, Images showing good quality

control and ePNT blastocysts. Arrowheads, ePNT blastocyst hatching through laser-induced opening in the zona pellucida. Scale bars, 20 μ m. **d**, Aneuploidy in cells sampled from blastocysts (grades A–F) detected by array-CGH blind to sample origin (n = blastocysts; not significant, Fisher's exact test). **e**, Aneuploidy in controls and ePNT blastocysts not significantly different from a reference population (Ref.) of IVF blastocysts (χ^2 test). Source data are available online for **b**.

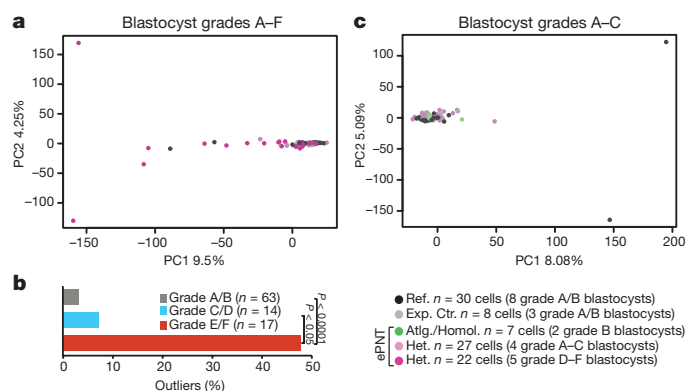


Figure 3 | Gene expression patterns in unmanipulated controls and ePNT blastocysts. **a**, PCA of single-cell RNA-seq data showing global gene expression profiles in a reference population ($n = 30$ samples; 8 blastocysts), experimental controls ($n = 8$ samples; 3 blastocysts) and ePNT blastocysts ($n = 56$ samples; 11 blastocysts). Each data point represents a single cell. ePNT blastocysts include heterologous (Het.), autologous (Atlg.) and homologous (Homol.) transfers (Extended Data Fig. 5b). The heterologous group is subdivided according to blastocyst grade. **b**, Graph shows an increased percentage of outliers in poor quality blastocysts (P values shown; Fisher's exact test). **c**, PCA of single-cell RNA-seq data comparing control samples with good quality ePNT blastocysts. PCA was performed blind to sample origin. The numbers of samples and blastocysts are shown.

we were able to distinguish distinct populations of cells corresponding to the three cell lineages of the mammalian blastocyst¹⁴ (Extended Data Fig. 6b). This was confirmed by t-distributed stochastic neighbour embedding (t-SNE), a nonlinear method for dimensionality reduction¹⁵ (Extended Data Fig. 6c). Consistent with this, unsupervised hierarchical clustering revealed that ePNT and control samples cluster together on the basis of lineage (Extended Data Fig. 7a). Together, these findings indicate that single-cell RNA-seq reliably detects differences in gene expression, and that global and lineage-associated gene expression is indistinguishable between control and ePNT blastocysts.

To address the question of whether ePNT specifically affects expression of mtDNA-encoded oxidative phosphorylation (OXPHOS) genes, we generated a heatmap after unsupervised hierarchical clustering. This revealed wide variation in the level of mtDNA OXPHOS gene expression within and between ePNT and control blastocysts. However, samples from both groups clustered together, irrespective of whether the karyoplast and cytoplasm contained the same, or different, mitochondrial genomes (Extended Data Fig. 7b). This suggests that switching nuclear genomes does not alter mitochondrial gene expression.

On the basis of evidence from a range of pathogenic mutations, the probability of developing or transmitting disease is low when mutation loads are $<18\%$ (ref. 16) and $<5\%$ (ref. 17), respectively. Thus, reducing the contribution of karyoplast mtDNA to $<5\%$ has the potential to prevent transmission to subsequent generations. The level of mtDNA carryover during transplantation of pronuclei was measured by pyrosequencing (Extended Data Fig. 8a–c) using clumps of cells from day 6 ePNT blastocysts ($n = 40$) generated by reciprocal transfer between zygotes from fresh and vitrified oocytes (Fig. 4a). Despite removal of excess cytoplasm before karyoplast fusion (Supplementary Video 2 and Fig. 1b), we found that heteroplasmy was $>5\%$ in a high proportion (28%) of samples enucleated in the presence of sucrose. This was significantly reduced by the omission of sucrose (Fig. 4b and Extended Data Fig. 8d), probably due to an osmotic effect. Carryover of mtDNA was further reduced in blastocysts whose cytoplasts originated from freshly harvested rather than vitrified oocytes (Fig. 4c), which may be explained by a high incidence of cytoplasmic leakage from the latter. Thus, the efficacy of ePNT in preventing mtDNA

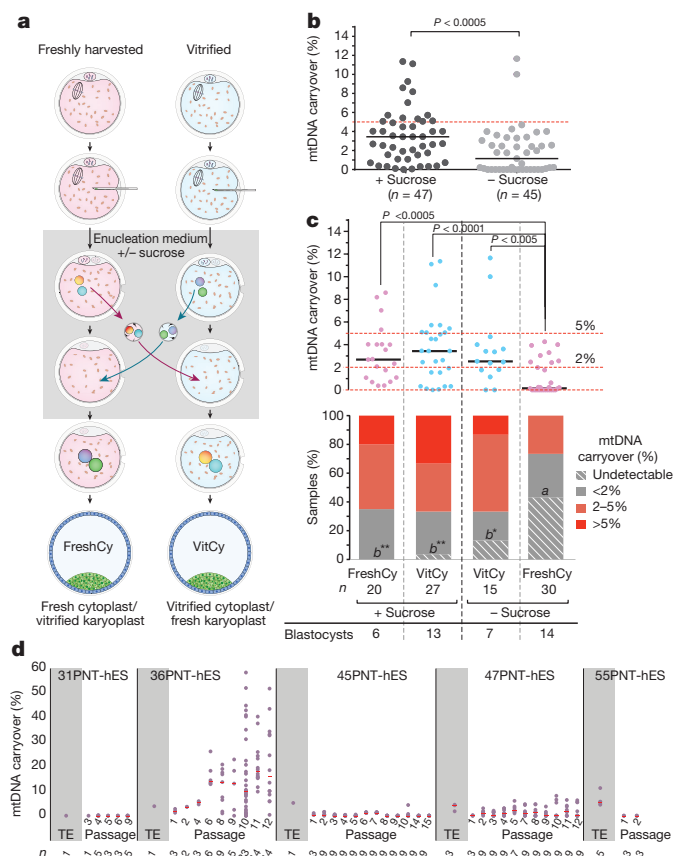


Figure 4 | Carryover of karyoplast mtDNA in ePNT blastocysts. **a**, Reciprocal ePNT between zygotes from fresh and vitrified oocytes, enucleated in the presence or absence of sucrose, resulting in four experimental groups: FreshCy \pm sucrose; VitCy \pm sucrose. **b**, mtDNA carryover in day 6 blastocysts arising from ePNT in the presence or absence of sucrose; horizontal lines represent means ($P < 0.0005$; two-sided Mann-Whitney U -test). **c**, mtDNA carryover in day 6 blastocysts (FreshCy and VitCy) after ePNT in the presence or absence of sucrose; horizontal lines represent medians (P values shown, two-sided Mann-Whitney U -test). Stacked graph showing the percentage of samples with specified levels of heteroplasmy. Groups with different letters have significantly different proportions of samples with undetectable levels of carryover ($*P < 0.05$; $**P < 0.01$; χ^2 test). **b**, **c**, Data points represent means of 2–3 technical replicates; n = number of samples, numbers of blastocysts as shown in **c**. **d**, mtDNA carryover in PNT-hES cell lines ($n = 5$). TE, trophectoderm. Data points represent 2–3 technical replicates. Median value (red) for each passage in which >1 sample was tested; n = number of samples tested for each passage. Source data files are available online for **b–d**.

disease is likely to be increased by vitrifying patient rather than donor oocytes. On the basis of our findings, this approach results in $<2\%$ heteroplasmy in the majority (79%) of blastocysts and none with $>5\%$ heteroplasmy (Extended Data Fig. 8e, f). Notably, those with $>2\%$ heteroplasmy were predicted by technical problems such as leakage from the cytoplasm or inadequate shearing of cytoplasm from the karyoplast. Such factors could be taken into account when selecting embryos for use in clinical treatment.

To assess the potential fate of karyoplast mtDNA under conditions in which it can replicate¹⁸, we derived human embryonic stem (hES) cell lines ($n = 5$) from ePNT blastocysts (Extended Data Fig. 9a–f). While all PNT-hES cell lines showed low levels of heteroplasmy at passage 1 (P1), one line (36PNT-hES), derived from a blastocyst with 4% mtDNA carryover, showed an upward drift with wide variation in heteroplasmy between colonies by P12 (Fig. 4d). This was confirmed by experiments in which individual colonies were subcloned and cultured for multiple passages (Extended Data Fig. 10). Interestingly,

the karyoplast and cytoplasm donors for 36PNT belonged to the same mtDNA haplogroup (Extended Data Fig. 9f), however, we cannot exclude the possibility that sequence variants in the karyoplast donor mtDNA might have conferred a replicative advantage¹⁹. While the biological basis remains to be established, the relevance of the increased heteroplasmy to development *in vivo* is unclear. For example, recent reports indicate that pluripotent cells derived from heteroplasmic fibroblasts exhibit a bimodal drift towards homoplasmy, which is not observed in the parental lines^{20,21}. Moreover, with the exception of one controversial case^{22,23}, a number of reports^{24,25}, together with our own unpublished data, indicate that the level of heteroplasmy in preimplantation embryos mirrors that in babies born after PGD. Nonetheless, the finding underscores the importance of reducing mtDNA carryover to the lowest possible levels and suggests that guaranteed prevention of disease will depend on complete elimination of karyoplast mtDNA.

The work reported here represents a considerable advance towards understanding the therapeutic potential of PNT in preventing transmission of mtDNA disease. Transplanting the pronuclei shortly after completion of meiosis resulted in improved survival. Further optimization of enucleation and embryo culture procedures promoted development of good quality blastocysts whose gene expression and incidence of aneuploidy did not differ from controls. Our findings also indicate that vitrification of patient rather than donor oocytes will probably minimize mtDNA carryover. This offers the added advantage of stockpiling patient oocytes before they become susceptible to age-related meiotic aneuploidy²⁶. Given the low levels of mtDNA carryover using optimized procedures, we believe that ePNT has the potential to reduce risk of mtDNA disease. However, until more is known about the postimplantation fate of karyoplast mtDNA, it should be considered in combination with prenatal screening.

Online Content Methods, along with any additional Extended Data display items and Source Data, are available in the online version of the paper; references unique to these sections appear only in the online paper.

Received 18 February 2015; accepted 3 May 2016.

Published online 8 June 2016.

- Schon, E. A., DiMauro, S. & Hirano, M. Human mitochondrial DNA: roles of inherited and somatic mutations. *Nature Rev. Genet.* **13**, 878–890 (2012).
- Craven, L. *et al.* Pronuclear transfer in human embryos to prevent transmission of mitochondrial DNA disease. *Nature* **465**, 82–85 (2010).
- Wallace, D. C. & Chalkia, D. Mitochondrial DNA genetics and the heteroplasmy conundrum in evolution and disease. *Cold Spring Harb. Perspect. Biol.* **5**, a021220 (2013).
- McFarland, R. *et al.* Multiple neonatal deaths due to a homoplasmic mitochondrial DNA mutation. *Nature Genet.* **30**, 145–146 (2002).
- Steffann, J. *et al.* Data from artificial models of mitochondrial DNA disorders are not always applicable to humans. *Cell Reports* **7**, 933–934 (2014).
- Richardson, J. *et al.* Concise reviews: assisted reproductive technologies to prevent transmission of mitochondrial DNA disease. *Stem Cells* **33**, 639–645 (2015).
- Tachibana, M. *et al.* Towards germline gene therapy of inherited mitochondrial diseases. *Nature* **493**, 627–631 (2013).
- Paull, D. *et al.* Nuclear genome transfer in human oocytes eliminates mitochondrial DNA variants. *Nature* **493**, 632–637 (2013).
- McGrath, J. & Solter, D. Nuclear transplantation in the mouse embryo by microsurgery and cell fusion. *Science* **220**, 1300–1302 (1983).
- Fenwick, J., Platteau, P., Murdoch, A. P. & Herbert, M. Time from insemination to first cleavage predicts developmental competence of human preimplantation embryos *in vitro*. *Hum. Reprod.* **17**, 407–412 (2002).
- Schatten, H. & Sun, Q. Y. The role of centrosomes in mammalian fertilization and its significance for ICSI. *Mol. Hum. Reprod.* **15**, 531–538 (2009).

- Niakan, K. K., Han, J., Pedersen, R. A., Simon, C. & Pera, R. A. R. Human pre-implantation embryo development. *Development* **139**, 829–841 (2012).
- Forman, E. J. *et al.* Oocyte vitrification does not increase the risk of embryonic aneuploidy or diminish the implantation potential of blastocysts created after intracytoplasmic sperm injection: a novel, paired randomized controlled trial using DNA fingerprinting. *Fertil. Steril.* **98**, 644–649 (2012).
- Blakeley, P. *et al.* Defining the three cell lineages of the human blastocyst by single-cell RNA-seq. *Development* **142**, 3151–3165 (2015).
- van der Maaten, L. & Hinton, G. Visualizing high-dimensional data using t-SNE. *J. Mach. Learn. Res.* **9**, 2579–2605 (2008).
- Hellebrekers, D. M. E. I. *et al.* PGD and heteroplasmic mitochondrial DNA point mutations: a systematic review estimating the chance of healthy offspring. *Hum. Reprod. Update* **18**, 341–349 (2012).
- Samuels, D. C., Wonnapijit, P. & Chinnery, P. F. Preventing the transmission of pathogenic mitochondrial DNA mutations: can we achieve long-term benefits from germ-line gene transfer? *Hum. Reprod.* **28**, 554–559 (2013).
- Facucho-Oliveira, J. M. & St John, J. C. The relationship between pluripotency and mitochondrial DNA proliferation during early embryo development and embryonic stem cell differentiation. *Stem Cell Rev.* **5**, 140–158 (2009).
- Burgstaller, J. P., Johnston, I. G. & Poulton, J. Mitochondrial DNA disease and developmental implications for reproductive strategies. *Mol. Hum. Reprod.* **21**, 11–22 (2015).
- Hämäläinen, R. H. *et al.* Tissue- and cell-type-specific manifestations of heteroplasmic mtDNA 3243A>G mutation in human induced pluripotent stem cell-derived disease model. *Proc. Natl Acad. Sci. USA* **110**, E3622–E3630 (2013).
- Lee, H. S. *et al.* Rapid mitochondrial DNA segregation in primate preimplantation embryos precedes somatic and germline bottleneck. *Cell Reports* **1**, 506–515 (2012).
- Treff, N. R. *et al.* Blastocyst preimplantation genetic diagnosis (PGD) of a mitochondrial DNA disorder. *Fertil. Steril.* **98**, 1236–1240 (2012).
- Mitalipov, S., Amato, P., Parry, S. & Falk, M. J. Limitations of preimplantation genetic diagnosis for mitochondrial DNA diseases. *Cell Reports* **7**, 935–937 (2014).
- Sallevelt, S. C. E. H. *et al.* Preimplantation genetic diagnosis in mitochondrial DNA disorders: challenge and success. *J. Med. Genet.* **50**, 125–132 (2013).
- Steffann, J. *et al.* Analysis of mtDNA variant segregation during early human embryonic development: a tool for successful NARP preimplantation diagnosis. *J. Med. Genet.* **43**, 244–247 (2006).
- Herbert, M., Kalleas, D., Cooney, D., Lamb, M. & Lister, L. Meiosis and maternal aging: insights from aneuploid oocytes and trisomy births. *Cold Spring Harb. Perspect. Biol.* **7**, a017970 (2015).

Supplementary Information is available in the online version of the paper.

Acknowledgements We are very grateful to those who donated gametes for this research and we thank M. Nesbitt and K. Lennox for obtaining their consent. We also thank P. Chinnery and V. Floros for helpful discussion. The work was funded by the Wellcome Trust (096919) and by grants from the National Institute for Health Research (NIHR) Newcastle Biomedical Research Centre and the Barbour Foundation. K.K.N. and co-workers are supported by The Francis Crick Institute, which receives its core funding from Cancer Research UK, the UK Medical Research Council (MC_UP_1202/9) and the Wellcome Trust, and by the March of Dimes Foundation (FY11-436). D.W. and co-workers are funded by the NIHR Oxford Biomedical Research Centre.

Author Contributions M.H. and L.A.H. conceived and designed the PNT experiments. L.A.H., L.I., L.C. and L.A. performed PNT experiments and embryo manipulations. J.R., D.K. and Q.Z. performed cell counts. D.W., E.F. and S.A. performed whole-genome amplification and array-CGH. K.K.N., P.B. and N.M.E.F. performed RNA-seq experiments. L.C., H.A.T. and D.M.T. measured mtDNA carryover and performed mtDNA haplogroup analysis. N.P., K.K.N., N.M.E.F., S.E.W., Y.T. and H.O'K. derived, cultured and characterized ES cell lines. K.K.N., P.B., M.L., J.R., L.A.H., L.C., Y.T., P.B. and M.H. analysed data. A.P.M. and M.C. coordinated the oocyte donation program. M.H. wrote the manuscript with input from D.M.T., D.W., K.K.N., J.R. and M.L.

Author Information Raw RNA-seq data and reads per kilobase per million mapped reads (RPKM) table have been deposited in the Gene Expression Omnibus under accession number GSE76284. Reprints and permissions information is available at www.nature.com/reprints. The authors declare no competing financial interests. Readers are welcome to comment on the online version of the paper. Correspondence and requests for materials should be addressed to M.H. (mary.herbert@ncl.ac.uk).

METHODS

Human oocytes and manipulations. The study was approved by the Newcastle and North Tyneside Research Ethics Committee and was licensed by the UK Human Fertilisation and Embryology Authority (HFEA). Informed consent was obtained from all donors by research nurses who were not directly involved in the research, or in the clinical treatments of women participating in the study. Human oocytes ($n = 523$) included in this study were donated either by women undergoing infertility treatment ($n = 44$ oocytes from 6 donors, age range 25–36 years) as part of an ‘egg sharing’ programme²⁷, or by non-patient donors ($n = 479$ oocytes from 57 donors, age range 21–36 years). Donors were compensated in accordance with current HFEA guidance on payments for donors²⁸. Non-patient donors received financial compensation of £500 per donation cycle. Compensation under the ‘egg share’ programme consisted of a subsidy (£1,500) from research funds towards the cost of treatment for self-funded patients²⁷, or an additional fully funded treatment cycle for those who did not become pregnant after NHS-funded treatment.

Oocytes were collected by ultrasound-guided follicle aspiration and the surrounding cumulus cells were removed using hyaluronidase (HYASE; Vitrolife). MII oocytes were identified by the presence of the 1st polar body and were fertilized by intracytoplasmic sperm injection (ICSI) using sperm donated specifically for this project. The experiments were not randomized. The investigators were not blinded to allocation during experiments and outcome assessment, except for aneuploidy and gene expression analysis.

Oocyte vitrification. MII oocytes were either vitrified or used immediately for PNT experiments. The majority ($n = 107$) of vitrified oocytes were vitrified at the MII stage. We also conducted a series of experiments in which vitrification was performed after completion of MII (at the 2PB stage; ~5.5 h post-ICSI; $n = 34$), to determine whether blastocyst development might be improved. Vitrification and warming were performed using the RapidVit and RapidWarm oocyte kits (Vitrolife, Sweden). Oocytes were stored in liquid nitrogen until required.

PNT. PNT was performed either at 16–20 h after ICSI (ltPNT), or at ~8–10 h after ICSI (ePNT). In the case of ePNT, two main series of experiments (series I and series II) were performed. A total of 51 zygotes from 10 donors were used for ltPNT ($n = 12$ controls; $n = 39$ ltPNT). For ePNT experiments, we used 58 zygotes from 13 donors in series I ($n = 19$ controls; $n = 39$ ePNT), and 131 zygotes from 30 donors in series II ($n = 30$ controls; $n = 101$ ePNT). Thirty-four zygotes from 13 donors were used for ePNT experiments involving oocytes vitrified at the 2PB stage.

Two types of PNT experiments were conducted: (1) autologous PNT, which involved removal and replacement of pronuclei in the same zygote, was performed to distinguish between technical and biological effects; (2) heterologous PNT involved reciprocal transfer between pairs of zygotes, either from the same or different donors. Heterologous PNT between zygotes from different donors involved reciprocal transfer between zygotes originating from fresh and vitrified oocytes. This gave rise to reconstituted zygotes consisting of cytoplasts from fresh oocytes and karyoplasts from vitrified oocytes, or vice versa. These combinations are termed FreshCy and VitCy, respectively (see Extended Data Fig. 4a). In one set of ePNT experiments, which gave rise to a single ePNT blastocyst, the two donors were sisters and therefore have the same mitochondrial genotype. For the purpose of the gene expression experiments, these are referred to as homologous transfers.

The PNT procedure was performed in an isolator-based workstation (Vitrosafe) with temperature, CO₂ and O₂ control²⁹ containing an inverted microscope (TE2000-U, Nikon) fitted with micromanipulators (Integra Ti, Research Instruments) and a laser objective (Saturn Active, Research Instruments). PNT procedures took ~15 min to complete and involved the following steps. First, zygotes in which 2PN were visible were placed in enucleation medium with cytoskeletal inhibitors. In all cases, nocodazole (10 µg ml⁻¹) was used to depolymerize microtubules. In ltPNT experiments we used either cytochalasin B (5 µg ml⁻¹) or latrunculin A (2.5 µM or 5 µM) to disable the actin cytoskeleton. We subsequently used latrunculin A (2.5 µM) for all ePNT experiments. For ltPNT and ePNT (series I) experiments, enucleation was performed in G-1 Plus medium (Vitrolife). We used Sydney IVF Embryo Biopsy Medium (Cook Medical), which does not contain Ca²⁺ and Mg²⁺ for ePNT (series II) experiments. Enucleation was performed in the presence or absence of sucrose (0.125 µM). Addition of sucrose increased the osmolarity of the enucleation medium from 280 mosm l⁻¹ to 449 mosm l⁻¹, which induced shrinkage of the cytoplasm, thereby facilitating enucleation. Second, a laser objective (Saturn Active, Research Instruments) was used to create an opening in the zona pellucida for insertion of the enucleation/fusion pipette. The inner diameter pipette measurements were 25–35 µm for ltPNT, and 17 µm for ePNT. Third, the pronuclei, surrounded by a small amount of cytoplasm, were aspirated into the enucleation pipette, either as a single karyoplast, or as two separate karyoplasts (see Supplementary Videos 1 and 2). Fourth, karyoplasts were briefly exposed to a suspension of HVJ-E; GenomONE-CF Ex

(Cosmo Bio). Undiluted suspension was used for ltPNT and ePNT (series I) and a 1:10 dilution was used for ePNT (series II). Fifth, the pipette containing the karyoplasts was inserted through the laser-drilled opening in the zona pellucida and karyoplasts were gently expelled into the perivitelline space and allowed to fuse with the cytoplasm. Sixth, reconstituted and control zygotes were cultured either in a sequential medium, G-1 Plus (day 1–3)/G-2 Plus (day 3–6) (Vitrolife; ltPNT and ePNT (series I)), or in the single-step G-TL medium (Vitrolife; ePNT (series II)) from day 1 to 6. Time-lapse embryo imaging was performed for three sets of ePNT (series II) experiments using the Primo Vision Time-lapse monitoring system (Vitrolife).

Overview of experiments on PNT zygotes. Survival of reconstituted zygotes was initially compared between ltPNT and ePNT (series I) and was subsequently recorded for all ePNT zygotes. In ePNT (series II), the first mitotic division was monitored by time-lapse imaging in three sets of experiments. All zygotes submitted to PNT were included in the analysis of development to the blastocyst stage. Zygotes (controls and PNT) that developed to the blastocyst stage were graded and included in the analysis of blastocyst quality. Blastocyst formation and grade were assessed on day 6 for ltPNT, and on days 5 and 6 for ePNT, except in the case of two ePNT (series II) experiments, which were assessed only on day 6. These experiments are not included in the day 5 analysis shown in Fig. 2b and in Extended Data Fig. 3d–f.

Blastocyst cell counts were performed primarily to gain insight into the causes of poor blastocyst quality in the ltPNT and ePNT (series I). Data on blastocyst cell counts were obtained from ltPNT ($n = 6$) and ePNT: series I ($n = 8$) and series II ($n = 5$). Further analyses, including aneuploidy, gene expression, mtDNA carryover, and hES cell derivation were conducted on series II blastocysts only. Where possible, we performed multiple investigations on individual blastocysts. In accordance with our Local Research Ethics Committee approval and HFEA licence, these were performed on day 6. Unmanipulated control blastocysts and ePNT blastocysts were used for aneuploidy and gene expression, or aneuploidy and hES cell derivation. The blastocyst grades shown for each of these analyses refer to the grades on day 6. The numbers of blastocysts used for each set of experiment were: aneuploidy screening (ePNT: $n = 30$ from 20 donors; control: $n = 11$ from 10 donors), gene expression analysis (ePNT: $n = 11$ from 10 donors; control: $n = 3$ from 3 donors), mtDNA carryover (ePNT: $n = 40$ from 28 donors), hES cell derivation (ePNT: $n = 15$ from 13 donors; control: $n = 6$ from 4 donors). **Embryo grading.** Embryos were graded using the UK National External Quality Assessment Service (NEQAS) grading schemes for embryos and blastocysts³⁰. Blastocysts were assigned a three-digit grade representing a score of: 1–6 for the extent of blastocoel expansion, 1–5 for the inner cell mass appearance and 1–3 for the trophectoderm appearance³¹. The grade was converted to a quality category using the table in Extended Data Fig. 2c.

Blastocyst nuclear counts. Day 6 blastocysts were fixed using 4% PFA at pH 7.4. Nuclear staining was carried out using DAPI (Vectashield). Blastocysts were imaged using an inverted confocal microscope (Nikon A1R) with a ×20 objective (Plan Apo, Nikon) and NIS-elements image software. Z-steps were taken at ~1 µm intervals and nuclear counts performed using ImageJ software.

Aneuploidy screening. Clumps of cells were harvested from ePNT blastocysts for whole-genome amplification followed by microarray-CGH analysis according to a previously validated protocol using 24Sure Cytochip (Illumina). Cells were obtained from the trophectoderm, ICM or both. Lysis and whole-genome amplification was performed using the SurePlex kit (Illumina) according to the manufacturer's instructions and blind to sample origin. Samples from ePNT blastocysts were labelled with Cy3 while a commercially available reference 46,XY DNA was labelled with Cy5 (Illumina)³². A laser scanner (InnoScan 710, Innopsys) was used to analyse the microarrays after washing and drying. The resulting images were analysed using BlueFuse Multi analysis software (Illumina).

Gene expression analysis by single-cell RNA-seq.

Blastocyst disaggregation. Blastocyst disaggregation was performed using an Olympus IX73 microscope and a Saturn 5 laser (Research Instruments) as described previously¹⁴. Embryos were placed in drops of G-MOPS solution (Vitrolife) on a Petri dish overlaid with mineral oil for micromanipulation. The separated ICM and polar trophectoderm were washed in Ca²⁺- and Mg²⁺-free PBS (Invitrogen) and incubated in 0.05% trypsin/EDTA (Invitrogen) for 5–10 min. Trypsin was quenched using Global Media supplemented with 5 mg ml⁻¹ LifeGlobal Protein Supplement. Single cells were isolated using a 30-µm inner diameter blastomere biopsy pipette (Research Instruments).

cDNA synthesis and amplification. cDNA was synthesized using SMARTer Ultra Low Input RNA for Illumina Sequencing-HV kit (Clontech Laboratories) according to the manufacturer's guidelines and as previously published¹⁴. cDNA was sheared using Covaris S2 with the modified settings 10% duty, intensity 5, burst cycle 200 for 2 min. Libraries were prepared using Low Input Library Prep Kit

(Clontech Laboratories) according to the manufacturer's instructions. Library quality was assessed with an Agilent 2100 BioAnalyser and concentration measured with a Qubit 2.0 Fluorometer (Life Technologies). Libraries were submitted for 50-bp paired-end sequencing using standard Illumina adapters on Illumina HiSeq 2500.

RNA-seq data analysis. The quality of the RNA-seq data was evaluated using the FastQC tool. Samples with primer contamination and amplification bias, identified by an unequal proportion of ATGC nucleotide percentages, were excluded from subsequent analysis. Reads were aligned to the human genome sequence hg19 using Tophat2 (ref. 33), and samples with low percentage mapping (<50%) were excluded from subsequent analysis. The number of reads mapping uniquely to each gene was counted using the program htseq-count³⁴. The individual count files for each sample were normalized using both the RPKM function in the edgeR package³⁵ and a variance-stabilizing transformation from the DESeq2 package³⁶.

A principal component analysis (PCA) of the top 12,000 most variably expressed genes was performed blind to sample origin on all ePNT and control samples to investigate differences in global gene expression. The PCA was generated using the R package prcomp, using both the scaling and centering options. A subsequent PCA excluded samples below grade C, which were generally aneuploid for multiple chromosomes. An R script was used to perform unsupervised hierarchical clustering and to generate a heatmap using the pheatmap R package. An alternative approach for data dimensionality reduction was performed using the t-SNE algorithm¹⁵. The top 5 principal components of the VST-normalized count data were used as input for the R implementation of t-SNE. DESeq2 was applied to the read counts for the ePNT and control data to identify differential expressed genes in the primitive endoderm, trophectoderm and epiblast samples.

mtDNA carryover analysis.

mtDNA extraction and mtDNA sequencing. The control region of the mitochondrial genome from oocyte donors was sequenced using ovarian follicular cells harvested at the time of oocyte retrieval, or cumulus cells removed from the oocyte in preparation for ICSI. DNA extraction from follicular cells was performed using the QIAamp DNA Mini kit according to the manufacturer's instructions (Qiagen). Cumulus cells were lysed for 2 h in a lysis buffer (50 mM Tris-HCl, pH 8.5, 1 mM EDTA, 0.5% Tween-20 and 200 µg ml⁻¹ proteinase K) at 55 °C. The enzyme was then inactivated by incubation at 95 °C for 10 min. The control region of the mitochondrial genome was amplified as described previously³⁷ with the following modification: secondary PCR reactions were performed with four sets of overlapping M13-tailed primers (primer nucleotide positions, D1F: 15758–15777 and D1R: 019–001; D2F: 16223–16244 and D2R: 129–110; D3F: 16548–16569 and D3R: 389–370; D4F: 323–343 and D4R: 771–752) with an annealing temperature of 58 °C. PCR products were purified using TSAP (Promega) then sequenced on an ABI3130 Genetic Analyser (Applied Biosystems) with BigDye Terminator cycle sequencing chemistries (v.3.1, Applied Biosystems). Sequences were directly compared to the revised Cambridge Reference Sequence for human mtDNA³⁸ (GenBank accession number AC_000021.2) using SeqScape software (v.2.1.1, Applied Biosystems).

Generation of heteroplasmic control DNA. The mtDNA control region containing either the wild-type or polymorphic nucleotide of interest was amplified using PCR primers (primer nucleotide positions: forward primer, 16016–16036; reverse primer, 571–552) with an annealing temperature of 58 °C. PCR products amplified from ovarian follicular cells were purified using the Agencourt AMPure XP purification system (Beckman Coulter) according to the manufacturer's instructions. PCR products amplified from cumulus cells were gel purified (QIAquick Gel Extraction kit, Qiagen) and cloned using the pGEM-T Easy Vector System (Promega) according to the manufacturer's instructions. Plasmid DNA was isolated using the QIAprep Spin Miniprep kit (Qiagen). Quantitative real-time PCR was performed using Platinum SYBR Green qPCR SuperMix-UDG (Invitrogen) and PCR primers (forward primer, L16016–16036; reverse primer, H16186–16167) to accurately determine the DNA concentration. Equimolar concentrations of DNA containing the wild-type or polymorphic nucleotide of interest were then combined in varying ratios to generate a range of heteroplasmic controls.

Pyrosequencing. Quantitative pyrosequencing was used to measure mtDNA carryover in samples from ePNT blastocysts and PNT-hES cell lines. Locus-specific PCR and a pyrosequencing primer were designed for each polymorphic nucleotide of interest the mtDNA using PyroMark Assay Design Software v.2.0 (Qiagen). Clumps of cells from ePNT blastocysts and from PNT-hES cell lines were lysed for 2 h in a lysis buffer (50 mM Tris-HCl, pH 8.5, 1 mM EDTA, 0.5% Tween-20 and 200 µg ml⁻¹ proteinase K) at 55 °C. The enzyme was then inactivated by incubation at 95 °C for 10 min. mtDNA amplification was performed before pyrosequencing analysis and pyrosequencing performed on the PyroMark Q24 and PyroMark Q96 instruments according to the manufacturer's instructions. Quantification of

the heteroplasmy level was achieved using the instrument software to directly compare the relevant peak heights of both the wild-type and polymorphic nucleotides at the relevant position¹⁴. A standard curve was generated by plotting expected heteroplasmy level against actual heteroplasmy level for the control samples. The standard curve was used to determine the level of heteroplasmy in the blastocyst and PNT-hES cell samples.

Mitochondrial haplogroups. Haplogroups were determined by next-generation sequencing analysis of whole mtDNA, amplified in two overlapping 9-kb fragments using primers L550–569 and H9839–9819 (set 1) and L9592–9611 and H645–626 (set 2), on an Ion Torrent Personal Genome Machine (Life Technologies)³⁹. Protocol modifications included use of a OneTouch 2 system and HiQ OT2 and sequencing kits. Samples were processed on Ion 316 chips and analysed with Torrent Suite Variant Caller plugin (v.4.6).

ES cell derivation. For ICM isolation, day 6 blastocysts were dissected in the embryo culture dish. The blastocysts were held in position by a holding pipette (Vitrolife) with the ICM at 3 o'clock. The ICM was held in position with a biopsy pipette (Origio, catalogue no. MPB-FP-30) and isolated from the majority of the trophectoderm cells by laser pulses (Saturn 5 Active, Research Instruments). The isolated ICMs were plated on inactivated feeders MEF (CF1 s), in medium containing KnockOut Serum Replacement (Invitrogen, catalogue no. 10828), KnockOut DMEM (Invitrogen, catalogue no. 10829), NEAA (Invitrogen, catalogue no. 11140), bFGF2 (Invitrogen, catalogue no. 13256), Glutamax (Invitrogen, catalogue no. 35050) and 2-mercaptoethanol (Invitrogen, catalogue no. 21985). Outgrowths were mechanically dissected from the surrounding cells and plated on fresh feeder cells, all subsequent passaging was performed mechanically. Embryonic stem cells were adapted to feeder-free culture conditions and maintained in mTeSR1 (STEMCELL Technologies) on growth-factor-reduced Matrigel (BD Biosciences). The hES cell lines generated during the course of this study will be deposited with the UK Stem Cell Bank (UKSCB). All the necessary tests, including mycoplasma testing will be performed by the UKSCB prior to distribution of the cell lines.

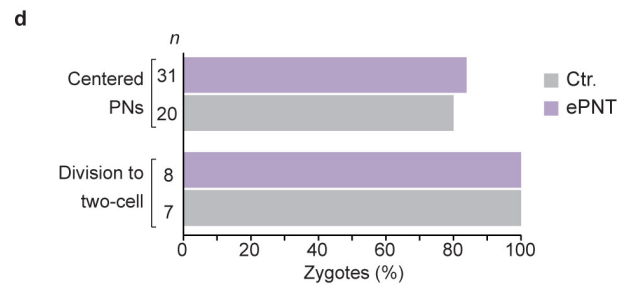
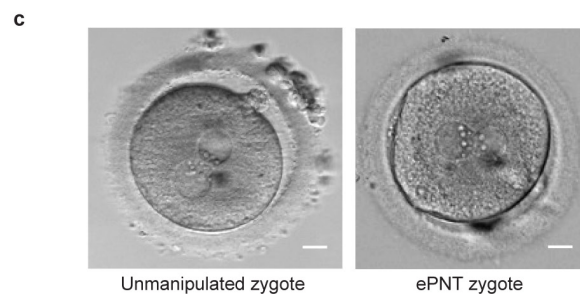
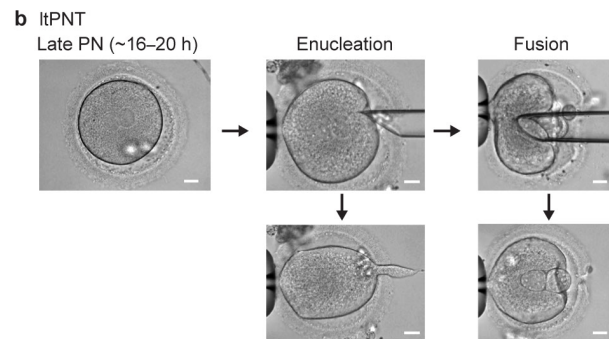
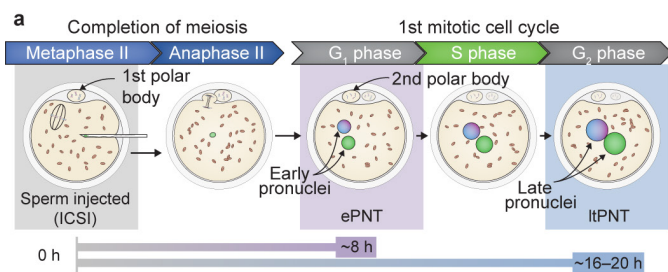
Quantitative RT-PCR. RNA was isolated using TRI Reagent (Sigma) and DNaseI treated (Ambion). cDNA was synthesized using a Maxima First Strand cDNA Synthesis Kit (Fermentas). qRT-PCR was performed using Quantace Sensimix on an Applied Biosystems 7500 machine (Life Technologies). Primer pairs used were previously published⁴⁰ and are as follows: NANOG forward GCAACCTGAAGAC GTGTGAA, reverse CTCGCTGATTAGGCTCCAAC; POU5F1 forward TATGGG AGCCCTCACTTCAC, reverse CAAAACCTGCGCACAAACT; SOX2 forward TTGTTCGATCCCAACTTTC, reverse ACATGGATTCTCGGCAGACT.

Immunohistochemistry and imaging. Samples were fixed in 4% paraformaldehyde at 4 °C overnight, permeabilized with 0.5% Tween in 1 × PBS for 20 min and blocked with 10% FBS diluted in 0.1% Tween in 1 × PBS for 1 h. Primary antibodies were diluted in blocking solution as indicated: AFP (Dako, A0008, 1:500), desmin (Neomarkers/Thermo, RB-9014-P, 1:50), NANOG (R&D, AF1977, 1:500), OCT4 (Santa Cruz, SC-5279, 1:500), SMA (Sigma, A5228, 1:250), SOX1 (R&D, AF3369, 1:500), SOX2 (Cell Signaling, 23064, 1:500), SOX17 (R&D, AF1924, 1:500), SSEA4 (DSHB, MC-813-70, 1:100), TUJ1 (Sigma, T2200, 1:500). Samples were incubated at 4 °C rotating overnight. Alexa Fluor secondary antibodies (Invitrogen, anti-mouse A21202, A21203; anti-rabbit A21206, A21207; anti-goat A11055, A11058) were diluted 1:300 in blocking solution and samples incubated for 1 h at room temperature, then washed and covered with 0.1% Tween in 1 × PBS containing DAPI Vectashield mounting medium (Vector Labs). Images were taken on an Olympus IX73 microscope with Cell^F software (Olympus Corporation).

Statistical analysis. Data were analysed using one-way ANOVA with Tukey's HSD test, Mann–Whitney *U*-test, χ^2 test and Fisher's exact test, as indicated in the figure legends. RNA-seq data were analysed by PCA using either RPKM- or VST-normalized counts.

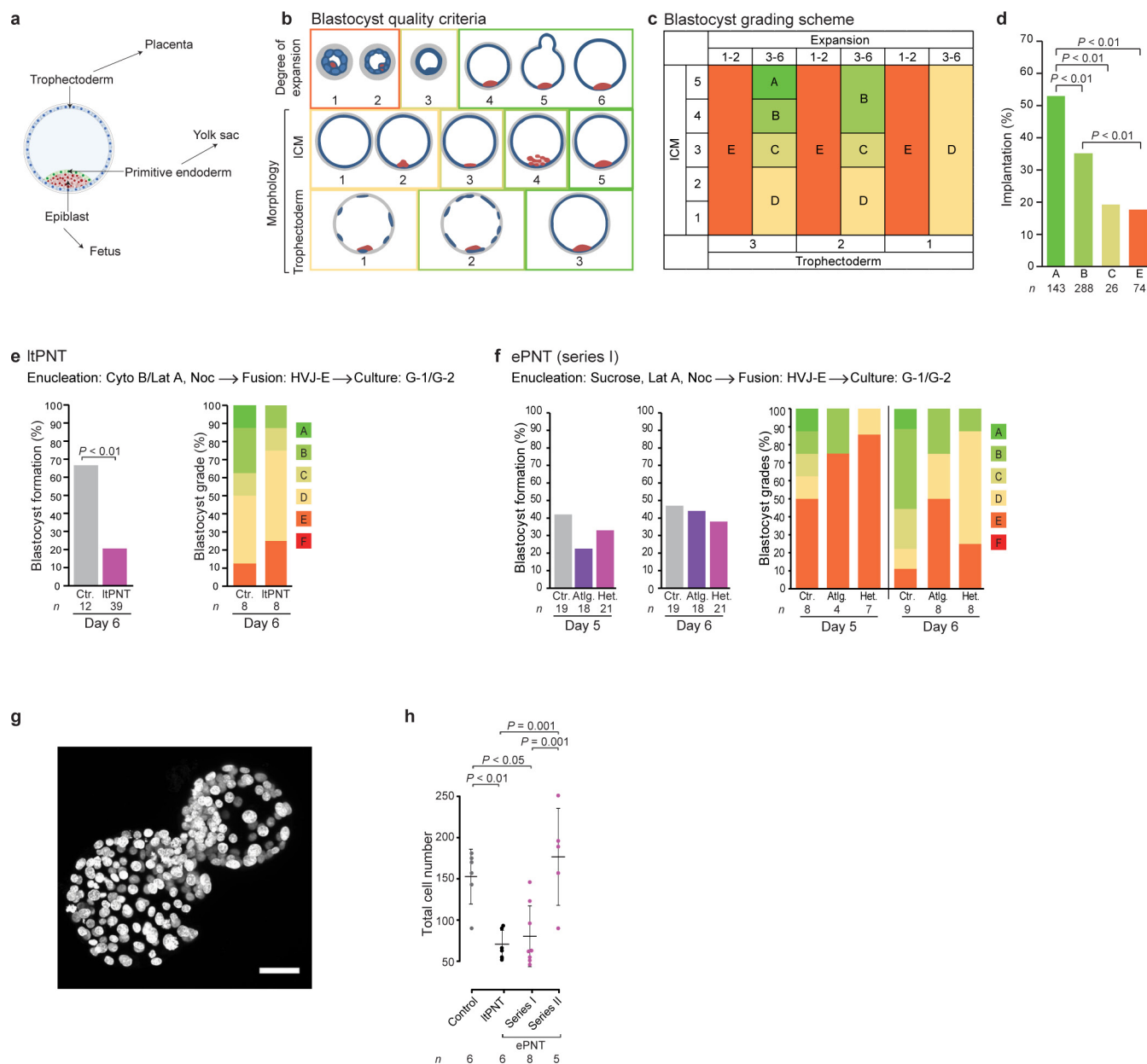
27. Choudhary, M. *et al.* Egg sharing for research: a successful outcome for patients and researchers. *Cell Stem Cell* **10**, 239–240 (2012).
28. HFEA Guidance on Payments for Donors. *HFEA Code of Practice* Section 13 <http://www.hfea.gov.uk/500.html> (Human Fertilisation and Embryology Authority, 2009).
29. Hyslop, L. *et al.* A novel isolator-based system promotes viability of human embryos during laboratory processing. *PLoS ONE* **7**, e31010 (2012).
30. Cutting, R., Morrill, D., Roberts, S. A., Pickering, S. & Rutherford, A. Elective single embryo transfer: guidelines for practice British Fertility Society and Association of Clinical Embryologists. *Hum. Fertil. (Camb.)* **11**, 131–146 (2008).
31. Stephenson, E. L., Braude, P. R. & Mason, C. International community consensus standard for reporting derivation of human embryonic stem cell lines. *Regen. Med.* **2**, 349–362 (2007).
32. Wells, D. *et al.* Clinical utilisation of a rapid low-pass whole genome sequencing technique for the diagnosis of aneuploidy in human embryos prior to implantation. *J. Med. Genet.* **51**, 553–562 (2014).

33. Kim, D. *et al.* TopHat2: accurate alignment of transcriptomes in the presence of insertions, deletions and gene fusions. *Genome Biol.* **14**, R36 (2013).
34. Anders, S., Pyl, P. T. & Huber, W. HTSeq—a Python framework to work with high-throughput sequencing data. *Bioinformatics* **31**, 166–169 (2015).
35. Robinson, M. D., McCarthy, D. J. & Smyth, G. K. edgeR: a Bioconductor package for differential expression analysis of digital gene expression data. *Bioinformatics* **26**, 139–140 (2010).
36. Love, M. I., Huber, W. & Anders, S. Moderated estimation of fold change and dispersion for RNA-seq data with DESeq2. *Genome Biol.* **15**, 550 (2014).
37. Taylor, R. W., Taylor, G. A., Durham, S. E. & Turnbull, D. M. The determination of complete human mitochondrial DNA sequences in single cells: implications for the study of somatic mitochondrial DNA point mutations. *Nucleic Acids Res.* **29**, e74 (2001).
38. Andrews, R. M. *et al.* Reanalysis and revision of the Cambridge reference sequence for human mitochondrial DNA. *Nature Genet.* **23**, 147 (1999).
39. Greaves, L. C. *et al.* Clonal expansion of early to mid-life mitochondrial DNA point mutations drives mitochondrial dysfunction during human ageing. *PLoS Genet.* **10**, e1004620 (2014).
40. Wamaitha, S. E. *et al.* Gata6 potently initiates reprogramming of pluripotent and differentiated cells to extraembryonic endoderm stem cells. *Genes Dev.* **29**, 1239–1255 (2015).
41. Mortazavi, A., Williams, B. A., McCue, K., Schaeffer, L. & Wold, B. Mapping and quantifying mammalian transcriptomes by RNA-Seq. *Nature Methods* **5**, 621–628 (2008).
42. White, H. E. *et al.* Accurate detection and quantitation of heteroplasmic mitochondrial point mutations by pyrosequencing. *Genet. Test.* **9**, 190–199 (2005).



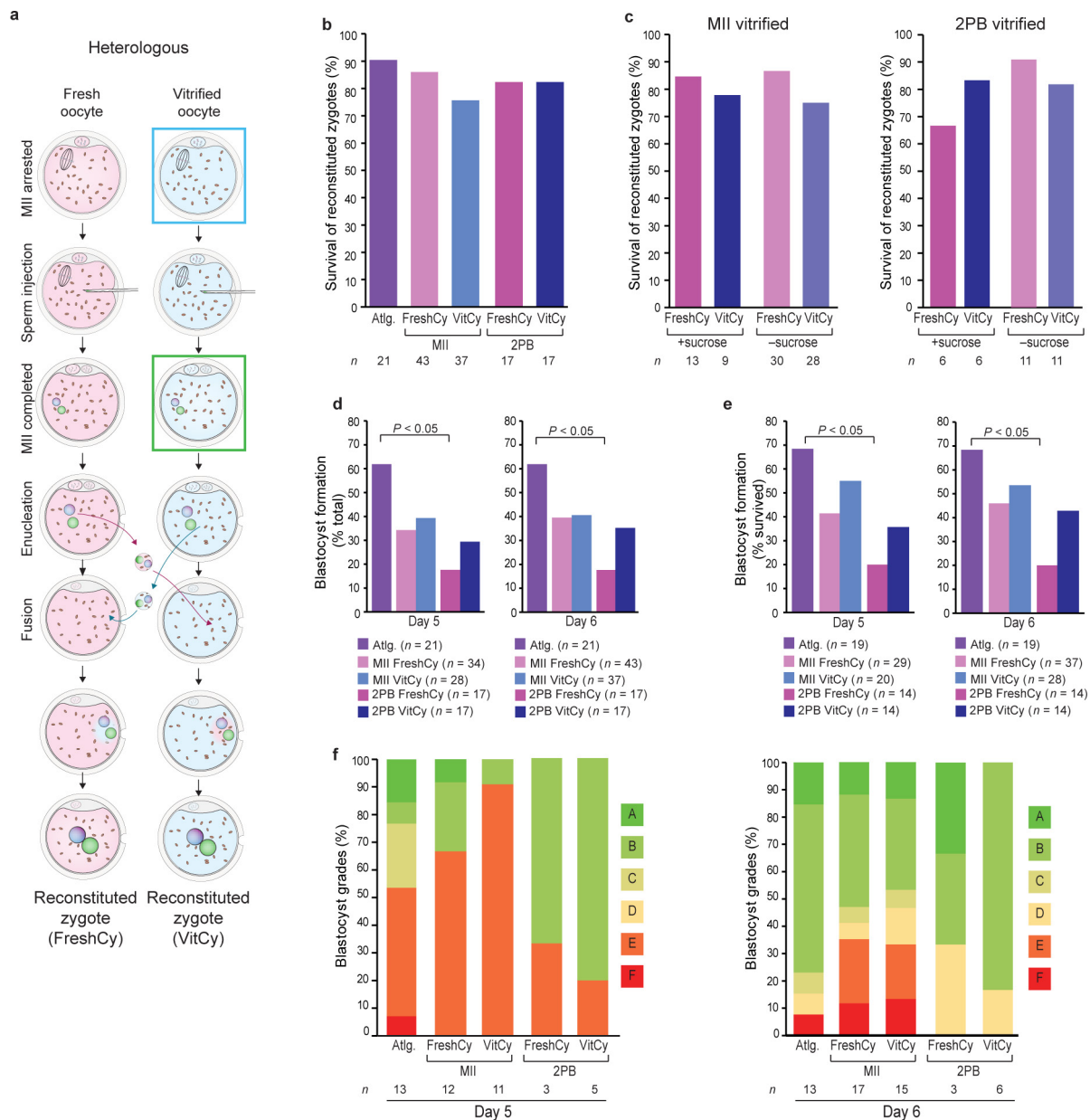
Extended Data Figure 1 | LtPNT and pronuclei centralization after ePNT. **a**, Schematic showing timing of LtPNT and ePNT. **b**, Images showing the stages of the LtPNT process: left, late pronuclear zygote; middle, enucleation; right, fusion. Scale bar, 20 μ m. Note large pronuclei and pipette size compared with Fig. 1b and Supplementary Videos 1 and 2.

c, Images show unmanipulated and ePNT zygotes at 16–18 h after fertilization. Scale bars, 20 μ m. **d**, Pronuclei centralization and division to the two-cell stage assessed by live cell imaging in control and ePNT zygotes (not significant). Comparisons by χ^2 test.



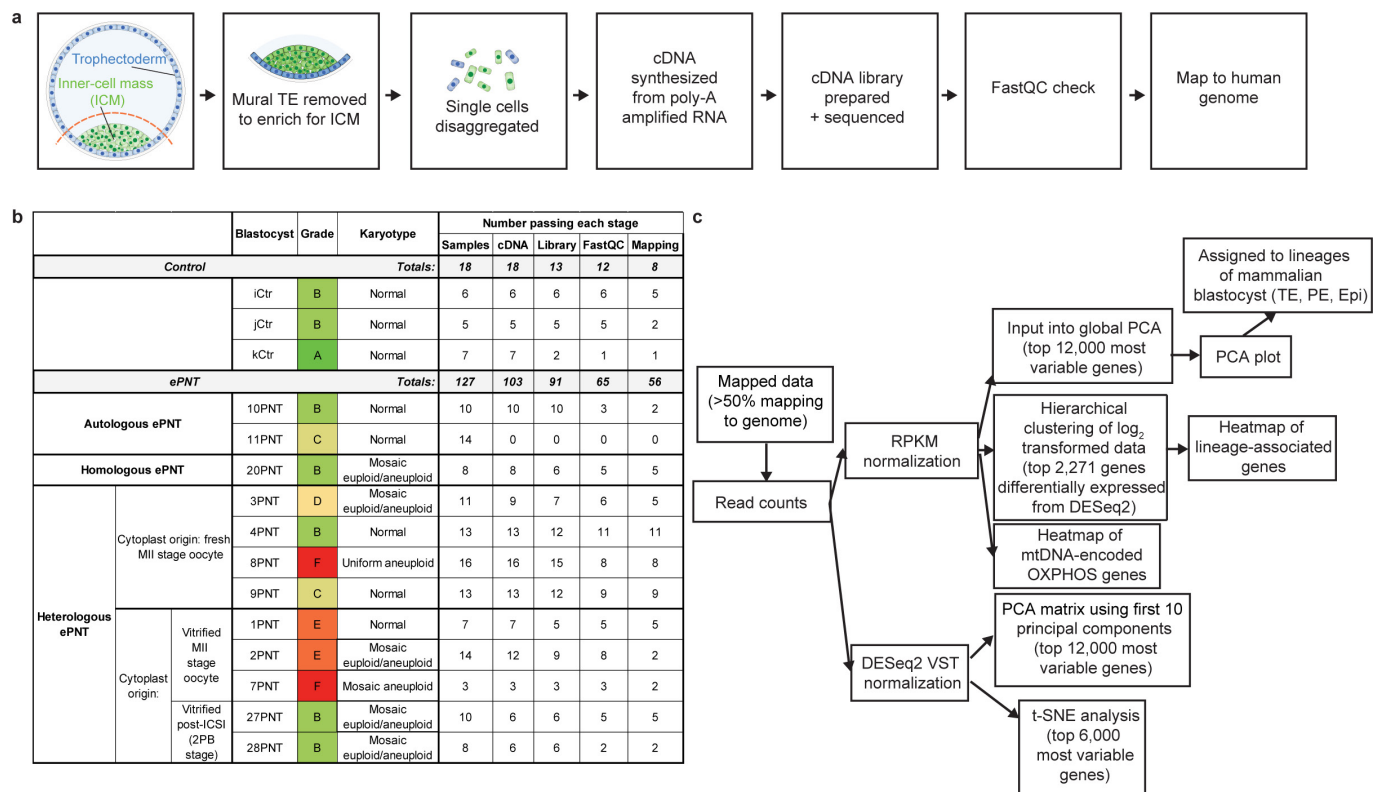
Extended Data Figure 2 | Blastocyst morphology and effect of PNT on blastocyst development and quality. **a**, Schematic showing cell lineages in a mammalian blastocyst: trophectoderm; primitive endoderm and epiblast. **b**, Morphological criteria and scoring system used for grading human blastocysts³¹. Top, degree of expansion ranging from an early, unexpanded blastocyst (score 1) to fully expanded (score 6). Middle, range of ICM morphologies from absent (score 1) to large but tightly packed (score 5). Bottom, range of trophectoderm morphologies from scant and discontinuous (score 1) to a fully formed layer of tightly packed cells (score 3). Box colours correspond to the grades shown in **c**. **c**, Table used to assign blastocyst grades, according to levels of expansion, and morphology of the ICM and trophectoderm. Grade F (not shown) was assigned to embryos that developed to the blastocyst stage but subsequently showed signs of degeneration. **d**, Graph showing the relationship between blastocyst grade and implantation. Data obtained from clinical IVF cycles ($n = 531$) in which unmanipulated single blastocysts were replaced on day 5. Implantation is defined by the detection of a fetal heartbeat at 6 weeks after IVF treatment. There was no case in which a grade D or F blastocyst

was replaced. P values are shown (χ^2 test). **e**, ItPNT experimental conditions, blastocyst formation ($P < 0.01$; χ^2 test) and quality. A total of 51 zygotes from 10 donors were allocated either to an unmanipulated control group (Ctr.; $n = 12$) or to ItPNT involving transfer between pairs of zygotes from the same donor ($n = 29$) or replacement back into the same zygote (autologous PNT (Atlg.) $n = 10$). **f**, ePNT (series I) experimental conditions, blastocyst formation and quality. This series of experiments involved a total of 58 zygotes from 13 donors. Zygotes were allocated to a control group ($n = 19$), or to ePNT involving either autologous ($n = 18$) or heterologous (Het.; $n = 21$) transfers. Differences are not significant (χ^2 test and Fisher's exact test). **g**, Image of an ePNT blastocyst fixed on day 6 and stained with 4',6-diamidino-2-phenylindole (DAPI). Scale bar, 50 μm . **h**, Cell number assessed by nuclear counts showing comparable numbers in control and ePNT (series II) blastocysts and significantly reduced numbers in ItPNT and ePNT (series I) blastocysts ($P = 0.001$; one-way analysis of variance (ANOVA) with Tukey's HSD test). Mean \pm standard deviation (s.d.) calculated from individual blastocysts, numbers indicated on the x -axis.



Extended Data Figure 3 | Survival and blastocyst development after ePNT between zygotes obtained from freshly harvested and vitrified oocytes. **a**, Experimental scheme for heterologous ePNT in series II. Because of unpredictability in the response to ovarian stimulation, heterologous transfers involved reciprocal ePNT between zygotes generated from freshly harvested and vitrified oocytes. This resulted in reconstituted zygotes whose cytoplasts originated from a fresh oocyte (FreshCy), or from a vitrified oocyte (VitCy). Oocytes for these experiments were vitrified predominantly at the MII stage (blue box; $n = 80$ zygotes; 25 donors). We also conducted a series of experiments to determine whether vitrification at the 2PB stage (green box; $n = 34$ zygotes; 13 donors) would promote improved blastocyst formation. **b**, Survival of reconstituted zygotes as a proportion of those submitted to autologous (Atlg.) and heterologous (Het.) ePNT according to the stage of vitrification (MI I or 2PB) and according to whether the cytoplast was derived from a fresh (FreshCy) or a vitrified (VitCy) oocyte. Loss

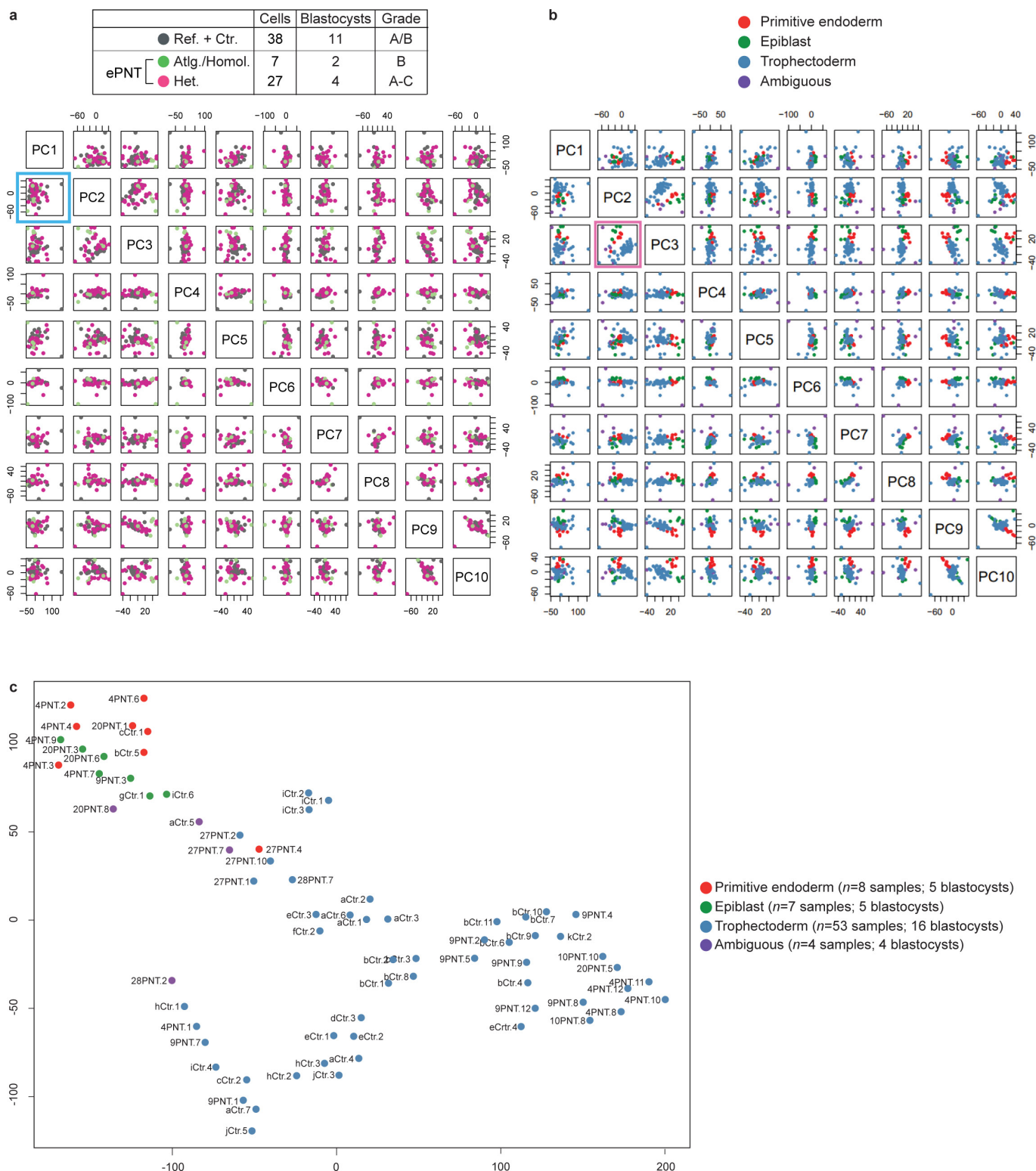
was generally due to karyoplast lysis, excessive leakage of cytoplasm, or degeneration of reconstituted zygotes during subsequent incubation. Differences are not significant (χ^2 test). **c**, Sucrose was initially included in the manipulation medium to facilitate enucleation and fusion, however, it was later removed because the data indicated that the osmotic effect resulted in increased mtDNA carryover (see Fig. 4b). Omission of sucrose from the enucleation medium had a small, but not significant, effect on survival of zygotes whose cytoplasts originated from vitrified MI I oocytes (χ^2 test). **d**, Blastocyst formation as a percentage of zygotes submitted to the ePNT procedure recorded on days 5 and 6 after fertilization. **e**, Blastocyst formation recorded on days 5 and 6 as a percentage of zygotes that survived the ePNT procedure. The numbers in each group and P values are shown, χ^2 test. **f**, Blastocyst quality grades (see Extended Data Fig. 2c, d) on days 5 and 6 (not significant; Fisher's exact test). Source data files are available online.



Extended Data Figure 5 | Experimental approach and bioinformatics analysis of single-cell RNA-seq data from ePNT and control blastocysts.

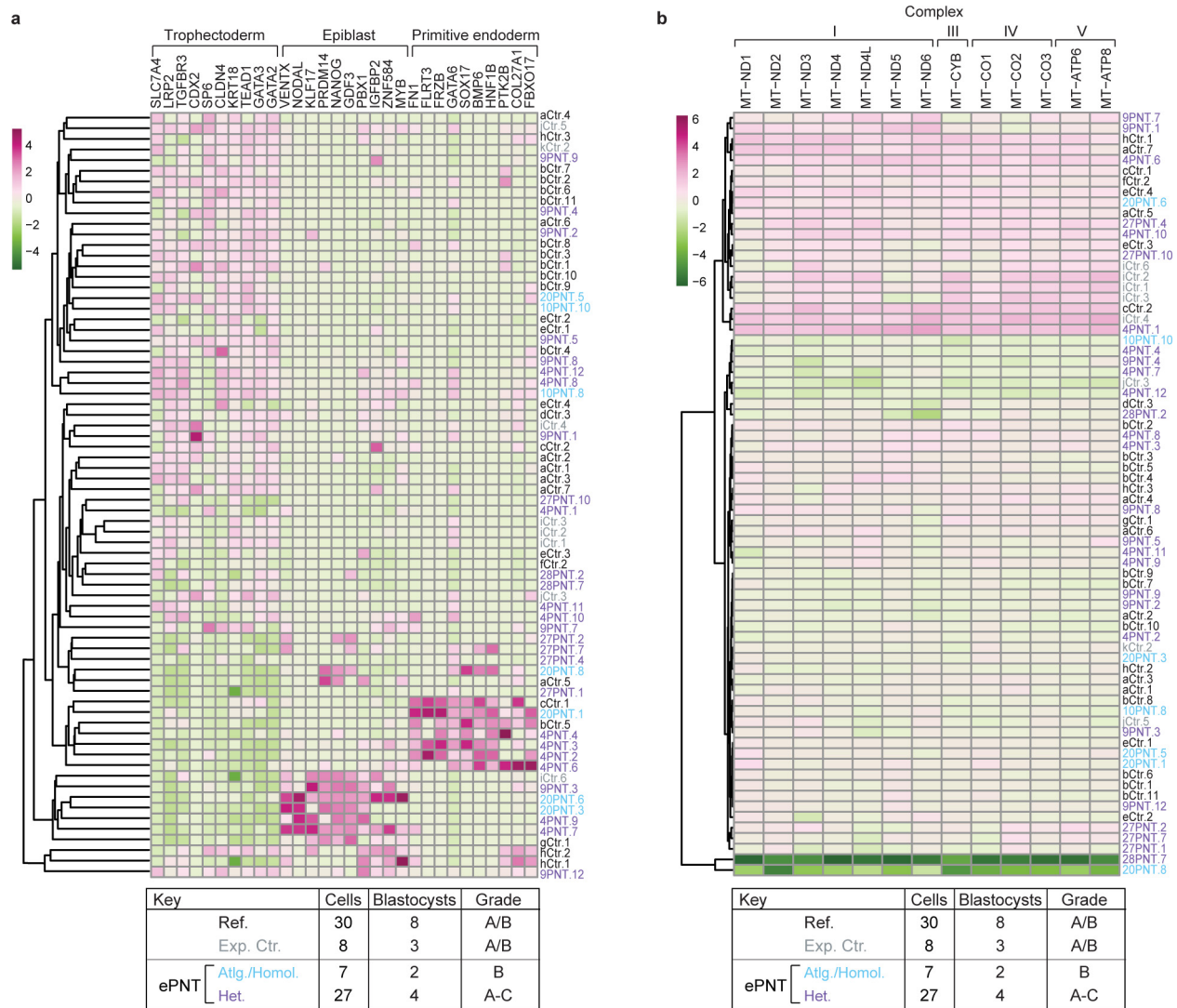
a, Flow diagram showing the steps involved in RNA-seq of single cells microdissected from human blastocysts. **b**, Summary table of control and ePNT blastocysts submitted for RNA-seq analysis. For the purpose of gene expression analysis, we distinguish between ePNT blastocysts derived from fusion of cytoplasts and karyoplasts with the same, and different, mitochondrial genomes. Those with the same mitochondrial genomes included blastocysts from autologous ePNT and from a zygote

pair donated by two sisters, which we refer to as homologous ePNT. Blastocysts arising from heterologous ePNT represent new combinations of nuclear and mitochondrial genome and are subgrouped according to the cytoplasm origin (see Extended Data Fig. 4). **c**, Flow diagram outlining the bioinformatics analysis of RNA-seq data. Data were normalized either as reads per kilobase per million mapped reads (RPKM)⁴¹ or using DESeq2 (ref. 36). Normalized data were used to generate PCA plots, t-SNE plots and heatmaps.



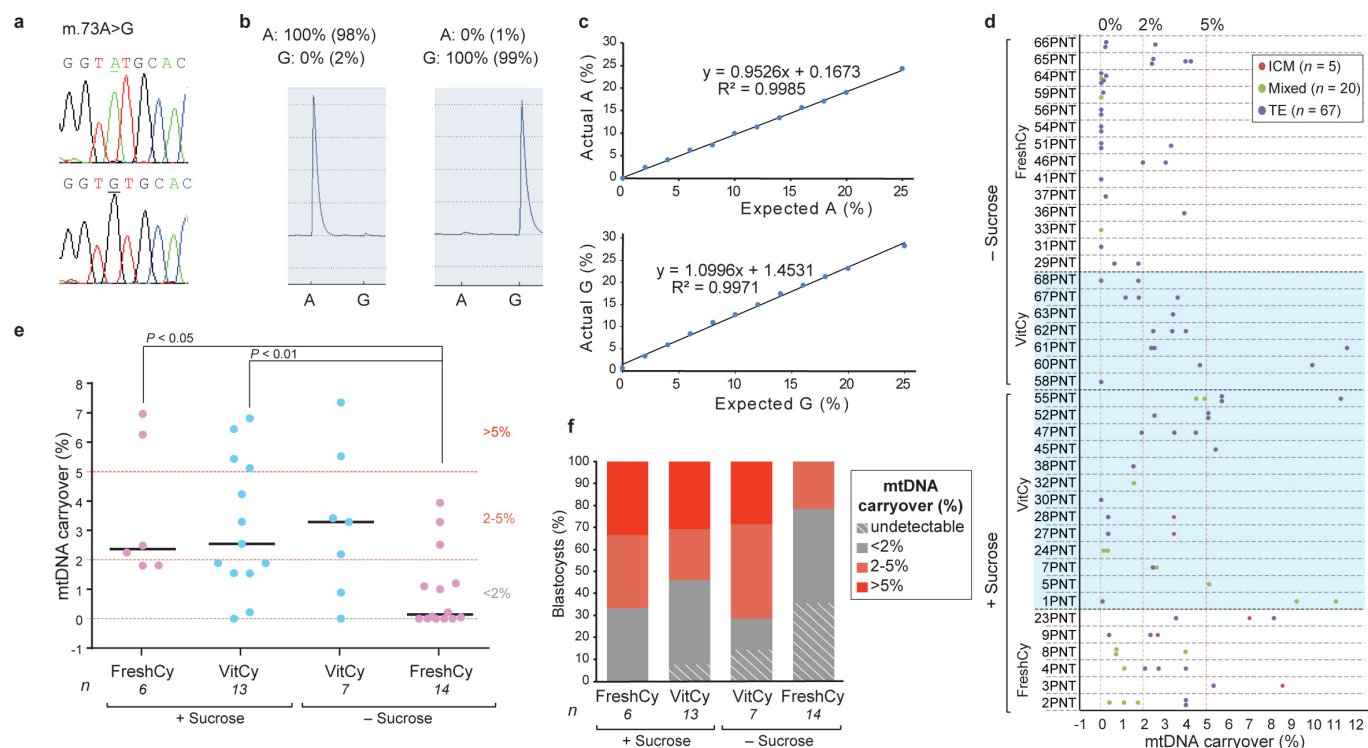
Extended Data Figure 6 | Analysis of differential gene expression in good quality ePNT and control blastocysts. a, PCA matrix using the first ten principal components of DESeq2 VST normalized data for the top 12,000 most variable genes. Global gene expression is indistinguishable between unmanipulated control and ePNT samples, PC1 versus PC2 highlighted in blue box. **b,** PCA matrix as shown in **a**, distinguished by lineage, clearly seen in PC2 versus PC3 (pink box). **c,** t-SNE analysis after DESeq2 VST normalization of 6,000 of the most variably expressed

genes, where samples were distinguished by lineage. Sample numbers and blastocyst grades are shown. Autologous and homologous ePNT samples are derived from blastocysts in which the karyoplast and cytoplast had the same mitochondrial genome. Heterologous ePNT samples were derived from pairs of zygotes with different mitochondrial genomes (Extended Data Fig. 5). Samples from experimental controls and reference population were combined for the purpose of the analyses shown in **a** and **b**.



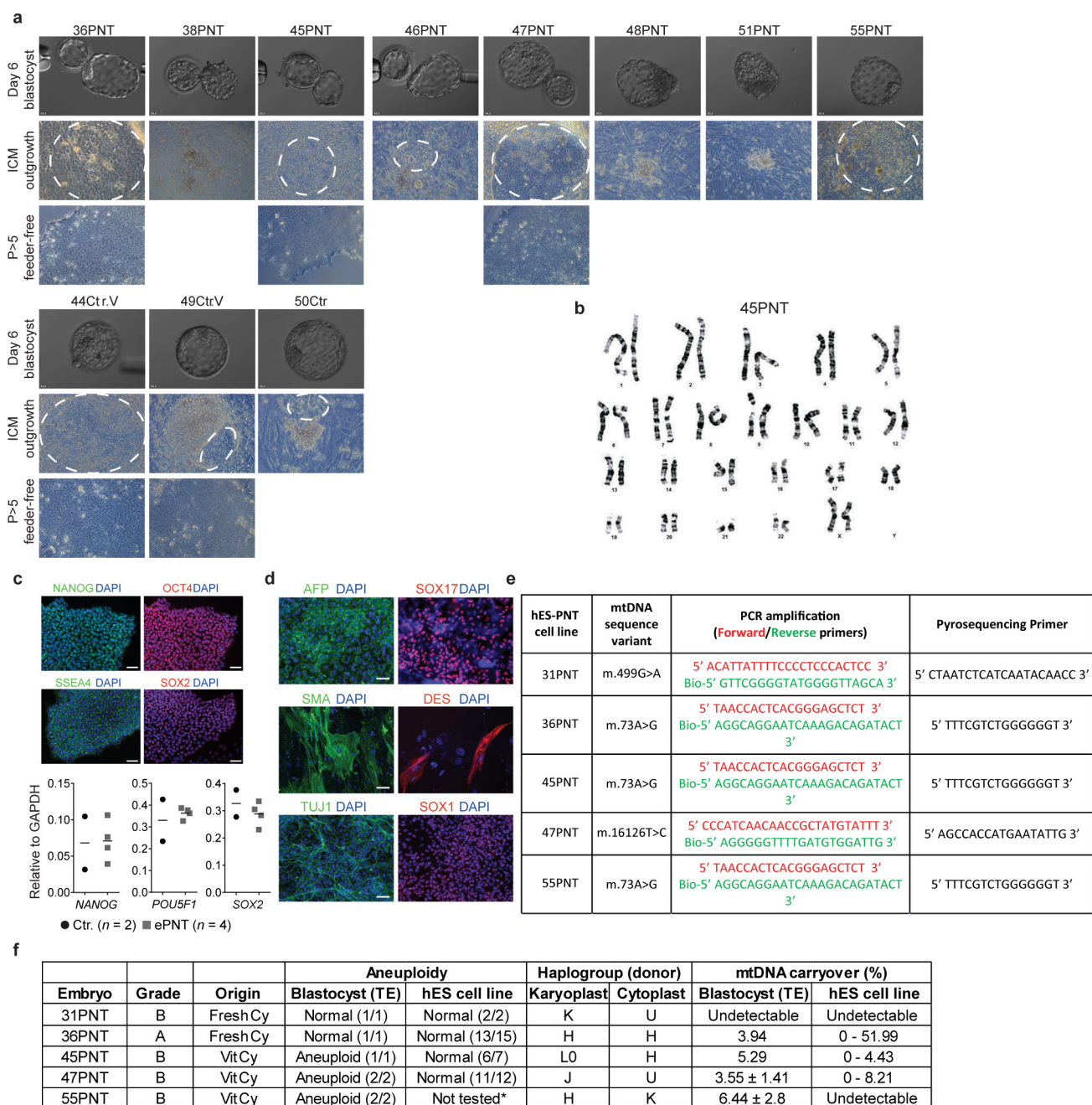
Extended Data Figure 7 | Expression of lineage-specific genes and mitochondrial OXPHOS genes in control and ePNT embryos.
a, Heatmap showing \log_2 -transformed RPKM values of selected differentially expressed genes in trophectoderm ($n = 10$), epiblast ($n = 10$) and primitive endoderm ($n = 10$) lineages. **b**, Heatmap showing expression of mitochondrial OXPHOS genes after unsupervised hierarchical clustering. Expression of OXPHOS genes encoded by mtDNA is variable both within and between blastocysts. Control and ePNT samples cluster together, irrespective of whether the cytoplasm and karyoplast had the

same (blue font) or different (purple font) mtDNA. Sample numbers and blastocyst grades are shown. The reference population includes a previously published series¹⁴. Autologous and homologous ePNT samples are derived from blastocysts in which the karyoplast and cytoplasm had the same mitochondrial genome. Heterologous ePNT samples were derived from pairs of zygotes with different mitochondrial genomes (Extended Data Fig. 5b). Expression levels are indicated on a high-to-low scale (purple–white–green). Source data files are available online for **a** and **b**.



Extended Data Figure 8 | Measurement of heteroplasmy due to mtDNA carryover during ePNT. **a**, Mitochondrial genotypes were determined by identifying polymorphic variants in the hypervariable mtDNA control regions of each donor. Sequence electropherograms of mtDNA non-coding control region with a sequence variant used for pyrosequencing (highlighted) (m.73A>G). **b**, Sequence pyrograms for the mtDNA variant (m.73A>G) in control samples. The expected level of variant is given along with the level determined by pyrosequencing (in brackets). **c**, Examples of the standard curve generated to increase accuracy in detecting low levels (0–25%) of heteroplasmy by pyrosequencing, which has previously been reported to accurately detect heteroplasmy at a level of 1% (ref. 42). Each data point represents the mean of 3–4 technical replicates. **d**, mtDNA carryover was measured by pyrosequencing using clumps of cells ($n = 92$) from day 6 blastocysts ($n = 40$; names shown on y axis). The cells were predominantly obtained from the trophectoderm

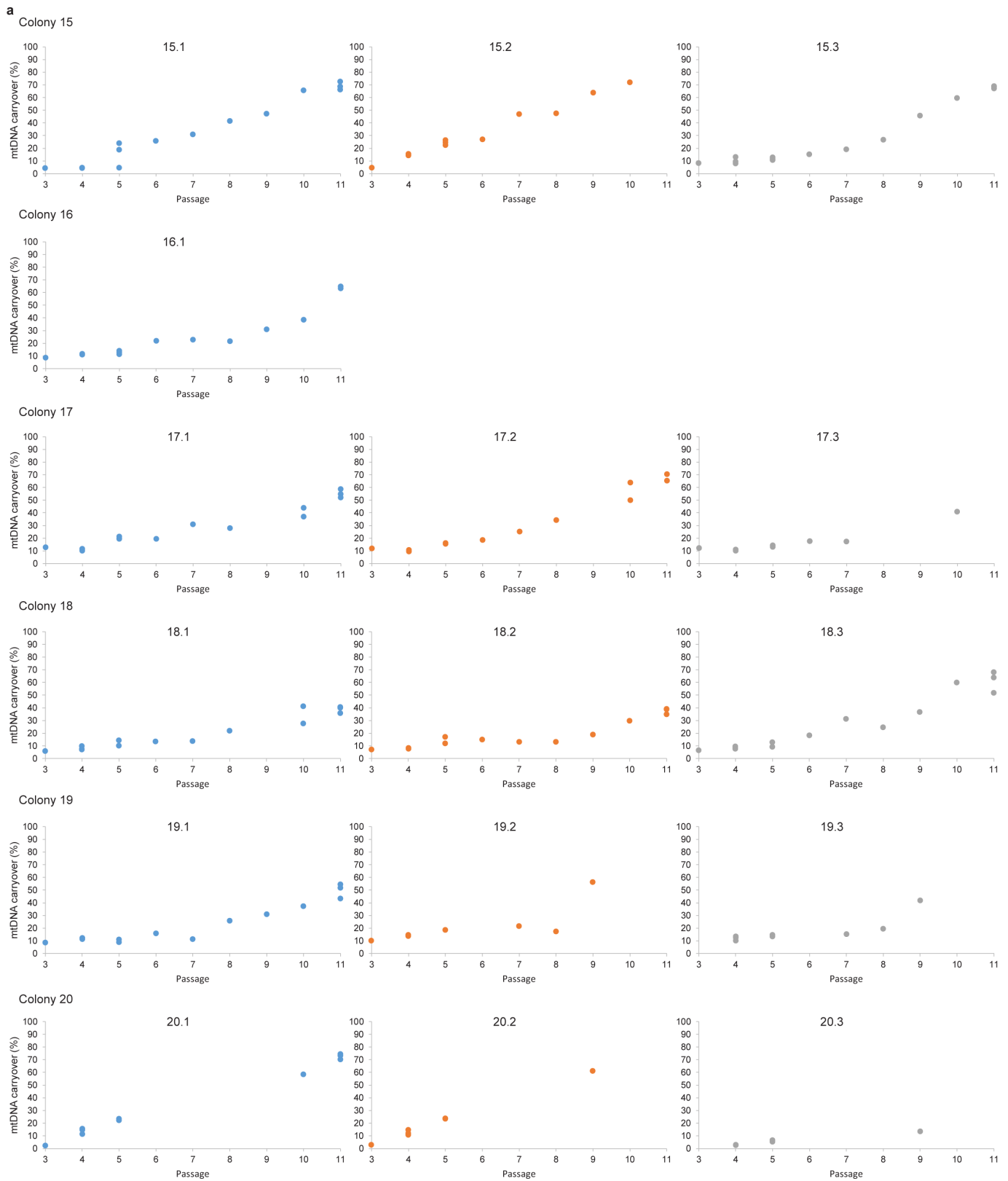
(TE) layer (purple, $n = 67$). ICM cells (red, $n = 5$) and cells of mixed trophectoderm/ICM origin (green, $n = 20$) were also analysed. Each data point represents the mean of 2–3 technical replicates. **e**, mtDNA carryover from individual blastocysts calculated from data shown in **d**. Each data point represents either the mean value where more than one sample was tested ($n = 28$ ePNT blastocysts), or a single value where only one sample was tested ($n = 12$ ePNT blastocysts). Horizontal lines show median values for each experimental group. Blastocysts arising from ePNT performed in the absence of sucrose and fused with a fresh cytoplasm (FreshCy) had significantly reduced mtDNA carryover compared with blastocysts where ePNT was performed in the presence of sucrose (P values and blastocyst numbers are shown; two-sided Mann–Whitney U -test). **f**, Graph showing the proportions of blastocysts ($n = 40$) with mtDNA carryover measurements falling within the specified levels (not significant: χ^2 test). Source data files are provided for **c–f**.



*Did not grow beyond passage 2

Extended Data Figure 9 | Derivation and characterization of human ES cells from control and ePNT blastocysts. **a**, Examples of outgrowths formed following explantation of the ICM from ePNT ($n=15$) and control ($n=6$) blastocysts used for hES cell derivations. The dashed white circle indicates the region picked for initial passage of the ICM outgrowth. Bottom, examples of hES cell colonies. **b**, Example of a normal karyogram from a PNT-hES cell line (45PNT); 4/4 lines tested showed a normal karyotype. The remaining hES cell line did not grow beyond passage 2 and was derived from a uniformly aneuploid blastocyst (55PNT; Extended Data Fig. 4). **c**, Immunostaining of representative PNT-hES cells (grown in mTeSR1) for NANOG, SSEA4 (green), SOX2 and OCT4 (red) with DAPI (blue) merge. Graph shows quantitative polymerase chain reaction with reverse transcription (qRT-PCR) analysis of control and PNT-hES cell lines for pluripotency transcripts NANOG, POU5F1 and SOX2. Horizontal

line shows the median value, which is similar between hES cells from unmanipulated control blastocysts (Ctr.; $n=2$ hES cell lines) and ePNT-hES cells ($n=4$ ePNT-hES cell lines). **d**, Immunostaining of representative PNT-hES cells after 20 days in basal MEF media, confirming differentiation into all three germ layers: endoderm (α -fetoprotein (AFP); SOX17), mesoderm (α -smooth muscle actin (SMA); desmin (DES)) and ectoderm (β -III tubulin (TUJ1); SOX1) in green or red, with DAPI (blue) merge. Scale bars, 50 μ m. **e**, Table showing the mtDNA variants and primers used to measure mtDNA carryover in PNT-hES cell lines. **f**, Summary table showing details of blastocysts and the corresponding hES cells. Aneuploidy in PNT-hES cell lines was analysed by metaphase spreads, except for 31PNT-hES, which was determined by array-CGH.



Extended Data Figure 10 | Heteroplasmy in subclones of the hES cell line derived from 36PNT. a, The 36PNT hES cell line was frozen at passage 3 (after derivation), thawed and subcloned to monitor heteroplasmy arising from the karyoplast donor mtDNA. Six colonies (15–20) were randomly selected at the first post-thaw passage (P3) and

clumps of cells were plated on 3 tissue culture wells; 5/6 colonies gave rise to 3 subclones, which were grown to P11. Subclones are distinguished by colour in the graphs. Each data point represents the mean of two technical replicates for a single cell sample. Source data file is available online.

Co-repressor CBFA2T2 regulates pluripotency and germline development

Shengjiang Tu^{1,2}, Varun Narendra^{1,2}, Masashi Yamaji³, Simon E. Vidal⁴, Luis Alejandro Rojas^{1,2}, Xiaoshi Wang⁵, Sang Yong Kim⁶, Benjamin A. Garcia⁵, Thomas Tuschl³, Matthias Stadtfeld⁴ & Danny Reinberg^{1,2}

Developmental specification of germ cells lies at the heart of inheritance, as germ cells contain all of the genetic and epigenetic information transmitted between generations. The critical developmental event distinguishing germline from somatic lineages is the differentiation of primordial germ cells (PGCs)^{1,2}, precursors of sex-specific gametes that produce an entire organism upon fertilization. Germ cells toggle between uni- and pluripotent states as they exhibit their own 'latent' form of pluripotency. For example, PGCs express a number of transcription factors in common with embryonic stem (ES) cells, including OCT4 (encoded by *Pou5f1*), SOX2, NANOG and PRDM14 (refs 2–4). A biochemical mechanism by which these transcription factors converge on chromatin to produce the dramatic rearrangements underlying ES-cell- and PGC-specific transcriptional programs remains poorly understood. Here we identify a novel co-repressor protein, CBFA2T2, that regulates pluripotency and germline specification in mice. *Cbfa2t2*^{-/-} mice display severe defects in PGC maturation and epigenetic reprogramming. CBFA2T2 forms a biochemical complex with PRDM14, a germline-specific transcription factor. Mechanistically, CBFA2T2 oligomerizes to form a scaffold upon which PRDM14 and OCT4 are stabilized on chromatin. Thus, in contrast to the traditional 'passenger' role of a co-repressor, CBFA2T2 functions synergistically with transcription factors at the crossroads of the fundamental developmental plasticity between uni- and pluripotency.

The germ line first segregates from somatic lineages via the specification of PGCs between embryonic day (E)6.25–7.25 in mice^{1,2}. PRDM14 regulates pluripotency^{5–7}, and is the only known transcription factor to specifically regulate germ cell specification⁴. To understand better the mechanism(s) underlying PGC development, we sought PRDM14-interacting proteins in the human germ-cell tumour cell line NCCIT. NCCIT cells stably expressing Flag–PRDM14 were subjected to affinity purification and proteomic analysis. In contrast with previous reports^{7–9}, neither EZH2 nor other polycomb repressive complex 2 (PRC2) components co-purified with PRDM14. Instead, the strongest identified interaction involved a co-repressor protein, CBFA2T2 (Extended Data Fig. 1a). Reciprocal affinity purification of Flag–haemagglutinin (HA)-tagged CBFA2T2 confirmed strong interaction with PRDM14 (Extended Data Fig. 1a). CBFA2T2, CBFA2T3 and ETO (also known as RUNX1T1) comprise a homologous gene family frequently targeted for translocation events in acute myeloid leukaemia^{10–13}. Despite 85% sequence similarity among homologues, their ubiquitous expression and capacity to form heterotetramers^{14–16}, ETO and CBFA2T3 were barely detectable (Extended Data Fig. 1a). This specificity for CBFA2T2 aligns with published microarray data indicating that it is the only family member upregulated during induced pluripotent stem (iPS) cell reprogramming¹⁷ and PGC specification¹⁸.

Further reciprocal immunoprecipitations confirmed endogenous PRDM14 and CBFA2T2 interaction in both NCCIT cells and mouse ES cells (Fig. 1a and Extended Data Fig. 1b, c). Gel filtration of the Flag eluate gave evidence of a larger than 600 kDa complex (Extended Data Fig. 1d), possibly due to CBFA2T2 oligomerization¹⁴. Moreover, a

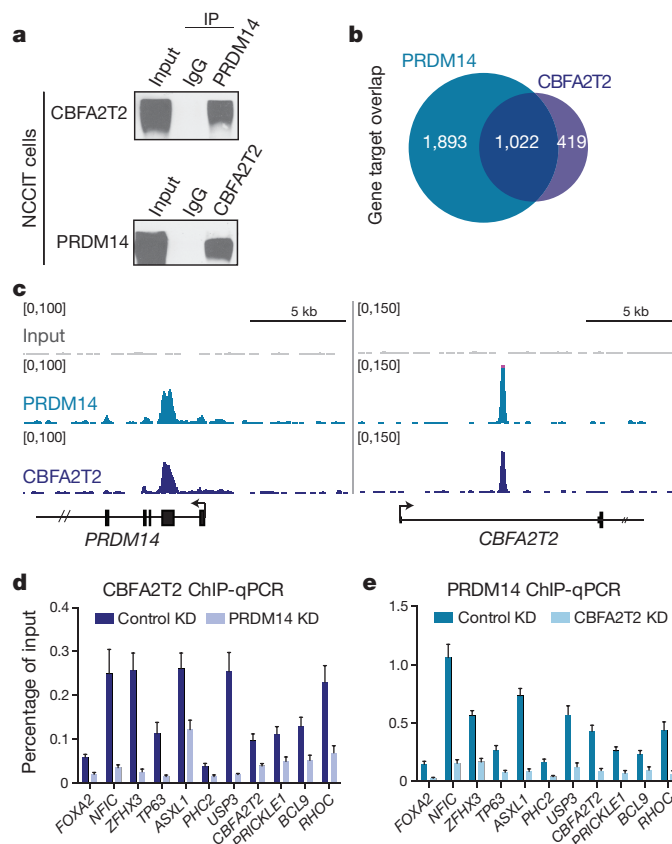


Figure 1 | PRDM14 and the co-repressor protein CBFA2T2 interact and bind to chromatin interdependently. **a**, Immunoprecipitation (IP) using antibodies against the indicated endogenous proteins in NCCIT cells. For all western blots, source gel data are included in Supplementary Fig. 1. **b**, Venn diagram depicting the overlap of PRDM14 and CBFA2T2 target genes as identified by ChIP-seq. **c**, Genome browser tracks showing PRDM14 and CBFA2T2 at their respective genomic loci. **d**, **e**, ChIP-qPCR at SERs found near the 11 indicated genes in NCCIT cells with siRNAs against CBFA2T2 (**e**) or shRNAs against PRDM14 (**d**) ($n = 3$ biological replicates). KD, knockdown. Error bars show standard deviation (s.d.). qPCR source data are included in the Supplementary Information.

¹Howard Hughes Medical Institute, New York University School of Medicine, New York, New York 10016, USA. ²Department of Biochemistry and Molecular Pharmacology, New York University School of Medicine, New York, New York 10016, USA. ³Howard Hughes Medical Institute, Laboratory for RNA Molecular Biology, The Rockefeller University, New York, New York 10065, USA.

⁴Skirball Institute of Biomolecular Medicine, Department of Cell Biology and Helen L. and Martin S. Kimmel Center for Biology and Medicine, New York University School of Medicine, New York, New York 10016, USA. ⁵Epigenetics Program, Department of Biochemistry and Biophysics, Perelman School of Medicine, University of Pennsylvania, Philadelphia, Pennsylvania 19104, USA.

⁶Rodent Genetic Engineering Core, NYU School of Medicine, New York, New York 10016, USA.

GAL4 recruitment assay demonstrated that GAL4–PRDM14 recruited CBFA2T2, but not EZH2, to the chromatinized luciferase promoter (Extended Data Fig. 1e).

To ascertain PRDM14 and CBFA2T2 colocalization on chromatin genome wide, we performed chromatin immunoprecipitation followed by sequencing (ChIP-seq) in wild-type NCCIT cells. In the case of CBFA2T2, 2,077 statistically enriched regions (SERs) were identified using a stringent *P*-value threshold of 1×10^{-15} , of which 1,384 overlapped with a PRDM14-binding event (Extended Data Fig. 2a and Supplementary Table 1). Global mapping of SERs to their nearest promoters identified 1,022 PRDM14/CBFA2T2 co-targeted genes (Fig. 1b), many of which are transcription factors involved in lineage commitment (Extended Data Fig. 2b, c). By contrast, PRDM14 exhibited very limited overlap with PRC2 or Polycomb repressive complex 1 (PRC1) (Extended Data Fig. 2a). Interestingly, PRDM14 and CBFA2T2 co-bind the genomic loci from which they are transcribed (Fig. 1c).

The sequence-specific DNA-binding capacity of PRDM14 coupled to the co-repressor activity of CBFA2T2 suggested a hierarchical model of chromatin recruitment. We performed knockdowns of *PRDM14* or *CBFA2T2* using short hairpin RNAs (shRNAs) or short interfering RNAs (siRNAs). As expected, *PRDM14* knockdown resulted in a loss of CBFA2T2 localization at 11/11 common target genes (Fig. 1d). Surprisingly, *CBFA2T2* knockdown caused a reciprocal loss of PRDM14 binding to the same genes (Fig. 1e), with minimal effect on *PRDM14* expression (Extended Data Fig. 2d). Thus, PRDM14 localization to chromatin depends on its DNA-binding activity and its association with CBFA2T2.

PRDM14 is required to repress lineage commitment genes and ensures naive pluripotency in mouse embryonic stem (mES) cells^{6,7}. To examine such a role for CBFA2T2, we generated *Cbfa2t2*- and *Prdm14*-knockout cells in KH2 mES cells¹⁹ using CRISPR–Cas9 genome editing²⁰. Guide RNAs (gRNAs) targeting the sixth exon (common to all *Cbfa2t2* isoforms) or the second exon of *Prdm14*, produced multiple lines harbouring distinct frameshift mutations and loss of the targeted protein (Fig. 2a and Extended Data Fig. 3a, b). Colonies of *Prdm14*- and *Cbfa2t2*-knockout mES cells displayed a flattened morphology (Extended Data Fig. 3c). Both mutant lines ceased to grow and could not be maintained in the absence of kinase inhibitors of MAPK/ERK and GSK3 (2i)²¹ (Extended Data Fig. 3d), as shown in the case of *Prdm14*-knockout lines⁷. After exposure to 2i-free conditions, three different knockout lines for both *Prdm14* and *Cbfa2t2*, alongside wild-type cells, were subjected to RNA sequencing (RNA-seq) analyses. Eighty-five per cent of genes differentially expressed in a *Prdm14*-knockout setting were also dysregulated upon loss of *Cbfa2t2* expression (Fig. 2b, Extended Data Fig. 3e and Supplementary Table 2). Moreover, the directionality of differential gene expression was nearly identical across mutants (Fig. 2c and Extended Data Fig. 3f). In both knockout ES cells, numerous pluripotency genes, including *Klf4*, *Pou5f1*, *Nr0b1* (also known as *Dax1*), *Lin28a* and *Myc*, were downregulated, whereas lineage commitment genes such as *Elf3*, *Cdx1* and *Pitx2* were upregulated. Similar to the case with PRDM14 (ref. 5), CBFA2T2 overexpression enhanced iPS cell reprogramming efficiency (Extended Data Fig. 3g, h). Thus, the CBFA2T2 co-repressor contributes positively to pluripotency.

Given that *Prdm14*^{−/−} mice displayed a major defect in germline development⁴, we tested the contribution of CBFA2T2 to both somatic and germline development by generating *Cbfa2t2*-knockout mice via CRISPR zygotic injection²². C57BL/6 zygotes were co-injected with *Cas9* messenger RNA and one of the gRNAs used in mES cells to target exon 6 of *Cbfa2t2* (Fig. 3a). We obtained multiple pups possessing a genetic lesion that caused a frameshift mutation and a dysfunctional truncated protein (Extended Data Fig. 4a). Genetic targeting was specific, as the ten most likely off-target genomic regions were unperturbed (Supplementary Table 3). Intercrossing of *Cbfa2t2*^{+/−} mice produced pups in a roughly normal Mendelian ratio (25% +/+ (30); 58% +/- (70); 17% -/- (21)) and *Cbfa2t2*^{−/−} animals appeared

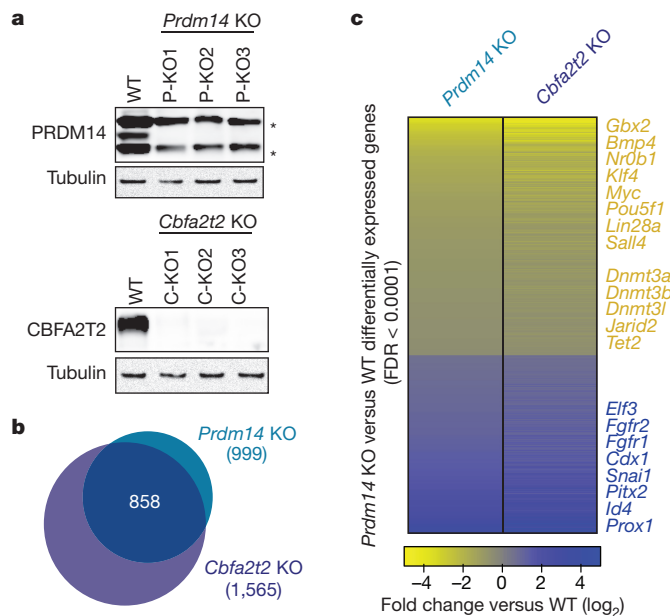


Figure 2 | PRDM14 and CBFA2T2 regulate pluripotency. **a**, Western blots confirming loss of PRDM14 or CBFA2T2 expression in knockout (KO) mES cells. Nonspecific bands are denoted with an asterisk. WT, wild type. P-KO and C-KO series represent three independently derived *Prdm14*- or *Cbfa2t2*-knockout lines, respectively. **b**, Venn diagram depicting the overlap of differentially expressed genes upon deletion of *Prdm14* or *Cbfa2t2* after removal of feeders from fetal bovine serum (FBS) plus leukaemia inhibitory factor (LIF) plus feeders culture. **c**, Heat map showing relative expression of all differentially expressed genes identified with a false discovery rate (FDR) less than 1×10^{-4} between wild-type and either *Prdm14*- or *Cbfa2t2*-knockout mES cells.

normal. However, crosses of those mice (two female and three male) with wild-type C57BL/6 counterparts failed to produce pups over 2 months.

To pinpoint the germline defect underlying the fertility phenotype of *Cbfa2t2*^{−/−} mice, we analysed anatomical and histological phenotypes of the reproductive organs. Female *Cbfa2t2*^{−/−} adult mice have underdeveloped ovaries (Fig. 3b), exhibiting a total absence of follicles with haematoxylin and eosin (H&E) stainings (Fig. 3c). Similarly, testes of male *Cbfa2t2*^{−/−} mice were reduced to ~30% of wild type (Fig. 3d and Extended Data Fig. 4b). Total number of sperm was reduced to less than 10% of wild type, while remaining sperm were largely immotile (Extended Data Fig. 4c) and unable to bind the zonae pellucidae of oocytes during *in vitro* fertilization. H&E staining of sections of *Cbfa2t2*^{−/−} testes showed that 41% of seminiferous tubules did not contain spermatogenic cells (Fig. 3e). Furthermore, postnatal day 0 (P0) male *Cbfa2t2*^{−/−} testes were almost completely devoid of gonocytes (Extended Data Fig. 4d). These data contrast with a previous study claiming that *Cbfa2t2*^{−/−} mice are fertile²³. This discrepancy may be due to differing purity of the genetic background.

To understand the germline phenotype observed in both sexes, we examined PGC development in *Cbfa2t2*^{−/−} embryos. Alkaline phosphatase staining of the genital ridge of E11.5 *Cbfa2t2*^{−/−} embryos showed greater than 95% reduction in the number of PGCs relative to wild type (Fig. 3f). This defect occurs even earlier, at E7.25–8.75 (Fig. 3g and Extended Data Fig. 4e, f). In accordance, SOX2 is not activated in the mutants (Extended Data Fig. 4g). Thus, CBFA2T2 is a novel factor required for specification and development of PGCs, and the defect in this process results in germ cell depletion.

We next mapped the genomic localizations of PRDM14 and CBFA2T2 in mES cells, relative to that of OCT4, SOX2 and NANOG (OSN) from published ChIP-seq data²⁴. CBFA2T2 and PRDM14 colocalize broadly across the genome in mES cells (Fig. 4a), and also exhibit

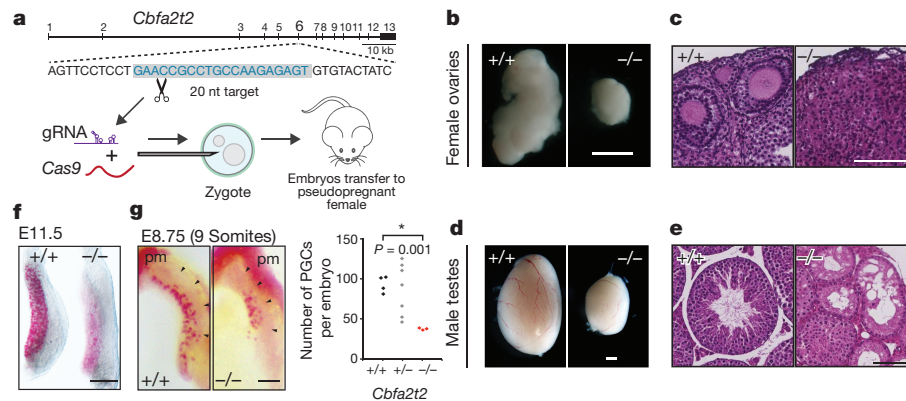


Figure 3 | *Cbfa2t2*^{-/-} mice are defective in their germ line. **a**, Schematic of *Cbfa2t2*-knockout mouse generation by CRISPR zygotic injection. nt, nucleotide. **b**, **d**, Image of dissected ovaries ($n = 8$) and testes ($n = 4$), respectively, in *Cbfa2t2*-knockout mice. Scale bars, 1 mm. **c**, **e**, Histological sections of ovaries and testes, respectively, stained by H&E. Scale bars, 100 μ m. **f**, Genital ridges of *Cbfa2t2*^{+/+} and *Cbfa2t2*^{-/-} embryos at E11.5

stained by alkaline phosphatase. Scale bar, 1 mm. **g**, Alkaline phosphatase staining of PGCs of E8.75 (9 somites) embryos is shown ($n = 3$). Arrowheads point to the boundary of the developing hindgut. pm, para-axial mesoderm. Scale bar, 100 μ m. PGC numbers in each embryo were plotted in the right panel, with the following values: +/+, 93 ± 5 ; +/-, 87 ± 5 ; -/-, 38 ± 1 .

considerable overlap with OSN, as reported for PRDM14 in human ES cells⁵. As in the case of NCCIT cells, CBFA2T2-PRDM14 target genes include numerous lineage-commitment transcription factors and chromatin regulators (Extended Data Fig. 5a and Supplementary Table 4), many of which are co-occupied by OCT4, including the histone H3K9 methyltransferase gene *Ehmt1* (Fig. 4b)²⁵.

The nervy homology 2 domain (NHR2) of ETO—a CBFA2T2 homologue—is required for self-renewal of haematopoietic stem cells in leukaemia¹⁴. NHR2 functions in homo- and heterotypic oligomerization by forming a four-helix bundle tetrameric structure. A seven amino acid 'm7' substitution within NHR2 disrupted oligomerization^{14,16}. To test whether CBFA2T2 oligomerization contributes

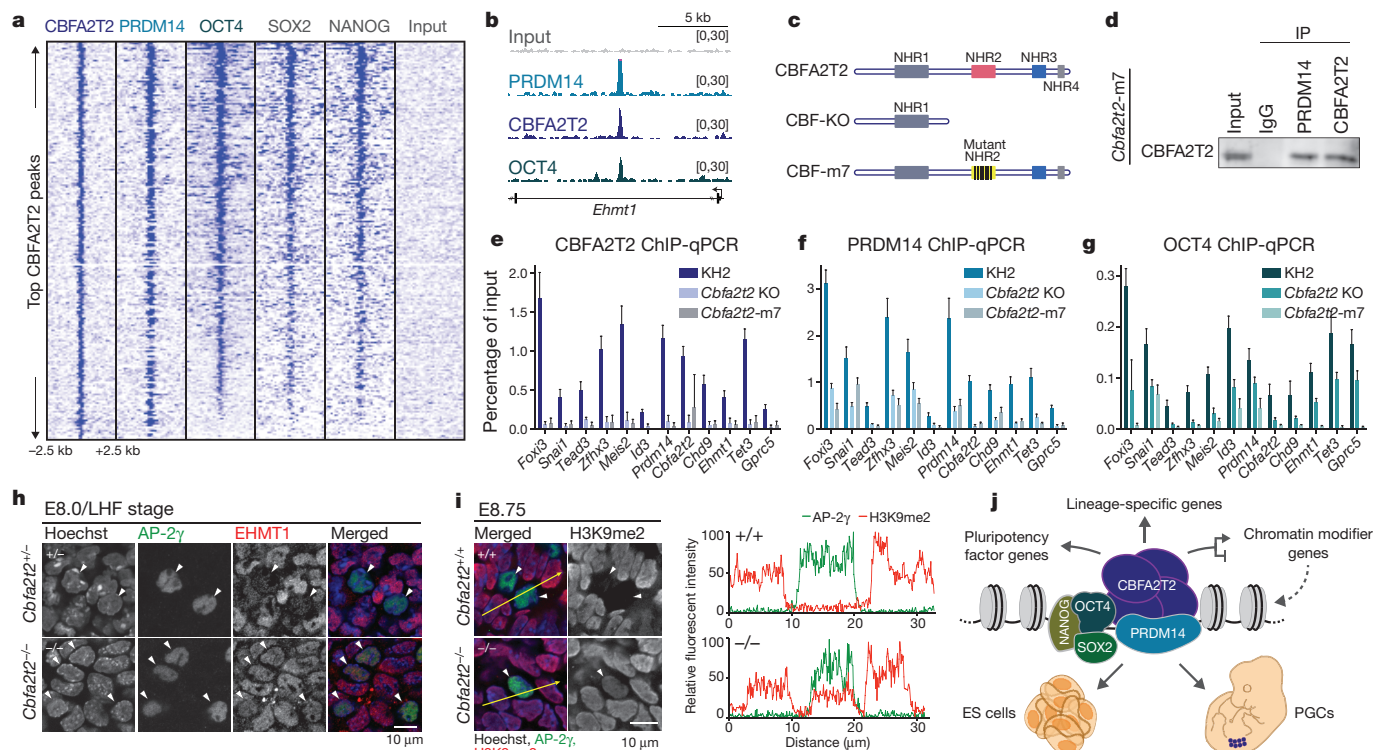


Figure 4 | Mechanism of CBFA2T2-PRDM14 complex chromatin binding and direct regulation of PGC epigenetic reprogramming. **a**, Heat map depicting CBFA2T2, PRDM14, OCT4, SOX2 and NANOG ChIP-seq read density centred about the top 299 CBFA2T2 SERs in mES cells. **b**, Representative genome browser tracks at the indicated *Ehmt1* locus in mES cells. **c**, Domain annotation of wild-type, *Cbfa2t2*-knockout (CBF-KO) and oligomerization-mutant m7 proteins. The 7 amino acids mutated in *Cbfa2t2*-m7 (CBF-m7) are depicted as lines within NHR2. **d**, Immunoprecipitation (IP) against the indicated proteins in *Cbfa2t2*-m7 mES cells followed by western blot. **e**–**g**, ChIP-qPCR using antibodies directed against CBFA2T2 (**e**), PRDM14 (**f**) or OCT4 (**g**) at SERs found

near the indicated genes ($n = 3$). Error bars, s.d. qPCR source data are included in the Supplementary Information. **h**, EHMT1 expression (red) in AP-2 γ -positive PGCs (green, arrowheads) in *Cbfa2t2*^{+/+} and *Cbfa2t2*^{-/-} embryos at E8.0, late head-fold (LHF) stage. **i**, Immunofluorescence analysis of H3K9me2 (red) of AP-2 γ -positive (green; arrowheads) PGCs in *Cbfa2t2*^{+/+} and *Cbfa2t2*^{-/-} embryos at E8.75. Line plot analysis on yellow-arrowed area are shown on the right. Scale bars, 10 μ m. Data are representative of three independent experiments. **j**, Model depicting the co-repressor CBFA2T2 oligomerizing to stabilize associated transcription factors (PRDM14 and OCT4) on chromatin.

to ES cell pluripotency, mES cells harbouring the m7 mutation in CBFA2T2 were generated using CRISPR–Cas9 technology (Fig. 4c and Extended Data Fig. 5b). Similar to *Cbfa2t2*^{−/−} cells, *Cbfa2t2*-m7 cells exhibited a flattened morphology (Extended Data Fig. 5c) and a total abrogation of CBFA2T2 occupancy at a number of target genes (Fig. 4e). Furthermore, while PRDM14 and OCT4 protein levels were unperturbed, as was biochemical interaction with PRDM14 (Extended Data Fig. 5d and Fig. 4d, respectively), CBFA2T2 oligomerization was required to stabilize PRDM14 and OCT4 on chromatin. ChIP with quantitative polymerase chain reaction (ChIP-qPCR) showed a significant reduction in PRDM14 and OCT4 occupancy across 12/12 target genes tested (Fig. 4f, g). Importantly, PRDM14–CBFA2T2-independent OCT4 targets retained OCT4 binding (Extended Data Fig. 5e). Thus, CBFA2T2 oligomerization is a critical molecular event underpinning a pluripotent network, providing a scaffolding function to stabilize essential transcription factors such as PRDM14 and OCT4 at their target sites.

CBFA2T2–PRDM14 targets comprise numerous components of the chromatin modifying machinery, such as EHMT1 (also known as GLP) (Fig. 4b, Extended Data Fig. 5a and Supplementary Table 4). During PGC development, H3K9me2 levels are reduced²⁶, potentially due to repression of the H3K9 methyltransferase EHMT1 via a presently unknown mechanism²⁷. Here, knockout of *Prdm14* or *Cbfa2t2* in mES cells caused derepression of *Ehmt1* (Extended Data Fig. 5f). Quantitative analysis showed a specific increase in H3K9me2 and H3K9me3 levels in *Prdm14*^{−/−}, *Cbfa2t2*^{−/−} and *Cbfa2t2*-m7 mutant mES cells (Extended Data Fig. 5g). Importantly, CBFA2T2–PRDM14-mediated repression was required to maintain appropriate levels of H3K9me2 in PGCs *in vivo*. PGCs in E8.0 *Cbfa2t2*^{−/−} embryos exhibited a specific EHMT1 derepression (Fig. 4h), with resultant increased H3K9me2 levels at E8.75 (Fig. 4i and Extended Data Fig. 5h, i). Thus, direct control of global levels of chromatin modifications is probably another mechanism by which PRDM14 and CBFA2T2 regulate the delicate balance between self-renewal and lineage specification (Fig. 4j).

In summary, CBFA2T2, a co-repressor protein, is a novel factor regulating pluripotency and is essential for germline development. In contrast to the long-held notion that co-repressors have a passive role in transcription factor recruitment, CBFA2T2, without intrinsic DNA-binding capacity, is required to stabilize both PRDM14 and OCT4 on chromatin via its oligomerization. While PRDM14 and OCT4 may independently bind DNA, their affinity-based 'on rate' is insufficient to generate a functional regulatory influence on transcription. Instead, CBFA2T2 oligomerization provides a larger interaction surface to limit its 'off rate' from chromatin, allowing for stable transcription factor binding (Fig. 4j). Such a model may extend to numerous transcription factors for which associated co-repressors or co-activators have yet to be identified.

Note added in proof: During the revision of this manuscript, another study utilized an *in vitro* differentiation system to determine the involvement of CBFA2T2 in PGC formation, in accordance with our *in vivo* findings²⁸.

Online Content Methods, along with any additional Extended Data display items and Source Data, are available in the online version of the paper; references unique to these sections appear only in the online paper.

Received 11 August 2015; accepted 13 April 2016.

Published online 8 June 2016.

1. Saitou, M., Barton, S. C. & Surani, M. A. A molecular programme for the specification of germ cell fate in mice. *Nature* **418**, 293–300 (2002).
2. Surani, M. A., Hayashi, K. & Hajkova, P. Genetic and epigenetic regulators of pluripotency. *Cell* **128**, 747–762 (2007).
3. Yeom, Y. I. *et al.* Germline regulatory element of Oct-4 specific for the totipotent cycle of embryonal cells. *Development* **122**, 881–894 (1996).
4. Yamaji, M. *et al.* Critical function of Prdm14 for the establishment of the germ cell lineage in mice. *Nature Genet.* **40**, 1016–1022 (2008).

5. Chia, N. Y. *et al.* A genome-wide RNAi screen reveals determinants of human embryonic stem cell identity. *Nature* **468**, 316–320 (2010).
6. Ma, Z., Swigut, T., Valouev, A., Rada-Iglesias, A. & Wysocka, J. Sequence-specific regulator Prdm14 safeguards mouse ESCs from entering extraembryonic endoderm fates. *Nature Struct. Mol. Biol.* **18**, 120–127 (2011).
7. Yamaji, M. *et al.* PRDM14 ensures naive pluripotency through dual regulation of signaling and epigenetic pathways in mouse embryonic stem cells. *Cell Stem Cell* **12**, 368–382 (2013).
8. Chan, Y. S. *et al.* A PRC2-dependent repressive role of PRDM14 in human embryonic stem cells and induced pluripotent stem cell reprogramming. *Stem Cells* **31**, 682–692 (2013).
9. Payer, B. *et al.* Tsix RNA and the germline factor, PRDM14, link X reactivation and stem cell reprogramming. *Mol. Cell* **52**, 805–818 (2013).
10. De Braekeleer, E. *et al.* RUNX1 translocations and fusion genes in malignant hemopathies. *Future Oncol.* **7**, 77–91 (2011).
11. Guastadisegni, M. C. *et al.* CBFA2T2 and C2orf112: two novel fusion partners of RUNX1 in acute myeloid leukemia. *Leukemia* **24**, 1516–1519 (2010).
12. Miyoshi, H. *et al.* The t(8;21) translocation in acute myeloid leukemia results in production of an AML1-MTG8 fusion transcript. *EMBO J.* **12**, 2715–2721 (1993).
13. Calabi, F. & Cilli, V. CBFA2T1, a gene rearranged in human leukemia, is a member of a multigene family. *Genomics* **52**, 332–341 (1998).
14. Liu, Y. *et al.* The tetramer structure of the Nervi homology two domain, NHR2, is critical for AML1/ETO's activity. *Cancer Cell* **9**, 249–260 (2006).
15. Hug, B. A. & Lazar, M. A. ETO interacting proteins. *Oncogene* **23**, 4270–4274 (2004).
16. Sun, X. J. *et al.* A stable transcription factor complex nucleated by oligomeric AML1-ETO controls leukaemogenesis. *Nature* **500**, 93–97 (2013).
17. Mikkelsen, T. S. *et al.* Dissecting direct reprogramming through integrative genomic analysis. *Nature* **454**, 49–55 (2008).
18. Kurimoto, K. *et al.* Complex genome-wide transcription dynamics orchestrated by Blimp1 for the specification of the germ cell lineage in mice. *Genes Dev.* **22**, 1617–1635 (2008).
19. Beard, C., Hochedlinger, K., Plath, K., Wutz, A. & Jaenisch, R. Efficient method to generate single-copy transgenic mice by site-specific integration in embryonic stem cells. *Genesis* **44**, 23–28 (2006).
20. Ran, F. A. *et al.* Genome engineering using the CRISPR-Cas9 system. *Nature Protocols* **8**, 2281–2308 (2013).
21. Ying, Q. L. *et al.* The ground state of embryonic stem cell self-renewal. *Nature* **453**, 519–523 (2008).
22. Yang, H., Wang, H. & Jaenisch, R. Generating genetically modified mice using CRISPR/Cas-mediated genome engineering. *Nature Protocols* **9**, 1956–1968 (2014).
23. Amann, J. M. *et al.* Mtgr1 is a transcriptional corepressor that is required for maintenance of the secretory cell lineage in the small intestine. *Mol. Cell. Biol.* **25**, 9576–9585 (2005).
24. Whyte, W. A. *et al.* Master transcription factors and mediator establish super-enhancers at key cell identity genes. *Cell* **153**, 307–319 (2013).
25. Tachibana, M. *et al.* Histone methyltransferases G9a and GLP form heteromeric complexes and are both crucial for methylation of euchromatin at H3-K9. *Genes Dev.* **19**, 815–826 (2005).
26. Seki, Y. *et al.* Extensive and orderly reprogramming of genome-wide chromatin modifications associated with specification and early development of germ cells in mice. *Dev. Biol.* **278**, 440–458 (2005).
27. Hajkova, P. *et al.* Chromatin dynamics during epigenetic reprogramming in the mouse germ line. *Nature* **452**, 877–881 (2008).
28. Nady, N. *et al.* ETO family protein Mtgr1 mediates Prdm14 functions in stem cell maintenance and primordial germ cell formation. *Elife* **4**, e10150 (2015).

Supplementary Information is available in the online version of the paper.

Acknowledgements We thank P. Andrews and X.-J. Sun for providing plasmids. We are grateful to L. Vales, M. E. Torres-Padilla and L. Bu for critical comments, H. Zheng for MS analysis, and D. Hernandez, C. Leek, M. Yamaji, A. Paradkar and M. Alu for excellent technical assistance. The work was supported by the Howard Hughes Medical Institute (HHMI) and National Institutes of Health (NIH; R01GM064844-12) (D.R.). B.A.G. acknowledges funding from NIH grant R01GM110174. T.T. was supported by the HHMI, NIH, Starr Foundation, and Tri-Institutional Stem Cell Initiative. M.Y. was a recipient of a Japan Society for the Promotion of Science (JSPS) Research Fellowship.

Author Contributions S.T. designed and performed majority of experiments; V.N. analysed ChIP-seq and RNA-seq data; S.E.V., S.T. and M.S. performed iPSC reprogramming experiments; X.W. and B.A.G. quantified histone modifications. S.Y.K. did CRISPR zygotic injection. S.T., S.Y.K., M.Y. and L.A.R. characterized mice. M.Y., S.T. and T.T. designed and performed PGC experiments. S.T., V.N., M.Y. and D.R. wrote the manuscript.

Author Information Sequencing data have been deposited in the Gene Expression Omnibus under accession number GSE71676. Reprints and permissions information is available at www.nature.com/reprints. The authors declare no competing financial interests. Readers are welcome to comment on the online version of the paper. Correspondence and requests for materials should be addressed to D.R. (danny.reinberg@nyumc.org).

METHODS

No statistical methods were used to predetermine sample size. For mouse studies, no randomization or blinding was done.

Cell lines and cultures. NCCIT cells (CRL-2073) were obtained from ATCC and grown in RPMI1640 media with 10% FBS, L-glutamine, penicillin/streptomycin and sodium pyruvate. 293Trex cells (ThermoFischer, #R710-07) were grown in DMEM with 10% FBS, L-glutamine and penicillin/streptomycin. KH2 ES cells, described previously¹⁹, were grown in DMEM supplemented with 15% FBS, L-glutamine, penicillin/streptomycin, non-essential amino acids, 0.1 mM β -mercaptoethanol, LIF and 2i inhibitors (1 μ M MEK1/2 inhibitor (PD0325901) and 3 μ M GSK3 inhibitor (CHIR99021)). On feeder conditions, 2i was omitted. Human fibroblast BJ cells were obtained from ATCC and maintained on fibroblast medium: DMEM knockout media with 10% FBS sera, 1% non-essential amino acids, L-glutamine, penicillin/streptomycin, non-essential amino acids and 0.1 mM β -mercaptoethanol. Human iPSC cell culture medium contains advanced DMEM/F12 plus 20% Knockout Serum Replacement, L-glutamine, penicillin/streptomycin, non-essential amino acids, 0.1 mM β -mercaptoethanol plus 10 ng ml⁻¹ FGF2 (Peprotech). Cell lines were verified by western blots and PCR, and tested for mycoplasma contamination.

To generate PRDM14 or CBFA2T2 NCCIT stable lines, CAG-eGFP vector²⁹ was used to clone N-terminal Flag-tagged and C-terminal HA-tagged target gene constructs. After 2 weeks puromycin selection, single colonies were picked and expanded. Similarly, GAL4-PRDM14 293 Trex stable line was generated by transfecting pcDNA4-T0 plasmid (ThermoFisher, #V1020-20) with an N-terminal GAL4, C-terminal HA fusion PRDM14 construct. For *Prdm14*- or *Cbfa2t2*-knockout KH2 lines, gRNAs were cloned into pSpCas9 (BB)-2A-eGFP vector (Addgene, px458)²⁰. For *Prdm14* knockout, the gRNA sequence was: GCGATGGCCTTACCGCCCTC. For *Cbfa2t2* knockout, two gRNAs were used: ACTCTCTTGGCAGGCGGTTC and CTGGCCCCAGGATTCATAA. For *Cbfa2t2* m7 knock-in lines, a gRNA sequence, AGAGAAACTAGGCGCTCCA, targeting the NHR2 domain was chosen for cloning into the Cas9 vector. For this knock-in, a donor 723 bp gBlock DNA centred at the NHR2 domain sequence was PCR amplified and purified. Mouse KH2 ES cells were transfected with the above Cas9-gRNA-eGFP plasmids with Lipofectamine 2000. In the case of m7 knock-in, the 723 bp template was included. Medium-to-high GFP population was FACS sorted and seeded at 20,000 cells per 15-cm plate. Seven days later, ES-cell single colonies were selected, expanded and genotyped.

Antibodies. Human PRDM14 antigen (N-terminal residue 1–243) was generated by using PreScission protease to cleave the recombinant fusion protein GST-PRDM14(1–243). Rabbit polyclonal antibody was affinity purified by affigel 15 matrix conjugated with a His₆-tagged antigen of PRDM14(1–243). Mouse PRDM14 antibody was described previously³⁰. Briefly, the N-terminal construct (amino acids 1–231) of mouse PRDM14 was cloned into pET30a vector (Novagen, #69909-3). The corresponding His₆-tagged protein was overexpressed and purified for rabbit polyclonal antigen production. The antibody was purified with Affi-gel 15 as mentioned earlier. In-house rabbit EZH2 antibody was reported previously³¹. Other antibodies used in this study were from commercial sources with the following catalogue numbers: anti-CBFA2T2, Bethyl A303-593A; anti-OCT4, Santa Cruz #sc-5279; anti-Ring1B, Bethyl #A302-869A; anti-SUZ12, Cell Signaling #3737S; anti-HA, Abcam #ab9110; anti-tubulin, Abcam #ab6046; anti-TRA-1-81 biotin, eBioscience #13-8883-82; Alexa Fluor 660 Streptavidin, Life Technologies s21377; HRP Streptavidin, Biolegend #405210; MVH, Abcam #ab13840.

Nuclear extracts, immunoprecipitation and affinity purification. Nuclear extracts were prepared with buffer A and buffer C, essentially as described³². Cytosol fraction was removed by buffer A (20 mM Tris, pH 7.9, 10 mM KCl, 0.5 mM dithiothreitol (DTT), 0.2 mM PMSF, 1 μ g ml⁻¹ Pepstatin A, 1 μ g ml⁻¹ Leupeptin, 1 μ g ml⁻¹ Aprotinin). The pellet was resuspended in buffer C (20 mM HEPES, pH 7.5, 20% glycerol, 420 mM NaCl, 0.5 mM DTT, 0.2 mM EDTA, 0.2 mM PMSF, 1 μ g ml⁻¹ Pepstatin A, 1 μ g ml⁻¹ Leupeptin, 1 μ g ml⁻¹ Aprotinin) and snap frozen with liquid nitrogen. For immunoprecipitation, 2–5 μ g antibody was incubated overnight with 0.8 mg nuclear extract and immobilized on 40 μ l of protein A:protein G beads (3:1 volume ratio). After 6 washes with BC350 (20 mM Tris, pH 7.9, 350 mM NaCl, 0.1% NP40, 0.2 mM PMSF, 0.2 mM DTT), the immunoprecipitate was separated by SDS-PAGE for western blot analysis. For loading controls, 5% of input nuclear extract was used. For Flag affinity purification, 10 mg nuclear extract was incubated with 100 μ l Flag M2 beads overnight, and washed six times with BC350, as described earlier. Immunoprecipitate was eluted with 0.2 mg ml⁻¹ Flag peptide in BC100 (20 mM Tris, pH 7.9, 100 mM NaCl, 0.2 mM PMSF, 0.2 mM DTT). The Flag eluate was run into an SDS-PAGE gel for 1 cm. The upper gel slices containing proteins were excised and subjected to trypsin digestion and liquid chromatography-mass spectrometry (LC-MS) analysis. Digested peptides were desalted and concentrated using C18 stagetips for LC-tandem MS (LC-MS/MS)

analysis. One hundred and twenty minute gradients (6–75% acetonitrile) were used (nanoLC1000, Thermo Scientific) and spectra were recorded on an Orbitrap Velos (Thermo Scientific) by selecting the 15 most intense precursor ions for fragmentation in each full scan.

PRDM14 and CBFA2T2 knockdowns. For PRDM14-knockdown experiments, the following shRNA sequences from Open Biosystems TRC pLKO.1 shRNA libraries were used: human PRDM14 shRNA 1: TTCTGTAGTGTCCATAGGACG; human PRDM14 shRNA 2: AACATGAAGAATGTGGATCCG; human PRDM14 shRNA 3: TTGAAGGGAGTCTTTATCCAG.

Lentiviruses from these shRNAs, as well as empty pLKO.1 vector were produced from 293T cells. Four million 293T cells were seeded on a 10-cm plate. Next day, 2.3 μ g plasmid (shRNA or control), 1.6 μ g psPAX2, and 1.1 μ g pMD2.G 2nd generation packaging plasmids (Addgene, #12260, #12259) were transfected with Lipofectamine 2000. Forty eight hours and sixty hours post-transfection, supernatants were collected. Viral particles were filtered through 0.45 μ m filters and enriched 100-fold by centrifugation at 20,000 r.p.m. for 1.5 h. For transduction of NCCIT cells by lentivirus, 0.20 million cells per well were seeded in 6-well plates. The next day, 20 μ l virus was transduced with polybrene at a final concentration of 8 μ g ml⁻¹. Forty eight hours post-transduction, 1 μ g ml⁻¹ Puromycin was added to select for transduced NCCIT cells. Transduced cells were expanded and harvested in 1 week for ChIP-qPCR.

For CBFA2T2-knockdown experiments, the following On-TARGETplus siRNA sequences from Thermo Scientific were used: GAUCAUCGUUUGACAGAAA; CAGAUUCUCUCAGCAAUGA; UAGAGGAUUAUGCAACUUC; CCACAG AGAUUCAGCAAG.

Qiagen AllStars negative siRNA was used as control. siRNA (final concentration, 10 nM) was transfected with 4 μ l Lipofectamine RNAiMAX (Life Technologies) in each well of 6-well plates. Seventy hours post-transfection, cells were harvested for western blot analysis. For ChIP chromatin preparation, CBFA2T2 siRNA transfection was scaled up to two 10-cm plates. Cells were split once before harvesting chromatin.

ChIP-qPCR and ChIP-seq. ChIP was done as described with biological replicates³³. Briefly, cells were crosslinked with 1% formaldehyde, lysed, and sonicated in buffer 3 (10 mM Tris, pH 7.9, 1 mM EDTA, 0.5 mM EGTA, 0.5% N-lauroylsarcosine) down to a desired chromatin size. Forty microlitres of 3:1 mixture of protein A and protein G Sepharose beads were blocked with 0.1 mg ml⁻¹ salmon sperm DNA and 1 mg ml⁻¹ bovine serum albumin (BSA). Approximately 100 μ g chromatin was pre-cleared by half of the blocked beads, and incubated with 2–5 μ g antibody overnight in Tris buffer (10 mM Tris, 10 mM EDTA, 1% Triton X-100, 0.1% sodium deoxycholate (DOC) and protease inhibitors). After 4 h incubation with the remaining protein A/G beads, samples were washed six times with RIPA buffer (0.5 M LiCl, 50 mM HEPES, pH 7.5, 1 mM EDTA, 1% NP-40, 0.7% DOC and protease inhibitors). After a brief wash with TE buffer (10 mM Tris, 1 mM EDTA, 50 mM NaCl), samples were resuspended in 200 μ l of T₅₀E₁₀S₁ (50 mM Tris, pH 8.0, 10 mM EDTA, 1% SDS) and incubated at 65 °C overnight to reverse crosslinks. Samples were digested at 55 °C for 3 h with 10 μ g each of RNase A and proteinase K. Digested samples were PCR column purified and diluted into 300 μ l water for qPCR. For qPCR quantification, 5 μ l SYBR Green I Master mix (Roche), ROX reference dye, 3 μ l water, 1 μ l 5 μ M primer pair, and 1 μ l DNA were mixed for PCR amplification. For GAL4 ChIP-qPCR, the primer sequences were: GAL4ChIPLucP5F: CACCGAGCGACCTGCATAAGC; and GAL4ChIPLucP5R: GCTTCTGCCCAACCGAACGGAC. Other qPCR primers are listed in Supplementary Table 3.

For PRDM14, CBFA2T2 and OCT4 ChIP-Seq, 40 μ l protein G beads per immunoprecipitation were used, and salmon sperm DNA was omitted in the blocking step. DNA was eluted in 30 μ l elution buffer for library construction as described later³⁴.

RNA-seq. Mouse KH2 cells and knockout lines were grown on feeders for three consecutive passages on 6-well plates with FBS sera media supplemented with LIF. After the 4th passage (day 5), feeder cells were removed by trypsinizing and then plating the cells on a T25 flask for 35 min. The unattached ES cells were spun down and lysed with TRIzol. Standard RNA-seq procedure was used³⁴.

Library construction. Libraries for ChIP-seq were prepared according to manufacturer's instructions (Illumina). Briefly, immunoprecipitated DNA (~5 ng) was end-repaired using End-It Repair Kit (Epicentre), tailed with deoxyadenine using Klenow exo- (New England Biolabs), and ligated to custom adapters with T4 Rapid DNA Ligase (Enzymatics). Fragments of 200–400 bp were size-selected using Agencourt AMPure XP beads, and subjected to PCR amplification using Q5 DNA polymerase (New England Biolabs). Libraries were quantified by qPCR using primers annealing to the adaptor sequence and sequenced at a concentration of 12 pM on an Illumina HiSeq. Barcodes were used for multiplexing. For RNA-seq libraries, polyA+ RNA was isolated using Dynabeads Oligo(dT)25 (Invitrogen) and

constructed into strand-specific libraries using the dUTP method. Once dUTP-marked double-stranded cDNA was obtained, the remaining library construction steps followed the same protocol as described earlier for ChIP-seq libraries.

Bioinformatic analysis. Sequenced reads from ChIP-seq experiments were mapped to the hg19 or mm9 genome with Bowtie, using the parameters $-v2$ and $-m4$. Normalized genome-wide read densities were computed using a custom script and visualized on the UCSC genome browser after extending to the estimated size of a ChIP fragment (~200 nt). Enriched regions (ERs) were identified using MACS 1.40rc2 with default parameters and an input control, and then filtered for ERs with at least 10 tags and an unadjusted P value of $<1 \times 10^{-15}$ for ChIPs performed in NCCIT cells, and $<1 \times 10^{-5}$ for ChIPs performed in KH2 mES cells. ERs were associated to gene targets using the HOMER tool. Heatmaps were generated using a custom code in which reads were mapped to non-overlapping 10-bp bins within peak-centred windows of 5–10 kb. Normalized cumulative read density across these bins is depicted. All Gene Ontology analysis was performed using the DAVID tool³⁵.

RNA-seq reads were assigned to genes using DEGseq (R package)³⁶ and the ENSEMBL annotation. FDR-adjusted P values for differential gene expression were calculated with DEseq (R package). Genes were considered to be 'differentially expressed' if their adjusted P value was <0.0001 .

Human iPS cell reprogramming. PRDM14 and CBFA2T2 lentiviral constructs were cloned into pHAGE-EF1 α -IRES-tdTomato and pHAGE-EF1 α -IRES-zGreen vectors, respectively. OKSM polycistronic vector under EF1 α control was used for the reprogramming experiments³⁷. Lentiviruses were produced as described previously³⁸. Supernatants were collected every 12 h on two consecutive days starting 48 h after transfection. Viral particles were concentrated by centrifugation at 20,000 r.p.m. for 1.5 h. Virus titre was quantified by flow cytometry and immunofluorescence, and high-titre viruses (greater than 60% transduction efficiency) were chosen for further human iPS cell reprogramming experiments. Human fibroblast BJ cells were seeded at 0.14 million cells per well of a 6-well plate. Twenty-eight hours after seeding, 10–15 μ l of concentrated OKSM, OKSM plus PRDM14, or OKSM plus CBFA2T2 virus combinations were used to transduce human fibroblasts with polybrene (final concentration of 8 μ g ml⁻¹). Forty hours post-transduction, tdTomato and GFP-positive cells were sorted and seeded onto irradiated mouse embryonic fibroblast (MEF) feeders (GLOBASTEM). Cells undergoing reprogramming were maintained on human fibroblast medium for the first week, and transferred into 100% human iPS culture medium at the end of the second week. At the end of the third week on feeders, human iPS cells were tested for live TRA-1-81 staining. Anti-human TRA-1-81 (Podocalyxin) Biotin solution (1:200 dilution in 4% FBS PBS solution) was directly added to each well. After washing, fluorescent secondary antibody Alexa Fluor 660 Streptavidin (1:200) was used for imaging. For colony counting, TRA-1-81 staining with secondary antibody conjugated with HRP was used with substrate DAB (Vector Labs, #SK-4100)³⁹. Error bars are based on three biological replicates of each condition.

Cbfa2t2-knockout mice. We generated *Cbfa2t2*-knockout mice via zygotic injection²². T7-gRNA DNA template was PCR amplified from one of the Cas9-gRNA plasmids for generation of *Cbfa2t2*-knockout ES cells. The gRNA sequence is ACTCTCTTGGCAGCGGTTT. The primer sequences are TTAATACGACTCACTATAGGGAGAATGGACTATAAGGACCACGAC and GCGAGCTCTAGGAATTCTTAC. Subsequently, T7-gRNA was generated by *in vitro* transcription with MEGAShortscript T7 kit. Similarly, Cas9 mRNA was generated with mMESSAGE mMACHINE T7 ULTRA kit (Life Technologies). Injection mix contained 100 ng μ l⁻¹ Cas9 mRNA, 50 ng μ l⁻¹ gRNA. Cytoplasmic injection was performed on 102 C57BL/6 zygotes. Of those, 72 embryos were transferred to three pseudopregnant female mice. A total of 30 pups were born and genotyped. Genotyping primers were TAGCAGTCTTCTGCTTTGG and CTTCTCGGTGTTCTAGCATCTT. Ten top potential off-target sites were tested by PCR sequencing. The ten primer pair sequences are listed in Supplementary Table 3. Crossing CRISPR mutant mice containing one allele of indel mutation with wild-type C57BL/6 mice resulted in *Cbfa2t2*^{+/-} mice. Intercrossing of these mice produced full *Cbfa2t2*-knockout mice (*Cbfa2t2*^{-/-}). Mouse studies were approved by the New York University Medical Center Institutional Animal Care and Use Committee.

Sperm counts and motility analysis and *in vitro* fertilization. Individual caudal epididymis was minced in 90 μ l MBCD medium. After 30 min incubation at 37 °C, sperm were separated by pipetting and passaging through a 70- μ m filter. Sperm counts and motility assessment were performed by using the DRM-600 CELL-VU Sperm Counting Cytometer. For *in vitro* fertilization (IVF), 28 egg donors were used in each experiment.

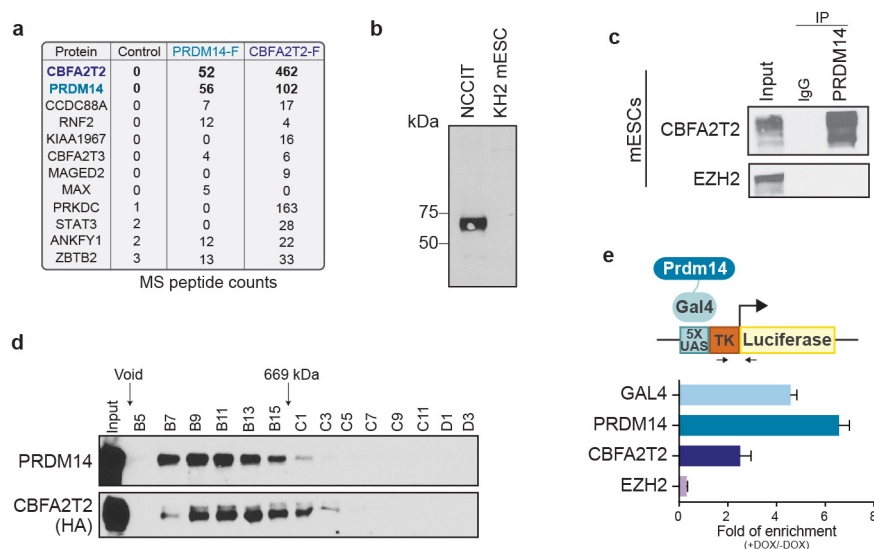
Tissue staining of sections. Mutant testes were weighed before fixation. Ovaries and testes were fixed in Bouin's fixative for 2–6 h, washed with PBS overnight, dehydrated with ethanol solution, embedded in paraffin and sectioned at 5 μ m.

Sections were stained by H&E. P0 testes were fixed with 4% PFA for 15 min. Slides of 10- μ m cryosections were stained with MVH antibody (1:250).

Whole-mount immunofluorescence analysis and alkaline phosphatase staining. Embryo isolation and staging were done as described previously⁴. The immunofluorescence analysis and alkaline phosphatase staining were performed essentially as described previously⁴. The primary antibodies used were as follows: anti-AP-2 γ rabbit polyclonal, 1:500 (catalogue no. sc-8977; Santa Cruz Biotechnology); anti-ETMT1/GLP mouse monoclonal, 5 μ g ml⁻¹ (catalogue no. PP-B0422-00; R&D Systems); anti-H3K9me2 mouse monoclonal, 1:500 (catalogue no. ab1220; Abcam); anti-SOX2 goat polyclonal, 1:200 (catalogue no. sc-17320, Santa Cruz Biotechnology). The following secondary antibodies from Molecular Probes were used at a dilution of 1:500: Alexa Fluor 488 goat anti-rabbit IgG; Alexa Fluor 568 goat anti-mouse IgG. The stained embryos were mounted with Vectashield Antifade Mounting Medium (catalogue no. H-1000; Vector Laboratories). The immunofluorescence images and the alkaline phosphatase staining images were taken by a confocal microscope (Zeiss LSM880) and a stereomicroscope (Leica M80), respectively. The image analyses were done by using ImageJ/Fiji software.

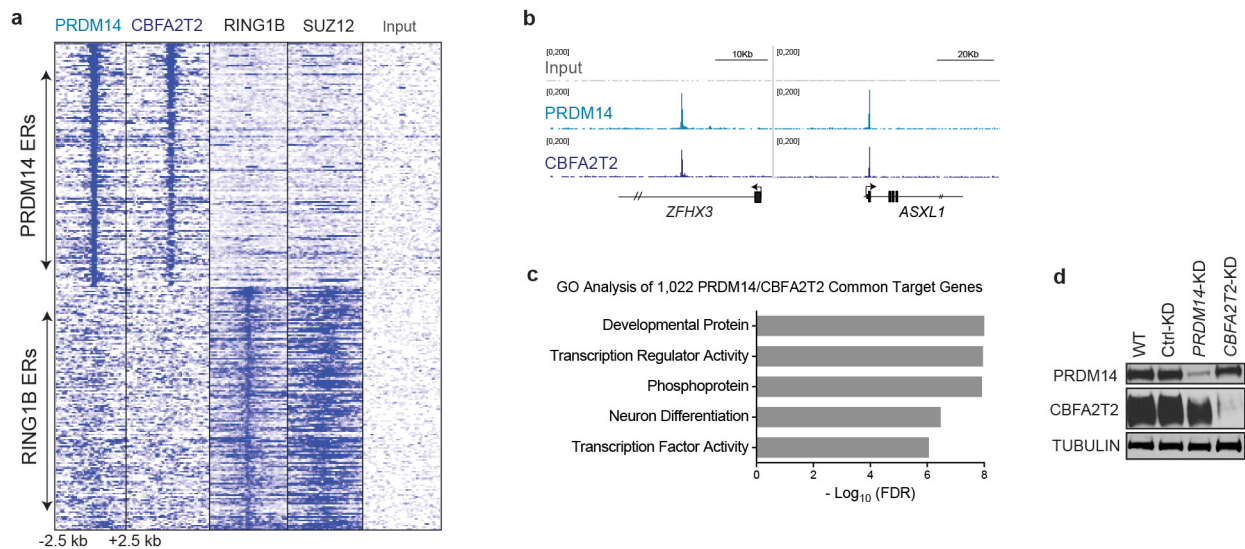
Histone modification quantification. Histones from mouse KH2 and knock-out mutant ES cells were purified by acid extraction⁴⁰. Approximately 100 μ g histones were derivatized with propionic anhydride. The reaction was repeated two times and then trypsinized. The newly formed N termini were then derivatized with propionic anhydride twice. The resulting peptides were purified with C18 stage-tip for MS analysis. Desalted histone peptides (1 μ g) were then loaded onto and separated by reversed-phase high-performance LC (HPLC) on a Thermo Scientific EASY-nLC 1000 system with a 75 μ m i.d. \times 15 cm (internal diameter and length) Reprosil-Pur C18-AQ 3 μ m nanocolumn run at 300 nl min⁻¹. Peptides were eluted with a gradient from 2% to 30% ACN (35 min) and to 98% ACN over 20 min in 0.1% formic acid. The HPLC was coupled to a Thermo Scientific Orbitrap Elite Hybrid Ion Trap-Orbitrap mass spectrometer. In each cycle, one full MS Orbitrap detection was performed with the scan range of 290 to 1,400 m/z , a resolution of 60 K and AGC of 1×10^6 . Then, data-dependent acquisition mode was applied with a dynamic exclusion of 30 s. MS2 scans were followed on parent ions from the most intense ones. Ions with a charge state of one were excluded from MS/MS. An isolation window of 2 m/z was used. Ions were fragmented using collision induced dissociation (CID) with a collision energy of 35%. Iontrap detection was used with normal scan range mode and normal scan rate. The resolution was set to be 15 K with AGC of 1×10^4 . Targeted scans were performed on a number of peptides to increase the identification of low-abundance modifications. Histone PTM quantification was performed by using in-house-developed software EpiProfile⁴¹.

29. Liew, C. G., Draper, J. S., Walsh, J., Moore, H. & Andrews, P. W. Transient and stable transgene expression in human embryonic stem cells. *Stem Cells* **25**, 1521–1528 (2007).
30. Burton, A. et al. Single-cell profiling of epigenetic modifiers identifies PRDM14 as an inducer of cell fate in the mammalian embryo. *Cell Reports* **5**, 687–701 (2013).
31. Kuzmichev, A., Jenuwein, T., Tempst, P. & Reinberg, D. Different EZH2-containing complexes target methylation of histone H1 or nucleosomal histone H3. *Mol. Cell* **14**, 183–193 (2004).
32. Dignam, J. D., Lebovitz, R. M. & Roeder, R. G. Accurate transcription initiation by RNA polymerase II in a soluble extract from isolated mammalian nuclei. *Nucleic Acids Res.* **11**, 1475–1489 (1983).
33. Takahashi, Y., Rayman, J. B. & Dynlacht, B. D. Analysis of promoter binding by the E2F and pRB families *in vivo*: distinct E2F proteins mediate activation and repression. *Genes Dev.* **14**, 804–816 (2000).
34. Narendra, V. et al. CTCF establishes discrete functional chromatin domains at the Hox clusters during differentiation. *Science* **347**, 1017–1021 (2015).
35. Huang, W., Sherman, B. T. & Lempicki, R. A. Systematic and integrative analysis of large gene lists using DAVID bioinformatics resources. *Nature Protocols* **4**, 44–57 (2009).
36. Wang, L., Feng, Z., Wang, X., Wang, X. & Zhang, X. DEGseq: an R package for identifying differentially expressed genes from RNA-seq data. *Bioinformatics* **26**, 136–138 (2010).
37. Sommer, C. A. et al. Induced pluripotent stem cell generation using a single lentiviral stem cell cassette. *Stem Cells* **27**, 543–549 (2009).
38. Mostoslavsky, G., Fabian, A. J., Rooney, S., Alt, F. W. & Mulligan, R. C. Complete correction of murine Artemis immunodeficiency by lentiviral vector-mediated gene transfer. *Proc. Natl Acad. Sci. USA* **103**, 16406–16411 (2006).
39. Onder, T. T. et al. Chromatin-modifying enzymes as modulators of reprogramming. *Nature* **483**, 598–602 (2012).
40. Lin, S. & Garcia, B. A. Examining histone posttranslational modification patterns by high-resolution mass spectrometry. *Methods Enzymol.* **512**, 3–28 (2012).
41. Yuan, Z. F. et al. EpiProfile quantifies histone peptides with modifications by extracting retention time and intensity in high-resolution mass spectra. *Mol. Cell. Proteomics* **14**, 1696–1707 (2015).



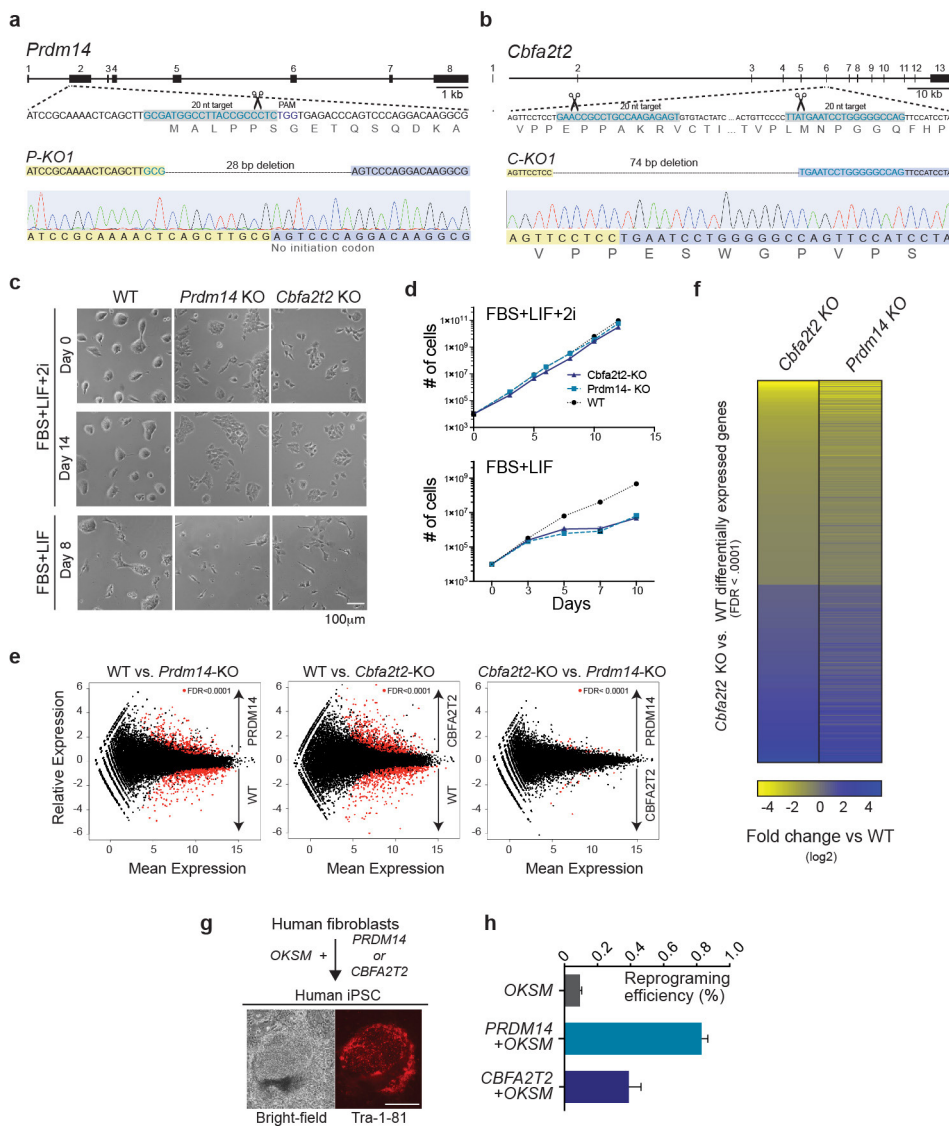
Extended Data Figure 1 | Biochemical interaction between PRDM14 and CBFA2T2. **a**, Mass spectrometry peptide counts from Flag affinity purification from NCCIT control cells and stable lines expressing Flag-HA-PRDM14 (PRDM14-F), and Flag-HA-CBFA2T2 (CBFA2T2-F). **b**, Characterization of in-house human PRDM14 antibody. Western blot performed using 30 μ g of NCCIT and KH2 mES cell lysate. Human PRDM14 antibody is specific and does not cross-react with mouse PRDM14. **c**, Immunoprecipitation (IP) using antibodies against the

indicated endogenous proteins in mES cells. **d**, Western blot of Superose 6 column fractionation of Flag-purified CBFA2T2 complex in NCCIT cells stably expressing Flag-HA-CBFA2T2. **e**, ChIP analysis using the indicated antibodies in 293T-REx harbouring a UAS-TK-Luciferase transgene. Fold enrichment represents the ratio of enrichment by ChIP-qPCR upon induction of GAL4-PRDM14 expression via doxycycline addition. Positions of the primer set are indicated by small arrows in the schematic. qPCR source data are included in the Supplementary Information.



Extended Data Figure 2 | PRDM14 and CBFA2T2 exhibit an overlapping and interdependent distribution on chromatin in NCCIT cells. **a**, Heat map depicting PRDM14, CBFA2T2, RING1B and SUZ12 read density across a 5-kb window centred about the PRDM14 (top) or RING1B (bottom) SERs identified in NCCIT cells. **b**, Representative

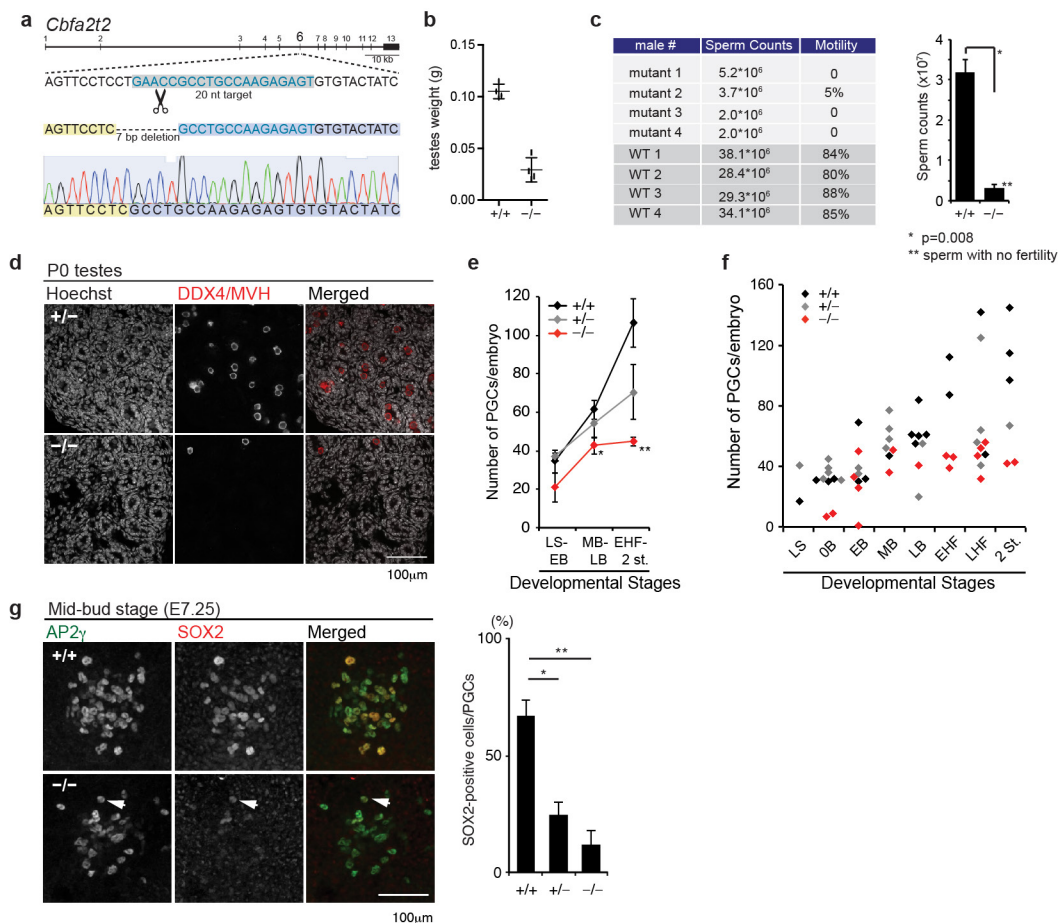
genome browser tracks depicting SERs at the indicated genomic loci. **c**, Gene Ontology (GO) analysis of PRDM14 and CBFA2T2 common target genes. **d**, Western blot analysis of PRDM14 and CBFA2T2 protein levels in knockdown (KD) experiments (Fig. 1d, e).



Extended Data Figure 3 | Characterization of knockout ES cell mutants and quantification of human iPS cell reprogramming efficiency.

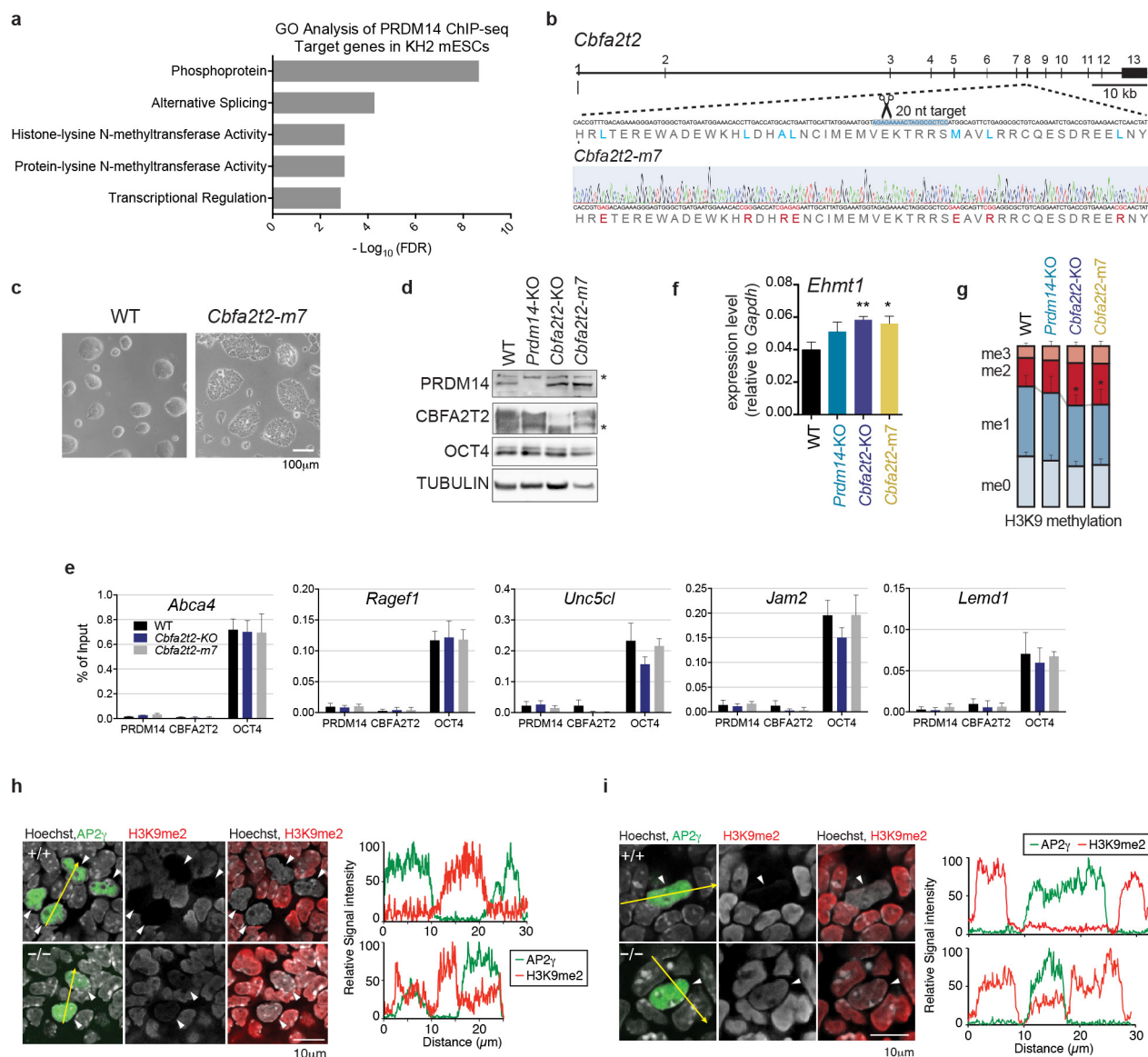
a, b, Strategy for generating *Prdm14*- and *Cbfa2t2*-knockout (KO) mES cells via CRISPR-Cas9 genome editing. Sequencing chromatograms confirming homozygous disruption of the locus are depicted. **c**, *Cbfa2t2*- and *Prdm14*-knockout ES cells require 2i to maintain growth. ES cell lines generated under FBS plus LIF plus 2i conditions were continuously cultured in FBS plus LIF plus 2i (top, middle), or switched to FBS plus LIF (bottom). Eight days after 2i withdrawal (FBS plus LIF), well-formed ES cell colonies were undetectable; instead, mutant ES cells appeared to be differentiated. Scale bar, 100 μ m. **d**, Proliferation rates of wild-type (WT) and mutant knockout ES cells as described in **c**. Data were obtained from three biological replicates. Please note error bars shown in the plots. Owing to the logarithmic scale used here, some error bars are very small and might be invisible. **e**, RNA-seq MA plot (log ratio (M) versus mean average (A)) in the indicated ES cells. Data are representative of three

biological replicate experiments for each line. Mean abundance is plotted on the x axis and enrichment (both in \log_2 scale) is plotted on the y axis. Genes depicted in red are differentially expressed with a FDR < 0.0001. **f**, Heat map showing relative expression of all differentially expressed genes as described in Fig. 2c. The only difference is now the heat map is centred on CBFA2T2 differentially expressed genes, rather than PRDM14 differentially expressed genes. **g**, Scheme of human fibroblast reprogramming to iPS cells. Fibroblasts were transduced with lentiviruses expressing polycistronic *OCT4/KLF4/SOX2/c-MYC* (OKSM) and either *PRDM14* or *CBFA2T2*. Three weeks later, bright-field images of successfully reprogrammed colonies (left) and live TRA-1-81 staining (right) were recorded. Scale bar, 500 μm . **h**, Quantification of human iPS cell reprogramming efficiency based on TRA-1-81 staining with secondary antibody conjugated with horseradish peroxidase (HRP) and substrate DAB. Error bars are based on four biological replicates of each condition. The source data are included in the Supplementary Information.



Extended Data Figure 4 | *Cbfa2t2*^{-/-} mouse genotypes and sperm defects. **a**, One representative *Cbfa2t2*^{-/-} mouse genotype wherein a 7-bp fragment is deleted. **b**, Testes of multiple wild-type ($n = 4$) and *Cbfa2t2*^{-/-} ($n = 4$) male mice at 8 weeks old were dissected and weighed. **c**, Number of sperm in the epididymis of *Cbfa2t2*^{+/+} ($n = 4$) and *Cbfa2t2*^{-/-} ($n = 4$) mice is shown with standard error of the mean. P value was determined by Student's t -test. **d**, Near loss of gonocytes in *Cbfa2t2*-knockout mutant P0 testes by DDX4 (MVH) staining. Visualization of MVH-positive (red) gonocytes in *Cbfa2t2*^{+/+} (top) or *Cbfa2t2*^{-/-} (bottom) testis at P0 stage. The merged images with Hoechst (left; white) are shown on the right. Scale bars, 100 μ m. **e**, Numbers of AP-2 γ -positive PGCs in *Cbfa2t2*^{+/+} (black), *Cbfa2t2*^{+/-} (grey) and *Cbfa2t2*^{-/-} (red) embryos at the indicated embryonic stages. LS, late-streak stage; EB, MB, and LB, early-, mid-, and

late-bud stage; EHF, early-head fold stage; 2 st., 2 somites stage. Student's t -test: $*P = 0.03$, $**P = 0.003$. **f**, Numbers of AP-2 γ -positive PGCs in *Cbfa2t2*^{+/+} (black), *Cbfa2t2*^{+/-} (grey) and *Cbfa2t2*^{-/-} (red) embryos at the indicated embryonic stages. 0B, zero-bud stage; LHF, late-head fold stage. **g**, Left, expression of SOX2 (red) in AP-2 γ -positive (green) PGCs in *Cbfa2t2*^{+/+} (top) or *Cbfa2t2*^{-/-} (bottom) embryo at mid-bud stage, E7.25, shown as z-projection images of posterial confocal sections. Arrow indicates a minor PGC with relatively normal activation of SOX2. Scale bar, 50 μ m. Right, percentage of SOX2-positive (red) cells in AP-2 γ -positive (green) PGCs in the indicated genotypes of *Cbfa2t2* at E7.0–E7.25 (zero- to mid-bud stage) are shown with statistical significance (Student's t -test: $*P = 0.0006$, $**P = 0.0001$; *Cbfa2t2*^{+/+}, $n = 7$; *Cbfa2t2*^{+/-}, $n = 5$; *Cbfa2t2*^{-/-}, $n = 5$).



Extended Data Figure 5 | *Cbfa2t2*-m7 mutant characterization and the related mechanism. **a**, Gene Ontology (GO) analysis of PRDM14 ChIP-seq target genes. PRDM14 target genes are enriched in histone methyltransferase activities by DAVID functional annotation tool analysis. **b**, *Cbfa2t2*-m7 mutant genotyping. The mutant 7 amino acids are in red and corresponding wild-type (WT) residues are highlighted in blue in the displayed protein sequences. **c**, Bright-field images of wild-type and *Cbfa2t2*-m7 mES cells. Scale bar, 100 μm . **d**, Western blot analysis of PRDM14, CBFA2T2 and OCT4 protein levels in *Prdm14*-knockout (KO), *Cbfa2t2*-knockout or m7 mutant ES cells under feeder-free FBS plus LIF plus 2i condition. Nonspecific bands are denoted with an asterisk. **e**, ChIP-qPCR using antibodies against PRDM14, CBFA2T2 or

OCT4 at selected OCT4 target genes. Occupancy is compared between wild-type, *Cbfa2t2*-knockout and *Cbfa2t2*-m7 mES cells. ChIP-qPCR primer sequences are included in Supplementary Table 3. **f**, RT-qPCR quantification of *Ehmt1* mRNA levels in wild-type and mutant lines. *P* values are 0.004 (**) and 0.0142 (*). The source data are included in the Supplementary Information. **g**, Mass spectrometry quantification of histone H3K9 modifications in wild-type and mutant lines. *P* values are 0.00956, 0.04248 (*). The source data are included in the Supplementary Information. **h**, **i**, Additional immunofluorescence analysis of H3K9me2 (red) of AP2 γ -positive (green; arrowheads) PGCs in *Cbfa2t2*^{+/+} and *Cbfa2t2*^{-/-} embryos at E8.75 as described in Fig. 4i.

Dissecting direct reprogramming from fibroblast to neuron using single-cell RNA-seq

Barbara Treutlein^{1,2*}, Qian Yi Lee^{1,3,4*}, J. Gray Camp⁵, Moritz Mall^{3,4}, Winston Koh¹, Seyed Ali Mohammad Shariati⁶, Sopheak Sim³, Norma F. Neff¹, Jan M. Skotheim⁶, Marius Wernig^{3,4,§} & Stephen R. Quake^{1,7,8,§}

Direct lineage reprogramming represents a remarkable conversion of cellular and transcriptome states^{1–3}. However, the intermediate stages through which individual cells progress during reprogramming are largely undefined. Here we use single-cell RNA sequencing^{4–7} at multiple time points to dissect direct reprogramming from mouse embryonic fibroblasts to induced neuronal cells. By deconstructing heterogeneity at each time point and ordering cells by transcriptome similarity, we find that the molecular reprogramming path is remarkably continuous. Overexpression of the proneural pioneer factor *Ascl1* results in a well-defined initialization, causing cells to exit the cell cycle and re-focus gene expression through distinct neural transcription factors. The initial transcriptional response is relatively homogeneous among fibroblasts, suggesting that the early steps are not limiting for productive reprogramming. Instead, the later emergence of a competing myogenic program and variable transgene dynamics over time appear to be the major efficiency limits of direct reprogramming. Moreover, a transcriptional state, distinct from donor and target cell programs, is transiently induced in cells undergoing productive reprogramming. Our data provide a high-resolution approach for understanding transcriptome states during lineage differentiation.

Direct lineage reprogramming bypasses an induced pluripotent stage to directly convert somatic cell types. Using the three transcription factors *Ascl1*, *Brn2* and *Myt1l* (BAM), mouse embryonic fibroblasts (MEFs) can be directly reprogrammed to induced neuronal (iN) cells within 2 to 3 weeks at an efficiency of up to 20%⁸. Several groups have further developed this conversion using transcription factor combinations that almost always contain *Ascl1* (refs 9–12). Recently, one of our groups showed that *Ascl1* is an ‘on target’ pioneer factor initiating the reprogramming process¹³, and inducing conversion of MEFs into functional iN cells alone, albeit at a much lower efficiency compared to BAM¹⁴. These findings raised the question whether and when a heterogeneous cellular response to the reprogramming factors occurs during reprogramming and which mechanisms might cause failure of reprogramming. We hypothesized that single-cell RNA sequencing (RNA-seq) could be used as a high-resolution approach to reconstruct the reprogramming path of MEFs to iN cells and uncover mechanisms limiting reprogramming efficiencies^{4,15,16}.

In order to understand transcriptional states during direct conversion between somatic fates, we measured 405 single-cell transcriptomes (Supplementary Data 1) at multiple time points during iN cell reprogramming (Fig. 1a and Extended Data Fig. 1a). We first explored how individual cells respond to *Ascl1* overexpression during the initial phase of reprogramming. We analysed day 0 MEFs and day 2 cells induced

with *Ascl1* only (hereafter referred to as *Ascl1*-only cells) using PCA and identified three distinct clusters (A, B, C), which correlated with the level of *Ascl1* expression (Fig. 1b–e). Cluster A consisted of all control d0 MEFs and a small fraction of day 2 cells (~12%) which showed no detectable *Ascl1* expression, suggesting these day 2 cells were not infected with the *Ascl1* virus. This is consistent with typical *Ascl1* infection efficiencies of about 80–90%. We found that the day 0 MEFs were surprisingly homogeneous, with much of the variance due to cell cycle (Extended Data Fig. 1b–g, Supplementary Data 3, Supplementary Information). Cluster C was characterized by high expression of *Ascl1*, *Ascl1*-target genes (*Zfp238*, *Hes6*, *Atoh8* and so on) and genes involved in neuron remodelling, as well as the downregulation of genes involved in cell cycle and mitosis (Fig. 1c, e, f and Supplementary Data 2). Cluster B cells represent an intermediate population that expressed *Ascl1* at a low level, and were characterized by a weaker upregulation of *Ascl1*-target genes and less efficient downregulation of cell cycle genes compared to cluster C cells. This suggests that an *Ascl1* expression threshold is required to productively initiate the reprogramming process. In addition, we found that forced *Ascl1* expression resulted in less intracellular transcriptome variance, a lower number of expressed genes (Fig. 1d) and a lower total number of transcripts per single cell (Extended Data Fig. 2a, b). Notably, the distribution of average expression levels per gene was similar for all experiments independent of *Ascl1* overexpression (Extended Data Fig. 2c). We observed that the upregulation of neuronal targets and downregulation of cell cycle genes in response to *Ascl1* expression are uniform, indicating that the initial transcriptional response to *Ascl1* is relatively homogenous among all cells (Fig. 1e). This suggests that most fibroblasts are initially competent to reprogram and later events must be responsible for the moderate reprogramming efficiency of about 20%.

To explore the effect of transgene copy number variation on the heterogeneity of the early response, we analysed single-cell transcriptomes of an additional 47 cells induced with *Ascl1* for two days from secondary MEFs derived via blastocyst injection from a clonal, *Ascl1*-inducible embryonic stem cell line. As expected, the induction efficiency of *Ascl1* was 100% since the secondary MEFs are genetically identical and all cells carry the transgene in the same genomic location (Fig. 1g). Nevertheless, these clonal MEFs had similar transcriptional responses and heterogeneity as primary infected MEFs at the day 2 time point, as well as comparable reprogramming efficiencies and maturation (Extended Data Fig. 3a). Finally, we compared the early response in our *Ascl1*-only single-cell RNA-seq data with our previously reported bulk RNA-seq data of *Ascl1*-only and BAM-mediated reprogramming¹³ (Extended Data Fig. 3b). We found similar downregulation of MEF-related genes and upregulation of pro-neural marker genes in both

¹Department of Bioengineering, Stanford University, Stanford, California 94305, USA. ²Department of Evolutionary Genetics, Max Planck Institute for Evolutionary Anthropology, Leipzig 04103, Germany. ³Institute for Stem Cell Biology and Regenerative Medicine, Stanford University School of Medicine, Stanford, California 94305, USA. ⁴Department of Pathology, Stanford University School of Medicine, Stanford, California 94305, USA. ⁵Department of Developmental Biology, Stanford University School of Medicine, Stanford, California 94305, USA. ⁶Department of Biology, Stanford University, Stanford, California 94305, USA. ⁷Howard Hughes Medical Institute, Stanford, California 94305 USA. ⁸Department of Applied Physics, Stanford University, Stanford, California 94305, USA.

*These authors contributed equally to this work.

§These authors jointly supervised this work.

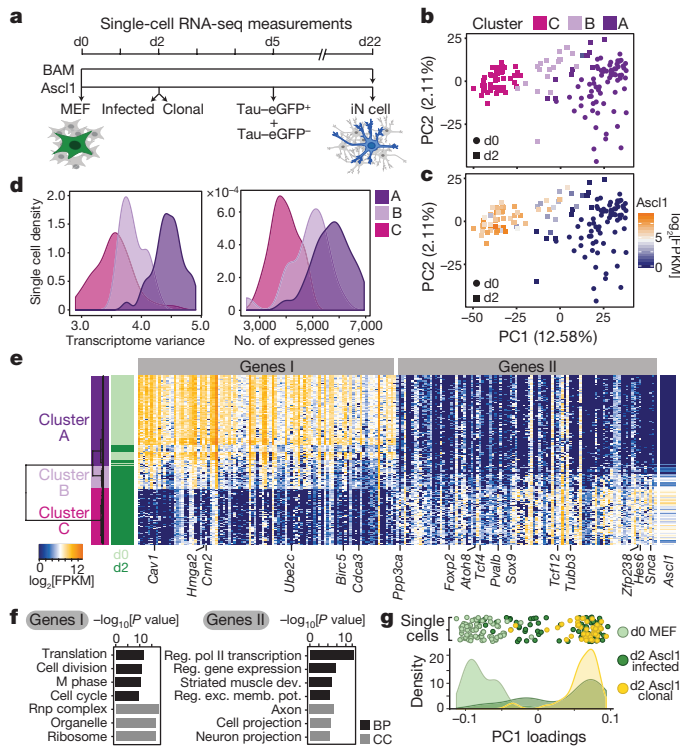


Figure 1 | Ascl1 overexpression elicits a homogeneous early response and initiates expression of neuronal genes. **a**, Mouse embryonic fibroblasts stably integrated with neuronal reporter Tau-eGFP⁸ were directly transformed to neuronal cells through overexpression of a single (Ascl1), or three factors (Brn2, Ascl1, Myt1l; BAM) as described⁸. Cells were sampled using single-cell RNA-seq at day 0 without infection (d0, 73 cells), day 2 (d2, 81 cells Ascl1-infected and 47 cells clonal), day 5 (d5, 55 cells, eGFP⁺ and eGFP⁻ cells), day 20 (d20, 33 cells, eGFP⁺ cells), and day 22 (d22, 73 cells, eGFP⁺ cells) post-induction with Ascl1. As a comparison, cells reprogrammed using all three BAM factors were analysed at 22 days (d22, 43 cells, eGFP⁺ cells). **b**, **c**, PCA of single-cell transcriptomes from day 0 MEFs (circle, 73 cells) and day 2 Ascl1-induced cells (square, 81 cells) shows reduced intercellular variation at day 2. Points are coloured based on hierarchical clustering shown in **e** (**b**), or Ascl1 expression (**c**). **d**, Left, distribution of transcriptome variance within single cells grouped by cluster assignment of **b** and **e** shows that Ascl1 expression reduces the intracellular transcriptome variance. Right, distribution of total number of genes expressed by single cells grouped by cluster assignment shows that Ascl1 overexpression reduces the range of gene expression. **e**, Hierarchical clustering of day 0 and day 2 cells (rows) using the top 50 genes (columns) correlating positively (genes I) and negatively (genes II) with PC1. Cells are clustered into three clusters (left sidebar): A (83 cells, MEFs), B (20 cells, intermediates), C (51 cells, day 2 induced cells). **f**, Top gene ontology enrichments of genes I and II (**d**) are shown with Bonferroni-corrected *P* values. BP, biological process; CC, cellular component; reg. exc. memb. pot., regulation of excitatory postsynaptic membrane potential. **g**, Distribution of PC1 loadings are shown for day 2 cells carrying variable numbers of *Ascl1* transgene copies (dark green, Ascl1-infected) or carrying the same *Ascl1* copy number and genomic location (yellow, clonal). PC1 effectively separates un-induced MEFs (cluster A) from induced cells highly expressing Ascl1-target genes (cluster C) and both, Ascl1-infected and clonal cells, productively initiate reprogramming. The induction efficiency is higher for clonally induced MEFs, however even in the clonal population Ascl1 induction is variable.

Ascl1- and BAM-mediated reprogramming. These data suggest that the overexpression of Ascl1 focuses the transcriptome and directs the expression of target genes.

We next analysed the transcriptomes of reprogramming cells on day 5. At this time point, the first robust Tau-eGFP signal can be detected in successfully reprogramming cells and we therefore purified

40 Tau-eGFP⁺ and 15 Tau-eGFP⁻ cells for transcriptome analysis by fluorescence-activated cell sorting. We found that Tau-eGFP⁻ cells lacked expression of neuronal Ascl1-target genes (genes B), and maintained expression of fibroblast-associated genes (genes A and C; Fig. 2a, b, Extended Data Fig. 4a, Supplementary Data 4). In addition, we found a positive correlation ($R^2 = 0.49$) between Ascl1 expression and Tau-eGFP intensities (Extended Data Fig. 4b, Fig. 2a, b). Quantitative real-time (qRT)-PCR and western blot analysis of Ascl1 expression on day 5 to day 12 Tau-eGFP-sorted cells validated a significant decrease in Ascl1 expression in Tau-eGFP⁻ cells compared to Tau-eGFP⁺ cells (Fig. 2c, Supplementary Data 5). Thus, Ascl1 expression is correlated to Tau-eGFP levels and expression of neuronal genes at day 5. This raises the hypothesis that Ascl1 is silenced in cells that fail to reprogram. Alternatively, cells with low or no Ascl1 expression at day 5 and day 22 might have never highly expressed Ascl1. To distinguish between these two mechanisms, we used live cell microscopy to track cells over a time course from 3–6 days after Ascl1 induction using an eGFP–Ascl1 fusion construct (Fig. 2d, Extended Data Fig. 5). We immunostained the cells at day 6 using Tuj1 antibodies recognizing the neuronal β 3-tubulin (Tubb3) to identify cells that differentiated towards neuronal fate. We found that transgenic Ascl1 protein levels varied substantially over time and, on average, continued to increase over time in Tuj1⁺ cells, but decreased or plateaued in Tuj1⁻ cells, leading to a significant difference in Ascl1 expression within six days of Ascl1 induction (Fig. 2e, Extended Data Fig. 4c). This time-lapse analysis demonstrated that Ascl1 is silenced in many cells that fail to reprogram.

We next analysed the maturation events occurring during late reprogramming stages. We performed principal component analysis (PCA) on the single-cell transcriptomes of all reprogramming stages analysed, including day 22 cells reprogrammed with Ascl1 alone or with all three BAM factors (Extended Data Fig. 6a). PC1 separated MEFs and early time points (day 2, day 5) from most of the day 22 cells. Surprisingly, PC2 separated most day 22 BAM cells from day 22 Ascl1-only cells despite robust Tau-eGFP expression in both groups. We used t-distributed stochastic neighbour embedding (tSNE) to organize all day 22 cells into transcriptionally distinct clusters, and identified differentially expressed genes marking each cluster (Fig. 3a). We identified 3 clusters, which contained cells expressing neuron (*Syp*), fibroblast (*Eln*), or myocyte (*Tnnc2*) marker genes, respectively (Fig. 3b). Consistent with this marker gene expression, cells in each cluster had a maximum correlation with bulk RNA-seq data from purified neurons, embryonic fibroblasts, or myocytes (Fig. 3c). Neuron- and myocyte-like cells expressed a clear signature of each cell type (Fig. 3d). Although we observed cells with complex neuronal morphologies in the Ascl1-only reprogramming experiments as we had reported previously¹⁴ (Fig. 3e), their frequency was too low to be captured in the single-cell RNA-seq experiments. All of the day 22 Ascl1-only cells, and 33% of BAM cells had a highest correlation with myocytes or fibroblasts.

We applied an analytical technique based on quadratic programming to quantify fate conversion and to predict when during reprogramming the alternative muscle program emerges (Extended Data Fig. 6b). This method allowed us to decompose each single cell's transcriptome and express each cell's identity as a linear combination of the transcriptomes from the three different observed fates (neuron, MEF, myocyte; Supplementary Data 6). Using this method, we observed that there is an initial loss of MEF identity concomitant with an increase in neuronal and myocyte identity over the first five days of Ascl1 reprogramming. The neuronal identity is maintained and matures in day 22 cells transduced with BAM (Extended Data Fig. 6c). However, the day 22 Ascl1-only cells failed to mature to neurons and adopted a predominantly myogenic transcriptional program. This divergence was already apparent in some day 5 cells (Extended Data Fig. 6d, e). These findings raised the question whether the additional two reprogramming factors Brn2 and Myt1l suppress the aberrant myogenic program. Compatible with this notion, we observed that Brn2 and Myt1l had low expression

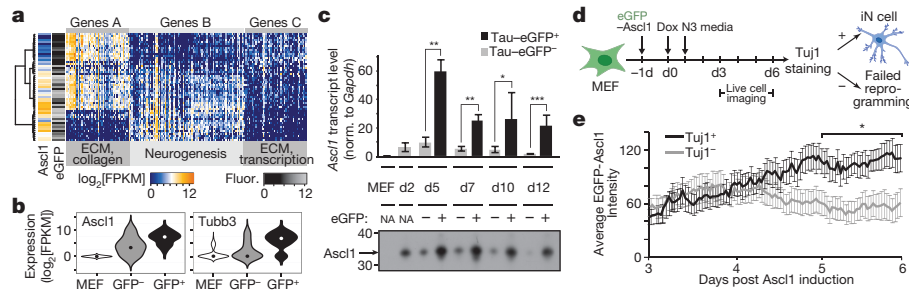


Figure 2 | Transgenic *Ascl1* silencing explains early reprogramming failure. **a**, Hierarchical clustering of day 5 cells using genes correlating positively and negatively with PC1 and PC2 from PCA of day 5 *Ascl1*-only cells. Note that eGFP fluorescence intensity and *Ascl1* mRNA expression shown in the left side bar appear correlated. **b**, Violin plots show the distribution of *Ascl1* and neuronal marker *Tubb3* in day 0 MEFs, as well as Tau-eGFP⁺ and Tau-eGFP⁻ day 5 cells. **c**, qRT-PCR for exogenous *Ascl1* expression (top, $n = 4$, biological replicates) and western blot of *Ascl1* protein levels (bottom, Supplementary Data 5) for unsorted control MEFs and day 2 cells (NA, not applicable), as well as day 5, day 7, day 10 and day 12 cells FAC-sorted using Tau-eGFP as a neuronal marker. Both

RNA and protein levels of *Ascl1* are significantly higher in Tau-eGFP⁺ cells, and gradually decrease in Tau-eGFP⁻ cells ($*P < 0.05$, $**P < 0.01$, $***P < 0.001$, two-tailed t -test; error bars, s.e.m.). **d**, Schematic for live cell imaging experiment. CD1 MEFs were infected with an eGFP-*Ascl1* construct at -1 day, induced with doxycycline at day 0, switched to N3 media at day 1 and imaged between 3 and 6 days post doxycycline. Cells were fixed at 6 days and stained for *Tubb3* expression. **e**, Average eGFP-*Ascl1* intensity (error bars, s.e.m.) was plotted at 45-min intervals for *Tuj1*⁺ ($n = 10$) and *Tuj1*⁻ ($n = 12$) cells between day 3 and day 6. *Tuj1*⁺ cells significantly (one-tailed t -test, $P < 0.05$) increased *Ascl1* expression through time compared to *Tuj1*⁻ cells, which appeared to silence *Ascl1*.

in the five day 22 BAM cells that expressed a myogenic program. To directly address this question, we infected MEFs with *Ascl1* alone or in combination with *Brn2* and/or *Myt1l* and assessed myogenic

and neurogenic fates at day 22 based on immunostaining and qRT-PCR (Fig. 3e, Extended Data Fig. 6f–i). Indeed, myocyte markers (*Myh3*, *Myo18b*, *Tnni3*) were upregulated in Tau-eGFP-positive versus negative cells and were strongly repressed when *Brn2* and/or *Myt1l* was overexpressed together with *Ascl1*. Moreover, *Brn2* and *Myt1l* enhanced the expression of the synaptic genes *Gria2*, *Nrxn3*, *Stmn3*, and *Snap25* but not the immature pan-neuronal genes *Tubb3* and *Map2*. As expected, fibroblast markers were repressed in Tau-eGFP⁺ cells.

We next set out to reconstruct the reprogramming path from MEFs to iN cells. By deconstructing heterogeneity at each time point as described above, we removed cells that appeared stalled in reprogramming due to *Ascl1* silencing or cells converging on the alternative myogenic fate. We used quadratic programming to order the cells based on fractional similarity to MEF and neuron bulk transcriptomes. This revealed a continuum of intermediate states through the 22-day reprogramming period (Fig. 4a, b). Notably, the total number of transcripts per single cell decreased as a function of fractional neuron identity (Extended Data Fig. 7a). Our ordering of cells based on fractional identities correlated well with pseudotemporal ordering using Monocle¹⁵, an alternative algorithm for delineating differentiation paths (Extended Data Fig. 7b–d). Heat map visualization of genes identified by PCA of all cells on the iN cell lineage revealed two gene regulatory events during reprogramming with many cells at intermediate stages (Fig. 4c, Supplementary Data 7). First, there is an initiation stage where MEFs exit the cell cycle upon *Ascl1* induction, and genes involved in mitosis are turned down or off (such as *Birc5*, *Ube2c*, *Hmga2*). Concomitantly, genes associated with cytoskeletal reorganization (*Sept3/4*, *Coro2b*, *Ank2*, *Mtap1a*, *Homer2*, *Akap9*), synaptic transmission (*Snc*, *Stxbp1*, *Vamp2*, *Dmpk*, *Ppp3ca*), and neural projections (*Cadm1*, *Dner*, *Klhl24*, *Tubb3*, *Map2* (Tau)) increase in expression. This indicates that *Ascl1* induces genes involved in defining neuronal morphology early in the reprogramming process. The initiation phase is followed by a maturation stage whereby MEF extracellular matrix genes are turned off and genes involved in synaptic maturation are turned on (*Syp*, *Rab3c*, *Gria2*, *Syt4*, *Nrxn3*, *Snap25*, *Sv2a*). These results are consistent with previous findings that *Tuj1*⁺ cells with immature neuron-like morphology can be found as early as three days after *Ascl1* induction, while functional synapses are only formed 2 to 3 weeks into the reprogramming process⁸. Finally, we constructed a transcription regulator network on the basis of pairwise correlation of transcription regulator expression across all stages of the MEF-to-iN cell reprogramming. This revealed three densely connected sub-networks identifying transcription regulators influencing MEF cell biology, iN cell initiation, and iN cell maturation

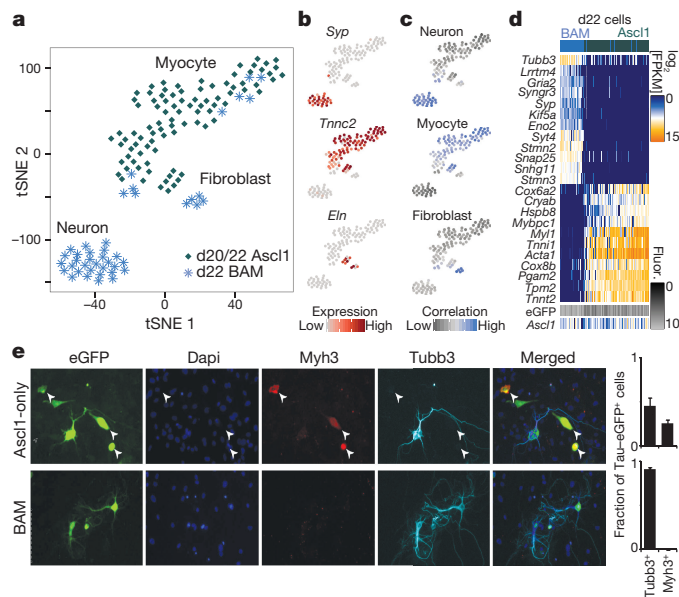


Figure 3 | iN cell maturation competes with an alternative myogenic cell fate that is repressed by *Brn2* and *Myt1l*. **a**, tSNE reveals alternative cell fates that emerge during direct reprogramming. Shapes and colours indicate the day 20/22 *Ascl1*-only (dark green) or day 22 BAM-induced (blue) cells. Note that all cells are Tau-eGFP⁺. **b**, **c**, tSNE plot from **a** with cells coloured based on expression level of marker genes (**b**), or correlation with bulk RNA-seq data from different purified cell types (neurons²⁴, myocytes²⁵, fibroblasts¹³, **c**). **d**, Heat map showing expression of genes marking the two alternative fates in day 20/22 *Ascl1*-only (upper sidebar, dark green) and day 22 BAM (upper sidebar, blue) Tau-eGFP⁺ cells. Genes (rows) have the highest positive and negative correlation with the first principal component in a PCA analysis on all day 20/22 cells and all genes. Columns represent 121 single cells, ordered based on their correlation coefficient with the first principal component. Lower sidebars, *Ascl1* transcript level and Tau-eGFP fluorescence for each cell. **e**, Immunofluorescent detection of Tau-eGFP (green), DAPI (blue), *Myh3* (red) and *Tubb3* (cyan) for day 22 cells infected with *Ascl1* alone, or with all BAM factors. Images are representative of four biological replicates. Right, mean fractions of eGFP⁺ cells that express either *Tubb3* or *Myh3*. Only *Tubb3*⁺ cells with a neuronal morphology were counted. Six or seven images were analysed for each of four biological replicates. Error bars, s.e.m.

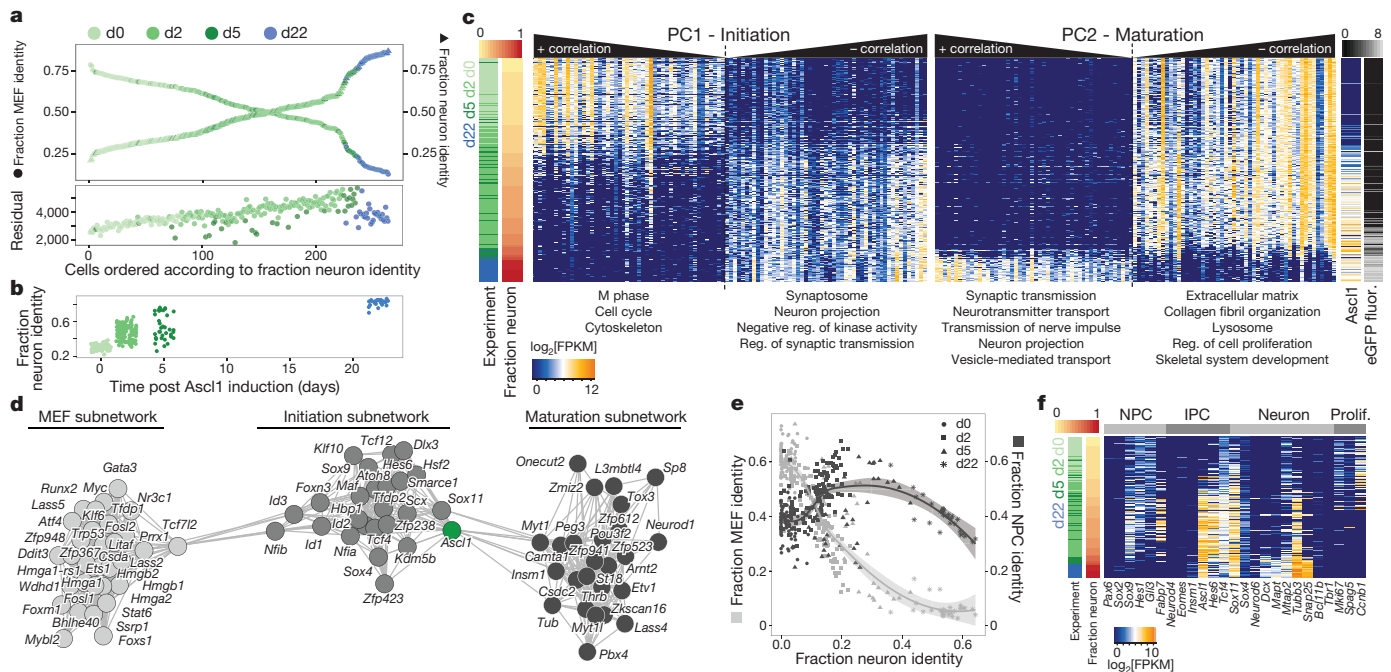


Figure 4 | Reconstructing the direct reprogramming path from MEFs to iN cells. **a**, Top, for each cell on the iN cell reprogramming path, the similarity to bulk RNA-seq from either MEFs¹³ or neurons²⁴ was calculated using quadratic programming and plotted as fractional identities (left axis, circle, fractional MEF identity; right axis, triangle, fractional neuron identity). Points are coloured based on the experimental time point. Bottom, Lagrangian residuals of the quadratic programming for each single cell ordered based on their fractional identity as above. Points are coloured based on the experimental time point. **b**, Fractional neuron identities of all cells on the iN cell reprogramming path are shown as a function of the experimental time point. **c**, Ordering of single cells (rows) according to fractional neuron identity revealed a cascade of gene expression changes leading to neuronal identity. Genes (columns) with the highest positive and negative correlation to PC1 and PC2 are shown. Left sidebars, experimental time point (green/blue) and fractional neuron identity (yellow/red). Right sidebars, *Ascl1* transcript levels (\log_2 [FPKM], blue/yellow) and eGFP fluorescence intensities (\log_{10} [RFU], black/white; RFU, relative fluorescence units). **d**, Transcriptional regulator covariance network during iN cell lineage progression. Shown are nodes (transcriptional regulators) with more than three edges, with each edge reflecting a correlation >0.25 between connected transcriptional regulators. **e**, Fractional MEF (left axis) or fractional neural precursor cell (NPC) identities (right axis) are plotted against fractional neuron identity for single cells on the MEF-to-iN cell lineage. Points are shaped based on the experiment. **f**, Expression of selected genes (columns) that mark NPCs, intermediate progenitor cells (IPCs), neurons, or proliferating cells (Prolif.) are shown for cells on the iN cell lineage (rows). Left sidebars, fractional neuron identity (yellow/red) and experimental time point (green/blue).

(Fig. 4d, Extended Data Fig. 8, Supplementary Data 8, Supplementary Information). Notably, *Ascl1* was found to strongly positively correlate with the transcription regulators in both the initiation and maturation subnetworks and negatively correlate with transcription regulators specific to MEFs. This data corroborates evidence that persistent *Ascl1* expression is required to maintain chromatin states conducive to iN cell maturation¹³.

It has been suggested that direct somatic lineage reprogramming may not involve an intermediate progenitor cell state as seen during induced pluripotent stem cell differentiation^{17–19}. However, our fractional analysis showed that the identity of intermediate reprogramming cells could not be explained by a simple linear mixture of the differentiated fibroblast and neuron identities, as revealed by an intermediary increase of Lagrangian residuals (Fig. 4a). Therefore, we tested whether a neural precursor cell (NPC) state is transiently induced by adding NPC bulk transcriptome data along with that of MEFs and neurons into the quadratic programming analysis (Fig. 4e). We found that the fractional NPC identity of cells increased specifically for cells at intermediate positions on the MEF-to-iN cell lineage path, and then decreased as a function of iN cell maturation. In addition, several NPC genes (that is, *Gli3*, *Sox9*, *Nestin*, *Fabp7*, *Hes1*) are expressed in intermediates of the iN cell reprogramming path²⁰ (Fig. 4f). However, canonical NPC marker genes such as *Sox2* and *Pax6* were never induced. This indicates that cells do not go through a canonical NPC stage, yet a unique intermediate transcriptional state is induced transiently that is unrelated to donor and target cell program

identity (yellow/red). Right sidebars, *Ascl1* transcript levels (\log_2 [FPKM], blue/yellow) and eGFP fluorescence intensities (\log_{10} [RFU], black/white; RFU, relative fluorescence units). **d**, Transcriptional regulator covariance network during iN cell lineage progression. Shown are nodes (transcriptional regulators) with more than three edges, with each edge reflecting a correlation >0.25 between connected transcriptional regulators. **e**, Fractional MEF (left axis) or fractional neural precursor cell (NPC) identities (right axis) are plotted against fractional neuron identity for single cells on the MEF-to-iN cell lineage. Points are shaped based on the experiment. **f**, Expression of selected genes (columns) that mark NPCs, intermediate progenitor cells (IPCs), neurons, or proliferating cells (Prolif.) are shown for cells on the iN cell lineage (rows). Left sidebars, fractional neuron identity (yellow/red) and experimental time point (green/blue).

similar to that which was observed for induced pluripotent stem cell reprogramming^{21–23}.

A fundamental question in cell reprogramming is whether there are pre-determined mechanisms that prevent the majority of the fibroblasts from reprogramming or whether all donor cells are competent to reprogram but the reprogramming procedure is inefficient. We did not observe any MEF subpopulations, other than cell cycle variation, that suggested differences in the capacity to initiate reprogramming. Furthermore, we observed that 48 h after infection the majority of the cells induced *Ascl1*-target genes and silenced MEF-associated genes. This does not preclude the possibility that underlying epigenetic variation in donor cells influences reprogramming outcomes; however, our analysis suggests that it is unlikely that MEF heterogeneity contributes significantly to reprogramming efficiency. We found that divergence from the neuronal differentiation path into an alternative myogenic fate, as well as *Ascl1* transgene silencing, were both significant factors contributing to reprogramming efficiency. Though *Ascl1* induces lineage conversion, it is inefficient in restricting cells to the neuronal fate. This suggests that intermediate stages of iN cell progression are unstable, perhaps due to epigenetic barriers, and additional factors promote cells to permanently acquire neuron-like identity, rather than revert to MEF-like or diverge towards the alternative myocyte-like fate. In summary, we present a single-cell transcriptomic approach that can be used to dissect direct cellular reprogramming pathways or developmental programs in which cells transform their identity through a series of intermediate states.

Online Content Methods, along with any additional Extended Data display items and Source Data, are available in the online version of the paper; references unique to these sections appear only in the online paper.

Received 10 March 2015; accepted 17 May 2016.

Published online 8 June 2016.

1. Xu, J., Du, Y. & Deng, H. Direct lineage reprogramming: strategies, mechanisms, and applications. *Cell Stem Cell* **16**, 119–134 (2015).
2. Arlotta, P. & Berninger, B. Brains in metamorphosis: reprogramming cell identity within the central nervous system. *Curr. Opin. Neurobiol.* **27**, 208–214 (2014).
3. Graf, T. Historical origins of transdifferentiation and reprogramming. *Cell Stem Cell* **9**, 504–516 (2011).
4. Treutlein, B. *et al.* Reconstructing lineage hierarchies of the distal lung epithelium using single-cell RNA-seq. *Nature* **509**, 371–375 (2014).
5. Shalek, A. K. *et al.* Single-cell transcriptomics reveals bimodality in expression and splicing in immune cells. *Nature* **498**, 236–240 (2013).
6. Zeisel, A. *et al.* Brain structure. Cell types in the mouse cortex and hippocampus revealed by single-cell RNA-seq. *Science* **347**, 1138–1142 (2015).
7. Ramsköld, D. *et al.* Full-length mRNA-seq from single-cell levels of RNA and individual circulating tumor cells. *Nat. Biotechnol.* **30**, 777–782 (2012).
8. Vierbuchen, T. *et al.* Direct conversion of fibroblasts to functional neurons by defined factors. *Nature* **463**, 1035–1041 (2010).
9. Pfisterer, U. *et al.* Direct conversion of human fibroblasts to dopaminergic neurons. *Proc. Natl Acad. Sci. USA* **108**, 10343–10348 (2011).
10. Yoo, A. S. *et al.* MicroRNA-mediated conversion of human fibroblasts to neurons. *Nature* **476**, 228–231 (2011).
11. Ambasudhan, R. *et al.* Direct reprogramming of adult human fibroblasts to functional neurons under defined conditions. *Cell Stem Cell* **9**, 113–118 (2011).
12. Caiazzo, M. *et al.* Direct generation of functional dopaminergic neurons from mouse and human fibroblasts. *Nature* **476**, 224–227 (2011).
13. Wapinski, O. L. *et al.* Hierarchical mechanisms for direct reprogramming of fibroblasts to neurons. *Cell* **155**, 621–635 (2013).
14. Chanda, S. *et al.* Generation of induced neuronal cells by the single reprogramming factor ASCL1. *Stem Cell Rep.* **3**, 282–296 (2014).
15. Trapnell, C. *et al.* The dynamics and regulators of cell fate decisions are revealed by pseudotemporal ordering of single cells. *Nat. Biotechnol.* **32**, 381–386 (2014).
16. Buettner, F. *et al.* Computational analysis of cell-to-cell heterogeneity in single-cell RNA-sequencing data reveals hidden subpopulations of cells. *Nat. Biotechnol.* **33**, 155–160 (2015).
17. Merkle, F. T. & Eggan, K. Modeling human disease with pluripotent stem cells: from genome association to function. *Cell Stem Cell* **12**, 656–668 (2013).
18. Perrier, A. L. *et al.* Derivation of midbrain dopamine neurons from human embryonic stem cells. *Proc. Natl Acad. Sci. USA* **101**, 12543–12548 (2004).
19. Li, X. J. *et al.* Specification of motoneurons from human embryonic stem cells. *Nat. Biotechnol.* **23**, 215–221 (2005).
20. Camp, J. G. *et al.* Human cerebral organoids recapitulate gene expression programs of fetal neocortex development. *Proc. Natl Acad. Sci. USA* **112**, 15672–15677 (2015).
21. Di Stefano, B. *et al.* C/EBP α poises B cells for rapid reprogramming into induced pluripotent stem cells. *Nature* **506**, 235–239 (2014).
22. Lujan, E. *et al.* Early reprogramming regulators identified by prospective isolation and mass cytometry. *Nature* **521**, 352–356 (2015).
23. Takahashi, K. *et al.* Induction of pluripotency in human somatic cells via a transient state resembling primitive streak-like mesendoderm. *Nat. Commun.* **5**, 3678 (2014).
24. Zhang, Y. *et al.* An RNA-sequencing transcriptome and splicing database of glia, neurons, and vascular cells of the cerebral cortex. *J. Neurosci.* **34**, 11929–11947 (2014).
25. Trapnell, C. *et al.* Transcript assembly and quantification by RNA-Seq reveals unannotated transcripts and isoform switching during cell differentiation. *Nat. Biotechnol.* **28**, 511–515 (2010).

Supplementary Information is available in the online version of the paper.

Acknowledgements The authors would like to acknowledge B. Passarelli and B. Vernot for discussions regarding bioinformatic pipelines, P. Lovelace for support with FACS and other Quake and Wernig laboratory members for discussions and support. This work was supported by NIH grant RC4NS073015-01 (M.W., S.Q.R., B.T.), the Stinehart-Reed Foundation, the Ellison Medical Foundation, the New York Stem Cell Foundation, CIRM grant RB5-07466 (all to M.W.), a National Science Scholarship from the Agency for Science, Technology and Research (Q.Y.L.), NIH grant GM092925 (S.A.M.S., J.S.), the German Research Foundation (M.M.) and a PhRMA foundation Informatics fellowship (J.G.C.). S.R.Q. is an investigator of the Howard Hughes Medical Institute. M.W. is a New York Stem Cell Foundation (NYSCF) Robertson Investigator and a Tashia and John Morgridge Faculty Scholar at the Child Health Research Institute at Stanford.

Author Contributions B.T., Q.Y.L., M.W. and S.R.Q. conceived the study and designed the experiments. Q.Y.L. performed direct reprogramming, qRT-PCR and western blot experiments; B.T., Q.Y.L., and S.S. performed single-cell RNA-seq experiments; N.F.N. assisted with single-cell RNA-seq experiments and sequenced the libraries; Q.Y.L., S.A.M.S. and M.M. performed time-lapse imaging experiments. B.T., J.G.C. and W.K. analysed single-cell RNA-seq data, Q.Y.L. analysed qRT-PCR and time-lapse imaging data, J.M.S., M.W. and S.R.Q. provided intellectual guidance in the interpretation of the data. B.T., Q.Y.L., J.G.C., M.W., and S.R.Q. wrote the paper.

Author Information The single-cell RNA-seq data were deposited on NCBI GEO with the accession number GSE67310. Reprints and permissions information is available at www.nature.com/reprints. The authors declare competing financial interests: details are available in the online version of the paper. Readers are welcome to comment on the online version of the paper. Correspondence and requests for materials should be addressed to S.R.Q. (quake@stanford.edu) and M.W. (wernig@stanford.edu).

Reviewer Information *Nature* thanks F. Tang and the other anonymous reviewer(s) for their contribution to the peer review of this work.

METHODS

No statistical methods were used to predetermine sample size. The experiments were not randomized and the investigators were not blinded to allocation during experiments and outcome assessment.

Cell derivation, cell culture and iN cell generation. Tau-eGFP reporter MEFs, tested negative for mycoplasma contamination, were isolated, infected with doxycycline (dox)-inducible lentiviral constructs and reprogrammed into iN cells as previously described⁸. Day 0 (d0) cells were uninfected MEFs that served as a negative control. Day 2 (d2) cells were infected with *Ascl1* and harvested two days after dox-induction. Day 5 (d5) cells were infected with *Ascl1*, FAC-sorted for Tau-eGFP⁺ and Tau-eGFP⁻ cells five days after dox induction and the two cell populations were mixed again in a 1:1 ratio. Day 20 or 22 (d20/d22) cells were infected either with *Ascl1* alone, or combined with *Brn2* and *Myt1l*, plated with glia seven days post dox induction, and FAC-sorted for Tau-eGFP⁺ iN cells 20 or 22 days after dox induction. Each of these groups was then loaded onto separate microfluidic mRNA-seq chips for preparation of pre-amplified cDNA from single cells.

Clonal *Ascl1*-inducible MEFs were derived as previously described¹³. Twelve-well plates were coated with Matrigel and incubated at 37°C overnight. 350,000 cells were then plated per well and kept in MEF media. Dox was added a day after plating. For single-cell RNA-seq, cells were harvested two days post dox induction and loaded onto a microfluidic mRNA-seq chip. To evaluate efficiency in reprogramming, MEF + dox media was switched out for N3 + dox media after 48 h, and cells were fixed for immunostaining 12 days post dox.

Capturing of single cells and preparation of cDNA. Single cells were captured on a medium-sized (10–17 µm cell diameter) microfluidic RNA-seq chip (Fluidigm) using the Fluidigm C1 system. Cells were loaded onto the chip at a concentration of 350–500 cells µl⁻¹, stained for viability (live/dead cell viability assay, Molecular Probes, Life Technologies) and imaged by phase-contrast and fluorescence microscopy to assess number and viability of cells per capture site. For d5 and d22 experiments, cells were only stained with the dead stain ethidium homodimer (emission ~635 nm, red channel) and Tau-eGFP fluorescence was imaged in the green channel. Only single, live cells were included in the analysis. cDNAs were prepared on chip using the SMARTer Ultra Low RNA kit for Illumina (Clontech). ERCC (External RNA Controls Consortium) RNA spike-in Mix (Ambion, Life Technologies)^{26,27} was added to the lysis reaction and processed in parallel to cellular mRNA. Tau-eGFP fluorescence intensity of each single cell was determined using CellProfiler²⁸ by first identifying the outline of the cell in the image of the respective capture site and then integrating over the signal in the eGFP channel.

RNA-seq library construction and cDNA sequencing. Size distribution and concentration of single-cell cDNA was assessed on a capillary electrophoresis based fragment analyser (Advanced Analytical Technologies) and only single cells with high quality cDNA were further processed. Sequencing libraries were constructed in 96-well plates using the Illumina Nextera XT DNA Sample Preparation kit according to the protocol supplied by Fluidigm and as described previously²⁹. Libraries were quantified by Agilent Bioanalyzer using High Sensitivity DNA analysis kit as well as fluorometrically using Qubit dsDNA HS Assay kits and a Qubit 2.0 Fluorometer (Invitrogen, Thermo Fisher Scientific). Up to 110 single-cell libraries were pooled and sequenced 100 bp paired-end on one lane of Illumina HiSeq 2000 or 75 bp paired-end on one lane of Illumina NextSeq 500 to a depth of 1–7 million reads. CASAVA 1.8.2 was used to separate out the data for each single cell using unique barcode combinations from the Nextera XT preparation and to generate *.fastq files. In total, the transcriptome of a total of 405 cells was measured from the following eight independent experiments: d0 (73 cells, 1 experiment), d2 (*Ascl1*-only in regular MEFs, 81 cells, 1 experiment; *Ascl1*-only in clonal MEFs, 47 cells, 1 experiment), d5 (*Ascl1*-only, 55 cells, 1 experiment) and d20 (*Ascl1*-only, 33 cells, 1 experiment) and d22 (BAM, 43 cells, 1 experiment; *Ascl1*-only, 34 and 39 cells, 2 independent experiments). See Supplementary Data 1 for the transcriptome data for all 405 cells with annotations (quantification in log₂[FPKM]).

Processing, analysis and graphic display of single cell RNA-seq data. Raw reads were pre-processed with sequence grooming tools FASTQC³⁰, cutadapt³¹, and PRINSEQ³² followed by sequence alignment using the Tuxedo suite (Bowtie³³, Bowtie2³⁴, TopHat³⁵ and SAMtools³⁶) using default settings. Transcript levels were quantified as fragments per kilobase of transcript per million mapped reads (FPKM) generated by TopHat/Cufflinks²⁵.

After seven days of reprogramming, Tau-eGFP reporter MEFs (with C57BL/6J and 129SvJae background) were co-cultured with glia derived from CD-1 mice. To determine if any feeder cells contaminated the 20–22-day time points, we used the single cell RNA-seq reads to identify positions that differ from the mouse reference genome (mm10, built from strain C57BL/6J mice). We used the mpileup function in samtools to generate a multi-sample variant call format file (vcf), and a custom python script to genotype the cells by requiring coverage in all cells for all positions, with a coverage depth of five reads, a phred GT likelihood = 0 for called genotype and ≥40 for next-best genotype. This resulted in 95 informative sites

distinguishing more than one cell from the reference genome. We clustered cells based on their genotype (homozygous reference, heterozygous, homozygous alternate), and identified cells that were strongly different from the reference genome. These cells expressed either astrocyte (*Gfap*) or microglia marker genes suggesting they were contaminants from the feeder cell culture. We removed these cells from subsequent analyses.

Approximate number of transcripts was calculated from FPKM values by using the correlation between number of transcripts of exogenous spike-in mRNA sequences and their respective measured mean FPKM values (Extended Data Fig. 2). The number of spike-in transcripts per single cell lysis reaction was calculated using the concentration of each spike-in provided by the vendor (Ambion, Life Technologies), the approximate volume of the lysis chamber (10 nl) as well as the dilution of spike-in transcripts in the lysis reaction mix (40,000×). Transcript levels were converted to the log-space by taking the logarithm to the base 2 (Supplementary Data 1). R studio³⁷ (<https://www.rstudio.com/>) was used to run custom R³⁸ scripts to perform principal component analysis (PCA, FactoMineR package), hierarchical clustering (stats package), variance analysis and to construct heat maps, correlation plots, box plots, scatter plots, violin plots, dendrograms, bar graphs, and histograms. Generally, ggplot2 and gplots packages were used to generate data graphs.

The Seurat package^{39,40} implemented in R was used to identify distinct cell populations present at d22 of *Ascl1*-only and BAM reprogramming (Fig. 3a–d). t-distributed stochastic neighbour embedding (tSNE) was performed on all d20/d22 cells using the most significant genes ($P < 1 \times 10^{-3}$, with a maximum of 100 genes per principal component) that define the first three principal components of a PCA analysis on the data set. To further estimate the identity of each cell on the tSNE plot, we colour coded cells based on Pearson correlation of each single cell's expression profile with the expression profile of bulk cortical neurons^{13,24}, myocytes²⁵, and MEFs¹³ (Fig. 3). The Monocle package¹⁵ was used to order cells on a pseudo-time course during MEF to iN cell reprogramming (Extended Data Fig. 7). Covariance network analysis and visualizations were done using igraph implemented in R⁴¹ (<http://igraph.sf.net>).

To generate PCA plots and heat maps in Figs 1c–e, 2a, 3a and 4c, PCA was performed on cells using all genes expressed in more than two cells and with a variance in transcript level (log₂[FPKM]) across all single cells greater than 2. This threshold resulted generally in about 8,000–12,000 genes. Subsequently, genes with the highest PC loadings (highest (top 50–100) positive or negative correlation coefficient with one of the first one to two principal components) were identified and a heat map was plotted with genes ordered based on their correlation coefficient with the respective PC (Figs 1e, 2a, 4c). Cells in rows were ordered based on unsupervised hierarchical clustering using Pearson correlation as distance metric (Figs 1e, 2a) or based on their fractional identity as determined by quadratic programming (Fig. 4c, see below).

Gene ontology enrichment analyses were performed using DAVID Bioinformatics Resources 6.7 of the National Institute of Allergy and Infectious Diseases⁴². Functional annotation clustering was performed and GO terms representative for top enriched annotation clusters are shown in Fig. 1f, Extended Data Figs 1e and 4a with their Bonferroni corrected *P* values. In addition, results of GO enrichment analyses are provided in the Supplementary Data.

To express a single cell transcriptome as a linear combination of primary cell type transcriptomes, we used published bulk RNA-seq data sets for primary murine neurons²⁴, myocytes²⁵, and embryonic fibroblasts¹³ (Extended Data Fig. 6b, c), neurons²⁴ and embryonic fibroblasts¹³ (Fig. 4a) or neurons²⁴, embryonic fibroblasts¹³ and neuronal progenitor cells¹³ (Fig. 4e). In each quadratic programming analysis, we first identified genes that were specifically (log₂ fold change of 3 or higher) expressed in each of the bulk data sets compared to the respective others (Supplementary Data 6). Using these genes, we then calculated the fractional identities of each single cell using quadratic programming (R package 'quadprog'). The resulting fractional neuron identities of cells on the MEF-to-iN cell reprogramming path (265 cells in total, excluding cells that were Tau-eGFP-negative at d5 or myocyte- and fibroblast-like cells at d22) were used to order cells in a pseudo-temporal manner (Fig. 4a–c, e, f). We compared this fractional neuron identity based cell ordering with pseudo-temporal ordering of cells based on Monocle (Extended Data Fig. 7b–d), an algorithm that combines differential dimension reduction using independent component analysis with minimal spanning tree construction to link cells along a pseudotemporally ordered path¹⁵. Monocle analysis was performed using genes differentially expressed between neuron²⁴ and embryonic fibroblast¹³ bulk RNA-seq data (same gene set that was used when calculating fractional neuron and fibroblast identities in Fig. 4a, genes listed in Supplementary Data 6).

For the transcription factor network analysis (Fig. 4d), we computed a pairwise correlation matrix (Pearson correlation, visualized in correlogram in Extended Data Fig. 8a) for transcriptional regulators annotated as such in the Animal

Transcription Factor Database (<http://www.bioguo.org/AnimalTFDB/>)⁴³ and identified those transcriptional regulators (TRs) with a Pearson correlation of greater than 0.35 with at least five other TRs (82 TRs, shown in Extended Data Fig. 8b). We used a permutation approach to determine the probability of finding TRs meeting this threshold by chance. We performed 500 random permutations of the expression matrix of all TRs across cells on the MEF-to-iN cell lineage, and calculated the pairwise correlation matrix for each permutation of the input data frame. All randomized data frames resulted in 0 TRs that met our threshold. This shows that our correlation threshold is strict, and all nodes and connections that we present in the TR network are highly unlikely to be by chance. We used the pairwise correlation matrix for the selected TRs as input into the function `graph.adjacency()` of `igraph` implemented in `R`⁴¹ (<http://igraph.sf.net>) to generate a weighted network graph, in which the selected TRs are presented as vertices and all pairwise correlations >0.25 are presented as edges linking the respective vertices. The network graph was visualized using the Fruchterman–Reingold layout and the three clear subnetworks (MEF, initiation, maturation) were manually colour coded.

We used Pearson correlation of each single cell expression profile with the expression profile of bulk cortical neurons^{13,24}, myocytes²⁵, and MEFs¹³ to further estimate the identity of each single cell and to estimate when alternative fates emerge (Fig. 3c, Extended Data Fig. 6d, e). For this analysis, we considered the same cell type specific gene sets that were used in the quadratic programming analysis, that is, were genes specifically expressed (\log_2 fold change of 3 or higher) in a respective bulk RNA-seq data set compared to the others (Supplementary Data 6).

To estimate intercellular heterogeneity of d0 MEFs, we calculated the variance for each gene across all MEF cells as well as across mouse embryonic stem cells under 2iLIF culture conditions⁴⁴ and across glioblastoma cells⁴⁵. We then plotted the distribution of variances for all genes per cell population as box plots.

Quantitative RT–PCR and immunostaining. Ascl1 infected Tau–eGFP reporter MEFs were FAC-sorted 5, 7, 10, 12 or 22 days post-Ascl1 induction with dox. RNA was then extracted from both Tau–eGFP positive and negative populations from each time point, as well as uninfected control MEFs and unsorted d2 Ascl1-infected MEFs using the TRIzol RNA isolation protocol (Invitrogen, 15596-018). Reverse transcription into cDNA was performed using the SuperScript III First-strand Synthesis System (Invitrogen, 18080-051) and qRT–PCR was performed using Sybr Green (Thermo Fisher Scientific, 4309155). Immunostaining was performed as previously described⁸. Antibodies and qRT–PCR primers are listed in the Supplementary Information.

Time-lapse imaging of Ascl1 expression. MEFs were isolated from E13.5 CD-1 embryos (Charles River) and infected with a dox-inducible, N-terminal-tagged eGFP–Ascl1 fusion construct using the protocol previously described¹. Cells were plated on 35 cm glass bottom dishes (MatTek), coated with polyornithine (Sigma P3655) and laminin (Invitrogen 23017-015). Imaging experiments were performed between 3 and 6 days post dox induction, in a temperature- and CO₂-controlled chamber. Images were taken for up to 10 positions per dish, for 3 dishes, every 45 min with a Zeiss AxioVert 200M microscope with an automated stage using an EC Plan-Neofluar 5×/0.16 NA Ph1 objective or an A-plan 10×/0.25 NA Ph1 objective. Cells were fixed at 6 days and immunostained using Tuj1 antibodies recognizing neuronal Tubb3 (Covance MRB-435P) to confirm neuronal identity. We used ImageJ to segment individual cells and measure the level of GFP for 7 Tuj1⁺ cells and 7 Tuj1[−] cells over time. Average intensity was obtained by normalizing the average intensity of a cell segment by the average background intensity of an adjacent segment of the same size. A *t*-test was performed comparing Tuj1⁺ and Tuj1[−] cells at each time point to evaluate significance.

Antibodies. Rabbit anti-Ascl1 (Abcam ab74065), chicken anti-GFP (Abcam ab13970), rabbit anti-Tubb3 (Covance MRB-435P), mouse anti-Tubb3 (Covance MMS-435P), mouse anti-Map2 (Sigma M4403), rabbit anti-Myh3 (Santa Cruzsc-20641), goat anti-Dlx3 (Santa Cruz sc-18143), mouse anti-β-Actin (Sigma A5441), rabbit anti-Tcf12 (Bethyl A300-754A).

Primers. General. *Gapdh* (forward: AGGTCCGTGTGAACGGATTGTG, reverse: TGTAGACCATGTAGTTGAGGTCA); *Ascl1* (TetO) (forward: CCGAA TTCGCTAGCCACCAT, reverse: AAGAAGCAGGCTGCGGG).

Initiation factors. *Atoh8* (forward: GCCAAGAAACGGAAGGAGTGA, reverse: CTGAGAGATGGTACACGGGC); *Dlx3* (forward: GCGCGCTCCAA GTTCAAAAA, reverse: GTGGTACCAGGAGTTGGTGG); *Hes6* (forward: TACCGAGGTGCAGGCCAA, reverse: AGTTCAGCTGAGACAGTGGC);

Sox11 (forward: CCTGTCGCTGGTGGATAAGG, reverse: CTGCGCCTCTC AATACGTGA); *Sox9* (forward: CGAGCACTCTGGGCAATCTCA, reverse: ATGACGTCGCTGCTCAGTTC); *Tcf4* (forward: CAGTGCGATGT TTTGCGCTC, reverse: ATGTGACCCAAGATCCCTGC); *Tcf12* (forward: GTCTCGAATGGAAGACCGCT, reverse: GTTCCGACCATCGAAGCTGA).

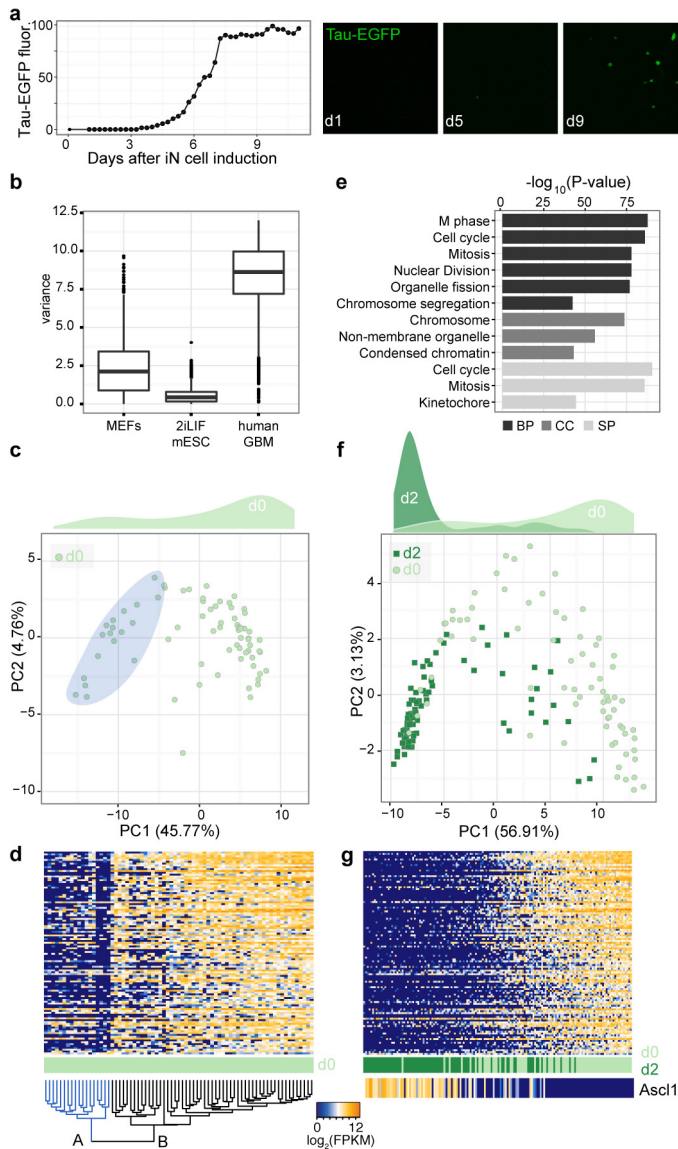
Maturation factors. *Camta1* (forward: CCCCTAAGACAAGACCCGAC, reverse: ACATAGCAGCCGTACAAGCA); *Insm1* (forward: GACCCGG CACATCAACAAGT, reverse: GAAGCGAAGCGAAGAGGACA); *Myt11* (forward: ATGTTCCCAACACACCA, reverse: TACCGCTTGGCATCG TCATA); *St18* (forward: TGCCAAGGGAGCTGAGATAGA, reverse: GAAGG CTGCTTGGCTTGAAT).

Neuronal genes. *Gria2* (forward: GGGGACAAGGCGTGGAATA, reverse: GTACCCAATCTTCCGGGGTCT); *Map2* (forward: CAGAGAAA CAGCAGAGGAGGT, reverse: TTTGTTCTGAGGTGGCGAT); *Nrxn3* (forward: TGTGAACCAAGTACAGATAAGAGT, reverse: CAGCTCAGGGGAC AAAGAGG); *Snap25* (forward: TTCATCCGCAGGGTAACAAA, reverse: GTTGACGTTGGTTGGCTT); *Stmn3* (forward: AGCACCCT ATCTGCCCTACAAG, reverse: TGGTAGATGGTGTTCGGGTG); *Tubb3* (forward: CAGATAGGGGCCAAGTTCTGG, reverse: GTTGTCGGGCCTGAATAGT).

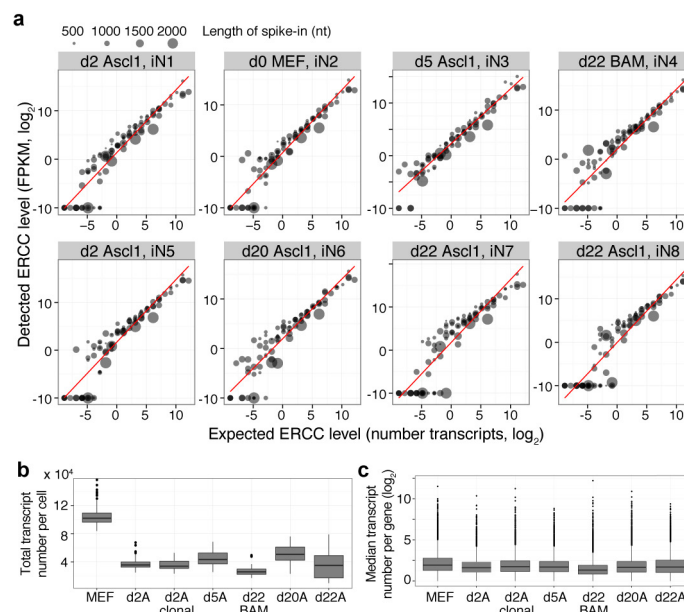
Myocyte genes. *Acta1* (forward: CTAGACACCATGTGCGACGA, reverse: CATACCTACCATGACACCCTGG); *Myh3* (forward: AAATGAAGGGGACG CTGGAG, reverse: CAGCTGGAAGGTGACTCTGG); *Myo18b* (forward: TGCCCTCTTCAGGGAAGGTA, reverse: GAGCTTCTCCACTGACACCC); *Tnni2* (forward: CAACCATGACGGACCAACAG, reverse: GTGTCTGCC CTAGCATCCTC).

Fibroblast genes. *Col1a2* (forward: AGTCGATGGCTGCTCCAAAA, reverse: ATTTGAAACAGACGGGGCCA); *Dcn* (forward: GCAAAATCAGT CCAGAGGCA, reverse: CGCCCAAGTTCTATGACAAGC).

26. Baker, S. C. *et al.* The External RNA Controls Consortium: a progress report. *Nat. Methods* **2**, 731–734 (2005).
27. Jiang, L. *et al.* Synthetic spike-in standards for RNA-seq experiments. *Genome Res.* **21**, 1543–1551 (2011).
28. Carpenter, A. E. *et al.* CellProfiler: image analysis software for identifying and quantifying cell phenotypes. *Genome Biol.* **7**, R100 (2006).
29. Wu, A. R. *et al.* Quantitative assessment of single-cell RNA-sequencing methods. *Nat. Methods* **11**, 41–46 (2014).
30. Babraham Institute. Babraham Bioinformatics. FASTQC. <http://www.bioinformatics.bbsrc.ac.uk/projects/fastqc>
31. Martin, M. Cutadapt removes adapter sequences from high-throughput sequencing reads. *EMBnet journal* **17**, 10–12 (2011).
32. Schmieder, R. & Edwards, R. Quality control and preprocessing of metagenomic datasets. *Bioinformatics* **27**, 863–864 (2011).
33. Langmead, B., Trapnell, C., Pop, M. & Salzberg, S. L. Ultrafast and memory-efficient alignment of short DNA sequences to the human genome. *Genome Biol.* **10**, R25 (2009).
34. Langmead, B. & Salzberg, S. L. Fast gapped-read alignment with Bowtie 2. *Nat. Methods* **9**, 357–359 (2012).
35. Trapnell, C., Pachter, L. & Salzberg, S. L. TopHat: discovering splice junctions with RNA-seq. *Bioinformatics* **25**, 1105–1111 (2009).
36. Li, H. *et al.* The sequence alignment/map format and SAMtools. *Bioinformatics* **25**, 2078–2079 (2009).
37. RStudio. Integrated Development for R. RStudio, Inc., Boston, MA URL <http://www.rstudio.com/> (2015).
38. R Core Team. R: A language and environment for statistical computing. R Foundation for Statistical Computing. <http://www.R-project.org/>
39. Macosko, E. Z. *et al.* Highly parallel genome-wide expression profiling of individual cells using nanoliter droplets. *Cell* **161**, 1202–1214 (2015).
40. Satija, R., Farrell, J. A., Gennert, D., Schier, A. F. & Regev, A. Spatial reconstruction of single-cell gene expression data. *Nat. Biotechnol.* **33**, 495–502 (2015).
41. Csardi, G. & Nepusz, T. The igraph software package for complex network research. *InterJournal* **1695** (2006).
42. Huang, W., Sherman, B. T. & Lempicki, R. A. Systematic and integrative analysis of large gene lists using DAVID bioinformatics resources. *Nat. Protocols* **4**, 44–57 (2009).
43. Zhang, H. M. *et al.* AnimalTFDB: a comprehensive animal transcription factor database. *Nucleic Acids Res.* **40**, D144–D149 (2012).
44. Kumar, R. M. *et al.* Deconstructing transcriptional heterogeneity in pluripotent stem cells. *Nature* **516**, 56–61 (2014).
45. Patel, A. P. *et al.* Single-cell RNA-seq highlights intratumoral heterogeneity in primary glioblastoma. *Science* **344**, 1396–1401 (2014).

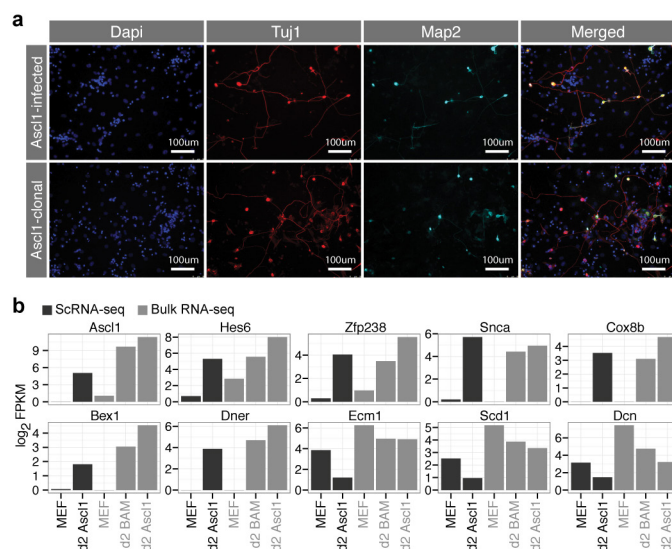


Extended Data Figure 1 | The majority of MEFs are actively undergoing cell cycle, but exit cell cycle upon *Ascl1* induction. **a**, Live cell imaging of Tau-eGFP reporter over the course of BAM-mediated iN cell reprogramming. Tau-eGFP fluorescence normalized to the maximum expression is shown in relation to days post-BAM induction. Tau-eGFP expression began at day 5 and reached a peak at day 8 after induction. Shown are representative images from day 0, day 5 and day 9. **b**, Box plots of intercellular transcriptome variance showed that MEFs are more heterogeneous than mouse embryonic stem cells under 2iLIF culture conditions⁴⁴ and less heterogeneous than glioblastoma cells⁴⁵. **c**, PCA of genes with most variance in day 0 MEFs revealed MEF heterogeneity (blue, A). Density plot showing the distribution of number of cells along PC1 loading is shown above the PCA plot. **d**, Heat map and hierarchical clustering of genes used for the PCA in panel c shows two major MEF subpopulations. Each column represents a single cell, and each row a gene. Subpopulation A is highlighted in blue in the dendrogram. **e**, GO enrichment for genes in c shows that MEF subpopulation A is distinguished by the low or lack of expression of genes enriched for cell cycle terms. **f**, **g**, PCA and heat map of the same genes used in panels c–e, this time including day 0 MEFs (circles, light green) and day 2 cells (squares, dark green), showed that most of the day 2 cells had the same cell cycle signature as MEF subpopulation A. Cells in columns of both heat maps are ordered based on PC1 loading.

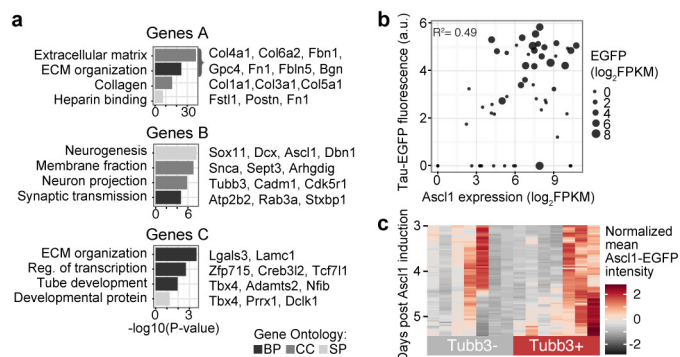


Extended Data Figure 2 | Total number of transcripts per cell decreases during MEF-to-iN cell reprogramming. **a**, Average detected transcript levels (mean FPKM, log₂) for 92 ERCC RNA spike-ins as a function of provided number of molecules per lysis reaction for each of the 8 independent single-cell RNA-seq experiments. Linear regression fits through data points are shown. The length of each ERCC RNA spike-in transcript is encoded in the size of the data points. No particular bias towards the detection of shorter versus longer transcripts is observed. The linear regression fit was used to convert FPKM values to approximate number of transcripts. **b**, Box plots showing the distribution of the total

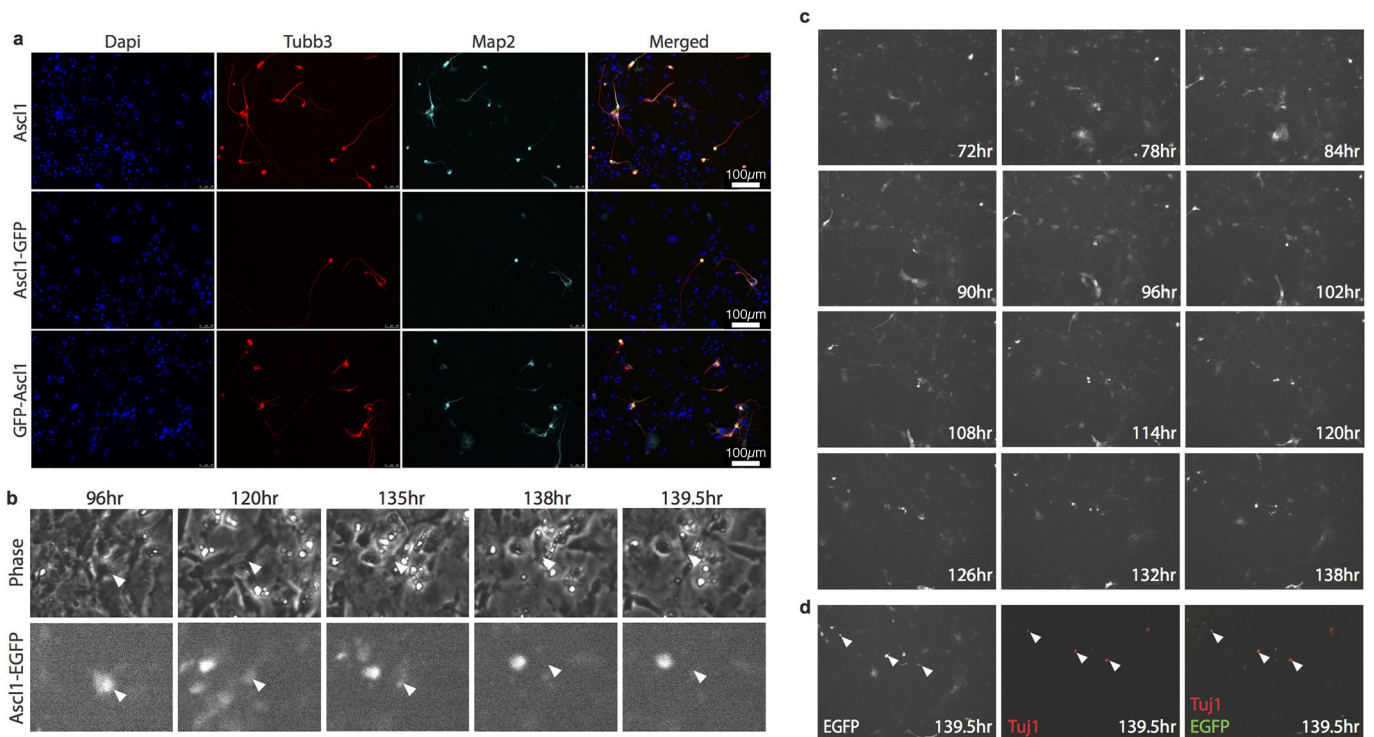
number of transcripts per single cell for each experiment. Number of transcripts per cell were calculated from the FPKM values of all genes in each cell using the correlation between number of transcripts of exogenous spike-in mRNA sequences and their respective measured mean FPKM values (calibration curves are shown in panel **a**). The total number of transcripts expressed by a single cell and detected by single-cell RNA-seq is highest in MEFs and is more than twofold decreased upon overexpression of Ascl1 or BAM. **c**, Box plots showing the distribution of the median transcript number per gene across all cells of one experiment. The distributions are similar over the course of iN cell reprogramming.



Extended Data Figure 3 | Clonal MEFs reprogram successfully into iN cells, and Ascl1-only and BAM induce similar responses during early iN cell reprogramming. **a**, Immunostaining of heterogenous Ascl1-infected MEFs and clonal MEFs with homogenous *Ascl1* transgene insertions, fixed 12 days after Ascl1 induction, using rabbit anti-Tubb3 (red) and mouse anti-Map2 (cyan) antibodies and DAPI (blue) as a nuclear stain. Reprogramming efficiencies are comparable regardless of variation in Ascl1 copy numbers. Images are representative for one reprogramming experiment. **b**, Bar plots showing expression of Ascl1-target genes (*Hes6*, *Zfp238*, *Snca*, *Cox8b*, *Bex1*, *Dner*) and MEF marker genes averaged across single cells from day 0 MEFs and day 2 Ascl1-only cells, as well as from bulk RNA-seq data from MEFs, day 2 BAM, and day 2 Ascl1-only cells. This data shows that the initiation of reprogramming at day 2 is similar for Ascl1-alone and BAM-mediated reprogramming.

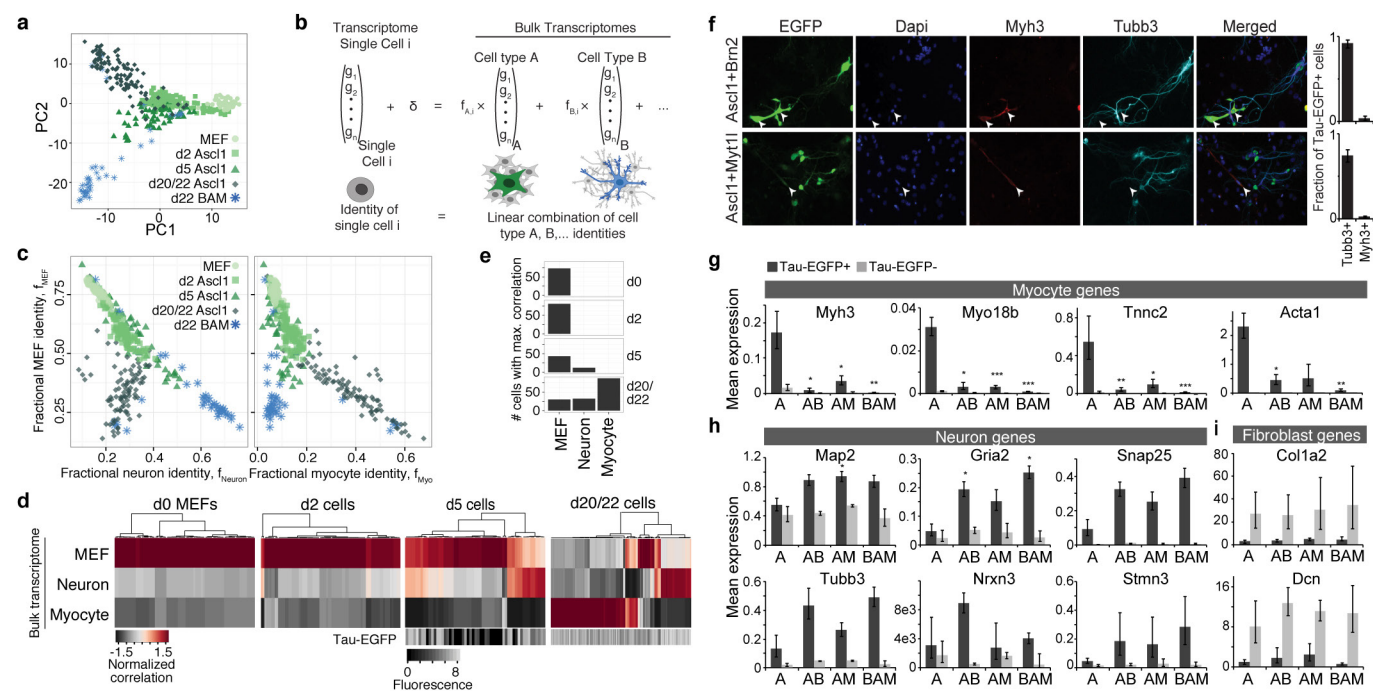


Extended Data Figure 4 | Failed reprogramming at day 5 correlates with silencing of *Ascl1*. **a**, Bonferroni-corrected P values for gene ontology enrichments are shown for each group of genes from Fig. 2a, with representative genes listed (Supplementary Data 4). **b**, Biplot showing Tau-eGFP fluorescence intensity as a function of *Ascl1* transcript level in day 5 cells. Point size is proportional to eGFP transcript levels in \log_2 [FPKM]. There is a positive correlation ($R^2 = 0.49$) indicating that cells with higher *Ascl1* expression are more likely to reprogram. **c**, Heat map of eGFP-*Ascl1* expression in 14 individual cells (columns) during live cell imaging. Rows represent time post *Ascl1* induction in 45-min intervals.



Extended Data Figure 5 | Live cell imaging shows diminishing of eGFP-Ascl1 signal in cells that fail to reprogram. **a**, Immunostaining for Tubb3 and Map2 at day 12 post induction of Ascl1, C-terminal tagged Ascl1-eGFP and N-terminal tagged eGFP-Ascl1 in CD-1 MEFs. eGFP-Ascl1 has comparable reprogramming efficiency with untagged Ascl1 while Ascl1-eGFP has a much reduced reprogramming efficiency, so eGFP-Ascl1 was chosen for live cell imaging. Images are representative for

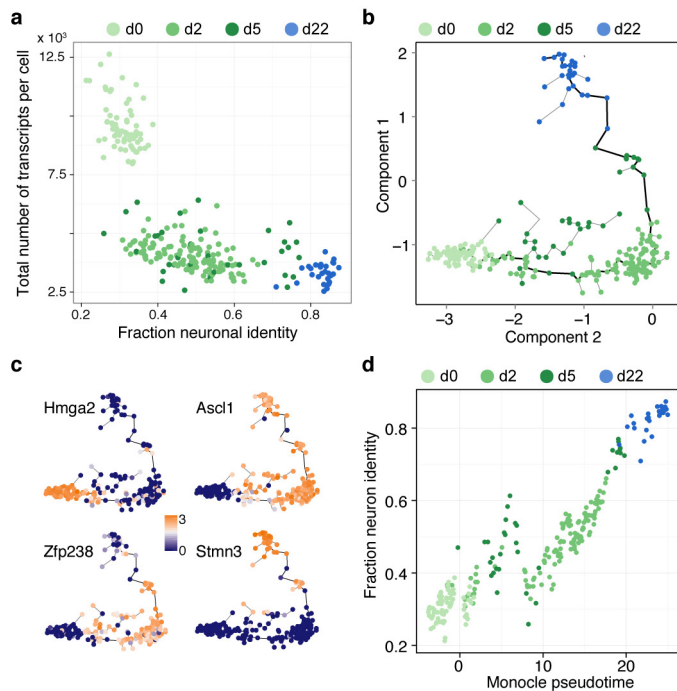
one reprogramming experiment per condition. **b**, Representative images from live cell imaging showing an example of diminishing of eGFP signal in a cell that failed to reprogram (that is, cell was TuJ1-negative at day 6). **c**, Live cell imaging of eGFP signal of eGFP-Ascl1 infected MEFs between 3–6 days post dox induction. **d**, eGFP imaging of live cells 6 days post induction of Ascl1 and corresponding immunostaining for Tubb3 after fixation.



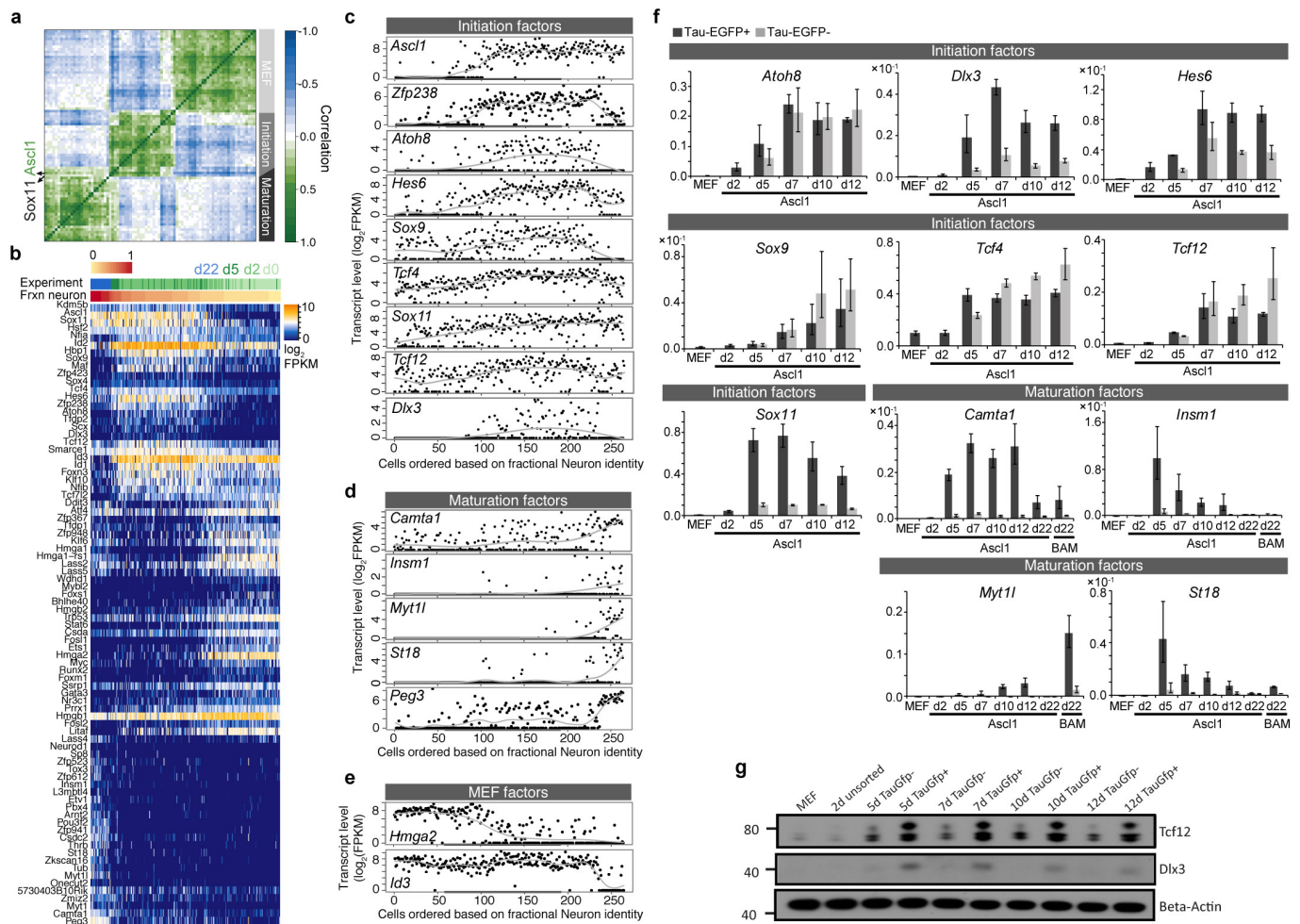
Extended Data Figure 6 | Brn2 and Myt1l repress alternative fates that compete with the iN cell fate during advanced Ascl1 reprogramming.

a, Scatter plot showing PC1 and PC2 loadings from principal component analysis (PCA) of single cells from all time points with experimental time point and reprogramming condition (Ascl1 versus BAM) encoded in point shape and colour. **b**, Overview of quadratic programming. Fractional identities are calculated assuming a linear combination of different cell fates. **c**, Biplots showing the fractional fibroblast identity as a function of fractional neuron (left) and fractional myocyte (right) identity for each cell with points shaped and colour coded based on reprogramming time point and condition. **d**, Correlation of transcriptomes from days 0, 2, 5, and 20/22 cells (Ascl1-only and BAM-induced) with bulk RNA-seq from MEFs, cortical neurons and myocytes. Bottom bars show Tau-eGFP fluorescence intensity. **e**, Bar plot quantifying the number of cells with a maximum correlation to bulk RNA-seq data from each of the observed fates (**d**). **f**, Immunofluorescent detection of Tau-eGFP (green), DAPI (blue), Myh3 (red) and Tubb3 (cyan) for day 22 cells that were infected

with Ascl1 co-infected with Brn2 or Myt1l. See Fig. 3e for respective data for cells infected with Ascl1-only or all three BAM factors. Images are representative for four biological replicates. Right, mean fractions of eGFP⁺ cells that express either Tubb3 or Myh3. Only Tubb3⁺ cells with a neuronal morphology were counted. Co-expression of Ascl1 with Brn2 and/or Myt1l increases fraction of Tau-eGFP⁺ cells that are also Tubb3⁺, while decreasing the number of cells that are Myh3⁺. Six or seven images were analysed for each of four biological replicates. Error bars, s.e.m. **g–i**, qRT-PCR of selected myogenic (**g**), neuronal (**h**), and fibroblast (**i**) markers using day 22 cells that are infected with Ascl1 only or co-infected with Brn2 or Myt1l or both and FAC-sorted by Tau-eGFP ($n = 3$, biological replicates; error bars, s.e.m.). Myogenic genes were significantly downregulated in Tau-eGFP⁺ cells that were co-infected with Brn2 and/or Myt1l compared to those infected with Ascl1 alone, while some neuronal genes are significantly upregulated (*Map2*, *Gria*) ($*P < 0.05$, $**P < 0.01$, $***P < 0.001$, two-tailed t -test).



Extended Data Figure 7 | Comparison of Monocle and quadratic programming with respect to ordering of neuronal cells through the reprogramming path. **a**, Biplot showing the total number of transcripts per cell for all cells on the MEF-to-iN cell lineage as a function of the fraction neuron identity of each cell (see Fig. 4). The total number of transcripts decreases during the reprogramming process. **b**, Cells (depicted as circles) are arranged in the 2D independent component space based on the expression of genes used for quadratic programming in Fig. 4a. Lines connecting cells represent the edges of a minimal spanning tree with the bold black line indicating the longest path. Time points are colour coded. **c**, Monocle plots with single cells coloured based on gene expression that distinguishes the stages of iN cell reprogramming. **d**, Biplot shows the correlation between ordering of cells based on pseudo-time (Monocle) and fractional identity (quadratic programming). Time points are colour coded. Pearson correlation coefficient = 0.91.



Extended Data Figure 8 | Neuronal maturation proceeds through expression of distinct transcriptional regulators. **a**, Correlogram showing transcriptional regulators (TRs) highly correlated within MEFs as well as the initiation phase and the maturation phase of reprogramming. **b**, Heat map shows expression of TRs that control the two stages of MEF to iN cell reprogramming (Fig. 4d) in cells ordered based on fractional neuron identity. Each row represents a single cell, each column a gene. Experimental time point (green/blue sidebar) and fractional neuron identity (yellow/red sidebar) are shown at the top. **c–e**, Pseudo-temporal expression dynamics of exemplary TRs marking the initiation stage (**c**) and the maturation stage (**d**) of iN cell reprogramming as well as MEF identity (**e**). Transcript levels of the TRs are shown across all single

cells on the MEF-to-iN cell lineage ordered based on fractional neuron identity. Growth curves based on a model-free spline method were fitted to the data. **f**, qRT-PCR of selected TRs from initiation and maturation subnetworks from Fig. 4d. Uninfected MEF controls and day 2–12 *Ascl1*-infected cells were assayed for all selected TRs, and day 22 *Ascl1*-alone and BAM-infected cells were additionally assayed for maturation TRs. Cells for day 5 to day 22 samples were FAC-sorted into Tau-eGFP⁺ and Tau-eGFP⁻ populations ($n = 4$ for all populations, biological replicates; error bars, s.e.m.). **g**, Western blot for selected TRs from the initiation subnetwork presented in panel **b**. β -Actin was used as a loading control (Supplementary Data 8).

Systemic RNA delivery to dendritic cells exploits antiviral defence for cancer immunotherapy

Lena M. Kranz^{1,2*}, Mustafa Diken^{1,3*}, Heinrich Haas³, Sebastian Kreiter^{1,3}, Carmen Loquai⁴, Kerstin C. Reuter³, Martin Meng³, Daniel Fritz³, Fulvia Vascotto¹, Hossam Hefesha³, Christian Grunwitz^{2,3}, Mathias Vormehr^{2,3}, Yves Hüseemann³, Abderraouf Selmi^{1,2}, Andreas N. Kuhn³, Janina Buck³, Evelyn Derhovanessian³, Richard Rae¹, Sebastian Attig^{1,2}, Jan Diekmann³, Robert A. Jabulowsky³, Sandra Heesch³, Jessica Hassel⁵, Peter Langguth⁶, Stephan Grabbe⁴, Christoph Huber^{1,3}, Özlem Türeci^{7§} & Ugur Sahin^{1,2,3§}

Lymphoid organs, in which antigen presenting cells (APCs) are in close proximity to T cells, are the ideal microenvironment for efficient priming and amplification of T-cell responses¹. However, the systemic delivery of vaccine antigens into dendritic cells (DCs) is hampered by various technical challenges. Here we show that DCs can be targeted precisely and effectively *in vivo* using intravenously administered RNA-lipoplexes (RNA-LPX) based on well-known lipid carriers by optimally adjusting net charge, without the need for functionalization of particles with molecular ligands. The LPX protects RNA from extracellular ribonucleases and mediates its efficient uptake and expression of the encoded antigen by DC populations and macrophages in various lymphoid compartments. RNA-LPX triggers interferon- α (IFN α) release by plasmacytoid DCs and macrophages. Consequently, DC maturation *in situ* and inflammatory immune mechanisms reminiscent of those in the early systemic phase of viral infection are activated². We show that RNA-LPX encoding viral or mutant neo-antigens or endogenous self-antigens induce strong effector and memory T-cell responses, and mediate potent IFN α -dependent rejection of progressive tumours. A phase I dose-escalation trial testing RNA-LPX that encode shared tumour antigens is ongoing. In the first three melanoma patients treated at a low-dose level, IFN α and strong antigen-specific T-cell responses were induced, supporting the identified mode of action and potency. As any polypeptide-based antigen can be encoded as RNA^{3,4}, RNA-LPX represent a universally applicable vaccine class for systemic DC targeting and synchronized induction of both highly potent adaptive as well as type-I-IFN-mediated innate immune mechanisms for cancer immunotherapy.

DCs initiate immune responses in lymphoid tissues upon early sensing of infectious pathogens⁵. Previous work aimed at gene delivery to DCs largely resorted to functionalization of nanoparticles with molecular ligands^{6–8}. Antigen-encoding RNA formulations have been used for local^{9–11} and systemic injection in various RNA vaccine studies and resulted in antigen-specific T-cell responses, albeit with low antitumour activity^{12,13}. We engineered RNA-containing nanoparticles differing in their molecular characteristics, for example, carrier composition, charge ratio (lipid to RNA ratio) and ionic conditions, and then analysed particle size, colloidal stability, RNA integrity, free RNA and zeta potential¹⁴. For *in vivo* testing, RNA nanoparticles encoding the reporter gene firefly luciferase (Luc-RNA) were injected intravenously (i.v.) into mice to assess biodistribution of the Luc signal. Whereas injection of naked Luc-RNA did not generate a

reporter signal, several of the carrier–RNA formulations gave characteristic patterns of *in vivo* organ transfection, indicating protection and efficient translation of RNA (Extended Data Fig. 1a). Positively charged particles with higher *in vitro* transfection efficiencies compared to neutral or negatively charged compositions have previously been the focus of *in vivo* studies for nucleic acid delivery^{15,16}. To systematically evaluate the effect of overall particle charge on *in vivo* targeting of DCs, which has remained unexplored to date, we varied lipid:RNA ratios. Cationic liposomes composed of the broadly used lipids DOTMA and DOPE formed colloiddally stable nanoparticulate RNA-LPX of reproducible particle size (200–400 nm) and charge (Fig. 1a, Extended Data Fig. 1b) with positive as well as negative excess charge. Slightly positively charged and near-neutral RNA-LPX (positive to negative charge ratio from 2.5:1 to 1.8:2), in contrast, were unstable, forming large aggregates immediately after preparation. Positively charged Luc-RNA-LPX (charge ratio of 5:1), as typically used for gene delivery¹⁶, targeted Luc expression predominantly in the lungs of mice and less in the spleen (Fig. 1b). Surprisingly, gradual decrease of the cationic lipid content shifted Luc expression from the lungs towards the spleen. Near-neutral and slightly negative particles (for example, charge ratio of 1.7:2) provided an exclusively splenic signal (Fig. 1b). RNA-LPX of further lowered charge ratio ($\leq 1.7:2$) were medium-sized (~ 200 – 320 nm), of low polydispersity, and were all expressed in the spleen. However, the transfection efficiency gradually declined with increasing negative charge, probably owing to increasing amounts of uncomplexed free RNA (Extended Data Fig. 1c). The unexpected selective targeting of negatively charged particles to the spleen prompted us to test various other well-characterized lipid compositions (for example, DOTAP, cholesterol). Irrespective of the lipids used, all particles with an excess negative charge exhibited pharmacologically suitable physicochemical properties (Extended Data Fig. 1d) and led to selective antigen expression in splenic cell populations (Extended Data Fig. 1e).

For further characterization, we selected an RNA-LPX formulation with a charge ratio of 1.3:2, which effectively targeted RNA to the spleen (Extended Data Fig. 1f), formed monodisperse and stable particles (Fig. 1c, Extended Data Fig. 1g) and was fully resistant to degradation by mouse serum at 37°C (Extended Data Fig. 1h). In CD11c-DTR mice (expressing diphtheria toxin receptor under control of the *Cd11c* promoter) depleted of CD11c⁺ cells before injection of this RNA-LPX, the reporter signal was almost undetectable in the spleen, indicating that APCs are the source of Luc expression (Fig. 1d).

¹TRON–Translational Oncology at the University Medical Center of the Johannes Gutenberg University gGmbH, Freiligrathstr. 12, Mainz 55131, Germany. ²Research Center for Immunotherapy (FZI), University Medical Center at the Johannes Gutenberg University, Langenbeckstr. 1, Mainz 55131, Germany. ³Biopharmaceutical New Technologies (BioNTech) Corporation, An der Goldgrube 12, Mainz 55131, Germany. ⁴Department of Dermatology, University Medical Center of the Johannes Gutenberg University, Langenbeckstr. 1, Mainz 55131, Germany. ⁵Department of Dermatology, Heidelberg University Hospital, Im Neuenheimer Feld 440, 69120 Heidelberg, Germany. ⁶Institute of Pharmacy and Biochemistry, Johannes Gutenberg University, Germany, Langenbeckstr. 1, Mainz 55131, Germany. ⁷Cluster for Individualized Immune Intervention, Kupferbergterasse 19, Mainz 55116, Germany.

*These authors contributed equally to this work.

§These authors jointly supervised this work.

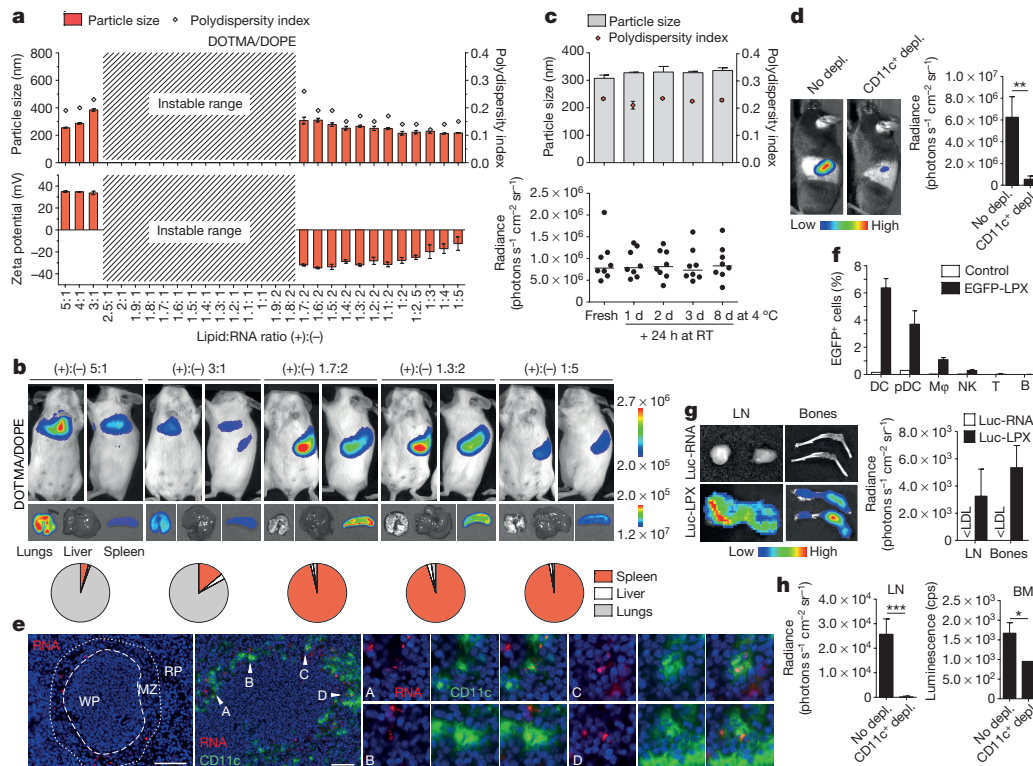


Figure 1 | RNA-LPX of negative net charge deliver RNA-encoded antigens body-wide to lymphoid-resident DCs. a, Particle size, polydispersity index (top) and zeta potential (bottom) ($n = 3$) of RNA-LPX constituted with DOTMA/DOPE liposomes and Luc-RNA at various charge ratios. **b**, Bioluminescence imaging of BALB/c mice ($n = 3$) after i.v. injection of Luc-LPX at various charge ratios. Pie charts show relative contribution of each organ to total signal. **c**, Particle size and polydispersity index of Luc-LPX either constituted freshly or stored at 4 °C followed by 24 h incubation at room temperature (top) and bioluminescence imaging of the spleens of BALB/c mice ($n = 8$, pooled from two experiments) after i.v. injection (bottom). **d**, Bioluminescence imaging after i.v. injection of Luc-LPX in CD11c-DTR mice ($n = 3$)

We identified CD11c⁺ conventional (c)DCs in the marginal zone, and plasmacytoid (p)DCs and macrophages in the spleen as the cell subsets internalizing RNA-LPX by a set of experiments in which RNA-LPX with Cy3- or Cy5-labelled RNA or enhanced green fluorescent protein (eGFP) was administered (Fig. 1e, f, Extended Data Fig. 2a, b).

The rate of RNA uptake was highest in macrophages (Extended Data Fig. 2a), whereas the highest eGFP transfection rate as measure for translation efficiency was observed in cDCs (Fig. 1f), indicating that DCs are more effective in cytoplasmic translocation and translation of RNA. Natural killer (NK), B and T cells, in contrast, did not exhibit relevant uptake. Concordant with the fact that the spleen, as the organ with the highest density of APCs, is known to be highly efficient in clearance of blood-borne pathogens, we found that i.v.-administered liposomal RNA was rapidly cleared from the blood within 1 h (Extended Data Fig. 2c).

Analysis of organs explanted after i.v. administration of RNA-LPX encoding Thy1.1 (enabling sensitive detection of Thy1.1⁺ transfected cells in Thy1.2 mice) or containing Cy5-labelled reporter RNA, revealed that not only APCs in the spleen are targeted. In the liver, we detected Cy5-labelled RNA in a small portion of cells, and Thy1.1 expression in CD11b⁺ macrophages (Extended Data Fig. 2d). Moreover, we detected Luc signals in lymph nodes from various body regions and in femur and tibia bone marrow (Fig. 1g, Extended Data Fig. 2e), as well as Cy5-labelled RNA and Thy1.1⁺CD11c⁺ cells in the bone marrow (Extended Data Fig. 2f). Again, depletion of CD11c⁺ cells before i.v. injection of

depleted (depl.) of CD11c⁺ cells. **e**, Splenic localization of CD11c and Cy3 double-positive cells in BALB/c mice ($n = 2$) 1 h after i.v. injection of Cy3-labelled RNA-LPX. Scale bar, 100 μ m. MZ, marginal zone; RP, red pulp; WP, white pulp. **f**, eGFP expression in splenic cell subsets of C57BL/6 mice ($n = 3$) 24 h after i.v. injection of eGFP-LPX by flow cytometry. **g**, Bioluminescence imaging of inguinal lymph nodes (LN), femur and tibia in BALB/c mice ($n = 3$) after i.v. injection of Luc-LPX. LDL, lower detection limit. **h**, Bioluminescence imaging of inguinal lymph nodes and *ex vivo* Luc assay of bone marrow (BM) single-cell suspensions after i.v. injection of Luc-LPX in CD11c⁺ cell-depleted CD11c-DTR mice ($n = 3$). Significance was determined using unpaired two-tailed Student's *t*-test. Error bars, median (c, bottom), otherwise mean \pm s.d.

Luc-LPX substantially reduced the reporter gene signal in these compartments (Fig. 1h).

We previously reported that DCs engulf naked RNA injected into lymph nodes by macropinocytosis¹⁷, which is constitutively active in immature DCs. RNA-LPX nanoparticles taken up by monocyte-derived human immature DCs almost completely co-localized with the macropinosome marker dextran (Extended Data Fig. 2g), whereas partial co-localization was observed with TLR7 and the early endosome marker EEA1 (Extended Data Fig. 2h). Moreover, rottlerin, a macropinocytosis inhibitor, and cytochalasin D, an inhibitor of phagocytosis and macropinocytosis, significantly inhibited RNA-LPX uptake by DCs *in vitro* (Extended Data Fig. 2i). Similarly, uptake of RNA-LPX was clearly reduced *in vivo* when lymph nodes were pre-injected with rottlerin (Extended Data Fig. 2j). DC maturation is known to prevent macropinocytosis¹⁸, whereas phagocytosis and receptor-mediated endocytosis remain unaffected¹⁹. Polyinosinic:polycytidylic acid (poly I:C)-matured DCs were unable to internalize Luc-RNA-LPX nanoparticles *in vitro* (Extended Data Fig. 2k). Similarly, in mice pre-treated with poly I:C before i.v. injection of RNA-LPX, the splenic Luc signal and reporter gene expression in CD8⁺ and CD8[−] cDCs were strongly reduced or completely lost (Extended Data Fig. 2l). Altogether, these findings identify macropinocytosis as the major uptake mechanism of RNA-LPX.

Investigating the biological effect of RNA-LPX *in vivo*, we found that a single i.v. injection of RNA-LPX encoding influenza virus hemagglutinin (HA), but not an empty control liposome carrier, induced

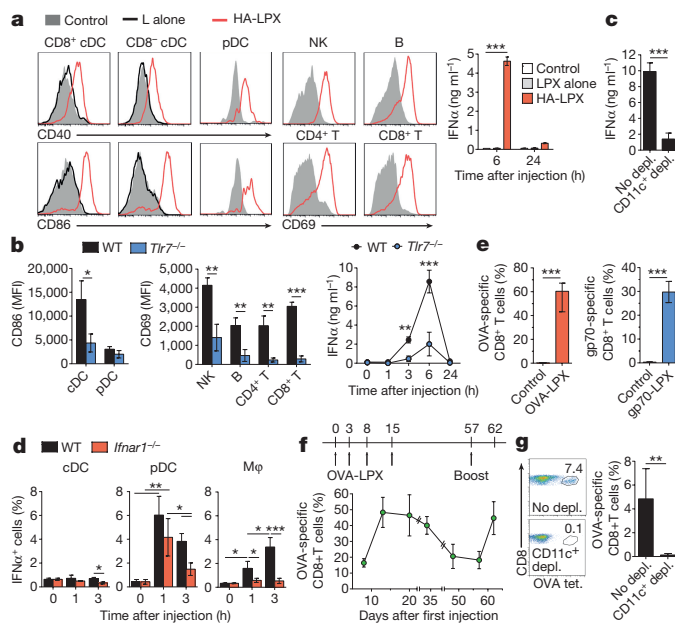


Figure 2 | RNA-LPX vaccines induce TLR7-triggered IFN α production, IFNAR-dependent activation of APCs and effector cells, and strong expansion of fully functional antigen-specific T cells. **a, b,** Activation markers measured 24 h after i.v. injection of HA-LPX by in splenic immune cell subsets ($n = 3$ per time point) and kinetics of IFN α serum levels ($n = 3$ per time point) in wild-type (a) or *Tlr7*^{-/-} (b) mice. **c,** IFN α serum levels in CD11c⁺ cell-depleted CD11c-DTR mice ($n = 3$) after i.v. injection of HA-LPX. **d,** Fraction of IFN α -expressing cells in splenic APC subsets after i.v. injection of HA-LPX in C57BL/6 and *Ifnar1*^{-/-} mice ($n = 3$ per time point). **e,** Fraction of OVA-specific (left) and gp70-specific CD8⁺ T cells (right) within CD8⁺ T cells in blood after *de novo* priming of C57BL/6 mice ($n = 5$) and BALB/c mice ($n = 5$) immunized i.v. with OVA-LPX or gp70-LPX (day 0, 3, 8), respectively. **f,** Kinetics of OVA-specific CD8⁺ T cell frequencies within CD8⁺ T cells in blood after i.v. immunization of C57BL/6 mice ($n = 5$) with OVA-LPX. **g,** Fraction of OVA-specific CD8⁺ T cells within CD8⁺ T cells in blood of CD11c⁺ cell-depleted BM-chimaeric CD11c-DTR mice ($n = 5$) immunized i.v. with OVA-LPX (day 0, 3). Significance was determined using two-way ANOVA and Bonferroni's multiple comparisons test (a, right, b, right, d), one-way ANOVA and Tukey's multiple comparisons test (d), and unpaired two-tailed Student's *t*-test (b, left, c, e, g). Error bars, mean \pm s.d.

maturation of splenic pDCs, CD8⁺ and CD8⁻ cDCs, which upregulated activation markers CD40 and CD86 (Fig. 2a, left). Activated CD11c⁺ cells redistributed from the red pulp and marginal zone into the T-cell-rich white pulp within 6 h after i.v. injection of RNA-LPX (Extended Data Fig. 3a). NK, B, CD4⁺ and CD8⁺ T cells were also strongly activated (Fig. 2a, middle), and a transient burst of serum IFN α peaking 6 h after RNA-LPX injection occurred (Fig. 2a, right). IFN α is typically produced in the context of RNA virus infections by APCs sensing dsRNA and ssRNA via endosomal TLR3 and TLR7, respectively, and is crucial for an efficient inflammatory, antiviral environment²⁰. In *Tlr7*^{-/-} mice, as compared to C57BL/6 wild-type mice, we found that splenocytes were moderately activated after i.v. injection of HA-LPX (Fig. 2b, left), and systemic IFN α release was not fully abrogated but significantly lower (Fig. 2b, right). By testing *Tlr3*^{-/-}, *Tlr4*^{-/-} and *Tlr9*^{-/-} mice, we excluded the contribution of these TLR signalling pathways and of DNA or LPS contamination to RNA-LPX-mediated effects (Extended Data Fig. 3b).

In C57BL/6 wild-type mice, expression of activation markers on cDCs, pDCs, NK cells, as well as B and T lymphocytes, increased continuously after i.v. injection of HA-LPX over a time period of 24 h. In C57BL/6 mice lacking IFN α receptor 1 (*Ifnar1*^{-/-}) and in BALB/c mice pre-treated with an anti-IFNAR1 blocking antibody, cDC, pDC, and NK-cell activation was significantly impaired and

restricted to the first 6 h, whereas no activation of CD4⁺ and CD8⁺ T cells and B cells occurred (Extended Data Fig. 3c–e). In CD11c-DTR mice depleted of CD11c⁺ cells before injection of HA-LPX, serum IFN α levels were markedly lower (Fig. 2c). These data support the role of type I IFN production and indicate that CD11c⁺ cells are the cellular source.

In C57BL/6 wild-type mice, splenic pDCs but not cDCs secreted IFN α immediately after RNA-LPX injection, which began to decrease 1 h after injection, whereas IFN α production by macrophages steadily increased over a period of 3 h (Fig. 2d). In *Ifnar1*^{-/-} mice, however, IFN α secretion by pDCs was moderately reduced, whereas macrophages did not produce IFN α . Expression profiling of sorted cells showed that macrophages and pDCs upregulate distinct IFN α isoforms (Extended Data Fig. 3f). Selective depletion of pDCs in BDCA2-DTR mice (expressing diphtheria toxin receptor under control of the *Bdca-2* promoter) or ablation of macrophages by pre-treatment with clodronate confirmed the role of these APC subsets for the TLR7-dependent biphasic IFN α production (Extended Data Fig. 3g).

Next, we studied antigen-specific T-cell stimulation upon vaccination. A single i.v. dose of HA-LPX induced strong proliferation of HA-specific T-cell receptor (TCR)-transgenic CD8⁺ and CD4⁺ T cells in blood, lymph nodes and spleen (Extended Data Fig. 3h). HA-specific T cells co-incubated with splenocytes from HA-LPX-treated mice *ex vivo* were strongly stimulated, indicating that HA-LPX delivered i.v. is efficiently internalized *in vivo* by splenocytes for functional antigen presentation (Extended Data Fig. 3i).

De novo priming of T-cell responses was analysed in C57BL/6 mice immunized with RNA-LPX encoding an ovalbumin epitope (OVA-LPX) and BALB/c mice immunized with gp70-LPX (an endogenous antigen of Moloney murine leukaemia virus integrated into the mouse genome). Three rounds of immunization with the respective RNA-LPX induced fully functional antigen-specific T cells reaching 30–60% of total CD8⁺ T cells (Fig. 2e, Extended Data Fig. 3j). Notably, repeated vaccination with RNA-LPX prevented the typical post-expansion T-cell retraction phase and high frequencies of antigen-specific T cells were maintained over several weeks (Fig. 2f). Concordantly, re-challenge of primed mice with OVA-LPX induced profound CD8⁺ T cell expansion, indicating the formation of memory cells (Fig. 2f, Extended Data Fig. 3k). Immune responses were not inducible in CD11c-DTR bone-marrow-chimaeric mice depleted of CD11c⁺ cells (Fig. 2g), whereas splenectomized mice vaccinated with RNA-LPX mounted a diminished but strong T-cell response, indicating the importance of APCs and the contribution of DCs in lymphoid tissues other than the spleen to RNA-LPX-mediated immunity (Extended Data Fig. 3l).

The prophylactic efficacy of RNA-LPX vaccines was assessed in two subcutaneous (s.c.) tumour models, B16-OVA and CT26: in both, immunization with OVA-LPX or gp70-LPX, respectively, led to complete and long-lasting protection upon tumour challenge, whereas all untreated mice died within less than 30 days (Fig. 3a).

Therapeutic efficacy was tested in several mouse tumour models. In a B16-OVA lung metastasis model, tumour-bearing C57BL/6 mice were immunized with three doses of OVA-LPX. The RNA-LPX-immunized mice cleared lung metastases completely and were free of tumours 20 days after the last immunization, whereas the lungs of mice immunized with control RNA exhibiting similar immune stimulatory properties were tumour-loaded (Extended Data Fig. 4a, b). In a lung metastases model with the melanocyte-differentiation antigen TRP-1 as vaccine target, strong CD8⁺ and CD4⁺ T-cell responses against this self-antigen were induced, and growing B16F10-Luc tumours were fully rejected (Fig. 3b, Extended Data Fig. 4c). Likewise, lung metastases derived from Luc-transduced or wild-type CT26 tumour cells were efficiently eradicated by vaccination with gp70-LPX (Fig. 3c, Extended Data Fig. 4d). Viral oncogenes and mutant neoepitopes are increasingly under investigation as clinically relevant vaccine-target classes. Vaccination with viral oncogene-coding E6/E7-LPX was successful at treating mice bearing advanced HPV16 E6- and E7-expressing TC-1

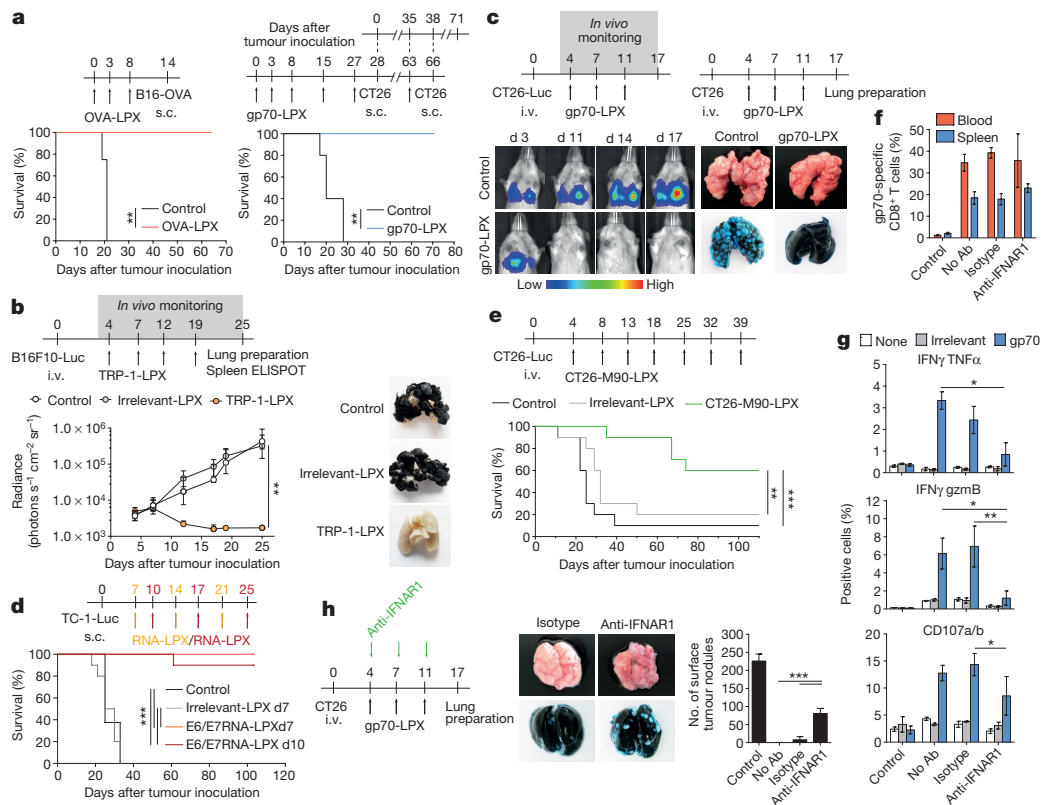


Figure 3 | RNA-LPX vaccines mediate rejection of advanced, aggressively growing tumours in mice. **a**, Prophylactic efficacy in OVA-LPX immunized C57BL/6 ($n = 6$) challenged s.c. with B16-OVA melanoma and gp70-LPX immunized BALB/c mice ($n = 5$) challenged and rechallenged s.c. with CT26 colon carcinoma. **b**, B16F10-Luc growth (left) and tumour load in lungs (right) of B6 albino mice ($n = 12$) immunized i.v. with TRP-1-LPX, irrelevant (empty vector)-LPX or control (untreated). **c**, CT26-Luc growth and CT26 tumour load in lungs of BALB/c mice ($n = 4-7$) immunized i.v. with gp70-LPX. **d**, Survival of C57BL/6 mice ($n = 10$) with advanced s.c. TC-1-Luc tumours immunized i.v. with E6/E7-LPX or irrelevant (OVA)-LPX. **e**, Survival of BALB/c mice ($n = 10$) with i.v. CT26-Luc colon carcinoma tumours immunized i.v. with

CT26-M90-LPX or irrelevant (OVA)-LPX. **f**, **g**, *De novo* priming in BALB/c mice ($n = 3$) immunized i.v. with gp70-LPX (day 0, 3, 8) and injected i.p. with anti-IFNAR1 antibody or isotype before each immunization. **f**, Fraction of gp70-specific CD8⁺ T cells within CD8⁺ T cells. **g**, Splenic CD8⁺ T cells upon *in vitro* restimulation with no (none), irrelevant (HA) or gp70 peptide. **h**, CT26 colon carcinoma load in lungs of BALB/c mice ($n = 5$) immunized i.v. with gp70-LPX and injected i.p. with anti-IFNAR1 antibody or isotype. Significance was determined using log-rank test (**a**, **d**, **e**), two-way ANOVA and Dunnett's multiple comparisons test (**b**), and one-way ANOVA and Tukey's multiple comparisons test (**g**, **h**). Error bars, median with interquartile range (**b**), otherwise mean \pm s.d.

tumours and protected C57BL/6 mice against tumour re-growth (Fig. 3d, Extended Data Fig. 4e). All mice starting treatment on day 7 and 90% of mice that started on day 10 survived. We vaccinated BALB/c mice bearing established rapidly growing CT26 lung tumours with the MHC class II neopeptide CT26-M90, derived from the P154S mutation in the *Aldh18a1* gene identified by exome sequencing²¹. This similarly led to efficient eradication of the lung tumours, highly significant long-term survival and protection from re-challenge, indicative of memory T-cell formation (Fig. 3e, Extended Data Fig. 4f).

To investigate the effect of RNA-LPX-induced IFN α on T cells, BALB/c mice were repeatedly immunized with gp70-LPX, but pre-treated either with an IFNAR1-blocking antibody or an isotype control before each immunization. Blocking IFNAR1 did not significantly affect expansion of gp70-specific CD8⁺ T cells in the blood and spleen (Fig. 3f). However, antigen-specific T cells primed under IFNAR1-blocking conditions failed to execute processes of pivotal effector function, such as secretion of granzyme B, IFN γ and tumour necrosis factor alpha (TNF α), and mobilization of degranulation marker CD107a/b (Fig. 3g). In another experiment, BALB/c mice with metastases derived from CT26 cells were immunized repeatedly with gp70-LPX, each preceded by injection of anti-IFNAR1 antibody or isotype control. Under IFNAR1-blocking conditions, lung metastases were only partially reduced and substantial residual tumour burden remained, whereas the lung tumours in control mice were completely rejected

(Fig. 3h). In conclusion, the ability of RNA-LPX to induce an IFN α response in lymphoid tissues appears to be critical for antigen-specific CD8⁺ T cells to acquire effector functions and execute potent *in vivo* anti-tumour activity.

These findings together with favourable outcomes of safety pharmacology studies with clinical grade material in mice and cynomolgus monkeys (Extended Data Table 1) encouraged the clinical translation of this concept.

A phase I dose-escalation trial with good manufacturing practise (GMP)-produced RNA-LPX vaccines encoding four tumour antigens (NY-ESO-1, MAGE-A3, tyrosinase and TPTE) for i.v. administration is currently recruiting patients with advanced malignant melanoma (NCT02410733). The first three patients were treated with a very low initial dose of RNA-LPX, followed by four weekly applications with moderately higher doses, but still below the absolute therapeutic dose levels used in mice (Extended Data Fig. 5a). All vaccine applications were well-tolerated with transient flu-like symptoms. All three patients had dose-dependent early release of IFN α and IP-10 (also known as CXCL10) peaking at 6 h (Fig. 4a), resembling the kinetics observed in mice (Fig. 2a). All patients developed *de novo* T-cell responses against the vaccine antigens. In patient 1, who had no T cells against NY-ESO-1 at baseline, cell counts of *de novo* induced NY-ESO-1-specific T cells four weeks after the last immunization reached the same range as those against immune-dominant HLA-class-I-restricted peptides from

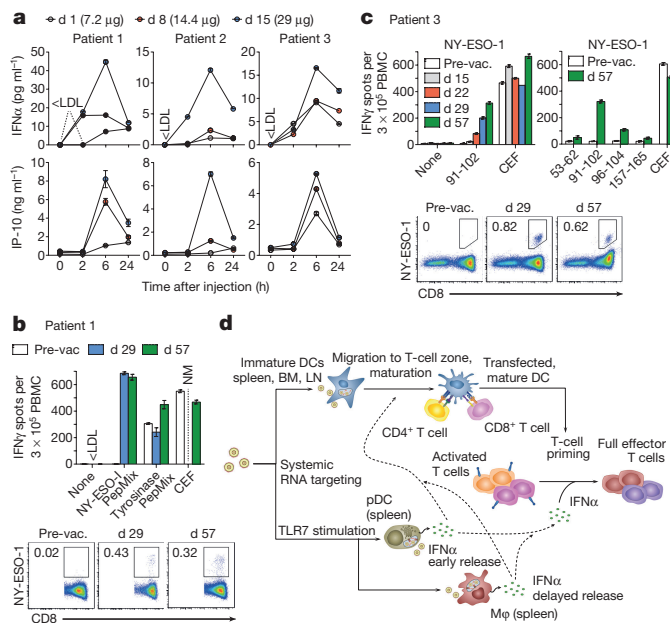


Figure 4 | Clinically administered RNA-LPX vaccines dose-dependently induce systemic IFN α and *de novo* priming and amplification of T cells against vaccine antigens. **a**, Serum cytokines before (0 h) and after injection of intra-patiently escalated doses. **b**, **c**, T-cell responses against NY-ESO-1 and tyrosinase determined by restimulation with overlapping peptide mixtures or NY-ESO-1 epitopes (indicated with the amino acid position) in IFN γ ELISPOT and NY-ESO-1 specific MHC class I dextramer staining for patients 1 (**b**) and 3 (**c**). CEF, cytomegalovirus, Epstein–Barr and influenza viruses peptide pool; NM, not measured; PepMix, peptide mixture; pre-vac., pre-vaccination. **d**, Mechanism of action for RNA-LPX. Error bars, mean \pm s.e.m.

cytomegalovirus, Epstein–Barr and influenza viruses (Fig. 4b, Extended Data Fig. 5b). HLA-B35 NY-ESO-1 dextramer analysis of blood samples showed a rapid induction of antigen-specific CD8 $^{+}$ T cells within two weeks of starting treatment, increasing with subsequent vaccinations. Moreover, the pre-existing T-cell response against tyrosinase in this patient was augmented. Imaging before and after vaccination showed regression of a suspected metastatic thoracic lymph node lesion (data not shown). Patient 2, whose metastases were surgically removed before vaccination, experienced induction of CD4 $^{+}$ T-cell responses against NY-ESO-1 and MAGE-A3 (Extended Data Fig. 5c) and was tumour-free at the time of this report (seven months after the start of vaccination). In patient 3, a strong NY-ESO-1-specific HLA-Cw03-directed *de novo* T-cell response (Fig. 4c) and a weaker response against MAGE-A3 (Extended Data Fig. 5d) were induced. This patient previously received various treatments and had eight lung metastases at recruitment, which remained clinically and radiologically stable (data not shown).

In summary, our study provides insights into a novel class of systemically administered nanoparticulate RNA vaccines, which act by body-wide delivery of encoded antigens to APCs in the spleen, lymph nodes and bone marrow, and concomitant initiation of a strong type-I-IFN-driven immunostimulatory program (Fig. 4d). Systemic antigen targeting in lymphoid DCs is more potent than local vaccine delivery (Extended Data Fig. 6) and has large therapeutic potential. To our best knowledge, RNA-LPX vaccines are the first example of a clinically applied systemic nanoparticulate vaccine which accomplishes this aim. Whereas the current model involves functionalization of nanoparticles with molecular ligands that target DCs^{6,8}, we show for the first time that precise DC targeting in lymphoid compartments can be accomplished using well-known lipid carriers such as DOTMA, DOTAP, DOPE and cholesterol, without functionalization, solely by adjusting negative net charge of the nanoparticles.

TLR7-driven type-I interferon release, the cellular source of which was unravelled in our study, appears to be essential for the full anti-tumour potency of this vaccine class, in contrast to previous reports that interferon counteracts locally applied RNA lipoplex vaccine responses¹⁰. Type I IFN as a key molecule in antigen-specific immunity against viral infections has further effects, for example, upregulation of MHC expression, promotion of maturation and cross-presentation in DCs²², and direct inhibition of regulatory T-cell functions^{23,24}, which were not investigated in our study but may contribute to the antitumour efficacy of RNA-LPX. Our findings connect effective cancer immunotherapy with host pathogen-defence mechanisms. Mechanisms of antiviral host defence are important for survival, conserved in all vertebrates and evolutionarily optimized for high sensitivity and potency. RNA-LPX vaccines appear to mimic infectious non-self and thus mobilize concomitantly adaptive and innate antiviral mechanisms^{25,26}. The i.v. delivery of RNA-LPX simulates a viraemic pathogen intrusion in the blood stream, and by reaching DCs in various lymphoid tissues, mobilizes the full T-cell repertoire for adaptive immune responses.

Our study shows profound expansion of effector T cells, even against self-antigens, and antitumour efficacy in various aggressively growing mouse tumour models induced by RNA-LPX. The dose-dependent IFN α response and stimulation of strong immune responses against self-antigens observed in the first cohort of patients supports the pre-clinically identified mode of action and strong potency of this approach in the clinical setting. RNA-LPX vaccines are fast and inexpensive to produce, and virtually any tumour antigen can be encoded by RNA. Thus, the nanoparticulate RNA immunotherapy approach introduced here may be regarded as a universally applicable novel vaccine class for cancer immunotherapy.

Online Content Methods, along with any additional Extended Data display items and Source Data, are available in the online version of the paper; references unique to these sections appear only in the online paper.

Received 28 December 2015; accepted 6 May 2016.

Published online 1 June 2016.

1. Zinkernagel, R. M. et al. Antigen localisation regulates immune responses in a dose- and time-dependent fashion: a geographical view of immune reactivity. *Immunol. Rev.* **156**, 199–209 (1997).
2. Stetson, D. B. & Medzhitov, R. Type I interferons in host defense. *Immunity* **25**, 373–381 (2006).
3. Boczkowski, D., Nair, S. K., Snyder, D. & Gilboa, E. Dendritic cells pulsed with RNA are potent antigen-presenting cells *in vitro* and *in vivo*. *J. Exp. Med.* **184**, 465–472 (1996).
4. Sahin, U., Karikó, K. & Türeci, Ö. mRNA-based therapeutics—developing a new class of drugs. *Nat. Rev. Drug Discov.* **13**, 759–780 (2014).
5. Banchereau, J. & Steinman, R. M. Dendritic cells and the control of immunity. *Nature* **392**, 245–252 (1998).
6. Tacke, P. J., de Vries, I. J. M., Torensma, R. & Figdor, C. G. Dendritic-cell immunotherapy: from ex vivo loading to *in vivo* targeting. *Nat. Rev. Immunol.* **7**, 790–802 (2007).
7. Phua, K. K. L. Towards targeted delivery systems: ligand conjugation strategies for mRNA nanoparticle tumor vaccines. *J. Immunol. Res.* 680620 (2015).
8. Mitragotri, S., Burke, P. A. & Langer, R. Overcoming the challenges in administering biopharmaceuticals: formulation and delivery strategies. *Nat. Rev. Drug Discov.* **13**, 655–672 (2014).
9. Brito, L. A. et al. A cationic nanoemulsion for the delivery of next generation RNA vaccines. *Mol. Ther.* **22**, 2118–2129 (2014).
10. Pollard, C. et al. Type I IFN counteracts the induction of antigen-specific immune responses by lipid-based delivery of mRNA vaccines. *Mol. Ther.* **21**, 251–259 (2013).
11. Zhou, W. Z. et al. RNA melanoma vaccine: induction of antitumor immunity by human glycoprotein 100 mRNA immunization. *Hum. Gene Ther.* **10**, 2719–2724 (1999).
12. Hess, P. R., Boczkowski, D., Nair, S. K., Snyder, D. & Gilboa, E. Vaccination with mRNAs encoding tumor-associated antigens and granulocyte-macrophage colony-stimulating factor efficiently primes CTL responses, but is insufficient to overcome tolerance to a model tumor/self antigen. *Cancer Immunol. Immunother.* **55**, 672–683 (2006).
13. Perche, F. et al. Enhancement of dendritic cells transfection *in vivo* and of vaccination against B16F10 melanoma with mannoseylated histidylated lipopolyplexes loaded with tumor antigen messenger RNA. *Nanomedicine* **7**, 445–453 (2011).
14. Blanco, E., Shen, H. & Ferrari, M. Principles of nanoparticle design for overcoming biological barriers to drug delivery. *Nat. Biotechnol.* **33**, 941–951 (2015).

15. Lee, E. R. *et al.* Detailed analysis of structures and formulations of cationic lipids for efficient gene transfer to the lung. *Hum. Gene Ther.* **7**, 1701–1717 (1996).
 16. Liu, Y. *et al.* Factors influencing the efficiency of cationic liposome-mediated intravenous gene delivery. *Nat. Biotechnol.* **15**, 167–173 (1997).
 17. Diken, M. *et al.* Selective uptake of naked vaccine RNA by dendritic cells is driven by macropinocytosis and abrogated upon DC maturation. *Gene Ther.* **18**, 702–708 (2011).
 18. Sallusto, F., Cella, M., Danieli, C. & Lanzavecchia, A. Dendritic cells use macropinocytosis and the mannose receptor to concentrate macromolecules in the major histocompatibility complex class II compartment: downregulation by cytokines and bacterial products. *J. Exp. Med.* **182**, 389–400 (1995).
 19. Platt, C. D. *et al.* Mature dendritic cells use endocytic receptors to capture and present antigens. *Proc. Natl Acad. Sci. USA* **107**, 4287–4292 (2010).
 20. Diebold, S. S., Kaisho, T., Hemmi, H., Akira, S. & Reis e Sousa & C. Innate antiviral responses by means of TLR7-mediated recognition of single-stranded RNA. *Science* **303**, 1529–1531 (2004).
 21. Kreiter, S. *et al.* Mutant MHC class II epitopes drive therapeutic immune responses to cancer. *Nature* **520**, 692–696 (2015).
 22. Le Bon, A. *et al.* Cross-priming of CD8⁺ T cells stimulated by virus-induced type I interferon. *Nat. Immunol.* **4**, 1009–1015 (2003).
 23. Bacher, N. *et al.* Interferon- α suppresses cAMP to disarm human regulatory T cells. *Cancer Res.* **73**, 5647–5656 (2013).
 24. Zitvogel, L., Galluzzi, L., Kepp, O., Smyth, M. J. & Kroemer, G. Type I interferons in anticancer immunity. *Nat. Rev. Immunol.* **15**, 405–414 (2015).
 25. Janeway, C. A. Jr The immune system evolved to discriminate infectious nonself from noninfectious self. *Immunol. Today* **13**, 11–16 (1992).
 26. Janeway, C. A. Jr & Medzhitov, R. Innate immune recognition. *Annu. Rev. Immunol.* **20**, 197–216 (2002).
- Acknowledgements** The authors thank M. Holzmann, R. Roth, U. Schmitt, M. Brkic, A. König, C. Worm, N. Kimmel, A.-K. Thiel, C. Bender, M. Suchan, A.-L. Popa, P. Bezerra Gomes, S. Herbert, M. Lux, D. Wintergerst, V. Bischoff, R. Krishna, Y. Hajime, J. Groß, A. Spruss, M. Erdeljan, S. Wöll, T. Bukur, H. Muramatsu and M. Baierdörfer for technical support, NIH Tetramer Core Facility for providing gp70 MHC class I tetramer, A. Kong for critical reading, A. Kemmer-Brück, D. Schwarck, S. Bolte for clinical operations support and K. Kariko for advice. This work was supported by the technology innovation program of the Rhineland Palatinate government, the InnoTop program, the Cl3 Cutting Edge Cluster Funding of the German Ministry of Technology (BMBF) and the Collaborative Research Group 1066 of Deutsche Forschungsgemeinschaft (DFG). L.M.K. was funded by the Graduate School of Immunotherapy 1043 of DFG.
- Author Contributions** U.S. was responsible for conception and experimental strategy of the study. Formulation development was performed by H.H. and P.L. Design and analysis of the experiments were done by L.M.K., M.D., H.H., S.K., M.M. and D.F. supported by K.C.R. and F.V. L.M.K., M.D., M.M., D.F., K.C.R., A.S., F.V., Y.H., Ho.He, C.G. and M.V. performed the experiments and acquired the data. C.L., J. H., J.D., A.N.K., J.B., R.J., S.H., S.G., E.D., R.R. and S.A. were involved in design, implementation or laboratory analyses of the clinical study. L.M.K., M.D., Ö.T. and U.S. interpreted the data and drafted the manuscript. C.H. supported the revision of the manuscript.
- Author Information** Reprints and permissions information is available at www.nature.com/reprints. The authors declare competing financial interests: details are available in the online version of the paper. Readers are welcome to comment on the online version of the paper. Correspondence and requests for materials should be addressed to U.S. (sahin@uni-mainz.de).
- Reviewer Information** *Nature* thanks O. Farokhzad, C. G. Figdor, C. Melief, L. Zhang and the other anonymous reviewer(s) for their contribution to the peer review of this work.

METHODS

Mice. C57BL/6 mice, as well as *Tlr3*^{-/-} and BDCA2-DTR mice²⁷ bred on a C57BL/6 background, and BALB/c mice were purchased from the Jackson Laboratory and Charles River. C57BL/6BrdCrHsd-Tyr^c (B6 albino) mice were purchased from Envigo EMS. C57BL/6 *Ifnar1*^{-/-} mice²⁸, derived from 129Sv *Ifnar1*^{-/-} mice²⁹ via backcrossing were a gift from J. Kirberg (Paul-Ehrlich-Institute). The following mice strains were provided from colleagues from the University Medical Center of the Johannes Gutenberg University Mainz: *Rag2*^{-/-} TCR-HA mice transgenic for the influenza virus hemagglutinin A HA₁₀₇₋₁₁₉ peptide-specific, I-E^d-restricted T cell receptor (TCR) (HA-TCRtg); BALB/c mice transgenic for the HA₅₁₈₋₅₂₆ peptide-specific, H2-K^d-restricted TCR (CL4-TCRtg); and BALB/c Thy1.1⁺ mice from U. Hartwig, *Tlr7*^{-/-} mice on a C57BL/6 background from H. J. Schild, CD11c-DTR³⁰ and *Tlr9*^{-/-} mice, both on a C57BL/6 background, by E. von Stebut-Borschitz, *Tlr4*^{-/-} mice by K. Steinbrink. For prolonged ablation of CD11c⁺ cells, bone-marrow chimaeras were generated by reconstitution of lethally irradiated (9.5 Gy) C57BL/6 mice with bone marrow cells from CD11c-DTR mice. Age-matched (6–12 weeks) female animals were used throughout all experiments. Experimental group sizes were approved by the regulatory authorities for animal welfare after being defined to balance statistical power, feasibility and ethical aspects. All mice were kept in accordance with federal and state policies on animal research at the University of Mainz and BioNTech AG.

Tumour cell lines. B16-OVA is a murine B16F10 melanoma cell line expressing the chicken ovalbumin gene (OVA) containing the H2-K^b-restricted OVA₂₅₇₋₂₆₄ epitope (SIINFEKL), which was a gift from U. Hartwig. CT26 (ATCC) is a murine colorectal cancer cell line endogenously expressing gp70 which is silent in most normal mouse tissues³¹. Luc-expressing CT26 (CT26-Luc) and B16F10 tumour cells (B16F10-Luc) were generated by lentiviral transduction. The Luc-expressing TC-1 tumour cell line (TC-1-Luc) derived from primary lung cells by immortalization and retroviral transduction with HPV16 E6 and E7³² as well as Luc³³ was obtained from E. Tartour (INSERM U970 PARCC) with the permission of T.-C. Wu (Johns Hopkins University). Master and working cell banks were generated immediately upon receipt, of which third and fourth passages were used for tumour experiments. Cells were tested for mycoplasma every three months. Reauthentication of cells was not performed after receipt.

RNA constructs and *in vitro* transcription. Plasmid templates for *in vitro* transcription of naked antigen-encoding RNAs were based on pSTI-A120 and pST1-MITD vectors³⁴. pST1-MITD features a signal sequence for routing to the endoplasmic reticulum and the major histocompatibility complex (MHC) class I transmembrane and cytoplasmic domains for improved presentation of MHC class I and II epitopes. pST1-eGFP-A120 (eGFP), pST1-OVA-MITD (OVA), pST1-Influenza-HA-MITD (HA) and pST1-Luciferase-A120 (Luc) vectors were described previously^{34–36}. The OVA construct encodes the H-2K^b-restricted, immunodominant epitope OVA₂₅₇₋₂₆₄, and the HA construct contains a codon-optimized partial sequence of influenza HA (aa 60–285 fused to aa 517–527; influenza strain A/PR/8/34) designed to combine all major immunodominant MHC epitopes. pST1-Thy1.1 encodes the murine Thy1.1 protein. pST1-gp70-MITD encodes the H-2L^d-restricted peptide antigen AH1₄₂₃₋₄₃₁ derived from Moloney murine leukaemia virus envelope glycoprotein 70 (gp70) with an amino acid substitution at position five (V/A; AH1-A5)³⁷. pST1-E6-MITD and pST1-E7-MITD encode human papillomavirus (HPV) 16 full-length E6 and E7³⁸, respectively, and the sequence encoding the point-mutated 27-meric peptide CT26-M90 of ALDH18a1 was cloned into the pST1-MITD vector. pST1-TRP-1-MITD encodes murine tyrosinase-related protein 1 (TRP-1). pST1-empty-MITD does not encode a protein and was used as an irrelevant RNA control. RNA was generated by *in vitro* transcription as described previously³⁹. For some experiments, Luc and Thy1.1 RNA was synthesized using 1-methyl-pseudouridine instead of uridine. Labelling of RNA with Cy3 or Cy5 was performed according to the manufacturer's instructions (Amersham Biosciences), and of total uridine triphosphate (UTP), 15% were replaced with labelled UTP during *in vitro* transcription of the HA construct.

Liposomes. Liposomes with positive (cationic) net charge were used to complex RNA for the formation of RNA-LPX and comprised of the cationic lipid DOTMA (Merck & Cie) or DOTAP (Merck Eprova), and the helper lipid DOPE (Avanti Polar Lipids or Corden Pharma) or cholesterol (Sigma-Aldrich). Liposomes were produced either by protocols based on the thin film hydration method^{40,41} or by an adopted proprietary protocol based on the ethanol injection technique⁴². For the film method, stock solutions of the individual lipids were prepared in 99.5% ethanol at a concentration of approximately 10 mg ml⁻¹ (exact concentrations controlled by HPLC), and appropriate amounts (volumes) of the stock solutions were mixed according to the intended lipid ratio. The solvent was evaporated and the obtained lipid film was dried for 1 h using a rotatory evaporator. The dry film was hydrated with RNase-free water by gently shaking to obtain a raw colloid with a total lipid concentration of approximately 6 mM which was left overnight at 4 °C for equilibration. For size adjustment, the dispersion was then extruded 10 times

through polycarbonate membranes with 200 nm pore size using the LIPEX 10 ml extruder (Northern Lipids Inc.). The lipid concentration was measured by HPLC and adjusted by further addition of H₂O to a fixed concentration of the cationic lipid.

RNA-LPX preparation and immunization. Lipoplex formation was performed with proprietary protocols, derived from extensive internal formulation development activities. The general procedures were derived from protocols for siRNA- and DNA-LPX preparation described elsewhere⁴³. A diversity of formulations complexed with the reporter firefly luciferase (Luc)-encoding RNA was assembled, with liposomes comprising different cationic and helper lipids to create various lipid:RNA ratios, which defined the charge ratio and overall RNA-LPX net charge. The charge ratios were calculated from the number of positive charges represented by lipid-specific head groups (one positive charge per head group) and the number of negative charges represented by RNA nucleotides, that is, from the RNA phosphodiester groups (one negative charge per phosphodiester). For the calculation of the molar ratio between RNA and cationic lipid, a mean molar mass of 330 Da per nucleotide was assumed. RNA was provided as a HEPES-buffered solution at an RNA concentration of 1 mg ml⁻¹. RNA-LPX were formed by diluting the RNA with H₂O and 1.5 M NaCl solution followed by adding an appropriate amount of liposome dispersion to reach the selected charge ratio at a final NaCl concentration of 150 mM. RNA-LPX size (triplicates, from each measured ten technical replicates) and zeta potential (triplicates) were measured by photon correlation spectroscopy (PCS; 380 ZLS submicron particle/zeta potential analyser, PSS Nicomp). Uncomplexed RNA and RNA integrity were determined after isolation of total RNA by capillary gel electrophoresis (Agilent 2100 Bioanalyzer, Agilent technologies) (2–7 replicates). For formulation screening studies, 20 µg RNA-LPX corresponding to 0.1 mg ml⁻¹ RNA per mouse were injected i.v. into the retrobulbar venous plexus. For stability experiments, prepared RNA-LPX were pre-incubated with 50% syngeneic mouse serum for 30 min at room temperature or stored for 1, 2, 3 or 8 days at 4 °C and another 24 h at room temperature before injection. For immunological and tumour experiments, mice were immunized three times with 40 µg RNA LPX unless stated otherwise. The generation of memory T cells was verified by the recall response 42 days after the last immunization. Control mice received NaCl or remained untreated. Arrows in vaccination schemes indicate immunization.

Cryogenic transmission electron microscopy. Each sample was preserved in vitrified ice supported by holey carbon films on 400-mesh copper grids. Samples were prepared by applying a 3 µl drop of sample suspension to a cleaned grid, blotted away with a filter paper, and immediately proceeding with vitrification in liquid ethane. Grids were stored under liquid nitrogen until being transferred to the electron microscope for imaging. Electron microscopy was performed using a FEI Tecnai T12 electron microscope, operating at 120 keV equipped with a FEI Eagle 4k × 4k CCD camera. Vitreous ice grids were transferred into the electron microscope using a cryostage that maintains the grids at a temperature below -170 °C. Images of each grid were acquired at multiple scales to assess the overall distribution of the specimen. After identifying potentially suitable target areas for imaging at lower magnifications, pairs of high magnification images were acquired at nominal magnifications of 110,000× (0.10 nm per pixel), 52,000× (0.21 nm per pixel) and 21,000× (0.5 nm per pixel). The images were acquired at a nominal underfocus of -2 µm (110,000×), -4 µm (52,000×) and -4 µm (21,000×), and electron doses of ~10–24 e Å⁻². Cryo-electron transmission microscopy measurements were performed at Nanoimaging Services, Inc.

Synthetic peptides. Peptides derived from gp70 (H2-L^d-restricted gp70₄₂₃₋₄₃₁ AH1-A5 SPSYAHQF), HA (H2-K^d-restricted HA₅₁₈₋₅₂₆ IYSTVASSL), OVA (H2-K^b-restricted OVA₂₅₇₋₂₆₄ SIINFEKL), TRP-1 (H2-D^b-restricted TRP-1₄₅₅₋₄₆₃ TAPDNLGYA; I-A^b-restricted TRP-1₁₁₃₋₁₂₆ CRPGWRGAACNQKI), CT26-M90 (LHSGQNHLKEMAISVLEARACAAAGQS) and vesicular stomatitis virus nucleoprotein (H2-K^b-restricted VSV NP₅₂₋₅₉ RGVVYQGL), NY-ESO-I (HLA-Cw03 NY-ESO-I₉₁₋₁₀₂ YLAMPFATPMEA (patient 2, 3), NY-ESO-I₉₆₋₁₀₄ FATPMEAEL (patient 2, 3); HLA-A31 NY-ESO-I₅₃₋₆₂ ASGPGGGAPR; HLA-A02 NY-ESO-I₁₅₇₋₁₆₅ SLLMWITQC (patient 3)), MAGE-A3 (HLA-A01 MAGE-A3₁₆₈₋₁₇₆ EVDPIGHLY; HLA-Cw7 MAGE-A3₂₁₂₋₂₂₀ EGDCAPEEK (patient 2); HLA-A02 MAGE-A3₁₁₂₋₁₂₀ KVAELVHFL; HLA-B44 MAGE-A3₁₆₇₋₁₇₆ MEVDPIGHLY; HLA-A02 MAGE-A3₂₇₁₋₂₇₉ FLWGPRALV (patient 3)) and overlapping 15-mer peptide mixes for NY-ESO-I and tyrosinase (patient 1) were obtained from Jerini Peptide Technologies.

Tissue preparation. Peripheral blood was collected from the orbital sinus. Spleens and lymph nodes were stored in PBS (Life Technologies). Spleen single-cell suspensions were prepared in PBS by mashing tissue against the surface of a 70-µm cell strainer (BD Falcon) using the plunger of a 3-ml syringe (BD Biosciences). Erythrocytes were removed by hypotonic lysis. Lymph nodes were digested with collagenase D (1 mg ml⁻¹; Roche) and passed through cell strainers. Bone marrow

cells were flushed from femur and tibia bones, homogenized and filtered, before erythrocytes were removed by hypotonic lysis.

Flow cytometry. Monoclonal antibodies for extracellular staining included CD4, CD8, CD11b, CD40, CD45RA, CD49b, CD69, CD86, Ly6C, NK1.1, Thy1.1, Thy1.2 (BD Pharmingen), GR-1 (BioLegend), F4/80 (Invitrogen), CD11c, PDCA-1 (Miltenyi Biotec), CD62L, CD127, CD317 and Siglec H (eBioscience). Intracellular cytokine staining was performed with antibodies against IFN γ , TNF α and CD107a and CD107b (BD Pharmingen) and cross-reactive human granzyme B (Invitrogen) using the cytofix/cytoperm kit (BD Pharmingen), after stimulation of 2×10^6 splenocytes with $4 \mu\text{g ml}^{-1}$ gp70 AH1-A5 or irrelevant HA peptide in the presence of $20 \mu\text{g ml}^{-1}$ brefeldin A (Sigma), $40 \mu\text{g ml}^{-1}$ GolgiStop (BD Pharmingen) and CD107a and CD107b for 5 h at 37°C . Intracellular IFN α (RMMA-1, R&D Systems) staining was performed using the fixation and permeabilization kit (eBioscience) after incubation of 2×10^6 splenocytes in the presence of $20 \mu\text{g ml}^{-1}$ brefeldin A (Sigma) for 5 h at 37°C . Quantification of OVA-specific CD8 $^+$ T cells with H-2K b /OVA₂₅₇₋₂₆₄ tetramer (Beckman-Coulter) was previously described³⁴, and CD8 $^+$ T cells recognizing gp70 AH1-A1 were detected with H-2L d /AH1₄₂₃₋₄₃₁ (SPSYVYHQF) tetramer kindly provided by the NIH tetramer core facility (Emory University Vaccine Center). Antigen-specific CD8 $^+$ T cells were determined five days after the last immunization. Viability was determined using 7-AAD (Sigma) or fixable viability dye (eBioscience). For patient samples, cryopreserved PBMC or freshly isolated PBMC (day 57) were stained for 10 min at room temperature in the dark with MHC dextramers (Immudex) bound to peptide (HLA-B35 NY-ESO-1₉₄₋₁₀₂ MPFATPMEA (patient 1), HLA-Cw03 NY-ESO-1₉₂₋₁₀₀ LAMPFPATPM (patient 3). Cell surface markers CD3, CD8, CD16, CD14, CD19 (all BD Pharmingen) and CD4 (Biolegend) were subsequently stained along with DAPI (BD Biosciences) for 20 min at 4°C in the dark. Antigen-specific CD8 $^+$ T cells were determined within the CD3 $^+$ CD8 $^+$ CD4 $^-$ lineage $^-$ population. Flow cytometric data were acquired on a FACSCanto II or, for patient samples, an LSR Fortessa SORP flow cytometer (both BD Biosciences) and analysed with FlowJo 7.6.5 software (Tree Star). For cell sorting, splenocytes were pre-enriched by simultaneous magnetic depletion of T and B cells using MACS magnetic microbeads coated with CD3 or CD19 antibodies and MACS columns (Miltenyi Biotec). cDCs (F4/80 $^-$ CD11c $^{\text{hi}}$), pDCs (F4/80 $^-$ CD11c $^{\text{int}}$ PDCA-1 $^{\text{hi}}$) and macrophages (F4/80 $^{\text{hi}}$) were then sorted on a FACSaria cell sorter (BD Biosciences) according to their surface marker expression. Purities of sorted populations: cDCs, 97.8%; pDCs, 99.7%; macrophages, 98.9%.

Immunofluorescence staining. Immunofluorescence was performed as previously described²¹. For colocalization studies with CD11c $^+$ cells, 8- μm sections of cryoconserved spleens were stained. Sections were fixed in 4% paraformaldehyde (PFA) for 10 min at room temperature in the dark, blocked using PBS supplemented with 1% BSA, 5% mouse serum, 5% rat serum and 0.02% Nonident for 1 h at room temperature in the dark. Fluorescence-labelled CD11c antibody (clone N418, BioLegend) was used to stain sections overnight at 4°C , followed by nuclear staining with Hoechst (Sigma). Uptake of Cy3-RNA-LPX by CD11c $^+$ cells was revealed by visualization of CD11c- and Cy3-double-positive cells. Immunofluorescence images were acquired using an epifluorescence microscope (ApoTome, Zeiss).

For biodistribution studies of Cy5-labelled RNA-LPX in the spleen and liver, cryoconserved organs were cut and 6- μm sections were fixed in 4% PFA for 10 s at room temperature in the dark, followed by nuclear staining with DAPI (Sigma). Immunofluorescence images were acquired using an epifluorescence microscope (Axio Scan.Z1, Zeiss). For *in vitro* uptake and colocalization studies with Cy3-labelled RNA-LPX, treated human monocyte-derived DCs were fixed in 4% PFA for 10 min at room temperature in the dark, blocked using PBS supplemented with 0.5% BSA, 0.01% saponin, 5% mouse serum and 5% goat serum for 1 h at room temperature in the dark. Primary antibody staining with TLR7 (polyclonal, Novus) and EEA1 (polyclonal, Cell signaling) was followed by secondary antibody (anti-rabbit IgG, Jackson ImmunoResearch) and Hoechst (Sigma) staining. Immunofluorescence images were acquired using a confocal microscope (SP8 Leica). For the quantification of RNA-Cy3-LPX uptake by DCs in absence or presence of inhibitors, images were acquired using an epifluorescence microscope (ApoTome, Zeiss). The area (as pixel square) of Cy3 $^+$ particles in individual cells was quantified as selected threshold areas using Fiji ImageJ 1.49.

Ex vivo luciferase assay. Single-cell suspensions were prepared from the bone marrow of femur and tibia bones from mice 6 h after injection of $100 \mu\text{g}$ Luc-RNA-LPX and 5×10^6 cells were plated in 96-well Nunc white plates (Thermo Scientific). Cell suspensions were treated with the equal volume of Bright-Glo luciferin reagent (Promega), incubated for 3 min on a microplate shaker and bioluminescence was measured with an Infinite M200 plate reader (Tecan) with an integration time of 1 s. Background luminescence measured in cells obtained from untreated mice were within the range of 15 ± 5 counts per second.

In vitro uptake studies. For uptake and maturation studies with whole blood, $30 \mu\text{l}$ fresh whole blood were coincubated with 2×10^5 freshly generated human

monocyte-derived immature DCs pre-treated with $50 \mu\text{g ml}^{-1}$ poly I:C for 40 h at 37°C or left untreated and transfected with $0.2 \mu\text{g}$ Luc-LPX. After incubation for 20 h at 37°C , luciferase assay was performed as described above. For colocalization and uptake inhibition studies, freshly generated human monocyte-derived immature DCs (2.5×10^5 or 5×10^5) were plated on poly-L-lysine-coated 12-mm cover slips or chamber slides (Nunc) and incubated overnight at 37°C . Cells were transfected with 0.8 or $1.25 \mu\text{g}$ Cy3-labelled RNA-LPX for 10 min and washed thoroughly with medium to remove extracellular RNA-LPX. For colocalization studies, cells were co-transfected with RNA-LPX and 1 mg ml^{-1} FITC-labelled dextran (70,000 kDa, ThermoFisher) and fixed directly after washing. For costaining with EEA1 and TLR7, cells were incubated for another 30 min before fixation. For inhibition studies, cells were treated with $10 \mu\text{M}$ cytochalasin D⁴⁴ (Sigma) for 3 h or $10 \mu\text{M}$ Rotterlin⁴⁵ (Sigma) for 1 h (inhibitors present during transfection) before transfection, and fixed directly after washing. All conditions were performed in duplicates.

Bioluminescence imaging. Uptake and translation of Luc-RNA were evaluated by *in vivo* bioluminescence imaging using the Xenogen IVIS Spectrum imaging system (Caliper Life Sciences). Unless stated otherwise, an aqueous solution of L-luciferin (250 μl , 1.6 mg; BD Biosciences) was injected intraperitoneally 6 h after i.v. injection of $20 \mu\text{g}$ Luc-RNA-LPX (*ex vivo* lymph nodes and bone marrow imaging: 24 h after i.v. injection of $100 \mu\text{g}$). Emitted photons from live animals or extracted tissues were quantified 10 min later with an exposure time of 1 min. Regions of interest (ROI) were quantified as average radiance (photons $\text{s}^{-1} \text{cm}^{-2} \text{sr}^{-1}$, represented by colour bars) (IVIS Living Image 4.0).

Ex vivo fluorescence measurements. Upon organ retrieval, individual tissues were homogenized in $500 \mu\text{l}$ PBS using Lysis Matrix D tubes and the MP Biomedicals FastPrep-24 5G Instrument. Lysed tissues were directly subjected to fluorescence measurements for Cy5 (excitation, 650 nm; emission, 680 nm) using a standard fluorescence reader (Tecan Reader, Software i-control).

Enzyme-linked immunospot (ELISPOT) assay. As described previously²¹, 5×10^5 freshly isolated splenocytes were incubated in a microtiter plate (Merck Millipore) coated with anti-IFN γ antibody ($10 \mu\text{g ml}^{-1}$, AN18, Mabtech) in the presence of $2 \mu\text{g ml}^{-1}$ peptide for 18 h at 37°C , and cytokine secretion was detected with anti-IFN γ antibody ($1 \mu\text{g ml}^{-1}$ R4-6A2, Mabtech). For analysis of T-cell responses in peripheral blood, PBMC were isolated via density gradient centrifugation, pooled and restimulated with $2 \mu\text{g/ml}$ peptide. From each biological replicate, three technical triplicates were performed. For *ex vivo* ELISPOT assay from patient samples (patient 1 and 3), cryopreserved peripheral blood mononuclear cells (PBMC) or freshly isolated PBMC (day 57) were used. Cryopreserved PBMC were thawed, resuspended in CTS OpTmizer T Cell Expansion serum-free medium (Thermo Fisher Scientific) and left for 2–5 h at 37°C before performing the assay. For *in vitro* stimulation (IVS) before ELISPOT (patient 2), cryopreserved PBMC were thawed in a 37°C water bath and immediately transferred into CTL-Wash serum-free wash buffer (Cellular Technology). CD4 $^+$ and CD8 $^+$ T cells were purified using CD4 or CD8 microbeads (Miltenyi Biotec) according to the manufacturer's instructions. Positive fractions were resuspended at 1×10^6 cells ml^{-1} in DMEM (ThermoFisher Scientific) containing 10% AB-human serum (Thermo Fisher Scientific) and left overnight at 37°C before performing the assay. Negative fractions were resuspended in RPMI (Thermo Fisher Scientific) containing 5% human serum, 0.5% penicillin-streptomycin $1 \times$ MEM non-essential amino acids and 1 mM Sodium Pyruvate (all from Thermo Fisher Scientific) and left to rest overnight at room temperature before being electroporated with RNA encoding vaccine antigens (BioNTech). Electroporated APCs were left to rest for 3 h at 37°C , followed by irradiation at 15 Gy. CD4 $^+$ /CD8 $^+$ effectors and electroporated and irradiated APCs were coincubated at an effector:target ratio of 2:1. One day after starting the IVS, fresh culture medium was added together with 10 U ml^{-1} IL-2 (Proleukin 2, Novartis Pharma) and 5 ng ml^{-1} IL-15 (Peprotech). IL-2 was added once again at the same concentration 7 days after setting up the IVS cultures, and the cultures were incubated for another 4 days. During incubation, IVS cultures were checked microscopically and fresh medium was added if necessary. ELISPOT was performed after 11 days of stimulation (50,000 cells per well). On multiscan filter plates (Merck Millipore) coated with antibodies specific for IFN γ (1-D1K, Mabtech), 3×10^5 PBMC were stimulated with overlapping peptides covering the whole length of the vaccine antigens (PepMix, JPT Peptide Technologies) or a mixture of HLA-class-I-restricted peptides from cytomegalovirus, Epstein-Barr and influenza viruses (CEF pool, JPT Peptide Technologies) for 16–20 h at 37°C . Plates were sequentially incubated with biotin-conjugated secondary anti-IFN γ antibody (7-B6-1, Mabtech) and Extravidin-Alkaline Phosphatase (Sigma-Aldrich) before cytokine secretion was detected by adding BCIP/NBT substrate (Sigma-Aldrich). For each patient, technical triplicates were performed. Plates were scanned and analysed using the ImmunoSpot Series S5 Versa ELISPOT Analyzer (S5Versa-02-9038), ImmunoCapture software 6.3 and ImmunoSpot software 5.0.3 (all Cellular Technology Ltd).

Depletion and blocking experiments. For depletion of CD11c⁺ cells, CD11c-DTR mice were treated i.p. with 4 ng g⁻¹ body weight (bone marrow chimaeras: 8 ng g⁻¹ body weight) diphtheria toxin diluted in 200 µl PBS 12 h before RNA-LPX administration (depletion efficiency of CD11c⁺ DTR⁺ cells: >97.2%). CD11c^{int} pDCs are hardly affected by depletion in CD11c-DTR mice⁴⁶. For depletion of pDCs, BDCA2-DTR mice were treated i.p. with 4.5 ng g⁻¹ body weight diphtheria toxin diluted in 200 µl PBS (depletion efficiency of CD11b⁺CD11c^{int}Siglec-H^{hi}Ly6C^{hi} pDCs: >97.2%). Macrophages were depleted by administration of 50 mg kg⁻¹ body weight of clodrolip⁴⁷ (4.46 mg ml⁻¹ clodronate formulated with 16 mM POPC and 14 mM cholesterol) in PBS i.p. 12 h before RNA-LPX administration (depletion efficiency of F4/80⁺CD11b⁺CD11c^{int} macrophages: >96.3%). Depletion of CD11c⁺ cells, pDCs and macrophages was specific, other cells were not affected. In some experiments, 100 µg anti-IFNAR1 blocking antibody (MAR1-5A3, BioXCell) or IgG1 isotype control (MOPC-21, BioXCell) diluted in 200 µl PBS were applied i.p. 1 h before RNA-LPX injection.

Cellular uptake, splenocyte activation, *in vivo* cytokine secretion. Mice were injected i.v. with 40 µg Cy3- or Cy5-labelled RNA-LPX or 80 µg eGFP RNA-LPX and spleens were recovered 1 h (Cy3, Cy5) or 24 h later (eGFP). For splenocyte activation and cytokine secretion, mice were injected i.v. with 40 µg HA RNA-LPX. Unless stated otherwise, splenocytes were prepared 24 h after injection to measure median fluorescence intensity of CD40, CD86 and CD69 expression on immune cell subsets. Serum was collected and production of IFNα was determined from samples stored at -20 °C (pan-IFNα ELISA kit, PBL assay science). For patient samples, serum was stored at -80 °C and IFNα and IP-10 levels were determined using the pan-IFNα ELISA kit (PBL assay science) and ECLIA multiplex assay (Meso Scale Discovery), respectively. Patient samples were measured in duplicates. Quantification of RNA in blood was performed by quantitative RT-PCR using antigen sequence-specific primers (IMGM Laboratories).

***In vivo* proliferation assay.** Splenocytes (1 × 10⁷) from BALB/c Thy1.2⁺ CL4-TCR-transgenic mice labelled with 1 µM carboxyfluorescein diacetate, succinimidyl ester (CFSE, Invitrogen) were adoptively transferred into BALB/c Thy1.1⁺ mice and immunized i.v. with 40 µg HA-RNA-LPX 18 h after transfer. Controls received Thy1.2⁺ CL4-TCR-transgenic CD8⁺ T cells but were not immunized. Four days after immunization, peripheral blood, splenocytes and LN cells were stained for Thy1.2⁺CD8⁺ T cells and proliferation analysed by flow cytometry.

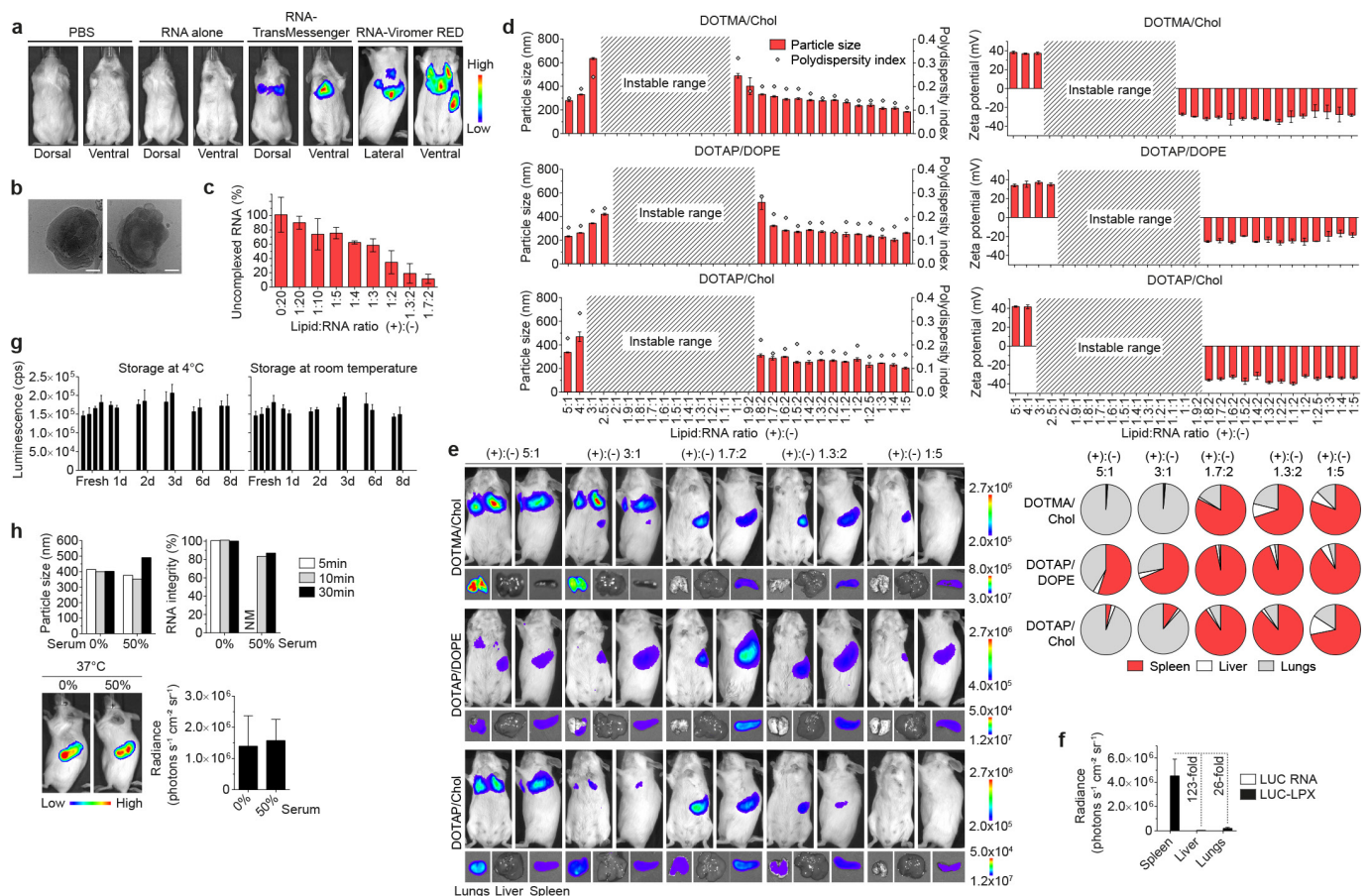
Tumour models. Protective immunity: BALB/c or C57BL/6 mice were immunized repetitively with 40 µg RNA-LPX. After the last immunization, 2 × 10⁵ CT26 or B16-OVA tumour cells, respectively, were inoculated s.c. into the flanks of mice. Therapeutic immunity: 1 × 10⁵ TC-1 tumour cells were inoculated s.c. and mice were immunized three times with 40 µg RNA-LPX (for E6/E7, 20 µg each). Tumour sizes were measured unblinded with a caliper every three to four days for calculating tumour volumes using the equation (a² × b)/2 (a, width; b, length). Animals were euthanized when exhibiting signs of impaired health or when the length of the tumour exceeded 15 mm. Metastasis models: 2 × 10⁵ CT26, CT26-Luc (immunization with CT26-M90 RNA-LPX: 5 × 10⁵), B16-OVA or 3 × 10⁵ B16F10-Luc tumour cells were injected i.v. and immunizations were initiated on day four after tumour inoculation. In some experiments, 1 mg of anti-IFNAR1 blocking antibody (MAR1-5A3, BioXCell) or IgG1 isotype control (MOPC-21, BioXCell) diluted in 200 µl PBS were applied i.p. 6 h before RNA-LPX injection. CT26-Luc and B16F10-Luc tumour growth kinetics were determined unblinded by bioluminescence *in vivo* imaging. Mice were randomized based on their average radiance values (ANOVA-P method, Daniel's XL Toolbox V6.53). When exhibiting impaired breathing, mice were killed and tumour burden was quantified unblinded after intratracheal ink (85 ml H₂O, 15 ml ink, two drops of ammonia water) injection (this step was omitted for B16-OVA model) and fixation with Fekete's solution (5 ml 70% ethanol, 0.5 ml formalin, and 0.25 ml glacial acetic acid)⁴⁸. After 2–6 h, tumour lesions were bleached whereas normal lung tissue remained stained.

Clinical trial design. The study protocol was approved by the relevant authority and ethics committee. The study was conducted in accordance with all applicable laws, regulations and in agreement with the ICH-GCP guidelines and the Declaration of Helsinki (Fortaleza 2013). Written informed consent from all patients was obtained before enrolment. For patient treatment, tumour antigen encoding RNA-LPX were prepared from GMP-manufactured components (BioNTech) in a dedicated pharmacy under GMP. Patients were injected i.v. with weekly escalating doses of RNA-LPX encoding antigens NY-ESO-1⁴⁹, tyrosinase⁵⁰, MAGE-A3⁵¹ and TPTE⁵² (1.9, 3.6 or 7.2 µg RNA-LPX of each antigen; see vaccination schemes in Extended Data Fig. 5a). Blood samples were obtained for cytokine measurements on day 1, 8 and 15 (0 (pre-vaccination), 2, 6, 24 h after each vaccination), for ELISPOT and MHC class I dextramer staining on day 0 (pre-vaccination), 15, 22, 29, 57. Blood samples for T-cell monitoring were obtained before vaccination on the respective vaccination day.

Statistical analyses and data presentation. All results are expressed as mean ± s.d., mean ± s.e.m. or median with or without interquartile range as indicated. Biological

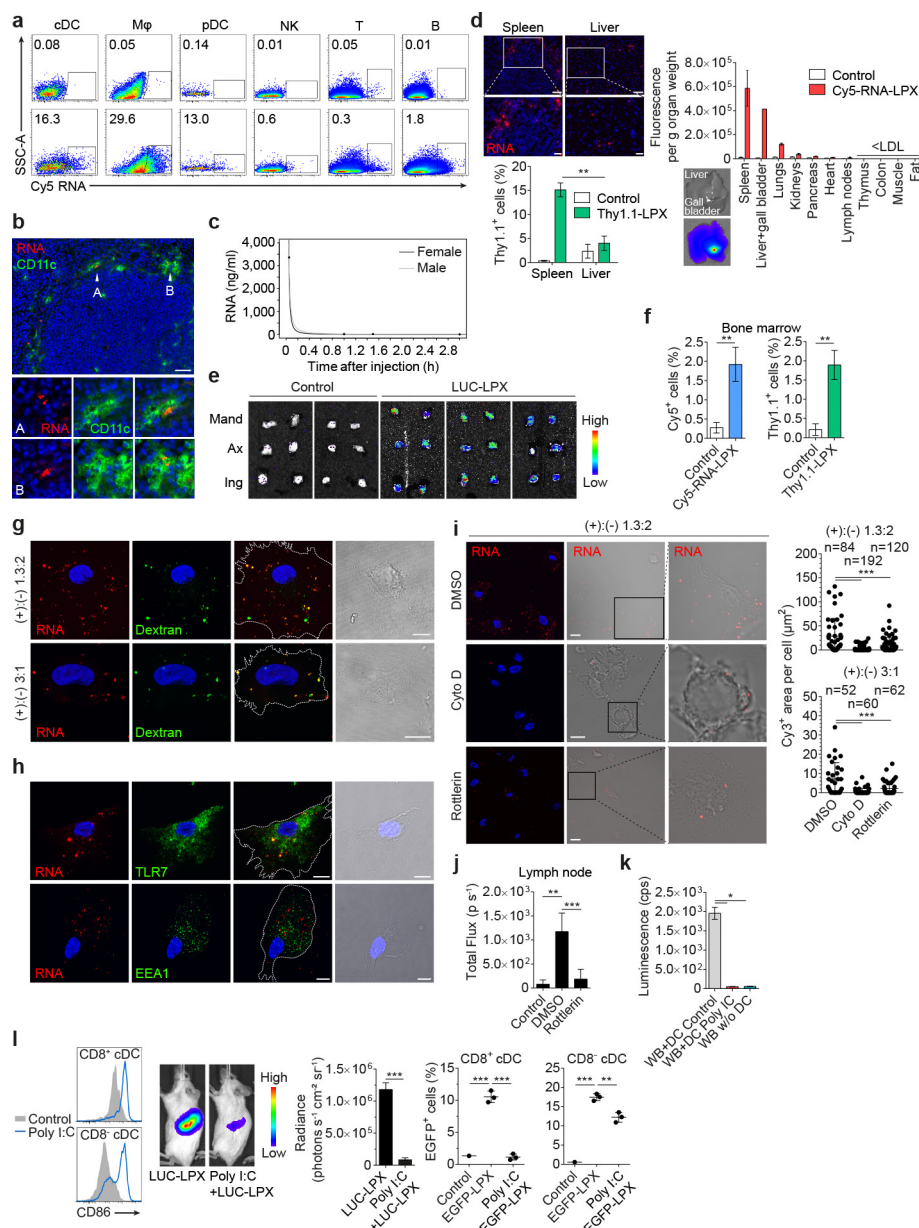
replicates were used in all experiments unless stated otherwise. Unpaired two-tailed Student's *t*-test was used for comparison of two groups. One-way analysis of variance (ANOVA) was performed when more than two groups were compared, and when determined significant (*P* < 0.05), multiple comparisons were performed using Tukey's post-hoc test. Two-way ANOVA was performed when both time and treatment were compared, and when significant (*P* < 0.05) multiple comparisons were performed using Bonferroni post-hoc tests or Dunnett's post-hoc test (Fig. 3b). Survival benefit was determined with the log-rank test. All statistical analyses were performed with GraphPad PRISM 6.01. **P* ≤ 0.05, ***P* ≤ 0.01, ****P* ≤ 0.001. In all experiments, representative images, dot plots and histograms are shown. Values below detection limit are marked with <LDL (lower detection limit). No statistical methods were used to pre-determine sample size for animal or other experiments.

27. Swiecki, M., Gilfillan, S., Vermi, W., Wang, Y. & Colonna, M. Plasmacytoid dendritic cell ablation impacts early interferon responses and antiviral NK and CD8⁺ T cell accrual. *Immunity* **33**, 955–966 (2010).
28. Kamphuis, E., Junt, T., Waibler, Z., Forster, R. & Kalinke, U. Type I interferons directly regulate lymphocyte recirculation and cause transient blood lymphopenia. *Blood* **108**, 3253–3261 (2006).
29. Müller, U. *et al.* Functional role of type I and type II interferons in antiviral defense. *Science* **264**, 1918–1921 (1994).
30. Jung, S. *et al.* *In vivo* depletion of CD11c⁺ dendritic cells abrogates priming of CD8⁺ T cells by exogenous cell-associated antigens. *Immunity* **17**, 211–220 (2002).
31. Huang, A. Y. *et al.* The immunodominant major histocompatibility complex class I-restricted antigen of a murine colon tumor derives from an endogenous retroviral gene product. *Proc. Natl Acad. Sci. USA* **93**, 9730–9735 (1996).
32. Lin, K.-Y. *et al.* Treatment of established tumors with a novel vaccine that enhances major histocompatibility class II presentation of tumor antigen. *Cancer Res.* **21**–26 (1996).
33. Chuang, C.-M., Monie, A., Wu, A. & Hung, C.-F. Combination of apigenin treatment with therapeutic HPV DNA vaccination generates enhanced therapeutic antitumor effects. *J. Biomed. Sci.* **16**, 49 (2009).
34. Holtkamp, S. *et al.* Modification of antigen-encoding RNA increases stability, translational efficacy, and T-cell stimulatory capacity of dendritic cells. *Blood* **108**, 4009–4017 (2006).
35. Kreiter, S. *et al.* Increased antigen presentation efficiency by coupling antigens to MHC class I trafficking signals. *J. Immunol.* **180**, 309–318 (2008).
36. Kuhn, A. N. *et al.* Phosphorothioate cap analogs increase stability and translational efficiency of RNA vaccines in immature dendritic cells and induce superior immune responses *in vivo*. *Gene Ther.* **17**, 961–971 (2010).
37. Slansky, J. E. *et al.* Enhanced antigen-specific antitumor immunity with altered peptide ligands that stabilize the MHC-peptide-TCR complex. *Immunity* **13**, 529–538 (2000).
38. Kenter, G. G. *et al.* Vaccination against HPV-16 oncoproteins for vulvar intraepithelial neoplasia. *N. Engl. J. Med.* **361**, 1838–1847 (2009).
39. Kreiter, S. *et al.* Simultaneous *ex vivo* quantification of antigen-specific CD4⁺ and CD8⁺ T cell responses using *in vitro* transcribed RNA. *Cancer Immunol. Immunother.* **56**, 1577–1587 (2007).
40. Bangham, A. D., Hill, M. W. & Miller, N. G. A. in *Methods in Membrane Biology* (ed. Korn, E. D.) 1–68 (Springer US, 1974).
41. Duzgunes, N. in *Methods in Enzymology* (Academic Press Inc, 2009).
42. Batzri, S. & Korn, E. D. Single bilayer liposomes prepared without sonication. *Biochim. Biophys. Acta* **298**, 1015–1019 (1973).
43. Barichello, J. M., Ishida, T. & Kiwada, H. Complexation of siRNA and pDNA with cationic liposomes: the important aspects in lipoplex preparation. *Methods Mol. Biol.* **605**, 461–472 (2010).
44. Racosin, E. L. & Swanson, J. A. Macrophage colony-stimulating factor (rM-CSF) stimulates pinocytosis in bone marrow-derived macrophages. *J. Exp. Med.* **170**, 1635–1648 (1989).
45. Sarkar, K., Kruhlak, M. J., Erlandsen, S. L. & Shaw, S. Selective inhibition by rottlerin of macropinocytosis in monocyte-derived dendritic cells. *Immunology* **116**, 513–524 (2005).
46. Bar-On, L. & Jung, S. Defining *in vivo* dendritic cell functions using CD11c-DTR transgenic mice. *Methods Mol. Biol.* **595**, 429–442 (2010).
47. Aichele, P. *et al.* Macrophages of the splenic marginal zone are essential for trapping of blood-borne particulate antigen but dispensable for induction of specific T cell responses. *J. Immunol.* **171**, 1148–1155 (2003).
48. Wexler, H. Accurate identification of experimental pulmonary metastases. *J. Natl. Cancer Inst.* **36**, 641–645 (1966).
49. Chen, Y. T. *et al.* A testicular antigen aberrantly expressed in human cancers detected by autologous antibody screening. *Proc. Natl Acad. Sci. USA* **94**, 1914–1918 (1997).
50. Brichard, V. *et al.* The tyrosinase gene codes for an antigen recognized by autologous cytolytic T lymphocytes on HLA-A2 melanomas. *J. Exp. Med.* **178**, 489–495 (1993).
51. Gaugler, B. *et al.* Human gene MAGE-3 codes for an antigen recognized on a melanoma by autologous cytolytic T lymphocytes. *J. Exp. Med.* **179**, 921–930 (1994).
52. Simon, P. *et al.* Functional TCR retrieval from single antigen-specific human T cells reveals multiple novel epitopes. *Cancer Immunol. Res.* **2**, 1230–1244 (2014).



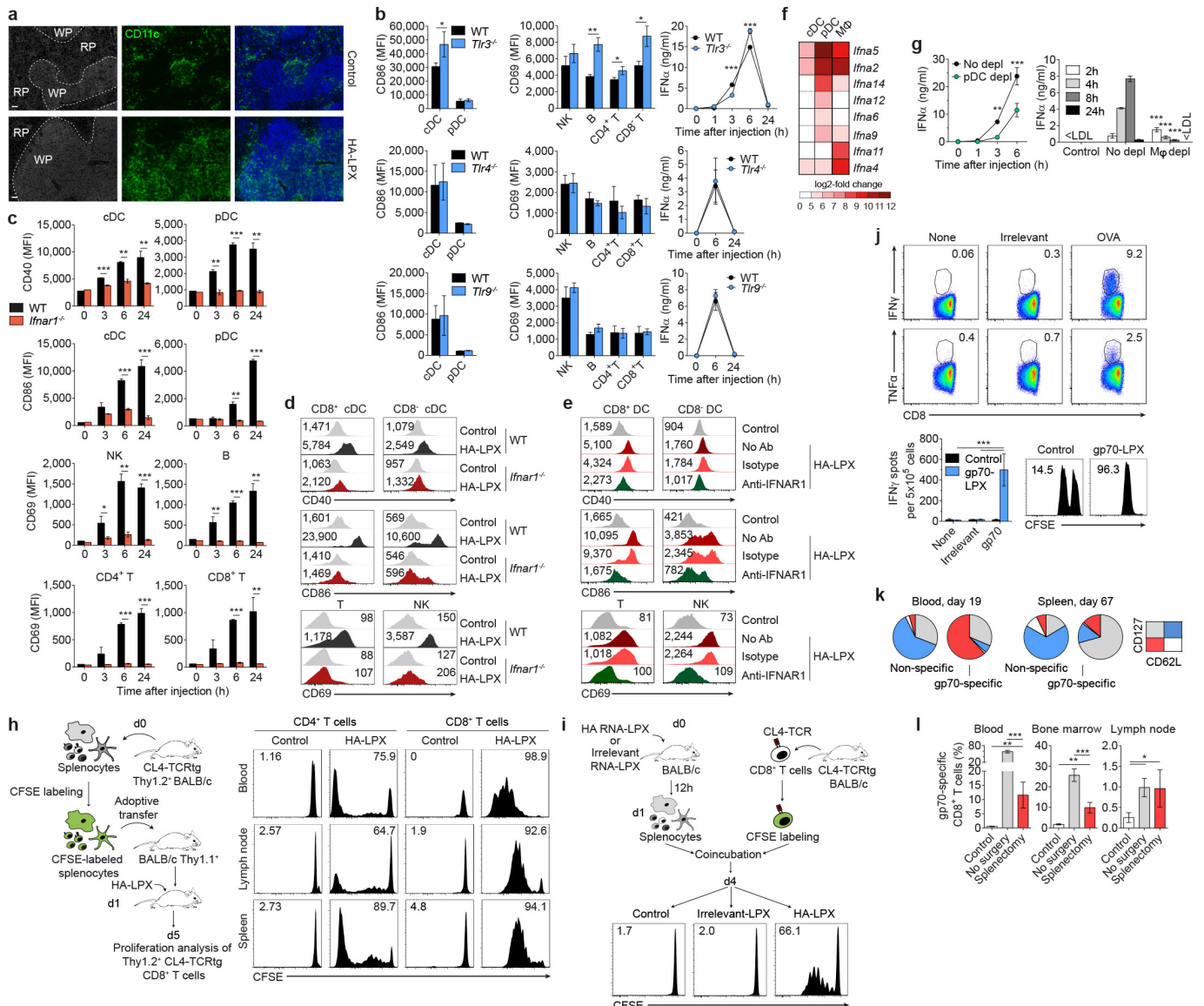
Extended Data Figure 1 | Physicochemical characteristics and biological activity of RNA-LPX constituted from different lipids at various charge ratios. **a**, Bioluminescence imaging of Luc expression in BALB/c mice 6 h after i.v. injection of different transfection reagents and controls: PBS ($n = 3$), 60 μ g Luc-RNA alone ($n = 3$), 25 μ g Luc-RNA complexed with TransMessenger (Qiagen) ($n = 3$), 5 μ g Luc-RNA complexed with Viromer RED (Lipocalyx) ($n = 3$). **b**, Cryo-TEM images of Luc-LPX constituted at a positive:negative ((+):(-)) charge ratio of 1.3:2 with DOTMA/DOPE liposomes. Scale bar, 100 nm. **c**, Fraction of uncomplexed RNA in Luc-LPX preparations constituted at different charge ratios with DOTMA/DOPE liposomes determined by capillary gel electrophoresis ($n = 2-7$). **d**, Particle size, polydispersity index (left) and zeta potential (right) ($n = 3$) of RNA-LPX constituted with Luc-RNA and differently constituted liposomes at various charge ratios. **e**, Bioluminescence imaging of BALB/c mice ($n = 3$) after i.v. injection

of Luc-LPX constituted with different liposomes at various charge ratios corresponding to **d**. Pie charts show relative contribution of each organ to total signal. **f**, Relative biodistribution of Luc expression in explanted organs of BALB/c mice ($n = 3$) after i.v. injection of Luc-LPX constituted with DOTMA/DOPE liposomes at a charge ratio of (+):(-) of 1.3:2 or Luc-RNA alone. **g**, Luc expression in human immature DCs transfected with 5 μ g Luc-LPX constituted freshly or stored after constitution for indicated time periods at 4°C (left) or room temperature (right). RNA-LPX tested in duplicates (stored) or quadruplets (fresh). Each bar represents triplicates. **h**, Particle size (upper left) and percentage of RNA integrity (upper right) of Luc-LPX ($n = 1$) incubated in 50% mouse serum for indicated time periods at 37°C. Bioluminescence imaging of Luc expression in BALB/c mice ($n = 5$) after i.v. injection of Luc-LPX preincubated in 50% mouse serum for 30 min at 37°C (lower left and right). NM, not measured. Error bars, median with interquartile range (**h**), otherwise mean \pm s.d.



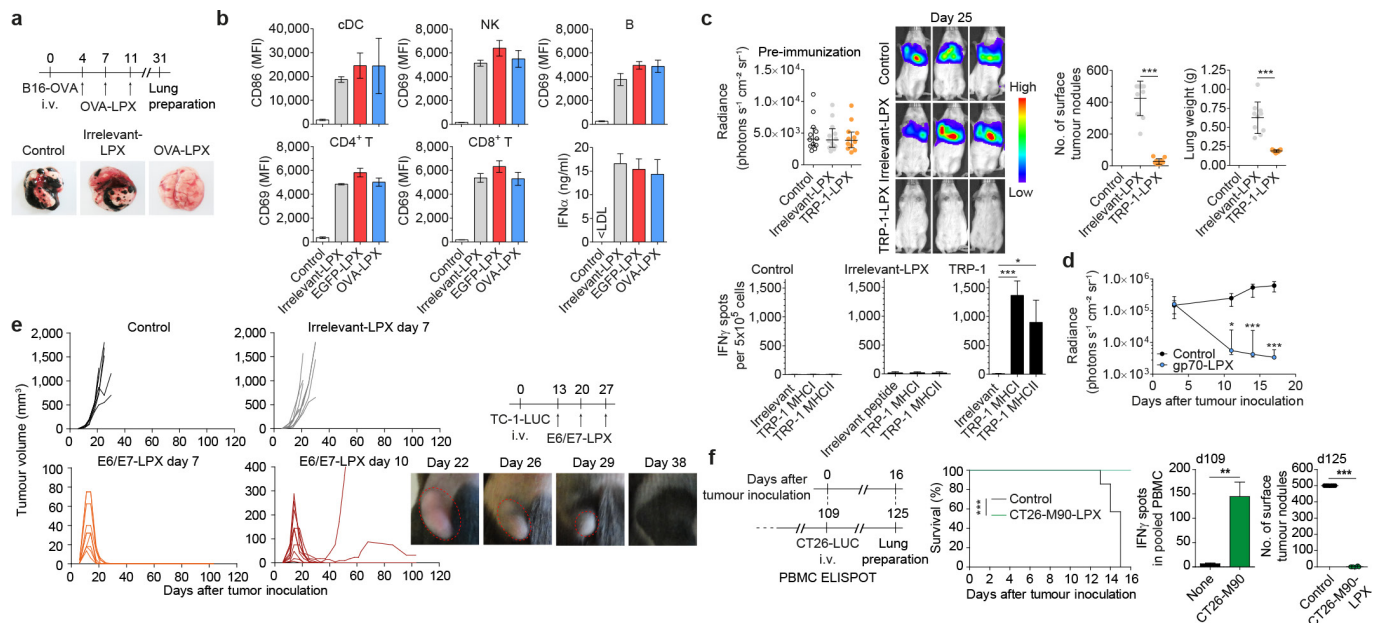
Extended Data Figure 2 | Biodistribution and cellular uptake mechanism of RNA-LPX vaccines. **a**, Uptake of Cy5-labelled RNA in splenic cell subsets of C57BL/6 mice ($n=3$) 1 h after i.v. injection of 40 μ g Cy5-labelled RNA-LPX. **b**, Localization of CD11c and Cy3 double-positive cells in the spleen of BALB/c mice ($n=2$) 1 h after i.v. injection of 40 μ g Cy3-labelled RNA-LPX. Nuclear staining in blue. Scale bar, 100 μ m. **c**, Half-life of RNA-LPX in circulation analysed by quantitative RT-qPCR in male and female C57BL/6 mice ($n=5$ per time-point) after injection of 60 μ g RNA-LPX constituted with NY-ESO-I, tyrosinase, MAGE-A3 and TPTE RNA (15 μ g each). **d**, Localization of Cy5⁺ (upper left) or Thy1.1⁺ cells (lower left) in spleen and liver of BALB/c mice ($n=5$) determined by microscopy or flow cytometry 1 h or 20 h after i.v. injection of 40 μ g Cy5-labelled RNA-LPX or 40 μ g 1-methyl-pseudouridine-modified Thy1.1-LPX, respectively. Nuclear staining in blue. Scale bar, 50 μ m (top), 20 μ m (bottom). Biodistribution of Cy5 signal in homogenized organs of BALB/c mice ($n=2$) (right). Note the signal in the liver is overestimated in this analysis owing to the strong signal in the gall bladder, probably reflecting biliary secreted free dye. **e**, Bioluminescence imaging of lymph nodes of BALB/c mice ($n=3$) 18 h after i.v. injection of 40 μ g 1-methyl-pseudouridine-modified Luc-LPX. ax, axillary; ing, inguinal; mand, mandibular. **f**, Flow cytometry analysis of Cy5 and Thy1.1 expression in CD11c⁺ cells in the bone marrow of C57BL/6 mice ($n=3$) 1 h or 20 h

after i.v. injection of 40 μ g Cy5-labelled RNA-LPX or 40 μ g 1-methyl-pseudouridine-modified Thy1.1-LPX, respectively. **g**, **h**, Localization of Cy3-labelled RNA in human immature DCs after co-transfection of 1.25 μ g Cy3-labelled RNA-LPX at a charge ratio of (+):(-) of 1.3:2 and 3:1 with dextran (**g**) or of 1.3:2 after staining for TLR7 or EEA1 (**h**). Nuclear staining in blue. Scale bar, 10 μ m. **i**, Visualization and quantification of inhibited uptake of positively as well as negatively charged Cy3-labelled RNA-LPX in human immature DCs pretreated with rottlerin or cytochalasin D. Scale bar, 10 μ m. **j**, Bioluminescence imaging of lymph nodes of BALB/c mice ($n=3$) injected intranodally with 10 μ M rottlerin in 10 μ l PBS 15 min before i.v. injection of 80 μ g Luc-LPX. **k**, Luminescence assay of whole blood enriched or not enriched with human immature DCs pretreated with poly I:C or not (control) before transfection with Luc-LPX at a charge ratio of 1.3:2. WB, whole blood. **l**, Poly-I:C-induced maturation determined by CD86 expression (left), bioluminescence imaging (middle) and eGFP expression in splenic cDC subsets (right) upon injection of BALB/c mice ($n=3$) with 50 μ g poly I:C i.p. 12 h before i.v. injection of 20 μ g Luc-LPX or 80 μ g eGFP-LPX, respectively. Significance was determined using unpaired two-tailed Student's *t*-test (**d**, lower left, **f**, **i**, middle) and one-way ANOVA and Tukey's multiple comparisons test (**i**-**k**, **l**, right). Error bars, mean \pm s.e.m. (**k**) or mean \pm s.d. otherwise.



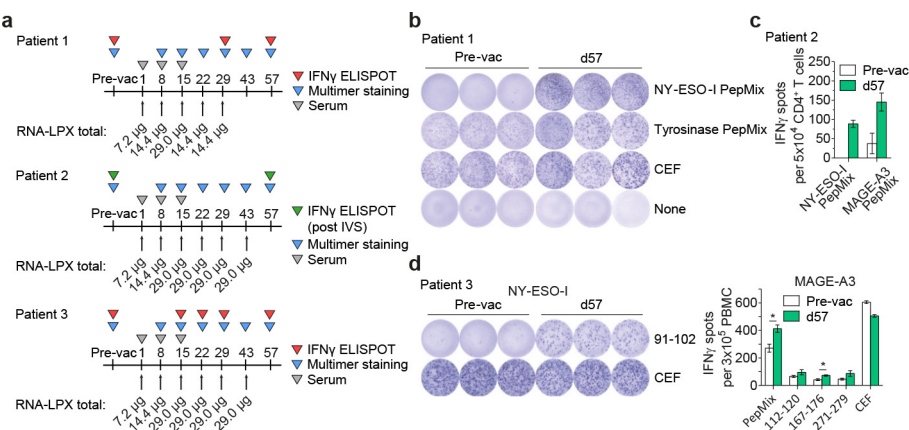
Extended Data Figure 3 | Systemic TLR7- and IFNAR-dependent activation of APCs and effector cells, IFNα production and strong expansion of fully functional antigen-specific T cells induced by RNA-LPX vaccines. **a**, Localization of splenic CD11c^{hi} cells at baseline (top) and 6 h after i.v. injection of 40 μg HA-LPX (bottom) into BALB/c mice (*n* = 2). Nuclear staining in blue. Scale bar, 100 μm. RP, red pulp; WP, white pulp. **b–e**, Activation marker expression in splenic cell subsets and kinetics of IFNα serum levels after i.v. injection of mice (*n* = 3 per time point) with HA-LPX in *Tlr3*^{-/-}, *Tlr4*^{-/-} and *Tlr9*^{-/-} mice (**b**), in *Ifnar1*^{-/-} mice (**c**, **d**), or in BALB/c mice treated with 100 μg anti-IFNAR1 antibody or isotype i.p. 1 h before i.v. injection of HA-LPX (**e**). Ab, antibody. **f**, mRNA levels of IFNα isoforms in sorted splenic APC subsets of C57BL/6 mice (*n* = 3) 1 h after i.v. injection of HA-LPX determined by qRT-PCR. Data expressed as log₂-fold change, as compared to control animals. **g**, IFNα serum levels after i.v. injection of HA-LPX in BDCA2-DTR mice (*n* = 3 per time point) depleted (depl) of pDCs (left) and in C57BL/6 mice (*n* = 3 per time point) depleted of macrophages (right). **h**, CFSE proliferation profile of HA-specific CD4⁺ T cells in lymphoid compartments of Thy1.1⁺ mice (*n* = 3) after adoptive transfer of HA-specific Thy1.2⁺ HA-TCR-transgenic CD4⁺ T cells and subsequent immunization with HA-LPX or control (untreated). Fraction of proliferated cells indicated. tg, transgenic. **i**, Priming of naive HA-specific CD8⁺ T cells *ex vivo*. BALB/c (*n* = 3) mice were immunized with 80 μg HA-LPX, irrelevant (eGFP)-LPX or NaCl (control). Splenocytes were prepared 12 h later and co-incubated with CFSE-labelled CL4-TCR-transgenic CD8⁺ T cells isolated using MACS magnetic microbeads coated with CD8 antibodies at an effector:target ratio of 1:6. Four days later, proliferation profiles were analysed by flow cytometry. Numbers indicate

the percentage of proliferated cells. **j**, Fraction of cytokine-secreting CD8⁺ T cells within CD8⁺ T cells in the spleen upon *de novo* priming in C57BL/6 mice (*n* = 5) immunized i.v. (day 0, 3, 8) with OVA-LPX after *in vitro* restimulation with no (none), irrelevant VSV (irrelevant) or OVA peptide and intracellular cytokine staining (top). Spleen *ex vivo* ELISpot assay upon *de novo* priming in BALB/c mice (*n* = 5) immunized i.v. (day 0, 3, 8) with gp70-LPX. Stimulation with no (none), irrelevant HA (irrelevant) or gp70 peptide (lower left). gp70-specific cytotoxicity *in vivo* (lower right). BALB/c mice (*n* = 5) were immunized i.v. (day 0, 3, 8) with 40 μg gp70-LPX. Naive splenocytes were labelled with 0.5 or 5 μM CFSE and pulsed with peptide (6 μg ml⁻¹) five days after the last immunization, and target cells (2 × 10⁷) were adoptively transferred into immunized recipients i.v. (irrelevant HA-loaded CFSE^{low}; gp70-loaded CFSE^{high} = 1:1). Recipient splenocytes were analysed by flow cytometry 18 h after transfer, and antigen-specific lysis was determined: specific lysis (%) = (1 – (percentage of cells pulsed with gp70/percentage of cells pulsed with HA)) × 100. **k**, Expression of memory markers CD127 and CD62L in gp70-specific, CD44⁺CD8⁺ T cells compared to non-specific CD8⁺ T cells in blood (day 19) and spleen (day 67) of BALB/c mice (*n* = 3) after priming with gp70-LPX (day 0, 7, 14). **l**, Fraction of gp70-specific CD8⁺ T cells within total CD8⁺ T cells in blood, bone marrow and lymph nodes determined by MHC class I tetramer staining after *de novo* priming of splenectomized BALB/c mice (*n* = 5–7) immunized with gp70-LPX (day 0, 7) or left untreated (control). Significance was determined using unpaired two-tailed Student's *t*-test (**b** left, **c**), two-way ANOVA and Bonferroni's multiple comparisons test (**b** right, **g**) and one-way ANOVA and Tukey's multiple comparisons test (**j**, **l**). Error bars, mean ± s.d.



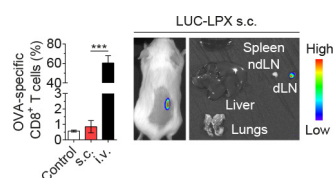
Extended Data Figure 4 | Potent antitumour immunity and rejection of advanced aggressively growing tumours in mice conferred by RNA-LPX vaccines. **a**, B16-OVA melanoma load in lungs of C57BL/6 mice ($n = 8$) immunized i.v. (days 4, 7, 11) with OVA-LPX or irrelevant (eGFP)-LPX. **b**, Expression of activation markers measured 24 h after i.v. injection of 40 μ g irrelevant (empty vector)-LPX, eGFP-LPX or OVA-LPX by flow cytometry in splenic immune cell subsets ($n = 3$) and IFN α serum levels ($n = 3$) 6 h after injection in C57BL/6 mice. **c**, Bioluminescence signal of tumours in different groups before immunization and on day 25 (upper left), tumour load and lung weights (upper right) and TRP-1-specific CD8 $^{+}$ and CD4 $^{+}$ T-cell responses in spleens of control (untreated), irrelevant (empty vector)-LPX and TRP-1-LPX-immunized B6 albino mice ($n = 12$) on day 25 detected by ELISPOT assay (bottom),

depicted in Fig. 3b. **d**, Bioluminescence imaging of CT26-Luc carcinoma in BALB/c mice ($n = 4-7$) depicted in Fig. 3c (left). **e**, TC-1-Luc tumour growth in C57BL/6 mice ($n = 10$) (left), depicted in Fig. 3d, and remission of established advanced TC-1-Luc tumours in C57BL/6 mice ($n = 10$) immunized i.v. with 40 μ g E6/E7-LPX (day 13, 20, 27) (right). **f**, Survival of BALB/c mice rechallenged with CT26-Luc colon carcinoma cells on day 109, depicted in Fig. 3e. Significance was determined using one-way ANOVA and Tukey's multiple comparisons test (c), two-way ANOVA and Bonferroni's multiple comparisons test (d), paired two-tailed Student's *t*-test (f, right), unpaired two-tailed Student's *t*-test (f, far right), and log-rank test (f, left). Error bars, median with interquartile range (d), mean \pm s.d. otherwise.



Extended Data Figure 5 | Clinical application of RNA-LPX vaccines and *de novo* priming and amplification of patient T-cell responses against encoded vaccine antigens. **a**, Vaccination scheme and monitoring for patients 1–3. **b**, Antigen-specific T-cell responses against NY-ESO-1 and tyrosinase determined by restimulation with overlapping peptide mixtures in IFN γ ELISPOT for patient 1. **c**, Antigen-specific T-cell responses against NY-ESO-1 and MAGE-A3, determined by post-IVS

IFN γ ELISPOT assay at indicated days for patient 2. Values are corrected for background (no peptide). **d**, Antigen-specific T-cell responses against NY-ESO-I and MAGE-A3, determined by *ex vivo* IFN γ ELISPOT assay at indicated days for patient 3. Numbers in ELISPOT data indicate the amino acid position of each epitope. Significance was determined using unpaired two-tailed Student's *t*-test. Error bars, mean \pm s.e.m.



Extended Data Figure 6 | Comparison of i.v. and s.c. routes for RNA-LPX administration in the context of T-cell priming and biodistribution of RNA-LPX upon s.c. administration. Fraction of OVA-specific CD8⁺ T cells within CD8⁺ T cells on day 13 in blood after *de novo* priming of C57BL/6 mice ($n = 5$) immunized i.v. with OVA-LPX (day 0, 3, 8) (left). Biodistribution of Luc expression 24 h after s.c. injection of Luc-LPX in BALB/c mice ($n = 3$) (right). Signal can only be observed at the injection site and the draining lymph node. Significance was determined using one-way ANOVA and Tukey's multiple comparisons test. Error bars, mean \pm s.d.

Extended Data Table 1 | Findings of non-GLP pilot pharmacokinetics and pharmacodynamics study in cynomolgus monkeys

Category	Findings
Local tolerance	No test item-related reactions at daily inspections of the infusion sites.
Mortality	No mortality occurred during the course of the study.
Clinical signs	No signs of systemic toxicity were noted for any of the treated animals.
Body weight and body weight gain	No test item-related changes.
Food and drinking water consumption	No test item-related changes.
Electrocardiography	No test item-related changes. In more detail, the quantitative evaluation of the ECG obtained on test days 15/16 did not reveal any test item-related influence on the heart rate, the RR interval, the QRS interval, the QT interval, the QTc values and the PQ interval for any of the animals treated in comparison to the control animals.
Troponin-I	No test item-related changes.
Circulatory functions	Normal levels of peripheral arterial systolic, diastolic and mean blood pressure reported for all animals.
Hematology	No influence on haematological parameters was noted for the liposome-treated group. A transient decrease of lymphocytes and a transient increase of neutrophils was found as test item-related findings in a dose-dependent manner, but were back to normal levels within 48 h.
Clinical biochemistry	No test item-related influence was rated on the biochemical parameters for the animals; one animal showed high LDH and CK values considered to be stress-related.
Cytokine	IL-6 showed a dose-dependent and test item-related induction. C_{\max} levels were reached at 30 min after completion of the treatment, and were back to predose levels after 24 h. In 2 animals also IFN α was detected.
Complement	No test item-related changes of complement factor 3a were noted.

ECG, electrocardiography. LDH, Lactate dehydrogenase. CK, Creatine kinase.

Aberrant *PD-L1* expression through 3'-UTR disruption in multiple cancers

Keisuke Kataoka^{1*}, Yuichi Shiraishi^{2*}, Yohei Takeda^{3*}, Seiji Sakata⁴, Misako Matsumoto³, Seiji Nagano⁵, Takuya Maeda⁵, Yasunobu Nagata¹, Akira Kitanaka⁶, Seiya Mizuno⁷, Hiroko Tanaka², Kenichi Chiba², Satoshi Ito², Yosaku Watatani¹, Nobuyuki Kakiuchi¹, Hiromichi Suzuki¹, Tetsuichi Yoshizato¹, Kenichi Yoshida¹, Masashi Sanada⁸, Hidehiro Itonaga⁹, Yoshitaka Imaizumi¹⁰, Yasushi Totoki¹¹, Wataru Munakata¹², Hiromi Nakamura¹¹, Natsuko Hama¹¹, Kotaro Shide⁶, Yoko Kubuki⁶, Tomonori Hidaka⁶, Takuro Kameda⁶, Kyoko Masuda⁵, Nagahiro Minato¹³, Koichi Kashiwase¹⁴, Koji Izutsu¹⁵, Akifumi Takaori-Kondo¹⁶, Yasushi Miyazaki¹⁰, Satoru Takahashi⁷, Tatsuhiro Shibata^{11,17}, Hiroshi Kawamoto⁵, Yoshiki Akatsuka^{18,19}, Kazuya Shimoda⁶, Kengo Takeuchi⁴, Tsukasa Seya³, Satoru Miyano² & Seishi Ogawa¹

Successful treatment of many patients with advanced cancer using antibodies against programmed cell death 1 (PD-1; also known as PDCD1) and its ligand (PD-L1; also known as CD274) has highlighted the critical importance of PD-1/PD-L1-mediated immune escape in cancer development^{1–6}. However, the genetic basis for the immune escape has not been fully elucidated, with the exception of elevated *PD-L1* expression by gene amplification and utilization of an ectopic promoter by translocation, as reported in Hodgkin and other B-cell lymphomas, as well as stomach adenocarcinoma^{6–10}. Here we show a unique genetic mechanism of immune escape caused by structural variations (SVs) commonly disrupting the 3' region of the *PD-L1* gene. Widely affecting multiple common human cancer types, including adult T-cell leukaemia/lymphoma (27%), diffuse large B-cell lymphoma (8%), and stomach adenocarcinoma (2%), these SVs invariably lead to a marked elevation of aberrant *PD-L1* transcripts that are stabilized by truncation of the 3'-untranslated region (UTR). Disruption of the *Pd-l1* 3'-UTR in mice enables immune evasion of EG7-OVA tumour cells with elevated *Pd-l1* expression *in vivo*, which is effectively inhibited by Pd-1/Pd-l1 blockade, supporting the role of relevant SVs in clonal selection through immune evasion. Our findings not only unmask a novel regulatory mechanism of *PD-L1* expression, but also suggest that *PD-L1* 3'-UTR disruption could serve as a genetic marker to identify cancers that actively evade anti-tumour immunity through PD-L1 overexpression.

Structural variations, including translocations, inversions, tandem duplications, and deletions, are widely observed across cancer genomes^{11,12}. Of particular interest are those involving non-coding sequences recently reported for activation of several oncogenic drivers, including *GFI1* (ref. 13) and *TERT*¹⁴, which have been less intensively investigated to date owing to the high-level complexity of SVs in cancer genomes^{11,12}. To clarify novel oncogenic mechanisms through such SVs, we recently developed a robust platform for sensitive capture of a wide spectrum of SVs based on whole-genome sequencing (WGS) (detailed in Methods), which was initially

applied to a set of WGS data from 49 cases of adult T-cell leukaemia/lymphoma (ATL), a retrovirus-associated aggressive peripheral T-cell neoplasm¹⁵. RNA sequencing (RNA-seq) data were also available for 43 samples (Extended Data Fig. 1a and Supplementary Table 1).

Genome-wide mapping of SV-associated breakpoints revealed a number of recurrent breakpoint cluster regions. Among these, the most prominent corresponded to breakpoints at chromosome 9p24.1 found in 13 (26.5%) samples, which were narrowly clustered in a 3.1 kilobase (kb) region within the 3' region of the *PD-L1* locus (Extended Data Fig. 1b and Supplementary Table 2). Depending on samples, a variety of SV types were observed, including a large deletion ($n = 1$), tandem duplications ($n = 4$), inversions ($n = 4$), and translocations ($n = 4$) (Fig. 1a and Extended Data Fig. 1c). However, irrespective of underlying SV types, an aberrant *PD-L1* allele was generated in all cases, where the authentic 3' exons were replaced by an ectopic sequence derived from the rearranged loci ($n = 12$) or a short 327 base pair (bp) sequence within the last exon was inverted (ATL017). It was apparent that these SVs were invariably associated with markedly elevated expression of *PD-L1*, except for a single case (ATL068) with very low tumour content (Fig. 1b). As expected from the underlying SV structure, all overexpressed *PD-L1* transcripts underwent structural alterations, which, on the basis of RNA-seq, fused varying lengths of the 5' region of the *PD-L1* sequence to a short tract of intronic or intergenic sequence derived from exogenous loci containing a putative polyadenylation (poly-A) signal¹⁶ ($n = 10$), or caused a premature termination within the authentic 3'-UTR using an alternative poly-A signal (ATL033 and ATL050) (Fig. 1c and Extended Data Figs 1d and 2a–d). In the remaining case (ATL017), unexpected cleavage of *PD-L1* transcripts occurred within the inverted 327 bp sequence of the 3'-UTR using a newly created poly-A signal sequence (Extended Data Fig. 2e). None of these aberrant *PD-L1* transcripts retained the intact 3'-UTR and therefore, the scarcity of 3'-UTR reads in RNA-seq in the majority of SV(+) samples indicated the predominance of the aberrant versus intact *PD-L1* transcripts, which was reflected by high relative

¹Department of Pathology and Tumor Biology, Graduate School of Medicine, Kyoto University, Kyoto 606-8501, Japan. ²Laboratory of DNA Information Analysis, Human Genome Center, Institute of Medical Science, The University of Tokyo, Tokyo 108-8639, Japan. ³Department of Microbiology and Immunology, Graduate School of Medicine, Hokkaido University, Sapporo 060-8638, Japan. ⁴Pathology Project for Molecular Targets, Cancer Institute, Japanese Foundation for Cancer Research, Tokyo 135-8550, Japan. ⁵Department of Immunology, Institute for Frontier Medical Science, Kyoto University, Kyoto 606-8507, Japan. ⁶Department of Gastroenterology and Hematology, Faculty of Medicine, University of Miyazaki, Miyazaki 889-1692, Japan. ⁷Laboratory Animal Resource Center and Faculty of Medicine, University of Tsukuba, Tsukuba 305-8575, Japan. ⁸Department of Advanced Diagnosis, Clinical Research Center, Nagoya Medical Center, Nagoya 460-0001, Japan. ⁹Department of Hematology, Sasebo City General Hospital, Sasebo 857-8511, Japan. ¹⁰Department of Hematology, Atomic Bomb Disease and Hibakusha Medicine Unit, Atomic Bomb Disease Institute, Nagasaki University, Nagasaki 852-8523, Japan. ¹¹Division of Cancer Genomics, National Cancer Center Research Institute, Tokyo 104-0045, Japan. ¹²Department of Hematology, National Cancer Center Hospital, Tokyo 104-0045, Japan. ¹³Department of Immunology and Cell Biology, Graduate School of Medicine, Kyoto University, Kyoto 606-8501, Japan. ¹⁴Department of HLA Laboratory, Japanese Red Cross Kanto-Koshinetsu Block Blood Center, Tokyo 135-8639, Japan. ¹⁵Department of Hematology, Toranomon Hospital, Tokyo 105-8470, Japan. ¹⁶Department of Hematology and Oncology, Graduate School of Medicine, Kyoto University, Kyoto 606-8501, Japan. ¹⁷Laboratory of Molecular Medicine, Human Genome Center, Institute of Medical Science, The University of Tokyo, Tokyo 108-8639, Japan. ¹⁸Department of Hematology, Fujita Health University School of Medicine, Toyoake 470-1192, Japan. ¹⁹Division of Immunology, Aichi Cancer Center Research Institute, Nagoya 464-8681, Japan.

*These authors contributed equally to this work.

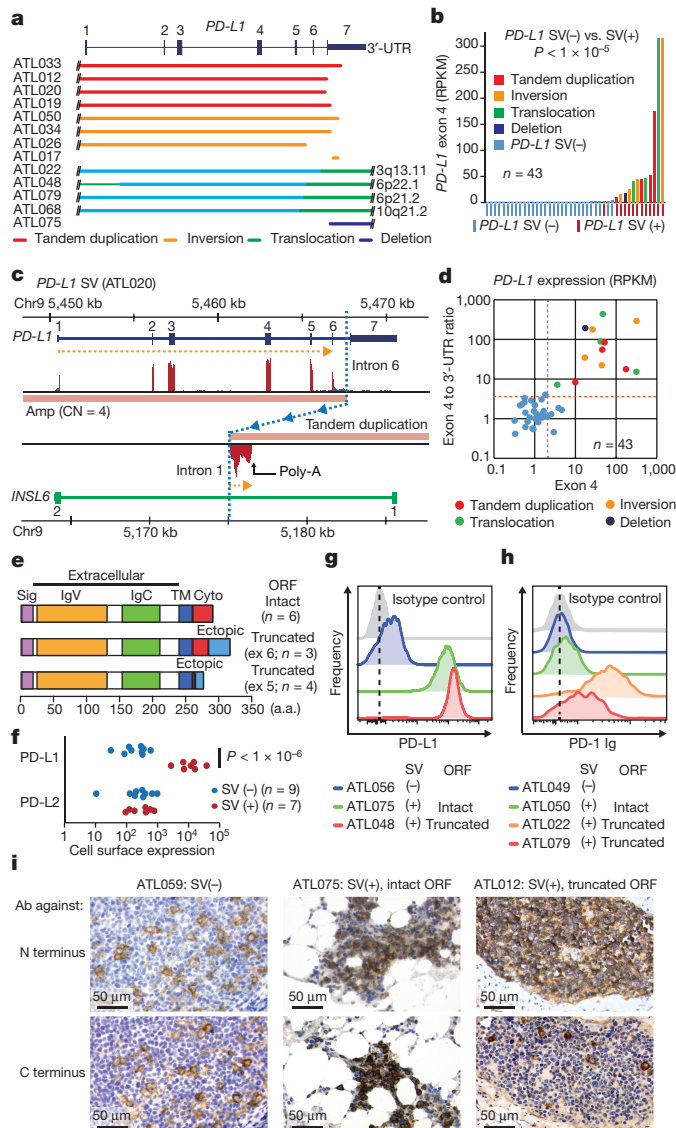


Figure 1 | Aberrant expression of PD-L1 in ATL samples with SVs involving *PD-L1* 3'-UTR. **a**, Different types of SVs commonly affecting 3' region of *PD-L1* are shown by indicated colours. **b**, *PD-L1* exon 4 expression (RPKM) in 43 ATL samples, coloured by *PD-L1* SV status. Welch's *t*-test. **c**, Genomic structure of the rearranged *PD-L1* locus and transcription (orange dotted lines) in a case (ATL020) with 3'-UTR-truncated *PD-L1* transcripts, in which *PD-L1* ORF is terminated before exon 7 and merged into an *INSL6* intronic sequence. Breakpoints (blue dotted lines) are shown with accompanying copy number (CN) alterations. Amp, amplification. **d**, *PD-L1* exon 4 expression (RPKM) and its relative value to that of 3'-UTR (exon 4 to 3'-UTR ratio) for 43 ATL cases. SV(+) cases are indicated by colours corresponding to each SV type. **e**, Predicted structures of wild-type and two representative C-terminal-truncated *PD-L1* fusion proteins. Sig, signal peptide; Ig, immunoglobulin; TM, transmembrane; Cyto, cytoplasmic. **f**, Summary of *PD-L1* and *PD-L2* expressions in ATL cells with ($n = 7$) or without *PD-L1* SVs ($n = 9$). Student's *t*-test. **g**, **h**, Representative plots for *PD-L1* surface expression (**g**) and *PD-1* Ig binding (**h**) for ATL cells with ($n = 7$) or without relevant SVs ($n = 9$). **i**, IHC of *PD-L1* SV(+) cases harbouring intact or truncated ORFs, compared with SV(-) cases using antibodies (Abs) specifically detecting N-terminal and C-terminal domains of *PD-L1*. Scattered stained cells are macrophages. See Extended Data Figs 1–4.

expression of exon 3 or 4 over 3'-UTR (>3.5) in SV(+) samples (Fig. 1d and Extended Data Fig. 3).

The entire *PD-L1* open reading frame (ORF) was completely preserved in six SV(+) cases, whereas in the remaining cases, the ORF

was interrupted by a rearrangement within intron 5 ($n = 4$) or 6 ($n = 3$), causing a premature truncation of the protein (Fig. 1e and Extended Data Fig. 4a). All of the predicted proteins from the aberrant transcripts retained the extracellular receptor-binding and transmembrane domains of *PD-L1* and were thought to be expressed on the cell surface with preserved receptor-binding capacity, which was confirmed for representative *PD-L1* variants derived from SV(+) samples (Extended Data Fig. 4b–d). Cell surface expression of different *PD-L1* proteins was also demonstrated in SV(+) primary ATL samples, which showed prominent overexpression of the proteins compared to SV(-) samples (Fig. 1f,g). By contrast, expression of *PD-L2* (also known as *PRCD1LG2*), another *PD-1* ligand encoded in the 3' vicinity of the *PD-L1* locus, remained the same between SV(+) and SV(-) samples (Fig. 1f and Extended Data Fig. 1c), indicating that these SVs did not affect *PD-L2* expression and also that increased cell surface binding of *PD-1* in these SV(+) samples (Fig. 1h) could be explained by overexpressed *PD-L1* proteins. Elevated expression of *PD-L1* proteins in SV(+) samples was further evidenced by immunohistochemistry (IHC) and western blotting (Fig. 1i and Extended Data Fig. 4e). Note that in SV(+) samples with a truncated ORF, *PD-L1* expression was detected only with an antibody directed against the N-terminal, but not the C-terminal, domain.

The highly recurrent nature of SVs converging on *PD-L1* 3'-UTR and their common consequence of markedly elevated expression of aberrant but apparently functional *PD-L1* proteins in ATL provide strong evidence that SV(+) ATL cells are clonally selected, most likely through escaping immune surveillance. Thus, we hypothesized that a similar mechanism of clonal selection and immune evasion might also operate in other, more prevalent human cancers. To investigate this, we next interrogated *PD-L1* 3'-UTR-involving SVs among 10,210 cancer samples from 33 tumour panels, for which RNA-seq data were available from the Cancer Genome Atlas (TCGA). Aberrant 3'-UTR-truncated *PD-L1* transcripts were screened by detecting *PD-L1*-containing gene fusions and/or a high exon 4 to 3'-UTR ratio (>3.5), together with increased absolute *PD-L1* exon 4 expression (reads per kb of transcript per million mapped reads (RPKM) >2.0) (Extended Data Fig. 5 and Methods). We identified 31 cases expressing 3'-UTR-truncated *PD-L1* transcripts (Fig. 2a, b, Extended Data Figs 5, 6, and Supplementary Table 3). In the majority, underlying SVs implicated in the abnormal transcripts were uniquely determined or suggested on the basis of whole-genome/exome sequencing and/or SNP array-karyotyping data, which were largely similar to those found in ATL cases (Extended Data Fig. 7a). Abnormal transcripts were most frequently seen in diffuse large B-cell lymphoma (DLBC) (4 out of 48 cases) and stomach adenocarcinoma (STAD) (9 out of 415 cases) (Fig. 2b). Three of the nine STAD cases were positive for Epstein-Barr virus (EBV) expression. Expression of the aberrant *PD-L1* transcripts was markedly elevated in all cases, of which 12 exhibited the highest expression levels within the corresponding 9 tumour types (Fig. 2b). *PD-L1* copy number was reported to correlate with *PD-L1* expression in Hodgkin lymphoma^{6,7} and the correlation was also observed for DLBC, STAD, and ATL in the present study (Fig. 2c). However, irrespective of the copy number status of the *PD-L1* gene, in the TCGA panel as well as in our ATL cases, *PD-L1* 3'-UTR disruption was significantly and independently associated with elevated *PD-L1* expression. *JAK2* is another potential target of SVs at 9p24.1 (refs 7, 10), but its expression was not significantly affected by SVs, although it did correlate with elevated genomic copy number frequently accompanied by these SVs (Extended Data Fig. 7b).

To investigate the anti-tumour response in SV(+) samples, we assessed the cytolytic activity score (a geometric mean of *GZMA* and *PRF1* expression) within the TCGA cohort, which was shown to be a reliable marker of cytotoxic T-cell infiltration and anti-tumour immune activity¹⁷. Probably reflecting adaptive response to anti-tumour immunity, the cytolytic activity significantly correlated with *PD-L1* expression within each tumour type ($P < 1 \times 10^{-15}$, generalized linear model (GLM)), where most of the *PD-L1* SV(+) samples

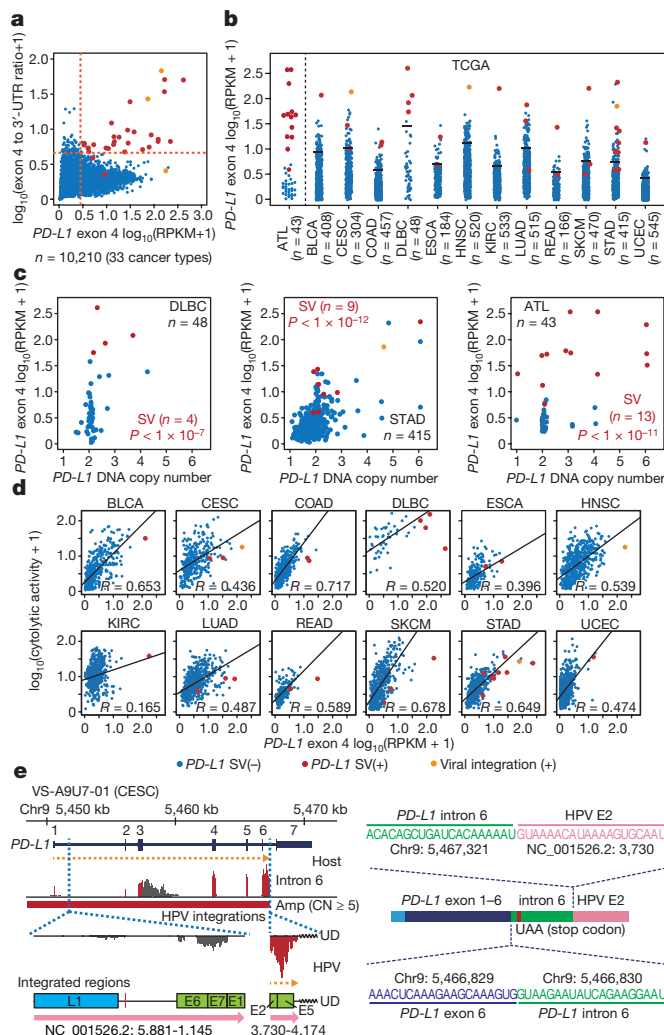


Figure 2 | *PD-L1* SVs associated with overexpression of aberrant *PD-L1* transcripts in multiple cancers. **a**, Exon 4 to 3'-UTR ratio versus *PD-L1* expression (exon 4) for 10,210 TCGA samples from 33 tumour types. **b**, *PD-L1* expression in each TCGA cancer type containing *PD-L1* SV cases. Each bar represents the 10th percentile. **c**, Effect of genomic copy number and SV on *PD-L1* transcript level for 48 DLBL (left), 415 STAD (middle), and 43 ATL (right) samples. P values for SV in GLM are provided. **d**, Cytolytic activity score (geometric mean of *GZMA* and *PRF1* expressions) versus *PD-L1* expression for each TCGA cancer type. Each black line represents a regression line with Pearson's correlation coefficient (R) for SV(−) cases. SV(+) samples (red) and those with virus integration around the *PD-L1* locus (orange) are indicated. BLCA, bladder urothelial carcinoma; COAD, colon adenocarcinoma; ESCA, oesophageal squamous cell carcinoma; KIRC, kidney renal clear cell carcinoma; LUAD, lung adenocarcinoma; READ, rectal adenocarcinoma; SKCM, skin cutaneous melanoma; UCEC, uterine corpus endometrioid carcinoma. **e**, Genomic structure of the rearranged *PD-L1* locus and transcription (orange dotted lines) in a case of CESC showing HPV16 integrations within the *PD-L1* gene (VS-A9U7-01) (left). Structure of the newly generated fusion transcript and breakpoint sequences are also shown (right). UD, undetermined sequence. See Extended Data Figs 5–7.

retained a high degree of cytotytic activity (Fig. 2d), supporting the hypothesis that *PD-L1* SV(+) cells are clonally selected in the presence of anti-tumour immunity through constitutively upregulating *PD-L1* expression. It is also interesting to note that compared to SV(−) samples with similar levels of *PD-L1* expression, SV(+) samples exhibited a significantly decreased cytotytic activity ($P < 1 \times 10^{-10}$, GLM), suggesting that there was an attenuation of anti-tumour immune response in SV(+) samples.

Viral infection is a major cause of several human cancers. Intriguing in this regard were those TCGA cases in which viral integration was implicated in the aberrant *PD-L1* transcription; in a case of cervical squamous cell carcinoma (CESC, VS-A9U7-01), human papillomavirus (HPV) 16 (ref. 18) was integrated into the *PD-L1* locus, causing an amplification of the virally interrupted *PD-L1* allele and transcription of a truncated *PD-L1* mRNA extending into HPV E2 and E5 genes (Fig. 2e). Motivated by this finding, we searched for viral integrations into or around the *PD-L1* locus in the TCGA panel (see Methods) and identified a similar defect caused by an HPV16 integration in a further case (CV-5443-01) of head and neck squamous cell carcinoma (HNSC), which had previously been implicated in possible alternative *PD-L1* transcripts¹⁹ but had escaped our initial screen relying on the exon 4 to 3'-UTR expression ratio, despite remarkably high *PD-L1* expression (Fig. 2b and Extended Data Fig. 7c). In the remaining case of STAD (FP-7998-01), a large 2.3 Mb segment containing an integrated EBV genome was amplified, where one of the breakpoints resided within the *PD-L1* 3'-UTR (Extended Data Fig. 7c). In cases of virally mediated cancers, viral integration is thought to have helped the infected cells escape not merely from anti-viral immunity during an early phase of infection, but also from later anti-cancer immunity.

On the basis of these findings, we reasoned that loss of 3'-UTR sequence could be the common mechanism of the markedly elevated *PD-L1* expression associated with these SVs. To test this hypothesis, we introduced large deletions/inversions involving almost the entire sequence of the *PD-L1* 3'-UTR in a variety of human and mouse cell lines using the CRISPR (clustered regularly interspaced short palindromic repeats)-Cas9 system²⁰, and evaluated their effects on *PD-L1* expression (Fig. 3a and Extended Data Fig. 8a). Only when cells were transfected with both, but not either, of the forward (F1 or F2) and reverse (R) single guide (sg) RNA vectors with Cas9, we were able to reproducibly obtain a small but discrete fraction of cells showing significantly elevated cell surface *PD-L1* expression, compared to parental or mock (Cas9 alone)-transfected cells (Fig. 3b, c and Extended Data Fig. 8b). The cells were purified and we confirmed the presence of intended deletions or inversions (Fig. 3d, e and Extended Data Figs 8c–e and 9a–d) and significantly elevated expression of corresponding 3'-UTR-truncated *PD-L1* transcripts and proteins (Fig. 3f–i and Extended Data Figs 8f, g and 9e). Further assessment of *PD-L1* transcripts using actinomycin-D-induced inhibition of *de novo* transcription demonstrated a delayed clearance of 3'-UTR-truncated, compared to wild-type *PD-L1* mRNA (Fig. 3j), suggesting a negative regulatory role of *PD-L1* 3'-UTR in mRNA stability. The effect of *PD-L1* 3'-UTR truncation on the upregulation of *PD-L1* expression was shown to be much greater than that of interferon- γ (IFN- γ), a major inducer of *PD-L1* expression⁴, suggesting a predominant regulation of *PD-L1* expression via the 3'-UTR sequence. Interestingly, however, when *PD-L1* 3'-UTR-disrupted cells were stimulated with IFN- γ , *PD-L1* expression was synergistically elevated (Extended Data Fig. 9f). Thus, 3'-UTR-disrupted cells can more effectively upregulate *PD-L1* expression in the presence of IFN- γ -secreting T cells to escape anti-tumour immunity.

Finally, we evaluated the biological consequence of loss of *PD-L1* 3'-UTR. When co-cultured with PD-1-expressing T cells (Jurkat), PC-9 cells with disrupted *PD-L1* 3'-UTR (and therefore with elevated *PD-L1* expression) markedly enhanced apoptosis of Jurkat cells compared to mock-treated PC-9 cells with intact *PD-L1* 3'-UTR, which was blocked by anti-PD-L1 antibody (Fig. 4a). Next, to investigate the effect of disruption of *Pd-l1* 3'-UTR on anti-tumour immunity, we adopted a tumour regression model, in which syngeneic C57BL/6 mice were subcutaneously inoculated with EG7-OVA cells with or without intact *Pd-l1* 3'-UTR, and anti-tumour (OVA) immunity was induced by immunostimulatory RNA polyinosinic-polycytidylic acid (poly(I:C))²¹ (Extended Data Fig. 10a). As previously demonstrated, in mice inoculated with EG7-OVA cells with intact *Pd-l1* 3'-UTR, peritumoral poly(I:C) treatment induced a marked tumour regression

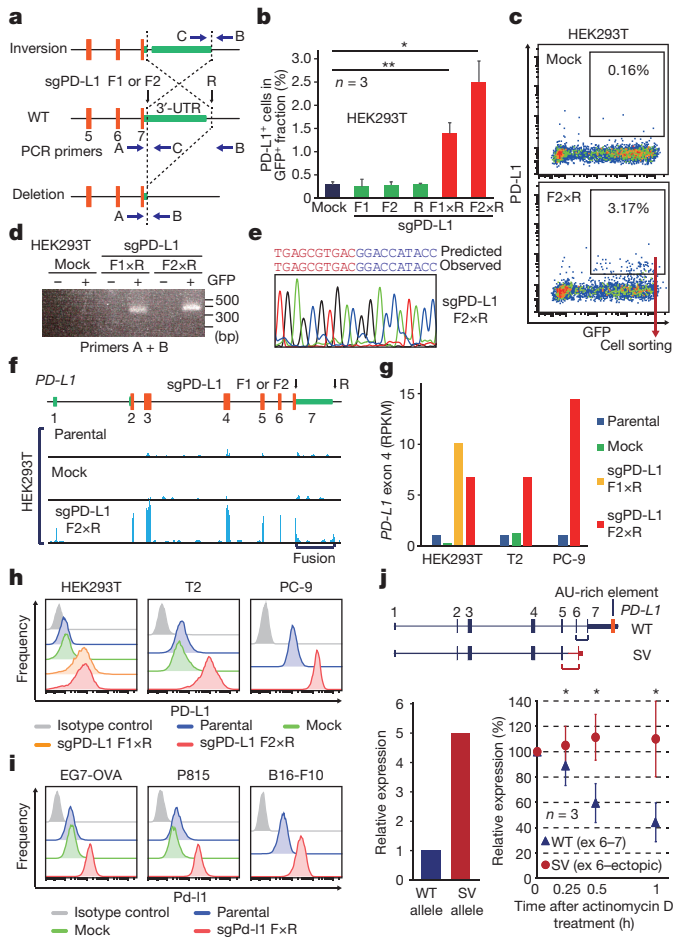


Figure 3 | 3'-UTR disruption by CRISPR-Cas9 induces PD-L1 overexpression. **a**, Positions of targeting sgRNAs and detection primers used for CRISPR-Cas9-mediated deletions and inversions of *PD-L1* 3'-UTR. WT, wild-type. **b**, Frequency of PD-L1⁺ cells in green fluorescent protein (GFP)⁺ fraction by flow cytometry in HEK293T cells transfected with Cas9 and no, single, or pairwise sgRNAs ($n = 3$). $*P < 0.05$, $**P < 0.005$, Welch's *t*-test. **c**, Sorting strategy of PD-L1⁺GFP⁺ cells. **d**, **e**, Validation of *PD-L1* 3'-UTR deletions by PCR (**d**) and Sanger sequencing (**e**) in sorted HEK293T cells targeted by indicated sgRNAs. **f**, RNA-seq reads for HEK293T cells transfected with indicated vectors. **g–i**, Expression of *PD-L1* transcripts (exon 4 RPKM) (**g**) and cell surface protein (**h**, **i**) in human (**g**, **h**) and mouse (**i**) cell lines transfected with indicated vectors. Representative of three independent experiments (**h**, **i**). **j**, Ratio of wild-type to truncated *PD-L1* mRNA in steady state (left) and their expression levels relative to 18S RNA (right) in ST-1 cells after transcriptional inhibition with 10 $\mu\text{g ml}^{-1}$ actinomycin D. $*P < 0.05$, Student's *t*-test. Data represent mean \pm s.d. See Extended Data Figs 8, 9.

with enhanced infiltration of CD8⁺ T cells into the tumour microenvironment (Fig. 4b, c and Extended Data Fig. 10b, c). By contrast, almost no tumour regression was observed in mice inoculated with 3'-UTR-disrupted cells with an attenuated CD8⁺ T-cell reaction, which was in accordance with *PD-L1* SV(+) human cancers (Fig. 2d), suggesting that *Pd-l1* 3'-UTR-disrupted cells can escape anti-tumour immunity mediated by cytotoxic T lymphocytes through activation of Pd-1/Pd-l1 signalling. In fact, blockade of the signalling with anti-Pd-l1 antibody restored CD8⁺ cytotoxic T lymphocyte induction and tumour regression in the mice carrying *Pd-l1* 3'-UTR-disrupted cells (Fig. 4d–f and Extended Data Fig. 10d). These results not only suggest that tumour-intrinsic PD-L1 overexpression due to 3'-UTR disruption promotes immune evasion and tumour cell growth, but also indicate that *PD-L1* 3'-UTR-involving SVs could be potentially actionable therapeutic targets.

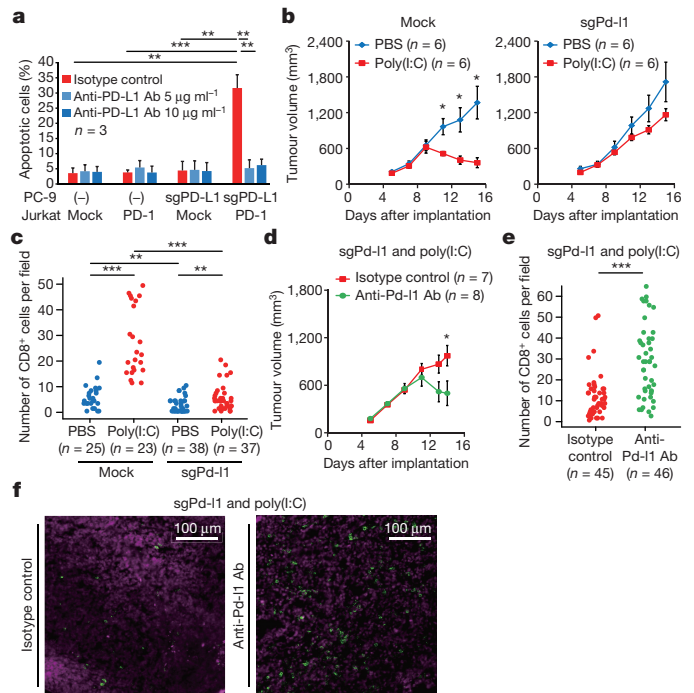


Figure 4 | PD-L1 activation by 3'-UTR loss promotes tumour growth and immune escape. **a**, Frequency (mean \pm s.d.) of mock- or *PD-L1*-transfected Jurkat T cells undergoing apoptosis after co-incubation with parental or sgPD-L1-transfected PC-9 cells in the presence of isotype control or anti-Pd-L1 antibody ($n = 3$). **b–f**, Mock- or sgPD-L1-transfected EG7-OVA tumours injected with PBS (blue) or poly(I:C) (red) (**b**, **c**), or poly(I:C)-treated, sgPD-L1-transfected EG7-OVA tumours administered with isotype control (red) or anti-Pd-l1 antibody (green) (**d–f**) were analysed for kinetics of tumour volume (**b**, **d**, $n = 6–8$ per group; mean \pm s.e.m.), and number of tumour-infiltrating CD8⁺ T cells per field by immunofluorescence staining (**c**, **e**, ≥ 20 random images from 2–3 animals per group). Representative images (from experiments in **e**) with CD8 (green) and DAPI (2',6'-diamidino-2-phenylindole, purple) staining shown (**f**). $*P < 0.05$, $**P < 0.005$, $***P < 0.0005$, Student's *t*-test (**a**, **b**, **d**) and Brunner–Munzel test (**c**, **e**). See Extended Data Fig. 10.

The unique SVs commonly targeting 9p24.1 in multiple cancers have unmasked a critical role of the 3'-UTR sequence in the regulation of *PD-L1* expression, which in turn provides new insights into how cancer cells exploit this regulatory mechanism to evade immune surveillance by disrupting the sequence. Although accounting only for a small fraction of patients in most cancer types, SVs affecting *PD-L1* are thought to represent common activating SVs in human cancers, like *BCR-ABL* and *ALK* fusions, affecting a substantial number of cancer patients. In some genes, typically those encoding transcription factors and cytokines, 3'-UTR is involved in post-transcriptional regulation of mRNA decay rate, which is a major determinant of mRNA abundance, and deregulation of this has been implicated in human diseases, including cancer^{22,23}. *PD-L1* is among such genes, as it has in its long 3'-UTR a number of *cis*-acting elements involved in mRNA decay, including an AU-rich element and potential microRNA-binding sites, such as those for miR-34 and miR-200 (Fig. 3j)^{24–28}. It would be interesting to determine the underlying molecular mechanisms of the 3'-UTR-mediated regulation of *PD-L1* expression and how these affect normal as well as abnormal immunity, and how cancer cells dispatch or deregulate these mechanisms to evade anti-cancer immunity, especially in *PD-L1*-involving SV(–) cancers, which account for the vast majority of cases in which *PD-L1* is overexpressed. Another important implication from the present study is that disrupted *PD-L1* 3'-UTR might serve as a genetic marker for identifying cancers that actively evade immune surveillance and therefore, potentially respond to immune checkpoint blockade using antibodies against

PD-1/PD-L1. A potential problem of detecting PD-L1 expression with a C-terminally directed antibody alone should also be highlighted. The surprisingly high efficacy of anti-PD-1/PD-L1 therapy in Hodgkin lymphoma, in which *PD-L1* overexpression is frequently associated with genetic defects in *PD-L1* (ref. 6), suggests that the above implication could be relevant for patients with ATL and other advanced cancers, particularly those for which no effective therapy is currently available.

Online Content Methods, along with any additional Extended Data display items and Source Data, are available in the online version of the paper; references unique to these sections appear only in the online paper.

Received 1 March 2015; accepted 29 April 2016.

Published online 23 May 2016.

- Iwai, Y. *et al.* Involvement of PD-L1 on tumor cells in the escape from host immune system and tumor immunotherapy by PD-L1 blockade. *Proc. Natl Acad. Sci. USA* **99**, 12293–12297 (2002).
- Topalian, S. L. *et al.* Safety, activity, and immune correlates of anti-PD-1 antibody in cancer. *N. Engl. J. Med.* **366**, 2443–2454 (2012).
- Brahmer, J. R. *et al.* Safety and activity of anti-PD-L1 antibody in patients with advanced cancer. *N. Engl. J. Med.* **366**, 2455–2465 (2012).
- Topalian, S. L., Drake, C. G. & Pardoll, D. M. Immune checkpoint blockade: a common denominator approach to cancer therapy. *Cancer Cell* **27**, 450–461 (2015).
- Page, D. B., Postow, M. A., Callahan, M. K., Allison, J. P. & Wolchok, J. D. Immune modulation in cancer with antibodies. *Annu. Rev. Med.* **65**, 185–202 (2014).
- Ansell, S. M. *et al.* PD-1 blockade with nivolumab in relapsed or refractory Hodgkin's lymphoma. *N. Engl. J. Med.* **372**, 311–319 (2015).
- Green, M. R. *et al.* Integrative analysis reveals selective 9p24.1 amplification, increased PD-1 ligand expression, and further induction via JAK2 in nodular sclerosing Hodgkin lymphoma and primary mediastinal large B-cell lymphoma. *Blood* **116**, 3268–3277 (2010).
- Steidl, C. *et al.* MHC class II transactivator *CIITA* is a recurrent gene fusion partner in lymphoid cancers. *Nature* **471**, 377–381 (2011).
- Twa, D. D. *et al.* Genomic rearrangements involving programmed death ligands are recurrent in primary mediastinal large B-cell lymphoma. *Blood* **123**, 2062–2065 (2014).
- Cancer Genome Atlas Research Network. Comprehensive molecular characterization of gastric adenocarcinoma. *Nature* **513**, 202–209 (2014).
- Mertens, F., Johansson, B., Fioretos, T. & Mitelman, F. The emerging complexity of gene fusions in cancer. *Nat. Rev. Cancer* **15**, 371–381 (2015).
- Garraway, L. A. & Lander, E. S. Lessons from the cancer genome. *Cell* **153**, 17–37 (2013).
- Northcott, P. A. *et al.* Enhancer hijacking activates *GFI1* family oncogenes in medulloblastoma. *Nature* **511**, 428–434 (2014).
- Peifer, M. *et al.* Telomerase activation by genomic rearrangements in high-risk neuroblastoma. *Nature* **526**, 700–704 (2015).
- Kataoka, K. *et al.* Integrated molecular analysis of adult T cell leukemia/lymphoma. *Nat. Genet.* **47**, 1304–1315 (2015).
- Beaudoing, E., Freier, S., Wyatt, J. R., Clavier, J. M. & Gautheret, D. Patterns of variant polyadenylation signal usage in human genes. *Genome Res.* **10**, 1001–1010 (2000).
- Rooney, M. S., Shukla, S. A., Wu, C. J., Getz, G. & Hacohen, N. Molecular and genetic properties of tumors associated with local immune cytolytic activity. *Cell* **160**, 48–61 (2015).
- Hu, Z. *et al.* Genome-wide profiling of HPV integration in cervical cancer identifies clustered genomic hot spots and a potential microhomology-mediated integration mechanism. *Nat. Genet.* **47**, 158–163 (2015).
- Parfenov, M. *et al.* Characterization of HPV and host genome interactions in primary head and neck cancers. *Proc. Natl Acad. Sci. USA* **111**, 15544–15549 (2014).
- Maddalo, D. *et al.* *In vivo* engineering of oncogenic chromosomal rearrangements with the CRISPR/Cas9 system. *Nature* **516**, 423–427 (2014).
- Matsumoto, M. *et al.* Defined TLR3-specific adjuvant that induces NK and CTL activation without significant cytokine production *in vivo*. *Nat. Commun.* **6**, 6280 (2015).
- Mayr, C. & Bartel, D. P. Widespread shortening of 3'UTRs by alternative cleavage and polyadenylation activates oncogenes in cancer cells. *Cell* **138**, 673–684 (2009).
- Schoenberg, D. R. & Maquat, L. E. Regulation of cytoplasmic mRNA decay. *Nat. Rev. Genet.* **13**, 246–259 (2012).
- Gong, A. Y. *et al.* MicroRNA-513 regulates B7-H1 translation and is involved in IFN- γ -induced B7-H1 expression in cholangiocytes. *J. Immunol.* **182**, 1325–1333 (2009).
- Wang, W. *et al.* A miR-570 binding site polymorphism in the *B7-H1* gene is associated with the risk of gastric adenocarcinoma. *Hum. Genet.* **132**, 641–648 (2013).
- Wang, X. *et al.* Tumor suppressor miR-34a targets PD-L1 and functions as a potential immunotherapeutic target in acute myeloid leukemia. *Cell. Signal.* **27**, 443–452 (2015).
- Chen, L. *et al.* Metastasis is regulated via microRNA-200/ZEB1 axis control of tumour cell PD-L1 expression and intratumoral immunosuppression. *Nat. Commun.* **5**, 5241 (2014).
- Cortez, M. A. *et al.* PDL1 Regulation by p53 via miR-34. *J. Natl. Cancer Inst.* **108**, djv303 (2015).

Supplementary Information is available in the online version of the paper.

Acknowledgements This work was supported by Grant-in-Aid from the Japan Agency for Medical Research and Development (Practical Research for Innovative Cancer Control (15A0106014h0002) and Medical Research and Development Programs Focused on Technology Transfer (15im0210102h0001)), Grant-in-Aid for Scientific Research (KAKENHI 22134006, 15H05909, 25250020), and National Cancer Center Research and Development Funds (26-A-6). We thank M. Sago, M. Nakamura and S. Baba for technical assistance, and R. Velaga for English editing. The supercomputing resources were provided by the Human Genome Center, the Institute of Medical Science, the University of Tokyo. This research also used computational resources of the K computer provided by the RIKEN Advanced Institute for Computational Science through the HPCI System Research project (hp140230, hp160219, and hp150232). The results shown here are partly based on data generated by the TCGA Research Network (<http://cancergenome.nih.gov/>).

Author Contributions K.Kataoka, Y.S., H.T., K.C., S.I., and S.Miyano performed sequencing data analyses. H.S., T.Y., Y.Totoki, H.N., N.H. and T.Shibata assisted sequencing data analyses. K.Kataoka, Y.N., Y.W., N.K., K.Y., M.S. and K.Kashiwase performed sequencing experiments. K.Kataoka, S.N., T.M., K.M., N.M., H.K., and Y.A. performed functional assays. S.Mizuno. and S.T. designed sgRNAs. Y.Takeda, M.M., and T.Seya performed *in vivo* experiments. S.S. and K.T. performed IHC assay. A.K., H.I., Y.I., W.M., K.Shide, Y.K., T.H., T.K., K.I., A.T.-K., Y.M., and K.Shimoda collected specimens. K.Kataoka, Y.S., and S.O. generated figures and tables and wrote the manuscript. S.O. led the entire project. All authors participated in discussions and interpretation of the data and results.

Author Information Sequencing data have been deposited in the European Genome-phenome Archive (EGA) under accession EGAS00001001296 (<https://www.ebi.ac.uk/ega/studies/EGAS00001001296>). Reprints and permissions information is available at www.nature.com/reprints. The authors declare no competing financial interests. Readers are welcome to comment on the online version of the paper. Correspondence and requests for materials should be addressed to S.O. (sogawa-ky@umin.ac.jp).

Reviewer information Nature thanks J. Cools, M. Meyerson and A. Ribas for their contribution to the peer review of this work.

METHODS

Patients and materials. A total of 49 ATL patients were enrolled in this study, of which 48 had been analysed by WGS previously¹⁵. Diagnosis and sub-classification were based on the WHO classification and the International Consensus Meeting proposal^{29,30} (Supplementary Table 1). All samples were collected from patients with informed consent according to the protocols approved by the Institutional Review Boards. This study was approved by the institutional ethics committees of the Graduate School of Medicine, Kyoto University and other participating institutes.

WGS analysis and SV detection. Methods of genomic DNA preparation and WGS were described previously¹⁵. Detection of SVs was performed using our in-house pipeline, Genom-SV (Y. Shiraishi *et al.*, in preparation), which enables sensitive and accurate detection of a variety of SVs, relying on both breakpoint-containing junction reads and improperly aligned read pairs for maximizing sensitivity. To identify significant breakpoint cluster regions, we divided the entire genome into 1-Mb windows, and enumerated the number of samples with at least one breakpoint within each window, as described in the literature^{13,14}. As ATL samples have frequent deletions in common fragile sites, which seem to be passenger events¹⁵, we first focused on the other SV types, that is, inversions, tandem duplications, and translocations to determine breakpoint cluster regions, and then all of the breakpoints were interrogated within the focused breakpoint cluster regions, regardless of SV types, that is, taking deletion-type SVs also into consideration. For those windows in which positive events were detected by the initial screen, breakpoints were visually inspected using Integrative Genomics Viewer (IGV).

RNA-seq analysis. Methods of preparation of RNA samples and RNA-seq were previously described¹⁵. Genome index generation and sequence alignment were performed using STAR software (version 2.4.0)³¹, followed by sorting and indexing of BAM files using SAMtools (version 1.2)³², where GRCh37 (human reference assembly) as well as NC_007605 (for EBV) and hs37d5 (from the 1000 Genomes Project Phase II for decoy sequences) sequences were used as reference genomes. RNA-seq reads were also aligned to cancer-related viral sequences (including those for HPV and hepatitis B virus) available from the NCBI Viral Genomes Resource³³ using BLAT³⁴. Positive identification of viral genomes required at least 1,000 read pairs properly mapped to viral sequences. For samples positive for a viral genome, realignment of the RNA-seq reads was performed after adding the corresponding viral sequence into the reference genomes. For transcriptome analysis of mouse samples, the GRCm38 mouse reference assembly was used as a reference. To detect fusion transcripts, we used our in-house program, fusionfusion, which enables effective selection of putative chimaeric transcripts generated by the STAR algorithm³¹. All samples positive for candidate *PD-L1*-containing fusions together with those harbouring genomic breakpoints within the *PD-L1* gene were manually reviewed using IGV. The transcription termination site was determined by detecting poly-A sequences and/or the genomic sequences at which the number of RNA-seq reads was abruptly reduced. Putative poly-A signal sequences (AAUAAA, UAUAAA, AUUAAA, or AGUAAA) were searched within 10–30 nucleotide upstream of the transcription termination site¹⁶. A modified version of RPKM was used for expression quantification³⁵. For *PD-L1* expression analysis, RPKM values for each exon and the distal part of 3'-UTR (chr9:5469203–5470567 for human and chr19:29386741–29388094 for mouse) were calculated.

Validation of *PD-L1* SVs and their products. The validation of *PD-L1* SVs and associated fusion transcripts was performed using both genomic and reverse transcription PCR, followed by Sanger sequencing. NCBI reference sequences (NM_014143 for nucleotide and NP_054862 for amino acid) were used as a reference.

Analysis of TCGA data sets. We analysed 10,210 TCGA samples from 33 cancer types, for which RNA-seq data were publically available, to interrogate whether 3'-UTR-disrupted aberrant *PD-L1* transcripts were found in cancer types other than ATL (Extended Data Fig. 5). Briefly, gene-level RNA-seq expression data (normalized RSEM (RNA-seq by expectation-maximization) value) were obtained from the standardized analysis-ready TCGA data, Broad GDAC Firehose std-data__2015_08_21 run (<http://dx.doi.org/10.7908/C18W3CNQ>) or otherwise, directly from the TCGA data portal (<https://tcga-data.nci.nih.gov/tcga/>) for DLBC and STAD samples. RNA-seq data for the corresponding samples were obtained from the Cancer Genomic Hub (<https://cghub.ucsc.edu>), and analysed through our in-house pipeline, as described above for sequencing alignment, *PD-L1* expression quantification, as well as detection of fusion transcripts and viral sequences. A sample was considered to have aberrant *PD-L1* transcripts, when the sample showed elevated expression of *PD-L1* exon 4 (RPKM > 2), together with a high *PD-L1* exon 4 versus 3'-UTR ratio in RPKM (> 3.5) or *PD-L1* fusion transcripts detected by fusionfusion. Candidate cases for aberrant *PD-L1* transcripts were further assessed by visual inspection using IGV. Cancer-related viral integration within or near the

PD-L1 gene was also investigated. Cytolytic activity was calculated as a geometric mean of *GZMA* and *PRF1* expressions (as expressed in RPKM, 0.01 offset), as previously described¹⁷. The effect of *PD-L1* SVs on cytolytic activity was assessed on the basis of a GLM using *PD-L1* expression and cancer type as covariates.

Copy number data. Copy number data for ATL were analysed to estimate total and allele-specific copy numbers using CNAG/AsCNAR^{36,37} and ASCAT³⁸ for Affymetrix GeneChip Human Mapping 250K NspI Array and Illumina Human610-Quad BeadChip, respectively. The level 3 segmented copy number data (Affymetrix Genome-Wide Human SNP Array 6.0) were downloaded from the TCGA data portal (<https://tcga-data.nci.nih.gov>) for (i) samples with abnormal *PD-L1* transcripts and (ii) all DLBC and STAD samples. Copy numbers for *PD-L1* exon 4 were used for further analysis.

IHC. IHC was performed on formalin-fixed paraffin-embedded tissue sections using antibodies directed against the N-terminal (E1J2J, Cell Signaling Technology) and C-terminal (SP142, Spring Bioscience) domains of PD-L1. The antigen–antibody complexes were visualized with Histofine Simple Stain MAX PO (Nichirei Bioscience).

Cell lines. HEK293T (human embryonic kidney), PC-9 (human lung cancer), and Jurkat (human T-cell leukaemia) cell lines were obtained from RIKEN Cell Bank, and P815 (mouse mastocytoma) cell line was from JCRB. T2 (human T and B lymphoblast hybrid), EG7-OVA (mouse T-cell lymphoma), ST-1 (human ATL), and B16-F10 (mouse melanoma) cell lines were gifts from H. Kawamoto, T. Seya, Y. Yamada, and N. Minato, respectively. Cell lines were authenticated by the provider and routinely tested for mycoplasma infection.

Gene transfer and retroviral transduction. Vector transfection was performed using X-tremeGENE 9 DNA Transfection Reagent (Roche) for HEK293T and PC-9, Lipofectamine 2000 Reagent (Thermo Fisher Scientific) for B16-F10, Neon transfection system (Thermo Fisher Scientific) for T2, EG7-OVA, and P815, and Amaxa Nucleofector (Lonza) for Jurkat, according to the corresponding manufacturer's protocol. PC-9 cells were transduced with retroviral supernatant from Phoenix-GALV packaging cells³⁹ (a gift from H. P. Kiem with permission from G. P. Nolan) transduced with the indicated vectors.

CRISPR-Cas9-mediated genome editing. Human and mouse *PD-L1* 3'-UTR sgRNA targeted sites were designed manually and checked *in silico*. The pSpCas9(BB)-2A-GFP (pX458) vector expressing Cas9 (Addgene plasmid 48138) was digested with BbsI and ligated to annealed and phosphorylated sgRNA oligonucleotides. The sgRNA sequences are listed in Supplementary Table 4. Human and mouse cell lines were transfected with indicated pX458 vectors and collected 48 h later. To validate CRISPR-mediated DNA cleavage occurring at the intended position, a genomic region containing the target sequence was amplified using KOD FX Neo DNA polymerase (TOYOBO) and gel purified. PCR primers used for validation are listed in Supplementary Table 5. Sequencing libraries were prepared from the PCR product using NEBNext Ultra DNA Library Prep Kit for Illumina (New England Biolabs) and sequenced on the Illumina HiSeq 2000/2500 platform as previously described¹⁵. To establish cell lines with *PD-L1* 3'-UTR deletions/inversions, cell lines were transfected with a pair of sgRNAs, collected 48 h later, and purified with FACSARIA II Cell Sorter (BD Biosciences) using GFP and PD-L1 expression as a surrogate marker for successful rearrangement. To validate deletions/inversions induced by introduction of a pair of sgRNAs targeting both ends of *PD-L1* 3'-UTR, genomic PCR flanking the breakpoint region and Sanger sequencing was performed. This was followed by RNA-seq to assess *PD-L1* expression and detect resultant truncation of *PD-L1* transcripts.

Plasmid constructs. GFP-tagged *PD-1/PDCD1* (NM_005018) cDNA in pCMV6-AC-GFP vector was obtained from OriGene. The fragments of wild-type *PD-L1* (NM_014143) and its fusion cDNA were obtained by PCR amplification of cDNA extracted from ATL samples without (ATL046) or with (ATL020 and ATL079) *PD-L1* SVs, respectively, then cloned into LZRSpBMN-Z vector (a gift from G. P. Nolan) using In-Fusion HD cloning kit (TaKaRa).

Western blot. Cells were lysed, subjected to SDS-PAGE, and transferred to a PVDF membrane (Millipore). The blot was incubated with the antibodies listed in Supplementary Table 6, and visualized by Immobilon Western Chemiluminescent HRP Substrate (Millipore).

Flow cytometry analysis. The list of antibodies used for flow cytometry is provided in Supplementary Table 7. Stained cells were analysed on FACS LSR Fortessa or FACSARIA II Cell Sorter (BD Biosciences). The data analyses were performed with FlowJo software (TreeStar). To assess PD-1 binding capacity of PD-L1 fusion proteins, ATL primary samples or PC-9 cells transduced with indicated PD-L1 were first incubated with recombinant human PD-1 Fc chimaera (R&D Systems) at 1 µg ml⁻¹. After 30 min, the cells were washed and further incubated for 30 min with APC anti-human IgG Fc (BioLegend) or APC mouse IgG2a, κ-isotype control (BioLegend). To analyse the effect of IFN-γ on PD-L1 expression, PC-9 cells were stimulated with different concentrations of human recombinant IFN-γ

(100 or 300 U ml⁻¹; Roche) for 48 h, followed by analysis of cell surface expression of PD-L1 using flow cytometry.

Assay for PD-L1 transcript stability. ST-1 cells harbouring wild-type and truncated *PD-L1* were collected at the indicated time points after transcription was inhibited by adding actinomycin D (Nacalai Tesque) in cell culture at the concentration of 10 µg ml⁻¹. Total RNA was extracted using RNeasy Mini Kit (QIAGEN), followed by cDNA synthesis with ReverTra Ace qPCR RT Kit (TOYOBO), and subjected to quantitative reverse transcription PCR with SYBR Premix Ex TaqII (Tli RNaseH Plus) (TaKaRa) and LightCycler 480 System (Roche) according to the manufacturer's instructions. PCR primers used are listed in Supplementary Table 8. All assays were performed in three technical replicates for each biological replicate and relative expression was normalized for 18S rRNA. We also searched for potential regulatory elements in *PD-L1* 3'-UTR sequence using UTRdb⁴⁰.

In vitro co-culture assay. Mock- or PD-1-transfected Jurkat T cells were co-incubated with parental or sgPD-L1-transfected PC-9 cells in the presence of anti-PD-L1 antibody (29E.2A3; BioLegend) or mouse IgG2b isotype control (MPC-11; BioLegend) for 18 h, and then assayed for apoptosis. For detection of apoptotic cells, cells were stained with DAPI and Annexin V-FITC (BD Biosciences) according to the manufacturer's protocol.

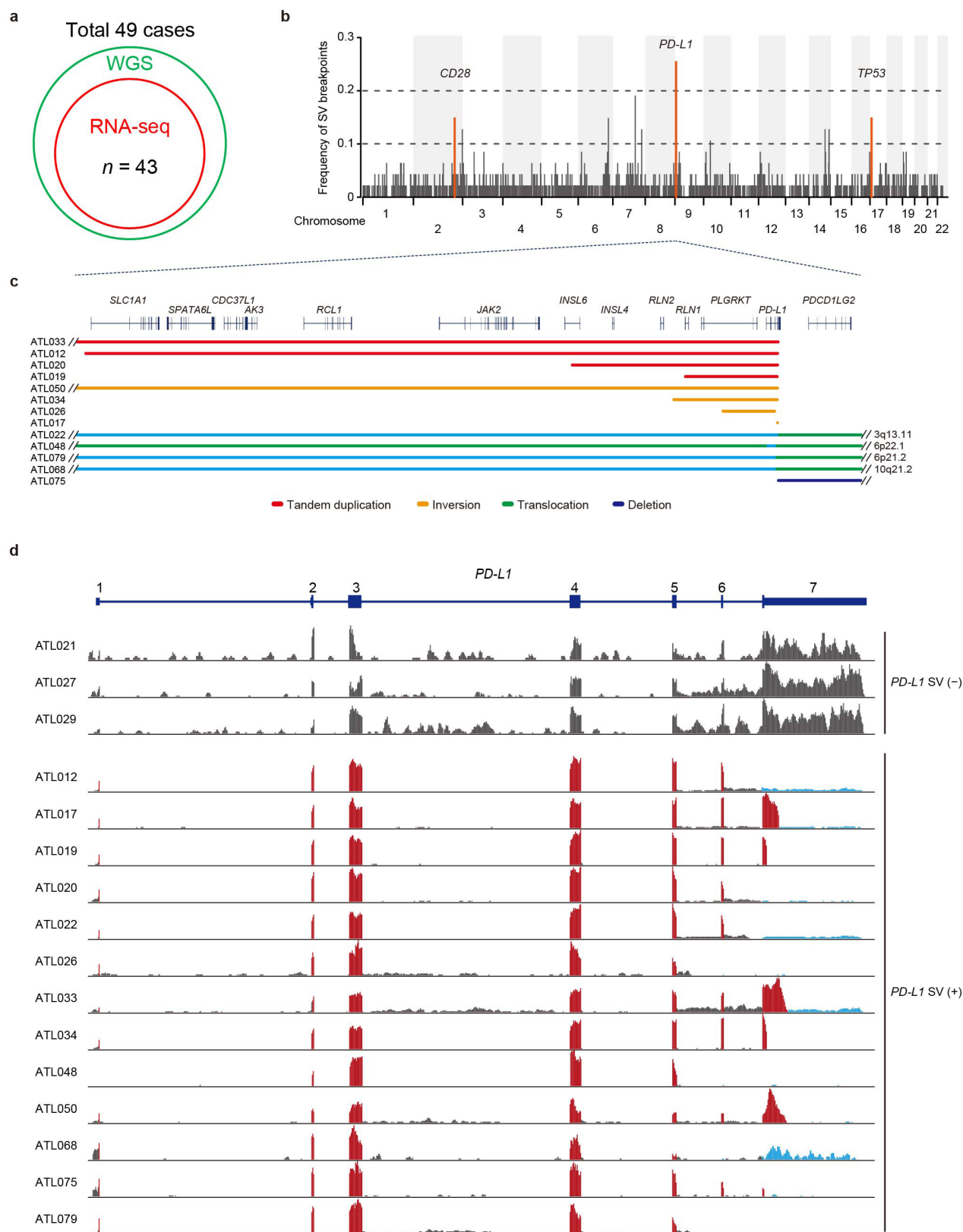
In vivo EG7-OVA tumour model. All animal experiments were approved by the Animal Research Committee, Graduate School of Medicine, Kyoto University and the Hokkaido University Animal Care and Use Committee and strictly adhered to their guidelines. Female C57BL/6 mice (6–10 weeks old) were obtained from CLEA Japan and maintained under pathogen-free conditions. Mice were subcutaneously transplanted with 2 × 10⁶ mock- or sgPD-L1-transfected EG7-OVA cells in PBS. On day 7, PBS or 50 µg poly(I:C) were subcutaneously injected around the tumour. On day 14 or 15, tumours were collected from tumour-bearing mice and further analysed. Tumour size was measured at regular intervals with a caliper, and calculated using the following formula: tumour size (cm³) = (long diameter) × (short diameter)² × 0.52. To examine the effect of Pd-1/Pd-l1 blockade, we intraperitoneally injected recipient animals with 200 µg anti-mouse Pd-l1 antibody (10F9G2; Bio X Cell) or rat IgG2b isotype control (LTF-2; Bio X Cell) on days 7, 9, 11, and 13. No statistical methods were used to predetermine sample size. No randomization or blinding was performed. No tumour exceeded the maximum size approved by the animal welfare committee and regulations.

Analysis of EG7-OVA tumours. For immunofluorescence imaging, 4% paraformaldehyde-fixed frozen sections were stained with anti-CD8α-APC antibody (53-6.7; BioLegend) and DAPI (Thermo Fisher Scientific), and examined using LSM510 META confocal microscope (Zeiss). The number of CD8⁺ T cells infiltrating into tumours was counted for randomly selected fields (0.2 mm² per field). For flow cytometric analysis, tumours were finely minced and treated with collagenase I (Sigma-Aldrich), collagenase IV (Sigma-Aldrich), hyaluronidase (Sigma-Aldrich), and DNase I (Roche) in Hank's Balanced Salt Solution at 33 °C for 10 min, and stained with antibody.

Statistical methods. Statistical analyses were performed with R3.1.3 software (The R Foundation for Statistical Computing). Normality of data distribution and homogeneity of variance were assessed by the Shapiro–Wilk's test and *F*-test, respectively. Student's two-tailed *t*-test was used to compare two groups and a Welch's correction was applied when comparing groups with unequal variance (*F*-test *P* < 0.05). Brunner–Munzel test was performed when normal distribution could not be assumed (Shapiro–Wilk's test *P* < 0.05). GLM was used to assess the effect of *PD-L1* SVs and DNA copy number on *PD-L1* and *JAK2* expression. The number of biological replicates (*n*) is indicated in the figure legends, if not otherwise specified.

Code availability. The codes for Genomon-SV and fusionfusion algorithms are available at <https://github.com/Genomon-Project/GenomonSV> and <https://github.com/Genomon-Project/fusionfusion>, respectively. The codes for virus detection and expression quantification are also available at <https://github.com/Genomon-Project/GenomonVirusChecker> and <https://github.com/Genomon-Project/GenomonExpression>, respectively.

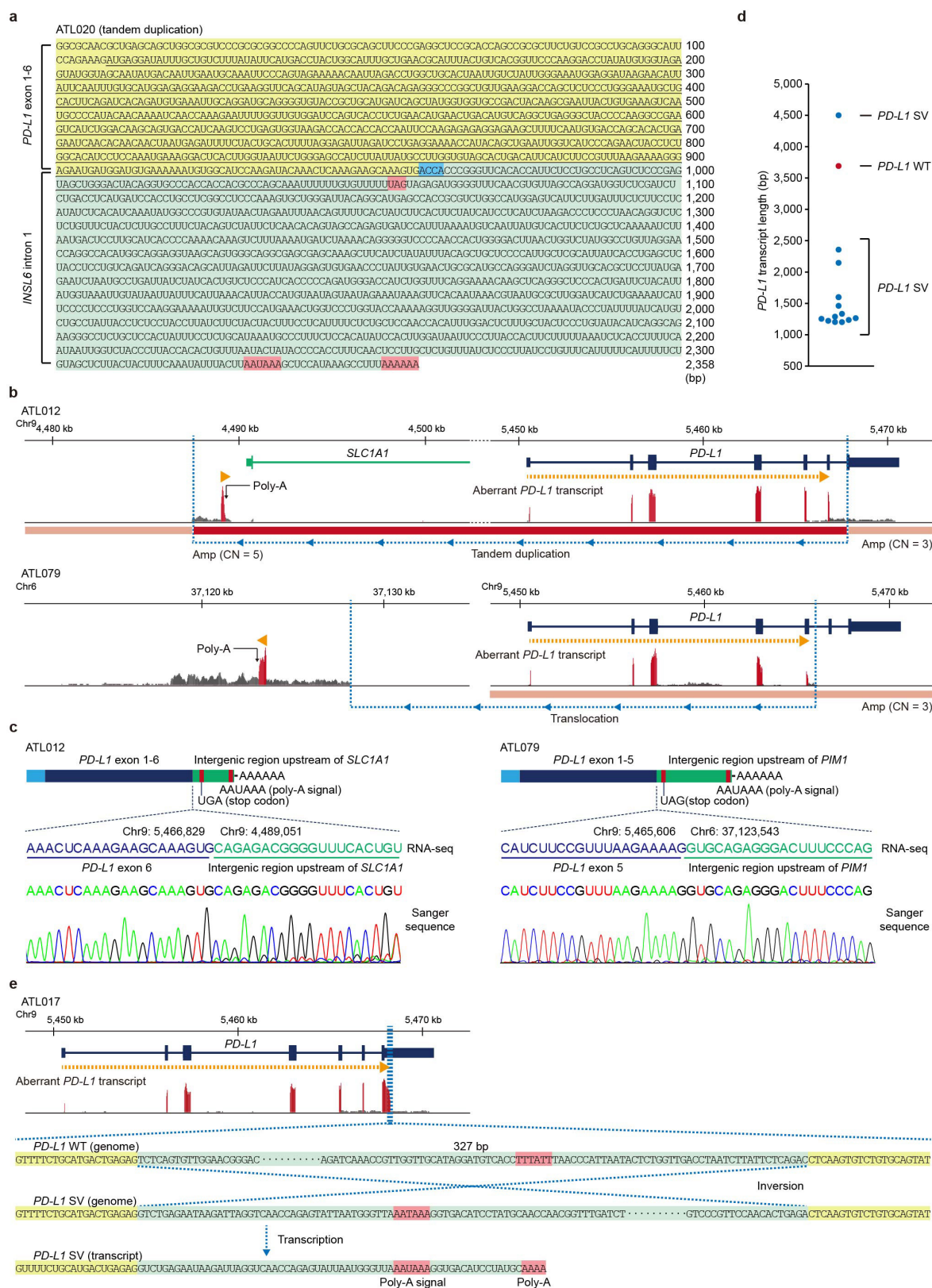
29. Tsukasaki, K. *et al.* Definition, prognostic factors, treatment, and response criteria of adult T-cell leukemia-lymphoma: a proposal from an international consensus meeting. *J. Clin. Oncol.* **27**, 453–459 (2009).
30. Swerdlow, S. *et al.* *WHO Classification of Tumours of Haematopoietic and Lymphoid Tissues* 4th edn, Vol. 2 (IARC Press, 2008).
31. Dobin, A. *et al.* STAR: ultrafast universal RNA-seq aligner. *Bioinformatics* **29**, 15–21 (2013).
32. Li, H. *et al.* The sequence alignment/map format and SAMtools. *Bioinformatics* **25**, 2078–2079 (2009).
33. Brister, J. R., Ako-Adjei, D., Bao, Y. & Blinkova, O. NCBI viral genomes resource. *Nucleic Acids Res.* **43**, D571–D577 (2015).
34. Kent, W. J. BLAT—the BLAST-like alignment tool. *Genome Res.* **12**, 656–664, 2002).
35. Mortazavi, A., Williams, B. A., McCue, K., Schaeffer, L. & Wold, B. Mapping and quantifying mammalian transcriptomes by RNA-seq. *Nat. Methods* **5**, 621–628 (2008).
36. Nannya, Y. *et al.* A robust algorithm for copy number detection using high-density oligonucleotide single nucleotide polymorphism genotyping arrays. *Cancer Res.* **65**, 6071–6079 (2005).
37. Yamamoto, G. *et al.* Highly sensitive method for genomewide detection of allelic composition in nonpaired, primary tumor specimens by use of affymetrix single-nucleotide-polymorphism genotyping microarrays. *Am. J. Hum. Genet.* **81**, 114–126 (2007).
38. Van Loo, P. *et al.* Allele-specific copy number analysis of tumors. *Proc. Natl Acad. Sci. USA* **107**, 16910–16915 (2010).
39. Horn, P. A., Topp, M. S., Morris, J. C., Riddell, S. R. & Kiern, H. P. Highly efficient gene transfer into baboon marrow repopulating cells using GALV-pseudotype oncoretroviral vectors produced by human packaging cells. *Blood* **100**, 3960–3967 (2002).
40. Grillo, G. *et al.* UTRdb and UTRsite (RELEASE 2010): a collection of sequences and regulatory motifs of the untranslated regions of eukaryotic mRNAs. *Nucleic Acids Res.* **38**, D75–D80 (2010).



Extended Data Figure 1 | *PD-L1* SVs affecting 3'-UTR in ATL.

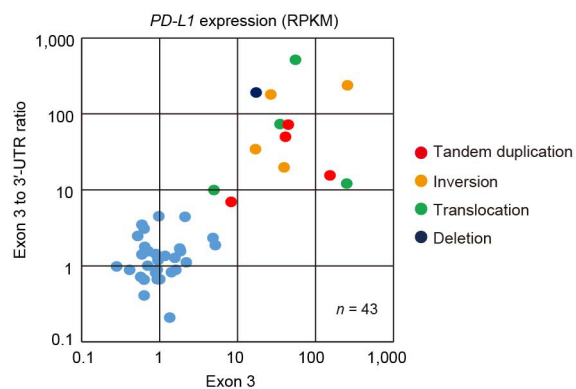
a, Diagram showing numbers of ATL samples investigated by WGS/RNA-seq. **b**, Genome-wide distribution of SV (without deletion) breakpoints in 49 ATL samples, showing a prominent peak at the *PD-L1* locus. **c**, Summary of different types of SVs commonly affecting 3' region of the

PD-L1 gene are shown by indicated colours. **d**, 3'-truncated *PD-L1* mRNA transcripts observed in ATL cases. RNA-seq data are visualized by IGV for ATL samples with or without *PD-L1* SVs. Aberrant *PD-L1* transcripts are shown in red.

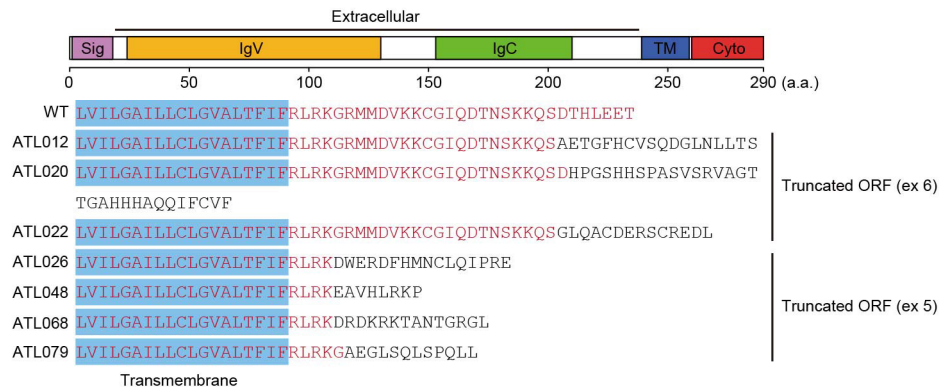
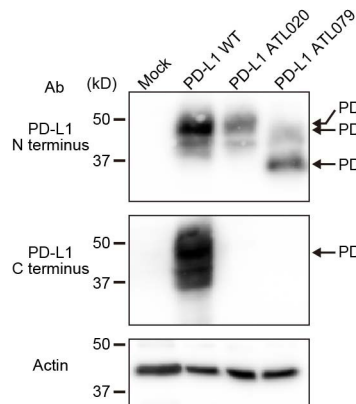
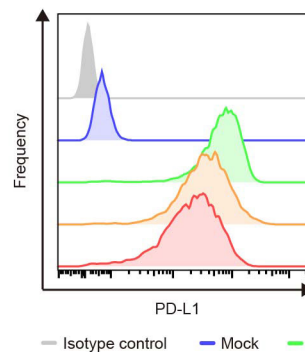
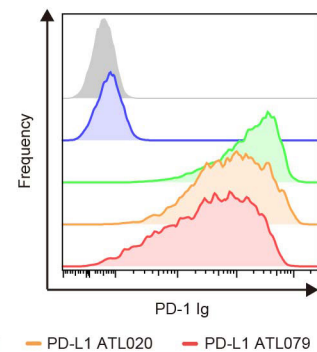
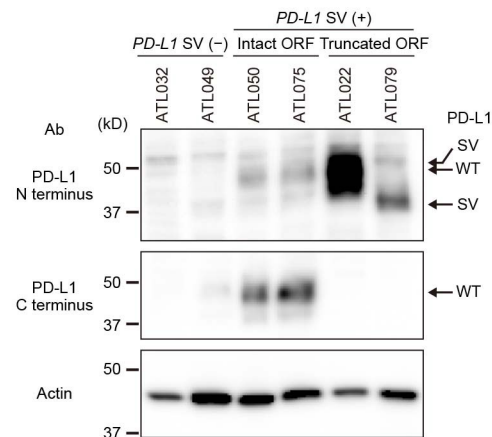


Extended Data Figure 2 | Fusion genes involving PD-L1 and non-coding sequences identified in ATL. **a**, ATL020 fused sequence: the sequences derived from PD-L1 exons 1–6 and INS6 intron 1 are marked in yellow and green, respectively. The non-template sequence is marked in blue, and stop codon (UAG), poly-A signal (AAUAAA) and poly-A in red. The putative translated region is underlined. **b**, Genomic structure of the rearranged PD-L1 locus and transcription in two representative cases (ATL012 and ATL079) with 3'-UTR-truncated PD-L1 transcripts, in which PD-L1 ORF is terminated before exon 6 or 7, and merged into

an intergenic sequence. Breakpoints (blue dotted lines) are shown with accompanying copy number alterations. **c**, Structure and breakpoint sequence of PD-L1 fusion transcripts (top) with Sanger sequencing chromatogram (bottom). **d**, Length of abnormal PD-L1 transcripts identified in ATL samples with PD-L1 SVs, compared with wild-type PD-L1. **e**, Genomic and transcript sequences from the PD-L1 locus containing 327 bp inversion within the last exon identified in case ATL017. Aberrant PD-L1 transcripts have a putative poly-A signal sequence in the inverted region, followed by poly-A tract.

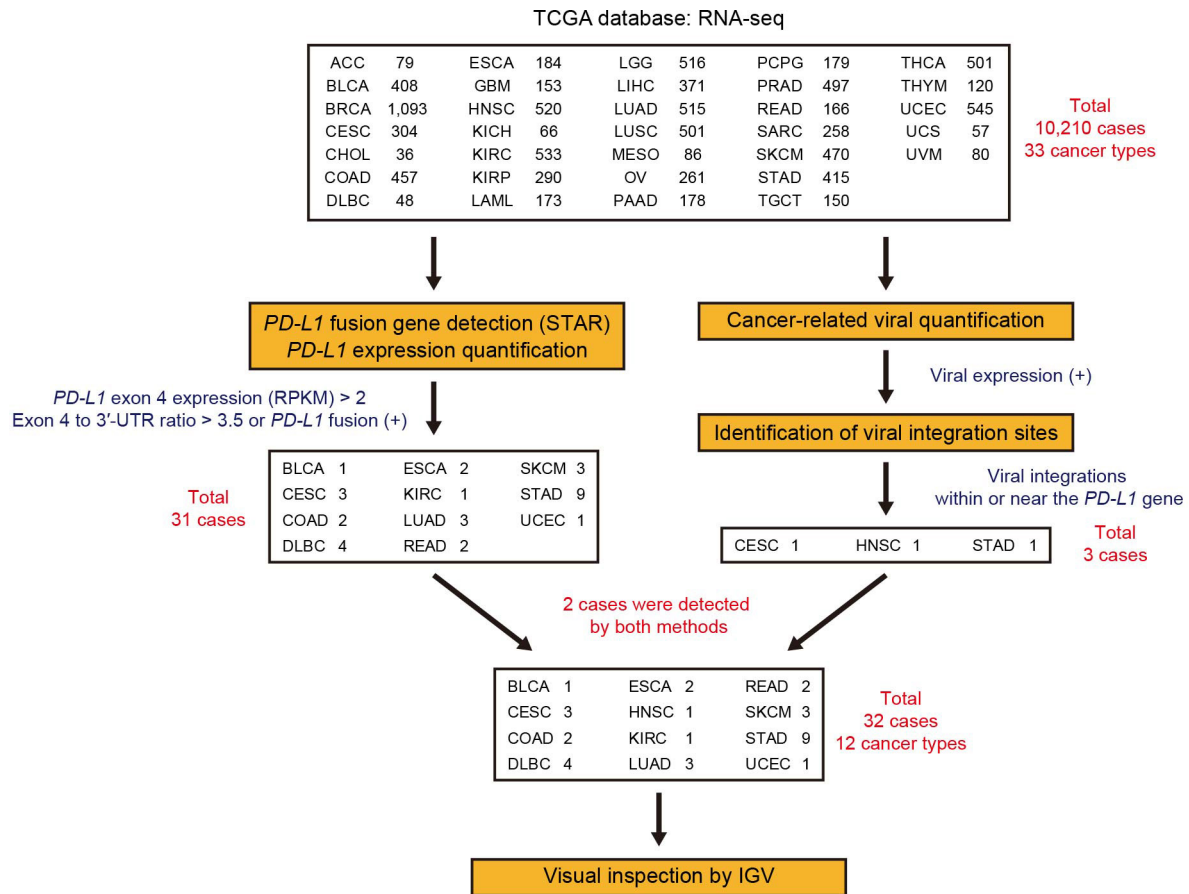


Extended Data Figure 3 | Elevated *PD-L1* mRNA expression in ATL according to *PD-L1* SV state. Diagonal plots between *PD-L1* exon 3 expression (RPKM) and its relative value to that of 3'-UTR (exon 3 to 3'-UTR ratio) for 43 ATL cases. SV (+) cases are indicated by corresponding colours to each SV type.

a**b****c****d****e**

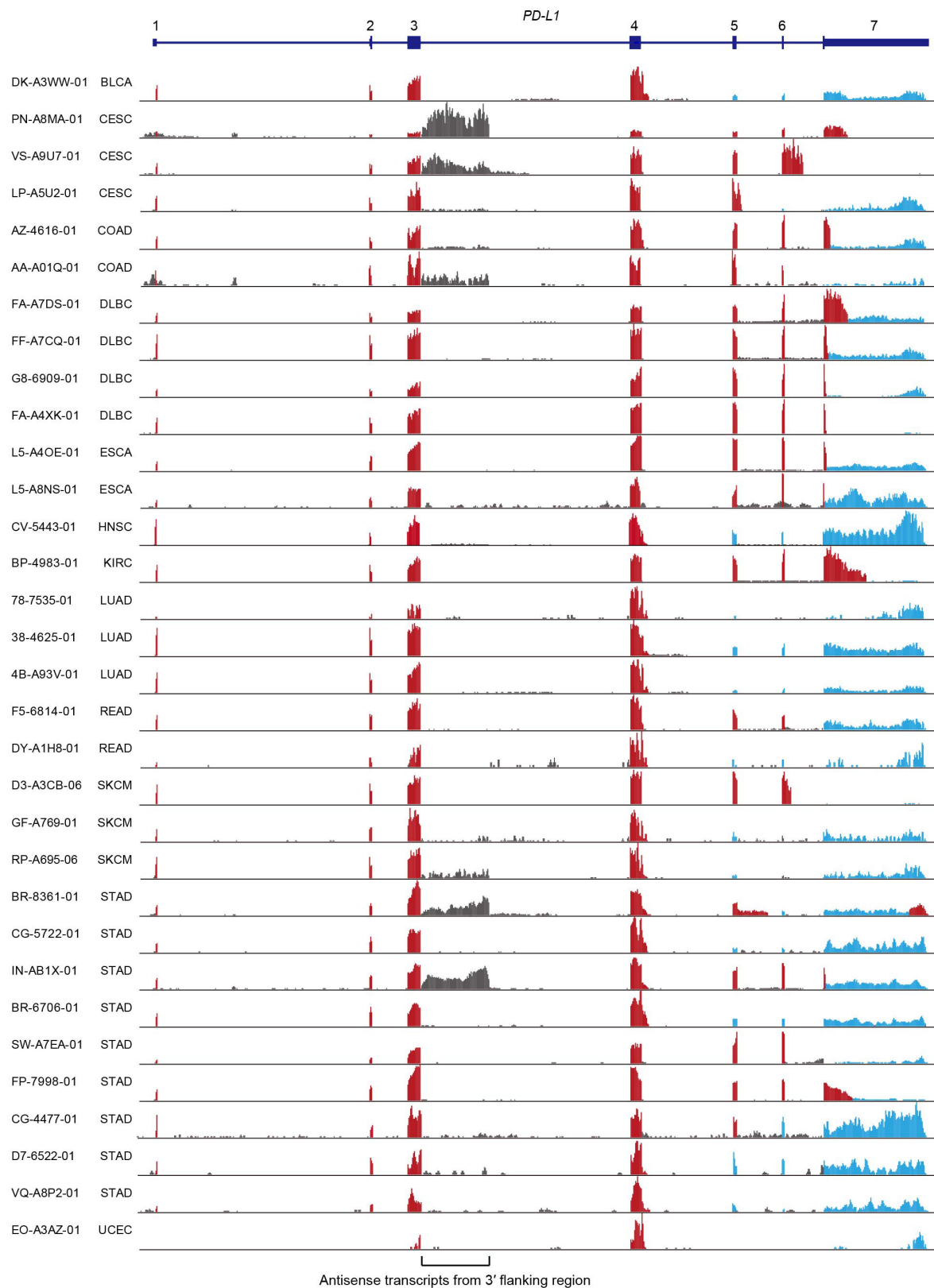
Extended Data Figure 4 | PD-L1 fusion proteins identified in ATL.
a, Amino acid sequence alignment of wild-type and truncated PD-L1 proteins. Transmembrane domain is shaded in blue. Conserved regions are shown in red. **b**, Western blot analysis with antibodies against the N-terminal and C-terminal domains of PD-L1 in PC-9 cells transduced with indicated *PD-L1* constructs. **c**, **d**, Flow cytometry plots for PD-L1

surface expression (**c**) and PD-1 Ig binding (**d**) in PC-9 cells transduced with indicated *PD-L1* constructs. **e**, Western blot of *PD-L1* SV(+) cases harbouring intact or truncated ORFs, compared with SV(-) cases using antibodies specifically detecting N-terminal and C-terminal domains of PD-L1. **b–e**, Representative of three independent experiments.



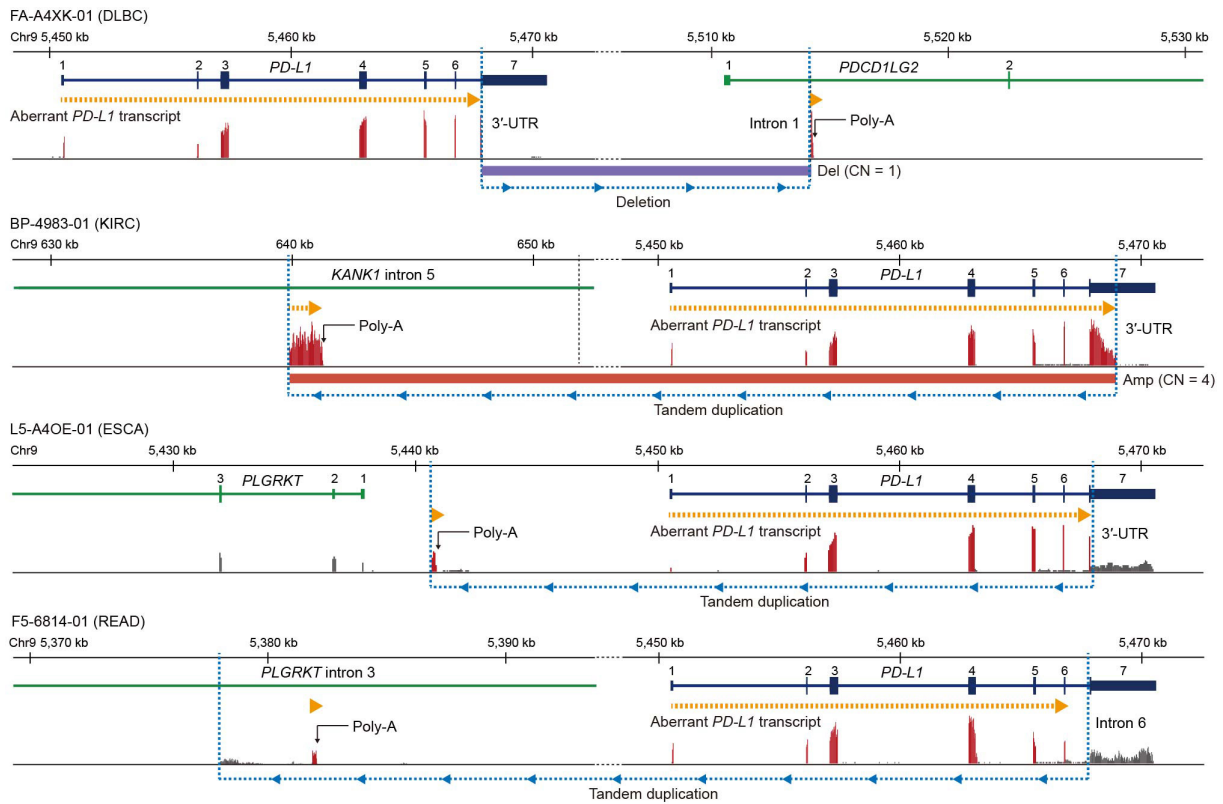
Extended Data Figure 5 | Flow chart for detecting abnormal *PD-L1* transcripts in the TCGA cohort. In total, 10,210 tumour samples in 33 tumour types, for which RNA-seq data were available in TCGA, were assessed by exon-level expression quantification and fusion detection by

STAR algorithm. Viral integration within or near the *PD-L1* gene was also searched in this cohort. After manual review by IGV, a total of 32 cases with aberrant *PD-L1* transcription were identified.

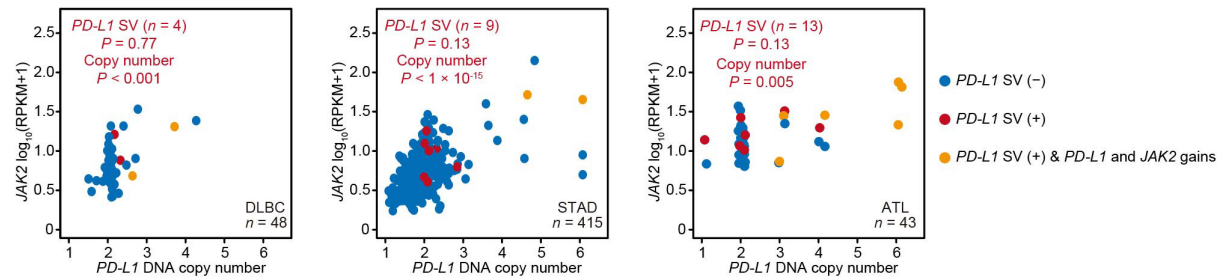


Extended Data Figure 6 | 3'-truncated *PD-L1* mRNA transcripts in the TCGA cohort. RNA-seq data are visualized by IGV for TCGA samples with abnormal *PD-L1* transcription. Aberrant *PD-L1* transcripts were shown in red.

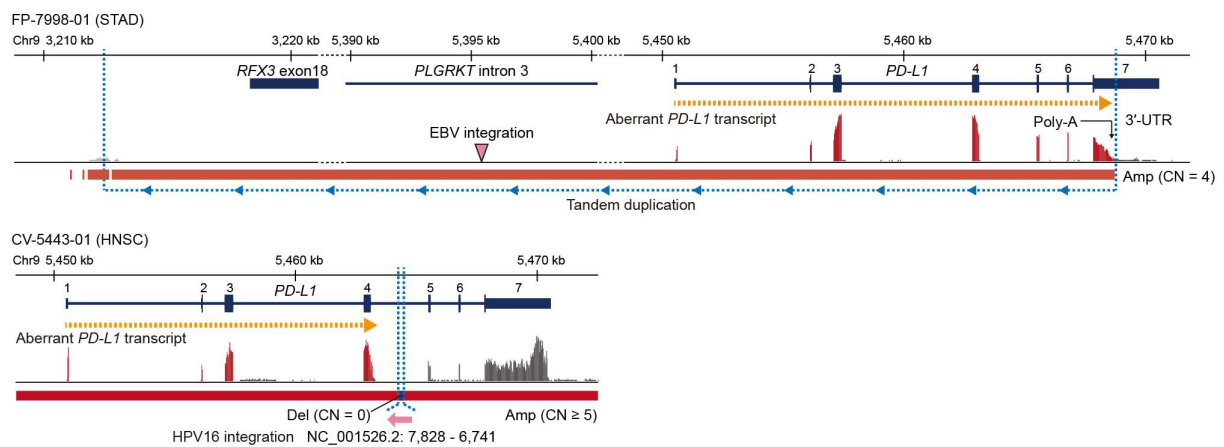
a



b

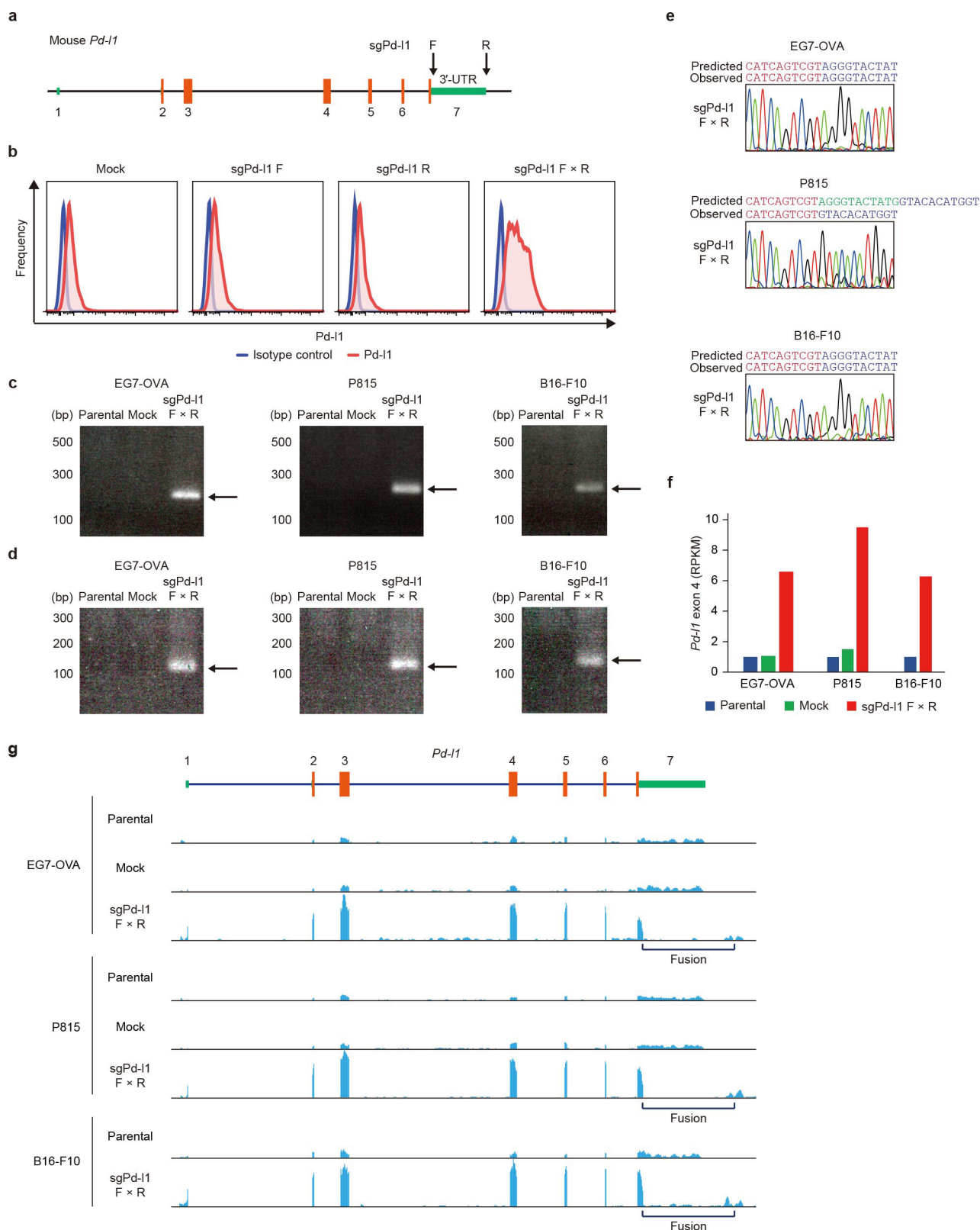


c



Extended Data Figure 7 | Aberrant transcription affecting *PD-L1* 3'-UTR and associated genomic alterations identified in multiple cancers. **a**, Genomic structure of the rearranged *PD-L1* locus and transcription in FA-A4XK-01 (DLBC), BP-4983-01 (KIRC), L5-L4OE-01 (ESCA), and F5-6814-01 (READ), showing loss of *PD-L1* 3'-UTR transcription and fusion transcripts between *PD-L1* and intronic or intergenic segments. Breakpoints (blue dotted lines) are shown with accompanying copy number alterations. Del, deletion. **b**, *PD-L1* DNA copy number versus *JAK2* mRNA expression across 48 DLBC (left), 415 STAD

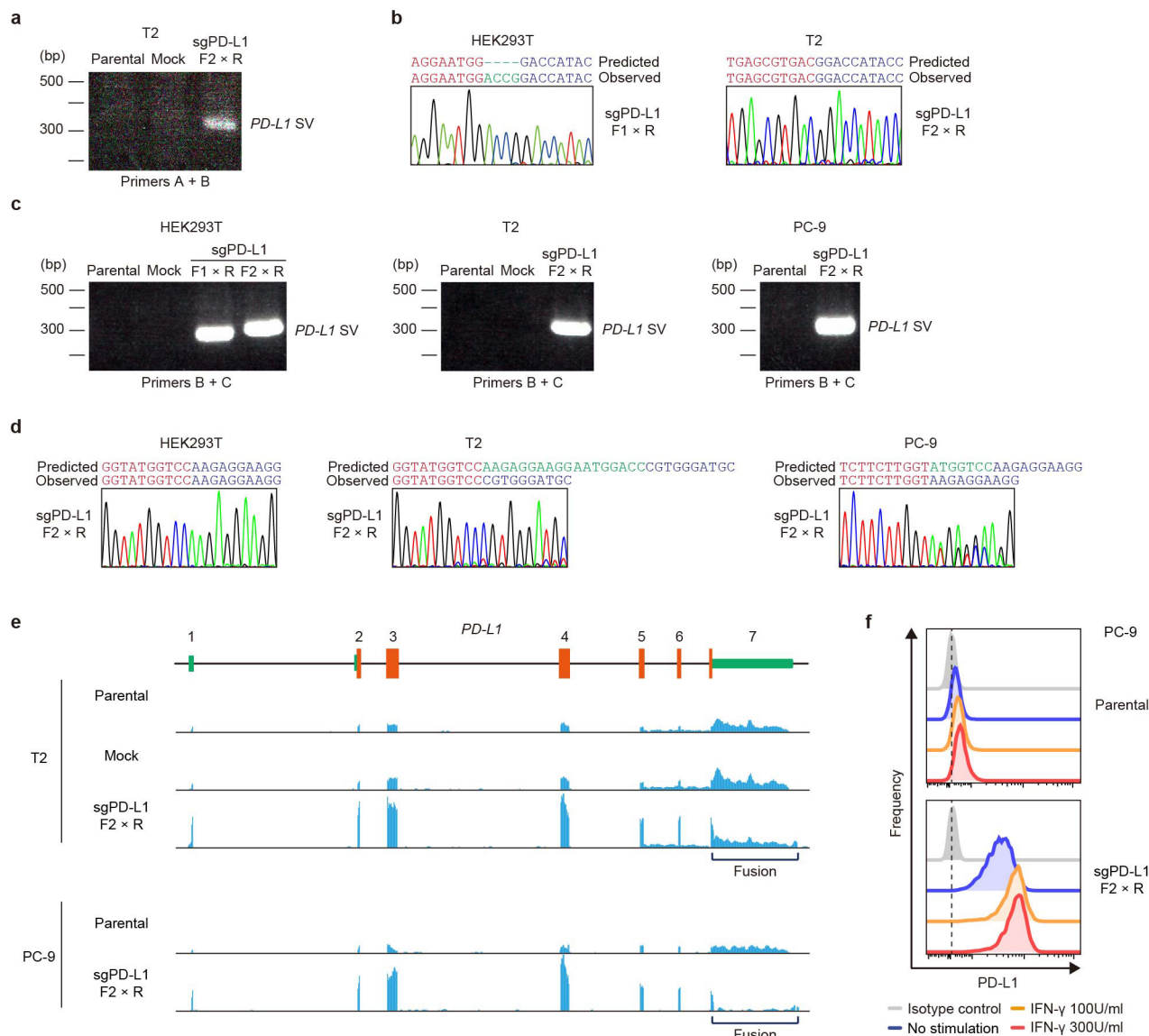
(middle), and 43 ATL (right) samples. SV(+) samples (red) and those with 9p24.1 copy number gains involving both *JAK2* and *PD-L1* genes (orange) are indicated. P values for the effects of *PD-L1* SVs and copy number on *JAK2* expression (GLM) are shown. **c**, Genomic structure of the rearranged *PD-L1* locus and transcription in two cases with viral integrations around the *PD-L1* gene; a STAD case (FP-7998-01) with an EBV integration (top) and an HNSC case (CV-5443-01), showing HPV16 integration, which was described previously¹⁹, and premature termination of *PD-L1* transcripts within intron 4 (bottom).



Extended Data Figure 8 | Induction of *Pd-1* 3'-UTR deletions and inversions in mouse cell lines using the CRISPR-Cas9 system.

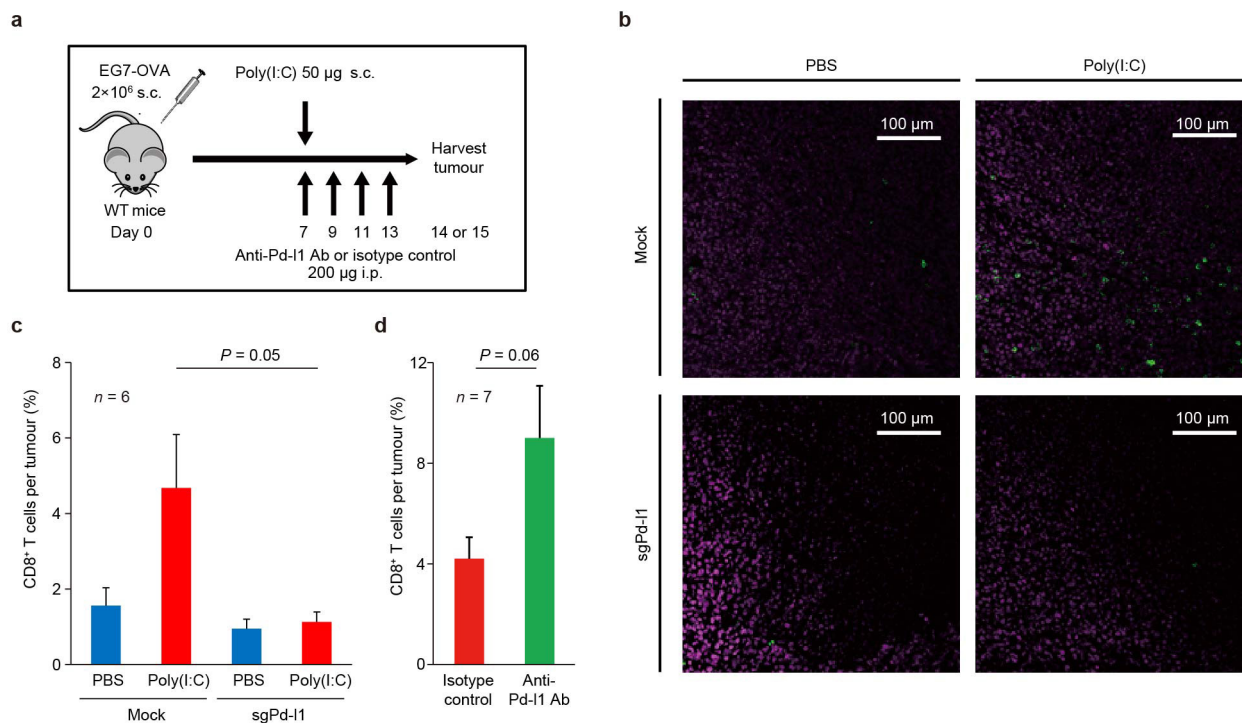
a, Positions of targeting sgRNAs used for CRISPR-Cas9-mediated disruption of *Pd-1* 3'-UTR are indicated by arrows. **b**, *Pd-1* surface expression in EG7-OVA cells transfected with Cas9 and no, single, or pairwise sgRNAs. Representative of three independent experiments. **c**, **d**, PCR detection of the *Pd-1* 3'-UTR deletion (**c**) or inversion (**d**) breakpoint junction from EG7-OVA, P815, and B16-F10 cells in which

Cas9 was expressed without (parental) or with no sgRNA (mock), or a pair of *Pd-1* sgRNAs. **e**, Sequence chromatogram of the detected *Pd-1* 3'-UTR deletions from sgPd-I1-transfected EG7-OVA, P815, and B16-F10 cells. **f**, **g**, *Pd-1* exon 4 mRNA expression (RPKM) was calculated from the RNA-seq data for EG7-OVA, P815, and B16-F10 cells in which Cas9 was expressed without (parental) or with no sgRNA (mock), or a pair of *Pd-1* sgRNAs (**f**). RNA-seq reads within the *Pd-1* gene were visualized by IGV (**g**).



Extended Data Figure 9 | Induction of *PD-L1* 3'-UTR deletions and inversions in human cell lines using the CRISPR-Cas9 system. **a**, PCR detection of the *PD-L1* 3'-UTR deletion breakpoint junction from T2 cells in which Cas9 was expressed without (parental) or with no sgRNA (mock), or a pair of *PD-L1* sgRNAs. **b**, Sequence chromatogram of the detected *PD-L1* 3'-UTR deletions from sgPD-L1-transfected HEK293T and T2 cells. **c**, PCR detection of the *PD-L1* 3'-UTR inversion breakpoint junction from HEK293T, T2, and PC-9 cells in which Cas9 was expressed

without (parental) or with no sgRNA (mock), or a pair of *PD-L1* sgRNAs. **d**, Sequence chromatogram of the detected *PD-L1* 3'-UTR inversions from sgPD-L1-transfected HEK293T, T2, and PC-9 cells. **e**, Visualization of RNA-seq reads within the *PD-L1* gene for T2 and PC-9 cells in which Cas9 was expressed without (parental) or with no sgRNA (mock), or a pair of *PD-L1* sgRNAs. **f**, Flow cytometric analysis of PD-L1 surface expression in parental or sgPD-L1-transfected PC-9 cells stimulated with IFN- γ (100 or 300 U ml⁻¹) for 48 h. Representative of three independent experiments.



Extended Data Figure 10 | Tumour-intrinsic Pd-11 activation by 3'-UTR loss suppresses CD8⁺ cytotoxic T lymphocyte recruitment within the tumour microenvironment. **a**, Strategy for evaluating the effect of *Pd-11* 3'-UTR disruption on anti-tumour immunity. **b**, Representative immunofluorescence images (from experiments in Fig. 4c) of CD8 (green) and DAPI (purple) staining in mock- and sgPd-11-transfected EG7-OVA tumours treated with PBS or poly(I:C). **c**, Flow cytometric analysis

showing frequency of CD8⁺ T cells infiltrating into mock- and sgPd-11-transfected EG7-OVA tumours treated with PBS or poly(I:C) ($n = 6$ per group; Welch's t -test). Data represent mean \pm s.e.m. **d**, Flow cytometric analysis showing frequency of CD8⁺ T cells infiltrating into sgPd-11-transfected, poly(I:C)-treated EG7-OVA tumours treated with isotype control or anti-Pd-11 antibody ($n = 7$ per group; Welch's t -test). Data represent mean \pm s.e.m.

Image-based detection and targeting of therapy resistance in pancreatic adenocarcinoma

Raymond G. Fox^{1,2,3,4*}, Nikki K. Lytle^{1,2,3,4*}, Dawn V. Jaquish^{4,5}, Frederick D. Park^{1,2,3,4,6}, Takahiro Ito^{1,2,3,4}, Jeevisha Bajaj^{1,2,3,4}, Claire S. Koechlein^{1,2,3,4}, Bryan Zimdahl^{1,2,3,4}, Masato Yano^{7†}, Janel L. Kopp^{3,8}, Marcie Kritzik^{1,2,3,4}, Jason K. Sicklick^{4,5}, Maike Sander^{3,8}, Paul M. Grandgenett⁹, Michael A. Hollingsworth⁹, Shinsuke Shibata⁷, Donald Pizzo¹⁰, Mark A. Valasek¹⁰, Roman Sasik¹¹, Miriam Scadeng¹², Hideyuki Okano⁷, Youngsoo Kim¹³, A. Robert MacLeod¹³, Andrew M. Lowy^{4,5} & Tannishtha Reya^{1,2,3,4}

Pancreatic intraepithelial neoplasia is a pre-malignant lesion that can progress to pancreatic ductal adenocarcinoma, a highly lethal malignancy marked by its late stage at clinical presentation and profound drug resistance¹. The genomic alterations that commonly occur in pancreatic cancer include activation of KRAS2 and inactivation of p53 and SMAD4 (refs 2–4). So far, however, it has been challenging to target these pathways therapeutically; thus the search for other key mediators of pancreatic cancer growth remains an important endeavour. Here we show that the stem cell determinant Musashi (Msi) is a critical element of pancreatic cancer progression both in genetic models and in patient-derived xenografts. Specifically, we developed Msi reporter mice that allowed image-based tracking of stem cell signals within cancers, revealing that Msi expression rises as pancreatic intraepithelial neoplasia progresses to adenocarcinoma, and that Msi-expressing cells are key drivers of pancreatic cancer: they preferentially harbour the capacity to propagate adenocarcinoma, are enriched in circulating tumour cells, and are markedly drug resistant. This population could be effectively targeted by deletion of either Msi1 or Msi2, which led to a striking defect in the progression of pancreatic intraepithelial neoplasia to adenocarcinoma and an improvement in overall survival. Msi inhibition also blocked the growth of primary patient-derived tumours, suggesting that this signal is required for human disease. To define the translational potential of this work we developed antisense oligonucleotides against Msi; these showed reliable tumour penetration, uptake and target inhibition, and effectively blocked pancreatic cancer growth. Collectively, these studies highlight Msi reporters as a unique tool to identify therapy resistance, and define Msi signalling as a central regulator of pancreatic cancer.

To understand the mechanisms that underlie pancreatic cancer development and progression, we investigated signals that control self-renewal, a key stem cell property often hijacked in cancer. In particular, we focused on the role of Msi, a highly conserved RNA binding protein originally identified in *Drosophila*⁵. While Msi has long been used as a marker of stem/progenitor cells⁶, the breadth of its functional impact is only beginning to emerge: genetic loss-of-function models have shown that Msi signalling is important for maintaining stem cells in the mammalian nervous system⁷, and more recently in normal and malignant haematopoiesis^{8–12}. However, the role of Msi in

pancreatic cancer biology and whether it may be a viable therapeutic target remains unknown.

To address these questions, we first analysed MSI expression in human pancreatic cancers. MSI1 and MSI2 were expressed in all primary tumour samples analysed, with expression increasing during progression (Extended Data Fig. 1). To track the function of Msi-expressing cells, we developed Msi knock-in reporters (Reporter for Musashi, REM) in which fluorescent signals reflected endogenous Msi expression (Fig. 1a, b, Extended Data Fig. 2a–c and ref. 31). To define whether Msi-expressing cells contribute to pancreatic cancer, we crossed REM mice to the *Kras*^{LSL-G12D/+}; *p53*^{f/f}; *Ptfla*^{CRE/+} model^{13–15} (Extended Data Fig. 2d–h). *In vivo* imaging of living tumours revealed clear Msi1 and Msi2 reporter activity within remarkable spatially restricted domains frequently surrounded by blood vessels (Fig. 1c, d, Extended Data Fig. 2i and Supplementary Video 1). Cells with high levels of Msi reporter expression were rare, and detected in 1.18% and 9.7% of REM1 and REM2 cancers, respectively (Fig. 1e, f). Because cancer stem cells can be similarly rare^{16,17}, we tested if Msi-expressing cells have preferential capacity for tumour propagation¹⁸. Consistent with this possibility, Msi⁺ cells expressed ALDH¹⁹, and were dramatically more tumorigenic *in vitro* and *in vivo* (Fig. 1g–i and Extended Data Fig. 3a–g). Most importantly, Msi2⁺ cells were highly lethal: while 100% of mice orthotopically transplanted with Msi2⁺ cells developed invasive tumours and died, none of the mice receiving Msi2[−] cells showed signs of disease (Fig. 1j and Extended Data Fig. 3h). Given the suggestion that certain markers may not consistently enrich for tumour propagating ability²⁰, our findings indicate that Msi expression can identify cancer stem cells at least in some contexts, and that Msi2⁺ cells preferentially drive pancreatic cancer growth, invasion, and lethality.

Msi2⁺ cells also represented a high proportion of circulating tumour cells, and were more tumorigenic than Msi2[−] circulating tumour cells (Fig. 1k, l). While this suggests that Msi2⁺ circulating tumour cells may pose a greater risk for tumour dissemination²¹, the fact that Msi was not consistently elevated in metastatic patient samples analysed leaves open the question of its role in metastasis. The Msi reporter also provided an opportunity to define if it could be used to identify therapy resistance. Exposure to gemcitabine led to preferential survival of Msi2⁺ cells even at high doses (Fig. 1m, n and Extended Data Fig. 3i–k). These experiments show that Msi2⁺ cells are a predominant gemcitabine-resistant population, and suggest Msi reporters could

¹Department of Pharmacology, University of California San Diego School of Medicine La Jolla, California 92093, USA. ²Department of Medicine, University of California San Diego School of Medicine La Jolla, California 92093, USA. ³Sanford Consortium for Regenerative Medicine, La Jolla, California 92037, USA. ⁴Moore's Cancer Center, University of California San Diego School of Medicine, La Jolla, California 92093, USA. ⁵Department of Surgery, Division of Surgical Oncology, University of California San Diego School of Medicine, La Jolla, California 92093, USA.

⁶Department of Medicine, Division of Gastroenterology, University of California San Diego School of Medicine, La Jolla, California 92093, USA. ⁷Department of Physiology, Keio University School of Medicine, Tokyo 160-8582, Japan. ⁸Department of Cellular and Molecular Medicine, University of California San Diego School of Medicine, La Jolla, California 92093, USA. ⁹Eppley Institute for Research in Cancer and Allied Diseases, Department of Pathology, University of Nebraska Medical Center, Omaha, Nebraska 68198, USA. ¹⁰Department of Pathology, University of California San Diego School of Medicine, La Jolla, California 92093, USA. ¹¹Center for Computational Biology and Bioinformatics, University of California San Diego School of Medicine, La Jolla, California 92093, USA. ¹²Department of Radiology, University of California San Diego School of Medicine, La Jolla, California 92093, USA. ¹³Department of Oncology Drug Discovery, Ionis Pharmaceuticals, Carlsbad, California 92010, USA. [†]Present address: Division of Neurobiology and Anatomy, Graduate School of Medical and Dental Sciences, Niigata University, Asahimachidori, Chuo-ku, Niigata 951-8510, Japan.

*These authors contributed equally to this work.

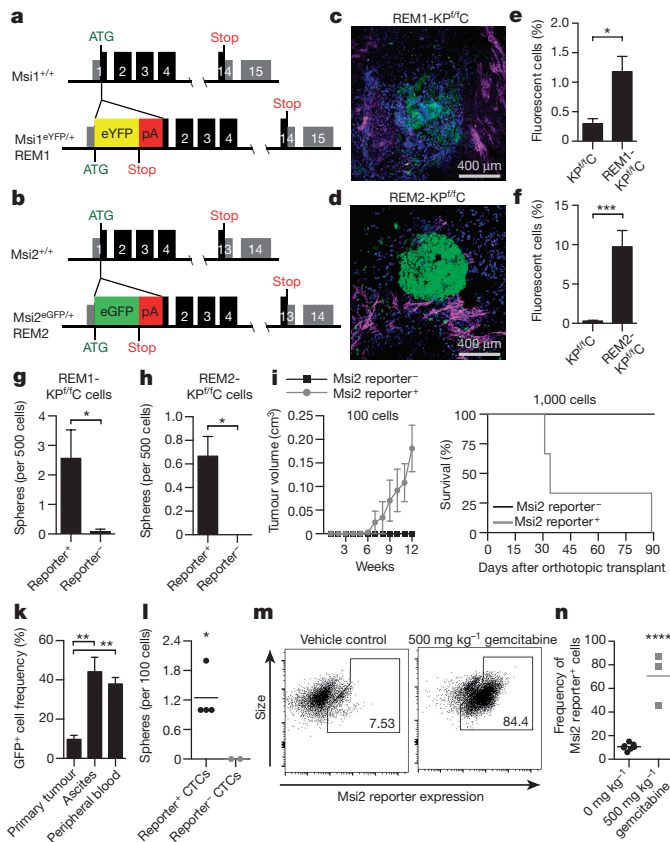


Figure 1 | Msi reporter⁺ pancreatic cancer cells are enriched for tumour-initiating capacity. **a, b**, Design of Msi reporter constructs (REM1, Msi1^{eYFP/+}; REM2, Msi2^{eGFP/+}). **c, d**, Live images of Msi reporter cells in (c) REM1-KP^{fl/c} and (d) REM2-KP^{fl/c} tumours; VE-cadherin (magenta), Hoechst (blue), Msi reporter (green). **e, f**, Msi1 and Msi2 reporter expression in dissociated tumours ($n = 6$). **g, h**, Sphere-forming ability of Msi2 reporter⁺ and reporter⁻ cells ($n = 8$; **g**, $n = 8$; **h**, $n = 6$). **i**, *In vivo* growth of Msi2 reporter⁺ tumour cells ($n = 8$). **j**, Survival of mice orthotopically transplanted with Msi2 reporter⁺ and reporter⁻ KP^{fl/c} tumour cells ($n = 6$). Log-rank (Mantel–Cox) survival analysis ($P < 0.05$). **k**, Reporter frequency in primary tumours ($n = 3$), and circulating tumour cells from ascites ($n = 3$) or peripheral blood ($n = 4$). **l**, Average frequency of tumour-spheres from Msi2 reporter⁺ and reporter⁻ circulating tumour cells ($n = 2$ –4 technical replicates). **m, n**, Reporter frequency in REM2-KP^{fl/c} mice treated with vehicle or 500 mg per kg (body weight) gemcitabine ($n = 6$). Data are represented as mean \pm s.e.m. * $P < 0.05$, ** $P < 0.01$, *** $P < 0.001$, **** $P < 0.0001$ by Student's *t*-test or one-way analysis of variance (ANOVA). Source data for all panels are available online.

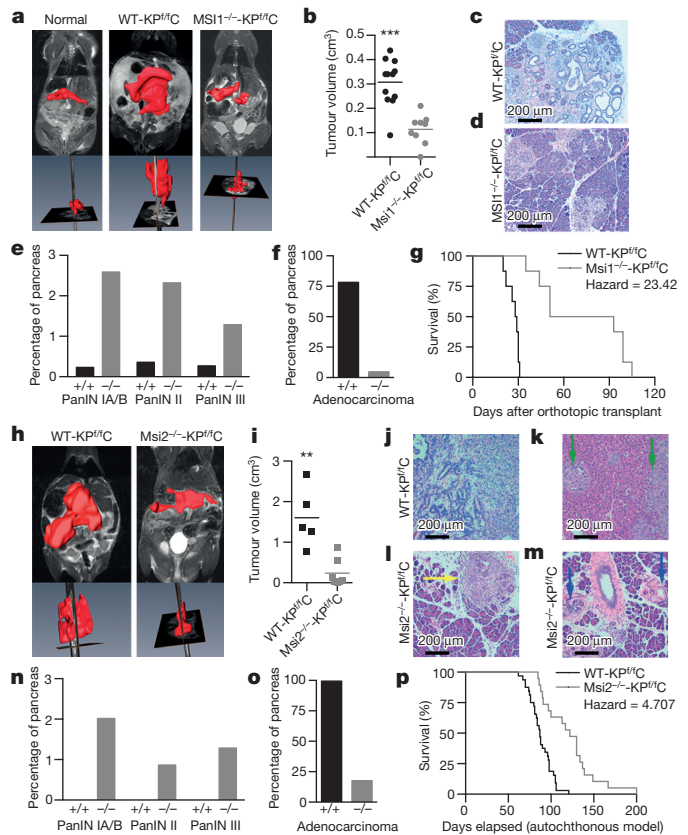


Figure 2 | Loss of Msi1 or Msi2 impairs tumour initiation and progression in a genetic mouse model of pancreatic cancer. **a**, Coronal and sagittal MRI images of normal, WT-KP^{fl/c}, and Msi1^{-/-}-KP^{fl/c} mice with three-dimensional volume rendering of tumour mass (red). **b**, Average volumes of isolated WT-KP^{fl/c} ($n = 13$) and Msi1^{-/-}-KP^{fl/c} tumours ($n = 9$). **c, d**, Histology and (e, f) quantification of PanIN and/or adenocarcinoma areas in WT-KP^{fl/c} and Msi1^{-/-}-KP^{fl/c} tumours. **g**, Survival of mice orthotopically grafted with Msi1^{-/-}-KP^{fl/c} or WT-KP^{fl/c} tumours ($n = 16$). Analysis of Msi1^{-/-}-KP^{fl/c} tumours (**h**) by MRI and (i) after isolation, WT-KP^{fl/c} ($n = 5$), Msi1^{-/-}-KP^{fl/c} ($n = 7$). **j–m**, Histology of WT-KP^{fl/c} and Msi1^{-/-}-KP^{fl/c} pancreatic tumours ($\times 40$ magnification); **k**, adenocarcinoma, liver invasion (green arrows); **l**, adenocarcinoma (yellow arrows); **m**, PanINs (blue arrows). **n, o**, Quantification of PanIN and/or adenocarcinoma areas in WT-KP^{fl/c} and Msi1^{-/-}-KP^{fl/c} tumours ($n = 6$). **p**, Survival of autochthonous Msi1^{-/-}-KP^{fl/c} ($n = 19$) or WT-KP^{fl/c} ($n = 32$) mice. Log-rank (Mantel–Cox) survival analysis ($P < 0.0001$). Data represented as mean \pm s.e.m. ** $P < 0.01$, *** $P < 0.001$ by Student's *t*-test. Source data for all panels are available online.

serve as a tool to visualize drug-resistant cells, and identify therapies to target them.

Because Msi expression rose during progression (Extended Data Figs 1f–k and 4a), and marked therapy-resistant cells, we tested if genetic or pharmacological targeting of Msi could eradicate this ‘high risk’ population. Deletion of Msi1 led to a fivefold reduction in tumour volume by magnetic resonance imaging (MRI) (Fig. 2a, b, Extended Data Fig. 4b and Supplementary Videos 2–4). Histologically, adenocarcinoma areas comprised 67% of wild-type (WT)-KP^{fl/c} but less than 10% of Msi1^{-/-}-KP^{fl/c} pancreata; further, while Msi1 loss allowed low-grade pancreatic intraepithelial neoplasias (PanINs) to form, it largely blocked progression to adenocarcinoma (Fig. 2c–f and Extended Data Fig. 4c, d). Finally, Msi1 deletion improved survival in orthotopic grafts: median survival for WT-KP^{fl/c} graft recipients was 28.5 days, and for Msi1^{-/-}-KP^{fl/c} grafts was 70.5 days, representing a 2.5-fold increase in survival time and a 23-fold decrease in risk of death (Fig. 2g).

Because both Msi1 and Msi2 are expressed in pancreatic cancer, we also analysed the impact of deleting Msi2 (ref. 9). MRI showed

no detectable tumour mass in most Msi2^{-/-}-KP^{fl/c} mice (Fig. 2h, i, Extended Data Fig. 4e and Supplementary Videos 2, 5 and 6). Histologically, KP^{fl/c} pancreata were mostly replaced by adenocarcinoma, often accompanied by extracapsular invasion into surrounding structures; in contrast, Msi2^{-/-}-KP^{fl/c} pancreata contained low-grade PanIN with rare high-grade PanIN and microscopic foci of adenocarcinoma within predominantly normal tissue (Fig. 2j–o). Median survival, tracked in the autochthonous model, was 122 days for Msi2^{-/-}-KP^{fl/c} versus 87 days for WT-KP^{fl/c} mice (Fig. 2p), representing a fourfold decreased risk of death. Collectively, our data show that Msi inhibition markedly improves disease trajectory, leading to an approximate doubling of survival. The fact that the mice ultimately succumbed to disease is probably due to the strong selection for Msi-expressing escaper cells in Msi1 and Msi2 single, or double, knockout mice (Extended Data Fig. 5). Additionally, some redundancy between Msi1 and Msi2, as well as a partial gene fragment present in Msi1^{-/-} mice (data not shown), may also exert compensatory activity.

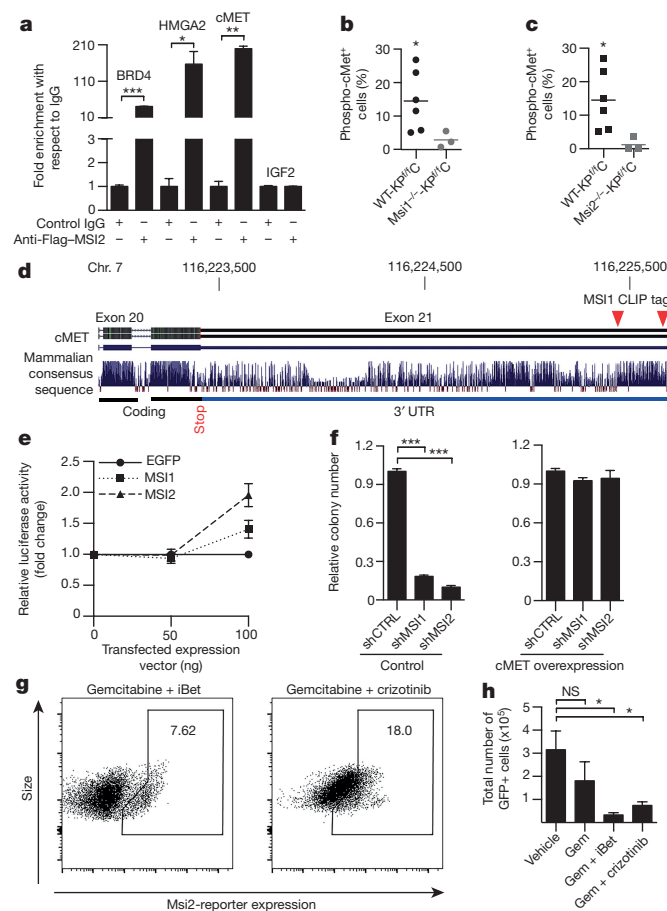


Figure 3 | Msi controls expression of key oncogenic and epigenetic signals. **a**, Msi RIP-PCR for indicated transcripts. **b**, **c**, Frequency of phospho-cMet⁺ cells in WT-KP^{flC}, Msi1^{-/-}-KP^{flC}, and Msi2^{-/-}-KP^{flC} mice (**b**, $n = 8$; **c**, $n = 6$). **d**, Schematic of cMET exons and 3' UTR. CLIP tags (red triangles) indicate MSI1 binding in 3' UTR. **e**, cMET 3' UTR luciferase reporter activity in the presence or absence of MSI1 or MSI2 ($n = 3$ independent experiments). **f**, Colony formation of MSI1 or MSI2 knockdown cells with or without cMET ($n = 4$ independent experiments). **g**, **h**, Fluorescence-activated cell sorting (FACS) analysis of tumours from gemcitabine-treated REM2-KP^{flC} mice, in the presence or absence of crizotinib and iBet762; vehicle ($n = 7$), gemcitabine ($n = 3$), gemcitabine + iBet762 ($n = 3$), gemcitabine + crizotinib ($n = 3$). Data represented as mean \pm s.e.m. * $P < 0.05$, ** $P < 0.01$, *** $P < 0.001$ by Student's t -test or one-way ANOVA. NS, not significant. Source data for all panels are available online.

To understand the molecular basis of the effects of Msi loss, we genomically profiled Msi deficient tumour cells (Extended Data Figs 6 and 7a–d). Msi loss led to downregulation of many key genes, including regulators of stem cell function (*Wnt7a*, *Aldh*, *Lin28*), proto-oncogenes (*cMet*, *Fos*, *Fyn*) and Regenerating (*Reg*) family genes, linked to gastrointestinal cancers. Among these, analysis of 3' untranslated regions (UTRs) for Msi binding sites and RNA immunoprecipitation (RIP)-qPCR identified *BRD4*, *cMET*, and *HMGA2* as potential direct targets (Fig. 3a and Extended Data Fig. 7e). We focused on cMET²², which was diminished in Msi null pancreatic cancer and bound MSI1 in ultraviolet-cross-linked immunoprecipitation followed by sequencing (CLIP-seq) experiments (Fig. 3b–d and Extended Data Fig. 7f, g). cMET could not only be activated molecularly by MSI but also effectively complemented MSI loss (Fig. 3e, f and Extended Data Fig. 7h). While these results suggest that cMet is a direct functional target of Msi, it is almost certainly one of many. In fact, the powerful impact of Msi on cancer is probably because of its ability to control a broad range of programs (Extended Data Fig. 6). In this context, *BRD4* and *HMGA2* may represent a particularly attractive class of targets^{23,24},

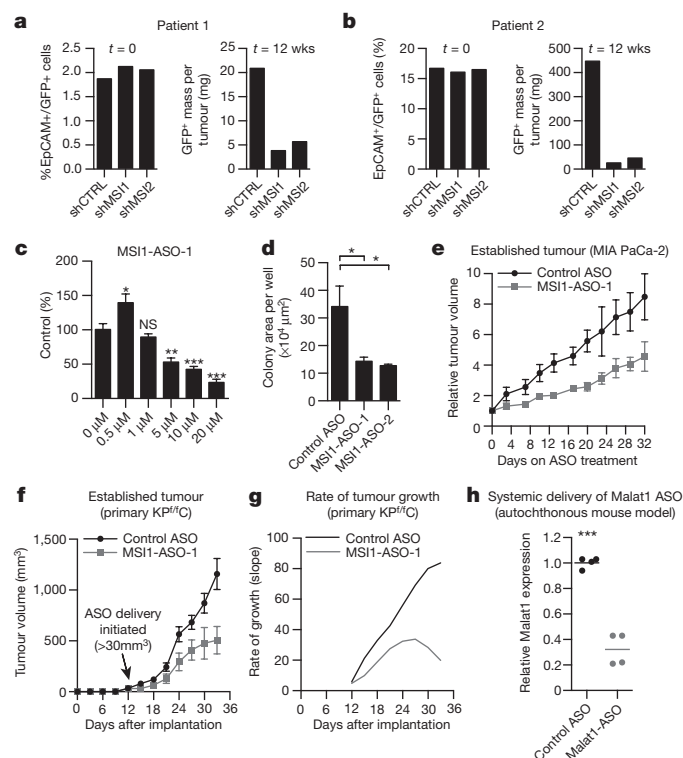


Figure 4 | Targeting MSI inhibits pancreatic cancer growth in patient-derived xenografts. **a**, **b**, Frequency of green fluorescent protein-positive (GFP⁺) tumour cells before and after transplantation. **c**, MSI1 expression after MSI1-ASO free uptake in human pancreatic cancer line ($n = 3$ independent experiments per dose). **d**, Colony formation of control or MSI1-ASO-treated human pancreatic cancer line ($n = 3$ independent experiments). **e**, *In vivo* growth of human cell-line-derived tumours in control or MSI1-ASO treated mice ($n = 10$). **f**, Relative tumour volume and (**g**) rate of growth of KP^{flC}-derived tumours in control or MSI1-ASO-treated mice ($n = 8$). **h**, Malat1 expression in autochthonous KP^{flC} tumours after systemic delivery of control or lead-optimized Malat1-ASO ($n = 6$). Data represented as mean \pm s.e.m. * $P < 0.05$, ** $P < 0.01$, *** $P < 0.001$ by one-way ANOVA. NS, not significant. Source data for all panels are available online.

as they could act at an epigenetic level with cMet to collectively mediate Msi function. Emphasizing such a potential convergence of epigenetic and oncogenic pathways, inhibitors of both *Brd4* and *cMet* effectively targeted gemcitabine-resistant Msi2⁺ cells (Fig. 3g, h).

To complement the mouse models, we tested the impact of MSI inhibition on primary patient samples, which harbour more complex mutations, and are uniformly drug resistant. Primary pancreatic cancer cells were infected with MSI short hairpin RNAs (shRNAs) and implanted as xenografts (Extended Data Fig. 8a). While shMSI cells were equivalently present at time of transplant, their ability to contribute to the tumour mass *in vivo* was reduced by 4.9- to 6.5-fold (Fig. 4a, b and Extended Data Fig. 8b, c), demonstrating that inhibition of either MSI1 or MSI2 results in marked suppression of primary human pancreatic cancer growth. Interestingly, MSI2 expression was more homogeneous in patients than in mouse models (Extended Data Figs 1a, b and 2d, e). This could be a consequence of selection due to treatment and end-stage disease in patients, or because MSI2 patterns differ between mouse models and human disease. However, regardless of the level of heterogeneity, our loss-of-function studies indicate that the mouse and human disease are both highly dependent on Msi signalling.

Given that inhibition of Msi has profound effects on pancreatic cancer progression, we explored its potential as a therapeutic target by developing antisense oligonucleotides (ASOs)^{25,26} specific for MSI1. Because ASO inhibitors are designed on the basis of target RNA sequences, they can be a powerful approach for inhibiting proteins such

as Msi, considered 'undruggable' by traditional approaches²⁷. Of 400 candidate MSI1-ASOs screened, the two most potent markedly reduced colony formation, as well as human cell line and KP^{fl/c} derived tumour growth *in vivo* (Fig. 4c–g and Extended Data Fig. 8d, e). The MSI1-ASOs have not yet been lead-optimized, a longer-term process designed to maximize therapeutic level efficacy with systemic delivery. To test if a lead-optimized ASO can penetrate the tumour microenvironment, a lead-optimized ASO against Malat1 was delivered intraperitoneally and was effective in knocking down its target both in stem and in non-stem cell fractions (Fig. 4h and Extended Data Fig. 8f–j). These studies provide proof-of-principle that deliverable Msi inhibitors can antagonize pancreatic cancer growth *in vivo*, and suggest that ASOs should be explored further as a new class of therapeutics in this disease.

The Msi reporters we describe here may be broadly applicable for cancer diagnostic and therapeutic studies. Because Msi reporter activity can be visualized through live imaging, these mice can be used to track cancer stem cells *in vivo*, and provide a dynamic view of cancer growth and dissemination within the native microenvironment. The fact that reporter⁺ cells are gemcitabine resistant raises the exciting possibility that this could serve as a platform to visualize resistance *in vivo*. Integration of such reporters during drug development may provide a powerful complement to conventional screens, and allow identification of therapies that can better target drug-resistant disease. Further, the spatially restricted distribution of Msi⁺ cells could have important implications for designing strategies to loco-regionally target cells that drive residual disease and relapse.

One of the biggest disappointments in pancreatic cancer therapy has been the failure of targeted agents to make a meaningful impact. Our data demonstrate that Msi function is critical for growth and progression of pancreatic cancer, and Msi therefore represents an attractive therapeutic target. We also show that cell-penetrating ASOs are able to antagonize Msi and inhibit growth of pancreatic cancer. These findings highlight the value of targeting Msi, and suggest that ASOs^{27–30} and other antagonists should be developed for pancreatic and other cancers marked by high Msi expression. Finally, the rise of Msi in pancreatitis (Extended Data Fig. 9) raises the possibility that Msi inhibition could serve as a strategy to decrease the risk of developing pancreatic cancer. In the long term, blocking Msi signalling could provide a new approach to controlling cancer establishment, progression, and therapy resistance.

Online Content Methods, along with any additional Extended Data display items and Source Data, are available in the online version of the paper; references unique to these sections appear only in the online paper.

Received 15 September 2015; accepted 7 April 2016.

Published online 6 June 2016.

1. Yachida, S. & Iacobuzio-Donahue, C. A. The pathology and genetics of metastatic pancreatic cancer. *Arch. Pathol. Lab. Med.* **133**, 413–422 (2009).
2. Almoguer, C. *et al.* Most human carcinomas of the exocrine pancreas contain mutant c-K-ras genes. *Cell* **53**, 549–554 (1988).
3. Hahn, S. A. *et al.* DPC4, a candidate tumor suppressor gene at human chromosome 18q21.1. *Science* **271**, 350–353 (1996).
4. Redston, M. S. *et al.* p53 mutations in pancreatic carcinoma and evidence of common involvement of homocopolymer tracts in DNA microdeletions. *Cancer Res.* **54**, 3025–3033 (1994).
5. Nakamura, M., Okano, H., Blendy, J. A. & Montell, C. Musashi, a neural RNA-binding protein required for *Drosophila* adult external sensory organ development. *Neuron* **13**, 67–81 (1994).
6. Okano, H., Imai, T. & Okabe, M. Musashi: a translational regulator of cell fate. *J. Cell Sci.* **115**, 1355–1359 (2002).
7. Sakakibara, S. *et al.* RNA-binding protein Musashi family: roles for CNS stem cells and a subpopulation of ependymal cells revealed by targeted disruption and antisense ablation. *Proc. Natl Acad. Sci. USA* **99**, 15194–15199 (2002).
8. Hope, K. J. *et al.* An RNAi screen identifies Msi2 and Prox1 as having opposite roles in the regulation of hematopoietic stem cell activity. *Cell Stem Cell* **7**, 101–113 (2010).
9. Ito, T. *et al.* Regulation of myeloid leukaemia by the cell-fate determinant Musashi. *Nature* **466**, 765–768 (2010).
10. Kharas, M. G. *et al.* Musashi-2 regulates normal hematopoiesis and promotes aggressive myeloid leukemia. *Nature Med.* **16**, 903–908 (2010).

11. Kwon, H. Y. *et al.* Tetraspanin 3 is required for the development and propagation of acute myelogenous leukemia. *Cell Stem Cell* **17**, 152–164 (2015).
12. de Andrés-Aguayo, L. *et al.* Musashi 2 is a regulator of the HSC compartment identified by a retroviral insertion screen and knockout mice. *Blood* **118**, 554–564 (2011).
13. Hingorani, S. R. *et al.* Preinvasive and invasive ductal pancreatic cancer and its early detection in the mouse. *Cancer Cell* **4**, 437–450 (2003).
14. Kawaguchi, Y. *et al.* The role of the transcriptional regulator Ptf1a in converting intestinal to pancreatic progenitors. *Nature Genet.* **32**, 128–134 (2002).
15. Tuveson, D. A. *et al.* Endogenous oncogenic K-ras(G12D) stimulates proliferation and widespread neoplastic and developmental defects. *Cancer Cell* **5**, 375–387 (2004).
16. Reya, T., Morrison, S. J., Clarke, M. F. & Weissman, I. L. Stem cells, cancer, and cancer stem cells. *Nature* **414**, 105–111 (2001).
17. Wang, J. C. & Dick, J. E. Cancer stem cells: lessons from leukemia. *Trends Cell Biol.* **15**, 494–501 (2005).
18. Hermann, P. C. *et al.* Distinct populations of cancer stem cells determine tumor growth and metastatic activity in human pancreatic cancer. *Cell Stem Cell* **1**, 313–323 (2007).
19. Kim, M. P. *et al.* ALDH activity selectively defines an enhanced tumor-initiating cell population relative to CD133 expression in human pancreatic adenocarcinoma. *PLoS ONE* **6**, e20636 (2011).
20. Dosch, J. S., Ziemke, E. K., Shettigar, A., Rehmetulla, A. & Sebolt-Leopold, J. S. Cancer stem cell marker phenotypes are reversible and functionally homogeneous in a preclinical model of pancreatic cancer. *Cancer Res.* **75**, 4582–4592 (2015).
21. Rhim, A. D. *et al.* EMT and dissemination precede pancreatic tumor formation. *Cell* **148**, 349–361 (2012).
22. Li, C. *et al.* c-Met is a marker of pancreatic cancer stem cells and therapeutic target. *Gastroenterology* **141**, 2218–2227 (2011).
23. Belkina, A. C. & Denis, G. V. BET domain co-regulators in obesity, inflammation and cancer. *Nature Rev. Cancer* **12**, 465–477 (2012).
24. Cleynen, I. & Van de Ven, W. J. The HMGA proteins: a myriad of functions (review). *Int. J. Oncol.* **32**, 289–305 (2008).
25. Hung, G. *et al.* Characterization of target mRNA reduction through in situ RNA hybridization in multiple organ systems following systemic antisense treatment in animals. *Nucleic Acid Ther.* **23**, 369–378 (2013).
26. Seth, P. P. *et al.* Short antisense oligonucleotides with novel 2'-4' conformationally restricted nucleoside analogues show improved potency without increased toxicity in animals. *J. Med. Chem.* **52**, 10–13 (2009).
27. Li, N., Li, Q., Tian, X. Q., Qian, H. Y. & Yang, Y. J. Mipomersen is a promising therapy in the management of hypercholesterolemia: a meta-analysis of randomized controlled trials. *Am. J. Cardiovasc. Drugs* **14**, 367–376 (2014).
28. Hong, D. *et al.* AZD9150, a next-generation antisense oligonucleotide inhibitor of STAT3 with early evidence of clinical activity in lymphoma and lung cancer. *Sci. Transl. Med.* **7**, 314ra185 (2015).
29. Lee, R. G., Crosby, J., Baker, B. F., Graham, M. J. & Crooke, R. M. Antisense technology: an emerging platform for cardiovascular disease therapeutics. *J. Cardiovasc. Transl. Res.* **6**, 969–980 (2013).
30. Saad, F. *et al.* Randomized phase II trial of custirsen (OGX-011) in combination with docetaxel or mitoxantrone as second-line therapy in patients with metastatic castrate-resistant prostate cancer progressing after first-line docetaxel: CUOG trial P-06c. *Clin. Cancer Res.* **17**, 5765–5773 (2011).
31. Koehnle, C. S. *et al.* High resolution imaging and computational analysis of hematopoietic cell dynamics in vivo. *Nature Comm.* (in the press).

Supplementary Information is available in the online version of the paper.

Acknowledgements We are grateful to I. Verma, M. Karin, and D. Cheresch for advice and comments on the manuscript, A. Luo and T. Wang for technical support, G. Yeo for advice on Msi targeting, K. Jenne for advice on MRI imaging, N. Patel and P. Mischel for reagents and experimental advice, and E. O'Conner and K. Marquez for cell sorting. R.F. is a recipient of a California Institute for Regenerative Medicine interdisciplinary stem cell training program fellowship and received support from T32 HL086344 and T32 CA009523. C.K. received support from T32 GM007752, N.K.L. received support from T32 GM007752 and a National Research Service Award F31 CA206416, J.L.K. received support from National Institutes of Health (NIH)-F32CA136124 and an Advanced Postdoctoral Fellowship from the Juvenile Diabetes Research Foundation, and B.Z. received support from T32 GM007184-33 (Duke University). F.P. is a recipient of a California Institute for Regenerative Medicine interdisciplinary stem cell training program fellowship and the University of California San Diego Clinical and Translational Research Institute KL2 Award. T.I. is the recipient of a California Institute for Regenerative Medicine interdisciplinary stem cell training program fellowship, J.B. is supported by a postdoctoral fellowship from National Cancer Center, and T.R. was supported in part by a Leukemia and Lymphoma Society Scholar Award. P.M.G. and M.A.H. are supported by a Specialized Program of Research Excellence (SPORE) in Pancreatic Cancer, CA127297, a TMEN Tumor Microenvironment Network U54, a National Cancer Institute Cancer Center Support Grant P30 CA36727, and an Early Detection Research Network (EDRN) U01 CA111294. M.Sa. is supported by NIH DK078803 and NIH CA194839. J.K.S. is supported by NIH K08CA168999. R.S. is supported by the Clinical and Translational Research Institute (CTRI) grant UL1TR001442,

and A.M.L. is supported by donations from Ride the Point. This work was also supported by CA155620 to A.M.L., DK63031, HL097767, DP1 CA174422, and R35 CA197699 to T.R., and CA186043 to A.M.L. and T.R.

Author Contributions R.F. designed and performed all experiments related to Msi expression and deletion, whole genome and target analysis, and ASO delivery in pancreatic cancer; N.K.L. designed and performed all live imaging of Msi reporter pancreatic tumours, and provided functional analysis of cancer stem cells, circulating tumour cells, and therapy resistance; R.F., N.K.L., and M.K. helped write the paper; D.V.J. performed histological analysis, and provided mouse and xenograft models; F.P., T.I., J.B., C.K., and B.Z. provided experimental data and advice; R.S. performed all bioinformatics analysis; M.Y., S.S., and H.O. provided Msi1^{-/-} mice and CLIP-seq analysis; M.V. and D.P. performed pathology/in situ hybridization

analysis; M.Sc. performed MRI analysis; J.K. and M. Sa. provided experimental advice, tumour samples, and mouse models; J.S., A.M.L., M.V., P.A.G., and M.A.H. provided patient samples; Y.K. and R.M. designed, synthesized, and screened MSI ASOs, and provided advice on ASO-related experiments. A.M.L. and T.R. conceived the project, planned and guided the research, and wrote the paper.

Author Information Microarray and RNA-seq data have been deposited in the Gene Expression Omnibus under accession numbers GSE73312 and GSE75797. Reprints and permissions information is available at www.nature.com/reprints. The authors declare competing financial interests: details are available in the online version of the paper. Readers are welcome to comment on the online version of the paper. Correspondence and requests for materials should be addressed to A.M.L. (alowy@ucsd.edu) or T.R. (treya@ucsd.edu).

METHODS

Mice. REM1 (*Msi1^{eYFP/+}*) and REM2 (*Msi2^{eGFP/+}*) reporter mice were generated by conventional gene targeting (Genoway; Fig. 1); all of the reporter mice used in experiments were heterozygous for the corresponding *Msi* allele. The *Msi1^{flf}* (*Msi1^{fllox/flox}*) mice were generated by conventional gene targeting by inserting LoxP sites around exons 1–4 (Genoway). The *Msi2* mutant mouse, B6; CB-*Msi2^{Gt(pU-21T)2lmg}* (*Msi2^{-/-}*) was established by gene trap mutagenesis as previously described⁹. H. Okano provided the *Msi1^{-/-}* mice as previously described⁷. The LSL-Kras G12D mouse, B6.129S4-Kras^{tm4Tyj}/J (stock number 008179), and the p53flox/flox mouse, B6.129P2-Trp53^{tm1Brn}/J (stock number 008462), were purchased from The Jackson Laboratory. M. Sander provided Ptf1a-Cre mice as previously described¹⁴. A. Lowy provided Pdx1-Cre mice as previously described¹³. Mice were bred and maintained in the animal care facilities at the University of California San Diego. All animal experiments were performed according to protocols approved by the University of California San Diego Institutional Animal Care and Use Committee. No sexual dimorphism was noted in any mouse model. Therefore, males and females were equally used for experimental purposes and both sexes are represented in all data sets.

Tumour analysis, tissue dissociation, and cell isolation. (A) Tumour wet weight was measured immediately following resection. Tumour volume was calculated using the standard modified ellipsoid formula $\frac{1}{2}(\text{length} \times \text{width}^2)$ (Figs 1i, 2b, 2i and 4e, f). (B) Mouse pancreatic tumours were washed in RPMI 1640 (Gibco, Life Technologies) and cut into 2–4 mm pieces immediately after resection. Dissociation into a single cell suspension was performed using a Miltenyi Biotec Mouse Tumour Dissociation Kit (130-096-730). Briefly, tumour pieces were collected into gentleMACS C tubes containing RPMI 1640 dissociation enzymes, and further homogenized using a gentleMACS Dissociator. Samples were incubated for 40 min at 37 °C under continuous rotation, then passed through a 70 µm nylon mesh (Corning). Red blood cells were lysed using RBC Lysis Buffer (eBioscience), and the remaining tumour cells were used for FACS analysis and cell sorting. (C) Freshly resected mouse brains were rinsed in PBS, placed in accutase (Life Technologies), and cut into <2 mm pieces. Samples were incubated for 15 min at 37 °C, then passed through a 70 µm nylon mesh (Corning). Red blood cells were lysed as above before FACS analysis and sorting of brain cells. (D) Bone marrow cells were suspended in HBSS (Gibco, Life Technologies) containing 5% FBS and 2 mM EDTA and were prepared for FACS analysis and sorting as previously described³². Analysis and cell sorting were performed on a FACS Aria III machine (Becton Dickinson), and data were analysed with FlowJo software (Tree Star).

Immunofluorescence and immunohistochemical staining. (A) Human primary pancreatic cancer tissues were fixed in 10% neutral buffered formalin and paraffin embedded at the Moores Cancer Center at University of California San Diego according to standard protocols. Sections (7 µm) were obtained and deparaffinized in xylene. The University of Nebraska Medical Center Rapid Autopsy Pancreas Program provided a second cohort of human primary pancreatic cancer tissues and matched liver metastases. Pancreatic cancer tissue from *KP^{flf}* mice were fixed in 4% paraformaldehyde and paraffin embedded at the University of California San Diego Histology and Immunohistochemistry Core at The Sanford Consortium for Regenerative Medicine according to standard protocols. Sections (5 µm) were obtained and de-paraffinized in xylene. Antigen retrieval was performed for 20–40 min in 95–100 °C 1 × citrate buffer, pH 6.0 (eBioscience). Sections were blocked in TBS or PBS containing 0.1% Triton X100 (Sigma-Aldrich), 10% goat or donkey serum (Sigma Aldrich), and 5% bovine serum albumin. (B) Single-cell suspensions from mouse pancreatic tumours and brain. Cells isolated by FACS were suspended in DMEM (Gibco, Life Technologies) supplemented with 50% FBS and adhered to slides by centrifugation at 42g. Twenty-four hours later, cells were fixed with 4% paraformaldehyde (USB Corporation), washed in PBS containing 0.1% Tween-20 (Sigma-Aldrich), and blocked with PBS containing 0.1% Triton X-100 (Sigma-Aldrich), 10% goat serum (Invitrogen), and 5% bovine serum albumin (Invitrogen). (C) Single-cell suspensions from mouse bone marrow. Cells were allowed to settle onto chambered cover glass (LabTek) coated with poly-L-lysine (Sigma) at 37 °C, fixed with 4% paraformaldehyde (USB Corporation), washed in 1 × Dako wash buffer (Dako), and blocked with Dako wash buffer containing 10% goat serum (Invitrogen). All incubations with primary antibodies were performed overnight at 4 °C. For immunofluorescent staining, incubation with Alexa Fluor-conjugated secondary antibodies (Molecular Probes) was performed for 1 h at 20–25 °C. 4',6-Diamidino-2-phenylindole (DAPI) (Molecular Probes) was used to detect DNA and images were obtained with a Confocal Leica TCS SP5 II (Leica Microsystems) or with a Nikon Eclipse E600 fluorescent microscope. For immunohistochemical staining, endogenous peroxidase was blocked by incubating slides in 3% H₂O₂ for 15 min before primary antibody. Incubation with biotinylated secondary antibodies (Vector Laboratories) was performed for 45 min at 20–25 °C. ImmPACT NovaRED Kit (Vector Laboratories) was used according to the manufacturer's protocol. Sections were counterstained with haematoxylin. The following

primary antibodies were used for human tissue sections: rabbit anti-Msi1 (Abcam, ab52865) 4 µg ml⁻¹; rabbit anti-Msi2 (Abcam, ab76148) 1 µg ml⁻¹; and mouse anti-Keratin (Abcam, ab8068) 1:20. The following primary antibodies were used to stain mouse tissues: rabbit anti-ALDH1 (Abcam, ab24343) 1:200; rabbit anti-cMet (Abcam, ab5662) 1:250; chicken anti-GFP (Abcam, ab13970) 1:250 (for pancreatic tumours and brain) or 1:200 (for bone marrow); rabbit anti-Msi2 (Abcam, ab76148) 1:500 (for pancreatic tumours and brain) or 1:200 (for bone marrow); rat anti-Ki67 (eBioscience, 14-5698) 1:1,000; rat anti-Msi1 (eBioscience, 14-9896-82) 1:500; mouse anti-Keratin (Abcam, ab8068) 1:10; and biotinylated DBA (Vector Laboratories, B-1035) 1:1,000.

Pancreatic tumoursphere formation assay. (A) Pancreatic tumoursphere formation assays were performed on freshly isolated mouse pancreatic tumour cells or circulating tumour cells from peripheral blood modified from ref. 33. Briefly, pancreatic tumours from 10- to 13-week-old REM1-KP^{flf}/C or REM2-KP^{flf}/C mice were dissociated and FACS sorted for YFP⁺ and YFP⁻ or EpCAM⁺/GFP⁺ and EpCAM⁺/GFP⁻ cells, respectively. One hundred to 500 cells were suspended in 100 µl DMEM F-12 (Gibco, Life Technologies) containing 1 × B-27 supplement (Gibco, Life Technologies), 3% FBS, 100 µM β-mercaptoethanol (Gibco, Life Technologies), 1 × non-essential amino acids (Gibco, Life Technologies), 1 × N2 supplement (Gibco, Life Technologies), 20 ng ml⁻¹ EGF (Gibco, Life Technologies), 20 ng ml⁻¹ FGF₂ (Gibco, Life Technologies), and 10 ng ml⁻¹ ESGRO mLIF (Millipore). Culture medium for circulating tumour cells also contained 20 ng ml⁻¹ mHGF (R&D Systems). Cells in medium were plated in 96-well ultra-low adhesion culture plates (Costar) and incubated at 37 °C for 7 days. Sphere images were obtained with a Nikon 80i fluorescence microscope. Sphere size was measured using ImageJ software version 1.47.

Lentiviral constructs and production. shRNA constructs were designed and cloned into plenti-hU6BX vector with a GFP tag by Cologentics. The target sequences were 5'-CCCAGATAGCCTTAGAGACTAT-3' for MSI1, 5'-CCCA GATAGCCTTAGAGACTAT-3' for MSI2, and 5'-CTGTGCCAGAGTCCTT CGATAG-3' for the control scrambled sequence. Additional (shRNA) target sequences were cloned into a plenti-FG12 vector with a TomatoRed tag. These target sequences were 5'-ATGAGTTAGATTCCAAGACGAT-3' for MSI2 and 5'-AGGAT TCCAATTCAGCGGGAGC-3' for the control scrambled sequence. Virus was produced in 293T cells transfected with plenti-shRNA constructs along with pRSV/REV, pMDLg/pRRE, and pHCMVG constructs. Viral supernatants were collected for 3 days followed by ultracentrifugation concentration at 50,000g for 2 h.

Agarose colony formation assays. MIA PaCa-2, Panc-1, Capan-2, and HPAC human pancreatic cancer cell lines were purchased from American Type Culture Collection, and cultured in the appropriate growth media as recommended by American Type Culture Collection. ASPC1, FG, and AA0779E human pancreatic cancer cell lines were provided by A. Lowy, and grown in DMEM containing 10% FBS, 1 × Glutamax, and 1 × penicillin and streptomycin. Human pancreatic cancer cell lines were infected with GFP-tagged or TomatoRed-tagged lentiviral particles containing shRNAs for MSI1, MSI2, and a scrambled control. Positively infected cells were sorted 72 h after transduction. For colony assays, 24-well plates were first coated with 0.6% agarose in DMEM without supplements. Cells were plated at a density of 2,000 cells per well in 0.3% agarose containing DMEM, 10% FBS, NEAA, penicillin and streptomycin, and Glutamax. Growth medium was placed over the solidified agarose layers and was supplemented every 3 days. Colonies were counted 14 days after plating.

MRI. MRI was used to determine the pancreatic volumes of the mice *in vivo*. Mice were anaesthetized using 1.5% isoflurane and imaged in a 7.0 T small animal scanner (Bruker-Biospin). Contiguous coronal slices were acquired using a multi-slice, rapid acquisition with relaxation enhancement (RARE) sequence: repetition time/echo time = 4826 ms/33 ms, field of view = 6 × 3 cm, and matrix = 126 × 128 with up to 44 slices with a thickness of 0.5 mm. Segmentation and volume rendering were performed using Amira software (FEI Visualization Sciences Group).

Histological analysis/quantification of PanIN and pancreatic ductal adenocarcinoma. Mouse tumours from 4.5- to 13-week-old *Msi1^{-/-}*-KP^{flf}/C, *Msi2^{-/-}*-KP^{flf}/C mice, and WT-KP^{flf}/C littermates were isolated, fixed in 4% paraformaldehyde, and paraffin embedded according to standard protocols. Sections (5 µm) were obtained for haematoxylin and eosin and periodic acid-Schiff/Alcian blue staining. To quantify tumour areas, each slide was digitally scanned with an Aperio slide scanner. Imagescope software was used to measure pancreatic ductal adenocarcinoma area, PanIN area, and normal pancreas area.

Gene expression microarray, RNA-seq, and bioinformatic analysis. (A) WT-KP^{flf}/C or *Msi1^{-/-}*-KP^{flf}/C mice were euthanized at 11 weeks of age. Tumours were harvested and total cellular RNAs were purified, labelled, and hybridized onto Affymetrix GeneChip Mouse Genome 430 2.0 arrays and raw hybridization data were collected (VA/VMR Microarray and NGS Core, University of California San Diego). Expression level data were extracted using R package gcRMA^{34,35}, and normalized using a multiple-loess algorithm as previously described³⁶. Probes whose

expression levels exceed a threshold value in at least one sample were considered detected. The threshold value is found by inspection from the distribution plots of \log_2 expression levels. Detected probes were sorted according to their q value, which is the smallest false discovery rate at which a probe is called significant³⁷. A false discovery rate value of α is the expected fraction of false positives among all genes with $q \leq \alpha$. False discovery rate was evaluated using significance analysis of microarrays and its implementation in the official statistical package samr³⁸. The samples were treated as 'two class paired' according to the date of RNA extraction. No genes reached a significance level of $\alpha = 0.1$. A heat map of selected genes was created using in-house software. (B) MIA PaCa-2 cells were infected with GFP-tagged or TomatoRed-tagged lentiviral particles containing shRNAs for MSI1, MSI2, MSI1 + MSI2, and a scrambled control. At 72 h after infection, positively infected cells were sorted and total cellular RNAs were isolated using a Qiagen RNeasy mini kit. RNA-seq fastq files were processed into transcript-level summaries using kallisto, an ultrafast pseudo-alignment algorithm with expectation maximization. Transcript-level summaries were processed into gene-level summaries by adding all transcript counts from the same gene. Gene counts were normalized across samples using DESeq normalization³⁹, and the gene list was filtered on the basis of mean abundance, which left 13,684 'detected' genes for further analysis. Differential expression was assessed with an R package limma⁴⁰ applied to \log_2 -transformed counts. Statistical significance of each test was expressed in terms of posterior error probability p^E using the limma function eBayes^{41,42}. Posterior error probability, also called local false discovery rate, is the probability that a particular gene is not differentially expressed, given the prior probabilities of the model. The list of genes sorted by p^E (in ascending order) was analysed for over-represented biological processes and pathways using a non-parametric version of gene set enrichment analysis^{43,44}. Denoting $p^E(1)$ as the probability that a gene is not differentially expressed in the Msi1 knockdown and $p^E(2)$ the probability that a gene is not differentially expressed in the Msi2 knockdown, the probability that a gene is differentially expressed in both samples was estimated as $[1 - p^E(1)][1 - p^E(2)]$. By the same token, the probability that a gene is differentially expressed in the Msi1 knockdown but not in the Msi2 knockdown was estimated as $[1 - p^E(1)]p^E(2)$; likewise with indices 1 and 2 switched.

Reverse transcription PCR. RNA was isolated using RNeasy Micro and Mini kits (Qiagen) and converted to cDNA using Superscript III (Invitrogen). Quantitative PCR was performed using an iCycler (BioRad) by mixing cDNAs, iQ SYBR Green Supermix (BioRad), and gene specific primers. Primer sequences are available upon request. All real-time data were normalized to actin or GAPDH.

In vivo transplantation assay and analysis. *In vivo* we focused on the tumorigenic potential of Msi2 reporter cells since Msi1⁺ cells were unable to form tumours in small numbers (100, 1,000), possibly because they are less tumorigenic or more quiescent (data not shown). Pancreatic tumours from 10- to 13-week-old REM2-KP^{fl/c} mice were dissociated and FACS sorted for EpCAM⁺/reporter⁺ (GFP⁺) and EpCAM⁺/reporter⁻ (GFP⁻) cells. GFP⁺ and GFP⁻ cells (100, 500, 1,000, or 5,000) were suspended in DMEM (Gibco, Life Technologies) containing 10% FBS, then mixed 1:1 with matrigel (BD Biosciences). Cells were injected subcutaneously into the left or right flank or orthotopically into the tail of the pancreas of 5- to 8-week-old NOD/SCID *Il2r γ* ^{-/-} (NSG) recipient mice. Subcutaneous tumour dimensions were measured with callipers every 7 days for 8–12 weeks. At endpoint, flank tumours were removed, volume calculated, and dissociated as described above. Tumour cells were stained with anti-mouse EpCAM antibody (eBiosciences) then analysed for GFP expression by flow cytometry on a FACSARIA III machine (Becton Dickinson), and data analysed with FlowJo software (Tree Star). Subcutaneous tumours did not exceed 2 cm in diameter as per the University of California San Diego Institutional Animal Care and Use Committee Policy on Experimental Neoplasia.

Patient-derived xenograft infection and in vivo transplant. Patient samples were obtained from Moores Cancer Center at the University of California San Diego from Institutional Review Board-approved protocols with written informed consent in accordance with the Declaration of Helsinki. All knockdown experiments were conducted with the construct shCTRL (scrambled), shMSI1, and shMSI2. Briefly, freshly dissociated (GentleMACS Dissociator, Miltenyi) patient-derived xenograft cells were plated in RPMI-1640 with 20% FBS, 1 \times glutamax, 1 \times non-essential amino acids, 100 IU ml⁻¹ penicillin, and 100 μ g ml⁻¹ streptomycin. Cells were transduced with GFP-tagged lentiviral shRNAs, and FACS analysis was performed after 24 h on a portion of the cells; the remaining cells were transplanted into the flank of 5- to 8-week-old NSG recipient mice. Tumour size was monitored by calliper measurement, and mice were euthanized when tumours reached 2 cm in diameter. Subcutaneous tumours did not exceed 2 cm in diameter as per the University of California San Diego Institutional Animal Care and Use Committee Policy on Experimental Neoplasia. Tumours were harvested, dissociated, and analysed by FACS.

RIP-qPCR. HEK 293T cells were transfected with MSCV-Flag-MSi2-IRES-tNGFR and lysed 72 h after transfection. RNA-immunoprecipitation was

performed with anti-Flag antibody (Sigma-Aldrich) or control immunoglobulin-G (IgG) using an EZ-Magna RIP kit according to the manufacturer's protocol (Millipore). Immunoprecipitated RNA was converted to cDNA and analysed for the expression of indicated genes by real-time PCR.

CLIP-seq. Briefly, MIA PaCa-2 cells were ultraviolet cross-linked with a Stratalinker (Model 2400, Stratagene). Cells were lysed and supernatant added to Dynabeads conjugated to MSI1 antibody (clone 14H1, eBiosciences). CLIP library preparation and sequencing, as well as sample preparation and sequencing, were performed as previously described⁴⁵. A total of 73,329 unique tags were obtained from MSI1-bound targets including tags with the binding core sequence 'rUAG' site, as reported previously⁴⁶.

MET rescue assay. Using gateway technology, pENTR-Human cMET was engineered into the pLENTI-PGK-PURO DEST vector. MIA PaCa-2 cells were infected with pLENTI PGK-MET or pLENTI PGK-EMPTY virus. After the establishment of the stable cell line over-expressing cMET, lentiviruses containing shRNAs for Control, MSI1, or MSI2 were delivered. Cells were sorted for GFP expression and plated into a soft agar colony assay. Colonies were counted 14 days after plating.

In vivo and in vitro drug therapy. Nine- to 10-week-old REM2-KP^{fl/c} mice were treated with gemcitabine alone or in combination with crizotinib or iBet762 for 6 days. On day 6, tumours were removed, dissociated (as described above), counted for total cellular content, stained with anti-mouse EpCAM antibody, and analysed for reporter expression by flow cytometry. Gemcitabine (Sigma, G6423) was resuspended in H₂O at 20 mg ml⁻¹ and delivered at 200 mg per kg (body weight) or 500 mg per kg (body weight) by intraperitoneal injection twice over 6 days (on days 0 and 3). Crizotinib (Selleckchem PF-02341066) was resuspended in dimethylsulfoxide (DMSO) at 50 mg ml⁻¹, diluted 1:10 in H₂O, and delivered at 100 mg per kg (body weight) per day for 6 days by oral gavage. iBet762 (Selleckchem S7189) was resuspended in DMSO at 50 mg ml⁻¹, diluted 1:10 in H₂O, and delivered at 30 mg per kg (body weight) per day by intraperitoneal injection for 6 days. For *in vitro* drug assay, low-passage Msi2 reporter KP^{fl/c} cells were loaded with 2 μ M DiI and imaged continuously for up to 48 h while receiving 10 μ M gemcitabine treatment.

ASO inhibitors. To identify human Msi ASO inhibitors, rapid throughput screens were performed to identify effective ASOs as previously described^{47,48}. ASOs were tested in full dose-response experiments to determine potency. The top two most effective ASOs were chosen to test free uptake and verify target knockdown in MIA PaCa-2 cells. The sequences of Gen 2.5 MSI1 ASOs used for the study were ASO-1, 5'-ATATGATACAGGACGG-3' and ASO-2, 5'-TTACATATGATACAGG-3', with underlined letters indicating cTET-modified bases. The sequence of Gen 2.5 scrambled (5'-GGCTACTACGCCGTCA-3') ASO with no perfect match for any known transcript was included as a negative control. (A) *In vitro*: MIA PaCa-2 cells were treated with 0.5–20 μ M of antisense compound for 24 h, after which cells were lysed and RNA isolated. Gene expression was assessed with Taqman probes for MSI1 and MSI2. Actin was used to normalize all real-time data. For functional testing, MIA PaCa-2 cells were plated in the colony assay as previously described. The growth medium was supplemented with 0.25–10 μ M of ASO. Cells were supplemented weekly with fresh antisense compound. Colonies were counted 21 days after the first ASO treatment. (B) *In vivo*: 5 \times 10⁵ MIA PaCa-2 cells were transplanted into the flank of 5- to 8-week-old NSG recipient mice. Once tumours were measurable at 2 weeks after transplant, 50 μ g of either control ASO or MSI1 ASO-1 in PBS was administered intratumorally. ASOs were delivered daily over the course of the study. Tumour measurements were recorded every 3 days. Subcutaneous tumours did not exceed 2 cm in diameter as per the University of California San Diego Institutional Animal Care and Use Committee Policy on Experimental Neoplasia. (C) *In vivo*: in 8-week-old WT-KP^{fl/c} mice, either control ASO or Malat1 ASO was delivered by intraperitoneal injection at a dose of 50 mg per kg (body weight). ASOs were delivered daily for 14 days. On day 15, mice were killed and the tumour removed. Tumours were harvested and used as follows: (1) flash frozen for RNA isolation and qPCR analysis for Malat1; (2) placed into 4% paraformaldehyde for paraffin embedding, sectioning, and *in situ* hybridization analysis for Malat1; and (3) dissociated and sorted for RNA isolation to compare Malat1 expression in EpCAM⁺/ALDH⁺ and EpCAM⁺/ALDH⁻ populations.

Tumour imaging. Eleven- to 12-week-old REM-KP^{fl/c} mice were anaesthetized by intraperitoneal injection of ketamine and xylazine (100/20 mg per kg (body weight)). To visualize blood vessels and nuclei, mice were injected retro-orbitally with Alexa Fluor 647 anti-mouse CD144 (VE-cadherin) antibody and Hoechst 33342 immediately after anaesthesia induction. Pancreatic tumours were removed and placed in HBSS containing 5% FBS and 2 mM EDTA. Images (80–100 μ m in 1024 \times 1024 format) were acquired with an HCX APO L20 \times objective on an upright Leica SP5 confocal system using Leica LAS AF 1.8.2 software. Videos were generated using Volocity 3D image analysis software and compressed using Microsoft Video 1 compression.

Circulating tumour cell analysis. Ten- to 13-week-old REM2-KP^{fl/c} mice were anaesthetized and approximately 100–500 μ l of peripheral blood and ascites was

collected in PBS containing 5 mM EDTA and 2% dextran. Samples were incubated at 37 °C and red blood cells were lysed using RBC lysis buffer (eBiosciences). Remaining cells were stained with anti-mouse EpCAM-PE (eBiosciences) and anti-mouse CD45-PE-Cy7 (eBiosciences) antibodies. Analysis was performed on a FACS Aria III machine (Becton Dickinson) and data analysed with FlowJo software (Tree Star).

In situ hybridization. Msi1 and Msi2 mRNA were detected in tumour samples using RNAscope, an RNA *in situ* hybridization method that allows signal amplification and background suppression. Human tissue was drop-fixed in neutral-buffered formalin and processed and embedded in paraffin. Tissue sections (4 µm) were collected in RNase-free manner and dried at room temperature overnight. Staining was initiated by baking the slides for 32 min at 60 °C, then they were deparaffinized, subjected to antigen retrieval, and treated with protease (two sequential incubations at 65 °C and 75 °C for 12 min each) to enhance probe penetration, as described by the manufacturer (Advanced Cell Diagnostics). Msi1-specific and Msi2-specific RNA target probe sets were generated and supplied by the manufacturer (Advanced Cell Diagnostics). Sequential amplification steps resulted in a large number of horseradish peroxidase molecules per mRNA. The probe was visualized by incubation with 3,3' diaminobenzidine (DAB). Sections were counterstained with haematoxylin. All steps of this procedure were performed using a Ventana Discovery Ultra (Roche). Slides were analysed by conventional light microscopy.

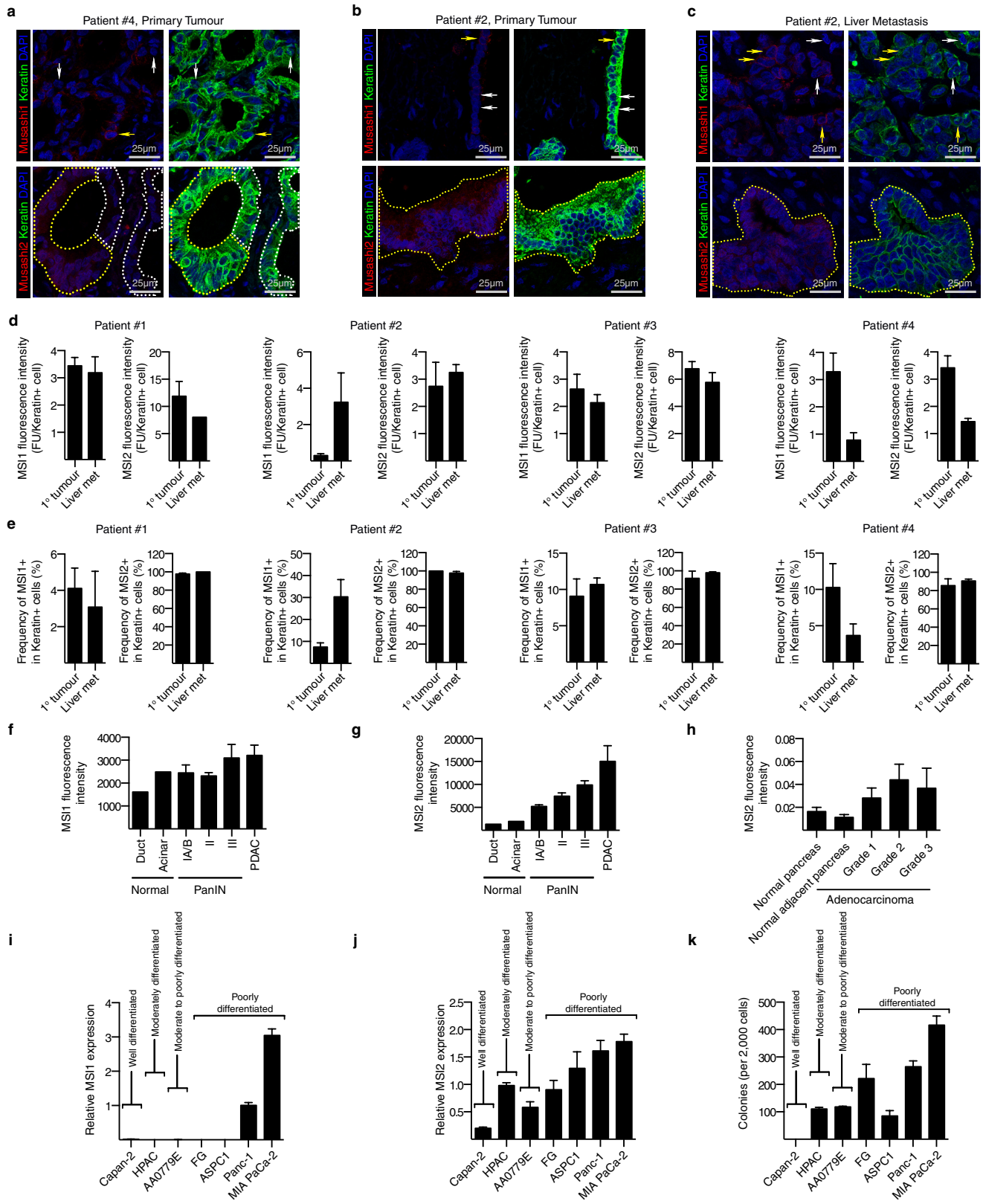
Msi1^{-/-}-KP^{fl/c} survival curve. For the Msi1^{-/-}-KP^{fl/c} mice, tracking survival was complicated by the incidence of hydrocephaly observed in the knockout mice reported previously⁷. To avoid confounding the data with deaths due to non-tumorigenic events, we performed orthotopic transplants. Briefly, Msi1^{-/-}-KP^{fl/c} and WT KP^{fl/c} mice at 8 weeks of age were killed and tumours collected. Tumours were divided into four equal chunks, and then surgically transplanted into the pancreas of 8-week-old NSG mice. After surgery, the orthotopically transplanted mice were tracked for survival.

Luciferase assay. A Lightswitch Luciferase Assay System (Active Motif) was used to assess MSI1 regulation of cMET. Briefly, 1 × 10⁴ MIA PaCa-2 cells were plated into 96-well plates and cultured for 24 h. Fifty nanograms of cMET 3' UTR GoClone (S811259, Active Motif) plasmid DNA and increasing concentrations (0 ng, 50 ng, and 100 ng) of either PGK-GFP or PGK-MSI1 plasmid vector DNA were co-transfected into MIA PaCa-2 cells. After 24 h, cells were lysed using Lightswitch Luciferase Assay Reagent (LS100, Active Motif) and luciferase activity measured using a plate scanner (Infinite 200, Tecan).

Caerulein-induced pancreatitis. Four-week-old C57BL/6 mice received 8 injections of 50 µg per kg (body weight) caerulein (Sigma-Aldrich) or PBS hourly each day for 2 consecutive days (for a total of 16 injections). Pancreata were isolated 2 days after the last injection, fixed in 4% paraformaldehyde, and paraffin embedded according to standard protocols. Sections (7 µm) were obtained, deparaffinized in xylene, and stained as described above.

Statistical analysis. Statistical analyses were performed using GraphPad Prism software version 6.0d (GraphPad Software). Sample sizes were determined on the basis of the variability of pancreatic tumour models used. Tumour-bearing animals within each group were randomly assigned to treatment groups. The investigators were not blinded to allocation during experiments and outcome assessment. Data are shown as the mean ± s.e.m. Two-tailed unpaired Student's *t*-tests with Welch's correction or one-way ANOVA for multiple comparisons when appropriate were used to determine statistical significance (**P* < 0.05, ***P* < 0.01, ****P* < 0.001, *****P* < 0.0001).

32. Domen, J., Cheshier, S. H. & Weissman, I. L. The role of apoptosis in the regulation of hematopoietic stem cells: overexpression of Bcl-2 increases both their number and repopulation potential. *J. Exp. Med.* **191**, 253–264 (2000).
33. Rovira, M. *et al.* Isolation and characterization of centroacinar/terminal ductal progenitor cells in adult mouse pancreas. *Proc. Natl Acad. Sci. USA* **107**, 75–80 (2010).
34. R Development Core Team. R: a language and environment for statistical computing (R Foundation for Statistical Computing, 2012).
35. Wu, J. *et al.* gcrma: background adjustment using sequence information. R package version 2.37.0.
36. Sásik, R., Woelk, C. H. & Corbeil, J. Microarray truths and consequences. *J. Mol. Endocrinol.* **33**, 1–9 (2004).
37. Benjamini, Y. & Hochberg, Y. Controlling the false discovery rate: a practical and powerful approach to multiple testing. *J. R. Stat. Soc. B* **57**, 289–300 (1995).
38. Tusher, V. G., Tibshirani, R. & Chu, G. Significance analysis of microarrays applied to the ionizing radiation response. *Proc. Natl Acad. Sci. USA* **98**, 5116–5121 (2001).
39. Anders, S. & Huber, W. Differential expression analysis for sequence count data. *Genome Biol.* **11**, R106 (2010).
40. Ritchie, M. E. *et al.* limma powers differential expression analyses for RNA-sequencing and microarray studies. *Nucleic Acids Res.* **43**, e47 (2015).
41. Efron, B. Microarrays, empirical Bayes and the two-groups model. *Stat. Sci.* **23**, 1–22 (2008).
42. Lonnstedt, I. & Speed, T. Replicated microarray data. *Stat. Sin.* **12**, 31–46 (2002).
43. Mootha, V. K. *et al.* PGC-1α-responsive genes involved in oxidative phosphorylation are coordinately downregulated in human diabetes. *Nature Genet.* **34**, 267–273 (2003).
44. Zimdahl, B. *et al.* Lis1 regulates asymmetric division in hematopoietic stem cells and in leukemia. *Nature Genet.* **46**, 245–252 (2014).
45. Licatalosi, D. D. *et al.* HITS-CLIP yields genome-wide insights into brain alternative RNA processing. *Nature* **456**, 464–469 (2008).
46. Ohyama, T. *et al.* Structure of Musashi1 in a complex with target RNA: the role of aromatic stacking interactions. *Nucleic Acids Res.* **40**, 3218–3231 (2012).
47. Carroll, J. B. *et al.* Potent and selective antisense oligonucleotides targeting single-nucleotide polymorphisms in the Huntington disease gene / allele-specific silencing of mutant huntingtin. *Mol. Ther.* **19**, 2178–2185 (2011).
48. Samuel, V. T. *et al.* Targeting foxo1 in mice using antisense oligonucleotide improves hepatic and peripheral insulin action. *Diabetes* **55**, 2042–2050 (2006).

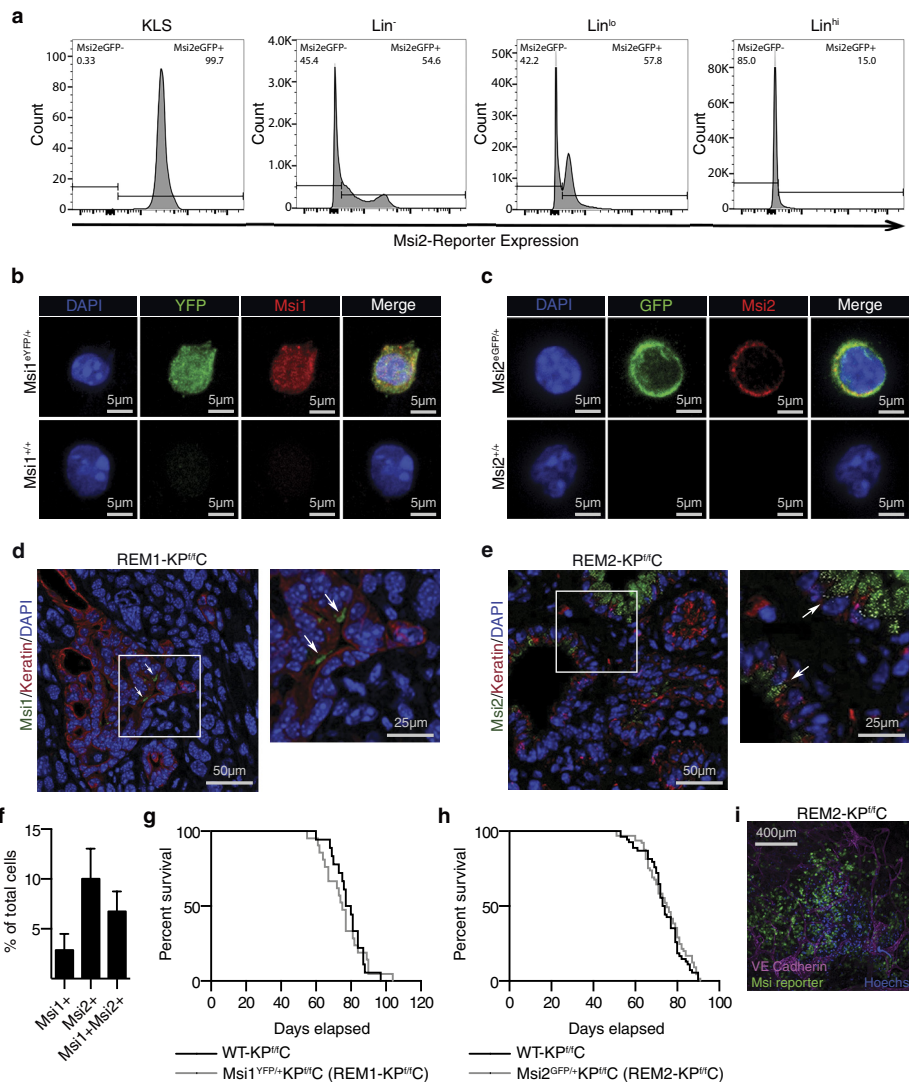


Extended Data Figure 1 | See next page for caption.

Extended Data Figure 1 | The Musashi genes *MSI1* and *MSI2*

are expressed in human pancreatic adenocarcinoma. **a**, Top row: representative images of a primary patient pancreatic adenocarcinoma sample stained with anti-keratin (green), DAPI (blue), and anti-*MSI1* (red) antibodies. White arrows indicate *MSI1*[−] cells; yellow arrow indicates a *MSI1*⁺ cell. **a**, Bottom row: representative images of a primary patient pancreatic adenocarcinoma sample stained with anti-keratin (green), DAPI (blue), and anti-*MSI2* (red) antibodies. White dotted regions indicate *MSI2*[−] cells while yellow dotted regions indicate *MSI2*⁺ cells. **b**, Top row: representative images of a primary patient pancreatic adenocarcinoma sample stained with anti-keratin (green), DAPI (blue), and anti-*MSI1* (red) antibodies. White arrows indicate *MSI1*[−] cells; yellow arrow indicates a *MSI1*⁺ cell. **b**, Bottom row: representative images of a primary patient pancreatic adenocarcinoma sample stained with anti-keratin (green), DAPI (blue), and anti-*MSI2* (red) antibodies. Yellow dotted region indicates *MSI2*⁺ cells. **c**, Top row: representative images of a matched liver metastasis from a patient with pancreatic adenocarcinoma stained with anti-keratin (green), DAPI (blue), and anti-*MSI1* (red) antibodies. White arrows indicate *MSI1*[−] cells; yellow arrows indicate *MSI1*⁺ cells. **c**, Bottom row: representative images of a matched liver metastasis from a patient with pancreatic adenocarcinoma stained with

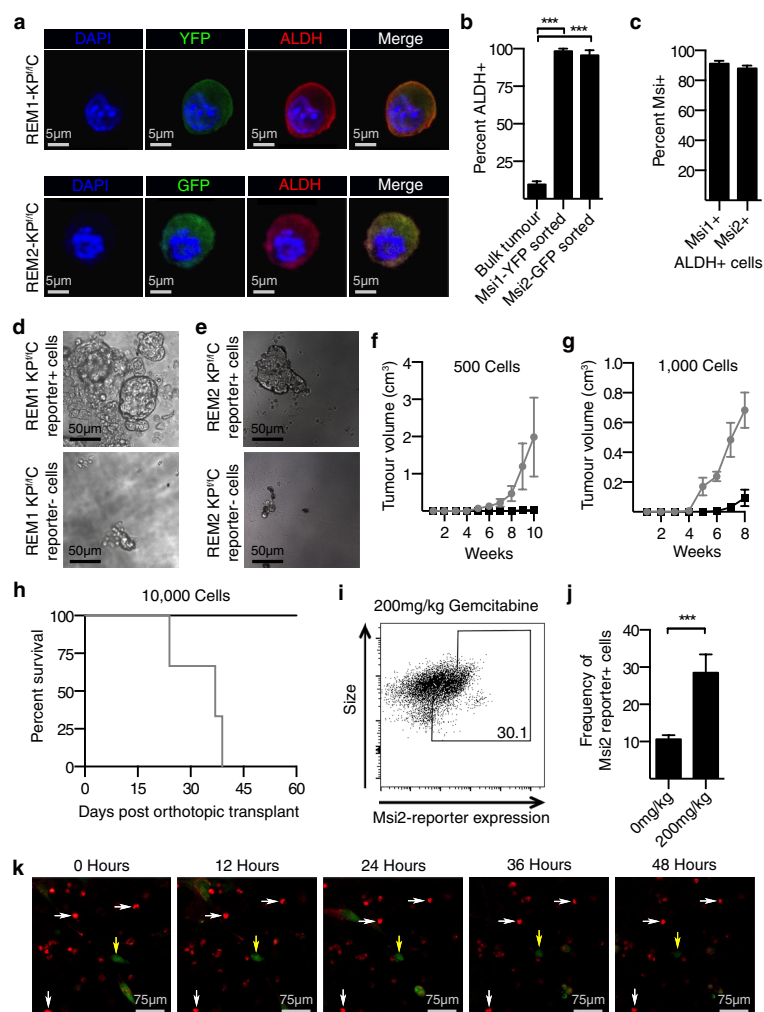
anti-keratin (green), DAPI (blue), and anti-*MSI2* (red) antibodies. Yellow dotted region indicates *MSI2*⁺ cells. **d**, Quantification of *MSI1* and *MSI2* expression in four patients comparing primary pancreatic adenocarcinoma to the patient-matched liver metastasis; four images analysed per patient. **e**, Quantification of the frequency of *MSI1*⁺ and *MSI2*⁺ cells in four patients comparing primary pancreatic adenocarcinoma to the patient-matched liver metastasis; four images analysed per patient. **f**, *MSI1* and **(g)** *MSI2* expression in normal pancreas ($n = 1$), PanIN ($n = 9$), and pancreatic adenocarcinoma samples ($n = 9$). **h**, Quantification of *MSI2* expression from a human tissue array comparing grade 1 (well-differentiated, $n = 9$), grade 2 (moderately differentiated, $n = 12$), and grade 3 (poorly differentiated, $n = 16$) adenocarcinoma relative to normal pancreas ($n = 14$) and normal adjacent pancreas ($n = 16$). **i**, *MSI1* and **(j)** *MSI2* expression in well-differentiated, moderately differentiated, and poorly differentiated human pancreatic cancer cell lines ($n = 3$ independent experiments). **k**, Colony formation of well-differentiated, moderately differentiated, and poorly differentiated human pancreatic cancer cell lines ($n = 3$ independent experiments). Data are represented as mean \pm s.e.m. Total magnification $\times 200$ (**a–c**). Source data for all panels are available online.



Extended Data Figure 2 | Validation of Msi1 and Msi2 reporter mice.

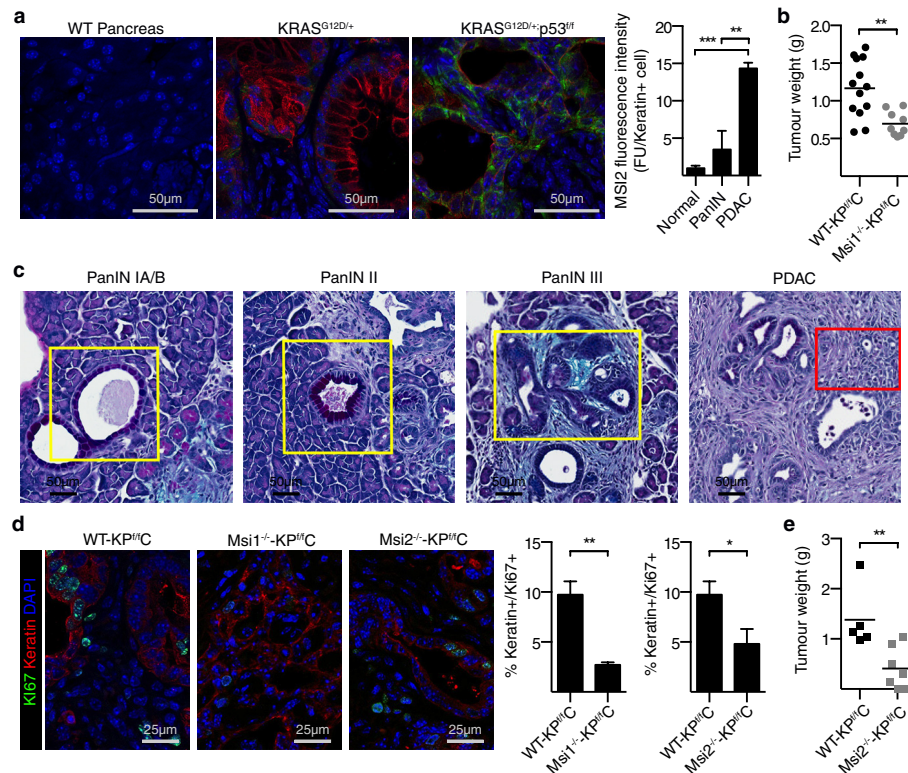
a, FACS analysis of Msi2 reporter expression in haematopoietic stem cells, progenitors, and lineage-positive differentiated cells. **b**, Representative image of Msi1 expression in FACS-sorted YFP⁺ neuronal cells; YFP (green), Msi1 (red), and DAPI (blue). **c**, Representative image of Msi2 expression in FACS-sorted GFP⁺ haematopoietic cells; GFP (green), Msi1 (red), and DAPI (blue). **d**, **e**, Msi-expression in keratin⁺ cells. **d**, Msi1-YFP reporter (green, white arrows) and keratin (red) staining was performed on tissue sections of REM1-KP^{fl/c} mice; **e**, Msi2-GFP reporter (green, white arrows) and keratin (red) staining was performed on tissue sections of REM2-KP^{fl/c} mice. DAPI staining is shown in blue. Rare cells

(<5%) were found to be keratin⁻ (possibly mesenchymal population). **f**, Immunofluorescence analysis of Msi1 and Msi2 expression overlap in isolated EpCAM⁺ KP^{fl/c} cells ($n = 3$, 1,000 total cells analysed from 3 independent experiments). Data are represented as mean \pm s.e.m. **g**, **h**, Survival of Msi reporter-KP^{fl/c} and WT-KP^{fl/c} mice. Survival curves of (**g**) Msi1^{YFP/+}-KP^{fl/c} (REM1-KP^{fl/c}, $n = 21$) or WT-KP^{fl/c} ($n = 18$) mice and (**h**) Msi2^{GFP/+}-KP^{fl/c} (REM2-KP^{fl/c}, $n = 65$) or WT-KP^{fl/c} ($n = 54$) mice. **i**, Live image of Msi2 reporter cells in REM2-KP^{fl/c} tumour; VE-cadherin (magenta), Hoechst (blue), Msi reporter (green). See also Fig. 1c, d. Source data for all panels are available online.



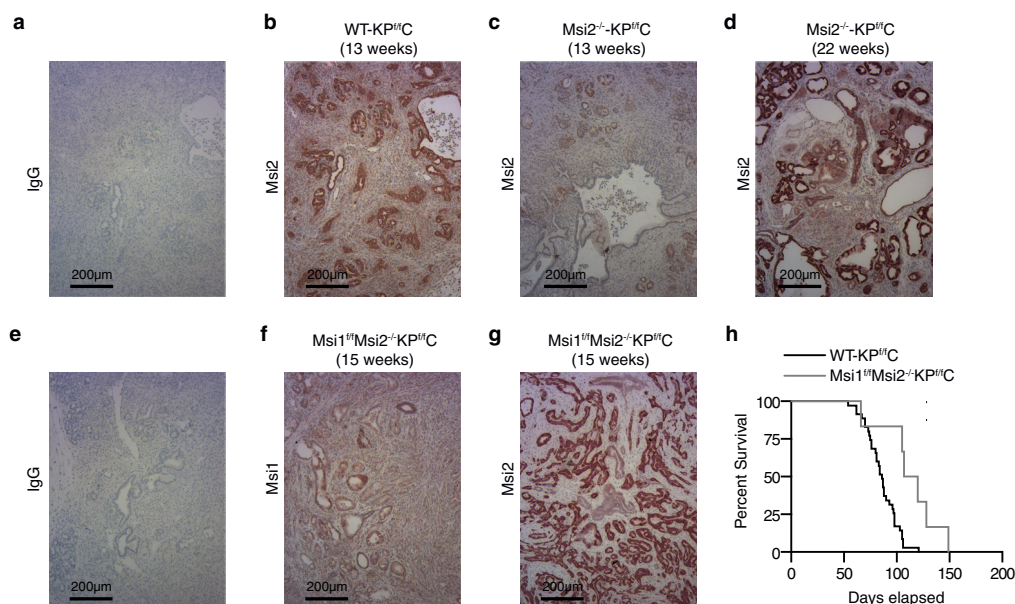
Extended Data Figure 3 | Analysis of stem cell traits in Msi1 and Msi2 reporter⁺ KP^{fl/c} populations. **a**, ALDH expression in reporter⁺ tumour cells sorted from REM1-KP^{fl/c} (top row) and REM2-KP^{fl/c} (bottom row) mice; ALDH1 (red), DAPI (blue), and GFP or YFP (green). **b**, Average ALDH expression in bulk or Msi1 and Msi2 reporter⁺ tumour cells (*n* = 3 each; 90 total cells analysed from 3 REM1-KP^{fl/c} and 150 total cells analysed from 3 REM2-KP^{fl/c}). **c**, Average Msi expression in ALDH⁺ cells from REM1-KP^{fl/c} and REM2-KP^{fl/c} tumours (*n* = 3 independent experiments for each genotype). **d, e**, Representative images of spheres formed from (d) Msi1 and (e) Msi2 reporter⁺ and reporter⁻ tumour cells. See also Fig. 1g, h. **f, g**, In vivo tumour growth of Msi2 reporter⁺ or Msi reporter⁻ KP^{fl/c} cells at (f) 500 or (g) 1,000 cells (*n* = 16). See also Fig. 1i. **h**, Survival of mice orthotopically transplanted with 10,000 Msi2 reporter⁺ and reporter⁻ KP^{fl/c} tumour cells (*n* = 6). See also Fig. 1j.

Log-rank (Mantel-Cox) survival analysis (*P* < 0.05). **i, j**, Reporter frequency in REM2-KP^{fl/c} mice treated with vehicle or 200 mg per kg (body weight) gemcitabine (*n* = 3 each). See also Fig. 1m, n for high-dose (500 mg per kg (body weight)) gemcitabine. Data are represented as mean ± s.e.m. ****P* < 0.001 by Student's *t*-test or one-way ANOVA. **k**, Msi2 reporter⁻ KP^{fl/c} cells do not turn on Msi2 expression after *in vitro* gemcitabine treatment, suggesting that Msi-reporter⁺ cells are differentially resistant to gemcitabine. Low-passage Msi2 reporter KP^{fl/c} cells loaded with DiI were live-imaged continuously for up to 48 h. Representative series of images from 10 μM gemcitabine treatment. Reporter⁻ cells (red); GFP reporter⁺ cells (green); tracking of Msi2 reporter⁻ cells (white arrows); tracking of Msi2 reporter⁺ cells (yellow arrows) (*n* = 3 independent experiments). Source data for all panels are available online.



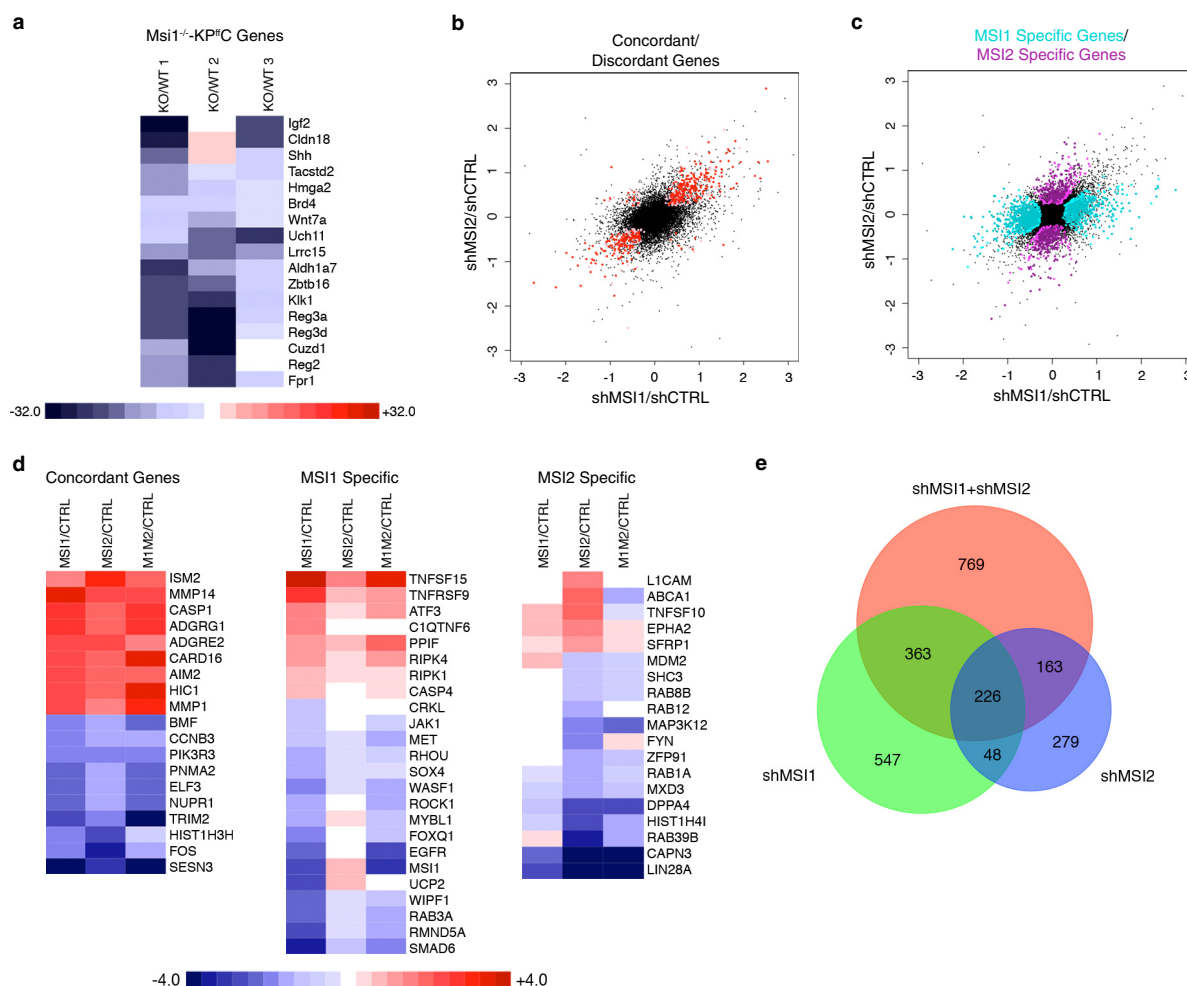
Extended Data Figure 4 | Analysis of tumours from Msi null KP^{fl/c} mice. **a**, Msi2 (green) and Keratin (red) immunofluorescent staining was performed on tissue sections from WT pancreas (normal, $n = 3$ samples), KRAS^{G12D/+};Ptf1a^{Cre/+} (PanIN, $n = 2$ samples), and KRAS^{G12D/+};p53^{fl/fl}; Ptf1a^{Cre/+} (pancreatic ductal adenocarcinoma, $n = 3$ samples) mice with quantification of Msi2 fluorescence in keratin⁺ cells. **b**, Average weights of WT-KP^{fl/c} ($n = 13$) and Msi1^{-/-}-KP^{fl/c} tumours ($n = 9$). See also Fig. 2a, b for tumour volume analysis. **c**, PAS and Alcian blue stained sections of pancreata isolated from WT-KP^{fl/c} represent areas used to identify the

stages of PanINs (yellow boxes) and adenocarcinoma (red box). **d**, Tumours from 11- to 13-week-old WT-KP^{fl/c} ($n = 6$), Msi1^{-/-}-KP^{fl/c} ($n = 3$), and Msi2^{-/-}-KP^{fl/c} ($n = 3$) mice were stained and quantified for percentage of Keratin⁺ tumour cells (red) expressing Ki67 (green); DAPI staining is shown in blue. **e**, Average weights of WT-KP^{fl/c} ($n = 5$) and Msi2^{-/-}-KP^{fl/c} tumours ($n = 7$). See also Fig. 2h, i for tumour volume analysis. Data are represented as mean \pm s.e.m. * $P < 0.05$, ** $P < 0.01$, *** $P < 0.001$ by Student's t -test or one-way ANOVA. Source data for all panels are available online.



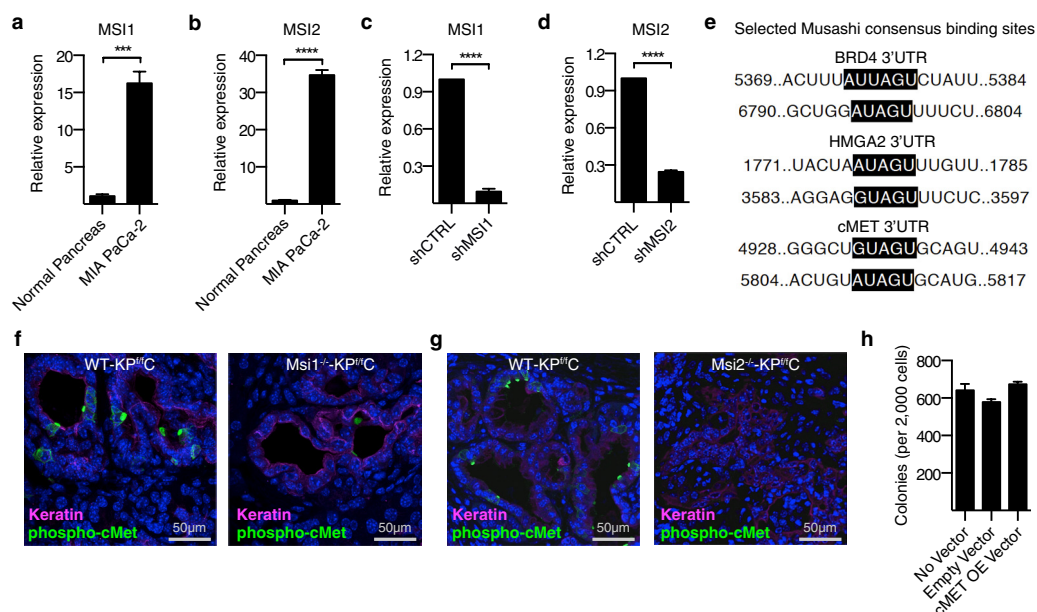
Extended Data Figure 5 | Selection for escaper Msi-expressing cells in Msi1, Msi2 single and double knockout KP^{flC} mice. **a–c**, Immunohistochemical staining for (a) IgG control ($n=4$) or (b, c, red) Msi2 in 13-week-old WT-KP^{flC} ($n=4$) and Msi2^{-/-}-KP^{flC} ($n=4$) mice. **d**, Immunohistochemical staining for Msi2 (red) in 22-week-old

Msi2^{-/-}-KP^{flC} mouse ($n=1$). **e–g**, Immunohistochemical staining for (e) IgG control, (f, red) Msi1, and (g, red) Msi2 in a 15-week-old Msi1^{fl}Msi2^{-/-}-double knockout KP^{flC} mouse ($n=1$). **h**, Survival curves of Msi1^{fl}Msi2^{-/-}-KP^{flC} ($n=6$) or WT-KP^{flC} tumours ($n=35$). Source data for all panels are available online.



Extended Data Figure 6 | Genome-wide analysis of Msi controlled programs in pancreatic cancer. **a**, Genome-wide expression analysis of dissociated pancreatic tumours. Microarray analysis was performed on RNA from three pairs of WT-KP^{fC} and Msi1^{-/-}-KP^{fC} matched littermates. Heat map shows differential expression of selected mRNAs identified as part of a stem-cell-associated gene signature. **b**, Concordantly (upper right and lower left quadrants) and discordantly (upper left and lower right quadrants) regulated genes (red) in MSI1-knockdown and MSI2-knockdown MIA PaCa-2 cells. **c**, Gene changes specific to

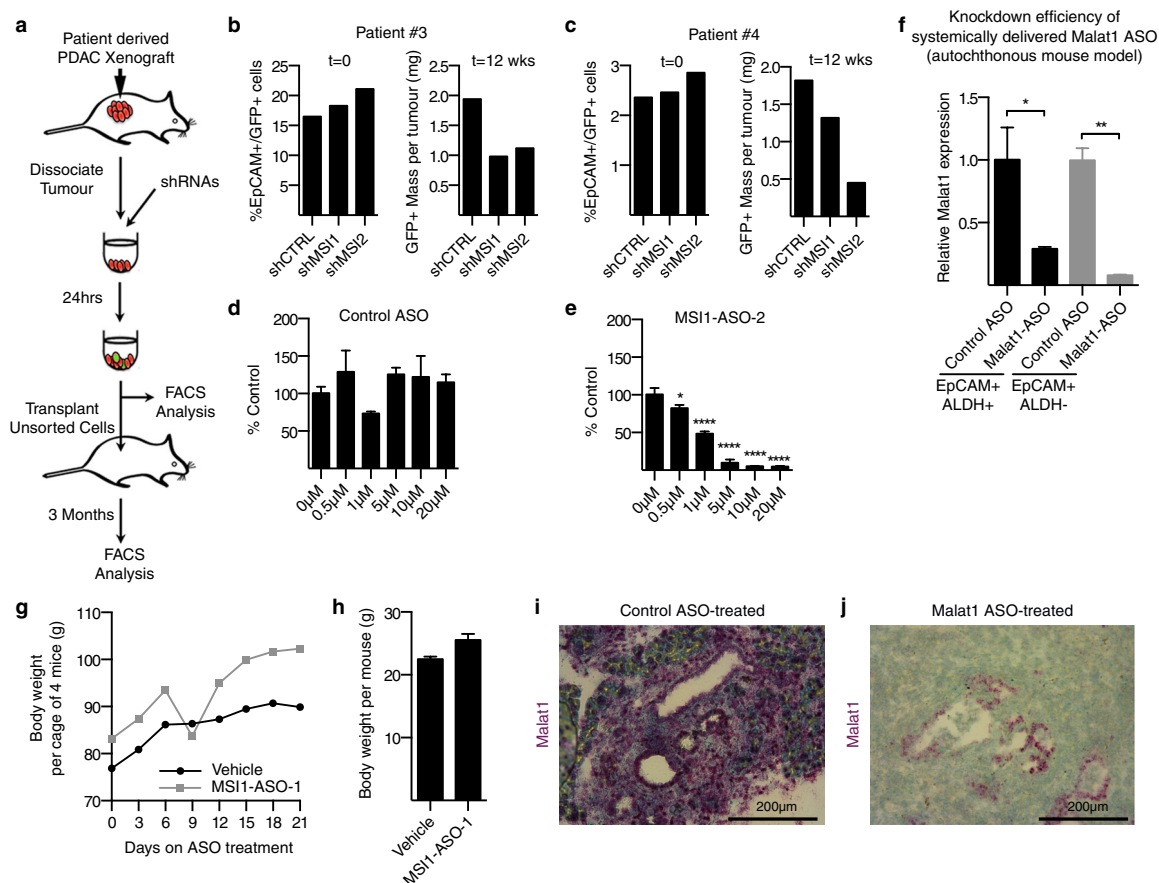
MSI1-knockdown (turquoise) or MSI2-knockdown (purple) in MIA PaCa-2 cells. **d**, Heat maps indicating concordant, MSI1-specific, and MSI2-specific genes. **e**, Venn diagram displaying the intersection of probe sets that are differentially regulated in MSI1-knockdown, MSI2-knockdown, and double knockdown of MSI1 and MSI2 in MIA PaCa-2 cells. Within scatterplots, lighter colour corresponds to a probability > 0.5 and the darker colour corresponds to a probability > 0.75. Source data for all panels are available online.



Extended Data Figure 7 | Molecular targets of Msi signalling.

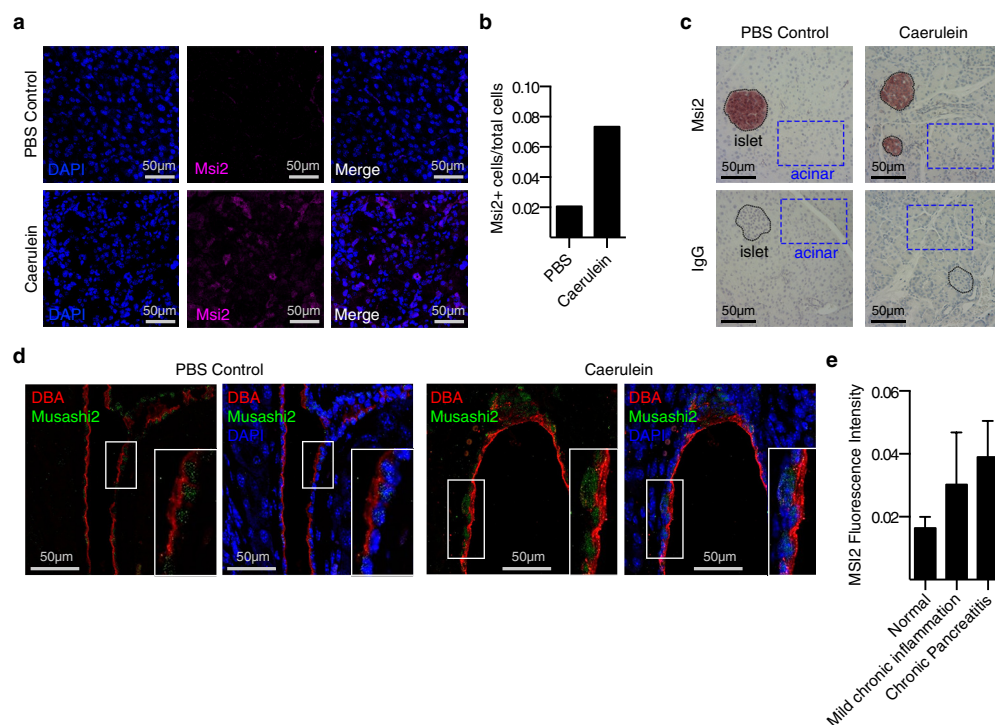
a, b, Quantitative PCR analysis of (a) Msi1 and (b) Msi2 expression in MIA PaCa-2 human pancreatic cancer cells relative to normal pancreas ($n = 3$ independent experiments). **c, d**, Analysis of shRNA knockdown efficiency in GFP⁺-sorted MIA PaCa-2 cells infected with GFP-tagged lentiviral shRNA against scrambled control sequences, (c) MSI1, or (d) MSI2 ($n = 3$ independent experiments). **e**, Analysis of direct Msi targets: Msi consensus binding sites in 3' UTR of BRD4, HMG2, and cMET transcripts. **f, g**, Phospho-cMet staining in WT-KP^{fl/c} and (f)

Msi1^{-/-}-KP^{fl/c}, (g) Msi2^{-/-}-KP^{fl/c} mice; keratin (magenta), phospho-cMet (green), DAPI (blue). See Fig. 3b–c for quantified data. **h**, Colony formation of MIA PaCa-2 cells infected with empty vector or cMET overexpression vector (three independent experiments) shows no impact of overexpressed cMet on control MIA PaCa-2 (control for cMet-mediated rescue of MSI knockdown in Fig. 3f). Data are represented as mean \pm s.e.m. *** $P < 0.001$, **** $P < 0.0001$ by Student's t -test. Source data for all panels are available online.



Extended Data Figure 8 | Analysis of impaired pancreatic cancer growth with shMSI and MSI1-ASOs. **a**, Schematic for inhibiting MSI in primary patient-derived xenografts. **b**, **c**, Frequency of GFP⁺ patient tumour cells before and after transplantation. See also Fig. 4a, b for patients 1 and 2. **d**, **e**, MSI1 expression after free uptake of (**d**) control ASO or (**e**) MSI1-ASO2 in human pancreatic cancer line ($n = 3$ per condition). See also Fig. 4c for impact of MSI1-ASO1. **f**–**j**, ASO delivery *in vivo*. **f**, Target knockdown efficacy of lead-optimized ASO in KP^{fl/c} stem cells. Malat1 expression in EpCAM⁺/ALDH⁺ and EpCAM⁺/ALDH⁻ cells after systemic delivery of control ASO or lead-optimized Malat1-ASO in autochthonous KP^{fl/c} model ($n = 3$ independent experiments). See also Fig. 4h for target knockdown in unfractionated EpCAM⁺ cells. **g**, **h**, Analysis of potential toxicity of MSI-ASO: **g**, cage weight of mice

receiving daily treatment of MSI1 ASO-1 (50 mg per kg (body weight)) or vehicle by intraperitoneal injection; four mice per cage; cage weight was measured every 3 days; **h**, average body weight of mice after 3 weeks of daily treatment with MSI1 ASO-1 (50 mg per kg (body weight)) or vehicle by intraperitoneal injection ($n = 4$ mice/cohort). *In vivo* delivery of MSI1 ASOs (50 mg per kg (body weight)) had no deleterious impact on body weight and maintained plasma chemistry markers (AST, ALT, BUN, T.Bil) within $3 \times$ upper limit of normal. **i**, **j**, Representative images of *in situ* hybridization for Malat1 (purple) in pancreatic tumours isolated from KP^{fl/c} mice treated by daily intraperitoneal injection with (**i**) control ASO (50 mg per kg (body weight)) or (**j**) Malat1-ASO (50 mg per kg (body weight)) for 14 days. Source data for all panels are available online.



Extended Data Figure 9 | Elevated expression of Msi in pancreatitis.

Msi2 expression in a caerulein-induced mouse model of pancreatitis, and in human pancreatitis. **a**, Msi2 staining and **(b)** quantification of ten images per group in pancreas from PBS-treated (**a**, top panels, $n = 1$) and caerulein-treated mice (**a**, bottom panels, $n = 1$). **c**, Msi2 immunohistochemical staining in islets (black dotted outlines) and acinar cells (blue squares) in caerulein-treated or PBS-treated mice ($n = 1$ for each group). **d**, Immunofluorescent staining of Msi2 (green)

in DBA⁺ ductal cells (red) treated with PBS (left panels) or caerulein (right panels) ($n = 1$ for each group); DAPI is shown in blue. **e**, Msi2 expression in human tissue arrays from patients presenting with mild chronic inflammation ($n = 4$) and chronic pancreatitis ($n = 6$) compared with normal pancreas ($n = 14$). Data are represented as mean \pm s.e.m. **** $P < 0.0001$ by Student's t -test. Source data for all panels are available online.

The bacterial DnaA–trio replication origin element specifies single–stranded DNA initiator binding

Tomas T. Richardson¹, Omar Harran¹ & Heath Murray¹

DNA replication is tightly controlled to ensure accurate inheritance of genetic information. In all organisms, initiator proteins possessing AAA+ (ATPases associated with various cellular activities) domains bind replication origins to license new rounds of DNA synthesis¹. In bacteria the master initiator protein, DnaA, is highly conserved and has two crucial DNA binding activities². DnaA monomers recognize the replication origin (*oriC*) by binding double-stranded DNA sequences (DnaA-boxes); subsequently, DnaA filaments assemble and promote duplex unwinding by engaging and stretching a single DNA strand^{3–5}. While the specificity for duplex DnaA-boxes by DnaA has been appreciated for over 30 years, the sequence specificity for single-strand DNA binding has remained unknown. Here we identify a new indispensable bacterial replication origin element composed of a repeating trinucleotide motif that we term the DnaA-trio. We show that the function of the DnaA-trio is to stabilize DnaA filaments on a single DNA strand, thus providing essential precision to this binding mechanism. Bioinformatic analysis detects DnaA-trios in replication origins throughout the bacterial kingdom, indicating that this element is part of the core *oriC* structure. The discovery and characterization of the novel DnaA-trio extends our fundamental understanding of bacterial DNA replication initiation, and because of the conserved structure of AAA+ initiator proteins these findings raise the possibility of specific recognition motifs within replication origins of higher organisms.

The master bacterial DNA replication initiator, DnaA, is a highly conserved multifunctional protein that utilizes distinct domains to achieve its two key DNA binding activities. DnaA recognizes double-stranded (ds)DNA using a helix–turn–helix motif (domain IV), whereas an ATP-dependent DnaA filament interacts with a single DNA strand using residues within the initiator specific motif (ISM; an α -helical insertion that distinguishes the family of replication initiators) of the AAA+ domain (domain III) (Extended Data Fig. 1a–d)^{4,5}. In contrast to DnaA, bacterial replication origins are diverse; they contain variable numbers of DnaA-boxes and seemingly lack a common architecture^{6,7}. Therefore, the sequence information within *oriC* that directs DnaA filament assembly onto a single DNA strand is unknown.

To investigate how DnaA filament formation could be localized to the DNA replication origin of *Bacillus subtilis*, we began by characterizing site-directed mutants of the DNA unwinding region *in vivo* (Fig. 1a and Extended Data Fig. 1e). To enable identification of essential sequences without selecting for suppressor mutations, we generated a strain in which DNA replication could initiate from a plasmid origin (*oriN*) integrated into the chromosome (Fig. 1b and Supplementary Information). Activity of *oriN* requires its cognate initiator protein, RepN; both of these factors act independently of *oriC*/DnaA⁸. Expression of *repN* was placed under the control of a tightly regulated inducible promoter, thus permitting both the introduction of mutations into *oriC* and their subsequent analysis after removal of the inducer to shut off *oriN* activity (Fig. 1c and Extended Data Fig. 2).

At the *B. subtilis* replication origin, DNA unwinding by DnaA is detected downstream of DnaA-box elements and includes a sequence of 27 continuous A:T base pairs that is thought to facilitate DNA duplex opening (Fig. 1a)⁹. Surprisingly, we were able to delete the entire AT-rich sequence ($\Delta 27$) without abolishing origin activity, although the mutant strain did display a slow growth phenotype indicating that the AT-cluster is required for efficient origin function (Fig. 1d). Interestingly, further deletions extending three or six base pairs ($\Delta 30$, $\Delta 33$) severely impaired *oriC*-dependent initiation (Fig. 1d), and a deletion series targeting the sequence between the GC-rich and AT-rich clusters confirmed that this region alone was essential for origin function (Fig. 1e). Scrambling this entire region also inhibited cell growth ($t1-t6^{scr}$), demonstrating that the specific sequence is required, rather than the spacing between the flanking elements (Fig. 1f). To explore this region in more detail, sequences were scrambled three base pairs at a time by exchanging each triplet for its complement. Phenotypic and marker frequency analyses revealed that disruption of sequences closest to the GC-cluster ($t1^{scr}$ and $t2^{scr}$) caused the greatest defect in DNA replication initiation, indicating that the region proximal to the DnaA-boxes is most important for origin activity (Fig. 1f). Although mutagenesis of neither $t4$ nor $t5$ alone produced a detectable effect on DNA replication initiation under the conditions tested, they may become important when origin firing is suboptimal as was observed in the AT-cluster deletion mutant (Fig. 1d).

To determine whether this essential DNA sequence between the GC- and AT-clusters has a role in DNA melting per se, an open complex formation assay was performed. DnaA was incubated with *oriC* plasmids containing either the wild-type or scrambled sequence ($t1-t6^{scr}$), potassium permanganate was added to oxidize distorted bases within the DNA, and base modification was detected by primer extension. Scrambling the sequence inhibited open complex formation, indicating that this region is necessary for DnaA-dependent unwinding (Fig. 1g).

DnaA monomers are thought to bind DnaA-boxes before ATP-dependent filament formation¹⁰. Using the strain capable of *oriC*-independent initiation, the seven DnaA-box sequences were individually scrambled to abolish DnaA binding¹¹. Culturing these strains in the absence of *oriN* activity revealed that mutation of DnaA-box6 severely inhibited growth, and mutation of DnaA-box7 resulted in a marked growth defect, while mutation of the remaining DnaA-boxes had no observable effect (Fig. 2a). Marker frequency analysis confirmed that mutation of DnaA-box7 markedly impaired origin activity, whereas mutation of the remaining DnaA-boxes resulted in only modest decreases in initiation frequency (Fig. 2a). These results indicate that DnaA-boxes proximal to the essential unwinding region are most critical for origin activity.

To directly test whether these DnaA-boxes promote DnaA filament assembly at the essential unwinding region we used a previously described DnaA filament formation assay¹². Here two cysteine residues are introduced within the AAA+ domain such that the protein remains functional and when the DnaA filament assembles

¹Centre for Bacterial Cell Biology, Institute for Cell and Molecular Biosciences, Newcastle University, Newcastle upon Tyne NE2 4AX, UK.

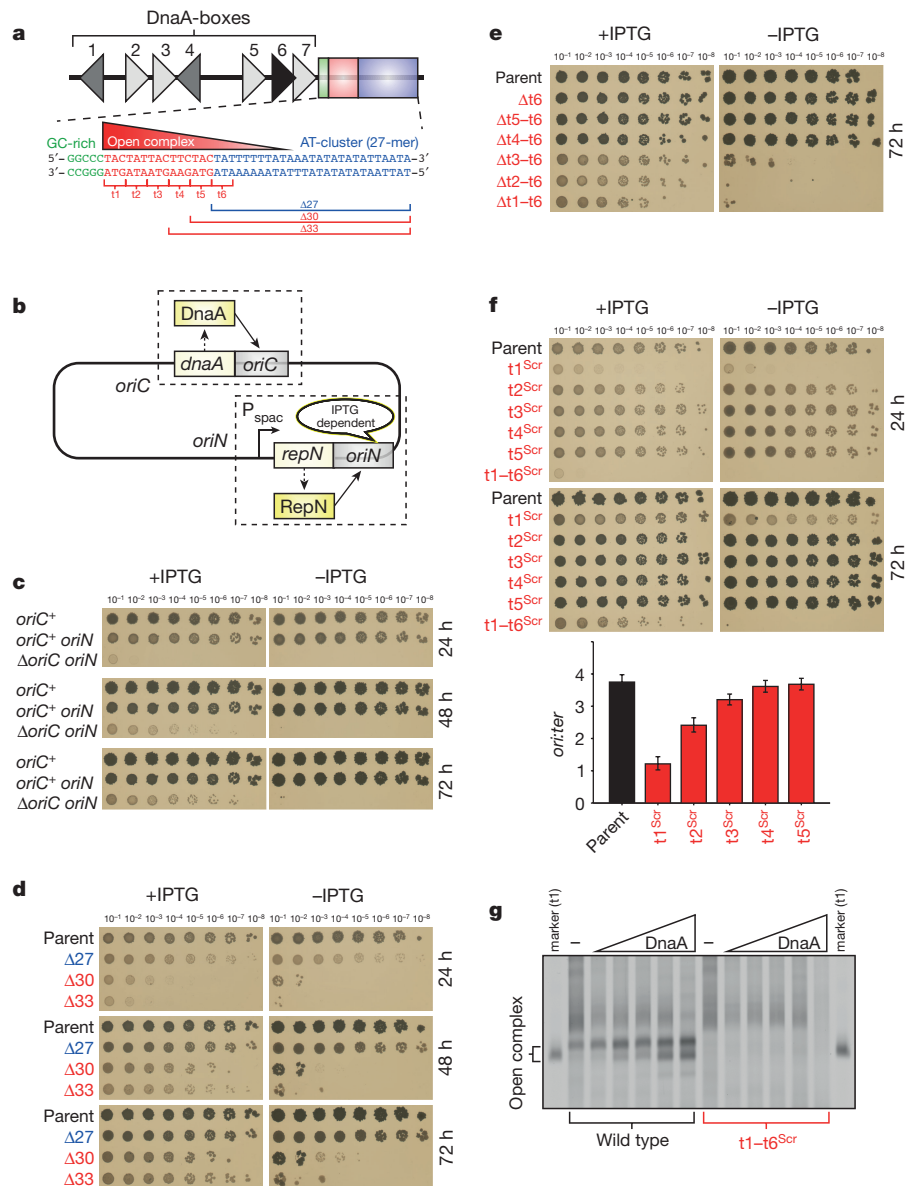


Figure 1 | Genetic analysis of the *oriC* DNA unwinding element reveals a critical region required for initiation activity. **a**, *B. subtilis* *oriC* unwinding region. DnaA-box colouring indicates conservation (consensus 5'-TTATCCACA-3' in black). **b**, The *oriC*-independent strain used for constructing replication origin mutations. **c**, Growth of an *oriC* deletion mutant is dependent upon *oriN* activity. **d**, Deletions extending beyond the AT-cluster into the initially unwound region inhibit cell growth.

the cysteine residues from interacting protomers come into close proximity. DNA scaffolds were assembled using oligonucleotides, and the cysteine-specific crosslinker bis(maleimido)ethane (BMOE; 8 Å spacer arm) was used to capture the oligomeric species formed on each substrate.

Incubation of DnaA with duplex substrates containing DnaA-box6, DnaA-box7 and the GC-rich region produced a dimeric species (Fig. 2b, c), whereas incubation of DnaA with a longer duplex substrate containing the unwinding region produced a set of larger oligomeric complexes. We wondered whether the larger species were being formed on the duplex DNA or on a single DNA strand. To test these models scaffolds containing single-stranded (ss)DNA tails were assembled. DnaA filaments readily formed on substrates containing a 5'-tail but were absent when the corresponding 3'-tail was provided (Fig. 2c and Extended Data Fig. 3). Formation of DnaA oligomers on the 5'-tailed substrate was dependent upon both ATP and the ssDNA

e, Sequences between the GC-rich and AT-rich clusters are essential for origin function. **f**, Sequences proximal to DnaA-boxes are most important for origin function. Marker frequency analysis was used to measure the rate of DNA replication initiation (mean and s.d. of three technical replicates). **g**, Open complex formation by DnaA requires the native sequence between the GC- and AT-clusters. DNA duplex unwinding was probed by KMnO₄ and detected by primer extension.

binding residue Ile190 located within the ISM of the AAA+ domain⁴, indicating that the assay was capturing DnaA filament formation on ssDNA (Fig. 2c, d and Extended Data Fig. 1d).

Critically, DnaA oligomer formation on the 5'-tailed substrate was specific. DnaA filament assembly was abolished when the DnaA-box sequences within the duplex region were scrambled and it was notably reduced when the single-stranded region was replaced with its complementary sequence (Fig. 2c). Taken together, these results suggest that DnaA filaments are loaded from duplex DnaA-boxes onto ssDNA bearing a 5'-tail. This model is consistent both with biochemical experiments showing that *Escherichia coli* DnaA preferentially interacts with the corresponding single-strand of its DNA unwinding element and with single molecule studies showing that *Aquifex aeolicus* DnaA filaments form with 3'→5' polarity^{11,13,14}.

DnaA oligomer size was proportional to the length of the 5'-tail up to the formation of a heptamer, after which further DNA extension

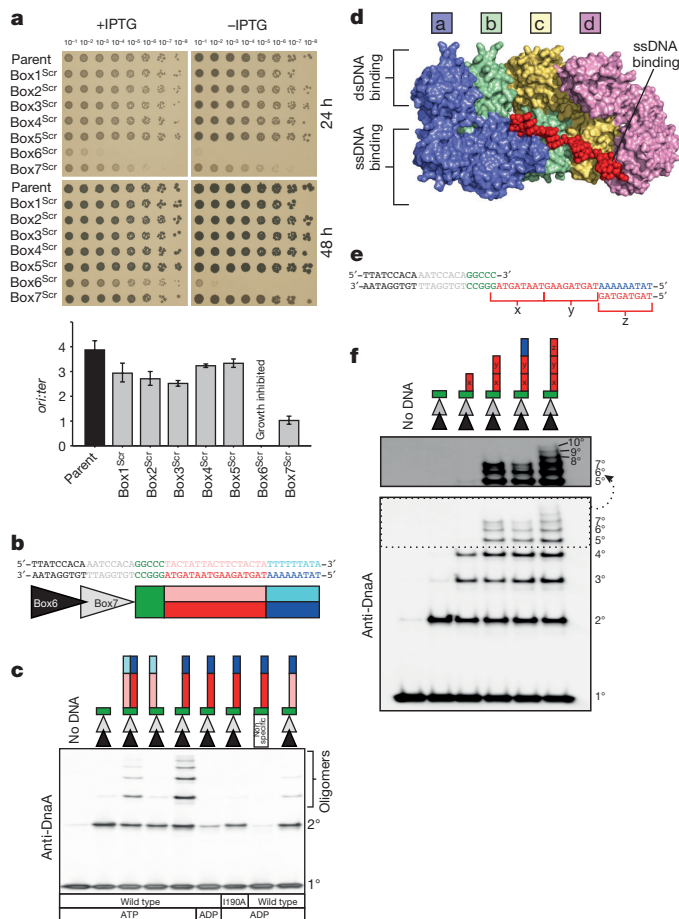


Figure 2 | DnaA filaments are loaded from DnaA-boxes onto a specific single-strand sequence within the initially unwound region. a, DnaA-boxes proximal to the unwinding region are most important for origin function. Marker frequency analysis was used to measure the rate of DNA replication initiation (mean and s.d. of three technical replicates). b, Sequence of the origin region used for constructing DNA scaffolds in c. c, DnaA filament formation using cysteine-specific crosslinking on DNA scaffolds. DnaA complexes were resolved by SDS–polyacrylamide gel electrophoresis (SDS–PAGE) and detected by western blot analysis. d, Crystal structure showing ssDNA (dA₁₂) bound to the DnaA filament through the AAA+ domain (Protein Data Bank (PDB) accession number 3R8F). e, Sequence of the origin region used for constructing DNA scaffolds in f. f, DnaA filament formation on tailed substrates is arrested by a poly(A) tract. Long oligomers highlighted within the dotted box are shown above with increased contrast.

did not promote longer filaments (Fig. 2e, f). We noted that this limit corresponded to a poly(A) tract in the DNA sequence and wondered whether this sequence inhibited DnaA filament formation. When the poly(A) tract was replaced by sequences from the beginning of the DNA unwinding region, DnaA oligomer length increased beyond a heptamer (Fig. 2e, f). This result suggests that the origin unwinding region is designed to limit DnaA filament formation to a precise position within *oriC*.

To identify a possible single-strand binding motif recognized by DnaA, individual base pairs within the essential unwinding region were inverted and origin activity was analysed *in vivo*. Marker frequency analysis revealed that altering either of two A:T base pairs, which were spaced three nucleotides apart from each other, resulted in the most significant loss of origin activity; in contrast the surrounding mutations had only modest effects (Fig. 3a). Re-examination of the unwinding region shows that A:T base pairs are spaced at three nucleotide intervals throughout this sequence (Fig. 1a). This observation is strikingly congruent with the mechanism proposed for binding of

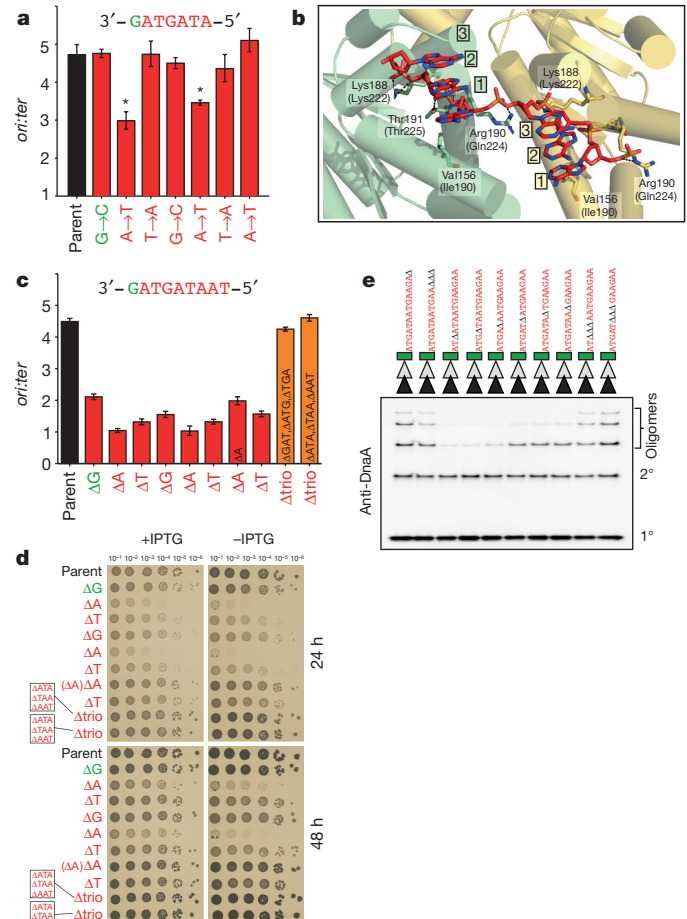


Figure 3 | Analysis of the key origin unwinding region provides evidence for functional trinucleotide repeats. a, Mutagenesis identifies A:T base pairs spaced three nucleotides apart are most critical for origin function. Marker frequency analysis was used to measure the rate of DNA replication initiation (mean and s.d. of three technical replicates). b, Crystal structure showing the interaction of DnaA with sets of three nucleotides (PDB accession number 3R8F). Residues for *A. aeolicus* indicated above; *B. subtilis* below. c, *In vivo* deletion analysis of the unwinding region. Isogenic deletions indicated in black. Marker frequency analysis was used to measure the rate of DNA replication initiation (mean and s.d. of three technical replicates). d, Growth of mutants used in c. e, *In vitro* deletion analysis of tailed substrates.

the DnaA filament to ssDNA, where each protomer engages a set of three nucleotides (Fig. 3b)⁴.

We hypothesized that an array of triplet nucleotide motifs recognized by DnaA are present within the unwinding region and that the motifs proximal to the DnaA-boxes are most important for origin activity. To test this model *in vivo* we created a set of nested deletions that removed either one or three base pairs (Extended Data Fig. 4). All of the single base-pair deletions significantly lowered the replication initiation frequency and several considerably inhibited cell growth (especially the same A:T base pairs noted above), whereas triplet deletions encompassing the single deletions had little or no effect (Fig. 3c, d). These results are consistent with the model that single base-pair deletions act both by disrupting a specific trinucleotide motif and by shifting the register of downstream trinucleotide motifs relative to the DnaA filament start point at the DnaA-boxes.

To test the model that the ssDNA binding motif is indeed a repeating trinucleotide, DnaA filament formation was analysed *in vitro* using tailed substrates that contained either single or triplet base deletions (Fig. 3e). Whereas deletion of one base produced shorter oligomers, deletion of three bases restored formation of full-length complexes.

Taken together with the *in vivo* deletions, these results indicate that DnaA filaments bind to ssDNA by recognizing a specific trinucleotide motif found within the unwinding region. We have termed this trinucleotide motif the 'DnaA-trio'.

To define the precise sequence of the DnaA-trio, DnaA filament formation was observed using a series of DNA scaffolds in which the 5'-tails were extended by increments of one nucleotide. We observed that additional oligomeric species appeared after the following sequences were added: 3'-GAT-5', 3'-AAT-5' and 3'-GAA-5', suggesting that these triplets represent individual DnaA-trio motifs (Fig. 4a).

However, it was surprising that a longer oligomer was not formed after addition of the first 3'-GAT-5' motif proximal to the GC-cluster, since mutagenesis of this sequence *in vivo* resulted in strong phenotypes (Fig. 3a, c, d). In structures of the archaeal initiator Orc1 bound to a replication origin the protein was observed to make two contacts with the DNA, one through its carboxy (C)-terminal DNA binding domain (analogous to DnaA domain IV) and another through its AAA+ motif^{15,16}. We wondered whether DnaA might similarly be capable of contacting both a DnaA-box and the first DnaA-trio, thereby accounting for the absence of a DnaA trimer. Importantly, BMOE crosslinking of cysteines in the AAA+ domain would not detect this activity as the assay captures DnaA oligomers formed on either dsDNA or ssDNA¹².

To test this hypothesis, we used the amine-specific crosslinker bis(sulfosuccinimidyl)suberate (BS³) which, in contrast to BMOE, only captures DnaA oligomers formed on a single DNA strand (Extended Data Figs 3 and 5). Crosslinking by BS³ reveals a DnaA dimer forming in the presence of the first 3'-GAT-5', indicating that DnaA does recognize this sequence (Extended Data Fig. 5). Taken together with the BMOE crosslinking showing that a DnaA dimer is formed on the dsDNA scaffold containing just DnaA-boxes 6 and 7 and the GC-cluster, the data suggest that the DnaA protein initially bound at DnaA-box7 undergoes a conformational change (detected by BS³) to engage the first DnaA-trio motif following the GC-cluster. Several lines of evidence support the notion that DnaA adopts distinct conformations when it engages either dsDNA or ssDNA^{17,18}.

To support the assignment of the DnaA-trio, we performed a targeted mutagenesis of the proposed sequence. The results indicate that each of the positions (3'-GAT-5') appears important for DnaA filament formation, specifically the nucleotides at positions 1 and 2, and the deoxyribose group at position 3 (Fig. 4b and Extended Data Fig. 6). Interestingly, in the crystal structure of DnaA bound to a ssDNA substrate, the protein makes no base-specific contacts⁴. These observations suggest either that the sequence of the DnaA-trios is important for an intermediate step in DNA duplex recognition and melting before full engagement of the product single-strand, or that the specific base sequence promotes the DNA backbone to adopt a favourable geometry for DnaA binding.

Using this information, we first searched for DnaA-trios within other well-characterized origin unwinding elements (Fig. 4c, underlined)^{19–21}. In these cases a set of at least three DnaA-trios could be identified. These DnaA-trios were located proximal to a DnaA-box that shared the same orientation as *B. subtilis* DnaA-box7, and the regions between the DnaA-box and the DnaA-trios were GC-rich. Using these additional criteria we next interrogated predicted bacterial DNA replication origins (DoriC²²) for similar patterns. Figure 4c shows that similar elements can be identified within putative *oriC* regions throughout the bacterial kingdom. A sequence logo of the DnaA-trios indicates that the preferred motif is 3'-G/AT-5' (Fig. 4d), with the central adenine being most highly conserved. We also observed that in most cases a pair of tandem DnaA-boxes preceded the GC-cluster (Extended Data Table 1).

We propose that the DnaA-trio constitutes a new element within bacterial replication origins. Our findings indicate that DnaA-trios play an essential role during DNA replication initiation by providing specificity for DnaA filament formation on a single DNA strand,

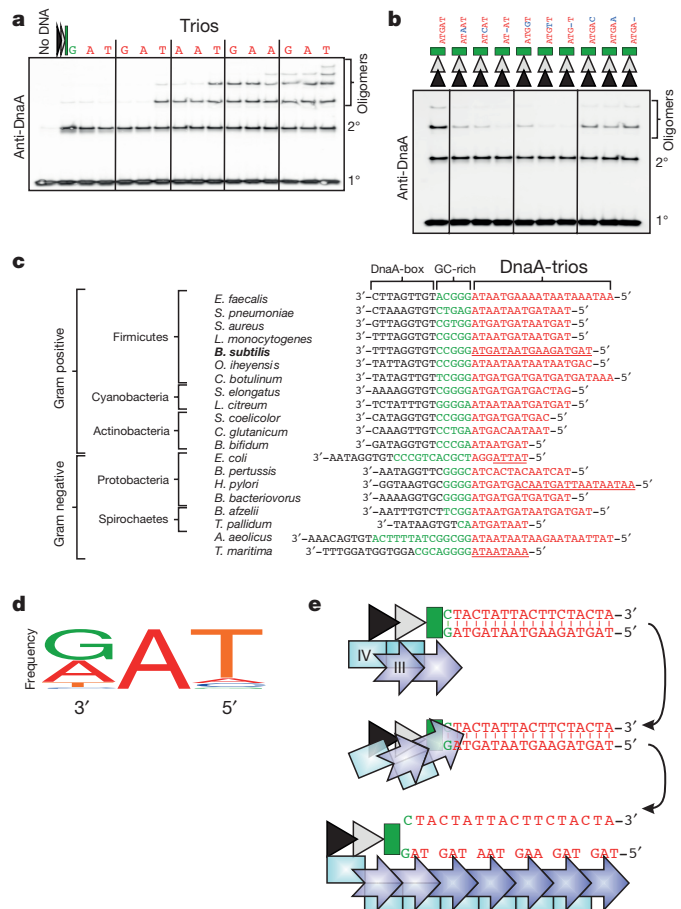


Figure 4 | Identification of the DnaA-trio motif. **a**, Varying the length of 5'-tailed substrates identifies the likely DnaA-trio sequence. Lane 2 shows DnaA filament formation on a duplex DNA scaffold (DnaA-box6, DnaA-box7, GC-rich cluster). Letters indicate the nucleotide sequentially added to the 5'-tail. **b**, Targeted mutagenesis of the proposed DnaA-trio motif. **c**, Bioinformatic analysis identifies DnaA-trio motifs adjacent to a DnaA-box throughout the bacterial kingdom. Underlined sequences indicate experimentally determined DnaA-dependent unwinding sites. **d**, DnaA-trios sequence logo (WebLogo²⁸). **e**, Schematic of DnaA filament formation from double-stranded DnaA-boxes (triangles) onto a single strand containing the DnaA-trios.

thereby promoting DNA duplex unwinding. Our analysis also indicates that the arrangement of tandem DnaA-boxes in close proximity to DnaA-trios is a widespread strategy used to direct DnaA filament growth onto the unwinding region, with a single DnaA protein probably binding dsDNA via domain IV before engaging a DnaA-trio via its AAA+ motif (Fig. 4e and Extended Data Fig. 5). Together our data are consistent with the two-step DnaA assembly model for DNA melting¹⁸.

We note that the configuration between DnaA-boxes and the DnaA-trios is not strictly required for DnaA to be loaded onto the single DNA strand *in vitro*. Scaffolds containing either a single DnaA-box or containing DnaA-boxes in reverse orientation are competent to promote DnaA filament formation from the duplex DNA onto the 5'-tail, although in the latter situation DnaA filament formation was reduced suggesting that DnaA-box orientation is important (Extended Data Fig. 7). Furthermore, loading does not require the flexibly tethered domains I/II of DnaA, consistent with previous observations suggesting that domains III/IV can adopt multiple conformations (Extended Data Fig. 7)^{12,17,18}. These results suggest that some plasticity can be accommodated between duplex and single-strand DNA binding elements, which is in agreement with recent reanalyses of essential DnaA-boxes in *E. coli* and might also explain the location of atypical origin unwinding sites^{23–26}.

Analysis of replication initiator proteins from both bacteria and archaea shows that the ISM within AAA+ domains is used for DNA binding, and the recent structure of the *Drosophila* origin recognition complex (ORC) suggests that this is also probably the case for eukaryotes, supporting the model that DNA binding by the ISM is a universal feature of replication initiators^{4,15,16,27}. We find here, for the first time, that the interaction of the *B. subtilis* replication initiator ISM with the origin involves recognition of a specific DNA sequence. We speculate that motifs analogous to the DnaA-trio might be present in replication origins of higher organisms and recognized by the ISM of ORC proteins. These sites need not be trinucleotides, nor would they necessarily share the same spacing observed for the DnaA-trios as they would need to accommodate the arrangement of AAA+ interactions within the respective heterohexameric ORC^{17,27}. The discovery of ISM binding motifs in higher organisms would greatly facilitate origin identification, an elusive problem precluding the understanding of DNA replication control in eukaryotes.

Online Content Methods, along with any additional Extended Data display items and Source Data, are available in the online version of the paper; references unique to these sections appear only in the online paper.

Received 9 November 2015; accepted 30 March 2016.

Published online 8 June 2016.

- Duderstadt, K. E. & Berger, J. M. A structural framework for replication origin opening by AAA+ initiation factors. *Curr. Opin. Struct. Biol.* **23**, 144–153 (2013).
- Messer, W. The bacterial replication initiator DnaA. DnaA and *oriC*, the bacterial mode to initiate DNA replication. *FEMS Microbiol. Rev.* **26**, 355–374 (2002).
- Fuller, R. S., Funnell, B. E. & Kornberg, A. The dnaA protein complex with the *E. coli* chromosomal replication origin (*oriC*) and other DNA sites. *Cell* **38**, 889–900 (1984).
- Duderstadt, K. E., Chuang, K. & Berger, J. M. DNA stretching by bacterial initiators promotes replication origin opening. *Nature* **478**, 209–213 (2011).
- Fujikawa, N. *et al.* Structural basis of replication origin recognition by the DnaA protein. *Nucleic Acids Res.* **31**, 2077–2086 (2003).
- Mackiewicz, P., Zakrzewska-Czerwinska, J., Zawilak, A., Dudek, M. R. & Cebat, S. Where does bacterial replication start? Rules for predicting the *oriC* region. *Nucleic Acids Res.* **32**, 3781–3791 (2004).
- Wolański, M., Donczew, R., Zawilak-Pawlik, A. & Zakrzewska-Czerwińska, J. *oriC*-encoded instructions for the initiation of bacterial chromosome replication. *Front. Microbiol.* **5**, 735 (2015).
- Hassan, A. K. *et al.* Suppression of initiation defects of chromosome replication in *Bacillus subtilis* dnaA and *oriC*-deleted mutants by integration of a plasmid replicon into the chromosomes. *J. Bacteriol.* **179**, 2494–2502 (1997).
- Krause, M., Rückert, B., Lurz, R. & Messer, W. Complexes at the replication origin of *Bacillus subtilis* with homologous and heterologous DnaA protein. *J. Mol. Biol.* **274**, 365–380 (1997).
- Leonard, A. C. & Grimwade, J. E. Regulation of DnaA assembly and activity: taking directions from the genome. *Annu. Rev. Microbiol.* **65**, 19–35 (2011).
- Speck, C. & Messer, W. Mechanism of origin unwinding: sequential binding of DnaA to double- and single-stranded DNA. *EMBO J.* **20**, 1469–1476 (2001).
- Scholefield, G., Errington, J. & Murray, H. Soj/ParA stalls DNA replication by inhibiting helix formation of the initiator protein DnaA. *EMBO J.* **31**, 1542–1555 (2012).
- Cheng, H. M., Gröger, P., Hartmann, A. & Schlierf, M. Bacterial initiators form dynamic filaments on single-stranded DNA monomer by monomer. *Nucleic Acids Res.* **43**, 396–405 (2015).
- Ozaki, S. *et al.* A common mechanism for the ATP-DnaA-dependent formation of open complexes at the replication origin. *J. Biol. Chem.* **283**, 8351–8362 (2008).
- Gaudier, M., Schuwirth, B. S., Westcott, S. L. & Wigley, D. B. Structural basis of DNA replication origin recognition by an ORC protein. *Science* **317**, 1213–1216 (2007).
- Dueber, E. L., Corn, J. E., Bell, S. D. & Berger, J. M. Replication origin recognition and deformation by a heterodimeric archaeal Orc1 complex. *Science* **317**, 1210–1213 (2007).
- Erzberger, J. P., Mott, M. L. & Berger, J. M. Structural basis for ATP-dependent DnaA assembly and replication-origin remodeling. *Nature Struct. Mol. Biol.* **13**, 676–683 (2006).
- Duderstadt, K. E. *et al.* Origin remodeling and opening in bacteria rely on distinct assembly states of the DnaA initiator. *J. Biol. Chem.* **285**, 28229–28239 (2010).
- Krause, M. & Messer, W. DnaA proteins of *Escherichia coli* and *Bacillus subtilis*: coordinate actions with single-stranded DNA-binding protein and interspecies inhibition during open complex formation at the replication origins. *Gene* **228**, 123–132 (1999).
- Donczew, R., Weigel, C., Lurz, R., Zakrzewska-Czerwinska, J. & Zawilak-Pawlik, A. *Helicobacter pylori oriC* – the first bipartite origin of chromosome replication in Gram-negative bacteria. *Nucleic Acids Res.* **40**, 9647–9660 (2012).
- Ozaki, S., Fujimitsu, K., Kurumizaka, H. & Katayama, T. The DnaA homolog of the hyperthermophilic eubacterium *Thermotoga maritima* forms an open complex with a minimal 149-bp origin region in an ATP-dependent manner. *Genes Cells* **11**, 425–438 (2006).
- Gao, F., Luo, H. & Zhang, C. T. DoriC 5.0: an updated database of *oriC* regions in both bacterial and archaeal genomes. *Nucleic Acids Res.* **41**, D90–D93 (2013).
- Kumar, S., Farhana, A. & Hasnain, S. E. *In-vitro* helix opening of *M. tuberculosis oriC* by DnaA occurs at precise location and is inhibited by IclA like protein. *PLoS ONE* **4**, e4139 (2009).
- Pei, H. *et al.* Mechanism for the TtDnaA-Tt-*oriC* cooperative interaction at high temperature and duplex opening at an unusual AT-rich region in *Thermoanaerobacter tengcongensis*. *Nucleic Acids Res.* **35**, 3087–3099 (2007).
- Kaur, G. *et al.* Building the bacterial orisome: high-affinity DnaA recognition plays a role in setting the conformation of *oriC* DNA. *Mol. Microbiol.* **91**, 1148–1163 (2014).
- Noguchi, Y., Sakiyama, Y., Kawakami, H. & Katayama, T. The Arg fingers of key DnaA protomers are oriented inward within the replication origin *oriC* and stimulate DnaA subcomplexes in the initiation complex. *J. Biol. Chem.* **290**, 20295–20312 (2015).
- Bleichert, F., Botchan, M. R. & Berger, J. M. Crystal structure of the eukaryotic origin recognition complex. *Nature* **519**, 321–326 (2015).
- Crooks, G. E., Hon, G., Chandonia, J. M. & Brenner, S. E. WebLogo: a sequence logo generator. *Genome Res.* **14**, 1188–1190 (2004).

Supplementary Information is available in the online version of the paper.

Acknowledgements We thank J. Errington and W. Vollmer for reviewing the manuscript. We thank G. Scholefield for preliminary data, A. Koh for research assistance and I. Selmes for technical assistance. Research support was provided to H.M. by a Royal Society University Research Fellowship and a Biotechnology and Biological Sciences Research Council Research Grant (BB/K017527/1), and to O.H. by an Iraqi Ministry of Higher Education and Scientific Research Studentship.

Author Contributions H.M. and T.T.R. conceived and designed experiments; H.M., T.T.R. and O.H. constructed plasmids and strains; H.M. and O.H. performed growth and marker frequency analysis experiments; H.M. performed microscopy experiments; T.T.R. purified proteins, performed the open complex assay, and performed the DnaA filament formation assays; H.M. and T.T.R. interpreted results and wrote the paper.

Author Information Reprints and permissions information is available at www.nature.com/reprints. The authors declare no competing financial interests. Readers are welcome to comment on the online version of the paper. Correspondence and requests for materials should be addressed to H.M. (heath.murray@newcastle.ac.uk).

METHODS

No statistical methods were used to predetermine sample size. The experiments were not randomized. The investigators were not blinded to allocation during experiments and outcome assessment.

Media and chemicals. Nutrient agar (Oxoid) was used for routine selection and maintenance of both *B. subtilis* and *E. coli* strains. For experiments in *B. subtilis* cells were grown using Luria-Bertani medium. Supplements were added as required: chloramphenicol (5 µg ml⁻¹), erythromycin (1 µg ml⁻¹), kanamycin (5 µg ml⁻¹), spectinomycin (50 µg ml⁻¹). Unless otherwise stated, all chemicals and reagents were obtained from Sigma-Aldrich.

Phenotype analysis of *oriC* mutants using the inducible *oriC*-independent strain. Strains were grown for 18–72 h at 37 °C on nutrient agar plates either with or without IPTG (1 mM). All experiments were independently performed at least twice and representative data are shown.

Marker frequency analysis. Genomic DNA was harvested from cells during the exponential growth phase and the relative amount of DNA from the replication origin (*ori*) and terminus (*ter*) was determined by qPCR. Strains were grown in Luria-Bertani medium to an absorbance, $A_{600\text{ nm}}$, of 0.3–0.5 whereupon sodium azide (0.5%) was added to prevent further metabolism. Chromosomal DNA was isolated using a DNeasy Blood and Tissue Kit (Qiagen). The DNA replication origin (*oriC*) region was amplified using primers 5'-GAATTCCTCAGGCCATTGA-3' and 5'-GATTTCTGGCGAATTGGAAG-3'; the region adjacent to *oriN* was amplified using primers 5'-CTTTCTGCCGCAAAGGATTA-3' and 5'-CCTCTTCATAGCCGTTTTC-3'; the DNA replication terminus (*ter*) region was amplified using primers 5'-TCCATATCCTCGTCTCTACG-3' and 5'-ATTCTGCTGATGTGCAATGG-3'. Either Rotor-Gene SYBR Green (Qiagen) or GoTaq (Promega) qPCR mix was used for PCR reactions. qPCR was performed in a Rotor-Gene Q Instrument (Qiagen). By use of crossing points (C_T) and PCR efficiency a relative quantification analysis ($\Delta\Delta C_T$) was performed using Rotor-Gene Software version 2.0.2 (Qiagen) to determine the origin:terminus (*ori:ter*) ratio of each sample. These results were normalized to the *ori:ter* ratio of a DNA sample from *B. subtilis* spores, which only contain one chromosome and thus have an *ori:ter* ratio of 1. Error bars indicate the standard deviation of three technical replicates. All experiments were independently performed at least twice and representative data are shown.

Protein expression. BL21 (DE3)-pLysS cells were transformed with the appropriate expression construct (Supplementary Table 2) and selected on nutrient agar plates containing 100 ng µl⁻¹ of ampicillin and 34 ng µl⁻¹ of chloramphenicol. A single transformant colony was used to inoculate an overnight starter culture grown at 37 °C, 180 rpm, in Luria-Bertani medium supplemented with 100 ng µl⁻¹ of ampicillin and 34 ng µl⁻¹ of chloramphenicol. The following morning a 1/100 dilution of overnight culture was used to inoculate 1,200 ml of Luria-Bertani medium supplemented with 100 ng µl⁻¹ of ampicillin and grown at 37 °C, 180 rpm, to $A_{600\text{ nm}} = 0.5$. Cells were induced with 1 mM IPTG and cultured for a further 3 h at 30 °C. Cells were pelleted at 3,000g, 4 °C for 10 min before resuspension in 45 ml of resuspension buffer (25 mM HEPES-KOH (pH 7.6); 500 mM potassium glutamate; 10 mM magnesium acetate; 20% sucrose; 30 mM imidazole; 1 × cComplete EDTA-free protease inhibitor tablet (Roche)). The cell suspension was then flash-frozen in liquid nitrogen.

Protein purification. DnaA (WT, WT-CC and I190A-CC) was purified as follows. A frozen 50 ml BL21 cell pellet suspension was thawed on ice with 32 mg of lysozyme and gentle agitation for 1 h then disrupted by sonication at 20 W for 5 min in 25 pulses. Cell debris was pelleted by centrifugation at 31,000g, 4 °C for 45 min and the supernatant further clarified by filtration (0.45 µm). All subsequent steps were performed at 4 °C unless otherwise stated. The clarified lysate was applied at 1 ml min⁻¹ to a 1 ml HisTrap HP column (GE), which had previously been equilibrated with Ni binding buffer (25 mM HEPES-KOH (pH 7.6); 250 mM potassium glutamate; 10 mM magnesium acetate; 20% sucrose; 30 mM imidazole). The loaded column was washed with a 10 ml one-step gradient of 10% Ni elution buffer (25 mM HEPES-KOH (pH 7.6); 250 mM potassium glutamate; 10 mM magnesium acetate; 20% sucrose; 30 mM imidazole). Specifically bound proteins were eluted using a 7.5 ml one-step gradient of 100% Ni elution buffer and the entire fraction collected and diluted into 42.5 ml of Q binding buffer (30 mM Tris-HCl (pH 7.6); 100 mM potassium glutamate; 10 mM magnesium acetate; 1 mM DTT; 20% sucrose). The diluted fraction was then applied at 1 ml min⁻¹ to a 1 ml HiTrap Q HP column (GE), which had previously been equilibrated with Q binding buffer. The loaded HiTrap Q HP column was washed with 10 ml of Q binding buffer then eluted using a linear 10 ml gradient of 0–100% Q elution buffer (30 mM Tris-HCl (pH 7.6); 1 M potassium glutamate; 10 mM magnesium acetate; 1 mM DTT; 20% sucrose) with 1 ml fractions collected. The peak 3 × 1 ml fractions, based on ultraviolet absorbance, were pooled and dialysed into 1 L of FactorXa cleavage buffer (25 mM HEPES-KOH (pH 7.6); 250 mM potassium

glutamate; 20% sucrose; 5 mM CaCl₂), using 3.5k MWCO SnakeSkin dialysis tubing (Life Technologies) at 4 °C overnight. The dialysed protein was diluted to 5 ml total volume in FactorXa cleavage buffer and incubated at 23 °C for 6 h with 80 µg of FactorXa protease (NEB). The sample was applied at 1 ml min⁻¹ to a 1 ml HisTrap HP column (GE), which had previously been equilibrated with Factor Xa cleavage buffer. The Factor Xa-cleaved fraction was eluted in 7.5 ml of Ni binding buffer. The eluted fraction was diluted into 42.5 ml of Q binding buffer and purified on a 1 ml HiTrap Q HP column as previously described. Peak fraction(s) were pooled and dialysed into 1 L of final dialysis buffer (40 mM HEPES-KOH (pH 7.6); 250 mM potassium glutamate; 1 mM DTT; 20% sucrose; 20% PEG₃₀₀), using 3.5k MWCO SnakeSkin dialysis tubing (Life Technologies) at 4 °C overnight before aliquoting, flash-freezing in liquid nitrogen and storage at –80 °C. Removal of the amino (N)-terminal His-tag, after incubation with FactorXa, was confirmed by anti-pentaHis (Qiagen) western blotting.

C-terminally His-tagged DnaA (WT-CC and Δ (domainI-II)-CC) purification was performed as for the tag-free variants, except that the protein was dialysed into final dialysis buffer after the first HiTrap Q HP column purification before aliquoting, flash-freezing and storing.

HBSu purification was performed exactly as for DnaA, except that the HiTrap Q HP column was substituted for a 1 ml HiTrap Heparin HP column (GE) and the composition of buffers was modified accordingly. Ni binding buffer (25 mM Tris-HCl (pH 8.0); 400 mM NaCl; 30 mM imidazole). Ni elution buffer (25 mM Tris-HCl (pH 8.0); 400 mM NaCl; 500 mM imidazole). Heparin binding buffer (25 mM Tris-HCl (pH 8.0); 100 mM NaCl; 1 mM EDTA). Heparin elution buffer (25 mM Tris-HCl (pH 8.0); 2 M NaCl; 1 mM EDTA). Factor Xa cleavage buffer (25 mM Tris-HCl (pH 8.0); 100 mM NaCl; 2 mM CaCl₂; 20% sucrose). Final dialysis buffer (25 mM Tris-HCl (pH 8.0); 400 mM NaCl; 2 mM CaCl₂; 20% sucrose; 20% PEG₃₀₀). Peak fractions were determined by SDS-PAGE and Coomassie staining owing to the absence of tryptophan, tyrosine and cysteine residues.

Open complex formation assays. KMnO₄ footprinting assays were essentially performed as described in ref. 9, except for the following changes. DnaA was not pre-incubated with ATP. The unwinding buffer contained 2 mM ATP, rather than 5 mM, and 500 ng of plasmid pTR541 (wild type) or pTR542 (t1-t6^{cc}) was used per 75-µl-scale reaction. DnaA was added to final concentrations of 0, 100, 250, 500 and 1,000 nM. Assembled reactions were incubated at 37 °C for 10 min. KMnO₄ treatment was then performed at 37 °C for 10 min. Six microlitres of β -mercaptoethanol was used to quench reactions; however, EDTA was omitted. KMnO₄-treated DNA was immediately purified using a Qiagen PCR clean-up kit, eluting in 20 µl of EB buffer. KMnO₄-treated templates were not linearized before primer extension. Primer extensions were performed on a 20 µl scale using 0.1 U µl⁻¹ of Vent exo- DNA polymerase (NEB) in 1 × manufacturer's reaction buffer supplemented with 4 mM MgSO₄, 200 µM each dNTP, 200 nM Cy5-labelled oligonucleotide (5'-Cy5-AGCTTCAGCAGCATGTAAAG-3') and 4 µl of PCR-purified template DNA per reaction. Reactions were subjected to thermocycling using a 3Prime thermal cycler (Techne) with 1 min initial denaturation at 98 °C, followed by 35 cycles of (10 s at 98 °C; 30 s at 55 °C; 30 s at 72 °C). Reactions were quenched by addition of an equal volume of stop buffer (95% formamide; 10 mM EDTA; 10 mM NaOH; 0.01% Orange-G) and products subjected to denaturing PAGE (6% acrylamide:bisacrylamide (19:1); 8 M urea in 1 × TBE). Resolved products were visualized using a Typhoon Trio Variable Mode Imager (GE Healthcare). The DnaA-trio marker was generated by primer extension performed under the same conditions as described for KMnO₄-treated substrates, but using a PCR product as template generated with a primer corresponding to the end of the first DnaA-trio (5'-TAGGGCCTGTGGATTGTG-3'). All experiments were independently performed at least twice and representative data are shown.

Filament assembly assays (BMOE). DNA scaffolds were prepared by mixing each oligonucleotide (50 nM final concentrations) in 10 mM HEPES-KOH (pH 7.6), 100 mM NaCl and 1 mM EDTA. Mixed oligonucleotides were heated to 98 °C for 5 min in a heat-block and slowly cooled to room-temperature in the heat-block before use. Filament formation was promoted by mixing DnaA-CC proteins (WT, I190A, Δ domainI-II) (200 nM final concentration) with DNA scaffold (15 nM) on a 20 µl scale in 30 mM HEPES-KOH (pH 7.0), 100 mM potassium glutamate, 100 mM NaCl, 10 mM magnesium acetate, 25% glycerol, 0.01% Tween-20 and 2 mM nucleotide (ADP or ATP). Reactions were incubated at 37 °C for 5–12 min before addition of 4 mM BMOE (ThermoFisher Scientific). Reactions were incubated at 37 °C for 5–12 min before quenching by addition of 60 mM cysteine. Reactions were incubated once more at 37 °C for 10–12 min before fixing in NuPAGE LDS sample buffer (ThermoFisher Scientific) at 98 °C for 5 min. Complexes were resolved by running 500 fmol of cross-linked DnaA from each reaction on a NuPAGE Novex 3–8% Tris-acetate gel (ThermoFisher Scientific) then transferred to Hybond 0.45 µm PVDF membrane (Amersham) in 0.5 × NuPAGE Tris-acetate SDS running buffer with 20% MeOH at 35 mA, 4 °C overnight using

wet transfer apparatus (Biorad). Complexes were visualized by western blotting using a polyclonal anti-DnaA antibody (Eurogentec). NB: all filament assembly assays were performed using tag-free proteins with the exception of that shown in Extended Data Fig. 7, in which C-terminally His-tagged proteins (Δ domainI-II-CC and wild-type-CC) were used. All experiments were independently performed at least twice and representative data are shown.

Filament assembly assays (BS³). Filament assembly assays using bis(sulfosuccinimidyl)suberate (BS³) were performed as described for BMOE, except a tag-free fully wild-type recombinant DnaA protein was used for Extended Data Fig. 3. Tag-free 'CC' variants of wild-type and I190A DnaA were used for Extended Data Fig. 5a, b. Crosslinking was performed using BS³ (15 mM final concentration) in place of BMOE and quenching performed by addition of Tris-HCl (pH 7.6) (30 mM final concentration). All experiments were independently performed at least twice and representative data are shown.

Microscopy. To visualize GFP-DnaN, starter cultures were grown overnight in defined minimal medium base (Spizizen minimal salts supplemented with Fe-NH₄-citrate (1 μ g ml⁻¹), MgSO₄ (6 mM), CaCl₂ (100 μ M), MnSO₄ (130 μ M), ZnCl₂ (1 μ M), thiamine (2 μ M)) supplemented with casein hydrolysate (200 μ g ml⁻¹) and glycerol (0.5%) with IPTG (1 mM) at 37 °C, diluted 1:100 into fresh medium with IPTG (1 mM) and allowed to grow at 37 °C for several generations until they reached $A_{600\text{ nm}} = 0.3$. Cells were collected by centrifugation, washed to remove IPTG, and resuspended into fresh medium at $A_{600\text{ nm}} = 0.1$ and allowed to grow until $A_{600\text{ nm}} = 0.6$. Cells were mounted on 1.5% agar pads (0.5 \times growth media) and a 0.13–0.17 mm glass coverslip (VWR) was placed on top. Microscopy was performed on an inverted epifluorescence microscope (Nikon Ti) fitted with a Plan-Apochromat objective (Nikon DM 100 \times /1.40 Oil Ph3). Light was transmitted from a 300 W xenon arc-lamp through a liquid light guide (Sutter Instruments) and images were collected using a CoolSnap HQ2 cooled CCD (charge-coupled device) camera (Photometrics). All filters were Modified Magnetron ET Sets from Chroma and details are available upon request. Digital images were acquired and analysed using METAMORPH software (version 6.2r6). All experiments were independently performed at least twice and representative data are shown.

Strains. Strains are listed in Supplementary Table 1. The genotype of all origin mutants was confirmed by DNA sequencing.

Oligonucleotides. All oligonucleotides were purchased from Eurogentec. Oligonucleotides used for plasmid construction are listed in Extended Data Table 2. Oligonucleotides used to construct DNA scaffolds are listed in Extended Data Table 3.

Plasmids. Plasmids are listed in the Supplementary Table 2 (sequences are available upon request). DH5 α (F⁻ Φ 80lacZ Δ M15 Δ (lacZYA-argF) U169 recA1 endA1 hsdR17(r_K⁻, m_K⁺) phoA supE44 thi-1 gyrA96 relA1 λ ⁻)²⁹ was used for plasmid construction, except where noted. Descriptions, where necessary, are provided below.

pHM327 derivatives were generated by quickchange mutagenesis using the oligonucleotides listed in Extended Data Table 2. After sequencing to confirm mutated regions, sequences were subcloned using BglII/FspAI.

pHM446 (*bla aprE' kan lacI* P_{spac}-MCS' *aprE*) is a derivative of pAPNC213 (ref. 30) with a kanamycin resistance cassette replacing the spectinomycin resistance cassette (gift from H. Strahl).

pHM453 (*bla rpna' rpmH erm Δ incAB* P_{spac}-*dnaA'*) was created in multiple steps. First, pJS1 was generated by ligation with a HindIII-BamHI PCR product containing 5' end of *dnaA* and pMUTIN4 (ref. 31) cut with HindIII-BamHI (gift from J. Errington). Second, pHM396 was generated by digestion of pJS1 with PvuII

(to remove *lacZ* and *lacI*) and ligation of the vector backbone. Finally, pHM453 was generated by ligation of an AatII PCR product containing *rpmH* and the 5' end of *rpna* (oHM319 + oHM320 and 168CA genomic DNA as template) with pHM396 cut with AatII.

pHM492 (*bla aprE' kan lacI* P_{spac}-*repN(oriN)* ' *aprE*) was generated by ligation of an EcoRI-XhoI PCR product containing *repN(oriN)* (oHM313 + oHM315 and MMB208 (ref. 32) genomic DNA as template) with pHM446 cut with EcoRI-SalI.

pHM560 (*bla rpna' rpmH erm Δ incA* P_{dnaA} Δ *incB dnaA'*) was generated by ligation of an EcoRV-HindIII PCR product containing the *dnaA* promoter (oHM510 + oHM511 and 168CA genomic DNA as template) with pHM453 cut with EcoRV-HindIII.

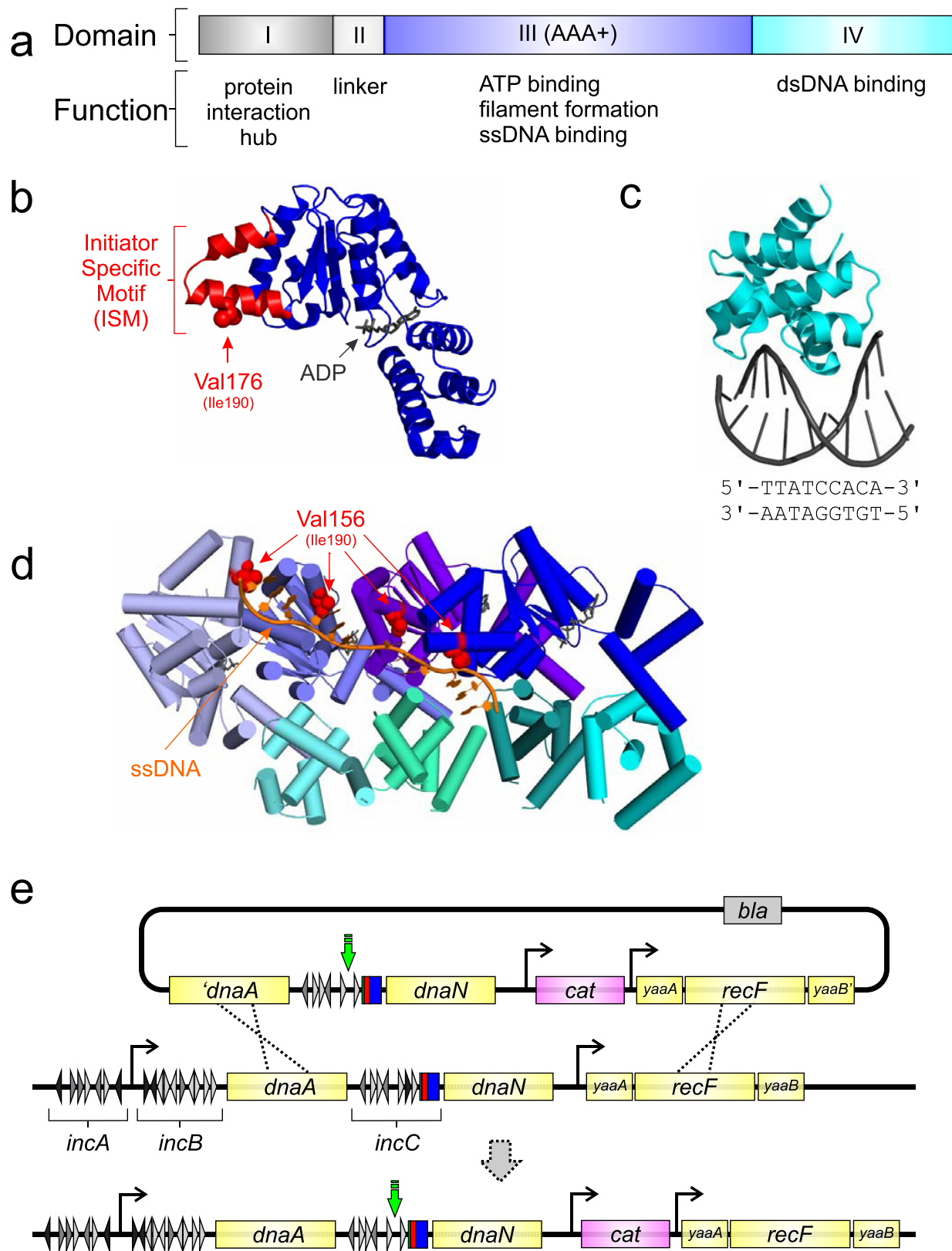
pTR72, pTR73, pTR74, pTR102, pTR168 were generated by quickchange mutagenesis using the oligonucleotides listed in Extended Data Table 2.

pTR208 was generated by two-fragment PCR. oTR384/oTR385 and oTR386/oTR387 were used to amplify products using pTR74 and *B. subtilis* 168CA genomic DNA as templates, respectively. An equal volume of each PCR product was mixed, heated to 98 °C and allowed to cool to room temperature before DpnI digestion and transformation.

pTR229 (*bla* P_{T7}(*his6-link-Xa-dnaA*)) was generated by subcloning a HindIII-XhoI fragment of *dnaA* from pHM239 into the pTR74 backbone.

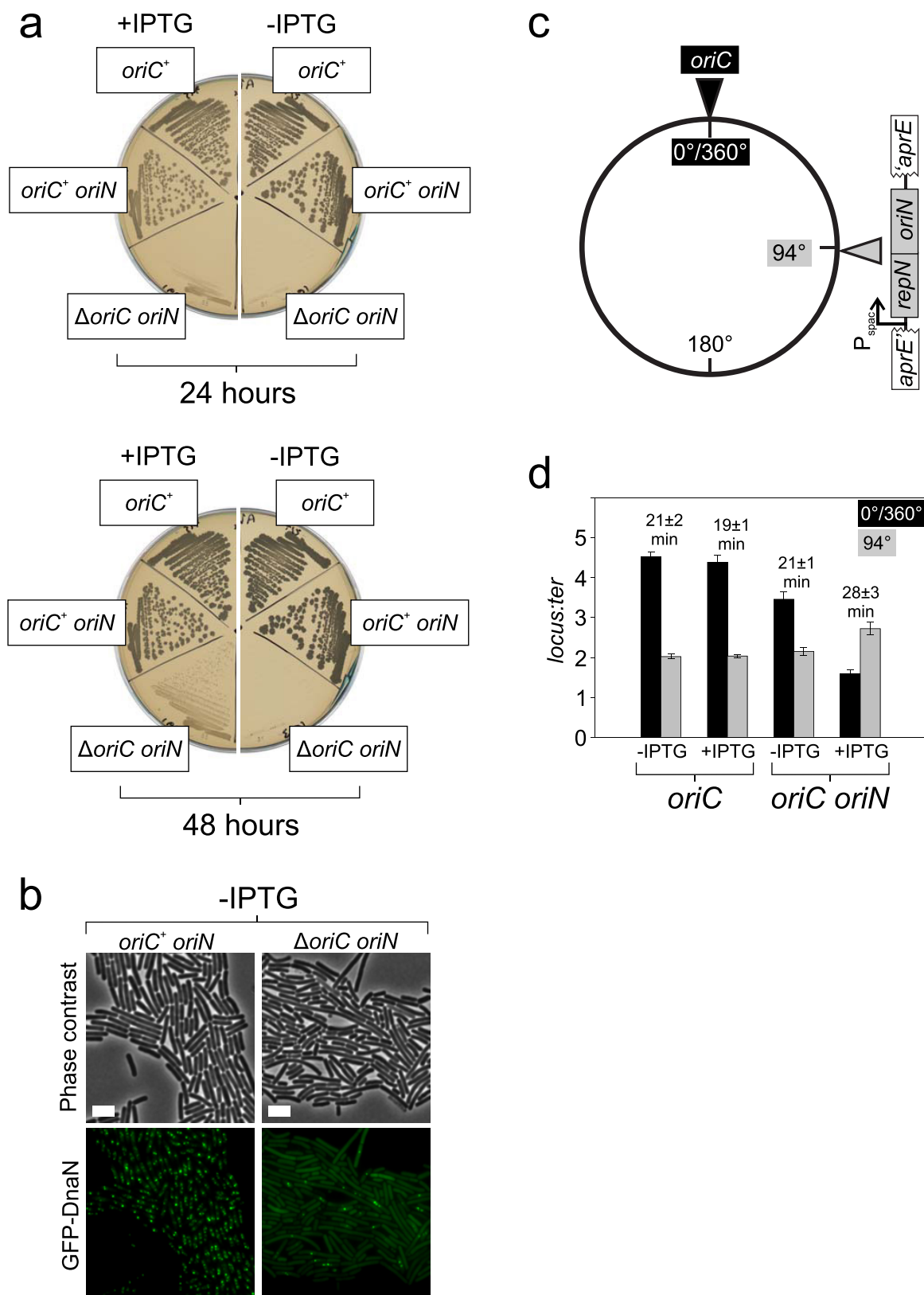
pTR541 and pTR542 were generated by two-fragment PCR. oTR537 and oTR538 were used to amplify the plasmid backbone of pSG1301. oTR535 and oTR536 were used to amplify *incC* with *B. subtilis* 168CA genomic DNA and pTR84 used as the templates for pTR541 and pTR542, respectively. An equal volume of each PCR product was mixed, heated to 98 °C and allowed to cool to room temperature before DpnI digestion and transformation into EH3827 (*asnB32 relA1 spoT1 thi-1 fuc-1 lysA ilv-192 zia::pKN500 Δ dnaA mad-1*)³³. DNA sequencing confirmed the construction of each origin including flanking sequences (>400 base pairs upstream and downstream).

29. Taylor, R. G., Walker, D. C. & McInnes, R. R. *E. coli* host strains significantly affect the quality of small scale plasmid DNA preparations used for sequencing. *Nucleic Acids Res.* **21**, 1677–1678 (1993).
30. Morimoto, T. et al. Six GTP-binding proteins of the Era/Obg family are essential for cell growth in *Bacillus subtilis*. *Microbiology* **148**, 3539–3552 (2002).
31. Vagner, V., Dervyn, E. & Ehrlich, S. D. A vector for systematic gene inactivation in *Bacillus subtilis*. *Microbiology* **144**, 3097–3104 (1998).
32. Berkmen, M. B. & Grossman, A. D. Subcellular positioning of the origin region of the *Bacillus subtilis* chromosome is independent of sequences within *oriC*, the site of replication initiation, and the replication initiator DnaA. *Mol. Microbiol.* **63**, 150–165 (2007).
33. Hansen, E. B. & Yarmolinsky, M. B. Host participation in plasmid maintenance: dependence upon *dnaA* of replicons derived from P1 and F. *Proc. Natl Acad. Sci. USA* **83**, 4423–4427 (1986).
34. Moriya, S., Atlung, T., Hansen, F. G., Yoshikawa, H. & Ogasawara, N. Cloning of an autonomously replicating sequence (*ars*) from the *Bacillus subtilis* chromosome. *Mol. Microbiol.* **6**, 309–315 (1992).
35. Oka, A., Sugimoto, K., Takanami, M. & Hirota, Y. Replication origin of the *Escherichia coli* K-12 chromosome: the size and structure of the minimum DNA segment carrying the information for autonomous replication. *Mol. Gen. Genet.* **178**, 9–20 (1980).
36. Calcutt, M. J. & Schmidt, F. J. Conserved gene arrangement in the origin region of the *Streptomyces coelicolor* chromosome. *J. Bacteriol.* **174**, 3220–3226 (1992).
37. Watanabe, S. et al. Light-dependent and asynchronous replication of cyanobacterial multi-copy chromosomes. *Mol. Microbiol.* **83**, 856–865 (2012).



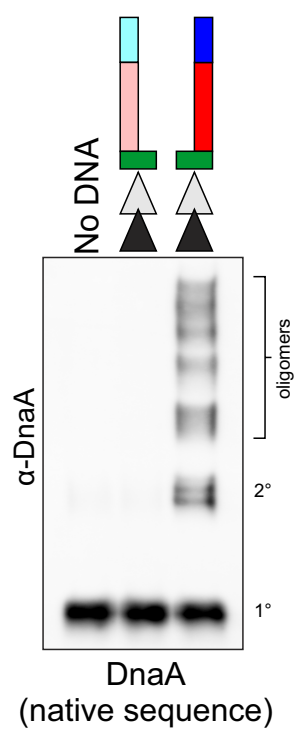
Extended Data Figure 1 | Structure of DnaA proteins. **a**, Primary domain structure of DnaA. Key functions are listed below the relevant domain. **b**, Structure of *Thermatoga maritima* DnaA domain III, highlighting the single-strand binding residue Val176 (Ile190 *B. subtilis*) within the ISM (PDB accession number 2Z4S). **c**, Structure of *E. coli* DnaA domain IV bound to a DnaA-box (PDB accession number 1J1V).

d, Structure of *A. aeolicus* DnaA domain III (blue shades) and domain IV (cyan shades) bound to a single DNA strand (orange), highlighting the single-strand binding residue Val156 (Ile190 *B. subtilis*) (PDB accession number 3R8F). **e**, Scheme used to construct mutants within the *B. subtilis* DNA replication origin. The green arrow highlights the location of a DnaA-box mutation.



Extended Data Figure 2 | Characterization of the inducible *repN/oriN* replication initiation system. Repression of *repN* expression inhibits DNA replication in a Δ *oriC* mutant. A large deletion was introduced into the *B. subtilis* replication origin using a strain harbouring the inducible *oriN/repN* construct. Strain growth was found to be dependent upon addition of the inducer IPTG. **a**, Strains streaked to resolve single colonies. **b**, A GFP-DnaN reporter was used to detect DNA replication after removal of IPTG from inducible *oriN/repN* strains. Scale bar, 5 μ m. **c**, Genetic map indicating the location of *oriN* at the *aprE* locus in strain HM1108.

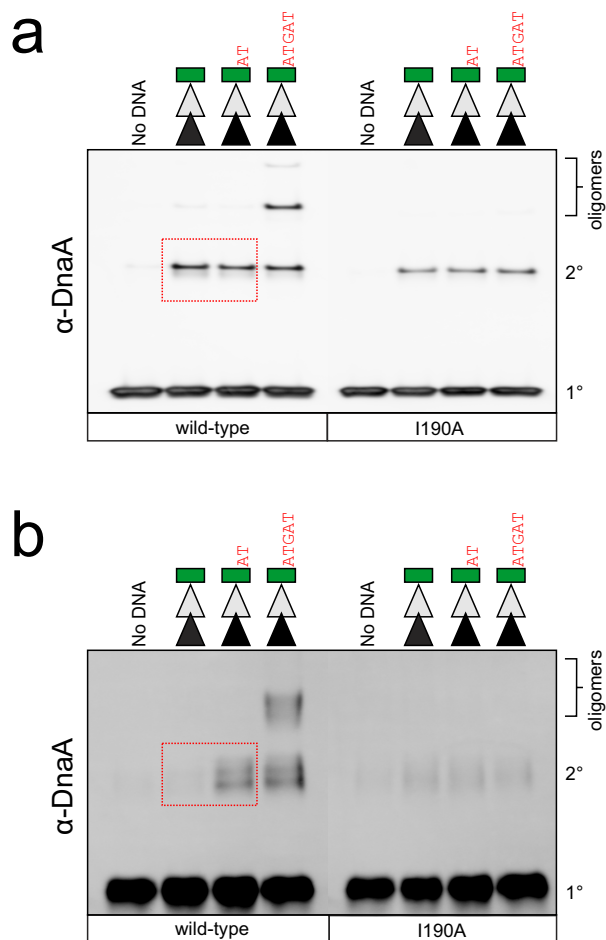
d, Analysis of DNA replication initiation at *oriC* and *oriN*. Marker frequency analysis was used to measure the rate of DNA replication initiation in the presence and absence of IPTG (0.1 mM). Genomic DNA was harvested from cells during the exponential growth phase and the relative amount of DNA from either the endogenous replication origin (*oriC*) or the *aprE* locus (*oriN*) compared with the terminus (*ter*) was determined using qPCR (mean and s.d. of three technical replicates). Cell doubling times (in minutes) are shown above each data set.



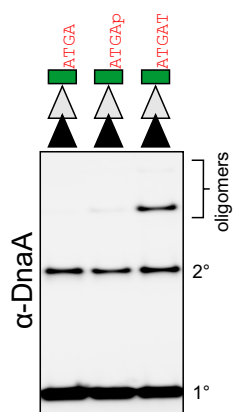
Extended Data Figure 3 | Wild-type DnaA assembles into filaments on 5'-tailed substrates. DnaA filament formation using amine-specific crosslinking (BS³) on DNA scaffolds (represented by symbols above each lane). Protein complexes were resolved by SDS-PAGE and DnaA was detected by western blot analysis.

	Strain	Wild-type sequence indicating deletions	Resulting sequence
Mononucleotide	Wild-type	3' - <u>G</u> <u>A</u> <u>T</u> <u>G</u> <u>A</u> <u>T</u> <u>A</u> <u>A</u> <u>T</u> <u>G</u> <u>A</u> <u>A</u> <u>G</u> <u>A</u> <u>T</u> - 5'	3' - <u>G</u> <u>A</u> <u>T</u> <u>G</u> <u>A</u> <u>T</u> <u>A</u> <u>A</u> <u>T</u> <u>G</u> <u>A</u> <u>A</u> <u>G</u> <u>A</u> <u>T</u> - 5'
	TR141	3' - <u>G</u> <u>A</u> <u>T</u> <u>G</u> <u>A</u> <u>T</u> <u>A</u> <u>A</u> <u>T</u> <u>G</u> <u>A</u> <u>A</u> <u>G</u> <u>A</u> <u>T</u> - 5'	3' - <u>A</u> <u>T</u> <u>G</u> <u>A</u> <u>T</u> <u>A</u> <u>A</u> <u>T</u> <u>G</u> <u>A</u> <u>A</u> <u>G</u> <u>A</u> <u>T</u> - 5'
	TR114	3' - <u>G</u> <u>A</u> <u>T</u> <u>G</u> <u>A</u> <u>T</u> <u>A</u> <u>A</u> <u>T</u> <u>G</u> <u>A</u> <u>A</u> <u>G</u> <u>A</u> <u>T</u> - 5'	3' - <u>G</u> <u>T</u> <u>G</u> <u>A</u> <u>T</u> <u>A</u> <u>A</u> <u>T</u> <u>G</u> <u>A</u> <u>A</u> <u>G</u> <u>A</u> <u>T</u> - 5'
	TR143	3' - <u>G</u> <u>A</u> <u>T</u> <u>G</u> <u>A</u> <u>T</u> <u>A</u> <u>A</u> <u>T</u> <u>G</u> <u>A</u> <u>A</u> <u>G</u> <u>A</u> <u>T</u> - 5'	3' - <u>G</u> <u>A</u> <u>G</u> <u>A</u> <u>T</u> <u>A</u> <u>A</u> <u>T</u> <u>G</u> <u>A</u> <u>A</u> <u>G</u> <u>A</u> <u>T</u> - 5'
	TR147	3' - <u>G</u> <u>A</u> <u>T</u> <u>G</u> <u>A</u> <u>T</u> <u>A</u> <u>A</u> <u>T</u> <u>G</u> <u>A</u> <u>A</u> <u>G</u> <u>A</u> <u>T</u> - 5'	3' - <u>G</u> <u>A</u> <u>T</u> <u>A</u> <u>T</u> <u>A</u> <u>A</u> <u>T</u> <u>G</u> <u>A</u> <u>A</u> <u>G</u> <u>A</u> <u>T</u> - 5'
	TR137	3' - <u>G</u> <u>A</u> <u>T</u> <u>G</u> <u>A</u> <u>T</u> <u>A</u> <u>A</u> <u>T</u> <u>G</u> <u>A</u> <u>A</u> <u>G</u> <u>A</u> <u>T</u> - 5'	3' - <u>G</u> <u>A</u> <u>T</u> <u>G</u> <u>T</u> <u>A</u> <u>A</u> <u>T</u> <u>G</u> <u>A</u> <u>A</u> <u>G</u> <u>A</u> <u>T</u> - 5'
	TR144	3' - <u>G</u> <u>A</u> <u>T</u> <u>G</u> <u>A</u> <u>T</u> <u>A</u> <u>A</u> <u>T</u> <u>G</u> <u>A</u> <u>A</u> <u>G</u> <u>A</u> <u>T</u> - 5'	3' - <u>G</u> <u>A</u> <u>T</u> <u>G</u> <u>A</u> <u>A</u> <u>A</u> <u>T</u> <u>G</u> <u>A</u> <u>A</u> <u>G</u> <u>A</u> <u>T</u> - 5'
	TR145	3' - <u>G</u> <u>A</u> <u>T</u> <u>G</u> <u>A</u> <u>T</u> <u>A</u> <u>A</u> <u>T</u> <u>G</u> <u>A</u> <u>A</u> <u>G</u> <u>A</u> <u>T</u> - 5'	3' - <u>G</u> <u>A</u> <u>T</u> <u>G</u> <u>A</u> <u>T</u> <u>A</u> <u>T</u> <u>G</u> <u>A</u> <u>A</u> <u>G</u> <u>A</u> <u>T</u> - 5'
	TR153	3' - <u>G</u> <u>A</u> <u>T</u> <u>G</u> <u>A</u> <u>T</u> <u>A</u> <u>A</u> <u>T</u> <u>G</u> <u>A</u> <u>A</u> <u>G</u> <u>A</u> <u>T</u> - 5'	3' - <u>G</u> <u>A</u> <u>T</u> <u>G</u> <u>A</u> <u>T</u> <u>A</u> <u>A</u> <u>G</u> <u>A</u> <u>A</u> <u>G</u> <u>A</u> <u>T</u> - 5'
Trinucleotide	Wild-type	3' - <u>G</u> <u>A</u> <u>T</u> <u>G</u> <u>A</u> <u>T</u> <u>A</u> <u>A</u> <u>T</u> <u>G</u> <u>A</u> <u>A</u> <u>G</u> <u>A</u> <u>T</u> - 5'	3' - <u>G</u> <u>A</u> <u>T</u> <u>G</u> <u>A</u> <u>T</u> <u>A</u> <u>A</u> <u>T</u> <u>G</u> <u>A</u> <u>A</u> <u>G</u> <u>A</u> <u>T</u> - 5'
	TR116	3' - <u>G</u> <u>A</u> <u>T</u> <u>G</u> <u>A</u> <u>T</u> <u>A</u> <u>A</u> <u>T</u> <u>G</u> <u>A</u> <u>A</u> <u>G</u> <u>A</u> <u>T</u> - 5'	3' - <u>G</u> <u>A</u> <u>T</u> <u>A</u> <u>A</u> <u>T</u> <u>G</u> <u>A</u> <u>A</u> <u>G</u> <u>A</u> <u>T</u> - 5'
		3' - <u>G</u> <u>A</u> <u>T</u> <u>G</u> <u>A</u> <u>T</u> <u>A</u> <u>A</u> <u>T</u> <u>G</u> <u>A</u> <u>A</u> <u>G</u> <u>A</u> <u>T</u> - 5'	3' - <u>G</u> <u>A</u> <u>T</u> <u>A</u> <u>A</u> <u>T</u> <u>G</u> <u>A</u> <u>A</u> <u>G</u> <u>A</u> <u>T</u> - 5'
		3' - <u>G</u> <u>A</u> <u>T</u> <u>G</u> <u>A</u> <u>T</u> <u>A</u> <u>A</u> <u>T</u> <u>G</u> <u>A</u> <u>A</u> <u>G</u> <u>A</u> <u>T</u> - 5'	3' - <u>G</u> <u>A</u> <u>T</u> <u>A</u> <u>A</u> <u>T</u> <u>G</u> <u>A</u> <u>A</u> <u>G</u> <u>A</u> <u>T</u> - 5'
		3' - <u>G</u> <u>A</u> <u>T</u> <u>G</u> <u>A</u> <u>T</u> <u>A</u> <u>A</u> <u>T</u> <u>G</u> <u>A</u> <u>A</u> <u>G</u> <u>A</u> <u>T</u> - 5'	3' - <u>G</u> <u>A</u> <u>T</u> <u>A</u> <u>A</u> <u>T</u> <u>G</u> <u>A</u> <u>A</u> <u>G</u> <u>A</u> <u>T</u> - 5'
	TR139	3' - <u>G</u> <u>A</u> <u>T</u> <u>G</u> <u>A</u> <u>T</u> <u>A</u> <u>A</u> <u>T</u> <u>G</u> <u>A</u> <u>A</u> <u>G</u> <u>A</u> <u>T</u> - 5'	3' - <u>G</u> <u>A</u> <u>T</u> <u>G</u> <u>A</u> <u>T</u> <u>G</u> <u>A</u> <u>A</u> <u>G</u> <u>A</u> <u>T</u> - 5'
		3' - <u>G</u> <u>A</u> <u>T</u> <u>G</u> <u>A</u> <u>T</u> <u>A</u> <u>A</u> <u>T</u> <u>G</u> <u>A</u> <u>A</u> <u>G</u> <u>A</u> <u>T</u> - 5'	3' - <u>G</u> <u>A</u> <u>T</u> <u>G</u> <u>A</u> <u>T</u> <u>G</u> <u>A</u> <u>A</u> <u>G</u> <u>A</u> <u>T</u> - 5'
		3' - <u>G</u> <u>A</u> <u>T</u> <u>G</u> <u>A</u> <u>T</u> <u>A</u> <u>A</u> <u>T</u> <u>G</u> <u>A</u> <u>A</u> <u>G</u> <u>A</u> <u>T</u> - 5'	3' - <u>G</u> <u>A</u> <u>T</u> <u>G</u> <u>A</u> <u>T</u> <u>G</u> <u>A</u> <u>A</u> <u>G</u> <u>A</u> <u>T</u> - 5'

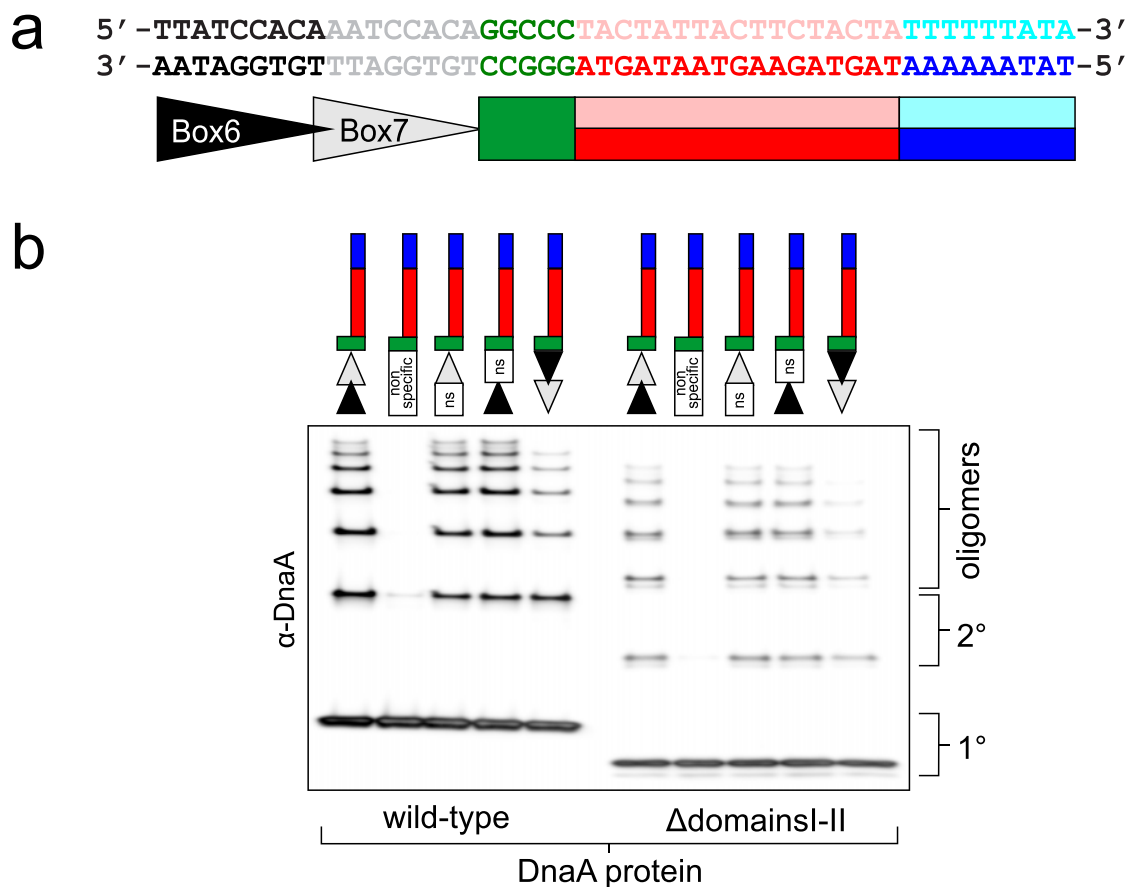
Extended Data Figure 4 | DNA sequence of unwinding regions after mononucleotide and trinucleotide deletions. Resulting sequences grouped in boxes are identical for more than one deletion.



Extended Data Figure 5 | Crosslinking with BS³ captures a distinct DnaA oligomer. DnaA was incubated with various DNA scaffolds and different crosslinking agents were added to capture distinct DnaA oligomers. **a**, Crosslinking with BMOE detects DnaA oligomers forming on both duplex and tailed substrates. **b**, Crosslinking with BS³ only detects DnaA oligomers forming on tailed substrates, revealing an interaction between DnaA and the first DnaA-trio motif located downstream of the GC-cluster.



Extended Data Figure 6 | The nucleotide at the third position of the DnaA-trio is required to stabilize DnaA. DNA scaffolds containing the first two nucleotides of a DnaA-trio either with or without a 5'-phosphate are unable to stabilize binding of an additional DnaA protomer, indicating that the nucleotide at the third position is required. Combined with the data shown in Fig. 4b where the position is abasic, the results suggest that the sugar at the third position plays a critical role in DnaA binding.



Extended Data Figure 7 | Relationship between the DnaA-box and the DnaA-trios. **a**, Sequence of the origin region used for constructing DNA scaffolds. Symbols below represent duplex DnaA-boxes (triangles), the GC-rich region (green rectangles), the two strands of the unwinding

region (red or pink rectangles) and the AT-rich region (blue rectangle). **b**, Loading of the DnaA filament onto a single-stranded 5'-tail requires a DnaA-box and DnaA domains III-IV, but the DnaA-box position and orientation are flexible.

Extended Data Table 1 | Bacterial replication origin regions in Fig. 4c

Organism	Genome accession #	Reference or DoriC accession # (ORI)	Genome position shown in Figure 4	Tandem DnaA-boxes (spacing)
<i>Aquifex aeolicus</i> VF5	NC_000918	¹⁷	166853 to 166897	N
<i>Bacillus subtilis</i> 168	NC_000964	³⁴	1860 to 1902	Y (-1)
<i>Bdellovibrio bacteriovorus</i> HD100	NC_005363	ORI10040030	1569 to 1597	N
<i>Bifidobacterium bifidum</i> PRL2010	NC_014638	ORI94010761	2048 to 2071	Y (0)
<i>Bordetella pertussis</i> Tohama I	NC_002929	ORI10030012	4084583 to 4084611	Y (+3)
<i>Borrelia afzelii</i> HLJ01	NC_018887	ORI96010684	460118 to 460149	Y? (+1)(+9)
<i>Clostridium botulinum</i> A str. Hall	NC_009698	ORI92010335	1517 to 1552	Y (-1)
<i>Corynebacterium glutamicum</i> ATCC 13032	NC_003450	ORI10010055	1984 to 2010	Y (0)
<i>Enterococcus faecalis</i> V583	NC_004668	ORI10010096	1498 to 1533	Y (0)
<i>Escherichia coli</i> MG1655	NC_000913	³⁵	3925780 to 3925809	N
<i>Helicobacter pylori</i> 26695	NC_000915	²⁰	1607488 to 1607525	Y (0)
<i>Leuconostoc citreum</i> KM20	NC_010471	ORI92310382	1790 to 1819	Y (0)
<i>Listeria monocytogenes</i> EGD-e	NC_003210	ORI10010047	1773 to 1802	Y (-1)
<i>Oceanobacillus iheyensis</i> HTE831	NC_004193	ORI10010074	1746 to 1778	Y (-1)
<i>Staphylococcus aureus</i> NCTC 8325	NC_007795	ORI10010183	2075 to 2104	Y (-1)
<i>Streptococcus pneumoniae</i> R6	NC_003098	ORI10010044	1458 to 1487	Y (0)
<i>Streptomyces coelicolor</i> A3(2)	NC_003888	³⁶	4270070 to 4270096	Y (0)
<i>Synechococcus elongatus</i> PCC 7942	NC_007604	³⁷	2695870 to 2695899	Y (0)
<i>Thermotoga maritima</i> MSB8	NC_000853	²¹	157010 to 157040	N
<i>Treponema pallidum</i> Nichols	NC_000919	ORI10010003	1568 to 1588	Y (-1)

References 17, 20, 21 and 34–37 are cited in the table.

Extended Data Table 2 | Oligonucleotides used for plasmid construction

Product	Template	Primer #1	Sequence (5'→3')	Primer #2	Sequence (5'→3')
pHM453	Genomic DNA	oHM319	AATAATGACGTCGGCAAATGTTTGAATTTGTC	oHM320	AATAATAGACGTCAGCCCACACGCAGTTTCATC
pHM492	Genomic DNA	oHM313	AATAATGAATCTTAATATCTAACCATTATAAACGGCAC	oHM315	AATAATCTCGAGCGCTTGGCAGCACTGAGCAAAACC
pHM560	Genomic DNA	oHM510	AATAATGATATCTAATAGGTGACCTATATAAGGCTAGATTGTGACAACCATTTG	oHM511	AATAAAAGCTTAGAGGAAAGGTAGGATTAG
pTR54	pHM327	oTR36	CTTCAACCATTTCCGTTAGAGGATAAAATGAAATTCAC	oTR37	GGATAATGGTAGAAGTAATAGTAGGGCCTGTGGATTTG
pTR72	pGS43	oTR156	CAGCTTAATGAGATCCGGCTGCTAACAAAGCCCGAAAGG	oTR157	CGGATCTCAITTAAGCTGTTCTTAAATTTCTTTACATGC
pTR73	pTR72	oTR158	CATCATCATCATCATCAGCGGAAATATATAGACCTGTGGAACCAAGCCCTTGCTCAAATC	oTR159	GCTGTGATGATGATGATGATGATGATGATATCTCCTCTTAAAGTTAAACAAAATTAATTC
pTR74	pTR102	oTR189	ATTCAAGGTGCGCATGGAAATATATAGACCTGTGGAACCAAGCCCTTG	oTR190	TTTCCATGCGACCTTGAATGCCGCTGCTGTGATGATGATGATGATGATG
pTR83	pHM327	oTR82	CACAGTCTTCCTTGCTGTGGATAGGCTGTGTTCTGCTCTTTTC	oTR83	ATCCACAGCAAGGAAGACTGTGTATGACTTCGGAAGTATTTC
pTR84	pHM328	oTR66	GCCCATGATAATGAAGATGATATTTTATAAATATATATTAATACATTATCCGTTAG	oTR67	AAAATATCATCTTCATTATCATGGCCTGTGGATTGTGGATAAGTTG
pTR85	pHM327	oTR118	GAAAGGCAAGGAAGCTTTTCGGGAAGTCATACACAGTCTGTGC	oTR119	AAAGCTTCCTTGCCCTTCCCCGATTGATCCCCGGTCTCTG
pTR86	pHM327	oTR123	GAAGCTTCCTTGGCTGTGCACATGTGGATAGGCTGTGTTTCC	oTR124	AGACGCAAGGAAGCTTCGGAAGATATTACACATTTCCCCGATTG
pTR87	pHM327	oTR125	ACAGCAAGGAAGGCTGTGTTCTCTGTCTTTTACAACCTATC	oTR126	CAGCCTTCCTTGCTGTGGACAGACTGTGTATGACTTCCGAAAG
pTR88	pHM327	oTR86	CCTGTCTCTCTGCACTTATCCACAATCCACAGGCCCTACTATTAC	oTR87	GGATAAGTGCAAGGAAGGACAGGAACACAGCCTATCCAC
pTR89	pHM327	oTR88	TCACAACCTTCCTTGAATCCACAGGCCCTACTATTACTTCTAC	oTR89	GTGGATTGCAAGGAAGGTTGTGAAAAAGACAGGAACACAGCCTATC
pTR90	pHM327	oTR090	CCACATTCCTTCGGCCCTACTATTACTTCTAC	oTR091	GGGCCGCAAGGAATGTGGATAAGTTGTGAAAAAGACAGGAAC
pTR102	pTR73	oTR187	CAGCAGCGGCATTGCAAAATATATAGACCTGTGGAACCAAGCCCTTG	oTR188	TTTCAATGCCGCTGCTGTGATGATGATGATGATGATGATGATATC
pTR146	pHM327	oTR247	CAGGCCCATGTATTACTTCTACTATTTTATAAATATATATTAATAC	oTR248	AATACATGGCCCTGTGGATTGTGGATAAGTTGTG
pTR147	pHM327	oTR249	GCCCTACATACTTCTACTATTTTATAAATATATATATAACATTATC	oTR250	AGTATATGAGGGCCTGTGGATTGTGGATAAGTTGTG
pTR148	pHM327	oTR251	CCCTACTATATGTTCTACTATTTTATAAATATATATATAACATTATCCGTTAG	oTR252	GAACATAGTAGGGCCTGTGGATTGTGGATAAGTTGTG
pTR149	pHM327	oTR254	AGTACTTGTAATAGTAGGGCCTGTGGATTGTGGATAAG	oTR263	CTACTATTACAAGTACTATTTTATAAATATATATATAACATTATCCGTTAGGAG
pTR150	pHM327	oTR255	TACTTCATGTATTTTATAAATATATATATAACATTATCCGTTAGGAG	oTR256	AATACATGAAGTAATAGTAGGGCCTGTGGATTGTG
pTR153	pHM327	oTR261	GATCAATCGGTATCCGTTAGGAGGATAAAATGAAATTC	oTR262	CTAACGGATACCGATTGATCCCCGGTCTGCTATTAAAG
pTR168	pTR74	oTR299	GAATTGCGCTGCTATCTCGAGATAATAATGC	oTR300	GAGCAGCGGAATTCGTTTGTAAATTTCTCAGAAG
pTR208	pTR74	oTR384	TCAAGGTGCGATGAACAAACGAACATTAATCAATG	oTR385	CGGATCTTATTTCCGGCACTGCGCTTTAAAGC
pTR208	Genomic DNA	oTR386	TTTTGTTCATGCGACCTTGAATGCCGCTGCTG	oTR387	CGGAAAAATAGATCCGGCTGCTAACAAAGCCCGAAAG
pTR284	pHM327	oTR449	GGCCCAACTATTACTTCTACTATTTTATAAATATATATATAACATTATC	oTR450	GTAATAGTTGGCCTGTGGATTGTGGATAAG
pTR285	pHM327	oTR451	GGCCCTTCTATTACTTCTACTATTTTATAAATATATATATAACATTATC	oTR452	GTAATAGAAGGCCTGTGGATTGTGGATAAG
pTR286	pHM327	oTR453	GGCCCTAGTATTACTTCTACTATTTTATAAATATATATATAACATTATCCG	oTR454	GTAATAGGGCCTGTGGATTGTGGATAAG
pTR287	pHM327	oTR455	CCCTACAATTACTTCTACTATTTTATAAATATATATATAACATTATCCGTTAG	oTR456	AGTAATGTAGGGCCTGTGGATTGTGG
pTR288	pHM327	oTR457	CCCTACTTTTACTTCTACTATTTTATAAATATATATATAACATTATCCGTTAG	oTR458	GAAGTAAAGTAGGGCCTGTGGATTGTGGATAAG
pTR289	pHM327	oTR459	CCCTACTACTATCTCTACTATTTTATAAATATATATATAACATTATCCGTTAG	oTR460	GATTAGTAGGGCCTGTGGATTGTGGATAAG
pTR301	pHM327	oTR469	CTTCTACTTTTATAAATATATATATAACATTATCCGTTAGGAGGATAAAATG	oTR470	TATAAAAGTAGAAGTAATAGTAGGGCCTGTGG
pTR302	pHM327	oTR471	TTACTTCTTTTATAAATATATATATAACATTATCCGTTAGGAGGATAAAATG	oTR472	TATAAAAGAAGTAATAGTAGGGCCTGTGGATTG
pTR303	pHM327	oTR473	CTATTACTTTTATAAATATATATATAACATTATCCGTTAGGAGGATAAAATG	oTR474	TATAAAAGTAATAGTAGGGCCTGTGGATTG
pTR304	pHM327	oTR475	CAGGCCCTACTATTTTATAAATATATATATAACATTATCCGTTAGGAG	oTR476	AATAGTAGGGCCTGTGGATTGTGGATAAG
pTR305	pHM327	oTR477	GGCCCTACTTTTATAAATATATATATAACATTATCCGTTAGGAGGATAAAATG	oTR478	TTATAAAAGTAGGGCCTGTGGATTGTG
pTR306	pHM327	oTR479	GGCCCTTTTATAAATATATATATAACATTATCCGTTAGGAGGATAAAATG	oTR480	TATAAAAGGCCTGTGGATTGTGG
pTR346	pHM327	oTR490	GGCCCACTATTACTTCTACTATTTTATAAATATATATATAATAC	oTR491	GAAGTAATAGTGGCCTGTGGATTGTGGATAAGTTG
pTR348	pHM327	oTR494	GGCCCTATTACTTCTACTATTTTATAAATATATATATAACATTATC	oTR495	AGAAGTAATAGGGCCTGTGGATTGTGGATAAGTTG
pTR349	pTR54	oTR496	ATTACTTCCATTATCCGTTAGGAGGATAAAATGAAATTC	oTR497	GATAATGGAAGTAATAGTAGGGCCTGTGGATTG
pTR350	pTR54	oTR498	ACTATTACCATTATCCGTTAGGAGGATAAAATG	oTR499	GGATAATGGTAATAGTAGGGCCTGTGGATTGTG
pTR377	pHM327	oTR539	GGCCCTATATACTTCTACTATTTTATAAATATATATATAACATTATC	oTR540	GTAATAGGGCCTGTGGATTGTG
pTR441	pHM327	oTR659	CCCTACATTACTTCTACTATTTTATAAATATATATATAACATTATC	oTR660	GTAGAAGTAATAGTAGGGCCTGTGGATTGTG
pTR443	pHM327	oTR663	CCCTACTACTTCTACTATTTTATAAATATATATATAACATTATC	oTR664	GTAGAAGTAGTAGGGCCTGTGGATTGTG
pTR452	pHM326	oTR698	GGCCGTACTATTACTTCTACTATTTTATAAATATATATATAATAC	oTR699	GTAATAGTACGGCCTGTGGATTGTGG
pTR453	pHM327	oTR700	AGGCCTACTATTACTTCTACTATTTTATAAATATATATATAATAC	oTR701	GTAATAGTAGGCCTGTGGATTGTGG
pTR456	pHM327	oTR706	GGCCTCTATTACTTCTACTATTTTATAAATATATATATAACATTATC	oTR707	AAGTAATAGAGGGCCTGTGGATTGTG
pTR457	pHM327	oTR708	CCCTACTTTACTTCTACTATTTTATAAATATATATATAACATTATCC	oTR709	GAAGTAAGTAGGGCCTGTGGATTG
pTR458	pHM327	oTR710	CCTACTATCTTCTACTATTTTATAAATATATATATAACATTATCC	oTR711	TAGAAGTAGTAGGGCCTGTGGATTG
pTR478	pHM327	oTR801	TACTATTCTTCTACTATTTTATAAATATATATATAACATTATCCGTTAG	oTR802	GTAGAAGAATAGTAGGGCCTGTGGATTGTG
pTR541	Genomic DNA	oTR535	ATTACGCCAGCTAGTGCTTTTATCTTCTGCAACCATAATAG	oTR536	ATTAATGCAGTTTATCTCTCTAACGGATAATG
pTR541	pSG1301	oTR537	AAAGCACTAGCTGGCGTAATAGCGAAGAGG	oTR538	GAGGATAAACTGCATTAAATGAATCGGCCAACG
pTR542	pTR84	oTR535	ATTACGCCAGCTAGTGCTTTTATCTTCTGCAACCATAATAG	oTR536	ATTAATGCAGTTTATCTCTCTAACGGATAATG
pTR542	pSG1301	oTR537	AAAGCACTAGCTGGCGTAATAGCGAAGAGG	oTR538	GAGGATAAACTGCATTAAATGAATCGGCCAACG

Extended Data Table 3 | Oligonucleotides used to assemble DNA scaffolds

Oligo 1	Sequence (5'→3')	Oligo 2	Sequence (5'→3')	Figure
oTR602	ACTTATCCACAAATCCACAGGCC	oTR603	GGGCCTGTGGATTGTGGATAAGT	2c, 2f, 4a, E5a, E5b
oTR602	ACTTATCCACAAATCCACAGGCC	oTR609	ATATATATTATAAAAAATAGTAGAAGTAATAGTAGGGCCTGTGGATTGTGGATAAGT	2c, E3, E7b
oTR602	ACTTATCCACAAATCCACAGGCC	oTR619	ATATATATTATAAAAAATCATCTTCATTATCATGGCCTGTGGATTGTGGATAAGT	2c
oTR602	ACTTATCCACAAATCCACAGGCC	oTR626	AGGGCCTGTGGATTGTGGATAAGT	4a
oTR602	ACTTATCCACAAATCCACAGGCC	oTR627	TAGGGCCTGTGGATTGTGGATAAGT	4a, E5a, E5b
oTR602	ACTTATCCACAAATCCACAGGCC	oTR628	GTAGGGCCTGTGGATTGTGGATAAGT	4a
oTR602	ACTTATCCACAAATCCACAGGCC	oTR629	AGTAGGGCCTGTGGATTGTGGATAAGT	4a, E6
oTR602	ACTTATCCACAAATCCACAGGCC	oTR630	TAGTAGGGCCTGTGGATTGTGGATAAGT	4a, 4b, E5a, E5b, E6
oTR602	ACTTATCCACAAATCCACAGGCC	oTR631	ATAGTAGGGCCTGTGGATTGTGGATAAGT	4a
oTR602	ACTTATCCACAAATCCACAGGCC	oTR632	AATAGTAGGGCCTGTGGATTGTGGATAAGT	4a
oTR602	ACTTATCCACAAATCCACAGGCC	oTR633	TAATAGTAGGGCCTGTGGATTGTGGATAAGT	4a, 2f
oTR602	ACTTATCCACAAATCCACAGGCC	oTR634	GTAATAGTAGGGCCTGTGGATTGTGGATAAGT	4a
oTR602	ACTTATCCACAAATCCACAGGCC	oTR645	AGTAATAGTAGGGCCTGTGGATTGTGGATAAGT	4a
oTR602	ACTTATCCACAAATCCACAGGCC	oTR646	AAGTAATAGTAGGGCCTGTGGATTGTGGATAAGT	4a, 3d
oTR602	ACTTATCCACAAATCCACAGGCC	oTR647	GAAGTAATAGTAGGGCCTGTGGATTGTGGATAAGT	4a
oTR602	ACTTATCCACAAATCCACAGGCC	oTR648	AGAAGTAATAGTAGGGCCTGTGGATTGTGGATAAGT	4a, 3d
oTR602	ACTTATCCACAAATCCACAGGCC	oTR649	TAGAAGTAATAGTAGGGCCTGTGGATTGTGGATAAGT	4a
oTR602	ACTTATCCACAAATCCACAGGCC	oTR754	TATAAAAAATAGTAGAAGTAATAGTAGGGCCTGTGGATTGTGGATAAGT	2f
oTR602	ACTTATCCACAAATCCACAGGCC	oTR831	TAGTAGAAGTAATAGTAGGGCCTGTGGATTGTGGATAAGT	2f
oTR602	ACTTATCCACAAATCCACAGGCC	oTR854	TAGTAGTAGTAGTAGAAGTAATAGTAGGGCCTGTGGATTGTGGATAAGT	2f
oTR602	ACTTATCCACAAATCCACAGGCC	oTR956	AAGAAGTAATAGTAGGGCCTGTGGATTGTGGATAAGT	3d
oTR602	ACTTATCCACAAATCCACAGGCC	oTR957	AAGAAGTAATAGTAGGGCCTGTGGATTGTGGATAAGT	3d
oTR602	ACTTATCCACAAATCCACAGGCC	oTR958	AAGAAGTAAGTAGGGCCTGTGGATTGTGGATAAGT	3d
oTR602	ACTTATCCACAAATCCACAGGCC	oTR959	AAGAAGTATAGTAGGGCCTGTGGATTGTGGATAAGT	3d
oTR602	ACTTATCCACAAATCCACAGGCC	oTR960	AAGAAGAAATAGTAGGGCCTGTGGATTGTGGATAAGT	3d
oTR602	ACTTATCCACAAATCCACAGGCC	oTR961	AAGAAGTAATAGGGCCTGTGGATTGTGGATAAGT	3d
oTR602	ACTTATCCACAAATCCACAGGCC	oTR962	AAGAAGTAGTAGGGCCTGTGGATTGTGGATAAGT	3d
oTR602	ACTTATCCACAAATCCACAGGCC	oTR965	pAGTAGGGCCTGTGGATTGTGGATAAGT	E6
oTR602	ACTTATCCACAAATCCACAGGCC	oTR970	*AGTAGGGCCTGTGGATTGTGGATAAGT	4b
oTR602	ACTTATCCACAAATCCACAGGCC	oTR971	T*GAGGGCCTGTGGATTGTGGATAAGT	4b
oTR602	ACTTATCCACAAATCCACAGGCC	oTR972	TA*TAGGGCCTGTGGATTGTGGATAAGT	4b
oTR602	ACTTATCCACAAATCCACAGGCC	oTR995	TAATAGGGCCTGTGGATTGTGGATAAGT	4b
oTR602	ACTTATCCACAAATCCACAGGCC	oTR996	TACTAGGGCCTGTGGATTGTGGATAAGT	4b
oTR602	ACTTATCCACAAATCCACAGGCC	oTR998	TGGTAGGGCCTGTGGATTGTGGATAAGT	4b
oTR602	ACTTATCCACAAATCCACAGGCC	oTR999	TTGTAGGGCCTGTGGATTGTGGATAAGT	4b
oTR602	ACTTATCCACAAATCCACAGGCC	oTR1001	CAGTAGGGCCTGTGGATTGTGGATAAGT	4b
oTR602	ACTTATCCACAAATCCACAGGCC	oTR1002	AAGTAGGGCCTGTGGATTGTGGATAAGT	4b
oTR603	GGGCCTGTGGATTGTGGATAAGT	oTR608	ACTTATCCACAAATCCACAGGCCCTACTATTACTTCTACTATTTTTATAAATATATAT	2c, E3
oTR608	ACTTATCCACAAATCCACAGGCCCTACTATTACTTCTACTATTTTTATAAATATATAT	oTR609	ATATATATTATAAAAAATAGTAGAAGTAATAGTAGGGCCTGTGGATTGTGGATAAGT	2c
oTR611	ACCTTCCTGCTTCCTTGCAGGCC	oTR612	ATATATATTATAAAAAATAGTAGAAGTAATAGTAGGGCCGCAAGGAAGCAAGGAAGGT	2c, E7b
oTR665	ATATATATTATAAAAAATAGTAGAAGTAATAGTAGGGCCTGTGGATTGCAAGGAAGGT	oTR667	ACCTTCCTTGCATCCACAGGCC	E7b
oTR666	ATATATATTATAAAAAATAGTAGAAGTAATAGTAGGGCCGCAAGGAATGTGGATAAGT	oTR668	ACTTATCCACATTCTTGCAGGCC	E7b
oTR946	ACTGTGGATTGTGGATAAGGCC	oTR623	ATATATATTATAAAAAATAGTAGAAGTAATAGTAGGGCCTATCCACAAATCCACAGT	E7b

Structural basis for amino acid export by DMT superfamily transporter YddG

Hirotohi Tsuchiya¹, Shintaro Doki¹, Mizuki Takemoto¹, Tatsuya Ikuta¹, Takashi Higuchi¹, Keita Fukui², Yoshihiro Usuda³, Eri Tabuchi³, Satoru Nagatoishi⁴, Kouhei Tsumoto⁴, Tomohiro Nishizawa¹, Koichi Ito⁵, Naoshi Dohmae⁶, Ryuichiro Ishitani^{1,7} & Osamu Nureki¹

The drug/metabolite transporter (DMT) superfamily is a large group of membrane transporters ubiquitously found in eukaryotes, bacteria and archaea, and includes exporters for a remarkably wide range of substrates, such as toxic compounds and metabolites¹. YddG is a bacterial DMT protein that expels aromatic amino acids and exogenous toxic compounds, thereby contributing to cellular homeostasis^{2,3}. Here we present structural and functional analyses of YddG. Using liposome-based analyses, we show that *Escherichia coli* and *Starkeya novella* YddG export various amino acids. The crystal structure of *S. novella* YddG at 2.4 Å resolution reveals a new membrane transporter topology, with ten transmembrane segments in an outward-facing state. The overall structure is basket-shaped, with a large substrate-binding cavity at the centre of the molecule, and is composed of inverted structural repeats related by two-fold pseudo-symmetry. On the basis of this intramolecular symmetry, we propose a structural model for the inward-facing state and a mechanism of the conformational change for substrate transport, which we confirmed by biochemical analyses. These findings provide a structural basis for the mechanism of transport of DMT superfamily proteins.

An important physiological function is the expulsion of various compounds from cells to the extracellular space, which is essential for cellular homeostasis. This process involves specific membrane transporters that export their substrates across the cellular membrane. An example is the exporters of toxic compounds, which are crucial for the growth of microorganisms in the presence of antibiotics and antiseptics^{4,5}. These drug exporters cause the emergence of multi-drug-resistant strains, which are a major obstacle to the effective treatment of bacterial infections^{6,7}. Furthermore, the exporters of metabolites, such as amino acids and sugars, are important for maintaining their appropriate concentrations in the cytosol^{8–10}. These metabolite transporters have crucial roles in multicellular organisms to direct metabolites to their appropriate locations, including tissues and cellular compartments.

The DMT superfamily is a large group of membrane transporters, comprising more than 32 families¹. Numerous members of this superfamily are involved in the export of a wide range of substrates, including drugs and metabolites, and DMT proteins are ubiquitously distributed in eukaryotes, bacteria and archaea. For example, nucleotide sugar transporter family proteins export nucleotide–sugar conjugates (such as UDP–galactose and CMP–sialate) to the Golgi apparatus and endoplasmic reticulum of eukaryotic cells to supply building blocks for the sugar chains of glycoproteins, glycolipids and polysaccharides^{11,12}. Many DMT proteins are predicted to contain ten transmembrane segments with a five-transmembrane unit internal repeat, which was probably formed by gene duplication^{1,13–15}. Despite the importance of the DMT superfamily proteins, their structural mechanism of drug/metabolite transport has remained elusive.

YddG, a bacterial inner-membrane protein belonging to the DMT superfamily, exports drugs and metabolites. YddG from *Salmonella enterica* sv. Typhimurium is involved in the efflux of the di-cationic herbicide methyl viologen, and is postulated to be important for the efflux of multiple toxic compounds². *E. coli* YddG (EcYddG) exports aromatic amino acids, and is essential for alleviating the growth inhibition caused by their excessive cytosolic accumulation³. To explore the substrate specificity of YddG further, we performed an *in vitro* functional analysis using YddG-reconstituted proteoliposomes (Fig. 1a). The results showed that EcYddG transports various amino acids, including threonine, methionine, lysine and glutamic acid (Fig. 1b), suggesting the broad substrate specificity of EcYddG. Although we could not examine the transport activity of aromatic amino acids in the *in vitro* assay system, because of their low solubility, YddG probably transports aromatic amino acids as well, based on a previous genetic analysis³. We also confirmed the *in vivo* amino acid export activity of EcYddG by a metabolomics analysis (Extended Data Fig. 1). We identified YddG from *S. novella* (SnYddG, 287 amino acids, 28% sequence identity with EcYddG) as a suitable candidate for structural studies, by the fluorescence-based screening method^{16,17}. The transport activity of SnYddG was confirmed using the *in vitro* assay system (Fig. 1), which showed that SnYddG is also an amino acid transporter with broad substrate specificity.

We determined the crystal structure of SnYddG by the single-isomorphous replacement with anomalous scattering method, using Hg-derivatized crystals, and refined it at 2.4 Å resolution (Extended Data Table 1, Extended Data Fig. 2a, b). The asymmetric unit of the crystalline lattice contains six SnYddG molecules with nearly identical structures, and they are superimposable with root mean square deviations

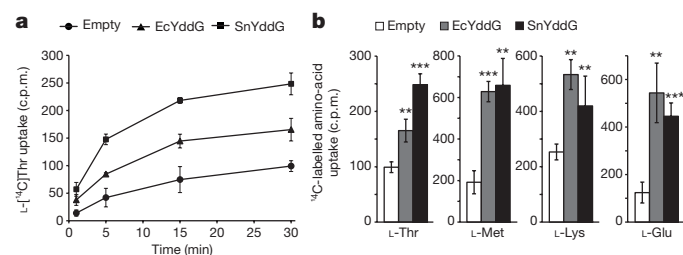


Figure 1 | Functional characterization of YddG. a, b, Liposome-based analyses of EcYddG and SnYddG transport activities. **a**, Time-dependent uptake of [¹⁴C]threonine into empty, EcYddG- and SnYddG-containing liposomes. **b**, Uptake of [¹⁴C]-labelled amino acids into empty, EcYddG- and SnYddG-containing liposomes, after 30 min. c.p.m., counts per minute. Error bars, s.d.; *n* = 3. ***P* < 0.01, ****P* < 0.001 compared with empty liposomes (Student's *t*-test).

¹Department of Biological Sciences, Graduate School of Science, The University of Tokyo, 2-11-16 Yayoi, Bunkyo-ku, Tokyo 113-0032, Japan. ²Research Institute for Bioscience Products & Fine Chemicals, Ajinomoto Co., Inc., 1-1 Suzuki-cho, Kawasaki-ku, Kawasaki 210-8681, Japan. ³Institute for Innovation, Ajinomoto Co., Inc., 1-1 Suzuki-cho, Kawasaki-ku, Kawasaki 210-8681, Japan. ⁴Department of Bioengineering, School of Engineering, The University of Tokyo, 7-3-1 Hongo, Bunkyo-Ku, Tokyo 113-8656, Japan. ⁵Department of Medical Genome Sciences, Graduate School of Frontier Sciences, The University of Tokyo, Chiba 277-8562, Japan. ⁶Biomolecular Characterization Unit, RIKEN Center for Sustainable Resource Science, Wako, Saitama 351-0198, Japan. ⁷Theoretical Molecular Science Laboratory, RIKEN, Wako, Saitama 351-0198, Japan.

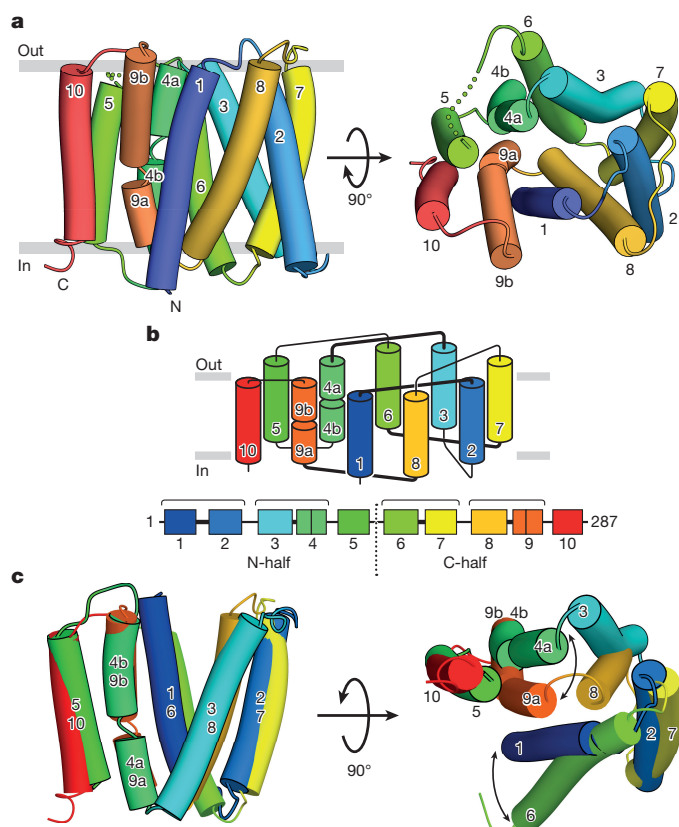


Figure 2 | Overall structure of *S. novella* YddG. **a**, Overall structure in cylinder representations, viewed from the plane of the membrane (left) and the periplasmic side (right). **b**, Topology diagram of SnYddG, coloured as in **a**. The primary structural organization of the transmembrane segments and the N and C halves is illustrated at the bottom. **c**, Structural superimposition of the N and C halves of SnYddG, viewed from two different directions. In the right panel, the transmembrane segments that do not overlap in the superimposition are indicated by arrows. All molecular graphics were illustrated with CueMol (<http://www.cuemol.org/>).

(r.m.s.d.) of less than 0.9 Å. Thus, we hereafter focus on molecule B in the asymmetric unit, as the quality of its electron density is the best among these molecules. The overall structure of YddG is basket-shaped, with a deep cavity facing the extracellular solvent (Fig. 2a, Extended Data Fig. 2c). As expected from previous informatics and biochemical analyses¹⁸, YddG comprises 10 α -helical transmembrane segments, with its N and C termini located on the intracellular side. The topology is composed of four pairs of two consecutive transmembrane segments forming two-helix hairpins; that is, transmembrane (TM) 1–TM2, TM3–TM4, TM6–TM7 and TM8–TM9, which are arranged alternately to surround the central cavity (Fig. 2b). Namely, the transmembrane segments in the N-half (TM1–TM5) and the C-half (TM6–TM10) surround the central cavity in anticlockwise and clockwise manners, respectively, as viewed from the periplasmic side (Fig. 2a, b). TM5 and TM10 form a four-helix bundle together with TM4 and TM9, which seals one side of the central cavity. TM4 and TM9 are respectively interrupted by short loops, with sequences that are well conserved among the YddG proteins from other species (Extended Data Fig. 3a), and thereby form the short helical segments, TM4a, TM4b, TM9a and TM9b. The N and C halves of SnYddG share weak sequence similarity (Extended Data Fig. 3b). Accordingly, the structures of these two halves are related by two-fold pseudo-symmetry with an axis running parallel to the membrane, and superimpose well with an r.m.s.d. of 2.7 Å for 90 C α atoms (Fig. 2c). Notably, the resulting topology of YddG is unique and completely different from those of membrane transporters with known structures.

Previous bioinformatics analyses suggested that the small multidrug resistance (SMR) family is the progenitor of the DMT proteins^{1,13–15}. *E. coli* EmrE is the best-characterized member of the SMR family^{19,20}. The crystal structure of EmrE at 3.8 Å resolution revealed its dimeric architecture, with four-transmembrane segment protomers²¹. Although there is no detectable sequence similarity and their transmembrane topologies are different, the superimposition of the transmembrane helices of YddG and the EmrE dimer (PDB accession 3B5D) revealed good structural alignment (r.m.s.d. of 2.9 Å over 127 C α atoms) (Extended Data Fig. 4a–c). The superimposition suggests the possible evolutionary relationship between the four-transmembrane SMR and other ten-transmembrane DMT proteins (see Supplementary Information).

The central cavity of YddG deeply penetrates the inner leaflet of the membrane, and is formed by six transmembrane segments: TM1, TM3, TM4, TM6, TM8 and TM9 (Fig. 3a). Notably, TM1, TM4, TM6 and TM9 contain several residues conserved among YddGs from other species (Extended Data Fig. 3a). At the centre of the molecule, the strictly conserved Trp residues, Trp17 (TM1), Trp101 (TM4a), and Trp163 (TM6), form the bottom of the cavity (Fig. 3a). The wall of the central cavity is created by the conserved hydrophobic residues, Leu20 (TM1), Phe40 (TM2), and Phe225 (TM8) (Fig. 3a). Notably, a large density blob is observed in the central cavity (Fig. 3a). The shape of this density fits well with the monoolein molecule used in the LCP crystallization, suggesting that monoolein is bound to this site. This density peak interacts with the conserved residues, including Trp17, Tyr78, Trp101 and Trp163. Thus, we proposed that this cavity functions as a substrate-binding pocket, where these conserved hydrophobic residues bind the hydrophobic groups of the substrates. Moreover, Tyr78 (TM3), Tyr82 (TM3), and Tyr99 (TM4) are located in the central cavity (Fig. 3a), and may provide both hydrophobic and hydrophilic environments for substrate binding. In addition, several hydrophilic residues, including His79 (TM3), Ser244 (TM9) and Ser251 (TM9), are also present in the central cavity (Fig. 3a), and may provide binding sites for the hydrophilic groups of the substrates.

To explore the functional importance of these conserved residues for the substrate recognition and transport activity, we measured the transport activities of SnYddG mutants by a liposome-based assay, using ¹⁴C-labelled threonine and methionine (Fig. 3b, c). The structural integrity of the mutant proteins was verified by gel-filtration chromatography at the final purification step (Extended Data Fig. 5a). The activity was normalized to the amount of protein reconstituted into the proteoliposomes (Extended Data Fig. 5b). The results showed that the His79Ala mutant abolished the transport activities for both threonine and methionine, thus revealing the critical role of this hydrophilic residue. Furthermore, the Trp101Ala and Trp163Ala mutants exhibited decreased transport activities for threonine, but not for methionine, suggesting the importance of these aromatic residues for specific types of substrates. In contrast, the Tyr78Ala mutation showed moderate effects on the transport activities of both threonine and methionine, suggesting that Tyr78 is involved in, but not crucial for, the recognition and/or transport of these substrates. The Tyr82Ala mutation enhanced methionine transport, and slightly reduced threonine transport. This mutation could increase the size of the substrate-binding site in the inward-facing state, which may facilitate the transport of large substrates. Taken together, our results strongly suggest that the central cavity functions as the binding site for a wide range of YddG substrates.

The intracellular side of the central cavity is closed by the intracellular gate, which is formed by the interactions among the side-by-side helices of TM4b and TM9a, and the intracellular tips of the TM6–TM7 and TM8–TM9a hairpins (Fig. 2a). Just beneath the central cavity, the conserved Trp228 (TM8) and Met232 (TM8) residues form the hydrophobic core of the intracellular gate (Fig. 3d). Trp228 hydrophobically interacts with the conserved Trp17 and Trp163, which form the bottom of the central cavity. The NE1 atom of the Trp228 side chain hydrogen bonds with the Ser167 (TM6) side chain. Furthermore, Met232 forms the hydrophobic core with Ile105 (TM4b), Val168 (TM6) and

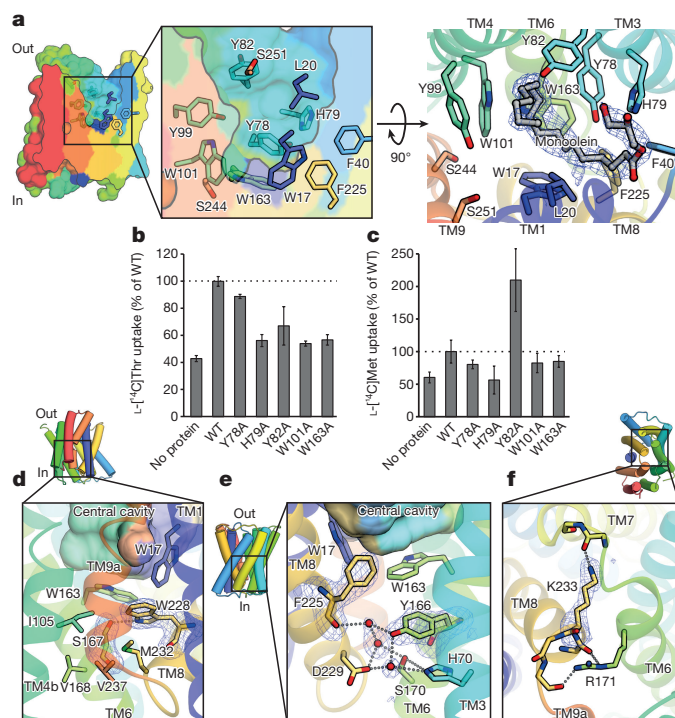


Figure 3 | Central cavity and intracellular gate. **a**, The structure of the central cavity. In the right panel, the monoolein molecule bound to the cavity and its $mF_o - DF_c$ omit map, contoured at 3σ , are shown. **b**, **c**, Liposome-based analyses of SnYddG mutants of the central cavity, using threonine (**b**) and methionine (**c**) as substrates. The substrate uptake activities were plotted as percentages of the wild-type transport activity. Error bars, s.d.; $n = 3$. **d–f**, The structure of the intracellular gate. The $mF_o - DF_c$ maps, calculated by omitting the key residues for the interactions and contoured at 3σ , are shown.

Val237 (TM9a), which are weakly conserved as hydrophobic residues among the YddGs from other species. In the vicinity of this hydrophobic core, the main-chain carbonyl group of Phe225 and the side chains of His70, Tyr166, Ser170 and Asp229 form a hydrogen-bonding network (Fig. 3e). Water molecules are captured by this hydrogen-bonding network, suggesting that the interactions in the intracellular gate are impermanent and can dissociate during the transport cycle. Furthermore, Arg171 (TM6) and Lys233 (TM8) form hydrogen bonds with the main-chain carbonyl groups in the TM8–TM9a and TM6–TM7 loops, respectively, which seal the intracellular side of the intracellular gate (Fig. 3f). Together, these tight interactions separate the central cavity from the intracellular space.

While the present crystal structure of YddG represents the outward-facing state in the alternating-access mechanism, the structural and sequence similarities between the N and C halves (Fig. 2c and Extended Data Fig. 3b) allowed us to generate a feasible structural model for the inward-facing state, as in other secondary transporters with inverted structural repeats^{22–24} (Fig. 4a, b). In this model of the inward-facing state, the intracellular gate interactions observed in the outward-facing structure are completely dissociated, thus opening the pathway directed towards the intracellular side (Fig. 4a). In contrast, the extracellular gate is formed by the interactions among the TM1–TM2 and TM3–TM4a hairpins, and TM4a and TM9b without any obvious steric clashes, and thus the substrate-binding site is occluded from the extracellular side. In the crystal structure of the outward-facing state, TM9a contains the Gly241 residue, which enables the tight side-by-side interaction between TM4b and TM9a (Fig. 4a). TM4a also contains the Gly95 residue, which could enable a similar side-by-side interaction between TM4a and TM9b in the inward-facing structure (Fig. 4b). Moreover, hydrophobic packing interactions are probably formed between the extracellular tips of the TM1–TM2 and TM3–TM4a hairpins, to create

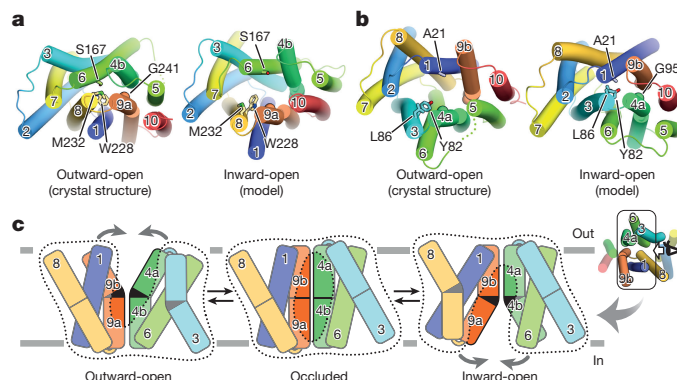


Figure 4 | The outward-inward conformational change of SnYddG.

a, Crystal structure of the outward-facing state (left) and the modelled structure of the inward-facing state (right), viewed from the cytoplasmic side. The residues involved in the intracellular gate are shown in stick models. **b**, The same structures as in **a**, viewed from the periplasmic side. The residues possibly involved in the extracellular gate are shown in stick models. **c**, Proposed transport mechanism, illustrating the bending motion of the transmembrane segments during the outward-inward conformational change. The molecular envelopes are indicated by dotted curves.

the extracellular gate. The side chain of Leu86 (TM3) may be surrounded by hydrophobic residues, including Ala21 (TM1) and Tyr82 (TM3), and Tyr82 may form the top of the substrate-binding site in the inward-open state (Fig. 4b). The results of the Cys-crosslinking experiment, as well as an evolutionary covariation analysis of YddG homologues, provide strong support for the extracellular gate formation and our inward-facing model structure (Extended Data Figs 6 and 7; see Supplementary Information for further discussion).

A comparison between the inward-facing model and outward-facing crystal structures provides further insights into the structural changes that occur during the transport cycle (Fig. 4c and Supplementary Video 1). The structures of TM3 and TM4 suggest the bending and straightening of the extracellular halves of these transmembrane segments, with the region around Gly71–Gly77 in TM3 (Extended Data Fig. 8a), as well as the intra-membrane loop in TM4, serving as hinges. The bending and straightening of the TM3–TM4 hairpin may further involve the tilting and upright motions of TM6, which collectively close and open the extracellular entrance of the central cavity (Fig. 4c). Similar structural changes may occur in TM8, TM9 and TM1, which are related by the intramolecular pseudo-symmetry to TM3, TM4 and TM6. Along with the tilting and upright motions of TM1, the hinge motions in the TM8–TM9 hairpin occur around Gly217–Gly222 in TM8 (Extended Data Fig. 8b) and the intra-membrane loop in TM9. These structural changes collectively close and open the intracellular entrance of the central cavity (Fig. 4c). The results from the molecular dynamics simulations also supported this structural change mechanism (Extended Data Fig. 9; see Supplementary Information for further discussion).

In summary, we determined the crystal structure of SnYddG at 2.4 Å resolution, which revealed the novel membrane transporter topology, with 10-transmembrane segments. The structural and complementary functional analyses suggested that YddG operates by a unique type of alternating-access mechanism, which is completely different from those of other known transporters. Our results provide further insight into the common transport mechanism shared among the DMT superfamily members, including the SMR transporters.

Online Content Methods, along with any additional Extended Data display items and Source Data, are available in the online version of the paper; references unique to these sections appear only in the online paper.

Received 16 July 2015; accepted 8 April 2016.

Published online 30 May 2016.

- Jack, D. L., Yang, N. M. & Saier, M. H. The drug/metabolite transporter superfamily. *Eur. J. Biochem.* **268**, 3620–3639 (2001).
- Santiviago, C. A. *et al.* The *Salmonella enterica* sv. Typhimurium smvA, yddG and ompD (porin) genes are required for the efficient efflux of methyl viologen. *Mol. Microbiol.* **46**, 687–698 (2002).
- Doroshenko, V. *et al.* YddG from *Escherichia coli* promotes export of aromatic amino acids. *FEMS Microbiol. Lett.* **275**, 312–318 (2007).
- Nikaido, H. Prevention of drug access to bacterial targets: permeability barriers and active efflux. *Science* **264**, 382–388 (1994).
- Paulsen, I. T., Brown, M. H. & Skurray, R. A. Proton-dependent multidrug efflux systems. *Microbiol. Rev.* **60**, 575–608 (1996).
- Poole, K. Efflux-mediated multidrug resistance in Gram-negative bacteria. *Clin. Microbiol. Infect.* **10**, 12–26 (2004).
- Piddock, L. J. V. Multidrug-resistance efflux pumps - not just for resistance. *Nature Rev. Microbiol.* **4**, 629–636 (2006).
- Krämer, R. Systems and mechanisms of amino acid uptake and excretion in prokaryotes. *Arch. Microbiol.* **162**, 1–13 (1994).
- Livshits, V. A., Zakataeva, N. P., Aleshin, V. V. & Vitushkina, M. V. Identification and characterization of the new gene *rhtA* involved in threonine and homoserine efflux in *Escherichia coli*. *Res. Microbiol.* **154**, 123–135 (2003).
- Bellman, A. *et al.* Expression control and specificity of the basic amino acid exporter LysE of *Corynebacterium glutamicum*. *Microbiology* **147**, 1765–1774 (2001).
- Ishida, N. & Kawakita, M. Molecular physiology and pathology of the nucleotide sugar transporter family (SLC35). *Pflugers Arch.* **447**, 768–775 (2004).
- Song, Z. Roles of the nucleotide sugar transporters (SLC35 family) in health and disease. *Mol. Aspects Med.* **34**, 590–600 (2013).
- Lolkema, J. S., Dobrowolski, A. & Slotboom, D. J. Evolution of antiparallel two-domain membrane proteins: tracing multiple gene duplication events in the DUF606 family. *J. Mol. Biol.* **378**, 596–606 (2008).
- Västermark, Å., Almén, M. S., Simmen, M. W., Fredriksson, R. & Schiöth, H. B. Functional specialization in nucleotide sugar transporters occurred through differentiation of the gene cluster *EamA* (DUF6) before the radiation of *Viridiplantae*. *BMC Evol. Biol.* **11**, 123 (2011).
- Bay, D. C. & Turner, R. J. Diversity and evolution of the small multidrug resistance protein family. *BMC Evol. Biol.* **9**, 140 (2009).
- Kawate, T. & Gouaux, E. Fluorescence-detection size-exclusion chromatography for precrystallization screening of integral membrane proteins. *Structure* **14**, 673–681 (2006).
- Hattori, M., Hibbs, R. E. & Gouaux, E. A fluorescence-detection size-exclusion chromatography-based thermostability assay for membrane protein precrystallization screening. *Structure* **20**, 1293–1299 (2012).
- Airich, L. G. *et al.* Membrane topology analysis of the *Escherichia coli* aromatic amino acid efflux protein YddG. *J. Mol. Microbiol. Biotechnol.* **19**, 189–197 (2010).
- Rapp, M., Seppälä, S., Granseth, E. & von Heijne, G. Emulating membrane protein evolution by rational design. *Science* **315**, 1282–1284 (2007).
- Schuldiner, S. EmrE, a model for studying evolution and mechanism of ion-coupled transporters. *Biochim. Biophys. Acta* **1794**, 748–762 (2009).
- Chen, Y.-J. *et al.* X-ray structure of EmrE supports dual topology model. *Proc. Natl Acad. Sci. USA* **104**, 18999–19004 (2007).
- Forrest, L. R. Structural biology. (Pseudo-)symmetrical transport. *Science* **339**, 399–401 (2013).
- Liao, J. *et al.* Structural insight into the ion-exchange mechanism of the sodium/calcium exchanger. *Science* **335**, 686–690 (2012).
- Mancuso, R., Gregorio, G. G., Liu, Q. & Wang, D.-N. Structure and mechanism of a bacterial sodium-dependent dicarboxylate transporter. *Nature* **491**, 622–626 (2012).

Supplementary Information is available in the online version of the paper.

Acknowledgements We thank H. Nishimasu and M. Hattori for comments on the manuscript; T. Tsukazaki and D. Drew for discussion; Y. Lee and A. Kurabayashi for technical assistance; the RIKEN BioResource Center for providing *Starkeya novella* genomic DNA; and the beam-line scientists at BL41XU and BL32XU of SPring-8 for assistance with data collection. The diffraction experiments were performed at SPring-8 BL41XU and BL32XU (proposals 2014A1091, 2014A1061, 2014A1093, 2014A1116 and 2014B1194). This work was supported by grants from the Platform for Drug Discovery, Informatics and Structural Life Science by the Ministry of Education, Culture, Sports, Science and Technology (MEXT), JSPS KAKENHI (grants 24227004, 25291011 and 26711003), the FIRST program, and a Grant-in-Aid for JSPS Fellows. Partial calculations were performed on the HOKUSAI GreatWave supercomputer system at RIKEN and the NIG supercomputer at ROIS National Institute of Genetics.

Author Contributions H.T., S.D., T.H., and E.T. constructed the expression systems. H.T. expressed, purified, and crystallized SnYddG, collected the diffraction data, determined the structure, and performed liposome-based assays. K.T. and S.N. assisted with the liposome-based assays. M.T., T.N. and R.I. assisted with the structure determinations. K.I. constructed the *E. coli* knockout strain. K.F. and Y.U. performed the metabolomics analysis. M.T. and T.I. performed the molecular dynamics simulations. N.D. performed disulphide-bond quantification. H.T., R.I. and O.N. wrote the manuscript. R.I. and O.N. directed and supervised all of the research.

Author Information The atomic coordinates and structure factors for SnYddG have been deposited in the Protein Data Bank (PDB) under accession number 5I20. Reprints and permissions information is available at www.nature.com/reprints. The authors declare no competing financial interests. Readers are welcome to comment on the online version of the paper. Correspondence and requests for materials should be addressed to O.N. (nureki@bs.s.u-tokyo.ac.jp) or R.I. (ishitani@bs.s.u-tokyo.ac.jp).

METHODS

Cloning and expression of YddG. The *S. novella yddG* gene (gi:502932551) was cloned from *S. novella* genomic DNA (Strain: JCM 20403) into a plasmid derived from the pET expression vector, which includes a C-terminal (His)₈-tag and a tobacco etch virus (TEV) protease cleavage site. The SnYddG protein was over-expressed in *E. coli* Rosetta2 (DE3) strain cells, grown in LB medium containing ampicillin (50 µg ml⁻¹). When the culture reached an absorbance at 600 nm of ~0.5, the cells were induced with 0.5 mM isopropyl β-thiogalactopyranoside (IPTG) for 2 h at 37 °C. The *E. coli yddG* gene (gi:152031741) was cloned from *E. coli* K-12 genomic DNA (strain: JCM 20135) into a plasmid derived from the expression vector pCGFP-BC16, which includes a C-terminal green fluorescent protein (GFP), a (His)₈-tag and a TEV protease cleavage site. The EcYddG protein was overexpressed in *E. coli* C41(DE3)ΔacrB cells, grown in LB medium containing ampicillin (50 µg ml⁻¹). When the culture reached an absorbance at 600 nm of ~0.5, the cells were induced with 0.5 mM IPTG for 18 h at 20 °C.

Purification and crystallization of SnYddG. The SnYddG protein for crystallization were purified according to the following procedure at 4 °C. The cells were pelleted by centrifugation at 4,500g, and were disrupted by a Microfluidizer (Microfluidics). After centrifugation (12,000g), the supernatant was ultracentrifuged (200,000g), and the membrane fraction was collected. The proteins were solubilized from the membrane fraction with 50 mM HEPES (pH 7.0), containing 300 mM NaCl, 20 mM imidazole, 1 mM phenylmethylsulfonyl fluoride, 1.2% (w/v) DDM, 0.24% (w/v) cholesteryl hemisuccinate (CHS), and were purified by the following three chromatography steps. The insoluble material was removed by ultracentrifugation (Beckman Type 70 Ti rotor, 150,000g, 30 min), and the supernatant was mixed with Ni-NTA resin (QIAGEN). The (His)₈-tag was cleaved by TEV protease at 4 °C overnight, and the proteins were re-chromatographed on a Ni-NTA column. The (His)₈-tag-cleaved protein was further purified by gel-filtration chromatography (Superdex 200 Increase 10/300 GL, GE Healthcare) in 20 mM HEPES (pH 7.0), containing 150 mM NaCl, 0.03% (w/v) DDM and 0.006% (w/v) CHS.

For crystallization, the purified protein was concentrated to approximately 15 mg ml⁻¹, using an Amicon Ultra 50K filter (Millipore). SnYddG was mixed with liquefied monoolein (Sigma) in a 2:3 protein to lipid ratio (w/v), using the twin-syringe mixing method. For the sandwich-drop crystallization, aliquots of the protein-LCP mixture were dispensed onto 96-well glass plates and overlaid with the precipitant solution, using a Gryphon LCP (Art Robbins Instruments, LLC). Initial crystallization conditions were searched, using screening kits including MemMeso, MemGold I and II, and MemStart/MemSys (Molecular Dimensions). The initial hits were optimized by changing the concentration of each component, as well as additive screening, using the hanging-drop crystallization method. For the hanging-drop crystallization, the protein-LCP drops were manually spotted onto siliconized glass coverslips and overlaid with the precipitant solutions, and then the coverslips were placed upside down onto 24-well plates and sealed with each well containing 300 µl of reservoir solution. We finally found that the addition of (NH₄)₂SO₄ to the precipitant solution markedly improved the size of the crystals. The native crystals were grown in hanging-drop plates at 20 °C, with 50 nl protein-LCP drops overlaid with 800 or 1,600 nl precipitant solution, which consisted of 32–34% PEG550MME, 100 mM Na-citrate (pH 4.5), 100 mM (NH₄)₂HPO₄, and 100 mM (NH₄)₂SO₄. The heavy atom-derivatized crystals were prepared by the soaking method. After the native crystals were grown on hanging-drop plates to the full size, the overlaid crystallization solution was replaced with 2,400 nl of the solution supplemented with a slightly higher concentration of PEG550MME and 1 mM CH₃HgCl. The crystals were incubated at 20 °C for 3 h. All of the crystals were flash-cooled in liquid nitrogen for data collection, using the reservoir solution as a cryoprotectant.

Data collection and structure determination of SnYddG. All diffraction data sets were collected at the station BL32XU at SPring-8. Data sets were processed with the program XDS²⁵ and the CCP4 suite²⁶. The data processing statistics are summarized in Extended Data Table 1. The structure was determined by the single isomorphous replacement with anomalous scattering method, using the native and CH₃HgCl-soaked SnYddG crystals. Twenty-four Hg atom sites were identified with the program SHELXD²⁷. The initial phases were calculated with the program SHARP²⁸. The resulting phases were improved by solvent flattening with the program SOLOMON²⁹ and six-fold non-crystallographic symmetry averaging with the program DM³⁰. The initial model was built into the map, using the program COOT³¹. The model was subsequently improved through alternating cycles of manual building with COOT and refinement with the program PHENIX³². The structural refinement statistics are summarized in Extended Data Table 1. Molecular graphics were illustrated with CueMol (<http://www.cuemol.org/>).

Metabolomics analysis. To construct the assay strain W3110 (DE3) ΔyddG::Km containing the IPTG-inducible T7 polymerase expression unit (λDE3), the *yddG* gene knockout allele was transferred to the destination *E. coli*

strain W3110 (DE3)³³ by P1 phage transduction from the systematic *E. coli* knockout library strain, with kanamycin resistance as the selection marker³⁴. The knockout allele was confirmed by a PCR analysis, using the DNA primers 5'-ATAGCGGTAGAAAAACGCACCA-3' and 5'-TGAGATATAAG-GTGAATTACTGGTATTG-3'. *E. coli* strains W3110 (DE3) and W3110 (DE3) ΔyddG::Km cells, cultivated on LB plates, were inoculated into 5 ml M9 medium, containing 0.5% glucose, and shaken at 37 °C. When the optical density reached 0.5, IPTG was added to the medium (final concentration 1 mM), and subsequently, the cells were cultivated for approximately 24 h. After the cells were removed by centrifugation and filtration, the supernatants were analysed by capillary electrophoresis-mass spectrometry (CE-MS) at Human Metabolome Technologies Inc.

Liposome-based assay. The SnYddG protein for liposome assay was purified by the same procedure as those for the crystallization, but 1.2% (w/v) DDM was used for solubilization and 0.25% (w/v) *n*-decyl-β-D-maltopyranoside (DM) was included in every step after solubilization to gel filtration. The EcYddG protein for liposome assay was also purified by the same procedure as the SnYddG protein. The purified SnYddG and EcYddG proteins were reconstituted into liposomes by the following procedure. An *E. coli* polar lipid extract (Avanti) was dissolved in chloroform and dried into a thin film. This film was then resuspended to a final concentration of 20 mg ml⁻¹ in 10 mM HEPES buffer (pH 7.0) containing 100 mM NaCl, and sonicated for 2 min to obtain the liposome solution. The purified proteins were added to the liposome solution at a lipid to protein ratio of 50:1 (w/w). The protein-liposome mixtures were incubated at 4 °C for 30 min, and then ultra-centrifuged (200,000g) at 4 °C for 3 h to remove the detergent. The proteoliposomes were re-suspended to a final concentration of 20 mg ml⁻¹ and stored at -80 °C. Protein-free liposomes were prepared by a similar procedure, except that the protein solution was replaced with the buffer used for the final purification step. The liposomes were sonicated immediately before the measurements to prepare uniformly-sized liposomes. The time-dependent [¹⁴C]Thr (175 mCi mmol⁻¹; Moravsek Biochemicals) uptake assay was initiated by mixing the liposome solution (45 µl) with an equal volume of the extraliposomal solution, consisting of 10 mM HEPES (pH 7.0), 100 mM NaCl, 100 µM amino acid, and 2% (v/v) [¹⁴C]amino acid. After the reaction at 37 °C, the aliquot (20 µl) of the reaction mixture were isolated by Sephadex G-50 (GE Healthcare) gel filtration, and the radioactivity of the incorporated [¹⁴C]amino acid was measured by liquid scintillation counting. The Met-, Glu- and Lys-uptake assays were also performed with a similar condition to that of Thr-uptake assay, using [¹⁴C]Met, [¹⁴C]Glu and [¹⁴C]Lys (55 mCi mmol⁻¹, 210 mCi mmol⁻¹ and 288 mCi mmol⁻¹, respectively; American Radiolabelled Chemicals). For mutational analyses, mutations were introduced by a PCR-based method. The mutant proteins were expressed, purified, and reconstituted into liposomes, and the transport activities were measured by a similar procedure to that for the wild type. The assays were initiated by mixing the liposome solution (25 µl) with an equal volume of the extraliposomal solution, and after the 30-min reaction at 37 °C, the aliquot (20 µl) were isolated for the subsequent radioactivity measurement. The reconstitution rates of the wild-type and mutant proteins were determined by fractionating the proteoliposome samples on an SDS-PAGE gel, and quantifying the amount of SnYddG protein by an LAS-3000 image analyser. All assays were repeated three times. Error bars represent s.d.

Cysteine cross-link analysis of SnYddG. The Cys-free mutant of SnYddG (C159A/C185A/195A/C271A) was constructed using a PCR-based method. The double-Cys mutants (A21C/P91C, A21C/A92C, T24C/A85C, T24C/L86C, A138C/A266C) were also constructed using a PCR-based method, based on the Cys-free mutant. The mutant proteins for the cross-link analysis were prepared by the same procedure as those for the crystallization, but 1.2% (w/v) DDM was used for solubilization and 0.03% (w/v) DDM was included in every step after solubilization to gel filtration. The purified mutant proteins were incubated with 10 mM tris(2-carboxyethyl) phosphine (TCEP) or 1 mM copper phenanthroline [Cu(phen)]₃ at 37 °C for 30 min, followed by trichloroacetic acid precipitation. The pellets were dissolved in SDS-PAGE sample buffer, containing 1% SDS and 20 µM tetramethylrhodamine maleimide (TMRM), incubated at 37 °C for 90 min, and then analysed by SDS-PAGE. The fluorescence of the TMRM-modified proteins was visualized with an LAS-3000 image analyser.

For quantification of intramolecular disulphide formation by SnYddG double-Cys mutants, they were subjected to reductive or non-reductive carboxymethylation. For reductive carboxymethylation, the protein (~2 µg) was dissolved in 20 µl of 1% dithiothreitol in 6 M guanidine hydrochloride, 1 M Tris-HCl (pH 8.5) and 10 mM EDTA, and was heated at 80 °C for 30 min. After cooling, alkylation was performed by the addition of 2 µl of a 25% iodoacetic acid solution in 1 N NaOH and an incubation at room temperature for 30 min in the dark. For non-reductive carboxymethylation, the protein was dissolved in 2.5% iodoacetic acid in 6 M guanidine HCl, 1 M Tris-HCl (pH 8.5) and 10 mM EDTA. The reaction mixtures were desalted with a Sephadex G-25 syringe (1 ml), and pooled fractions

of the carboxymethylated protein were dried and hydrolysed in 6N HCl vapour at 110 °C for 20 h. The acid hydrolysate was derivatized with 6-aminoquinolyl-N-hydroxysuccinimidyl carbamate, and was quantified as described previously³⁵ (Extended Data Fig. 6b).

Co-evolutionary analysis. The co-evolutionary analysis of YddG homologues and other DMT proteins was performed using the EVcoupling³⁶ web interface (<http://evfold.org/evfold-web/evfold.do>). The default parameters of the web interface were employed for the calculations, except that the E-value threshold for generating the sequence alignment was changed to -30 . The resulting number of YddG and DMT homologue sequences used for the calculation was 59,114. The subsequent 3D-structure prediction of SnYddG was performed by the program EVfold_membrane³⁷. The default parameters of the web interface were employed for the calculation, except that the 'membrane protein' option was turned on and the numbers of flanking upstream and downstream residues in the secondary structure prediction were changed to 0.

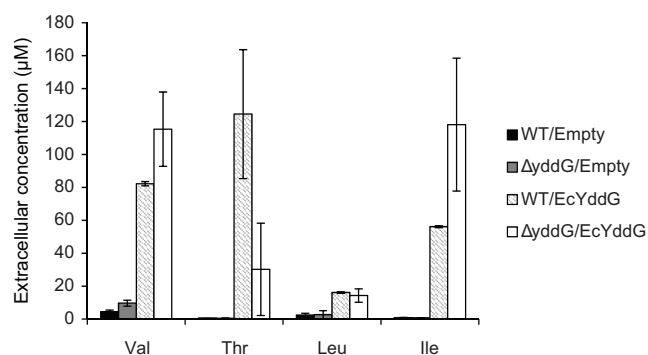
Molecular dynamics simulation. The atomic coordinates of the crystal structure of SnYddG (molecule B) were used for the simulation. The disordered region (Ala138–Gly144) was modelled by adding the corresponding coordinates in molecule E. All of the water molecules observed in the crystal structure were kept. The missing hydrogen atoms were built with the program VMD³⁸. A periodic boundary system, including explicit solvent and a phosphorylloleoylphosphatidylethanolamine (POPE) lipid bilayer³⁹, was prepared. The net charge of the simulation system was neutralized through the addition of 150 mM NaCl. The simulation system was $96 \times 96 \times 96$ Å, and contained 80,530 atoms. The molecular topologies and parameters from the Charmm36 force field³⁹ were used for the protein, lipid and water molecules.

Molecular dynamics simulations were performed with the program NAMD 2.10 (ref. 40). The systems were first energy minimized for 1,000 steps with fixed positions of the non-hydrogen atoms, and then for another 1,000 steps with 10 kcal mol⁻¹ restraints for the non-hydrogen atoms, except for the lipid molecules within 5.0 Å from the proteins. Next, equilibrations were performed for 0.01 ns under NVT conditions, with 10 kcal mol⁻¹ restraints for the heavy atoms of the protein. Finally, equilibrations were performed for 0.5 ns under NPT conditions with the 1.0 kcal mol⁻¹ restraints. In the equilibration and production processes, the pressure and temperature were set to 1.0 atm and 310 K, respectively. Constant temperature was maintained by using Langevin dynamics. Constant pressure was maintained by using the Langevin piston Nosé–Hoover method⁴¹. Long-range electrostatic interactions were calculated by using the particle mesh Ewald method⁴². The production run of the equilibrium simulation was performed for 500 ns, starting from the crystal structure. The outward-to-occluded simulation run was also performed for 500 ns, starting from the crystal structure, with a harmonic distance restraint (force constant = 10.0 kcal mol⁻¹ Å⁻²) between centres of mass of the C α atoms of TM4a (Pro91–Ala98) and TM9b (Ala246–Leu253). The equilibrium distance of the harmonic restraint was gradually decreased from 15 Å to 9 Å during the 500-ns run. Next, the occluded-to-inward simulation run was performed, starting from the final snapshot of the outward-to-occluded simulation.

A similar harmonic distance restraint was applied between centres of mass of the C α atoms of TM4b (Trp101–Phe108) and TM9a (Val237–Ser244), with the equilibrium distance gradually increased from 9 Å to 15 Å.

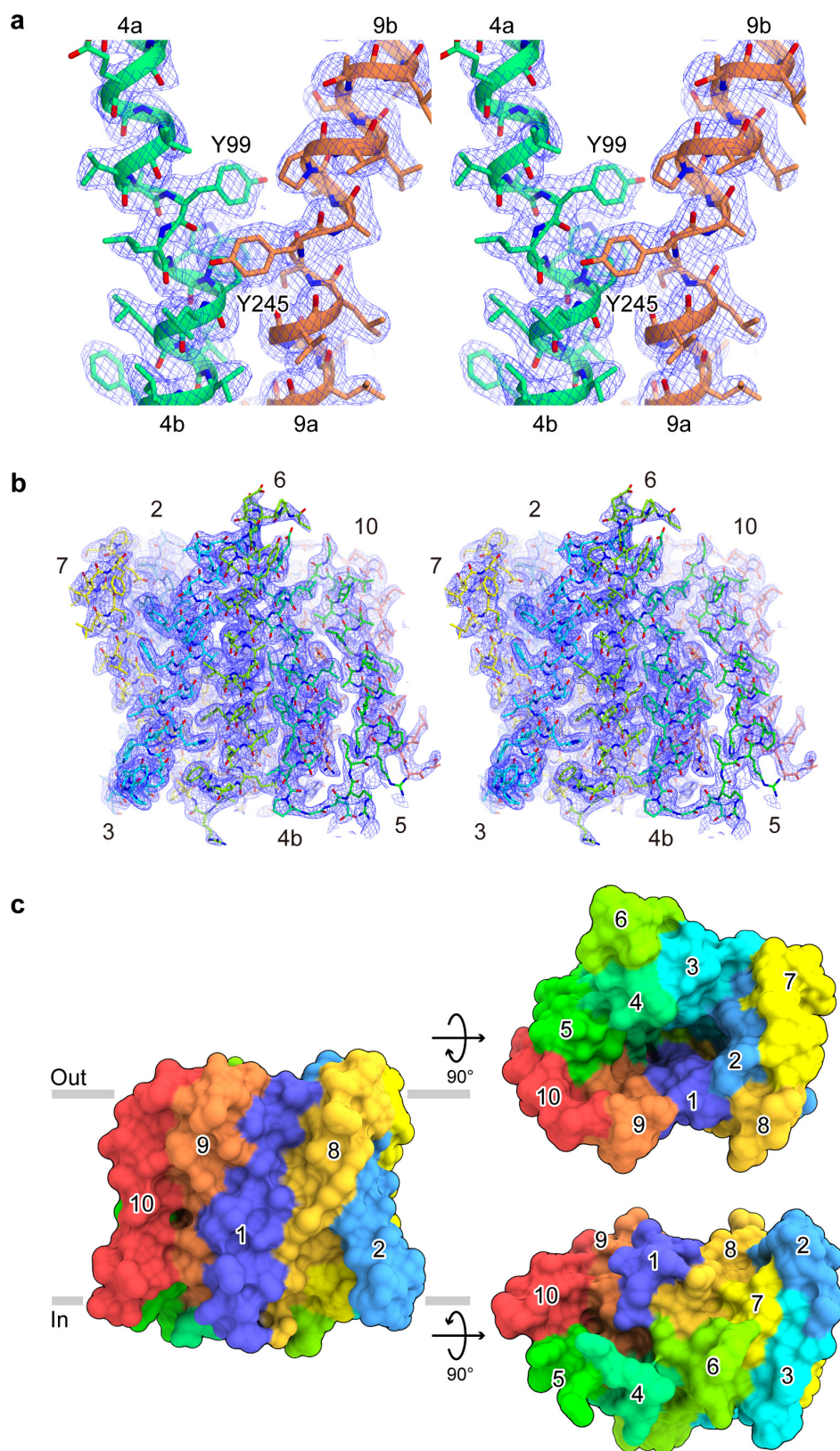
Statistical analyses. The statistical significance of differences in mean values was calculated using unpaired, two-tailed Student's *t*-test. No statistical methods were used to predetermine sample size.

25. Kabsch, W. XDS. *Acta Crystallogr. D* **66**, 125–132 (2010).
26. Winn, M. D. *et al.* Overview of the CCP4 suite and current developments. *Acta Crystallogr. D* **67**, 235–242 (2011).
27. Schneider, T. R. & Sheldrick, G. M. Substructure solution with SHELXD. *Acta Crystallogr. D* **58**, 1772–1779 (2002).
28. De La Fortelle, E. & Bricogne, G. Maximum-likelihood heavy-atom parameter refinement for multiple isomorphous replacement and multiwavelength anomalous diffraction methods. *Methods Enzymol.* **276**, 472–494 (1997).
29. Abrahams, J. P. & Leslie, A. G. Methods used in the structure determination of bovine mitochondrial F1 ATPase. *Acta Crystallogr. D* **52**, 30–42 (1996).
30. Cowtan, K. D. & Main, P. Improvement of macromolecular electron-density maps by the simultaneous application of real and reciprocal space constraints. *Acta Crystallogr. D* **49**, 148–157 (1993).
31. Emsley, P., Lohkamp, B., Scott, W. G. & Cowtan, K. Features and development of Coot. *Acta Crystallogr. D* **66**, 486–501 (2010).
32. Adams, P. D. *et al.* PHENIX: Building new software for automated crystallographic structure determination. *Acta Crystallogr. D* **58**, 1948–1954 (2002).
33. Hattori, M. *et al.* Mg²⁺-dependent gating of bacterial MgtE channel underlies Mg²⁺ homeostasis. *EMBO J.* **28**, 3602–3612 (2009).
34. Baba, T. *et al.* Construction of *Escherichia coli* K-12 in-frame, single-gene knockout mutants: the Keio collection. *Mol. Syst. Biol.* **2**, 2006.0008 (2006).
35. Masuda, A. & Dohmae, N. Examination of an absolute quantity of less than a hundred nanograms of proteins by amino acid analysis. *Anal. Bioanal. Chem.* **405**, 8073–8081 (2013).
36. Marks, D. S. *et al.* Protein 3D structure computed from evolutionary sequence variation. *PLoS ONE* **6**, e28766 (2011).
37. Hopf, T. A. *et al.* Three-dimensional structures of membrane proteins from genomic sequencing. *Cell* **149**, 1607–1621 (2012).
38. Humphrey, W., Dalke, A. & Schulten, K. VMD: visual molecular dynamics. *J. Mol. Graph.* **14**, 33–8, 27–8 (1996).
39. Brooks, B. R. *et al.* CHARMM: the biomolecular simulation program. *J. Comput. Chem.* **30**, 1545–1614 (2009).
40. Phillips, J. C. *et al.* Scalable molecular dynamics with NAMD. *J. Comput. Chem.* **26**, 1781–1802 (2005).
41. Feller, S. E., Zhang, Y., Pastor, R. W. & Brooks, B. R. Constant pressure molecular dynamics simulation: The Langevin piston method. *J. Chem. Phys.* **103**, 4613 (1995).
42. Darden, T., York, D. & Pedersen, L. Particle mesh Ewald: An *N*-log(*N*) method for Ewald sums in large systems. *J. Chem. Phys.* **98**, 10089 (1993).
43. Krissinel, E. & Henrick, K. Secondary-structure matching (SSM), a new tool for fast protein structure alignment in three dimensions. *Acta Crystallogr. D* **60**, 2256–2268 (2004).

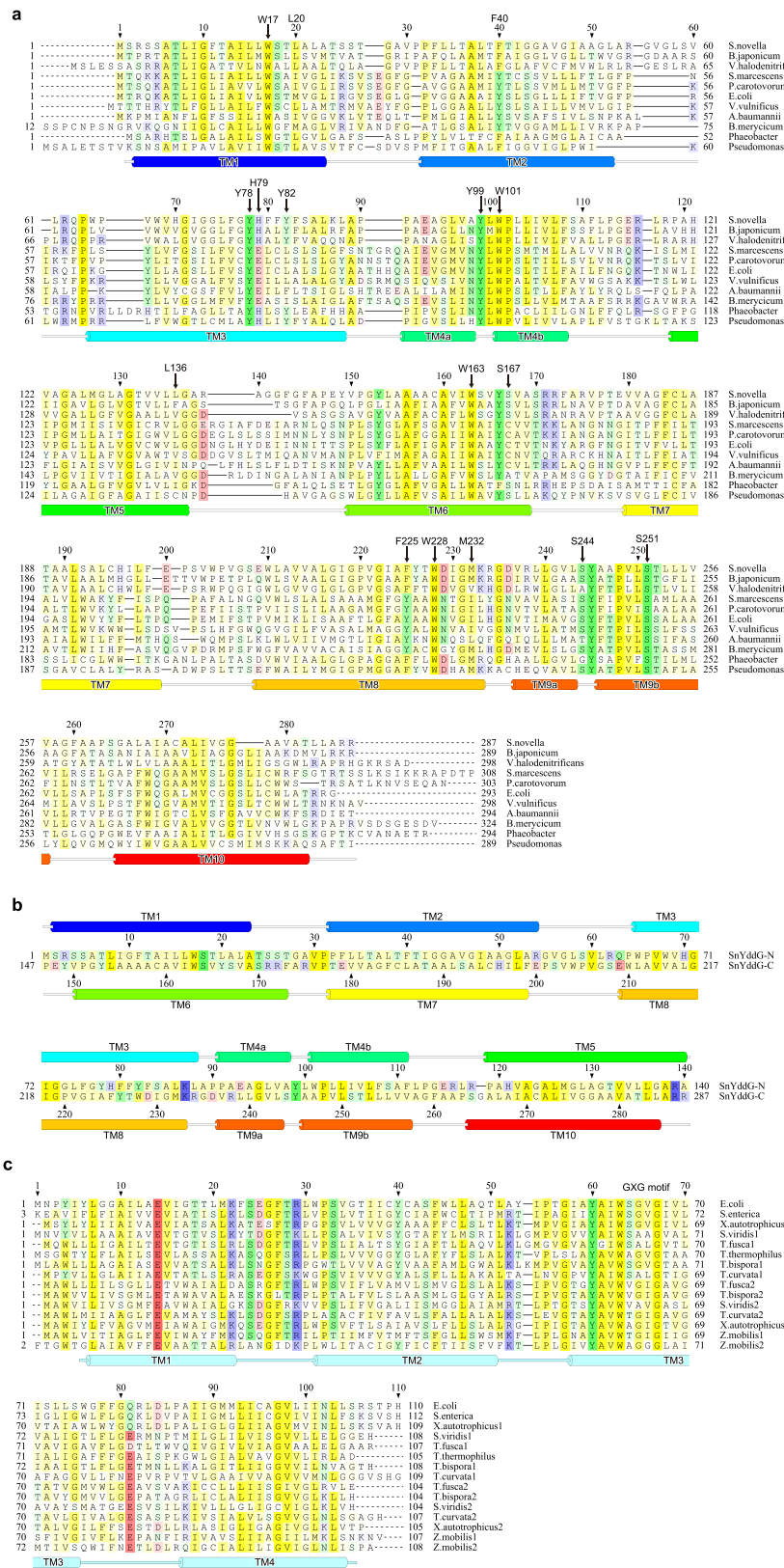


Extended Data Figure 1 | Metabolomics analysis of the *E. coli* W3110 wild-type (WT) and YddG knockout ($\Delta yddG$) strains, containing either the empty vector or the EcYddG protein expression vector.

We analysed the 110 well-known metabolites in the culture media of wild-type and $\Delta yddG$ cells, transformed with an empty vector or the pET-derived vector containing the EcYddG gene. The amounts of the metabolites in the media that exhibited more than threefold increases in both the wild-type and $\Delta yddG$ strains are plotted. The results showed the consistent increases of valine, threonine and isoleucine, in the medium of the EcYddG-expressing cells, as compared to the negative controls. These results are consistent with those from the *in vitro* liposome-based analysis of EcYddG (Fig. 1), supporting the notion that YddG transports a wide range of metabolites, as well as amino acids.



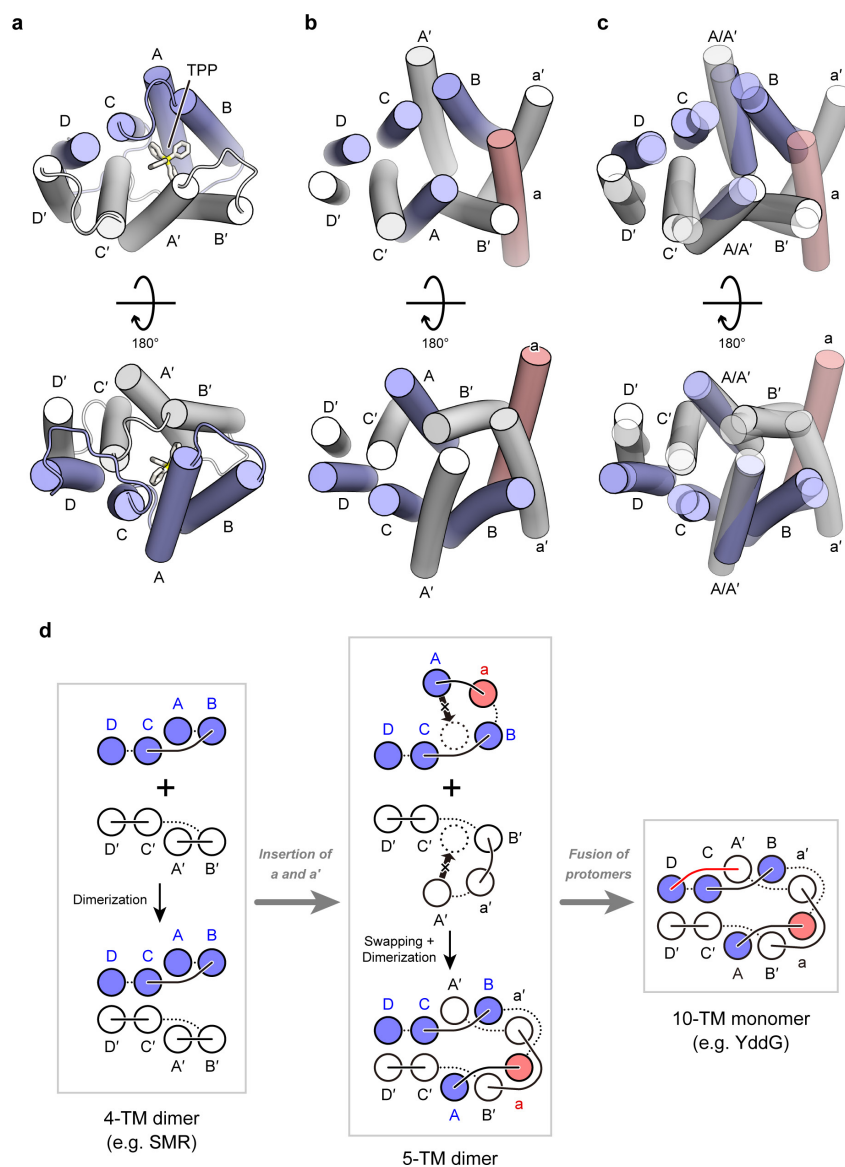
Extended Data Figure 2 | The 2.4-Å electron density map and molecular surface of SnYddG. a, b, A stereo view of the unbiased $2mF_o - DF_c$ maps around TM4 and TM9 (a), and an overall view of molecule B in the crystal asymmetric unit, contoured at 1.1σ (b) are shown. c, Molecular surface of SnYddG, viewed from different directions. The transmembrane segments are coloured as in Fig. 2.



Extended Data Figure 3 | See next page for caption.

Extended Data Figure 3 | Conserved residues of YddG and SMR homologues. **a**, Amino acid sequence alignment of SnYddG and other YddG homologues, from *Bradyrhizobium japonicum* (UniProtKB ID: A0A0A3YL06), *Virgibacillus halodenitrificans* (GenBank ID: CDQ34001.1), *Serratia marcescens* (UniProtKB ID: L0MHZ3), *Pectobacterium carotovorum* (UniProtKB ID: A0A0E2ZTH4), *E. coli* (UniProtKB ID: P46136), *Vibrio vulnificus* (UniProtKB ID: Q7MDM6), *Acinetobacter baumannii* (UniProtKB ID: A0A009YGQ0), *Bifidobacterium merycicum* (UniProtKB ID: A0A087BD75), *Phaeobacter inhibens* (UniProtKB ID: I7EXD9), and *Pseudomonas sp.* (UniProtKB ID: B2Z3V9). The conserved amino acids involved in the transport

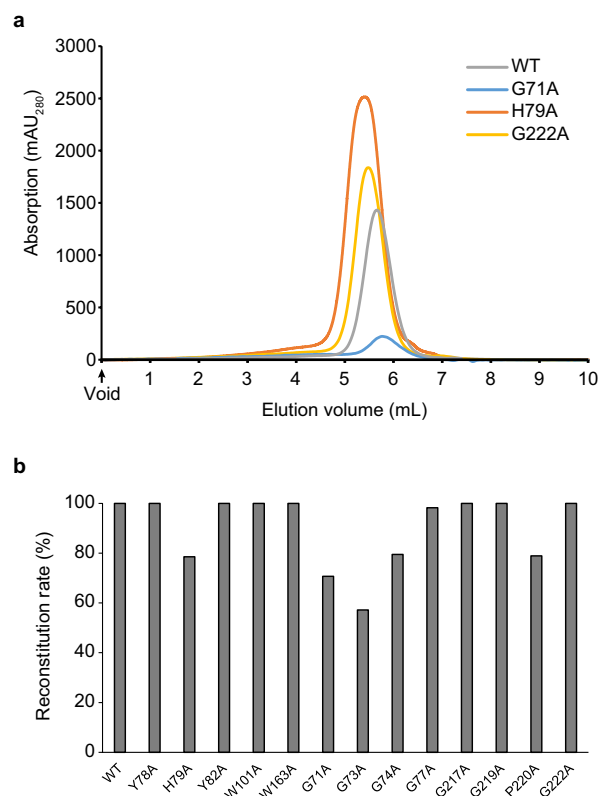
mechanism and discussed in the main text are indicated. **b**, Amino acid sequence alignment of the N and C halves of SnYddG. **c**, Amino acid sequence alignment of EmrE homologues, from *E. coli* (UniProtKB ID: P23895), *S. enterica* (UniProtKB ID: X5AXH0), *Xanthobacter autotrophicus* (UniProtKB IDs: A7IJY9 and A7IN30), *Saccharomonospora viridis* (UniProtKB IDs: C7MRM1 and C7MSE0), *Thermobifida fusca* (UniProtKB IDs: Q47R92 and Q47QH0), *Thermus thermophilus* (UniProtKB ID: Q72K82), *Thermobispora bispora* (UniProtKB IDs: D6YBB5 and D6Y4B6), *Thermomonospora curvata* (UniProtKB IDs: D1A404 and D1AD18), and *Zymomonas mobilis* (UniProtKB IDs: Q5NPN9 and Q5NRC2).



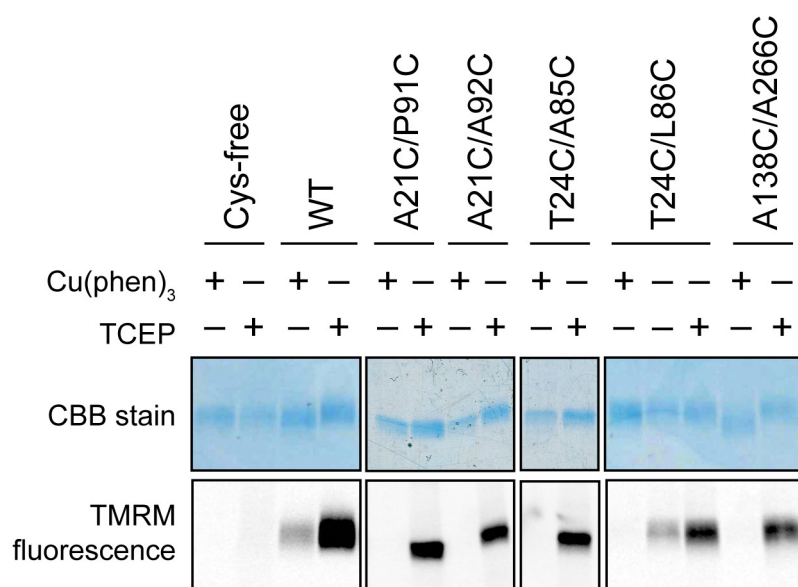
Extended Data Figure 4 | Molecular evolution of the DMT superfamily.

a, Crystal structure of *E. coli* EmrE (PDB accession 3B5D)²¹. The bound tetraphenylphosphonium (TPP) is shown as a stick model. The transmembrane segments are coloured and labelled as in **d**. **b**, The present crystal structure of SnYddG. Only the transmembrane segments are shown in cylinder models. The transmembrane segments are coloured and labelled as in **d**. **c**, Molecular superimposition of EmrE and SnYddG, calculated by the SSM algorithm⁴³. The cylinder model of EmrE is shown with the same colouring as in **d**. The semi-transparent cylinder model of

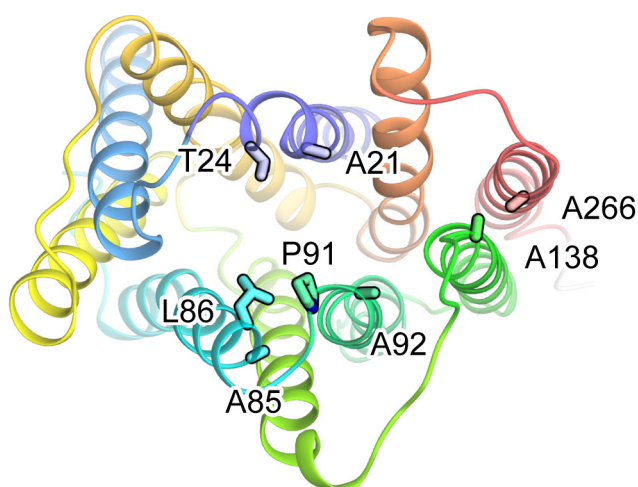
SnYddG is shown with the same colouring as in **d**. **d**, Schematic illustration of the possible evolutionary path of the DMT family transporters. The transmembrane segments are indicated by circles, and the connecting loops are indicated by solid and dotted curves. The black arrows indicate the folding of the transporter, while the grey arrows indicate the possible evolutionary pathway. Transmembrane segments originating from one protomer of SMR are coloured blue, while the newly inserted transmembrane segments (TM a) are coloured red.



Extended Data Figure 5 | Preparation of the reconstituted proteoliposomes containing the SnYddG mutants. **a**, The chromatograms of the final purification step by the gel-filtration chromatography column. The results of the wild type, as well as the mutants with the decreased activities in the liposome-based assay (that is, G71A, H79A and G222A), are shown. **b**, Reconstitution rates of the wild-type and SnYddG mutants, determined by the SDS-PAGE analysis. The reconstitution rates were measured as a percentage of the total amount of protein used for the reconstitution.

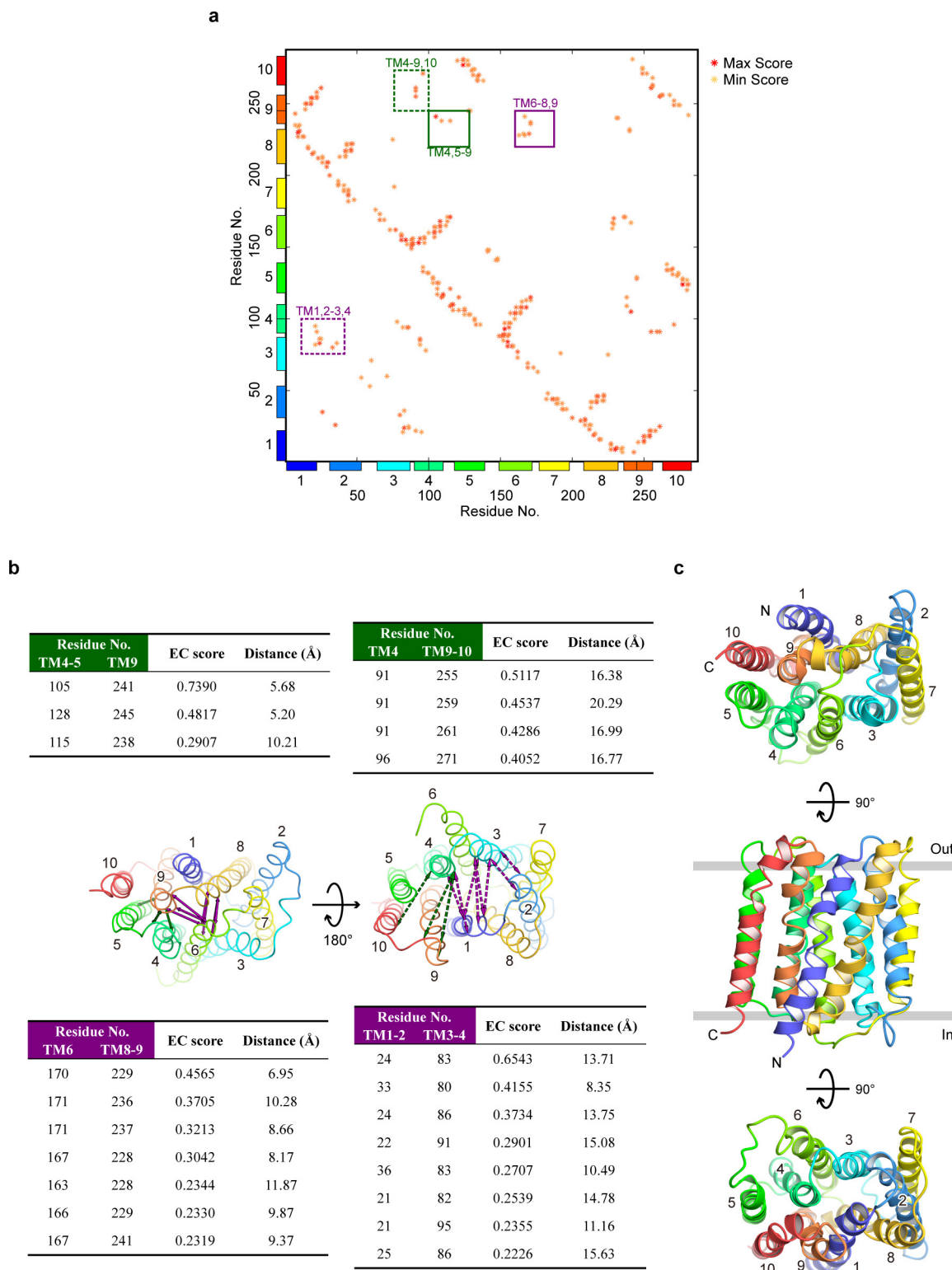
a**b**

Double-Cys mutant	Percentage of disulfide bond formation (%)
A21C/P91C	84.69
A21C/A92C	83.45
T24C/A85C	100.00
T24C/L86C	83.04

c

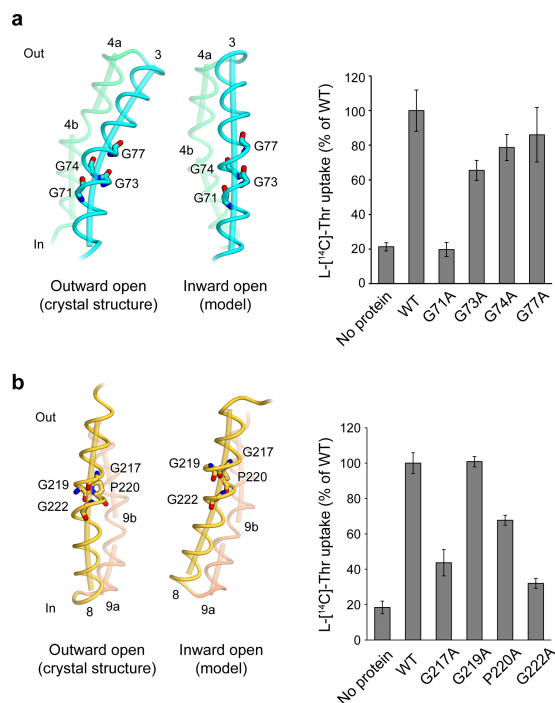
Extended Data Figure 6 | Cys-crosslink analysis of the residues on the periplasmic sides of TM1 (Ala21, Thr24) and TM3 (Ala85, Leu86, Pro91, Ala92). **a**, The Cys-free mutant of SnYddG (C159A/C185A/C195A/C271A) was created, and then pairs of Cys residues to the residues in TM1 and TM3 or TM1 and TM4, which may form the intracellular gate, were introduced. The purified double-Cys mutant proteins were oxidized or reduced, and then modified by the Cys-reactive fluorescent reagent, tetramethylrhodamine maleimide (TMRM). The double-Cys mutants

were completely masked from the Cys-modification by TMRM under the oxidized conditions, indicating that these residues are close enough to form disulfide bonds. **b**, The results of the quantification of the amino acid composition of the cross-linking products of the YddG double-Cys mutants. The percentages of disulfide bond formation for each mutant were calculated from the amounts of carboxymethylated Cys under the oxidizing and reducing conditions. **c**, The positions of the mutated residues are indicated in the crystal structure viewed from the periplasmic side.

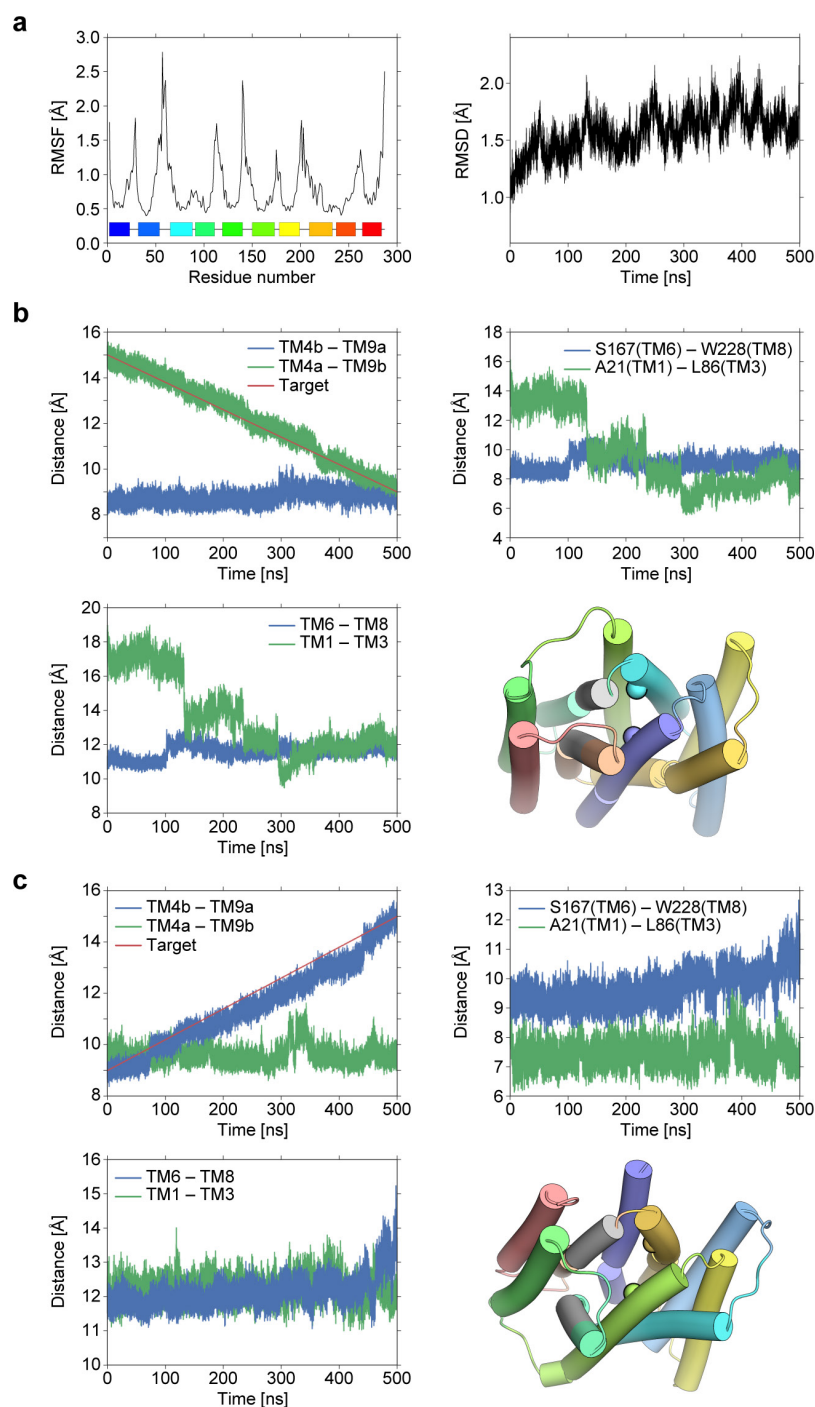


Extended Data Figure 7 | Evolutionary covariation analysis of YddG and DMT protein homologues. **a**, Contact maps of the top-ranked 170 evolutionary constraints (ECs), calculated from the 59,114 homologue sequences using the program EVcoupling. The ECs are indicated by stars, coloured proportionally according to their EC scores, from orange to red. The solid and dashed rectangles indicate the ECs corresponding to the observed extracellular gate and the putative intracellular gate interactions, respectively. **b**, The ECs mapped onto the outward-open crystal structure

of SnYddG. The ECs indicated in **a** and tabulated in the top and bottom panels are indicated as arrows connecting the corresponding residues in the SnYddG structure. The solid and dashed arrows indicate the ECs corresponding to the observed extracellular gate and the putative intracellular gate interactions, respectively. **c**, The SnYddG structure predicted from the top-ranked 170 ECs, using the program EVfold_membrane.



Extended Data Figure 8 | The kinks of TM3 and TM8 around the conserved Gly and Pro residues. **a**, The kinks of TM3 around the conserved Gly residues, in the outward-open crystal structure and the inward-open model. **b**, The kinks of TM8 around the conserved Gly and Pro residues, in the outward-open crystal structure and the inward-open model. In **a** and **b**, the Gly and Pro residues are shown by stick models, and the axes of the transmembrane helices are indicated by cylinders. In the right panel, the activities of SnYddG mutants of the TM3 and TM8 kinks, measured by the liposome-based analysis using threonine as a substrate, are plotted, respectively. The substrate uptake activities measured after 30 min were plotted as percentages of the wild-type transport activity. Error bars, s.d.; $n = 3$.



Extended Data Figure 9 | Molecular dynamics simulation of SnYddG.

a, The results of the 500-ns run of the non-biased simulation. Left, a plot of the root mean square fluctuations of each C α atom from the initial crystal structure. Right, a plot of the root mean square deviation over all C α atoms from the initial crystal structure, during the course of the simulation. **b**, The results of the outward-to-occluded simulation. Top left, a plot of the distances between the C α atoms of TM4a (Pro91–Ala98) and TM9b (Ala246–Leu253), and between TM4b (Trp101–Phe108) and TM9a (Val237–Ser244). The equilibrium distance of the harmonic restraint applied between TM4a and TM9b is plotted with a red line. Top right, time series of the distances between the C α atoms of Ser167 (TM6) and Trp228 (TM8), and between Ala21 (TM1) and Leu86 (TM3). Bottom left, time series of the distances between the C α atoms of TM1 (17–24) and TM3 (81–88) and the C α atoms of TM6 (163–170) and TM8 (225–232). Bottom right, the final snapshot of the outward-to-occluded simulation. The C α atoms of Ala21 (TM1) and Leu86 (TM3) are shown

as spheres. The parts of TM4a and TM9b subjected to harmonic restraints are coloured grey. The arrows indicate the distances plotted in the graphs in **b** and **c**. **c**, The results of the occluded-to-inward simulation. Top left, plot of the distance between the C α atoms of TM4a (Pro91–Ala98) and TM9b (Ala246–Leu253), and between TM4b (Trp101–Phe108) and TM9a (Val237–Ser244). The equilibrium distance of the harmonic restraint applied between TM4b and TM9a is plotted with a red line. Top right, time series of the distances between the C α atoms of Ser167 (TM6) and Trp228 (TM8), and between Ala21 (TM1) and Leu86 (TM3). Bottom left, time series of the distances between the C α atoms of TM1 (17–24) and TM3 (81–88) and between the C α atoms of TM6 (163–170) and TM8 (225–232). Bottom right, the final snapshot of the occluded-to-inward simulation. The C α atoms of Ser167 (TM6) and Trp228 (TM8) are shown as spheres. The parts of TM4b and TM9a subjected to harmonic restraints are coloured grey. The arrows indicate the distances plotted in the graphs in **b** and **c**.

Extended Data Table 1 | Data collection and refinement statistics

	Native	CH ₃ HgCl derivative
Data collection		
X-ray source	Spring-8 BL32XU	
Wavelength (Å)	1.0	1.0
Space group	<i>P</i> 2	<i>P</i> 2
Cell dimensions		
<i>a</i> , <i>b</i> , <i>c</i> (Å)	105.84, 84.65, 112.25	106.67, 85.89, 112.85
α , β , γ (°)	90, 108.46, 90	90, 109.44, 90
Resolution (Å)	50–2.4 (2.54–2.4)*	50–3.5 (3.59–3.5)
<i>R</i> _{sym}	0.120 (1.269)	0.272 (1.26)
<i>I</i> / σ (<i>I</i>)	13.25 (1.91)	6.11 (1.54)
Completeness (%)	99.8 (99.8)	99.8 (99.9)
Multiplicity	8.47 (8.45)	4.95 (4.98)
CC _{1/2}	0.998 (0.619)	0.989 (0.572)
Refinement		
Resolution (Å)	50–2.4	
No. reflections	73,750	
<i>R</i> _{work} / <i>R</i> _{free}	0.2264/0.2495	
No. atoms		
Protein	11,564	
Ligand/ion/lipid	349	
Water	11	
<i>B</i> -factors (Å ²)		
Protein	66.44	
Ligand/ion/lipid	69.43	
Water	47.96	
R.m.s. deviations		
Bond length (Å)	0.003	
Bond angle (°)	0.751	
Ramachandran plot		
Favored (%)	98.07	
Allowed (%)	1.87	
Outliers (%)	0.06	

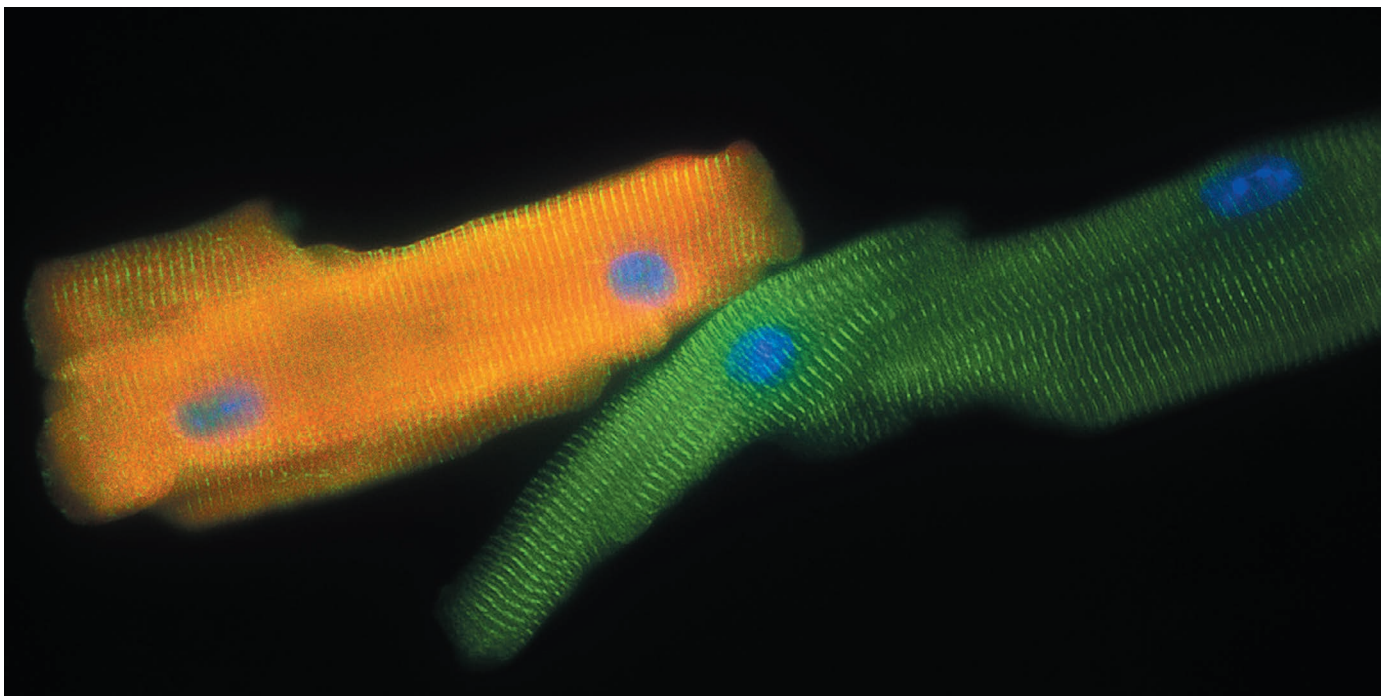
*Values in parentheses are for highest-resolution shell.

TECHNOLOGY FEATURE

A SIMPLER TWIST OF FATE

Ways to directly convert one mature cell type into another may eventually offer a safer, faster strategy for regenerative medicine.

COURTESY OF THE GLADSTONE INSTITUTES



The green heart muscle cells are 'natural'. The orange ones were fibroblasts that have been directly reprogrammed to become heart muscle cells.

BY MICHAEL EISENSTEIN

Until the day it dies, a cell that has become a skin cell remains a skin cell — or so scientists used to think. Over the past decade, it has become clear that cellular identity is not written in stone but can be rewritten by activating specific genetic programs. Today, the field of regenerative medicine faces a question: should this rewriting take the conventional route, in which mature cells are first converted back into stem cells, or, where feasible, a more direct approach?

'Terminally differentiated' is a term that sums up the old way of thinking — that skin, muscle or other mature cells cannot be coaxed to adopt a drastically different fate. That idea began to falter a decade ago, when cell biologist Shinya Yamanaka of Kyoto University in Japan showed that a handful of genes could transform adult fibroblast (connective tissue)

cells into induced pluripotent stem (iPS) cells¹. Like embryonic stem cells, iPS cells can develop into any cell type, a property called pluripotency. They can also be produced in unlimited quantities, unlike embryonic stem cells, which must be harvested from human embryos and therefore come with considerable political baggage.

Just a few years after Yamanaka's discovery — which earned him a share of the 2012 Nobel Prize in Physiology or Medicine — researchers began uncovering shortcuts for switching cell types that they called 'direct reprogramming'. Mature cells of one kind could be coaxed to directly become another, with no pluripotent middleman. Researchers have learned how to turn skin cells into neurons or heart cells, and stomach cells into insulin-producing pancreatic β -cells. "It's amazing to watch the cells change right before your eyes," says Benedikt Berninger of the Johannes Gutenberg

University of Mainz in Germany, who uses direct reprogramming to generate neurons.

Research into direct reprogramming is more preliminary than work on iPS cells, but it is stirring excitement in regenerative medicine. Directly reprogrammed cells might be safer than cells that pass through a pluripotent state, because the latter share with tumour cells a capacity for extensive proliferation — making them potentially cancer-causing Trojan horses.

Clinical interventions based on iPS cells must be done carefully to ensure that no pluripotent cells are transplanted along with the fully mature cells. "There's a risk that you could lose control of these cells and that they start proliferating uncontrollably after transplantation," says Malin Parmar, a neurobiologist at Lund University in Sweden who hopes to use direct reprogramming to reverse the loss of neurons in people with Parkinson's disease. ►

► “But if you bypass the pluripotent stage, it’s a lot quicker and potentially safer.”

CHANGING PROGRAMS

Rewriting cellular identities first requires an understanding of how those identities are established. Every cell in the body can trace its ancestry back to a single progenitor: the fertilized egg. As embryonic cells divide and mature, their destiny is determined by the specific genes that are switched on and off over the course of development. Proteins called transcription factors regulate this process by binding certain DNA sequences in the genome, and subsequently activating or suppressing adjacent genes. The ones that govern the fate of a developing cell are often called master regulators because they operate at the summit of complicated cascades of gene activity.

“These master regulators are basically all defined by their pivotal roles in embryogenesis in the development of certain cell types,” says Qiao Zhou, a cell biologist at Harvard Stem Cell Institute in Cambridge, Massachusetts. “Perhaps a progenitor cell can become cell A or B or C, but if you force it to express a certain master regulator, it will inevitably choose A.”

An early demonstration of the usefulness of master regulators for direct reprogramming came as far back as 1987, when Harold Weintraub, Andrew Lassar and their colleagues at the Fred Hutchinson Cancer Research Center in Seattle, Washington, showed that forcing fibroblasts to express a certain portion of DNA put them on a developmental path to become muscle cells; they later discovered that the single gene responsible encodes the transcription factor MyoD². “That was a paradigm-shifting observation, and people in the field thought that most other cell types would have that one key factor that would be powerful enough to convert the fate of a cell,” says Deepak Srivastava, a heart development researcher at the Gladstone Institute of Cardiovascular Disease in San Francisco, California.

But it wasn’t that simple. The hunt for individual master regulators that could initiate reprogramming would yield many years of disappointment — until Yamanaka’s work on iPS cells revealed that the secret of effective reprogramming was not a single factor, but rather combinations of multiple genes. As researchers started to mix and match different sets of master regulators, success stories began to emerge.

In 2008, Zhou was part of a team led by Harvard scientist Douglas Melton that transformed one type of pancreatic cell into another, generating the insulin-secreting β -cells that are needed by many people with diabetes. “Our study concluded that you need a minimum of three master regulators to make that happen,” says Zhou. In 2010, a group led by stem-cell scientist Marius Wernig of Stanford University in California turned fibroblasts into neurons, also using a trio of genes³. Further refinements and extensions of this work gave rise to a host

of different, specialized neurons, with each type producing or responding to distinct neurotransmitter signals.

Most of these pioneering demonstrations of direct reprogramming have been achieved with cultured cells. Yet many researchers see much greater promise for regenerative medicine if cell conversions can be prompted inside the body. Pools of cells that are relatively abundant in an organ could be transformed into other kinds of mature cells that are more desperately needed. So far, there have been a handful of triumphs in animal experiments. Parmar’s group, for example, found that glial cells can be converted into functional neurons by injecting viruses laden with genes for reprogramming factors into the brains of mice. And Srivastava has likewise turned mouse fibroblasts inside the heart into beating cardiac muscle cells, a strategy that may offer a way to repair damage caused by a heart attack. “You’ve got this vast pool of cells that are already in the organ that you can harness for regeneration,” he says. But no one has so far tried direct reprogramming inside a human.

IDENTITY CRISIS

For now, most research is focused on ensuring the success of the reprogramming process. Investigators not only have to work out a successful combination of master regulators that turns on the genes that define a certain cell type; they also, ideally, have to discover the smallest possible set. This is because the most reliable way to force a cell to express master

regulator genes is to deliver additional copies of these genes to it, and delivering many genes into a cell is a much tougher technical challenge than providing just a few. Working out the minimal set of master regulators can be a slog: often the roster of candidate combinations is huge, and the only way through a thicket of options is to systematically test each one. Parmar’s team started with 12 candidate genes for generating dopamine-producing neurons, for example, before eventually narrowing it down to 2.

Some researchers have started to create software specifically for direct reprogramming that incorporates information about which master regulators control the formation of tissues. A team spread over three continents has developed an experiment-planning tool called Mogrify⁴, which brings together large quantities of gene-expression data from a long list of cell types with rules about the gene networks that different master regulators control. Mogrify uses these to predict the combination of reprogramming factors that will cause a desired cellular identity change. The idea is to provide researchers with a way to computationally identify the fewest possible master regulator genes that can directly reprogram one particular cell type into another.

But providing active master regulator genes isn’t always enough to ensure complete reprogramming: the master regulators may successfully set a cell on a developmental path, but then leave it stranded in an immature, precursor

Better modifying through chemistry

Transcription factors are a natural choice for reprogramming overall gene activity, but the genes encoding them first have to be delivered into target cells. This process is laborious and raises potential safety concerns for clinical applications.

Chemical biologist Sheng Ding has found an alternative method: inducing direct reprogramming with cocktails of chemicals. In his lab at the Gladstone Institute of Cardiovascular Research in San Francisco, California, he has spent much of the past decade building a library of compounds that can greatly modify gene expression. Using chemical agents such as A83-01 and LDN193189, which can switch off certain cellular signalling pathways, Ding has successfully reprogrammed adult cells with no transcription factors whatsoever.

He thinks his approach is much less artificial because he externally triggers innate cellular mechanisms that lead to reprogramming, rather than abruptly forcing cells to produce proteins that they normally wouldn’t. “It’s really a gradual

reprogramming process,” he says.

In a pair of recent experiments, Ding and his colleagues converted fibroblasts into neural stem cells⁷ and cardiac muscle⁸ by applying different cocktails, each consisting of nine different compounds, some of them pharmaceuticals. Although the results are impressive, heart researcher Deepak Srivastava, who collaborated with Ding at Gladstone on this work, notes that the heart muscle cells produced in this way are more developmentally immature than those reprogrammed with transcription factors.

But the approach offers far more precise control over reprogramming in cell culture than direct reprogramming with transcription factors alone, and advocates of Ding’s strategy think that it could avoid some of the regulatory complications around gene therapy. Only a handful of labs have tried this chemistry-alone approach, but many have quickly become converts, among them Hongkui Deng of Peking University in Beijing. “We see chemical reprogramming as the future,” he says. **M.E.**

state. Then the task is to identify which additional genes must be active to finish the process, and add them to the delivery package.

Stem-cell biologist Hongkui Deng at Peking University in Beijing struggled with this problem for years. His initial efforts to directly turn skin cells into liver cells through the forced expression of master regulator genes alone yielded cells that failed to perform key, liver-like functions. Then, during a second round of screening, he identified additional genes that could complete the reprogramming⁵. He calls them maturation factors — genes that are unimportant for initiating the conversion but crucial for obtaining functionally mature cells.

Other researchers have found that they can boost the success rate of direct reprogramming by augmenting the effects of master regulator genes with chemicals that act on cellular signalling pathways to promote reprogramming — occasionally, chemicals alone can prompt a cell-type transformation (see ‘Better modifying through chemistry’).

Even with the appropriate gene and chemical deliveries, it is hard to prove that any direct reprogramming is truly complete. Peering through a microscope can reveal whether a transformation has taken place — for example, whether flat, star-shaped fibroblasts have formed long, axon-like projections — but deeper analysis of the cell’s inner workings is also needed. Put simply, how can one be certain that a reprogrammed skin cell has truly become a neuron, and is not merely ‘neuron-like’?

Measuring the downstream activity of master regulator genes can offer insights into how well reprogramming has succeeded. If the introduced master regulators are doing their job, they should cause grand shifts in the overall patterns of gene expression in the cell nucleus, which should match the patterns found in mature cells of the target tissue. There are several ways to survey a cell’s total gene expression — for example, sequencing all of the RNA molecules in it. Researchers at Boston University and Harvard University in Massachusetts have drawn on this kind of data in their development of CellNet, a software program that can assess how well the gene activity in reprogrammed cells matches that of target cells⁶.

Still, the identity test that really matters is whether reprogrammed cells can functionally replace naturally differentiated cells. “If they look like neurons and have gene expression like neurons, that doesn’t mean they’re really neurons,” says Chun-Li Zhang, a neurobiologist at the University of Texas Southwestern Medical Center in Dallas. Convincing proof requires a battery of assessments, such as electrophysiological measurements that confirm whether a newly formed neuron is firing and is therefore capable of activating other neurons that are linked to it by synapses. No one characteristic can provide sufficient evidence in isolation, says Zhou. His group’s attempts to reprogram liver cells into pancreatic β -cells



Researchers studying reprogrammed neurons in Malin Parmar’s lab at Lund University in Sweden.

yielded only dysfunctional intermediates. “They synthesized and released insulin in large quantities — so much so that the animals died from hypoglycaemia,” he says. This is because the cells lacked pancreatic cells’ ability to sense and respond to blood glucose levels.

One of the findings of these diagnostic tests is that prompting reprogramming within a target organ often works better than efforts with cultured cells. “Most of our cells only partially reprogram to cardiac muscle when they’re on plastic,” says Srivastava. “But in their natural environment, the majority go all the way to a beating state, where they’re electrically coupled with their neighbours.” This may be due to chemical cues generated by other neighbouring cells in the organ, or because of features of the 3D tissue environment that are hard to replicate in the lab. Whatever the reason, it bodes well for developing clinical applications.

PATH TO THE CLINIC

Researchers agree that there are many hurdles to overcome before these methods can be tested in people. In general, human cells have proven more challenging to directly reprogram than mouse cells: they tend to take longer to go through the reprogramming process and often require additional transcription factors to those that are sufficient in animal experiments.

Gene delivery also poses formidable challenges, especially to organs such as the brain. In some cases, viruses that preferentially infect particular cell types could help to guide reprogramming factors to specific sites of disease or injury, but delivery to unintended sites may still pose risks.

Then there’s the issue of ‘robbing Peter to pay Paul’. Transforming glia into neurons in the brain reduces the number of glia there — which might pose a hazard. “These cells are not just for decoration,” says Berninger. “They have

important functions, and how do we replace them if we take them away?” One possibility is to reprogram cells to a proliferative — but non-tumorigenic — neural progenitor state. That way, a few glia could yield numerous neurons.

Heart treatments are probably closest to the clinic. Srivastava’s team has already begun studies to turn fibroblasts inside pig hearts into cardiac muscle cells. “We have initial proof of concept that even in a big heart like ours, we can achieve efficacy,” he says. The team is now carrying out safety studies and refining their gene delivery method with the aim of gaining regulatory approval for human trials. Importantly, heart fibroblasts are self-replenishing, so concerns over cell loss are less acute.

Zhou’s team is also making headway towards the clinic in its attempts to switch cultured human gastrointestinal cells directly into β -cells. The gut cells are easily obtained by biopsy, and after cultivation and reprogramming they could, in theory, be transplanted into the pancreases of volunteers who have diabetes.

Direct reprogramming is beginning to garner interest from industry, although biotechnology and pharmaceutical companies are not quite ready to jump in with both feet. Although research into iPS cells and embryonic stem cells has a head start in this respect, the gap may close as the advantages of direct cell-type switching come into focus. “There is not yet a comparable amount of resources and manpower going into this approach,” says Zhou. “But the field is quickly catching up, and I can’t wait to see where it’s going.” ■

Michael Eisenstein is a science writer based in Philadelphia, Pennsylvania.

1. Takahashi, K. & Yamanaka, S. *Cell* **126**, 663–676 (2006).
2. Tapscott, S. J. *et al. Science* **242**, 405–411 (1988).
3. Vierbuchen, T. *et al. Nature* **463**, 1035–1041 (2010).
4. Rackham, O. J. L. *et al. Nature Genet.* **48**, 331–335 (2016).
5. Du, Y. *et al. Cell Stem Cell* **14**, 394–403 (2014).
6. Cahan, P. *et al. Cell* **158**, 903–915 (2014).
7. Zhang, M. *et al. Cell Stem Cell* **18**, 653–667 (2016).
8. Cao, N. *et al. Science* <http://dx.doi.org/10.1126/science.aaf1502> (2016).

CAREERS

SATELLITE ARCHAEOLOGY Citizen science could save ancient sites from destruction **p.427**

STARTING SALARIES In pay negotiations, knowledge is power **go.nature.com/1zacnl6**

NATUREJOBS For the latest career listings and advice **www.naturejobs.com**



LANGUAGE STUDIES

Learn the local lingo to get ahead

English is widely spoken in science, but mastering another language can open doors, especially when working abroad.

BY CAMERON WALKER

Joshua Plotnik pursued a different kind of instruction along with his PhD studies on the psychology of animal behaviour at Emory University in Atlanta, Georgia. Several times a month, he would go to a nearby Buddhist temple to practise writing and reading Thai with native speakers.

He had decided to learn the language after finding field sites in Thailand where he could study elephants. He put his lessons to good use the following year, when he returned to the sites for his dissertation research. In rural Thailand, few people spoke more than a few words of English. So Plotnik threw himself into speaking Thai, no matter how ridiculous he might sound. He carried notebooks to write down phrases,

got help from a US researcher who had spent decades in the country and made local friends.

Now at Mahidol University near Bangkok, Plotnik says that learning to speak (and read) Thai was essential for his doctoral research — as well as for his work today at the university, where he lectures in Thai, and as the executive director of Think Elephants International, a non-profit conservation organization that he founded in 2011. He would never, he says, have been able to develop relationships with locals who care for native elephants or talk to government officials about the animals' role in tourism. "If you really want to have an impact in a place, and develop collaborations, partnerships and relationships," he says, "you need to learn the language."

Although English is the universal language of science, many scientists have found that learning to speak and read the native language of the nation in which they work or study can open doors to new research projects and job opportunities, and can enhance life satisfaction. Early-career scientists who plan to look for postdoctoral positions or fellowships abroad, or wish to collaborate with researchers around the globe can seek formal instruction before their arrival (see 'Where to find your voice'). Once in the country, they should spend as much time as possible speaking, listening to, reading and writing the language.

SMOOTH INTERACTIONS

Although some international institutions conduct much of their official business in English, scientists who work in such places find that learning the native tongue can help to smooth interactions and relationships. Many of the Chilean staff at Cerro Tololo Inter-American Observatory, which has its offices in La Serena, Chile, speak English in addition to their native Spanish. But observatory director Steve Heathcote says that speaking Spanish can be helpful for visiting international researchers who need, for example, to choose optical filters — some of their names sound very similar in Spanish — or to navigate life in La Serena. "It gets complicated sometimes," he says about potential misunderstandings in English. "And there's plenty of room for confusion."

Junior scientists who travel abroad may find that they can make important connections in the field far more easily by speaking in the local tongue. Wildlife researcher Owen Bidder grew up speaking Welsh and English, and wanted to learn German after he accepted a postdoc at the University of Veterinary Medicine Hannover ►

► in Germany. As part of his fellowship, he took German language classes and lived with a family in the nearby area for two months before starting his programme — to great effect. In the field, where he works with local hunters who trap foxes that he needs for blood samples, no one speaks much English (or any Welsh). His ability to chat with the hunters in German has forged a camaraderie: they grin at his linguistic mistakes and cheer his successes. It's a victory, he adds, because they are wary of researchers after conflicts in the past over some of the animals they hunt. By speaking in German, he says, "I'm trying to meet them halfway".

His proficiency in German has also helped him in other ways. Last September, he presented his research at an annual mammalian-biology meeting in Germany. He gave most

of his talk in English, but introduced himself and his work in German. Outside the presentation, he answered questions in both German and English. This, he says, helped attendees to relate to his research and improved their comprehension of his responses. "They'd say, 'Oh — now I understand,'" he says.

OVERCOMING INTIMIDATION

There's little question that learning a language can be intimidating at first, even for those like Bidder who already speak more than one. It helps, says Gabriel Hernández Valdivia, to practise the language in informal settings. Valdivia, who is a transportation-systems graduate student at the Technical University of Munich in Germany, knew early on that he wanted to study in the country because of

Germany's transportation expertise. But even though he had taken German courses in his native Mexico, he was overwhelmed when he first arrived in Germany. "It took me an hour to read three pages," he says of technical textbooks. He worked to pick up technical vocabulary, but his overall speaking skills improved vastly after he joined extracurricular activities, such as playing Frisbee, that let him hone his language skills outside the classroom. He also uses an app that provides closed captioning so that he can see films in German and read along in the same language.

When Bidder was first learning German, he picked out a few idioms to use in conversation that served as a source of amusement — and connection. One of his favourites is *das Gelbe vom Ei* — 'the yellow of the egg' — which he uses as the equivalent of the English phrase 'cream of the crop'. The hunters get a laugh out of it, he says, because it's a quaint expression. He says it so often that his colleagues have affixed a poster with the phrase to his office door.

To boost comprehension and fluency, it helps to attend meetings. Ana San Gabriel, who is from Spain, went to Japan for a three-year veterinary-science fellowship at the University of Tokyo and was initially bored at the frequent meetings. Then she realized that they offered a great opportunity for her to learn technical and lab-related words and phrases. She soon felt much more comfortable asking students and staff members for help in Japanese. "If you learn the key words, it's easier for you to speak about issues in the lab," she says.

THROW CAUTION TO THE WIND

Even if you fret about sounding foolish, it's important to keep throwing yourself into situations in which you're forced to speak the local language. When Maria Jimenez-Sanchez started a PhD programme in Spain, she worried that she wasn't proficient enough in English to compete for a postdoc abroad. So she did a three-month exchange programme in a US lab, and another in a Swiss lab where English was spoken. She gained enough confidence — and mastery of English — to apply for her neuroscience postdoc at the University of Cambridge, UK. Today, she's the vice-president of the Spanish Society of Researchers in the United Kingdom, a group that offers support in areas such as career development and networking, mainly in English. International researchers need to lose their self-consciousness and talk, she says. "When people are listening to you, they just want to hear what you have to say."

There are other, more nuanced benefits to learning the native tongue of a country where you work or study. San Gabriel found that learning Japanese gave her insight into the nation's culture and the hierarchal nature of Japanese society. In turn, she learned to recognize how and when to seek opportunities such as grants, pay rises and advancement. "You have to learn the art of discussion," she

LANGUAGE COURSES

Where to find your voice

Many universities provide language lessons for their students, staff and faculty members. Some institutions and programmes are open to all.

United States

- Emory College Language Center in Atlanta, Georgia, offers language instruction, events, options for independent language study and online resources (go.nature.com/1srhufn).
- The University of Chicago's English Language Institute in Illinois runs three-week intensive English courses every summer (go.nature.com/1x2sizh).
- Middlebury Language Schools in Vermont holds intensive courses each summer in Arabic, Chinese, German, Japanese, Russian and more (go.nature.com/25envje).
- Concordia Language Villages in Minnesota holds week-long immersion courses for adults in Spanish, German, French and Japanese (go.nature.com/288h5e8).
- CRDF Global in Arlington, Virginia, organizes multi-week, intensive English courses for early-career scientists in a wide range of countries. Participants work on career skills, discuss research and participate in excursions and social events, all in English. The programme often ends with a mock conference (go.nature.com/1zizroz).
- An online manual, *Scientific English as a Foreign Language*, covers short lessons in scientific communication, from commonly confused words and phrases to tips on writing mathematical equations and papers (go.nature.com/1o7frcr).

Germany

- The Alexander von Humboldt Foundation

in Bonn will cover the fees for four months of intensive German courses, including accommodation and a stipend, for research fellows at German institutions and their spouses (go.nature.com/1tseqt7).

- The Goethe Institute has a range of intensive German courses, with some tailored to the medical field. Others combine language instruction with a four-week internship in fields such as mechanical engineering. Online tutorials are also available (go.nature.com/22cilcp).

Japan

- The Japanese MEXT scholarship funds six months at a Japanese language institute (go.nature.com/25eolq9).

Latin America

- Cerro Tololo Inter-American Observatory, based in La Serena, Chile, funds Spanish courses for incoming staff and their families (go.nature.com/20x3mkv).
- The National Autonomous University of Mexico's Learning Center for Foreigners in Mexico City offers courses for all levels of Spanish as well as classes focused on Mexican culture (go.nature.com/1zj0q1d).

United Kingdom

- The University of Manchester has programmes of varying lengths in both general and academic English (go.nature.com/22bsgu0).
- Studio Cambridge provides intensive English courses for adult learners all year round (go.nature.com/1ujpfwa).
- Cambridge University Press offers *Cambridge English for Scientists*, a book on written and spoken English that comes with audio CDs (go.nature.com/1tzbyo). **C.W.**

says. “You can still say what you think, but you have to learn where and when.”

Even if a researcher doesn't move to another country, learning a new language can be helpful for collaborating with colleagues abroad and understanding the research in their field. While studying auklets as a PhD student in Newfoundland, Canada, Alex Bond found that several crucial papers and reports, as well as older publications about the small seabirds from the North Pacific Ocean, were in Russian. He could neither read nor speak it.

He converted his laptop keyboard to Cyrillic and turned to Google Translate, Wikipedia and a Russian-to-English dictionary for help. Soon, he could recognize names of places and species. When he started a postdoc at the University of

“If you learn the key words, it's easier for you to speak about issues in the lab.”

Saskatchewan in Canada, he arranged for tutoring in Russian and, after two years, his reading skills had improved. He felt that he was more of an asset

to the Russian researchers with whom he was collaborating — he could understand papers that they wanted him to read, and incorporate studies in English into their co-authored papers. “Just because something's not in English doesn't mean you should ignore it,” says Bond, now a senior conservation scientist at the Royal Society for the Protection of Birds in Sandy, UK.

Fluency in the tongue of one's adopted nation also has advantages that may not directly affect research, but can boost life satisfaction. Heathcote spoke little Spanish for the first 3 years after he arrived in Chile more than 30 years ago. Then he met a Chilean woman. In three months, he went from having almost no Spanish to great eloquence — albeit with terrible grammar, he says. As for his new Spanish-speaking friend? He married her. ■

Cameron Walker is a freelance writer in Santa Barbara, California.

CORRECTIONS

The caption for the main image accompanying the Careers Feature ‘Change is in the air’ (*Nature* **532**, 403–404; 2016) named the wrong silver-spotted skipper. The picture is actually of *Epargyreus clarus*, not *Hesperia comma*. The Careers Feature ‘Take my advice’ (*Nature* **532**, 531–533; 2016) erroneously called Michael Lang a co-founder of milEAD. He was one of the first consultants, but did not help to found the company.

TURNING POINT

Aerial archaeologist

Sarah Parcak helped to establish the use of satellite imagery to identify potential archaeological sites. Last year, she was awarded US\$1 million from TED, the non-profit organization devoted to spreading ideas. Parcak, a remote-sensing expert at the University of Alabama at Birmingham, plans to use the money to fulfil her dream of creating an online portal for citizen scientists to help discover archaeological treasures.



How did you get the idea to apply satellite imaging to archaeology?

My grandfather, Harold Young, a forestry professor at the University of Maine in Orono, was a pioneer in the use of aerial photography to look at forests. He would measure tree heights and look at the health of forests that were going to be used in paper manufacturing. I wondered how to apply that technology. He had passed away by the time I was an undergraduate. I was surprised to find that aerial imaging hadn't been applied to archaeology before.

Were you the first to use this technology?

There was a cohort of about six of us working mainly in the Middle East — in Turkey, Syria, Iraq and Egypt — to explore how to use satellite data, which has now helped practitioners move beyond their traditional focus on one site for an entire career. To understand sites in a broader context, it's not efficient to do work on the ground. You have to think big, look from above and follow old river courses.

How is your work changing archaeology?

I hope that I've encouraged colleagues to think of the scale of sites differently. Most recently, we discovered what may be a Viking settlement in Newfoundland, Canada. It was the first time that the technology had been used in the search for potential Norse sites. Using high-resolution satellite imagery, we found two potential sites that, when ground-truthed, yielded one likely Viking site. These techniques give you robust data that can be used to focus field efforts.

What about its use in previously studied areas?

Using high-resolution imagery, colleagues and I recently found what appeared to be a massive rectangular platform in one of the most well-surveyed archaeological zones in Petra, Jordan. Chris Tuttle, the executive director of the non-profit Council of American Overseas Research Centers in Washington DC, used drones to survey the object, and confirmed that it's massive — 80 metres by 40 metres — and dates to

2,000 years ago. Despite the site having been studied for 150 years, we missed what was probably a large ritual structure. Imagine what else we haven't found.

How did TED impact your work?

I gave a short TED talk in 2012 that aired on National Public Radio, and I was made a senior TED fellow two years later. The TED prize was very unexpected, to put it mildly. I got a message last summer saying that I'd been nominated. I filled out a ‘what would your wish be’ questionnaire. Then I had 18 minutes in February to make a public case for Global Xplorer, which is an online citizen-science platform to train an army of global explorers. I celebrated the work of colleagues but also gave the sense of real urgency that our field faces with so much destruction — from conflict to climate change — around the world. The prize completely changed my life. It's both an opportunity and major responsibility.

What do you expect Global Xplorer to accomplish?

Our team has scientific training and expertise; the bottleneck is the time spent searching through images. We have been scouring images to detect looting in the wake of the 2011 Arab Spring, and it has been one of the most depressing things ever. I believe to my core that the only chance we have to save cultural heritage sites around the world is to turn everyone into explorers. By turning people into what I call ‘space archaeologists’, they will develop a sense of pride and ownership in preserving our cultural heritage. I think it's one of the only chances to save the past. ■

INTERVIEW BY VIRGINIA GEWIN

This interview has been edited for length and clarity.

nature

THE INTERNATIONAL WEEKLY JOURNAL OF SCIENCE

January 27, 2011



PLURIPOTENCY UNDER THE MICROSCOPE

A decade of iPS cells – what we've learned **1001**

REVIEW
CRISPR
REPAIRING GENES BY
editing the genome
with CRISPR/Cas9
1005

REVIEW
SUSTAINABLE
SLAUGHTER
Animal cell-based meat
production: a review
1011

REVIEW
FORGIVING
NEBIO
How a bio-inspired
robot is changing the
way we think
1017

REVIEW
REPAIRING
GENES
CRISPR/Cas9
1023

SIX NAMES FOR THE END

Time to say goodbye.

BY KEN HINCKLEY

LAST GASP

The silver dollar clunks through the innards of the coin-box and out of the return with a hollow ring.

"What's wrong Daddy?" asks my daughter, Clematissa, from her faded stallion of hand-painted plastic.

"Nothing, Tissa, don't worry about it," I reply, using the diminutive she accepts only from me.

In a fit of sentimentality I had named her after the extinct vines that once trellised the gardens of the world. Now, the pout furrowing her brow mocks the geometry of pink tulle (improvised by her mother, of course) that ruffles her dress.

"Then why won't the horsies go?"

The abandoned shopping centre reeks of stale air salted with dust, baked too many years under an oven of cracked skylights that turn the firmament into a shattered dream. Punctured soup cans and protein-jerky wrappers litter the carousel, but I thought maybe one last go-round on Tissa's favourite stallion would give her something to remember me by.

Guess not.

"I think they're just all tuckered out, sweetie," I say, as I roll up the sleeves of my work-jersey. "They need to rest up for the big trip too."

Her lower lip curls and her eyes brim with tears.

"Hang on a minute," I say, with a wink. I fix the leather strap around Tissa's waist. Then I jump down, grab one of the tarnished brass poles, and push. There's no music and the lights on the mirrors stare back at me like so many dead eyes, but at least the up-and-down of the horses accompanies my exertions.

I run round and round till I'm drenched in sweat, my jersey ripe with the fug of it. Out of shape, gasping for air.

"Thank you, Daddy," she says as I lift her off the stallion, and the look in her eyes almost melts my heart. "You smell awful!"

QUIETUS

I've read the last story and there she is, my little angel gone to sleep. Her chest rises and falls atop the mattress and I pull the fleece blanket, patterned with pink and purple hearts, over her tiny body.

It's the last thing I can do for her.

The apartment is quiet, too quiet. No hum of the fridge. No clink of a radiator warming

up. I settle on the musty-smelling carpet next to Tissa.

It's gonna be a long, long night.

TERMINUS

Our marriage ended badly, this awkward union of Barbara and Wilbur, like so many other things on this world. Even our names sounded terrible together. It should have been a clue.

But at least I won partial custody. For a time.

Everyone's so busy getting ready to leave this place behind that they've forgotten their roots. Forgotten where they come from. It makes them light in the head, spending all their time in such rarefied air.

The Lagrange staging-points are bustling. The brilliant flares of the departing starships make an inferno of the sky, night after night after night.

I tell Tissa it's the dawn of new hope, even though I can't come round to believing it myself.

Because someone has to stay behind.

And someone always does.

FINIS

They say we can't long survive here. That soon there'll be nothing left to save. The world's done. Finito. Finis.

Well, colour me sceptical. Or just stubborn.

I intend to fight to the end.

But what ties me to this piece of rock? What is it really that makes me stay?

My father died here, and his father before him. I can taste the salt of the evaporating oceans on the air.

I imagine what's left is filled with tears. All the tears of every man, woman and child who ever lived. I can't let that dry up. I can't let that all be for nothing.

The oceans will brim again.

SAYONARA

I don't tell Tissa it's the last visit. I don't tell her it's the end. I don't even say goodbye.

I just drop her with the governess at the station. Kiss her on the cheek. Pretend it's just another time I'm sending her back to Mommy.

All this strength, this hard shell I put on, hides a weak man.

Sayonara to me.

RAPTURE

Tissa's mother comes down from the sky.

The transport roars as it touches down, unsettling the earth, sending the dust off in a fruitless search of heaven.

A stairway drops, a uniformed steward leads a line of children to the bottom, and they ascend, clutching plush dolls and security blankets to their cheeks.

I catch sight of Tissa as she hesitates near the top.

She searches for me in the thin crowd, but I'm too far away,

my wave too feeble and a moment too late to catch her attention.

She's gone.

My resolve wavers and suddenly I'm clomping down the aluminium bleachers, sprinting across the tarmac.

But I'm not running to her.

No, I'm putting as much distance between myself and the transport as my iffy knees will allow.

I've made my choice. I'm going to forge something of this broken-down Earth. It's where I belong.

But that doesn't mean I can bear to watch Tissa go.

I know she'll find her new home out there, in the stars, after I'm long dead. It's a light-speed journey, or nearly so. My Tissa, my only daughter, is destined to live a million years.

And when she gets there, I like to think that she might even remember this one-trick pony she once called Daddy, that she'll look back on an Earth born anew.

But right now I can't get far enough away.

As I run, the transport accelerates past Mach 1, a pressure wave that fractures the sky.

It makes the sound of my heart breaking in two. ■

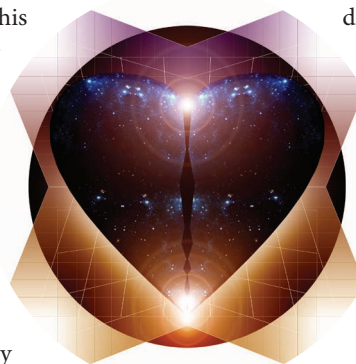


ILLUSTRATION BY JACEY

Ken Hinckley — writer, principal scientist (Microsoft Research) and editor-in-chief (Transactions on Computer-Human Interaction) — invents the future of sensors, mobility and multi-modal interaction. Follow: kenhinckley.wordpress.com